ISBN: 978-4-909106063 C3051

GEOMATE PROCEEDINGS

(Geotechnique, Construction Meterials & Environment)

Edited by

Zakaria Hossain

3-5 Nov. 2021 Kyoto, Japan

PROCEEDINGS OF THE ELEVENTH INTERNATIONAL CONFERENCE – GEOMATE 2021
GEOTECHNIQUE, CONSTRUCTION MATERIALS AND ENVIRONMENT, KYOTO, JAPAN
03-05 NOVEMBER, 2021

Geotechnique, Construction Materials and Environment

Edited by

Prof. Zakaria Hossain
Department of Environmental Science and Technology
Graduate School of Bioresources
Mie University, Japan

THE GEOMATE INTERNATIONAL SOCIETY

Published by:
The GEOMATE International Society
Tsu city, Mie, Japan
E-mail: society@geomate.org
http://www.geomate.org/

ISBN Number: 978-4-909106063 C3051

Eleventh International Conference on Geotechnique, Construction Materials and Environment,
Kyoto, Japan, 3-5 November 2021, ISBN: 978-4-909106063 C3051

Table of Contents

Preface

On behalf of the GEOMATE 2021 Organizing Committee, we would like to welcome you in attending the International Conference on Geotechnique, Construction Materials and Environment held at Kyoto Research Park, Kyoto, Japan in conjunction with The GEOMATE International Society, Useful Plant Spread Society, Glorious International, AOI Engineering, HOJUN, JCK, CosmoWinds and Beppu Construction, Japan.

On Friday 11 March 2011, at 14:46 Japan Standard Time, the northeast of Japan was struck and severely damaged by a series of powerful earthquakes which also caused a major tsunami. This conference was first dedicated to the tragic victims of the Tohoku-Kanto earthquake and tsunami disasters. The Geomate 2021 conference covers three major themes with 17 specific themes including:

- Advances in Composite Materials
- Computational Mechanics
- Foundation and Retaining Walls
- Slope Stability
- Soil Dynamics
- Soil-Structure Interaction
- Pavement Technology
- Tunnels and Anchors
- Site Investigation and Rehabilitation
- Ecology and Land Development
- Water Resources Planning
- Environmental Management
- Public Health and Rehabilitation
- Earthquake and Tsunami Issues
- Safety and Reliability
- Geo-Hazard Mitigation
- Case History and Practical Experience

Due to COVID-19, this year we have received less number of paper submissions from different countries. The participated countries are Australia, Bangladesh, China, Germany, India, Indonesia, Iraq, Israel, Japan, Philippines, Saudi Arabia, Singapore, South Korea, Thailand, and Vietnam. The technical papers were selected from the vast number of contributions submitted after a review of the abstracts. The final papers in the proceedings have been peer reviewed rigorously and revised as necessary by the authors. It relies on the solid cooperation of numerous people to organize a conference of this size. Hence, we appreciate everyone who supports as well as participate in this joint conferences.

Last but not least, we would like to express our gratitude to all the authors, session chairs, reviewers, participants, institutions and companies for their contribution to GEOMATE 2020. We hope you enjoy the conference and find this experience inspiring and helpful in your professional field. We look forward to seeing you at our upcoming conference next year.

Best regards,

Prof. Zakaria Hossain,
Mie University, Japan
Chairman (General)

Dr. Dr. John V. Smith
RMIT University,
Australia Chairman
(Vice-chairman)

Organization

Conference Honorary Chairmen:

Emeritus Professor Dr. Sohji Inoue, Mie University, Japan
Emeritus Professor Dr. Teruo Nakai, Nagoya Institute of Technology, Japan
Emeritus Professor Dr. Fusao Oka, Kyoto University, Japan
Prof. Dr. Bajang B.K. Huat, UPM, Malaysia

Scientific Committees:

Conference Chairmen:
Prof. Dr. Zakaria Hossain, Mie University, Japan (Chairman)
A/Prof. Dr. John V. Smith, RMIT Univ. Australia (Vice-chairman)

Conference Organizing Committee:

Dr. Zakaria Hossain, Prof. Mie University, Japan (Chair)
Dr. Satoshi Kaneco, Prof., Mie University, Japan (Co-Chair)
Dr. Sohji Inoue, E/Prof. Mie University, Japan (Co-Chair)
Dr. Toshinori Sakai, Prof. Mie University, Japan (Co-Chair)
Dr. Takamitsu Kajisa, Prof. Mie University, Japan (Co-Chair)
Dr. Masaaki Kondo, A/Prof. Mie University, Japan (Co-Chair)

National & International Advisory Committee:

Prof. Dr. Fumio Tatsuoka, Tokyo University of Science, Japan
Prof. Dr. Junichiro Takeuchi, Kyoto University, Japan
Prof. Dr. Kingshuk Roy, Nihon University, Japan
Prof. Dr. Sai Vanapalli, University of Ottawa, Canada
Prof. Dr. Musharraf Zaman, Univ. of Oklahama, USA
Prof. Dr. Rafiqul Tarefder, University of New Mexico, USA
Prof. Dr. M. Bouassida, National Sch. of Engg. of Tunis
Prof. Dr. L.R. Austriaco, Angles Univ. Found., Philippines
Prof. Dr. M. Ibn Ibrahimy, Int. Islamic Univ., Malaysia
Prof. Dr. Bujang B.K. Huat, Univ. Putra Malaysia
Prof. Dr. Nemy Banthia, Univ. of British Columbia, Canada
Prof. Dr. Ian Jefferson, Univ. of Birmingham, UK
Prof. Dr. John Bolander, Univ. of California, USA
Prof. Dr. Shamsul Chowdhury, Roosevelt Univ., USA
Prof. Dr. Isabel Pinto, University of Coimbra, Portugal
Prof. Dr. Mark Jaksa, University of Adelaide, Australia
Prof. Dr. Hj. Ramli Bin Hj. Nazir, UTM, Malaysia
Prof. Dr. M.S. Hossain, International Islamic Univ. Bangladesh
Prof. Dr. Suksun Horpibulsuk, Suranaree Uni of Tech, Thailand
Dr. Muzamir Hasan, Director, CERRM, Univ. Malaysia Pahang
Dr. Afshin Asadi, S/Lecturer, Int. College of Auckland, New Zealand

International Technical Program Committee:

Prof. Sai Vanapalli, University of Ottawa, Canada
Prof. Alaa Masoud, Tanta University, Egypt
Prof. Aly Ahmed, Beni-Suef University, Egypt
Prof. Aminaton Marto, Universiti Teknologi Malaysia, Malaysia
Prof. Bandari Shankar, Osmania University, India
Prof. Bashir Ahmed Mir, National Institute of Technology, India
Prof. Hamidi Abdul, Aziz, Universiti Sains Malaysia (USM), Malaysia
Prof. Hussein Elarabi, University of Khartoum, Sudan
Prof. M. Shohidullah Miah, International Univ. of Business Agriculture &Tech., Bangladesh
Prof. Nazar Oukaili, University of Baghdad, Iraq
Prof. Michele, Casagrande, Pontifical University Catholic of Rio De Janeiro, Brazil
Prof. Radim Cajka, Technical University of Ostrava, Czech Republic
Prof. Rajaraman Jambunathan, AMET University, India
Prof. Reshma Chandran T., Global Institute of Architecture, India
Prof. Roslan Hashim, University of Malaya, Malaysia
Prof. Seyed Naser Moghaddas Tafreshi, K.N. Toosi University of Technology, Iran
Prof. Valeriy Perminov, Tomsk Polytechnic University, Russia
Prof. Quanmei Gong, Tongji University, China
A/ Prof. Abdoullah Namdar, Sichuan University, China
A/ Prof. Abdul Naser Abdul Ghani, Universiti Sains Malaysia, Malaysia
A/ Prof. Alaeddinne Eljamassi, Islamic University of Gaza, Palestine
A/ Prof. Alina Paranina, Herzen State Pedagogical University of Russia, Russia
A/ Prof. Ashraf Elmoustafa, Ain Shams Univeristy, Egypt
A/ Prof. Bindu C S, Cochin University of Science& Technology, India
A/ Prof. Chee-Ming Chan, Universiti Tun Hussein Onn Malaysia, Malaysia
A/ Prof. Chidanand Naik, Anjuman Instistute of Technology and Management, India
A/ Prof. Dahlia Hafez, Cairo University, Egypt
A/ Prof. Deepa G Nair, Isfahan University of Technology, India
A/ Prof. Dolrerdee Hormdee, Khon Kaen University, Thailand
A/ Prof. Farhad Behnamfar, Isfahan University of Technology, Iran
A/ Prof. Gabriela B. Cazacu, Geotech Dobrogea, Romania
A/ Prof. Hadi Khabbaz, University of Technology, Sydney (UTS), Australia
A/ Prof. Homayoon Ganji, Herat Univercity Badghis, Afghanistan
A/ Prof. Hudson Jackson, US Coast Guard Academy, United States
A/ Prof. Inazumi Shinya, Shibaura Institute of Technology, Toyosu, Koto, Tokyo, Japan
A/ Prof. John Smith, RMIT University, Australia
A/ Prof. Kasinathan Muthukkumaran, National Institute of Technology, India
A/ Prof. Lindrianasari Lindrianasari, Universitas Lampung, Indonesia
A/ Prof. Mahdi Karkush, Baghdad University, Iraq
A/ Prof. Mohamed Redha Menani, Batna University, Algeria
A/ Prof. Navid Khayat, Ahvaz Branch, Islamic Azad University, Iran
A/ Prof. Salam, Bash AlMaliky, AlMustansiriya University, Iraq
A/ Prof. Shailesh Kumar Jha, Indian Institute of Technology, India
A/Prof. Teodor Lucian Grigorie, University of Craiova, Romania
A/Prof. Paresh Dalal, Shri Vitthalrao Shankarrao Naik Arts, Commerce and Science College, India
A/Prof. Muhammad Qasim, Abdul Wali Khan University Mardan, Pakistan
A/Prof. R. S. Ajin, GeoVin Solutions Pvt. Ltd., India
Dr. Abdul Karim M. Zein, University of Khartoum, Sudan
Dr. Abdull Halim Abdul, Universiti Teknologi MARA, Malaysia
Dr. Afshin Asadi, University Putra Malaysia, Malaysia
Dr. Ahmad Safuan Bin A Rashid, Univeristi Teknologi Malaysia, Malaysia
Dr. Akindele Okewale, Federal University of Petroleum Resources, Nigeria
Dr. Akinola Johnson Olarewaju, Federal Polytechnic Ilaro, Nigeria
Dr. Ali Sobhanmanesh, Universiti Teknologi Malaysia (UTM), Malaysia
Dr. Alireza Bahiraie, Semnan University, Iran
Dr. Allan Manalo, Centre of Excellence in Engineered Fibre Composites, Australia
Dr. Aniza Ibrahim, National Defence University of Malaysia, Malaysia

Dr. Arif Ali Baig Moghal, King Saud University, Saudi Arabia
Dr. Aslan S. Hokmabadi, University of Technology, Sydney (UTS), Australia
Dr. Ather Ashraf, PUCIT, Old Campus Punjab University, Pakistan
Dr. Atsuko Sato, Cicil Engineering Research Institute for Cold Region, Japan
Dr. Ben-Hur Silva, Military Institute of Engineering, United States
Dr. Choy Soon Tan, Univeristi Teknologi Malaysia, Malaysia
Dr. David Thorpe, University of Southern Queensland, Australia
Dr. Delsye Ching Lee Teo, Universiti Malaysia Sarawak, Malaysia
Dr. Domenico Lombardi, University of Manchester, United Kingdom
Dr. Ehsan, Jorat Newcastle University, United Kingdom
Dr. Ganesh Kumar Shanmugam, National Institute of Ocean Technology, India
Dr. Helsin Wang, Institute of Bridge Engineering, Taiwan
Dr. Hossein Moayedi, Kermanshah University of Technology, Iran
Dr. Hossein MolaAbasi, Babol University of Technology, Iran
Dr. James Hambleton, University of Newcastle, Australia
Dr. James Hambleton, University of Newcastle, Australia
Dr. Janaka Kumara, Tokyo University of Science, Japan
Dr. Jirayut, Suebsuk Rajamangala University of Technology Isan, Thailand
Dr. Juhyung Lee, Korea Institute of Civil Engineering and Building Technology, South Korea
Dr. Jun Sugawara, Advision - WorleyParsons Group, Australia
Dr. Lamia Touiti Bouebdellah, Ecole Nationale d'Ingénieurs de Gabes, Tunisia
Dr. Luky Handoko, Universitas Atma Jaya Yogyakarta, Indonesia
Dr. M. Mohammad Ali, California Public Utilities Commission, United States
Dr. Marfiah Ab.Wahid, Universiti Technologi Mara, Malaysia
Dr. Maryam Naeimi, Semnan University, Iran
Dr. Mehdi Mokhberi, Islamic Azad University, Shiraz, Iran
Dr. Mohd Hairy Ibrahim, Sultan Idris Education University, Malaysia
Dr. Neelima Satyam, International Institute of Information Technology, India
Dr. Nor Zurairahetty Mohd Yunus, Univeristi Teknologi Malaysia, Malaysia
Dr. Siavash Zamiran, Southern Illinois University Carbondale, United States
Dr. Subha Vishnudas, Cochin University of Science and Technology, India
Dr. Sunggi Jin, SK E&C, South Korea
Dr. Sunil Pusadkar, Govt. College of Engineering, Amravati, India
Dr. Teresa Lopez-Lara, Universidad Autonoma De Queretaro, Mexico
Dr. Usama Juniansyah Fauzi, University of Tokyo, Japan
Dr. Yusep Muslih Purwana, Sebelas Maret University, Indonesia
Dr. Ana Almerich-Chulia, Universitat Politecnica de Valencia, Spain
Dr. Khor Shing Fhan, Universiti Malaysia Perlis, Malaysia
Dr. Afshin Asadi, International College of Auckland, New Zealand

Conference Correspondence:

Prof. Dr. Zakaria Hossain, Conference Chairman,
Dept. of Env. Sci. & Tech., Mie University, Japan,
E-mail: conference@geomate.org
Tel & Fax: +81-59-231-9578

Editorial Committee and Executive Committee:

Prof. Zakaria Hossain, Prof. Mie University, Japan

Keynote Paper

11th Int. Conf. on Geotechnique, Construction Materials & Environment,
Kyoto, Japan, 3-5 November 2021, ISBN: 978-4-909106063 C3051

DEVELOPMENTS IN SLOPE STABILITY IN ENGINEERING PRACTICE: A REVIEW OF RESEARCH PUBLISHED BY GEOMATE

John Victor Smith

RMIT University, Australia and CMW Geosciences, Australia

ABSTRACT

Many papers have been published in the International Journal of GEOMATE making some contribution to the topic of slope stability. A selection of these papers have been reviewed with the aim of classifying the types of contributions made. Three main areas of application focus have been identified: 1) Context, 2) Mechanics and 3) Techniques. Context refers to papers which address the risk posed to people or infrastructure in the location and also refers to papers which are identified as case studies of a particular slope failure event or slope region. Mechanics refers to papers which focus on the mechanism of failure or on the properties of the materials in which failure has occurred. Techniques refers to papers which focus on presenting methods of data collection, modelling and methods of stabilization and protection for slopes. Each of these different focus areas is shown to be a distinctive way that papers have contributed to the integrated knowledge of slope stability.

Keywords: Slope Stability, Risk Assessment, Case Study, Mechanism, Stabilization

INTRODUCTION

The International Journal of GEOMATE "aims to become an efficient mean of publishing and distributing high quality information from researchers, scientists and engineers." The journal scope covers the main areas of Geotechnique, Construction Materials and the Environment.

This contribution has been prepared as a Keynote presentation to the 11th annual conference held in Kyoto, Japan in 2021. The paper presents a review of selected papers from the journal which have a focus on slope stability. A framework of studies will be presented to assist future researchers and practitioners to recognize the diverse types of investigations and to assist in identifying opportunities for future research and improvements to engineering practice.

METHODOLOGY

The review covers papers in the journal from Issues 1 to 85. Papers were initially selected for the review based on the title containing some reference to slopes or slope stability. It is possible some papers with relevance to slope stability have been omitted.

As the list of relevant references was compiled, each paper was assigned to a grouping based on the main aspects of the paper. The nature of the groupings emerged as the examples were compiled. This process was subjective according to this author's interpretation. It is possible that other authors and authors of the original papers may choose a different categorization for individual papers.

It is not suggested that any paper is restricted to a particular category. The categories are intended to recognize the main way in which each paper contributes to the broad field of slope stability research and practice.

As categories of studies emerged from the review these categories were arranged into a hierarchy. A three-level hierarchy has been developed. It is intended that this hierarchy may be a useful tool for future studies to recognize their main area of contribution to the field.

RESULTS

A summary of the categories of studies identified in the review is provided in Fig.1.

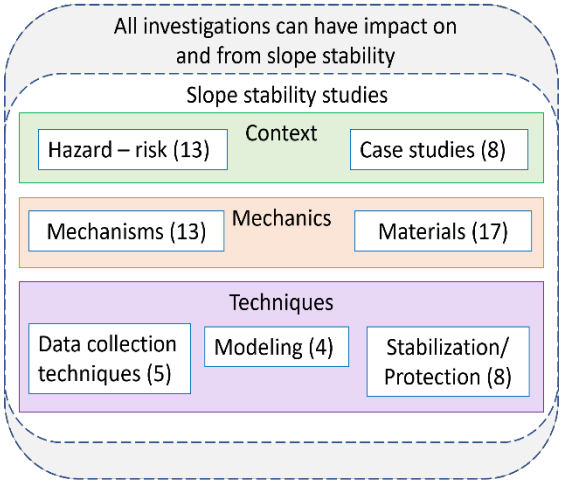

Fig. 1 Framework of the review (from papers published in J. GEOMATE Issues 1-85)

The outer boundary of Fig.1 acknowledges that slope stability is not an isolated field. Many other

fields of study are relevant to slope stability or benefit from the outcomes of slope stability research.

The first level of categories identified as the main areas of application focus are: 1) Context, 2) Mechanics and 3) Techniques (Fig.1). Context refers to papers which address the risk posed to people or infrastructure in the location and also refers to papers which are identified as case studies of a particular slope failure event or slope region. The context includes the application of susceptibility mapping methods. Mechanics refers to papers which focus on the mechanism of failure or on the properties of the materials in which failure has occurred. Techniques refers to papers which focus on presenting methods of data collection, modelling and methods of stabilization and protection for slopes.

A third level of hierarchy was identified under each category. These sub-categories are summarized in Fig.2.

DISCUSSION

The research on slope stability published in the journal is based on work in the field and laboratories of many countries. The brief comments in this discussion highlight only a small number of research examples and opportunities.

Development Areas

Case Studies

The importance of case studies is a feature of slope stability research. It is only through the on-going study of field examples that new problems and issues can be identified.

Where there is a significant historic or current slope instability event it is essential that the context and contributing factors are collated and published. Each study not only makes a contribution to the understanding of the location investigated but also contributes the database of factual information which is fundamental to future research.

A case study, as a secondary function, can also address other categories of investigation including those listed in Fig.2. However, these secondary issues emerge in a case study as needed to understand the conditions found in the location.

Rainfall and Water Infiltration

A significant number of papers were observed to investigate the role of rainfall and water infiltration. This field is constantly developing as the understanding of unsaturated soil mechanics has progressed in recent decades [23].

Rainfall is commonly observed to be a trigger for slope instability so these studies also make significant contributions to risk assessment [9-10]. It is also noted that probabilistic methods of analysis are becoming more common in this field of study [22].

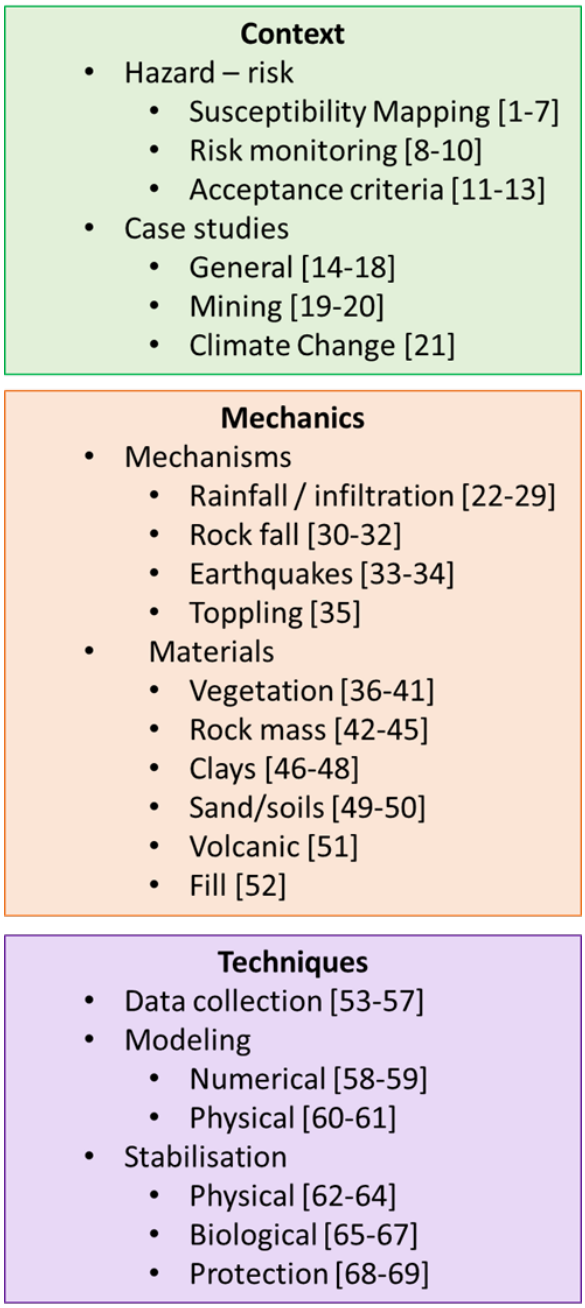

Fig. 2 Categories of study focus in the review framework, with the paper references listed

Integration of Soil and Rock Mechanics

Throughout much of the history of scientific and engineering progress soil mechanics and rock mechanics have remained separate disciplines. However, these fields need to become integrated as both material types contribute to slope instability.

Landslide scars often show that structures in the bedrock have contributed to slope failure by planar

sliding, wedge sliding or toppling [18], [27].

Use of material strength parameters from the field of rock mechanics, such as the Hoek-Brown criteria can be incorporated into the range of material property models used in slope stability analysis [42].

The field of rockfall is an areas where rock mechanics plays an important role. It is also a field of investigation where numerical and physical models have made a significant contribution e.g. [32].

Vegetation

Vegetation has long been recognized as a stabilizing influence on slopes. Methods for quantifying the strength improvement by field and numerical studies of root strength and other aspects of vegetation have the potential to influence engineering practice e.g. [38].

Future Developments

This review framework can provide impetus to guide future research in the field. For example, researchers may recognize items in Fig.2 where they could make a contribution based on their own investigations. Alternatively researchers may observe gaps in the items in Fig.2 and may seek out opportunities to expand the range of topics.

Unstable and potentially unstable slopes are a common feature of rural and urban settings (Fig.3). Future research into the context, mechanics and techniques for investigations are needed to inform future developments in engineering practice.

Fig. 3 Photograph of an unstable slope in an urban setting

CONCLUSIONS

A review of papers on slope stability published in the International Journal of GEOMATE has been conducted to develop a framework of investigation categrories. The framework provides a scheme to assist researchers to contribute to existing threads of research or to identify gaps needing new research contributions. The theoretical, laboratory and field data in these papers and others provides a basis for future developments in engineering practice with the aim of improving the living conditions and safety of communities in many parts of the world.

ACKNOWLEDGMENTS

The many authors of papers in the International Journal of GEOMATE are thanked for their contributions.

REFERENCES

[1] Ito S., Oda K., Koizumi K., and Usuki Y., Identification of Slopes with Higher Risk to Slope Failures Based on Information Processing Techniques. International Journal of GEOMATE, Vol. 8, Issue 16, 2015, pp. 1226-1231.

[2] Wang L., Sawada K., and Moriguchi S., Landslide Susceptibility Mapping by Using Logistic Regression Model with Neighborhood Analysis: A Case Study in Mizunami City. International Journal of GEOMATE, Vol. 1, Issue 2, 2011, pp. 99-104.

[3] Zhang S., and Zhang L., Assessment of Human Risks Posed by Deadly Debris Flow in the Wenchuan Earthquake Area. International Journal of GEOMATE, Vol. 8, Issue 15, 2015, pp. 1207-1211.

[4] Sinarta I.N, Rifa'i A., Fathani T.F., and Wilopo W., Geotechnical Properties and Geologic Age on Characteristics of Landslides Hazards of Volcanic Soils in Bali, Indonesia. International Journal of GEOMATE, Vol.11, Issue 26, 2016, pp. 2595-2599.

[5] Le T.T., and Kawagoe S., Study on Landslide Category Base on Temporal-Spatial Characteristic Distribution in Northern Vietnam Using Satellite Images. International Journal of GEOMATE, Vol. 14, Issue 43, 2018, pp. 118-24.

[6] Priyono K.D., Jumadi A.S., and Fikriyah V.N., Risk Analysis of Landslide Impacts on Settlements in Karanganyar, Central Java, Indonesia. International Journal of GEOMATE, Vol.19, Issue 73, 2020, pp. 100-107.

[7] Triyatno, Bert, I., Idris, Hermon, D., and Putra A., Hazards and Morphometry to Predict the Population Loss Due of Landslide Disasters in Koto Xi Tarusan - Pesisir Selatan. International Journal of GEOMATE, Vol. 19, Issue 76, 2020, pp. 98-103.

[8] Motakabber S.M., and Ibrahimy M.I., An Approach of Differential Capacitor Sensor for Landslide Monitoring. International Journal of GEOMATE, Vol. 9, Issue 18, 2015, pp. 1534-1537.

[9] Athapaththu A.M., Yabuki K., and Tsuchida T., Geotechnical Assessment of Natural Slopes and Valleys Based on Real Time Rainfall Data. International Journal of GEOMATE, Vol. 10, Issue 19, 2016, pp. 1584-1594.

[10] Iida T., Fujimoto M., Kumakura N., Takasaki D., Hiraoka N., and Fukagawa R., A Method to Judge Slope Failures Using Soil Moisture Characteristics. International Journal of GEOMATE, Vol.10, Issue 22, 2016, pp. 2094-2100.

[11] Kanjanakul C., and Chub-Uppakarn T., Method to Estimate the System Probability of Failure for Slope Stability Analysis. International Journal of GEOMATE, Vol.14, Issue 45, 2018, pp. 162-169.

[12] Cahyaningsih C., Asteriani F., Crensonni P.F., Choanji T., Yuskar Y., Safety Factor Characterization of Landslide in Riau-West of Sumatra Highway. International Journal of GEOMATE, Vol.17, Issue 63, 2019, pp. 323-330.

[13] Purwanto, Zakaria Z., Paripurno E.K., and Boy Yoseph C.S.S.S.A., Angle of Slope and Slope Safety Factor Relationship in Gendol River, Southern Slope of Merapi Volcano Yogyakarta. International Journal of GEOMATE, Vol.17, Issue 64, 2019, pp. 93-99.

[14] Ali S., Ivan G., and Kim D.H., Rock Slope Stability Problems in Gold Coast Area, Australia. International Journal of GEOMATE, Vol. 4, Issue 7, 2013, pp. 501-504.

[15] Sugawara J., Characteristics of Slope Failures in Makinohara, Japan. International Journal of GEOMATE, Vol. 5, Issue 10, 2013, pp. 717-723.

[16] Sugawara J., Landslides in Tea Plantation Fields in Shizuoka, Japan. International Journal of GEOMATE, Vol. 4, Issue 7, 2013, pp. 495-500.

[17] Patuti I.M., Rifa'i A., and Suryolelono K.B., Mechanism and Characteristics of the Landslides in Bone Bolango Regency, Gorontalo Province, Indonesia. International Journal of GEOMATE, Vol. 12, Issue 29, 2017, pp. 1-8.

[18] Sonnekus M., and Smith J.V., A Review of Selected Unexpected Large Slope Failures. International Journal of GEOMATE, Vol. 15, Issue 48, 2018 pp.66-73.

[19] Almandalawi M., You G., Dahlhaus P., Dowling K., and Sabry M., Slope Stability and Rockfall Hazard Analysis in Open Pit Zinc Mine. International Journal of GEOMATE, Vol. 8, Issue 15, 2015, pp. 1143-1150.

[20] Mandalawi M.A., You G., Dowling K., and Dahlhaus P., Kinematic Assessment of Slopes at handlebar Hill Open Cut Mine, Mt. Isa, Queensland, Australia. International Journal of GEOMATE, Vol. 10, Issue 19, 2016, pp. 1575-1583.

[21] Chaithong T., Soralump S., Pungsuwan D., and Komori D., Assessing the Effect of Predicted Climate Change on Slope Stability in Northern Thailand: A Case of Doi Pui. International Journal of GEOMATE, Vol. 13, Issue 38, 2017, pp. 38-48.

[22] Chaithong T., Analysis of Extreme Rainfall-Induced Slope Failure Using a rainfall Infiltration-Infinite Slope Analysis Model. International Journal of GEOMATE, Vol. 13, Issue 35, 2017, pp. 156-165.

[23] Ibrahim A., Ahmad I.K., and Taha M.R., 3 Dimension Real Time Images of Rainfall Infiltration into Unsaturated Soil Slope. International Journal of GEOMATE, Vol. 14, Issue 43, 2018, pp. 31-35.

[24] Thanh D.T., Nguyen T.L., and Le T.T., Analysis the Effects of the Degree of Saturation on the Slopes Stability Using Modelling and Numerical Simulation. International Journal of GEOMATE, Vol. 17, Issue 63, 2019, pp. 119-125.

[25] Tran T.V., Pham H.D., Hoang V.H., and Trinh M.T., Assessment of the Influence of the Type of Soil and Rainfall on the Stability of Unsaturated Cut-Slopes – A Case Study. International Journal of GEOMATE, Vol. 20, Issue 77, 2021, pp. 141-148.

[26] Wada T., Kodani R., and Miwa H., Spatial Analysis on Occurrence Factors of Multiple Slope Failures Using Topographic and Rainfall Indices with High Spatial Resolutions. International Journal of GEOMATE, Vol. 20, Issue 79, 2021, pp. 89-97.

[27] Chaithong T., Komori D., Sukegawa Y., Touge Y., Mitobe Y., and Anzai S., Landslides and Precipitation Characteristics During the Typhoon Lionrock in Iwate Prefecture, Japan. International Journal of GEOMATE, Vol. 14, Issue 44, 2018, pp. 109-14.

[28] Arimitsu Y., Fujimoto M., Hiraoka N., Danjo T., Ishida Y., and Fukagawa R., Characteristics of Rain Infiltration in Soil Layers on the Hillslope Behind Important Cultural Asset. International Journal of GEOMATE, Vol. 10, Issue 22, 2016,

pp. 2109-2115.

[29] Ishida Y., Kibayashi T., Konegawa T., Fujimoto M., and Fukagawa R., Influence of Antecedent Precipitation on Slope Failures at the Yokogaki-Toge Pass. International Journal of GEOMATE, Vol. 11, Issue 26, 2016, pp. 2626-2632.

[30] Alzo'ubi A.K., Stability of a Rock Slope Susceptible to Seasonal Movements. International Journal of GEOMATE, Vol. 6, Issue 11, 2014, pp. 800-805.

[31] Alzo'ubi A.K., Rock Slopes Processes and Recommended Methods for Analysis. International Journal of GEOMATE, Vol. 11, Issue 25, 2016, pp. 2520-2527.

[32] Ma G., Sawada K., and Saitoh H., Study on Evaluating Rock Block Stability by Using a remotely Positioned Laser Doppler Vibrometer. International Journal of GEOMATE, Vol. 2, Issue 4, 2012, pp. 247-252.

[33] Kohno M., and Ono Y., Evaluation of Earthquake-Induced Slope Failure Distribution Using the AHP Method and GIS. International Journal of GEOMATE, Vol. 20, Issue 79, 2021, pp. 74-81.

[34] Ono Y. Simulating Earthquake-Induced Slope Failures Using a Solid-Fluid Coupling Model Based on the Smoothed Particle Hydrodynamics Framework. International Journal of GEOMATE, Vol. 20, Issue 82, 2021, pp. 1-6.

[35] Alzo'ubi AK. The Role of Block Ratio and Layer Thickness on Rock Slopes Movement Style. International Journal of GEOMATE, Vol. 8, Issue 16, 2015, pp. 1271-1277.

[36] Arase T., and Okano T., Influence of Fertilization on Native Plants and Exotic Pasture Grasses on the Fascined Landslide Slopes in Mikura-Jima Island, Japan. International Journal of GEOMATE, Vol. 8, Issue 16, 2015, pp. 1316-1322.

[37] Hytiris N., Fraser M., and Mickovski S.B., Enhancing Slope Stability with Vegetation. International Journal of GEOMATE, Vol. 9, Issue 18, 2015, pp. 1477-1482.

[38] Tiwari R.C., Bhandary N.P., Yatabe R., and Bhat D.R., Simulation of Root-Reinforcement Effect in Natural Slopes Based on Progressive Failure in Soil-Root Interaction. International Journal of GEOMATE, Vol. 1, Issue 1, 2011, pp. 32-38.

[39] Okano T., and Arase T., Vegetation Recovery Process on Landslide Steep Slope after Alnus Sieboldiana and Miscanthus Condensatus Planting with Simple Terracing Work in Mikurajima Island, Japan. International Journal of GEOMATE, Vol. 10, Issue 21, 2016, pp. 1884-1890.

[40] Hasyim A.W., Gusti H.I., and Prayitno G., Determination of Land Cover as Landslide Factor Based on Multitemporal Raster Data in Malang Regency. International Journal of GEOMATE, Vol. 18, Issue 69, 2020, 254-261.

[41] Chaithong T. A Model for Assessment of Tree Stability and Entrainment of Woody Debris by Flow Slides and Shallow Slope Failure. International Journal of GEOMATE, Vol. 19, Issue 71, 2020, pp. 77-83.

[42] Kusumawardani R., Upomo T.C., and Faizal M., Back-Analysis of Hoek-Brown Criterion: Rock Slide Case in Manado. International Journal of GEOMATE, Vol. 11, Issue 27, 2016, pp. 2808-2814.

[43] Rakhman A.N., Zakaria Z., Muslim D., Haryanto I., and Mulyaningsih S., Modification of Rock Mass Classification in the Rock Slope Platy Jointed Andesite at Seloharjo Area. International Journal of GEOMATE, Vol. 16, Issue 53, 2019, pp. 163-170.

[44] Choanji T., Yuskar Y., Putra D.B., Cahyaningsih C., Suryadi A., and Antoni S., Clustering Slope Stability Using DEM Lineament Extraction and Rock Mass Rating in Pangkalan Koto Baru, West Sumatra, Indonesia. International Journal of GEOMATE, Vol. 17, Issue 60, 2019, pp. 225-230.

[45] Dafalla M.A., Al-Shamrani M., and Al-Refeai T., Founding Heavy Structures Along the Slope of Schist Formation. International Journal of GEOMATE, Vol. 17, Issue 60, 2019, pp. 239-243.

[46] Zein A.K., and Karim W.A., Stability of Slopes on Clays of Variable Strength by Limit Equilibrium and Finite Element Analysis Methods. International Journal of GEOMATE, Vol. 13, Issue 38, 2017, pp. 157-164.

[47] Salih A.G., and Ismael A.M., Influence of Clay Contents on Drained Shear Strength Parameters of Residual Soil for Slope Stability Evaluation. International Journal of GEOMATE, Vol. 17, Issue 59, 2019, pp. 166-172.

[48] Ubay I.O., Alfaro III M., Alfaro M., and Blatz J., Stability Assessment of an Aging Earth Fill Dam Considering Anisotropic Behaviour of Clay, International Journal of GEOMATE, Vol. 18, Issue 66, 2020, pp. 84-91.

[49] Ravindran S., and Gratchev I., Estimation of Shear Strength of Gravelly and Sandy Soils from Shallow Landslides. International Journal of

GEOMATE, Vol. 18, Issue 70, 2020, 130-137.

[50] Abdiev B., Kasymova G., Kalmatayeva B., Adirbekov K., Abdullayeva K., and Abdraimov R., Determination of Reduced Physicomechanical Properties of Two-Phase Soils Peculiar to Landslides of Northern Tian Shan International Journal of GEOMATE, Vol. 20, Issue 81, 2021, pp. 52-58.

[51] Purwanto Z.Z., and Paripurno E.T., Boy Yoseph C.S.S.S.A., Volcanic Eruption Products and its Slope Stability in Merapi Volcano, Yogyakarta. International Journal of GEOMATE, Vol. 15, Issue 51, 2018, pp 167-172.

[52] Murao H., Nakai K., Yoshikawa T., and Noda T., Progressive Failure of Unsaturated Fill Slope Caused by Cumulative Damage Under Seepage Surface. International Journal of GEOMATE, Vol. 20, Issue 78, 2021, pp. 1-8.

[53] Furuya T., and Jiang J.C., Determination of Slip Surfaces in Fracture Zone Landslides Using Oriented Borehole Core Samples. International Journal of GEOMATE, Vol. 8, Issue 15, 2015, pp. 1151-1158.

[54] Susilo A., Suryo E.A., Fitriah F., Sutasoma M., and Bahtiar., Preliminary Study of Landslide in Sri Mulyo, Malang, Indonesia Using Resistivity Method and Drilling Core Data. International Journal of GEOMATE, Vol. 15, Issue 48, 2018, pp. 161-168.

[55] Amalia D., Mochtar I.B., and Mochtar N.E., Application of Digital Image Technology for determining Geometry, Stratigraphy, and Position of Cracks Inside Earth Slope. International Journal of GEOMATE, Vol. 17, Issue 63, 2019, pp. 297-306.

[56] Suryo E., Zaika Y., Gallage C., and Trigunarsyah B., A Non-Destructive Method for Investigating Soil Layers of an Individual Vulnerable Slope. International Journal of GEOMATE, Vol. 18, Issue 69, 2020, pp. 1-8.

[57] Tao S., Uchimura T., Tang J., and Fukuhara M., Estimation of The Instability of Slope Surface Layer by Elastic Wave Attenuation Changing with Soil Moisture and Deformation. International Journal of GEOMATE, Vol. 18, Issue 70, 2020, pp. 81-87.

[58] Hiraoka N., Oya A., Bui H.H., Rajeev P., and Fukagawa R., Seismic Slope Failure Modelling Using the Mesh-Free SPH Method. International Journal of GEOMATE, Vol. 5, Issue 9, 2013, pp. 660-665.

[59] Adajar J.B., Ubay I.O., Alfaro M., and Chen Y., Discrete Element Model Parameters to Simulate Slope Movements. International Journal of GEOMATE, Vol. 18, Issue 65, 2020, pp. 192-199.

[60] Repadi J.A., Bari F., Junaidi, Ismail F.A., Andriani and Hakam A., Slip Surface in a Clay-Sand Mixture Slope Test Using Scaled Laboratory Models, International Journal of GEOMATE, Vol. 21, Issue 85, 2021, pp.17-23.

[61] Alrammahi F., Khassaf S., Abbas S., Madhloom H., Aljaradin M., and Al-Ansari N., Study the Slope Stability of Earthen Dam Using Dimensional Analysis Techniques. International Journal of GEOMATE, Vol. 21, Issue 83, 2021, pp. 125-131.

[62] Surjandari N.S., Dananjaya R.H., and Utami E.C., Slope Stability Analysis Using Mini Pile: A Case Study in Cigempol River, Karawang, West Jawa. International Journal of GEOMATE, Vol. 13, Issue 38, 2017, pp. 49-53.

[63] Munawir A.A., On the Nailed Soil Slopes Research Development. International Journal of GEOMATE, Vol. 13, Issue 38, 2017, pp. 69-78.

[64] Asoudeh A., and Oh E., Strength Parameter Selection in Stability Analysis of Residual Soil Nailed Walls. International Journal of GEOMATE, Vol. 7, Issue 13, 2014, pp. 950-954.

[65] Omar R.C., Taha H., Roslan R., and Baharuddin I.N., Geotextile from pineapple leaves and bio-grout for slope stabilization and erosion control. International Journal of GEOMATE, Vol. 17, Issue 60, 2019, pp. 219-224.

[66] Ready B., Krisnamurti K., and Nurtjahjaningtyas I., Analysis of Slope Stability in Soft Soil Using Hardening Soil Modeling and Strengthening of Bamboo Mattress. International Journal of GEOMATE, Vol. 19, Issue 73, 2020, pp. 226-234.

[67] Moqsud M.A., Slope Soil Stabilization Through Biocementation by Native Bacteria in Chugoku Region, Japan. International Journal of GEOMATE, Vol. 21, Issue 83, 2021, pp. 36-42.

[68] Maegawa K., Tajima T., Yokota T., and Tohda M., Experiments on Rockfall Protection Embankments with Geogrids and Cushions. International Journal of GEOMATE. Vol. 1; Issue 1, 2011, pp.19-24.

[69] Van P.T., and Maegawa K. Experiments and Numerical Modeling of a Rockfall Protective Wire Rope. International Journal of GEOMATE, Vol. 2, Issue 4, 2012, pp. 219-226.

Technical Papers

Geotechnique

11th Int. Conf. on Geotechnique, Construction Materials & Environment, Kyoto, Japan, 3-5 November 2021, ISBN: 978-4-909106063 C3051

EVALUATING THE EFFECTS OF POLYMERS ON MICROBIALLY INDUCED CARBONATE PERCIPITATION

Zhen Yan[1], Sivakumar Gowthaman[2], Kazunori Nakashima[2], and Satoru Kawasaki[2]

[1]Graduate School of Engineering, Hokkaido University, Sapporo, Japan
[2]Faculty of Engineering, Hokkaido University, Sapporo, Japan

ABSTRACT

Microbially induced carbonate precipitation (MICP) is relatively a new environmentally friendly soil improvement method. In MICP process, the formation of calcium carbonate occurs within the soil matrix as the consequence of biochemical process mediated by ureolytic bacteria. The objective of this preliminary work is to evaluate the effects of adding polymers on MICP process. Basically, the polymers are organic macromolecules and have potential to offer several benefits such as increasing solution viscosity, extending supply time, localization of cementation reactions, reduction of harmful byproduct ammonium and enhancement of strength. For the above-mentioned objective, two different types of polymers are studied: (i) Polyvinyl alcohol (PVA) and (ii) Polyacrylic acid (PAA). *Lysinibacillus xylanilyticus* are cultivated in the standard medium with varying contents of polymers. The growth and urease activity of the bacteria are determined with the incubation time. In addition, set of test tube tests is performed to assess the precipitation characteristics of calcium carbonate at the presence of polymers. The outcomes indicated that the polymers do not have any adverse effects on the growth of bacteria. However, the PAA is found significantly enhance the urease activity compared with typical bacteria culture medium, whereas it is not evidenced in PVA. Moreover, compared to the typical MICP process, the addition of polymers produce more spherical-shaped calcium carbonate crystals, which highly differ from typical rhombohedral-shaped crystals. With the above findings, future works are recommended on soil to investigate the cementation efficiency and adsorption of ammonium by-products.

Keywords: Microbially induced carbonate precipitation (MICP), soil improvement, polymer, urease activity, crystal morphology

INTRODUCTION

In recent years, the biological method has attracted attention as an environmentally friendly method of ground improvement. Microbial Induced Carbonate Precipitation (MICP) is one of such kind of novel geotechniques. In MICP process, precipitation of $CaCO_3$ is induced by non-pathogenic bacteria that mediate the hydrolysis of the urea [1]. The sequential bio-chemical reactions that occur during the MICP process are listed in Eqs. (1-3).

$$CO(NH_2)_2 + H_2O \xrightarrow{\text{Urease}} H_2NCOO^- + NH_4^+ \quad (1)$$

$$H_2NCOO^- + H_2O \rightarrow HCO_3^- + NH_3 \quad (2)$$

$$Ca^{2+} + HCO_3^- + NH_3 \rightarrow CaCO_3 + NH_4^+ \quad (3)$$

Most of the MICP related research works attempt to involve *Sporosarcina pasteurii* which is a popular gram positive bacteria with high urease activity [2]–[4]. In due course, few researchers worked on identifying some other potential ureolytic bacteria for MICP purposes. Their outcomes indicate that the use of indigenous bacteria, instead of popular exogenous bacteria, offers numerous benefits in terms of reliability and bio-safety. *Lysinibacillus xylanilyticus* is one of such reliable species, and which was previously isolated from Hokkaido expressway slope, Japan [5]. Following the demonstration by Japan MICP researchers, the species were repeatedly used in many MICP related works [6]–[7]. Due to their consistence performance, the *Lysinibacillus xylanilyticus* is used in this study to evaluate the effects of polymers in MICP process.

Use of additives such as polymers to improve the weak soil is an alternative biological approach to the MICP process [8]. Number of researches has done previously to investigate the applicability of hydrophilic polymers. Hydrophilic polymer solution can restrain the desiccation of the cementation solution and extend the time window for MICP-related reactions following one-shot injection, which can be critical for certain applications where the treated surficial soils are exposed to air and sunlight. Owing to these favorable characteristics, hydrophilic polymers have increasingly been utilized for assisting mineral precipitation-based improvement and remediation approaches in the field of civil engineering [9].

Previously, the effect of polyvinyl alcohol (PVA) on strengthening was investigated. Using PVA to increase the surface erosion resistance of MICP treated soil also studied. Their outcomes indicats

that the polymers provide additional cohesive forces [10]. In another instance, polyacrylic acid (PAA) was applied to not only improving the mechanical strength of the loose soil but also mitigating excessive ammonium contamination [11]. It is worth mentioning, however, only a very few studies focused on the effect of polymer on biological and bio-chemical responses, providing insufficient information in the scientific literature.

Thus, the objectives of this original work are to evaluate the (i) effects of polymers on the biological responses and (ii) efficacy of incorporating polymers in MICP process. For the assessment, two popular polymers: PVA and PAA, are chosen in this study. The experimental program mainly involves urease activity measurements and assessments of precipitation characteristics.

MATERIALS AND METHOD

2.1 Polymers used

The PVA used herein was obtained from Wako Pure Chemical Industries Ltd., Tokyo, Japan. The average degree of polymerization is between 400 to 600. The average molecular mass of PAA (Wako Pure Chemical Industries Ltd., Tokyo, Japan) used is 25000. Chemical structures of the PVA and PAA are shown in Fig. 1(a) and Fig. 1(b), respectively.

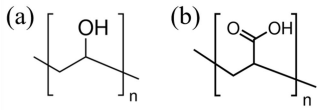

Fig. 1 Structures of the polymers (a) PVA (b) PAA

2.2 Preparation of bacteria culture

The gram-positive ureolytic bacteria *Lysinibacillus xylanilyticus*, previously identified from the Hokkaido slope were used in this research study. Firstly, to prepare the preculture, 5 mL of NH_4 -YE medium was inoculated by the stock bacteria (preserved at -80 ℃) and kept in the shaking incubator at 25 ℃ and 160 rpm for 24 hours. Secondly, 1 mL of the preculture was added into 100 mL of NH_4-YE medium with varying quantities of PVA or PAA (hereinafter referred to as main culture). The main culture was then kept in the shaking incubator under the same condition as preculture.

The culture mediums tested herein are all have 1.57 g of Tris buffer, 1 g of Ammonium sulfate and 2 g of Yeast extract per 100 mL. The additional adding polymers clearly presented in Table 1.

From case V1 to V6, the content of PVA increases. Similarly, from case A1 to A6, the content of PAA gradually increases. But for the case C, neither PVA nor PAA was added. It was used as a control group to compare the effects of additional polymers on microorganisms.

Table 1. The compositons of main culture

Case No.	PVA (g/L)	PAA (g/L)
V1	5	0
V2	10	
V3	20	
V4	40	
V5	60	
V6	80	
C	0	0
A1		2.5
A2		5
A3		7.5
A4		10
A5		12.5
A6		15

2.3 Urease activity test

Urease activity of the bacteria culture was measured using indophenol spectrophotometry method. 0.5 mL of bacterial culture was taken from main culture and added in 50 mL phosphate buffer solution with 0.1 mol/L urea. At the presence of hypochlorite, the ammonium ions produced from the urea hydrolyses react with phenol and produce the blue colour indophenol dye in the alkaline medium. The intensity of indophenol dye was measured via the wave length of 630 nm (OD_{630}) at every 5 min interval of catalyzation. Using a calibration curve established between ammonium ion concentration and intensity (OD_{630}), the rate of urea hydrolysis and urease activity can be obtained [12].

2.4 Precipitation test

After 1 ml bacteria samples separately took from each case in Day 3, centrifugated and removed supernatant and each sample tube was added 10 mL same concentration (0.3 mol/L) of $CaCl_2$ and Urea solution. Samples were kept in the shaking incubator under 25 ℃ and 160 rpm speed for 24 hours. Then the reaction mixture was centrifuged to collect the precipitate, and supernatant of tubes were removed separately by using filter paper (11 μm).

Both of the filter papers and the tubes with the precipitate were oven dried at 60 ℃ for 48 hours and dry weights were measured. Weight of the precipitate was calculated by subtracting the empty weight of the tube and the empty weight of the filter paper from the dry weight of the tube and the dry weight of the filter paper.

2.5 Scanning Electron Microscopy (SEM) analysis

The shape of calcium carbonate crystals can be affected by many factors. In order to minimize interference from organic components in the culture medium and different urease activities from different cases, using 1 ml of bacteria sample in the same control case C in day 3. After centrifugation and supernatant removement, 3 groups both added with the 10 mL of same concentration (0.3 mol/L) of Urea and $CaCl_2$ solution. One group was added with 1 g/L of PVA, and the other group was added with 1 g/L of PAA, one group left as control group.

Samples were kept in the shaking incubator under 25 ℃ and 160 rpm speed for 24 hours. Then the reaction mixture was centrifuged to collect the precipitate. After 48 hours of 60 ℃ oven dry, scanning electron microscopy (SEM) was performed using Miniscope TM3000, Hitachi (Tokyo, Japan) to identify the morphology of the precipitated calcium carbonate crystals.

RESULTS

3.1 Growth of the bacteria

Variation of the population of samples under different polymers concentrations are given in the Fig. 2. It can be seen from the Fig. 2(a) that the PVA has no obvious inhibitory effect on the growth of bacteria, bacteria can still grow, even at a high concentration up to 80 g/L. In contrast, PAA strongly inhibits bacterial growth when the concentration is higher than 10 g/L (Fig. 2(b)).

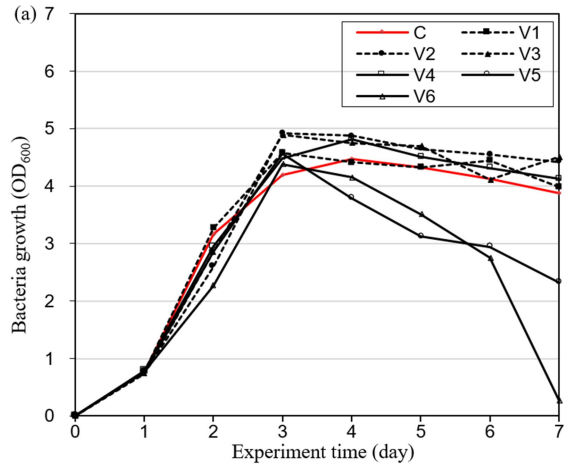

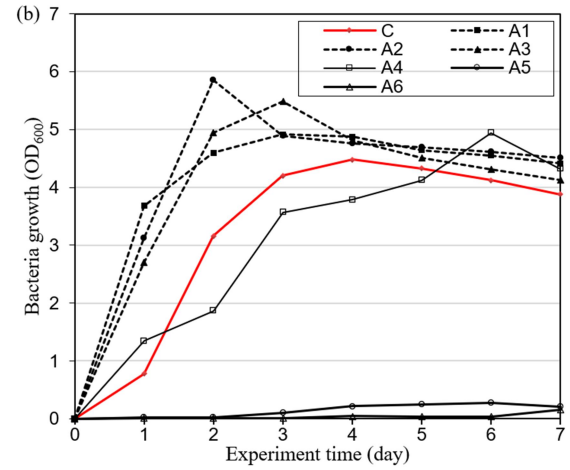

Fig. 2 Variation of the bacteria population with adding polymer (a) PVA (b) PAA

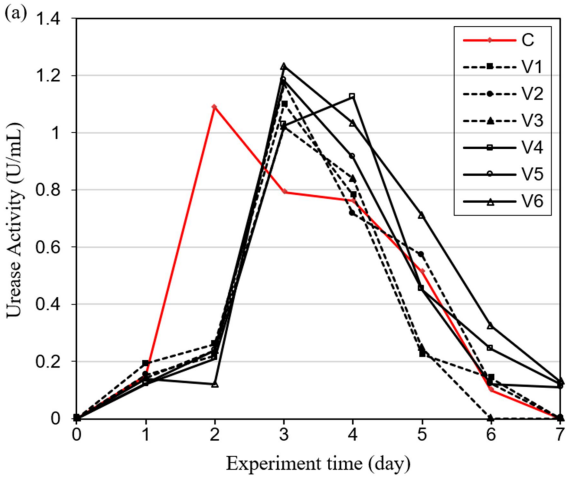

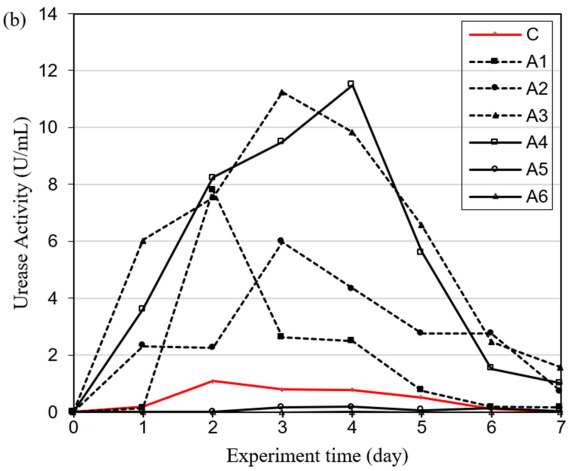

Fig. 3 Variation of the urease activity with adding polymer (a) PVA (b) PAA

3.2 Urease activity

Figure 3 shows that different concentrations of PVA have no obvious effect on the activity of bacteria. The activities were almost similar to that observed of the control. On the other hand, the low concentrations of PAA have a very obvious promotion effect on urease activity. For instance, at the concentration of 10 g/L, the urease activity is found to be relatively optimum, that exceeds of a value over 11 U/mL. However, when the PAA concentration further increases, the urease activity dramatically diminishes.

3.3 Amount of $CaCO_3$ precipitation

Figure 4 shows the variation of the amount of $CaCO_3$ for the different considered cases. In the cases of adding PVA do not show any evident trend (no significant changes). But, for the PAA cases, when the concentration increases, the amount of precipitation shows an increasing tendency. However, when the concentration increases above 10 g/L, it suddenly drops very close to 0 g.

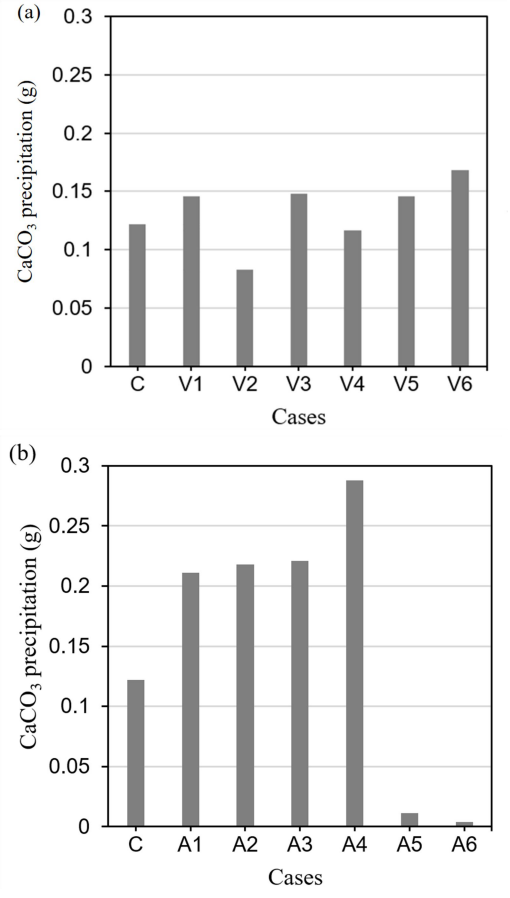

Fig. 4 Variation of the $CaCO_3$ amount with different polymer cases (a) PVA (b) PAA.

3.4 Morphology of the precipitated crystals

According to Fig. 5, scanning electron microscope (SEM) images of various morphologies are shown at the same scale.

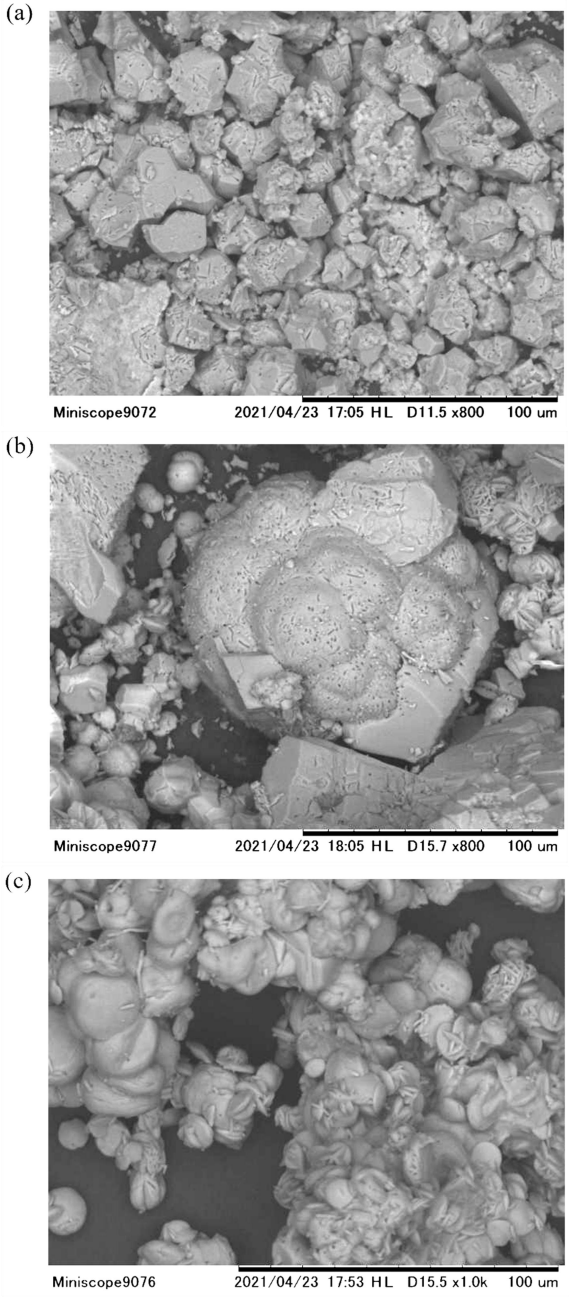

Fig. 5 Variation of the $CaCO_3$ morphology under different condition (a) no polymer adding (b) PVA (c) PAA.

The calcium carbonate crystal morphology without any polymers is shown in Fig. 5(a) (control), indicating the formation of typical rhombohedral-shape crystals. When the PVA is added to the medium, relatively spherical-shaped crystals are precipitated. At the same time, an accumulation of

pallets-like calcium carbonate crystals could be seen in the PAA added cases. It should be noted that the morphology of the crystals seen in Fig. 5(a) significantly different from that observed in Fig. 5(b). This suggests that the crystallization effects highly rely on the intrinsic characteristics of polymers.

DISCUSSION

From the outcomes, it is found that the PVA does not inhibit both the growth and urease activity of bacteria, regardless of its concentration in the reaction medium. In contrast, the addition of PAA was found to favor the urease activity of the bacteria, which showed an increase over more than two-folds. However, the concentration over 10 g/L strongly inhibited the bacteria growth, urease activity and precipitation efficiency. This could probably be attributed to the characteristics of the polymer. The PVA is a neutral polymer, while the PAA is an acidic one; therefore, the low pH conditions caused by high concentration of PAA (above 10 g/L) were extremely unfavorable and harsh for bacterial growth.

In consideration of both Fig. 3 and Fig. 4, there were no considerable positive or adverse influences observed from the PVA on the MICP process. Interestingly, the lower concentrations of the PAA (below 10 g/L) promoted the ureolytic performance of the bacteria, hence the mineralization efficiency. One possible explanation could be that the preferential consumption of PAA by the bacteria that aided to produce more amino acids. Nevertheless, the clear mechanism for the incredible performance is still unclear, needing further investigation (left for the future work).

It was evident (from the SEM analysis) that with the addition of polymer, the morphology of the crystals transitioned from rhombohedral to round/ spherical-shaped crystals with more aggregation. The morphology changes could possibly be due to the adsorption of the polymers on the crystal surface, which led to the formation of new crystal faces.

CONCLUSIONS

According to the obtained results, a moderate amount of PAA has a significant positive effect on urease activity, which has great significance to the practical application of engineering and can be used to achieve high strength cementation in the future research. On the contrary, PVA does not promote or inhibit MICP, even at high concentrations. It also has potential application value which can be used to adjust the viscosity of the cementation solution to control the occurrence position of the MICP.

Morphology of the crystals changes from the polyhedral crystals to agglomeration of round crystals with the attendance of polymer. The relationship between the crystal morphology and ground improvement is still not clear. However, this is a quite important point in MICP. It thus should be revealed in the future work by comparing the crystal polymorph and the strength of cured soil.

REFERENCES

[1] Dhami N. K., Reddy M. S., and Mukherjee M. S., Biomineralization of calcium carbonates and their engineered applications: A review, Frontiers in Microbiology, Vol. 4, Issue OCT, 2013, pp. 1–13.

[2] Whiffin V. S., van Paassen L. A., and Harkes M. P., Microbial carbonate precipitation as a soil improvement technique, Geomicrobiology Journal, Vol. 24, Issue 5, 2007, pp. 417 – 423.

[3] van Paassen L. A., Ghose R., van der Linden T. J. M., van der Star W. R. L., and van Loosdrecht M. C. M., Quantifying Biomediated Ground Improvement by Ureolysis: Large-Scale Biogrout Experiment, Journal of Geotechnical and Geoenvironmental Engineering, Vol. 136, Issue 12, 2010, pp. 1721–1728.

[4] Gomez M. G., Anderson C. M., Graddy C. M. R., DeJong J. T., Nelson D. C., and Ginn T. R., Large-Scale Comparison of Bioaugmentation and Biostimulation Approaches for Biocementation of Sands, Journal of Geotechnical and Geoenvironmental Engineering, Vol. 143, Issue 5, 2017, pp. 04016124.

[5] Gowthaman S., Mitsuyama S., Nakashima K., Komatsu M., and Kawasaki S., Biogeotechnical approach for slope soil stabilization using locally isolated bacteria and inexpensive low-grade chemicals: A feasibility study on Hokkaido expressway soil, Japan, Soils and Foundations, Vol. 59, Issue 2, 2019, pp. 484–499.

[6] Gowthaman S., Iki T., Nakashima K., Ebina K., and Kawasaki S., Feasibility study for slope soil stabilization by microbial induced carbonate precipitation (MICP) using indigenous bacteria isolated from cold subarctic region, SN Applied Sciences, Vol. 1, Issue 11, 2019, pp. 1–16.

[7] Gowthaman S., Nakashima K., and Kawasaki S., Effect of wetting and drying cycles on the durability of bio-cemented soil of expressway slope, International Journal of Environmental Science and Technology, Vol. 4, Issue 1, 2021 .

[8] Nawarathna T. H. K., Nakashima K., Fujita M., Takatsu M., and Kawasaki S., Effects of Cationic Polypeptide on CaCO3 Crystallization and Sand Solidification by Microbial-Induced Carbonate Precipitation, ACS Sustainable Chemistry and Engineering, Vol. 6, Issue 8, 2018, pp. 10315–10322.

[9] Wang X., and Tao J., Polymer-modified microbially induced carbonate precipitation for one-shot targeted and localized soil improvement, Acta Geotechnica, Vol. 14, Issue 3, 2019, pp. 657–671.

[10] Wang X., and Tao J., Polymer-modified Microbially-Induced Carbonate Precipitation Treatment Method for Surface Erosion Prevention. 2018.

[11] Zhao Z., Hamdan N., Shen L., Nan H., Almajed A., Kavazanjian E.,and He X., Biomimetic hydrogel composites for soil stabilization and contaminant mitigation, Environmental Science and Technology, Vol. 50, Issue 22, 2016, pp. 12401–12410.

[12] W. T. Bolleter, C. J. Bushman, and P. W. Tidwell, Spectrophotometric Determination of Ammonia as Indophenol, Analytical Chemistry, Vol. 33, Issue 4, 1961, pp. 592–594.

11th Int. Conf. on Geotechnique, Construction Materials & Environment, Kyoto, Japan, 3-5 November 2021, ISBN: 978-4-909106063 C3051

HIGH WATER CONTENT PEAT SOIL IMPROVED BY MICP TECHNIQUE WITH FIBER-REINFORCEMENT

Meiqi Chen[1], Sivakumar Gowthaman[2], Kazunori Nakashima[2], Shin Komatsu[3] and Satoru Kawasaki[2]

[1]Graduate School of Engineering, Hokkaido University, Sapporo, Japan
[2]Faculty of Engineering, Hokkaido University, Sapporo, Japan
[3]Meiwa Seishi Genryo Co., Ltd., Osaka, Japan

ABSTRACT

Peat soil is referred to as problematic soil that uniquely forms under anaerobic and water-saturated conditions. It is usually characterized as organic soil of high compressibility, high water content, and low shear strength. To reduce the environmental impact, instead of using cement products to stabilize it, a relatively novel technique based on the bio-mineralization principle, microbially induced carbonate precipitation (MICP), was adopted to improve the soil matrix. Besides, this study introduced wastepaper fibers from the paper recycling process onto MICP treatment. The objectives were to investigate the effects of fiber reinforcement (0-50% addition) on the undrained shear strength (USS) improvement and contributing factors to the MICP effectiveness. Furthermore, the fiber-reinforced and MICP treated samples were subjected to dispersive crumb tests to examine their stability under a water-logged environment. The results showed a significant improvement in USS up to 360 folds observed when 50% of fibers were introduced onto MICP treatment. The dispersion tests revealed a stable state of MICP treated sample with fiber reinforcement, while the fiber reinforcement alone showed a swelling behavior.

Keywords: Peat soil, Microbially induced carbonate precipitation (MICP), Wastepaper fiber, Fall cone test, Dispersive crumb test

INTRODUCTION

According to the latest report on the global distribution of peatland, peat soil covers approximately 2.84% of the world land area [1]. Formed under extreme conditions of high acidity and waterlogging, this type of soil usually exists at high organic and water levels [2]. Peat deposits possess undesirable engineering properties, so improving this marginal land has been challenging for engineers [3]. For the past several decades, most conventional methods using many cement products have been accused of contributing significantly to CO_2 emissions [4]. Nowadays, since we are facing an unprecedented crisis due to global warming, engineers now tend to consider more undesirable consequences that may come with the improvement than before, generating more and more novel technologies of sustainability.

Microbial induced carbonate precipitation (MICP) is one of these techniques, and now it is increasingly described as a green and reliable alternative to conventional methods in many research fields. Unlike conventional techniques, in MICP process, urease produced by living organisms plays a vital role in controlling the reaction rate flexibly. The following equations explain how the bio-mineralization occurs [5, 6]:

$$CO(NH_2)_2 + 2H_2O \xrightarrow{\text{Urease}} 2NH_4^+ + CO_3^{2-} \quad (1)$$

$$CO_3^{2-} + Ca^{2+} \longrightarrow CaCO_3\downarrow \quad (2)$$

This technique has broad application prospects, including soil stabilization, liquefaction prevention, coastal erosion control, fugitive control, etc. [7, 8]. In this study, the focus is concentrated on soil improvement, aiming to enhance one type of high-water content peat soil. The use of wastepaper fibers recycled from a paper mill differs this research from most other reports. Due to its excellent water holding capacity, the wastepaper fiber was expected to stabilize the excessive water in the peat. Globally, the recycling rate of wastepaper fibers keeps at a low level in developing countries. If these wastes could become useful materials in the construction industry, the increasing recovery rate would contribute to sustainable development.

The objectives of this study are i) to investigate the factors that determine the effectiveness of MICP on peat soil; ii) to examine the feasibility of stabilizing high water content peat soil using wastepaper fiber-reinforced MICP technique; iii) to evaluate the performance of the treated soil samples in a water-clogging condition. Strength improvement data were obtained using fall cone test. The effectiveness of MICP was evaluated by the measurement of calcium carbonate content and dispersive crumb test. These experimental works provide a fresh insight into the reuse of waste materials and generate sustainable ideas that combine wastes with novel techniques to achieve a win-win situation.

MATERIALS AND METHODOLOGY

Peat Soil

Peat soil samples were collected from Iwamizawa, Hokkaido, Japan. Table 1 presents the basic characteristics of Iwamizawa peat. The distinguishing characteristics between Iwamizawa peat and normal soils are its high water content (around 800%) and pH lower than 5.

Table 1 Basic characteristics of Iwamizawa peat

Parameters	Values
Water content	711 - 824 %
Density	1.821 g/cm^3
Ignition loss	65.815 %
pH	4.6 - 4.8
k	10^{-4} - 10^{-5} cm/s

Note: Samples were examined from the lower layer to the upper layer; *k* is the permeability coefficient.

Wastepaper Fiber

Wastepaper fibers (WPF) are a mixture of waste materials produced in a paper mill, with cellulose fibers, the basic structural constituent of all plant fibers, and ash content as two dominant components. Meiwa Seishi Genryo Company, Japan, provided the fibers used in this study. The image captured by scanning electron microscopy (SEM) illustrates the appearance of WPF (see Fig. 1 below). Basically, a wide range of fiber lengths from 20 to 500 µm was observed.

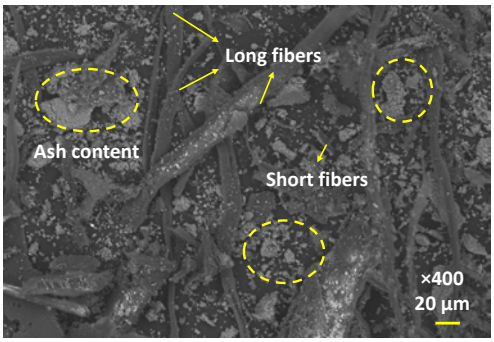

Fig. 1 SEM image of WPF

Bacteria

The ureolytic bacterium (as a source of urease) used in this study is *Lysinibacillus xylanilyticus*, a gram-positive species with a rod shape (8-10 µm long) which was previously isolated from Hokkaido by Gowthaman et al. [9]. Its urease activity tends to peak at around 3.5 U/mL at a neutral condition (pH 7-8) after 72 hours of cultivation at 25℃ [9]. Since the previous report has corroborated its reliability, the bacterial preparation was done following the same method, using NH_4-YE (ATCC 1376) as the culture medium and 25 ℃ as the cultivation temperature.

Table 2 Experimental Cases

	Category	Conc. of $CaCl_2$ & urea	Fiber addition
Set 1	Effect of fiber addition	non	0% 10% 30% 50%
Set 2	Effect of initial pH	pH 4.5 pH 7	non
	Effect of conc. of $CaCl_2$ & urea	1 M 2 M 3 M	
Set 3	MICP treatment reinforced by fibers	1 M	0% 10% 30% 50%

Experimental Cases

Cases set in this experiment were depicted in Table 2. In this study, considering the characteristics of peat soil, MICP treatment was conducted by mixing all the materials added in the following order: 0.5% of CaO_2, for pH adjustment; WPF at different ratios; $CaCl_2$ & urea; and bacterial culture solutions, with an OD_{600} around 10. It should be mentioned that all the ratios presented in this study refer to proportion by the weight of soil. For each 182 g (100 cm^3) of peat soil, 15 mL of bacteria were added. The concentration of cementation materials was calculated based on the volume of soil. Molded samples were sealed and then put into an incubator with a constant temperature of 25℃ for curing. Strength examinations were carried out three times: right after the sample preparation, 24 hours, and day 7.

Evaluations

Fall cone test

The fall cone apparatus (release-stop type DH-22NM, cone angle=60°) is provided by Seikensha, Tokyo, Japan. The tests are conducted according to the JGS 0142-2009 [10]. It has been reported that this test could be a feasible and reliable method to estimate the shear strength for soft clay materials. For Iwamizawa peat, this test is a quick way to examine the strength improvement over time. The estimation is based on an approximate relation between the undrained shear strength (s_u) and the depth of penetration (h), as presented in Eq. 3.

$$s_u = k(mg/h^2) \quad (3)$$

Where fall cone factor k=0.29, cone mass m=60 g, and earth gravity acceleration g=9.81 N/kg.

Calcium carbonate measurement

The measurement of calcium carbonate is achieved by using a sealed container equipped with a pressure gauge, which was developed by Fukue et al. [11]. It is based on a simple principle: the pressure inside the container increases due to the carbon dioxide produced by the reaction between calcium carbonate and hydrochloric acid. This change in pressure could be transformed into the mass of calcium carbonate using an established calibration curve. For each test, 2 g of dry samples were taken from the sample and reacted with 20 mL of HCl solution (2 mol/L).

RESULTS

Fiber Reinforcement

The first test was carried out to measure the variation in strength with different fiber contents, as shown in Fig. 2. It can be found that the addition of WPF enhanced the USS significantly. When the fiber content was up to 50%, an improvement ratio of 200 folds and a significant reduction of water content were observed. It is considered that the water reduction is responsible for the improvement since the high water content controls the shear strength of Iwamizawa peat.

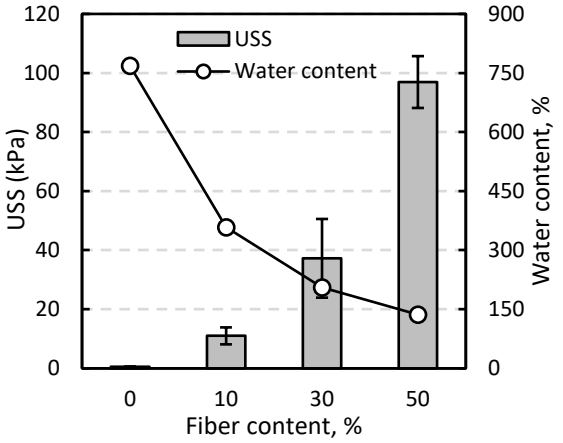

Fig. 2 Effect of fiber addition on undrained shear strength (USS) improvement and the water content

Contributing Factors of MICP Treatment

Effect of initial pH

Having an acidic condition (pH 4.5) makes it quite challenging to improve the peat by MICP treatment because it inhibits the urease activity of bacteria and the precipitation of carbonate. Therefore, to tackle this problem, the acidic peat was adjusted to a neutral condition (around pH 7) by adding 0.5% of CaO_2 (agricultural fertilizer). A comparison of the adjusted and unadjusted strength is illustrated in Fig. 3(a), revealing a significant difference in strength improvement. What is striking here is that a doubled improvement ratio when the acidic condition was altered into a neutral one, which indicates a significant enhancement in the effectiveness of MICP.

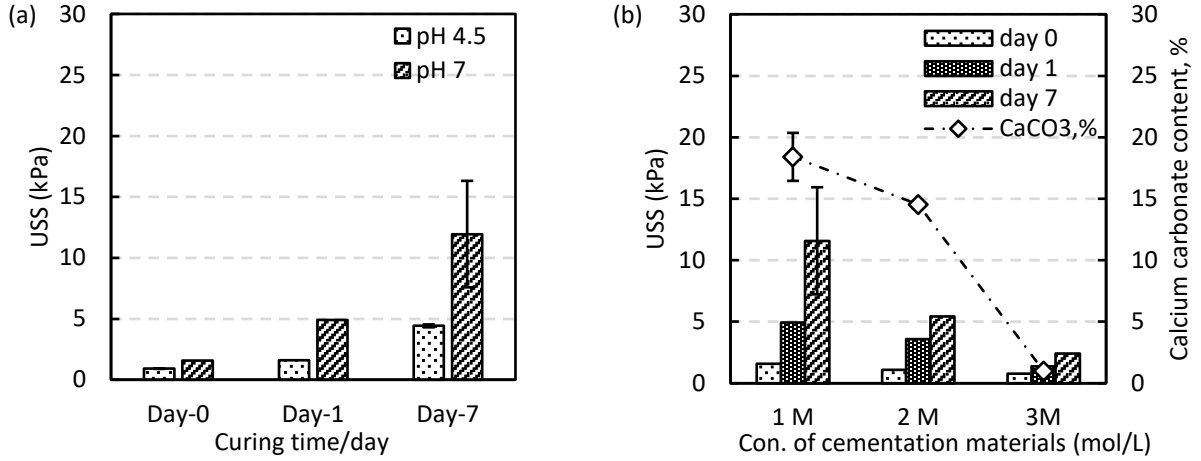

Fig. 3 Contributing factors of MICP: (a) effect of initial pH; (b) effect of concentration of cementation materials

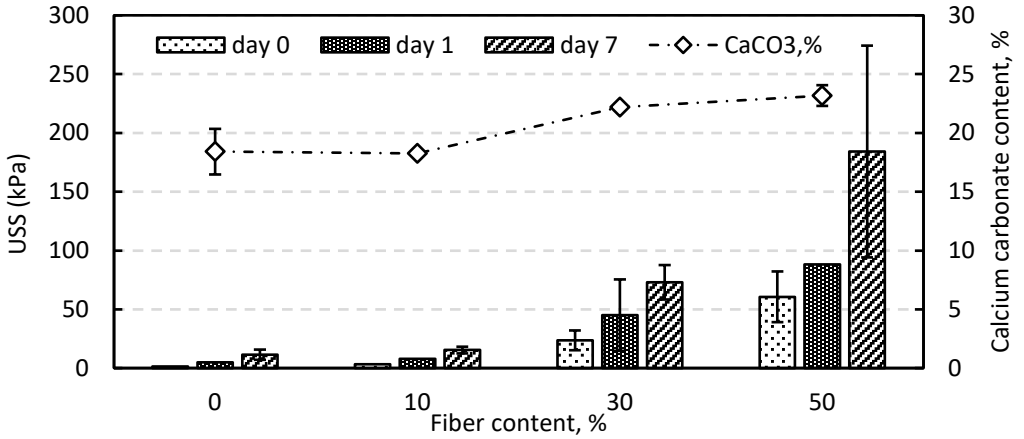

Fig. 4 MICP treatment reinforced by different fiber content (10%, 30%, 50%), with carbonate content shown by the dash-dotted line

Concentration of $CaCl_2$ & urea

To investigate the effect of different concentrations of cementation materials, a set of MICP treated samples with 1 mol/L, 2 mol/L and 3 mol/L of $CaCl_2$ & urea were prepared. From the bar chart in Fig. 3(b), it can be seen that samples with a higher concentration appeared to be less improved by the treatment. Strong evidence was found in the results of calcium carbonate content. The 1 M case yielded a calcium carbonate precipitation of 18%, while only 1% of precipitation was obtained in the 3 M case. The concentration of 1 mol/L was the optimum among three cases, with an improvement ratio of more than 20 times.

Fiber Reinforced MICP Treatment

Figure 4 illustrates the enhanced strength by WPF (10%, 30%, 50%) reinforced MICP treatment during 7-day curing. It is apparent from this figure that a small amount of fiber addition did not enhance the effectiveness of MICP, which can be explained by the similar calcium carbonate precipitation obtained from 0% case and 10% case. However, when the addition was up to 30%, one-week strength increased by six folds compared to the 0% case. What stands out in this figure is that 50% of fiber addition contributed an improvement ratio of 15 times. Meanwhile, the calcium carbonate content was increased by 25% compared to the 0% case.

The enhancement observed in this figure can be compared with the results shown in Fig. 2. As mentioned before, fibers enhanced the strength significantly by holding the water. Incorporated with MICP treatment, a nearly doubled enhancement was obtained in cases with high fiber content.

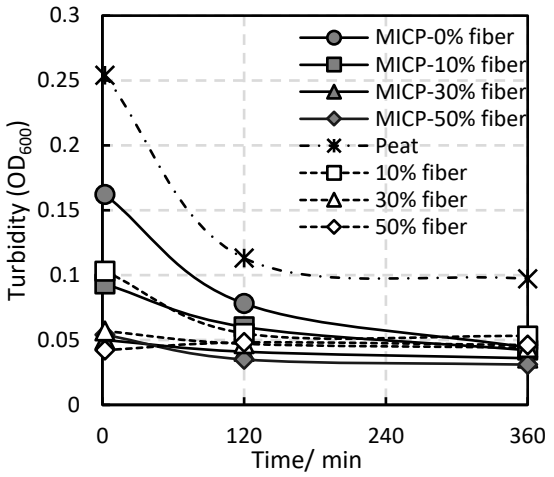

Fig. 5 Turbidity-time curve in crumb tests conducted on untreated peat, fiber-reinforced samples, and fiber-MICP treated samples

Dispersive Crumb Test

Since the peat was formed in conditions with excessive water, investigating how the stabilized peat performs under water-clogging is essential. Therefore, both untreated and treated peat samples were subjected to crumb tests. The results were presented both in pictures and statistics. As shown in Fig. 5, the quantified turbidity of treated samples verified the remarkable improvement in dispersive properties. Pictures in Fig. 6 illustrate the samples kept in a water-logging condition after 6 hours. High water content peat collapsed immediately when samples were subjected to water immersion (Fig. 6(a)). It is evident from Fig. 6(b-h) that samples became more stable with the increasing fiber addition, with less crumbled material observed at the bottom of the beaker. Remarkably, almost no crumb was found in the MICP case with 50% of fiber addition. It is worth noting here that the fiber-reinforced samples exhibited a swelling behavior during the 7-day curing

period, as shown in Fig. 6(c), which accelerated the damaging process when soaking into water. Closer observation on the crumb settled at the bottom of the beaker suggests that fiber-reinforced MICP treated samples are more stable in water for the reason that suspended particles in peat were connected by the bio-cementation.

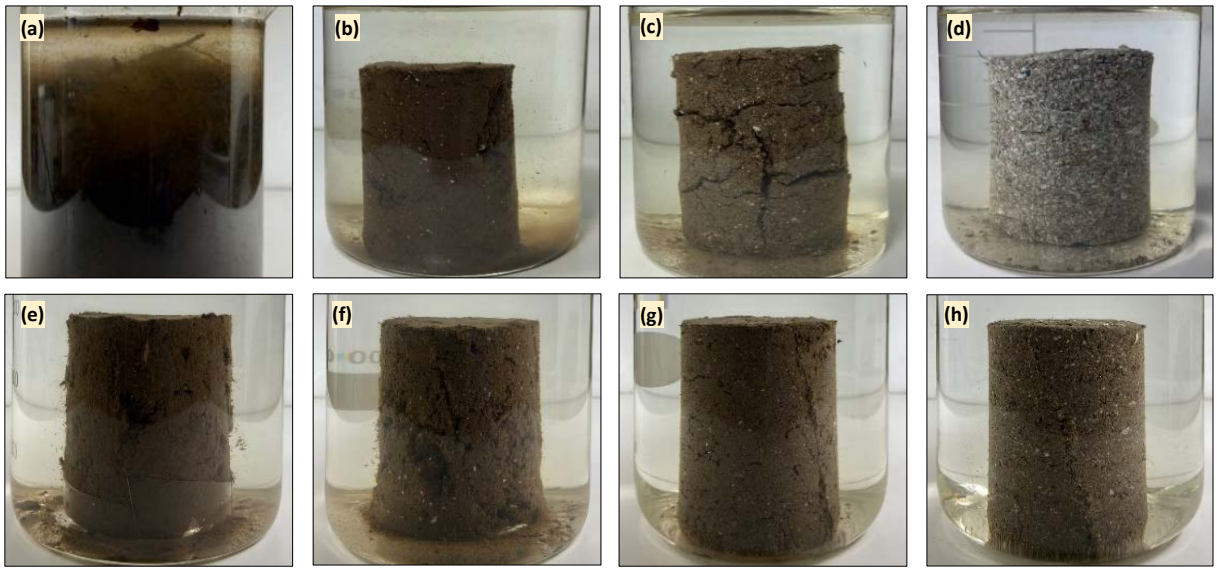

Fig. 6 Demolded samples in a water-clogging state with a 6-hour duration: (a) untreated peat soil; (b) 10%, (c) 30%, and (d) 50% of fiber-reinforced peat; (e) MICP treated sample (1 mol/L); (f) MICP treatment reinforced by 10%, (g) 30% and (h) 50% of fibers

DISCUSSION

A previous experimental study on improving Iwamizawa peat combined bamboo fibers and MICP treatment [12]. Due to the limited urease activity of the native bacteria, the treated soil remained weak. Overall, it has been confirmed that fiber materials could stabilize high water content soil, which further aids the MICP treatment.

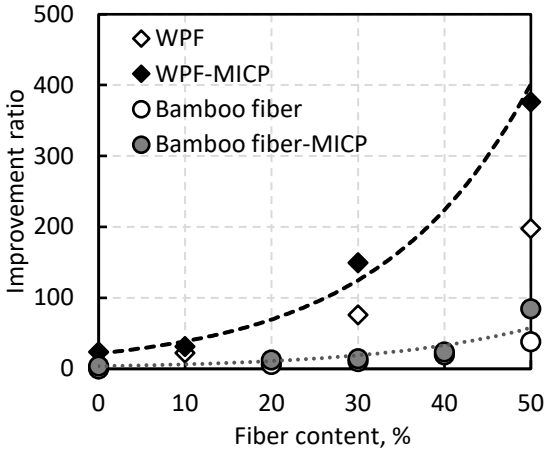

Fig. 7 Improvement ratio by fibers and fiber-MICP [12]

Similarly, in this study, bacteria of higher urease activity and fibers (finer) with a larger specific surface area were used to enhance the strength further. What stands out in this study is that the improvement ratio by wastepaper fibers was more than 5-fold as that by bamboo fibers when the addition was up to 50%. It can be explained by their difference in the capacity of moisture reduction. Compared to bamboo fibers, wastepaper fibers possess a larger specific surface area, thus holding more water, which leads to a significant enhancement in the shear strength.

The results of the dispersive crumb test illuminate a significant improvement in peat soil's stability. As generally known, cellulose fibers hold water and expand, which explains why a relatively poor performance was observed in fiber-reinforced samples. However, it seems that fiber-reinforced MICP treatment could overcome this obstacle since the precipitation functions as a cementitious material that binds the loose fibers.

Considering the organic matter, mainly humic substances in the peat soil, the addition of CaO_2 might have affected the solubility of some substances since the pH condition was greatly altered. Furthermore, when mixing the calcium carbonate and urea, there is a severe fluctuation in temperature. Both these chemical and physical changes disturbed the original structure of the soil, which might inhibit the MICP to

some extent. As reported in the previous study, the humic substances are of great cation exchange capacity (particularly humic acids), which could be the most challenging part of MICP treatment considering the indispensable role of calcium ions [12]. In soil humus science, these substances, unfortunately, are remained elusive to scientists. Therefore, to obtain a deeper understanding of these substances' role in the MICP process, more efforts need to be made.

CONCLUSIONS

The present study was designed to investigate the effect of fiber-reinforcement on high water content peat improvement, two contributing factors of MICP treatment on peat, and evaluate the effectiveness of fiber-reinforced MICP treatment. The first set of experiments conducted in this research has identified a remarkable enhancement in soil strength when reinforced by wastepaper fibers. The second set confirmed a favorable condition for effective MICP treatment. The results of the third set revealed a doubled improvement in shear strength when fiber reinforcement was combined with MICP treatment, followed by dispersive crumb test, which indicates an essential finding of the treated samples' stability. A discussion of samples' durability lies beyond the scope of this study, which is recommended for future work.

In general, this study suggests an essential role for wastepaper fibers in amending high water content peat and highlights the feasibility of MICP treatment on soil improvement.

ACKNOWLEDGMENTS

The authors express their gratitude to Civil Engineering Research Institute for Cold Region, Sapporo, Japan, for their contribution and technical support.

REFERENCES

[1] Xu J., Morris P.J., Liu J., Holden J., PEATMAP: Refining estimates of global peatland distribution based on a meta-analysis. Catena, Vol. 160, 2018, pp.134-140.

[2] Huat B.B.K., Kazemian S., Prasad A., Barghchi M., State of an art review of peat: General perspective. International Journal of the Physical Sciences, Vol. 6, Issue 8, 2011, pp.1988-1996.

[3] Kazemian S., Huat B.B.K., Prasad A., Barghchi M. A state of art review of peat: Geotechnical engineering perspective. International Journal of the Physical Sciences, Vol. 6, Issue 8, 2011, pp.1974-1981.

[4] United Nations Environment Programme, Emissions Gap Report 2020.

[5] DeJong J.T., Mortensen B.M., Martinez B.C., Nelson D.C., Bio-mediated soil improvement. Ecological Engineering, Vol. 36, 2010, pp. 197-210.

[6] Mujah D., Shahin M.A., Cheng L., State-of-the-Art Review of Biocementation by Microbially Induced Calcite Precipitation (MICP) for Soil Stabilization. Geomicrobiology Journal, Vol. 34, 2017, pp.524-537.

[7] Dejong J.T., Soga K., Kavazanjian E., Burns S., Van Paassen L.A., Al Qabany A., Aydilek A., Bang S.S., Burbank M., Caslake L.F., et al., Biogeochemical processes and geotechnical applications: Progress, opportunities and challenges. Géotechnique, Vol. 63, Issue 4, 2013, pp. 287-301.

[8] Jiang N.J., Tang C.S., Hata T., Courcelles B., Dawoud O., Singh D.N., Bio-mediated soil improvement: The way forward. Soil Use Management. Vol. 36, Issue 2, 2020, pp.185-188.

[9] Gowthaman S., Mitsuyama S., Nakashima K., Komatsu M., Kawasaki S., Biogeotechnical approach for slope soil stabilization using locally isolated bacteria and inexpensive low-grade chemicals: A feasibility study on Hokkaido expressway soil, Japan. Soils and Foundations, Vol. 59, Issue 2, 2019, pp. 484-499.

[10] JGS Testing Methods and Their Interpretation for Geotechnical Materials (in Japanese). 2009.

[11] Fukue M., Nakamura T., Kato Y., Cementation of Soils Due to Calcium Carbonate. Soils and Foundations, Vol. 39, Issue 6, 1999, pp. 55-64.

[12] Chen M., Gowthaman S., Nakashima K., Kawasaki S., Evaluating Mechanical Strength of Peat Soil Treated by Fiber Incorporated Bio-Cementation. International Journal of GEOMATE, Vol. 20, Issue 78, pp.121-127.

11th Int. Conf. on Geotechnique, Construction Materials & Environment, Kyoto, Japan, 3-5 November 2021, ISBN: 978-4-909106063 C3051

OFF-CENTER TETRAHEDRAL WEDGES

John Victor Smith [1]

[1]RMIT University, Australia

ABSTRACT

Tetrahedral wedges in rock slopes can have symmetric and asymmetric shapes. Asymmetry is commonly recognized as differences in dip angles of the sliding planes. This form of asymmetry is known to influence the kinematic feasibility and stability of a wedge. Asymmetry also influences the appearance of wedges and therefore the ability to recognize wedges in rock faces and in data from rock masses. The relative orientation of the sliding planes in relation to the lower and upper slope faces is also part of the asymmetry system. In particular, the direction of the line of intersection which determines the sliding direction of two planes, relative to the direction of the slope of the rock face introduces an additional type of asymmetry. This form of asymmetry is defined here as off-center wedges. A detailed terminology for asymmetric tetrahedral wedges is presented and the implications for kinematic feasibility, sliding mechanism and stability analysis are discussed. A field example from Auckland New Zealand is presented.

Keywords: Wedge, Kinematic stability, Rock slope, Sliding

INTRODUCTION

The stability of a tetrahedral wedge exposed in a rock slope has been shown to be influenced by its shape in both static [1-3] and dynamic [4-6] conditions. Wang et al. [7] demonstrated limit-equilibrium and numerical solutions to wedge stability including comparison of symmetrical and asymmetrical examples. In a probabilistic analysis of wedge stability it was found that the reliability results were very sensitive to variations in the shape and therefore symmetry of the wedge [8].

Large amounts of discontinuity orientation data need to be investigated in field and synthetic rock mass characterization projects [9]. Stereographic methods form the initial step in wedge stability assessment in many rock engineering investigations [10-17]. In a summary of conventional stereographic methods, Wyllie and Mah [18] indicated that wedge-forming poles are restricted to inside the daylighting envelope of the slope face plane. However, the limits to wedge-forming poles has been shown to be more complex and defined by limits to the orientations of great circles on which wedge-forming pole pairs can lie [19].

Stereographic methods have also been used to distinguish between mechanisms of single-plane and two-plane sliding mode of wedges using the line of intersection [20] or the poles and daylighting envelope [21].

This paper is focussed on tetrahedral wedges defined by two sliding planes and an upper and lower slope face. The presence of tension cracks or basal sliding planes is not considered. Asymmetry is developed by the relationship between all four faces. The typical distributions of planes which can form kinematically feasible wedges are considered in terms of the shape and symmetry of a tetrahedral wedge. The typical shapes of feasible wedges are illustrated on a stereograph. Examples of applications of the approach are given for data from jointed and faulted sedimentary rock in Auckland, New Zealand. The feasibility and factor of safety are shown to be related to the shapes of the wedges, including the off-center asymmetry of some wedges.

TERMINOLOGY

Angle Between Sliding Planes

The angle between sliding planes is an important geometric parameter of wedges. The term dihedral angle can be used to specifically identify the angle measured in a plane perpendicular to the line of intersection of the planes. The terms thin and thick were applied by Hudson and Harrison [3] up to a dihedral angle of 90^o. They did not extend their analysis beyond that value. When higher dihedral angles are considered the wedges become thinner with respect to the slope face. Therefore, the terms narrow (for thin) and open (for thick) are adopted. The term very open is applied to wedges where the two sliding planes are approaching parallelism with each other (Table 1). As wedges become increasingly open, they can approach the dip direction of the slope face and therefore approach the planar sliding case which represents a minimum stability for that dip angle. On a stereograph, that appears as poles to sliding planes approaching the opposite direction to the dip direction of the slope face. Lateral limits of planar sliding are typically accepted as +/-20^o [18]. These limits are a general reference only and do not define a change in failure mechanism. As will be shown below, the change in mechanism from single

plane to two-plane sliding varies according to the degree to which wedges are off-center.

Wedge Symmetry

The symmetry of a tetrahedral wedge must be considered in two ways. First, the symmetry of the two sliding planes relative to each other. Second, the symmetry of the sliding planes relative to the slope face also needs to be considered. These aspects of symmetry can be considered to be related to the sliding plane dip and dip directions, respectively. If the two sliding planes have the same dip then a plane halfway between them would be vertical. If the two sliding planes have the different dips then a plane halfway between them would be dipping. Hudson and Harrison [3] refer to this as upright and inclined, respectively. For simplicity, the dip angle of each plane will be compared and will be termed equal or unequal. An arbitrary 10^o difference in dip between the planes is applied here to separate the two terms.

Regarding the influence of dip direction, if a wedge is oriented such that its sliding direction (intersection line) is the same as the dip direction of the slope face that will be described here as a centered wedge. Other sliding directions will be referred to as off-center. Therefore, the symmetry of the tetrahedral wedge is a combination of its centered or off-center characteristics and its equal versus unequal characteristics (Table 1). A symmetrical wedge must be both centered and equal. Note that the sliding direction can be directly observed as the pole to the great circle on which the wedge-forming poles lie [19].

Off-center Wedges

Poles lying in other locations other than on a centered great circle are capable of forming a wedge. Such poles will typically lie on a great circle which has a different strike to the strike of the slope face. An off-center example has a pole (equivalent to line of intersection of wedges) trending northeast (Fig. 1). For simplicity, a southeast trending example is not shown, as the principle can be applied in a mirror image for comparison. On this basis, a wide range of wedge-forming possibilities can be considered for example, the eight general locations of poles shown as numbered stars on Fig. 1.

Location 1 represents a pole close to the lateral limit of planar sliding near where the centered and off-center great circles intersect. Location 2 and location 3 occur on the same side of the stereograph, between the lateral limit and the primitive circle (outer edge of the stereograph) on the off-center great circle. Locations 4 and 5 occur on the same side of the stereograph as location 1, between the lateral limit and the primitive circle on the off-center great circle. Location 5 lies close to the primitive circle on the

Table 1 Terminology used to describe features of tetrahedral wedges observable on a stereographic representation

Application	Term	Comment/ Quantification
Describes the (dihedral) angle between two sliding planes forming a wedge	Narrow	<60^o (>120^o pitch on stereograph between poles on opposite sides of the slope face)
	Open	60^o-120^o (60^o-120^o pitch angle on stereograph)
	Very open	>120^o (<60^o pitch on stereograph between poles on opposite sides of the slope face)
Describes the overall shape of a tetrahedral wedge (defined by four planes)	Symmetric	Only possible for centered, equal wedges
	Asymmetric or Non-symmetric	Asymmetry of a tetrahedral wedge can be due to off-centered orientation of the great circle joining the sliding plane poles and/or unequal dip of sliding planes
Describes the direction of two-plane sliding relative to the slope direction	Centered	Great circle joining sliding plane poles dips 180^o from slope face direction
	Off-center	Great circle joining sliding plane poles dips 180^o +/- <30^o from slope face direction
	Highly off-center	Great circle joining sliding plane poles dips 180^o +/- >30^o from slope face direction
Describes the difference in dip of the wedge sliding planes	Equal	Difference of dip <10^o
	Unequal	Difference of dip >10^o

off-center great circle and is distinguished by dipping back into the slope face. The numbering of these locations is entirely arbitrary and they have been selected for the purpose of illustrating general examples of shapes of kinematically feasible wedges according to the position of poles on a stereograph.

Any combination of poles from great circle distribution (e.g. any pair of poles form locations 1-5 forms a wedge with the same intersection plunge (red star on Fig. 1). The shape will differ greatly for each pair of planes. For example, the wedge formed by poles at locations 1 and 2 are very open whereas a wedge formed by poles at locations 3 and 5 would be narrow.

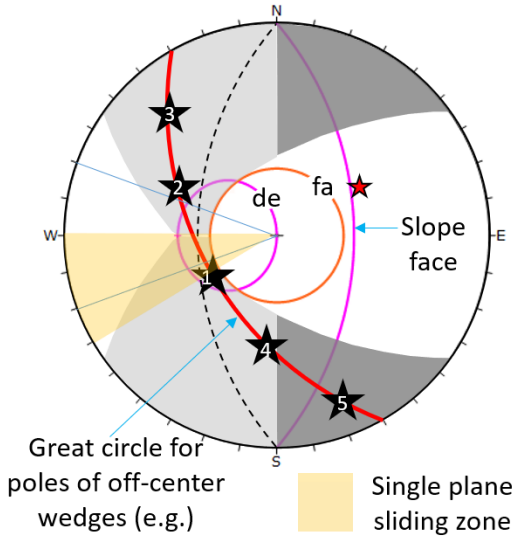

Fig.1 Stereograph of potential wedge-forming poles (black stars) illustrating off-center wedges

Wedge Sliding Mode

The lateral limits of planar sliding are recognized as an arbitrary range for practical purposes [18]. The occurrence of single plane sliding wedges and two-plane sliding wedges depends on other geometric relationships [20,21]. For centered wedges, the single plane sliding mode cannot occur. Even two planes one degree either side of the plane perpendicular to the slope face will form a two-plane sliding pair, in the centered case. Where a pair of planes (poles) are joined by an off-center great circle the zone of single plane sliding is defined by the difference between the strikes of the slope face and the off-center great circle. The example in Fig. 1 has a 30° difference and therefore the range of the single plane sliding zones is 30° as shown on Fig. 1. A wedge formed by a pair of poles with one of those poles being in that zone will have the mechanism of single plane sliding on that plane. A wedge formed by a pair of poles both of which are outside that zone will have the mechanism of two plane sliding.

FIELD EXAMPLE: AUCKLAND, NEW ZEALAND

The rocks in the field area are interbedded sandstone and siltstone of the Miocene age Waitemata Group. Weathered rock and soil approximately 2 m thick is present at the top of the cliff. Coastal retreat in sedimentary rocks north of Auckland, New Zealand is controlled by bedding, joints and faults [22]. A report on a fatal rockfall at Rothesay Bay, in the northern suburbs of Auckland New Zealand by Hancox [23] concluded that the failure occurred by joint-controlled sandstone block failure related to erosional undercutting of a sandstone bed with heavy rain two weeks prior and a low to moderate earthquake 16 hours prior was likely to have influenced the timing.

Bedding dips very gently to the west (into the cliff face). Joints are close-spaced and clustered in two main sets with vertical to steep easterly dipping and northeasterly dipping orientations (Fig. 2, Table 2). Faults are also present with moderate to steep dips. Kinematic analysis shows that wedges can form with combinations of joints with faults and faults with other faults (Fig.3, Table 3).

Table 2 Structural readings from Rothesay Bay, Auckland, New Zealand

Dip	Dip Dir.	Structure	Notes
78	013	Joint set 1	N=41, SD=12.4
86	100	Joint set 2	N=40, SD=9.5
81	310	Fault 1a	
54	140	Fault 1b	
79	320	Fault 2a	
69	140	Fault 2b	
68	110	Fault 3	
49	290	Fault 4a	
55	076	Fault 4b	

Slope face orientation 70-063, height 30 m. N=number of points, SD=Angular standard deviation based on Fischer dispersion

DISCUSSION

The common practice of assessing wedge kinematic stability according to the line of intersection of the sliding planes fails to provide information on the shape of the wedges.

The method of assessing kinematic stability from the poles of sliding planes allows the shape of the wedges to be observed concurrently. This approach allows symmetrical and non-symmetrical wedges to be distinguished on the stereograph. Symmetry of wedges is observable according to the two factors: (1) the dip directions of sliding planes relative to the

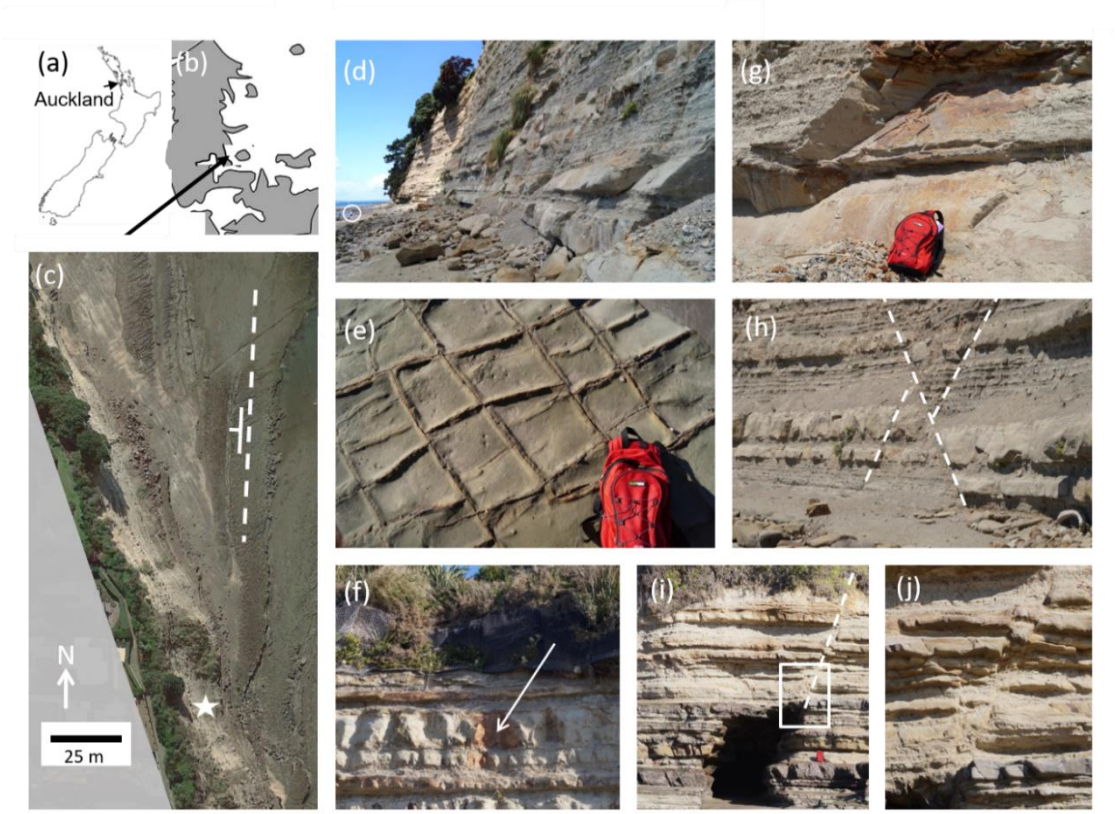

Fig. 2 Location maps (a-b) and satellite image (c) of the rocky cliffs south of Rothesay Bay, Auckland, New Zealand (Google Earth). Star shows approximate location of rockfall reported by Hancox [29]. Dashed line shows the strike of bedding on the rock platform. (d) Cliffs approximately 30 m high (person circled for scale) and slope of approximately 70º (dashed line). (e) Typical jointing pattern on the surface of a bed (backpack is approximately 30 cm wide. (f) Location near top of cliff where a joint-block in a bed has fallen from the cliff (arrow). (g) Joint surface dipping out of the slope face. (h) Conjugate faults (dashed lines). (i & j) A sea cave formed in the hangingwall of a fault

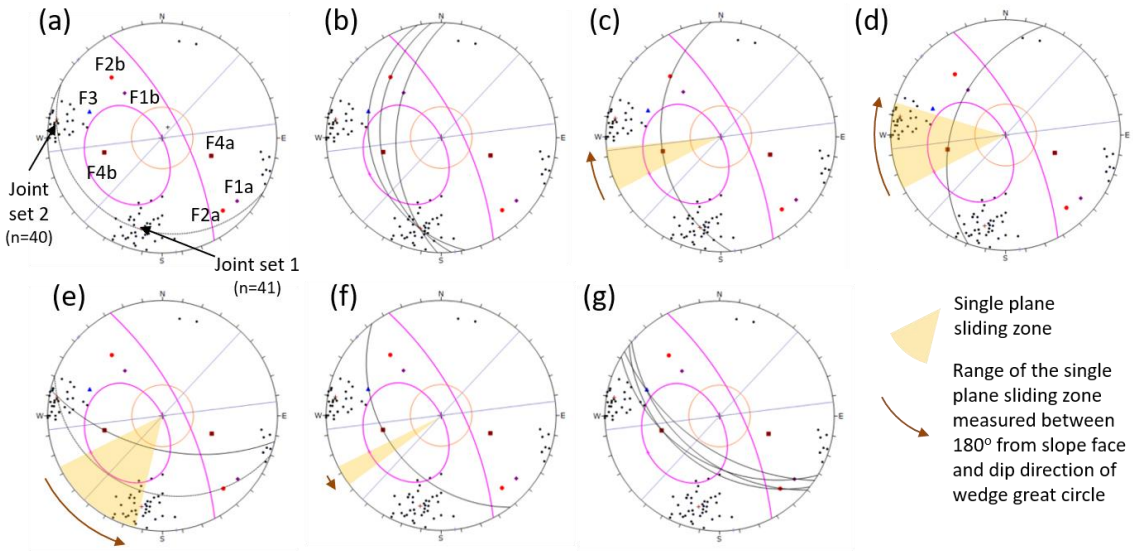

Fig. 3 Stereographic representations (equal angle, lower hemisphere) of structural data from the coastal cliff south of Rothesay Bay, Auckland. (a) Stereograph with joint sets and faults labelled F1-4 with conjugate pairs labelled a and b. The northeast facing slope is shown as a great circle and its daylight window (pink lines). The great circle (black line) between joints does not pass through the daylight window indicating stability. (b) Wedges between joint set 1 and east-southeast-dipping faults. (c,d) Single plane sliding on F4b forming a wedge with joint set 1 and faults. (e-g) Wedges formed by F4b, joint set 2 and other faults

Table 3 Potential wedges, Rothesay Bay, Auckland, New Zealand

Wedge	Wedge angle (°)	FoS	Mech	Fig.
W(J1-J2)	95	NW		5a
W(J1-F1b)	68	1.0524	1&2	5b
W(J1-f2b)	61	0.7515	1&2	5b
W(J1-f3)	88	0.386	1&2	5b
W(J1-f4b)	59	0.4043	slide on f4b	5c
W(F1b-F4b)	53	0.4043	slide on f4b	5d
W(J2-f1a)	32	NW		5e
W(J2-f2a)	43	NW		5e
W(J2-F4b)	38	2.5318	1&2	5e
W(F2a-F4b)	75	0.7825	1&2	5g
W(F3-F4b)	32	0.9316	1&2	5f
W(F2b-F4b)	57	0.4043	slide on f4b	5c
W(F1a-F3)	36	2.9526	1&2	5g
W(F2a-f3)	44	1.766	1&2	5g

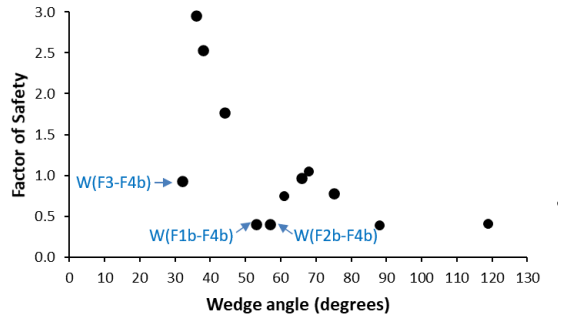

Fig.4 Stability and shape of wedges in Table 3. Anomalous low FoS cases are labelled

slope face and (2) the similarity dip of the sliding planes.

The factor of safety is closely related to the wedge shape and symmetry (Fig. 4). The factor of safety has been calculated by the limit-equilibrium method in the software 'Roscience SWedge' which is based on methods developed by Evert Hoek and colleagues [1]. Wedges with one or more of the planes close to the planar sliding direction (e.g. F4b) have lower factors of safety than the general trend (Fig. 4). This situation occurs in both single plane and two-plane sliding cases.

CONCLUSIONS

The relationship between wedge sliding compared to a rock slope face dip direction is described here as centered or off-center. This feature can be observed by the position of the poles of the sliding planes along their shared great circle. Only off-center wedges can slide with a single plane sliding mechanism.

The shapes of wedges are defined in terms of narrow, open and very open. This property can also be readily observed on a stereograph using the circle method of wedge analysis. The further apart are the poles along the great circle, the more narrow is the wedge. The closer the poles are located to each other the more open the wedge is. The more open a wedge is, the lower the factor of safety tends to be.

ACKNOWLEDGMENTS

The author acknowledges the discussions with Dr Christian Arnhardt, British Geological Survey on stereographic analysis of wedges.

REFERENCES

[1] Hoek E., Bray J. W., and Boyd, J. M., The stability of a rock slope containing a wedge resting on two intersecting discontinuities. Quarterly Journal of Engineering Geology and Hydrogeology 6 (1) 1973, pp. 1-55.

[2] Chan H.C. and Einstein H.H., Approach to complete limit equilibrium analysis for rock wedges—the method of "artificial supports". Rock Mechanics 14 (2) 1981, pp.59-86.

[3] Hudson J.A. and Harrison J.P., Engineering Rock Mechanics: An Introduction to the Principles. Elsevier. 1997, pp.1-444.

[4] Ghosh A. and Haupt W., Computation of the seismic stability of rock wedges. Rock Mechanics and Rock Engineering 22 (2) 1989, pp. 109-125.

[5] Aydan Ö., Kumsar H., An experimental and theoretical approach on the modeling of sliding response of rock wedges under dynamic loading. Rock Mechanics and Rock Engineering 43 (6), 2010, pp. 821-830.

[6] Kumsar H., Aydan Ö., and Ulusay R., Dynamic and static stability assessment of rock slopes against wedge failures. Rock Mechanics and Rock Engineering 33 (1) 2000, pp.31-51.

[7] Wang Y.J., Yin J.H., Chen Z., and Lee, C.F., Analysis of wedge stability using different methods. Rock Mechanics and Rock Engineering 37 (2) 2004, pp.127-150.

[8] Jimenez-Rodriguez R., and Sitar N., Rock wedge stability analysis using system reliability methods.

Rock Mechanics and Rock Engineering 40 (4) 2007, pp.419-427.

[9] Grenon M. and Hadjigeorgiou J., A design methodology for rock slopes susceptible to wedge failure using fracture system modelling. Engineering Geology 96(1-2), 2008, pp.78-93.

[10] Paronuzzi P., Bolla A., and Rigo E., 3D Stress–Strain Analysis of a Failed Limestone Wedge Influenced by an Intact Rock Bridge. Rock Mechanics and Rock Engineering 49, 2016, pp. 3223-3242.

[11] Mandalawi M.A., You G., Dowling K,. and Dahlhaus, P., Kinematic assessment of slopes at handlebar hill open cut mine, Mt. Isa, Queensland, Australia. International Journal of GEOMATE, 10(1), 2016, pp.1575-1583

[12] Alzo'ubi A.K., Rock slopes processes and recommended methods for analysis. International Journal of GEOMATE, 5(25), 2016, pp.2520-27.

[13] Barla G., Wedge Instability on the Abutment of a Gravity Dam in Italy. Geotechnical and Geological Engineering 35, 2017, pp.3025-3033.

[14] Basahel H., and Mitri H., Application of rock mass classification systems to rock slope stability assessment: A case study. Journal of Rock Mechanics and Geotechnical Engineering 9, 2017, pp.993-1009.

[15] Cerri R.I., Reis F.A.G.V., Gramani M.F., Rosolen V., Luvizotto G.L., do Carmo Giordano L., and Gabelini B.M., Assessment of landslide occurrences in Serra do Mar mountain range using kinematic analyses. Environmental Earth Sciences 77, 2018, pp.325.

[16] Sonnekus M. and Smith J.V., A review of selected unexpected large slope failures. International Journal of GEOMATE, 15(48), 2018, pp.66-73.

[17] Iyaruk A., Phien-wej N., and Giao P.H., Landslides and debris flows at Khao Phanom Benja, Krabi, southern Thailand. International Journal of GEOMATE, 16(53), 2019. pp.127-134.

[18] Wyllie D.C. and Mah, C., Rock Slope Engineering. Taylor & Francis. 2004, pp.1-456.

[19] Smith J.V., A method for assessing discontinuity poles for potential wedge sliding. Engineering Geology 202, 2016, pp.55-61.

[20] Öcal A. and Özgenoğlu A., Determination of sliding mode of tetrahedral wedges in jointed rock slopes. Rock Mechanics and Rock Engineering 30 (3) 1997, pp.161-165.

[21] Smith J.V. and Arnhardt C., Distinguishing between single and double plane sliding of tetrahedral wedges using the circle method. Engineering Geology 25, 2016, pp.98-101.

[22] Moon V.G. and Healy T.R., Mechanisms of coastal cliff retreat and hazard zone delineation in soft flysch deposits. Journal of Coastal Research 10, 1994, pp.663–680.

[23] Hancox G., Report on the fatal rock fall on the coastal cliff south of Rothesay Bay, Auckland, on 2 July 205, GeoNet Response Report No. 460W6000, 205, pp.1-7.

11th Int. Conf. on Geotechnique, Construction Materials & Environment,
Kyoto, Japan, 3-5 November 2021, ISBN: 978-4-909106063 C3051

IMPACTS OF SUFFUSION FACTOR ON HETEROGENIZATION OF SOILS

Koji Nakashima[1], Katsuyuki Kawai[1] and Takayuki Fumoto[1]

[1] Department of Civil and Environmental Engineering, Kindai University, Japan

ABSTRACT

In recent years, embankment structures have often failed due to extreme weather events, such as typhoons and torrential rains. Suffusion, in which finer particles within the soils are transported by seepage flow, causes heterogenization of the soils and may lead to deterioration of the embankment. Various suffusion factors, such as material properties and hydraulic conditions, have been confirmed. However, the impact of these factors on the degree of heterogenization is uncertain. In this study, repeated seepage tests on cylindrical specimens with different relative densities were conducted. X-ray CT scans of the specimens during the test were also performed. A greater erosion rate was observed in the first seepage flow experience, and a decreasing trend during seepage was observed to differ depending on the hydraulic gradient. It was confirmed that the relative density had a larger impact on the occurrence of suffusion compared to the hydraulic gradient or the number of seepage events. Investigation of CT images demonstrated that heterogenization of soil had occurred by the formation of lower density zones within the samples.

Keywords: Seepage, Erosion rate, Hydraulic gradient, Relative density

INTRODUCTION

In recent years in Japan, embankment structures, such as levees and earth dams, have often failed due to the torrential rain and devastating flood events that accompany climate change. Causes of levee failure, such as overtopping, increasing pore water pressure and piping, have mainly been mentioned. Furthermore, the existence of deteriorated areas within the structures also proves critical in terms of operation and maintenance and should be carefully considered.

Natural soil materials are used for construction of the embankment structures; hence, it is thought that they have irregular homogeneity in terms of material (*e.g.* particle size distribution, density) and mechanical (*e.g.* permeability, strength) properties. Internal erosion, which is the migration of soil within the embankment, also has a large impact on the heterogenization of the soil materials and may lead to deterioration of structures and, in the worst case, catastrophic failure during a flood event. Internal erosion can be classified into four types: suffusion, backward erosion, contact erosion and concentrated leak erosion [1]. This study focuses on suffusion, in which finer soil particles are transported among the voids of the coarse fraction following seepage flow (Figure 1). Void change due to migration of fines induces various geotechnical concerns. Several laboratory experiments have previously revealed suffusion factors, such as material properties and hydraulic conditions [2]. However, the impact of these factors on the degree of heterogenization is uncertain. Understanding them is vital to improving the resilience of the embankment structure against extreme rain and flooding events.

On the other hand, suffusion is a microscopic phenomenon; hence, it is quite difficult to visually understand the deterioration of the structures derived from it. Internal visualization using X-ray CT images is useful for investigating the mechanical behavior of engineering materials, and several laboratory experiments have previously utilized this method in the geotechnical engineering field as well. Nguyen et al. [3] captured CT images during a suffusion test and investigated the microstructural changes during the suffusion process, such as strain fields, spatial distribution and fines content.

In this study, repeated seepage experiments on cylindrical specimens with different relative densities were conducted. X-ray CT scans of the specimens during the test were also performed.

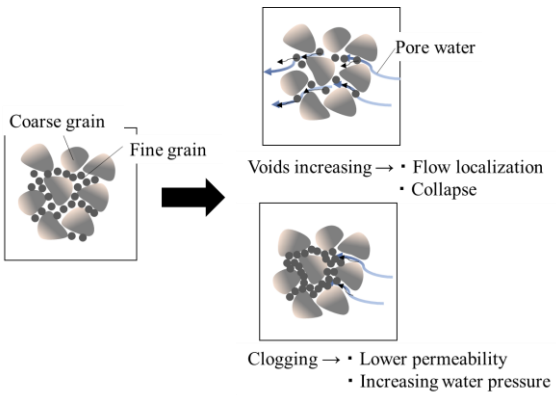

Fig. 1 Schematic illustration of suffusion

EXPERIMENTAL STUDY

Test material

The test material was prepared by mixing No.3 and No.7 silica sands, in equal portions by weight. The particle size distribution curve of the test material is shown in Figure 2. The test material is generally classified as gap-graded soils, which are often internally unstable. Chang and Zhang [4] proposed the criterion of internal instability by applying gap ratio G_r, as illustrated in Figure 3. This is defined as the ratio of the maximum particle size d_{max} and the minimum particle size d_{min}. Soils which have fines content of less than 10% are classified as stable when the gap ratio is smaller than 3.0. The gap ratio of the test material was G_r=4.72 (d_{max}=1.18mm, d_{min}=0.25mm). Alternatively, the criterion proposed by Kenny and Lau [5] is well known for classifying internal stability of soils and can be defined by two parameters, H and F, which are obtained from particle size distribution curves (Figure 3). Soils which have minimum H/F of more than 1.3 are classified as stable. From the particle size distribution curve of the test material, minimum H/F was calculated as $(H/F)_{min}$=0.05. According to both of these criteria, the test material can be interpreted as having the potential for instability to internal erosion. The material properties are presented in Table 1.

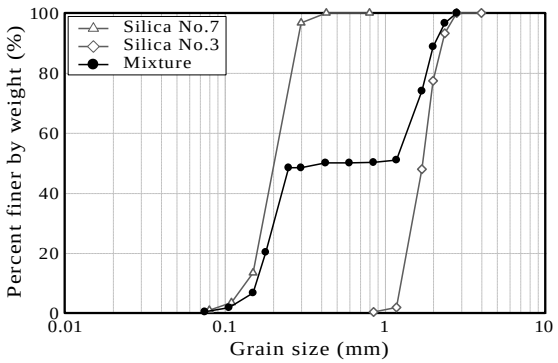

Fig. 2 Particle size distribution curve

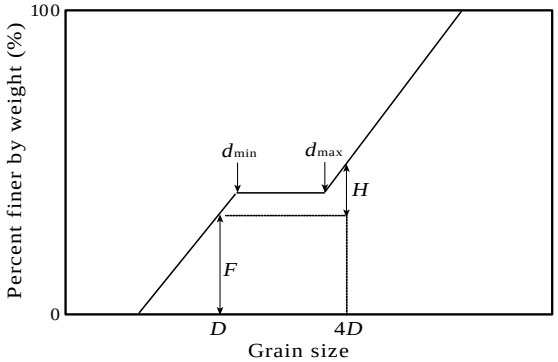

Fig. 3 Definition of parameters for internal instability

Table 1 Material properties

Specific gravity G_s	Uniformity coefficient U_c	Maximum void ratio e_{max}	Minimum void ratio e_{min}
2.60	8.81	0.83	0.48

A constant head permeability test of the test material was conducted for 24 hours. Figure 4 shows the fluctuation of the coefficient of permeability k during the permeability test. The results indicate that permeability slightly decreased with time.

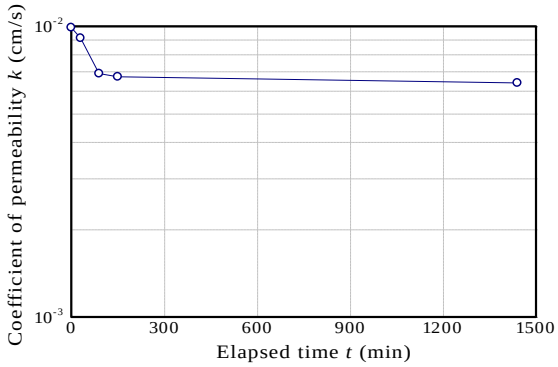

Fig. 4 Results of constant head permeability test

Test procedures

The prepared unsaturated test material was installed into a cylindrical acrylic column, and the specimen was constructed by compaction of five layers at a target relative density. Figure 5 illustrates an overview of the test equipment. A 0.23mm mesh filter was set to allow the washing away of finer particles. Water from the upper tank was supplied to the bottom of the specimen. A hydraulic gradient was constantly maintained by the water level difference between the upper tank and top of the specimen.

The repeated seepage tests were conducted to investigate heterogenization of the soils due to cyclic hydraulic power, as shown in Figure 6. The cylindrical column was installed into the X-ray testing apparatus (Figure 7), and CT scans were also performed at points (a)~(f) shown in Figure 6. CT images were captured under the acquisition conditions explained in Table 2. After specimen preparation, the specimen was saturated with water for 24 hours. The upper tank was then lifted to the target position where the hydraulic gradient would be the critical hydraulic gradient i_c. This position was maintained for 0.5 hours. Drainage water from the top of the specimen was collected every 6 minutes, for 5 collections in total; flow rates and turbidity were measured. After seepage, the water supply was stopped, and the CT images of the specimen were captured. Next, the upper tank was lifted so that the

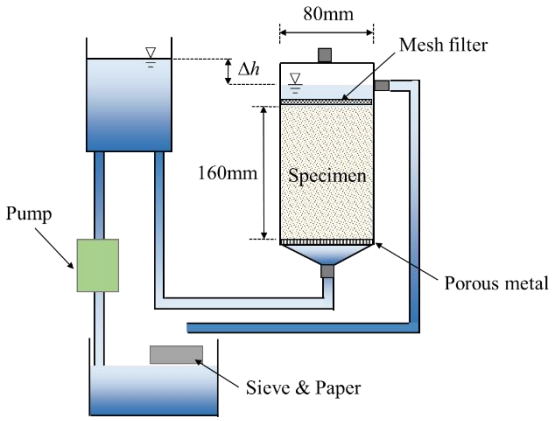

Fig. 5 Overview of test equipment

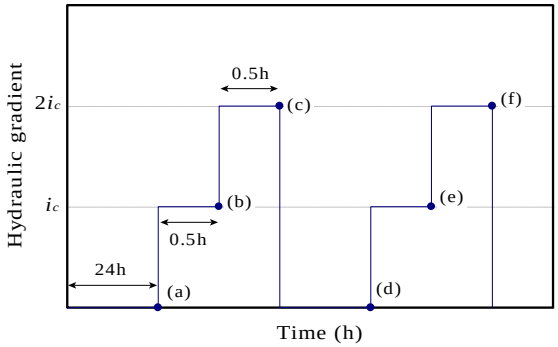

Fig. 6 Test condition

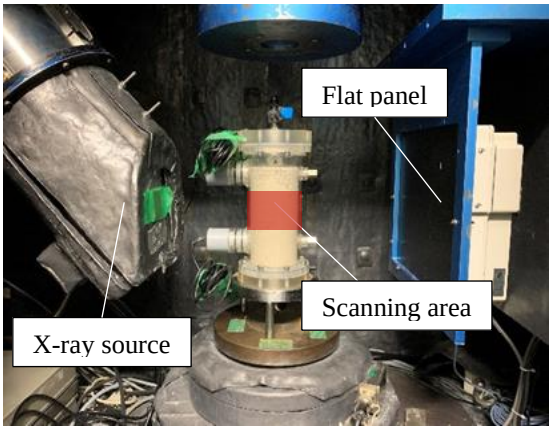

Fig. 7 X-ray testing apparatus

Table 2 Acquisition conditions of CT images

Voltage (kV)	Current (μA)	Frame rate (fps)	Projection views	Resolution (mm/pixel)
180	100	3.0	2000	0.0615

hydraulic gradient would be $2i_c$, and measurements and X-ray CT scans were conducted. After the CT scan, the water within the specimen was temporary drained by gravity. The soil was again saturated with water, and the seepage test was performed in the same manner as in the first cycle described above.

In this study, the seepage tests were performed on specimens with relative densities of D_r=60% and 80%. The theoretical critical hydraulic gradient i_c is 0.98 for the specimen of D_r=60%, and 1.03 for D_r=80%. Hereinafter, in the test results section below, the graph legend is displayed as "relative density"-"hydraulic gradient"-"cycle". For example, d60-i2-c2 means the result of the test at $2i_c$ of the second cycle for the specimen compacted at the relative density of 60%.

TEST RESULTS

The following sections explain the test results in terms of erosion response, fluctuation of permeability, and CT images. For the soil specimen with relative density of 60%, boiling failure was immediately observed at $2i_c$ of the first seepage cycle, as displayed in Figure 8. Because of this, the seepage test was then finished at this point.

Fig. 8 Failure state of the specimen

Erosion and permeability response

Figure 9 shows the results of turbidity during the seepage tests. The turbidity tended to gradually decrease in each case. Greater turbidity was confirmed in the results for D_r=60% compared to those for D_r=80%. As shown by the results for D_r=80%, the greatest turbidity was observed at the beginning point of i_c in the first seepage cycle. It is

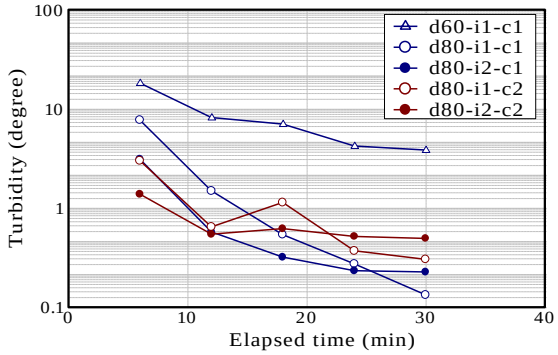

Fig. 9 Turbidity during seepage

presumed this was because the sands had never experienced an erosion history. Hence, less turbidity was observed at the beginning point of the second seepage cycle compared to the first seepage cycle. It was also confirmed that the turbidity of the beginning point of the second cycle was greater than that of the terminate point of the first cycle. This is probably because soil structure changed due to the downward drainage by gravity after the first cycle.

Turbidity of the artificial suspension was measured in advance. The relationship between the turbidity and the density of the soil in the suspension was then investigated, and can be approximated by a linear function, as shown in Figure 10. Using this, the values of the turbidity measured from each test can be converted into density. As an example, the result of d60-i1-c1 is shown in Figure 11. The eroded soil mass can be obtained by applying a non-linear approximation, as follows, and integrating it.

$$M_e(t) = -a\left[1-\exp\left(-bt\right)\right]+c \qquad (1)$$

Where, a, b and c are the constant determined by fitting, and t denotes the elapsed time. Subsequently, an instantaneous erosion rate was calculated from the following formula [6]

$$R_e(t) = \frac{M_e(t)}{M(t)} \qquad (2)$$

Where, $M_e(t)$ is the eroded soil mass obtained from Eq. (1). $M(t)$ is the total soil mass at a certain time. The fluctuations of the instantaneous erosion rate are shown in Figure 12. For the results of seepage with i_c, the instantaneous erosion rate decreased linearly with time; whereas, for the results of $2i_c$, the trend showed a smooth curvature. The cause of this is uncertain, yet, it implies that the seepage condition has some sort of influence on erosion progression. Figure 13 shows the relationship between the erosion rate and hydraulic gradient. The erosion rate is plotted as the rate of total eroded soil mass to initial total soil mass. In the figure, the hydraulic gradient is shown as the value obtained from the test condition. For D_r=60%, greater erosion rate was confirmed compared to results for D_r=80%. Therefore, the relative density of soils have larger impacts on the degree of suffusion compared to the hydraulic gradient or the number of seepage events.

Marot et al. [7] proposed the expanded energy equation, which is the time integration of the instantaneous power dissipated by water seepage for the experimental duration, as follows.

$$E_{flow}(t) = \sum_{0}^{t} Q\gamma_w \Delta h \Delta t \qquad (3)$$

where, Q (m^3/s) is the flow rate of water; γ_w (kN/m^2) is the unit weight of water; Δh is the difference of water level between the upstream section and the

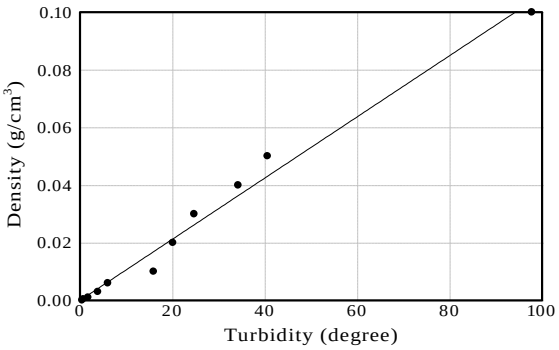

Fig. 10 Relationship between turbidity and density

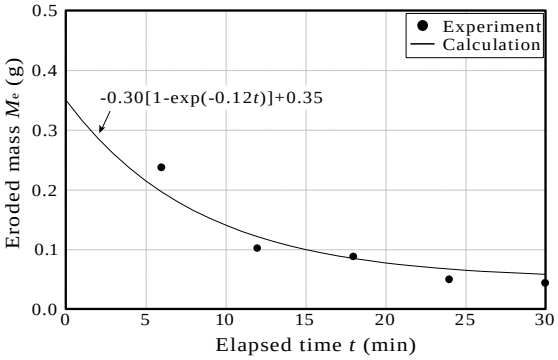

Fig. 11 Eroded soil mass

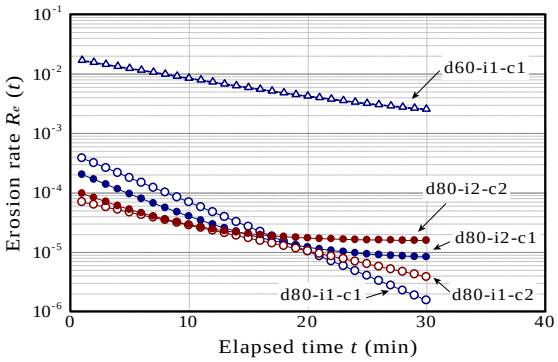

Fig. 12 Instantaneous erosion rate

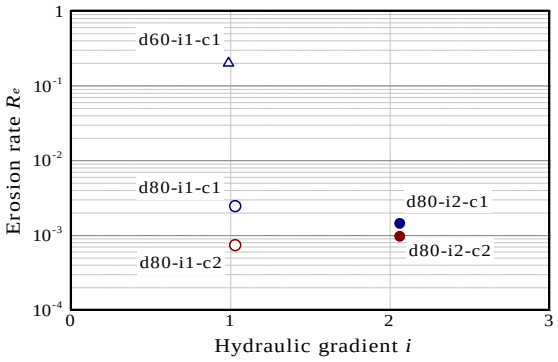

Fig. 13 Relationship between erosion rate and hydraulic gradient

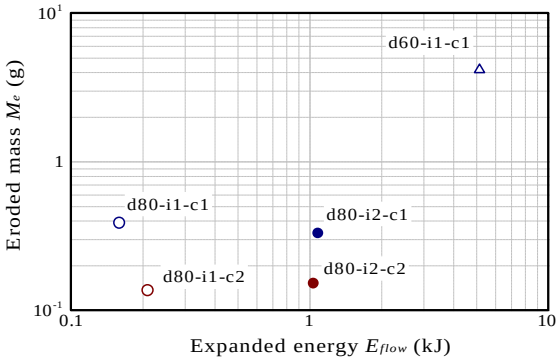

Fig. 14 Relationship between eroded mass and expanded energy

downstream section; and Δt is the time for a certain duration. Figure 14 represents the relationship between the total eroded soil mass and the expanded energy. According to the previo column us results [7], the eroded mass increased in agreement with an increase in the expanded energy. The results obtained from this study show approximately similar trends.

Figure 15 shows the fluctuation of the coefficient of permeability during the seepage tests. The coefficient of permeability tended to gradually decrease with time in each case. The trend appeared significant with the first seepage event, and the magnitude decreased about a tenth. A similar trend was also confirmed from the constant head permeability test, as represented above. Moreover, this trend roughly corresponded to the turbidity fluctuation. It could be interpreted that the decreasing turbidity implies a clogging of fine particles, thus forming a poorly permeable area. It can be observed that permeability at the beginning of the second seepage cycle recovered compared to that of the terminate point of the first cycle. This is because the soil structure changed due to the downward drainage of gravity between the cycles, as mentioned before, and the permeable area could change.

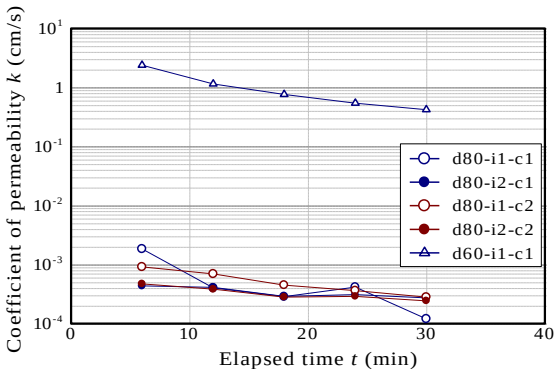

Fig. 15 Fluctuation of the coefficient of permeability

Heterogenization under seepage history

For investigating the heterogenization of soils due to the seepage force, the gray values of the CT images were analyzed. Figure 16 shows the results obtained by subtracting the gray values of CT images at each point in Figure 6. The white parts of the images indicate the area where the density increases due to seepage. The results for D_r=80% explicitly show the remarkable heterogenization of soil in the layer where the density had potentially become loose. Less heterogenization can be observed around the layer boundary where the soils were densely compacted during specimen preparation. Greatest variation was confirmed at i_c of the second seepage cycle, yet an obvious variation related to the magnitude of hydraulic gradient cannot be specifically observed. Results for D_r=60%, as opposed to the results of D_r=80%, seem to indicate that the heterogenization of the entire soil dominates, rather than local heterogenization; however, further investigation is needed on this point.

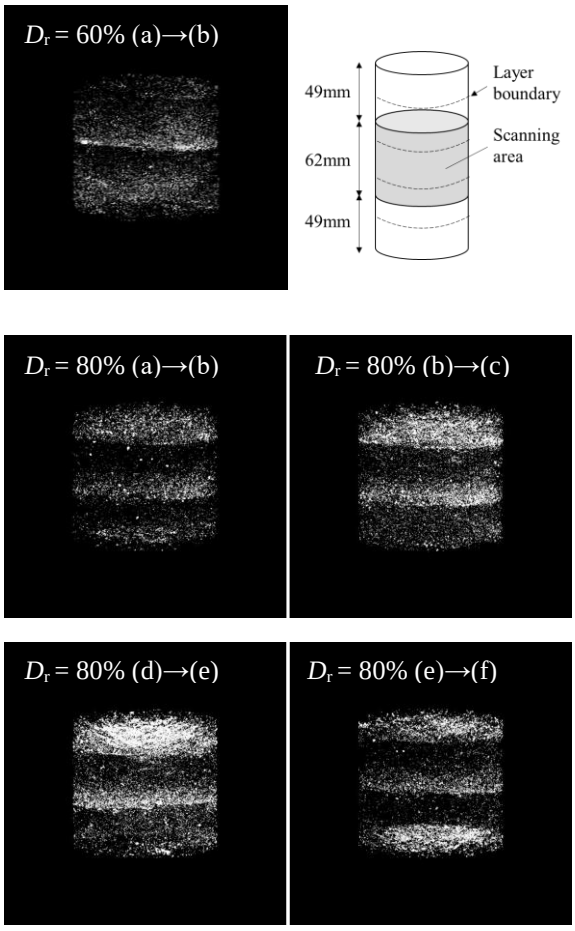

Fig. 16 Heterogenization due to seepage

CONCLUSIONS

In this paper, repeated seepage tests on specimens with different relative densities were conducted to investigate the impact of suffusion factors on the degree of heterogenization of soils. Visualization of the progressive changes within the soils using CT images of the specimen under seepage histories was also performed. The following conclusions were drawn;

1) Turbidity under seepage tended to gradually decrease with time regardless of the test condition. Greater turbidity was confirmed for D_r=60% compared to D_r=80%. The decreasing trend of instantaneous erosion rate during seepage differed depending on the hydraulic gradient. In general, the relative density of soils have larger impacts on the degree of suffusion compared to the hydraulic gradient or the number of seepage events.
2) The coefficient of permeability tended to gradually decrease with time in each case. The trend appeared significantly in the first seepage event. Additionally, it was observed that this trend roughly corresponded to turbidity fluctuation.
3) Investigation of CT images demonstrated that heterogenization of soil had occurred by the formation of lower density zones within the samples. An obvious variation related to the magnitude of hydraulic gradient could not be observed.

REFERENCES

[1] Fell, R., Fry, J.J., State of the art on the likelihood of internal erosion of dams and levees by means of testing. In: Bonelli, S. (Ed.), Erosion in Geomechanics Applied to Dams and Levees. ISTE-Wiley, London, UK, 2013, pp.1-99, Chapter 1.

[2] Horikoshi, K., Takahashi, A., Suffusion-induced change in spatial distribution of fine fractions in embankment subjected to seepage flow, Soils and Foundations, Vol. 55(5), 2015, pp. 1293-1304.

[3] Nguyen, C.D., Benahmed, N., Andò, E., Sibille, L., Philippe, P., Experimental investigation of microstructural changes in soils eroded by suffusion using X-ray tomography, Acta Geotechnica, Vol.14, 2019, pp. 749-765.

[4] Chang, D.S., Zhang, L.M., Extended internal stability criteria for soils under seepage, Soils and Foundations, Vol. 53(4), 2013, pp.569-583.

[5] Kenny, T.C., Lau, D., Internal instability of granular filters. Canadian Geotechnical Journal, 22(2), 1985, pp.215-225.

[6] Sato, M., Kuwano, R., Suffusion and clogging by one-dimensional seepage tests on cohesive soil, Soils and Foundations, Vol. 55(6), 2015, pp.1427-1440.

[7] Marot, D., Rochim, A., Nguyen, H.H., Bendahmane, F., Sibille, L., Assessing the susceptibility of gap-graded soils to internal erosion: proposition of a new experimental methodology, Natural Hazards, 83, 2016, pp.365-388.

11th Int. Conf. on Geotechnique, Construction Materials & Environment,
Kyoto, Japan, 3-5 November 2021, ISBN: 978-4-909106063 C3051

MEASUREMENT OF THE FROST HEAVE ACTING ON THE FULL SIZE GROUND ANCHOR AND SOIL NAILING

Atsuko Sato[1], Osamu Hatakeyama[1], Hirochika Hayashi[1], Masahiko Yamaki[1], Jun Ikeda[2], Takayuki Iizuka[2], Noboru Mikami[2], Tuyoshi Nakamura[3], Fumitada Mikami[3] and Yuji Kyouden[3]

[1]Civil Engineering Research Institute for Cold Region, Japan; [2]Nittoc Construction Co., Ltd., Japan; [3]Japan Foundation Engineering Co., Ltd., Japan

ABSTRACT

In snowy and cold regions such as Hokkaido, ground anchor and soil nailing are damaged by frost heaves, and their functions are considered to be degraded, which is a problem in maintenance. However, the relationship between the degree of frost heaving power and the time of action and damage has not been clarified. For this reason, a design method and a maintenance management method that take into account frost heave prevention technology have not been established for slope structures. In order to understand the mechanism of damage caused by frost heave and to study the technology for countermeasures against frost heave, a full-scale test and construction was performed on the ground anchors and the soil nailings, and the applied load was measured. For ground anchors, we focus on the free length, introduced tension load, and pressure receiving area, and for soil nailings, we focus on the length of the reinforcing material and the area of the pressure receiving plate. As a result of the measurement, the frost heaving force exceeding the design load was applied to the ground anchors and the ground reinforcement soil works in the winter period. It was also found that the freezing depth could be reduced by covering the ground with continuous fiber reinforced soil and rubber mat.

Keywords: Frost heaving force, ground anchors, soil nailings, frost depth, full size

INTRODUCTION

In cold, snowy regions such as Hokkaido, frost heave damages ground anchors and soil nailngs, reducing the functionality of these structures. Administrators have considered this damage as an issue to be addressed in order to improve maintenance and management techniques for these structures [1]. However, the relationship between the degree and the period of frost heave force acting on these structures and the resulting damage has not been clarified. Therefore, design methods and maintenance and management methods that consider frost heave countermeasure technologies for slope retaining structures have not been established. To clarify the mechanism behind frost heave damage to ground anchors and soil nailngs, we constructed full-scale experiment models for these two types of soil nailngs and measured the loads acting on the structures. As investigation items for ground anchors, we focused on the free length, the initial tension load, and the area of the pressure plate. For soil nailngs, we focused on the length of reinforcing materials and the area of the pressure plates. We investigated a frost heave countermeasure for ground anchoring and earth reinforcement work. The pressure plates of the ground anchors and the soil nailngs were covered with continuous fiber-reinforced soil or rubber mats, which were the insulating materials, and we measured and compared the temperatures of the ground under each insulation material to those without a countermeasure [2], [3]. This paper summarizes the results.

TEST METHODS

Basic data for the ground anchor systems and the soil nailngs

To measure the frost heave force that acts on ground anchor and earth reinforcement work using soil nailings, we constructed these two types of structures at an experiment site in Tomakomai, Hokkaido, the northernmost prefecture of Japan. The basic data for the constructed ground anchors and the soil nailings are shown in Tables 1 and 2.

The ground anchor and the soil nailing were installed at the locations shown in Fig. 1. Investigations were done comparing the target parameters set for the 6 ground anchors. The difference based on the free length was tested using GA-1 and GA-2. The difference based on the tensioning strength was tested using GA-3, GA-4, and GA-5. The difference based on the area of the pressure plate was tested using GA-5 and GA-6. Comparison investigations were also done for the soil nailings. RB-1 and RB-3 were for comparison of different lengths of reinforcement materials. The difference in the areas of the pressure plates was examined by using the pair of RB-1 and RB-3 and that of RB-2 and RB-4. The design area of the pressure plate is determined depending on the bearing capacity

Table 1 The basic data for the constructed ground anchors

	Type	Anchoring load (kN)	Allowable load (kN) 0.6Tus(JIS) Ordinary condition	0.9Tys(JIS) During earthquakes	0.9Tys Test table	Apparent free length (m)	Anchoring length (m)	Area of pressure plate (m^2)
GA-1	PC steel wire φ15.2	70	156.6	199.8	227	7.00	10.0	3.13
GA-2						14.00	4.0	
GA-3	PC steel wires φ9.5×7	235	428.4	547.2	648	18.85	6.0	5.62
GA-4								
GA-5		400						
GA-6						18.71		4.14

Tus: Tensile load Tys: Yield load

Table 2 The basic data for the constructed soil nailings.

	Type	Anchoring load (kN)	Allowable load (kN)	Anchoring length(m)	Area of pressure plate(m^2)
RB-1	SD345-D25	20	137	7.0	0.16
RB-2				5.0	
RB-3				7.0	0.10
RB-4				5.0	

Fig. 1 Installation location of ground anchor and soil nail

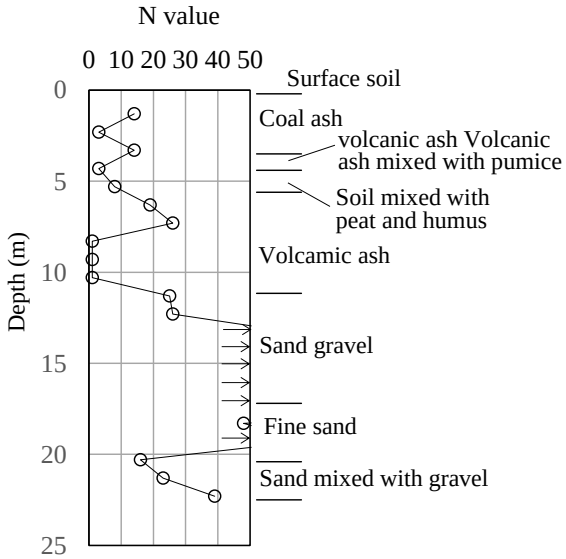

Fig. 2 Columnar section of construction site.

of the ground (the bearing power of soil), on which the pressure plate is installed, and on the design load. In the experimental installation in this study, pressure plates with different areas were used to investigate the possibility of reducing the frost heave force acting on the pressure plates according to the differences in the area. The pressure plates used with the ground anchors were steel, and those used with the soil nailing were glass fiber or carbon fiber composite reinforced plastic grids

Construction method

We installed the ground anchors and soil nailings in ground whose geologic columnar section is shown in Fig. 2. To equalize the conditions for frost heaving force for the ground anchors and soil nailings, we replaced the soil layer at the installation site. A 90cm-deep soil layer was replaced with frost susceptible material that has the basic physical properties shown in Table 3. When ground anchors and soil nailings are constructed on the slope, water supply from the back of the structures affects frost heaving, depending on the height of the structure on the slope. In this study, we constructed the ground anchors and soil nailings on flat ground to equalize the frost heaving conditions for all structures. The replaced material had a high

Table 3 Basic physical properties of the frost susceptible material

Physical characteristics		Value
Soil particle density ρ_s (g/cm^3)		2.678
Natural water content w_n (%)		50.0
Grain size characteristics	2mm-(%)	25.6
	75μm-2mm (%)	30.9
	-75m (%)	43.5
Ground material classification		SFG
Liquid limit w_L(%)		63.3
Plastic limit w_P (%)		42.4
Cone index q_c (kN/m^2)		667
Frost-susceptible	Frost heave rate (mm/hr)	0.78
	Degree of compaction (%)	94.6
Max. dry density ρ_{dmax} (g/cm^3)		1.125
Optimum moisture content w_{opt} (%)		42.9

frost susceptibility, with a freezing rate of 0.78mm/h [4]. The cone index of this material with natural water content was 667kN/m^2. Construction machines such as bulldozers were able to travel on this material safely; however, roller compaction machines such as tier rollers were not [5]. Because of the strength properties of the material, the test ground was prepared by using a bulldozer. We considered that installing these structures on the slope would not result in equal the water supply conditions because of the different installation heights of the structures. Therefore, we constructed the ground anchors and the soil nailings on flat ground. The covering materials were a layer of 20cm-thick continuous-fiber reinforced soil and a 2cm-thick rubber mat. Each covering material is 2m long and 2m wide, and the construction area is 4m^2.

Measurement method

The load acting on the pressure plate was assumed as the frost heaving force acting on the ground anchors or soil nailing. This load was measured by installing a hollowed load cell between the pressure plate and the bearing plate of each structure. To understand the freezing conditions of the ground, soil temperatures were measured by using temperature sensors installed at an interval of 10cm in the depth direction from the ground surface. The air temperature at the height of 1.5m was also measured. The load and temperatures were automatically measured every hour. The frost heave-induced displacements for the ground anchors and soil nailings were surveyed every two weeks at the locations shown in Fig. 3. The snow depth was measured at the same time as these measurements. To measure the changes in height, concrete blocks were placed as markers on the continuous fiber-reinforced

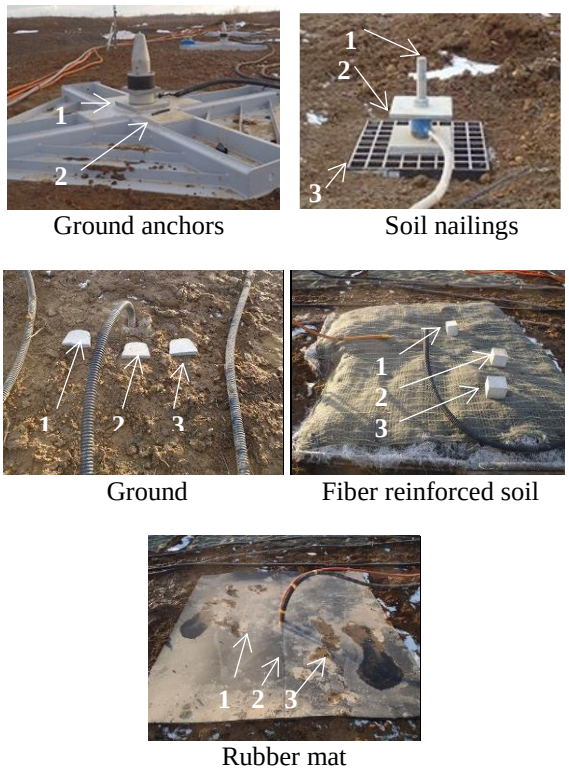

Ground anchors Soil nailings

Ground Fiber reinforced soil

Rubber mat

Fig. 3 Measurement position.

soil and the ground without a reinforcing structure, and marks were painted on the rubber mat.

TEST RESULTS

Deformation of the ground anchors and the acting load

Fig. 4 shows the air temperature, snow depth, and freezing conditions of the ground. Fig. 5 shows the displacements of the ground anchors, and Fig. 6 shows the loads acting on the ground anchors. When the ground started to freeze and the cumulative daily average air temperatures were negative, the load acting on the pressure plate started to increase. Which indicated that the frost heaving force was starting to act on the structure. After reaching the maximum, the frost heaving force gradually decreased. When the daily average air temperatures became constantly above the freezing point, the frost heaving force of the ground anchors became smaller than the fixing load. The displacement of GA-2, whose free length is greater than that of GA-1, was greater than the displacement of GA-1. The load acting on GA-2 was slightly lower than that acting on GA-1. The frost heave force was thought to be controlled in GA-2, whose free length was great. The greater displacement of GA-2 is thought to have absorbed the frost heave force. In the comparison among the ground anchors with different tension strengths (GA-

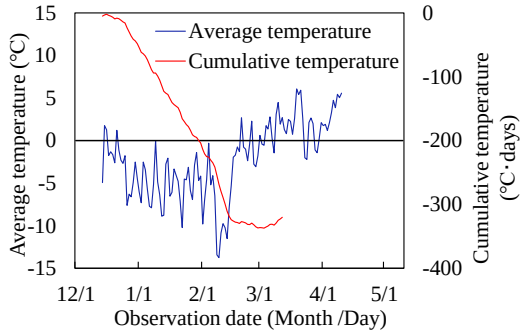

Average temperature and Cumulative temperature

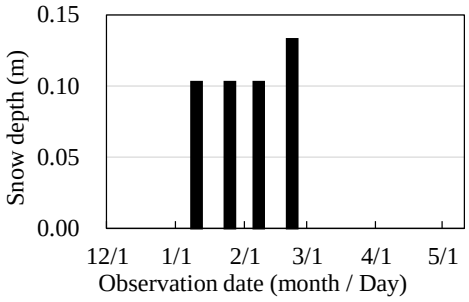

Snow depth

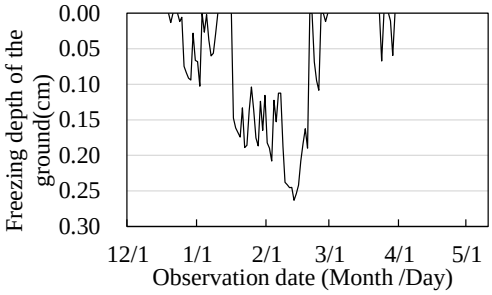

Freezing depth of the ground

Fig. 4 Status of measurement points.

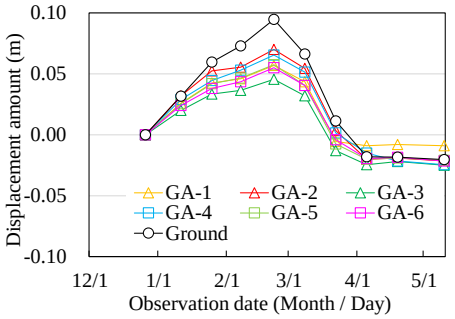

Fig. 5 Displacement amount of ground anchors.

3, GA-4 and GA-5), the load was greater for GA-5, whose tension strength was the greatest. From this, we found that it is necessary to be careful about setting the tension strength of the ground anchors when installing them in ground where frost heave force may act on them. The frost heave force acting

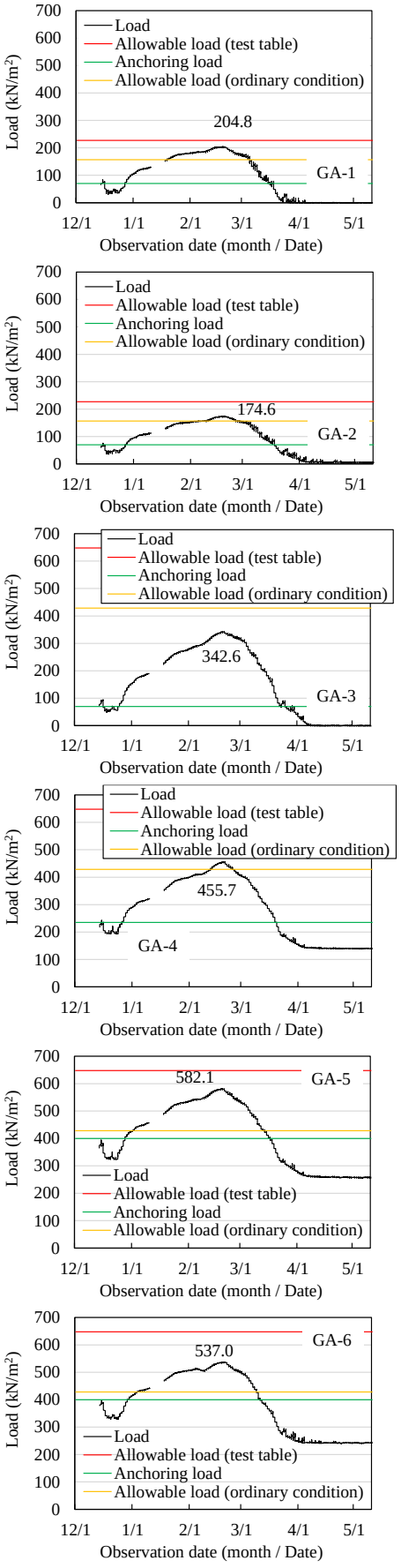

Fig. 6 Loads acting on the ground anchors.

on the unit area of the pressure plate under the same soil and freezing conditions is equal. For GA-5 and GA-6, in which the areas receiving pressure were different, the frost heave force acting on the ground anchors, whose pressure-receiving area was small, was considered to be small. In the measurement, we found that the frost heave force at GA-6, whose pressure-receiving area was small, was slightly smaller than that of GA-5. The displacement in GA-6 was also smaller than that of GA-5. In constructing ground anchors, if we only consider the frost heave force, it is possible to control that force by designing the pressure plate such that its area is small. We also found that loads which were far greater than the normal-time allowable load acted on five of the pressure plates, excluding that for GA-3. When the air temperature rose and the ground started to melt at each ground anchor, the frost heave force became small, even smaller than the original fixing load. The displacement at this time indicated that the heights of the markers were lower than the original heights. It is considered that the real fixing load for the ground anchor was smaller than the design fixing load because the ground around the ground anchors at the application of the initial tension was slightly frozen. This initial state of ground is also considered to be why the final heights of the markers were lower than those at the start of the observation. The construction and tensioning of ground anchors should be done before the ground freezes.

Deformation of the soil nailings and the acting load

Fig. 7 shows the displacement of the soil nailings, and Fig. 8 shows the loads acting on the soil nailings. There was almost no displacement due to frost heaving in soil nailings. Similar to the load condition of the ground anchors, the load acting on the pressure plates of the soil nailings started to increase when the ground around them started to freeze, and it became small when the frozen ground melted. It is understood that frost heave force acted on the pressure plates.

The loads acting on RB-1 and RB-2 (soil nailings with greater areas) were compared with those acting

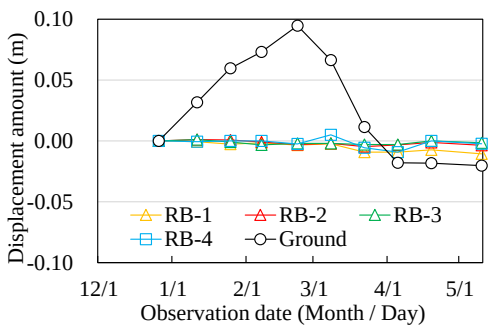

Fig. 7 Displacement amount of soil nailings.

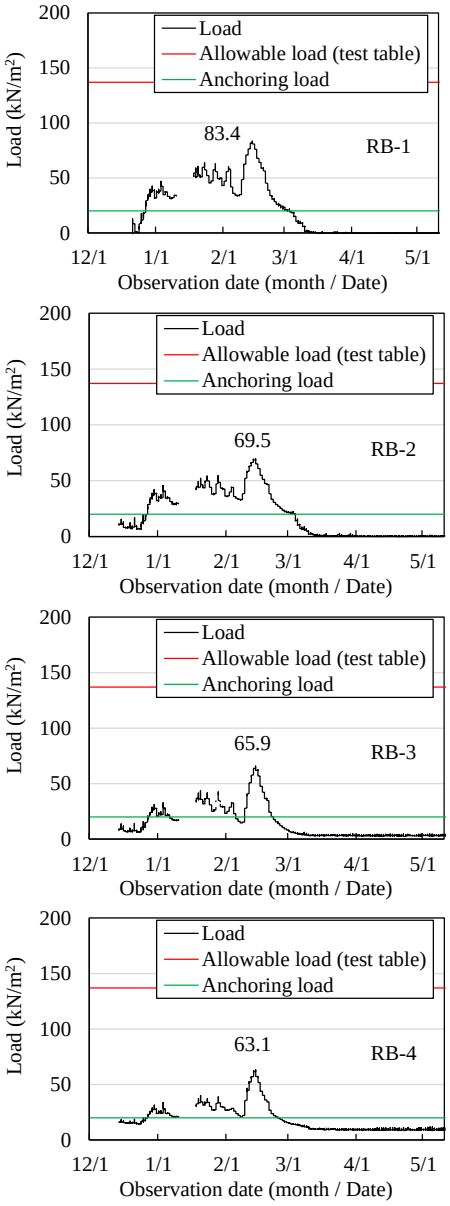

Fig. 8 Loads acting on the soil nailings.

on RB-3 and RB-4 (soil nailings with a smaller areas). It was found that the loads acting on the pressure plates with greater areas were slightly smaller than those acting on the pressure plates with smaller areas. When the areas of two pressure plates were equal but the lengths of the reinforcement material were different, the loads acting on them were nearly equal.

Deformation from frost heaving of the covered structures, and control of the loads acting on the structures

The displacement of the ground depending on the difference in covering are shown in Fig. 9. The frost penetration depth of the ground depending on the

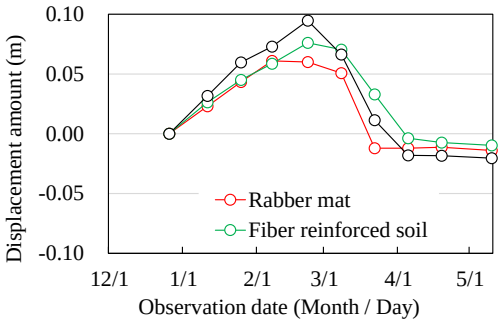

Fig. 9 Displacement of the covering part.

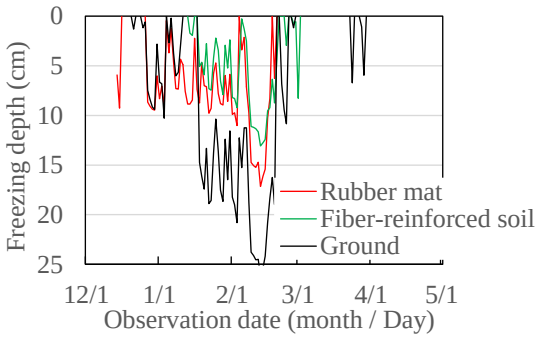

Fig. 10 Freezing depth of the ground at the covered area.

difference in covering are shown in Fig. 10. The heights of the continuous fiber-reinforced soil and the rubber mat started to increase at the same time that the displacement of the ground without covering started to increase from frost heaving, and these heights started to decrease when the heaving from freezing in the ground without covering started to decrease. The two test structures with covering had lower heights at the end of the measurements than before the start of measurements. This is thought to be because the ground was already frozen on the day when the measurement was started. The displacements of the soil nailings with covering were about 2cm smaller than those of the soil nailing without covering. The soil nailing covered with a rubber mat returned to its original height about two weeks earlier than the ground without covering did. The continuous fiber-reinforced soil took longer than the other two to return to its original height. The frost penetration depth of the ground without covering was the greatest, that of the rubber mat covering was next, and that of the continuous fiber-reinforced soil was the shallowest. In controlling the frost penetration depth and the deformation from frost heaving, it considered effective to cover the structures with rubber mats or continuous fiber-reinforced soil.

SUMMARY

Ground anchors and soil nailings were constructed on frost-susceptible ground, and deformation of the structures from frost heaving was investigated. The effects of covering on the structures were also investigated. The findings are as follows.

[1] Frost heave force that exceeded the design load (normal time) acted on the ground anchors. The pressure plates of the ground anchors were lifted with the increase in the frost heaving. The frost heave force acting on the pressure plate was greater for greater free lengths, greater tension strengths, and greater areas of the pressure plate.

[2] The frost heave force of the ground acted on the soil nailing; however, no considerable deformation from frost heaving was observed. For the pressure plate of the soil nailing with a greater area, the frost heave force was slightly greater.

[3] Covering the structures with rubber mats or continuous fiber-reinforced soil was found to be effective in controlling the frost penetration depth and the deformation from frost heaving.

REFERENCES

[1] Study Group Concerning an Investigation and Design Method of Frost-Heaving Countermeasure, Investigation and design manual for frost protection of slopes (Draft), Public Interest Incorporated Association, The Japanese Geotechnical Society, Hokkaido Branch, 2016 (in Japanese).

[2] Masahiko Yamaki, Atsuko Sato, Osamu Hatakeyama, Jun Ikeda, Takayuki Iizuka and Tsuyoshi Nakamura, A Consideration on Heat Conduction Analysis for Frost Heave Countermeasures, Japan Society of Civil Engineers Hokkaido Branch Paper Report, No. 76, 2020, C-02 (in Japanese).

[3] Atsuko Sato, Osamu Hatakeyama, Jun Ikeda, Takayuki Iizuka, Noboru Mikami,Tsuyoshi Nakamura, Fimitada Miura and Yuji Kyouden, , Measurement of the frost heave acting on the full size ground anchor and soil nailing, 54rd Japan National conference on Geotechnical Engineering, No.54, 2019, pp.789-790 (in Japanese).

[4] Japanese Geotechnical Society, “Test method for frost heave measurement” and “Test method for frost susceptibility” in the Japanese Standards and Explanations of Laboratory Tests of Geomaterials, 2020, pp. 249-281 (in Japanese).

[5] Japan Road Association, Road Construction Summary, 2009, p.287 (in Japanese).

11th Int. Conf. on Geotechnique, Construction Materials & Environment,
Kyoto, Japan, 3-5 November 2021, ISBN: 978-4-909106063 C3051

THE RECOVERY CHARACTERISTICS OF SHEAR STRENGTH OF CEMENT-STABILIZED CLAY

Tomoro Ueda[1], Kiyonobu Kasama[2] and Masaki Kitazume[3]

[1,3] Civil and Environmental Department, Tokyo Institute of Technology, Japan;
[2]Civil Engineering Department, Kyushu University, Japan

ABSTRACT

Many cement stabilization techniques have been frequently applied for various types of infrastructures and for various improvement purposes. The target strength of stabilized soil depends on the type of technique and improvement purpose, but is usually of the order of a couple MPa. The cement stabilized soil is subjected to large earthquakes, which may induce local failure in the stabilized soil even for stabilized soil with large strength. As it is practically quite difficult to repair such a damaged soil after earthquake, it is desirable for stabilized soil to have a sort of self-curing phenomenon where the damaged soil strength is recovered to same extent during the further curing. And the cement stabilized soil is expected to have the self-curing phenomenon due to the cement hydration. The self-curing phenomenon of the cement stabilized soil by the bio-chemical additives has been investigated. However, they are very limited. In this research, a series of laboratory direct shear tests was carried out on the cement stabilized soil to investigate the effects of the initial shear and additives on the strength recovery.

Keywords: Cement stabilization, Strength recovery, Direct shear strength test, Clay

INTRODUCTION

Many cement stabilization techniques have been frequently applied for various types of infrastructures and for various improvement purposes. This technique is one of the essential techniques for developing infrastructures worldwide. The strength of cement stabilized soil is usually controlled by the type and amount of cement. The target strength depends on the type of technique and the improvement purpose, but is usually of the order of a couple MPa.

The cement stabilized soil is subjected to large earthquakes, which may induce local failure in the stabilized soil even with large strength. As it is practically quite difficult to repair such a damaged soil after earthquake, it is desirable for stabilized soil to have a sort of self-curing phenomenon where the damaged soil strength is recovered to same extent during the further curing. And the cement stabilized soil is expected to have the self-curing phenomenon due to the cement hydration. In the concrete engineering, many research efforts have been conducted to investigate the self-curing phenomenon of the concrete mixed with fly ash and/or silica fume as an additive[1,2)]. In the geotechnical engineering, the self-curing phenomenon of the cement stabilized soil by the bio-chemical additives have been investigated[3,4)]. However, they are limited that focus on the strength recovery phenomenon of the cement stabilized soil subjected the initial shearing in young curing stage.

In this research, a series of laboratory direct shear tests was carried out on the cement stabilized soils to investigate the effects of the initial shear and additives on the strength recovery.

MATERIALS AND TEST PROCEDURE

Clay and binder

Two type clays were used in the tests, Kawasaki clay and Kaolin clay, the physical properties of which are summarized in Table 1. Ordinal Portland cement was used as a binder and blast furnace slag fine powder was also used as an additive.

Table 1. Physical properties of clay samples.

	Kawasaki clay	Kaolin clay
Specific gravity, *Gs*	2.66	2.63
Plastic limit, w_P (%)	51.0	82.1
Liquid limit, w_L (%)	25.6	34.7
Liquid index	25.4	47.4
Ignition loss (%)	6.0	13.0

Test procedure

The soils with the initial water content of 100% were stabilized with ordinal Portland cement of the binder content, *aw* of 10% to achieve the target shear strength of about 150 kPa. The chemical additives of blast furnace slag fine powder were also mixed with the stabilized soil changing the *cw* of 0, 5 and 10% of the dry weight of the clay. The stabilized soil and cement mixture were poured into a mold of 60 mm in diameter and 20 mm in height for the direct shear test and cured in a laboratory.

In the case of the initial shearing sample, the sample was subjected to the initial shear to the shear stress of about 90 % of the peak stress at either 3, 7 or 14 days curing. This corresponds the stress condition after peak strength at the residual stage (called as post sample) and before the peak strength (called as pre sample).

After subjecting the initial shearing, the sample was cured without overburden pressure. The sample was subjected to the direct shear test at 28 days curing where the sample was subjected to the horizontal displacement of about 3 mm, the total of about 7 mm, again to measure the strength. The test procedure followed the Japanese Geotechnical Society standard (JGS-0561)[6]. In the direct shearing, the overburden pressure was 100 kPa for Kawasaki clay and it was changed 50, 100 and 150 kPa for Kaolin clay to investigate its effect on the shear behavior.

TEST RESULTS AND DISCUSSION

Shear stress and horizontal displacement curve

Figure 1(a) shows examples of the shear stress and horizontal displacement curves of stabilized Kawasaki clays with the *aw* of 10% and the *cw* of 0% at various curing days. The shear stress is increased very rapidly with the increase of the horizontal displacement to show the clear peak stress, and followed by the gradual decrease in the shear stress to the residual stage. Similar phenomenon can be seen in the other sample at the different curing days, while the peak stress is decreased with the short curing days.

Similar phenomenon can be seen in the case of stabilized Kaolin clay, Figure 1(b), where the shear stress is increased rapidly with the horizontal displacement to show the clear peak stress followed by the gradual strength decrease to the residual stage.

Figure 2 shows examples of the stress and horizontal displacement curves for the intact and the initial sheared samples at 28 days for the cement content, *aw* of 10% and *cw* of 0% under the vertical pressure of 100 kPa. In the case of stabilized Kawasaki clay, Fig. 2(a), the shear stress is increased rapidly with the horizontal displacement to show the peak strength of about 187 kPa, after then the stress was decreased to the residual stage of about 110 kPa. In the case of the initial shearing sample, the shear stress at 7 days is also increased rapidly with the horizontal displacement to show the maximum strength of about 136 kPa but the shear stress was almost constant with further increase of the horizontal displacement to about 3 mm. The sample was sheared again at 28 days curing. In the second shearing at 28 days, the shear stress is increased very rapidly again with the increase of the horizontal displacement to show the peak strength of about 171 kPa, which is almost the same order of the peak strength of the intact sample at 28 days. The Young's modulus in the second shearing stage at 28 days is larger than that in the initial shearing stage at 7 days. In the case of stabilized Kaolin clay, Fig. 2(b), a similar phenomenon can be seen. The intact sample at 28 days shows a clear peak strength followed by the gradually decreased residual strength with the increase of the horizontal displacement. The initial sheared sample at 7 days shows the rapid increase in

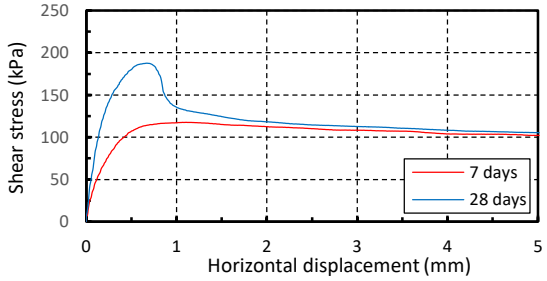

(a) Kawasaki clay

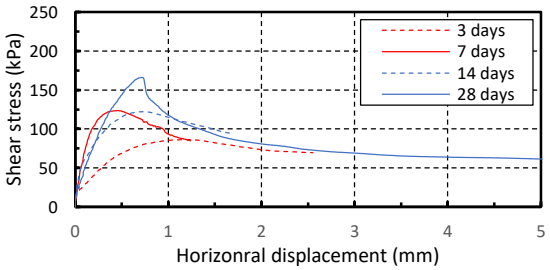

(b) Kaolin clay

Fig. 1. Shear stress and horizontal displacement curves of intact sample at various curing days.

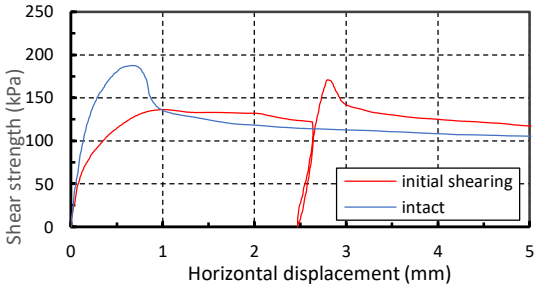

(a) Kawasaki clay

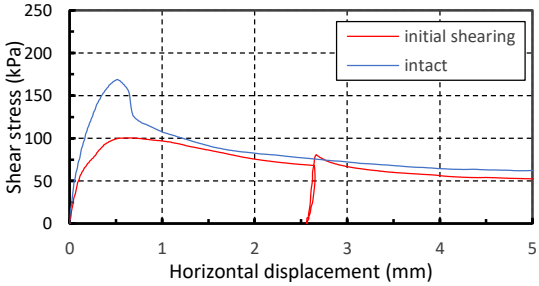

(b) Kaolin clay

Fig. 2. Shear stress and horizontal displacement curves of intact and initial sheared samples.

the strength to show a peak strength at the horizontal displacement of about 1 mm, and followed by the gradually decreased to the residual stage. In the second shearing stage at 28 days, the shear stress is increased very rapidly again with the increase of the horizontal displacement to show a clear peak strength followed by the gradually decrease to the residual stage. The peak strength at the second shearing stage is smaller than that in the first shearing stage, which is the different from the case of Kawasaki clay.

Effect of initial shearing on 28 days' strength

Figure 3 shows the relationship between the shear strength at 28 days and the curing period for the stabilized Kaolin clay with the *aw* of 10% and the *cw* of 0%, which were measured at the vertical pressure of 100 kPa in the direct shear test. The shear strength of the intact sample is rapidly increased at the beginning with the curing period and gradually increase further curing period. The test data of the sample subjected to the initial shear at 3 and 7 days (post sample) are also plotted in the figure. The strength at 28 days becomes small for the sample subjected to the initial shearing: 114 kPa for the initial shearing at 3 days and 108.4 kPa for the initial shearing at 7 days. It is found that the strength decrease is the almost same irrespective of the day at the initial shearing.

Figure 3 is replotted in Fig. 4 in which the strength ratio of the shear strength to the shear strength of the intact sample at 28 days is plotted on the vertical axis. The shear strength ratio at 3 days is about 0.4 but is increased with the curing period. The strength ratio of the sample subjected to the initial shearing at 3 and 7 days are about 0.55 and 0.76 respectively. By comparing the shear strength at the initial shearing at 3 and 7 days, the shear strength is slightly increased at 28 days.

Figure 5 shows the strength ratio, which is the shear strength of the initial sheared sample at 28 days to the initial shear stress. In the figure, two types of sample are plotted; the sample sheared beyond the peak strength, "post sample", and the sheared before the peak strength, "pre sample". In the case of "post sample", the strength ratio is about 1.2 to 1.5, which means that the shear stress is increased to 1.2 to 1.5 at 28 days of the magnitude of the initial shear. In the case of "pre sample", the strength ratio is about 1.5 to 2.0, which is larger than that of the "post sample". It can be seen that the strength ratio is large at the 3 days rather than the 14 days, which indicates that the shear strength recovery is dominant in the early stage shearing.

Figure 6 shows the effect of the strength ratio of shear stress of the sheared sample at 3, 7 and 14 days to the shear strength of intact sample at 28 days. In the figure, two types of sample are plotted; the

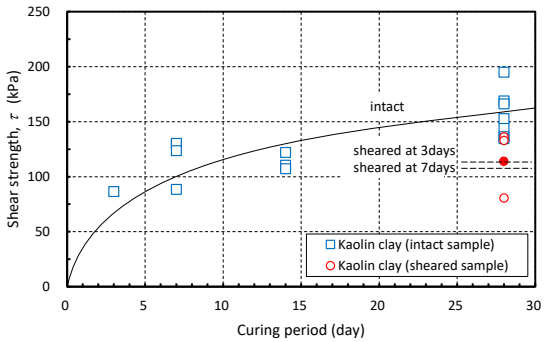

Fig. 3. Relationship between the shear strength and curing period for stabilized Kaolin clay with the *aw* of 10% and the *cw* of 0%.

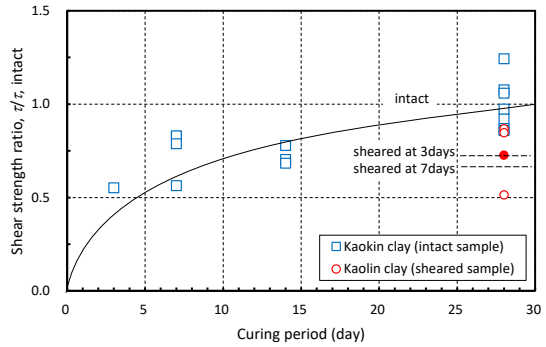

Fig. 4. Relationship between the shear strength ratio and curing period for stabilized Kaolin clay with the *aw* of 10% and the *cw* of 0%.

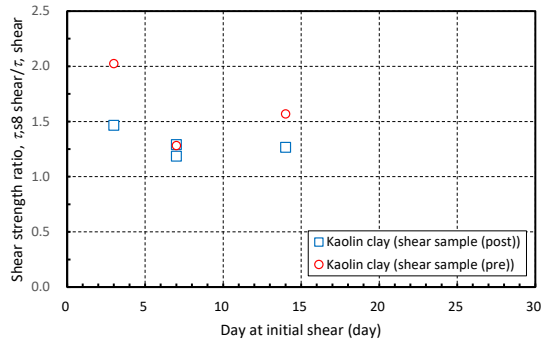

Fig. 5. Relationship between the strength ratio and the day at initial shearing.

sample sheared beyond the peak strength, "post sample", and the sheared before the peak strength, "pre sample". In the case of the "post sample", the strength ratio at 28 days is ranging about 0.5 to 0.87, which is slightly larger than the shear stress level. This indicates that the shear stress of sample shows the strength gain even after the initial shearing, but not to that of the intact sample. In the case of the "pre sample", the strength ratio is almost 1 irrespective of the time of the initial shearing, which means that the shear stress of sample subjected to the initial

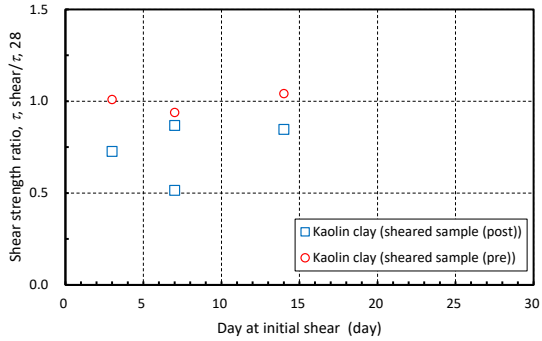

Fig. 6. Effect of initial shear on shear strength at 28 days.

shearing shows the large strength gain to that of the intact sample at 28 days.

Effect of blast furnace slag fine powder on 28 days' strength

Figure 7(a) shows the effect of content of blast furnace slag fine powder on the strength of stabilized soil of the *aw* of 10% at 28 days, which were measured at the vertical stress of 100 kPa in the direct shear test. It is found that the shear strength is almost linearly increase of the increase of the blast furnace slag fine powder in the stabilized Kawasaki clay. Similar phenomenon can be seen in the stabilized Kaolin clay as shown in Fig. 7(b), but the effect of slag on the strength increment is dominant in stabilized Kawasaki clay.

Evaluation of Mohr-Coulomb failure criteria

Figure 8 show that the Mohr-Coulomb failure criteria for the Kaolin clay stabilized with ordinal Portland cement with the *aw* of 10 % and the slag content, *cw* of 0% for the peak and residual conditions respectively.

Figure 8(a), the shear strength at the peak is increased with the increase of the vertical stress for the intact sample, "post shear sample" and "pre shear sample". Though there is a lot of scatter in the test data, the shear strength is increased almost linearly with the vertical stress irrespective of the type of sample. The friction angle, defined as the shear strength increment to the vertical stress increment, is about 28.8 degree, almost the same irrespective of the type of sample, while the cohesion, the intersect to the vertical axis, is largest for the intact sample and the lowest for the "sheared sample (post)".

In the residual stage, Fig. 8(b), the shear strength is also increased with the increase of the vertical stress irrespective of the type of sample. The friction angle and the cohesion are almost constant of about 21 degree and 20 kPa respectively irrespective of the type of sample. The friction angle is slightly smaller

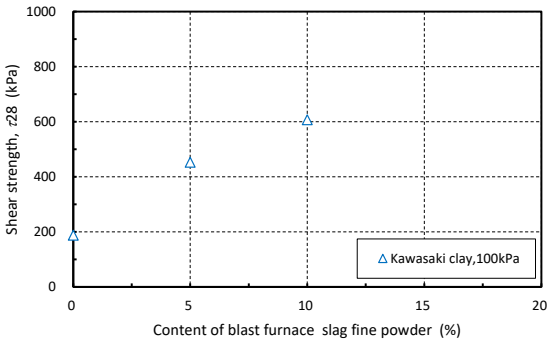

(a) Kawasaki clay

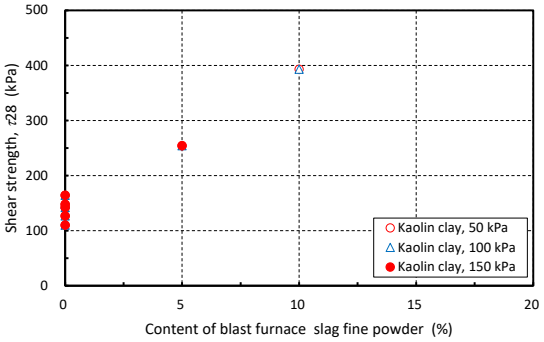

(b) Kaolin clay

Fig. 7. Effect of amount of slag on shear strength at 28 days.

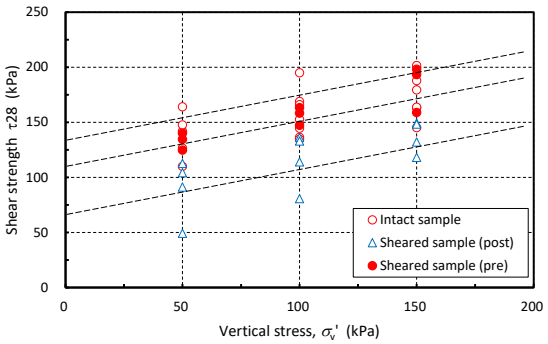

(a) Peak strength

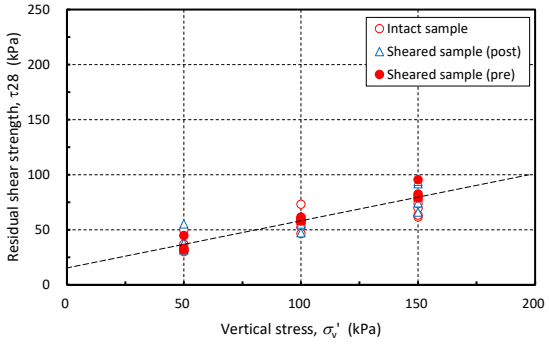

(b) Residual strength

Fig. 8. Vertical stress and shear strength of Kaolin clay with the *aw* of 10 % and the *cw* of 0%.

than that of the peak strength, but the cohesion is quite smaller than that of the peak. This indicates that the cohesion component is loosed in the stabilized soil when subjecting to the shear deformation.

Chemical composition at shear plane by Powder X-ray diffraction test

Table 2 summarized the chemical formula of the clay mineral and chemical compounds derived from chemical reaction between cement and water. The clay mineral and chemical compounds were targeted for XRD test. Kaolin clay used in our study mainly consists of Kaolinite, $Al_4Si_4O_{10}(OH)_8$, and silica, SiO_2. Tricalcium silicate, Ca_3SiO_5, Dicalcium silicate, Ca_2SiO_4, Tetracalcium aluminoferrite, $Ca_4Al_2Fe_2O_{10}$, and Calcium hydroxide,$Ca(OH)_2$, are main chemical compounds of Portland cement. Calcium carbonate, CaCO3, Calcium silicate hydrate, $nCaO\text{-}SiO_2\text{-}mH_2O$, and Ettringite, $3CaO\text{-}Al_2O_3\text{-}3CaSO_4\text{-}32H_2O$ are chemical compounds resulted from hydration chemical reaction between cement and water.

Figure 9 and Table 3 show the X-ray diffraction (XRD) test results on the three samples of stabilized Kawasaki clay with the *aw* of 10% and the *cw* of 10%, which was subjected to the shear at 7 days, the shear at 28 days and the initial shear at 7 days and the second shear at 28 days. And they were sheared under the vertical stress of 100 kPa. The figure shows the weight ratio of compounds, which shows that the amount of Ettringite and Calcium aluminate hydrate are increased with the curing period, which indicates that the cement hydration is still proceeded after the initial shearing. This hydration enhances the strength increase with the curing period.

CONCLUSIONS

In this study, a series of direct shear tests was carried out on Kawasaki clay and Kaolin clay stabilized with ordinary Portland cement with/without blast furnace slag fine powder, in which the vertical stress was also changed in the shear test. The major conclusions derived in the test are as follow:

The shear strength of the stabilized soil is increased with the increase of the curing period irrespective of the type of soil.

The stabilized soil with the initial shearing shows the strength recovery during the curing, the magnitude of the strength recovery is depend on the soil type and amount of additives content and also by the vertical pressure at shearing.

According to the Mohr-Coulomb failure criteria, the friction angle at the peak strength stage is almost constant irrespective of the initial shearing, while the cohesion depends on the sample type, largest for the intact sample. In the residual stage, the friction angle and the cohesion are almost constant irrespective of the type of sample.

The amount of Ettringite and Calcium aluminate hydrate is increased with the curing period, which indicates that the cement hydration is still proceeded after the initial shearing. This hydration enhances the strength increase with the curing period.

Table 2. Chemical formula of clay mineral and chemical compounds for XRD test

Name		Chemical Formula
Mineral (Kaolinite) Mineral	Mineral	$Al_4Si_4O_{10}(OH)_8,SiO_2$
Tricalcium silicate	C3S	Ca_3SiO_5
Dicalcium silicate	C2S	Ca_2SiO_4
Tetracalcium aluminoferrite	C4AF	$Ca_4Al_2Fe_2O_{10}$
Calcium hydroxide	Calcium hydrate	$Ca(OH)_2$
Calcium carbonate	Calsite	$CaCO_3$
Calcium silicate hydrate	C-A-H	$nCaO\text{-}SiO_2\text{-}mH_2O$
Ettringite	Ettringite	$3CaO\text{-}Al_2O_3\text{-}3CaSO_4\text{-}32H_2O$

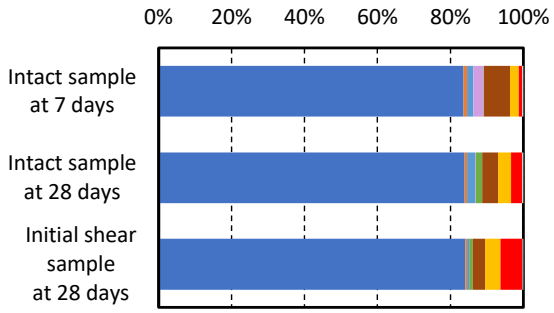

Fig. 9. Chemical composition at shear plane by Powder X-ray diffraction test.

Table 3. The result of XRD test.

	Initial shear sample at 28 days	Intact sample at 28 days	Intact sample at 7 days
Mineral	83.90	83.90	83.90
C3S	0.45	0.66	0.95
C2S	0.55	2.31	1.80
C4AF	0.05	0.16	2.80
Calcium hydroxide	1.00	1.65	0.10
Calcite	3.45	4.40	7.10
Ettringite	4.15	3.57	2.40
C-A-H	5.90	3.02	0.90
Others	0.30	0.33	0.39

ACKNOWLEDGEMENT
This research was supported by JSPS KAKENHI Grant Number 19H02233.

REFERENCES

[1] Seung-hyun, N., Hama, Y., Taniguchi, M. and Sagawa, T. The self-healing performance of concrete using ground granulated blast-furnace slag and fly ash, Proceedings of the Japan Concrete Institute, Vol. 34, No. 1, pp. 1402-1407, 2012 (in Japanese).

[2] Ueda, R., Kawano, J., Iiboshi, T. and Eriguchi, A., Influence of dosage of amino acid on self-healing performance of concrete, Cement Science and Concrete Technology, Vol. 70, No. 1, pp. 321-327, 2012 (in Japanese).

[3] Kawasaki, S., Present status of ground improvement technologies using microbial functions, Journal of MMIJ, Vol. 131, No. 5, pp. 155-163, 2015 (in Japanese).

[4] Hata, T., Tateno, N. and Abe, H., Evaluation of coastal region microbial carbonate precipitation using urease produced microorganisms, Japanese Geotechnical Journal, Vol. 6, No. 2, pp. 305-315, 2011 (in Japanese).

[5] Japanese Geotechnical Society, Practice for making curing stabilized soil specimens without compaction (JGS 0821-2000), Laboratory Testing Standards of Geomaterials, pp. 426-434, 2009 (in Japanese).

[6] Japanese Geotechnical Society, Method for consolidated constant volume direct box shear test on soils (JGS 0560-2000), Laboratory Testing Standards of Geomaterials, pp. 666-670, 2009 (in Japanese).

[7] Nakamura, S. and Gibo, S., The recovered strength of landslide soils and its relation to the effective normal stress, Journal of the Japan Landslide Society, Vol. 37, No. 3, pp. 18-24, 2000 (in Japanese).

11th Int. Conf. on Geotechnique, Construction Materials & Environment,
Kyoto, Japan, 3-5 November 2021, ISBN: 978-4-909106063 C3051

VISUALIZATION OF LIQUEFACTION PHENOMENON BY COUPLED CAE ANALYSIS OF MPS AND DEM

Koki Nakao[1], Katsumi Ookori[2], Tsuyoshi Takahashi[2] and Shinya Inazumi[3]

[1]Graduate School of Engineering and Science, Shibaura Institute of Technology, Japan;
[2]Aomi Construction Co. Ltd., Japan;
[3]College of Engineering, Shibaura Institute of Technology, Japan

ABSTRACT

The mechanism of liquefaction and the factors that cause liquefaction have already been examined and evaluated both analytically and experimentally, and liquefaction countermeasure construction is being implemented based on these findings. However, there are no cases in which the mechanism of liquefaction generation in the original ground and the effects of liquefaction countermeasures were visually examined and evaluated. Therefore, this study theoretically visualizes the mechanism of liquefaction generation and evaluate the behavior of particles in the ground. Specifically, MPS-DEM coupled CAE analysis is used to visualize the inside of the ground when an external force acceleration is applied, simulating seismic waves, and reveal the behavior inside the ground. The MPS-DEM coupled CAE analysis succeeded in visualizing the liquefaction phenomenon by applying an external force acceleration that simulates a seismic wave to the ground modeled three-dimensionally. This study is expected to clearly show the mechanism of liquefaction generation, and to contribute to the design and accountability of more efficient and economical liquefaction countermeasures, regardless of the field of specialization.

Keywords: CAE, DEM, Liquefaction, MPS, Visualization

INTRODUCTION

In Japan, the history of study on liquefaction is short. Since it was recognized that the sandy ground became liquid during the 1964 Niigata earthquake, study began to be actively conducted, and only a quarter of a century has passed since then [1], [2]. With the 1964 Niigata earthquake, liquefaction study has been energetically conducted, and nowadays, the ground conditions that are easily liquefied have become clear. However, the damage caused by liquefaction caused by the 2011 off the Pacific coast of East Japan Earthquake extended to the Kanto region, and the metropolitan area also suffered great damage [3]. The mechanism of liquefaction and the factors that cause liquefaction have already been examined and evaluated both analytically and experimentally, and despite the fact that liquefaction countermeasure construction is being implemented based on these findings, The liquefaction damage caused by the 2011 off the Pacific coast of East Japan Earthquake was enormous. One of the reasons for this is that there are no cases in which the effects of the construction of liquefaction countermeasures were visually examined and evaluated. At present, Japan has a large number of soft ground composed of fine particles such as sand, and earthquakes are likely to occur due to the positional relationship of rocks on the earth. Therefore, in order to prevent damage caused by liquefaction, efficient and economical liquefaction measures are indispensable.

Based on the above background, in this study, the mechanism of liquefaction generation is theoretically visualized using the coupled computer aided engineering analysis (CAE) of the moving particle semi-implicit (MPS) and the discrete element method (DEM) [4], [5]. The CAE is a general term for technology that simulates and analyzes prototypes on a computer created by a computer-aided design (CAD) and so on, considering the site conditions. The CAE in this study is executed by an algorithm in which both MPS and DEM methods are combined.

In this study, external force acceleration that simulates seismic waves is applied to the ground modeled three-dimensionally by the coupled CAE analysis of the MPS and the DEM, and the purpose is to reveal the behavior. Evaluate the behavior of particles in the ground and examine whether liquefaction occurs. By visualizing the liquefaction phenomenon, it is expected that the mechanism of liquefaction generation will be clearly shown and that it will contribute to the design and accountability of more efficient and economical liquefaction countermeasures. By utilizing CAE analysis in the field of liquefaction, it is possible to visualize the generating mechanism of liquefaction, which cannot be seen originally, and solve complicated problems associated with the liquefaction [4], [5]. In addition, since design and evaluation can be performed while comparing and examining various condition patterns, it is considered that the design quality can be

improved at an early stage and a more effective construction method can be designed.

GENERALAS OF LIQUEFACTION

With the 1964 Niigata earthquake and the 1995 Great Hanshin-Awaji earthquake, study on liquefaction has been actively conducted [1], [2] [6]. And the understanding, prediction, and countermeasure technology for liquefaction have been almost established. Liquefaction during an earthquake is a phenomenon in which when saturated sand ground is repeatedly subjected to shear stress, the shear rigidity decreases as the effective stress decreases, and finally the shear resistance is lost like a viscous fluid. Therefore, in order to analyze the mechanical behavior of soil during the liquefaction process, the process of change from solid to fluid must be considered.

Effective stress analysis is one of the typical methods for analyzing ground deformation during liquefaction [7], [8]. The effective stress analysis incorporates the constitutive law of sand into the equation of the field in which the soil skeleton and the interstitial water are coupled, which is obtained based on solid dynamics. The effective stress analysis covers the initial state of the ground, the dynamic behavior of the ground during an earthquake, and the occurrence of liquefaction. So far, many constitutive equations of sand based on solid-state mechanics have been proposed based on the results of laboratory tests on the repeated shear behavior of sand [9], [10]. These sand constitutive equations can reproduce stress-strain relationships and dilatancy behavior under various stress conditions. As the constitutive equation of sand, a repetitive elasto-plastic model, an elasto-plastic underload surface model, a densification model and so on have been proposed. On the other hand, analysis methods targeting only the flow process after liquefaction has occurred have also been proposed, and these can be divided into methods based on solid-state mechanics and methods based on fluid mechanics. As a method based on solid-state mechanics, for example, Yasuda et al. [11], [12] have proposed a residual deformation analysis method that can analyze the flow associated with liquefaction with simple and practical accuracy. As a method based on fluid mechanics, for example, Uzuoka et al. [13] proposed a method to analyze liquefied sand as a Bingham fluid, and quantitatively show the flow force and large deformation after flow, although under relatively simple boundary conditions.

The above-mentioned analysis method has been proposed by paying attention to each of the solid property and the fluid property of the liquefied sand, and is not a fusion of the two properties. In the actual liquefaction phenomenon, the phase change process between solid and fluid is considered to occur non-uniformly both spatially and temporally. At a certain time, a region having a solid property and a region having a fluid property are mixed. In order to deal with such problems, it is necessary to develop an analysis method that can express the transition region between solid and fluid.

In this study, the authors propose a CAE analysis that combines a MPS as one of the typical particle based methods (PBMs) and the DEM as an analysis model that can express the phase change process during liquefaction. This is a combination of sand particles in the target ground analyzed by the individual element method and interstitial water by the PBM. An analysis will be performed using this method to examine the effectiveness of the analysis model.

MPS-DEM COUPLED CAE ANALYSIS

A computer aided engineering (CAE) is an alternative technology for large-scale experiments, conducted in a room or in-situ, using prototypes that have been prepared in a study as part of the development process of “manufacturing”. In other words, CAE is a general term for technology that simulates and analyzes prototypes on a computer created by a computer-aided design (CAD) and so on, considering the site conditions [14], [15], [16], [17]. At the same time, CAE may refer to computer-aided engineering work or its tools for the prior examination, design, manufacturing, and process design of construction methods and products. In the field of geotechnical engineering, CAE can be used not only to visualize the inside of the ground and the stress loading on the inside of the ground, but also to estimate the results of experiments that would require huge costs and/or phenomena that would be difficult to reproduce. In addition, by performing appropriate post-processing, it is possible to communicate with other people in a visually easy-to-understand manner.

In this study, external force acceleration that simulates seismic waves is applied to the ground modeled three-dimensionally by the coupled CAE analysis of the moving particle semi-implicit (MPS) as one of the typical particle based methods (PBMs) and the discrete element method (DEM), and the particles in the ground are subjected to the loading. The purpose is to clear the behavior.

ANALYSIS MODEL AND CONDITIONS

The analytical model is shown in Fig. 1. Sand particles and water particles are arranged according to the void ratio on a 3000 mm square cube. The sand particles are expressed in yellow and the water particles are expressed in blue to visually express the ground. In addition, the ground simulating liquefaction countermeasures will be reproduced. The pile model is shown in Fig. 2. The piles are 400 mm in diameter and 3000 mm in length, and 6 piles are

arranged on each side. The piles are set as a distance function. Place the pile shown in Fig. 2 on the ground shown in Fig. 1 and performs the analysis.

In this study, liquefaction is expressed by applying an external force acceleration that simulates a seismic wave to the ground. Assumed parameters of the external force acceleration are shown in Fig. 3. Acceleration is given in the X-axis direction every 0.01 seconds for a total of 59.99 seconds. Figure 4 shows the relationship between acceleration and seismic intensity [18]. The maximum value of acceleration is adopted as a parameter representing seismic intensity. The maximum value of the external force acceleration parameter is 207.33 (cm/s^2), which corresponds to an earthquake with a seismic intensity of 5 or higher, as shown in Fig. 4. The reason for setting this seismic intensity is that the liquefaction phenomenon often occurs with an earthquake with a seismic intensity of 5 or higher.

In this study, water is set as fluid by the MPS and sand is set as powder particles by the DEM. Table 1 shows the physical characteristics of water particles modeled by the MPS, and Table 2 shows the physical characteristics of sand particles modeled by the DEM. All of these physical property parameters refer to and cite previous experimental values [4], [5], [16], [19], [20], [21]. Attention should be paid to the DEM parameters for sand particles shown in Table 2, especially the setting of sand particle diameter and density. The typical sand particle diameter and density are 0.2 mm and 2.634 g/cm^3 respectively. In this study, the diameter and density of the sand particles modeled by DEM are set so that the particle sedimentation velocity of Stokes fluid [22], [23] is

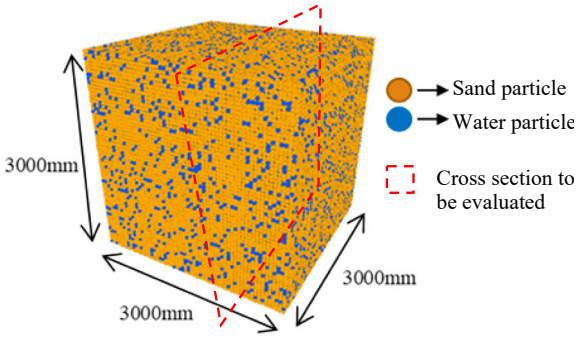

Fig. 1 Cross-section model assumed for analysis (Case 1 and Case 2)

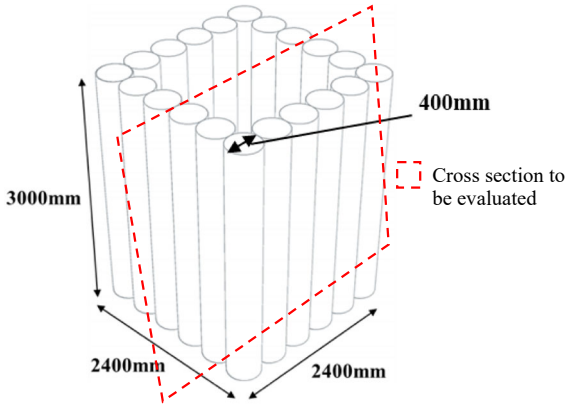

Fig. 2 Cross-section model assumed for analysis (Case 3; lattice-shaped ground improvement pile)

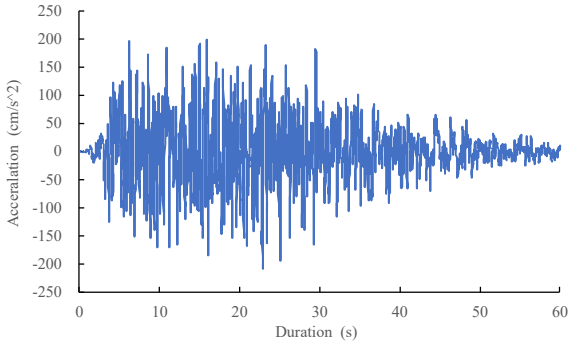

Fig. 3 Assumed external force acceleration

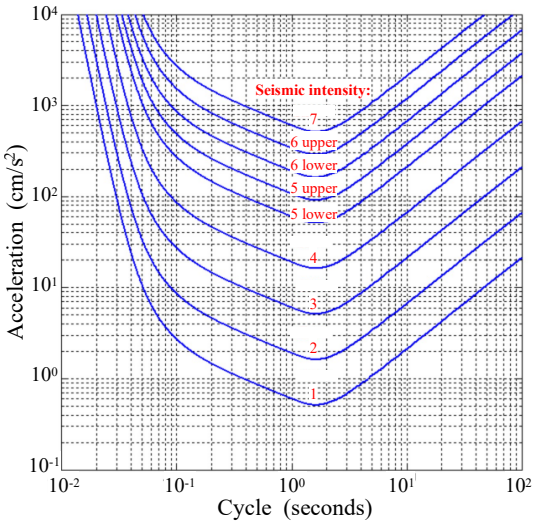

Fig. 4 Relationship between period and acceleration in each seismic intensity scale 4)

Table 1 MPS parameters for water particles

	Water
Particle density (kg/m^3)	1000
Particle size (m)	0.03
Rheology model	Newtonian fluid

Table 2 DEM parameters for sand particles

	Sand
Particle density (kg/m^3)	1000.118
Particle size (m)	0.03
Young's modulus (GPa)	1
Poisson's ratio	0.485

Table 3 Assumed gap ratio of sand ground (typical value of sand ground is adopted)

	Sand ground
Maximum void ratio	1.19
Minimum void ratio	0.71

equal to that of typical sand particle and sand particle modeled by DEM. The authors focus on the void ratio and express the sand ground by void ratio using the maximum and minimum void ratios of typical sand ground. The void ratio is shown in Table 3. The void ratio of 1.19 is Case 1, the void ratio of 0.71 is Case 2, and the void ratio of 1.19 with piles is Case 3.

RESULTS AND DISCUSSIONS

Figures 5, 6 and 7 display the analysis results on Case 1, Case 2 and Case 3 respectively at the avaluating cross section witn Figs. 1 and 2. These figures show from 0 seconds to 59.99 seconds every 10 seconds, respectively. Because Case 3 surrounds the ground with piles, Fig. 7 that is the analysis result of Case 3 is shown as a cross-sectional view. In all cases, it is confirmed that sand particles are deposited at the bottom of the analysis model over time and water particles are floating. In other words, this analysis was able to roughly visualize the liquefaction of the ground when an external force acceleration simulating a seismic wave was applied.

The mechanism of the liquefaction phenomenon is that when a sand soil saturated with water receives a large shaking, the skeletal structure of the sand particles that make up the ground collapses and the sand particles try to fall into the void spaces. As a result, excessive pore water pressure is generated and accumulated inside the ground. Furthermore, when the excess pore water pressure becomes equal to the effective loading pressure of the ground before it receives a large shaking, the effective stress loading between the soil particles becomes zero, and as a result of the above, a liquefaction phenomenon occurs. The analysis results shown in Figs. 5, 6 and 7 also show the same phenomenon as the above-mentioned liquefaction generation mechanism. In addition, when comparing the central part and the four corners of the analysis model in all cases, it is confirmed that the amount of sedimentation of water particles in the four corners is smaller than that in the central part. This is because the rearrangement of water particles and sand particles occurs due to external force, and the sand particles try to settle and deposit at the bottom of the model. While sand particles settle and deposit, water particles try to rise to the top of the model. As a result, the sand particles at the four corners are sedimented at the bottom of the model and then flow out to the center of the model, resulting in a rearrangement of the particles.

Comparing Case 1 and Case 2 with different void ratios, in Case 1, water particles are floating in

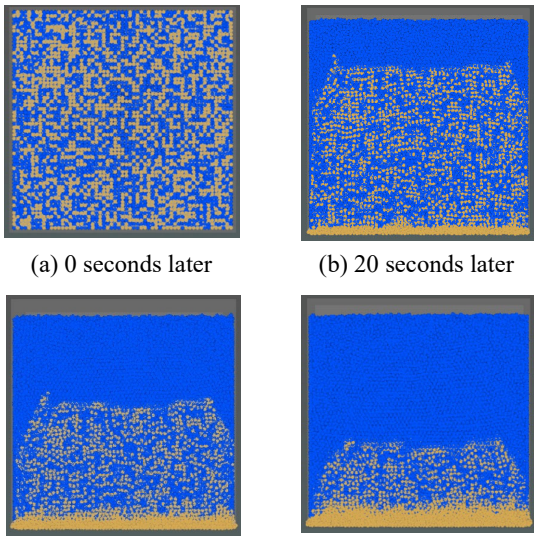

(a) 0 seconds later (b) 20 seconds later

(c) 40 seconds later (d) 60 seconds later

Fig. 5 Liquefaction occurrence in Case 1 with external acceleration (void ratio: 1.16)

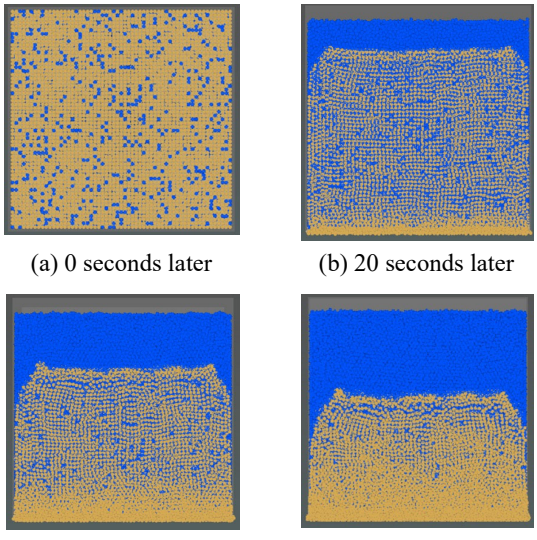

(a) 0 seconds later (b) 20 seconds later

(c) 40 seconds later (d) 60 seconds later

Fig. 6 Liquefaction occurrence in Case 2 with external acceleration (void ratio: 0.71)

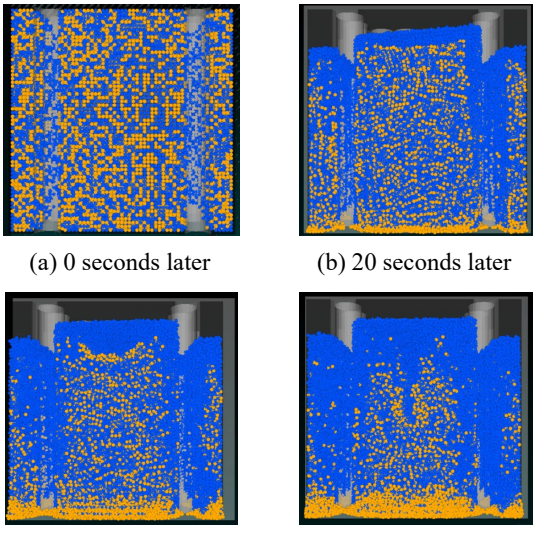

(a) 0 seconds later (b) 20 seconds later

(c) 40 seconds later (d) 60 seconds later

Fig. 7 Liquefaction occurrence in Case 3 with external acceleration (void ratio: 1.16, with piles)

the upper part of the model. It can be considered that this is the mechanism of the liquefaction phenomenon, that the loosely deposited sandy ground and the higher groundwater level are more likely to cause the liquefaction phenomenon. Comparing Case 1 and Case 3 with respect to the presence or absence of liquefaction countermeasure, sand particles are stopped on the model at the inner part of the pile in Case 3. From this, it is considered that liquefaction measures that surround the ground with piles are effective. The physical principle of liquefaction countermeasures by piles is to keep the shear deformation caused by seismic motion small, block the propagation of pore water pressure from the surroundings, and prevent the outflow of pore water and sand into the supported layer [24], [25]. This analysis was able to reproduce the same phenomenon as the physical principle of liquefaction countermeasures using piles.

CONCLUSIONS

The behavior of water particles and sand particles inside the ground, in which an external force acceleration simulating a seismic wave loaded on the ground, was evaluated using MPS-DEM coupled CAE analysis, and an attempt was made to visualize the liquefaction phenomenon in this study.

The results and findings obtained in this study are shown below.

(1) MPS-DEM coupled CAE analysis succeeded in visualizing the liquefaction phenomenon by applying an external force acceleration that simulates a seismic wave to the ground modeled three-dimensionally.
(2) The effect of ground conditions such as void ratio on the behavior of particles in the ground during an earthquake was visualized. By using MPS-DEM coupled CAE analysis, it is possible to evaluate the behavior of particles in the ground during an earthquake and examine whether liquefaction occurs.
(3) The liquefaction phenomenon on the ground with piles simulating the liquefaction countermeasure work was visualized. By visualizing the liquefaction phenomenon, it can be expected to contribute to the design and accountability of efficient and economical liquefaction countermeasures.

In order to visually evaluate the need for liquefaction countermeasures, it is necessary to simulate and analyze more actual liquefaction countermeasures.

REFERENCES

[1] Kuribyashi, E. and Tatsuoka, F. (1975) : Brief review of liquefaction during earthquakes in Japan, Soils and Foundations, Vol. 15, No. 4, pp. 81-92.
[2] Onoue, A., Yasuda, S., Toyota, H., Inotsume, T., Kiku, H., Yamada, S., Hosaka, Y., Tsukamoto, Y., Towhata, I., Wakai, A., Ugai, K. (2011): Review of topographic and soil conditions for liquefaction-related damage induced by the 2007 off Mid-Niigata earthquake, Soils and Foundations, Vol. 51, Issue 3, pp. 533-548, doi: 10.3208/sandf.51.533.
[3] Yasuda, S., Harada, K., Ishikawa, K. and Kanemaru, Y. (2012): Characteristics of liquefaction in Tokyo Bay area by the 2011 Great East Japan Earthquake, Soils and Foundations, Vol. 52, Issue 5, pp. 793-810, doi: 10.1016/j.sandf.2012.11.004.
[4] Inazumi, S., Jotisankasa, A., Nakao, K. and Chaiprakaikeow, S. (2020a): Performance of mechanical agitation type of ground-improvement by CAE system using 3-D DEM, Results in Engineering, Vol. 6, doi: 10.1016/j.rineng.2020.100108.
[5] Inazumi, S., Kuwahara, S., Jotisankasa, A. and Chaiprakaikeow, S. (2020b): MPS-CAE simulation on dynamic interaction between steel casing and existing pile when pulling out existing piles, International Journal of GEOMATE: Geotechnique, Construction Materials and Environment, Vol. 18, Issue 70, pp. 68-73, doi: 10.21660/2020.70.9166.
[6] Kazama, M., Kawai, T., Mori, T., Kim, J. and Yamazaki, T. (2018): Subjects of the liquefaction research seen to the liquefaction damage of the great East Japan earthquake disaster, Journal of Japan Association for Earthquake Engineering, Vol. 18, No. 3, pp. 26-39, doi: 10.5610/jaee.18.3_26.
[7] Rapti, I., Caballero, F.L., Razavi, A.M.F., Foucault, A. and Voldoire, F. (2018): Liquefaction analysis and damage evaluation of embankment-type structures. Acta Geotechnica, Vol. 13, pp. 1041–1059, doi: 10.1007/s11440-018-0631-z.
[8] Finn, W.D.L. (2000): State-of-the-art of geotechnical earthquake engineering practice, Soil Dynamics and Earthquake Engineering, Vol. 20, pp. 1-15, doi: 10.1016/S0267-7261(00)00033-6.
[9] Wu, W., Lin, J. and Wang, X. (2017): A basic hypoplastic constitutive model for sand, Acta Geotechnica, Vol. 12, pp. 1373-1382, doi: 10.1002/nag.1610181203.
[10] Tasiopoulou, P. and Gerolymos, N. (2016): Constitutive modeling of sand: Formulation of a new plasticity approach, Soil Dynamics and Earthquake Engineering, Vol. 82, pp. 205-221, doi: 10.1016/j.soildyn.2015.12.014.
[11] Yasuda, S., Yoshida, N., Adachi, K., Kiku, H. and Ishikawa, K. (2017): Simplified evaluation method of liquefaction-induced residual displacement, Journal of Japan Association for Earthquake Engineering, Vol. 17, No. 6, pp. 1-20, doi: 10.5610/jaee.17.6_1.
[12] Yasuda, S., Yoshida, N., Adachi, K., Kiku, H., Gose, S. and Masuda, T. (1999): A simplified practical method for evaluating liquefaction-induced flow, Journal of Geotechnical Engineering, Proceedings of JSCE, No. 638/III-49, pp. 71-89, doi: 10.2208/jscej.1999.638_71.
[13] Uzuoka, R., Yashima, A., Kawakami, T. and Konrad, J.M. (1998): Fluid dynamics based prediction of liquefaction induced lateral spreading, Computers and Geotechnics, Vol. 22, No. 3, pp. 243-282, doi: 10.1016/S0266-352X(98)00006-8.
[14] Chang, K.H. (2014): Product Design Modeling using CAD/CAE: The Computer Aided Engineering Design Series, Elsevier.

[15] Pan, Z., Wang, X., Teng, R. and Cao, X. (2016): Computer-aided design-while-engineering technology in top-down modeling of mechanical product, Computers in Industry, Vol. 75, pp. 151-161, doi: 10.1016/j.compind.2015.05.004.

[16] Inazumi, S., Tanaka, S., Komaki, T. and Kuwahara, S. (2021): Effect of insertion of casing by rotation on existing piles in removal of existing pile, Geotechnical Research, Vol. 8, Issue 1, pp. 25-37, doi: 10.1680/jgere.20.00042.

[17] Adeli, B.H. and Kumar, S. (2020): Distributed Computer-Aided Engineering for Analysis, Design, and Visualization, CRC Press, doi: 10.1201/9781003067795.

[18] Sakai, A. (2019): Relationship between acceleration waveforms determined in addordance with acceleration response spectra and various seismic intensity levels and long-period seismic intensity, Division A1 (Structural Engineering & Earthquake Engineering), Journal of Japan Society of Civil Engineers, Vol. 75, No. 3, pp. 266-279, doi: 10.2208/jscejseee.75.266.

[19] Inazumi, S., Kaneko, M., Shigematsu, Y. and Shishido, K. (2018): Fluidity evaluation of fluidisation treated soils based on the moving particle semi-implicit method, International Journal of Geotechnical Engineering, Vol. 12, Issue 4, pp. 325-336, doi: 10.1080/19386362.2016.1277618.

[20] Inazumi, S., Kaneko, M., Tomoda, Y., Shigematsu, Y. and Shishido, K. (2017): Evaluation of flow-ability on fluidization treated soils based on flow analysis by MPS method, International Journal of GEOMATE: Geotechnique, Construction Materials and Environment, Vol. 12, Issue 29, pp. 53-58.

[21] Inazumi, S., Kaneko, M., Shigematsu, Y. and Shishido, K. (2018): Fluidity evaluation of fluidisation treated soils based on the moving particle semi-implicit method, International Journal of Geotechnical Engineering, Vol. 12, Issue 4, pp. 325-336, doi: 10.1080/19386362.2016.1277618.

[22] Makino, M. (2020): Lateral migration of particles dispersed in Stokes fluid, Japanese Journal of Multiphase Flow, Vol. 34, No. 1, pp. 3-10, doi: 10.3811/jjmf.2020.T001.

[23] Doi, M. and Makino, M. (2005): Sedimentation of particles of generl shape, Physics of Fluids, Vol. 17, 43601, doi: 10.1063/1.1884625.

[24] Saha, P., Horikoshi, K. and Takahashi, A. (2020): Performance of sheet pile to mitigate liquefaction-induced lateral spreading of loose soil layer under the embankment, Soil Dynamics and Earthquake Engineering, Vol. 139, 106410, doi: 10.1016/j.soildyn.2020.106410.

[25] Liu, W.M.B., Rasouli, R., Aoyama, S. and Towhata, I. (2019): Performance of piles with different configurations subjected to slope deformation induced by seismic liquefaction, Engineering Geology, Vol. 263, 105355, doi: 10.1016/j.enggeo.2019.105355.

11th Int. Conf. on Geotechnique, Construction Materials & Environment,
Kyoto, Japan, 3-5 November 2021, ISBN: 978-4-909106063 C3051

BEARING CAPACITY BEHAVIOR OF SINGLE PILE DURING GROUNDWATER LEVEL CHANGE BY CENTRIFUGE MODEL

Sutasinee Intui[1], Suttisak Soralump[2] and Shinya Inazumi[3]

[1]Graduate School of Engineering and Science, Shibaura Institute of Technology, Japan;
[2]Faculty of Engineering, Kasetsart University, Thailand;
[3]Department of Civil Engineering, Shibaura Institute of Technology, Japan

ABSTRACT

The recent decrease in the groundwater level in the Bangkok area has mainly occurred due to inappropriate water pumping for industrial and agricultural activities. This inappropriate pumping is not only causing land subsidence, but it is also affecting the load capacity of the soil around the piles. At present, the groundwater level in the Bangkok area is showing a tendency to increase to the ground surface thanks to the reduction in groundwater pumping. This is an important issue of research into the soil load capacity behavior around piles with changes in the groundwater level. This study focuses on the behavior of a single pile by comparing the results of centrifuge tests and the results of previous studies. The test results are compared for each groundwater level. Finally, the results of the tests are summarized into two parts. The first part is that the bearing capacity of the sand around the pile is related to the changing groundwater level, but in an inverse manner. The soil strength is seen to decrease as the groundwater level increases or rises up to the ground surface. The bearing capacity in clay mainly depends on the consolidation process. The second part is that the results of the pile load behavior from the centrifuge tests tend to be like those of the previous studies. Therefore, centrifuge test results can be used to evaluate and design pile foundations in the Bangkok area with changing groundwater levels.

Keywords: Bangkok clay, Centrifuge test, Bearing capacity, Settlement, Groundwater

INTRODUCTION

At present, most constructions in soft soil areas use pile or deep pile foundations. The type of pile is chosen by the characteristics of each construction, the type of building, and the load of the structure. Thus, the bearing capacity is the most important factor to analyze in terms of the pile performance. The significant parameters affecting the pile capacity are the groundwater level and the soil characteristics.

Bangkok and its vicinity are located in a soft soil area that used to be part of the sea. The soil profile shows alternating layers of sand and clay from soil deposits. The first soil layer is a top clay crust with a thickness of 1 to 2 meters from the ground surface. The second soil layer is a very soft to soft clay layer with a thickness of about 14 meters. The third soil layer is a medium stiff to very stiff clay layer, extending to a depth of about 25 meters, followed by a medium dense sand layer, referred to as the first sand layer, extending to a depth of 40 meters. The deeper layers comprise alternating layers of stiff clay and dense sand, reaching great depths that have very high soil strength.

In terms of the groundwater situation in Bangkok, the groundwater level changes in relation to the quantity of groundwater pumping. The Department of Groundwater Resource evaluated the groundwater level by installing piezometers at many stations [1]. The results showed that the groundwater level was draw down to the minimum level around 1997 due to groundwater pumping. Then, a decrease in the groundwater pumping rate led to the recovery of the groundwater level to the ground surface. The groundwater level is presently recovering to the ground surface thanks to monitoring at piezometer stations in Bangkok and its vicinity.

Much research has been done on the strength of the Bangkok area soil. The strength and stiffness of Bangkok clay has been monitored at Sukhumvit MRT Station using the PLAXIS 3D model to compare the hardening soil model and the Mohr-Coulomb model [2]. The results revealed that the Bangkok clay characteristics of the hardening soil model were better than those of the Mohr-Coulomb model for excavation work. The numerical model proved that the results of the hardening soil model can be employed to analyze and predict the ground surface settlement in both 2D and 3D analyses. A comparison of the load capacity between barrette piles and bored piles at similar depths found that barrette piles, with dimensions of 1.5x3.0 meters and a depth of 57 meters, have a higher bearing capacity than bored piles in Bangkok, Thailand [3]. Additionally, the bearing capacity of the two types of piles is not

different. Thus, that research recommends barrette piles for high pile capacity designs. On the contrary, the soil strength estimated through a numerical method showed that the positive skin friction value of barrette piles is more than that of bored piles [4]. The strength of soft Bangkok clay was measured using the recompression and SHANSEP techniques [5]. The results of their comparison of the undrained shear stress values showed that recompression tests yield higher values than those estimated from the SHANSHEP technique by about 28%. Finally, the research proved that the corrected field vane shear tests match the SHANSHEP triaxial data well. Additionally, the undrained shear strength of the MRT blue line project and the MRT blue line extension project, Bangkok, Thailand was examined [6]. Their research used a single pile with a diameter of 1.5 meters and a length of 55 meters. The results revealed the undrained shear strength of stiff clay of about 40 to 100 kN/m^2 by triaxial tests and the undrained shear strength of soft clay of about 10 to 50 kN/m^2 by vane shear tests. The development of negative skin friction was found on piles driven into soft Bangkok clay [7]. This research showed that the undrained shear strength values of medium stiff to stiff clay and sand are 3 to 8 t/m^2 and 18 to 25 t/m^2, respectively, by direct shear tests (DSs), field vane shear tests (FVs), Dutch Cone tests (DCs), and Ko consolidated undrained triaxial tests (CKoUs). The results of the pile load tests conducted in the Bangkok area by driven piles and bored piles have been summarized. For the stiff clay layer, the undrained shear strength is 200 to 250 kN/m^2 by unconfined compression tests and standard penetration tests, and the average skin friction is about 100 kN/m^2 [8].

It is important to give consideration to the groundwater level in constructions since the bearing capacity of the soil affects the safety of the structures. This is because the water level, in terms of the pore water pressure, will reduce the soil strength. The present research shows the results of centrifuge tests performed during the recovery or rising up of the groundwater level. The results were verified with the data from the previous research by the authors [9]. Thus, this research will show the bearing capacity of a single pile while the groundwater level changes from the surface and then experiences groundwater level drawdown due to water pumping until the recovery of the groundwater level to the ground surface.

METHODOLOGY

This research focuses on the bearing capacity behavior of a single pile, and attempts to model a single pile while changing the groundwater level at different intervals. The centrifuge tests were divided into three stages for one model to represent a bored pile under the impact of engineering structures during the changes in groundwater level by means of geotechnical centrifuge tests done at Hong Kong University of Science and Technology [10].

Model preparation

Load distribution

The soil strength theory depends on many parameters, such as the soil layers, soil properties, and groundwater level. Following the previous study [3], this research chooses two soil layers to represent the soil condition in the Bangkok area for the model because they have a very high load transfer. Following Fig. 1, the load distribution refers to the percentage of load transfer to each soil layer of the barrette and bored piles. Most of the load is transferred to the medium dense sand layer, followed by the hard clay layer and then the stiff clay layer.

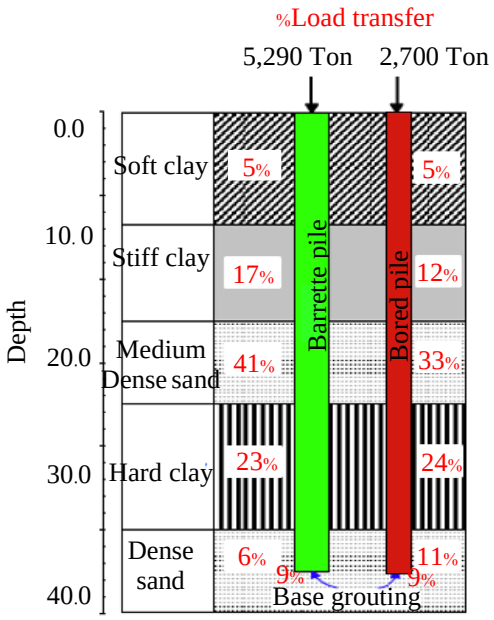

Fig. 1 Percentage of load transfer to each soil layer in pile load tests.

Soil model

Following the capacity of the soil from the previous study, medium dense sand and stiff clay were chosen for this research to simplify the model preparation and to represent the Bangkok soil profile that has alternating layers of clay and sand. Even though the hard clay layer has the 2nd highest percentage of load transfer for both types of piles, it is almost impossible to prepare this layer to attain the density of the hard clay layer in the centrifuge model.

Thus, Kaolin clay and Toyoura sand were used as the stiff clay and medium dense sand, respectively. The Speswhite Kaolin clay was prepared at a water content of 27%, a density of 1.65 t/m^3, and undrained shear strength of 35 kPa. The Toyoura sand was prepared with a controlled density of 1.53 t/m^3.

Water flow system

The water flow system in the centrifuge tests was modeled by installing a standpipe at the bottom of a strongbox. A standpipe is a PVC tube covered with a geotextile. The end of the standpipe was connected to a hole in the strongbox and a reservoir or water tank next to the strongbox. This system was installed to control the water level at each stage of the tests, as mentioned previously

Single pile model

The model for the single pile was an aluminium tube equipped with strain gauges. The dimensions of the model pile are a diameter of 2.4 meters (30 mm for the pile model) and a length of 50.4 meters (630 mm for the pile model). Wheatstone bridge strain gauges were installed at seven levels in the pile to measure the values of the pile movement during testing. The aluminium tube was divided into six segments because doing so would make it easy to install the strain gauges inside the pile segments. In order to prevent the electric circuit installed in each segment from water, tape was wrapped around the circuit to protect it, as shown in Figs. 2 and 3. After connecting the pile segments together, the pile model was coated with a thin layer of liquid epoxy to form a watertight layer.

Fig. 2 Strain gauges by full Wheatstone bridge circuit.

Fig. 3 Single pile model.

Bored piles

Three bored piles were installed in the model in order to perform a pile load test at each water level. The diameter of the pile was 2.4 meters and the length was 50.4 meters. The three single piles were installed in the strongbox, as shown in Fig. 4.

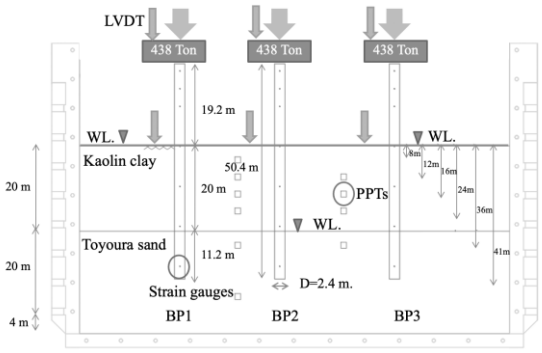

Fig. 4 Testing procedure of centrifuge tests.

Instruments

The focus of the tests is the results of the pile bearing capacity. Three types of instruments were installed in the soil model. Firstly, linearly variable differential transformers (LVDTs) were installed at the pile caps and the ground surface to measure the surface soil displacements. Secondly, pore water pressure transducers (PPTs) were installed in both soil layers. Thirdly, strain gauges were installed inside the model pile. After all centrifuge tests had been performed, the undrained shear strength of the soil was measured by pocket vane shear tests. Additionally, cameras were installed around the strongbox to monitor the external movement and groundwater level in the model during the testing.

Testing procedures

This study uses a 2D model box. The model had the dimensions of 350x750x1245 mm. A water system was installed at the bottom of the model box with two holes to control the groundwater level and distribute the water. Then, the two soil layers were prepared. Toyoura sand was released from a rate hopper and spread to a fixed height to control the density of the sand (1.53 t/m^3). The sand was filled in, layer by layer, with a maximum thickness of 50 mm per layer, until reaching a total thickness of 300 mm. After that, the groundwater level was increased by the standpipe system to saturate the sand for about 24 hours. Then, water was released from the model box by the standpipe system to make the uniform density of the sand layer. Next, the Kaolin clay was compacted on top of the sand layer by a density

control method to a thickness of 250 mm. Then, the soil model was drilled to install the three-pile model, as shown in Fig. 4. The piles were installed in both the stiff clay layer and the medium dense sand layer. The pile tips were driven into the medium dense sand layer about 140 mm from the interface of the sand layer. After installing all the instruments in the model box, a balance weight was equipped on the opposite side of the model box to balance the centrifuge machine during testing. A summary of the centrifuge test is given in Table 1. The testing model consisted of the model box and one water tank to control the water level.

Table 1 Summary of centrifuge test

Testing No.	Water level in prototype (m)	Water level in model (mm)	Initial water content (%)
BP1	0	0	27
BP2	20	250	27
BP3	0	0	27

Note: BP refers to the type of pile, namely, a bored pile, and the number after BP is the number of single piles.

The centrifuge test consisted of three stages that were carried out at an acceleration equal to 80 times the force of gravity (80 g). Each stage is related to the groundwater level at a different period of time. The three stages are called BP1, BP2, and BP3. The first stage, BP1, refers to the stage in which the bearing capacity behavior of the soil around a single pile is investigated by performing a pile load test after the groundwater level reaches the ground surface. This stage represents the original groundwater in the past before the occurrence of the pumping issue. The second stage, BP2, refers to the stage in which the groundwater level decreases to the interface of the sand layer and clay layer after which a pile load test is performed. This stage represents the decrease in groundwater due to the high pumping rate during the period of increasing industrial development. The third stage, BP3, is similar to the BP1 stage. The groundwater level reaches the ground surface again after the BP2 stage and a pile load test is performed on the pile head. Every test was performed at an acceleration of 80 g with the pile load test rate of 2 mm/min by ASTM, as in [11].

RESULTS AND DISCUSSION

The results of the pile load tests in the centrifuge test will be detailed here. The results of the three stages were separated into three parts. The first set of results shows the settlement of the pile and the ground surface during the pile load tests. The second set of results shows the bearing capacity and the unit skin friction during the pile load tests. The last set of results shows the undrained shear strength values after testing at 0 g.

Settlement

Based on Figs. 5 to 7, the settlement behavior between a single pile and the ground surface in each stage condition of the groundwater level during the pile load tests is given. The circular marker in each test, representing the settlement of the ground surface, shows that small settlement occurred in all the tests compared with pile settlement. On the other hand, the triangular marker shows that very large settlement occurred in the first pile load test due to the soil model just starting to consolidate and the voids between the soil particles filling with water due to groundwater level reaching the ground surface. In the same way, it was found that the second test had the smallest settlement because of the decrease in water level to the soil interface between the clay and the sand as the clay layer was consolidated. The last test showed that more settlement occurred than in the second test, but still less than in the first test. These results confirm that the groundwater level directly affects the settlement behavior of the soil around the piles in every stage.

Bearing Capacity

The pile load capacity is discussed in this section. The strain gauge results represent the strength of the soil around the piles. Based on Fig. 8, the pile load is directly affected by the changing water level. The first stage has the smallest load capacity due to the high groundwater level and the short-term consolidation. After consolidation, the bearing capacity is significantly increased. Especially in the last stage, BP3, the condition is represented whereby the groundwater level rises up and the Kaolin clay layer has already consolidated for the longest period. Fig. 9 confirms that the period of consolidation has a huge effect on the strength of the soil around a single pile. However, the unit skin friction results for the sand layer are not related to the consolidation condition in each test. The third stage has a lower unit skin friction value than the second stage because the groundwater rises up to the ground surface leading to high pore water pressure. The soil strength of each test is explained in terms of the effective stress in Fig. 10. The effective stress is equal to the total stress minus the pore water pressure. The groundwater level at each stage refers to the pore water pressure that

directly affects the effective stress. Thus, the second test has the highest effective stress due to the decrease in water to the interface of the soil.

Soil strength

The undrained shear strength, after the centrifuge tests done at 0 g, is discussed here. Fig. 11 shows a comparison of the undrained shear strength between the centrifuge test results and the results obtained by other researchers. The results revealed that many researchers obtained almost the same undrained shear strength values at every depth [12]–[15]. Even the results of the pocket vane shear tests showed higher strength than in the tests done by others researchers, but still with the same trend. Additionally, the authors confirm the values when using the Modified Cam-Clay theory to recheck the values of the pocket vane shear tests, as seen in Fig. 12. The results reveal that the values of the undrained shear strength from the vane shear tests are lower than those of the Modified Cam-Clay theory at each soil depth.

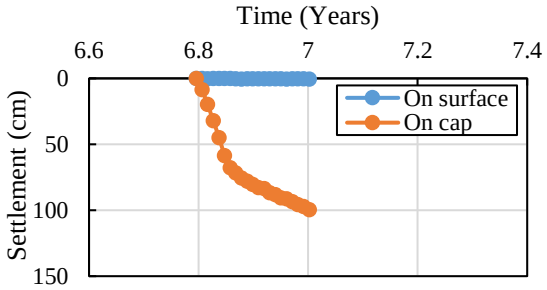

Fig. 5 Settlement during first pile load test.

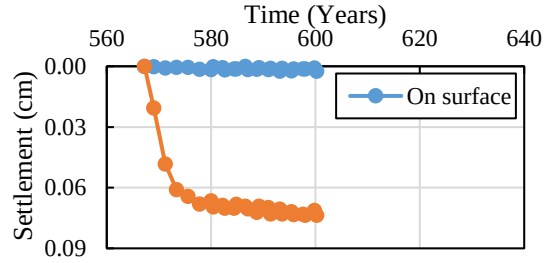

Fig. 6 Settlement during second pile load test.

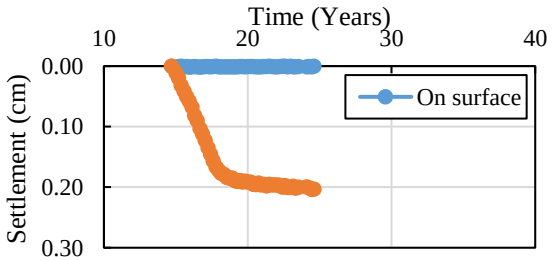

Fig. 7 Settlement during third pile load test.

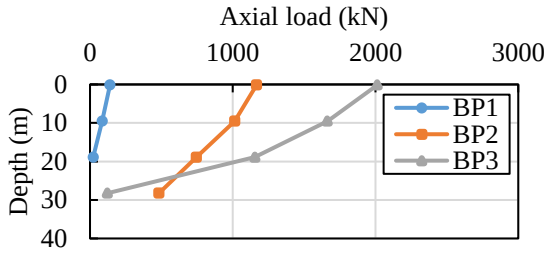

Fig. 8 Comparison of axial load of each test.

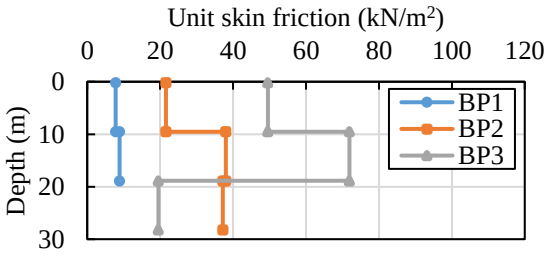

Fig. 9 Unit skin friction of each test.

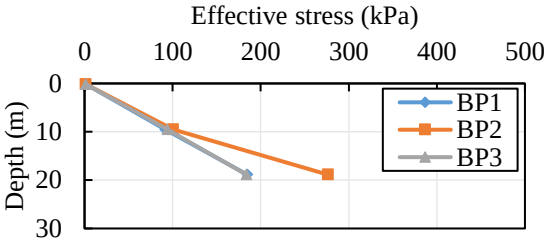

Fig. 10 Effective stress of each test.

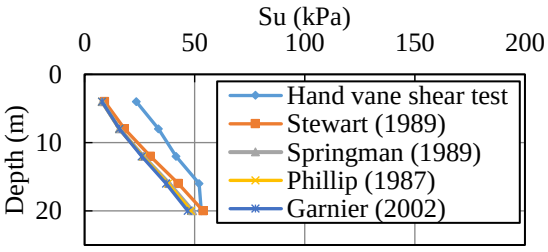

Fig. 11 Comparison of undrained shear strength.

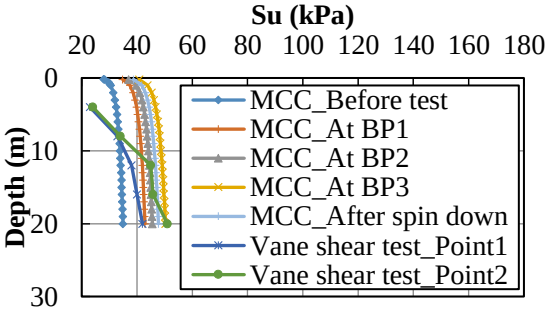

Fig. 12 Comparison of undrained shear strength.

CONCLUSIONS

This paper focused on a comparison of the behavior of a single pile during changing groundwater levels by considering the soil strength parameters, ground settlement, and pile head settlement. All the results of this research were compared with those of a previous study. It was proven by hand calculation that the trends of the results are the same. For the axial load behavior of a single pile, the bearing capacity of the soil around the pile was found to be related to the water level and the consolidation of the soil. The bearing capacity of the clay layer increased because of an increase in the effective stress due to a decrease in the groundwater level. On the other hand, the bearing capacity in the last of the three stages was seen to increase because of the consolidation process in the clay layer when the groundwater rose up again. However, the bearing capacity in the sand layer was found to depend on the groundwater level or the pore water pressure, as in the effective stress theory. Therefore, this research can be used to estimate and design the bearing capacity of soil with changing groundwater levels.

ACKNOWLEDGMENTS

The research was supported in every aspect by the Geotechnical Research and Development Center (GERD). The writers would like to thank each researcher of the Geotechnical Engineering Research and Development Center (GERD) and each technician of the Geotechnical Centrifuge Facility, the Hong Kong University of Science and Technology (HKUST), for providing the machines and other necessary equipment.

REFERENCES

[1] Department of Groundwater Resource (DGR), Groundwater situation in Bangkok and urban area, 2012.

[2] Likitlersuang S., Cheng C., Soraral C. and Balasubramaniam A., Strength and stiffness parameters of Bangkok clays for finite element analysis, Geotechnical Engineering Journal of the SEAGS & AGSSEA, Vol. 49, No. 2, 2018, pp. 150-156.

[3] Singtokaew K., Submaneewong C. and TANSENG P., The highest static load which ever been tested on piles in Bangkok subsoils, 40th anniversary the foundation of success, 2001, pp. 103-108.

[4] Hosoi T., Yagi N. and Enoki M., Consideration to the skin friction of diaphragm wall foundation, Interconference on deep foundation practice incorporating PILETALK, Singapore, 1994.

[5] Seah T.H. and Lai K.C., Strength and deformation behavior of soft Bangkok clay, Geotechnical Testing Journal, Vol. 26, No. 4, 2003, pp. 1-11.

[6] Likitlersuang S., Surarak C., Wanatowski D., Oh E. and Balasubramaniam A., Geotechnical parameters from pressuremeter tests for MRT Blue Line Extension in Bangkok. Geomechanics and Engineering: An International Journal, Vol. 5, No. 2, 2013, pp. 99-118.

[7] Indraratna B. and Arumugam B., Development of negative skin friction on driven pile in soft Bangkok clay, Canadian Geotechnical Journal, Vol. 29, 1992, pp. 393-404.

[8] Balasubramaniam A.S., Phienwej N. and Oh Y.N., Back-analysis and interpretations of driven and bored pile tests data in Bangkok sub-soils, Conference proceedings, International Society for Soil Mechanics and Geotechnical Engineering, 2004, pp. 81-87.

[9] Intui S. and Soralump S., The Vertical Bearing Capacity Behavior of Single Pile by Geotechnical Centrifuge, Kasetsart Engineering Journal, Vol. 31, No. 104, 2018, pp. 55-68.

[10] Ng C.W.W., Zhang L.M. and Wang Y.H., Proceedings of 6th Int. Conf. on Physical Modeling in Geotechnics (TC2), 2006.

[11] ASTM, Standard test method for deep foundations under static axial compressive load, ASTM D1143-81 (Reapproved 1994), In Annual Book of ASTM Standards. New York, 1994, pp. 1-15.

[12] Stewart D. I., Groundwater effect on in-situ walls in stiff clay, Ph.D. Thesis, University of Cambridge, 1989.

[13] Springman, Lateral loading in piles due to simulated embankment construction, Ph.D. Thesis, Cambridge University Engineering Department, UK, 1989.

[14] Phillip, R., Ground deformation in the vicinity of a trench heading, Ph.D. dissertation, Cambridge University, 1987.

[15] Garnier S.M., Properties of soil samples used in centrifuge models, Physical Modelling in Geotechnics: ICPMG'02, 2002.

11th Int. Conf. on Geotechnique, Construction Materials & Environment,
Kyoto, Japan, 3-5 November 2021, ISBN: 978-4-909106063 C3051

SURFACE TREATMENT ON ANODE ELECTRODES FOR THE HIGHER BIOELECTRICITY GENERATION IN PLANT MICROBIAL FUEL CELLS

Shohei Uramoto[1], and Md.Azizul Moqsud[2]

[1,2]Department of Civil and Environmental Engineering, [1,2]Yamaguchi University, Japan

ABSTRACT

In this study, plant microbial fuel cells (PMFCs) were constructed to enhance the power generation by using chemical treatment of carbon-based anode materials. To increase the power output to utilize it for the real-life usage is the biggest challenge in the microbial fuel cell research. Iron (Fe) , Manganese (Mn) and both of the chemicals coated anode materials have been prepared in the laboratory for the efficient electron transfer and used in PMFCs with *Monstera* plants. It was observed that the anode which was treated with both Iron and Manganese generated the highest power density, which was 46%～69 higher than Cells whose anode was coated by either Iron or Manganese. Voltage generation and stability of voltage variation were also improved with Iron and Manganese. So, the surface treatment of the carbon-based electrode materials by this environment-friendly chemical can be used for the plant microbial fuel cell application in the future.

Keywords: Plant Microbial Fuel Cells, Anode surface treatment, Bio electricity, Iron, Manganese

INTRODUCTION

Recently, massive energy revolution has been occurred, especially in the developed nations over the world. Although solar power generation, wind power generation, and water power generation are the dominant clean・sustainable energy source, some drawbacks are also observed such as instability of its power output due to weather conditions, huge area of construction, and damage to the environment. Therefore, noble energy source called Microbial Fuel Cell (MFC) is gathering an attention.[1,2]

Microbial Fuel Cells introduced plants in its system called as PMFCs are promising technology [3,4] due to the fact of that organic matters which are necessary for bacteria's activity are theoretically supplied by plants permanently in the soil. This is expected to become new sustainable energy source, however; the biggest drawback in PMFC has been low power output. Some researchers have been attempting to overcome the problem, [5,6]
Recently, it was discovered that anode electrodes treated with Fe and Mn shows higher power output in Microbial Fuel Cells. [7]

Since there is few research which tries to improved PMFCs' power generation based on conventional MFCs' technologies, this report will attempt to construct PMFCs by utilizing previous MFCs' researches.

The main objective in this paper is to construct PMFCs with chemically treated anode. In addition, to compare power characteristics between treated and untreated anode was also set as a research purpose.

MATERIALS AND METHODS

Experimental set-up of PMFCs

Three PMFCs were prepared with organic soil, Monstera plants, bacteria, and chemically treated electrodes in laboratory. The properties of organic soil are shown in table 1, and Fig 1.

Table 1. Soil properties

Sample soil	Organic soil
Water content (%)	190
pH	6.36
Electrical conductivity (mS/cm)	0.24
Loss On Ignition (%)	51.7

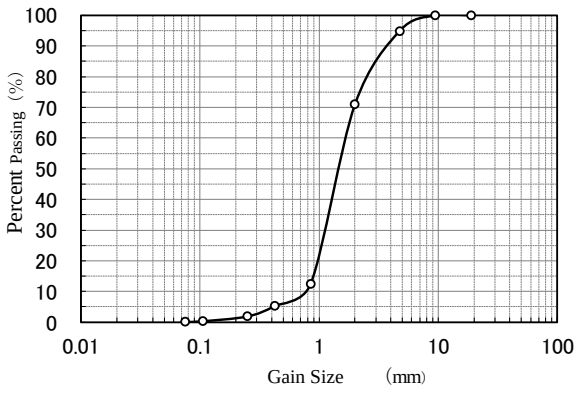

Fig 1. Grain size distribution curve of organic soil

Regarding plant species, *Monstera deliciosa*, which is one typical house plant was chosen due to the fact of that this has shade tolerance, as well as tolerance to high temperature, humidity. These properties are ideal for the indoor experiment. Herein, *Monstera Deliciosa* is abbreviated to *Monstera.*
Figure 2 shows diagram of *Monstera*'s PMFC.

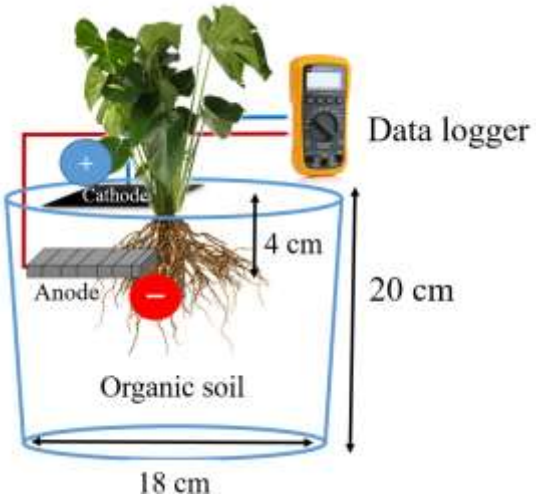

Fig 2. Plant Microbial Fuel Cell using *Monstera*

Shewanella Oneidensis (Japan Collection of Microoganisms) was chosen as the electroactive bacteria. *Shewanella Oneidensis* was cultured in the petri dish at Incubator at 28℃. The medium consisted of Trypto-soya agar (Nissui Pharmaceutical Co., Ltd.) at 40g, and distilled water at 1000mL.
Three types of anode electrodes were prepared in order to evaluate the effect of Iron and Manganese.

Procedure of Anode Surface Treatment

First of all, bamboo charcoals curled with iron wire were combined with Polyethylenimine (PEI) solution. Bamboo charcoal curled with iron wire had been discovered to have higher performance due to the lower internal resistance in previous study. [8]
To form the combination of bamboo charcoal and PEI, bamboo charcoals with iron wire was submerged in PEI (10g/L) for 3 hours while stirring with magnetic stirrer at 100rpm to be mixed thoroughly, and rinsed with distilled water, and then left to air dry for 12hours in the laboratory in which air temperature was set at 25℃. This process was conducted in all electrodes.

Secondly iron (Ⅲ) particles seeding process was conducted with the two PEI-Bamboo charcoals out of three because one electrode was supposed to contain only manganese. PEI-Bamboo charcoals were first placed in a Fe(Ⅲ) solution (Fe_3O_4 ; 1g/L) and submerged to absorb the solution while mixing at 100rpm for 2 hours, and rinsed with distilled water, and then left to air dry for 12 hours in the laboratory. The ratio of mol concentration between iron and manganese was decided to be at 1:1 because of the previous work which had discovered this ratio is an optimum. [7]

A base growth iron (Ⅱ) solution was prepared consisting of iron (Ⅱ) sulfate heptahydrate ($FeSO_4 \cdot 7H_2O$) at 1mmol in distilled water. Sodecylbenzenesulfonate (SDBS) surfactant was added to this iron growth solution. Given the amount of iron (Ⅱ) particles, the SDBS surfactant's mol concentration was adjusted to be 0.02M in the beaker. The dried PEI-Fe(Ⅲ)-Bamboo charcoals were placed in this solution while stirring at 100rpm for an hour.

To activate the growth reaction of the Fe nanoparticles, an aqueous solution of 5.0M NaOH was added and quickly mixed to produce the characteristic green suspension.
Before moving to the next step, one electrode which was supposed to have only Iron was removed and left in solution for 48 hours.
After 5 min, 1 mM aqueous solution of potassium permanganate (KMnO4) was added and mixed to create a murky brownish precipitate. The PEI-Iron(Ⅱ) Bamboo charcoals were left in this solution to promote the Fe(Ⅲ)-Mn(Ⅶ) growth process for 48 h. The bamboo charcoals were then removed from the solution and rinsed thoroughly with distilled water to ensure the termination of the growth process. Finally, the completed samples were left to air-dry overnight before use within PMFC testing. Green suspension and a murky brownish precipitate which were appeared in the experimental process are shown in Fig 3.

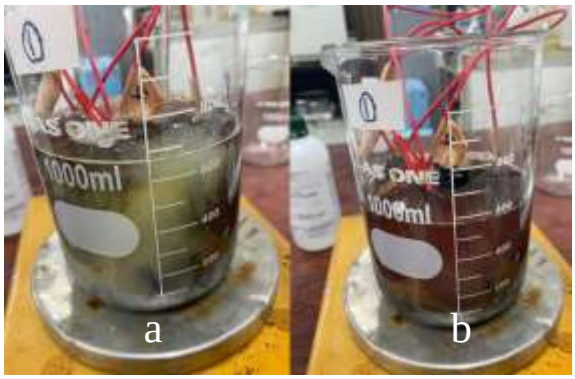

Fig 3. a) Green suspension, b) Murky brownish precipitate

When it comes to electrode which was supposed to be treated by manganese, SDBS treatment and 1 mM aqueous solution of potassium permanganate (KMnO4) was conducted, then left to the solution for

48 hours.
These anode electrodes were submerged in *Shewanella Oneidensis*' bacteria solution for hour, then used in PMFCs. Electrode distance was fixed at 4 cm in all cells.
Figure 4 illustrates anode electrode treated with Iron, Manganese, and both of them respectively.

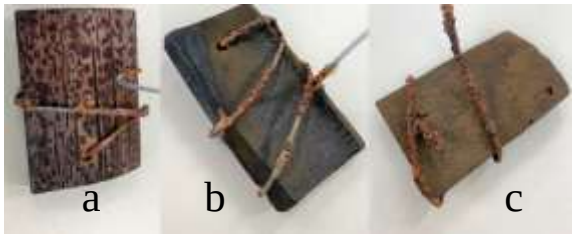

Fig 4. Chemically treated anodes a) Fe-anode, b) Mn-anode, c) Fe・Mn-anode

RESULTS AND DISCUSSION

Voltage Variation

Figure 5 illustrates voltage variation for 5 days with PMFCs whose anode electrodes were coated by Iron, Manganese, and both Iron and Manganese.

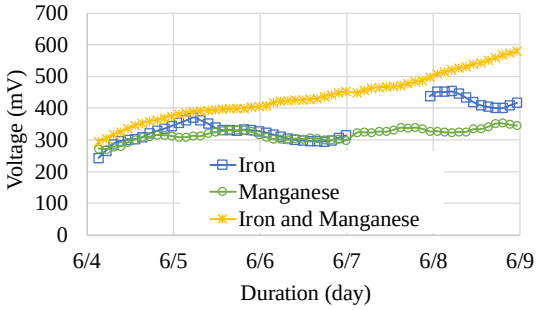

Fig 5. Voltage variation with time

Herein, each cell will be denoted as Fe-PMFC, Mn-PMFC, and Fe・Mn-PMFC respectively for simplify. In the initial stage, it is observed that all voltages are almost the same, value. Fe・Mn-PMFC generated 293.9 mV. When it comes to Fe-PMFC and Mn-PMFC, its initial voltages were 242. 5 mV and 272.0 mV respectively.
After that, Fe・Mn-PMFC's voltage increased gradually without voltage drops, and the highest voltage was produced at the end of duration, which was 578.9 mV. On the other hand, Fe-PMFC and Mn-PMFC experienced some fluctuation during 5 days. Regarding Mn-PMFC, voltage generation changes slightly. After the initial voltage, its value went up marginally until June 5th. However, voltage started to decline from the time, and it reached first bottom at 15:26 on June 5th. This kind of slight changes were seen four times, but in average, its voltage was fixed at approximately 320 mV. Turning to Fe-PMFC, voltage begun to increase from the initial stage, and this trend seems to the same as Fe-Mn PMFC's voltage increase. However, Fe-PMFC suddenly experienced voltage decrease at the middle of June 5th, then its gradual voltage decline continued by June 7th. The blank seen between June 7th and 8th was occurred by mechanical trouble of data logger. The highest voltage of Fe-PMFC was obtained at June 8th's afternoon whose value was 453.3 mV. An order of the highest voltage in whole duration is Fe・Mn-PMFC, Fe-PMFC, then Mn-PMFC, and its voltage was 578.9 mV, 453.3 mV, and 352.9 mV respectively.
It was no voltage drop that Iron and Manganese coated anode's cell was discovered to have extremely high performance. This indicates that both metal ion, Iron and Manganese are essential factors for the stable, and higher voltage generation.

Power Generation

Figure 6 explains power characteristics of Fe・Mn-PMFC, Fe-PMFC, and Mn-PMFC respectively. These power characteristics were measured after June 9th shown in voltage variation section. This graph was obtained with data logger (Crenova digital multimeter, Crenova Ink, Japan) as well as external resistances.

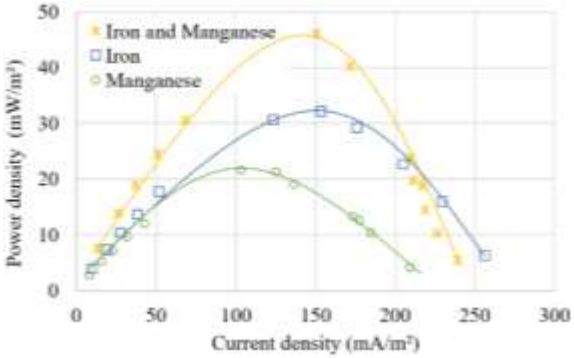

Fig 6. Power characteristics in three PMFCs

First of all, peak power density of Fe・Mn-PMFC was 46.0 mW/m^2 which is the highest value out of three PMFCs. This highest power was generated when 993 ohm's external resistance was connected. That is to say, this cell's internal resistance is calculated to 993 ohm.

Secondly, Fe-PMFC's highest power density was calculated to 32.1 mW/m^2, which is around 15mW lesser than Fe・Mn-PMFC. Internal resistance determined with the same method described above was 668 ohm. Although the peak power is smaller in Fe-PMFC, the internal resistance was better in Fe coating anode than Fe・Mn coating anode's PMFC.

Thirdly, Mn-PMFC's maximum power was 21.6

mW/m^2, which was the lowest in all cells. Its internal resistance was 993 ohm, and this is the same value as Fe・Mn-PMFC, however; due to the lower highest open circuit voltage, Mn-PMFC's power was lesser than Fe・Mn-PMFC by around 25 mW.
Although the maximum power density was highest in Fe・Mn-PMFC, internal resistance was lower in Fe-PMFC by 325 ohm. Further research will be necessary in order to identify the reason of this, however; difference between this experiment and previous experiment [7] was bacteria's species. This might be the cause of higher power performance in Fe coated anode since some researchers [9] reported the power generation can be improved with the supplement of Fe(Ⅲ).

Image Analysis by Scanning Electron Microscope

Figure 7 illustrates the comparison of untreated anode, and Iron-Manganese treated anode using SEM.

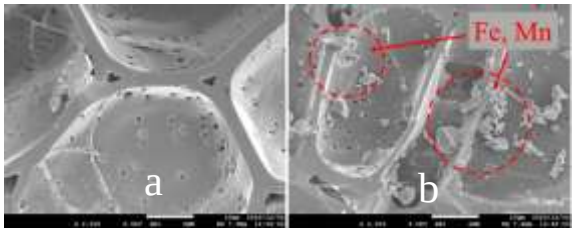

Fig 7. Comparison of anodes, a) Untreated anode, b) Fe and Mn treated anode

In both figures, some unique porous structure of bamboo material can be observed in the background. A number of small particles are also shown in the section a) in Fig 7's Fe・Mn treated anode surface. They are iron and manganese nano particles. These nano particles are still captured on the surface of electrode even though electrodes were rinsed with distilled water. Thus, a function of polyethienine as an adhesive is thought to be working well. As previous research [7] explains, the reason of higher power generation in Enhanced anode PMFC is that countless particles can play an essential role as an edge which enables bacteria to stay on the surface easier. By contrast, these nano chips are not observed in section b) in Fig.7

CONCLUSIONS

This research was conducted in order to construct Plant Microbial Fuel Cells based on recent developments which had reported in Microbial Fuel Cells' study. Moreover, to compare power characteristics between treated and untreated anode was also purpose in order to determine which metal plays more essential role.

First, it was discovered that Iron and Manganese coated anode exhibited highest voltage generation in which no voltage decline occurred in PMFCs.

Secondly, PMFC whose anode was treated by Fe and Mn showed the highest power, which implies that both Iron and Manganese are essential for the improvement in PMFC.

Thirdly, although future research will be required to identify the cause of gaps in Fe-PMFC, and Mn-PMFC, this is considered that there may be optimum metal ion for each bacterium.

ACKNOWLEDGMENTS

The authors acknowledged the financial support of the Chugoku Denryoku for conducting this research.

REFERENCES

[1] P.M.D. Serra, Espirito Santo A., Sourcing power with microbial fuel cells: A timeline. Journal of Power Souces, Vol 482, 2021
[2] Mostafa E. Elshobary, Hossain M.Zabed, Junhua Yun, Guoyan Zhang, Xianghui Qi., Recent insights into microalgae-assisted microbial fuel cells for generating sustainable bioelectricity. Internal Journal of Hydrogen Ennergy, Vol 46, Issue 4, 2021, pp 3135-3159
[3] Rukhsar Shaikh, Afshan Rizvi, Marzuqa Quraish, Soumya Pandit, Abhilasha Singh Mathuriya, Piyush Kumar Gupta, Joginder singh, Ram Prasad., Bioelectricity production using plant-microbial fuel cell: Present state of art. South African Journal of Botany. 2020
[4] Chiranjeevi.P, Yeruva,D.Y, Kumar,A.K, Mohan,V, Varjani,S., Plant- Microbial Fuel Cell Technology. Microbial Electrochemical Technology, 2019, pp.549-564
[5] Moqsud,M.A J. Yoshitake, Q.S. Bushra, M. Hyodo, K. Omine, David Strik., Microbial fuel cell (MFC) for bioelectricity generation from organic wastes. Waste management, Vol 36, 2015, pp 63-69
[6] Helder,M, Buisman,C.J.N, Hamelers,H.V.M, Strik,D.P.B.T.B., Design criteria for the Plant-Microbial Fuel Cell Electricity generation with living plants from lab to application. 2012, pp 4-5.
[7] Duarte,K.D.Z, Kwon,Y., Enhanced extracellular electron transfer of yeast-based microbial fuel cells via one pot substrate-bound growth iron-manganese oxide nanoflowers. Journal of Power Source, Volume 474, 2019.
[8] Moqsud.M.A, Omine,K, Yasufuku,N, Hyodo,M, Yukio,N., Microbial fuel cell (MFC) for bioelectricity generation from organic wastes.Waste management, Vol 33, Issue 11, 2013, pp.2465-2469

[9] Di Wu, Defeng Xing, Lu Lu, Ma Wei, Bingfeng Liu, Nanqi Ren., Ferric iron enhances electricity generation by Shewanella oneidensis MR-1 in MFCs. Bioresource Technology, Vol 135, 2013, pp 630-634

11th Int. Conf. on Geotechnique, Construction Materials & Environment, Kyoto, Japan, 3-5 November 2021, ISBN: 978-4-909106063 C3051

PLANT ENZYME INDUCED CARBONATE PRECIPITATION FOR SAND CEMENTATION

Linyu Wu[1], Linchang Miao[2] and Satoru Kawasaki[3]

[1,2]Transport School, Southeast University, China; [3]Faculty of Engineering, Hokkaido University, Japan

ABSTRACT

Enzyme-induced carbonate precipitation (EICP) is an emerging biogeotechnology for enhancing the engineering properties of granular soil. In this study, to lower the cost of urease used in EICP, urease was extracted from soybeans. The effects of temperature and pH on soybean urease activity were studied. Then the test-tube experiments of urease-induced calcium carbonate precipitation were carried out by controlling cementation solution concentration. Based on this, sand was cemented by injecting urease solution and cementation solution circularly. The ultrasonic test and unconfined compressive strength test were performed to evaluate the cementation effect of sand solidified with EICP. The results show that the optimum pH of soybean urease is 8, and the maximum urease activity is observed at 75°C. With the increase of cementation solution concentration, the precipitation ratio of calcium carbonate increases first and then decreases, and when the cementation solution concentration is 0.75 M, the precipitation ratio of calcium carbonate arrives at the highest during tests. The calcium carbonate induced by soybean urease cements the loose sand into a strong sand column. The longer the cementing time is, the more compact the treated sand is and the higher the unconfined compressive strength is. Overall, soybean urease has a great potential to replace commercial urease for sand treated via EICP.

Keywords: Sand cementation; Soybean urease; Enzyme induced carbonate precipitation (EICP); Unconfined compressive strength

INTRODUCTION

Microbially induced carbonate precipitation (MICP) is a promising method of improving soil [1, 2]. MICP is mostly based on a high-yield urease microorganism that uses its own metabolic activity to produce urease, which hydrolyzes urea into NH_4^+ and CO_3^{2-}, and then CO_3^{2-} combines with Ca^{2+} in the surrounding environment to form carbonate, so as to cement sand particles into a whole, causing an increase in strength of the soil [3]. Due to its mild reaction conditions and weak negative effects, this technology has been widely used in geotechnical engineering and environmental engineering and other fields in recent years.

Although MICP technology has been successfully applied in both laboratory and field scales, there are still some challenges in improving soil. The size and aerobic nature of the urease-producing bacteria limit the application of MICP, including the type and depth of the treated soil [4]. Plant-derived enzyme induced carbonate precipitation (EICP) is an alternative method to MICP for the enhancement of soil. EICP technology has two significant advantages over MICP. First, small size free urease induces carbonate precipitation to be less prone to biological clogging and can penetrate finer grained soil. Second, free urease is degradable, avoiding long-term impact on the environment [5, 6].

In recent years, Neupane et al. [7] injected the mixture of urea, calcium chloride and urease into PVC cylinders containing sand to obtain cemented sand samples, confirming the effectiveness of EICP technique. Neupane et al. [8] reported that the maximum unconfined compressive strength of enhanced sand specimens using EICP was 380 kPa. Carmona et al. [9] studied the application of EICP technology in sand cementation, and found that it can effectively enhance the mechanical properties of sand. However, the cost of urease greatly restricts the promotion of EICP technology. According to the current price of urease, the cost of urease accounts for the main part of the total cost of EICP technology. Commercial urease is produced in high-purity form for medical, food and other industries, so the price is high [10]. Therefore, the potential of using plant-derived urease-induced carbonate precipitation has been demonstrated. Nam et al. [11] extracted urease from jack bean with phosphate buffer, indicating that the crude urease extract of the plant had the potential to replace the purified urease for improving the strength of the material. Dilrukshi et al. [12] used crude urease extracted from crushed watermelon seeds to cement sand and obtained estimated unconfined compressive strength of several kPa to MPa. Javadi et al. [13] applied a method of blending, filtration, and acetone fractionation to extract and purify urease from watermelon seeds for EICP treatment of soil. They reported the urease activity of approximately 611 U/mL and demonstrated the formation of $CaCO_3$ precipitation.

Soybean is rich in urease and has a wide range of

sources [14, 15]. In this study, in order to reduce the cost of urease used in EICP, a simple method was investigated to crudely extract soybean urease. The effects of various factors on soybean urease activity were studied. Then, urease was used in calcium carbonate precipitation test to obtain the optimum cementation solution concentration. Furthermore, soybean urease and cementation solution with optimum concentration were used to cement sand, and the cementation effect was evaluated by ultrasonic test and unconfined compressive strength. Finally, the X-ray diffraction (XRD) test and scanning electron microscope (SEM) test were performed to explore the cementation mechanism of the treated sand.

MATERIALS AND METHODS

Soybean Urease Extraction

The soybean flour was obtained by pulverizing dried commercial soybeans and passing through a 100 mesh sieve. 100 g of soybean flour was placed in a conical flask, and then 1 L of distilled water was added, which was thoroughly shaken for 30 min. After being stored in a refrigerator at 4°C for 24 h, the soybean flour solution was centrifuged at 3000 r/min for 15 min. The supernatant was collected as urease solution for subsequent tests.

Urease Activity Test

The urease activity can be obtained by measuring the change in conductivity of the solution [16]. In this study, 3 mL urease solution was mixed with 27 mL urea solution with a concentration of 1.5 M, and the conductivity change in 10 min was monitored. The temperature of the whole process remained constant. The value of conductivity change per minute was calculated, and then it can be converted to the urea hydrolysis rate representing urease activity (mM urea hydrolysed·min^{-1}).

In order to determine the effective temperature range where cementation is possible, urease solution and urea solution were mixed at different temperatures ranging from 15-85°C. To investigate the changes of urease activity with different acid-base conditions, the temperature was 25°C and the pH varied from 6 to 10 to obtain the influence of pH on urease activity.

Calcium Carbonate Precipitation Test

The cementation solution was the mixture of urea and an equal molar concentration of calcium acetate. In order to investigate the optimum cementation solution concentration, cementation solution with different concentrations (0.25, 0.5, 0.75, 1, 1.25 and 1.5 M) was prepared. In the test tube, 10 mL of urease solution was uniformly mixed with 10 mL of cementation solution, and then the tube was placed in an incubator at 30°C for 24 h.

The theoretical amount of calcium carbonate is calculated by C×V×M, where C is the cementation solution concentration in moles per liter, V is the volume of the cementation solution in liters, and M is the molar mass of calcium carbonate of 100.09 g/mol [7]. The actual amount of calcium carbonate was obtained by the acid digestion method: After the reaction, the reactant was filtered through filter paper. Then the precipitate and filter paper were oven-dried at 60°C, and the total mass of them was weighted (M1). Subsequently, hydrochloric acid with a concentration of 4 M was used to rinse until no bubbles were produced, followed by rinsing with deionized water. The insoluble matter and filter paper were oven-dried to obtain the total mass (M2). The difference in mass before and after the acid digestion was the actual amount of calcium carbonate (M1–M2). The ratio of the actual amount of calcium carbonate to the theoretical amount was represented as the precipitation ratio of calcium carbonate.

Sand Cementation Test

Sand column treatment

In this study, the commercial sand was dried at 105°C before being placed in PVC cylinders with an inner diameter of 4.7 cm and a height of 15 cm. The particle size distribution curve was shown in Fig. 1. The median diameter of the sand grains was 0.65 mm, and according to ASTM D2487 [17], the sand was classified SP. 300 g of sand was packed into the PVC cylinder by layered compaction method. All samples had a same initial dry density of 1.73 g/cm^3 and a height of 10 cm.

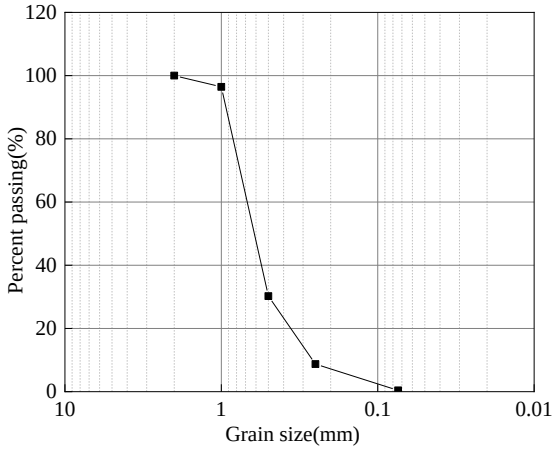

Fig. 1 The grading curve of sand

All samples were placed vertically, and the urease solution was injected from the bottom of samples at a speed (2 mL/min) until it reached saturation, and

approximately 50 mL of urease solution was used. After two hours, 50 mL of cementation solution (0.75 M urea and 0.75 M calcium acetate) was injected into samples at 2 mL/min as well. After 1 day, new urease solution and cementation solution with the same concentration and volume were added. In this way, new urease solution and cementation solution were added daily until required cementing time was attained. The required cementing time of samples was 2, 4, 6, 8 days.

Ultrasonic test

After the sand was cemented, deionized water was injected to flush out the byproducts of ammonium ions, and then samples were placed in an oven at 60°C for 48 h. Then every soil specimen with a height of 10 cm was divided into three sections along the vertical length, and the measuring points were selected at the middle points of each section, denoted as A, B and C successively, which was 17, 50 and 83 mm from the bottom of the sample respectively. Ultrasonic wave propagated along the diameter of samples at each measuring point, and the compactness of the samples was determined by comparing the sound time values of different samples.

Unconfined compressive strength test

The sand columns were trimmed to make them flat at the top and bottom before unconfined compressive strength (UCS) test. Under the condition that the sample had no lateral pressure, the loading rate of 1mm/min was controlled, the axial pressure was applied until the sample failed, and the maximum axial stress was taken as the UCS.

RESULTS AND DISCUSSION

Urease Activity Test

Effect of temperature

At high temperatures, urease will be inactivated due to degeneration [18]. In this study, urease activity was investigated between 15 and 85°C. The urease activity at different temperatures is shown in Fig. 2. Temperature had a significant effect on urease activity. The urea hydrolysis rate of urease was 5.36 mM per minute at 15°C, at the same temperature, this soybean urease activity was about 13 times higher than microbial urease activity previously studied by Whiffin [16], which demonstrated that the extracted soybean urease activity was higher. Afterward, urease activity increased and approached the maximum at 75°C. Then, it dropped sharply at 85°C, this might be due to the inactivation of urease at high temperatures, which meant that excessive temperature was not conducive to urease development.

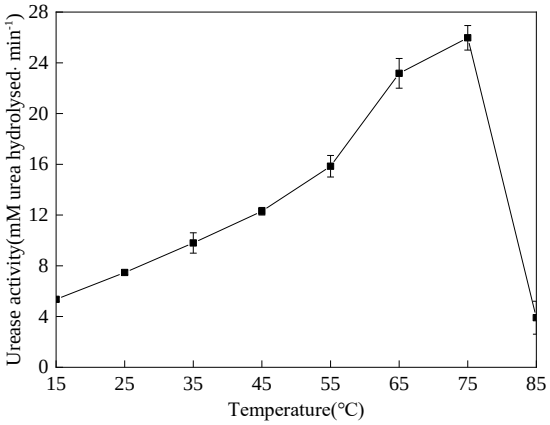

Fig. 2 The urease activity at different temperatures

Effect of pH

Each enzyme has an optimal pH at which it has the greatest activity [19]. The urease activity at different pH is shown in Fig. 3. The urease activity increased first and then decreased with an increase in pH from 6 to 10. The urea hydrolysis rate reached maximum at the pH of 8, i.e., 7.55 mM per minute. Therefore, the optimal pH of urease is 8. For the pH of 6 and 10, the urea hydrolysis rate was 7.32 and 7.17 mM per minute, respectively, and it was noticed that there was no significant` decrease in the urea hydrolysis rate compared with the pH of 8, which showed that urease had strong tolerance to moderately acid and alkali environment. During the EICP process, urease hydrolyses urea into NH_4^+ and CO_3^{2-}, resulting in the increase of pH, which creates a conducive environment to carbonate precipitation [20], hence, the resistance of urease to acid and alkali is beneficial to its application in practical engineering.

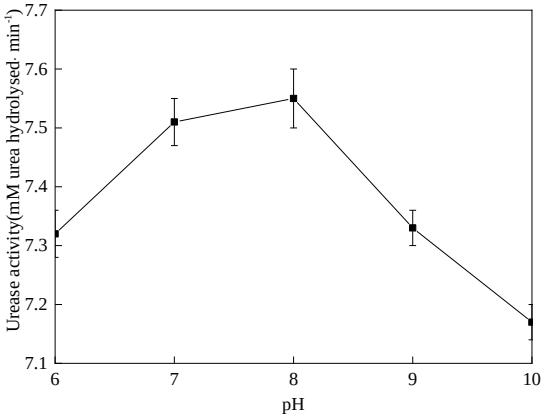

Fig. 3 The urease activity at different pH values

Calcium Carbonate Precipitation Test

The comparison between the actual and theoretical amount of calcium carbonate at different cementation solution concentrations is shown in Fig.

4. As can be seen from the figure, when the cementation solution concentration increases from 0.25 to 0.75 M, the actual amount of calcium carbonate gradually increased and the precipitation ratio also increased. Afterward, the actual amount of calcium carbonate gradually deviated from theoretical amount when the concentration of cementation solution continued to increase, that is, the precipitation ratio of calcium carbonate decreased. This might be due to that the concentration of urease was too high relative to the cementation solution concentration as the cementation solution concentration was low, which might suppress the calcium carbonate precipitation reaction [7, 21]. Therefore, if the cementation solution concentration is appropriately increased at this stage, the precipitation ratio of calcium carbonate will increase. However, when the concentration of cementation solution exceeds the optimum concentration, the function of urease will be limited, leading to the reduction of the catalytic hydrolysis capacity of urease and the reduction of calcium carbonate precipitation ratio. Considering that the precipitation ratio of calcium carbonate is up to 84% at the cementation solution concentration of 0.75 M, hence, 0.75 M is taken as the optimum cementation solution concentration, and the cementation solution with this concentration is adopted in subsequent sand cementation test.

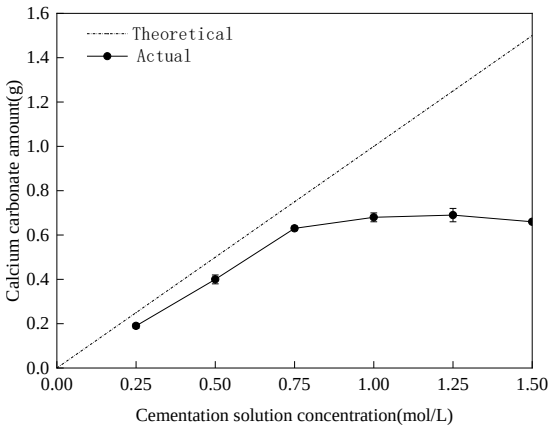

Fig. 4 The calcium carbonate production at different cementation solution concentrations

Sand Cementation Test

Ultrasonic test

The propagation velocity of ultrasonic wave varies with the degree of medium compactness. Therefore, sound time value is taken as an index to evaluate the compactness of cemented samples. The difference of sound time value of each sample indicates that the degree of compaction is different, that is, the degree of cementation is different. The sound time value of the sample after cementing is shown in Fig. 5. With the increase of cementing time, the sound time value of each test position of the sand column decreased. Because more urease solution and cementation solution were injected as the cementing time was increased, and more precipitation was formed, the sample was more compact.

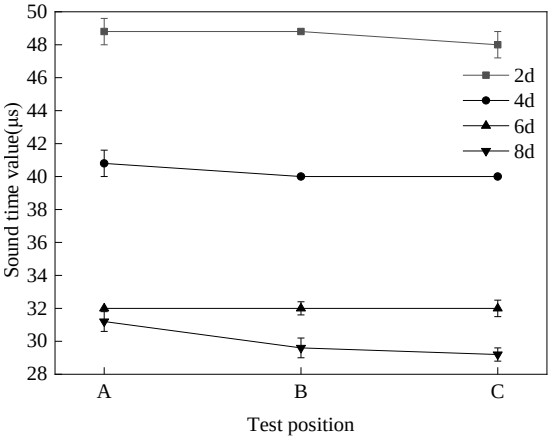

Fig. 5 The sound time value of cemented samples

Unconfined compressive strength test

The UCS of the sample after cementing is shown in Fig. 6. It could be seen from the figure that the cementing time had a significant influence on the UCS of the sample. The UCS of the sample increased with the increase of the cementing time. The UCS of the sample was only 0.07 MPa at the cementing time of 2 days, and when the cementing time was 8 days, the UCS of the sample could reach 2.18 MPa, which was 31 times greater than the cementing for 2 days. In general, the more compact the material is, the stronger it is. The ultrasonic test results showed that the samples were more compact with the increase of cementing time, hence, the UCS of the sample increased.

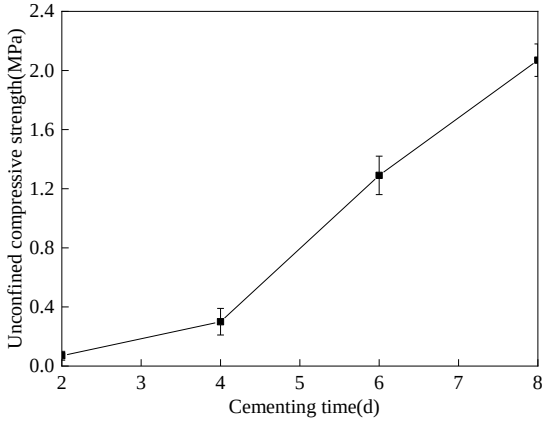

Fig. 6 The unconfined compressive strength of cemented samples

XRD Test and SEM Test

The XRD test was conducted with the dried precipitate. Figure 7 presents the X-ray diffraction pattern of precipitate products. According to the diffraction peak, the mineral composition of the soybean urease induced precipitation is calcite.

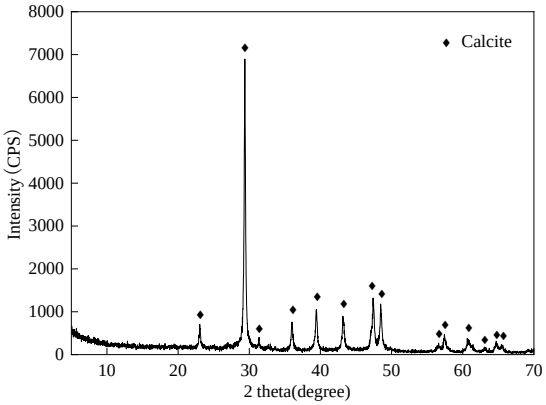

Fig. 7 The X-ray diffraction pattern of precipitate product

Figure 8 shows the SEM image of the cemented sand sample. It could be seen that there were calcium carbonate crystals on the surface of sand grains and between adjacent sand grains (Fig. 8(a)). With the development of EICP reaction, the size of generated calcium carbonate crystals kept growing. Some calcium carbonate crystals cemented between sand particles, while others filled the pores among sand particles, thus making loose sand particles a whole. However, there were still some pores in the sand, which indicated that calcium carbonate crystals generated by EICP reaction were not enough to fill all the pores in the sand. This explained why the longer the cementing time was, the more compact the sample was. Figure 8(b) shows the SEM image with magnification of 10000 times. As shown in the figure, the morphology of calcium carbonate crystals induced by soybean urease was spherical or spherical aggregates with different sizes, which might be related to the sedimentary environment.

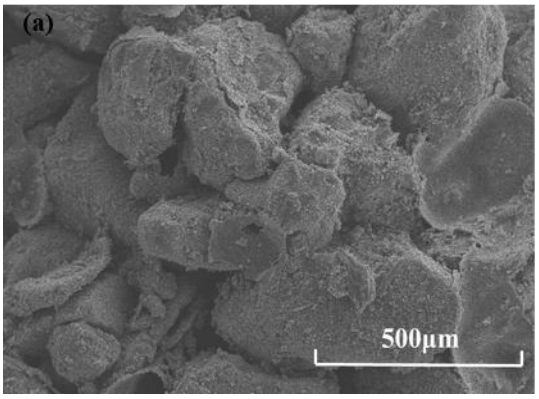

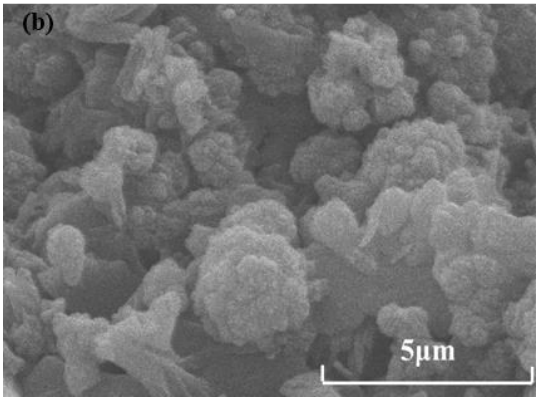

Fig. 8 The SEM images of the cemented sample: (a) magnification of 100 times and (b) magnification of 10000 times

CONCLUSIONS

Urease was extracted from soybeans at low cost. On the basis of studying influencing factors of urease activity and calcification, the soybean urease cemented sand test was carried out. The following conclusions can be drawn:

(1) Plant enzyme is simple and economical. The extracted soybean urease has higher urease activity, and its optimal pH is 8. Compared with pH, temperature has a more significant effect on urease activity, and the urease has a temperature optimum at 75°C.

(2) The cementation solution concentration has great influence on calcification. When the cementation solution concentration is low (<0.75 M), increasing cementation solution concentration will increase the precipitation ratio of calcium carbonate, while excessively high concentration of cementation solution will reduce the precipitation ratio of calcium carbonate.

(3) EICP technology can successfully cement loose sand particles into a whole. As for cementing samples, with the increase of cementing time, more calcium carbonate is generated to cement and fill the sand, which improves the compactness and the UCS of the sample. The UCS of the sample can reach 2.18 MPa after cementing for 8 days. It demonstrates that EICP technology can appreciably improve the mechanical properties of soil and has a broad application prospect.

It is recommended to optimize the soil treatment parameters and conduct some large-scale field tests before EICP technology can be used in practical engineering.

ACKNOWLEDGMENTS

This work was supported by the National Natural Science Foundation of China (No. 51578147). The authors thank the valuable comments from the

reviewers.

REFERENCES

[1] Mitchell J. K. and Santamarina J. C., Biological considerations in geotechnical engineering, Journal of geotechnical and geoenvironmental engineering, Vol. 131, Issue 10, 2005, pp. 1222-1233.

[2] Van Paassen L. A., Daza C. M., Staal M., Sorokin D. Y., van der Zon W. and van Loosdrecht M. C., Potential soil reinforcement by biological denitrification, Ecological Engineering, Vol. 36, Issue 2, 2010, pp. 168-175.

[3] DeJong J. T., Mortensen B. M., Martinez B. C. and Nelson D. C., Bio-mediated soil improvement, Ecological Engineering, Vol. 36, Issue 2, 2010, pp. 197-210.

[4] Hamed Khodadadi T., Kavazanjian E., van Paassen L. and DeJong J., Bio-grout materials: A review, in Proc. Grouting, 2017, pp. 1-12.

[5] Hamdan N., Kavazanjian Jr E. and O'Donnell S., Carbonate cementation via plant derived urease, in Proceedings of the 18th International Conference on Soil Mechanics and Geotechnical Engineering, 2013, pp. 2-6.

[6] Kavazanjian E. and Hamdan N., Enzyme induced carbonate precipitation (EICP) columns for ground improvement, in Proc. Int. Foundation Congress and Equipment Exposition, 2015, pp. 2252-2261.

[7] Neupane D., Yasuhara H., Kinoshita N. and Unno T., Applicability of enzymatic calcium carbonate precipitation as a soil-strengthening technique, Journal of Geotechnical and Geoenvironmental Engineering, Vol. 139, Issue 12, 2013, pp. 2201-2211.

[8] Neupane D., Yasuhara H., Kinoshita N. and Ando Y., Distribution of mineralized carbonate and its quantification method in enzyme mediated calcite precipitation technique, Soils and Foundations, Vol. 55, Issue 2, 2015, pp. 447-457.

[9] Carmona J. P., Venda Oliveira P. J., Lemos L. J. and Pedro A. M., Improvement of a sandy soil by enzymatic calcium carbonate precipitation, in Proceedings of the Institution of Civil Engineers-Geotechnical Engineering, Vol. 171, Issue 1, 2017, pp. 3-15.

[10] Larsen J., Poulsen M., Lundgaard T. and Agerbaek M., Plugging of Fractures in Chalk Reservoirs by Enzyme-Induced Calcium Carbonate Precipitation, SPE Production & Operations, Vol. 23, Issue 4, 2008, pp. 478-483.

[11] Nam I. H., Chon C. M., Jung K. Y., Choi S. G., Choi H. and Park S. S., Calcite precipitation by ureolytic plant (Canavalia ensiformis) extracts as effective biomaterials, KSCE Journal of Civil Engineering, Vol. 19, Issue 6, 2015, pp. 1620-1625.

[12] Dilrukshi R. A. N., Nakashima K. and Kawasaki S., Soil improvement using plant-derived urease-induced calcium carbonate precipitation, Soils and foundations, Vol. 58, Issue 4, 2018, pp. 894-910.

[13] Javadi N., Khodadadi H., Hamdan N. and Kavazanjian Jr E., EICP treatment of soil by using urease enzyme extracted from watermelon seeds, in Proc. Int. Foundation Congress and Equipment Exposition, 2018, pp. 115-124.

[14] Kerr P. S., Blevins D. G., Rapp B. J. and Randall D. D., Soybean leaf urease: comparison with seed urease, Physiologia plantarum, Vol. 57, Issue 3, 1983, pp. 339-345.

[15] Kumar S. and Kayastha A. M., Soybean (Glycine max) urease: Significance of sulfhydryl groups in urea catalysis, Plant Physiology and Biochemistry, Vol. 48, Issue 9, 2010, pp. 746-750.

[16] Whiffin, V. S., Microbial CaCO3 precipitation for the production of biocement (Doctoral dissertation, Murdoch University), 2004.

[17] ASTM Committee D-18 on Soil and Rock, Standard Practice for Classification of Soils for Engineering Purposes (Unified Soil Classification System) 1, ASTM international, 2017.

[18] Kumar S., Dwevedi A. and Kayastha A. M., Immobilization of soybean (Glycine max) urease on alginate and chitosan beads showing improved stability: Analytical applications, Journal of Molecular Catalysis B: Enzymatic, Vol. 58, Issue 1-4, 2009, pp. 138-145.

[19] Van der Schoot B. H. and Bergveld P., The pH-static enzyme sensor: An ISFET-based enzyme sensor, insensitive to the buffer capacity of the sample, Analytica chimica acta, Vol. 199, 1987, pp. 157-160.

[20] Hamdan N. and Kavazanjian Jr E., Enzyme-induced carbonate mineral precipitation for fugitive dust control, Géotechnique, Vol. 66, Issue 7, 2016, pp. 546-555.

[21] Chandra A. and Ravi K., Application of Enzyme-Induced Carbonate Precipitation (EICP) to Improve the Shear Strength of Different Type of Soils, In Problematic Soils and Geoenvironmental Concerns, Vol. 88, 2021, pp. 617-632.

11th Int. Conf. on Geotechnique, Construction Materials & Environment,
Kyoto, Japan, 3-5 November 2021, ISBN: 978-4-909106063 C3051

STRENGTH AND PERMEABILITY CHARACTERISTICS OF EXPANSIVE SOIL WITH GYPSUM AND RICE HUSK ASH USED FOR ROADWAY CONSTRUCTION

Angelo B. Edora[1] and Mary Ann Q. Adajar[1]

[1]Gokongwei College of Engineering, De La Salle University, Philippines

ABSTRACT

The presence of expansive soils in the site poses threats not only for built residential houses and superstructures but also for roadway construction. The shrink-swell behavior of expansive soils creates a continuous strain on the pavements which can result in cracking and settlements. Therefore, there is a need to stabilize such problematic soils. This study aims to establish a more economic and environmental-friendly way of stabilizing clay loam from Kauswagan, Lanao del Norte. Varying combinations of gypsum and rice husk ash (RHA) were used in soil stabilization. Untreated and treated soil specimens were tested for their California Bearing Ratio (CBR) and coefficient of permeability per ASTM Standard D1883 and D2434 respectively. The CBR of the soil slightly increased with the addition of 15% gypsum. While the addition of 10% RHA with the same amount of gypsum dramatically increased the soaked CBR index of the soil. A peak average value of 21.11% was recorded for 15% gypsum + 10% RHA soil specimen. Falling head permeability tests showed that as the amount of gypsum in gypsum + 10% RHA soil specimen increases, the coefficient of permeability of the soil also increases. A direct relationship was then formed between strength and permeability. This can be attributed to the formation of micropores in the soil specimen with the addition of 10% RHA, allowing an easier flow of water through it. The stabilized soil passed the DPWH Standard for the subgrade layer but slightly fell short of the requirement for the subbase layer.

Keywords: Expansive soil, Roadway construction, CBR, Permeability, Soil stability

INTRODUCTION

Expansive soils are characterized for their drastic volume change depending on the water present in them [1]. This behavior is attributed to the most detrimental clay mineral in expansive soils which is the montmorillonite. Expansive soils exhibit three characteristics that are considered problematic in construction – expansiveness, crack, and over-consolidation. These characteristics are highly dependent on the amount of water or moisture in the soil and may manifest during dry-wet cycles [2]. Excessive expansion and shrinking of these soils produce continuous ground movement which causes multiple damages to the overlying structure. Also, the propagation of cracks in the soil reduces its overall integrity and strength and increases its sliding ability. Another thing to consider is the over-consolidation characteristics of these soils which hinder the drainage of tightly packed particles of soil. In solving these, soil stabilization techniques are implemented to improve the properties of the soil and make it more suitable for its served purpose. The use of heavy equipment and mechanically stabilizing the soil on-site are the usual ways of improving the strength properties of soil however, these practices have various negative impacts on the environment and are not economically possible for all instances. One of the more economical ways of stabilizing soils is chemical soil stabilization. This is done by altering several properties of the soil by incorporating additives, to improve the necessary parameters for engineering purposes. Cementitious materials such as cement and lime are the typical characteristics of additives used. However, the use of cement in soil stabilization contributes to the rising carbon footprint of construction. Therefore, the use of waste materials exhibiting the same properties is the focus of research nowadays to promote sustainable construction.

Gypsum is known for its application in the flash setting of cement however, the larger percentage of use of gypsum is in the production of plasterboards. In Japan, the sudden rise in construction demand increases the consumption and disposal of excess and under quality plasterboards which poses environmental problems in their country [3]. With this, an opportunity to use it as a soil stabilization additive was established by past studies [4],[5]. It was found that gypsum combined with rice husk ash (RHA) was able to improve the strength properties and control the expansion of expansive soils [5].

Agricultural wastes such as RHA were also used in soil stabilization techniques because of their abundance. In the Philippines, the top ten rice-producing provinces produced nearly about 9 million metric tons of rice per year which can also be associated with the huge amount of rice husk waste. The viability of RHA in the field of soil stabilization

was proven by past studies [6],[7]. It was found that RHA has pozzolanic properties due to its silica and aluminum content. This characteristic is important in the development of the strength property of soils.

The main objective of this study is to determine the optimum mix proportions of waste gypsum and RHA that will yield the maximum values of the strength property and permeability acceptable for roadway embankment application. In determining the improvement on the strength property of the soil, CBR tests are done using untreated and treated soil specimens. On the other hand, falling head permeability tests are done in determining the mix proportion of gypsum and RHA that yields the peak value for the coefficient of permeability. Empirical models are then formulated to describe the relationship of soaked CBR index and coefficient of permeability with the amount gypsum in a mixed proportion.

With the implementation of the 'Build, build, build' program of the government, the demand for construction materials and the waste generated including gypsum increases. And considering the effect of gypsum on the environment, this increase in a waste generation may cause environmental problems in the future [8]. Considering the country's rice production, using RHA in stabilizing soils is ideal. This promotes a more sustainable, economical, and eco-friendly way of improving the geotechnical properties of soils.

MATERIAL AND METHODS

Source of the Expansive Soil Sample

The soil sample used in this study was extracted from Kauswagan, Lanao del Norte, Philippines. The sample was extracted at a depth of at least 2 meters ensuring that no organic matter will be included. The area was used for a proposed landfill site. While dealing with moist samples, color streaks and some of the soil were left when forming bigger clumps of soil as seen in Figure 1. These traits were attributed to clay minerals in soils [9]. On the other hand, the soil exhibited cracks and loss in total volume when oven-dried for 24 hours at 105 degrees Celsius as can be in Figure 2.

Source of Gypsum

The gypsum used in this study was sourced from a hardware store, selling it as plaster. This form of gypsum was grounded to powder and heated in production plants at a temperature depending on their application. Typically, gypsum wastes are collected from plasterboard excess and rejects during production. These wastes are then recycled by recycling companies and repurposing for plaster and tile grout used. Figure 3 shows the gypsum used.

Fig. 1 Soil sample formed in big clumps.

Fig. 2 Crack propagation in Kauswagan soil sample.

Fig. 3 Recycled powdered gypsum used in the study.

Source of Rice Husk Ash

The rice husk ash used in this study was collected from a biomass powerplant in Muntinlupa City, Metro Manila. Huge hauls of rice husk from the Central Luzon provinces were collected and brought to the said powerplant to incinerate. The resulting product of the said incineration process was the rice husk ash. Figure 4 shows the rice husk ash used in this study.

Fig. 4 Rice husk ash sample used in the study.

EXPERIMENTAL PROGRAM

Considering the objectives of the study, the essential parameters to be determined are the soaked CBR index and coefficient of permeability of the untreated and treated soil specimens. But before conducting the main experimental program, preliminary experiments per ASTM Standards must be done. These experiments are summarized in Table 1.

Table 1 Preliminary Experiments

Laboratory Test	ASTM Standard
Grain Size Analysis	ASTM D422
Moisture-Density Relationship	ASTM D698
Maximum Index Density	ASTM D4253
Minimum Index Density	ASTM D4254

Using the results of these tests, the soaked CBR index and coefficient of permeability of all the soil specimens were analyzed and compared. The parameters obtained in these tests were also used to determine if the soil passed the requirements mandated by the Department of Public Works and Highways (DPWH). Table 2 and Table 3 summarize the requirements for the subgrade and subbase layer.

Table 2 Summary of Subgrade Requirements

Subgrade course	
Laboratory Test	Requirement
Grain Size Analysis	All particles shall pass 75 mm square openings and not more than 15% passing no. 200 sieve
Atterberg Limits	Plasticity Index of not more than 6. Liquid Limit of not more than 30.

Table 3 Summary of Subbase Requirements

Subbase Course	
Laboratory Test	Requirement
Grain Size Distribution	Percent passing no. 200 sieve shall not be greater than two-thirds of the percent passing no. 40 sieve
Atterberg Limits	Percent passing no. 40 sieve shall have PI < 12 and LL < 35
CBR Test	Soaked CBR values not less than 30%

TEST RESULTS

Grain Size Analysis

The soil in this study was tested for its grain size distribution and the average percent passing sieve no. 200 is 59.14% [5]. Based on the results of tests done, all mix proportions passed the grading requirement for subgrade materials. The particles of treated soil samples have a range of 1.28% to 5.54% passing no. 200 sieve. Moreover, upon calculating the two-thirds of percent passing no. 40 sieve and comparing it to the percent passing of no. 200 sieve, all treated samples passed the grading requirements of subbase layer. Figure 5 shows the grain size distribution curve of 15% gypsum + 10% RHA + soil mix proportion.

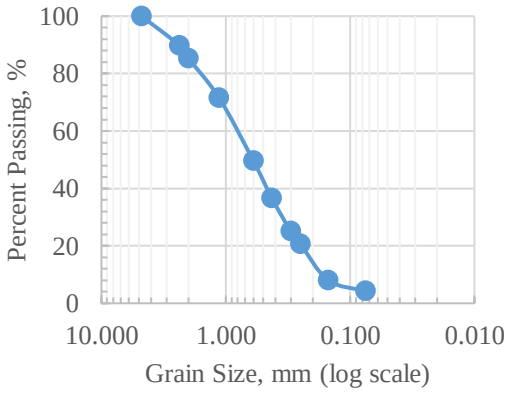

Fig. 5 Grain Size Distribution Curve of Kauswagan Soil + 15% Gypsum + 10% RHA.

Moisture-Density Relationship

Table 4 summarizes the results of Proctor compaction tests conducted for each mix proportion. Based on the results, it is noticeable that there is an increase in the maximum dry density (MDD) and a decrease in optimum moisture content (OMC) as gypsum is added to the soil sample. The same trend is

true as a constant value of 10% RHA is introduced in the specimen. Typically, the compaction curves of clays are bell-shaped [10]. This can be observed in the compaction curve of plain soil and soil with 15% gypsum specimens. On the other hand, the addition of RHA in the soil specimens induced the shifting of compaction curves to the left. This kind of compaction curve is common to silt with sand [11]. The change in the trend of the compaction curves proves the effectivity of the admixtures used. Better visualization of the comparison of curves is shown in Figure 6.

Table 4 Average Optimum Moisture Content and Maximum Dry Density of each Soil Mix Proportion

Material	OMC (%)	MDD (kN/m^3)
Kauswagan Soil	42.719	11.772
15% Gypsum + 85% Soil	37.374	12.681
5% Gypsum + 10% RHA + 85% Soil	34.435	13.173
10% Gypsum + 10% RHA + 80% Soil	32.190	13.247
15% Gypsum + 10% RHA + 75% Soil	31.496	13.695

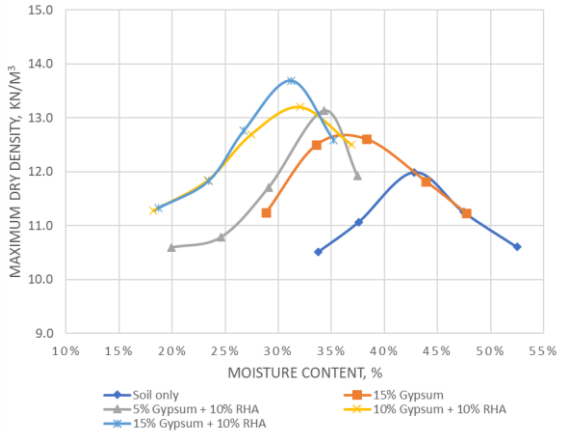

Fig. 6 Comparison of moisture-density curves of untreated and treated soil sample.

Maximum and Minimum Index Density Test

The maximum and minimum index density tests are used to determine the state of compactness of the soil specimen. From the calculated maximum and minimum index densities, the relative density of the specimen is determined. In this study, a constant value of 90% relative density was used. This is the maximum relative density that can be achieved by manual tamping [11]. The resulting maximum value for e_{max} and the resulting minimum value for e_{min} in all trials for each mix proportion were adopted. Using these values, the masses of each mix proportion to be used in the permeability test were determined. Table 5 summarizes the resulting values for e_{max} and e_{min}.

Table 5 Maximum and Minimum index densities of each Soil Mix Proportion

Material	e_{max}	e_{min}
Kauswagan Soil	2.554	1.616
15% Gypsum + 85% Soil	2.529	1.727
5% Gypsum + 10% RHA + 85% Soil	2.515	1.736
10% Gypsum + 10% RHA + 80% Soil	2.484	1.754
15% Gypsum + 10% RHA + 75% Soil	2.476	1.692

California Bearing Ratio Test

In assessing the effectiveness of the additives used in this study to stabilize expansive soils, one important factor to consider is its effect on the strength of the soil. In this study, the bearing strengths of the untreated and treated soil specimens were determined using the soaked CBR test per ASTM D1883 which is the standard test method for identifying the CBR value of soils. The soil specimens were soaked for 96 hours after compacting them in the CBR mold. Table 6 summarizes the average soaked CBR values of the soil specimens at 2.54 mm and 5.08 mm penetrations.

Table 6 Average Soaked CBR Values (%) of each specimen at 2.54 mm and 5.08 mm penetration

Material	CBR @ 2.54 mm (%)	CBR @ 5.08 mm (%)
Kauswagan Soil	1.46	1.76
15% Gypsum + 85% Soil	2.74	2.97
5% Gypsum + 10% RHA + 85% Soil	6.88	7.32
10% Gypsum + 10% RHA + 80% Soil	10.72	11.13
15% Gypsum + 10% RHA + 75% Soil	20.43	21.11

Based on the results, the recorded soaked CBR value for pure Kauswagan soil is 1.76%. This value is considered extremely low for roadway construction but is completely normal for soils classified as MH

(heavy silt). Soaked CBR values ranging from 1.35% to 2.20% were recorded for soils classified under MH (heavy silt) [12]. While the addition of 15% gypsum in the soil specimen yields a 69% increase in the soaked CBR value of the soil, yet it is still considerably low to pass the roadway construction requirements. On the other hand, the introduction of a constant amount of 10% RHA in the soil specimen dramatically increases the strength of the soil. At 15% Gypsum + 10% RHA sample, which yields the peak average soaked CBR value of 21.11%, a 600% increase in the soaked CBR value compared to its gypsum-only soil mixture counterpart, was recorded. The bearing strength improvement of 15% Gypsum+10% RHA soil specimens can be used for subgrade fill if it will also allow good drainage for water.

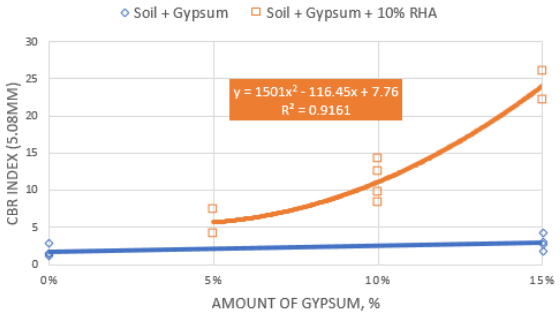

Fig. 7 Correlation between the gypsum content and soaked CBR index at 5.08 mm penetration for both Gypsum only and Gypsum+10% RHA samples.

In calculating for the CBR index of Gypsum+10% RHA soil specimens at 5.08 mm penetration, Eq. 1 can be used:

$$\text{CBR} = 1501\, X_{gypsum}^2 - 116.45 X_{gypsum} + 7.76 \quad (1)$$

Where:
CBR – soaked CBR index at 5.08 mm penetration
X_{gypsum} – the amount of gypsum in decimal form

Falling Head Permeability Test

The coefficient of permeability, k, of the treated and untreated soil specimens were determined using a rigid wall permeameter with an internal diameter of 6.305 cm and a specimen height of 14.6 cm. The condition of the permeability tests was falling head at a constant minimum hydraulic gradient of 1.5. Moreover, a constant relative density of 90% was achieved in all test specimens as it was the highest value attainable by manual thumping [11]. The coefficient of permeability, k, was calculated using Darcy's Law. Table 7 shows the summary of the coefficient of permeability of the untreated and treated soil specimens.

Table 7 Average Coefficient of Permeability of each soil specimen

Material	Permeability, cm/s
Kauswagan Soil	$\mathbf{3.958 \times 10^{-4}}$
15% Gypsum + 85% Soil	$\mathbf{1.599 \times 10^{-3}}$
5% Gypsum + 10% RHA + 85% Soil	$\mathbf{8.943 \times 10^{-4}}$
10% Gypsum + 10% RHA + 80% Soil	$\mathbf{2.308 \times 10^{-3}}$
15% Gypsum + 10% RHA + 75% Soil	$\mathbf{2.960 \times 10^{-3}}$

Based on the results, Kauswagan soil recorded a coefficient of permeability value of 3.958×10^{-4}cm/s which is classified as poor in the table of drainage characteristics of soils [13]. The addition of 15% Gypsum in the soil yields a significant increase in the k value and improved the drainage capacity of soil into good. Further increase in the permeability was recorded for gypsum +10% RHA soil specimens. As the amount of gypsum increases, the coefficient of permeability also increases. A peak value of 3.114×10^{-3} cm/s and an average value of $2.960 \times 10^{-3}$was attained by 15% Gypsum+10% RHA soil specimens which are considered as good drainage capacity. This is 647.85% greater than the pure soil specimen and 85.11% greater than the gypsum-only soil specimen counterpart.

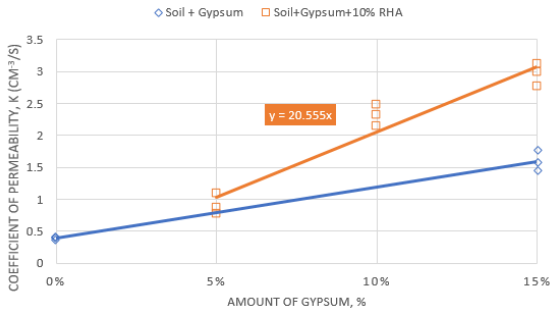

Fig. 8 Correlation between the gypsum content and Coefficient of Permeability for both Gypsum only and Gypsum + 10% RHA samples.

In calculating the coefficient of permeability of Gypsum + 10% RHA soil specimens, Eq. 2 can be used:

$$k = 20.555 X_{gypsum} \quad (2)$$

Where:
k – coefficient of permeability of Gypsum + 10% RHA soil specimens
X_{gypsum} – the amount of gypsum in percentage (%)

CONCLUSIONS

Based on this study, the following conclusions can be drawn:

Physical properties of the soil were described. Color streaks of the soil were left when molded into bigger clumps. When dried, visible cracks and loss in volume in the soil were also observed. Based on the Unified Soil Classification System (USCS), Kauswagan soil is classified as MH (high plasticity silt). These characteristics proved that the soil is expansive.

For the bearing capacity, pure soil has a very low soaked CBR value of 1.76%. The addition of 15% gypsum in the soil resulted in a 69% increase in the soaked CBR index but still considerably low to pass the roadway construction requirements. On the other hand, the introduction of 10% RHA in the mix proportion dramatically increased the bearing capacity of Kauswagan soil. An increasing soaked CBR index trend was observed as the number of gypsum increases in the mix proportion. A peak average value of 21.11% was recorded for 15% Gypsum+10% RHA soil specimens. Therefore, the optimum mix proportion in improving the strength property of Kauswagan soil is 15% Gypsum + 10% RHA mix.

Kauswagan soil was also tested for its coefficient of permeability, and it showed that it has a poor drainage capacity. The addition of 15% gypsum reduces the number of voids present in the soil but slightly increases the permeability of the soil. This unusual effect on the soil remains consistent as 10% RHA was added to the soil. As the amount of gypsum increases in Gypsum+10% RHA soil specimens, the void ratio and coefficient of permeability of the soil increases. A peak value of 3.114×10^{-3} cm/s and an average value of $2.960 \times 10^{-3}$was attained by 15% Gypsum+10% RHA soil specimens which are considered as good drainage capacity. Therefore, the optimum mix proportion in improving the permeability characteristics of Kauswagan soil is 15% Gypsum + 10% RHA. The addition of RHA in the mix proportion, which is bigger than the soil, reduced the cohesion among soil particles which creates micropores in the soil specimen

Considering the improvement of the strength and permeability characteristics of Kauswagan soil due to the combination of gypsum and RHA, the soil is recommended for subgrade use.

ACKNOWLEDGMENTS

The authors would like to express their deepest gratitude to DOST-ERDTR for providing the necessary resources to complete this research, ABC Infrageoservices, and to Engr. Jonathan Tiongson for the procurement of materials.

REFERENCES

[1] Dang, L., Hasan, H., Fatahi, B., Jones, R., & Khabbaz, H., Enhancing the Engineering Properties of Expansive Soil Using Bagasse Ash and Hydrated Lime. International Journal of GEOMATE, Vol. 11, Issue 25, 2016, pp. 2447-2454.

[2] Shi, B., Zheng, C., & Wu, J., Research Progress on Expansive Soil Cracks under Changing Environment. The Scientific World Journal, 2014.

[3] Ahmed, A., Ugai, K., & Kamei, T., Investigation of recycled gypsum in conjunction with waste plastic trays for ground improvement. Construction and Building Materials, Volume 25, pp. 208-217.

[4] Ahmed, A., Ugai, K., & Kamei, T., Laboratory and Field Evaluations of Recycled Gypsum as a Stabilizer Agent in Embankment Construction. Soils and Foundations, Volume 51, Issue 6, 2011, pp. 975-990.

[5] Tan, J. F., & Adajar, M. A. Q., Recycled Gypsum and Rice Husk Ash as Additives in the Stabilization of Expansive Soil. International Journal of GEOMATE, Volume 18, Issue 70, 2020, pp. 197-202.

[6] Behak, L., Soil Stabilization with Rice Husk Ash. Rice Technology and Production, 2017, pp. 31-45.

[7] Yadav, A. K., Gaurav, K., Kishor, R., & Suman, S. K., Stabilization of alluvial soil for subgrade using Rice Husk Ash, Sugarcane Bagasse Ash, and Cow Dung Ash for Rural Roads. International Journal of Pavement Research and Technology, Volume 10, 2017, pp. 254-261.

[8] Claisse, P. A., & Ganjian, E., Gypsum: Prospects for Recycling. Proceedings of the ICE – Construction Materials, Volume 159, Issue 1, 2006, pp. 3-4.

[9] Finch, H. J. S., Samuel, A. M., & Lane, G. P. F., Lockhart & Wiseman's Crop Husbandry Including Grassland, 9th ed., Woodhead Publishing, 2014.

[10] Budhu, M., Soil Mechanics and Foundations, 3rd ed., John Wiley & Sons, Inc., 2010.

[11] Dungca, J. R., & Jao, J. L., Strength and permeability characteristics of road base materials blended with fly ash and bottom ash. International Journal of GEOMATE, Volume 12, Issue 31, 2017, pp. 9-15.

[12] Nagaraj, H. B., & Suresh, M, Influence of clay mineralogy on the relationship of CBR of fine-grained soils with their index and engineering properties. Transportation Geotechnics, Volume 15, 2018, pp. 29-38

[13] Liu, C., & Evett, J. B., Soil Properties: Testing, Measurement, and Evaluation, 6th ed., Pearson Education, Inc., 2009.

11th Int. Conf. on Geotechnique, Construction Materials & Environment,
Kyoto, Japan, 3-5 November 2021, ISBN: 978-4-909106063 C3051

OPTIMIZATION OF THE STRENGTH PROPERTIES OF EXPANSIVE SOIL STABILIZED WITH AGRICULTURAL WASTES

Mary Ann Q. Adajar[1] and Kigia R. Valbuena[1]

[1]De La Salle University, Manila, Philippines

ABSTRACT

Expansive soils are problematic soils that exhibit shrink-swell behavior. Previous research has shown that 20% rice husk ash (RHA) effectively reduces the swelling potential of expansive soils, but it does not increase the strength of the soil. An improved admixture composed of RHA and a binder is used to treat the expansive soil. Different types of binders are used; three of which are agricultural wastes namely coconut shell ash (CSA), rice straw ash (RSA), and sugarcane bagasse ash (SCBA). Ordinary Portland cement (OPC) is used as a comparison for the other binders. The untreated and treated soil mixtures were evaluated mainly through the unconfined compressive strength (UCS) and expansion index (EI). The effectivity of the admixture is evaluated through ASTM D4609. The treated specimens exhibited an increase in the strength by as much as 745.38 kPa, 859.90 kPa, 799.46 kPa, 2428.31 kPa for the mixtures with CSA, RSA, SCBA, and cement, respectively. A response surface methodology was performed for the UCS of the soil mixtures with the binder types CSA, RSA, and SCBA. The binder content and curing period are the numerical factors and the response is the UCS. Contour plots and response surface plots show that the optimum strength for the mixtures with CSA, RSA, and SCBA is at the highest curing period (35 days) and lowest binder content (5% content). The binder type that has the highest maximum value for the predicted response is the RSA, therefore, the optimum mixture is the soil with 5% RSA.

Keywords: Expansive soils, Agricultural wastes, Unconfined compressive strength, Expansion index, Response surface methodology

INTRODUCTION

Expansive soils are clay soils that shrink and swell, exhibiting an extreme change in volume. The damaging effects of expansive soils are exacerbated in fluctuating climates such as the Philippines. Temperature changes trigger the shrink-swell phenomena in the soil that will lead to the failure of the soil and ultimately the structure above it. Expansive soils are prevalent in the Philippines due to the extensive deposition of volcanic ash [1]. The Philippines is also abundant in fertile soils, among which include smectite type of clays, which are very much prone to shrinking and swelling upon drying and wetting [2]. Expansive soils can cause extensive damage to structures if undetected and overlooked before construction. It is stipulated in the National Structural Code of the Philippines (NSCP) that where expansive soils are present under foundations, they should be removed or stabilized around and beneath the structure [3].

There are already numerous existing mechanical or chemical solutions for expansive soils. However, these are not always practical or economical. Removal and replacement of expansive soils can also be done but it is not always preferred due to its high cost. A sustainable and more cost-effective alternative would be to make use of admixtures composed of agricultural waste that have cementitious properties. It has been found that waste materials can replace cement even up to 70% while providing environmentally safe, sound, and low-cost structures [4]. RHA has already been found to be successful in mitigating the swelling potential of expansive soils; however, it does not increase the strength of the soil alone [5]. A binding agent should be used together with RHA to improve its quality and efficiency as a soil stabilizer.

Agricultural wastes are pozzolanic, making them good supplementary cementitious materials [6]. In the Philippines, large quantities of agricultural wastes are abandoned yearly, creating a pollution problem. Rice husk, sugarcane bagasse, and coconut shells produced more than three million metric tons, over five million metric tons, and more than two million metric tons of waste biomass from 2010-2011, respectively. Rice straw produced a staggering amount of over sixteen million metric tons during the same period [7]. The environmental burden caused by agricultural wastes can be reduced by using them as admixtures.

There is great potential for using agricultural wastes as binders particularly CSA, RSA, and SCBA due to their pozzolanic characteristic [8]-[10]. Coconut shells subjected to uncontrolled combustion to produce CSA were found to be a suitable partial replacement for cement in the production of concrete [8]. RSA satisfies the minimum requirements of a pozzolana according to the ASTM standards, making it a good replacement for cement [9]. SCBA has a high percentage of silica which allows it to have a

binding property. In a study, an increase in the strength of expansive soil was observed when SCBA and lime were used. Further, the addition of SCBA to lime is more effective than lime alone in decreasing the swelling potential of the soil [10].

The main objective of this study is to determine the optimum amount of admixture in treating expansive soils under dry curing conditions that will reduce the swelling potential and produce the maximum strength of the soil. The RHA-soil mixture for controlling soil expansion will be enhanced by adding different proportions of CSA, SCBA, and RSA to find the optimum mix design. The effectivity of the admixture is evaluated using the Expansion Index (EI), Atterberg limits, Maximum Dry Density (MDD), Optimum Moisture Content (OMC), and Unconfined Compressive Strength (UCS). The response surface methodology (RSM) was used to optimize the response of interest, the UCS, which is influenced by the type of binder, binder content, and the curing period.

MATERIALS AND METHODS

Material Sourcing

The expansive soil was obtained from Kauswagan, Lanao del Norte. It was already used in a previous study that confirmed its shrink-swell tendencies [11]. RHA was obtained from Restored Energy Development Corporation in Muntinlupa City. CSA was produced in Morong, Bataan. RSA was sourced from local rice farmers in Anao, Mexico, Pampanga. SCBA was bought from a commercial establishment.

Experimental Procedure

The index properties of the untreated soil were obtained for soil classification. The index properties were evaluated using the NSCP specifications for expansive soil in Table 1 to determine the potential expansion of the soil.

Table 1 NSCP Specifications for Expansive Soil [3]

Property	Required Value
Percent Passing No. 200 Sieve (%)	>10%
Percent Passing 5 μm (%)	>10%
Liquid Limit, LL (%)	>50%
Plasticity Index, PI (%)	>15%
Expansion Index, EI	>20

Standard procedures from ASTM were followed for all of the laboratory tests shown in Table 2. These tests were performed on both untreated and treated samples. The preliminary data includes the specific gravity, grain size analysis, Atterberg limits, and the moisture-density relationship. The effectiveness of the admixture is evaluated through ASTM D4609. The indicators for improvement are in Table 3.

Table 2 Laboratory Tests

Experimental Program	Test Standard
Specific Gravity	ASTM D854
Grain Size Analysis	ASTM D422
Atterberg Limits	ASTM D4318
Moisture-Density Relationship	ASTM D698
Expansion Index	ASTM D4829
Unconfined Compressive Strength	ASTM D2166

Table 3 Criteria to Gauge the Effectiveness of Admixture (ASTM D4609)

Property	Indicator for Improvement
Liquid Limit	Significant reduction
Plasticity Index	Significant reduction
Maximum Dry Density	Increase by more than 80 kg/m^3
Optimum Moisture Content	Decrease by more than 15%
Unconfined Compressive Strength	Increase by 345 kPa or more

Mixture Preparation

Dry mix proportioning made use of the preliminary data. The soil mixtures were created by replacing a percentage of the untreated soil's volume with RHA and binder. The RHA content is always 20%; the binder content ranges from 5% to 20% in increment of 5%. Twenty percent RHA is used in this study as the stabilizer because it is the recommended value to effectively reduce the swelling potential of expansive soil [5].

The dry mixture was mixed with water at optimum moisture content to make the total soil mixture for the EI test and the UCS test. For the UCS test, there were five specimens prepared for each variation of the soil mixture.

The samples were placed in airtight containers to cure for at least 16 hours. The cured samples were compacted into molds then extruded. Immediately after casting, the specimens were sealed with plastic wrap for at least seven days. The specimens were unsealed after seven days and subjected to the drying curing condition. The specimens were cured up to 14, 21, 28 and 35 days from casting.

TEST RESULTS

Soil Classification

The index properties of the soil used in this study met most of the criteria set by the NSCP for expansive soils as shown in Table 4. The soil is classified as expansive because of its expansion index that is the governing property to classify expansive soils. Its expansion index value of 98 indicates that it has high expansion potential. Based from the Unified Soil Classification System (USCS), the soil sample is elastic silt (MH).

Table 4 Summary of Soil Classification

Property	Required Value	Result	Remarks
Percent Passing No. 200 Sieve (%)	>10%	54.82	Pass
Percent Passing 5 μm (%)	>10%	N/A	Fail
Liquid Limit, LL (%)	>50%	76.93	Pass
Plasticity Index, PI (%)	>15%	32.85	Pass
Expansion Index, EI	>20	98	Pass

Evaluation of Effectiveness of Admixture

Atterberg Limits

The behavior of the soil under varying moisture contents can be determined using the Atterberg limits. According to ASTM D4609, an admixture is effective when there is a significant reduction in the liquid limit and the plasticity index. The summary of the test results for the Atterberg limits is shown in Table 5.

The liquid limit and the plasticity index values of the mixtures are generally decreasing. The reduction in the liquid limit and plasticity index is due to the replacement of clay particles with non-plastic materials.

The liquid limit dropped by as much as 7.23% and 17.77% for the mixtures with RSA and cement, respectively. Conversely, it could be observed that the mixtures containing CSA and SCBA have liquid limit values significantly higher compared to the untreated soil. The microstructure of the CSA and SCBA allowed more water to be absorbed.

The plasticity index was reduced by as much as 11.89% when RSA acted as the binder. Cement mixtures also show a reduction by as much as 39.73% in the plasticity index. A study that used cement and RHA as additives also saw a reduction in the plasticity of the soil [12]. On the other hand, most mixtures with CSA and SCBA have values for plasticity index higher than the untreated soil. In a study that used coconut shell powder, the plasticity index also increased as the additive increased [13]. In another study that used SCBA, the liquid limit and plasticity index decreased as the additive increased [14]. This difference in the trend observed could be because the SCBA used in this study was not burned in a controlled condition. Overall, the RSA and cement improved the soil while the CSA and SCBA did not.

Table 5 Summary of Results for Atterberg Limits

Binder Content	Liquid Limit, LL (%)	Plastic Limit, PL (%)	Plasticity Index, PI (%)
0%	77	44	33
5% CSA	93	49	44
10% CSA	83	46	37
15% CSA	83	47	36
20% CSA	82	45	37
5% RSA	75	46	29
10% RSA	75	45	29
15% RSA	74	45	30
20% RSA	72	42	30
5% SCBA	81	45	36
10% SCBA	80	46	34
15% SCBA	79	43	36
20% SCBA	77	47	30
5% OPC	74	46	27
10% OPC	72	47	25
15% OPC	67	43	24
20% OPC	65	41	24

Moisture-Density Relationship

Most soils show a relationship between their moisture content and dry density when placed under a compactive effort. The optimum moisture content (OMC) and maximum dry density (MDD) are performance indicators of the admixture as per ASTM D4609. Table 6 shows the summary of the results obtained through the Standard Proctor Test.

The reduction in the MDD observed for all mixtures could be attributed to the lower specific gravity of the stabilizer and binder compared to the soil. The RHA used in this study has a specific gravity of 1.555 [5]. The CSA, RSA, and SCBA have specific gravity values of 1.154, 1.844, and 1.544, respectively, while the soil has a specific gravity of 2.713.

The OMC of the soil increased by 2.24% to 34.23% when incorporated with the stabilizer and different types of a binder. The increase in the OMC

is attributed to the porosity of the RHA [12]. The presence of 20% RHA in all the mixtures greatly affected the results of the moisture-density relationship test. Overall, none of the binders showed an improvement in the compaction characteristics of the soil.

Table 6 Summary of Results for Moisture-Density Relationship

Binder Content	Maximum Dry Density (kN/m^3)	Optimum Moisture Content (%)
0%	14.03	35.73
5% CSA	9.55	44.9
10% CSA	10.06	46.93
15% CSA	9.61	46.53
20% CSA	9.36	47.35
5% RSA	11.03	40.08
10% RSA	11.20	40.23
15% RSA	11.38	39.2
20% RSA	11.67	38.85
5% SCBA	9.53	47.96
10% SCBA	9.84	46.94
15% SCBA	9.66	48.57
20% SCBA	9.50	47.76
5% OPC	11.83	30.58
10% OPC	12.23	36.53
15% OPC	12.76	37.31
20% OPC	12.38	37.88

Unconfined Compressive Strength

Most of the soil mixtures met the required provisions set by ASTM D4609 for the indication of improvement in strength. The treated specimens exhibited an increase in strength by as much as 745.38 kPa (227.82%), 859.90 kPa (262.82%), 799.46 kPa (187.61%), 2428.31 kPa (569.85%) for the mixtures with CSA, RSA, SCBA, and cement, respectively. The consistency of the specimens changed from very stiff to hard under the drying curing condition and with an increased curing period. A similar study also found that the specimens under drying conditions yielded a higher compressive strength than that of the sealed condition due to carbonation and suction [15].

The mixtures with cement did not show a trend for the curing period and binder content because the dry curing condition inhibited the hydration process. The increase in strength after the 35-day curing period is represented in Fig. 1. A high strength could be achieved by the soil mixtures with RSA and SCBA with the minimum binder content while the soil mixtures with cement require the maximum binder content to achieve a strength that may not always be as high. OPC is not an ideal binder for expansive soils not only for being uneconomical but also because of its poor and inconsistent performance when subjected to the dry curing condition.

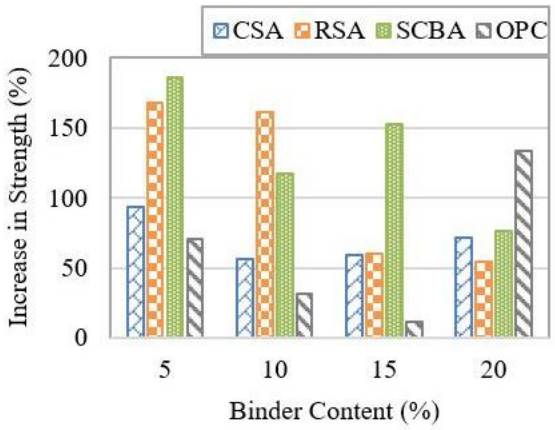

Fig. 1 Increase in strength after 35 days

Expansion Index

With the addition of the stabilizer and binder, the potential expansion of the mixtures became very low. The EI of the mixtures ranged from 0 to 2 only. This reaffirms the effectiveness of 20% RHA as a stabilizer. It also indicates that the binder had little to no effect on the expansion of the soil, even though the microstructures of CSA, RSA, and SCBA allow more water to be absorbed by the mixture.

Optimization of the Strength Using Response Surface Methodology

The optimum mixture is chosen based on the response surface method. The response surface methodology was performed using the Design-Expert software. The curing period and binder content are the numerical factors. The minimum value of the curing period is 14 days while the maximum is 35 days. The minimum value for the binder content is 5% while the maximum is 20%. Cement is not considered in the optimization because it only served as a comparison for the other binders in terms of effectiveness. A response surface quadratic model was produced for each binder type. Statistical analysis revealed that the models are significant and adequate to represent the relationship between the response and the independent variables. There is only one response which is the unconfined compressive strength.

Three-dimensional (3D) surface plots are produced by the models shown in Figs. 2 to 4. The highest strength is always achieved in the upper left portion of the surfaces, which means that the optimum strength is at the highest curing period (35 days) and lowest binder content (5% content) for the

binder types CSA, RSA, and SCBA. The strength of the CSA, RSA, and SCBA mixtures increases over time due to the drying curing condition that gives the specimens a hard consistency. Additionally, the cohesion of the particles is improved over time. The ashes are non-cohesive and they have a microstructure full of voids; therefore, the lowest binder content is desirable.

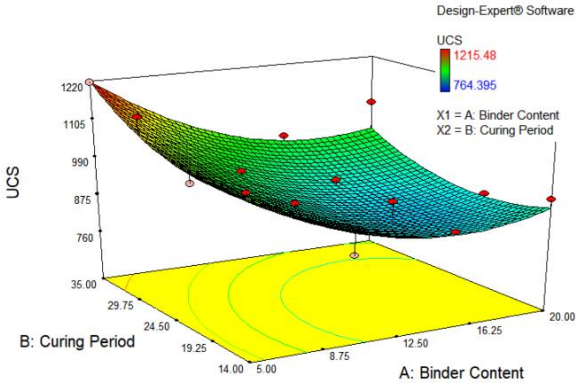

Fig. 2 Response surface plot of curing period and binder content (CSA as binder type)

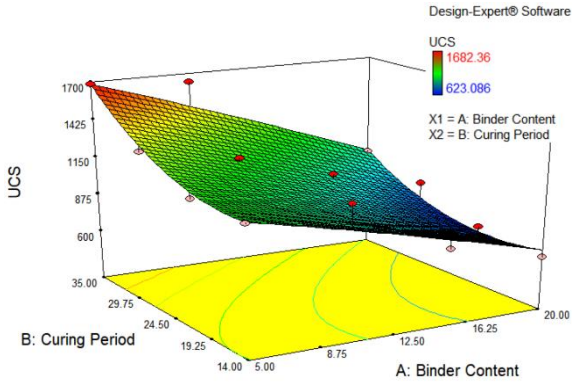

Fig. 3 Response surface plot of curing period and binder content (RSA as binder type)

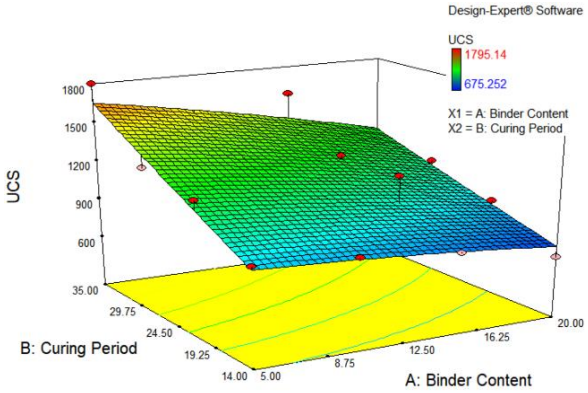

Fig. 4 Response surface plot of curing period and binder content (SCBA as binder type)

The equations of the UCS generated from the ANOVA were used to obtain the predicted maximum value of the strength for each binder type. The equations produced by the models are as follows:

$$UCS_{CSA} = 1432.809 - 49.460(BC) - 18.361(CP) - 0.27(BC)(CP) + 1.746(BC^2) + 0.555(CP^2) \quad (1)$$

$$UCS_{RSA} = 1582.026 - 16.791(BC) - 39.551(CP) - 0.695(BC)(CP) - 0.242(BC^2) + 1.385(CP^2) \quad (2)$$

$$UCS_{SCBA} = 426.154 + 9.277(BC) + 35.513(CP) - 0.840(BC)(CP) - 0.329(BC^2) + 0.075(CP^2) \quad (3)$$

Where:
UCS_{CSA} = UCS of Mixtures with CSA (kPa)
UCS_{RSA} = UCS of Mixtures with RSA (kPa)
UCS_{SCBA} = UCS of Mixtures with SCBA (kPa)
BC = Binder Content (%)
CP = Curing Period (days)

The UCS can be obtained using the final equation in terms of the actual factors. The equations for the predicted response in terms of the actual factors were used to compare the maximum UCS values as shown in Table 7. The values used for the factors are those that would produce the maximum, which is 5% for the binder content, and 35 days for the curing period. The binder type that has the highest maximum value for the predicted response is the RSA, therefore, the optimum mixture is the soil with 5% RSA.

Table 7 Maximum Values for the Predicted UCS for Each Binder Type

Binder Type	Binder Content (%)	Curing Period (days)	Predicted UCS (kPa)
CSA	5	35	1219.120
RSA	5	35	1682.124
SCBA	5	35	1651.952

CONCLUSIONS

The soil used in this study was sourced from Kauswagan, Lanao del Norte. It is identified as an expansive soil due to its index properties meeting the criteria set by the NSCP for expansive soils. 20% RHA was used as the stabilizer for the soil since it has been proven to effectively reduce the swelling potential of the soil. CSA, RSA, SCBA, and OPC

were added in varying percentages from 5% to 20% in steps of 5% as the binder.

With the addition of the stabilizer and binder, the potential expansion of the mixtures became very low. Only the mixtures with RSA and OPC showed improvement in the consistency limits, and none of the mixtures showed improvement in the compaction characteristics. Improvement in strength was observed for all binder types. OPC is not an ideal binder for expansive soils because of its poor performance in drying conditions.

A response surface methodology was performed for the UCS of the soil mixtures. The optimum strength for each binder is at the lowest binder content, and the strength increases with the curing period. The optimum mixture is the soil with 5% RSA because it yielded the highest maximum value for the predicted UCS.

It is recommended to investigate the long-term strength of the treated expansive soils and with curing methods that will simulate the actual condition on site.

ACKNOWLEDGMENTS

Thank you to my adviser, Dr. Mary Ann Q. Adajar for the guidance throughout this research. Thank you to Engr. Joenel G. Galupino, Engr. Miller DL. Cutora, and Dr. Erica Elice S. Uy for answering my queries. I would like to thank DOST-ERDT as well for the funding.

REFERENCES

[1] Morales E. and Morales M. K., Expansive Soils - Identification, Detection and Remediation Strategies, Retrieved from http://www.pgatech.com.ph, 2007.

[2] Carating, R. B., Galanta, R. G., and Bacatio, C. D., The Soils of the Philippines, Springer Science & Business, 2014.

[3] Association of Structural Engineers of the Philippines (ASEP), National Structural Code of the Philippines, 2010.

[4] Khan, R., Jabbar, A., Ahmad, I., Khan, W., Khan, A., and Mirza, J., Reduction in Environmental Problems using Rice-husk Ash in Concrete. Construction and Building Materials, Vol. 30, 2011, pp. 360-365.

[5] Adajar, M. Q., Aquino, C. P., Dela Cruz II, J. D., Martin, C. H., and Urieta, D. G., Investigating the Effectiveness of Rice Husk Ash as Stabilizing Agent of Expansive Soil. International Journal of GEOMATE, Vol. 16, Issue 58, 2019, pp. 33-40.

[6] Alex, J., Dhanalakshmi, J., and Ambedkar, B., Experimental investigation on rice husk ash as cement replacement on concrete production. Construction and Building Materials, Vol. 127, 2016, pp. 353-362.

[7] Baconguis, S. R., and Pasagdan, A. R., Waste biomass statistics in the Philippines. Canopy International, 2013, pp. 8-9.

[8] Adajar, M., Galupino, J., Frianeza, C., Aguilon, J., Sy, J., and Tan, P., Compressive Strength and Durability of Concrete with Coconut Shell Ash as Cement Replacement. International Journal of GEOMATE, Vol. 18, Issue 70, 2020, pp. 183-190.

[9] El-Sayed, M. A., and El-Samni, T. M., Physical and Chemical Properties of Rice Straw Ash and Its Effect on the Cement Paste Produced from Different Cement Types. Journal of King Saud University - Engineering Sciences, Vol. 19, Issue 1, 2006, pp. 21-29.

[10] Hasan, H., Dang, L., Khabbaz, H., Fatahi, B., and Terzaghi, S., Remediation of Expansive Soils Using Agricultural Waste Bagasse Ash. Procedia Engineering, Vol. 143, 2016, pp. 1368-1375.

[11] Tan, J. F., and Adajar, M. Q., Recycled Gypsum and Rice Husk Ash as Additives in the Stabilization of Expansive Soil. International Journal of GEOMATE, Vol. 18, Issue 70, 2020, pp. 197-202.

[12] Basha, E. A., Hashim, R., Mahmud, H. B., and Muntohar, A. S., Stabilization of Residual Soil with Rice Husk Ash and Cement. Construction and Building Materials, Vol. 19, Issue 6, 2005, pp. 448-453.

[13] Oluwafemi, I. J., Laseinde, T. O., and Akinwamide, J., Data Showing the Effects of Geotechnical Properties of Lateritic Soil Mixed with Coconut Shell Powder in Ado-Ekiti, South Western Nigeria. Data in Brief, Vol. 24, 2019.

[14] Barasa, P. K., Too, D., Jonah K., and Mulei, S., Stabilization of Expansive Clay Using Lime and Sugarcane Bagasse Ash. International Journal of Science and Research, 2015, pp. 2112-2117.

[15] Ho, L. S., Nakarai, K., Ogawa, Y., Sasaki, T., and Morioka, M., Strength Development of Cement-treated Soils: Effect of Water Content, Carbonation, and Pozzolanic Reaction under Drying Curing Condition. Construction and Building Materials, pp. 703-712.

11th Int. Conf. on Geotechnique, Construction Materials & Environment, Kyoto, Japan, 3-5 November 2021, ISBN: 978-4-909106063 C3051

DEVELOPMENT OF SITE FACTOR FOR SURFACE SPECTRAL ACCELERATION CALCULATION AT THE ALLUVIAL SOILS

Windu Partono[1], Masyhur Irsyam[2], Ramli Nazir[3], Frida Kistiani[1], Undayani Cita Sari[1]

[1]Engineering Faculty, Diponegoro University, Semarang 50275, Indonesia; [2]Faculty of Civil and Environmental Engineering, Bandung Institute of Technology, Bandung 40132, Indonesia; [3]Centre of Tropical Geoengineering, Faculty of Civil Engineering, Universiti Teknologi Malaysia, Malaysia

ABSTRACT

Calculation of surface spectral acceleration (SMS) is one of the important steps in seismic design. The SMS value can be obtained from bedrock spectral acceleration and multiplied it with site factor. According to ASCE/SEI 07-16, for short period spectral acceleration (0.2 sec / S_S) greater than 1g and long period (1 sec / S_1) greater than 0.2g, site specific propagation analysis (SSA) shall be used for site factor development. SSA can be performed using three different data, bedrock elevation, dynamic soil profile and acceleration time histories. The site factor can be calculated by comparing the surface to bedrock spectral acceleration obtained from SSA. This paper describes the development of site factor at the alluvial area (soft soil area) at Semarang city, Indonesia. The site factor was calculated at 23 boring positions. Microtremor tests were conducted at this area to predict soil dynamic profile. Five different acceleration time histories having magnitude from 6.5 Mw to 7 Mw and epicenter distance less than 10 km were collected for SSA. The average F_{PGA}, F_a and Fv values developed at this area were smaller compared to the site factor calculated using 2019 Indonesian Seismic Code.

Keywords: Acceleration Time Histories, Bedrock, Microtremor, Site Factor, Site Specific Propagation Analysis

INTRODUCTION

Site factor is one of the important values used for development surface spectral acceleration. Three different site factor F_{PGA} (Peak Ground Acceleration), Fa (short period or 0.2 sec) and Fv (1 sec) are required for seismic design of buildings. According to Indonesian seismic code 2019 [1] these three site factors can be obtained using Risk-targeted Maximum Considered Earthquake MCE_G, MCE_R-S_S and MCE_R-S_1, respectively. The problem of Fa and Fv calculation was occurred during the development of new 2019 Indonesian Seismic Code. ASCE/SEI 7-16 [2] as one of the references used by Indonesian Seismic Code introduced a different method for developing Fa value for soft soil (SE) area having MCE_R-S_S greater than 1 g and for Fv value having MCE_R-S_1 greater than 0.2 g. Site Specific Propagation Analysis (SSA) should be conducted for developing Fa and Fv at SE (soft soil) area. Not all Civil Engineering in Indonesia familiar with this new method. An alternative approach for developing these two values were applied following the research conducted by [3].

Two different problems occurred during the development Site Specific Propagation Analysis at site class SE area. The first problem related with the investigation of bedrock elevation and the soil profile from bedrock elevation up to the surface. The second problem related with the acquisition of acceleration time histories of specific earthquake events data which can be used for Site Specific Propagation Analysis. This paper describes 1D (one dimension) Site Specific Propagation Analysis (1D-SSA) for developing site factor at the study area. The analysis was performed at 23 boring positions at the alluvial area. Figure 1 shows the study area and the related soil investigations performed at the study area. The 1D-SSA was performed using bedrock elevation observed from single and array microtremor at the study area [4]-[7]. The study was performed at the northern part of Semarang, Indonesia. Based on the geological map information, the majority of soft soil area is located at the alluvial area at the northern part of the City. Figure 2 shows the geological map of the city.

According to the previous 2015–2020 research conducted at the study area the bedrock elevation was predicted at a minimum of 225 meters below the surface level. Figure 3 shows the predicted bedrock elevation contour map developed based on the single station microtremor investigation. A comparative investigation was also performed using array microtremor. The investigation was performed at 5 different locations. The purpose of the array microtremor investigation was to verify the bedrock elevation at the study area. Figure 4 shows two different results of the bedrock elevation investigation. As can be seen in these figures the bedrock elevation was predicted at a minimum 250 meter below the surface level. The shear wave velocity (Vs) values were used as a parameter for bedrock elevation measurement. Rock sample having at least 1500 m/sec was conducted as a parameter

used for bedrock elevation. The predicted soft-rock elevation (Vs ≥750 m/sec) or SB soil class [1], [2] is predicted in between 100 to 250 m below the surface level.

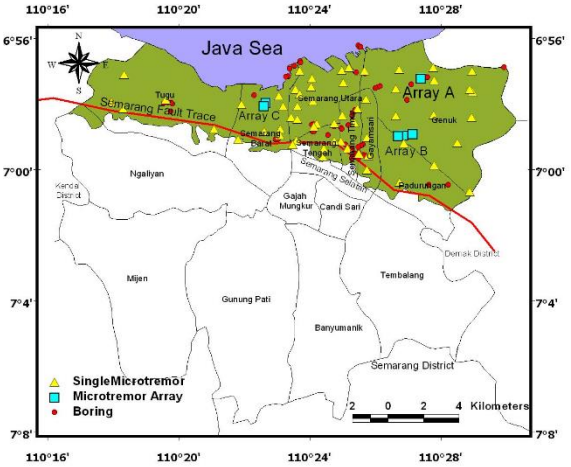

Fig. 1 The study area and soil investigations (boring, single microtremor and array microtremor) performed at the study area

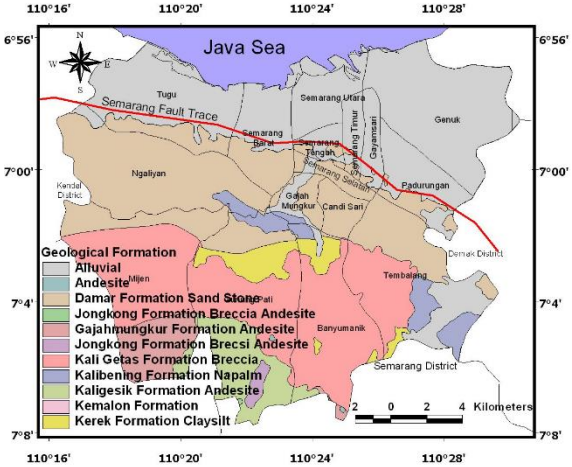

Fig. 2 Geological Map

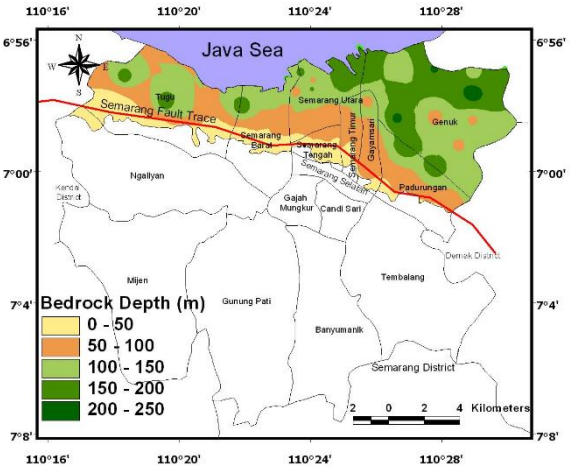

Fig. 3 Predicted bedrock depth

Due to the difficulties in development of soil profile, a 250 meters soil model was conducted for 1D-SSA. The distribution of soil dynamic parameters was calculated based on the empirical correlation of Vs (shear wave velocity) and NSPT (Standard Penetration Test) and also between G (Shear Modulus) and NSPT.

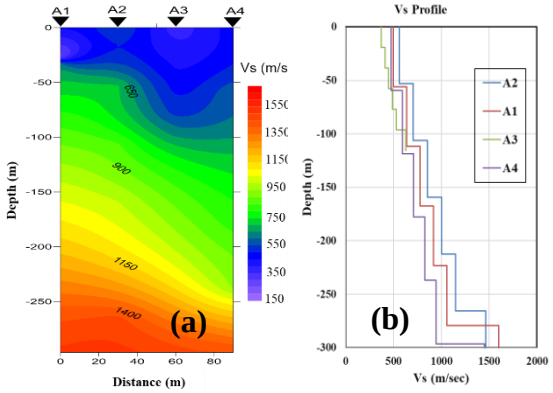

Fig. 4 Predicted bedrock depth based on array microtremor investigation at Array C position

METHODOLOGY

The site factor F_{PGA}, Fa and Fv development at the study area were conducted following three basic steps, de-aggregation analysis, response spectral matching and 1D-SSA. The objective of de-aggregation analysis is to find the predicted magnitude (M) and distance (R) of earthquake scenario in terms of acceleration time histories that can be used for 1D-SSA. The second approach related with the matching analysis of time histories collected from earthquake event. The spectral acceleration MCE_G, MCE_R-S_S and MCE_R-S_1 were conducted as a target spectral acceleration used for spectral matching analysis. These three spectral accelerations were calculated based on Indonesian seismic code 2019. The final steps of site factor calculation related with the development of 1D-SSA. The site factor can be developed by comparing the surface and bedrock spectral acceleration.

Figure 5 shows an example of de-aggregation analysis results of three different spectral acceleration (PGA, 0.2 sec and 1 sec) of shallow crustal fault seismic source model. The de-aggregation analysis was performed for the whole part of the city. According to these de-aggregation charts, the earthquake magnitude that can be used for the study area is in between 6.5 and 7 Mw. The correlation earthquake epicenter distance developed based on the de-aggregation analysis is in between 0-40 km. The alluvial area within the city is located at the north side of the Semarang fault trace [8]. The maximum distance of the study area against the seismic source

is less than 10 km. According to these seismic earthquake scenarios, 5 (five) shallow crustal fault earthquake time histories were collected for site factor development. All earthquake data and time histories were collected based on reverse fault seismic model from Pacific Earthquake Engineering Research ground motion database. Table 1 shows the information of 5 earthquake events used in this study.

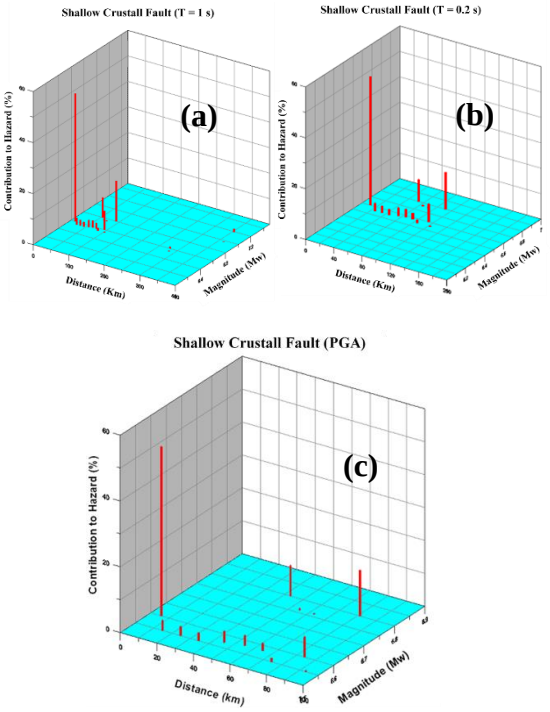

Fig. 5 De-aggregation analysis results of shallow crustal fault source model for spectral 1 sec (a), spectral 0.2 sec (b) and PGA (c).

Table 1 Earthquake event and related magnitude and epicenter distance used for site factor calculation

Earthquake Event	M (Mw)	R (km)
Nahanni (Canada, 1985)	6.76	4.93
Niigata (Japan, 2004)	6.63	6.27
Chuetsu Oki (Japan, 2007)	6.8	5.0
Northridge (USA, 2004)	6.69	5.26
San Simeon (California, 2003)	6.52	5.07

The response spectral matching analysis was conducted to 5 (North-South/270 and East-West/360) direction ground motion data. Three Risk-targeted Maximum Considered Earthquake (MCE_G, MCER-S_S and MCER-S_1) used as a spectral acceleration target. Figure 6 shows matching spectral acceleration result conducted at boring no 15. Three spectral acceleration 0.3722 g, 0.8394 g and 0.3667 g displayed in this figure represent MCE_G, MCE_R-S_S and MCE_R-S_1 calculated at boring no 15 position. These three spectral accelerations were calculated based on Indonesian Seismic Code 2019. Fig. 7 shows an example of two directions original acceleration time histories of Chuetsu-Oki earthquake data conducted at boring no 15. Fig. 8 shows the corresponding matched time histories developed from matching spectral acceleration analysis. The original and matched acceleration time histories developed for all 5 acceleration time histories were conducted at bedrock elevation.

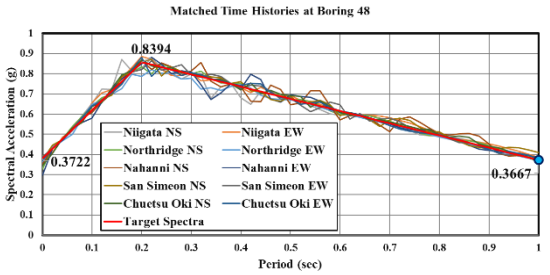

Fig. 6 Matching spectral acceleration for 5 (two direction) acceleration time histories at boring no 15

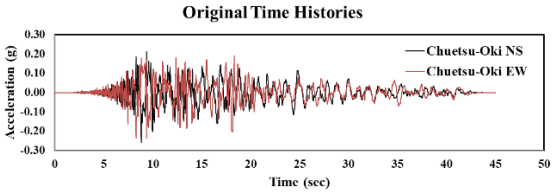

Fig. 7 Chuetsu-Oki original time histories

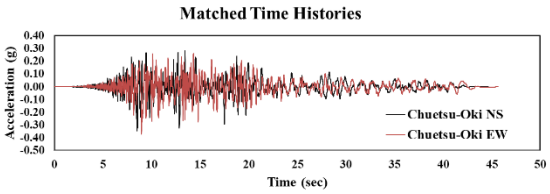

Fig. 7 Chuetsu-Oki matched time histories at boring no 15

The final analysis for site factor calculation was performed to obtain the surface spectral acceleration. One soil profile model having predicted bedrock elevation 250 meter was conducted for 1D-SSA. Four different Vs-NSPT correlation model was elaborated for developing VS profile of each boring position. Table 2 shows 4 different Vs-NSPT (shear wave velocity and N standard penetration) correlation. The "a" and "b" values displayed in this table represents correlation coefficients as displayed in Eq. 1. The NSPT (N Standard Penetration Test) are N_{60} standard penetration value. Eq. 2 shows the empirical correlation of shear modulus of soil and NSPT. Three shear modulus and NSPT correlation was applied for development of shear modulus (G) values. Table 3

shows "c" and "d" values used for development of the soil shear modulus.

The 1D-SSA conducted at the study area was performed at 23 soil boring positions. The 1D-SSA was performed to obtain the F_{PGA}, Fa and Fv site factor. Fig. 8 shows three example soil parameters at boring no 15. Fig 9 shows the related soil profile developed from bedrock up to surface elevation.

$$Vs = aN^b \quad (1)$$

$$G = cN^d \quad (2)$$

Table 2 Vs and NSPT correlation parameters

Correlation Model	a	b
Ohta & Goto (1978) [9]	82.1	0.35
Imai &Tonouchi (1982) [10]	93.7	0.31
Ohsaki & Iwasaki (1973) [11]	78.0	0.39
Partono et al. (2021) [12]	105.98	0.2643

Table 3 G and NSPT correlation parameters

Correlation Model	c	d
Ohsaki & Iwasaki (1973) [11]	11500	0.8
Imai &Tonouchi (1982) [10]	14070	0.68
Seed et al. (1983) [13]	6220	1.0

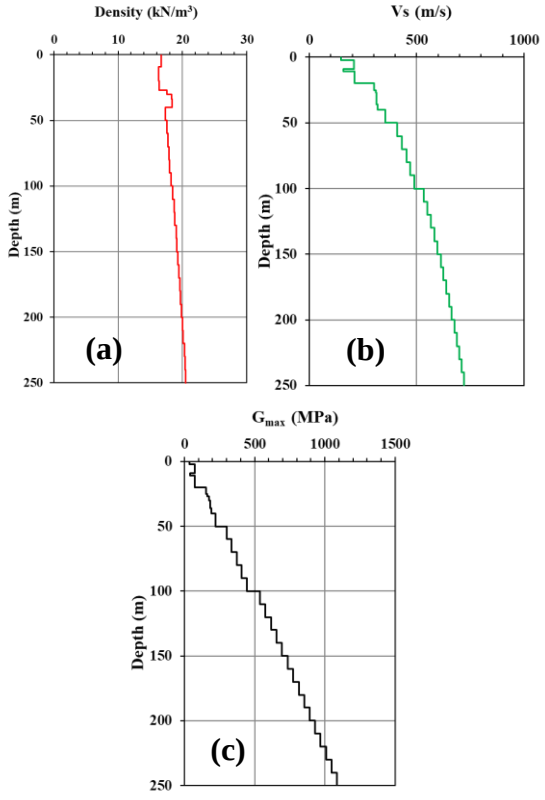

Fig. 8 Soil parameters used for 1D-SSA at boring no 15, soil density (a), shear wave velocity (b) and soil shear modulus (c)

The MCE_G, MCE_R-S_S and MCE_R-S_1 calculated at 23 boring positions shown at Fig. 10. The MCE_G and MCE_R-S1 calculated at 23 boring positions are almost equal, and distributed in between 0.30-0.40 g. The MCE_R-S_S calculated at 23 boring positions are almost constant and distributed form 0.7 up to 0.89 g. Based on ASCE/SEI 7-16, for MCE_R-S_S greater than 1 g and the building located at soft soil area (average N30 less than 15), the site factor Fa for spectral acceleration 0.2 sec shall be calculated using site analysis. Even-though the MCE_R-S_S at 23 boring positions less than 1 g, the comparative study for site factor calculation was conducted at the study area.

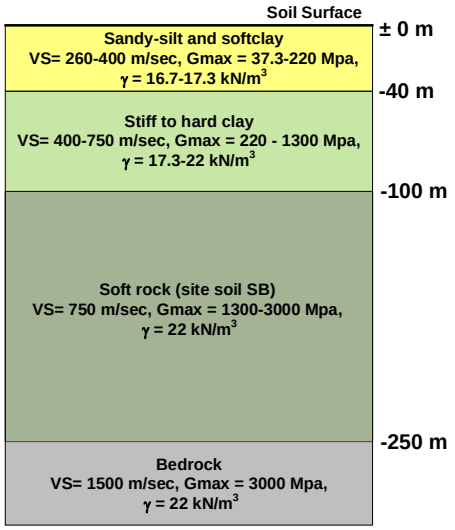

Fig. 9 Sample soil profile and parameters used for 1D-SSA at boring no 15

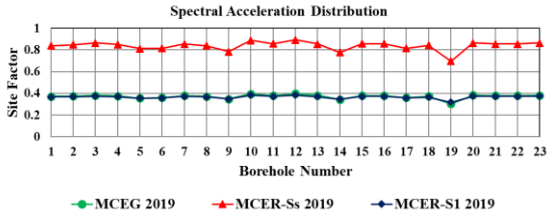

Fig. 10 MCE_G, MCE_R-S_S and MCE_R-S_1 calculated at 23 borehole position

The predicted bedrock elevation at this boring position is 250 m. The thickness of each boring investigation for all 23 boring positions are not equal. The minimum depth of boring investigation is 30 m. However, the maximum soil boring investigation is 60 m. Most of the soil boring investigations performed at the study area were conducted following the requirement for foundation design. The F_{PGA}, Fa and Fv site factors were calculated by comparing the surface to bedrock peak ground acceleration and spectral acceleration at 0.2 sec and 1 sec period. Figure 11 shows an example of bedrock and surface spectral acceleration obtained from 1D-SSA at boring

position no 15. Based on this sample 1D-SSA analysis result, the average F_{PGA}, Fa and Fv site factor calculated from two directions Chuetsu Oki scenario earthquake are 1.4646, 1.1592 and 2.8369, respectively. The analysis was conducted using NS and EW acceleration time histories of Chuetsu-Oki earthquake.

RESULT AND DISCUSSIONS

The site factors developed using 1D-SSA analysis and conducted at 23 boring positions were evaluated and compared to the same site factor obtained from Indonesian seismic code 2019. Fig. 12 shows the three site factors F_{PGA}, Fa and Fv developed based on Indonesian seismic code 2019. According to this figure the site factor developed at the study area are almost constant. The F_{PGA} site factor are distributed in between 1.39 and 1.59. The Fa site factor obtained at 23 boring positions are also constant and the value are distributed in between 1.17 and 1.38. However, the Fv site factor calculated at 23 soil boring positions are distributed in between 2.45 and 2.73. The average values of F_{PGA}, Fa and Fv calculated using Indonesian seismic code 2019 are 1.46, 1.23 and 2.54 respectively.

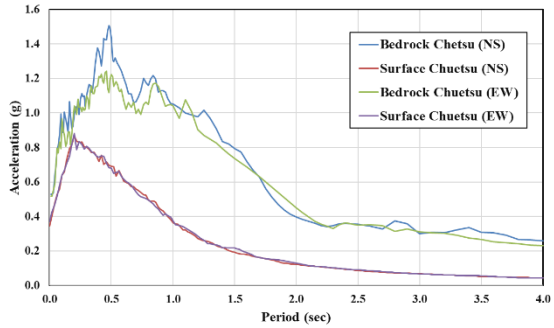

Fig.11 Surface and bedrock (SB) spectral acceleration developed from 1D-SSA at boring position no 15

Fig. 13 shows the three site factors distribution developed using 1D-SSA. All site factors developed using 1D-SSA are not constant and the values are varied between 0.6 and 3. The site factor F_{PGA} are distributed between 0.97 and 2.74. The site factor Fa are distributed from 0.68 to 1.85. And the Fv site factor are distributed in between 1.97 and 2.32. In average the F_{PGA} site factor developed using 1D-SSA is greater than the Fa and Fv site factor. In average the F_{PGA}, Fa and Fv calculated at the study area are 1.62, 1.23 and 1.48, respectively. Table 3 shows average site factor calculated using 1D-SSA and 5 different seismic scenarios.

Compared to the site factor developed using Indonesian seismic code 2019, in average the site factor F_{PGA} and Fa developed using 1D-SSA and Indonesian seismic code 2019 are almost equal. However, the Fv site factor developed using 1D-SSA are smaller compared to the same site factor calculated based on Indonesian seismic code 2019. Figure 14 shows the differences of three site factors developed using 1D-SSA and Indonesian seismic code 2019.

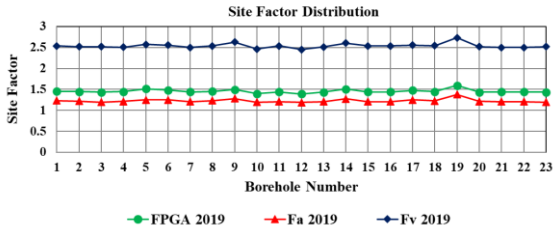

Fig.12 FPGA, Fa and Fv distribution developed at 23 boring positions calculated using Indonesian seismic code 2019

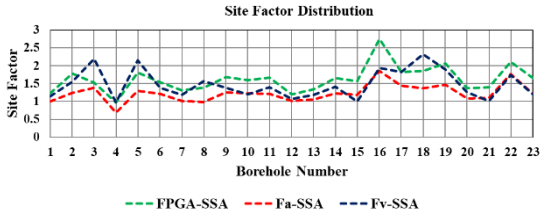

Fig.13 FPGA, Fa and Fv distribution developed at 23 boring positions calculated using 1D-SSA

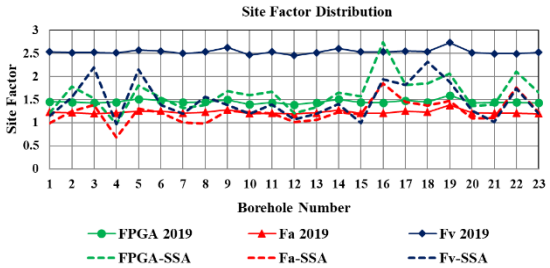

Fig. 14 FPGA, Fa and Fv distribution developed at 23 boring positions calculated using 1D-SSA and Indonesian seismic code 2019

Table 3 Average F_{PGA}, Fa and Fv site factor calculated using 1D-SSA and 5 earthquake scenarios

SA	Ch	Ni	Na	No	Sa
PGA	1.93	1.44	1.95	1.37	1.38
Ss	1.16	1.01	1.75	1.15	1.09
S1	1.55	1.11	1.76	1.40	1.57

Note: Ch: Chuetsu Oki; Ni: Niigata; Na: Nahanni; No: Northridge and Sa: San Simeon Earthquake. SA: Spectral acceleration. PGA: Peak Ground Acceleration. Ss and S1: spectral acceleration 0.2 sec and 1 sec respectively

According to these two calculation methods in developing site factor F_{PGA}, Fa and Fv, the site factor developed using 1D-SSA at alluvial or soft soil area as already suggested by ASCE/SEI 7-16 should be taken into account. Even-though the Ss values calculated at 23 boring positions at the study area are less than 1 g. The Fv values are smaller compared to the same site factor calculated using Indonesian seismic code 2019.

CONCLUSIONS

Site factor calculation at the alluvial area was conducted at 23 different boring positions. According to the Indonesian seismic code 2019, the average N30 at these 23 boring positions are less than 15. The alluvial area is located at soft soil area.

The three site factors F_{PGA}, Fa and Fv calculated and analyses based on Indonesian seismic code are not equal compared to the same site factor developed using 1D-SSA. The F_{PGA} and Fa calculated based on these two approaches are almost equal. However, the Fv site factor calculated using 1D-SSA are smaller compared to the same value calculated based on Indonesian seismic code 2019.

The site factor Fa and Fv for building upper structures calculation at the alluvial or soft soil area shall be evaluated due to the difference results calculation. Two different approaches shall be performed to get the real Fa and Fv site factor at alluvial area.

ACKNOWLEDGMENTS

This study was financially supported by the Directorate Research and Community Devotion, Deputy of Research Empowerment and Development, Ministry of Research and Technology / National Research Council and Innovation, through research grant 2021.

REFERENCES

[1] SNI 1726:2019, Seismic Resistance Design Codes for Building and Other Structures, Indonesian National Standardization Agency, 2019.

[2] ASCE/SEI 7-16, Minimum Design Loads and Associated Criteria for Buildings and Other Structures. American Society of Civil Engineers, 2017.

[3] Partono W., Wardani S. P. R., Irsyam M. and Maarif S., Seismic Microzonation of Semarang, Indonesia Based on Site Response Analysis Using 30 m Soil Deposit Model, Jurnal Teknologi, 78:8-5, pp. 31-38, 2016.

[4] Sengara I. W. and Komerdevi Det, 2020, Site-Specific Response Analysis (SSRA) and pairs of ground- motions time-history generation of a site in Jakarta, E3S Web of Conferences 156, 03009 (2020), Volume 156, 2020, 4th International Conference on Earthquake Engineering & Disaster Mitigation (ICEEDM 2019).

[5] Nguyen V. Q., Aaqib M. , Nguyen D. D., Nguyen V. L. and Park D., A Site-Specific Response Analysis: A Case Study in Hanoi, Vietnam, Applied Science, MDPI, Vol. 10 3972, 2020.

[6] Natepra P., Boonpichetvong M., Pannachet T. and Chintanapakdee C., Seismic Response of Deteriorated Residential RC Buildings in The Northeasthern Region of Thailand, Intenational Journal of Geomate, Vol. 9, 2020.

[7] Fathani T. F. and Wilopo W., Seismic Microzonation Studies Considering Local Site Effects for Yogyakarta City, Indonesia, International Journal of Geomate, Vol. 12, 2017.

[8] National Center for Earthquake Studies, Indonesian Seismic Sources and Seismic Hazard Maps 2017, Centre for Research and Development of Housing and Resettlement, Ministry of Public Works and Human Settlements), ISBN 978- 602-5489-01-3, 2017, pp. 1-377.

[9] Ohta, Y. and Goto, N., Empirical Shear Wave Velocity Equations in Terms of Characteristic Soil Indexes, Earthquake Engineering and Structural Dynamics, 6, pp. 167-187, 1978.

[10] Imai, T. and Tonouchi, K., Correlation of N-value with S-Wave Velocity and Shear Modulus, Proc. Of second European Symposium on PenetrationTesting, Amsterdam, The Netherlands, pp. 67-72, 1982.

[11] Ohsaki Y. and Iwasaki R., On Dynamics Shear Moduli and Poisson's Ratio of Soil Deposits, Soil and Foundations, JSSMFE, Vol. 13, N.4, Dec., pp.59-73, 1973.

[12] Partono W., Asrurifak M., Tonnizam E. , Kistiani F., Sari U.C. and & Putra K. C. A., Site Soil Classification Interpretation Based on Standard Penetration Test and Shear Wave Velocity Data, J. Eng. Tech, Sci., Vol. 53, No. 2, 2021.

[13] Seed H.B., Idriss I.M. and Arango I., Evaluation of Liquefaction Potential Using Fields Performance Data, Journal Geotechnic Eng. Div., ASCE, Vol 109 No. 3, March, pp. 458- 482, 1983.

11th Int. Conf. on Geotechnique, Construction Materials & Environment,
Kyoto, Japan, 3-5 November 2021, ISBN: 978-4-909106063 C3051

METROPOLITAN MANILA SEISMIC HAZARD MAP USING MIDORIKAWA & HORI SITE AMPLIFICATION MODEL

Jonathan R. Dungca[1] and Mariamae Francia G. Montejo[2]

[1,2]Civil Engineering Department, Gokongwei College of Engineering, De La Salle University, Philippines

ABSTRACT

Since Metropolitan Manila is known to be susceptible to seismic hazards, it is necessary to consider multiple factors in assessing this hazard. Aside from ground motion, the properties of soil which lead to the amplification of seismic waves should be considered. This study aimed to develop a seismic hazard map for Metro Manila considering the soil properties in the area by using Midorikawa & Hori site amplification model. Probabilistic seismic hazard assessment was conducted using earthquake data within 250 km of Metropolitan Manila for 10% and 2% probabilities of exceedance. The site amplification factors were computed using calculated shear wave velocities from SPT-N values. The calculated ground motions were amplified using the site amplification factors considering short-period and mid-period amplifications. The constructed maps of amplified peak ground acceleration (PGA) values showed how soil properties affect the ground motion. It was found that for a short-period amplification, the average PGAs are 0.538 g, and 0.659 g for 10%, and 2% probabilities of exceedance, respectively. While for mid-period amplification, the average PGAs are 0.589 g, and 0.830 g for 10%, and 2% probabilities of exceedance. Using the amplified seismic hazard maps, a better approximation of seismic hazards can be generated for future use.

Keywords: Site amplification, Shear wave velocity, Peak ground acceleration, Probabilistic seismic hazard assessment, Metro Manila

INTRODUCTION

Since the Philippines is situated within the Pacific Ring of Fire, the country is considered highly vulnerable to natural hazards such as earthquakes. Typically the damage caused by earthquakes is defined by the magnitude of the event and the distance from the site to the source. However, it is also necessary to consider the varying geological conditions in the area as it also affects the hazards caused by earthquakes [1]. These varying geological conditions include the stability of slopes in the area, its liquefaction susceptibility, and the possibility of site amplification.

Site amplification refers to the amplification of the earthquake waves as they travel from the source through the soil due to the local geological conditions in the site [2]. Only a few research in the country have been conducted which consider the effect of site amplification on earthquake hazards due to a general shortage of data for soil profiles and shear wave velocities. Since Metropolitan Manila or Metro Manila is regarded to be susceptible to earthquake hazards and site amplification due to its variable geology [3], it is necessary to include the effects of the soil conditions in the evaluation to provide a more accurate representation of ground motion intensities.

In a previous study [4], a reference for site amplification of Metro Manila was developed, however, the model used is only applicable to strains less than 1% and for periods that are less than or equal to 0.5 seconds. With this, the study aims to develop seismic hazard maps considering site amplification of Metro Manila using a site amplification model [5] that is designed for higher strains and different periods. The developed seismic hazard maps show the amplified peak ground accelerations in the study area for probabilities of exceedance of 10% and 2%. With this, a reference and a basis are provided to determine how local site conditions affect ground motion intensities. Moreover, the maps will be able to provide a more accurate representation of seismic hazards for future planning and assessments.

METHODOLOGY

The location of the study covers the area of Metro Manila, formally known as the National Capital Region (NCR). The region has a total of sixteen (16) cities and one (1) municipality. In this study, a probabilistic seismic hazard assessment (PSHA) was conducted to determine the peak accelerations at bedrock (PA_{rock}) within the study area. The site amplification factors were then identified using the average shear wave velocities (V_{S30}) in Metro Manila and were used to amplify PA_{rock} and obtain the peak accelerations at the ground surface.

Probabilistic Seismic Hazard Assessment

In conducting PSHA, the equation of the probability theorem [7] is shown in Eq. (1). The equation shows the computation of the probability of exceeding a value of a ground motion parameter, considering the possible magnitudes or locations of an earthquake.

$$\lambda_{y^*} = \sum_{i=1}^{N_S} \sum_{j=1}^{N_M} \sum_{k=1}^{N_R} v_i P\left[Y > y^* \middle| m_j, r_k\right] P\left[M = m_j\right] P[R = r_k] \quad (1)$$

where:
λ_{y^*} = total mean annual exceedance rate for peak acceleration level y^*;
N_S = total number of potential earthquakes source i in the study area;
N_M = total number of magnitude intervals j considered;
N_R = total number of distance intervals k considered;
v_i = average rate of magnitude exceedance for source i;
$P\left[Y > y^* \middle| m_j, r_k\right]$ = probability that a ground motion parameter Y will exceed the peak acceleration level y^* at a specific magnitude interval m_j and a specific distance interval r_k;
$P\left[M = m_j\right]$ = probability that a magnitude M will be included in the magnitude interval m_j;
$P[R = r_k]$ = probability that a distance R will be included in the distance interval r_k.

In this study, the earthquake sources within 250 kilometers (km) of Metro Manila were considered and categorized as either linear sources or areal sources. For linear sources, the probability density function by [6] is used. For areal sources, the magnitude-fault area relation [7] was used. The area was further divided into square elements and the probability distribution was obtained considering the shortest distance from the center of each element to the site being considered.

The probability distribution for magnitude was computed using the probability density function by [6]. In computing the probability distribution of the exceedance of a ground motion parameter, the ground motion prediction equations (GMPE) by [8] were used for shallow earthquakes. The GMPE by [9] shown was used for earthquakes generated by subduction zones.

The value of $P\left[Y > y^* \middle| m_j, r_k\right]$ is computed using the equation by [6]. The value of $F_Y(y^*)$ was then computed using the standard normal variate. When the values of λ_{y^*} were computed considering the target accelerations from 0.05 g to 1.0 g, the seismic hazard curve was constructed by plotting the accelerations against the mean annual rate of exceedance. By combining the seismic hazard curve with the Poisson model [6], the peak accelerations at bedrock (PA_{rock}) for probabilities of exceedance of 10% and 2% in 50 years were computed.

Evaluation of Site Amplification

The average shear wave velocities (V_{S30}) and the PA_{rock} were used to quantify the site amplification. To calculate V_{S30}, the SPT-N data or RQD values from the borehole data in Metro Manila were gathered and processed.

For SPT-N values, the model by [10] is used to calculate the shear wave velocity (V_S) as shown in Eq. (2).

$$V_S = 77.13N^{0.377} \quad (2)$$

where:
N = raw standard penetration resistance.

For RQD values, interpolation is done using the table of typical values of V_S for a given RQD by [11].

After computing V_S for each soil layer, the V_{S30} for each site is computed. For soil data with depths greater than 30 meters, the equation by [12] in Eq. (3) was used, otherwise, an extrapolation shown in Eq. (4) was conducted as proposed by [13].

$$V_{S30} = \frac{\sum_{i=1}^{N} h_i}{\sum_{i=1}^{N} \frac{h_i}{v_i}} \quad (3)$$

$$\log V_{S30} = c_0 + c_1 \log V_{SZ} + c_2 (\log V_{SZ})^2 \quad (4)$$

where:
h_i = thickness of soil layer;
v_i = shear wave velocity at the i^{th} layer at the top 30 meters;
V_{SZ} = average shear wave velocity at termination depth;
c_n = regression coefficients [13].

The shear wave velocity map of Metro Manila was then constructed in a mapping software using the computed V_{S30} values. The V_{S30} and PA_{rock} values were used to compute the site amplification factors using the model by [5] shown in Eq. (5).

$$\ln AF = a \ln V_{S30} + b \quad (5)$$

where:
AF = amplification factor;
a, b = regression coefficients in the function of PA_{rock}.

The regression coefficients [5] are computed depending on whether the amplification being considered is short-period amplification or mid-

period amplification. Short-period amplification (F_a) covers a period of 0.1 to 0.5 seconds while mid-period amplification (F_v) covers a period of 0.4 to 2.0 seconds.

The amplification factors were used to amplify the peak acceleration values computed from the GMPEs, from which new seismic hazard curves were constructed. With this, the amplified peak ground acceleration (PGA) values are computed for 10% and 2% probabilities of exceedance.

RESULTS AND DISCUSSION

In this study, earthquake data with a minimum magnitude of 4.0 and spanning from the years 1907 to 2020 were obtained from the Philippine Institute of Volcanology and Seismology (PHIVOLCS). The geotechnical data, on the other hand, were collected from past studies by [4] and [14]-[18].

Seismic Hazard Maps

In developing the seismic hazard maps, Geographic Information System (GIS) was used similar to [19]. Considering the probabilities of exceedance (POE) of 10% and 2%, the PA_{rock} values in Metro Manila were computed. It was found that the average PA_{rock} values in Metro Manila vary from as low as 0.296 g in Navotas and as high as 0.475 g in Muntinlupa for 10% POE. Considering 2% POE, the average PA_{rock} values range from 0.437 g to 0.706 g, which are also in Navotas and Muntinlupa, respectively. Graphical representations of the actual values of PA_{rock} are shown as maps in Fig. 1 and Fig. 2

Fig. 1 Map of PA_{rock} in Metro Manila for 10% POE

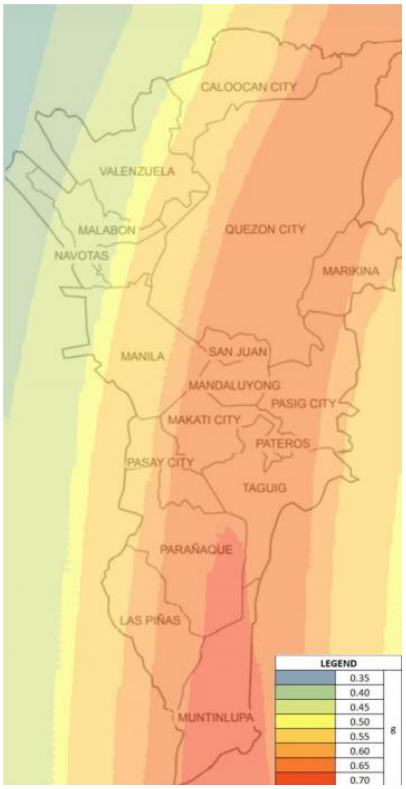

Fig. 2 Map of PA_{rock} in Metro Manila for 2% POE

As shown in the maps, the Muntinlupa area has the highest PA_{rock} values. The contour then spreads outwards, decreasing gradually as the distance from the center increases. The highest PA_{rock} is at the center due to the presence of the West Valley Fault, which also shows that this fault has the biggest influence in the seismic behavior in Metro Manila. The PA_{rock} also increases as the probability of exceedance decreases, since large-scale earthquakes are less common than smaller earthquakes.

Shear Wave Velocity Map

To create the shear wave velocity map, a total of 1412 borehole data were collected, 1372 of which are within Metro Manila and 40 are gathered from nearby provinces to complete the interpolation. Relating the number of data used and the area of the study area, a density of 2 borehole data for every square meter was used. Using the different geotechnical data gathered within Metro Manila, the V_{S30} in the study area were computed and mapped. From the computation, it was found that the average V_{S30} values in Metro Manila range from 206.48 m/s in Manila up to 554.08 m/s in Quezon City. These values describe the stiffness of the soil in each location, which is also attributed to the types of soil present in the area, and their corresponding SPT-N or RQD values. Figure 3 shows the V_{S30} map of Metro Manila.

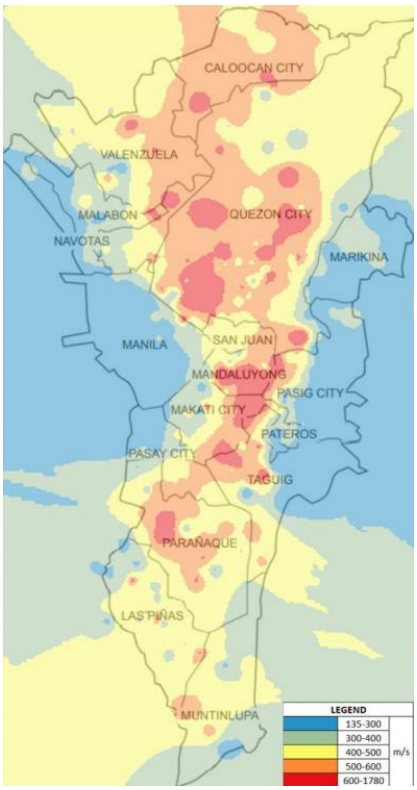

Fig. 3 Map of V_{S30} in Metro Manila

As seen in Fig. 3, the west and east sides of Metro Manila are almost similar with low V_{S30} values, while the center has high V_{S30} values. The low values on the western side, comprised of Navotas, Malabon, Manila, and Pasay, can be attributed to the area being near Manila Bay. The west is also comprised of quarterly alluvial soil where SPT-N values are very low at the surface and are average at deeper layers [14].

The areas in the eastern part, comprised of Marikina, Pasig, Pateros, and Taguig. have slightly higher V_{S30} values when compared to the west since the areas are far from Manila Bay. However, the soil composition in these areas is similar to the west, with almost the same SPT-N patterns.

The remaining cities aligned at the center, which are Caloocan, Valenzuela, Quezon City, San Juan, Mandaluyong, Makati, Muntinlupa, Las Piñas, and Parañaque have the highest V_{S30} values. This is due to the tuff and rock formations that are common in the central part of the region [14]. With this, the SPT-N values are generally higher, and refusal can be achieved even in shallow depths.

Amplified Seismic Hazard Maps

Using the PA_{rock} values and the V_{S30} values, the site amplification factors F_a and F_v were computed. To see the relationship between PA_{rock}, V_{S30}, and the amplification factors F_a and F_v, theoretical values for the first two parameters are used to compute the amplification factors. Table 1 shows the values of F_a and F_v for increasing V_{S30} values, assuming that PA_{rock} is constant.

Table 1 Resulting amplification factors for increasing V_{S30} values

V_{S30} (m/s)	F_a	F_v
150	2.737	3.405
250	2.135	2.399
350	1.813	1.905
450	1.605	1.603
550	1.456	1.397

Based on the data in Table 1, the values of F_a and F_v decrease as V_{S30} increases. This shows that softer soils cause stronger amplification of ground motion compared to stiff soils. It can also be observed that considering the amplification factors at the highest and lowest V_{S30}, the value of F_a is 1.88 times smaller, while the value of F_v is 2.43 times smaller. This shows that V_{S30} dependency is stronger for mid-period amplification since the rate of change of its value is greater.

On the other hand, Table 2 shows the values of F_a and F_v for increasing PA_{rock} values, assuming that V_{S30} is constant.

Table 2 Resulting amplification factors for increasing PA_{rock} values

PA_{rock} (g)	F_a	F_v
0.25	1.813	1.905
0.35	1.627	1.873
0.45	1.445	1.845
0.55	1.269	1.819
0.65	1.104	1.797

From the data in Table 2, Fa and F_v also decrease as PA_{rock} increases. This is due to the nonlinearity of soil behavior [20]. When the ground accelerations are high, the soil response is governed by its high damping ratio, which results in low amplification in the soils. This also shows that amplification is greater for earthquakes with low magnitudes at farther distances. Also, similar to Table 1, the data in Table 2 show that the mid-period amplification is generally greater than the short-period amplification.

Comparing the amplification factors at the highest and lowest PA_{rock} values, it can be seen that F_a became 1.65 times smaller and F_v became 1.06 times smaller. This shows that short-period amplification is more dependent on the change in the PA_{rock} values. After incorporating the amplification factors into the PSHA, the amplified PGAs are computed and mapped.

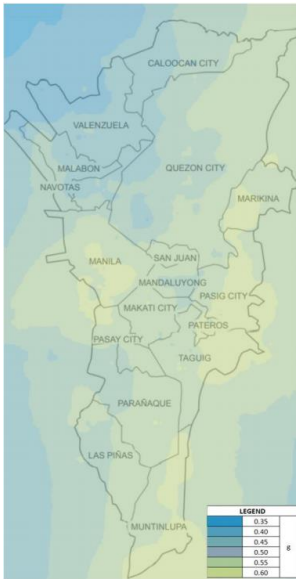

Fig. 4 Map of amplified PGAs in Metro Manila (10% POE, short-period amplification)

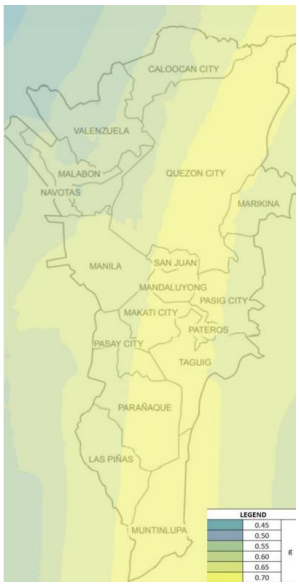

Fig. 5 Map of amplified PGAs in Metro Manila (2% POE, short-period amplification)

Figure 4 and Fig. 5 show the maps of amplified PGAs considering short-period amplification. It can be seen that he contour in Fig. 4 is more random, with the highest accelerations at the west and east. The areas with the highest PGAs are also the areas with the lowest V_{S30}, which shows that areas with softer soils experience greater amplification.

In Fig. 5, it is observed that the contour of the map is more similar to Fig. 2, where the accelerations are higher at the center, and gradually decrease as they move away towards the sides. This shows how short-period amplification is more influenced by PA_{rock}.

Figure 6 and Fig. 7 show the maps of amplified PGAs considering mid-period amplification. Here, the shape of the contour remains the same. The maps in Fig. 6 and Fig. 7 show that the west and east of the region have the highest PGAs. The main difference between the short-period and mid-period amplification is that, for the latter, the areas with the highest PGAs for 10% POE are still the same areas with the highest PGAs for 2% POE. This shows that mid-period amplification is more dependent on V_{S30} which is constant regardless of the POE considered.

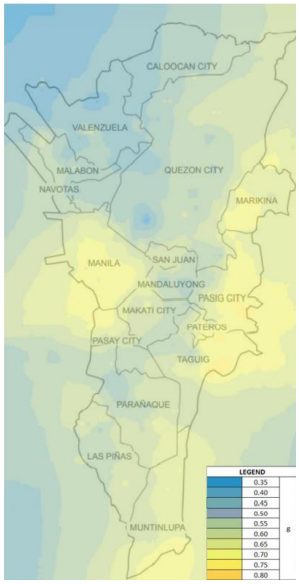

Fig. 6 Map of amplified PGAs in Metro Manila (10% POE, mid-period amplification)

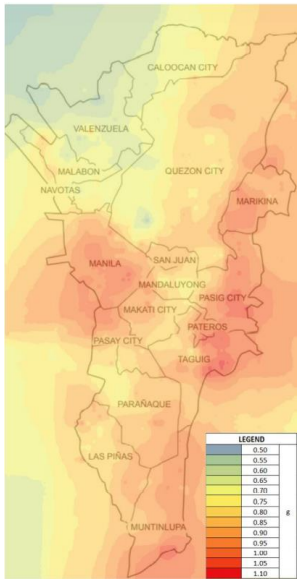

Fig. 7 Map of amplified PGAs in Metro Manila (10% POE, mid-period amplification)

Based on the results, the average amplified PGAs in the region are 0.538 g and 0.589 g for short-period and mid-period amplification, respectively, considering 10% POE. For 2% POE, the amplified

PGAs for short-period and mid-period amplification are found to be 0.659 g and 0.830 g, respectively.

CONCLUSION

Due to the susceptibility of Metro Manila to seismic hazards, it is necessary to consider the local soil conditions which intensify the damages from these hazards. It was seen that short-period amplification has a stronger dependency on PA_{rock}, while mid-period amplification is more dependent on V_{S30}. Considering short-period amplification, Metro Manila has an average PGA of 0.538 g and 0.659 g for 10% and 2% POE, respectively. Meanwhile, for mid-period amplification, the region has an average PGA of 0.589 g and 0.830 g for 10% and 2% POE.

REFERENCES

[1] Monahan, P., Levson, V., McQuarrie, E., Bean, S., Henderson, P., and Sy, A., Relative Earthquake Hazard Map of Greater Victoria, Showing Areas Susceptible to Amplification of Ground Motion, Liquefaction, and Earthquake-induced Slope Instability, Geoscience Map, 2000, Ministry of Energy and Mines, British Columbia.

[2] Navidi, S., Development of a Site Amplification Model for Use in Ground Motion Prediction Equations, The University of Texas at Austin, 2012.

[3] Sali, A., Seismic Hazard Assessment of Metro Manila (A Foundation Engineering Analysis), Geological Society of the Philippines, 2004.

[4] Dungca, J. and Macaraeg, C., Development of a Reference for Seismic Amplification: The Case of Metro Manila, Conference proceedings, in 19th IABSE Congress Stockholm, 2016, pp. 1015-1022.

[5] Midorikawa, S. and Hori, A., Nonlinear Site Amplification Model Derived From Strong Motion Records Including Records of the 2011 Tohoku, Japan Earthquake, Conference proceedings, in 16th European Conference on Earthquake Engineering, 2018.

[6] Kramer, S., Chapter 4, Geotechnical Earthquake Engineering, Prentice Hall, 1996, pp. 117-138.

[7] Singh, S., Bazan, E. and Esteva, L., Expected Earthquake Magnitude from a Fault, Bulletin of the Seismological Society of America, Vol. 70, 1980, pp. 903-914.

[8] Joyner, W. and Boore, D., Peak Horizontal Acceleration and Velocity from Strong Motion Records Including Records from the 1979 Imperial Valley, California Earthquake, Bulletin of the Seismological Society of America, Vol. 71, Issue 6, 1981, pp. 2011-2038.

[9] Youngs, R., Chiou, S., Silva, W. and Humphrey, J., Strong Ground Motion Attenuation Relationships for Subduction Zone Earthquakes, Seismological Research Letters, 1997, pp. 58-73.

[10] Marto, A., Soon, T. and Kasim, F., A Correlation of Shear Wave Velocity and Standard Penetration Resistance, Electronic Journal of Geotechnical Engineering, Vol. 18, 2013, pp. 463-471.

[11] Hunt, R., Geotechnical Engineering Investigation Manual, Mc Graw Hill Book Co., 1984.

[12] Ahmad, I., Hashash, Y., Khan, A. and Waseem, M., Site Amplification Factor at Mardan, Journal of Himalayan Earth Sciences, Vol. 44, Issue 2, 2011, pp. 61-70.

[13] Boore, D., Thompson, E. and Cadet, H., Regional Correlations of V_{S30} and Velocities Averaged Over Depths Less Than and Greater Than 30 m, Bulletin of the Seismological Society of America, Vol. 101, Issue 6, 2011, pp. 3046-3059.

[14] Dungca, J., Concepcion, I., Limyuen, M., See, T. and Vicencio, M., Soil Bearing Capacity Reference for Metro Manila, Philippines, International Journal of GEOMATE, Vol. 12, Issue 32, 2017, pp. 5-11.

[15] Dungca, J. and Chua, R., Development of a Probabilistic Liquefaction Potential Map for Metro Manila, International Journal of GEOMATE, Vol. 10, Issue 2, 2016, pp. 1804-1809.

[16] Dungca, J., Pua, R., Raynold, N., Sangalang, A. and Tan, A, Mat Foundation Design Reference for Metro Manila Reference, International Journal of GEOMATE, Vol. 15, Issue 47, 2018, pp. 42-47.

[17] Dungca, J., A Reference for the Allowable Soil Bearing Capacities in Quezon City, Philippines, International Journal of GEOMATE, Vol. 19, Issue 71, 2020, pp. 42-47.

[18] Dungca, J., Gozum, N., Telan, J., Torres, V. and Uytengsu, T., Deep Foundation Reference for Metro Manila, Philippines, International Journal of GEOMATE, Vol. 14, Issue 45, 2018, pp. 16-21.

[19] Galupino, J., Garciano, L., Paringit, M. and Dungca, J., Location Based Prioritization of Surigao Municipalities Using Probabilistic Seismic Hazard Analysis (PSHA) and Geographic Information System (GIS), Conference proceedings, in HNICEM 2019 – 9th International Conference on Humanoid, Nanotechnology, Information Technology, Communication and Control, Environment and Management, 2017.

[20] Kumar, A., Harinarayan, N. and Baro, O., High Amplification Factor for Low Amplitude Ground Motion: Assessment for Delhi, Disaster Advances, Vol. 8, Issue 12, 2015, pp. 1-11.

11th Int. Conf. on Geotechnique, Construction Materials & Environment, Kyoto, Japan, 3-5 November 2021, ISBN: 978-4-909106063 C3051

DEVELOPMENT OF SOIL TYPE REFERENCE OF METROPOLITAN MANILA USING GENETIC ALGORITHM

Jonathan R. Dungca[1] and Izzhar Christian P. Sumagaysay[2]

[1] Faculty, De La Salle University, Philippines; [2] Graduate Student, De La Salle University, Philippines

ABSTRACT

A soil type reference of Metropolitan Manila was developed using an optimization algorithm called Genetic Algorithm (GA). In this study, a program was created to perform a Genetic Algorithm on each meter soil layer ranging from 40 meters below mean sea level up to 100 meters above mean sea level for specified points with 2km grid intervals. The program utilized the Unified Soil Classification System (USCS) and a borehole database of the study area and surrounding provinces to predict the soil types. Two variables were chosen to assess the fitness of the prediction: the likeness of the soil type with surrounding boreholes, and the distance of the boreholes from a specified grid point. A total of 216 points were used in the study each containing 40 to 130 soil layers. The results were then compiled and plotted to create a total of 38 soil profiles of the study area for the longitudinal and transverse directions. The profiles followed the expected soil types based on the geologic zones of the study area: sands and clays for the coastal lowlands, rocks and sands for the central plateau, and clays and silts for Marikina Valley. Validation of the profiles suggests the Genetic Algorithm as a suitable tool for the development of soil type reference of the study area.

Keywords: Genetic Algorithm, USCS, Soil Types, Metropolitan Manila

INTRODUCTION

Metropolitan Manila, or more locally known as Metro Manila, is the capital region of the Philippines. It has about 13% of the total population of the country and it is where the majority of government offices along with important business and commercial infrastructures are located. It has a land area of 619.54 square kilometers bordered by the Manila Bay at the west and the Laguna de Bay at the east.

Due to its unique location and the shifts in tectonic plates in its geologic past, a fault system was formed leading to the frequent earth movements up until the present [1], [2] As such, there is a need for proper planning and design for all infrastructure. Furthermore, policymakers and disaster response teams need to know these hazards to create a robust disaster reduction and management plan. Currently, there were a lot of studies [3]-[10] that tried to evaluate the geotechnical properties of the study area. However, even being a major component of these studies, there was no available soil type reference for Metropolitan Manila except for the city of Quezon [11] The discussion on the effect of soil type on their respective studies was only discussed concerning the different geologic zones of the study area. Usually, researchers would divide Metro Manila into several zones with the Central Plateau, Marikina Valley, and the Coastal lowlands as the most prominent zones [5]. The problem with this, however, is that a detailed soil profile is absent along with the thicknesses of each soil layer. Thus, this study focuses on creating a soil type reference to map the locations and boundaries of the different soil layers present in the study area.

Mapping of geotechnical parameters is not uncommon as there were several studies already making use of Graphic Information System (GIS) to create maps and projections of the different soil characteristics [3]-[13]. However, current GIS software has no functions fit for mapping the profiles needed for this study, as such, the soil type reference was patterned to the soil profiles presented by Galupino and Dungca [11] in their study on the Quezon City soil profile reference

To create the soil profile reference of Metro Manila, an algorithm was used to predict the existing soil type in specified locations. The use of machine learning and other algorithms is becoming common in the field of Geotechnical Engineering [15]-[17]. One of the fast and easy algorithms is the Genetic Algorithm (GA). GA follows the idea of survival of the fittest wherein fitter individuals have a higher chance to survive and pass on their genes to the next generation. Several studies [15], [18] have already applied GA to geotechnical engineering and the results are very promising. The application of GA, however, is unique for each problem. With this, a fitness function was created for this specific application of GA to the prediction of soil types.

This study aims to create a soil type reference for Metropolitan Manila that will aid engineers, policymakers, and other stakeholders in knowing the expected soil type in their respective project sites.

METHODOLOGY

Borehole logs located in Metropolitan Manila and other surrounding provinces are collected. Erroneous borehole logs were removed and a representative borehole was determined for sites with multiple borehole logs. A grid system with 2km intervals was also placed in the study area. the grid intersections will be the location where the Genetic Algorithm will be deployed. The grid was labeled alphabetically from west to east and numerically from north to south. The borehole locations and the grid system were presented in Fig. 1.

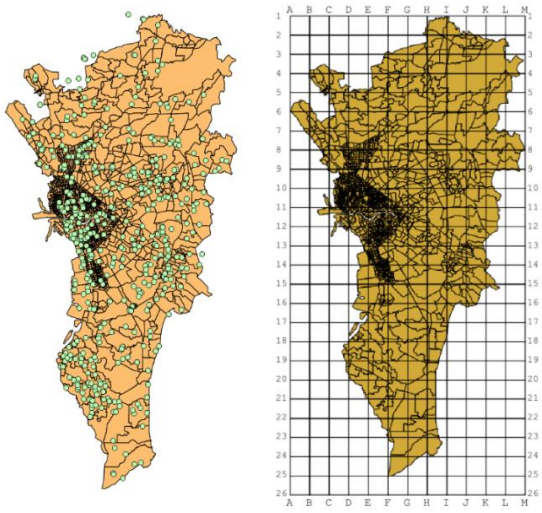

Fig. 1. Borehole locations and grid system of Metropolitan Manila.

The elevations of the borehole logs and the grid intersections were plotted to create a 3D Elevation map shown in Fig. 2. This was crucial as each borehole was adjusted to its correct meter elevations with the mean sea level as the reference elevation.

Fig. 2. 3D elevation Map of Metropolitan Manila.

The soil types were grouped into classes based on the Unified Soil Classification System. The classes were adjusted to cover the different soil type reporting given by the borehole logs. A total of 24 soil types were used in this study, including the 15 original soil types from USCS, unspecified or general Gravel, Sand, Clay, and Silt, and 5 classifications for Rock. The summary of the soil types with their short description was shown in Table 1.

Table 1. Summary of soil types.

General Soil Type	Soil Type Origin	Specific Soil Type	Description
G Gravel	USCS	GW	Well-graded gravel
	USCS	GP	Poorly-graded gravel
	USCS	GC	Clayey gravel
	USCS	GM	Silty gravel
	Added	G	Unspecified gravel
S Sand	USCS	SW	Well-graded sand
	USCS	SP	Poorly-graded sand
	USCS	SC	Clayey sand
	USCS	SM	Silty sand
	Added	S	Unspecified sand
C Clay	USCS	CH	High-plasticity clay
	USCS	CL	Low-plasticity clay
	Added	C	Unspecified clay
M Silt	USCS	MH	High-plasticity silt
	USCS	ML	Low-plasticity silt
	Added	M	Unspecified silt
R Rock	Added	GR	Boulders and large-sized gravel
	Added	SR	Sandstone
	Added	CR	Mudstone
	Added	MR	Siltstone
	Added	R	Tuff and other unspecified rock
PT Peat	USCS	PT	Peat
O Organic Fines	USCS	OH	High-plasticity organic fines
	USCS	OL	Low-plasticity organic fines

The process of a Genetic Algorithm (GA) starts with the creation of a random initial population followed by the fitness evaluation then the crossover and mutation operations to create the next generation population. The new generation replaces the initial population and the process is repeated until a given set of generations or if the convergence criteria are attained [17]. The method is shown in Fig. 3.

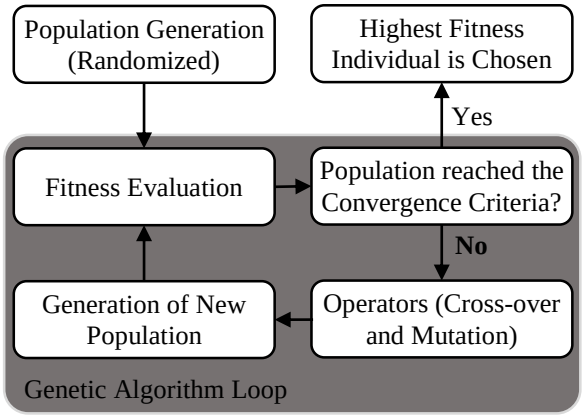

Fig. 3. Genetic Algorithm Flowchart

The GA used in the creation of the program was deployed in the grid intersection. GA was used as its process is a fast and easy way for the program to converge into a prediction of the soil type. The program scores the prediction based on their accuracy to surrounding borehole logs. The maximum distance of the referenced borehole logs was set at 2.5km from the respective grid intersections. Furthermore, the influence of the borehole logs in the scoring of the predictions was adjusted in relation to their distance to a specific grid point. Usually, Euclidean distance is used in these applications [11], however, due to the size of the study area, the great-circle distance was used.

For GA to function, it required a set of variables to optimize, its mutation rates and the fitness function to quantify the accuracy of the prediction. The created program used two variables: the soil type and the maximum distance of boreholes to be considered. The range of this distance was set from 500 meters to 2500 meters from the grid intersection points. This was implemented to lessen the irrelevant data points for the comparison of the prediction. The soil type variable was set as categorical data following the specific soil type presented in Table 1. The mutation rates for these variables are set to be 0.10 and 0.30 for the soil type and the maximum distanced considered. Lastly, the fitness function incorporated the weights used in k-Nearest Neighbor by Galupino and Dungca [11], and a 'likeness' function. The fitness formula was shown in Eq. (1).

$$F = L_{ij} W_{ij} = \frac{\sum L_{ij} e^{-D_{ij}}}{\sum e^{-D_{ij}}} \quad (1)$$

Where: L_{ij} is the 'likeness' function of the specific soil layer of grid intersection point i to the j^{th} borehole under the training data set. L_{ij} has a value of 1 if the specific soil layer has the same soil type as the j^{th} borehole, otherwise, the value is 0. Meanwhile, W_{ij} is the distance weights introduced by Galupino and Dungca [11] and D^{ij} is the great-circle distance between grid intersection point i to the j^{th} borehole

The genetic algorithm was deployed in each grid intersection point for each meter soil layer. The extents of the elevations were set at 40 meters below sea level up to 100 meters above sea level. The program skips those grid intersections without surrounding boreholes under a 2.5km radius. Once all elevation points were completed for all grid intersections, the results were compiled and soil profiles were plotted in CAD.

RESULTS

Metropolitan Manila is composed of different geologic zones due to its locations. The study area can be divided into 4 main areas: Central Plateau composed of mainly Guadalupe Tuff, Marikina Valley composed of delta deposits from the Marikina River, the coastal lowlands composed of delta deposits from Pasig River, and the Coastal swamp/wetlands on the north-west [5], [7]. It is surrounded by Manila Bay on the west, and Laguna de Bay on the east. It is bordered by the province of Bulacan in the north, Rizal to the north-east, and the provinces of Cavite and Laguna in the south.

For this specific study, the highest ground elevation from the borehole logs inside the study area was determined to be 88 meters above sea level, however, there were borehole logs in the neighboring province of Rizal that exceeded 100 meters above sea level. These excess soil layers were disregarded as they were beyond the set extents of the study area.

For the plot of the soil profiles in CAD, the soil layers were grouped and color-coded based on their general soil types following Table 1. Gravels were shaded with dark green, sands were shaded in light blue, clays with orange, silts with light green, rocks with brown, and organic fines as pink. There was no predicted soil type for peat. The generalization of the soil types was done for the simplicity of the plotting as well as to easily observe the trend and movement of the soil types throughout the study area.

Longitudinal Sections

Due to the Guadalupe Tuff formation, different rock classes were observed to be prevalent in the study area with the only exception for this was on the western and eastern sides near the bodies of water. Samples of the soil profile in the longitudinal direction were shown in Fig. 4 and Fig. 5.

Longitudinal grid H, shown in Fig. 4, passed through the entire length of the central plateau area along with the cities of Quezon, Mandaluyong, San Juan, Makati, Taguig, and some parts of Muntinlupa. It was also the longest grid present in the area. In the area of Quezon City, It was observed to be composed of different rock types, which was expected based on past studies [5], [11]. The topsoil, however, did not

conform with the predictions of Galupino and Dungca [11] as a different technique was used in their study.

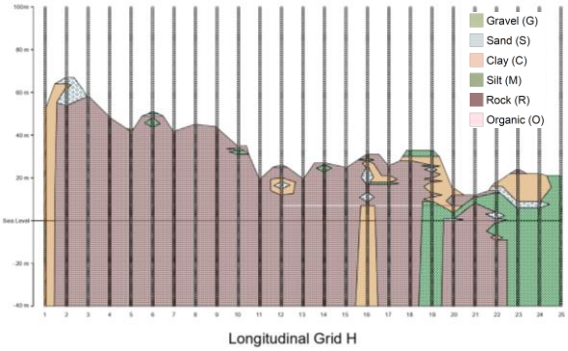

Fig. 4. The soil profile of longitudinal grid H.

Looking at a grid nearer the western coast, longitudinal grid E, presented in Fig. 5, showed a prevalent sand top layer, especially in the central area in grid E10 to E15. These grid points were located in the cities of Manila and Pasay where the mouth of the Pasig River was located. Furthermore, some parts of these locations were also reclamation areas. Traveling further south, revealed a transition from clay to a mixture of rocks and silts as the soil type underneath the sand topsoil.

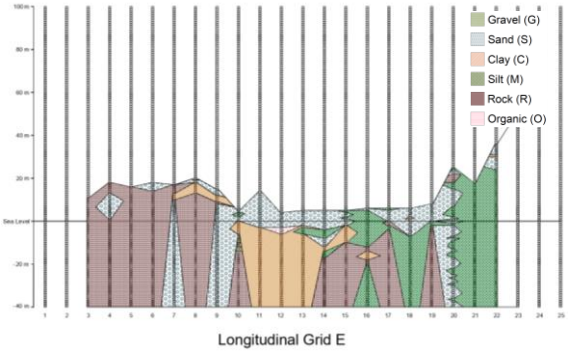

Fig. 5. The soil profile of longitudinal grid E.

The different parts of the study area followed the expected soil types based on the geologic zones. Other parts of the central plateau not shown by Fig. 4 and Fig. 5 were mainly composed of rock types with a 5-meter topsoil depth composed of mixtures of sand, clays, and silts. Furthermore, the Marikina Valley showed prevalent clay and silt layers. The topsoil for this area was a mix of clay, silt, and sands.

Transverse Sections

The transverse soil profiles gave the perspective of the different geologic zones of the study area. The central plateau was easily seen together with the coastal lowlands on the west and the Marikina Valley in the east. Shown in Fig. 6 was Grid 11.

As mentioned before, the three areas of coastal lowlands, the central plateau, and the Marikina Valley were visible in this soil profile. The differences in the soil composition of these three main areas were observed in Fig. 6. The western coast has clay and rock layers overlain by sands and silts, meanwhile, the eastern coast has silt and sand layers overlain by clays. Gravels were also present in the lower layers of Grid G5. The soil types in the western coast were expected from the Pasig River Delta deposits draining to Manila Bay. Additionally, tide changes and ocean movement in Manila bay may have contributed to the soil types present on the western coast. As for the soil types in the Marikina Valley, it was as expected from the Marikina River Delta deposits. Surrounding areas of the Marikina Valley were also composed of the central plateau and the Antipolo Plateau of the province of Rizal. These surrounding areas were previously identified to be mostly composed of Tuff formations [11]

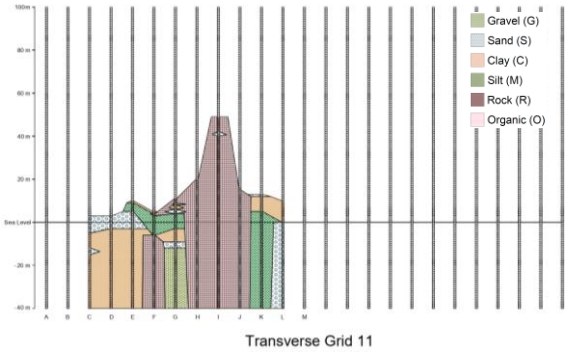

Fig. 6. The soil profile of transverse grid 11.

Genetic Algorithm Analysis and Validation

A total of 551 borehole logs were used in the program to predict the soil profile. 56 borehole logs were put aside for the validation of the results of the GA program. The results of the profile were compared to this validation subset. Since there were varying depths of boreholes, it was better to compare the accuracy of prediction on each meter depth. From these 56 borehole logs, a total of 1113 soil layers were obtained. These soil layers were compared to the closest grid intersection point in relation to their respective elevations. The number of correct soil layers was tallied and grouped per city. Overall, the accuracy of the prediction is 52.83% and 74.75% for the specific and general soil types respectively.

The higher accuracy of the general soil types was expected as there were multiple soil types under a single general soil type. Confusion matrices, shown in Fig. 7 and Fig. 8, were created to visualize these inaccuracies. The number of predicted layers under each actual layers were given in these matrices. The distribution was then shaded to highlight the concentration of the prediction.

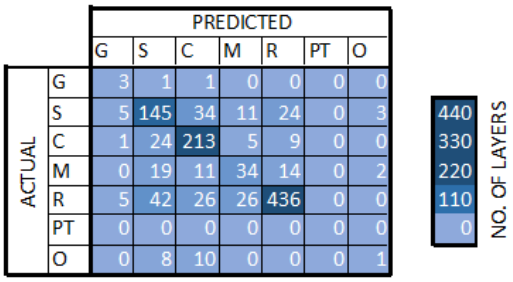

Fig. 7. Confusion matrix for the general soil types.

In Fig. 7, the confusion matrix for the general soil types was shown. The main diagonal had a higher value than other parts and was reflective of the overall 74.75% accuracy of the prediction. Only organic fines had a lower value for the main diagonal. Most of the organic fines were predicted as clays or sands. This prediction error can be attributed to their location as organic fines were commonly found in the western coastal lowlands surrounded by sands and clays.

Looking at Fig. 8, this confusion matrix shows the detailed distribution of the prediction for the specific soil types. The low accuracy of the prediction was observed in this matrix as there were prediction deviation from the main diagonal. Some of these wrong predictions, however, were not as severe such as high-plasticity clays being predicted as low-plasticity clays and vice versa. As such, it is still necessary for engineers to perform additional tests to determine the different geotechnical parameters to properly design a safe and economical foundation.

CONCLUSION

This study was able to create a soil type reference of Metropolitan Manila using a Genetic Algorithm and a compilation of borehole logs collected from the study area and surrounding provinces. This soil profile hopes to serve as a reference for engineers, policymakers, and other stakeholders.

A program was created to perform a Genetic Algorithm to predict the soil type. The soil type was classified using a revised Unified Soil Classification System (USCS). This program was deployed at specific points with 2km grid intervals from 40 meters below mean sea level up to 100 meters above mean sea level. The genetic algorithm was programed to predict the soil type based on the soil types of surrounding boreholes and the distance of these boreholes to the grid intersection points. A fitness function was presented which incorporates the weights used on k-Nearest Neighbor by Galupino and Dungca [11] and a 'likeness' function. The results were then compiled and the soil profiles were plotted in CAD.

The soil profiles followed the expected soil types based on the geologic zones of the study area. Rocks were prevalent in the Central Plateau, Clays overlain by sands and silts were observed in the western coastal lowlands, and silts overlain by clays were found in the Marikina Valley. Validation of the results was done by comparing a subset of the borehole database to the closest grid intersection point of the soil profiles. It was determined that the

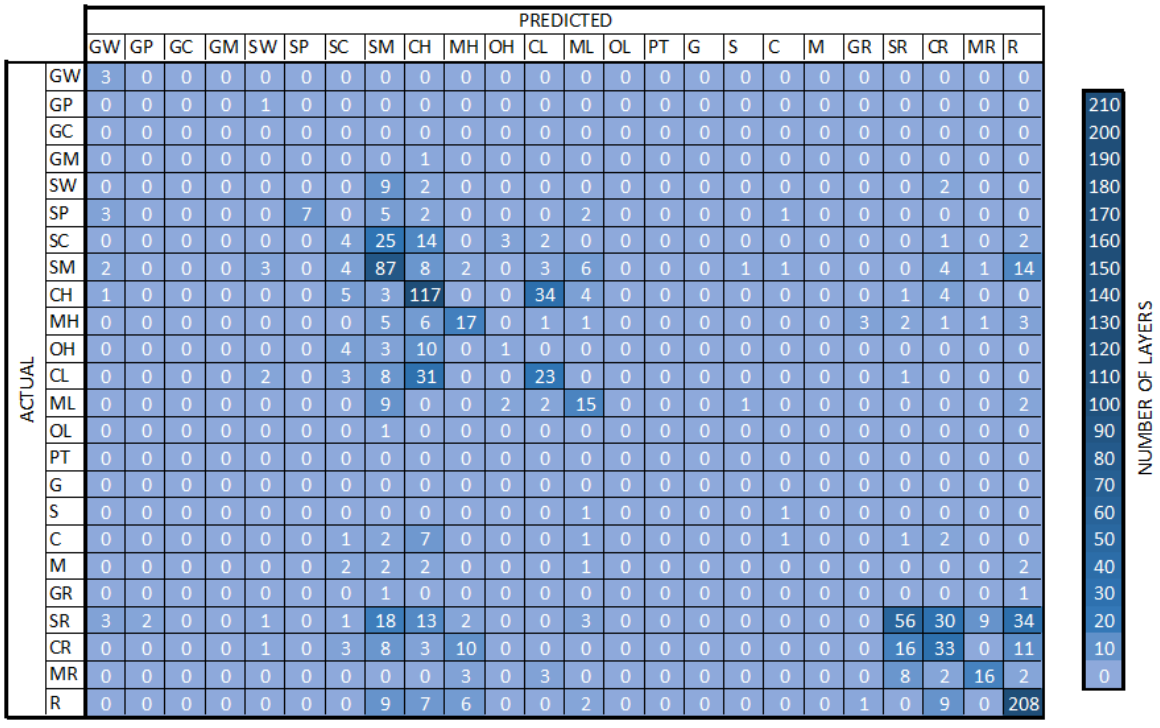

Fig. 8. Confusion matrix for the specific soil types

predictions were 74.75% and 52.83% accurate for general and specific soil types. Confusion matrices were also created to show the distribution of the prediction across the soil types. This accuracy was satisfactory considering the size of the Metropolitan Manila and the distribution of borehole logs throughout the study area

ACKNOWLEDGEMENTS

The researchers would like to thank the Engineering Research and Development (ERDT) of the Department of Science and Technology (DOST) of the Philippines for funding this study, Dr. Erica Elice Uy for introducing Genetic Algorithm, and Joaquin Ramos and other previous researchers under the Department of Civil Engineering of DLSU for sharing their borehole logs for the study area This would have not been completed without their support.

REFERENCES

[1] Kurita, K., Kinugasa, Y., Deguchi, T., Rimando, R.E. and Watanabe, M., Monitoring Aseismic Surface Creep along the Western Valley (Marikina) Fault, 11th International Workshop on Seismic Microzoning and Risk Reduction, Granada, Spain, 2016

[2] Ramos, E., Shifts in Tectonic Stresses around Metro Manila, 2019 Annual Geological Conference of the Geological Society of the Philippines, doi:10.13140/RG.2.2.10532.91528

[3] Dungca, J. R., A Reference for the Allowable Soil Bearing Capacities in Quezon City, Philippines, International Journal of GEOMATE, Vol. 19, Issue 17, 2020, pp. 42-47

[4] Dungca, J. R., and Macaraeg, C. M., Development of a Reference for Seismic Amplification: The Case of Metro Manila, 19th Congress of International Association for Bridge and Structural Engineering, Stockholm, Sweden, 2016

[5] Dungca, J. R., Concepcion, I., Limuren, M., See, T., and Vicencio, M., Soil Bearing Capacity Reference for Metro Manila, Philippines, International Journal of GEOMATE, Vol. 12, Issue 32, 2017, pp. 5-11

[6] Dungca, J. R., Gozum, N. L. C., Telan, J. A. S., Torres, V. C. F., and Uytengsu, T. S. Y., Deep Foundation Reference for Metro Manila, Philippines, International Journal of GEOMATE, Vol. 14, Issue 45, 2018, pp. 16-21

[7] Dungca, J. R., Pua, R. Y., Que, N. Q., Sangalang, A. K. M., and Tan, A. N., Mat Foundation Design Reference for Metro Manila, International Journal of GEOMATE, Vol. 15, Issue 47, 2018, pp. 42-47

[8] Dungca, J. R., and Chua, R. A. D., Development of a Probabilistic Liquefaction Potential Map for Metro Manila, International Journal of GEOMATE, Vol. 10, Issue 2, 2016, pp. 1804-1809

[9] Uy, E. S., Dadios, E., P., and Dungca, J. R., Preliminary Assessment of Liquefiable Area in Ermita, Manila Using Genetic Algorithm, Conference Proceedings, in IEEE 8th International Conference Humanoid, Nanotechnology, Information Technology Communication and Control, Environment and Management (HNICEM), 2015

[10] Velasco, J. N., Tirao, J. M., Enoria, A. S., San Juan, S. Q., and Ubaldo, H. F., Liquefaction Potential Mapping of the City of Valenzuela, Philippines, Conference Proceedings, in IEEE 11th International Conference Humanoid, Nanotechnology, Information Technology Communication and Control, Environment and Management (HNICEM)

[11] Galupino, J. G., and Dungca, J. R., Quezon City Soil Profile Reference, International Journal of GEOMATE, Vol. 16, Issue 58, 2019, pp. 48-54

[12] Khatri, S., and Suman, S. Mapping of Soil Geotechnical Properties using GIS, Geotechnical and Geo-Environmental Engineering (ICGGE-2019, Prayagraj, India, 2019

[13] Galupino, J., Garciano, L., Paringit, M., and Dungca, J., Location Based Prioritization of Surigao Municipalities Using Probabilistic Seismic Hazard Analysis (PSHA) and Geographic Information System (GIS), Conference Proceedings, in 9th International Conference Humanoid, Nanotechnology, Information Technology Communication and Control, Environment and Management (HNICEM), 2019

[14] Elevado, K. J. T., Galupino, J. G., and Gallardo, R. S., Artificial Neural Network (ANN) Modelling of Concrete Mixed with Waster Ceramic Tiles and Fly Ash, International Journal of GEOMATE, Vol. 15, Issue 51, 2018, pp. 154-159

[15] Alamanis, N., Uncertainties and Optimization in Geotechnical Engineering, American Scientific Research Journal for Engineering, Technology and Sciences (ASRJETS), Vol. 38, Issue 1, pp. 92-111

[16] Suguna, N., and Thanushkodi, K., An Improved k-Nearest Neighbor Classification Using Genetic Algorithm, IJCSI International Journal of Computer Science Issues, Vol. 7, Issue 4, 2010, pp. 18-21

[17] de Santos, C., Backanalysis Methodology based on Multiple Optimization Techniques for Geotechnical Problems, Universitat Politencia de Catalunya – BarcelonaTECH, 2015

[18] Fasna, M., Fathima Zuhara, T., and Krishnankutty, S. V., Prediction of Optimum Mosture Content using Genetic Algorithm, Asian Journal of Engineering and Technology, Vol. 5, Issue 3, 2017, pp. 71-76

11th Int. Conf. on Geotechnique, Construction Materials & Environment, Kyoto, Japan, 3-5 November 2021, ISBN: 978-4-909106063 C3051

PREVENTION OF SLOPE FAILURE USING NATIVE MICROORGANISMS

Ryosuke Kawano, Md. Azizul Moqsud

Faculty of Engineering, Yamaguchi University, Ube city, Japan

ABSTRACT

In this study, the solidification of soil by using native microorganisms living in Japan has been carried out. The slope soil failure is one of the main geo-disasters in Japan and the traditional methods to improve the slope soil are not environmental friendly. Microbially induced calcium precipitate (MICP) is becoming popular for the bio-geotechnical engineering purposes in the world. In this study , the native microorganisms were used to bio-stabilize the slope soil. Laboratory experiments were conducted in the constant room temperature to solidify the slope soil by using the native bacteria for 21 days. Direct shear tests were conducted for the measurement of the strength. A model slope was also prepared and solidified with the native bacteria. The generated calcium carbonate was measured. It was observed that the strength has increased significantly after 21days of bio-stabilization by using the native bacteria. The calcium carbonate amount was found maximum in the bottom part of the model slope which indicated the bio-stabilization was more effective at the bottom than the upper part of the slope.

Keywords: Microbial induced calcium precipitation, Slope soil, Model slope, Native bacteria

INTRODUCTION

In Japan, where the ratio of topography in the mountains and hills of the country occupies about 70%, and the area above 500 m above sea level occupies a quarter of the total, a magnitude 6 earthquake occurred in 20% of the world [1]. In addition, 120 million people live in Japan, which has an area of 380,000 km^2, and many people live near the mountains, and the climate is temperate and rainy, so it is susceptible to erosion. There are geo-disasters such as slope failure and landslides occurred each year. With these background, it can be said that it is necessary to improve the technology to prevent the collapse of mountain slopes.

Currently, many of them use concrete as a measure to prevent the collapse of mountain slopes. This is very effective, but not very suitable given its appearance and impact on the ecosystem. However, slope stabilization by using chemical cement is not environment friendly. MICP is a promising technology in where natural bacteria can be used to solidify the soil by producing the calcium carbonate and binds the soil particle and hence increase the geotechnical properties of the soil [2,3,4]. The MICP method by using foreign bacteria is not good for bio-safety and many times they do not active in different weather condition. In recent years, it has been attracting attention that ground improvement technology by microbial metabolism may have less impact on the environment. In recent years, research on the calcium carbonate method has been progressing as the technology.

The calcium carbonate method is a method of solidifying soil by binding soil particles to each other by precipitating calcium carbonate from carbon dioxide produced by the metabolism of microorganisms and calcium existing in the soil.

・ Urea hydrolysis

$$CO(NH_2)_2 + 3H_2O \rightarrow 2NH_4^+ + 2OH^- + CO_2 \quad (1)$$

・ Calcium precipitation reaction

$$CO_2 + H_2O \rightarrow HCO_3^- + H^+ \quad (2)$$

$$HCO_3^- + Ca^{2+} + OH^- \rightarrow CaOH_3 + H_2O \quad (3)$$

So the main objective of this research is to use the native bacteria to solidify the slope soil in the Chugoku region of Japan by conducting the direct shear test and model slope MICP method.

MATERIALS AND METHODS

Culture Solution

The culture solution was prepared using pure chemicals, which are generally used in standard laboratory experimentation. The compositions od the culture solutions are clearly described and presented in Table 1. The amounts were expressed for 1 liter of distilled water. All the chemicals were added to the distilled water and shook adequately to mix. The prepared mix was filtered before applying it to the soil.

Cementation Solutions

The cementation solution was prepared by using

pure chemicals. The detail of the composition of cementation solutions is summarized in Table 2. The composition is shown for 1 liter of distilled water. The chemicals were mixed with the distilled water and filtered.

Table 1 Composition of the culture solution

Subdtance	Amount (g)
Amonium sulfate	10
Yeast Extract	20
Tris-buffer	15.7
Distilled water	1L

Table 2 Composition of cementation solution

Substance	Amount (g)
Calcium chloride	55.5
Urea	30
Nutrient broth	3
Distilled water	1L
Sodium Acetate	7

The soil used in this study is the slope soil on the premises of the Faculty of Engineering, Yamaguchi University, Ube city, Yamaguchi prefecture, Japan which is located in the Chugoku region and to compare the natural slope soil commercial available Mikawa silica sand was also used. The microorganism used was *Psychrobacillus*, which is easily found in the slope soils in Japan [5]. Many researchers of MICP used *Pasteurii*, however, the reason why this study uses a microorganism called *Psychorobacillus* is that *Pasteutii* does not inhabit in Japan. Biohazard and other problems will come up if it will be used in the field. Therefore, as an alternative, native microbes will be used.

Direct Shear Test

Fig. 1 Direct shear tester

Direct shear tests were conducted as it is a simple method for measuring the strength according to ASTM D 3080. In general, the test is performed by deforming a specimen at a controlled strain rate on or near a single shear plane determined by the configuration of the apparatus. Three or more samples were tested, each under different normal stresses, to determine the effects upon shear resistance and displacement and strength properties. In this research, the condition of shear displacement of 7 mm, speed of 0.2 mm/min, and the three normal loads ware 50,100 and 150 kN, respectively. The loss on ignition test was conducted to check the generated calcium carbonate amount.

Scanning electron Microscope Images

Scanning electron microscope images were completed with a Hitati S-4100 field emission SEM at an acceleration voltage of 2 kV and magnification of 100x. Before imaging, cemented samples were oven-dried for at least 1-day. Soil samples were collected from the bio-cemented and un-cemented soil samples.

The above formula expresses the process of carbon dioxide emission by hydrolysis of urea and the mechanism of calcium carbonate precipitation by reacting with calcium ions in the soil. As a measuring method, after the solidification of the soil is completed, the calcium carbonate content is examined by an ignition loss test.

The amount to calcium carbonate was measured by using the ignition loss test. The SEM was also done to see the change of the calcium carbonate between the soil particles.

Amount of calcium ions during the experiment

By measuring the calcium ion concentration during the experiment, it is possible to roughly grasp the degree of microbial propagation and the degree of calcium carbonate precipitation reaction during the experiment period.

The experiment was conducted for 21 days, and the amount of calcium ions at that time was measured using LAQUAtwin.

Ignition weight loss test

The ignition loss test is a test to determine the content of organic matter contained in soil, and is a test used to obtain the physical and mechanical properties of soil.

Microbial culture conditions

Add 5.0 g of soil containing Psychrobacillus, a microorganism used in this study, and 45 mL of distilled water into a beaker to prepare a 10-fold diluted sample solution. Collect 5 mL from the prepared 10-fold diluted sample solution and mix it with 45 mL of distilled water in a beaker to prepare a 100-fold diluted sample solution. At the same time, an agar medium is prepared in a petri dish. The material of the agar medium is the same material as the culture solution and 10 g of agar, and the material is autoclaved to prepare. Apply a 100-fold diluted sample solution to a petri dish containing agar medium thinly on the surface with a large stick, and propagate in an incubator for 2 days at 30 ° C.

Preparation conditions for specimens

Divide into 5 layers in a 60 mm x 20 mm mold, and compact each layer 100 times. The culture solution is permeated with 8 ml only on the first day, and the nutrient solution is permeated with 8 ml once a day at a predetermined time. This is done for 21 days, and after 21 days, the sample is frozen and the specimen is taken out. Photo 1 shows a specimen made of decomposed granite soil in Ube on the left and a specimen made of silica sand in Mikawa on the right.

The other type is made in a specimen with a width of 13.5 cm, a height of 10 cm, and a depth of 10 cm. The culture solution is permeated with 45 ml only on the first day, and the nutrient solution is permeated with 45 ml once a day.

Picture 1 Specimens of decomposed granite soil (left) and silica sand Mikawa (right)

Biocementation of model slope

Measured separately in the upper layer, middle layer, and lower layer.

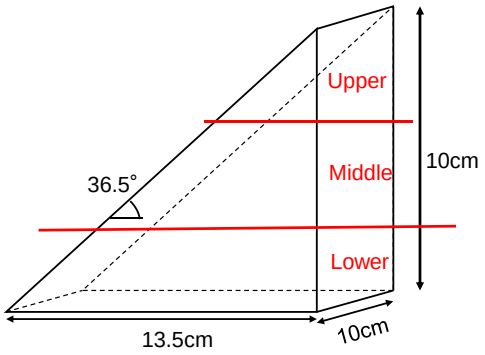

Fig. 2 Schematic diagram of the model slope

From the results, it can be seen that the microorganisms were actively working in the lower layer because the content in the lower layer was higher than the content of calcium carbonate in the upper layer. In this experiment, the nutrient solution and the like easily permeated, and it is considered that the microorganisms themselves were gathered in the lower layer because of the large amount, or that the large amount of the microorganisms flowed out together with the liquid.

In addition, in the calcium carbonate precipitation method, the content is generally about 3 to 5%. Therefore, the content of decomposed granite soil in Ube was almost as expected, but the calcium carbonate content of Mikawa silica sand was extremely low. Regarding this, Ube's decomposed granite soil originally used natural soil, so microorganisms could easily propagate in the soil, but Mikawa silica sand was bought soil and has a finer particle size than Ube's decomposed granite soil. Since there was no variation and it was constant, the propagation of microorganisms did not reach the details. Therefore, it is considered that even if a nutrient solution was added and a precipitation reaction was expected, it did not work and such a result was obtained.

RESULTS AND DISCUSSION

Direct Shear Test

A constant pressure direct shear test was performed at restraint pressures of 50, 100, and 150 kN / m².

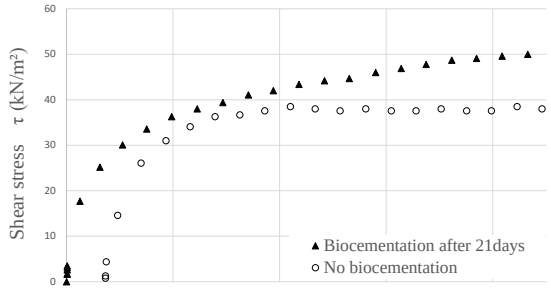

(c) 150 kN/m^3 normal stress

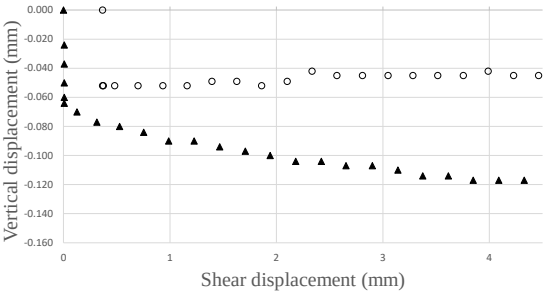

(a) 50 kN/m^2 normal stress

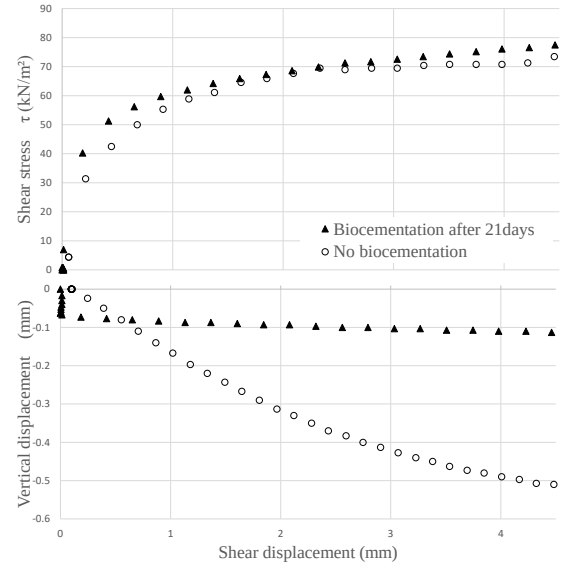

(b) 100 kN/m^2 normal stress

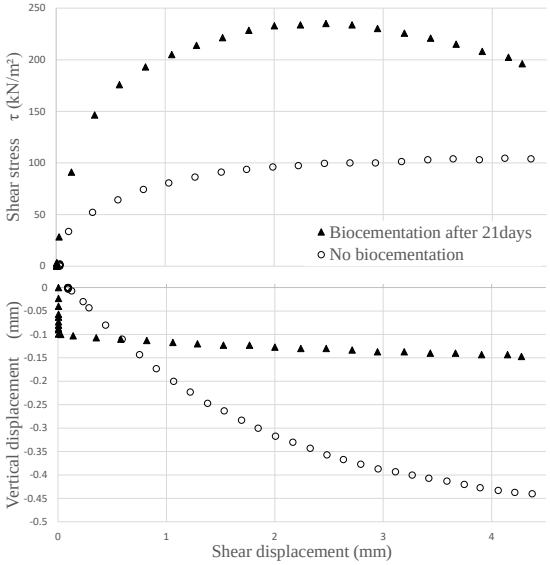

Fig. 3 Variation of vertical displacement with shear displacement

This figure compares before and after the calcium carbonate experiment on a specimen of decomposed granite soil in Ube. As can be seen from the figure, the shear stress of the sample in which the culture solution and the nutrient solution were impregnated with microorganisms for 21 days was larger than that of the sample before the experiment. In other words, it was found that soil solidification by microorganisms is possible. In particular, the shear stress of the specimen with a confining pressure of 150 kN / m² increased significantly.

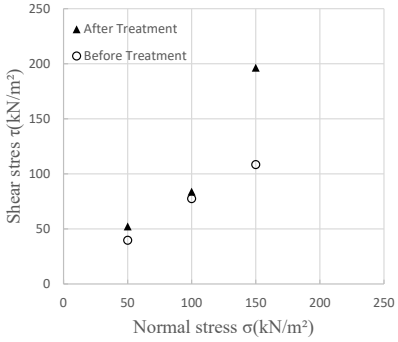

Fig. 4 Relationship of shear stress and the normal stress

From Fig. 4, the adhesive strength of the specimen on the first day was 7.5 kN / m² and the effective stress φd was 30.4 °, and the adhesive strength of the specimen soaked with nutrient solution for 21 days was 22.5 kN / m² and the effective stress was 36.6 °. became. Both the adhesive strength and the effective stress are increased in the specimens infiltrated with the nutrient solution. From this, it is considered that the experiment in this study can raise the soil strength.

Ignition weight loss test

The precipitation rate of calcium carbonate after 21 days was 4.97% for decomposed granite soil and 2.72% for Mikawa silica sand. In the Ube decomposed granite specimen, the precipitation rate of calcium carbonate is slightly higher. Even if it is not saturated, it exceeds the precipitation rate, so it is considered important to allow microorganisms to propagate on the first day in solidifying the soil. Since it was confirmed that the Mikawa silica sand was precipitated at a low rate of 2.72%, it was found that calcium carbonate was precipitated even in soil with a substantially constant particle size.

Calcium ion amount for 21 days

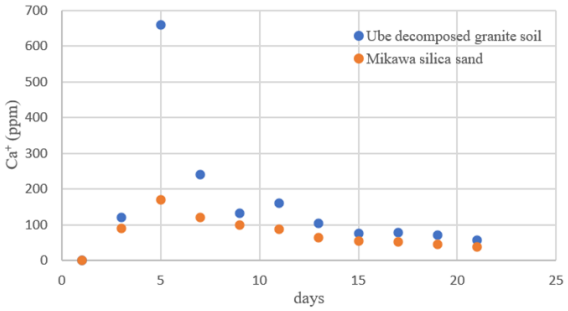

Fig. 5 Variation of calcium ion with time

The maximum content during this period was 660ppm for decomposed granite soil in Ube on the 5th day and 170ppm for Mikawa silica sand on the 5th day. Other papers also measured the highest content on 5-7 days, which was in line with expectations. However, at the scale of the specimen in this study, the maximum content should have been measured around 1000ppm. It is considered that the main reason for this is that the specimen could not be kept saturated because it was a specimen with a slope.

In addition, the specimens using Mikawa silica sand are far below the expected values. This is because the particle size of Mikawa silica sand is almost constant, so it is thought that the propagation of microorganisms in the soil did not go well.

Regarding the fact that the graph has a convex shape with the apex on the 5th day, the microorganisms reached the specimen on the 5th day in the scale of the cylindrical specimen in this study. As a result, it is considered that the reaction of the microorganisms appeared remarkably when the nutrient solution was infiltrated. In addition, the reaction gradually decreased in the latter half of the experimental period. This is related to the fact that it took longer for the nutrient solution to penetrate in the latter half. In other words, the precipitation reaction was active in the upper part of the specimen in the first half of the experiment, so the nutrient solution may not have penetrated into the details of the soil, or it may have been difficult to penetrate. It is also possible that, although unlikely, the soil in the upper layer had solidified, and the air did not reach the soil, hindering the reaction of microorganisms.

From these, reduce the amount of nutrient solution and culture solution from 45 ml, change the size of the specimen because the scale of the specimen was small and it was difficult to perform an experiment to measure the strength of the specimen, and once propagate the microorganisms in Mikawa silica sand Improvements such as starting the experiment after that are necessary.

CONCLUSIONS

Since it was confirmed that the calcium carbonate content increased due to the change in culture conditions, the strength of the solidified soil can be expected to improve.

Calcium carbonate precipitation rate is lower than that of the cylindrical model because the solidification cannot be maintained in the upper layer mainly in the inclined model.

As the number of curing days increases, the precipitation rate of calcium carbonate also increases. The action of microorganisms could be confirmed from the calcium ion concentration for 21 days when the culture conditions were changed.

It was found that the shear stress of the cylindrical test piece increased due to changes in culture conditions.

As the number of curing days increases, the precipitation rate of calcium carbonate also increases.

ACKNOWLEDGMENTS

The authors acknowledged the financial help of the Geo-science Center Foundation for conducting the research.

REFERENCES

[1]. Bhutange.P.S. Chakrabarti.T., 2020. Studies on efficacy of biocementation of cement mortar using soil extract. Journal of Cleaner Production. Volume 274.

[2]. Gowthaman.S. Miysuyama.S. Nakashima.K. Komatsu.M. Kawasaki.S., 2019. Microbial induced slope surface stabilization using industrial-grade chemicals:a preliminary laboratory study. Volume 17, Issue 60, pp.110-116.

[3]. Sharaky.M.A. Shredah.M.N., 2018. Application of microbial biocementation to improve the physico-mechanical properties of sandy soil. Volume 190. Page 861-869.

[4]. Sato.T. Otani.J., 2018. Development of a new loading test apparatus for microfocus Xray CT and its application to the investigation of soil

behavior surrounding driven opensection piles. Volume 58, Issue 3, June 2018, Pages 776-785.

[5]. Moqsud, M.A. (2021). Slope soil stabilization through biocementation by native bacteria in Chugoku region, Japan. International Journal of GEOMATE. (Accepted).

[6]. Cheng, L., Cord-Ruwisch, R., Shahin, M.A. Cementation of sand soil by microbially induced calcite precipitation at various degrees of saturation. Can. Geotech. J. Vol. 50,2013, pp. 91-90

[7]. Dejong, J.T., Mortensen, B.M., Martinez, B.C., Nelson, D.C. Biomediated soil improvement. Ecol. Eng. 36, 2010, pp. 197-210.

[8]. Dhami, N.K., Reddy, M.S., Mukherjee, A. Significant indicators for biomineralization in sand of varying grain sizes. Constr. Build. Mater. 104, 2016, pp. 198-207

[9]. Stocks-fisher, S., Galinat, J.K., Bang, S.S. Microbiobial precipitation of CaCO3. Soil Biology and Biochemistry Vol. 31(11),199, pp. 1563-1571

[10]. Bao, R., Li, J., Chen, L.. Effect of microbial induced calcite precipitation on surface erosion and scour of granular soils proof of concept. Journal of granular soils proof of concept. Journal of transportation research board, Vol. 2657, 2017, pp. 10-18.

11th Int. Conf. on Geotechnique, Construction Materials & Environment,
Kyoto, Japan, 3-5 November 2021, ISBN: 978-4-909106063 C3051

DESIGNING A TRAPEZOIDAL MODULAR BLOCK WALL WITH NONLINEAR OPTIMIZATION

Vuttichai Chatpattananan[1], Somchai Prayongphan[2], Thanadol Kongsomboon[3], and Vatanavongs Ratanavaraha[4]

[1,3]School of Engineering, King Mongkut's Institute of Technology Ladkrabang, Thailand;
[2]Department of Civil Engineering, Kasetsart University, Kamphaeng Saen, Nakhon Pathom, Thailand;
[4]Suranaree University of Technology, Nakhon Ratchasima, Thailand

ABSTRACT

A rectangular wall is better in terms of stability and ease of calculation than a trapezoidal wall. However, a trapezoidal wall is sometimes inevitable such as a retaining wall construction near rockface. FHWA provides simplified rules to design a trapezoidal wall. However, FHWA does not give an example to follow, and the rules need trial and error to implement. BS8006 gives an exact dimension of the block heights, but designing still needs to adjust the block widths. A 16-meters high modular block wall project near rock face in Thailand as an example to illustrate a calculation detail in external stability checking follow FHWA simplified rules and BS8006. The illustrations are trapezoidal walls with two zones, three zones, and four zones. Nonlinear optimization models are also used to minimize the wall base length to facilitate the construction instead of jacking the near rock face to build a rectangular wall. Optimization models also help to relax FHWA simplified rules and BS8006 guidelines. Using an optimization model can decrease the base length from *0.7H* to 0.6*H* for a rectangular wall or even 0.5*H* for a rectangular wall with competent foundation soil. Optimization models can also achieve a base length down to 0.48*H* with a decrease in the cross-sectional area down to 0.92 for a three zones trapezoidal wall. A simple three zones wall with exact dimensions is also proposed in the competent foundation soil conditions.

Keywords: Nonlinear optimization, MSE wall, Trapezoidal wall, Uneven reinforcement lengths

INTRODUCTION

A mechanically stabilized earth wall or MSE wall is a retaining wall that allows more displacement than a rigid reinforced concrete wall. There are two MSE wall types commonly used, which are segmental precast concrete panel (SPCP) and modular block wall (MBW). SPCP uses precast concrete panel as its facing unit and metal strips as its reinforcements, while MBW uses modular block as its facing unit and geogrid as its reinforcements. Reinforcements help to add tension because the tensile strength of soils is negligible.

Designing a Rectangular MSE Wall

An MSE wall has to resist the failure modes in external stability, internal stability, and global stability. External stability requires this rigid body MSE wall to pass the safety factor in sliding, overturning and bearing capacity. Internal stability prevents the failure inside the MSE wall by setting safety factors in rupture and pullout. Global stability considers all other failures that may occur anywhere, especially outside the MSE wall.

Designing MSE deals with specifying the reinforcement length, reinforcement length spacing reinforced soil strength property. For a rectangular MSE wall, FHWA [1] and BS8006 [2] give a preliminary minimum reinforcement length (*L*) of 0.7*H*. FHWA also recommends *L/H* to be not greater than 1.1. Shored MSE wall [3] suggests that the reinforcement length can be as narrow as *0.3L/H*.

Design for external stability for a rectangular MSE wall is simply to specify the reinforcement lengths to handle the sliding, overturning, and bearing capacity. The design for internal stability is slightly different for the SPCP wall and MBW wall. SPCP wall, which is an inextensible wall, adjusts the number of metal strips, spacings, and lengths to resist the rupture and pullout mainly from lateral earth with its trapezoidal (or bilinear) maximum tension force line. MBW wall, which is an extensible wall with less rigid reinforcements than SPCP wall, adjusts the geogrid tensile strengths with its triangular (or linear) maximum tension force line to resist the pullout. Global stability design is implemented by using either the limit equilibrium method (LEM) or finite element method (FEM).

Designing an Uneven Length Reinforcement MSE Wall

Uneven length reinforcement MSE wall is needed due to the limited right of way base, near rock face that is difficult to widen the base, and shored MSE wall is also not an optional. FHWA gives simplified rules used in external stability checking for uneven

length reinforcement MSE walls as follow: 1) the wall is represented by a rectangular block (L_o, H) having the same total height and the same cross-sectional area as the trapezoidal section for external stability calculations, as shown in Fig. 1 (left). 2) minimum base length (L_3) is 0.4H, with the difference in length in each zone being less than 0.15H. 3) Internal stability is designed using the same methods as the rectangular MSE wall. 4) Global stability analysis is also needed in the design. 5) Trapezoidal wall is considered given a rock base or competent foundation soil.

BS8006 gives more specific trapezoidal wall dimensions. Fig. 1 (right) shows the three zones wall where $Z_1 = 0.5H$, $Z_2 = 0.75H$, $Z_3 = H$, $L_1 \geq 0.4H$, $\Delta L \leq 0.15H$. D_m is wall embedment length. For the two zones wall, BS8006 recommends minimum reinforcement lengths at the top at 0.7H and at the bottom at 0.4H or 3 meters. BS8006 also recommends $0.55 \leq L/H \leq 0.75$ and $0.125 \leq S_v/H \leq 0.222$ where S_v is reinforcement vertical spacing.

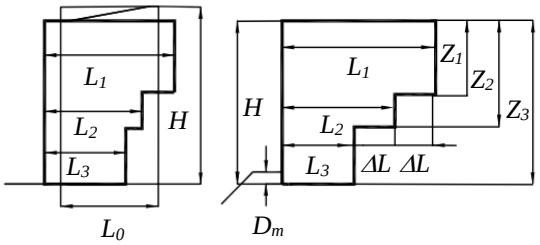

FHWA BS8006

Fig. 1 Dimensioning uneven reinforcement lengths wall guided by FHWA [1] and BS0006 [2]

Nonlinear Optimization Techniques in Designing Uneven Length Reinforcement MSE Wall

Optimization techniques have been applied popularly in civil engineering for both practitioners and researchers. The techniques are well suited to handle problems on hand that demand solutions under limitations. Uneven MSE wall design, which is a retaining wall design, is also an optimization problem that seeks a safe and the most economical solution under its narrowest base limitation.

Numerous optimization techniques have been applied to retaining wall designs, such as Dungca [4], which applies linear optimization of soil mixes in designing vertical cut-off walls. Optimization is also applied in some other areas, such as Bala [5], in mix design optimization of asphalt mixtures.

Narrow retaining walls near rock faces are addressed in some studies. Chen [6] pays attention to its translational mode. Leshchinsky [7] developed a design chart for narrow SPCP walls. Dai [8] illustrated a project of uneven reinforcement lengths of trapezoidal walls, which is a shored MSE wall 8 meters high and 4 meters base width.

Aim, Limitations, and Significance of the Study

From these studies, there is no example showing a design of uneven reinforcement lengths MSE wall. There exist guidelines such as BS8006 and the simplified rules provided by FHWA to design this unconventional trapezoidal wall geometry. Hence, this study aims to provide an example in designing this uneven reinforcement lengths MSE wall.

A 16-meter high retaining wall project in Thailand is chosen to illustrate the design. Four different geometries of MSE walls are proposed. The first wall is a rectangular MBW wall. The second wall is a 2-block trapezoidal MBW wall. The third wall is a 3-block trapezoidal MBW wall. The fourth wall is a 4-block trapezoidal MBW wall.

Nonlinear optimization using GAMS (General Algebraic Modeling Software) program with NLP solver [9] is also used to dimension these MBW walls. The optimization models mainly follow the simplified rules from FHWA and BS8006. The nonlinear optimization models consider both external and internal stability checking. Internal stability can be adjusted by varying the geogrid reinforcement lengths and spacings for each block. Global stability is omitted due to space limitations.

This study helps illustrate the design of an uneven reinforcement length MBW wall. The optimization models proposed also give an approach in dimensioning the 2-block, 3-block, and 4-block trapezoidal MBW walls. A simple 3-block wall with exact dimensions is also proposed. Optimality and convergence problems for nonlinear optimization are also addressed.

WALL GEOMETRY AND PARAMETERS

Wall Geometry

Geometry for nonlinear optimization models is shown in Fig. 2. Those models are the rectangular (1-block) wall, the trapezoidal walls with two zones (2-block), three zones (3-block), and four zones (4-block). Those walls are MBW walls, not the SPCP wall, because its resistant zone is triangular (linear) according to FHWA.

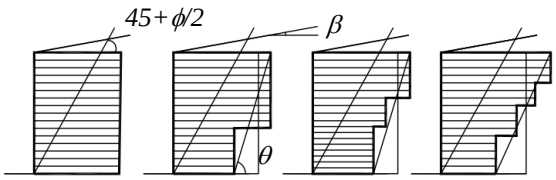

Fig. 2 Wall geometry for the three walls

Parameters

Materials
The reinforced soil density, γ_r, is 18 kN/m^3
The reinforced soil friction angle, ϕ_r, is 32 degrees
The back soil density, γ_b, is 18 kN/m^3
The back soil friction angle, ϕ_b, is 30 degrees
The foundation soil density, γ_f, is 18 kN/m^3
The foundation soil friction angle, ϕ_f, is 35 degrees
The soil cohesion, c, is 0 kPa.

Bearing capacity parameters
The bearing capacity parameters are defined by the following equations from Meyerhof [10].
For the foundation soil, N_{qf} = 33.3, N_{cf} = 46.1, $N_{\gamma f}$ = 37.2. For the reinforced soil, N_{qr} = 23.2, N_{cr} = 31.7, $N_{\gamma r}$ = 22.

Other parameters
The wall height, H, is 16 meters.
The surcharge, q, is 10 kN/m^2.
The retained soil backslope, β, is 0 degrees.
The active earth pressure coefficient is from Rankine equation [10]. K_{ab} for back soil is 0.31, and K_{ar} for reinforced soil is 0.33.

RECTANGULAR MBW WALL

1-Block Wall Geometry

The geometry of the rectangular MBW wall or 1-block wall, as well as its force diagram, is shown in Fig. 3.

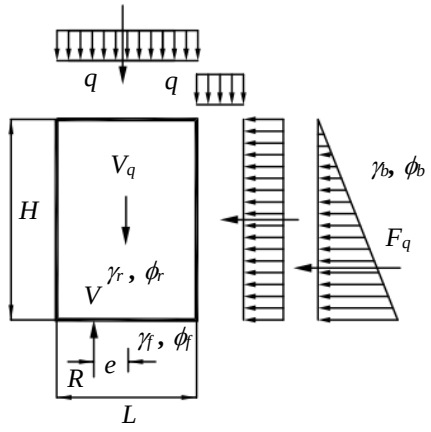

Fig. 3 1-block rectangular wall force diagram

FHWA Design Criteria

Additional notations
V is the vertical load in kN/m.
V_q is the vertical surcharge load in kN/m.
F is the horizontal load in kN/m.
F_q is the horizontal surcharge load in kN/m.
P_R is the resisting force in kN/m.
P_D the driving force in kN/m.
M is the overturning moment in kN-m/m.
M_R is the resisting moment kN-m/m
M_{RBP} is the resisting moment in the bearing pressure in kN-m/m.
L' is the effective bearing width in m.
σ_V is the maximum bearing pressure in kN/m^2.
σ_{utl} is the ultimate bearing capacity of the foundation soil in kN/m^2.

The design calculation details from FHWA [1] are as follows.

Factor of safety - sliding

$$FSS = \frac{P_R}{P_D} = \frac{V tan\emptyset_f}{F+F_q} = \frac{\gamma_b HL tan\emptyset_f}{{}^1/_2 \gamma_b H^2 K_{ab} + qHK_{ab}} \quad (1)$$

Factor of safety - overturning

$$FSO = \frac{M}{M_{RO}} = \frac{V(L/2)}{F(H/3)+F_q(H/2)} \quad (2)$$

Eccentricity (m)

$$e = \frac{L}{2} - \frac{M_{RBP}-M}{V+V_q} = \frac{L}{2} - \frac{\gamma_b HL\left(\frac{L}{2}\right) - F\left(\frac{H}{3}\right) - F_q\left(\frac{H}{2}\right)}{\gamma_b HL + qL} \quad (3)$$

Factor of safety – bearing capacity

$$FSB = \frac{\sigma_{ult}}{\sigma_V} = \frac{0.5L'\gamma_f N_{\gamma f}}{(V+V_q)/L'} = \frac{0.5(L-2e)\gamma_f N_{\gamma f}}{(\gamma_b HL + qL)/(L-2e)} \quad (4)$$

Under FHWA [1] design criteria for external stability checking, $L \geq 0.7H$, $FSS \geq 1.5$, $FSO \geq 2.0$, $e \leq L/6$ and $FSB \geq 2.5$. FHWA also recommends global stability factor of safety ≥ 1.3.

1-block Wall Optimization Models

F

The optimization model for 10 meters high 1-block wall is done by relaxing the design criteria of $L \geq 0.7H$ and tries to minimize L. Note that the constraint $L \geq 0.3H$ is added to guarantee the optimality.

1-block $L/6$ optimization model (1-block $L/6$)

Minimize	L
Subject to	*FSS in* (1) ≥ 1.5
	FSO in (2) ≥ 2.0
	e in (3) $\leq L/6$
	FSB in (4) ≥ 2.5
	$L \geq 0.3H$

(5)

FHWA also recommends maximum allowable eccentricity for competent foundation soil at $L/4$. Another 1-block optimization model for competent foundation soil is developed by replacing *e in* (3) $\leq$

L/6 in (5) with *e in* (3) $\leq$ *L*/4.

Using an optimization model can decrease the base length from *0.7H* to 0.6*H* for a rectangular wall or even 0.5*H* for a rectangular wall with competent foundation soil.

2- BLOCK TRAPAZOIDAL MBW WALL

2-Block Wall Geometry

The geometry of the 2-block trapezoidal MBW wall or 2-block wall and its force diagram is shown in Fig. 4.

FHWA Simplified Rules Optimization Models (FHWA Model)

Simplified rules from FHWA are applied to design this uneven reinforcement length wall. The equal sectional area can be stated as:
Equal areas

$$L_B H_B + L_T H_T = L_o H \quad (6)$$

where the minimum L_o is 0.7*H*.

This simplified rule is simply to guarantee that the trapezoidal wall gains a little less sliding factor of safety in (11) than the original rectangular wall. The decrease in the trapezoidal factor of safety is due to the extra length ($L_T - L_o$) of the surcharge load (q).

FHWA simplified rule also limits the different zone lengths to be less than 0.15*H*. This rule can be stated as:

Different zone length

$$L_T - L_B \leq 0.15H \quad (7)$$

Another FHWA simplified rule is the minimum base width, or base reinforcement length (L_B) is *0.4H*, stated as:

Minimum base length

$$L_B \geq 0.4H \quad (8)$$

Accompanying with FHWA simplified rules in (6), (7), and (8) to specify the base layer height (H_B) and the top layer height (H_T) in Fig. 4, one more relationship between the top layer height (H_T) and the top layer width (L_T - L_B) is needed. This relationship can be set through the top rear slope angle (θ_T) in Fig. 4. BS8006 in Fig. 4 for 3-block wall also implies that the upper block height should be greater than the lower block height and the different zone lengths as $Z_1 = 0.5H$, $Z_2 = 0.75H$, $Z_3 = H$, $L_1 > 0.4H$, $\Delta L < 0.15H$. The rear slope is from 1.67V1H to 3.33V1H.

In the authors' opinion, the rear slope is set for the following reasons; 1) Facilitate the slip plane to be outside the global stability with 1.3 factor of safety; 2) Ensure that the reinforcement lengths are beyond the MBW internal stability resistant zone at $tan(45 + \emptyset_2/2)$; 3) Adjust to the actual construction restriction such as the slope needed to avoid jacking the rock surface at the back of the wall; 4) Balance the moment equilibrium at point *O'* in Fig. 4 that geogrid hold enough strength to hold the right-wing of the top block to not fall due to the insufficient bearing capacity of the foundation soil. The authors use reason 4) in setting the rear slope angle or the top block height by taking the moment equilibrium at point O' in Fig. 4, stated as follows:

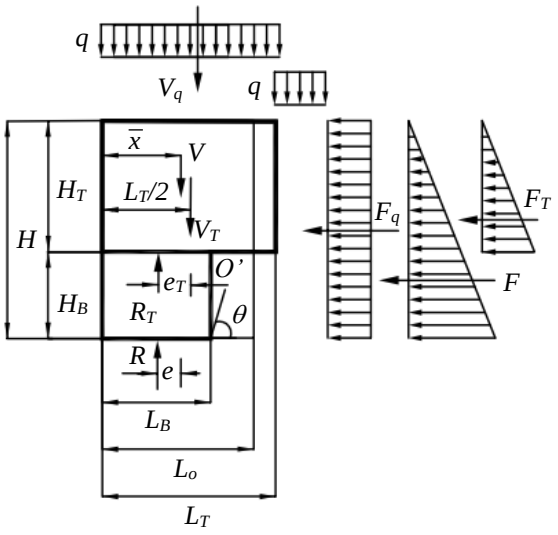

Fig. 4 2-block trapezoidal wall force diagram

Top block height

$$K_{ar}\frac{1}{2}\gamma_r {H_T}^2\left(\frac{H_T}{3}\right) + K_{ar} q H_T \frac{H_T}{2} \geq \gamma_r H_T (L_T - L_B)\frac{L_T - L_B}{2} + \mathrm{q}(L_T - L_B)\frac{L_T - L_B}{2} \quad (9)$$

In (9), the moment from geogrid strength derived from the lateral earth pressure and the surcharge (MO_{RW}) must be greater than the moment from the right-wing weight of the top block (MR_{RW}). To keep good stability, the overturning factor of safety of this right-wing block (FSO_{RW}) should be close to 1.

Internal stability is also in consideration. FHWA requires the reinforcement lengths at all layers in the resistant zone to be at least 1 meter, stated as follows.

Internal stability

$$L_B \geq H_B \tan(45 + \emptyset_r/2) + 1 \quad (10)$$

An optimization model for a 2-block wall

following FHWA simplified rules for external stability to minimize the base width (L_B) is set as follows:

2-block FHWA optimization model (2-block FHWA)

Minimize	*Base length (L_B)*
Subject to	*FSS in (1) of top block* $\geq$ *1.5*
	FSO in (2) of top block $\geq$ *2.0*
	e_T in (3) of top block $\leq$ *L_T/6*
	FSB in () top block $\geq$ *2.5*
	FSS in (1) of 2-block $\geq$ *1.5*
	FSO in (2) of 2-block $\geq$ *2.0*
	e in (3) of 2-block $\leq \bar{x}/3$
	FSB in (4) 2-block $\geq$ *2.5*
	Equal areas in (6)
	Different zone lengths in (7)
	Minimum base in (8), $L_B \geq 0.4H$
	Top block height in (9)
	Internal stability in (10)
	$L_T \geq 0.7H$
	$L_T - L_B \geq H/20$

(11)

In (11), 2-block means the whole block, including the top block and the bottom block. $\bar{x}$ in (11) shown in Fig. 4 is the center of mass for the whole block. Meyerhof's effective bearing length for the 2-block wall is replaced $L' = L - 2e$ with $L' = \bar{x} - 2e$. For top-block wall, $L'_T = L_T - 2e_T$.

The minimum different zone length $L_T - L_B \geq H/20$ and the minimum bottom block height $H_B \geq 0.15H$ are added to set lower bounds for this nonlinear optimization model to avoid the optimality and convergence problems. H/20 in the minimum different zone constraint is set following FHWA in designing superimposed MSE walls that if the difference is offset for the upper wall and the lower wall is less than H/20, the two-tier wall can be treated as one wall. The bottom block height can be adjusted lower or higher according to the rock face at the back of the wall.

BS8006 Optimization Model (BS Model)

BS8006 recommends the top block reinforcement length to be at least 0.7H, the bottom reinforcement to be at least 0.4H, and the different zone lengths to be less than 0.15H. Equal areas constraint is not imposed as FHWA. The 2-block BS optimization model is similar to the 2-block FHWA model in (11) except that the equal areas constraint in (6) is relaxed.

Relaxing Minimum Top Length Model (Proposed Model)

In decreasing the base length, the minimum top length at 0.7H is relaxed. Omitting $L_T \geq 0.7H$ still guarantees the wall stability since both external stability (sliding, overturning, bearing, and eccentricity) and internal stability in (10) are checked at both the top block and the whole 2-block wall. The 2-block proposed model is similar to the 2-block FHWA in (11) and BS8006 model except that the equal areas constraint in (6) and minimum top reinforcement length at 0.7H are relaxed. Wall stability is guaranteed through external and internal stability of the top block and the whole 2-blocks.

Comparison of 2-Block Wall Models

The optimized result for the three optimized models for 2-blocks walls is shown in Table 1. The different zone lengths (7) and top block height (9) are binding constraints for all three models. The additional binding constraint for the FHWA model in (11) is the equal areas (6). The additional constraint for the BS model is the top reinforcement length. The additional constraint for the Proposed model is the eccentricity.

Table 1 2-block wall output

Description	FHWA	BS	Proposed
L_B/H	0.64	0.55	0.52
L_T/H	0.79	0.7*	0.67
$(L_T - L_B)/H$	0.15*	0.15*	0.15*
H_T/H	0.42*	0.42*	0.42*
FSO_{RW} H_T	1.0*	1.0*	1.0*
2-block *FSS*	2.75	2.41	2.30
2-block *FSO*	4.04	3.11	2.84
2-block *e* (m)	1.33	1.52	1.59*
2-block al. *e* (m)	1.88	1.65	1.59
2-block *FSB*	5.68	3.79	3.21
Area (m^2)	179.2*	156.9	150.0
Area/($0.7H^2$)	1.0*	0.88	0.84

Note: 2-block means the whole block. Top means the top block. al .e means allowable eccentricity. * is the binding constraint.

The top block external stability is sliding, overturning, and bearing capacity are not the critical constraints in the design. This can be seen from its factors of safety and eccentricity. Practically, top block stability can be ignored in the design.

3-BLOCK AND 4 BLOCK TRAPEZOIDAL MBW WALLS

The 3-block and 4-block MBW wall use the same design parameters as the 2-block MBW wall. Its force diagram is similar to Fig. 4 of the 2-block wall, except that there is one middle block between the top and the base block for the 3-block model, and there are two middle blocks for the 4-block model. Table 2

compares only the proposed model for rectangular 1-block, trapezoidal 2-block, 3-block, and 4-block optimized models.

From Table 2, 4-block performs better than 3-block, 2-block, and 1-block models in base length (L_B) with the trade-off in increasing top length (L_T). In terms of the area, 1-block and 2-block are better than 3-block and 4-block because they have fewer constraints to achieve. For trapezoidal 2-block, 3-block, and 4-block, foundation soil bearing capacity (*FSB*) is a binding constraint. The follows the recommendation by FHWA that trapezoidal wall should be considered under competent foundation soil conditions.

Table 2 Comparison of the Proposed model output

Description	1	2	3	4
L_B/H	0.6	0.52	0.48	0.48
L_T/H	0.6	0.67	0.78	0.87
FSS	2.34	2.30	2.66	2.79
FSO	2.90	2.84	3.82	4.26
e (m)	1.59*	1.59*	1.36	1.28
al *e* (m)	1.59	1.59	1.84	1.96
FSB	4.76	2.5*	2.5*	2.5*
Area (m^2)	152.6	150.0	165.5	181.9
Area/($0.7H^2$)	0.85	0.84	0.92	1.02

Note: 1 is the rectangular wall in (11). 2 is the 2-block wall. 3 is a 3-block wall. 4 is the 4-block wall. * is the binding constraint

The authors suggest using three zones block is the best option since the 4-block needs to use a subjective upper bound of the second top height to avoid infeasibility. A simple rule recommended by the authors is to combine both the FHWA simplified rules in equal areas and BS8006 guidelines resulted in a simple three zones block with $Z_1 = 0.5H$, $Z_2 = 0.75H$, $Z_3 = H$, $\Delta L = 0.15H$, $L_1 = 0.5125H$. The dimension of this three zones wall is simple to use with sufficient stability under competent foundation soil conditions.

CONCLUSIONS

Optimization techniques can help design MSE walls with economic and safe solutions. The reinforcement length can be decreased from $0.7H$ to 0.6H for or even 0.5H for a rectangular wall with competent foundation soil. For a trapezoidal wall, the three zones wall seems to be the best option in terms of the minimum base length and optimality difficulty. The three zones wall proposed by this study can reduce the base length ratio (L_B/H) to 0.48 and reduce the cross-sectional area down to 0.92. from the area of 1.0 of rectangular walls with the reinforcement ratio of $0.7L/H$. A simple three zones wall without optimization following BS8006 guideline with $0.5125H$ base length is also recommended.

REFERENCES

[1] FHWA-NHI-00-043, Mechanically stabilized earth walls and reinforced soil slopes design and construction guidelines, U.S. Department of Transportation – Federal Highway Administration, 2001.

[2] BS8006, Code of practice for strengthened/reinforced soils and other fills, The British Standards Institution, 2010.

[3] FHWA-CFL/TD-06-001, Shored Mechanically Stabilized Earth (SMSE) Wall Systems Design Guidelines, U.S. Department of Transportation–Federal Highway Administration, 2006.

[4] Dungca J., Galupino J., Sy C., Chiu S. F., Linear Optimization of Soil Mixes in the Design of Vertical Cut-off Walls. International Journal of GEOMATE, Vol.14, Issue 44, 2018, pp.159-165.

[5] Bala N., Napiah M. and Kamaruddin I., Application of Response Surface Methodology for Mix Design Optimization of Nanocomposite Modified Asphalt Mixtures, International Journal of GEOMATE, Nov., Vol.13, Issue 39, 2017, pp.237-244.

[6] Chen F., Yang J. and Lin, Y., Active Earth Pressure of Narrow Granular Backfill against Rigid Retaining Wall Near Rock Face under Translation Mode, International Journal of Geomechanics, Vol. 19, Issue 12. 2019,

[7] Leshchinsky D., Hu, Y. and Han, J., Limited Reinforced Space in Segmental Retaining Walls, Geotextiles and Geomembranes, Vol. 22, No. 6, 2004, pp. 543-553.

[8] Dai C., and Livingston J., MSE Wall with Uneven Reinforcement Lengths (Trapezoidal Walls) – Design Development and Challenges, Proceedings of China-Europe Conference on Geotechnical Engineering pp 1668-1671.

[9] Brooke A., Kendrick D., Meeraus A., Raman R., GAMS: A User's Guide, GAMS Development Corporation, 1992.

[10] Bowles J. E., Foundation Analysis and Design, McGraw-Hill, 2001.

11th Int. Conf. on Geotechnique, Construction Materials & Environment,
Kyoto, Japan, 3-5 November 2021, ISBN: 978-4-909106063 C3051

ESTIMATION OF SUBSURFACE STRUCTURE OF LANDSLIDE AREA BASED ON MICROTREMOR OBSERVATION IN THE HOJOJIMA, NAWASHIRO AND AMEDAKI AREA, TOTTORI, JAPAN

Tatsuya Noguchi[1], Isamu Nishimura[1] and Takao Kagawa[1]

[1]Faculty of Engineering, Tottori University, Japan

ABSTRACT

Investigating the ground structure of a landslide area is important in considering the hazards of slope disasters in that area. In this study, microtremor exploration was carried out in three areas (Hojojiima, Nawashiro and Amadaki) in Tottori prefecture that were judged to be landslide topography, and the ground structure was estimated. The target areas are based on the landslide topography distribution map published by the National Research Institute for Earth Science and Disaster Prevention. As a result, it was found that the characteristics of tremors in the target area differ between landslide moving mass, main scarp, and original ground areas. In addition, the velocity structure and thickness distribution of the landslide sedimentary layer in each area could be estimated. In the Hojojima area, where the building was damaged by the 2016 Central Tottori Earthquake, it was found that landslide moving mass was deposited on the alluvium. In the Nawashiro area, landslides occurred in three areas, and it was found that the geology and sedimentary layer thickness differed in each area. In the Amedaki area, it was found that the soft sedimentary layer of the moving mass was thin and widely distributed. In the future, it will be necessary to evaluate landslide hazards based on this ground structure information.

Keywords: Landslide area, Microtremor, Subsurface structure, Tottori Prefecture

INTRODUCTION

In recent years, earthquakes have caused large-scale landslide damage. Strong ground motions caused widespread landslides in the 2009 West Sumatra Earthquake [1] and the 2018 Hokkaido Eastern Iburi Earthquake [2]. Volcanic ash and weathered rock strata exist in the area, and landslides may have occurred repeatedly in the past. The strong ground motions triggered widespread landslides in the area. Therefore, it is important to investigate the ground structure in landslide areas in order to consider slope hazards in those areas.

In this study, microtremor surveys were conducted in three areas (Hojojima, Nawashiro and Amedaki area) in Tottori Prefecture, Japan (Fig.1) that were determined to be landslide terrain based on the landslide topography distribution map published

Fig. 1 Location of observation area (red frame)

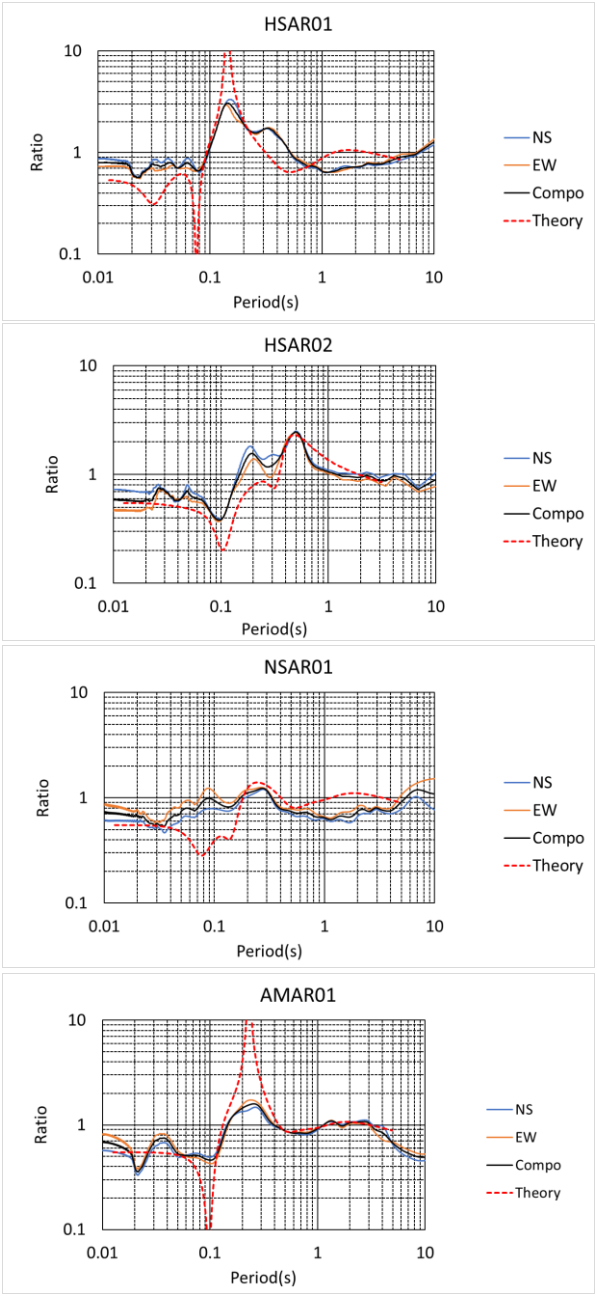

Fig. 2 H/V spectra of microtremors

by the National Research Institute for Earth Science and Disaster Prevention [3] [4]. In the Hojojima area, where the building was damaged by the 2016 Central Tottori Earthquake [5]. The microtremor data were analyzed to understand the ground motion characteristics in the target area. In addition, the layer thickness distribution of the landslide moving mass was determined by estimating the ground structure.

OBSERVATION

For microtremor observations, single-site observations of three-components were conducted to determine the dominant period and amplification characteristics of the subsurface structure, and array observations were conducted to estimate the S-waves velocity structure. A three-component acceleration-type seismometer (JU410) was used for the observations. JU410 is a device that can record microtremors with a period of 0.05 - 10 s.

A total of 80 sites three-component single-site observations were conducted at Hojojima (35 sites), Nawashiro (28 sites), Amedaki (17 sites), at intervals of 100 m to 200 m. The sampling frequency for the measurement was 200 Hz, and the observation time was 10 min for each site.

Array observations were carried out at 4 sites: 2 sites at Hojojima (HSAR01, HSAR02), Nawashiro (NSAR01), and Amedaki (AMAR01). In Hojojima, the ground structure is assumed to be different depending on the topography, and array observation points were set up at two locations with different topography. In the array observation, one point was placed at the center of the circle and three points were placed at equal intervals on the circumference of the circle, and the radius of the circle (array radius) ranged from 1 to 20 meters. Each device was synchronized using a GPS clock. Since the power of the microtremors was expected to be small, three to four people jumped at the same time at about 5 m from the outer seismometer to give an artificial seismic source and observed the waveform. The sampling frequency for the measurement was 200 Hz, and the observation time was 10 - 15 min for each array.

ANALYSIS

For the analysis of the three-component single-site observation data, at least 10 sections of 20.48 s periods without artificial noise were selected from the array observation records. The spectra were smoothed using a log-window [6] with a coefficient of 20. The averaged Fourier spectra of the selected data for each component was used to compose the horizontal components and the horizontal-to-vertical spectral ratio (H/V spectrum) was calculated. The predominant periods were read from the H/V spectra obtained at each site. The H/V spectra obtained from the seismometer at the center of the array observation are shown in Fig. 2 (NS, North-South; EW, East-West; Comp, composition, where the red dashed lines are the theoretical values of the Rayleigh waves using the subsurface structural model). The distribution of H/V spectral predominant periods for each region area shown in Fig. 3.

For the array observation data, Using the open analyzing tool [7], the phase velocity dispersion curves were estimated based on the CCA method [8]. The conditions for the analysis are as follows: At least five sections were selected through an automatic extraction using the RMS value of the microtremor record of each seismograph with a segment length of

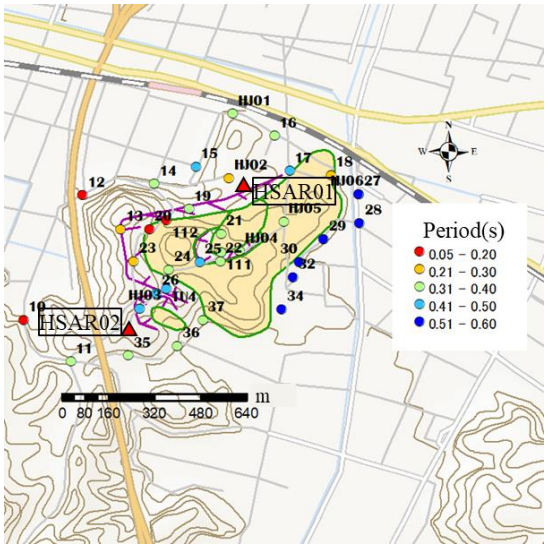

(a) Hojoshima area

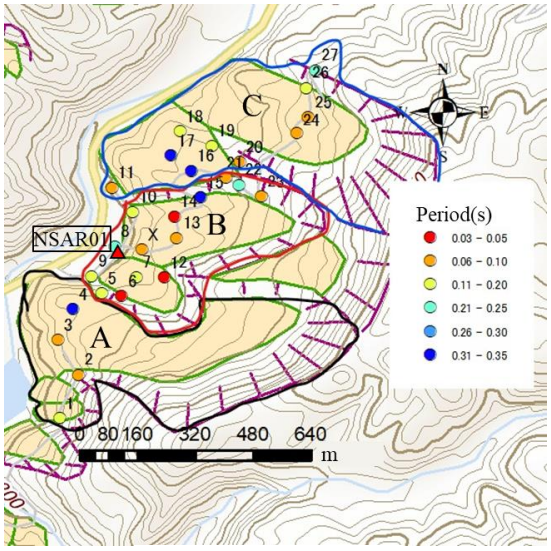

(b) Nawashiro area

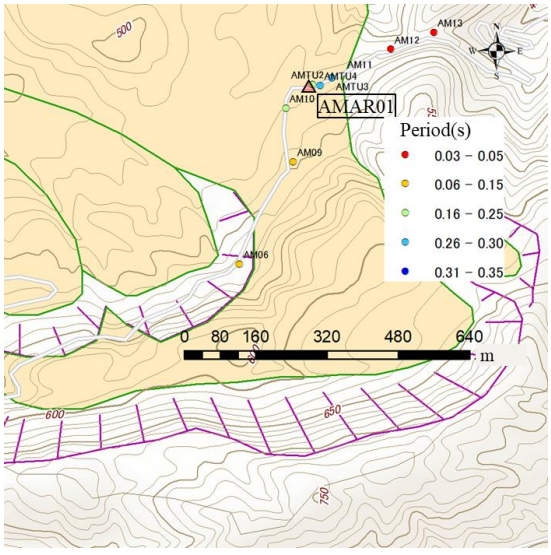

(c) Amadaki area

Fig. 3 Distribution of predominant period

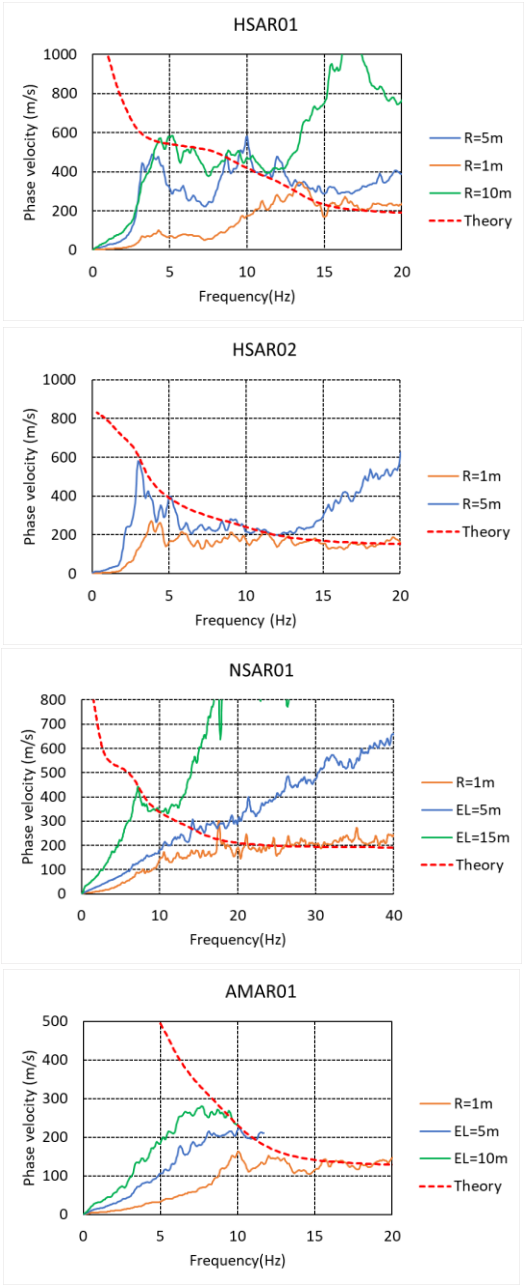

Fig. 4 Dispersion curves of phase velocity

10.24 s. The power spectrum of these sections was smoothed using a Parzen window with a bandwidth of 0.3 Hz and then averaged. Using the power spectrum of each seismograph, the phase velocity dispersion curve was obtained based on the CCA method [8]. The dispersion curves of the phase velocity for each site are shown in Fig. 4 (solid lines are curves obtained for each radius. Red dashed lines are the theoretical values of the Rayleigh waves using the subsurface structural model). We determined the subsurface structures to satisfy the H/V spectra and the dispersion curves of the phase velocity by using the fundamental mode of Rayleigh waves within the frequency range of 2 - 40 Hz. The subsurface

Table 1 Subsurface structural models

HSAR01

Thickness (m)	ρ (g/cm^3)	Vp (m/s)	Vs (m/s)
1.5	1.7	1420	120
6	1.9	1500	200
100	2.0	1950	600
200	2.1	2300	900
∞	2.2	2600	1200

HSAR03

Thickness (m)	ρ (g/cm^3)	Vp (m/s)	Vs (m/s)
3	1.6	1450	145
4	1.7	1480	170
13	1.8	1620	300
15	1.9	1730	400
35	2.0	1840	500
150	2.1	2170	800
∞	2.2	2280	900

NSAR01

Thickness (m)	ρ (g/cm^3)	Vp (m/s)	Vs (m/s)
6	1.7	1460	200
15	1.8	1560	350
100	1.9	1970	600
250	2.1	2300	900
∞	2.2	2620	1200

AMAR01

Thickness (m)	ρ (g/cm^3)	Vp (m/s)	Vs (m/s)
5	1.6	1460	130
8	1.7	1570	250
100	1.9	1970	600
250	2.1	2300	900
∞	2.2	2620	1200

Table 2 Average S-wave velocity

	S-wave velocity (m/s)
HSAR01	184
HSAR02	315
NSAR01	307
AMAR01	204

structures were determined using forward calculations based on geological situations from borehole data [9]. The parameters of the subsurface structure models are the number of layers, density, P-wave velocity: V_p, S-wave velocity: V_s, and the layer thickness. Densities were set referring previous research in Japan [10], and P-wave velocities were set from S-wave velocities [11]. The parameters of the obtained subsurface structure model are shown in Table 1.

The predominant period of the H/V spectrum is considered to correspond to the layer thickness of the sedimentary layer of the landslide moving mass. Therefore, the average S-wave velocity of the sedimentary layer of the landslide moving mass was calculated from the obtained subsurface structure model. The average S-wave velocity was calculated by a weighted average of the layer thickness. The thickness of the layer was estimated from the average S-wave velocity and the predominant period based on the 1/4 wavelength rule. The average S-wave velocity used to calculate the layer thickness in each region is shown in Table 2. For the calculation of Hojojima, the average S-wave velocity of either HSAR01 or HSAR02 is used because the ground structure is different depending on the topography. Which S-wave velocity is used is determined by location and topography. Fig. 5 shows which model was used for

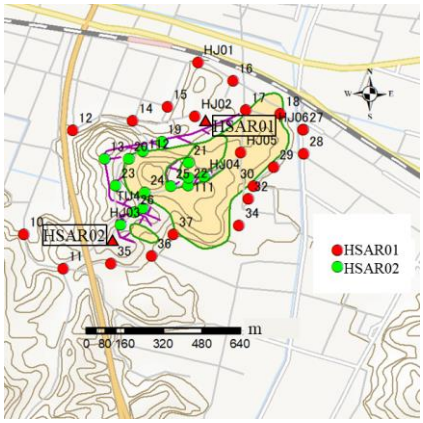

Fig. 5 Location of average S-wave velocity of HSAR01 or HSAR02 at each site in Hojojima

each station. The distribution of thickness of landslide moving mass for each region area shown in Fig. 6.

RESULTS

Distribution of predominant periods

The predominant period distribution in the Hojojima area (Fig. 3(a)) is about 0.1 s with a short period for scarp (purple line) and mountainous areas, and about 0.2 - 0.5 s with a long period for landslide moving mass (yellow-green line, cream-colored areas) and flat areas. The dominant period distribution in the Nawashiro area (Fig. 3(b)), which is topographically divided into three blocks (A, B, and C), shows a random distribution of short and long period points in the range of 0.1 - 0.3 s. The distribution trend is independent of the areas of scarp and landslide moving mass. In the Amedaki area (Fig. 3(c)), the predominant period is about 0.1 - 0.3 s for the landslide moving mass. In the area of the scarp,

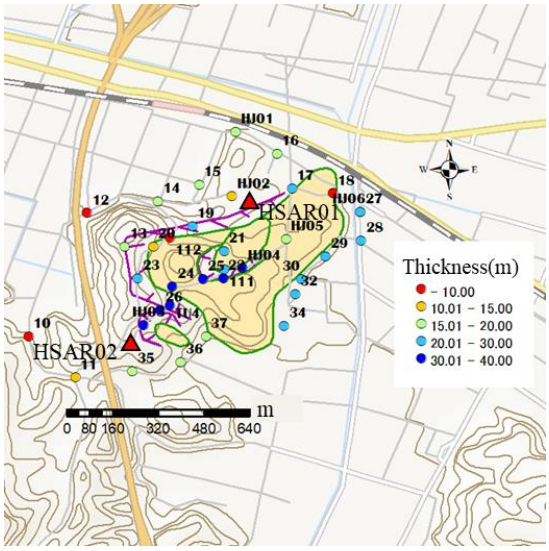

(a) Hojojima area

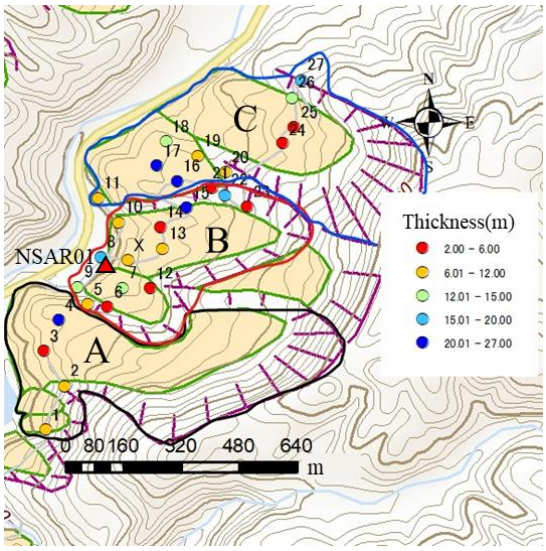

(b) Nawashiro area

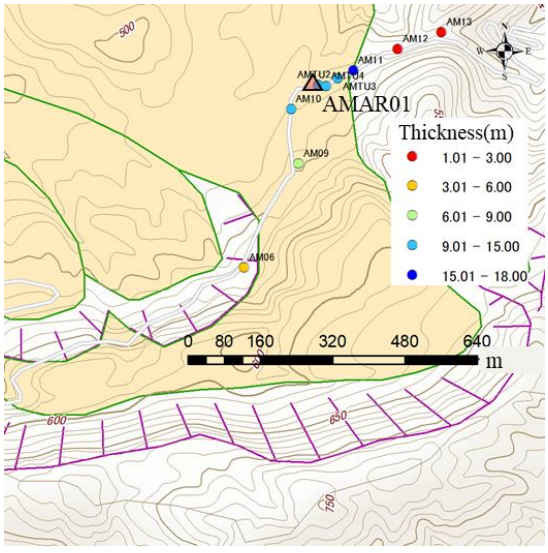

(c) Amadaki area

Fig. 6 Distribution of thickness of sediment layer

predominant period was not found from H/V spectra. The geology of each area is as follows: Hojojima is dominated by andesite, Nawashiro is dominated by andesite with localized mudstone, and Amedaki is dominated by andesite and tuff conglomerate.

Subsurface structure

From the ground model in Table 1, the S-wave velocity structure is as follows. In Hojojima (HSAR01, HSAR02), the S-wave velocity of the sedimentary layer of the landslide moving mass is quite low (120m/s - 200m/s) and the layer thickness is about 7m. It is considered that the S-wave velocity of the rock mass distributed around HSAR02 is gradually changing due to weathering and other effects. In Nawashiro (NASR01), the S-wave velocity of the sedimentary layer of the landslide moving mass is high (200m/s - 350m/s) and the layer thickness is 21m, which is thicker than the other two regions. NASR01 model shows the subsurface structure of block B, and it is considered that other blocks are similar. In Amedaki (AMAR01), the S-wave velocity of the sedimentary layer of the landslide moving mass is low (130m/s - 250m/s) and the layer thickness is 13 m. The area is an extensive landslide terrain, and the observation point is almost in the middle of the moving object.

The layer thickness distribution is as follows. In Hojojima (Fig. 6(a)), the sedimentary layers are thickened from the southwestern scarp to the northwestern landslide moving mass, with a maximum thickness of about 30 m. In Nawashiro (Fig. 6(b)), the sedimentary layer tends to be thicker in the center of the moving mass at lower elevations and thinner closer to the scarp, and the thickness of the layer exceeds 20 m at some points. In Amedaki (Fig. 6(c)), the sedimentary layer tends to be thicker from the west to the east, with a maximum thickness of about 15 m.

CONCLUSIONS

Based on the landslide topography distribution map, microtremor surveys were conducted in three areas in Tottori Prefecture that were determined to be landslide terrain. As a result, the distributions of microtremor period, the subsurface structure model, and the layer thickness distributions of the sedimentary layer of the landslide moving mass were obtained for each region. Microtremor observation is an excellent method for investigating the subsurface geological structures, especially for estimating the predominant period and S-wave velocity structure of the subsurface. These results provide essential information for the evaluation of earthquake ground motions in landslide areas.

ACKNOWLEDGMENTS

Part of this research is based on the results of the graduation thesis by Mr. Atsushi Shimada, who belonged to the Faculty of Engineering, Tottori University. This work was supported by JSPS Grant-in-Aid for Scientific Research JP20K05028 (Principal Investigator: Tatsuya Noguchi).

REFERENCES

[1] Faris F. and Fawu W., Investigation of the initiation mechanism of an earthquake- induced landslide during rainfall: a case study of the Tandikat landslide, West Sumatra, Indonesia, Geoenvironmental Disasters 2014 1:4., doi:10.1186/s40677-014-0004-3, 2014.

[2] Osanai. N, Yamada T., Hayashi S., Kastura S., Furuichi T., Yanai S., Murakami Y., Miyazaki T., Tanioka Y., Takiguchi S., Miyazaki M., Characteristics of landslides caused by the 2018 Hokkaido Eastern Iburi Earthquake, Landslides, DOI:10.1007/s10346-019-01206-7, 2019.

[3] National Research Institute for Earth Science and Disaster Prevention, Landslide Maps, Series 21 "The Miyazu and Tottori Region", Explanations of Landslide Distribution Maps, Vol.260, 2005 (in Japanese).

[4] National Research Institute for Earth Science and Disaster Prevention, Landslide Maps, Series 25 "The Matsue and Takahashi Region", Explanations of Landslide Distribution Maps, Vol.278, 2005 (in Japanese).

[5] Kagawa,T., Noguchi,T., Yoshida,S. and Yamamoto, S., Effect of the surface geology on strong ground motionsdue to the 2016 Central Tottori Earthquake, Japan, Earth Planets and Space, Vol69, DOI10.1186/s40623-017-0689-0, 2017.

[6] Konno K. and Ohmachi T., A smoothing function sutable for estimation of amplification factor of the surface ground from microtremor and its application, Journal of JSCE, No.524/1-33, 1995, pp.247-259 (in Japanese with English abstract).

[7] Cho I., Tada T. and Shinozaki Y., Possibility of microtremor array opened up by general theory: Release of analysis tool BIDO, Seismological Society of Japan Fall Meeting in 2009, 2009 (in Japanese).

[8] Cho I., Tada T. and Shinozaki Y., Centerless circular array method: Inferring phase velocities of Rayleigh waves in broad wavelength ranges using microtremor records, Journal of Geophysical Research, 2006, Vo.111, B09315.

[9] National Research Institute for Earth Science and Disaster Resilience, Geo Station (https://www.geo-stn.bosai.go.jp), [Viewed on June 14, 2021]

[10] Noguchi T., Nishikawa H., Yoshida S. and Kagawa T., Estimation of subsurface structure and characteristics of ground vibration based on microtremor and seismic observation in the central Tottori Prefecture, Japan, Journal of Japan Association for Earthquake Engineering, Vol. 19, Issue 6, 2019, pp. 258-271. (in Japanese with English abstract)

[11] Kitsunezaki C., Goto N., Kobayashi Y., Ikawa, T., Horike M., Saito T., Kurota T., Yamane K., Okuzumi K., Estimation of P- and S- wave velocities in deep soil deposits for evaluating ground vibrations in earthquake, Natural disaster science, 1990, 9-3, 1-17. (in Japanese with English abstract)

11th Int. Conf. on Geotechnique, Construction Materials & Environment,
Kyoto, Japan, 3-5 November 2021, ISBN: 978-4-909106063 C3051

SUBSURFACE STRUCTURES BASED ON MICROTREMOR OBSERVATIONS IN LANDSLIDE AREA OF TANDIKAT, WEST SUMATRA, INDONESIA

Isamu Nishimura[1], Tatsuya Noguchi[1], Yusuke Ono[1] and Masanori Kohno[1]

[1]Graduate school of Engineering, Tottori University, Japan

ABSTRACT

The 2009 West Sumatra Earthquake (M7.5) caused landslides in Padang Pariaman, West Sumatra, Indonesia, and severe damage was occurred in Tandikat. Previous studies of the damage reported that the sliding surfaces are pumice layers with about 2 m thickness on hard clay layers. In this study, we carried out microtremor observations at the landslide areas to estimate ground motion characteristics from H/V spectral ratios and subsurface structures from phase velocity dispersion curves of array measurements.

The predominant periods of H/Vs are distributed in the range of 0.1-0.4 seconds. The H/Vs in the damaged area have sharp unimodal peaks and the peak values tend to be smaller in area without landslides. They might reflect the difference of the velocity structures between the areas with and without landslides through the 2009 earthquake. Harder subsurface structures are suggested in the areas without landslides. From the subsurface structure models derived from array observations, however soft surface layers with S-wave velocity 200 m/s or less are estimated over the whole areas even in the areas without landslides. The layers are considered to be past landslide deposits including pumice layers. We are afraid future coseismic landslides due to the deposit even in the areas without landslides under this event. We hope the results contribute to landslide disaster prevention in the area.

Keywords: Microtremor observation, Subsurface structure, Landslide, The 2009 West Sumatra Earthquake

INTRODUCTION

At local time 5:16 p.m. on September 30, 2009, a magnitude 7.5 earthquake occurred off the coast of Padang in western Sumatra, Indonesia, and caused strong motions (Fig.1) and extensive damage mainly in Padang and Pariaman in western Sumatra [1,2]. Figure 2 shows the distribution of landslides caused by the earthquake. In Tandikat, Padang Pariaman, where the damage was particularly severe. Many flat-roofed houses and schools collapsed due to the earthquake induced landslides, and many people were killed [3]. According to Wang et al. [3], the slip surfaces are composed of about 2 m of pumice layers deposited on top of solid clay layers.

As shown above, coseismic landslides have caused large-scale damage in recent years. It is important to clarify the ground motion characteristics of landslide areas because landslides often occur repeatedly in the particular areas due to the past landslide deposits. Microtremor surveys have been widely used to evaluate the ground conditions in landslide areas [e.g.,4]. This is due to the fact that the sediments above the slip surfaces are very soft and the velocity contrast against basement is distinct. In this study, we carried out microtremor observations at Tandikat where earthquake induced landslide occurred, to estimate landslide deposits.

OBSERVATIONS

Single-point observations of microtremors were conducted at 11 sites in Tandikat mainly in the area of observed landslides. JU410, three-component accelerometer with a 24-bit recorder, was used for data acquisition. We used the following specifications, amplification factor of 100, sampling frequency of 200 Hz, and recording time between 10-15 minutes. Observation at TDK08, TDK10 and TDK11 were carried out at the same time.

As shown in Fig. 3, we made array observations at two sites where landslides were observed (TDKAR1 and TDKAR3) and another site at higher elevations (TDKAR2). The measurements were conducted using four JU410s synchronized by GPS clocks and four geo-phones (UD component only, natural frequency 4.5 Hz) and a data logger HKS9700 (resolution 27 bit). One seismometer was placed at the center of a circle, and the other three were set around the circumference to form an equilateral triangle. The specifications were 200-Hz sampling frequency, radius of the array 1 to 10 m, and recording duration around 15 minutes. The single-point observation records at TDK08, TDK10 and TDK11 were to form an irregular triangular array with synchronized by GPS to guarantee simultaneous observations. The results of this analysis are used in TDKAR3 case.

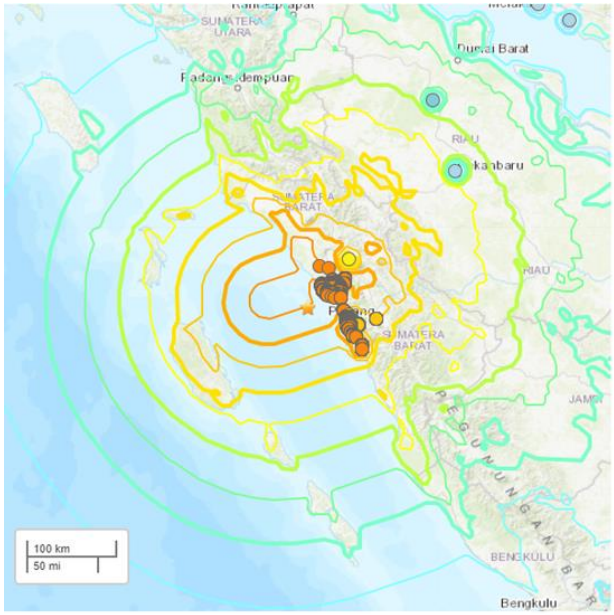

PERCEIVED SHAKING	Not felt	Weak	Light	Moderate	Strong	Very strong	Severe	Violent	Extreme
POTENTIAL DAMAGE	none	none	none	Very light	Light	Moderate	Mod./Heavy	Heavy	Very Heavy
PEAK ACC.(%g)	<0.05	0.3	2.8	6.2	12	22	40	75	>139
PEAK VEL.(cm/s)	*<0.02*	*0.1*	*1.4*	*4.7*	*9.6*	*20*	*41*	*86*	*>178*
INSTRUMENTAL INTENSITY	I	II–III	IV	V	VI	VII	VIII	IX	X+

Scale based upon Worden et al. (2012)

Fig. 1 Estimated seismic intensity distribution for the 2009 West Sumatra Earthquake [2]

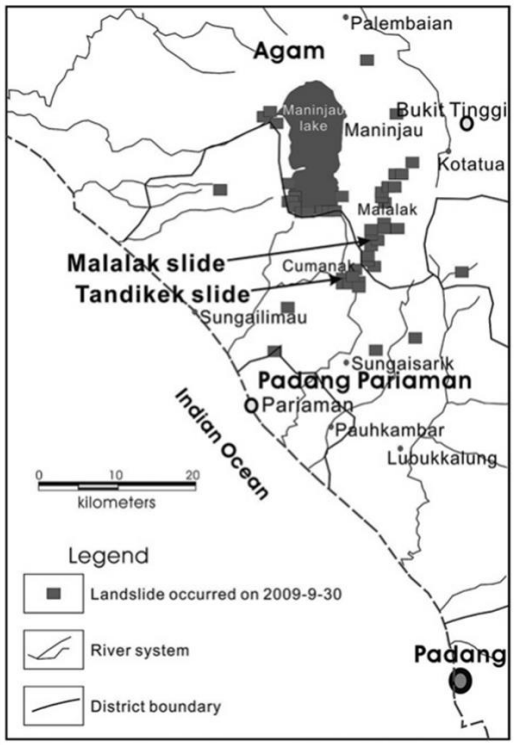

Fig. 2 Landslide distribution prepared by the Geological Survey of Padang, Indonesia [3]

ANALYSIS

Fourier spectra were calculated from single-point observation records of 20.48 sec length and were smoothed using a log window with a coefficient of 20 [5]. Average spectra were evaluated from at least 10 stable sections. Horizontal to vertical (H/V) spectral ratios were calculated from the Fourier spectra, and the predominant periods were visually estimated. Many H/Vs were identified as unimodal with a single distinct peak. The predominant period distribution in Tandikat is shown in Fig. 3.

An analysis of the array observations was conducted with the following procedure: the phase velocity dispersion curves of the array observation records were estimated based on the SPAC method [6] or the CCA method [7]. Using the open analysis tool [8], at least ten sections were selected by automatic extraction using the root mean square values of microtremor recordings with 10.24-s length segments. Only for the irregular triangle array of TDKAR3, 20.48-s length segments were used. Then, the power spectra of those sections were smoothed with a 0.3-Hz bandwidth Parzen window, and the average was estimated. Finally, the phase velocity dispersion curves were determined for an array with a radius. And those obtained at different radius were integrated at each observation site, with respect to their continuity.

Assuming that microtremors are Rayleigh waves, their propagation characteristics allow us to estimate subsurface structures [e.g.,9]. Therefore, subsurface structure models were estimated by trial and error so that these phase velocity dispersion curves and the microtremor H/Vs obtained at the center of the array matched the theoretical phase velocity dispersion curves and the theoretical H/Vs based on the Rayleigh wave fundamental mode, respectively. S-wave velocities of the first layers were estimated from the minimum and constant phase velocity in higher frequencies, and the base layer was fixed for Vs=700m/s. As shown in Fig. 4, number of layers were determined with reference of previous studies [3]. Then, modeling was performed by modifying the thicknesses of layers. P-wave velocities were derived from S-wave velocities [10]. The resulting subsurface structure model is presented in Table 1. Figure 5 shows the phase velocity dispersion curves of the fundamental mode of Rayleigh waves overlaid on those derived from array observations. Figure 6 shows observed and theoretically calculated microtremor H/V spectrum at the center point of array observation sites.

DISCUSSIONS

Predominant Periods of The Horizontal to Vertical Spectral Ratios of Microtremors

Figure 3 shows that the predominant periods are about 0.4-s at TDK01, TDK05, and TDK07, those are

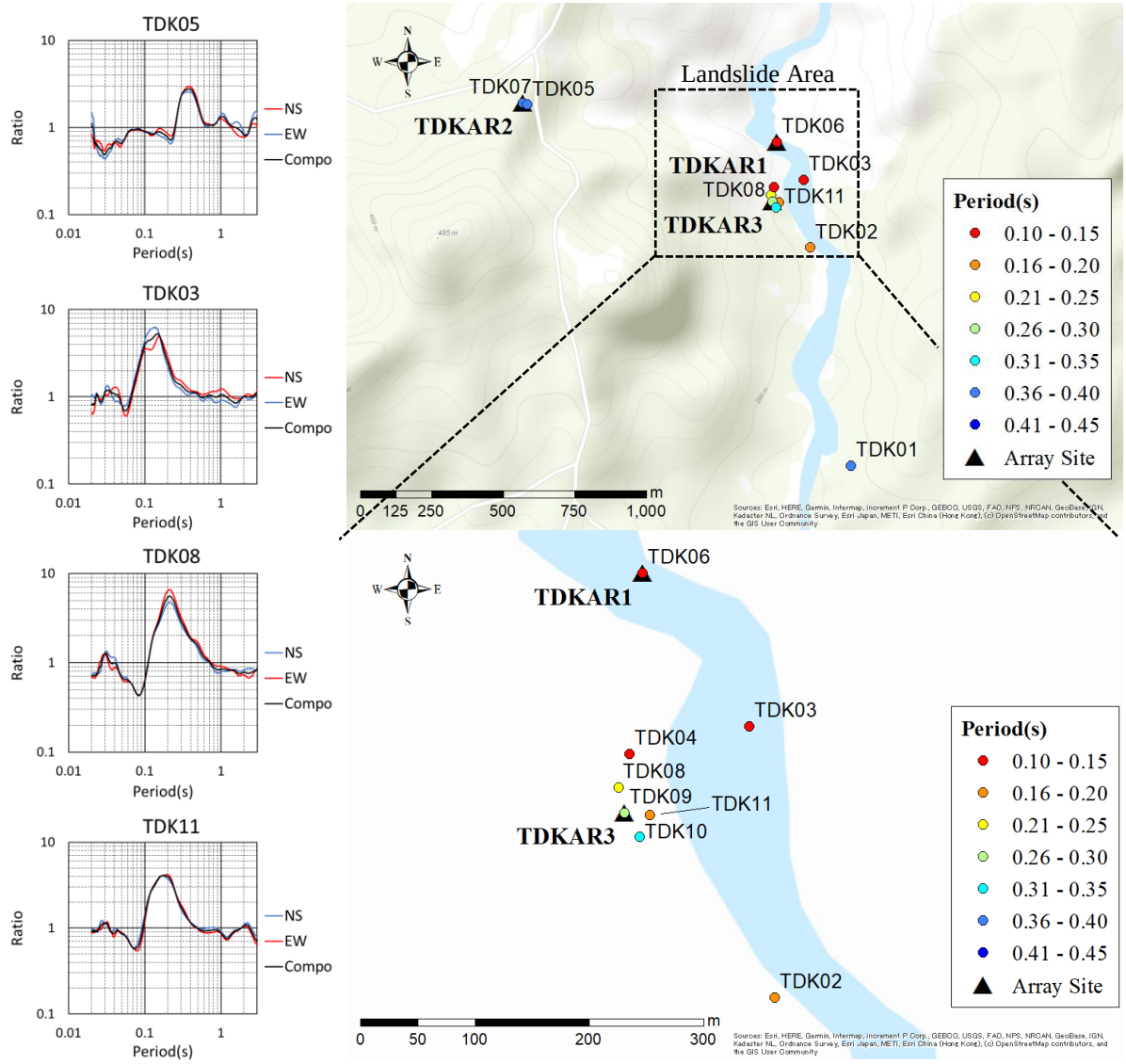

Fig.3 H/V spectral ratios and predominant period distribution

far from the landslide areas. And the periods are shorter at the other stations. Around TDK08 to 11 sites, the dominant period changes even in small areas, which may reflect the quick change of layer thickness deposited by the landslide. According to Fikri and Wang [1], the landslides occurred along several valleys eastward from TDKAR2 in Fig. 3. And the areas around TDK02, TDK03 and TDK06 are considered to be the top of landslide mass. In addition, the sedimentary conditions are expected to be very complicated because of confluence of several valleys. TDK01 is located on a flatland far from the collapse sites, and is assumed to be long-period due to the thick layers on the river terraces. Focusing on the spectral shape of microtremor H/Vs, we observed many single-peak H/Vs in the range of 0.1-0.4 seconds. The peak ratios of TDK05 and TDK07 are smaller than those of other stations. This suggests that the velocity contrast against the base layers is smaller than that at the area observed landslides.

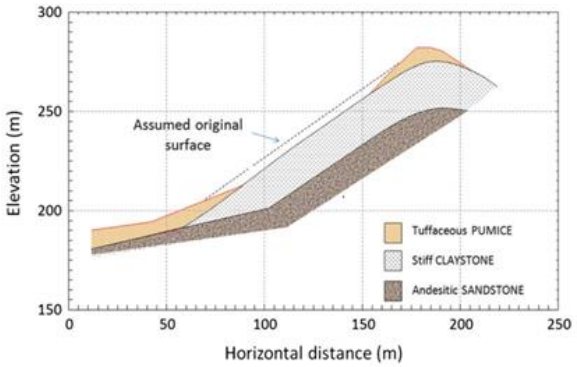

Fig.4 Interpretation of landslide sequences from geological surveys [3]

Table 1 Subsurface structures based on array observations

Site	Thickness (m)	density (t/m³)	V_P(m/s)	V_S(m/s)
TDKAR1	5	1.7	1430	200
	∞	2.1	2070	700
TDKAR2	6	1.6	1400	100
	10	1.8	1620	300
	∞	2.1	2070	700
TDKAR3	3	1.5	1350	50
	∞	2.1	2070	700

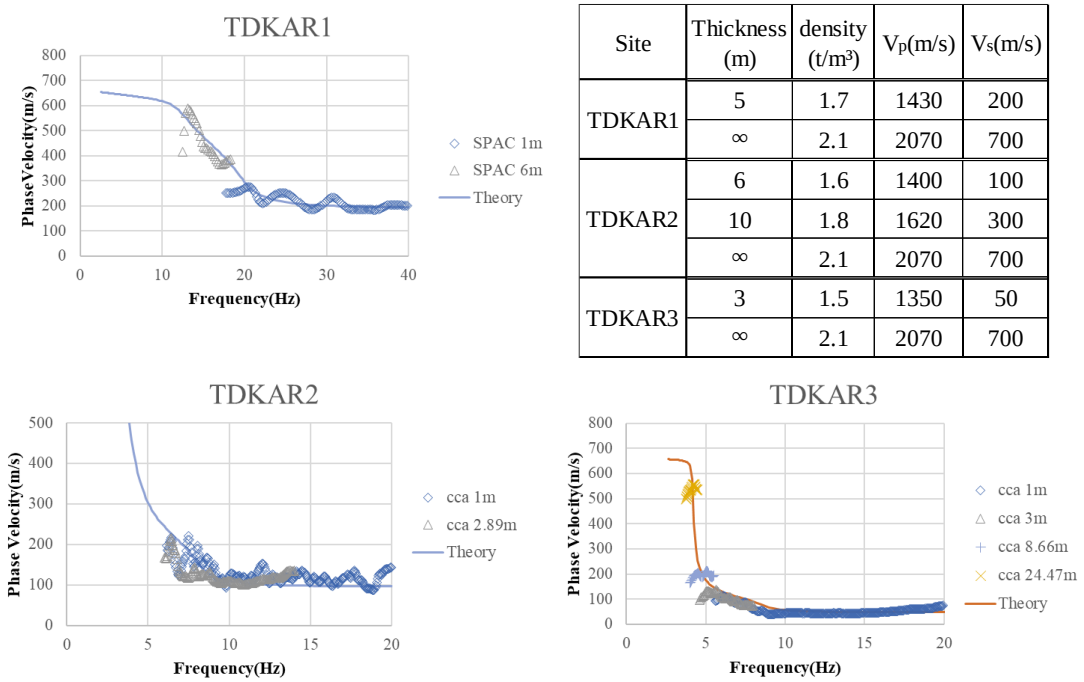

Fig. 5 Phase velocity dispersion curves

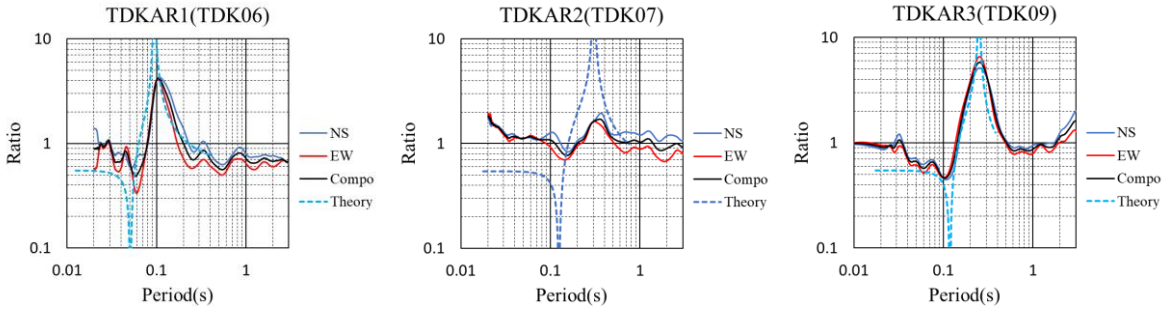

Fig.6 H/V spectral ratios at the center of the array observation sites

Estimation of Subsurface Structures

Table 1 shows that TDKAR1 and TDKAR3 at the mountainsides have several meters of low-velocity layers with S-wave velocities of 100 m/s or less on the surface, and their S-wave velocities are different even at very nearby stations. In TDKAR2, in addition to this low-velocity layers, an intermediate layer with S-wave velocity of 300 m/s was identified with 10 m thickness. Previous studies reported that the sliding surfaces are pumice layers with about 2 m thickness on hard clay layers containing gravel [3]. Soft surface layers with S-wave velocities of 200 m/s or less are estimated over the whole areas including the areas even without landslides from the subsurface structure models in this study. The layers are considered to be past landslide deposits including pumice layers. TDK05 and TDK07 (TDKAR2) have longer predominant periods than the other sites, because of the thick intermediate layer with S-wave velocity of 300 m/s. Therefore, the intermediate layers is considered to be sediments that did not collapsed due to the landslide in this area, and there is concern about the next coseismic landslides in the future.

CONCLUSIONS

This research investigated microtremor observations in the areas of landslide damaged due to the 2009 West Sumatra Earthquake in Tandikat. The relationship between subsurface structures and earthquake induced landslide damages were considered. Consequently, the following findings are noted.

The predominant periods of microtremor H/Vs are distributed in the range of 0.1-0.4 seconds, and the peak ratios of H/Vs tended to be small in the area

without landslide damage. They might reflect the difference in the velocity structures between the landslide deposits with sediments such as clay and pumice layers and bedrock layers. The subsurface structures without landslides are considered to be harder.

Surface layers with S-wave velocity 200 m/s or less were estimated overall the area derived from array observations. An intermediate layer with an S-wave velocity of 300 m/s was estimated at the site where no landslide occurred this time. We are afraid future coseismic landslides due to the deposit. We would like to mention the need for continuous monitoring of the deposits.

ACKNOWLEDGMENTS

We would like to express our gratitude to all individuals for their cooperation in the preparation of this paper. We appreciate to whom supported our investigations. This research was supported by JSPS Grants-in-Aid for Scientific Research (Grant-in-Aid for Scientific Research (B), PI: Yusuke Ono, Project No.: 18H01523).

REFERENCES

[1] Fikri F. and Wang F.: Investigation of the initiation mechanism of an earthquake- induced landslide during rainfall: a case study of the Tandikat landslide, West Sumatra, Indonesia, Geoenvironmental Disasters 2014 1:4., doi:10.1186/s40677-014-0004-3, 2014.

[2] USGS : M 7.6 - southern Sumatra, Indonesia, <https://earthquake.usgs.gov/earthquakes/eventpage/usp000h237 /impact>[Viewed on 1 June 2021]

[3] Wang F., Muhammad W. A. N., Zhang F. and Takeuchi A.: Tandikek and Malalak rapid and long runout landslides triggered by West Sumatra earthquake 2009 (M7. 6) in Indonesia, Journal of the Japan Landslide Society Vol.48, No.4, July, pp.215-220, 2011. (in Japanese with English abstract)

[4] Takahashi K., Tsuji T., Ikeda T., Nimiya H., Nagata Y. and Suemoto Y.: Underground structures associated with horizontal sliding at Uchinomaki hot springs, Kyushu, Japan, during the 2016 Kumamoto earthquake, Earth, Planets and Space volume 71, Article number: 87, 2019

[5] Konno K. and Ohmachi T.: A smoothing function suitable for estimation of amplification factor of the surface ground from microtremor and its application, Jornal of the Japan Society of Civil Engineers, No525/I-33, 1995, pp247-259. (in Japanese with English abstract).

[6] Aki K.: Space and time spectra of stationary stochastic waves, with special reference to microtremors, Bull.Earthq.Res.Inst., 35, pp415-456, 1957.

[7] Cho I., Tada T. and Shinozaki Y.: Centerless circular array method: Inferring phase velocities of Rayleigh waves in broad wavelength ranges using microtremor records, J. Geophys. Res., 111, B09315, 2006.

[8] Cho I., Tada T. and Shinozaki Y.: Possibility of microtremor array opened up by general theory: Release of analysis tool BIDO, Seismological Society of Japan Fall Meeting in 2009. (in Japanese)

[9] Ohmachi T., Konno K., Endou T. and Takumi Toshinawa T.: Refinement and application of an estimation procedure for site natural periods using microtremor, Jornal of the Japan Society of Civil Engineers, No489, 1994, pp251-260. (in Japanese with English abstract).

[10] Kitsunezaki C., Goto N., Kobayashi Y., Ikawa, T. Horike M., Saito T., Kurota T., Yamane K. and Okuzumi K.: Estimation of P- and S- wave velocities in deep soil deposits for evaluating ground vibrations in earthquake, Natural disaster science, 9-3, 1-17, 1990. (in Japanese with English abstract)

11th Int. Conf. on Geotechnique, Construction Materials & Environment, Kyoto, Japan, 3-5 November 2021, ISBN: 978-4-909106063 C3051

INVESTIGATION OF TUNNEL RESPONSE DUE TO THE EFFECT OF ADJACENT LOADED PILE ROW BY 3D SIMULATION ANALYSIS

Puckjira srikaewsai[1], Narunat Heama[1], Prateep Lueprasert[1], and Suchatvee Suwansawat[1]

[1]Department of Civil Engineering, School of Engineering, King Mongkut's Institute of Technology Ladkrabang, Bangkok, Thailand

ABSTRACT

Construction of tunnels for transportation, wastewater, or electricity, etc., in the major cities has flourishing. In the meantime, other infrastructures such as elevated trains, flyovers, are continually constructed for urbanization. Under a soft ground condition, they are supported by the pile foundations required pile rows which are possibly located along the existing tunnel. A common challenge encountered the loaded pile row of the new adjacent structures is inevitably induces soil stress changes and deformation of existing tunnels. Thus, an assessment of the impact of piles under loading on the integrity of the existing tunnels is essential. The three-dimensional finite element analyses (3D FEA) with two pile conditions were carried out. The tunnel responses in terms of the transversal deformation and additional forces are presented. The maximum response of those were shown at the monitoring section (center of pile row section), Meanwhile, the torsion deformations are maximum as the 10 m and 27 m away from monitoring section. For both cases of short and long pile, in transverse section, the existing tunnel show obvious asymmetrical characteristic, and the maximum values of additional forces were at θ of approximately $105^o - 120^o$ and 45^o. In longitudinal direction, the tunnel gradually rotates in range of 0 - 27 m. In addition, the pile length may not affect on tunnel responses in longitudinal direction.

Keywords: Transversal deformation, Torsional deformation, Tunnel response, 3D finite element analysis

INTRODUCTION

Construction of tunnels for transportation, wastewater, electricity, or communication cables, etc., is flourishing around the major cities in the world and has become focus of urban infrastructure development. In the meantime, other infrastructures such as elevated trains, flyovers, crossing bridges, are continually constructed for urbanization. Under a soft ground condition, they are supported by the pile foundations. A common challenge encountered is that the loaded piles of the new adjacent structures are inevitably close to the existing tunnels. Typically, the displacement of soil generated by pile settlement (under loading) induces additional deformation and change in structural forces to adjacent existing tunnel. Such changes may lead to the extremely negative effects on the integrity and serviceability of the tunnels. Thus, an assessment of tunnel response due to the impact of piles under loading is crucial.

The numerical analysis has become an increasingly popular and powerful analytical tool for modeling. A three-dimensional finite element analysis (3D-FEA) is often used to study in the tunneling works [1]-[5]. In analyses of existing tunnel response due to a new construction (i.e., deep excavation, tunneling), the internal forces, deformation monitored at different transverse section and the torsion behavior are determined [6], [7].

During the past few decades, many investigations of the influence of loaded pile on adjacent or underlying existing tunnels have been concerned. The parameters of adjacent loaded pile (i.e., pile diameter, pile length, pile spacing, and number of pile) were considered to only evaluate the tunnel transversal deformation and structural forces in tunnel lining in soft soil profile. The analysis results were used to suggest the mechanisms behind tunnel-soil-pile interaction and safe clearance between the tunnel and pile or pile row [8]-[10]. However, the tunnel responses due to adjacent loaded pile were presented in only one transverse section at monitoring section or center of the model. Their results at different transverse section and torsional deformation have been neglected.

Specifically, this research focuses on the effect of adjacent loaded pile row on existing tunnel. The simulations were carried out by 3D finite element (FE) models. There were two simulation models: 3D FE full models with short pile row and long pile row. For the pile row, there were simulated by embedded pile. The existing tunnels responses (e.g., the lining deformation and additional structural forces) are presented and discussed. Typically, the torsion behavior of the existing tunnel after pile row under loading is highlighted.

Table 1 Parameters for soil layer of 3D and 2D simulation models.

Layer	1	2	3	4	5	6	7	8
Soil type	Made Ground	Soft Clay	Medium Clay	1st Stiff Clay	1st Clayey Sand	2nd Stiff Clay	Hard Clay	2nd Clayey Sand
γ_{soil} (kN/m^3)	18	16.5	17.5	19.5	19	20	20	20
c' (kPa)	1	5	15	25	0	30	40	0
$\emptyset'$ (°)	25	27	27	28	33	28	28	36
Ψ' (°)	0	0	0	0	5	0	0	5
E_{oed}^{ref} (MPa)	45.6	5	20	60	80	60	60	80
E_{50}^{ref} (MPa)	45.6	5	20	60	80	60	60	80
E_{ur}^{ref} (MPa)	136.8	15	100	180	240	180	180	240
v_{ur}	0.2	0.2	0.2	0.2	0.2	0.2	0.2	0.2
m	1	1	1	1	0.5	1	1	0.5
K_0^{nc}	0.58	0.6	0.6	0.5	0.55	0.5	0.5	0.5
R_f	0.9	0.9	0.9	0.9	0.9	0.9	0.9	0.9
G_{max} (MPa)	-	15	45	80	200	80	130	240
$\gamma_{0.7}$	-	0.08	0.11	0.12	0.014	0.12	0.15	0.02
Analysis type	Drained	Undrained	Undrained	Undrained	Undrained	Undrained	Undrained	Undrained

Table 2 Material properties of the 3D and 2D FE simulation models.

	Young's modulus (E, kN/m^2)	Poisson's ratio (v)	Unit weight (γ, kN/m^3)
Tunnel lining	31 x 10^6	0.20	24
Loaded pile	31 x 10^6	0.20	24
EPB shield	210 x 10^6	0.28	78
Grouting layer	1 x 10^6	0.30	21

FINITE ELEMENT SIMULATION

The continuous tunnel lining and embedded pile row were modeled by Plaxis 3D software version 2018. In engineering practice, the tunnel is constructed by segmental lining. However, in case of the tunnel where the location is shallow, the modeling of continuous lining is sufficient for consideration of the structural forces in tunnel lining [11]. The pile row was modeled by embedded pile row which can reduce the complexity of a high number of pile models [12]. The wished-in-place bored piles are modeled on one side of tunnel. The total displacement was reset to zero, and thus only the tunnel deformation attributable to adjacent loaded pile row was investigated. The working load is 40% of the ultimate pile capacity determined from α-method [13]. The pile row consisted of 13 piles to eliminate the edge effect [14].

Characteristics of Model

In Fig. 1, the lining thickness, T, of 0.3 m, outer diameter, D_{tunnel}, of 6.3 m, and the center of the tunnel below the ground surface, Z_{tunnel}, of 20.5 m are fixed throughout this study. The diameter of bore pile, D_{pile}, of 1.0 m, and clearance, C, of 0.5 m are also fixed. The pile spacing, S, of 3 m, positions of pile tips, Z_{pile}, are at the 17.35 m and 57.0 m below the ground surface, representing the short pile and long pile conditions for determining the existing tunnel response, respectively.

The soil profile at Sukhumvit station, one of the MRTA Blue Line Project's stations (section CS-8C of the project), was chosen to simulate and analyze in the study. Figure 2 depicts the geological conditions, which include (1) Made Ground or fill material at 0–2.5 m, (2) Soft Clays at 2.5–12 m, (3) Medium Clays at 12–14 m, (4) 1st Stiff Clays at 14–20 m, (5) A thin seam of 1st Clayey Sand is found at 20-21.5 m, (6) 2nd Stiff Clays at 21.5-26.5 m, (7) Hard Clays at 26.5-54 m, and (8) 2nd Clayey Sand at 54–80 m. The groundwater condition is piezometric drawdown due to the over pumping of the ground water in the past as shown in Fig. 2.

Fig. 1 Geometric parameters in the modeling

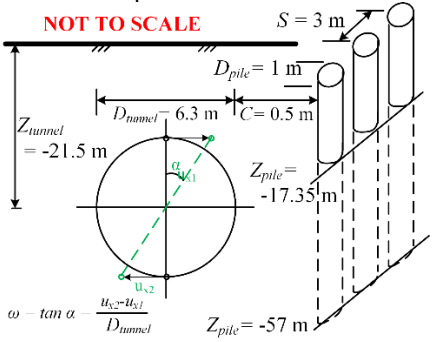

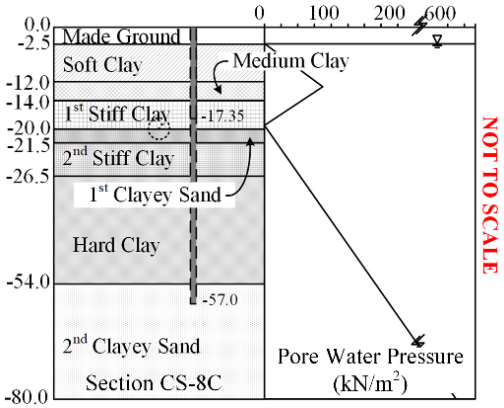

Fig. 2 Soil profile and pore water pressure

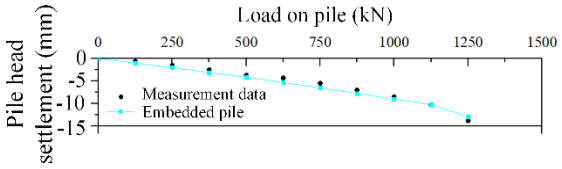

Fig. 3 Loaded single pile simulation

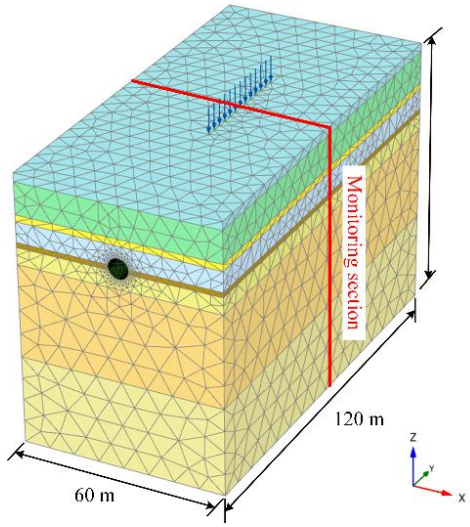

Fig. 4 Boundary and FE mesh

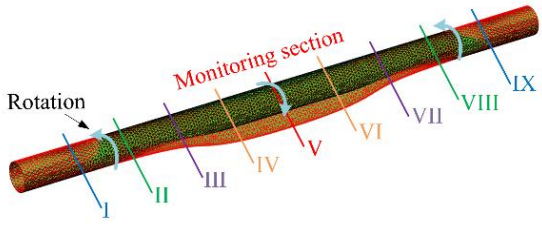

Fig. 5 Torsion behavior of tunnel due to adjacent loaded pile row (pile length of 17.35 m)

Model Properties

In the 3D simulation models, the hardening soil model with small-strain stiffness (HSS) was adopted to model all layers of soils except the Made Ground Layer which is modeled by Hardening Soil model (HSM). Table 1 presents the parameters of soil profile of the capital Bangkok. The properties of the Bangkok subsoil were adopted from previous study [15], [16]. The tunnel lining, EPB shield, grouting layer and bored pile were modeled as a linear elastic material. The material parameters listed in Table 2 were used in the study. The interface friction value (R_{inter}) between the structural elements (EPB, tunnel lining, or bored piles), and the surrounding soil was chosen to be 0.9 as suggested in previous research [9], [17].

The soil layer and grouting layer were discretized into the volume elements or the 10-node tetrahedral elements. The 6-node triangular plate element was used to model the tunnel lining and EPB shield. The embedded pile consists of beam elements which can be 3-node line elements. For the embedded pile, the input parameters consist of diameter (D), the unit weight (γ) and young's modulus (E). In the model, the unit weight of embedded pile ($\gamma_{embedded}$) was subtracted by unit weight of soil (γ_{soil}) [12].

Model Validation

The static pile load test of a 23-storey residential complex at or near the CS-8C section (It is located approximately 500 m away) was used to validates against the computed single-pile head settlements from FE model.

Figure 3 shows comparing between the static pile load test and simulated pile head settlements, given the pile diameter of 1 m and pile length of 57.0 m. The results were generally agreeable. This implies that the properties of soil and pile are reasonable to subsequently evaluate the effect on existing tunnel due to adjacent loaded pile row for this study. Note that the simulation of 17.35 m pile length (short pile) was not compared due to unavailability of field static pile load test data of the short pile.

3D Simulation Model

From a previous study, the sufficient boundary of 3D numerical model with TBM tunneling suggested by Mroueh and Shahrour [18], was the advancement of $4.0D_{tunnel}$ behind and ahead of the face of tunnel excavation and lateral distance from the edge of the tunnel of $3.5D_{tunnel}$. Thus, the lateral distance from a tunnel edge of $4.25D_{tunnel}$, and the advancement of $5.5D_{tunnel}$ behind and ahead of the monitoring section in this study as shown in Fig. 4, are enough to fully model the 3D tunneling problem.

On the lateral boundaries of the 3D model, the lateral displacements in the x- and y-directions were fixed, while vertical displacement in the z-direction was permitted. The horizontal and vertical displacements were both fixed at the bottom boundary. For a good level of accuracy result, finer meshes are generated in zone around tunnel and pile. The total number of elements was approximately 260,000, and the total number of nodes was approximately 320,000. The loaded pile row was located on one side of the existing tunnel.

SIMULATION RESULTS AND DISCUSSION

Transversal Deformation

In this study, the tunnel deformations in transverse direction were investigated along the longitudinal direction of the existing tunnel as shown in Fig. 5. This figure presents the tunnel deformation. in transverse direction with 12 m of horizontal distance between cross-sections (section I to section IX). The reference of tunnel lining is represented by bold line, the tunnel deformation along longitudinal direction with a magnification ratio of 1:1000. Note that the deformation after tunneling is excluded.

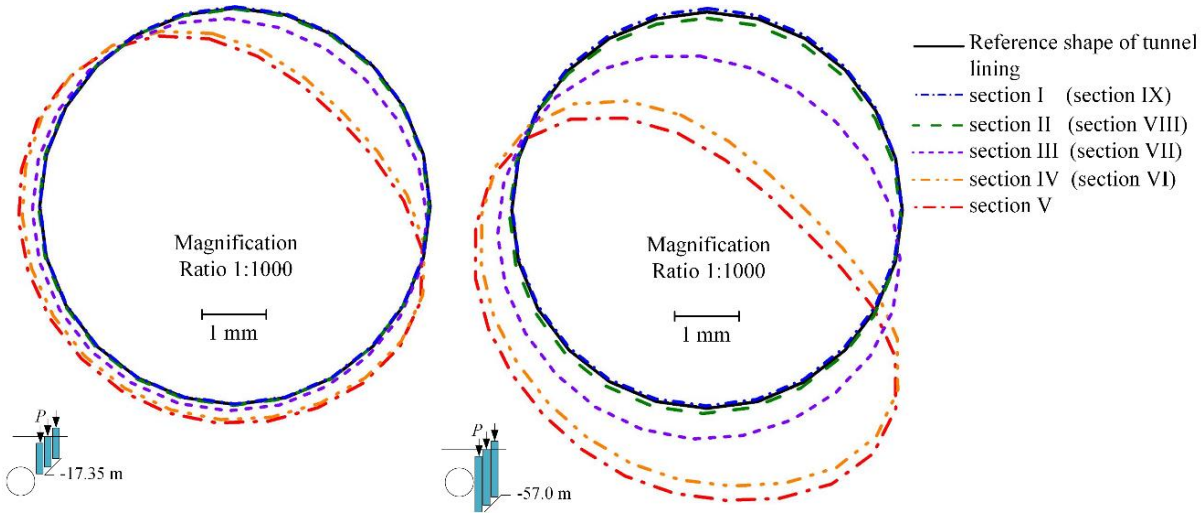

(a) Pile length of 17.35 m (short pile) (b) Pile length of 57.0 m (long pile)

Fig. 6 Simulated tunnel deformation as a result of adjacent loaded pile row

It can be seen that, for both short and long pile conditions, the lining at the section III to section VII distorts into a kidney or ellipse shape inclined to the side closer to the pile. The tunnel deformation slightly changes at the sections I, II, VIII and IX as shown in Fig. 6, it is attributed to the different degrees of adjacent loaded pile row effect. With the distance considered from the monitoring section (section V), the transversal deformations of the tunnel lining decrease with increasing distance.

Considering the pile conditions, the effect of long pile row is larger than short pile row. This is similar to the previous study [9]. However, it is worthy noted that, with the dual influences of adjacent loaded pile row, the tunnel deformation slightly changes at the section II and VIII in both short and long pile cases. The pile length may not affect on transversal deformation in longitudinal direction.

Torsion Behavior

Figure 7 shows the distribution of rotation indexed by ω of the existing tunnel along the longitudinal direction due to nearby loaded pile row in both short and long pile condition. In order to identify the rotation behavior of the tunnel, a qualitative evaluation method is proposed as follows [6]:

$$\omega = \tan\alpha = \frac{u_{x2} - u_{x1}}{D_{tunnel}} \quad (1)$$

where, ω is rotation index. α is the rotation angle of the tunnel. u_{x1} and u_{x2} are the horizontal displacement of the crown and invert of the tunnel, respectively (see Fig. 1). D_{tunnel} is the diameter of the tunnel.

The ω is assumed to be positive when tunnel rotates anticlockwise and negative when it rotates clockwise. In short pile condition, the tunnel rotates anticlockwise at the monitoring section. The ω slightly increases as the distance away from monitoring section in range of 0 – 12 m. Then, the ω gradually decrease in range of 12 – 24 m. The tunnel gradually turned from anticlockwise rotation to clockwise rotation with increase of the distance away from 24 m. The maximum and minimum of ω located about 10 m and 27 m away from the monitoring section, respectively.

In long pile case, the tunnel rotates clockwise along the longitudinal direction. The ω increase and gradually decrease in range of 0 - 14 m and 14 – 28 m. Then ω increases with increasing distance. The minimum of ω located about 27 m. In this research, the rotation of the existing tunnels caused by the nearby loaded pile in ranges from 0.07×10^{-4} to -0.02×10^{-4} and -0.01×10^{-4} to -0.07×10^{-4} for short pile and long pile cases, respectively. These results reveal that the maximum or minimum of ω are not located at the monitoring section.

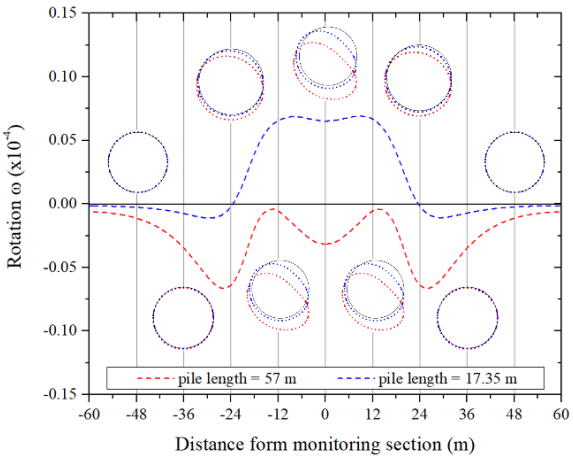

Fig. 7 Rotation of existing tunnel along longitudinal direction

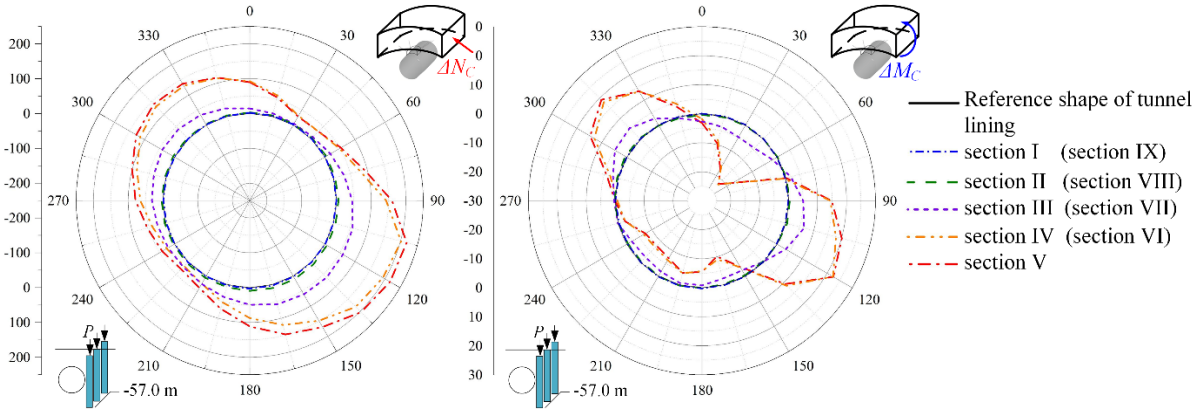

(a) bending moment: pile length of 57 m (b) axial force: pile length of 57 m

Fig. 8 additional lining forces in circumferential direction

In some tunnel works, structural forces in tunnel lining are the main concern, and torsional deformation may be neglected [19]. However, the ω due to adjacent loaded pile row may also experience large torsional deformation, which may lead to track distortion and even pose a risk to safe operation of train. Therefore, the effect of adjacent loaded pile row on existing tunnel, not only be careful to the structural forces in tunnel lining but also the torsional deformation of tunnel should be concern.

Additional Forces in Tunnel Lining

Figure 8 shows the additional bending moment (ΔM) and axial force (ΔN) in circumferential direction due to adjacent loaded pile row, given pile length of 57 m. The tunnel crown is an origin ($\theta = 0^o$). In the figure, the ΔM and ΔN were obtained at different cross-sections (section I to section IX) as the same the section assigned to monitoring the tunnel deformation. The calculation of the additional bending moment and axial force are shown in Eq. (2) and (3). When M_1, N_2 are structural forces in tunnel lining before pile loading and M_2, N_2 are structural forces after pile loading. In this research, a positive value of ΔM and ΔN represents an increasing value, whereas a negative value represents a decreasing value.

$$\Delta M = M_2 - M_1 \quad (2)$$

$$\Delta N = N_2 - N_1 \quad (3)$$

The ΔM increases in the range of $\theta = 285^o$ to 0^o and 70^o to 140^o and decrease in the range of $\theta = 0^o$ to 70^o and 140^o to 285^o for both short and long piles. The maximum positive and negative ΔM were at θ of approximately 105^o and 45^o for the short pile and approximately 120^o and 45^o for the long pile as shown in Figs. 8(a). By comparison, the ΔM obtained from short pile case were similar tendencies to long pile case, with smaller magnitude. It is seen from the figure that the ΔM decreases when distance considered from the monitoring section (section V) increases. In the sections I, II, VIII and IX, the ΔM slightly changes or remains almost constant.

Figure 8(b) illustrate the ΔN in circumferential direction, given pile length of 57 m. The ΔN only increases with maximum value at θ of approximately 105^o for both short and long piles. For comparison in both short and long pile conditions, ΔN are similar to ΔM . Their results closely resembled the tunnel deformation in longitudinal direction. This supports that the effect on existing tunnel in longitudinal direction may not depend on pile length.

CONCLUSIONS

This study investigated the effect on existing tunnel due to adjacent loaded pile row in terms of tunnel deformation, torsional deformation, and additional lining force (bending moment and axial force). The simulations were carried out by Plaxis 3D software, with 13 piles within the row. The simulation results were discussed. The pile diameter was 1 m, and the pile lengths were 17.35 m (short pile) and 57.0 m (long pile), respectively. The pile spacing (S) and edge-to-edge clearance (C) were fixed at 3 m and 0.5 m, respectively. The conclusions are as follows:

1. The adjacent loaded pile row leads to tunnel responses (deformation and variation of internal forces) in transverse direction accordingly. The tunnel deformation and additional forces (bending moment and axial force) become significant at the center of pile row. Meanwhile, the torsion deformations are maximum as the 10 ($\approx 1.5D_{tunnel}$) m and 27 m ($\approx 4.5D_{tunnel}$) away from center of pile row.
2. The unrecoverable torsional deformation of the tunnel was induced by loaded pile row, which is distinct from the perpendicular case. For both short and long pile conditions, the tunnel gradually rotates in range of 0 - 27 m. ($\approx 0D_{tunnel}$ - $4.5D_{tunnel}$)

3. The tunnel deformation and additional forces in tunnel lining in transverse sections slightly changes or remains almost constant as the distance away from 36 m ($\approx 6D_{tunnel}$) in both cases of short and long pile.

This study, the pile diameter (D_{pile}) and pile spacing (S) were fixed and tunnel lining was simulated based on continuous lining. The future work considering the effects of joints and varying D_{pile} and S should be done to extent the scope of study.

ACKNOWLEDGMENTS

The authors wish to express their thankfulness to Faculty of Engineering, King Mongkut's Institute of Technology Ladkrabang and TRF Basic Research for the financial support through Grant KREF016317 and Contract PHD60I0032.

REFERENCES

[1] Dang V. K., Dias D., Do N. A., and Vo T. H., Impact of blasting at tunnel face on an existing adjacent tunnel, International Journal of GEOMATE, Vol. 15, Issue 47, 2018, pp.22-37.

[2] Shiau J. and Sams M., Estimation of tunneling induced ground settlement using pressure relaxation method, International Journal of GEOMATE, Vol. 13, Issue 39, 2017, pp.132-139.

[3] Chaiyasarn K., Sharma M., Ali L., Khan W., and Poovarodom N., Crack detection in historical structures based on convolutional neural network, International Journal of GEOMATE, Vol. 15, Issue 51, 2018, pp.240-251.

[4] Lueprasert P., Jonpradist P., and Suwansawat S., Tunneling simulation in soft ground using shell elements and grouting layer, International Journal of GEOMATE, Vol. 12, Issue 31, 2017, pp.51-57.

[5] Zheng G., Pan J., Li Y., Cheng X., Tan F., Du Y., and Li, X. (2020), Deformation and Protection of Existing Tunnels at an Oblique Intersection Angle to an Excavation",International Journal of Geomechanics, 20, 2020.

[6] Lin X. T., Chen R. P., Wu H. N., and Cheng H. Z., Deformation behaviors of existing tunnels caused by shield tunneling undercrossing with oblique angle, Tunnelling Underground Space Technol. 89, 2019, pp.78–90.

[7] Zheng G., Pan J., Li Y., Cheng X., and Li X., Deformation and protection of existing tunnels at an oblique intersection angle to an excavation, International Journal of Geomechanics, Vol. 20, No. 8, 2020.

[8] Heama N., Jongpradist P., Lueprasert P., and Suwansawat S., Investigation on tunnel responses due to adjacent loaded pile by 3D finite element analysis, International Journal of GEOMATE, Vol. 12, Issue 31, 2017, pp.63-70.

[9] Lueprasert P., Jongpradist P., Jongpradist P., and Suwansawat S., Numerical investigation of tunnel deformation due to adjacent loaded pile and pile-soil-tunnel interaction, Tunnelling and Underground Space Technology, 70, 2017, pp.166-181.

[10] Nematollahi M. and Dias D., Three-dimensional numerical simulation of pile-twin tunnels interaction – Case of the Shiraz subway line, Tunnelling and Underground Space Technology, 86, 2019, pp.75-88.

[11] Michael K., Dimitris L., Ioannis V., and Petros, F., Development of a 3D finite element model for shield EPB tunnelling, Tunnelling and Underground Space Technology, 65, 2017, pp.22-34.

[12] Tschuchnigg F. and Schweiger H. F. (2015), The embedded pile concept - Verification of an efficient tool for modelling complex deep foundations, Computers and Geotechnics, 63, 2015, pp.244–254.

[13] Skempton A. W., Cast In-Situ Bored Piles in London Clay, Géotechnique, 9, 1959, pp.153–173.

[14] Heama N., Jongpradist P., Lueprasert P., and Suwansawat S., Investigation on pile-soil-tunnel interaction due to adjacent loaded pile row by 3D FEM, The International Conference on Engineering, Applied Sciences and Technology (ICEAST), 192, 2018, pp.792-795.

[15] Likitlersuang S., Teachavorasinskun S., Surarak C., Oh E., and Balasubramaniam A., Small strain stiffness and stiffness degradation curve of Bangkok Clays, Soils and Foundations, 53, 2013, pp.498–509.

[16] Rukdeechuai T., Jongpradist P., Wonglert A., and Kaewsri T., Influence of Soil Models on Numerical Simulation of Geotechnical works in Bangkok subsoil, Journal of Research and Development, 20, 2009.

[17] Mathew G. V. and Lehane B. M., Numerical back-analyses of greenfield settlement during tunnel boring, Canadian Geotechnical Journal, 50, 2013, pp.145–152.

[18] Mroueh H. and Shahrour I., Three-dimensional finite element analysis of the interaction between tunneling and pile foundations, International Journal for Numerical and Analytical Methods in Geomechanic, 2002.

[19] Chen H. H., Li J. P., and Li L., Performance of a zoned excavation by bottom-up technique in Shanghai soft soils, Journal of Geotechnical and Geoenvironmental Engineering, Vol. 144, Issue)11(, 2018.

11th Int. Conf. on Geotechnique, Construction Materials & Environment,
Kyoto, Japan, 3-5 November 2021, ISBN: 978-4-909106063 C3051

VERTICAL LOADING TESTS ON LOCAL SCOURED SPREAD FOUNDATION ON ALUMINUM RODS MODEL GROUND

Yuna Sasaki[1] and Hidetoshi Nishioka[2]

[1, 2]Faculty of Science and Engineering, Chuo University, Japan

ABSTRACT

In recent years, the damage to bridge foundations caused by heavy rainfall and scouring has increased. In some cases, the entire bridge is carried away, whereas, in others, damage mainly occurs in the foundation, such as settlement and inclination. In the latter cases, it is expected that the damaged bridge is shortly reused after minor repairs are performed only on the superstructure while retaining the residual displacement of the foundation. However, it is difficult to predict whether a foundation with residual displacement possesses the bearing capacity needed to resume emergency use of the damaged bridge. This study focuses on the residual bearing capacity of a shallow foundation after scouring. We performed vertical loading tests on scoured shallow foundations on an aluminum rod ground model to clarify the mechanism. The scouring of the ground was simulated by manually pulling out the aluminum rods. The residual displacement induced by the dead load was measured, and the loading was continued until the residual bearing capacity became clear. We systematically evaluated the effects of scouring volume and shape on the behavior of the foundation. It was found that the residual displacement increased with scouring, but the residual bearing capacity did not necessarily decrease. These findings suggest the possibility of expanding the conditions for the early resumption of damaged foundations and will be helpful for future emergency disaster operations of damaged river bridges.

Keywords: Bearing Capacity, Scour, Ground Spring Constant, Residual Performance, Image Analysis

INTRODUCTION

Background and objective of study

Scouring is caused by the erosive action of flowing water that removes the soil around hydraulic structures, such as bridge piers. This phenomenon often occurs with heavy rainfall and typhoons. The number of scouring disasters has been increasing in recent years owing to global warming. Half of the bridge scour cases are classified as medium-scale scours, which mainly damage foundations, such as settlements and inclinations without significant damage, for example, the outflow of girders [1].

Figure 1 shows an example of the medium-scale damage, the Hino Bridge across the Tama River, whose foundation has settled, owing to scours produced by the typhoon in Eastern Japan in October 2019. The road was closed because of settlement, and the transportation network was interrupted. The damaged pier was not reused because its long-term safety could not be guaranteed. Instead, the damaged pier and two girders were removed, and a new girder double the span length was fabricated and erected. It took seven months for the bridge to be reopened.

In this case, the bridge is partially rebuilt. However, it is unrealistic to apply the rebuilding operation to all damaged bridges in medium-scale scouring cases. In some cases, the bridge is expected to be used after immediate repair operations, even when its foundation is damaged, such as through settlements and inclinations. For early resume operations with the reuse of damaged piers, these resistances must be evaluated. However, most previous studies on bridge scouring have focused on scouring, and a few studies have focused on the bearing capacity of scoured foundations. Therefore, it is unclear whether residual resistance with residual displacement retains the bearing capacity required for reuse.

In this study, we performed vertical loading tests on a scoured foundation on an aluminum rod ground model to reveal the mechanism of the residual bearing capacity of a scoured foundation. The target structure was limited to a river bridge with a shallow foundation, and the target conditions were limited to local scours. By varying the local scour depth, we considered the expected condition in which the residual bearing capacity required for resuming operations will exist. We also performed an image

Fig. 1 Example of medium-scale damage

analysis to clarify the mechanism.

The findings of this study suggest the possibility of expanding the conditions for the early resumption of bridges with damaged foundations and is valuable for future emergency disaster operations of damaged river bridges. Finally, these findings will improve the resilience of transportation networks.

Performance of residual bearing capacity of scoured foundation

This study focused on the residual bearing capacity of scoured foundations based on the following concept (Fig. 2) [2] [3].

The load–settlement curve starting from the origin represents the performance of the bearing capacity before the disaster. After a scoured disaster, the performance changes, and the curves can have a wide variety of shapes. We believe that the performance of the residual bearing capacity can be determined by identifying the shape of the curve.

After the disaster, we can easily determine the residual settlement and dead load as a single point (Fig. 2). However, it is difficult to predict the following load–settlement curve from this single point; thus, it is almost impossible to determine whether the bridge pier can be repaired.

If the damaged bridge is reused, emergency restoration, such as jacking up and additional repair concrete, will be performed. Therefore, safety confirmation loading tests, such as static loading tests and slow train passing tests, were conducted in this study. In addition, the settlement was measured to obtain information as a second point in the load–settlement curve.

Through this process, it is possible to limit the candidates for the load–settlement curve of the damaged foundation. The performance of the residual bearing capacity after a disaster can then be evaluated.

VERTICAL LOADING TESTS ON ALUMINUM RODS

Experimental devices

The experimental devices used for the tests are shown in Figs. 3 and 4. Vertical loading tests were performed on the aluminum rod ground model produced by mixing two types of aluminum rods with diameters of 1.6 and 3.0 mm and layered with 60% and 40% weight content, respectively. The ground model was generated in an experimental container with a width of 600 mm and a depth of 220 mm.

Compaction was performed for each spreading depth of 50 mm using a hand vibrator machine. The weight per unit volume γ and angle of repose ϕ_r of the ground model were measured using a measuring box (width = 250 mm; depth = 50 mm). Here, the angle between the measuring box tilt and the aluminum rod

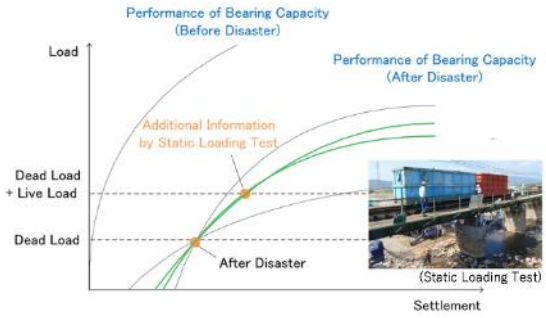

Fig. 2 Concept of change in performance of bearing capacity by scouring disaster

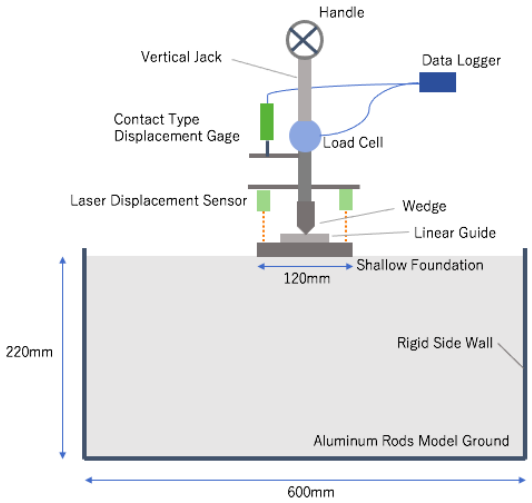

Fig. 3 Outline of experimental devices

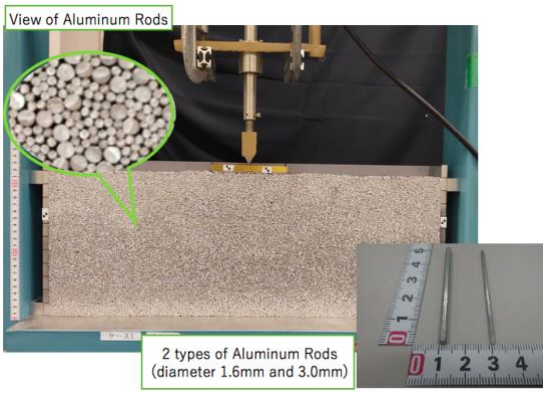

Fig. 4 Aluminum rod ground model

collapse (Fig. 5) is defined as the angle of repose ϕ_r. After five tests, average values of γ = 21.3 kN/m^3 and ϕ_r = 29° were obtained.

A rigid plate with a thickness of 10 mm, width of 120 mm, and length of 50 mm was used as the shallow foundation model. A linear guide was installed on the top surface of the foundation to enable the foundation to rotate and slide horizontally. It was loaded

Fig. 5 Measurement of angle of repose

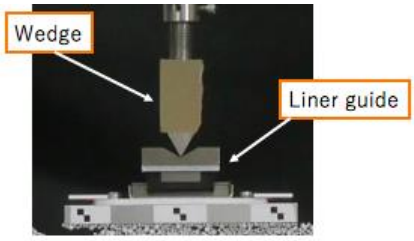

Fig. 6 Connection structure between load jack and foundation model

vertically using a wedge at the point of the vertical displacement-controlled jack (Fig. 6).

The load cell was set between the wedge and the vertical jack to measure the vertical load. In this experiment, the actual load resistance was the total load value output by the data logger and the self-weight of the foundation (3.9 N) because the foundation was not connected to the vertical jack. The displacement of the jack was measured using a contact-type displacement transducer. The angle of inclination of the foundation was obtained by measuring the displacement of both sides of the foundation using laser displacement transducers.

Loading procedure

After the aluminum rod model ground was produced, the foundation was placed on the ground. At this time, the values of the load and settlement were zero. First, a 22.5 N load was applied to simulate a dead load. This condition represents the state of the foundation before the scouring damage occurs. This value (22.5 N) was obtained by dividing the ultimate bearing capacity obtained in the previous experiment without scouring by a safety factor of 3.

During the tests, loading and unloading were repeatedly applied several times until the displacement of the jack exceeded 10% of the foundation width. The loading speed in each settlement phase was controlled to 0.25 mm/min in 0–3 mm, 0.5 mm/min in 3–6 mm, and 1 mm/min in more than 6 mm. Figure 7 shows the variations in the settlement and load with time for vertical loading

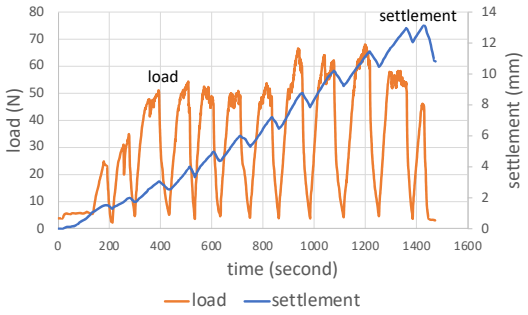

Fig. 7 Time-history curves of load and displacement of model before scouring

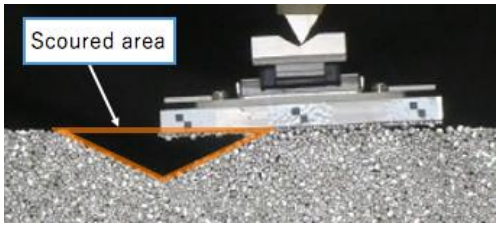

Fig. 8 Modeling of Local scour by removing aluminum rods

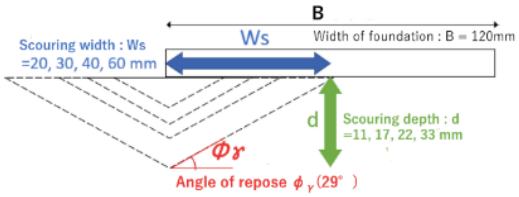

Fig. 9 Test cases of local scour area

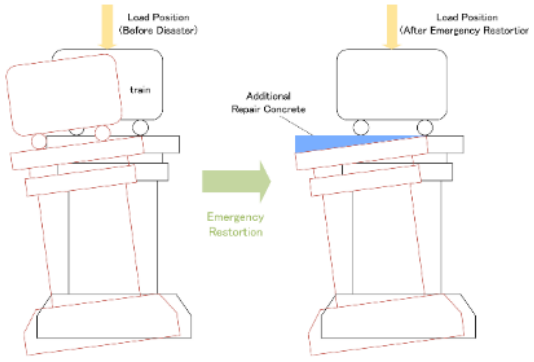

Fig. 10 Modeling of loading position after emergency restoration

tests performed for the model before scouring.

Modeling of local scour

Aluminum rods in the local scour area were removed to simulate a situation in which local scouring occurred just below the foundation on the

upstream side (Fig. 8). The shape of the local area was an isosceles triangle with an angle of repose (29°) and the depth of the local scour. The loading tests were performed for four cases by varying the depth of the local scour, d = 11, 17, 22, and 33 mm (Fig. 9).

While the displacement of the vertical jack was maintained, aluminum rods were removed to simulate local scouring. During the removal of the aluminum rods, most of the reaction force was lost because the position of the vertical jack was fixed. Subsequently, the displacement of the vertical jack increased again, and the load–settlement curve after the disaster was plotted.

In practice, the dead load is eccentric because the foundation is inclined after a local scour appears. However, this eccentricity was not modeled in our study because of the following reasons. In emergency restorations, the girders are generally jacked up and moved horizontally to return to their original position and then fixed by adding repair concrete (Fig. 10). In other words, the loading position of the live load before and after the disaster remained unchanged.

EXPERIMENTAL RESULTS

Load–settlement curves

The load–settlement curves obtained from the tests are shown in Fig. 11. For d = 33 mm, the curve could not be plotted because the foundation could not carry its self-weight and moved by rotating from its initial position during the aluminum rod removal. In the other three cases, each curve showed a slight gradient during the initial loading phase. However, from the middle phase of loading, the curve warped up, indicating a high load value. This increase occurred when all foundation base widths reached the ground after the foundation was inclined along the slope owing to local scouring.

Residual settlement and residual inclination

In Fig. 12, the horizontal axis indicates the local scour depth, and the vertical axis represents the settlement and inclination when the load reaches the dead load after local scouring. These settlements and inclinations correspond to the residual settlement and inclination that occur in actual situations after a foundation is damaged by disasters because the settlement and inclination increase with local scouring under dead loads. The graphs indicated that the residual settlement and inclination increased with the local scour depth.

Inclination of foundation

Figure 13 shows the changes in the inclination of the foundation with an increasing settlement. The plots （●）in the graph represent the state when

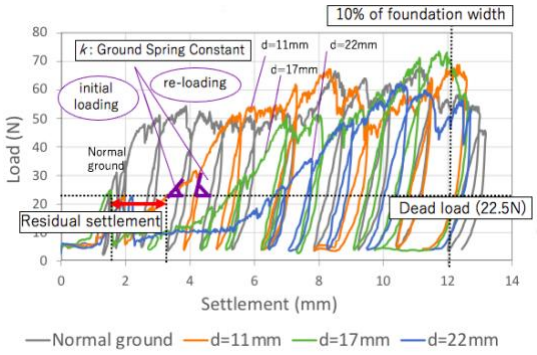

Fig. 11 Load–settlement curves

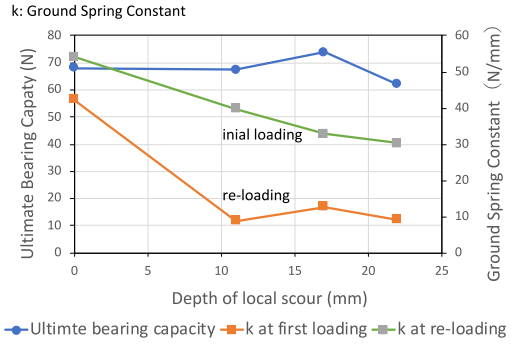

Fig. 12 Changes in residual settlement and inclination with depth of local scour

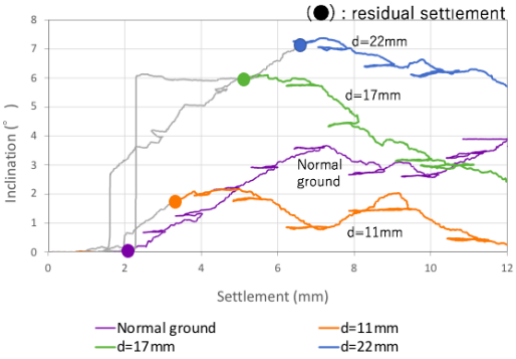

Fig. 13 Changes in inclination of foundation with settlement

loaded with 22.5 N after removing the aluminum rods. These graphs indicate the residual settlement caused by the dead load immediately after the scouring disaster. In each scouring case, the inclination of the foundation under the dead load decreased gradually, and it decreased by at least 1° after the test when the settlement reached 12 mm. It was assumed in this study that repair would be conducted to return the loading position (which moved slightly owing to scouring) to the initial position (Fig. 10). The inclination of the foundation returned to the stable direction, suggesting that there is minimal concern

about exceeding the limit state of inclination when the foundation is reused with appropriate repair (Fig. 13).

Ultimate bearing capacity and ground spring constant

In Figure 14, the horizontal axis indicates the local scour depth, and the left vertical axis shows the ultimate bearing capacity. In this study, the ultimate bearing capacity was defined as the maximum value of the load before the settlement reached 12 mm, which was 10% of the foundation width. The ultimate bearing capacity maintained a steady value (Fig. 14), which was almost the same as that for normal ground loading.

The right vertical axis in Figure 14 represents the ground spring constant *k*, defined as the slope of the load–settlement curve from the dead load (22.5 N) to 1.2 × the dead load (27.5 N). This load increment was simulated as a live load. We calculated two types of ground spring constants (Fig. 11): the ground spring constants at the initial loading immediately after local scouring and during reloading. On the one hand, the ground spring constant at the initial loading can be used to calculate the increase in settlement during restoration work, such as the jack-up, adding repair concrete, and static loading tests. On the other hand, the ground spring constant at reloading can be used to evaluate the behavior under live load after the resumption of service.

Both ground spring constants tended to decrease with local scour depth (Fig. 14). Although the ground spring constant at the initial loading decreased significantly, the incremental settlement at the restoration work was smaller than the overall residual settlement owing to the dead load only (Fig. 11). This increment can be handled easily through restoration work. Moreover, the ground spring constant at reloading had a higher value than the ground spring constant at the initial loading in all cases. The effect of the local scour depth on the ground spring constant at reloading was less significant than that at initial loading.

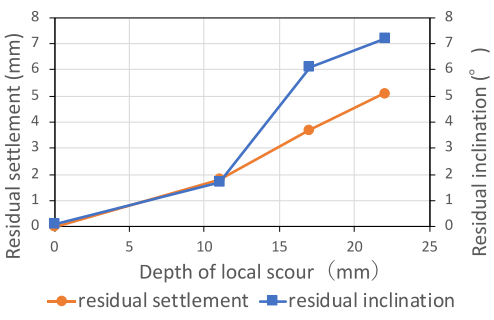

Fig. 14 Changes in ultimate bearing capacity and ground spring constant with local scour depth

In summary, in cases where the foundation does not collapse under the dead load, it is likely for its ultimate bearing capacity to not decrease even if the it is damaged by local scouring. Therefore, the foundation of the bridge might be safe, with there also being the possibility of its reuse. In addition, the decrease in the ground spring constant at reloading is expected to remain within the acceptable range after resumption. However, the sum of the residual deformation and increment at initial loading must be less than the value of the maximum limit that the restoration work can accommodate.

IMAGE ANALYSIS

We performed image analyses to calculate the displacement and visualize the slip lines on the ground for all cases. In the image analysis, tracking points were set on the image for the tests on the aluminum rod ground model. The displacements at each point were calculated by changing the points. In addition, slip lines were observed to chase the trajectories of each point.

Figures 15 and 16 show the image analysis results, and we compared the changes in the slip lines under the dead load and 10% of the foundation width (12 mm). In all cases under the dead load, tiny slip lines were observed. In contrast, at 12 mm settlement, more extensive slip lines appeared than those under the dead load. For d = 17 and 22 mm, significant slip lines were observed at the unscoured side (right side) of the foundations, as shown in Fig. 16. On the scoured side, a slip surface was observed, although the movement was slight. This surface indicated that the ground resistance at the scoured area at the bottom of the foundation recovered. It was also confirmed from the image analyses that the bearing capacity increased during the loading tests, even when the foundation scoured.

CONCLUSIONS

In this study, we performed vertical loading tests on a scoured spread foundation on aluminum rods and conducted image analysis to clarify the mechanism of the bearing capacity of the locally scoured foundation.

The results suggest that it is possible to resume the service of bridges because the ultimate bearing capacity will remain, even if the foundation is damaged if the residual settlement and inclination are recoverable through simple emergency restoration, and if the reduction in the ground spring constant is limited. Additionally, the inclination of the foundation will be gentle, and the settlement will not increase when the repair, such as fixing the loading position to the original location before resuming, is performed.

In future research, we will perform tests by

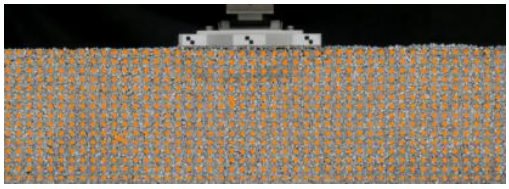

a) Case of normal ground

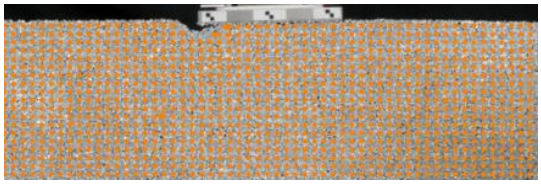

b) Case of d = 11 mm

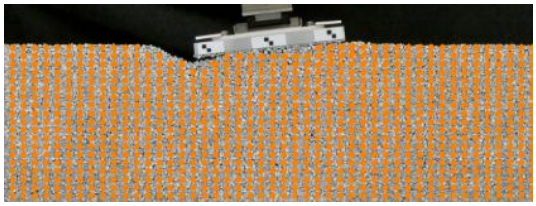

c) Case of d = 17 mm

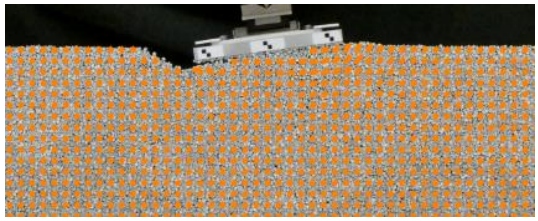

d) Case of d = 22 mm

Fig. 15 Ground displacement at residual settlement

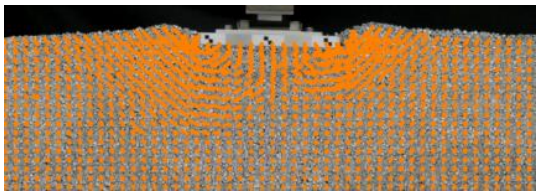

a) Case of normal ground

b) Case of d = 11 mm

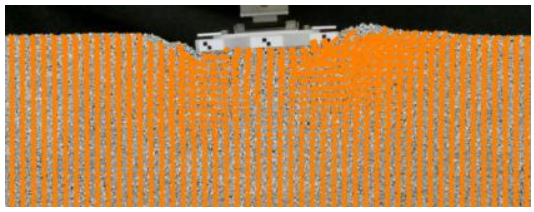

c) Case of d = 17 mm

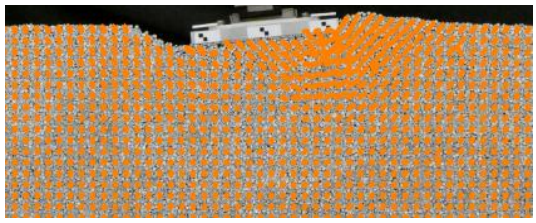

d) Case of d = 22 mm

Fig. 16 Ground displacement from residual settlement to 12 mm

varying the diameters of aluminum rods and the size distributions of the aluminum rods. Moreover, we will analyze the bearing capacity mechanism in detail through image analysis.

ACKNOWLEDGMENTS

This work was supported by the JSPS KAKENHI Grant-in-Aid for Scientific Research (C) (Grant Number JP20K04687).

We would like to thank Editage (www.editage.com) for English language editing.

REFERENCES

[1] H. Nishioka, Evaluation Method of Residual Bearing Capacity of Bridge Pier Foundation Damaged by Scouring, Monthly Report in Railway Technical Research Institute, 2018 (in Japanese) https://bunken.rtri.or.jp/doc/fileDown.jsp?RairacID=0040002746

[2] H. Nishioka, T. Sanagawa, and Y. Otake, Reliability Assessment for Residual Bearing Capacity of a Railway Bridge Foundation after Scouring, In Proceedings of 7th Asian-Pacific Symposium on Structural Reliability and Its Applications (APSSRA2020), October 4-7, 2020, Tokyo, Japan, pp.467–472

[3] H. Nishioka, M. Shinoda, Y. Sumi, and H. Yamate, The Vertical Loading Test to the Bridge Pier of Spread Foundation which was Damaged by Scouring Settlement, In Proceedings of Japan National Conference on Geotechnical Engineering 2013, July 23-25, 2013, Toyama, Japan, pp.203-204 (in Japanese)

[4] M. Amada, On Trial of Bearing Capacity Apparatus in Geotechnical Engineering – Experiments by Using Ground Material of Aluminum Rods, Journal of Japanese Society for Engineering Education, March, 1992, Vol. 40, Issue 2 (in Japanese)

11th Int. Conf. on Geotechnique, Construction Materials & Environment,
Kyoto, Japan, 3-5 November 2021, ISBN: 978-4-909106063 C3051

THREE-DIMENSIONAL ANALYSIS OF SOIL-PILE-STRUCTURE INTERACTION PROBLEM ON HIGH RISE BUILDING ON IMPROVED SOFT SOIL

Thanapon Tipsunavee[1], Goran Arangjelovski[2]

[1,2]King Mongkut's University of Technology Thonburi, Bangkok, Thailand

ABSTRACT

This study presents the numerical simulation of flexible wall barrel soil-pile-structure interaction analysis. Soil-Structure Interaction (SSI) is usually assumed beneficial during an earthquake. However, SSI can also increase permanent deformation and decrease the stiffness of the pile foundation system which affects seismic response and displacement in the overall structure, especially high-rise buildings. Non-linear 3D FEM models with a gap/slap mechanism have been developed in ABAQUS to simulate the effect of soil-pile-structure interaction (SPSI). The objectives of this research are to study the effect of SPSI on soil response, kinematic properties of the superstructure, and the modeling of SPSI problem with the superstructure, and to increase horizontal stiffness of foundation system by using the cement-mixing method. The analyses in this study include superstructure analysis with fix-based, SPSI and SPSI with cement-mixing. The constitutive models in this study are Mohr-Coulomb for soil material and Linear-elastic for the upper structure. The calibration of the flexible wall barrel modeling technique was successfully calibrated with a shaking table reference case with some variation of the results. It is observed that SPSI provides flexibility and damping to the superstructure. The gap/slap mechanism is clearly observed on the contact surfaces between soil and superstructure at a shallow level. Cement-mixing soil improvement increases horizontal stiffness resulting in a stiffer response of superstructure and reduction of pile stress during earthquakes. The influence of SPSI on superstructure and comparisons between simulation cases are then discussed. However, this study does not consider consolidation and the contraction properties have been simplified.

Keywords: 3D FEM/ ABAQUS/ Seismic/ Soil-pile-structure interaction

INTRODUCTION

Nowadays, a number of high-rise buildings in Thailand are increasing dramatically, especially in Bangkok, the capital of Thailand. Most of the design methods in Thailand are based on the assumption that the foundations of the building are assumed to be rigid or fixed. This kind of simplification can reduce the complication of the problem and also reduce the time required to analyze the problem, thus this simplification can help engineers to work easier and also save the cost for designing the building. However, this simplification is excluding soil-structure interaction and the flexibility of soil and foundation will be ignored.

Many design codes suggest neglecting the soil-structure interaction. Neglecting SSI is usually considered beneficial because the soil-structure interaction can increase the damping of the structural system. In addition, a lot of previous research found that SSI is reasonably neglected for low-rise structures and structures supported with very stiff soil. However, SSI will have a significant influence on a structure that is supported with soft soil, especially for high-rise buildings. [1]-[3].

Even though the Bangkok area is located in a low seismic hazard zone, most of the soil profile at a shallow depth are soft soils which are potentiality influenced from far distance earthquakes. Since SSI has high influence on the upper structure subjected to seismic load, post-seismic records in the past such as 1985 Mexico City, 1994 Northridge, and 1995 Kobe earthquakes provided adequate reasons to prove that the SSI effects should be investigated [4], [5].

Cement mixing is one of the cost-effective soil improvement technique that can improve the strength and stiffness of the weak soil area [6]. The improved area of the surrounding soil can potentially reduce the negative effect of SSI by increasing the horizontal stiffness. Moreover, additional numerical analyses to validate this approach are needed.

In the past, most of the numerical research about SSI was simplified to be linear elastic in order to reduce the complication of the problem. As computer hardware improved a lot over the past few years, FEM software also improved and allow computers to analyze the non-linear problem with great efficiency. Even though some of the previous research implements a non-linear soil model with non-linear Winkler spring models to the SSI problem, the effect of SSI still not clearly understand. Winkler spring model is the spring model based on the Winkler spring theory which uses beam elements to model the pile and uses the spring element to model the soil along the embedded pile surface. This model will consider only the load and displacement of the soil

and springs are independent of each other which exclude shear coupling between the springs.

In this study, a powerful engineering numerical simulation program based on the finite element method, ABAQUS, is adopted to simulate the 3D SSI behavior of pile foundations subjected to seismic load with the continuum SSI model. This continuum model will include normal pressure, shear drag, and gap/slap mechanism between soil and pile. The response of the structure is then observed.

APPROACH FOR SOIL-STRUCTURE INTERACTION IN NUMERAICAL ANALYSIS

Soil-Structure Interaction Interface Properties

According to previous research, most suitable interface properties for SSI is combination of normal behavior (Pressure-Over closure) and Tangential behavior [7]. In the past, most of SSI model was based on Winkler spring theory, but recently many researchers developed SSI model to compatible with continuum model such as gap element. The behavior of SSI was modeled as surface contact behavior between subsoil and pile. The master surface and slave surface are assigned to pile and soil respectively.

Normal Behavior (Pressure-Over Closure)

Normal behavior is defined as Pressure-Over closure that is transmitted between soil and pile while both surfaces are in contact with each other. The most appropriate type of normal behavior is "hard contact". Hard contact means that there is a zero-penetration condition between each surface. In addition, if surfaces are in contact, any contact pressure can be transmitted between them. The surfaces separate if the contact pressure reduces to zero. Separated surfaces come into contact when the clearance between them reduces to zero. in other words, this behavior will allow gap/slap mechanism to occur.

Tangential Behavior

The most suitable tangential behavior for SSI is penalty friction. Unlike the spring model, this type of friction can provide drag force to the system. This friction model base on Coulomb friction. As the basic theory of the Coulomb friction model, two surfaces that contacting to each other can carry shear drag stress up to a certain point across their interface before they start sliding relative to one another. The Coulomb friction model defines this critical shear stress, τ, at which sliding of the surfaces starts as a fraction of the contact pressure, p.

$$\tau_{crit} = \mu p \qquad (1)$$

Where μ is known as the coefficient of friction. The coefficient of friction, μ, is equal to tan (δ) where δ is the interface frictional angle of the soils [8]. The interface frictional angle (δ) was estimated using the equation as shown in Eq. (2) [9].

$$\delta = tan^{-1}[\sin\phi\,'\cos\phi\,/(1+\sin^2\phi)] \qquad (2)$$

Simulation of Shaking Table

To demonstrate the soil-structure interaction behavior such as gap/slap mechanism, the numerical analysis approaches are calibrated by simulating the physical model shaking table test. A flexible wall container on a shaking table is proven to be accurate and provides the best response spectra when compared to other types of shaking table containers. Thus, a single pile model with a flexible wall container shaking table test was adopted as reference case [10]. The single pile model with superstructure is the best model to observe soil-pile-structure interaction behavior. The single pile model with head masses of 25, 100, and 160 lbs. The piles were subjected to Loma Prieta earthquake motion with a maximum horizontal acceleration of 0.16g. The numerical model assembly of shaking table are shown in Fig.1.

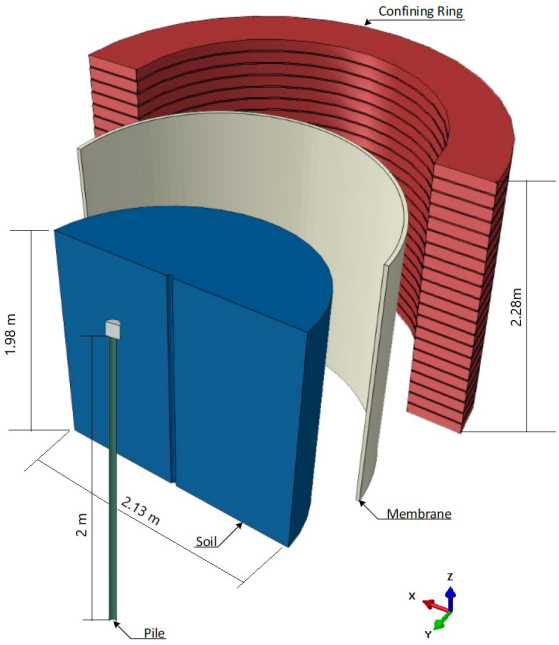

Fig.1 Numerical model assembly of shaking table.

The boundary conditions in the numerical model are the same as a flexible wall barrel container. At the bottom of each confining ring and rubber membrane, the displacements are restrained in the vertical direction and will allow to move freely in the horizontal direction. The combination of confining ring and rubber membrane confined the soils and help

the soil maintain its geometry. The soil model is displacement restrained with roller support in the vertical direction at the bottom of the model.

The result from the simulation shows a good correlation with the observed from the experiment as shown in Fig.2. Most of the soil-structure interaction effect can be observed such as Gap/slap mechanism and shows the influence of the kinematic forces from the soil to the pile, and the influence from the inertial forces from the super-structure.

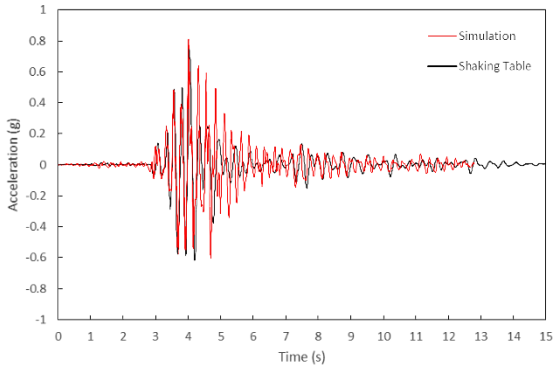

Fig.2 Acceleration time history at the pile head with 160 lbs. mass.

Figure 3 shows gap/slap mechanism which causes free vibration and reduction of pile stiffness. Even though some results have a small deviation, it can be confirmed that physical shaking table test with flexible wall barrel container can be successfully simulated by using 3-D FEM program, ABAQUS.

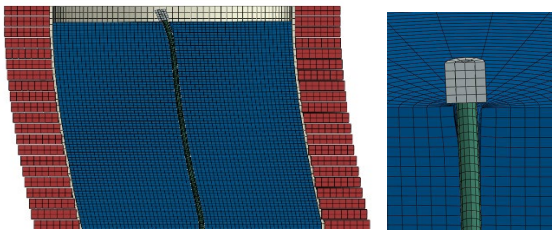

(a) (b)

Fig.3 Gap deformation (a) during earthquake motion (b) permanent deformation.

ANALYSIS OF SOIL-PILE-STRUCUTRE INTERACTION

The modeling technique used the contact properties from the calibration model to simulate the effect of SSI on the Pile-foundation system and superstructure. This model includes a pile foundation system and an 18-floor building with natural periods of 1.79 and 1.44s in x and y direction, respectively. The superstructure in this study is simplified from an existing 18-floor building, for the purpose to achieve symmetry in both axes. The earthquake motion is applied to both directions of the building. Floor to floor height in of the superstructure was 3 m., with 1.5 m. clearance between the first floor and the ground level. The superstructure composes of columns, beams, slabs, elevator shafts, and footings. The columns have two different sizes of a cross-section which are 0.4x0.8 m. and 0.4x0.15 m. The slab thickness is 0.25m. The beam cross-section including the slab thickness is 0.5x0.25m. Figure 4 shows the foundation system of the superstructure consists of several types of pile and piled-raft footings, with a pile length of 40m., and a pile cap thickness of 1.7m.

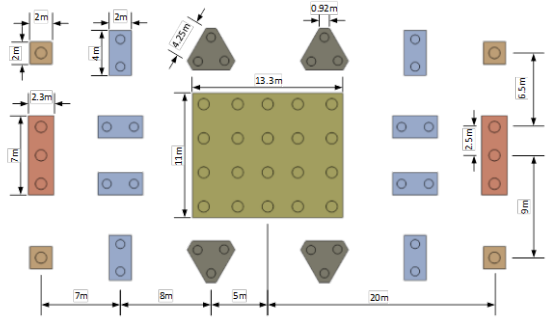

Fig.4 Foundation system layout of the superstructure.

The soil layer boundaries in this study are 235m deep and 100m in diameter. The superstructure has 18 stories with a combined height of 55.5 m. The building has a width of 18.8 m. and a length of 40.4m. as shown in Fig. 5. The boundary conditions in this part are similar to the previous one. The soil parameters in this study are adopted from previous researches [11], [12]. The material properties and soil parameters are shown in Table 1.

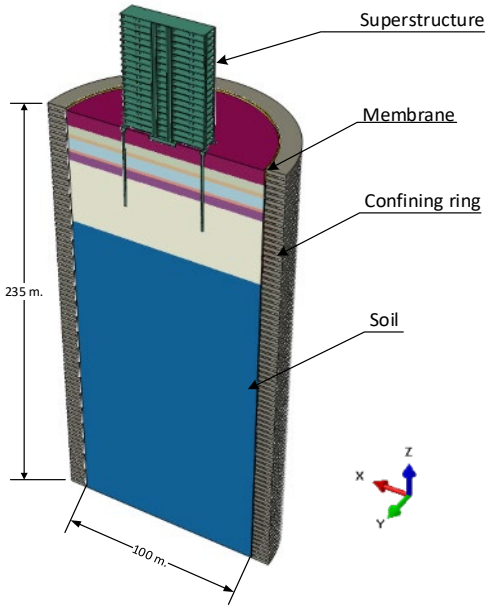

Fig.5 Assembly of SPSI model with high-rise building.

Figure 6 shows three cases that consider in this study which are (1) structure only; (2) structure with soil layers; and (3) structure with cement-mixing improved soil.

Table 1 Material properties and soil parameter (Likitlersuangetal et al., 2013; Arai and Yamazaki, 2002)[11], [12]

Material	Depth (m)	Model	γ (kN/m^3)	Su (kPa)	Friction Angle(ϕ)	Eu, E' (mPa)	v	Rayleigh damping
Soil								
Soft Clay1	0-7.5	MCM	16.5	20	-	10	0.5	5%
Soft Clay2	7.5-12	MCM	16.5	39	-	20.5	0.5	5%
Medium Clay	12-14	MCM	17.5	55	-	27.5	0.5	5%
Stiff Clay1	14-20	MCM	19.5	80	-	40	0.5	5%
Sand	20-21.5	MCM	19	-	27	53	0.5	5%
Stiff Clay2	21.5-26	MCM	20	120	-	72	0.5	5%
Hard Clay1	26-60	MCM	20	240	-	240	0.5	5%
Hard Clay2	60-235	MCM	20	400	-	1350	0.5	5%
Cement mixing	-	MCM	16	300	-	221.9	0.5	5%
Concrete		LEM	23			35000	0.2	5%
Confining Ring		Rigid	0	-	-	-	-	-
Membrane		LEM	0	-	-	Vary*	-	-

* Elastic modulus of the Membrane is depends on the soil layer

** MCM = Mohr-Coulomb Model

** LEM = Linear Elastic Model

The third case attempts to increase the horizontal stiffness of the foundation system of the superstructure by using a soil cement mixing method [12]. The interaction was applied to all contact surfaces including the contact surface between cement mixing soil and existing soil.

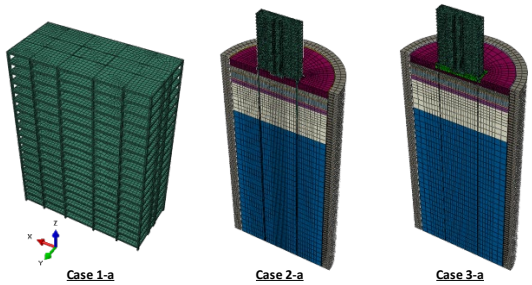

Fig.6 Assembled 3-D model and mesh of analysis case 1-3.

The model was subjected to the Loma Prieta earthquake as shown in Fig.7. The earthquake time history is applied at bottom of the model in Case 2 and Case 3 while the acceleration time history obtained from the free-field analysis is applied to the bottom boundary of Case 1. The earthquake wave was propagating from the bottom to the soil surface. As the wave travels through different soil layers, the wave was modified by transfer functions as shown in free-field motion analysis. Thus, the wave propagation in this model was more realistic than the model that applied the earthquake motion at the side boundary of the model. After the model was subjected to earthquake time history, permanent gap formations are clearly observed on most of the footing and piles.

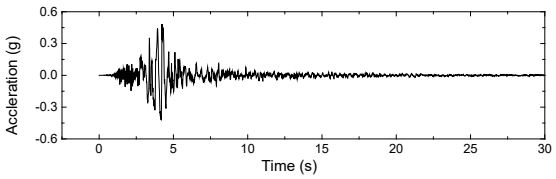

Fig.7 Acceleration time history of Loma Prieta Earthquake, Gilroy Array, 1989.

RESULTS

The acceleration time history and spectral acceleration of both cases are shown in Fig. 8 and Fig. 9. In the case2-a, superstructure vibrates in modes 1 through 4. Due to SPSI, the frequency of vibration for case 2 was lower than the case 1. In case 2, where SPSI is included in the analysis, the vibration frequency of the superstructure was shifted from 0.57Hz to 0.5Hz for mode 1 and 0.69Hz to 0.53Hz for mode 2. Figure 9 shows a comparison of acceleration time history between case 1 and case 2. The soil-structure-interaction provides additional damping and flexibility to the superstructure, thus the amplitude of acceleration was lower and the period increased [1]. The SSI also reduced the relative displacement of the superstructure. Gap/slap mechanism can be observed in Fig.10. Once the gap is forming the unconfined area of the piles and footings increases, which leads to an increase in the natural period of the superstructure.

The acceleration time history and spectral acceleration for cases 2 and 3 are shown in Fig. 11 and Fig. 12. The vibration characteristic between case 2 and case 3 is almost similar, however, ground improvement by using cement-mixing can increase the stiffness of the weak soil layer which resulting in a stiffer respond from the super structure.

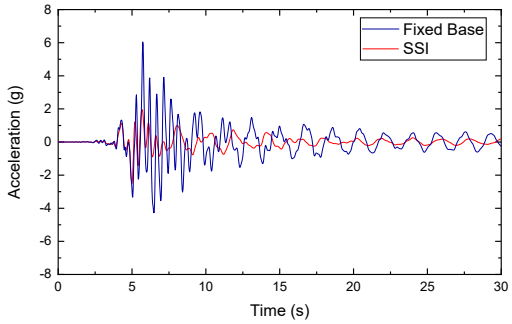

Fig.8 Comparison of acceleration time history between case 1-a(Fixed Base) and case 2-a(SSI) at the top of the superstructure.

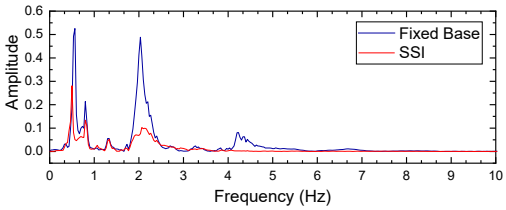

Fig.9 Comparison of Spectral acceleration between case 1-a(Fixed Base) and case 2-a(SSI) at the top of the superstructure.

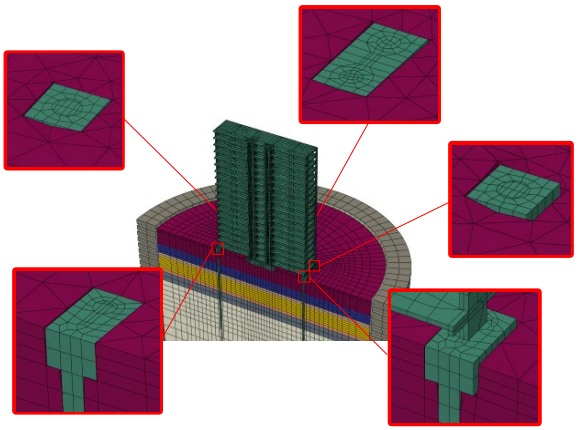

Fig.10 Permanent gap around footings in case 2-a.

Since there is a very high number of piles in this study, some of the piles were selected from each type of footings to show the change of vertical stresses during the earthquake. The vibration of the superstructure generates a significant amount of bending moment on the piles. The stresses in each pile are shown in Fig.13 and Fig.14. The cement-mixing soil improvement increases the horizontal stiffness of the soil which resulted in better axial stress distribution among the piles. When the gap is formed, the unconfined area increasing and the influence from the moment from the superstructure to the pile also increasing. As the cement-mixing increases the strength and stiffness of the surrounding soil, the gap deformation is reduced. Although most of the stress in the piles decreased due to the cement-mixing soil improvement, the efficiency of cement-mixing also depends on the non-improved soil. The elastic modulus and cohesion between improved area and non-improved soil are significantly different, thus the gap can be observed between the contract surfaces as shown in Fig. 15.

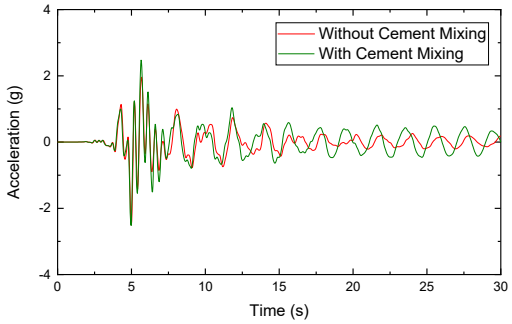

Fig.11 Comparison of acceleration time history between case 2-a and case 3-a at the top of the superstructure.

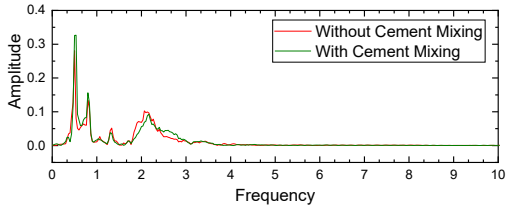

Fig.12 Comparison of Spectral acceleration between case 2-a and case 3-a at the top of the superstructure.

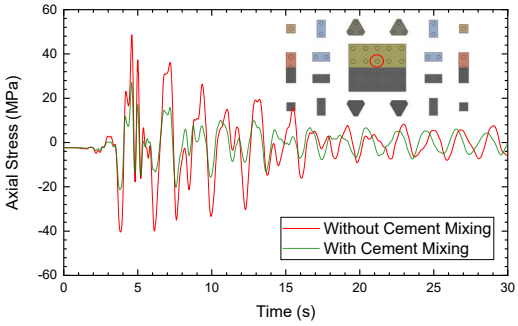

Fig.13 Comparison of the axial stresses between case 2-a and case 3-a for the pile in the middle of pile raft.

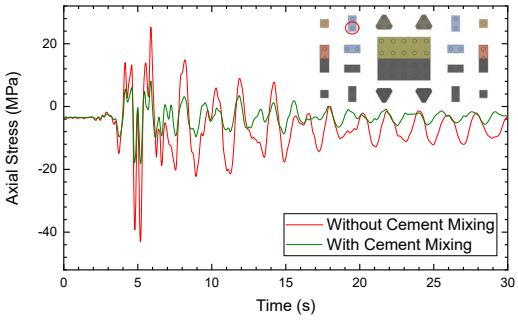

Fig.14 Comparison of the axial stresses between case 2-a and case 3-afor the pile of 2-pile footing.

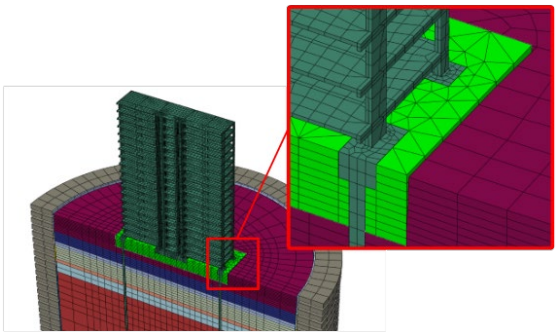

Fig.15 Permanent gap between cement-mixing and environmental soil in case 3-a.

CONCLUSION

Soil-pile-structure interaction behavior can be successfully simulated by using 3-D finite element software "ABAQUS". The gap/slap mechanism was clearly observed. Soil-pile-structure interaction provides damping and flexibility to the superstructure. The natural period of the superstructure was increased. The acceleration and displacement of the superstructure were significantly decreased. Cement-mixing soil improvement increases the horizontal stiffness of the foundation system which results in better stress distribution among the piles and the gap position was changed from the contract surfaces between soil and piles to contact surfaces between non-improved soil and cement-mixing soil.

ACKNOWLEDGMENT

The authors would like to express their gratitude for financial support from King Mongkut's University of Technology Thonburi (KMUTT) through The Petchra Pra Jom Klao PhD scholarship under contract Grant No. 2/2559.

REFERENCES

[1] Guin, J. and Banerjee, P. K., Coupled soil-pile-structure interaction analysis under seismic excitation, Journal of Structural Engineering, Vol. 124, No. 4, 1998, pp. 434-444.

[2] Han Y., Seismic response of tall building considering soil-pile-structure interaction," Earthquake Engineering and Engineering Vibration, Vol. 1, 2002, pp. 57–64.

[3] Mylonakis, G. and Gazetas, G., Seismic soil structure interaction: Beneficial or Detrimental, Journal of Earthquake Engineering, Vol. 4 No.3 2000.

[4] Mizuno, H., Iiba, M. and Hirade, T., Pile damage during the 1995 Hyogoken-Nanbu earthquake in Japan, 11th World Conf. on Earthquake Engineering, Association for Earthquake Engineering (IAEE), Tokyo, No. 977, 1996.

[5] Phanikanth, V., Choudhury, D. and Reddy, G., Behavior of Single Pile in Liquefied Deposits during Earthquakes, International Journal of Geomechanics, 2013, pp. 454–462.

[6] Rollins, K. and Brown, D., "Design Guidelines for Increasing the Lateral Resistance of Highway-Bridge Pile Foundations by Improving Weak Soils," National Cooperative Highway Research Program Report, Washington, D.C., 2011, pp. 697

[7] Lv, Y., Liu, H., Charles, W.W. Ng, Ding X. and Gunawan, A., Three-dimensional numerical analysis of the stress transfer mechanism of XCC piled raft foundation, Computers and Geotechnics, Vol. 55, 2014, pp. 365-377.

[8] Lee, C. J., Bolton, M. D. and Al-Tabbaa, A., Numerical modelling of group effects on the distribution of dragloads in pile foundations, Geotechnique, Vol. 52, No. 5, 2002, pp. 325-335.

[9] Randolph, M.F. and Wroth, C.P., Application of the failure state in undrained simple shear to the shaft capacity of driven piles, Geotechnique, Vol. 31, 1980, pp. 143–57.

[10] Meymand, P.J., Shaking Table Scale Model Tests of Nonlinear Soil-Pile-Superstructure Interaction In Soft Clay, Doctor of Philosophy Dissertation, University of California, Berkeley, 1998.

[11] Likitlersuang, S., Surarak, C., Wanatowski, D., Oh, E. and Balasubramaniam, A., Finite element analysis of a deep excavation: A case study from the Bangkok MRT, Soils and Foundations, Vol. 53, No.5, 2013, pp. 756-773.

[12] Arai, H. and Yamazaki, F., Exploration of S-Wave Velocity Structure Using Microtremor Arrays in the Greater Bangkok,Thailand, EDM Technical Report No.15, Earthquake Disaster Mitigation Research Center (EDM), 2002.

[13] Muraleetharan, K.K., Ravichandran, N. and Norton, S.L., Fully Ccoupled Dynamic Soil-Structure Interaction Analysis of Pile Foundation in Weak Soil, 4th International Conference on Earthquake Geotechnical Engineering, No. 1177, 2007.

11th Int. Conf. on Geotechnique, Construction Materials & Environment,
Kyoto, Japan, 3-5 November 2021, ISBN: 978-4-909106063 C3051

RELATIONSHIP BETWEEN LIQUEFACTION STRENGTH OF SAND WITH FINE FRACTION AND VARIOUS VOID RATIOS

Kentaro Ishii [1], Wen LIU[1], and Shoji KAMAO[2]

[1]Graduate Student, Department of Civil Engineering, Nihon University, JAPAN
[2]Associate Professor, Department of Civil Engineering, Nihon University, JAPAN

ABSTRACT

Liquefaction damage has been reported in the ground containing fine fractions. It is necessary to investigate the effect of soil containing fine particles on liquefaction strength. This study aims to clarify the relationship between the liquefaction strength and the skeleton void ratio, representing the skeletal structure of the soil and the fine fraction void ratio. For the utilized samples, Toyoura sand was used as the coarse fraction, Kaolin clay worked as the fine fraction, and mixed soil in which the mixing ratio was altered in the range of 0 to 40% was applied. Besides, considering the difference in the fine fraction properties, the experimenter made use of Fujimori clay, Kasaoka clay, and the three combined soils. The specimens were prepared using the dry tamping method and repeatedly subjected to cyclic undrained triaxial tests. As a result, when the skeleton void ratio does not exceed the maximum void ratio of sand, it is located on the same line as the liquefaction strength regardless of the types of fine fractions. We can declare that it is a unique relationship. When the skeleton void ratio exceeds the maximum void ratio of sand, there is an excellent correlation between the fine fraction void ratio and the liquefaction strength. However, it is represented by two curves of Kaolin mixed soil and other mixed soil due to the distinction in the magnitude of the plasticity index, and it can be remarked that the fine fraction void ratio is not distinctly related to the liquefaction strength.

Key words: liquefaction strength, fines content, undrained cyclic test, sand clay

INTRODUCTION

The main grounds where seismic liquefaction events occur are generally recognized as loosely deposited, saturated sand grounds. However, liquefaction of fine fraction has been confirmed by the 1995 Hanshin Earthquake and the 2011 Great East Japan Earthquake[1], which caused severe liquefaction of reclaimed land in the Tokyo Bay area from Shinkiba to Urayasu. And the researches have been carried out to clarify the liquefaction mechanism of fine fraction and its effects on liquefaction strength. As a result of these studies, it was found that (1) The liquefaction strength decreases with the increase of fine fraction content, and there is a fine fraction content with the lowest liquefaction strength [2] [3]. (2) There is a good correlation between the skeleton void ratio and the liquefaction strength, where a part of the fine grain content is considered as a void [4] [5]. However, there is no unified view on the effect of fine fraction of liquefaction strength, due to different methods of density control and specimen preparation among researchers. In particular, few studies have been conducted on samples that contain a large amount of fine fraction up to the region where fine fraction are dominant. And the effect of fine fraction on liquefaction strength in the region where fine fraction is dominant has not been clarified. So far, the authors have repeatedly conducted the undrained cyclic triaxial tests using a mixed sample in which the void ratio e is constant and the fine fraction content is changed in the range of 0 to 40% [6] [7]. In the region with a skeleton void ratio e_s that does not exceed the maximum void ratio of sand only ($e_s<e_{max}$), the liquefaction strength R_{20} is categorically related to the Skeleton void ratio e_s, notwithstanding the type of fine fraction. With a skeleton void ratio es above the maximum void ratio for sand only ($e_s>e_{max}$), the liquefaction strength R_{20} has a good correlation with the "Fine fraction void e_{ff}" in the region where the fine fraction is predominant. An intermediate region exists between these two regions. The R_{20} is approximately equal to the R_{20} when the skeleton void ratio e_s is total up to the maximum void ratio of sand only.

The purpose of this study is to clarify the effect of fine fraction on liquefaction characteristics by performing undrained cyclic triaxial tests on specimens with the same method from small to large fine fraction. In this study, the skeleton void ratio e_s [6] [7] [8] [9] is defined as the void ratio of all the fine grains in the sand as pore space. The fine fraction void ratio e_{ff} [6] [7] [8] [9] is the void ratio that ignores the volume of the coarse grains and focuses only on the fine fraction. It is an indicator of the degree of fine fraction blockage.

EXPERIMENT OVERVIEW

In this study, undrained cyclic triaxial tests were carried out to determine the liquefaction strength of each sample. An overview of the experiment is given below

Sample

For the base material sample used in this study, Toyoura sand was used as the coarse fraction, and Kaolin clay, Fujinomori clay, and Kasaoka clay were used as the fine fraction. The sample used was Toyoura sand whose grain size was adjusted to 75 μm to 2 mm as the coarse fraction content, and kaolin clay as the low plastic fine fraction content, and the mixing ratio. The author used kaolin-mixed clay in which was changed by 5% in the range of 0% to 40%. In addition, Fujinomori clay and Kasaoka clay were used to examine the effect of different properties of fine fraction. The author used Fujinomori clay whose grain size was adjusted to 75 μm or less. The fine fraction content of the Fujinomori mixed soil is 3%, 5%, 10%, 15%, 20%, and 25%. The fine fraction content of the Kasaoka mixed soil is 5%, 10%, and 20%. Each mixed soil is called K5, F3, or KS5, according to the acronym of the fine fraction' name and the mixing ratio. This study mixing ratio is the

Table 1 Main soil property values of Toyoura sand

Corse fraction	Soil particle density	Mean diameter	Fine fraction content	Clay fraction content
	ρ_s (g/cm^3)	D_{50}	FC (%)	CC (%)
Toyoura sand	2.64	0.161	0	0

Table 2 Main soil property values of fine-grained soil

Fine fraction	Soil particle density	Plastisity index	Fine fraction content	Clay fraction content
	ρ_s (g/cm^3)	I_P	FC (%)	CC (%)
Kaolin clay	2.714	13.7	100	64
Fujinomori clay	2.535	20.4	92	37
Kasaoka clay	2.710	30.8	99.8	46

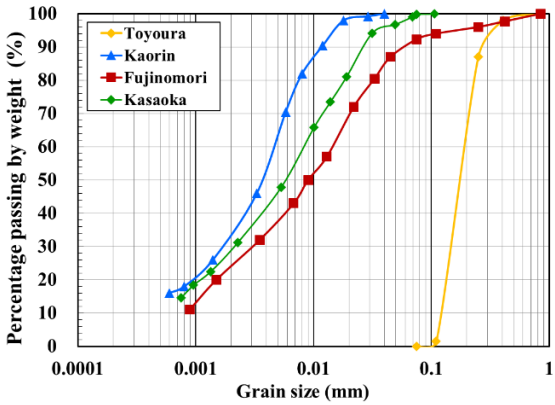

Fig. 1 grain size accumulation curves the sample

Table 3 Test conditions for cyclic triaxial tests

Sample	Density	Initial void ratio	Consolidation time	Cyclic stress ratio
	( ) indicates D_r (%)	e_0	t (hour)	R(=$\sigma_d/2\sigma_c'$)
Toyoura	Loose (40)	0.828	0.5	0.12, 0.13, 0.15
	Medium (60)	0.757	0.5	0.16, 0.17, 0.18
	Dense (80)	0.687	0.5	0.21, 0.22, 0.24
K5	Loose	0.828	1	0.09, 0.10, 0.14
	Medium	0.757	1	0.12, 0.14, 0.16
	Dense	0.687	1	0.15, 0.17, 0.18
K10	Loose	0.828	5	0.08, 0.10, 0.12
	Medium	0.757	5	0.08, 0.10, 0.12
	Dense	0.687	5	0.10, 0.11, 0.12
K15	Loose	0.828	12	0.08, 0.10, 0.12
	Medium	0.757	12	0.08, 0.10
K20	Medium	0.757	24	0.07, 0.08, 0.09
K25	Medium	0.757	24	0.08, 0.09
K30	Medium	0.757	24	0.10, 0.12, 0.15
K35	Loose	0.828	24	0.08, .0.09
	Medium	0.757	24	0.09, 0.11, 0.13
K40	Loose	0.828	24	0.09, 0.13
	Medium	0.757	24	0.11, 0.13, 0.15
F3	Medium	0.757	0.5	0.2, 0.17, 0.125
F5	Medium	0.757	1	0.16, 0.14, 0.12
F10	Medium	0.757	5	0.12, 0.11
F15	Medium	0.757	15	0.11, 0.09
F20	Medium	0.757	18	0.105, 0.115
F25	Medium	0.757	24	0.11, 0.12
KS5	Medium	0.757	1	0.17, 0.13
KS10	Medium	0.757	5	0.15, 0.12, 0.10
KS20	Medium	0.757	15	0.11, 0.10

*The Confining pressure of Consolidation is 100 kPa

*The load repeats with a sinusoidal wave of 0.1 Hz frequency at the specified cyclic stress ratio

percentage of the dry mass of the mixed fine-grained sample to the total dry mass. Each mixed soil was prepared by mixing each sample in an air-dried state until it became homogeneous in a container. main physical properties and particle size distributions of each sample are shown in Table 1 and Table2, Fig. 1.

Experimental Method

The specimen is a cylindrical sample of 5 cm in diameter and 10 cm in height. The specimens were divided into ten equal parts and then divided into ten layers, each layer of which was solidified with a rammer. After the specimens were prepared at a predetermined density, the specimens were first allowed to stand on their own at a constraint pressure of 20 kPa, and was saturated by aerating carbon dioxide, passing sufficient degassed water, and then saturated by applying 200 kPa of back pressure, which is about three times the volume of the specimens. Subsequently, consolidation was performed with effective constraint pressure σ_c'=100 kPa. The consolidation time was set as shown in Table 3 for each sample, taking into account that the consolidation could be completed sufficiently. After the consolidation was completed, the B-value was measured to confirm the saturation, and the back pressure was further applied to make the B-value more than 0.95. After confirming that the B-value was more than 0.95, the material was repeatedly loaded with a sinusoidal wave of 0.1 Hz frequency at the prescribed cyclic stress ratio R($=\sigma_d/2\sigma_c'$). The test conditions for each sample are shown in Table 3.

Density Management Method

In the field of liquefaction, the relative density D_r is often used as a parameter expressing the density of specimens, and even in study using samples mixed with fine fraction, the relative density controls the density, and the same relative density is used. There are many examples of comparing densities with each other. For example, the reason why the relative density is often used is that in the case of sand, the relationship between the relative density and the liquefaction strength is proportional. but the "minimum/maximum density test of sand (JIS)" for determining the relative density the range of soil to which A 1224) is applied is said to be sand in which 95% or more remains in a 75 μm sieve, and when using a sample containing a large amount of fine fraction as used in this study, the relative density It is difficult to control the density using, and it is considered inappropriate.

Therefore, in this study, the most densely packed sand is called "Dense", the most loosely packed sand is called "Loose", and the sand with a density in between is called "Medium". When only Toyoura sand was used, in order to take into account the effect of density change, the relative densities were adjusted in three ways: D_r=40% (Loose), D_r=60% (Medium) and D_r=80% (Dense). When the same test was conducted using mixed soil, the density was controlled so that the initial pore ratio e_0 was e_0=0.828 (Loose), e_0=0.757 (Medium), and e_0=0.684 (Dense), respectively, which was the same value as the initial pore ratio e_0 when the density was adjusted using only Toyoura standard sand. Therefore, the density control method in this study can be considered as a constant void ratio.

Liquefaction Strength Curve

Figure. 2(a)~(d) shows the liquefaction test results for each sample. It shows the relationship between the cyclic stress ratio R and the number of cycles N required to reach both amplitude axial strains DA=5%. Fig. 2(a) shows the liquefaction strength curve when the undrined cyclic triaxial test was repeatedly performed using Toyoura standard sand. As the density of Toyoura sand increases, the cyclic stress ratio at a certain number of loading cycles increases, the curve moves upward, and the resistance to liquefaction increases. In Dense, the liquefaction intensity curve, commonly seen in dense sand, tends to rise. Fig. 2(b) shows the cyclic strength curves for K5 to K15 with varying densities; as for K5, the curve moves upward with increasing density, as in the case of Toyoura sand, but it becomes weaker as the content of K10, K15 and Kaolin clay increases. For the same densities, the cyclic strength curve is located at the bottom of the curve as the fines content increases. Fig. 2(c) shows the cyclic strength curves for the cyclic triaxial tests using from K20 to K40. It was found that the curve was located upward for samples with higher fines content, and the resistance to liquefaction was higher. Fig. 2 (d) shows the cyclic strength curves for the cyclic triaxial tests using from F3 to F25 and KS5 to KS20. In Fujinomori mixed soil, the liquefaction strength curve moves to the bottom as the fine fraction content increases, and the liquefaction strength gradually increases beyond FC = 15%, increasing the resistance to liquefaction. In addition, the Kasaoka mixed soil shows the same tendency as the Fujinomori mixed soil.

Relationship Between Fine Fraction Content And Liquefaction Strength

In this study, the cyclic shear stress R was used as "liquefaction strength R_{20}" to indicate the resistance to liquefaction when both amplitudes of strain DA=5% were reached at 20 times of cyclic loading (shown as dashed line in Fig.2). The relationship between the liquefaction strength, R_{20}, and the Fine fraction content FC, is shown in Fig.3. From the

figure, the R_{20} of kaolin mixed soil Medium

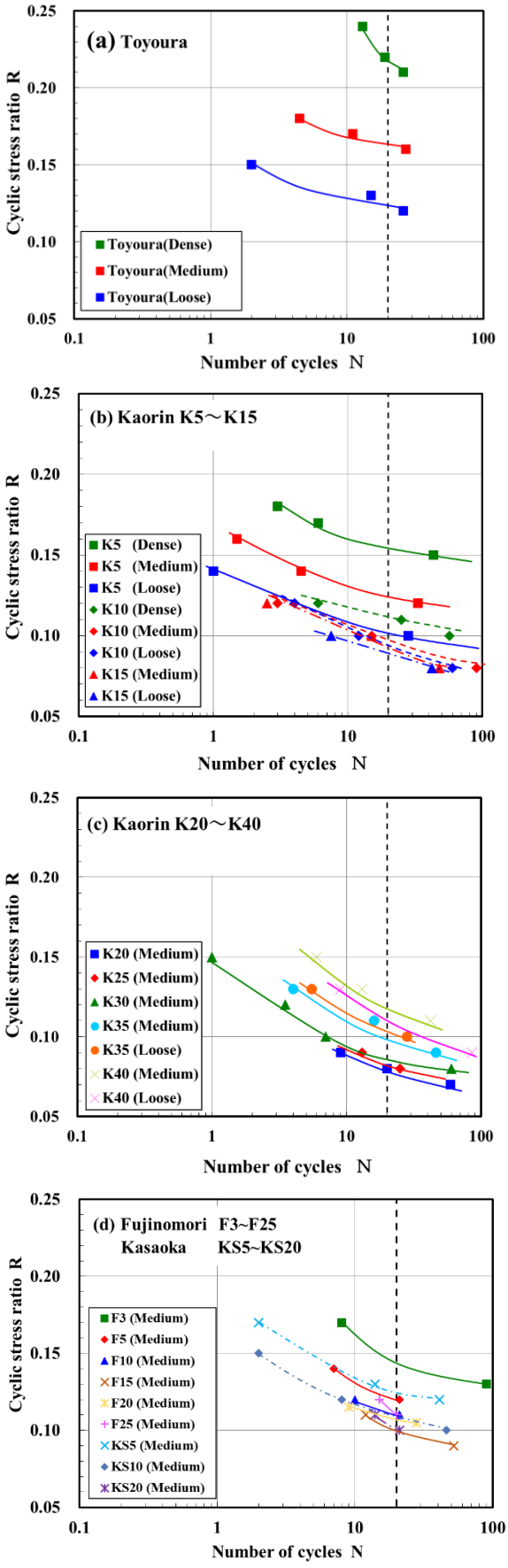

Fig. 2 Cyclic strength for each sample

decreased with the increase of Fine fraction content, showed the lowest R_{20} at FC=20%, and then increased. In the range of FC=0~15%, the R_{20} of Kaolin mixed soil increases with the increase of density of specimen, but the effect of density of specimen on liquefaction strength gradually decreases with the increase of fine grain content. at FC=15%, the strength of Loose and Medium are almost the same. The R_{20} of Fujinomori mixed soil Medium decreased with the increase of Fine fraction content. The lowest R_{20} was observed at FC=15% and then increased. The R_{20} of Kasaoka mixed soil Medium decreased with the increase of FC. After FC=10%, under the same density of specimen, Fujinomori mixed soil and Kasaoka mixed soil show higher liquefaction strength than Kaolin mixed soil.

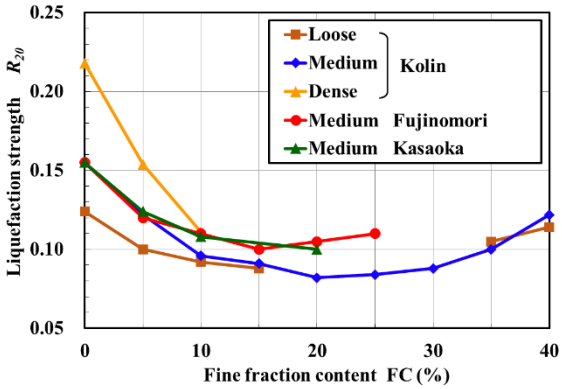

Fig. 3 Effect of fine fraction content on liquefaction strength R_{20}

Relationship Between Various Void Ratios And Fine Fraction Content

When investigating the strength of a soil with a grain size intermediate between sand and clay, such as the sample used in this study, it is very important to pay attention to the skeletal structure of the soil.

Therefore, in this study, the effect of fine fraction on liquefaction properties was considered using " Skeleton void ratio e_s" and "Fine fraction void ratio e_{ff} ". The skeleton void ratio e_s is the void ratio when all fine fractions are considered as pores while the skeleton void ratio e_s is the void ratio. The fine fraction void ratio e_{ff} is a void ratio that ignores the volume of coarse-grains and focuses only on the fine fraction content, which is an indicator of how well the fine fraction content is plugged. The void ratio can be calculated by the following equations (1) and (2). Equations (1) and (2) use the symbols shown in Fig. 4.

Skeleton void ratio $$e_s = \frac{V_v + V_{s(silt)} + V_{s(clay)}}{V_{s(sand)}} \quad \cdots(1)$$

Fine fraction void ratio $e_{ff} = \frac{V_v}{V_{s(clay)}+V_{s(silt)}}$ ⋯(2)

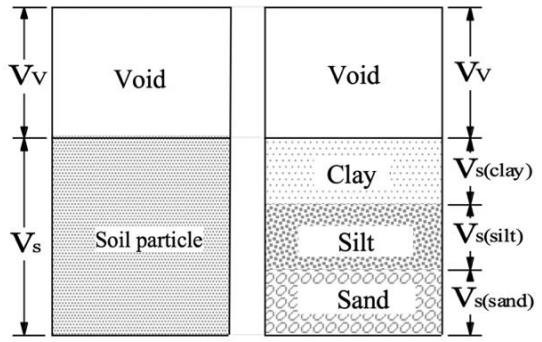

Fig. 4 Schematic of mixed samples

Fig. 5 and Fig. 6 show the changes in the skeleton void ratio e_s and the fine fraction void ratio e_{ff} due to the increase in the fine fraction content in the medium of each mixed soil. The various void ratios in the figure are the values at the time of preparing the specimen. From Fig. 5, the value of the skeleton void ratio does not change regardless of the type of fine fraction, and the skeleton void ratio increases as the fine fraction content increases. The skeleton void ratio e_s exceeds the maximum void ratio e_{max} of sand only (broken line in Fig. 5) near FC = 10%. Therefore, before FC = 10%, a skeleton of sand particles is formed and fine fraction are formed. After FC = 10%, it is considered that the fine fractions enter between the sand particles to form a skeleton, or the sand particles are floating in the fine fraction. Fig. 6 shows the relationship between the fine fraction void ratio e_{ff} and the fine fraction content FC. As FC increases, the fine fraction void ratio e_{ff} decreases.

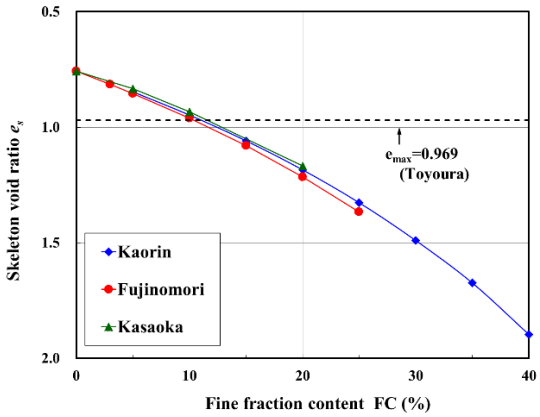

Fig. 5 Relationship between fine fraction content and skeleton void ratio e_s

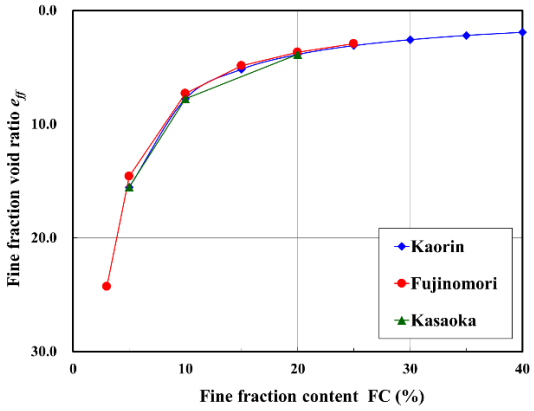

Fig. 6 Relationship between fine fraction content and fine fraction void ratio e_{ff}

Relationship Between Various Void Ratios And Liquefaction Strength

The relationship between the Skeleton void ratio es and liquefaction strength R_{20} is shown in Fig. 7. When the Skeleton void ratio e_s does not exceed the maximum void ratio of Toyoura sand only e_{max} (dashed line in the figure), the Skeleton void ratio e_s and liquefaction strength are on the same curve regardless of the type of fine fraction or the density of the specimen. This indicates that the skeletal structure of the sample is formed by sand and fine fraction does not affect the liquefaction strength, and R_{20} is determined by the Skeleton void ratio e_s, within the range of the maximum void ratio of sand only. Furthermore, the Skeleton void ratio e_s gradually increases after e_{max}. The liquefaction strength starts to increase after reaching the lowest point, suggesting that the skeletal structure of the soil is similar to that the fine fraction does not fit into the spaces between the sand grains, and the sand grains float in the fine fraction.

Therefore, in such a state, the liquefaction strength R_{20} is presumed to be influenced by the state of fine fraction and is considered to be closely related to the Fine fraction void ratio e_{ff}. The relationship between the Fine fraction void ratio e_{ff} and the liquefaction strength R_{20} is shown in Fig. 8. Focusing on the kaolin mixed soil in Fig. 8, R_{20} is located on almost the same line regardless of the fine fraction content and density, and R_{20} increases sharply from around FC = 30%. From this, it was found that there is a good correlation between the liquefaction strength R_{20} and the Fine fraction void ratio e_{ff} in the region where the fine particles of FC = 30 to 40% are predominant. The same change tendency is shown in the Fujinomori mixed soil and the Kasaoka mixed soil. However, due to the difference in the magnitude of the plasticity index I_p, the results were represented by two curves, kaolin mixed soil ($I_p < 15$) and other mixed soil (Ip $>$ 20).

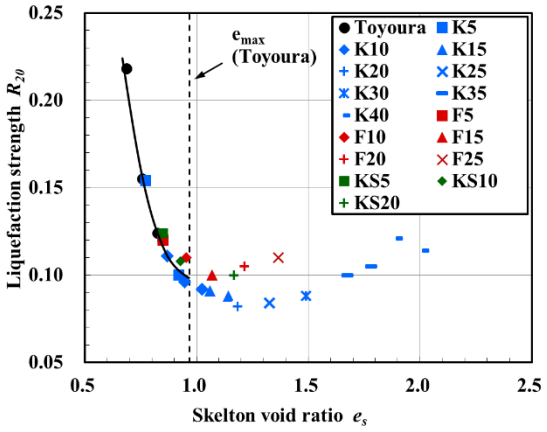

Fig. 7 Relationship between Skeleton void ratio e_s and Liquefaction Strength R_{20}

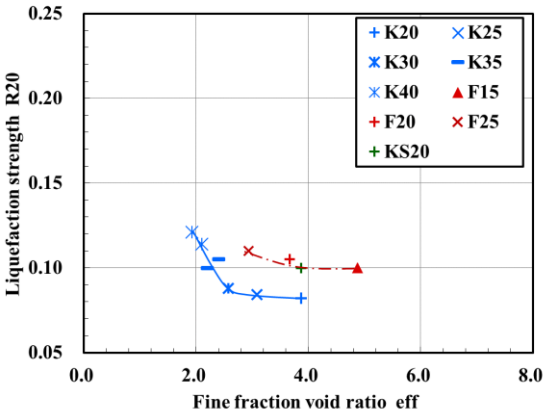

Fig. 8 Relationship between Fine fraction void ratio e_{ff} and liquefaction strength R_{20}

CONCLUSION

The authors investigated an evaluation method using various void ratios as indicators for the liquefaction strength of sand and sandy soil through experiments. As a result, the following findings were obtained.

(1) In the region with a skeletal pore ratio es that does not exceed the maximum pore ratio of sand only ($e_s < e_{max}$), the fine fraction makes no difference to the liquefaction strength. And the liquefaction strength R_{20} is categorically related to the "Skeleton void ratio e_s", notwithstanding the type of fine fraction.

(2) With a skeleton void ratio es above the maximum void ratio for sand only ($e_s > e_{max}$), the liquefaction strength R_{20} has a good correlation with the "Fine fraction void e_{ff}" in the region where the fine fraction is predominant.

(3) With a skeleton void ratio es above the maximum void ratio for sand only ($e_s > e_{max}$), The liquefaction strength and the Fine fraction void ratio e_{ff} are not uniquely related, and the liquefaction strength tends to change depending on the difference in the plasticity index of fine fraction.

REFERENCES

[1] Kazama M., Kagatani T., Yanagisawa E., Peculiarities of liquefaction resistance of masado, Journal of JSCE No.645/III-50 pp153-160, 2000. (In Japanese only)

[2] Kuwano J., Iimura H., Nakazawa H., Sugihara K., Liquefaction strength of sand containing kaolin clay , 50th JSCE Annual meeting, pp.506-507, 1995. (In Japanese only)

[3] Yazima J., Numata Y., Nkane A., A Study on liquefaction strength evaluation methods and liquefaction properties of fine containing sand, Journal of JSCE No.624/III-47, pp.113-122, 1999.6 (In Japanese only)

[4] Ishikawa S., Masayuki H., Ikuko S., Rolando O., Nakata Y., Norimasa Y., Cyclic shear properties of non-plastic low plastic fine fraction mixed soil, 42nd JGS Annual meeting, pp.158-159, 2007. (In Japanese only)

[5] Nabeshima Y., Nagasaw T., Tamotsu M., Evaluation of liquefaction strength of sands containing fines based on clay fraction, 38th JGS Annual meeting, pp.239-240, 2003. (In Japanese only)

[6] Liu W., Kamao S., Yokoyama K., Effect of fines content on liquefaction characteristics, 10th Int. Conf. on Geotechnique, Construction Materials and Environment, Melbourne, Australia, 11-13 November 2020

[7] Liu W., Ishii K., Kamao S., Effect of fines content on liquefaction characteristics, International Journal of GEOMATE, June., 2021, Vol.20, Issue 82, pp.40-45

[8] Sato M., Oda M., Kazama H., Ozeki K., Fundamental study on the effect of fines on liquefaction strength of reclaimed ground, Journal of JSCE No.561/III-38, pp.271-282, 1997. (In Japanese only)

[9] Thevanayagam S., Shenthan T., Mohan S., Liang J., Undrained fragility of clean sands, silty sands, and sandy silts, Journal of geotechnical and geoenvironmental engineering 128 (10), pp.849-859, 2002.

11th Int. Conf. on Geotechnique, Construction Materials & Environment,
Kyoto, Japan, 3-5 November 2021, ISBN: 978-4-909106063 C3051

MONITORING AND PREDICTION OF SETTLEMENT USING ASOKA METHOD AND HYPERBOLA METHOD WITH PREFABRICATED VERTICAL DRAIN AS GROUND IMPROVEMENT METHOD

Muhammad Haziq Taqiuddin bin Rezuwan[1], Saiful Azhar bin Ahmad Tajudin[2]

[1]Faculty of Civil Engineering and Built Environment, University Tun Hussein Onn, Malaysia,

ABSTRACT

Surcharge preloading together with prefabricated vertical drains (PVDs) have been widely used to improve properties of thick clay deposits to accelerate consolidation settlement. To assess the performance of soil improvement works, the average degree of consolidation needs to be estimated. Based on the formula, Hyperbola method and Asoka method is proposed to predict the ultimate settlement and calculate the coefficient of consolidation using field settlement monitoring data. This research compares the effectiveness and accuracy of Hyperbola method against Asoka method compared to predicted design settlement through the analysis of the degree and time of consolidation. Comparisons between the Hyperbola method and the Asoka method indicate that Hyperbola method give a less than 1.0% higher ultimate settlement than the Asoka method if initial data on 60% consolidation were not recorded. The results show a close relationship between the stability of predicted results by curve fitting methods when monitoring work done between days 380 till days 540.

Keywords: Settlement, Asoka, Hyperbola,

INTRODUCTION

For clay deposit improvement, preloading method is generally used by using surcharge fill and Prefabricated Vertical Drains (PVDs) [1]. As an alternative method to improve soft soil condition [2], PVDs are made to counter structural failure due to settlement by increasing the soil shear strength, decreases compressibility of soil and impede on reduction of substantial consolidation [3], [4]. Degree of soil improvement is evaluated by estimating the average Degree of Consolidation. Degree of consolidation is current settlement percentage to ultimate primary consolidation settlement [5]. There are several empirical and predictive models of curve fitting systems, such as the Hyperbola method and the Asoka method [6], [7].

However, the potential and effectiveness for both methods are still in study to justify its accuracy. Especially on cases using prefabricated vertical drain for marine clay [5], [8]. Several justifications stated that Hyperbola method are more accurate than Asoka method yet over predicted. On the other hand, Asoka method are much more accurate, but it predicted the value slight smaller than predicted settlement [9]–[11]. Thus, from this observation which method are more accurate when predict settlement and the result are close by to actual designed settlement. However, in this research initial data on 60% consolidation were not recorded on settlement gauge and settlement marker. Furthermore, settlement marker was installed after surcharge rest period. This condition will bring controversy on accuracy for both method and allowable adjustment during data analysis.

SITE DESCRIPTION AND MEASUREMENT

This research is focus on evaluate, predict and determine the settlement using Asoka method and Hyperbola method. The study is Located at Kampung Jawa, Parit Jalil, Batu Pahat, Johor. Figure 1 shows the location of the field test at Kampung Jawa, Parit Jalil, Batu Pahat, Johor

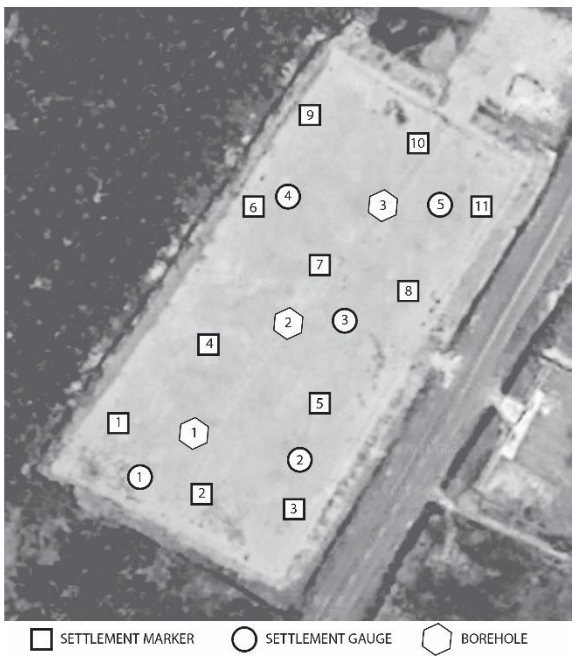

Fig. 1 Site location and detail at Kampung Jawa

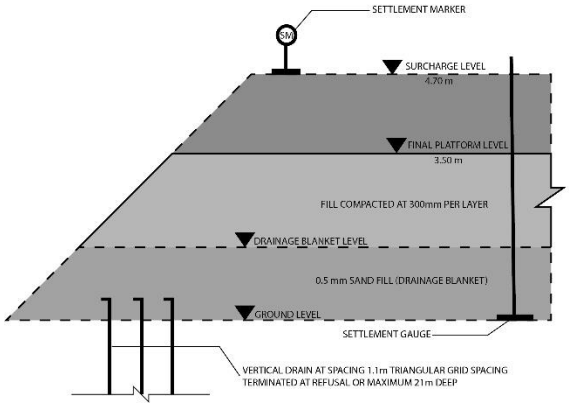

Fig. 2 Cross-section of ground treatment with PVD and surcharge

Generally, this site consists of 5 settlement gauge and 11 settlement markers install in the site as shown in figure 1 and figure 2. Three boreholes were drilled to provide information as reference for settlement analysis. The structures of the soil for the site were consistent with clayey type of soil. Surcharge and Prefabricated vertical drain (PVD) were applied through the whole site. The detail for both ground improvement method was summarized as below:

Table 1: Surcharged and Prefabricated Vertical Drain (PVD) summary

No.	Description	BH1	BH2	BH3
1	PVD Spacing	1.1 m	1.1 m	1.1 m
2	PVD Length	21 m	21m	21 m
3	Clay thickness	21 m	21 m	18 m
4	Surcharge Height	1.3 m	1.3 m	1.3 m
5	Embankment Height	2.5 m	2.5 m	2.5 m
6	Total height	3.8 m	3.8 m	3.8 m
7	Predicted settlement	1.034 m	1.101 m	0.993 m
8	Degree consolidation	90 %	90 %	90 %

GRAPHICAL METHOD IN PREDICTIING GROUND SETTLEMENT

In this research, two field tests are conducted to monitor the settlement. Hence, other relevant theories were used to justify and predict the ultimate settlement.

ASOKA METHOD

Asoka method [12] is based on the one-way consolidation equation of Terzaghi [6], its linear fitting equations (Fig. 3 & Fig. 4) as follows [13]:

$$S_{tj} = \beta_0 + \beta_1 S_{tj-1} \quad (1)$$

Since β0 and β1 indicate undetermined constants and independent, the time series data will be plotted via same straight line. When S_{tj} equals $S_{tj\text{-}1}$, final settlement S_∞ can be calculated by formula:

$$S_\infty = \beta_0 / (1 - \beta_1) \quad (2)$$

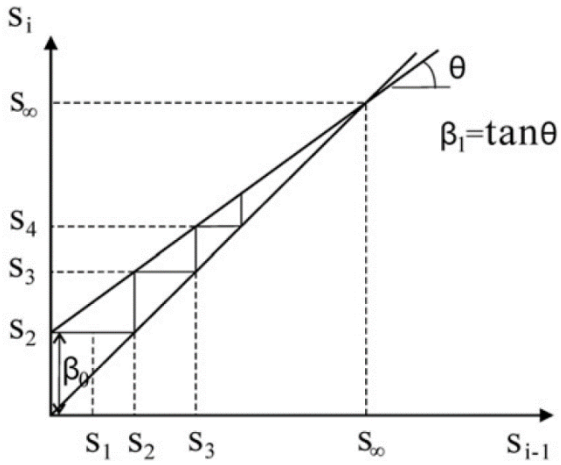

Fig. 3 Graphical plot of Asoka method [9]

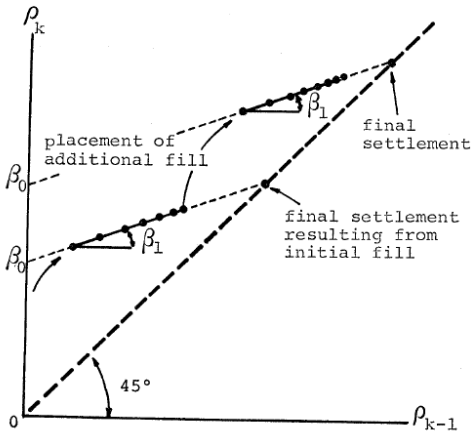

Fig 4 Asoka method for settlement prediction [12]

The accuracy of Asoka method depends on time interval. The longer the time, the higher the accuracy.

HYPERBOLA METHOD

It is assumed that the settlement rate of ground decreases with time in hyperbola method [6], [14], [15], the settlement calculation formula of hyperbola method [14], [11] is as follows:

$$S_t = S_0 + \frac{t - t_0}{\alpha + \beta(t - t_0)} \quad (3)$$

In the formula**,** t_0 and S_0 respectively indicate the observation time and the settlement of the starting point in the fitting calculation; t and St respectively indicate any time point of fitting curve and the corresponding settlement; α and β respectively indicate the intercept and slope of the line. When the parameter t tends to be infinite, final settlement S_∞ could be obtain by using [16]:

$$S_\infty = S_{0+} \frac{1}{\beta} \quad (4)$$

After a period of loading, residue settlement ΔS can be calculated by formula:

$$\Delta S = S_\infty - S_t \quad (5)$$

The S_{60} and S_{90} slope can be determine by:

$$S_{60} = S_i \frac{\propto_{60}}{\propto_i} \text{ and } S_{60} = S_i \frac{\propto_{60}}{\propto_i} \quad (6)$$

Where ultimate primary settlement can be obtained by following ratio:

$$\delta_f = \frac{\propto_i}{s_i} = \frac{\delta_{60}}{0.6} = \frac{\delta_{60}}{0.9} \quad (7)$$

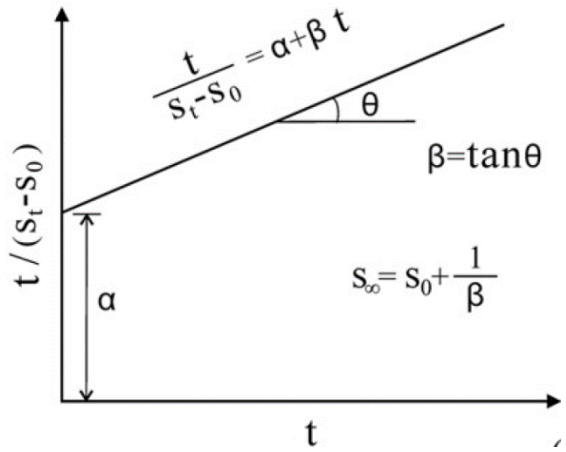

Fig.4 Hyperbola method for settlement prediction [9]

In reality, due to the fact that settlement assessment at the beginning of consolidation is often not taken, it is more efficient to use $(t - t_i)/(s - s_i)$ versus $(t - t_i)$, where S_i are settlement after time as shown in Fig. 4. This method of plotting is also useful as it allows the results to be reinitialized whenever appropriate [17].

PREDICTION OF ULTIMATE SETTLEMENT

The calculation results of ultimate settlement of settlement gauge and settlement marker based on two methods studied in this research. Monitoring work were done between days 380 till days 540. The data obtain were analyze and summarized in table 2 and table 3.

ASOKA METHOD

The results show that predicted settlement for settlement gauge and settlement marker were different by using Asoka and Hyperbola method. As a result of different initial data record for settlement marker and settlement gauge, the predicted data using both method for both instruments were also contribute to different result.

Settlement marker were installed and monitored after embankment are almost filled while settlement gauge was installed and monitored during initial ground level. From this case, the monitoring record affect the prediction of the ultimate settlement using Asoka and Hyperbola method as shown in table 2 and table 3.

Table 2: Ultimate Settlement for Settlement Marker using both method

Soil Instrument	Predicted Design Settlement	Method	
		Asoka	Hyperbola
	S_{ult} (mm)	S_{ult} (mm)	S_{ult} (mm)
SG 01	1034	1100	2380.4
SG 02		1225	2297.2
SG 03	1100	1060	1943.8
SG 04		1050	1997.6
SG 05	993	1386	2632.2

Table 3: Ultimate Settlement for Settlement Gauge using both method

Soil Instrument	Predicted Design Settlement	Method	
		Asoka	Hyperbola
	S_{ult} (mm)	S_{ult} (mm)	S_{ult} (mm)
SM 01	1034	650	1152
SM 02		650	856
SM 03		410	707
SM 04		690	1064
SM 05		620	798
SM 06	1100	643	1120
SM 07		520	-

SM 08		595	963
SM 09		560	1124
SM 10	993	700	1458
SM 11		600	1296

Based on Asoka plot for settlement gauge (Fig 5, Fig 6, Fig 7, Fig 8 and Fig 9) and settlement marker (Fig 10, Fig 11, Fig 12, Fig 13, Fig 14, Fig 15, Fig 16, Fig 17, Figure 18, Figure 19, Figure 20) shows that settlement are linearly increase proportional to settlement [18].

According to Asoka method [12], the predicted ultimate settlement were obtain from previous observation time series of settlement data. from Eq. 1, a line of best fit was constructed, and the predicted ultimate settlement determined from the interception of $\boldsymbol{\beta_1}$ with the 45^o line.

However, Table 2 and Table 3 shows that the predicted ultimate settlement obtained from settlement gauge were more identical than settlement marker. Since time interval of settlement monitoring for settlement gauge were much longer than settlement marker, the accuracy to attain predicted ultimate settlement were much higher considering self-reliant period of $\boldsymbol{\beta_1}$ and $\boldsymbol{\beta_0}$.

The time interval of monitoring for settlement gauge were begin after 386 days while settlement marker was on initial stage of 14 days. Therefore, the predicted ultimate settlement of settlement gauge was in average of 1000mm to 1300mm while settlement marker was in between 600mm to 650mm.

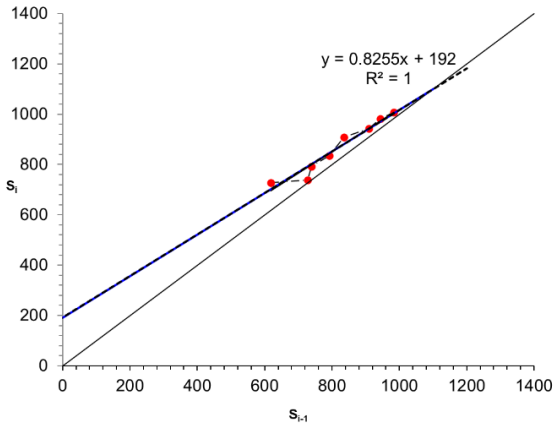

Fig. 5 Asoka plot for Settlement Gauge, SG 01

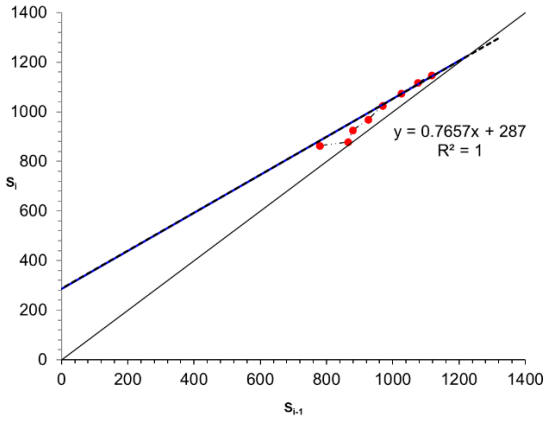

Fig. 6 Asoka plot for Settlement Gauge, SG 02

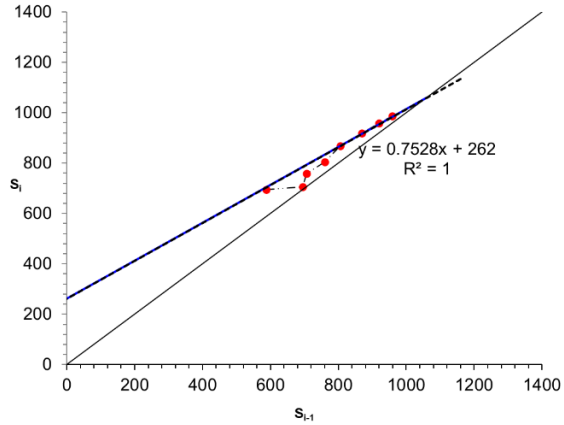

Fig. 7 Asoka plot for Settlement Gauge, SG 03

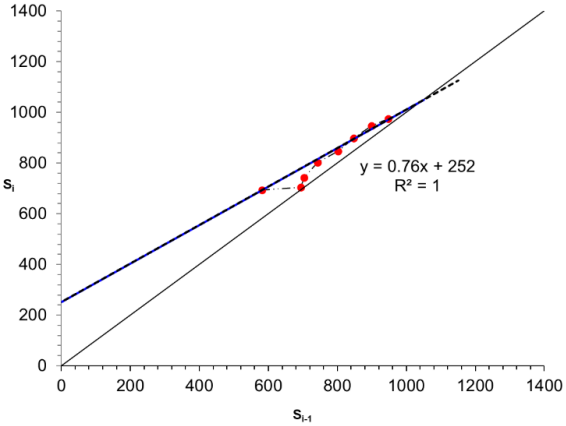

Fig. 8 Asoka plot for Settlement Gauge, SG 04

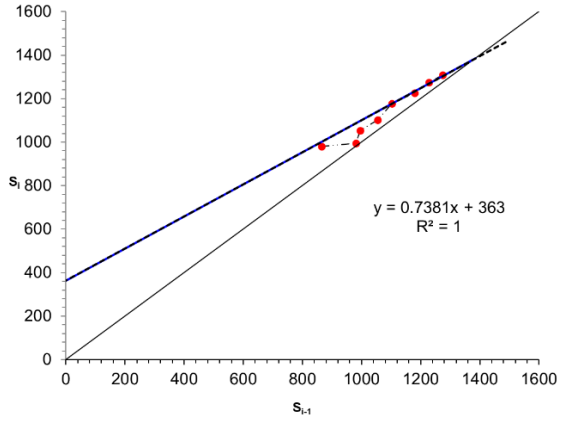

Fig. 9 Asoka plot for Settlement Gauge, SG 05

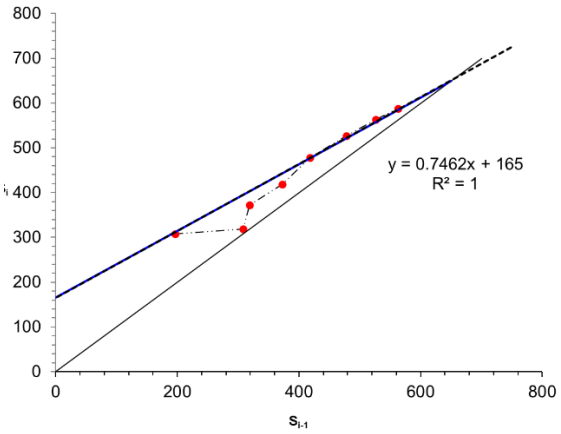

Fig. 10 Asoka plot for Settlement Marker, SM 01

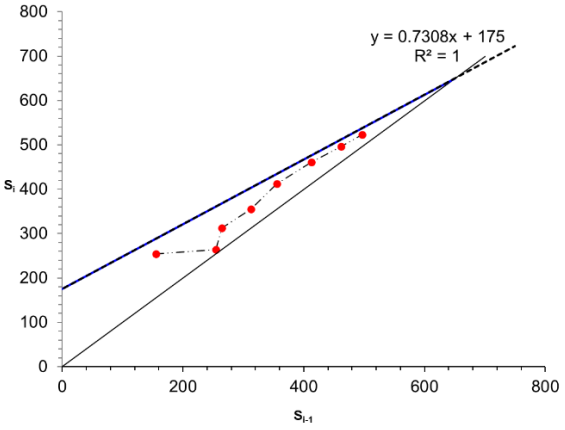

Fig. 11 Asoka plot for Settlement Marker, SM 02

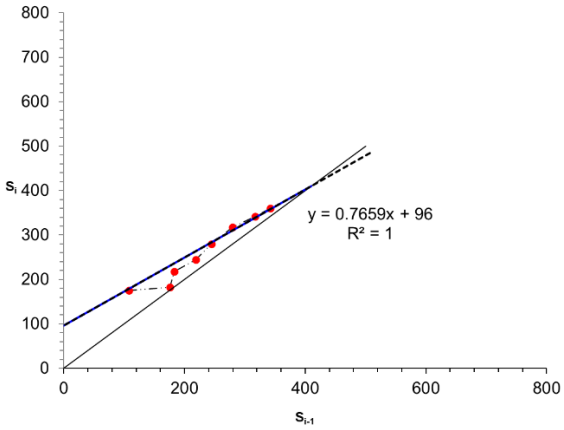

Fig. 12 Asoka plot for Settlement Marker, SM 03

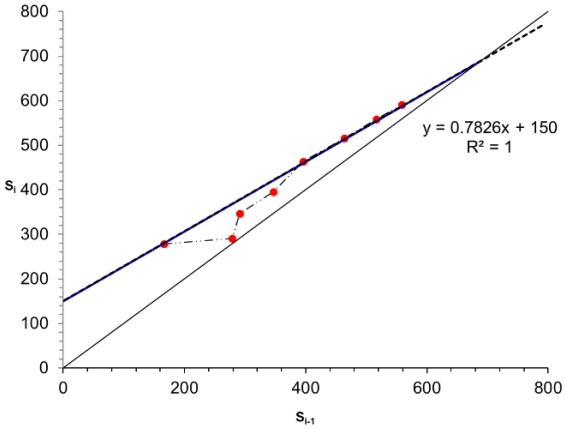

Fig. 13 Asoka plot for Settlement Marker, SM 04

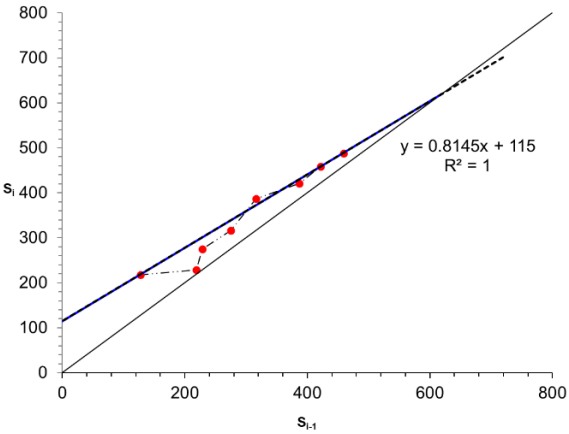

Fig. 14 Asoka plot for Settlement Marker, SM 05

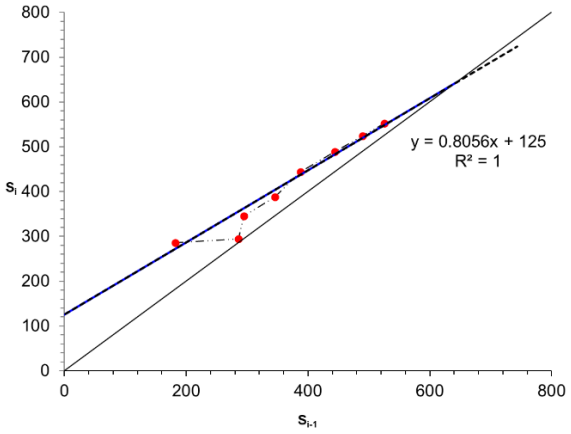

Fig. 15 Asoka plot for Settlement Marker, SM 06

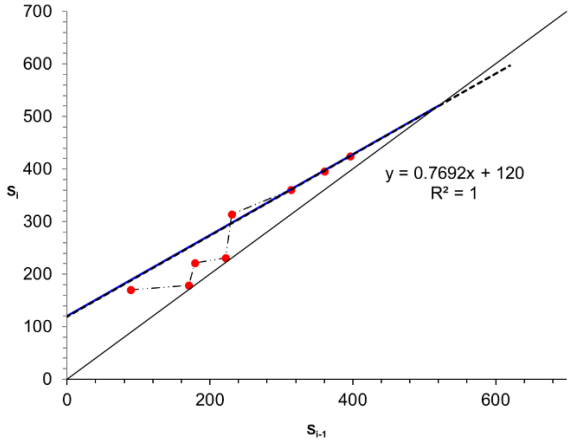

Fig. 16 Asoka plot for Settlement Marker, SM 07

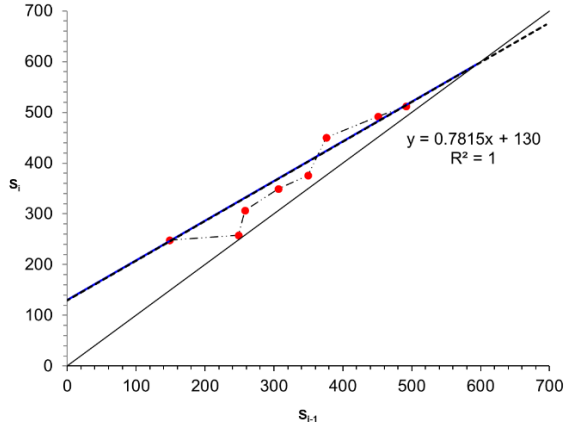

Fig. 17 Asoka plot for Settlement Marker, SM 08

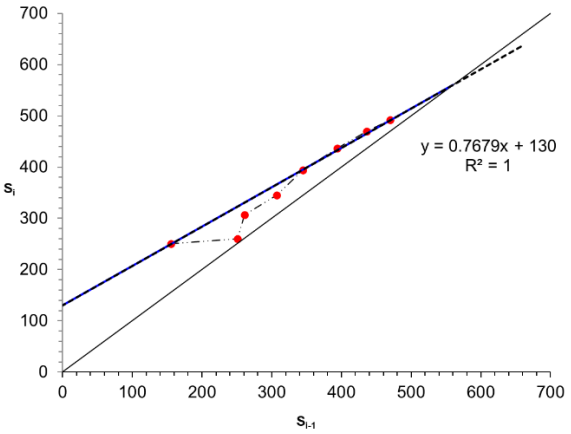

Fig. 18 Asoka plot for Settlement Marker, SM 09

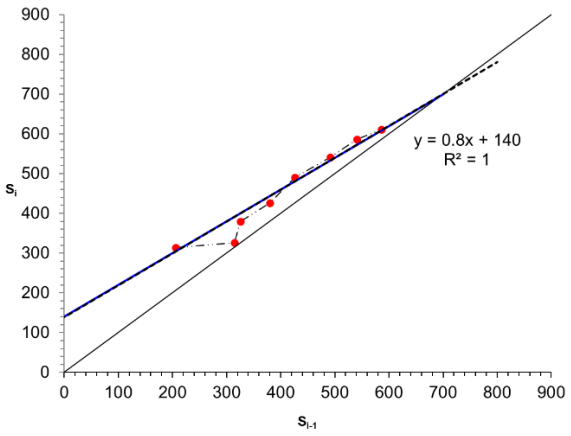

Fig. 19 Asoka plot for Settlement Marker, SM 10

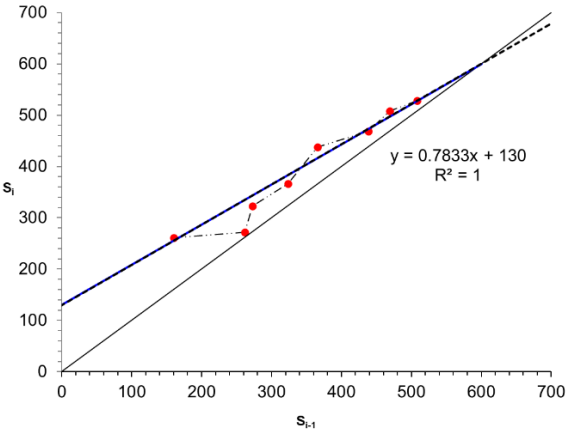

Fig. 20 Asoka plot for Settlement Marker, SM 11

HYPERBOLA METHOD

According to Hyperbola method [14] the predicted ultimate settlement were obtain based on field data which in this case, the collected data during monitoring work. From Eq. (4), it is more reasonable to use to obtain S_i because it allows to re-compute the result on any needed occasion and if another load is added. Especially on consolidation with non-homogeneous and non-linear properties.

Based on the hyperbolic plot for settlement marker (Fig 26, Fig 25, Fig 26, Fig 27, Fig 28, Fig 29, Fig 30, Fig 31, Figure 32, Figure 33, Figure 34), it is shows that the data follows a hyperbola pattern and possible to predict the ultimate settlement, ultimate settlement at 60% and 90% stages [15]. However, due to the monitoring record did not consist of initial level of the field reading, the hyperbolic plot misses the early stage of information to construct a best fit curve. Especially for settlement gauge (Fig 21, Fig 22, Fig 23, Fig 24, Fig 25).

Therefore, settlement gauge hyperbolic line did not intersect with t_{60} and t_{90} line while settlement marker only intercept on t_{90} line during initial plot both data. Although the analysis may be not accurate, hyperbola method [14] were still possible although the pattern were nonlinear and initial stage are nonhomogeneous.

Considering 90% of max settlement must be achieved to obtain the ultimate settlement [6], [17], by increase the maximum value of time over settlement, t_s the t_{60} and t_{90} value that corresponding to $t_{60/s}$ and $t_{60/s}$ from settlement gauge hyperbola graph were obtain although maximum value of t_s must be based on current maximum value of t_s. From this modification, the result as shown on settlement gauge hyperbola plot (Fig 21, Fig 22, Fig 23, Fig 24, Fig 25) clearly indicate that hyperbola method was not bounded to limited settlement.

Therefore, the justification influences the respective settlement gauge data as well as values of intersection of S_{60} and S_{90} when intersect with Hyperbola curve. Hence, to attain the value of t/δ_{60} and t/δ_{90} that correspond to the intersection point of S_{60} and S_{90} and the hyperbolic curve. Next, the value of δ_{60} and δ_{90} are calculated which give the determination of ultimate settlement, ultimate settlement at 60% and 90% stage. However, due to the maximum value of time over settlement, t_s increase, the predicted ultimate settlement will also increase.

Moreover, settlement marker 07 were unable to plot hyperbolic graph. This case was able to be expected because during filling surcharge work on 42 days. The settlement marker was missing and unable to relocate and retrieved. So, a new settlement marker 07 were establish and off set 1 meter from original location. Therefore, the settlement reading afterward were unable to comply with first reading from original location. Hence, effect the best fit line of hyperbola curve even though the value of the settlement is modified.

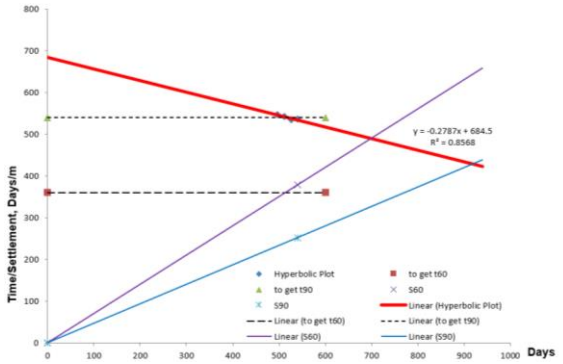

Fig. 21 Hyperbola plot for Settlement Gauge, SG 01

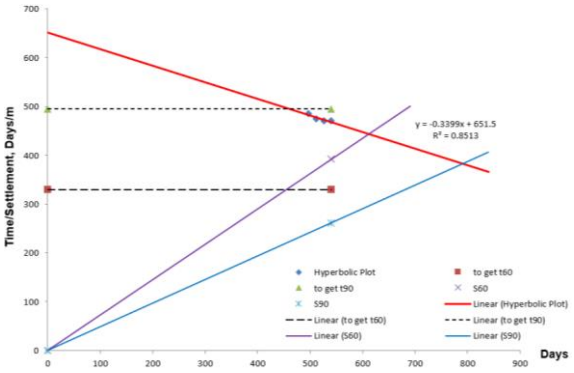

Fig. 22 Hyperbola plot for Settlement Gauge, SG 02

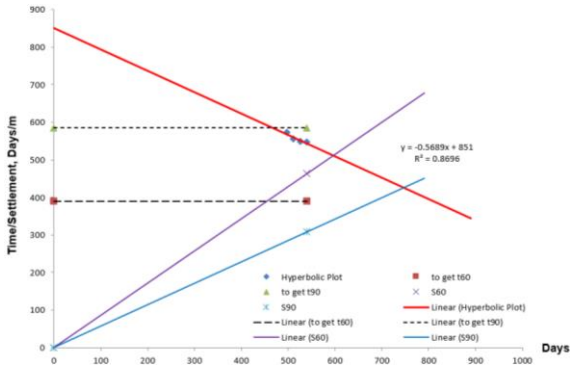

Fig. 23 Hyperbola plot for Settlement Gauge, SG 03

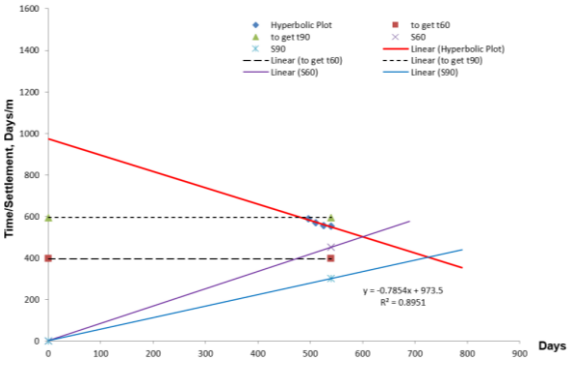

Fig. 24 Hyperbola plot for Settlement Gauge, SG 04

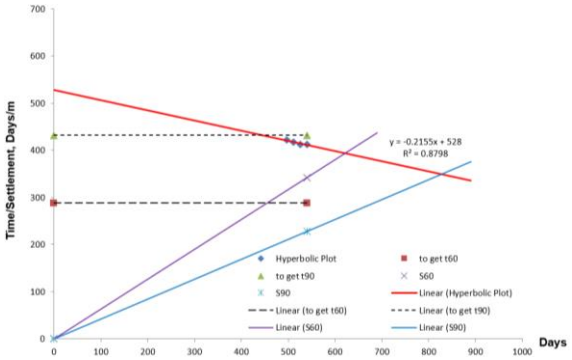

Fig. 25 Hyperbola plot for Settlement Gauge, SG 05

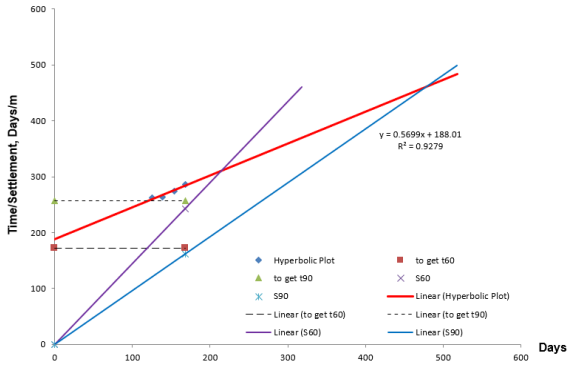

Fig. 26 Hyperbola plot for Settlement Marker, SM 01

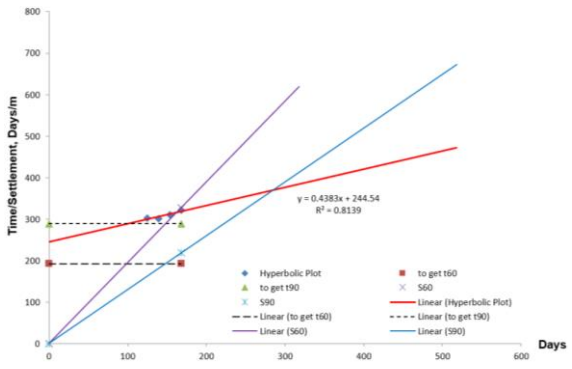

Fig. 27 Hyperbola plot for Settlement Marker, SM 02

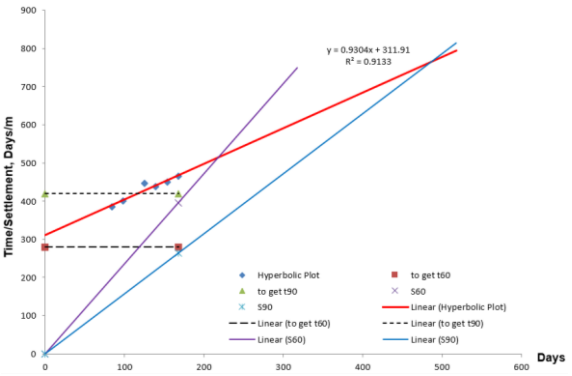

Fig. 28 Hyperbola plot for Settlement Marker, SM 03

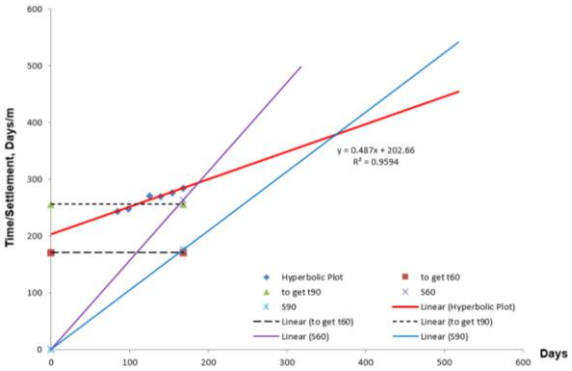

Fig. 29 Hyperbola plot for Settlement Marker, SM 04

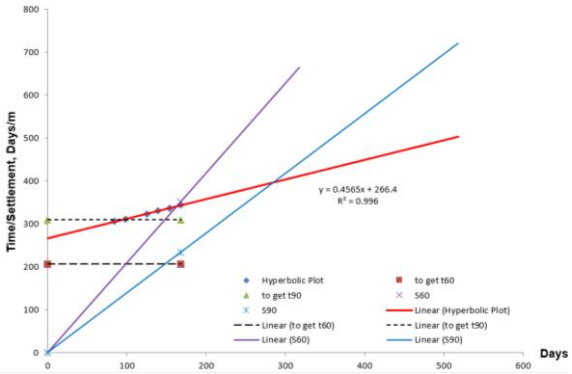

Fig. 30 Hyperbola plot for Settlement Marker, SM 05

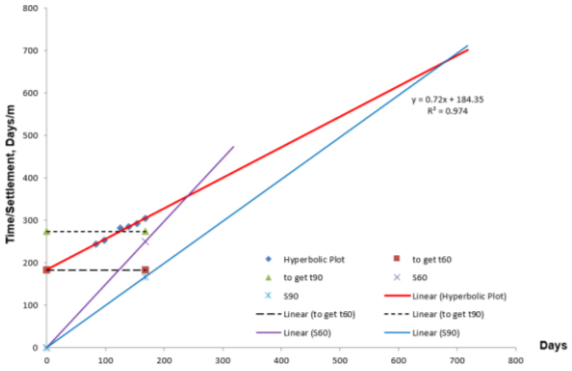

Fig. 31 Hyperbola plot for Settlement Marker, SM 06

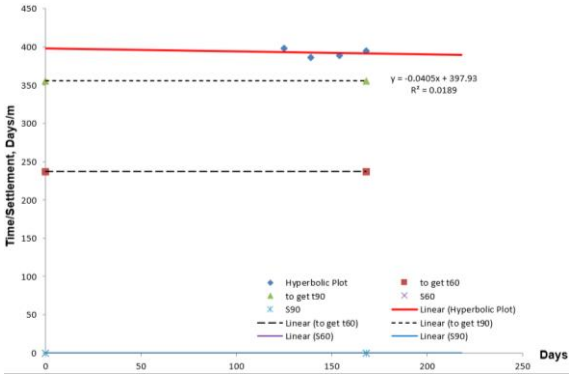

Fig. 32 Hyperbola plot for Settlement Marker, SM 07

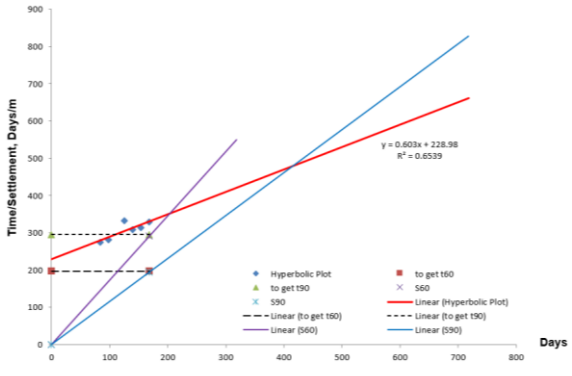

Fig. 33 Hyperbola plot for Settlement Marker, SM 08

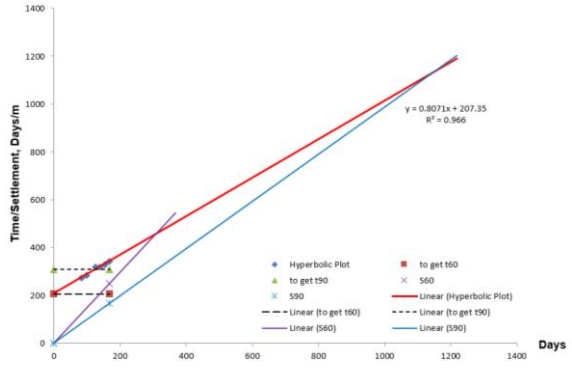

Fig. 34 Hyperbola plot for Settlement Marker, SM 09

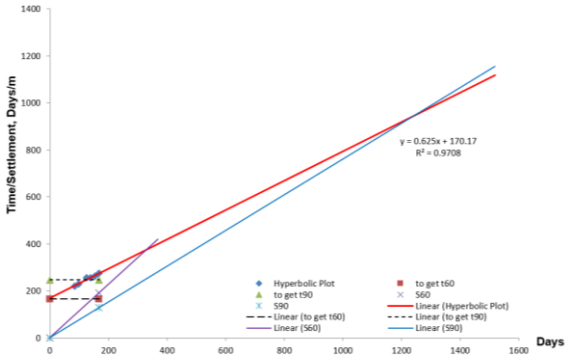

Fig. 35 Hyperbola plot for Settlement Marker, SM 10

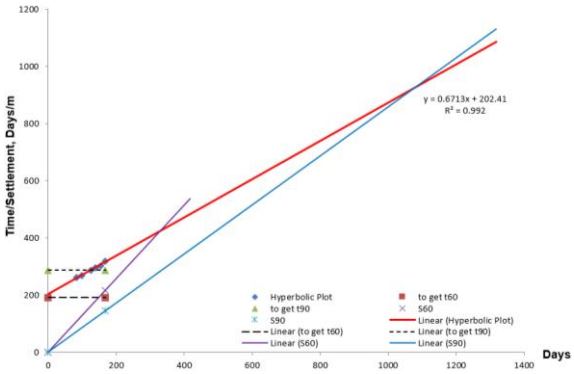

Fig. 36 Hyperbola plot for Settlement Marker, SM 11

CONCLUSION

Based on the settlement record, it can be concluded that both methods require settlement data beyond 60% consolidation stage to provide accurate predictions. However, if the initial settlement data from settlement marker and settlement gauge were unrecorded, the prediction using Asoka method were 90% more accurate than Hyperbola method.

Asoka method graph consist of current settlement versus previous settlement plot and simpler. It had more advantage and accurate when predicting short-term settlement. This is because, it relies on previous monitoring data. However, if the time interval is longer, the prediction will more accurate and identical with actual design settlement. Although the data obtain were only a few months it manages to predict the settlement, but it will underestimate the prediction as the data time interval were shorter.

Hyperbola method had disadvantage on this condition. Due to hyperbola method relies on construction settlement data that need more detail and

numbers of data. This is because the plot consists of time over settlement versus time. The longer the period the tendency to predict of the settlement will more accurate although it was slightly tedious and complex. From this observation, if hyperbola method data are not satisfying it tend to overestimate the ultimate settlement.

ACKNOWLEDGEMENT

Special thanks to Hidayat, Ain, Ayme, Ashraf, Iqbal, Faid and Faiq for their help during soil sampling and monitroring work. Hence, special appreciation and recognition to those who contribute directly and indirectly in this finding.

REFERENCES

[1] M. W. Bo, A. Arulrajah, S. Horpibulsuk, A. Chinkulkijniwat, and M. Leong, "Laboratory measurements of factors affecting discharge capacity of prefabricated vertical drain materials," *Soils Found.*, vol. 56, no. 1, pp. 129–137, 2016.

[2]J. D. Hussin, "Methods of soft ground improvement," *Found. Eng. Handb.*, pp. 529–565, 2006.

[3] A. Suhendra, R. P. Putra, and F. Absari, "Effectiveness study of prefabricated vertical drain using vacuum preloading and surcharge preloading," *Earth Environ. Sci.*, 2018.

[4] L. G. Lam, D. T. Bergado, and T. Hino, "PVD improvement of soft Bangkok clay with and without vacuum preloading using analytical and numerical analyses," *Geotext. Geomembranes*, vol. 43, no. 6, pp. 547–557, 2015.

[5] W. Guo, J. Chu, and W. Nie, "An observational method for consolidation analysis of the PVD-improved subsoil," *Geotext. Geomembranes*, vol. 46, no. 5, pp. 625–633, 2018.

[6] B. Ahcène and B. Mohamed, "Comparative study of four consolidation settlement estimation methods of a railway," vol. 06002, pp. 1–15, 2017.

[7] S. G. Chung, H. J. Kweon, and W. Y. Jang, "Observational method for field performance of prefabricated vertical drains," *Geotext. Geomembranes*, vol. 42, no. 4, pp. 405–416, 2014.

[8] R. B. Kelly, S. W. Sloan, J. A. Pineda, G. Kouretzis, and J. Huang, "Outcomes of the Newcastle symposium for the prediction of embankment behaviour on soft soil," *Comput. Geotech.*, vol. 93, pp. 9–41, 2018.

[9] H. Il Park, K. S. Kim, and H. Y. Kim, "Field performance of a genetic algorithm in the settlement prediction of a thick soft clay deposit in the southern part of the Korean peninsula," *Eng. Geol.*, vol. 196, pp. 150–157, 2015.

[10]M. Zhang, J. J. Li, and C. H. K. Qin, "Analysis and discussion on post-construction settlement of soft soil foundation treatment test section of highway," *IOP Conf. Ser. Earth Environ. Sci.*, vol. 81, no. 1, pp. 0–7, 2017.

[11]W. Zhu, J. Yan, and G. Yu, "Vacuum preloading method for land reclamation using hydraulic filled slurry from the sea: A case study in coastal China," *Ocean Eng.*, vol. 152, no. February, pp. 286–299, 2018.

[12]A. Asaoka, "NII-Electronic Library Service," *Soils Found.*, vol. 18, no. 4, 1978.

[13]S.-H. C. Siew-Ann Tan, "Comparison of the Hyperbolic and Asoka Observational Method of Monitoring Consolidation with Vertical Drains," *Chem. Pharm. Bull.*, vol. 17, no. 11, pp. 1460–1462, 1994.

[14]T. Tan, A. Member, T. Inoue, and S. Lee, "Hyperbolic Method for Consolidation Analysis," *Geotech Eng.*, vol. 117, no. 11, pp. 1723–1737, 1992.

[15]T. Shin, Yeon-Sil Mori, Takeshi Okita, Masatsugu Gemma, Tsuyoshi Kai, Chieko Mikami, "Validation of Hyperbolic Method for Settlement in Clays with Vertical Drains," *Soils Found.*, vol. 35, no. 1, pp. 101–113, 1995.

[16]A. J. Puppala, P. Ruttanaporamakul, and S. S. C. Congress, "Design and construction of lightweight EPS geofoam embedded geomaterial embankment system for control of settlements," *Geotext. Geomembranes*, vol. 47, no. 3, pp. 295–305, 2019.

[17]M. A. Al-Shamrani, "Applying the hyperbolic method and Cα/Cc concept for settlement prediction of complex organic-rich soil formations," *Eng. Geol.*, vol. 77, no. 1–2, pp. 17–34, 2005.

[18]R. Nazir, H. Moayedi, P. Subramaniam, and S. Ghareh, "Ground improvement using SPVD and RPE," *Arab. J. Geosci.*, vol. 10, no. 23, 2017.

11th Int. Conf. on Geotechnique, Construction Materials & Environment,
Kyoto, Japan, 3-5 November 2021, ISBN: 978-4-909106063 C3051

AN EXPERIMENTAL STUDY ON TEMPERATURE EFFECTS ON ELASTIC AND CREEP DEFORMATION BEHAVIOURS OF A SAND

Yodphao Punya-in[1], and Warat Kongkitkul[2]

[1,2]Department of Civil Engineering, Faculty of Engineering,
King Mongkut's University of Technology Thonburi, Thailand

ABSTRACT

An automated triaxial loading system that can accurately control both the loading and temperature histories was developed. A series of unconventional triaxial compression tests with an air-dried sand sample were performed. Various loading histories consisting of: i) continuous monotonic loading (ML); ii) sustained (creep) loading (SL); and iii) cyclic loading (CL) with small amplitude were employed in this study. Shearing the sand sample with these different loading histories was performed under different but constant controlled temperatures surrounding the sample to study the temperature effects on the elastic and creep deformation behaviours of the sample. The followings are found from the experimental results. The peak and residual shear strengths tend to decrease with an increase temperature. The equivalent elastic Young's modulus increases with increasing stress level in a hypo-elasticity manner, but at the same stress level, it decreases significantly with increasing temperature. Creep strain is obvious and it increases with the increasing stress level and temperature.

Keywords: Triaxial test, Shear strength, Elastic, Creep, Temperature, Sand

INTRODUCTION

In a number of geological and geotechnical engineering projects such as nuclear waste repositories [1], high voltage electric cables [2], energy piles [3] - [5], thermally-active embankments [6], thermally-active retaining walls [7], geothermal tunnel linings [8], highway pavements [9], geosynthetic reinforced soil (GRS) structure [10], the soils are subjected to non-isothermal conditions [11]. That is, the ambient temperature surrounding them change cyclically or arbitrarily. Therefore, for such a circumstance, it is necessary to understand the stress-strain behaviours, which are affected by the change in the temperature. In the literature, the thermal effects on yield stress of clays have been widely investigated throughout temperature-controlled conditions such as triaxial compression test, one dimensional compression test and isotropic compression test [12] - [15].

The deformation characteristics of granular material (i.e., gravel and sand) at a small-strain level are important for many geotechnical engineering problems. For instance, they are necessary for a precise prediction of the settlement of the foundation supporting a megastructure or the ground movement caused by a deep excavation. In such cases, strains mobilised in the ground by working loads are usually smaller than about 0.1%, or at the largest, about 0.5% [16], [17]. At such a small-strain level, the soil behaviours are significantly elastic, and therefore the elastic deformation properties, i.e., the elastic stiffness, are essential design parameters.

The dependency of elastic properties of geomaterials on various factors have been investigated by many researches. For example, Kohata [18] performed a series of triaxial compression tests on Hostun sand sample employing a comprehensive loading history (e.g., cyclic loading during otherwise monotonic loading) and showed that the elastic deformation characteristics of granular materials depend on the stress state. Hitcher [19] investigated the elastic properties of various soil types (e.g., sand, gravel, clays) by subjecting them to very small strains in triaxial compression and extension. Elasticity was found to be nonlinear because the elastic modulus depends on the mean effective stress in a nonlinear manner. Although there are many studies on the dependency of elasticity on the stress-state in the literature, little has been attempted to investigate the effect of temperature on the elasticity of granular materials, especially for sands.

On the other hand, it is known that geomaterials also exhibit creep deformation upon sustained loading. Creep deformation depends on soil type, stress level, and so on. Tatsuoka [20] explained that creep is a deformational response due to the material viscous properties, and can be explained by a non-linear three-component model, by which creep depends on the initial strain rate, viscosity type, rate-sensitivity, stress level, and decay characteristic. The study by Lu [21] showed that the change of temperature can affect to the creep deformation of saturated marine deposit. Understanding creep deformation is an important key for predicting the long-term deformation of foundations of megastructures, whereas the immediate settlement can be predicted by the elastic properties.

Nevertheless, to the best of the authors' knowledge, little has been known on how the temperature alters the creep deformation of geomaterials, especially with the dried sand.

Among the limitedly available studies on the temperature effects on sands, most of them focused only on the shear strength behaviours. For instance, Liu [22] performed hollow cylinder tests on Fujian standard quartz sand sample. The sample was heated under a drained condition, and then isotropically-consolidated, and finally sheared under an undrained condition. Their test results showed that the shear-induced pore pressure of the heated quartz sand greatly increased, and thus weakening the shear strength. Shoa-Heng He [23] performed another test on a calcareous sand so as to compare with Fujian standard quartz sand. The sample was heated under a drained condition, subjected to K_0 consolidation, and then sheared under a drained condition. Their results showed that with increasing the temperature, the strength and dilatancy of the quartz sand are improved, but the opposite was found with the calcareous sand. This is because an increase in the temperature aggravated the particle breakage for the calcareous sand during shearing, while for the quartz sand the discharge of pore water and the densification.

In view of the above, this paper aims to study temperature effects on elasticity and stress - strain deformation behaviours of a sand by performing a series of special triaxial compression tests. An air-dried sample was used so that the complexity of setting up the triaxial loading system with a temperature control unit was minimized. This was also to avoid pore pressure induced by the heating, consolidation, and shearing stages. The sample once erected was subjected to heat until reaching the target temperature, after which held constant thorough the test. During the above-mentioned three stages, the sample was allowed to drain by connecting the specimen's inside to the atmosphere. The stress-strain deformation behaviours were studied by subjecting the sample to various loading patterns (i.e., monotonic loading, sustain loading, cyclic loading) under different constant controlled-temperatures.

TEST APPARATUS AND MATERIAL

Test apparatus

A new temperature-controlled triaxial test apparatus shown in Fig. 1 has been developed in the present study. It consists of: i) a cylindrical cell of which the cell water pressure is automatically controlled by an electro-pneumatic (E/P) transducer and the cell water temperature by temperature control unit; and ii) an automatic axial loading system with a precise gear. The newly developed temperature control unit consists of a heater, a temperature controller unit and a circulating pump. A temperature transducer (k-type thermocouple) was installed inside the triaxial cell and connected to a computer for recording. Complicated shear loading histories (e.g., small-strain cyclic loading, creep) can be successfully performed by the precise gear loading system which can response sharply to control the loading directions and the speed [24]. After finishing the specimen preparation, the triaxial cell was then sealed and connected to the temperature control unit. Next, the cell water temperature was elevated to the target value by circulating the water throughout a heater located outside. The heater is automatically controlled by the temperature controlling unit. After achieving the target value, the temperature was maintained constant with an accuracy of ± 0.5 ◦C as shown in Fig. 2.

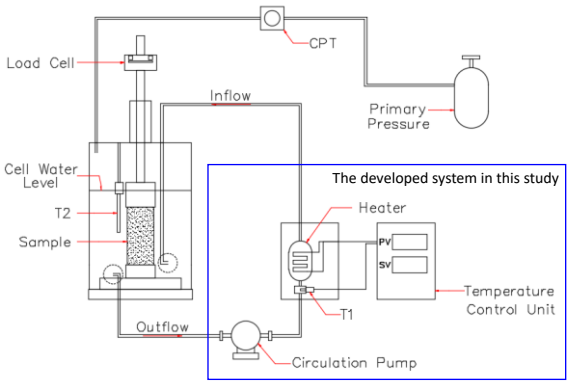

Fig. 1 Temperature-controlled triaxial test apparatus newly developed

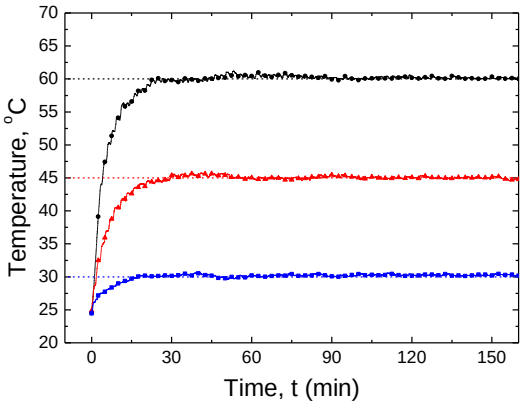

Fig. 2 Typical time histories of the measured temperature of the cell water

Test material

A river bed sand in Thailand was used as the test material in the present study. It was treated by sieving and only the portion that passed through the sieve no. 40 but retained on the sieve no. 100 was used. Then, it was cleaned by flushing with tap water to remove

any remaining fines attracted on the particle's surface, and then oven-dried. This sand is sub-angular in the grain shape. It has specific gravity (*Gs*) of 2.640, an effective particle size (D_{50} (of 0.285 mm, and a coefficient of uniformity (C_u) of 1.879 .The maximum and minimum void ratios are 1.035 and 0.665, respectively.

TEST METHOD

Specimen preparation

A split mould with the inner diameter of 70 mm and height of 150 mm was used to prepare the test sample. After adhering the membrane with the mould and placed on the pedestal, the sand was filled in by using the air pluviation technique [25] using a multiple-sieving apparatus so as to achieve high uniformity. The relative density in a range of 88 - 95 % was achieved by this method. Table 1 lists the values of initial void ratio and relative density for all the test specimens. After sealing the membrane with the top cap, a partial vacuuming with 20 kPa was applied to specimen so as to be able to remove the mould. The specimen was then waited for reaching an equilibrium stage for 30 min (Fig. 3a)). After sealing the triaxial chamber, the partial vacuuming was replaced by the cell water pressure by gradually increasing the cell water pressure and reducing the partial vacuuming at the same time until the cell water pressure reached 20 kPa. After that, the specimen was further isotropically consolidated until the confining pressure reached 30 kPa (Fig. 3b)). By maintaining the cell pressure constant at 30 kPa, the cell water was then circulated to the heater of the temperature control unit until reaching the target temperature. Another waiting period of 90 min was employed for allowing the specimen to achieve an equilibrium stage, and them the shearing process commences while holding the cell water temperature constant.

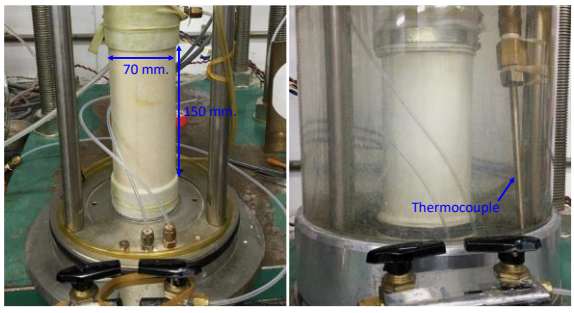

a) b)

Fig. 3 Preparation of the sand sample for triaxial compression test upon: a) applying a partial vacuuming of 20 kPa; and b) having been isotropically consolidated by the cell water pressure of 30 kPa.

Test program

In this study, a comprehensive series of shear loading histories were employed to investigate the elastic and creep deformation behaviours of the test sand. The details are listed in Table 1 and shown in Fig. 4, which can be described as follows.

Loading type a)-ML: Continuous monotonic loading (ML) is performed at a constant strain rate of 0.03 %/min.

Loading type b)-SL-CL: ML with the strain rate of 0.03%/min is performed until reaching the target stress ratio (*R*), after which the sustained loading (SL) is hold for three hours for allowing the test specimen to exhibit creep deformation. At the end of SL, the specimen is considered behaves significantly only elastic behaviour, by which cyclic loading with a double deviator stress amplitude (Δq) of 15 kPa (or equal to ΔR of 0.5) is applied for 10 cycles for evaluating the quasi-elastic Young's modulus (E_{eq}). After finishing CL, ML is restarted to the next target *R* value. For this loading type, the target *R* values are equal to 2.0, 3.5, and 5.0.

Loading type c)-SL-CL: This loading type is the same as the loading type b), except the values of target *R* are equal to 2.75, 4.25, and 5.75.

For each loading type mentioned above, the cell water temperature surrounding the test specimen is controlled constant at either 30 ºC, 45 ºC, or 60 ºC throughout the shearing process. This range of temperature is consistent with the values used in the studies with sands by Hong Liu [22] and Shao Heng-he [23]. In addition, there was also limitation of the triaxial loading system used in the present study in that: i) there was no system to cool down the temperature below the room temperature; and ii) the maximum temperature was limited at 60 ºC for avoiding any damage to the measuring devices (e.g., pressure transducer).

Table 1 Triaxial compression test program with different shearing histories and different temperatures

Test No.	e_0 (-)	*Dr* (%)	Loading Type	*T* (ºC)	Target *R*
1	0.686	94.39	a)-ML	30	-
2	0.695	92.02	a)-ML	45	
3	0.707	88.52	a)-ML	60	
4	0.703	89.73	b)-SL-CL	30	2, 3.5, 5
5	0.717	85.87	b)-SL-CL	45	
6	0.714	86.72	b)-SL-CL	60	
7	0.689	93.41	c)-SL-CL	30	2.75, 4.25, 5.75
8	0.683	95.10	c)-SL-CL	45	
9	0.691	93.05	c)-SL-CL	60	

TEST RESULTS AND DISCUSSION

Effect of temperature on shear strength

Fig. 5 shows the relationships between the stress ratio (R) and axial strain (ε_a) obtained with loading type a)-ML for different temperatures. With increasing temperature surrounding the test specimen, the R - ε_a relationships observably degrade. The shear strength of the test sand can be expressed in terms of internal friction angles at the peak state, ϕ_{peak}, from R at the peak state, and at the residual state, ϕ_{res}, from R at the residual state defined at the ε_a equal to 12%. Due to the sand used in the experiment was very clean without any fines, the cohesion was assumed null. Thus the internal friction angle can be determined from the test employing only a single value of confining pressure as shown in Eq. (1). The values of the R and ϕ at the peak and residual states are listed in Table 2. It can be seen that both ϕ_{peak} and ϕ_{res} tend to decrease with increasing temperature. In addition, it may be seen from Fig. 5 that not only the shear strength but also the stiffness of the R - ε_a relationship decreases with an increase in the temperature. This issue is discussed in detail later in this paper.

$$\phi = \sin^{-1}\left(\frac{R-1}{R+1}\right) \quad (1)$$

Table 2 Strengths of test KMUTT sand obtained from ML with different constant temperatures

T (ºC)	R_{peak}	ϕ_{peak}	R_{res}	ϕ_{res}
30	7.052	48.73	5.752	44.73
45	6.849	48.18	5.067	42.09
60	6.720	47.81	4.465	39.35

Stress-strain relationships during cyclic loading

Fig. 6a) and 6b) show the relationship between R and ε_a for different constant temperatures with loading type b)-SL-CL and c)-SL-CL, respectively. In these tests, CLs were performed by unloading-reloading for 10 cycles with a small stress-amplitude (Δq) of 15 kPa at different specified R values, applied after SL has been completed, during otherwise ML at a constant strain rate. The trends of R - ε_a behaviours from loading types b) - SL-CL and c) - SL-CL can be described as follows.

1. The R-εa relationships for different temperatures tend to rejoin to the respective ones that could be obtained by continuous ML tests without intermission of SL and CL. This importantly implied that the peak shear strength is maintained, while is not degraded with SL and CL applied at the pre-peak loading history. Thus, it can be postulated that although creep strain is obvious, it does not degrade the shear strength, unlike the temperature.
2. The R-ε_a relationships immediately after the restart of ML at the end of CL show a very high stiffness, which is very close to the elastic stiffness.
3. For the same temperature, creep deformation increases with increasing R value. That is, SL performed at the stress state nearer to the failure results in more creep deformation. Most interestingly, for the same R value, creep deformation increases with an increase in the temperature.

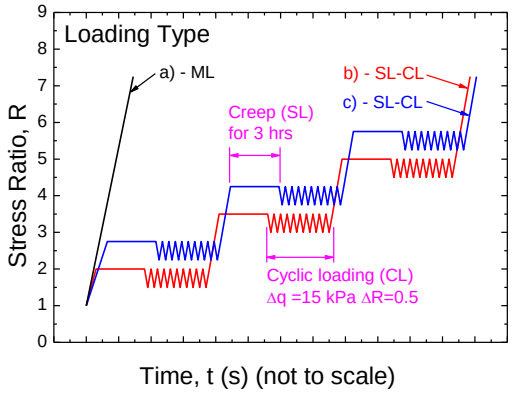

Fig. 4 Illustration of time histories of stress ratio (R) for loading types a), b) and c) according to the test program.

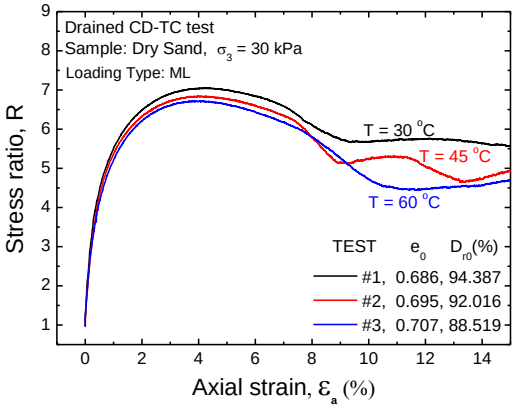

Fig. 5 R-ε_a relationships for different constant temperatures with loading type a)-ML.

Elastic stiffness

Determination of elastic stiffness

Fig. 7 shows an enlarged portion of Fig. 6a) around the R value equal to 5.0. In this figure, the R value presented on the vertical axis was converted to the major principal stress (σ_1). This figure shows typical stress-strain characteristics during SL and then CL as well as upon the restart of ML at the end

of CL of the present study. It can be clearly observed that the behaviour during small unload-reload cycles is highly linear-elastic, as noted by the facts that: i) the stress-strain loops generated during the respective unload-reload cycles are very small, exhibiting negligible energy dissipation; and ii) the residual strain developed by the respective unload-reload cycles was very small.

Fig. 8a) - 8c) show the last five unloading σ_1 - ε_a branches by CLs at R of 5.0 (Fig. 7) for different temperatures of 30ºC, 45ºC and 60ºC, respectively. It can be seen from these figures that the unloading branches exhibit a highly linear-elastic behaviour for the whole stress amplitude (15 kPa). Thus, it is relevant to evaluate the equivalent elastic Young's modulus (E_{eq}) from a linear relation fitted to the respective portions of the unloading σ_1 - ε_a branches presented in Fig. 8. The value of E_{eq} is fairly constant during the last five unload-reload cycles for the respective CL stages. This fact indicates that the deformation during these unloading σ_1 - ε_a branches is essential elastic.

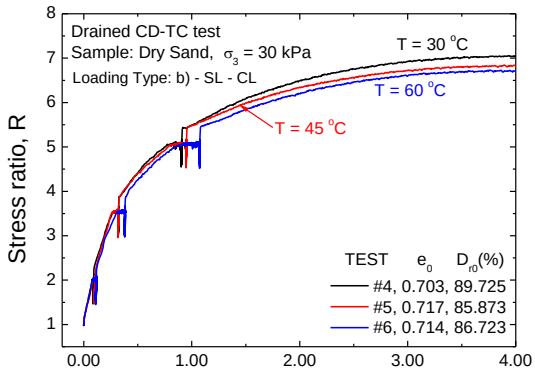

a)

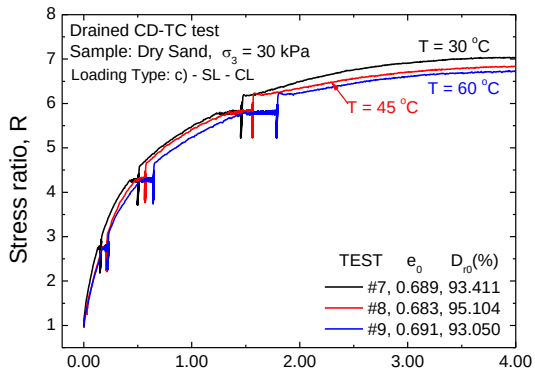

b)

Fig. 6 R - ε_a relationships for different constant temperatures with: a) loading type b) - SL-CL; and b) loading type c) - SL-CL

Determination of elastic stiffness

The averaged E_{eq} and σ_1/σ_0 relationships were then plotted in the full-log scale for respective temperatures as shown in Fig. 9. Here, σ_0 is the reference stress equal to 100 kPa. It can be seen that E_{eq} is not constant but increases with an increase of σ_1/σ_0 ratio. The dependency of elastic modulus with the stress level can be expressed with hypo-elasticity expressed by Eq. (2). With respect to the hypo-elastic properties, the trend that the elastic stiffness of geomaterial increases with an increase in the major principal stress for which the elastic modulus is defined has been observed in triaxial tests of many types of unbound geomaterial [26] - [28]. The lines were best-fitted to the test data points, and the values of E_0 and m for respective temperatures are shown in Fig. 9a). With different temperatures, the E_{eq} - σ_1/σ_0 relationships exhibit the same trend of behaviours. For the same value of the σ_1/σ_0 ratio, it is clearly noticed that the E_{eq} decreases with increasing temperature.

$$E_{eq} = E_0 \left(\frac{\sigma_1}{\sigma_0} \right)^m \quad (2)$$

Considering at the m value, it could be seen that the m values obtained from the tests with different temperatures are quite similar. This implies that the characteristics of increasing E_{eq} with σ_1 for different temperatures are very similar. For this reason, averaging the m values was attempted and the averaged m value (m_{avg}) of 0.624 was obtained. Then, regression analysis was re-performed for different temperatures using Eq. (2) but with the fixed value of $m = m_{avg}$, as shown in Fig. 9b). The coefficient of determination (R^2-value) value for each respective temperature is also shown in Fig. 9b).

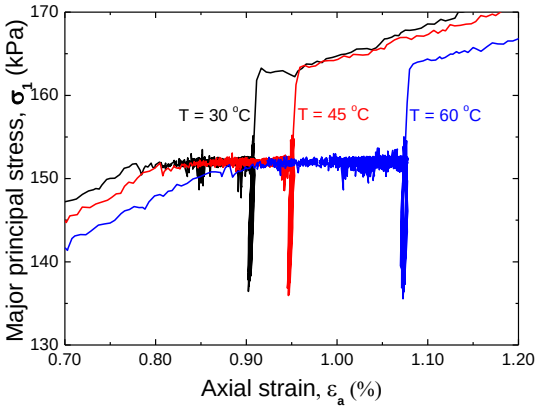

Fig. 7 Enlarged portion of Fig. 6a) showing σ_1 - ε_a relationships at R = 5.0.

Creep deformation

Fig. 10 shows the time histories of creep strain during 3-hr SL at different stress levels for the temperature equal to 30 °C. The trend of increasing creep axial strain with increasing stress ratio is obviously noticed.

Fig. 12 compares the creep strains at the end of 3-hr SL for different *R* values at which the SL was performed and different temperatures. The trend of increasing of creep axial strain with an increase in the temperature as well as with an increase in the stress level can be clearly seen. However, it can be seen that the stress level has more influence than temperatures on creep strains.

The end of strain during sustained loading for a period of 3 hours at different stress ratio levels from a)-SL-CL and b)-SL-CL tests with respective temperature. The trend of increasing of creep axial strain with an increase in temperature can be seen. However, it clearly seen that the stress ratio level has a larger influence than the temperature on the creep strain development.

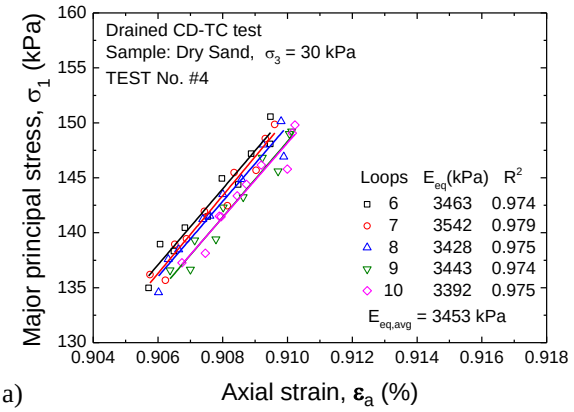

a)

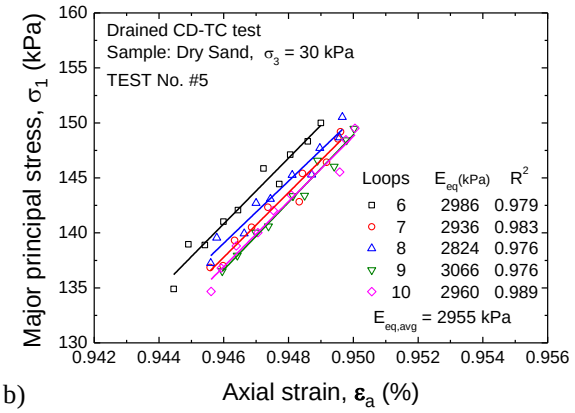

b)

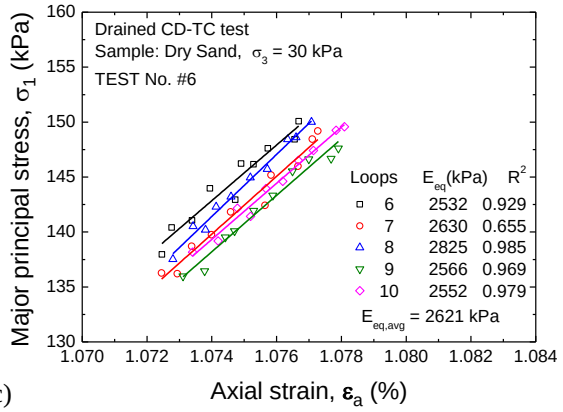

c)

Fig. 8 Determination of equivalent elastic Young's modulus (E_{eq}) from unloading branches of small-amplitude unload-reload cycles at R = 5 presented in Fig. 7 for temperatures equal to: a) 30 °C; b) 45 °C; and c) 60 °C.

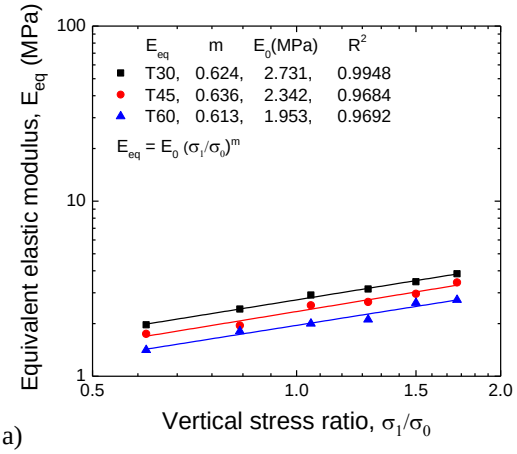

a)

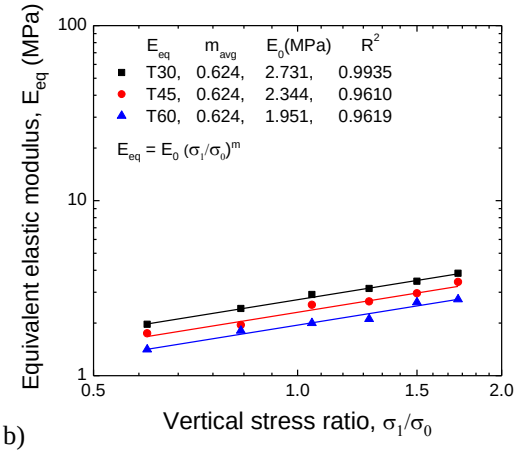

b)

Fig. 9 Dependency of E_{eq} on the stress level and temperature with respective trend lines fitted by using: a) respective m values; and b) common averaged m value.

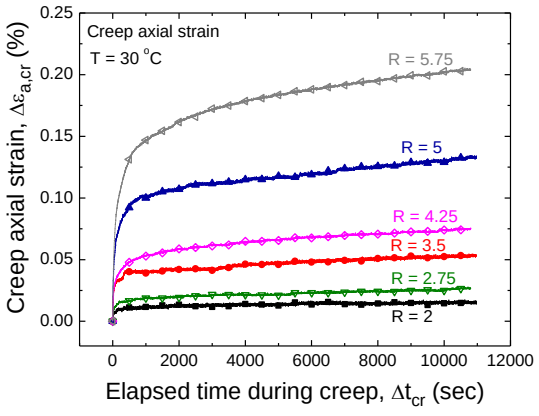

Fig. 10 Time histories of creep strain by 3-hr SL at different stress levels with temperature equal to 30.

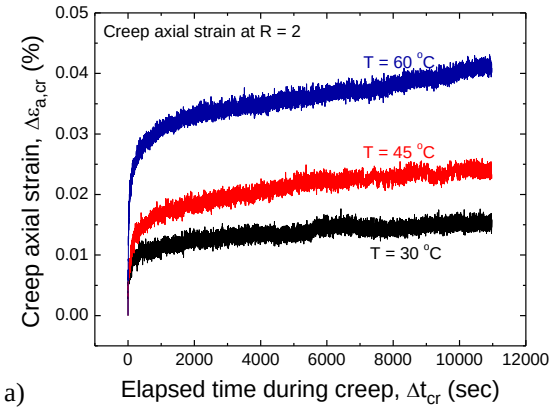

a)

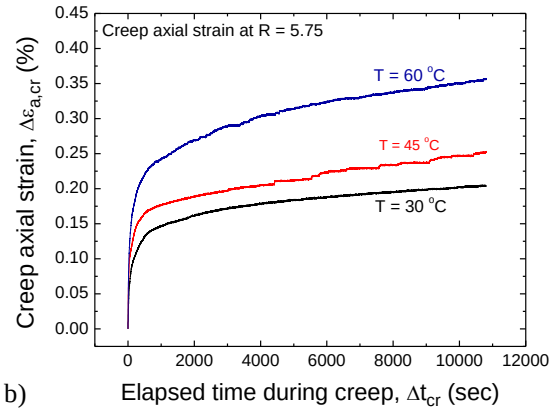

b)

Fig. 11 Comparison of time histories of creep axial strain for different temperatures by SL performed at *R* equal to: a) 2.0; and b) 5.75.

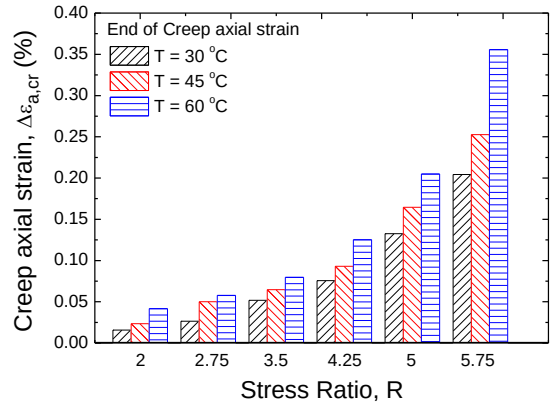

Fig. 12 Comparison of creep strain at the end of 3-hr SL for different stress ratio levels and temperatures.

CONCLUSIONS

The following conclusions can be derived from the triaxial compression test results of the studied sand.

1. A newly triaxial loading apparatus that can accurately control both the loading and temperature histories in an automated manner was successfully developed.

2. With increasing temperature, the internal friction angles both at the peak and residual states decrease. In addition, the stress-strain characteristics by continuous ML degrade.

3. With increasing stress level, the E_{eq} value significantly increases, exhibiting a hypo-elastic behaviour. On the other hand, by comparing at the same stress level, the E_{eq} value noticeably decreases with increasing temperature.

4. Creep strain increases with increasing the stress level and the temperature. The effect of stress level on the creep strain development seems to be more dominant than that of temperature.

ACKNOWLEDGMENTS

The authors would like to express their gratitude for financial support from King Mongkut's University of Technology Thonburi (KMUTT) through The Petchra Pra Jom Klao PhD scholarship under contract Grant No. 3/2559.

REFERENCES

[1] Gens A., Sanchez M., Guimaraes L.D.N., Alonso E.E., Lloret A., Olivella S., Villar M.V., Huertas F., A full-scale in situ heating test for high-level nuclear waste disposal: observations, analysis and interpretation, Geotechnique 59 (4), 2009, pp. 377–399.

[2] Brandon T.L., Mitchell J.K., Cameron J.T., Thermal instability in buried cable backfills, J. Environ. Eng. 115 (1), 1989, pp. 38–55.

[3] Knellwolf C, Peron H, Laloui L, Geotechnical analysis of heat exchanger piles, J. Geotech Geoenviron 137(10), 2011, pp. 890–902.

[4] Liu H.L., Wang C.L., Kong G.Q., Ng C.W.W., Che P., Model tests on thermo-mechanical behavior of an improved energy pile, Eur. J. Environ. Civil Eng., 2016, pp. 1–16.

[5] Olgun C.G., McCartney J.S., Outcomes from international workshop on thermoactive geotechnical systems for near-surface geothermal energy: from research to practice, J. Deep Found. Inst. 8 (2), 2014, pp. 59–73.

[6] Coccia C.J.R., McCartney J.S., Impact of heat exchange on the thermo-hydro-mechanical response of reinforced embankments, In:Proceedings of GeoCongress 2013, ASCE(3–5), 2013, pp. 343–352.

[7] Stewart, M.A., Coccia, C.J.R., McCartney, J.S., Issues in the implementation of sustainable heat exchange technologies in reinforced, unsaturated

soil structures. In: Proceedings of GeoCongress 2014 (GSP 234), 2014 pp. 4066–4075.
[8] Brandl H., Energy foundations and other thermo-avtive ground structures, Geotechnique 56 (2), 2066, pp. 81–122.
[9] Kertesz R., Sansalone J., Hydrologic transport of thermal energy from pavement, Journal of Environmental Engineering, 140 (8), 2014, 04014028.
[10] Tatsuoka F., Tateyama M., Koda M., Kojima K.-i., Yonezawa T., Shindo Y., Research and construction of geosynthetic-reinforced soil integral bridges, Transp. Geotech. 8, 2016, pp.4-25.
[11] Gens A., Soil–environment interactions in geotechnical engineering, Géotechnique 60 (1), 2010, pp. 3–74.
[12] Tidfors M., Sällfors S., Temperature effect on preconsolidation pressure, Geotech. Test. J. 12 (1), 1989, pp. 93–97.
[13] Cekerevac C., Laloui L., Experimental study of thermal effects on the mechanical behaviour of a clay. Int. J. Numer. Anal. Methods Geomech. 28 (3), 2004, pp. 209–228.
[14] Tang A.M., Cui Y.J., Barnel N., Thermo-mechanical behaviour of a compacted swelling clay, Géotechnique 58 (1), 2008, pp. 45–54.
[15] Di Donna, A., Laloui, L., Response of soil subjected to thermal cyclic loading: experimental and constitutive study. Eng. Geol. 190, 2015, pp. 65–76.
[16] Burland, J. B., Ninth Laurtis Bjerrum Memorial Lecture. Small is beautiful – the stiffness of soils at small strains. Can. Geotech. J. 26, 1989, pp. 499 –516.
[17] Tatsuoka, F., Kohata, Y., 1995. stiffness of Hard soils and soft rocks in engineering applications. In: Shibuya, S. (Ed.), Keynote Lecture, Proceedings of the International Symposium Pre-failure Deformation of Geomaterials, vol. 2. Balkema, pp. 947–1063.
[18] Kohata Y., Tatsuoka, F., Wang, L., Jiang, G. J., Hoque, E., Kodaka, T., Modelling the non-linear deformation properties of stiff geomaterials. Geotechnique, 47(3), 1997, pp. 563–580.
[19] Hitcher, Elastic properties of soils. J. Geotech. Engrg, 1996, pp. 641-648.
[20] Tatsuoka, F., Di Benedetto, H., Enomoto, T., Kawabe, S., and Kongkitkul, W., Various viscosity types of geomaterials in shear and their mathematical expression. Soils and Foundations., Vol.48, No. 1, 2008, pp. 41–60.
[21] Lu, R., Cheng, C., Nagel, T. et al. What process causes the slowdown of pressure solution creep. Geomech. Geophys. Geo-energ. Geo-resour. 7, 57 (2021).
[22] Hong Liu, Hanlong Liu, Yang Xiao, John S. McCartney, Effects of temperature on the shear strength of saturated sand. Soils and Foundations 58, 2018, pp.1326–1338.
[23] Shao-Heng He, Hua-Feng Shan, Tang-Dai Xia, Zhi-Jun Liu, Zhi Ding, Fan Xia, The effect of temperature on the drained shear behavior of calcareous sand. Acta Geotechnica, 2020, pp. 613-633.
[24] F. Santucci de Magistris, J. Koseki, M. Amaya, S. Hamaya, T. Sato, and F. Tatsuoka, A Triaxial Testing System to Evaluate Stress-Strain Behavior of Soils for Wide Range of Strain and Strain Rate. Geotechnical Testing Journal 22, no. 1, 1999, pp. 44-60.
[25] Miura S., Toki S., A sample preparation method and its effect on static and cyclic deformation-strength properties of sand. Soils and Foundations, Vol. 22, No. 1, pp. 61-77.
[26] Shibuya, S., Tatsuoka, F., Teachavorasinskun, S., Kong, X. J., Abe F., Kim, Y. S., Park, C. S., Elastic deformation properties of geomaterials. Soils and Foundations, Vol. 32, No.3, pp. 26-46.
[27] Tatsuoka, F., Sato, T., Park, C., Kim, Y., Mukabi, J., Kohata, Y., Measurements of elastic properties of geomaterials in laboratory compression tests. Geotech. Testing J., Vol. 17, No. 1, pp. 80-94
[28] Hoque, E., Tatsuoka, F., Anisotropy in the elastic deformation of materials. Soils and Foundations, Vol. 38. No. 1, pp.163-179.

11th Int. Conf. on Geotechnique, Construction Materials & Environment, Kyoto, Japan, 3-5 November 2021, ISBN: 978-4-909106063 C3051

ANALYSIS OF SOIL-PIPE INTERACTION SUBJECTED TO NORMAL AND REVERSE FAULTING USING THE DISCRETE ELEMENT METHOD

Yusuke Ono[1]

[1]Faculty of Engineering, Tottori University, Japan

ABSTRACT

Although buried pipelines are essential components of lifelines, they have been repeatedly damaged by earthquakes. Fault displacement is one of the major factors that cause damage to buried pipelines. In this study, the deformation and cross-sectional forces of buried conduits subjected to ground displacement caused by reverse or normal faults were calculated using the distinct element method, which can appropriately model the nonlinear behavior of the ground. By comparing the results obtained from the individual element method analysis with the results of finite element analysis, which is widely used in practice, the characteristics of deformation, bending moment, and axial force in buried pipelines subjected to these fault displacements are summarized. In the case of a buried pipe subjected to a reverse fault, the coupled effect of the pipe deformation and the axial force should be appropriately considered, and in the case of a buried pipe subjected to a normal fault, it is crucial to evaluate the ground reaction force to prevent the pipe from uplifting.

Keywords: Buried pipeline, Soil-pipe interaction, Fault movement, Discrete element method, Finite element method

INTRODUCTION

Fault displacement is one of the most common causes of damage to buried pipelines during earthquakes. For example, in the 1971 San Fernandez earthquake, more than 1,400 buried water, sewage, and gas pipelines were damaged due to the fault displacement near the ground surface [1]. In the 1999 Chi-Chi earthquake in Taiwan, it was confirmed some steel pipes subjected to fault displacement were deformed in a z-shape [2]. In the 2014 Kamishiro Fault Earthquake in Nagano Prefecture, a sewer pipe that intersected a reverse fault was damaged by a vertical displacement of about 80 cm and a horizontal displacement of about 40 cm. In the 2016 Kumamoto earthquake, a ductile iron pipe for water supply crossing the fault in Mashiki Town was bent significantly and pulled out at the joint [4].

The design of buried pipelines against fault displacement has been developed in the past. Newmark and Hall [5] developed a method to calculate the pipe elongation by considering the non-uniform distribution of frictional forces between the pipe and the surrounding ground under fault displacement. Kennedy et al. [6] extended the method of Newmark and Hall [5] to calculate the bending moment of the pipe. Wang and Yeh [7] proposed a method to model the ground as an elastic spring and the pipe as a beam. Takada et al. [8] developed a finite element analysis method that combines shell and beam elements to accurately determine the strains in the pipe at fault crossings. Suzuki [9] developed a method for calculating the deformation and cross-sectional force of a buried pipe subjected to fault displacement by solving the elastic equation of the beam with the range of yielding of the ground as the unknown in a model in which the buried pipe is represented as an elastic beam and the ground around the pipe as elasto-plastic springs. Talebi and Kiyono [10] developed a new governing equation including exact nonlinear axial and transverse soil-pile interaction terms for a strike-slip fault crossing. At present, finite element analysis, in which the pipe is modeled as a beam element and the ground as a nonlinear spring, is commonly used in design practice to evaluate the cross-sectional force generated in buried conduits subjected to fault displacement. The restoring force characteristics of the nonlinear springs in the ground can be set based on the guidelines released by American Lifelines Alliance (ALA) [11].

Yoshizaki et al. [12] conducted large-scale experiments to analyze in detail the effects of permanent ground displacement (PGD) on buried steel conduits. Ha et al. [13]–[15] and Abdoun et al. [16] conducted centrifuge experiments on a reduced model to investigate the relationship between the cross-sectional forces generated in a buried pipe subjected to fault displacement and the characteristics of the pipe and the surrounding soil in detail. In these studies, the effectiveness of the finite element model analysis was also verified by comparing the experimental results.

Numerical studies have also been carried out to investigate the effects of experimental limitations and many loading conditions. Most of them are based on finite element analysis. Finite element analysis was also used in the experimental studies described above [12]-[16], and the consistency between experiment

and analysis has been confirmed. Rahman and Taniyama [17] proposed a hybrid model that treats the ground as a discretized element method and the pipe as a finite element method using beam elements and investigated the characteristics of the interaction between the pipe and the ground near the fault intersection. They discussed the effects of displacements due to reverse and lateral faults and the bending stiffness of the pipe. Their analysis was performed on a limited number of models, and it is necessary to perform discretized element analysis on many models to clarify the characteristics of the interaction between the pipe and the ground acting on the pipe subjected to fault displacement.

In this study, the deformation and cross-sectional force characteristics of a buried pipeline are analyzed by using the three-dimensional discrete element method. The analyzed models are different from those of Rahman and Taniyama [17]. The fault displacement analyzed is pure vertical displacement. A high-density polyethylene (HDPE) pipe is examined. The burial depths of the pipes analyzed are 2.4, 4.8, and 7.2 times the outer pipe diameter.

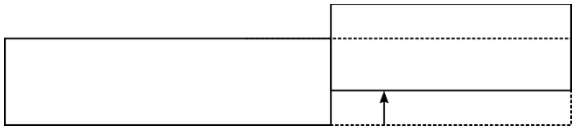

(a) Vertical dislocation

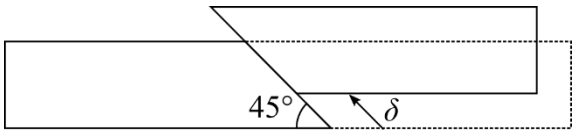

(b) Reverse fault

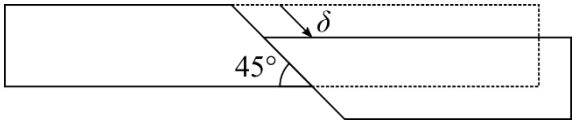

(c) Normal fault

Fig. 1 Types of fault movements considered in the present study.

METHOD

The Discrete Element Method

The Discrete Element Method (DEM) [18] is widely used in geotechnical engineering as a numerical tool that can directly deal with the granular properties of the ground. The deformation of the ground is represented by a result of the motion of many rigid bodies. In general, spheres are used as a rigid body because of their simplicity in detecting contact. In this study, the ground is also modeled as a set of spheres.

The contact between spheres is determined by the relationship between their radii and the distance to the center of gravity; when the radii of the two spheres are r_1 and r_2, respectively, and the distance between the centers of gravity is r_{12}, the two spheres are in contact if they satisfy the relationship as follows:

$$r_1 + r_2 \leq r_{12} \tag{1}$$

When contact occurs, virtual springs and dashpots are generated in the tangential and normal directions of the contact point, respectively, and the contact force acting on the sphere is calculated. The equation of motion of the sphere is given by the following equation,

$$m\ddot{x}_i = F_i \tag{2}$$

where F_i is the i-directional component of the sum of all contact forces acting on the sphere; m is the mass of the spere; $\ddot{x}_i$ is acceleration. In the discrete element method, not only the translational motion of the object but also the rotational motion is considered. The equation of motion for rotation is given by,

$$I_i\ddot{\omega}_i = M_i \tag{3}$$

where i is the index representing the central axis of rotation, I_i is the rotational inertia, $\ddot{\omega}_i$ is the rotational acceleration, and M_i is the moment.

The maximum shear force F^s_{max} is determined as follows:

$$F^s_{max} = \mu F^n \tag{4}$$

where F^n is the normal contact force, and μ is the frictional coefficient between the spheres.

The computer code used in this study is the open-source software Yade 2020.01a [19]. Spherical elements are used for the ground, while a chained cylinder element is used to represent the buried pipe. The chained cylinder model deforms according to the elastic beam theory. However, the chained cylinder model [20], [21] implemented in the Yade does not support a hollow cross-section such as a pipe. Therefore, we needed to change the original source code slightly.

Analytical Model

The ground model of 14 m length, 1 m width, and 1 m height are placed in a rigid box, as shown in Fig.2. The box is divided into two parts, one of them is fixed, and the other is movable. For normal or reverse fault analysis, the fault plane was tilted 45 degrees to the fixed side. The movement of the fault is simulated by moving the movable side of the box at a constant

speed of 0.5 m/s. The maximum fault movement δ is 0.30 m. The box is modeled using the facet elements provided by Yade. In the actual analytical mode, a flat plate is placed at the bottom of the box to prevent the spherical elements from spilling through the gap created by the movement of the fault.

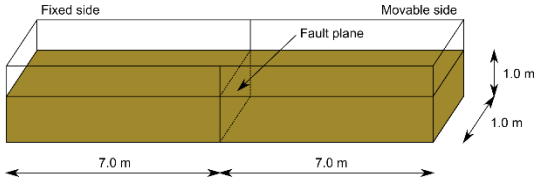

(a) Vertical dislocation type

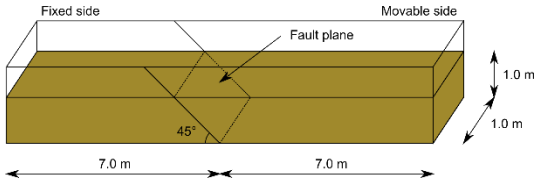

(b) Normal and reverse fault type

Fig. 2 Dimension of the analytical model.

Table 1 Parameters for the spherical elements

Parameter	Value
Radius (m)	0.040
Density (kg/m^3)	2.4×10^3
Elastic modulus (N/m^2)	3.0×10^7
Poisson's ratio	0.15
Internal friction angle	35.0°

Table 2 Parameters for the pipe model

Parameters	Value
Diameter (m)	0.125
Thickness (m)	0.0114
Elastic modulus (N/m^2)	1.0×10^9
Poisson's ratio	0.46

Table 3 Summary of the analytical cases

Case	Fault type	Buried depth (m)
111	Vertical dislocation	0.30
112	Reverse fault	0.30
113	Normal fault	0.30
121	Vertical dislocation	0.60
122	Reverse fault	0.60
123	Normal fault	0.60
131	Vertical dislocation	0.90
132	Reverse fault	0.90
133	Normal fault	0.90

The buried depth is defined by the depth from the ground surface to the centerline of the pipe.

Table 1 summarizes the parameters of the spherical elements. The sizes of the spherical elements used in the analysis are all equal. When analyzing the ground using the discrete element method, it is desirable to keep the size of the spherical elements as small as possible. However, if the size of the spherical elements is too small, the number of required elements becomes too large, and the analysis cannot be performed realistically. In this study, therefore, the diameter of the spherical element was set to 0.04 m, as a guideline that one analysis case can be completed in a few hours. As a result, the number of spherical elements used was 319,726.

An HDPE pipe with an outer diameter of 0.125 m is analyzed. The parameters of the pipe are shown in Table 2. Although HDPE is a strain-rate-dependent material, it is treated as an elastic material. The variation of the cross-sectional shape of the pipe is not considered. The modeled pipe is buried horizontally in the center of the width according to the specified depth. The ends of the pipe are rigidly fixed to the walls of the rigid box.

The frictional coefficient μ between the surface of the pipe and the spherical elements is determined by Eq.(5) using the internal friction angle φ between the spherical elements,

$$\mu = \tan f\varphi \tag{5}$$

where f is the coating coefficient of the pipe, and which is set to 0.6 according to the ALA guideline [11].

Analytical Cases

The analysis was conducted for nine cases shown in Table 3. The three types of faults are vertical longitudinal dislocation, 45-degree reverse fault, and 45-degree normal fault as shown in Fig. 1. The pipe burial depths (distance from the ground surface to the central axis of the pipe) are 0.30 m, 0.60 m, and 0.90 m.

Simulation Procedure

First, spherical elements of a specified size were randomly generated in the prepared box, deposited under gravity, and stabilized until the motion of the spherical elements was sufficiently settled. The number of spherical elements to be generated was adjusted by trial and error so that the height of the ground after stabilization was approximately 1.0 m. At this point, the friction between the elements was set to zero so that the spherical elements would be as dense as possible. Next, the spherical elements were removed from the buried position of the pipe, and the pipe was placed in the vacant space. After confirming that the motion of the spherical element was sufficiently settled under the action of gravity, the fault displacement was applied. Figure 3 shows the

ground model just before the fault displacement was applied. The spherical elements are colored in a grid pattern so that the deformation of the ground can be observed. The porosity of the ground at this time was 0.490.

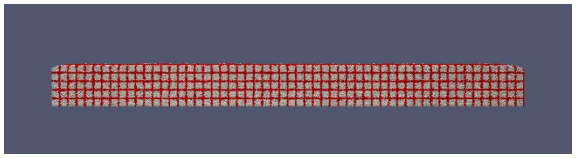

Fig. 3 Side view of the ground model before application of the fault movement.

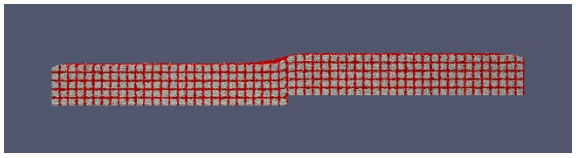

(a) Vertical dislocation

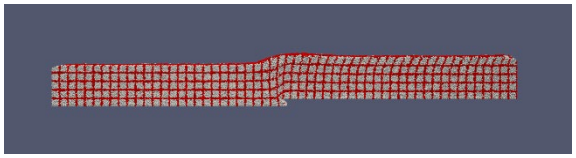

(b) Reverse fault

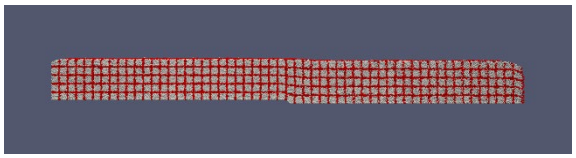

(c) Normal fault

Fig. 4 Deformation of the ground models after application of the fault movement

RESULTS AND DISCUSSION

Deformation of the Ground Model

Figure 4 shows a side view of the ground model after a fault displacement of 0.30 m was applied. Depending on the burial depth of the pipe, there are some differences in the ground surface deformation. However, the pipe with a burial depth of 0.30 m is shown here as an example. In the model with vertical dislocation, a gentle slope was formed just above the fault due to the flow of the spherical elements. In the model with reverse faulting, the ground was significantly compressed above the fault plane. The ground on the fixed side was hardly deformed, while the ground on the moving side was deformed over a wide area. In particular, the ground near the surface was deformed up to the rightmost boundary. In the case of the normal fault, the subsidence of the ground surface was smaller than that of the vertical direction of the bottom of the moving side. This is because the ground could not follow the movement of the fault sufficiently and the pore of the ground became large. Near the right boundary, the ground could not keep up with the movement of the boundary, and a gap was created between the wall and the ground.

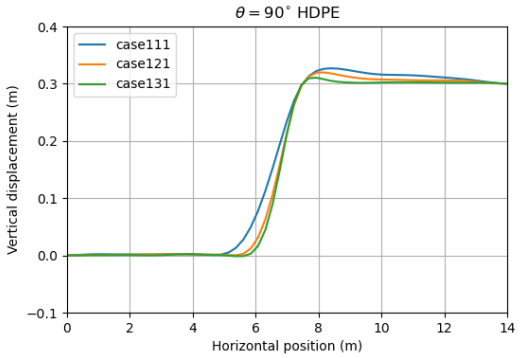

(a) Vertical dislocation

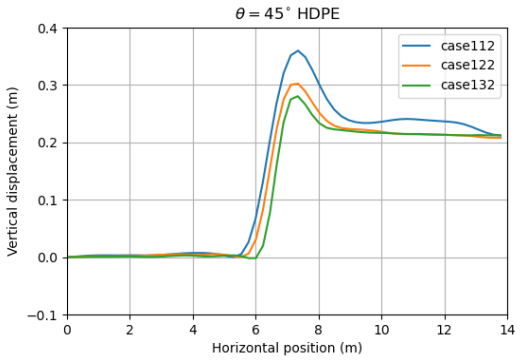

(b) Reverse fault

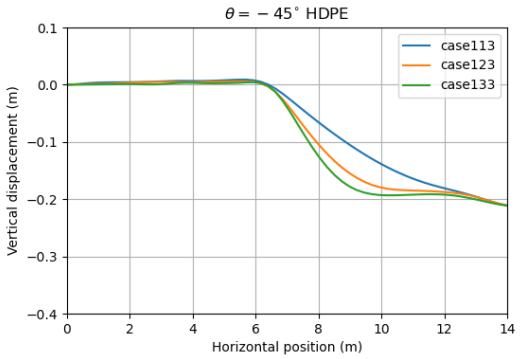

(c) Normal fault

Fig. 5 Deformation of the pipe along the axial direction.

Deformation of the Pipe

The deformation of the buried pipe when the displacement of each fault movement pattern reaches 0.30 m is shown in Fig. 5. The pipe shows characteristic deformation according to the fault pattern.

In the case of vertical dislocations, the pipe deformed slightly upward from just above the fault to the moving side. The deformation of the pipe on the

fixed side occurs only near the fault. The vertical upward displacement of the pipe is more significant when the depth of burial is shallower. This is because the downward force acting on the pipe is smaller when the depth of burial is shallower. In the case of reverse faulting, the pipe bends upward significantly on the moving side near the fault.

In the case of reverse faulting, the pipe bends upward significantly on the moving side of the ground near the fault. In this case, the pipe is compressed by the fault movement, so the upward deformation of the pipe is larger. In this case, the upward deformation of the pipe is larger because the pipe is compressed by the fault movement. The downward restraining force acting on the pipe is smaller when the burial depth is shallower, so the pipe is bent larger when the burial depth is shallower. In the case with the shallowest burial depth, the pipe deforms even near the boundary of the moving box (left side of the figure), indicating that the boundary affects the analysis results.

In the model with normal faults given, the pipe deforms gently, unlike the models with the other two fault types. In the case with the shallowest burial depth, the deformation of the pipe continues to the left boundary, unlike the cases with different burial depths.

Bending Moment of the Pipe

The bending moment generated in the pipe is shown in Figure 6. In the case where the vertical discrepancy is given, the bending moment on the fixed side is positive and that on the moved side is negative. The bending moment of the pipe is almost zero at the intersection with the fault. The bending moment of the pipe is larger when the depth of burial is deeper. The point where the bending moment is the largest on the fixed side is farther from the fault location as the burial depth becomes shallower. On the other hand, the position of the maximum bending moment on the moving side is almost the same regardless of the burial depth. The maximum value of the bending moment is larger on the moving side than on the fixed side.

The shape of the distribution of the bending moment of the pipe in the results of the reverse faulting is similar to that of the results of the vertical dislocation. The position where the pipe intersects the fault and the position where the bending moment becomes zero are almost the same. The bending moment of the pipe is positive on the fixed side and negative on the moving side. The maximum magnitude of the bending moment is larger when the pipe is buried deeper in both the fixed side and the moving side. The position where the maximum bending moment appears is constant regardless of the burial depth on the fixed side, while it becomes closer to the fault on the moving side as the burial depth becomes deeper.

In the case of normal faulting, the bending moment generated in the pipe is smaller than the results of the case with vertical dislocation or reverse faulting. The bending moment is negative for the fixed side and positive for the moving side, which is opposite to the other two cases. The tendency of the magnitude of the bending moment to increase with the depth of burial is the same as in the other cases.

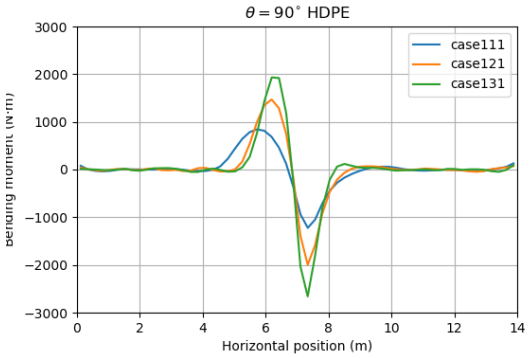

(a) Vertical dislocation

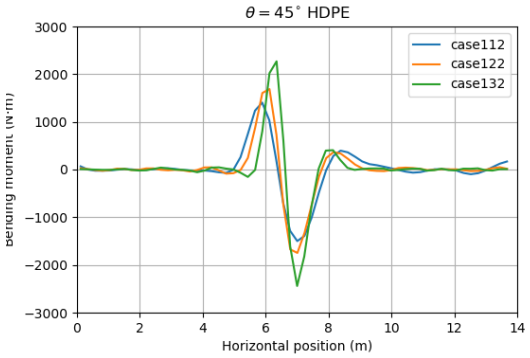

(b) Reverse fault

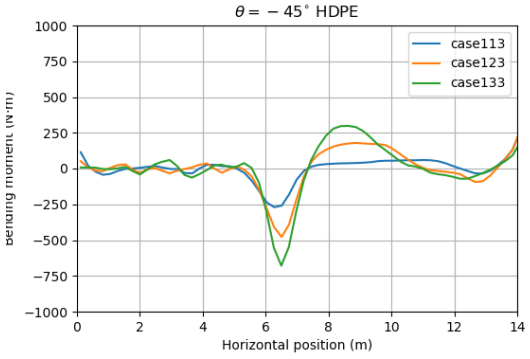

(c) Normal fault

Fig. 6 Bending moment of the pipe at the different buried depths.

Axial Force of the Pipe

Figure 7 shows the axial force of a pipe. The axial force is positive in tension and negative in compression. In the model with vertical dislocation

and the model with normal fault, tensile force is acting on the pipe. On the other hand, in the model with reverse faults, compressive forces are acting on the pipe.

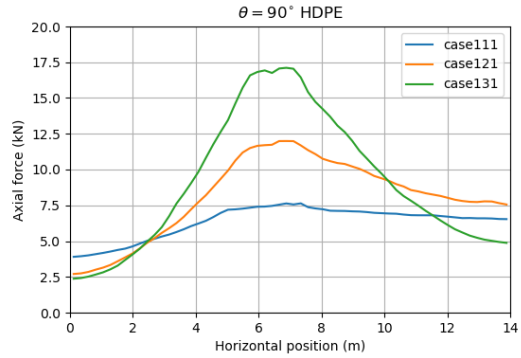

(a) Vertical dislocation

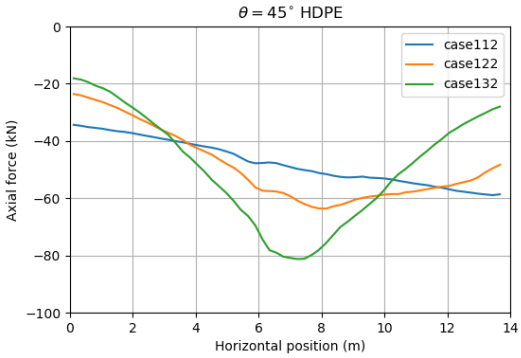

(b) Reverse fault

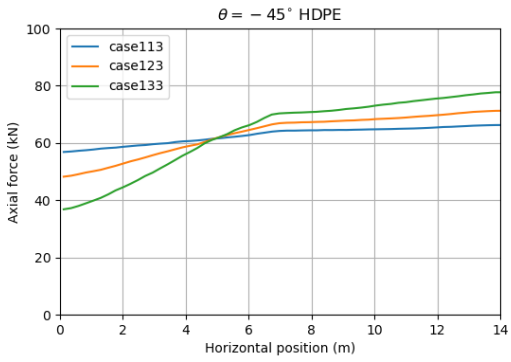

(c) Normal fault

Fig. 7 Axial force of the pipe at the different buried depths.

In the model with vertical dislocation, the tensile force acting on the pipe is large near the fault and decreases as it approaches the lateral boundary. The axial force is almost constant near the fault, indicating that the reaction force acting from the ground has reached its maximum value. Near the fault, the axial force is larger as the depth of the pipe increases. From the difference in the slope of the axial force graph, it can be seen that the reaction force acting from the ground is larger as the pipe burial depth becomes deeper. Near the right and left boundaries, the axial force decreases with the depth of burial. The axial force at the right boundary is larger than that at the left boundary, which may be due to dynamic effects.

In the reverse fault model, the compressive force on the pipe at the intersection with the fault is the largest at the deepest case132. In case 132, where the depth of burial is the deepest, the compressive force on the pipe is the largest at the intersection with the fault, and the graph flattens near the maximum compressive force, indicating that the ground reaction force has reached its maximum. On the other hand, in case112, where the soil cover is the shallowest, the compressive force increases monotonically from the left boundary to the right boundary, showing a different trend from the case with the deepest burial depth. In the intermediate case122, the compressive force is maximum near the fault and decreases toward the boundary. The rate of change of the compressive force is different between the fixed and moving sides.

In the normal fault model, the tensile force is maximum at the boundary on the moving side and decreases toward the boundary on the fixed side. The rate of change of tensile force is different on both sides of the intersection of the pipe and the fault, and the rate of change of tensile force on the moving side is lower than that on the fixed side.

Comparison to the Finite Element Analysis

The deformations, bending moments, and axial forces of the pipes obtained by the discrete element method were compared with the results obtained by finite element analysis. The finite element analysis software used was OpenSeesPy [22] that enables to control OpenSees [23] from Python script.

Finite element model

The pipe is modeled as an elastic beam element and the ground as soil springs. The ground springs are applied in the axial and the transverse directions. The transverse soil springs generate reaction forces against the upward or downward movement of the pipe. Both ground springs are modeled as elastic-perfectly-plastic models following the ALA guidelines [11]. The maximum force F_{max} and yield displacement δ_y of each soil spring are determined as follows, respectively, according to the ALA guidelines [11].

The maximum force per unit length F_{max} and the yield displacement δ_y (m) on the axial direction are given by,

$$F_{max} = \pi D H \bar{\gamma} \frac{1+K_0}{2} \tan(f\phi) \quad (6)$$

$$\delta_y = 0.003 \quad (7)$$

where D is the outer diameter of the pipe, H is the depth of the centerline of the pipe from the ground

surface, $\bar{\gamma}$ is the unit weight of the ground, K_0 is the coefficient of pressure at rest, ϕ is the internal friction angle of the ground, and f is the factor of pipe coating that is set to be 0.6 in the study.

For the vertical uplift soil spring, the maximum force per unit length and the yield displacement δ_y is given by,

$$F_{\max} = \left(\frac{\phi H}{44D}\right)\bar{\gamma}\mathrm{HD} \quad (8)$$

$$\delta_y = 0.01H \quad (9)$$

The maximum force per unit length $F_{\max}$ and the yielding displacement δ_y for the vertical bearing soil spring are,

$$F_{\max} = e^{(\pi tan\phi)} tan^2\left(45 + \frac{\phi}{2}\right) + e^{(0.18\phi - 2.5)}\gamma\frac{D^2}{2} \quad (10)$$

$$\delta_y = 0.1D \quad (11)$$

This finite element analysis model does not consider the coupling of bending moment and axial force in the pipe. In addition, the coupling between axial (horizontal) and transverse (vertical) ground springs is not considered.

Results

Figure 8 shows the deformation of the pipe for each fault type. For the vertical dislocation model, the results from the discrete element method and the finite element method are in general agreement. However, in the discrete element analysis, the pipe is slightly raised at the fault intersection. The results of the discrete element method and the finite element method for the pipe deformation in the model with reverse faulting are very different. The upward convex deformation of the pipe at the fault intersection seen in the results of the distinct element method is not seen in the results of the finite element method. This is because the finite element method does not take into account the effect of the axial force on the bending of the pipe. In the normal fault results, the deformations of the pipes on the moving side are different from each other. The finite element method results show that the pipe is pushed down to a deeper position than the discrete element method results. This means that the force exerted on the pipe by the ground above the moving pipe is excessive in the finite element method.

Figure 9 compares the distribution of bending moments of the pipes. The results of the discrete element method and the finite element method are very similar for the bending moment of the vertical dislocation model. For the reverse fault model, the peak values of the bending moments are different for both the fixed and moving sides. In particular, the peak bending moment on the fixed side is much lower in the finite element method than in the discrete element method. For the peak bending moment caused by the normal fault, the finite element method results are higher than the individual element method results, contrary to the case of the reverse fault.

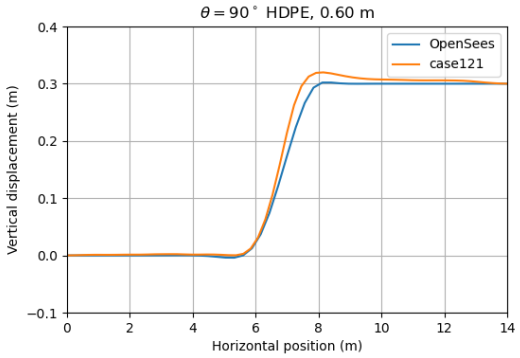

(a) Vertical dislocation

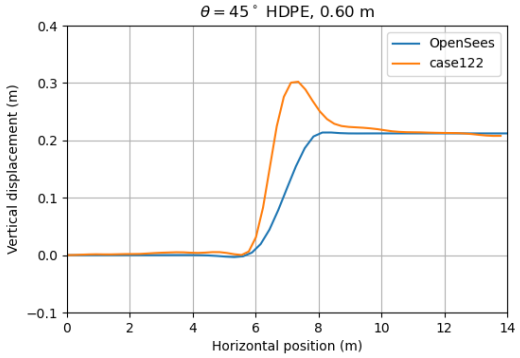

(b) Reverse fault

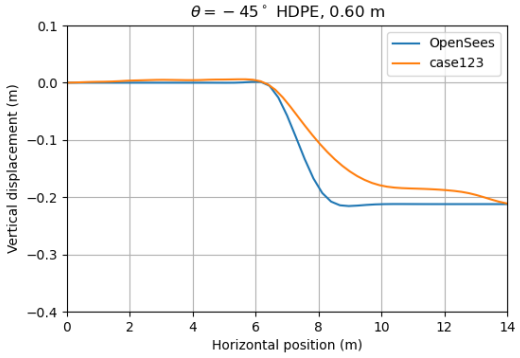

(c) Normal fault

Fig. 8 Comparison of the pipe deformation to that from the FE analysis.

Figure 10 shows the axial force generated in the pipe. In this figure, the axial force obtained from the results of the discrete element method varies along the pipe, while the value obtained from the finite element analysis is constant. This is due to the fact that the axial slip between the pipe and the ground occurs at a relative displacement as small as 3 mm in the ground spring used in the finite element analysis, and the effect of the force acting perpendicular to the

axis of the pipe on the maximum friction force is not taken into account.

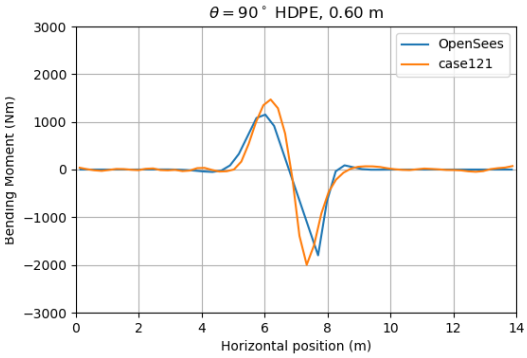

(a) Vertical dislocation

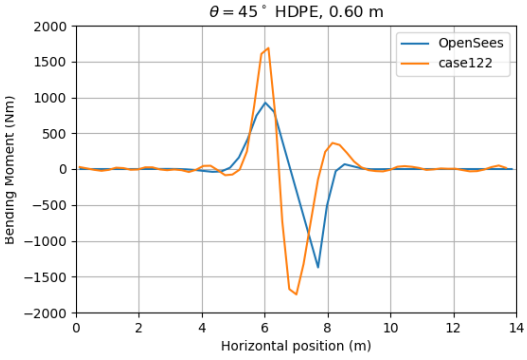

(b) Reverse fault

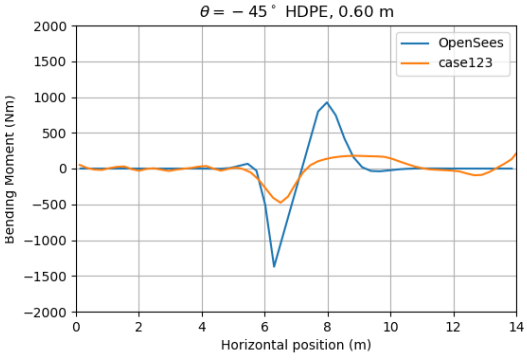

(c) Normal fault

Fig. 9 Comparison of bending moment of the pipe to that from the FE analysis.

CONCLUSIONS

In this study, the deformation, bending moment, and axial force generated in a buried pipe subjected to vertical dislocation, reverse fault, and normal fault, respectively, were calculated using the three-dimensional discrete element method. For comparison, a finite element analysis was also conducted. The main findings are as follows: for the buried pipe subjected to reverse faulting, the coupling of axial force and bending deformation should be considered appropriately; in the case of a buried pipe subjected to a normal fault, it is necessary to properly evaluate the ground reaction force acting in the direction perpendicular to the pipe axis that prevents the pipe from uplifting.

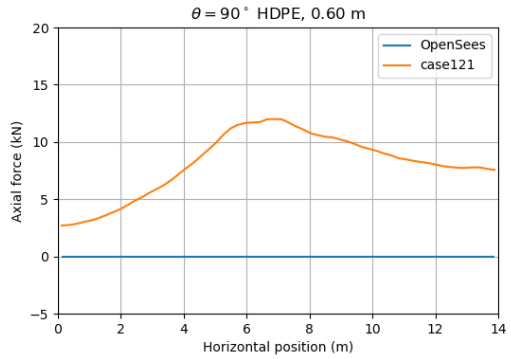

(a) Vertical dislocation

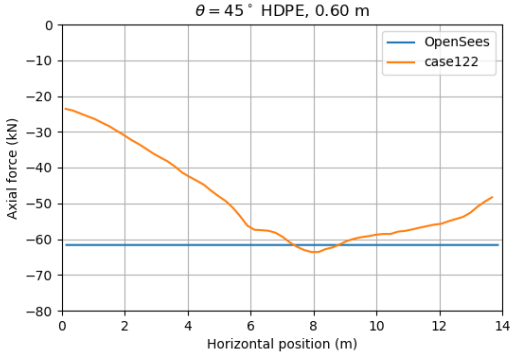

(b) Reverse fault

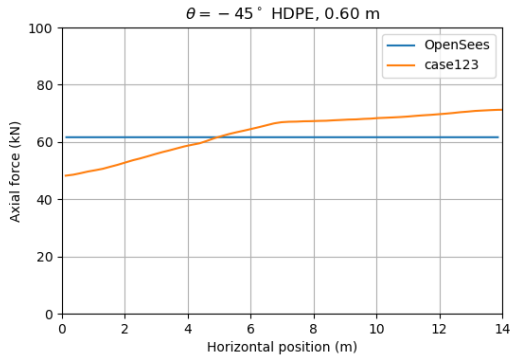

(c) Normal fault

Fig. 10 Comparison of axial force of the pipe to that from the FE analysis.

It is well known that the results of ground deformation analysis by the discrete element method depend on the size of the elements used. It is necessary to carefully confirm that the findings obtained in this study do not depend greatly on the size of the spherical elements. In addition, individual element analysis requires a large number of elements to be used, so the computation time is large. In addition, it is not easy to set the ground conditions such as porosity and unit volume weight as expected. Therefore, there are still many problems to be solved before the individual element method can be used as

a major tool in practical design. In the future, we will try to incorporate the knowledge obtained in this study into the method of setting ground springs used in finite element analysis with high computational efficiency.

REFERENCES

[1] MaCaffrey M. A., and O'Rourke T. D., Buried pipeline response to reverse faulting during the 1971 San Fernando Earthquake., ASME, PVP. Vol.77, 1983, pp.151-159.

[2] Shih B.J., and Chang C.H., Damage survey of water supply systems and fragility curve of PVC water pipelines in the Chi–Chi Taiwan earthquake, Natural Hazards, Vol.37, No.1-2, 2006, pp.71-85.

[3] Japan Association for Earthquake Engineering, Report of the investigation team on the 2014 earthquake in northern Nagano Prefecture, 2015 (in Japanese).

[4] Committee for the Evaluation of Seismic Performance of Polyethylene Pipes for Water Distribution, Guide to Seismic Design of Polyethylene Pipes for Water Distribution, Reference Materials, 2018, pp.46-47 (in Japanese).

[5] Newmark N.M., and Hall W.J., Pipeline design to resist large fault displacement, Proceedings of US national conference on earthquake engineering. 1975, pp.416-425.

[6] Kennedy R.P, and Kincaid R.H., Fault crossing design for buried pipelines for seismic-induced ground distortions, Proceeding of 4th National Congress on Pressure Vessel and Piping Technology, 1983, pp.1-24.

[7] Wang L.R.L., and Yeh Y.H., A refined seismic analysis and design of buried pipeline for fault movement, Earthquake engineering & structural dynamics, Vol.13, No.1, 1985, pp.75-96.

[8] Takada S., Hassami N., and Fukuda K., A new proposal for simplified design of buried steel pipes crossing active faults, Earthquake engineering & structural dynamics, Vol.30, No.8, 2001, pp.1243-1257.

[9] Suzuki T., Approximate calculation method for beam model supported by inelastic springs in enforced displacement, Doboku Gakkai Ronbunshu, Vol.2001, No.689, 2001, pp.109-116 (in Japanese).

[10] Farzad Talebi and Junji Kiyono, A refined nonlinear analytical method for buried pipelines crossing strike-slip faults, Earthquake Engineering and Structural Dynamics, Vol.50, No.11, 2021, pp.2915-2938.

[11] American Lifelines Alliance, Seismic guidelines for water pipelines, 2005.

[12] Yoshizaki K., O'Rourke T.D., and Hamada, M., Large scale experiments of buried steel pipelines with elbows subjected to permanent ground deformation, Structural Engineering/Earthquake Engineering, Vol.20, No.1, 2003, pp.1-11.

[13] Ha D. et al., Buried high-density polyethylene pipelines subjected to normal and strike-slip faulting—a centrifuge investigation, Canadian Geotechnical Journal, Vol.45, No.12, 2008, pp.1733-1742.

[14] Ha D. et al., Centrifuge modeling of earthquake effects on buried high-density polyethylene (HDPE) pipelines crossing fault zones, Journal of Geotechnical and Geoenvironmental engineering, Vol.134, No.10, 2008, pp.1501-1515.

[15] Ha D. et al., Earthquake faulting effects on buried pipelines–case history and centrifuge study, Journal of earthquake engineering, Vol.14, No.5, 2010, pp.646-669.

[16] Abdoun, T.H., et al., Factors influencing the behavior of buried pipelines subjected to earthquake faulting, Soil Dynamics and Earthquake Engineering, Vol.29, No.3, 2009, pp.415-427.

[17] Rahman M.A., and Taniyama H., Analysis of a buried pipeline subjected to fault displacement: A DEM and FEM study, Soil Dynamics and Earthquake Engineering, Vol.71, 2015, pp.49-62.

[18] Cundall P.A., and Strack O.D.L., A discrete numerical model for granular assemblies, Geotechnique, Vol.29, No.1, 1979, pp.47-65.

[19] Kozicki J. , and Donze F.V., YADE-OPEN DEM: An open-source software using a discrete element method to simulate granular material, Engineering Computations, 2009.

[20] Effeindzourou, A., et al., A general method for modelling deformable structures in DEM, Proc. of the IV International Conference on Particle-Based Methods: fundamentals and applications, 2015.

[21] Wu W., et al., effect of vegetation on stability of soil slopes: numerical aspect, Recent advances in modeling landslides and debris flows, 2015, pp.163-177.

[22] Zhu M., McKenna F., and Scott M.H., OpenSeesPy: Python library for the OpenSees finite element framework, SoftwareX, Vol.7, 2018, pp.6-11.

[23] McKenna F., Scott M.H., and Fenves G.L., Nonlinear finite-element analysis software architecture using object composition, Journal of Computing in Civil Engineering, Vol.24, No.1, 2010, pp.95-107.

11th Int. Conf. on Geotechnique, Construction Materials & Environment,
Kyoto, Japan, 3-5 November 2021, ISBN: 978-4-909106063 C3051

THE APPLICATION OF STRUCTURE FROM MOTION METHOD FOR ROCKFALL ANALYSIS, A CASE STUDY ON ENDE-MAUMERE ROAD KM 18+600, EAST NUSA TENGGARA

Cahya Ahmad Gumilar[1] and Muhammad Rizaldi Nuraulia[2]

[1,2] Geotechnical, Tunnel and Structure Division, Directorate General of Highways, Ministry of Public Works and Housing Republic of Indonesia

ABSTRACT

Rockfall often happens on Ende-Maumere Km 18+600 road, Ende Regency, East Nusa Tenggara because that location has an intense geological structure condition, such as fault, joint, and plane discontinuity. That condition affected the rock slope is vulnerable to rockfall occurrences. Rockfall identification and analysis such as rock mass rating (RMR) and slope mass rating (SMR) to identify rock slope characteristics and kinematic analysis to determine the type of rockfall failure must be conducted properly. Structure from Motion (SfM) is an image-based method to identify the characteristics of discontinuity plane from the photogrammetric using UAV/Drone to generates high-resolution 3D images rock surfaces and outcrops with a lower cost compared to Terrestrial Laser Scanning (TLS) and can map the location that can't be done by geological compass. The measurement using a geological compass and SfM on the toe of slope compared, and the results show no significant differences of discontinuity with differences of only ± 10°. The photogrammetric images show RMR and SMR values between 50° to 70°. The average strike/dip of discontinuity using the SfM method at the toe of the slope is N 190° E/55°. This data is then used as input parameters for kinematic analysis, resulting in the type of rockfall failure wedge and toppling.

Keywords: structure from motion, rock mass rating, slope mass rating, kinematic analysis

INTRODUCTION

The development of the structure from motion (SfM) method has acquired high-resolution topographic data cheaper and more manageable. SfM allows acquisitions using ordinary digital cameras that can be done alone, thereby significantly reducing the number of experts required to collect topographical models using this method (Micheletti et al., 2015).

In this study, the SfM method was used to create a three-dimensional model of a slope segment on the Ende-Maumere road Km 18+600, Ende Sub-District, Ende Regency, East Nusa Tenggara.

GEOLOGICAL CONDITIONS

Regional stratigraphy was taken based on the Geological Map of the Ende Quadrangle, East Nusa Tenggara (Fig. 1) (Suwarna et al., 1989).

Old Volcanic Results (QTv): consists of lava, breccia, agglomerates with local inserts of tuff and tuff of lapilli, a thin layer of silt and coral limestone. Lava is composed of andesitic pyroxene, locally showing a columnar and sheeting joint structure. Andesitic and basalt fragments and agglomerates, loose material. In some places, this unit exhibits a columnar structure. This unit was deposited in a shallow water environment (Suwarna et al., 1989).

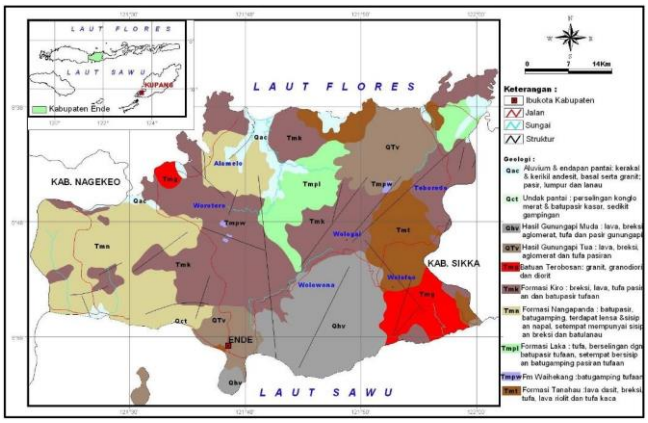

Fig. 1 Geological Map of the Ende (Suwarna et al., 1989)

ROCK MASS RATING (RMR)

RMR was established by Bieniawski (1973-1989) to evaluate the quality of rock masses for underground projects. The RMR system consists of five basic parameters that represent different conditions of the rock and its discontinuities. These parameters are (1) UCS of intact rock, (2) RQD, (3) spacing between discontinuities, (4) condition of discontinuities, and (5) groundwater. This RMR system is known as "the basic RMR" and gives a value ranging from 0 to 100 (Bieniawski, 1989).

Table 1 Classification parameter and their ratings

	Parameter		Range of values						
1	Strength of intact rock material	Point-load strength index (MPa)	> 10	4 – 10	2 – 4	1 – 2	For the low range, uniaxial compression test is preferred		
		Uniaxial compressive strength (MPa)	> 250	100 – 250	50 – 100	25 – 50	5 – 25	1 – 5	< 1
		Rating	15	12	7	4	2	1	0
2	Drill core RQD (%)		90 – 100	75 – 90	50 – 75	25 – 50	< 25		
		Rating	20	17	13	8	3		
3	Spacing of discontinuities		> 2 m	0.6 – 2 m	20 – 60 cm	6 – 20 cm	< 6 cm		
		Rating	20	15	10	8	5		
4	Condition of discontinuities (see Table 2)		Very rough surfaces Not continuous No separation Unweathered wall rock	Slightly rough surfaces Separation < 1 mm Slightly weathered walls	Slightly rough surfaces Separation < 1 mm Highly weathered walls	Slickensided surfaces or Gouge < 5 mm thick or Separation 1 – 5 mm (Continuous)	Soft gouge > 5 mm thick or Separation > 5 mm (Continuous)		
		Rating	30	25	20	10	0		
5	Groundwater	Inflow per 10 m tunnel length (L/min)	None	< 10	10 – 25	25 – 125	> 125		
		Ratio of joint water pressure to major principal stress	0	< 0.1	0.1 – 0.2	0.2 – 0.5	> 0.5		
		General condition	Completely dry	Damp	Wet	Dripping	Flowing		
		Rating	15	10	7	4	0		

Note: After Bienawski, 1989

Table 2 Guidelines for classification of discontinuity conditions

Parameter	Ratings				
Discontinuity length (persistence/continuity)	< 1 m	1 – 3 m	3 – 10 m	10 – 20 m	> 20 m
	6	4	2	1	0
Separation (aperture)	None	< 0.1 mm	0.1 – 1 mm	1 – 5 mm	> 5 mm
	6	5	4	1	0
Roughness	Very rough	Rough	Slightly rough	Smooth	Slickensided
	6	5	3	1	0
Infilling (gouge)		Hard filling		Soft filling	
	None	< 5 mm	> 5 mm	< 5 mm	> 5 mm
	6	4	2	2	0
Weathering	Unweathered	Slightly weathered	Moderately weathered	Highly weathered	Decomposed
	6	5	3	1	0

Note: After Bienawski, 1989

Table 3 Rock mass classes from total ratings

Rating	Class	Description
100 – 81	I	Very good rock
80 – 61	II	Good rock
60 – 41	III	Fair rock
40 – 21	IV	Poor rock
< 20	V	Very poor rock

Note: After Bienawski, 1989

SLOPE MASS RATING (SMR)

SMR is a classical lump-rating classification system for rock slopes developed by Romana (1985). The SMR system is derived initially from the RMR system, where adjustment parameters representing the discontinuity orientations concerning the slope attitude are added to the basic RMR and the effect of the excavation method. SMR score is obtained by

subtracting a factor from RMR depending on the joint-slope relationship, and adding an element depending on the excavation method, as expressed in the following equation.

$$SMR = RMR + (F_1 \times F_2 \times F_3) + F_4 \quad (1)$$

Where F_1 is an adjustment factor, which depends on the parallelism between the joint strike (α_j) (or the plunge direction of the intersection line of two planes (α_i) and the slope face strike (α_s). It ranges from 1, when the joint and the slope face strikes are near parallel, to 0.15, when the angle between strikes is 30° (see Table 4).

F_2 refers to joint dip angle (β_j) in the planar failure or the plunge of the line of intersection of two planes (β_i) in the wedge-type failure mode. It varies from 1 for joints dipping more than 45° to 0.15 for joints dipping less than 20° (see Table 4).

F_3 reflects the effect of the angle between the slope face dip (β_s) and the joint dip (β_j) or the plunge of the intersection line of two planes (β_i). It ranges from 0 (very favourable) when $\beta_j - \beta_s$ or $\beta_i - \beta_s$ is more than 10°, to – 60 (very unfavourable) when $\beta_j - \beta_s$ or $\beta_i - \beta_s$ is less than – 10°.

F_4 is an adjustment factor that depends on the excavation method. The values are selected empirically as shown in Table 5.

Table 5 Adjustment factor F_4 for excavation method

Method of excavation	F_4 value
Natural slope	15
Pre-splitting	10
Smooth blasting	8
Normal blasting or mechanical excavation	0
Deficient blasting	-8

Note: After Romana, 1985

Planar-type and toppling-type failure modes are considered in the SMR system. Anbalagan et al. (1992) added a wedge failure to Romana's classification. Wedge-type and planar-type failure modes will be addressed separately, where the inclination and the direction of the line of intersection of two planes are considered for wedge failure analysis. This modified SMR (Anbalagan et al., 1992) is used in this paper, and three types of structurally controlled failures, i.e., planar, wedge, and toppling, are used. These are identified in Table 4 as 'P' for planar, 'W' for wedge and 'T' for toppling. Different classes of SMR scores that describe the slope and its stability condition are listed in Table 6.

Table 6 SMR classes

Class	SMR	Description	Stability
I	81 – 100	Very good	Completely stable
II	61 – 80	Good	Stable
III	41 – 60	Fair	Partially stable
IV	21 – 40	Bad	Unstable
V	0 – 20	Very bad	Completely unstable

Note: After Romana, 1985

RESEARCH METHODS

Field Geology Method

Morphology description of the outcrop and the type of rock is carried out, and then the scanline method is measured by the stretching of the measuring tape along a length of 50 meters where the strike dip value is calculated from each discontinuity that is passed by the tape measure (Fig. 2).

Descriptions of rock mass rating (RMR) and slope mass rating (SMR) are also carried out by observing outcrops in the field.

Structure From Motion Method

First, the outcrop photo captured was done using a DJI Mavic 2 Pro drone with a 20 megapixel Hasselblad camera with global coordinates. Image captured was done using DroneDeploy software to create flight routes and outcrop areas to be captured. (Fig. 3). The resulting 253 photos were processed using Agisoft Photoscan Professional software.

Fig. 2 Field observations using tape and compass

Then, the global coordinates are converted to UTM 48S projection coordinates. After that, the photos were aligned to produce a sparse point cloud which has 120,857 points. Then the sparse point cloud is then processed into a dense point cloud with 16,223,542 points (Fig. 4).

Table 4 Adjustment ratings for F_1, F_2, and F_3

Case of slope failure		Very favourable	Favourable	Fair	Unfavourable	Very unfavourable
P	$\lvert\alpha_j - \alpha_s\rvert$					
T	$\lvert\alpha_j - \alpha_s - 180°\rvert$	> 30°	30° – 20°	20° – 10°	10° – 5°	< 5°
W	$\lvert\alpha_i - \alpha_s\rvert$					
P/T/W	F_1	0.15	0.4	0.7	0.85	1
P	$\lvert\beta_j\rvert$	< 20°	20° – 30°	30° – 35°	35° – 45°	> 45°
W	$\lvert\beta_i\rvert$					
P/W	F_2	0.15	0.4	0.7	0.85	1
T	F_2	1	1	1	1	1
P	$\beta_i - \beta_s$	> 10°	10° – 0°	0°	0° to –10°	< –10°
W	$\beta_j - \beta_s$					
T	$\beta_j + \beta_s$	< 110°	110° – 120°	> 120°	–	–
P/T/W	F_3	0	-6	-25	-50	-60

Note: After Romana, 1985 modified by Anbalagan et al., 1992

Fig. 3 Flight routes to capture the photos

Then, the dense point cloud is processed into a 3D model through a meshing process. Furthermore, the 3D model is exported in ASPRS LAS (.las) format for further analysis using CloudCompare software.

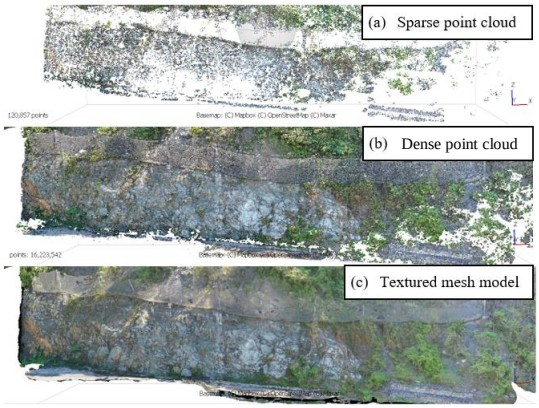

Fig. 4 SfM method data processing using Agisoft Photoscan Professional

Strike and dip calculations can be performed using the Compass plugins found in the CloudCompare software.

KINEMATIC ANALYSIS

Field Geology Method

The results of the strike and dip calculations carried out in the field as shown in Table 7 were analyzed using the Rocscience Dips software. The wedge failure as shown in Figure 5 occurs at 1084 points of joint intersection with a significance of 13.57 % of the total points of joint intersection. The pink area on the stereonet indicates the critical area for wedge failure, while the yellow zone indicates the semi-critical area for wedge failure.

Table 7 The difference between the calculation of the field model and the SfM model

Field Model		SfM Model		Difference	
Strike	Dip	Strike	Dip	Strike	Dip
235	47	245	39	+10	-8
34	42	29	49	-5	+7
205	60	210	64	-5	+4
30	37	36	41	+6	+4
217	64	224	66	+7	+2
215	67	209	60	-6	-7
210	55	205	53	-5	-2
270	40	263	34	-7	-6
340	33	330	27	-10	-6
200	54	196	45	-4	-9
205	38	215	46	-10	+8
217	48	212	41	-5	-7
195	50	200	57	+5	+7
197	55	203	63	+6	+8
190	62	197	64	+7	+2

Note: This only shows 15 data examples; 127 data of the field model and 250 data of the SfM model.

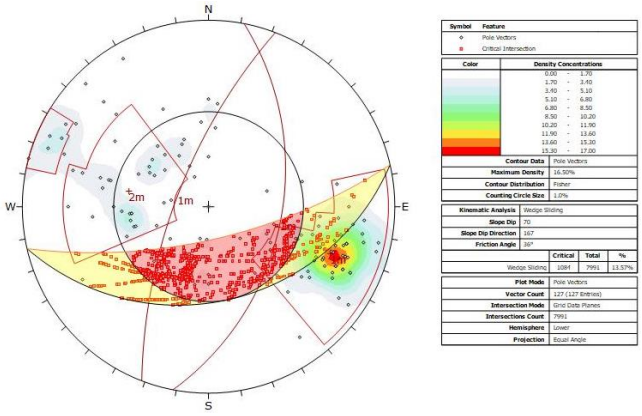

Fig. 5 Wedge failure configuration on field model

The direct toppling failure as shown in Figure 6 occurs at 800 points of joint intersection with a significance of 10.01 % of the total points of joint intersection. The pink area on the stereonet indicates the critical area for direct toppling failure, while the yellow zone indicates the semi-critical area for oblique toppling failure.

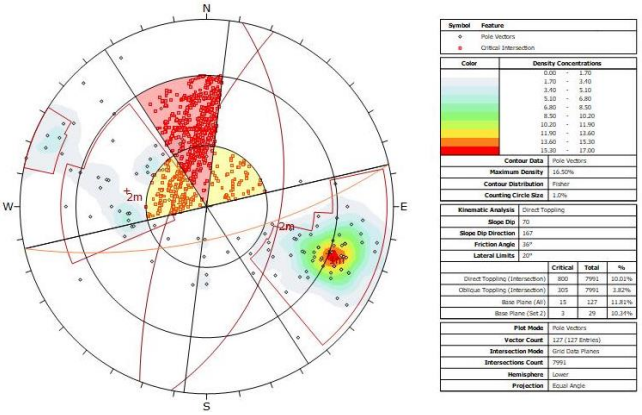

Fig. 6 Toppling failure configuration on field model

Structure From Motion Method

The results of the strike and dip calculations carried out in the field as shown in Table 7 were analyzed using the Rocscience Dips software. The wedge failure as shown in Figure 7 occurs at 4614 points of joint intersection with a significance of 14.83 % of the total points of joint intersection. The pink area on the stereonet indicates the critical area for wedge failure, while the yellow zone indicates the semi-critical area for wedge failure.

The direct toppling failure shown in Figure 8 occurs at 2797 points of joint intersection with a significance of 8.99% of the total points of joint intersection. The pink area on the stereonet indicates the critical area for direct toppling failure, while the yellow zone indicates the semi-critical area for oblique toppling failure.

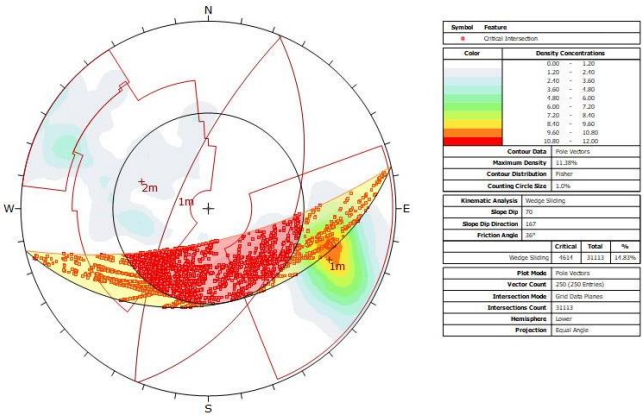

Fig. 7 Wedge failure configuration on SfM model

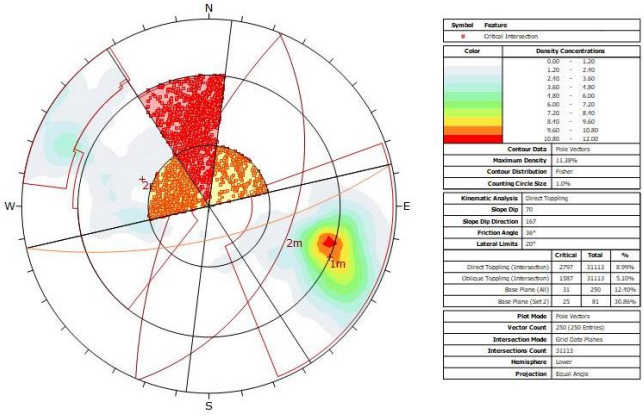

Fig. 8 Toppling failure configuration on SfM model

DISCUSSION

Strike Dip Measurements

In this study, the strike dip measurement was carried out by direct measurement in the field and using the SfM method (Table 7). The difference in the calculation with a range of values of ± 10°. This difference is due to some discontinuity planes minimal surface area and the lack of firm boundaries on the discontinuity planes.

Therefore, data acquisition using the SfM method, which is only based on the front view of the outcrop, also causes the resulting depth maps to be less accurate due to the shadow effect indirectly captured by the camera.

RMR and SMR Calculation

In this study, there were two calculations of RMR and SMR, which were carried out through field observations and using the SfM method. The comparison on RMR and SMR calculations shown on

Table 8 Comparison of the calculation RMR values of the field model with the SfM model

Model	Strength of intact rock material		RQD		Spacing of discontinuity		Condition of discontinuity		Groundwater		RMR values
	UCS	Rating	%	Rating	Spacing	Rating	Description	Rating	Condition	Rating	
Field Model	100-250 MPa	12	75 – 90	17	6 – 20 cm	8	Discontinuity length 3-10 m, separation 1-5 mm, no filling, slightly weathered	19	Dry	15	71
SfM Model	97 MPa	7	73.57	13	6 – 20 cm	8	Discontinuity length 3-10 m, separation 1-5 mm, no filling, slightly weathered	19	Dry	15	61

Note: Based on Bieniawski, 1989

Table 9 Comparison of the calculation SMR values of the field model with the SfM model

Model	RMR values	Slope angle recommendation and class						Slope support recommendation
		F_1	F_2	F_3	F_4	SMR	Class	
Field Model	71	1.00	0.15	-60	0	62°	IIb	Toe ditch or fence. Nets. Spot or systematic bolting
SfM Model	61	1.00	0.15	-60	0	52°	IIIa	Toe ditch and/or nets Spot or systematic bolting Spot shotcrete

Note: Based on Romana, 1985 modified by Anbalagan et al., 1992

Table 8 and Table 9 are more conservative using the SfM method. This happens because the SfM methods calculations generated more data, 250 data in the SfM method, and 127 data in field observations, shown in Table 7 notes.

Kinematic Analysis

In this study, two kinematic analysis calculations were carried out through field observations and using the SfM method. Comparison of the kinematics analysis results through field observations and using the SfM method shows the calculation results are more conservative, with 14.83 % chances for wedge failure in the SfM method and 13.57 % in the field model. In toppling failure, with 8.99 % chances in the SfM method and 10.01 % in the field observations. The possibilities for wedge failure are more extensive than toppling failure because the joint measurement results in a more intersected joint, which means the wedge failure are more influential in this type of failure on the slope.

Both models produce the same three types of failure, wedge failure, direct toppling failure, and oblique toppling failure. However, there are significant differences in the kind of failure in each model. This happens because the discontinuity data obtained through the SfM method is more numerous than through field observations.

In addition, with the help of the SfM method, engineering geologists can observe outcrops in more detail and more freely in a 3D model.

CONCLUSIONS

Based on the results of data analysis and discussion that has been described previously, the following conclusions are obtained:

1. The SfM method approach is suitable for small-scale outcrops such as outcrops in the study area because of its flexibility in delineating the discontinuity area.
2. The research area has two sets of joint set with an average orientation N 203°E / 70° in set 1 and N 22°E / 42° in set 2. The measurement using a geological compass and SfM on the toe of slope compared, and the results show no significant differences of discontinuity with differences of only ± 10°.
3. There are differences in the calculation results of the RMR value using the field model, which has 71 values, and the SfM model has 61 values. Meanwhile, the difference in the calculation of the SMR values using the field model has 62° SMR values and the SfM model with 52° SMR values.
4. The field model is classified in IIb classes with recommendations for supporting using toe ditch or fence, nets, spot, or systematic bolting, while the SfM model is classified in IIIa classes with recommendations for supporting using toe ditch and/or nets, spot or systematic bolting, spot shotcrete.
5. Slope failure in the study area has three types of failure that may occur, wedge failure, direct toppling failure, and oblique toppling failure. There is a significant result from the field method and the SfM method, where the SfM method is more conservative because the chance of failure is bigger with 14.83 % compared to 13.57 % in the field model.

ACKNOWLEDGMENTS

Thank you to the Head of the Geotechnical, Tunnel and Structures Division, Directorate General of Highways, Ministry of Public Works and Housing Republic of Indonesia for granting permission and providing funds for this research to complete this paper.

REFERENCES

[1] Anbalagan R., Sharma S., Raghuvanshi T. K. Rock mass stability evaluation using modified SMR approach. In: proceeding of the 6th National Symposium on Rock Mechanics; 1992. p. 258-68.
[2] Bieniawski Z. T. Classification rock masses for engineering. John Wiley & Sons; 1989.
[3] Hafiz A., Setianto A. Aplikasi Metode Structure from Motion dalam Penentuan Kedudukan Bidang Gelincir di Desa Ngoro-Oro, Kecamatan Patuk, Kabupaten Gunungkidul, Daerah Istimewa Yogyakarta. Prosiding Seminar Nasional Kebumian ke-12 Universitas Gadjah Mada; 2019. p. 1362-1375.
[4] Micheletti N., Chandler J., and Lane S. Struture from Motion (SfM) photogrammetry. British Society for Geomorphology; 2015.
[5] Romana M. New adjustment ratings for application of Bieniawski classification to slopes. In: Proceedings of international symposium on the rock of rock mechanics. Zacatecas: ISRM; 1985. p. 49-53.
[6] Suwarna N. Geological Map of the Ende Quadrangle, East Nusa Tenggara. Pusat Penelitian dan Pengembangan Geologi; 1989.

11th Int. Conf. on Geotechnique, Construction Materials & Environment,
Kyoto, Japan, 3-5 November 2021, ISBN: 978-4-909106063 C3051

EFFECT OF COCONUT SHELL ASH ON PORE WATER PRESSURE CHANGES IN SAND

Gabriel Jose G. Lim[1], Mary Ann Q. Adajar[2], and Erica Elice S. Uy[2]

[1]Graduate Student, De La Salle University, Philippines; [2]Faculty, De La Salle University, Philippines

ABSTRACT

Previous studies showed that addition of coconut shell ash (CSA) to soil improved the California Bearing Ratio, Maximum Dry Density, and Unconfined Compressive Strength. But the effect of CSA in deceasing soil susceptibility to static liquefaction has yet to be investigated. Static liquefaction is a major concern because it is defined when soil loses its strength and behaves like a fluid. This causes settlements, damages to buildings, and endangers lives. The loss in soil strength is attributed to the increase in pore water pressure. Pore water pressure buildup is more likely to happen in loose and saturated sands. This study hypothesizes that the particle size and the chemical property of CSA can reduce the liquefaction susceptibility of sands by decreasing pore water pressure buildup when the sand is subjected to vertical loads. For the experiment, the consolidated undrained (CU) triaxial test was conducted. The Cam-Clay model was used to analyze soil behavior between the control samples and the samples mixed with CSA. Results show that administering 5 % CSA expanded the soil's yield surface, improving soil's ability to respond elastically to deformations. Five percent CSA decreased pore water pressure buildup in the samples subjected to 50 kPa and 100 kPa consolidating pressures by 6.53 % and 5.55 %, respectively. However, for the sample subjected to 25 kPa consolidating pressure, 5 % CSA caused an adverse effect by increasing pore water pressure buildup by 10.73 %. The low consolidating pressure negates the effect of CSA and there should be a sufficiently high consolidating pressure to decrease pore water pressure buildup.

Keywords: Coconut Shell Ash, Critical State, Cam-Clay Model, Pore Water Pressure Buildup

INTRODUCTION

Soil liquefaction is a phenomenon where the strength of soil is decreased by loads. Soils are made up of an assemblage of individual soil particles. The weight of these particles produces contact forces among the particles. Contact forces are responsible for holding the particles together and give the soil its strength. Liquefaction occurs in saturated soils, which are soils with voids filled with water. During loading, soils breaks down into a denser configuration. The water in the voids is compressed, and water pressure is generated. Water pressure decreases the contact forces among the soil particles. In severe cases, high water pressures cause the particles to completely lose contact with each other. This causes soil to behave like a liquid [1]-[4]. The current trend in geotechnical engineering is to improve soil using waste materials instead of conventional processes and additives, like fly ash and cement [5]-[16]. Using locally available waste materials will help the environment and reduce construction costs [17]-[28]. Previous experiments concluded that the introduction of additives like slag, Bassanite, fibers, grout and denitrifying bacteria decreased pore water pressure generation in soils. However, past studies have yet to investigate the effect of coconut shell ash (CSA) in reducing pore water pressure generation [29]-[34]. With a scanning electron microscope, the mean particle size of CSA was 34.3 microns. With its small particle size, CSA can occupy soil voids and reduce the amount of water held by the soil, which can decrease pore water pressure buildup [35]. The effect of CSA as a stabilizer for base course of pavements has been investigated. Dosages of 5 %, 10 %, and 15 % CSA were tested, and it was found that 5 % CSA produced the best results [36]. The Philippine Institute of Volcanology and Seismology (PHILVOCS) declared the areas of Malabon, Manila, Pasay, Marikina, Pateros, Pasig and the coastal area of Muntinlupa to have very high liquefaction susceptibility. Heavy loads from buildings in these areas can trigger pore water pressure buildup [37]. It is the objective of this study to measure and compare the generation of the pore water pressure, under consolidated undrained (CU) triaxial test, among the sand samples at 0 % and 5 % CSA mixtures, at a target relative density. The objective also includes determining shear strength parameters and validating stress-strain responses of modified soil through obtaining overconsolidation ratio.

CAM-CLAY MODEL

The Cam-Clay model is a useful tool for geotechnical engineers because it incorporates

volume changes in modeling soil behavior. The Cam-Clay Model states that all soils will fail in a unique failure surface defined by deviatoric stress (q), effective mean stress (p'), and void ratio (e). It is used when sufficient soil tests cannot be conducted or when there is a need to estimate soil responses to changes in loading during and after construction. An example is when a client makes a last-minute change by adding another story to a structure but does not want to finance any further soil testing. The Cam-Clay model is used to determine whether the soil can support an additional story [38]. It is known that the buildup of pore water pressure accelerates after soil yields. With void ratio considered, the Cam-Clay model defines the range of stresses that would result to soil yielding. With this, engineers can determine when to slow down the rate of construction or how to manage heavy machinery on the construction site, to avoid failure caused by excess pore water pressure generation [39]. There are other models that incorporate critical state concepts, like the Modified Cam-Clay model and the Nor-Sand model. The Cam-Clay model was used because it is simple, consistent, and arguably still the most influential soil model proposed [40]. Many sophisticated critical state models have been proposed but these models still adopt the original Cam-Clay model as their backbone [41].

In this study, the original Cam-Clay model was used for undrained analysis, proving its suitability for this study. The elements of the Cam-Clay model include the yield surface, critical state line in the q-p' space, critical state line in the e-ln p' space, and normal consolidation line. These are defined by Eq. 1, Eq. 2, Eq. 3, and Eq. 4, respectively. The Cam-Clay model also consists of the total stress path and the effective stress path. The total stress path and the effective stress path are plotted using the data from the consolidated undrained triaxial test.

$$\frac{q}{Mp'} + \ln\left(\frac{p'}{p_{o'}}\right) = 0 \quad (1)$$

$$q = Mp' \quad (2)$$

$$e = \Gamma + \lambda \ln p' \quad (3)$$

$$e = N_p + \lambda \ln p' \quad (4)$$

EXPERIMENTAL PROGRAM

Index Tests

The index properties of the CSA were obtained in accordance to ASTM standards. The following are the tests performed: Specific Gravity Test (ASTM D854), Maximum Void Ratio Test (ASTM D4253), and Minimum Void Ratio Test (ASTM D4254).

Consolidated Undrained Triaxial Test

The consolidated undrained triaxial test was performed based on ASTM D4767 – 02. The sample preparation method used was the air pluviation method. Two percentages of CSA were adopted in this study. Zero percent and five percent CSA were mixed with loose Ottawa sand. For the saturation phase, the cell pressure is kept at a pressure difference of 5 kPa from the back pressure to prevent sample swelling. A fully saturation condition is attained when Skempton's B-value is greater than 0.95, this is defined by Eq. 5.

$$B = \frac{\Delta u}{\Delta \sigma_3} > 0.95 \quad (5)$$

For the consolidation phase, the consolidating pressures were set at 25 kPa, 50 kPa, and 100 kPa. In this study, the samples are allotted thirty minutes to consolidate. For the shearing phase, the rate of loading for an undrained condition is usually 1 % axial strain, but this did not cause any significant change in pore water pressure. The axial strain was slowly increased to 2 % and 5 %, before settling for a 10 % axial strain. Ten percent axial strain caused enough pore water pressure generation required for the purpose of this study. The strain was applied until the stroke limit was reached.

RESULTS AND DISCUSSION

Index Properties

Summarized in Table 1 are the index properties of CSA. The specific gravity of CSA falls within the range of values found from previous studies [42-43].

Table 1. Index Properties

Index Property	Value
Specific Gravity (G_s)	1.525
Maximum Void Ratio (e_{max})	1.778
Minimum Void Ratio (e_{min})	0.804

Strain Curves

Larger consolidating pressures allow sand to take more stress at the same strain. The samples subjected to the 100kPa consolidating pressure are denser than the other samples subjected to 25 kPa and 50 kPa consolidating pressures. A peak is observed in the samples subjected to 100k Pa consolidating pressure because denser soils tend to dilate and exhibit peaks. Critical state was taken at 10 % axial strain. The stress strain curves for the samples are shown in Fig. 1 and Fig. 2.

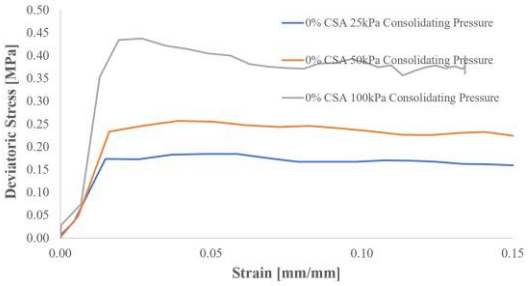

Fig. 1 Stress Strain Curve for 0% CSA Group

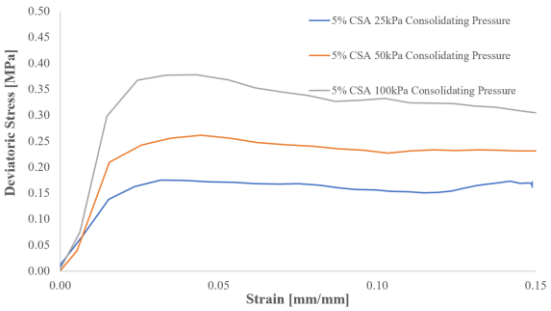

Fig. 2 Stress Strain Curve for 5% CSA Group

Pore Water Pressure Buildup

The pore water pressure-strain curves of the samples are shown in Fig. 3 to 5. It is observed that pore water pressure fluctuates much more in samples that were subjected to the 25kPa consolidating pressure. Samples that were subjected to the 100kPa consolidating pressure exhibited less fluctuations and much flatter curves. Larger consolidating pressures decreased pore water pressure changes. Observing Figure 3, the graph of 0% CSA resembled a flat line once 5 % axial strain was reached, while the graph of 5 % CSA exhibited relatively more fluctuations. While both samples were subjected to 50kPa consolidating pressure, the sample mixed with 5 % CSA exhibited a flat stress-strain curve. Five percent CSA was shown to decrease fluctuations, thus resulting to more stable pore water pressure-strain curve behavior. The same is observed from the graphs in Figure 4 and Figure 5.

Shear Strength Parameters

The Mohr Coulomb failure envelope for both total and effective stress conditions are shown in Fig. 6 and Fig. 7. The best fit tangent line is drawn to obtain the friction angles. The effective friction angle is used to find the slope of the critical state line in the Cam-Clay model. Tabulated in Table 2 are the friction angles in the total stress and effective stress condition. The five (5) percent CSA caused the friction angle in the total stress condition to increase from 31.7595° to 38.1076°. The five (5) percent CSA did not cause significant increase in friction angle in the effective stress condition.

Table 2. Friction Angles

CSA	ϕ	ϕ'
0%	31.7595°	38.2902°
5%	38.1076°	38.2073°

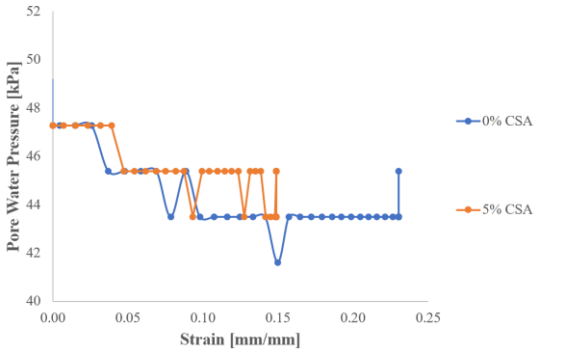

Fig. 3 Pore Water Pressure-Strain Curve at 25kPa Consolidating Pressure

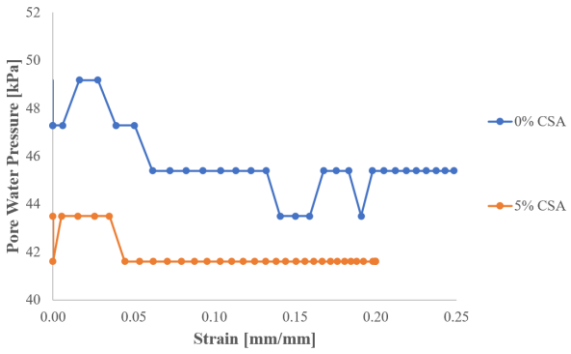

Fig. 4 Pore Water Pressure-Strain Curve at 50kPa Consolidating Pressure

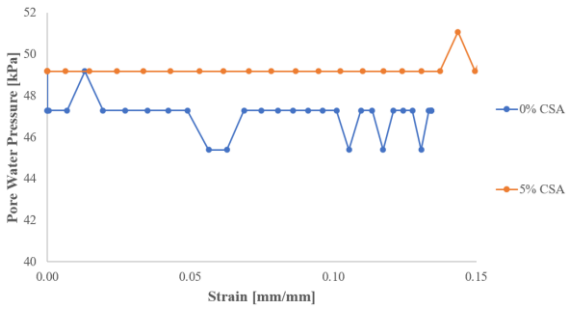

Fig. 5 Pore Water Pressure-Strain Curve at 100kPa Consolidating Pressure

Cam-Clay Model

The Cam-Clay model in the q-p' space for the sample at 5 % CSA and subjected to 25 kPa consolidating pressure is presented in Fig. 8. The

stress paths lie to the right of the critical state line. The same is also observed in all the other samples. This indicates that all samples are normally consolidated and lightly overconsolidated soils. Thus, the samples will compress and undergo strain hardening. For the sample at 5% CSA and subjected to 25 kPa consolidating pressure, the equations for the yield surface and critical state line in the q-p' space are defined by Eq. 6 and Eq. 7, respectively.

$$\frac{q}{1.558p'} + \ln\left(\frac{p'}{122.619}\right) = 0 \quad (6)$$

$$q = 1.558p' \quad (7)$$

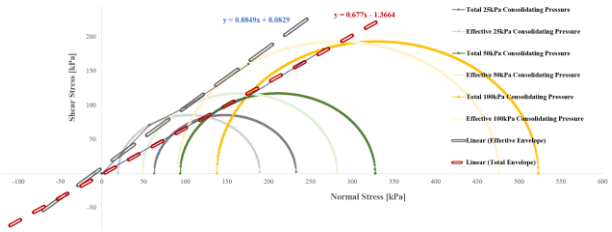

Fig. 6 Mohr's Circle and Failure Envelope at 0% CSA

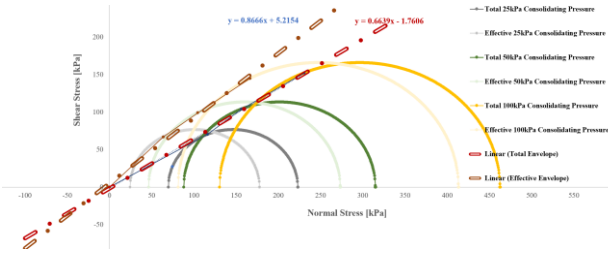

Fig. 7 Mohr's Circle and Failure Envelope at 5% CSA

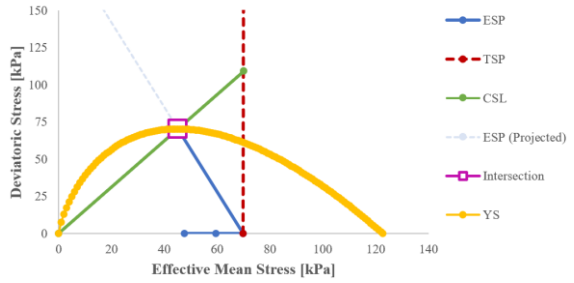

Fig. 8 Mohr's Circle and Failure Envelope at 5% CSA and 25kPa Consolidating Pressure

The Cam-Clay model in the q-p'-e space is a 3D model which shows the boundary surface. All combinations of deviatoric stress, effective mean stress, and void ratio within the boundary surface will not result in soil failure and are considered safe. The boundary surface shows that the yield surface decreases as the void ratio increases. Soil becomes more susceptible to failure at larger void ratios, or at looser soil states. In other words, the soil's ability to exhibit elastic responses improves at lower void ratios, or at denser soil states. The Cam-Clay model in the q-p'-e space for the sample at 5 % CSA and subjected to 25 kPa consolidating pressure is presented in Fig. 9. For the same sample, the critical state line in the e-ln p' space and normal consolidation line are defined by Eq. 8 and Eq. 9, respectively.

$$e = 0.441 + 0.0156\ ln\ p' \quad (8)$$

$$e = 0.456 + 0.0156\ ln\ p' \quad (9)$$

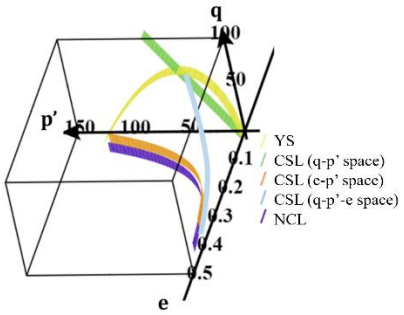

Fig. 9 3D Cam-Clay Model at 5% CSA and 25kPa Consolidating Pressure

The friction angle for dense sands range between 36° and 41°. The samples in the study have a relative density of 70 %, indicating dense sand. The friction angles obtained fall within the range for dense sands, verifying that the samples are in the dense state [44]. Summarized in Table 4 are the pore water pressure buildup at failure for the samples. Five percent CSA decreased pore water pressure buildup by 6.53 % and 5.55 % for the samples subjected to consolidating pressures of 50 kPa and 100 kPa, respectively. The decrease in pore water pressure buildup is attributed to the small particle size of CSA, which occupy the soil voids and reduces the amount of water that occupy the soil voids. However, an adverse effect was observed in the sample subjected to 25 kPa consolidating pressure when mixed with 5 % CSA. The sample exhibited a 10.73 % increase in pore water pressure buildup. The low consolidating pressure negated the effect of CSA. Sufficient consolidating pressure is required for 5 % CSA to decrease pore water pressure buildup. The effect of CSA on the yield surface is analyzed by comparing the yield surfaces at 0 % CSA and at 5 % CSA. Plastic deformations are unrecoverable and occur when stress states lie beyond the yield surface. Within the yield surface, soils exhibit elastic responses to deformations. An expanded yield surface indicates that soil is more able to respond elastically to heavier loads. In other words, soil deformations become much more recoverable. It was observed that for 5 % CSA mixture with 25 kPa and 100 kPa consolidation pressure their yield surface expanded. However, for 50 kPa consolidation pressure 5 % CSA did not

experience expansion. It was observed upon inspection of the sample after the experiment most of the CSA settled at the bottom. This was due to the lack of contact of CSA to the soil sample.

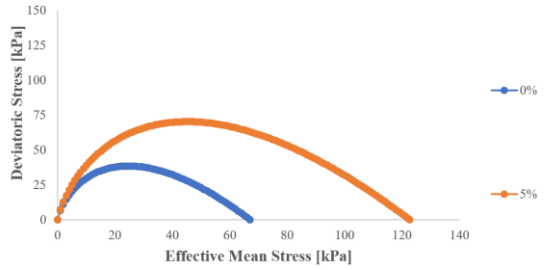

Fig. 10 Yield Surfaces at 25kPa Consolidating Pressure

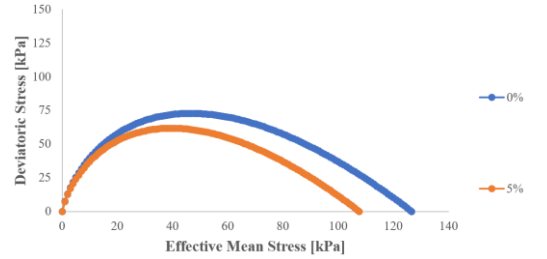

Fig. 11 Yield Surfaces at 50kPa Consolidating Pressure

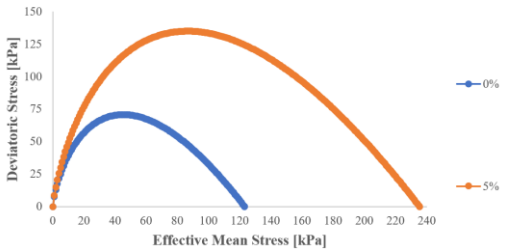

Fig. 12 Yield Surfaces at 100kPa Consolidating Pressure

From the Cam-Clay model graphs, Eq. 10 is formulated to calculate the pore water pressure change at failure (Δu_f) [38]. The critical state parameters and the void ratio after consolidation phase (e_c) of the samples are summarized in Table 3.

$$\Delta \boldsymbol{u_f} = \boldsymbol{\sigma_3} + (\frac{\boldsymbol{M}}{\boldsymbol{3}} - \boldsymbol{1})(\boldsymbol{\exp}[\frac{\boldsymbol{\Gamma - e_c}}{\boldsymbol{\lambda}}]) \quad (10)$$

With Eq. 1, the preconsolidation stress (p_o') is estimated from the deviatoric stress and effective mean stress at critical state. It is then used to compute for the overconsolidation ratio (R_o) with Eq. 11. The overconsolidation ratio is used to validate if the samples are normally consolidated and lightly overconsolidated soil.

$$\boldsymbol{R_o} = \frac{\boldsymbol{p_o'}}{\boldsymbol{\sigma_3}} \quad (11)$$

Table 3. Cam-Clay Model Parameters and Void Ratio After Consolidation Phase

Sample	M	Γ	e_c	λ
0%CSA 25kPa	1.562	0.463	0.429	0.0108
0%CSA 50kPa	1.562	0.416	0.365	0.0144
0%CSA 100kPa	1.562	0.436	0.415	0.0052
5% CSA 25kPa	1.558	0.441	0.390	0.0156
5% CSA 50kPa	1.558	0.477	0.388	0.0256
5%CSA 100kPa	1.558	0.472	0.402	0.0181

Table 4. Pore Water Pressure Buildup at Failure

Consolidation Pressure[kPa]	$\Delta u_{0\%CSA}$ [kPa]	$\Delta u_{5\%CSA}$ [kPa]	$\%_{Decrease}$
25	51.890	57.460	-10.73
50	77.506	72.442	6.53
100	113.746	107.429	5.55

Summarized in Table 5 are the preconsolidation stresses, the current consolidating pressures (σ_3), and the overconsolidation ratios. R_o values less than or equal to 2 define normally consolidated and lightly overconsolidated soil. From the R_o values obtained, all samples fall into the classification of normally consolidated and lightly overconsolidated soil. Normally consolidated soil is expected to have a stress-strain behavior that does not exhibit a linear elastic state. For this type of soil, strain hardening is more pronounced and it behaves as an elastoplastic material. For a lightly overconsolidated soil is expected to exhibit a linear elastic state then followed by strain hardening. Also for this type of soil, it behaves as an elastoplastic material. To a considerable extent, the stress-strain curves of the samples, shown in Fig. 1 and Fig. 2, resemble the expected behavior of both a normally consolidated and lightly soil, respectively.

Table 5. Overconsolidation Ratios

Sample	p_o' [kPa]	σ_3 [kPa]	R_o
0%CSA 25kPa	67.008	63.000	1.1
0%CSA 50kPa	126.627	94.100	1.3
0%CSA 100kPa	123.086	138.100	1.0
5% CSA 25kPa	122.619	69.800	1.8
5% CSA 50kPa	107.662	88.000	1.2
5%CSA 100kPa	235.364	130.500	1.8

CONCLUSION

No liquefaction occurred in all samples because the pore water pressure buildup for all samples were insufficient to induce liquefaction. The five (5) percent CSA resulted to decreased fluctuations in the pore water pressure-strain graphs. A reduction in pore water pressure generation was also observed from the graphs. Five percent CSA effectively expanded the yield surface, which makes soil more able to respond elastically to heavier loads and recover from deformations. Five percent CSA reduced the pore water pressure buildup in the samples subjected to 50kPa and 100kPa consolidating pressure by 6.53% and 5.55%, respectively. Therefore, five (5) percent CSA is effective in decreasing pore water pressure generation in sands at 70% relative density. To a considerable extent, the expected stress-strain behavior of soil is in agreement with the actual soil behavior of the samples. The Cam-Clay model validated the samples to be normally consolidated and lightly overconsolidated soil.

ACKNOWLEDGMENTS

I would like to express my gratitude to my thesis adviser, Dr. Mary Ann Q. Adajar, and to Dr. Erica Elice S. Uy, for giving me the opportunity to conduct this research study. Their expertise proved vital for conducting this study. Without their continuous guidance, this paper would not have been possible. I express my appreciation to my parents for their constant support and encouragement throughout the entire process of this paper. Their confidence in me have proven to be an important factor for the completion of this research. I would also like to express my gratitude to the Engineering Research and Development for Technology and the Civil Engineering Department of De La Salle University. And of course, to God, who has equipped me with perseverance and discipline.

REFERENCES

[1] Johansson. (2000). What is soil liquefaction? Retrieved from https://depts.washington.edu/liquefy/html/why/why1.html.

[2] Uy, E. E. S., Noda, T., Nakai, K., & Dungca, J. R. (2018). Monitoring the triggering of liquefaction using image processing. International Journal of GEOMATE, 15(51), 180-187. doi:10.21660/2018.51.02150

[3] Uy, E. E. S., Noda, T., Nakai, K., & Dungca, J. R. (2018). Non-contact estimation of strain parameter-triggering liquefaction. International Journal of GEOMATE, 16(57), 82-88. doi:10.21660/2019.57.4722

[4] Ann Adajar, M., Galupino, J., Frianeza, C., Faye Aguilon, J., Sy, J. B., & Tan, P. A. (2020). Compressive strength and durability of concrete with coconut shell ash as cement replacement. International Journal of GEOMATE, 17, 183-190.

[5] Dungca, J. R., Galupino, J. G., Alday, J. C., Barretto, M. A. F., Bauzon, M. K. G., & Tolentino, A. N. (2018). Hydraulic conductivity characteristics of road base materials blended with fly ash and bottom ash. International Journal of GEOMATE, 14(44), 121-127. doi:10.21660/2018.44.7145

[6] Elevado, K. J. T., Galupino, J. G., & Gallardo, R. S. (2019). Compressive strength optimization of concrete mixed with waste ceramics and fly ash. International Journal of GEOMATE, 16(53), 135-140. doi:10.21660/2019.53.14268

[7] Galupino, J., Adajar, M. A., Uy, E. E., Koa, N. C., Lao, A. L., Lao, R. N., & Tan, J. C. M. (2020). Performance of concrete mixed with fly ash and plastic when exposed to fire. International Journal of GEOMATE, 19(74), 44-51. doi:10.21660/2020.74.9198

[8] Galupino, J. G., & Dungca, J. R. (2015). Permeability characteristics of soil-fly ash mix. ARPN Journal of Engineering and Applied Sciences, 10(15), 6440-6447.

[9] Adajar, M. A. Q., Aquino, C. J. P., dela Cruz, J. D., Martin, C. P. H., & Urieta, D. K. G. (2019). Investigating the effectiveness of rice husk ash as stabilizing agent of expansive soil. International Journal of GEOMATE, 16(58), 33-40. doi:10.21660/2019.58.8123

[10] Dungca, J. R., & Jao, J. A. L. (2017). Strength and permeability characteristics of road base materials blended with fly ash and bottom ash. International Journal of GEOMATE, 12(31), 9-15. doi:10.21660/2017.31.6508

[11] Dungca, J. R., Lao, W. D. T., Lim, M., Lu, W. D., & Redelicia, J. C. P. (2019). Radial flow permeameter: A proposed apparatus to measure horizontal hydraulic gradient of fly-ash based geopolymer-soil mix. International Journal of GEOMATE, 16(58), 218-223. doi:10.21660/2019.58.4524

[12] Elevado, K. T., Galupino, J. G., & Gallardo, R. S. (2018). Compressive strength modelling of concrete mixed with fly ash and waste ceramics using K-nearest neighbor algorithm. International Journal of GEOMATE, 15(48), 169-174. doi:10.21660/2018.48.99305

[13] Elevado, K. J. T., Galupino, J. G., & Gallardo, R. S. (2018). Artificial neural network (ANN) modelling of concrete mixed with waste ceramic tiles and fly ash. International Journal of GEOMATE, 15(51), 154-159. doi:10.21660/2018.51.58567

[14] Dungca, J. R., & Galupino, J. G. (2017).

Artificial neural network permeability modeling of soil blended with fly ash. International Journal of GEOMATE, 12(31), 76-83. doi:10.21660/2017.31.6549

[15] Dungca, J. R., & Galupino, J. G. (2016). Modelling of permeability characteristics of soil-fly ash-bentonite cut-off wall using response surface method. International Journal of GEOMATE, 10(4), 2018-2024. doi:10.21660/2016.22.5173

[16] Nicoleta-Maria, Farcas, Gherman, Vesile & Popa. (2015) Soils efficient improvement solutions with waste materials and binders. *Journal of Environmental Protection and Ecology*, 16, 1397-1406. Retrieved from https://www.researchgate.net/publication/295114373_Soils_efficient_improvement_solutions_with_waste_materials_and_binders/citation/downloa

[17] Uy, E. E. S., Adajar, M. A. Q., & Galupino, J. G. (2021). Utilization of philippine gold mine tailings as a material for geopolymerization. International Journal of GEOMATE, 21(83), 28-35. doi:10.21660/2021.83.9248

[18] Adajar, M. A. Q., & Cutora, M. D. L. (2018). The effect of void ratio, moisture content and vertical pressure on the hydrocompression settlement of copper mine tailing. International Journal of GEOMATE, 14(44), 82-89. doi:10.21660/2018.44.7108

[19] Adajar, M. A. Q., de Guzman, E., Ho, R., Palma, C., & Sindico, D. (2017). Utilization of aggregate quarry waste in construction industry. International Journal of GEOMATE, 12(31), 16-22. doi:10.21660/2017.31.6511

[20] Adajar, M. A. Q., & Pabilona, W. N. K. (2018). Soil-structure interface behavior of cemented-paste backfill material mixed with mining waste. International Journal of GEOMATE, 14(44), 102-108. doi:10.21660/2018.44.7109

[21] Adajar, M. A. Q., & Zarco, M. A. H. (2014). An empirical model for predicting hydraulic conductivity of mine tailings. International Journal of GEOMATE, 7(2), 1054-1061.

[22] Adajar, M. A. Q., & Zarco, M. A. H. (2016). Predicting the stress-strain behavior of mine tailing using modified hyperbolic model. International Journal of GEOMATE, 10(3), 1834-1841. doi:10.21660/2016.21.5127

[23] Uy, E. E. S., Adajar, M. A. Q., & Dungca, J. R. (2019). Volume change behavior of sea water exposed coal ash using hyperbolic model. International Journal of GEOMATE, 16(58), 97-103. doi:10.21660/2019.58.8171

[24] Uy, E. E. S., & Dungca, J. R. (2018). A comparative settlement prediction of limestone blended materials using asaoka and hyperbolic method. International Journal of GEOMATE, 14(43), 63-69. doi:10.21660/2018.43.7170

[25] Uy, E. E. S., & Dungca, J. R. (2018). Hyperbolic model parameters of philippine coal ash. International Journal of GEOMATE, 15(47), 95-102. doi:10.21660/2018.47.7171

[26] Dungca, J. R., & Dychangco, L. F. T. (2016). Strength properties of road base materials blended with waste limestones. International Journal of GEOMATE, 11(3), 2493-2498.

[27] Dungca, J., Galupino, J., Sy, C., & Chiu, A. S. F. (2018). Linear optimization of soil mixes in the design of vertical cut-off walls. International Journal of GEOMATE, 14(44), 159-165. doi:10.21660/2018.44.7146

[28] He, J., Ivanov, V. & Chu, J. (2013). Mitigation of liquefaction of saturated sand using biogas. *Géotechnique*, 63(4), 267-275.

[29] Ibraim, Diambra, Wood, & Russell. (2010). Static liquefaction of fiber reinforced sand under monotonic loading. *Geotextiles and Geomembranes, 28(4)*. Retrieved August 4, 2018.Kimura S., Journal Paper Title, J. of Computer Science, Vol. 1, Issue 2, 1987, pp. 23-49.

[30] Muhammad, Zakaria, & Namdar. (2013). Liquefaction Mechanisms and Mitigation. *Research Journal of Applied Sciences, Engineering and Technology.* Retrieved August 4, 2018, from file:///C:/Users/user1/Downloads/v5-574-578 (1).pdf.Hossain M.Z. and Awal A.S.M.A., Experimental Validation of a Theoretical Model for Flexural Modulus of Elasticity of Thin Cement Composite, Const. Build. Mat., Vol.25, No.3, 2011, pp.1460-1465.

[31] Porcino, D., Marciano, V., & Granata, R. (2012). Static and dynamic properties of a lightly cemented silicate-grouted sand. *Canadian Geotechnical Journal*, 49(10), 1117-1133. Retrieved August 4, 2018.

[32] Sabbar, A., Chegenizadeh, A., & Nikraz, H. (2016). Static liquefaction of very loose sand–slag–bentonite mixtures. Soil and Foundations, 341-356. doi: https://doi.org/10.1016/j.sandf.2017.05.003

[33] Sato. (2013). A method of suppressing liquefaction using a solidification material and tension stiffeners. Retrieved from http://www.cfms-sols.org/sites/default/files/Actes/1547-1550.pdf

[34] Liyanage, C., & Pieris, M. (2015). A Physico-Chemical Analysis of Coconut Shell Powder. *International Symposium on Applied Chemistry*, 222-228. doi: 10.1016/j.proche.2015.12.045

[35] Gandia, Famero, & Sarno. (2014). Coconut Shell Ash as Stabilizer for Base Course. Retrieved August 13, 2018, from https://thesis.dlsud.edu.ph/2766/1/CE 041 2014.pdf.

[36] Jain, A. (2016). Liquefaction Potential In and

Around Manila. Retrieved from http://www.air-worldwide.com/Blog/Liquefaction-Potential-In-and-Around-Manila/

[37] Budhu. (2007). Soil Mechanics and Foundations.

[38] Powrie. (2004). Soil Mechanics Concepts and Applications.

[39] Uy, E. E. S., & Dungca, J. R. (2017). Constitutive modeling of coal ash using modified cam clay model. International Journal of GEOMATE, 12(31), 88-94. doi:10.21660/2017.31.6558

[40] Uy, E. E. S., & Adajar, M. A. Q. (2017). Assessment of critical-state shear strength properties of copper tailings. International Journal of GEOMATE, 12(32), 12-18. doi:10.21660/2017.32.6565

[41] Kumar, N., & Kumar, D. (2014). Utilization of Coconut Shell in Different Forms in Concrete. *International Journal for Scientific Research & Development*, 2(7), Retrieved from file:///C:/Users/63917/Downloads/Utilization_of_Coconut_Shell_in_Differen.pdf

[42] Wadhwa, Rajprasad, & Thamilarasu. (2016). An experimental investigation on physical, chemical and mechanical properties of concrete blocks mixed partially with burnt coconut shell powder. *International Journal of Chemical Sciences*, 14, 353-358. Retrieved from https://www.researchgate.net/figure/Specific-gravity-of-burnt-coconut-shell-powder_tbl2_317026550

[43] Peck, R., Hanson,W., and Thornburn, T. (1974). Foundation Engineering Handbook. Wiley, London.

11th Int. Conf. on Geotechnique, Construction Materials & Environment, Kyoto, Japan, 3-5 November 2021, ISBN: 978-4-909106063 C3051

EXPERIMENTAL STUDY ON THE EFFECT OF ANISOTROPIC PRESSURIZING AND UNPRESSURIZING THE TBM-SEGMENTS

Haruka Mashiko[1], Naotaka Kikkawa[2], Nobutaka Hiraoka[2] and Kazuya Itoh[3]

[1, 3]Architecture and Civil Engineering, Tokyo City University, Japan; [2]National Institute of Occupational Safety and Health, Japan

ABSTRACT

In recent years, there has been an increasing demand for the TBM method, which is considered to be an effective method for tunnel construction in urban areas in Japan. Although morphologies and construction methods have been established for various geological and construction conditions, it is difficult to cover all safety criteria in their design, and unexpected external forces during construction may cause the segments to collapse, resulting in accidents. The purpose of this study is to understand the behavior of segments under various loading conditions and to indicate the safety criteria. In this paper, a small segment model was fabricated, and each segment was subjected to anisotropic pressurizing and un-pressurizing from the circular direction, and the segment behavior was evaluated using the failure criteria of bending moment and normal force. The differences between the segments with and without reinforcement and joints were also investigated. The results showed that under anisotropic pressure, the bending moment and normal force exceeded the failure criteria, part of the concrete in the segment was damaged, and the bending moment increased not only in the segment under anisotropic pressure but also in the adjacent segments (Ring). Furthermore, based on the value of the maximum bending moment, the bending moments were dispersed and reduced when it was assumed that there was a joint. Therefore, it can be seen that in situations where the pressure is unbalanced due to external forces, a stronger joint between the segments will result in a safer design. 245words (150~250)

Keywords: Shield segment, Bending moment, Normal force, Failure envelope

INTRODUCTION

The TBM method involves excavating a tunnel while avoiding the collapse of the surrounding ground and constructing a segment ring of A-, B-, and K-segments in the tunnel. The mechanical behavior of these segments depends on the cross-sectional shape of the tunnel and the tunnel construction method, in addition to ground conditions such as isotropic earth pressure from the ground, water pressure, and ground reaction forces. During segment assembly, anisotropic pressure may be generated due to competition between the tunnel boring machine and the segment during construction.

It has been found that the compressive action of the tunnel boring machine concentrates cracks and failures in critical and adjacent segments, and understanding the behavior of segments due to the attitude of the tunnel boring machine is one of the important factors to be studied (Mo et al. 2008)[1].

In order to avoid the collapse of segmental rings, maximum safety should be considered at the design stage of the tunnel, and it is important to identify the structure regarding the composition of the joints, the interaction between the ground and the structure, and the load redistribution capability of the lining with the adjacent rings (Molins et al. 2011)[2].

In this study, a small segment model was used to reproduce the segment behavior caused by the tunnel structure deformation. The segment behavior under various compressive loads from the circular direction was investigated using the failure criteria of bending moment (M) and axial force (N) [3] to investigate the collapse mechanism. In addition, four different models were made and compared to confirm the change in segment behavior due to the tightness of the joint and the effect of reinforcement. The durability of the segment was also verified.

Translated with www.DeepL.com/Translator (free version)

OUTLINE OF EXPERIMENT

For the model tests in this study, a miniature physical segment model was produced using a PVC mold with an outer diameter of 150 mm and an inner diameter of 137.5 mm as shown in Fig.1.

Preparation Procedure for Miniature Physical Model of Segments

The dimensions of the models are shown in Table 1. The dimension of segment models were 6.25 mm in thickness and 37mm in width. The segments consisted of six segments: K-, A1-, A2-, A3-, B1- and B2-segments. After coating the mold-releasing agent to the surface of the mold, the mass ratio of mortar

Fig.1 Mold for making a physical model of segment/ring

Table 1 Dimensions of the miniature segments/ring

Each item	Segment	Ring (Integrated segment)
Outer diameter (mm)	150	150
Inner diameter (mm)	137.5	137.5
Thickness (mm)	6.25	6.25
Width (mm)	37.5	37.5
Number of segments comprising the ring	6	-

(Toyoura sand : high early-strength Portland cement : water = 2.0 : 1.0 : 0.65) was poured. “Reinforced” segment model with reinforcing steel inserted as reinforcement and an "Unreinforced" segment model without reinforcing steel inserted in the segment were produced, respectively. Furthermore, the segments shown in Fig. 2 and the segmental ring (integrated segments) shown in Fig.3 were prepared. The ring is designed to simulate the condition where the segments are connected to each other by joints.
Four types of segments and rings were produced: "(1) Segments without reinforcement," "(2) Ring without reinforcement," "(3) Segments with reinforcement," "(4) Ring with reinforcement." After the model was removed from the mold, it was cured in water, and the total number of curing days was 28 days from casting.

Procedure of Experimental Test

In this experiment, we used a pressurizing/un-pressurizing system to apply load from the circular direction as shown in Fig. 4. A total of 12 hydraulic cylinders were installed to position the segment models, and by simultaneously or individually extending and retracting them, loads can be applied from any direction, reproducing the condition of unbalanced pressure on the segments.

Pressurizing and un-pressurizing device

Water is connected to a pressure-resistant tank, and high-pressure air is fed into the tank using a compressor to reproduce the load acting on the

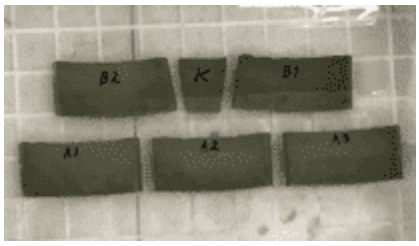

Fig.2 Segments

Fig.3 Ring (Integrated segment)

segments by the water pressure. By changing the air pressure in the tank in stages, the device can pressurize and un-pressurize the segments and ring. It is assumed here that the pressure of the air supplied to the pressure-resistant tank is not equal to the pressure acting on the segments. The value of the pressure acting on the segments was obtained by dividing the load value of the small load cell installed by the cross-sectional area of the loading jig. For both pressurizing and un-pressurizing, the pressure can be applied from 0 kN/m^2 to a maximum of about 320 kN/m^2 (0.32 N/mm^2).

Experimental case

First, the procedure of isotropic pressurizing and un-pressurizing is shown below.
(1) Pressurizing up to 320 kN/m^2 in the entire area.
(2) Un-pressurizing up to 0 kN/m^2.
The schematic diagram of the isotropic pressurizing and un-pressurizing is shown in Fig.5.

Next, the procedure of the anisotropic pressurizing and un-pressurizing is described. The following is the procedure of the anisotropic pressurizing and un-pressurizing to the K-segment.

(1) The pressure is applied isotropically up to 160 kN/m^2. (2) Pressurizing up to 320 kN/m^2 with the hydraulic cylinders of No. 2 to No. 11 fixed and of No. 1 and No. 12 unfixed. This simulates that the tail of TBM pressurizes the K-segment or the position of

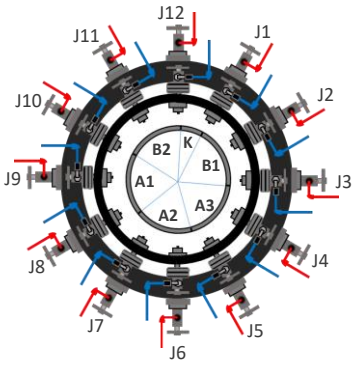

Fig.4 Sketch of pressurizing/un-pressurizing device

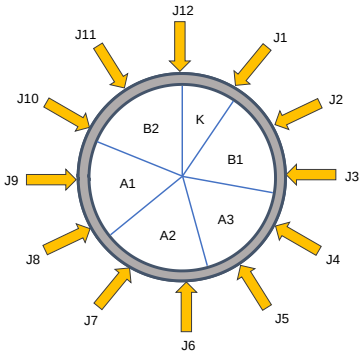

Fig.5 Sketch of Isotropic pressure

Table 2 Segment position of applied anisotropic pressure and the jack to be controlled at that time

Position of pressurizing/un-pressurizing	Unfixed hydraulic cylinder
Isotropic	None
K	J12, J1
B2	J10, J11
A1	J8, J9
A2	J6, J7

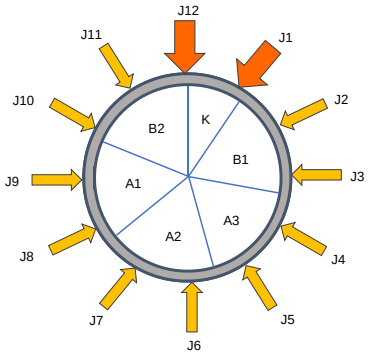

Fig.6 Sketch of anisotropic pressure

K-segment of the ring. This stress state becomes anisotropic in the segments or ring. (3) From the state of (2), remove the pressure to 0 kN/m^2. That simulates the state of the segments or ring at the opposite directions of (2). (4) Pressurizing up to 160 kN/m^2 once again and then the segments or ring becomes at the isotropic stress condition again. (5) Releasing to fix the hydraulic cylinders of No. 2 to No. 11, and remove the pressure to 0 kN/m^2 isotropically.

As an example, here is a schematic diagram of the timing of loading and unloading pressure on the K segment is shown in Fig.6.

Other anisotropic pressures were also applied to the B2, A1, and A2 segments locations. The anisotropic pressures for B2, A1, and A2 were applied in the same procedure as described above, and the unfixed jacks are shown in Table 2. Therefore, a total of 5 cases of pressurizing and un-pressurizing tests were carried out for each of them.

Preparation for the experimental test

A small load cell and a plate bent to the same shape as the periphery of the segments (long side: 400 mm, short side: 300 mm) were installed between the hydraulic cylinder and the segments to reduce the intensive load and to monitor the loading. In order to reduce the friction between the segments and the plate, the grease was pasted and the teflon sheets were installed.

RESULTS AND DISCUSSIONS REGARDING EXPERIMENTAL TEST BY FAILURE ENVELOPE

Failure Envelope of Bending moment and Normal force

The M-N failure envelope is shown in Fig.7. The red dotted line is the failure envelope of concrete and the light blue solid line is the failure envelope of reinforced concrete. First, uniaxial compression tests were conducted on cylindrical specimens made with the same mixing ratio as the segments to calculate the compressive and tensile strengths. The compressive and tensile forces were calculated by multiplying both strengths by the cross-sectional area of the segments. The failure points of compressive and tensile forces were at the intersection of the horizontal axis and the dotted line in Fig.7.

Next, the failure point of pure bending were obtained from the average values of the single bending tests conducted on A1, A2 and A3-segments. It corresponds to the intersection of the dotted line in Fig.7 and the vertical axis. The failure point balanced between compression and tension was calculated using Equations (1) and (2) from Reference [3].

$$\sigma_c' = \frac{N'}{A} + \frac{M}{Z} = \left(\frac{1}{A} + \frac{e}{Z}\right) N' \quad (1)$$

$$\sigma_t = \frac{N'}{A} - \frac{M}{Z} = \left(\frac{1}{A} - \frac{e}{Z}\right) N' \quad (2)$$

Here, σ_c' : compressive strength of concrete (= 46.2N/mm^2), σ_t : tensile strength of concrete (= 4.62N/mm^2), N': normal compressive force (N), M: bending moment (N·mm), A: cross-sectional area (= 234mm^2), Z: cross-section coefficient (= 244mm^2), e: eccentricity.

Next, the failure envelope of reinforced concrete is developed. The compressive and tensile strengths of the reinforced concrete are obtained by adding the compressive and tensile strengths of the reinforcement to those of the concrete. The failure point balanced between compression and tension was calculated using equations (3), (4) and (5) from the reference [3].

$$M_{ub} = k_3 f'_{cd} b a_b \left(d_1 - \frac{a_b}{2}\right) + A_{s2} f'_y (d_1 - d_2) - N'_{ub} y_t \quad (3)$$

$$N'_{ub} = -k_3 f'_{cd} b a_b - A_{s2} f'_y + A_{s1} f_y \quad (4)$$

$$a_b = \frac{\beta_1 \varepsilon'_{cu}}{\varepsilon'_{cu} + f_y / E_s} d_1 \quad (5)$$

Here, M_{ub} : ultimate bending moment balanced between compression and tension (N·mm), N'_{ub} : ultimate normal force balanced between compression and tension (N), k_3 : ratio of maximum stress in concrete to compressive strength of standard specimen f_c' (here set to 1.0), f_c' : compressive strength of concrete (= 46.2 N/mm^2), f_y': compressive yield strength of reinforcement (= 345 N/mm^2), f_y: tensile yield strength of reinforcement (= 345 N/mm^2), b: section width (= 37.5 mm), a_b: equivalent stress block length (= 2.28 mm), d_1: distance from top edge distance from top edge to tension bar (= 4.25mm), d_2: distance from top edge to compression bar (= 2.00 mm), A_{s1}: cross-sectional area of tension bar (= 2.61 mm^2), A_{s2} : cross-sectional area of compression bar (= 2.61 mm^2), y_t: length from center of gravity to edge (= 3.125 mm), f'_{cd}: design value of material strength (here f_c'), β_1: ratio of average stress to maximum stress ($k_3 f_c$') in concrete (here set to 0.8), ε'_{cu}: ultimate compressive strain of concrete (= 0.0035), E_s: elastic modulus of reinforcement (= 200,000 N/mm^2).

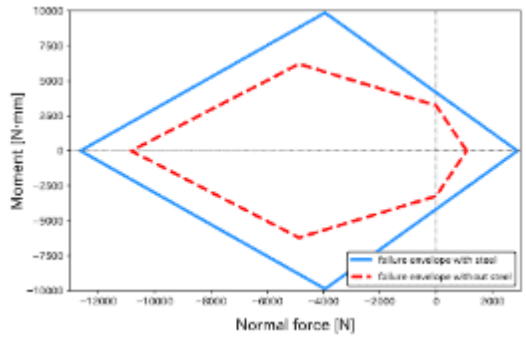

Fig. 7 Failure envelope (red-dotted line: failure envelope of concrete, blue-solid line: failure envelope of reinforced concrete)

Table 3 Simplified table of parameter values for failure envelope of concrete

Notation	Value	Unit
σ_c'	46.2	N/mm^2
σ_t	4.62	N/mm^2
A	234	mm^2
Z	244	mm^3

Results of Pressurizing/Un-pressurizing Experimental Test

The results of the segmented type experiment conducted in the previous experiment [4] are used to compare with the results of the ring type experiment in this study. The results of anisotropic pressurizing and un-pressurizing at K-position for "(1) Segments without reinforcement" and "(2) Ring without reinforcement" are shown in Fig.8 and 9. "(3) Segments with reinforcement" and "(4) Ring with reinforcement" are shown in Fig.10 and 11, respectively. The results of anisotropic pressurizing and un-pressurizing at the A1 position for (3) and (4) are shown in Fig.12 and 13, respectively. The tension side is positive and the compression side is negative value in the x-axis (the normal force, N).

At first, it was confirmed that the M-N curves of each segment returned to near the origin after the isotropic load un-pressurizing. The same trend was

Table 4 Simplified table of parameter values for failure envelope of reinforced concrete

Notation	Value	Unit
$f_{ç}$	46.2	N/mm^2
f_v	345	N/mm^2
f_y	345	N/mm^2
b	37.5	mm
a_b	2.28	mm
d_1	4.25	mm
d_2	2.00	mm
A_{s1}	2.61	mm^2
A_{s2}	2.61	mm^2
y_t	3.125	mm
β_1	0.8	–
ε_{cu}	0.0035	–
E_s	200,000	N/mm^2

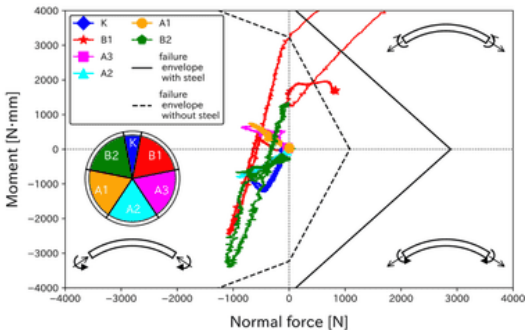

Fig.8 Bending moment and normal force behavior (anisotropic pressure to K-segment at the "(1) Segments without reinforcement")

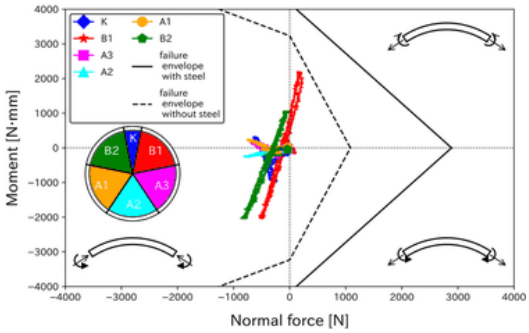

Fig.9 Bending moment and normal force behavior (anisotropic pressure to the position of K-segment in the "(2) Ring without reinforcement")

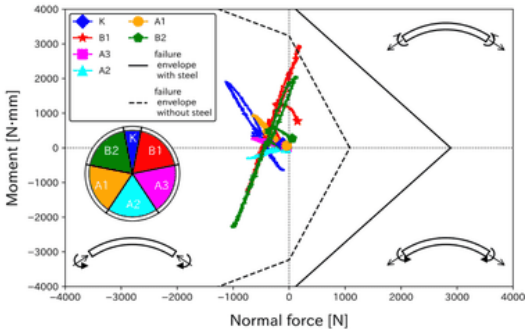

Fig.10 Bending moment and normal force behavior (anisotropic pressure to K-segment at the "(3) Segments with reinforcement")

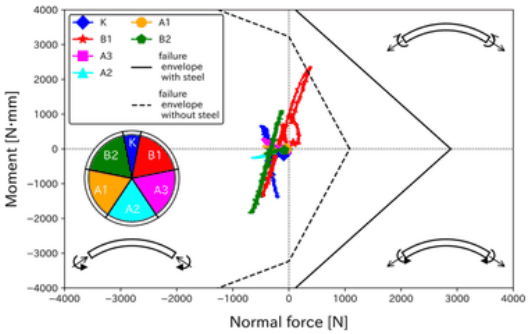

Fig.11 Bending moment and normal force behavior (anisotropic pressure to the position of K-segment in the "(4) Ring with reinforcement")

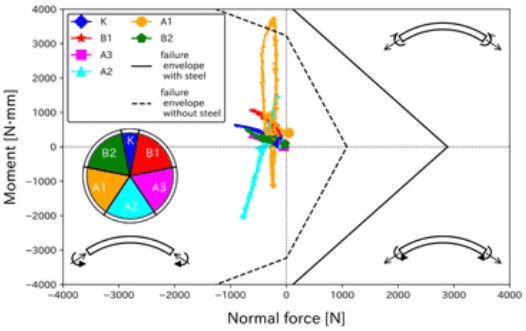

Fig.12 Bending moment and normal force behavior (anisotropic pressure to A1-segment at the "(3) Segments with reinforcement")

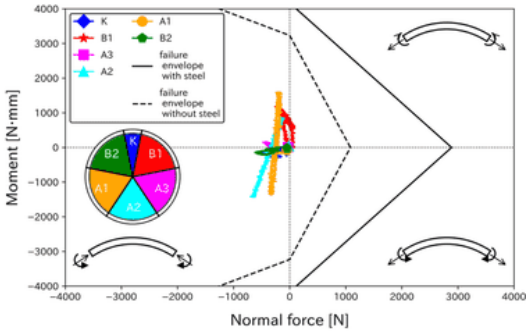

Fig.13 Bending moment and normal force behavior (anisotropic pressure to the position of A1-segment in the "(4) Ring with reinforcement")

observed for all segments (1) to (4), indicating elastic deformation. It was found that in the case of anisotropic load pressurizing and un-pressurizing at position K for the "(1) Segments without reinforcement," the B1 segment significantly exceeded the failure envelope after unloading, indicating that the concrete may have been damaged or destroyed. On the other hand, in the "(2) Ring without reinforcement," each segment was within the failure envelope. This indicates that the impact on the "(1) Segments without reinforcement" is larger than the "(2) Ring without reinforcement." It was also found that the behavior of the B1 and B2-segments tended to be larger in both (1) and (2) for the anisotropic un-pressurizing to the K position.

Next, for the steel-reinforced segments, the B1-segment exceeded the failure envelope in the anisotropic pressurizing at the K position for "(3) Segments with reinforcement." In addition, the B1-segment exceeded the failure envelope in (4), although no damage could be confirmed visually. It was found that the behavior of the B1 and B2-

segments tended to be larger even when the steel bars were included. The A1-segment exceeded the failure envelope only in (3), although the maximum bending moment of the A1 and A2-segments increased in both (3) and (4). The same pattern was observed in the other cases of anisotropic pressurizing and un-pressurizing on B2, A1 and A2-segments. This indicates that the applying of anisotropic pressure not only increases the bending moment of the segment where the anisotropic pressure is applied, but also increases the bending moment of the adjacent segments. It can also be seen that the M-N behavior of the ring type is smaller than that of the unreinforced and reinforced types when compared with the segments and rings in Figures 8 and 9 and 10 and 11.

Results of maximum bending moment

The measured values of maximum bending moment and normal force for unreinforced and reinforced segments and rings are shown below. Table 5 shows the values of maximum bending moment and normal force for (1) and (2), and Table 6 shows the values of maximum bending moment and normal force for (3) and (4). Comparing the unreinforced (1), (2) and reinforced (3), (4) of segment and ring, the values of maximum bending moment for both are larger for the segment type, suggesting that the force is more concentrated, while the force is relatively distributed for the ring type. Comparing (1) to (4), the values of maximum bending moment are smaller in the order of "(1) Segment without reinforcement", "(3) Segment with reinforcement", "(2) Ring without reinforcement", and "(4) Ring with reinforcement".

Table 5 Maximum bending moment

Position of pressurizing/un-pressurizing	(1) Segments without reinforcement		(2) Ring without reinforcement	
	Bending moment	Normal force	Bending moment	Normal force
Isotropic	-2426	-1136	-1228	-835
K	14950	10504	2201	134
B2	–	–	-1923	-806
A1	–	–	1715	-544
A2	–	–	-1584	-292

Table 6 Maximum bending moment value

Position of pressurizing/un-pressurizing	(3) Segments with reinforcement		(4) Ring with reinforcement	
	Bending moment	Normal force	Bending moment	Normal force
Isotropic	1075	-892	1381	-434
K	2950	158	2367	357
B2	2750	-20	1287	113
A1	3769	-249	1596	-205
A2	2061	-718	-1524	-232

CONCLUSIONS

In this study, the behavior of each segment/ring model was confirmed and evaluated from the behavior of the bending moment and normal force of each. This experiment showed that the concrete may be damaged by exceeding the failure envelope when a segment is an-isotropically pressurized/un-pressurized, and that the bending moment of not only the segment at the position of the anisotropic pressure but also the adjacent segments increases. It was suggested that the values of maximum bending moment measured under anisotropic pressure/un-pressure were smaller for reinforced concrete than for unreinforced concrete, and for ring(integrated segment) than for segmented ones.

In other words, the physical joints between segments are very effective.

ACKNOWLEDGMENTS

I would also like to thank Mr. Furuhata Takuma for his careful guidance on the experimental approaches.

REFERENCES

[1] Mo, H.H., Chen, J.S., “Study on inner force and dislocation of segments caused by shield machine attitude”, Science Direct, Tunnelling and Underground Space Technology 23, 2008 pp.281–291

[2] Molins, C., Arnau, O., “Experimental and analytical study of the structural response of segmental tunnel linings based on an in situ loading test. Part 1: Test configuration and execution”, Tunnelling and Underground Space Technology 26, 2011, pp.764-777

[3] Yoshikawa, H., *Analysis and Design of Reinforced Concrete*, Tokyo, 1995, pp.97-122. (in Japanese)

[4] Furuhata, T, “M-N behavior of a shield segment model”, The 47th Kanto Branch is one of the Branches of JSCE, Ⅲ-42, 2020. (in Japanese)

[5] Liao, L., de la Fuente, A., Cavalaro, S.H.P., Aguado, A., Carbonari, G., “Experimental and analytical study of concrete blocks subjected to concentrated loads with an application to TBM-constructed tunnels”, Tunnelling and Underground Space Technology 49, 2015, pp-295-306

11th Int. Conf. on Geotechnique, Construction Materials & Environment,
Kyoto, Japan, 3-5 November 2021, ISBN: 978-4-909106063 C3051

MONITORING OF ROCKFALL NET FENCE TECHNOLOGY BY AERIAL PHOTOGRAPHY TECHNOLOGY IN ENDE, NUSA TENGGARA TIMUR, INDONESIA

Ihwan Fauzi[1], Cahya Ahmad Gumilar[2] and Muhammad Rizaldi Nuraulia[3]

[1,2,3]Office of Geotechnical Tunnels and Structures, Directorate of Road and Bridge Engineering Development, Directorate General of Highways, Ministry of Public Work and Housing, Indonesia

ABSTRACT

Different types of technological solutions to protect road against rockfall has developed. It is needed to prevent transportation from material detaching from rock walls. Barrier technology is important for controlling, intercepting or deviating the material during rock fall movement. Ende is one of district which has many rock wall as geological structure that baypassed by national road. To reduce the impact of rock falls on the road it need to build a rockfall net fence. This study describes the characteristics of the rocks in Ende using aerial photography using drones, hammer test sampling on random rackwall. Aerial photography used a data cloud that can produce a 3D model and shows the rack wall image for rock classification. The geometry of the rock wall can be measured from the results of aerial shooting data processing. Furthermore, the performance of the net fence that has been installed can be assessed on its condition quickly and safely. So that the existing rockfall net fence and transportation safety can be maintained.

Keywords: Rockfall, Aerial Photogrphic, geological, Net Fence

INTRODUCTION

Geographic position potentially effected Indonesia as a country with many natural hazards. Rockfall are one of the natural disasters that often occur in hilly areas. As a result of this natural disaster, of course, has an impact on human activities. An extreme hazard in transportation such as roads and railways in steeply mountainous terrain should be affected by rockfall [1]-[2]. Rockfall is a potentially hazardous mountain areas affect to transportation infrastructure [3]. Rockfall that hit the road will affect the safety of road users. In addition to causing casualties, rockfall that cover the road will result in the paralysis of cities and regencies connected by the road.

Landslides are among the most frequent natural disasters occurring in Indonesia. They occur regularly throughout the entire Kabupaten Ende. The term landslides comprises a lot of different types of mass movements, including rock falls, debris flows, slumps, and many others. Geological, geomorphological, geographical, and land use characteristics define their predisposition. They are triggered either by heavy rainfall or earthquake related shaking. Landslides are natural geological processes but their predisposition can be increased by human activities, e.g. inappropriate land use or deforestation. Human activities, such as road cuts, can also trigger landslides. However, the most common triggering factor for landslides is heavy rainfall. The geological and topographic characteristics of Kabupaten Ende are in general very favorable for landslides to occur, it could be seen on Fig 1. The most severe types of landslides in Kabupaten Ende are debris flows. Relatively recent events occurred in November 1988 and April 2003, when extremely heavy rainfall caused many landslides, debris flows and floods in Ende District. Especially debris flows endanger many villages in the region. In addition to the immediate danger for people and buildings, the impacts of these disasters are also indirect through disrupted roads, telecommunication lines, water supplies, to name a few. Among the areas hit most severely in the recent past were the Kecamatans Ende, Detusoko, Ndona Timur, Nangapada, Maurole, Wolowaru and South Ende [4]. No exception in a number of areas in East Nusa Tenggara (NTT) experiencing landslides due to rain. In Ende Regency, Flores, a landslide hit a road section, precisely at KM 18 heading for Ende-Maumere. As a result of this landslide, 9 districts on the mainland of Flores were isolated.

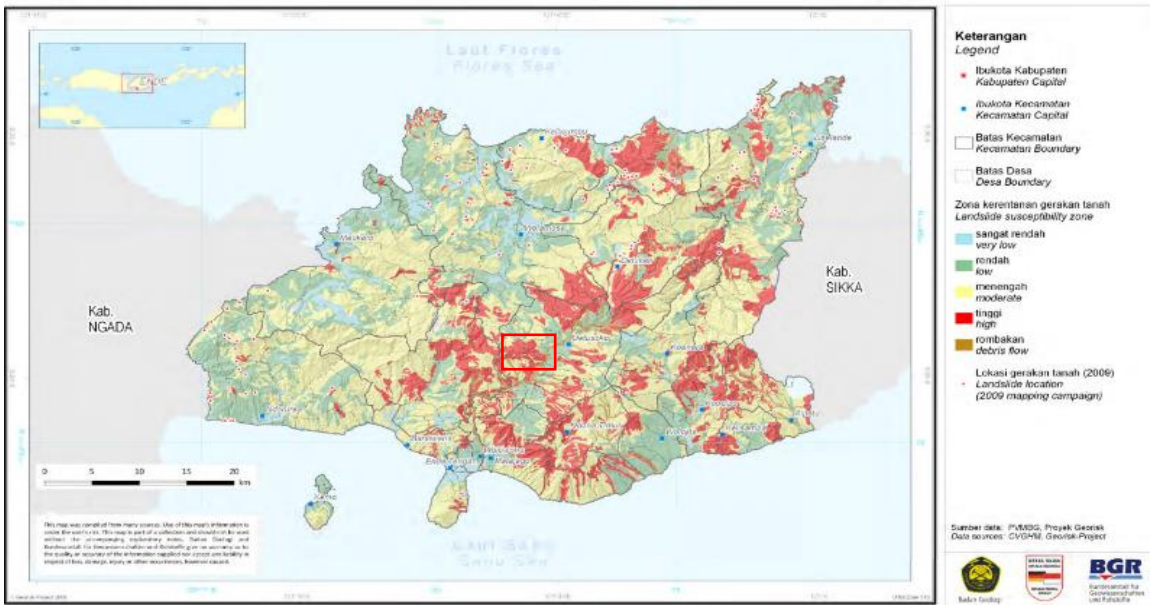

Fig. 1 Study area on Ende Landslide susceptibility map [4]

Research on rockfall related topics is an important task and advances are clearly visible. In addition, structural countermeasures also based on uncertainty models are also of practical interests [5]. Rockfall can be described as the quick bouncing, rolling and sliding movement of one (or several) boulders down a slope which can reach significant kinetic energy as it (they) travels, speed values range from a few metres per second to up to 25-30 m/s [6]. The rockfall handling technology that has been implemented in Ende, precisely at KM 18, is the rockfall net fence made of metallic meshes. The design of rockfall net fences had a high tensile wire and this is a new technology been constructed in Indonesia. Monitoring rockfall hazardous is needed to assist in the management and maintenance of rockfall protection devices during their lifetime. Ensuring risk mitigation would be fulfilled by identifying loss in efficiency and monitoring slope of rock wall [7]. In this paper the results of a site survey on 60 meters length rockfall net fence at KM 18+000 Ende-Datusuko, national road. The use of Unmanned Aerial Vehiucle (UAV) technology in monitoring work provides convenience and safety at work at rock slope locations. This study we use UAV to obtain information on the geometry of rock slopes at the location of the application of rockfall net fence technology. Local geometry is main factor of installation rockfall protection net fences problems [8].

Aerial photography using UAV data produces orthomosaic map and Digital Elevation Model (DEM). Through image processing orthomosaic image, we can classify the distribution of rocks located on the rock slopes above the rockfall net fence. Classification using unsupervised and supervised methods on Geographic Information System (GIS) software.

MATERIAL AND METHOD

Rockfall Net Fence

Rockfall net fence systems are used to mitigate rockfall and generally consist of flexible nets or panels that are connected to a post system with energy absorbing braking elements. Rockfall fence systems are currently designed and given an energy rating based on full-scale field testing to determine the energy capacity or energy reduction of a single rockfall event with variable considerations for serviceability after specific impacts [9].

A number of variable factors influence the rock fall process. The factors that influence the occurrence and behavior of individual falling rocks can be divided into internal parameters and external influences. Internal parameters means the source rock mass and slope intrinsically. External influences are conditions sometimes changing very rapidly, and change the force acting on the rock source so that it triggers the rockfall [10]. Internal parameters: rock mass properties (rock type, discontinuities, strength, block size/shape), slope morphology (height, angle, profile shape), slope materials, vegetation, groundwater. External influences: weathering, erosion, climate (rain, snow, freeze/thaw), seismic activity, human activity (excavation, blasting, water table changes, surface water control, deforestation). Together these factors Fig. 2 influence the frequency of rockfall and the path, speed, mode of travel (eg bouncing, rolling, etc) and travel distance of rocks as well as their resistance to breaking apart during travel.

it is important to understand and document these factors as they play a role in the selection and design of rockfall mitigation measures.

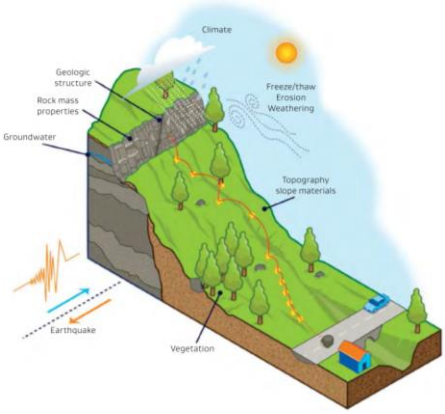

Fig. 2 Factor that influences the rockfall [10]

Technological solutions have been developed to provide the need for protection against rockfall. One of the devices technology to intercept and stop blocks detaching from rock walls most frequently used to is net fence Rockfall net fence is able to both prevent blocks from and to control, intercept or deviate the blocks during movement. [6]. Rockfall Fences Fig.3 referred to as flexible rockfall barriers, are designed to stop individual rockfall events, rockfall fences typically consist of panels (interception structure), infrastructure (support structure), friction brakes (energy-absorbing devices or connections), and foundations. These systems are commonly tested and certified by various European testing agencies and are rated between 100 and 8,000 kilojoules (kJ) for a single rockfall event [9].

Fig. 3 Rockfall Net Fence KM18 Ende-Datusuko, Flores Indonesia

Figure 3 shows rockfall fences applied at KM18 Ende-Datusuko national road. Rock slope with a height of 100 meters with a slope angle above 65 degrees. A rockfall barrier with a net fence is installed at a height of 8 meters above the road. The distribution of rock types on rock slope bodies is very diverse. The possibility of rock falling from rockfall sources can be mapped using aerial photography showed Fig.4. To ensure work safety at rock slope locations, the use of UAVs to document the rockfall net fence during monitoring can be seen in Fig. 5 oblique photos can be taken using a UAV, so that the slope conditions of the rockfall net fence can be seen.

Fig. 4 Aerial photography of Rockfall Fence KM18 Ende-Datusuko, Flores Indonesia

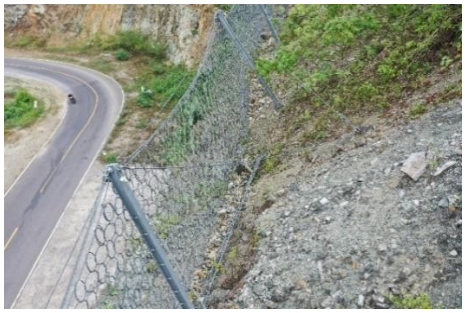

Fig. 5 Monitoring by UAV of Rockfall Fence KM18 Ende-Datusuko, Flores Indonesia

The rockfall net fence installed on KM18 Ende-Detusuko national road can withstand rockfall energy of 3000 kJ. It consists of several types depending on the amount of energy or the weight of the rock to be retained. GBE Rockfall Protection Barrier from 100 kJ to 3000 kJ showed on Fig. 6.

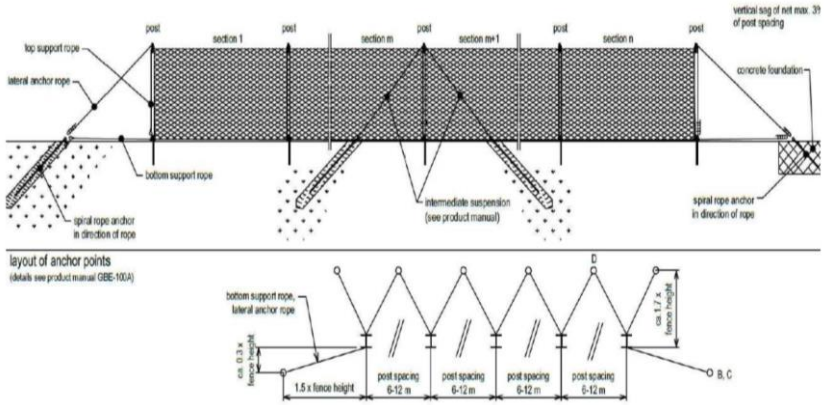

Fig. 6 GBE Rockfall Protection Barrier (100 kJ to 3000 kJ) [11]

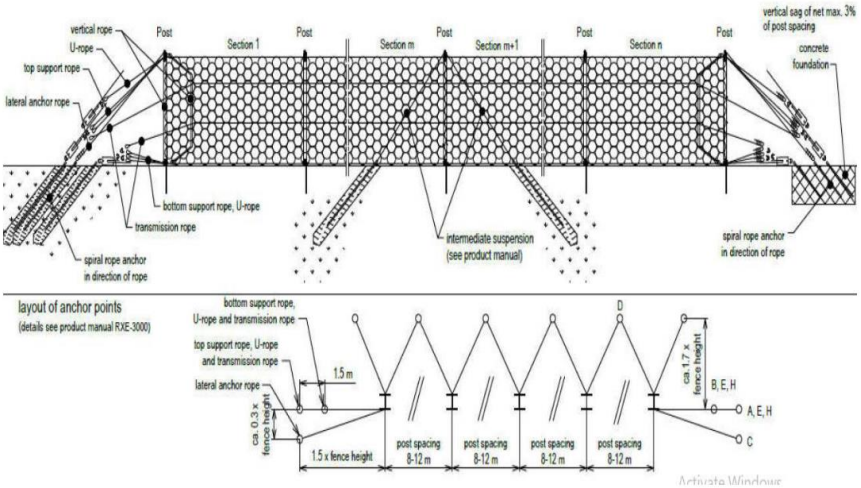

Fig. 7 RXE Rockfall Protection Barrier (500 kJ to 8000 kJ) [11]

RXE Rockfall Protection Barrier dari 500 kJ sampai dengan 8000 kJ showed Fig. 7

Unmanned Aerial vehicle (UAV)

An unmanned aerial vehicle (UAV) is a type of aircraft that is remote controlled by pilot on the ground, the most common types used in small-format aerial photogrammetry; Quadcopters and Wing planes [12]. Various fields to facilitate work currently apply to this technology. Monitoring activity used UAV for site survey, inspection, thermography, infrared, photogrammetry, transport applications, marketing activities [13] and monitoring of natural hazards in mapping and monitoring slope failures [14]. UAV is able to give monitoring system to detect the warning effectively. Loose and potentially dangerous on rock slope could be checked by visual inspection using UAV. The deterioration slope caused by weathering, erosion, cutting and blasting damage could be identified. Recording the number and width of cracks at regular time intervals could occur the crack. It could reduce potential hazard [13].

On photogrammetry using UAV taken a block of images by flying in straight lines on flight plan. Overlap at least 60% of each another to be able to get orthofoto [12]. On this monitoring we use 2 types of drone, DJI Phantom 4 Pro and DJIMavic 2 Pro.

(a) (b)

Fig. 8 (a) DJI Phantom 4 Pro; (b) DJI Mavic 2 Pro [12]

The DJI Phantom 4 is an onboard cameras quadcopter drone, could be shown on Fig. 8 (a) An uprated camera is equipped with a 1-inch 20-megapixel sensor capable of shooting 4K/60fps video and Burst Mode stills at 14 fps. The adoption of

titanium alloy and magnesium alloy construction increases the rigidity of the airframe and reduces weight, making the Phantom 4 Pro similar in weight to the Phantom 4. The Flight Autonomy system adds dual rear vision sensors and infrared sensing systems for a total of 5-direction of obstacle sensing and 4-direction of obstacle avoidance [15].

The DJI™ MAVIC™ 2 Pro features omnidirectional Vision Systems and Infrared Sensing Systems*, and a fully stabilized 3-axis gimbal with a 1" CMOS sensor camera (jointly developed by DJI and Hasselblad) that shoots 4K video and 20-megapixel photos shown at Fig. 8 (b) DJI signature technologies such as Obstacle Sensing and Intelligent Flight Modes like HyperLapse, ActiveTrackTM 2.0, QuickShot, Panorama, and Advanced Pilot Assistance Systems, help you capture complex shots effortlessly. The Mavic 2 Pro boasts a maximum flight speed of 44.7 mph (72 kph) and a maximum flight time** of 31 minutes [16].

Rock Size Classification for RGB Images

The unsupervised and supervised algorithms used to identify rock size from RGB images are taken from UAV. The visual camera assigns to each pixel a value of the primary colors Red, Green and Blue [17]. This trichromy is additive: this means that secondary colors are generated by the summing of three values corresponding to each pixel. The main elements noticeable from an RGB image of rock by size.

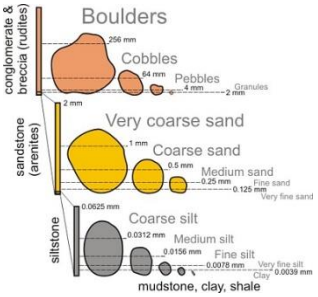

Fig. 9 Grain size [18]

A maximum-likelihood (ML) algorithm is one of the wide classifiers has been used for supervised image classification in different remote sensing application [19]. ML classification [20] is used this present, regions of interest (ROIs) associated with the training pixels for 4 classes of rock wall were determined based on difference rock sizes Fig. 10.

Training areas were established by choosing one or more polygons for each rock size class. In order to select a good training area for a class, the important properties taken into consideration are its uniformity and how well they represent the same class throughout the whole image. Accuracy assessment of the ML classification is determined by means of the confusion matrix (sometimes called error matrix), which compares, on a class-by-class basis, the relationship between reference data (ground truth) and the corresponding results of a classification [20]. This approach works by computing weighted distances and/or likelihood D relate to an unknown vector X belong to known classes. However, Mc is regarding Bayesian equation [19]:

$$D = \ln(ac) - [0.5\ln([Cov\ c])] - [0.5(X - Mc)T(Cov\ c - 1)(X - Mc] \quad (1)$$

Where, C is a particular class, ac refers to the percent probability for any candidate pixel of class C. when Covc refers to pixels covariance matrix in class c. However, |Covc| is a Covc determinant, (Covc-1) inverse of Covc, the T refers to transposition function [19].

RESULT AND DISCUSION

UAV images data are processed by Dronedeploy, and visualized by GIS Software. The result are Orthomosaic Map, Digital Terrain Model, Cross section and Classification by Maximum Likelihood supervised.

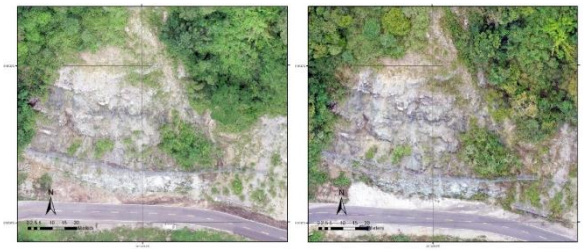

(a) (b)

Fig. 10 Orthomosaic Map

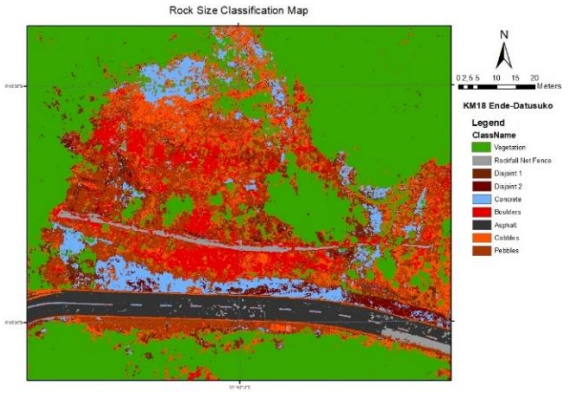

Fig. 11 Rock size classification map

Orthomosaic map used to check may fall rock held by rockfall net fences on Fig. 10 (a) is the result

of mapping using the DJI Phantom 4 Pro, while Fig.10 (b) is surveyed by aerial photos using the DJI Mavic 2 Pro at different times. Small size rockfall net fences can be seen, rocks with smaller sizes fall under the net. Rock size classification is obtained from the supervised maximum likelihood process in GIS software Fig. 11.

CONCLUSIONS

The use of UAV technology in monitoring rock slopes with a rockfall net fence guarantees work safety. Rock classification using the maximum likelihood supervised with images from the UAV provides an overview of the size distribution of rocks on the rock slopes so that it can be estimated what size they fall. Furthermore, by taking into account the rock mass, the rockfall net fence's ability to withstand falling rocks can be more measured.

ACKNOWLEDGMENTS

The authors would like to express their sincere appreciation to Mr. Fahmi Aldiamar, Head of Office of Geotechnical Tunnels and Structures, Directorate of Road and Bridge Engineering Development, Directorate General of Highways, Ministry of Public Work and Housing, Indonesia.

REFERENCES

[1] P. T. Van and K. Maegawa, Experiments And Numerical Modeling Of A Rockfall Protective Wire Rope Fence, Int. J. GEOMATE, vol. 2, no. 2, 2012, pp. 219–226.

[2] G. Lollino et al., Engineering Geology For Society and Territory – Volume 2: Landslide Processes, Eng. Geol. Soc. Territ. - Vol. 2 Landslide Process., no. January, 2015, pp. 1–2177.

[3] M. Grošić, Ž. Arbanas, and D. Udovič, Designing and Constructing Rockfall Barriers - Experiences in Republic of Croatia, Rock Eng. Difficult Gr. Cond. - Soft Rocks Karst - Proc. Reg. Symp. Int. Soc. Rock Mech. EUROCK 2009, no. May 2014, 2010, pp. 703–708.

[4] M. Resources, B. Geologi, and G. Agency, Geological Hazard and Risk Assessment Kabupaten Ende , Nusa Tenggara Timur, 2010, no. 57.

[5] A. Volkwein et al., Rockfall Characterisation and Structural Protection - A Review, Nat. Hazards Earth Syst. Sci., vol. 11, no. 9, 2011, pp. 2617–2651.

[6] D. Peila and C. Ronco, Technical Note: Design of Rockfall Net Fences and The New ETAG 027 European Guideline, Nat. Hazards Earth Syst. Sci., vol. 9, no. 4, 2009, pp. 1291–1298.

[7] F. Rinaudo, F. Chiabrando, A. Lingua, and a Spanò, Politecnico di Torino Porto Institutional Repository, ISPRS - Int. Arch. Photogramm. Remote Sens. Spat. Inf. Sci., vol. XXXIX n. B, 2012, pp. 583–588.

[8] A. Luciani, M. Barbero, D. Martinelli, and D. Peila, Maintenance and Risk Management of Rockfall Protection Net Fences Through Numerical Study of Deteriorations, Nat. Hazards Earth Syst. Sci. Discuss., vol. 0, no. March, 2016, pp. 1–12.

[9] B. Arndt, B. Arpin, J. D. Higgins, and P. Thompson, Guidelines for Certification and Management of Flexible Rockfall Protection Systems, Guidel. Certif. Manag. Flex. Rockfall Prot. Syst., 2016, no. December 2015.

[10] M. Easton, ROCKFALL Design Considerations for Passive Protection Structures, 2004, pp. 1–71.

[11] A. H. Putra, Metode Pelaksanaan Pekerjaan Rockfall Protection Barrier, 2021, Jakarta.

[12] S. Syring and J. Nylund, Introducing UAS and Photogrammetry for Surveying and Surveilling New Project Sites, 2018.

[13] N. Ngadiman, I. A. Badrulhissham, M. Mohamad, N. Azhari, M. Kaamin, and N. B. Hamid, Monitoring Slope Condition Using UAV Technology, Civ. Eng. Archit., vol. 7, no. 6, 2019, pp. 1–6.

[14] S. K. Nagendran, M. A. M. Ismail, and W. Y. Tung, Integration of UAV Photogrammetry and Kinematic Analysis for Rock Slope Stability Assessment, Bull. Geol. Soc. Malaysia, vol. 2019, no. 67, 2019, pp. 117–123.

[15] Dji, Phantom 4 Pro/Pro+Series, vol. 3304, no. January. 2012.

[16] Mavic Air User Manual 2021.05. 2021.

[17] P. Cinat, S. F. Di Gennaro, A. Berton, and A. Matese, Comparison of Unsupervised Algorithms for Vineyard Canopy Segmentation from UAV Multispectral Images, Remote Sens., vol. 11, no. 9, 2019, pp. 1–24.

[18] Earth Sience Australia, Grain Size, [Online]. Available: http://earthsci.org/mineral/rockmin/identification/identification.html. [Accessed: 15-Jun-2021].

[19] Z. Abbas and H. S. Jaber, Accuracy Assessment of Supervised Classification Methods for Extraction Land Use Maps Using Remote Sensing and GIS Techniques, IOP Conf. Ser. Mater. Sci. Eng., vol. 745, 2020, no. 1.

[20] A. Ahmad and S. Quegan, Comparative Analysis of Supervised and Unsupervised Classification on Multispectral data, Appl. Math. Sci., vol. 7, no. 73–76, 2013, pp. 3681–3694.

11th Int. Conf. on Geotechnique, Construction Materials & Environment, Kyoto, Japan, 3-5 November 2021, ISBN: 978-4-909106063 C3051

PERMEABILITY OF THE DIKE 1'S MATERAILS OF KAENG KRACHAN DAM, THAILAND

Uba Sirikaew[1], Witthawin Hopeancharoen[2] and Uma Seeboonruang[3]

[1,2,3]School of Engineering, King Mongkut's Institute of Technology Ladkrabang, Thailand

ABSTRACT

Dike 1 of Kaeng Krachan Dam located in Phetchaburi province of Thailand constructed in 1966 with the reservoir capacity of 710 million m^3. This large-scale project provides more than 55 years of irrigation purposes. Risk evaluation of dam is needed to be carried out. Calibration of engineering properties of the Dike 1 is conducted because there is no database of those properties. The existing Dike 1 cross section is a soil model, used for calculated. Piezometric level and flow rate obtained from the dam instruments was calibrated with the hydraulic head and the flowrate determined by SEEP/W model. The permeability coefficient of the Dike 1 materials can be analyzed by calibration technique. The data of the dam instruments is a helpful information and computer program is friendly use. The coefficient of permeability of soil of the Dike 1 of Kaeng Krachan Dam is determined and applied for risk analysis.

Keywords: Permeability, Soil Model, Calibration and Dam Instruments

INTRODUCTION

Dike 1 of Kaeng Krachan, located in Phetchaburi province of the southern of Thailand, with 33 m height and 305 m length with capacity of 704,000 m^3 of earth fills. Dike 1 was constructed in between 1966 and 1968. It is fully operated more than 55 years which under the dam safety program of Royal Irrigation Department of Thailand (RID). Since the lack of permeability data of the construction materials and there is no budget for soil testing, therefore, the objective of the study is to determine the permeability of soil by calibrating the calculated and measured data using mathematical model. The measured data was monitored by the piezometers, installed along the alignment of the Station +130 km and seepage flow at the down-stream, as shown in Fig. 1. The study scoped with the trial calculated value by assuming the representative one for calculation. The monitored data obtained by piezometer and seepage flow meter was collected at a certain period at the water level of +96.000 m (msl). 2D SEEP/W with the mesh size of 0.5 to 3.0 m was applied to determine the seepage.

DESCRIPTION AND INSTRUMENT

The soil model of Dike 1 consisted of clay core, selected outer core zone, chimney and blanket drain as shown in Fig.2. Eight zones of the earth embankment can be summarized in Table 1, separated by permeability coefficient. First, the core zone (C), soil group of core zone has permeability in the range of 1×10^{-9} to 1×10^{-7} m/s which value closed to the impervious state. Second, the foundation rock zone comprised of greywacke, claystone, mudstone and shale. Third layer is natural ground, lean clay (CL) showed impervious one like the core zone. Fourth, quarry-run-rock (QR) mainly consisted of coarse aggregate and rock fragment made from greywacke or high strength rock mass. Aggregate's permeability showed 1×10^{-3} to 1×10^{-1} m/s. Fifth, Random zone (R) comprised of silty gravel (GM) or clayey sand (SC) showed permeability as 1×10^{-8} to 1×10^{-6} m/s. Sixth, the chimney drain zone (SP) presents permeability as 1×10^{-7} to 1×10^{-5} m/s. Seventh, selected random zone (SR) shows very high value of permeability as 1×10^{-3} to 1×10^{-1} m/s. Eighth, transition zone shows silty gravel (GM) with 1×10^{-7} to 1×10^{-5} m/s.

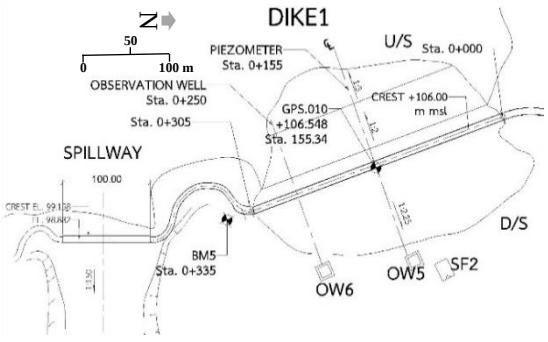

Fig.1 Dike 1's site plan and dam instruments

Vibrating wire piezometers P1, P2, and P3 are installed at the core zone, off set from the center line of Dam 4.00 m at the elevation of 59.940, 70.000 and 85.000 m (msl), respectively. Piezometer P4 and P8

are installed and monitored the foundation off set from the center line of dam at 25.00 and 50.00 m at elevation of 60.079 and 75.050 m (msl). Piezometer P5, P6 and P7 are installed at the random zone off set from the center line 25.00, 50.00 and 50.00 meters, at the elevation of 85.079, 58.000 and 75.000 m (msl), respectively as showed in Table 2.

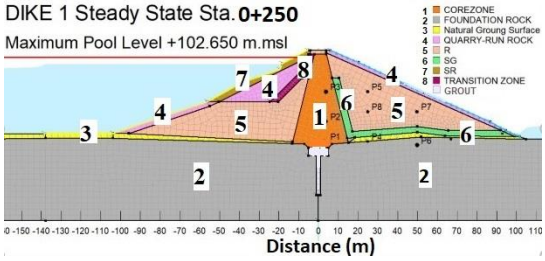

Fig.2 Cross section of Sta.1

Table 1 Zoned materials of Dike 1

Reference [1]		Dike 1's	
USCS	k, m/sec	Zone	Soil/Rock type
CL	10^{-9} - 10^{-7}	1. Core	CL, GC
-	-	2. Foundation	claystone
CL	10^{-9} - 10^{-7}	3. Ground	CL, SC
GW	10^{-3} -10^{-1}	4. Quarry rock	Aggregate
SC	10^{-8} -10^{-6}	5. Random	GM, SC
SM	10^{-7} -10^{-5}	6. Filter/drain	SP, SM
GW	10^{-3} -10^{-1}	7. Selected rock	Fragment
GM	10^{-7} -10^{-5}	8. Transition	GM, SM

Table 2 Detail of Piezometer

Representative	Zone	Off-set-dam, m	Elevation m, msl
P1, 59.940	core	4/DS	+59.940
P2, 70.000	core	4/DS	+70.000
P3, 85.000	core	4/DS	+85.000
P4, 60.079	foundation	25/DS	+60.079
P5, 85.079	random	25/DS	+85.079
P6, 58.000	foundation	25/DS	+58.000
P7, 75.000	random	50/DS	+75.000
P8, 75.059	random	50/DS	+75.059

Note: from Argus Web Monitoring System

Seepage flow meter (SF2), V-Notch weir was installed on ground at Sta.0+120 of Dike 1 which located 150 m downstream (DS) from the center line of dam. The seepage flow can be monitored by sensor and measured by manual. There is no significant error of flowrate counter measured from sensor and direct measuring. Dike 1's seepage flow rate increased with reservoir water level, which similar to the seepage condition of Khassa Chai Dam, Iraq [2].

There are two observation wells, OW5 and OW6 which located at Sta.0+150 and Sta.0+250 which offset 250 m and 200 m from the center line of Dike 1 to downstream (Fig. 1). Subsurface water level was depicted and used for determine hydraulic gradients at the Dike 1's toe. Local RID office provided maintenance program of dam instrument and dam safety inspection. Dike 1's instrument for seepage analysis, purpose and maintenance are tabulated in Table 3.

Monitored and recorded data were obtained by Argus software, checked its reliability**.** It supposed that change in water pressure of the vibrating wire piezometers, flow seepage meter and observation well depend on changing of the reservoir water level**.** However, there is an error due to sensor mounting, a broken electric wire, and sensor**'**s calibration.

Table 3 Dike 1's instrument for seepage analysis

Instrument	Type	Purpose
Piezometer	Vibrating Wire	Pressure head
Seepage	Sensor and	Flow rate
flow meter	V notch weir	Flow rate
Observation	Bore hole with	Hydraulics
Well	sensor	gradient

SITE CHARACTERIZATION

Existing data obtained from the drawing of Kaeng Krachan Dam was carried out by RID and Engineering Consultants Inc. Denver Colorado U.S.A**.,** defined zone of core and filter as impervious and sand and gravel, no permeabilities' testing results of construction materials and rock foundation [3].

Soil boring logs of the adjacent areas show clayey (SC), clayey and silty sand (SC and SM) lean clay (CL) in majority. Dense to very dense coarse grain sand with fines, SC and SC-SM, contain with fines in the range of 13 % to 44 % with the median value of 33 % of fines contents. Fines show liquid limit and plastic index in the range value of 15.90-21.45% and 3.15-8.34 %. About three meters thick of ground presented the natural moisture content, dry unit weight, compressive strength from pocket penetrometer and N-value in the range of 5.95-12.86%, 1.96-2.08 t/m^3, 4.5 ksc and 35-95 blows/ft., respectively. At the depth greater than 3 meters, very dense to dense silty gravel (GM) with the non-plastics fines has been found in thin layer. It shows fine contents, natural moisture content and dry unit weight of 13.72-17.30%,6.91-10.47% and 1.95-1.96 t/m^3, respectively.

Sandy Clay (CL) consists of about 70 % fines with 30% sand with low plasticity. Two meters of stiff clay layer presents moisture content, dry unit weight and N value of 21.34%, 1.34 t/m^3 and 16 blows/fts. Medium dense to dense poorly graded sand (SP) was found below 3 meters of ground. Percentage of fines, natural moisture content, dry unit weight and N-value

shows in the range of 3.06 - 4.77%, 7.72-8.66%, 1.73-2.02 t/m^3 and 28-93 blows/ft, respectively [4].

It remarks that soil groups in adjacent area is the same as shown in drawing of Kaeng Krachan Dam and as soil group classified based on ASTM D 2488. The open-end tests perform at the representative random zone showed permeability of 7.5× 10^{-7} -5.3 × 10^{-8} m/s of sandy clay (CL). Field test and visual-manual procedure for soil classification can be operated only on shallow surfaces. Core material and random zone can be classified as lean clay, sandy clay (CL) and clayey sand (SC) and sandy clay (CL). Spillway located at the right abutment of Dike 1 shows good rock mass of mudstone, shale and fine grained graywacke which conform with work of Department of Mineral Resources [5]. Dike 1's and grounds' materials has been tabulated in Table 4.

Table 4 Materials of Dike 1

Location	Spection method	Classified
Core (right abutment)	Visual manual	Lean Clay (CL), hard clay with sand.
Random zone (D/S)	Visual manual & open-end test	Clayey Sand (SC)& Sandy clay, *k*=7.5× 10^{-7} - 5.3 ×10^{-8} m/sec
Rock mass at spillway	Rock mass rating	mudstone, shale graywacke, good & & tight joints
Adjacent D/S	Visual manual and review	Sandy Clay& Lean soil symbols; CL, SC SC-SM, GM, SM, SP

Based on geological map showed rock unit of mudstone, shale and graywacke, colluvium and alluvium at Dike 1 and adjacent area. Rock unit has been found at the elevation of +80 - +250 m (msl). Generally, the drawing stated that rock quarry had been performed by blasting the mountain located in the reservoir area. Aggregate and block of graywacke, mudstone and shale were mainly used in number 4 zone of quarry run rock, number 7 zone of selected material and riprap. Residual soils altered from those parent rocks mostly consisted of lean clay, clayey sand and lateritic soil, predominantly. It is about 2-3 meters thick and impermeable soil. Colluvium soil mostly consisted of rock fragments, gravel, sand, silt and clay which scattered along the slope and hilly area which covered at the elevation of +60-+80 m (msl). It is medium to very dense silty-clayey sand. Alluvium mainly consisted of silty sand (SM) and poorly graded sand (SP). It is loose to medium dense sand layer which scattered along the canal and river. This flood plain shows the elevation +45 – +60 m (msl). Site characterization meets requirements of good rock foundation as water tightness and high quality and quantity of earthen construction materials for Dike 1.

SEEPAGE ANALYSIS IN EARTH DAM

Bernoulli's equation and Darcy's law are applied for understanding water flow through porous media. Bernoulli's equation can be explained as in

$$H = z + \frac{p}{\gamma_w} + \frac{v^2}{2g} \quad (1)$$

Where, $\boldsymbol{H}$ is the total head, z is the elevation head, P is pressure head, v is velocity head and $\boldsymbol{g}$ is gravitational acceleration.

For steady-state flow between two points (a-b), Eq. (1) expressed the head loss equation as in

$$\Delta h = Ha - Hb \quad (2)$$

Where, Δh is head loss, or head change between point a to point b, Ha is the total head at point a, Hb is the total head at point b.

Combination of Eq. (2) and Darcy's law can be used to define hydraulic conductivity of soil as in

$$\boldsymbol{Q} = \boldsymbol{KiA} \quad (3)$$

hydraulic conductivity, $\boldsymbol{K} = Ki\frac{\gamma_w}{\mu}$ (4)

hydraulic gradient, $i = \frac{\Delta h}{\Delta L}$ (5)

Where, Q is the flow rate (volume over time), K is the hydraulic conductivity, Ki is the intrinsic permeability, γ_w is the unit weight of water, μ is water viscosity, i is the hydraulic gradient, Δh is the head loss, ΔL is the horizontal distance between two points, A is the cross-sectional area [6].

There are many computed tools used for study dam behavior which calculated results agree with measured data [7], [8] and [9]. This uses 2D SEEP/W to analyze seepage through Dike 1 of Kaeng Krachan Dam. In practice, hydraulic conductivity of soil is an important factor for seepage analysis besides consideration of the boundary conditions. Finite element program, 2D SEEP/W program provides 3 parts, data input, solving and result output. Input part composed of defying the dam model, boundary condition and mesh. It depends on user's requirement to select function of transient flow or steady state, saturated or unsaturated condition, for instance. Solving part is an analysis of total head, hydraulic gradient and flow rate which depend on the method of selection. An output results generate flow net of the earth dam mode, total head of water and flowrate of the model section.

The calculated seepage flow is calibrated with flow rate measured by SF2 which V notch weir presented the calibration equation as in

$$Q = CwH^{5/2} \quad (6)$$

Where, *Q* is flow rate (liter/min), *Cw* is discharge coefficient of weir (82,800), *H* is height in milli meter of water measured from V notch weir's sharp edge.

STUDY METHOD

Study methods purposed for achieving the objectives which tabulated in Table 5. It consisted of reviewing the existing data of Dike 1, seepage analysis by 2D SEEP/W, verification of materials' permeability in Dike 1 and report writing. The existing data was reviewed to understand engineering properties of construction materials of Dike 1 and site and to classify the drawing and dam instrument. Seepage analysis gives the result of hydraulics conductivity of Dike 1's soil model. Field permeability test has been carried out to verify the calibrated hydraulic conductivity which obtained from SEEP/W. Finally, this study is reported and established to the local organization who response for dam safety program. It confirmed the Dike 1's behavior and instruments which work properly and needed to be regularly inspected.

Table 5 Study method and result

Study Method	Result
Reviewing data	site characterization and reliability of data
Seepage analysis	Calibrated k value of Dike 1's materials
Verification of calibrated k value by field permeability test	Permeability of soil (random sampling)
Report writing	Dike 1's safety plan

Seepage analysis diagram of Fig. 3 briefly presents the detailed calibration of hydraulic conductivity of Dike 1's materials. Step (1) applying SEEP/W of GeoStudio program limits for the two dimensions. Step (2) finite element model was generated and defined mesh size and boundary condition. Key in material property and trial k value in the soil model as given step (3). Step (4) The program of 2D SEEP/W had been executed. Step (5) shows comparison of computed data and the value from instrument data as earlier mentioned in Table 3. Trial and error process, step (6), has been considered if there is the different value in those compared data. End of seepage analysis is completely done when the computed data is closed to the measured data. This study limits with the cross section Sta 0+130 which the piezometer had been installed. The computed flow rate of Dike 1 is calibrated with the seepage flow meter (SF2).

The standard field permeability test of Royal Irrigation Department which based on USBR manual has been conducted at the shallow subsurface ground of the Dike 1 [10]. According to no permission on drilling for investigation purpose, five locations are randomly chosen, 3 from Dike 1 and 2 from the two abutments.

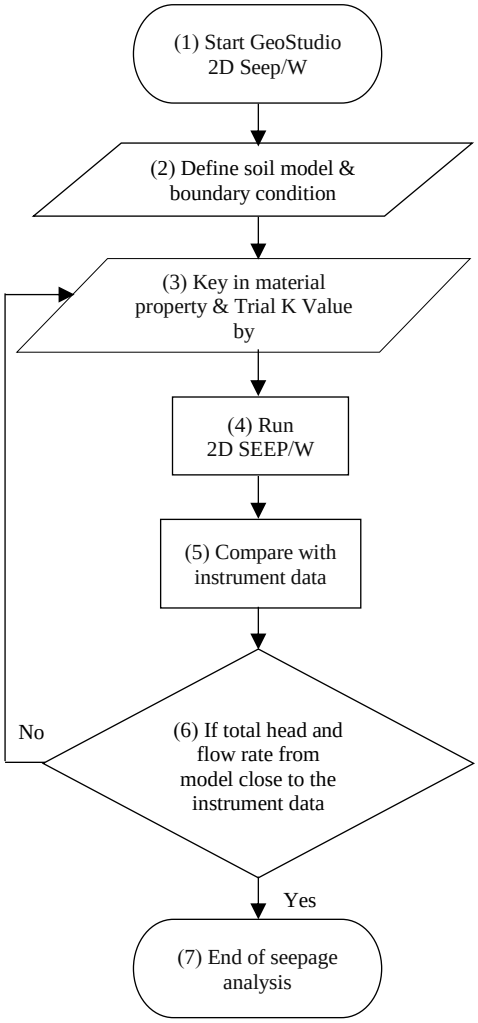

Fig.3 Seepage analysis diagram

Duration of field test is rainy season, July 2019 which made high moisture content of the shallow ground. testes section was developed by using 3 inched diameters of auger, drilled into the ground with the depth of 1.5 meter. Shallow bore hole was installed with the 3 inches diameter of PVC pipe with about 2.5 meters length. The length of PVC pipe is 1 meter above the surface. Clean the hole bottom and fill with clean water, left soil fully saturated and plug the PVC case about 24 hours. Period of test is about 20 minutes per set, test 3 sets with the constant head and measure the flow rate. Leakage of water during testing needed to be avoided. Average permeability of soil can be calculated as in

$$k = \frac{Q}{cHr} \quad (7)$$

Where, k is average permeability in cm/sec, Q is flow rate (cm^3/s), c is dimensionless parameters as a function of test length and radius of hole (use 5.5 for about 3 inches diameters), H is total head (section of constant head in centimeter), r is radius of the PVC pipe in centimeter.

RESULT AND DISISCUSSION

The existing data of the Dike 1 provided some engineering properties of soils which applied as the permeability functions of soil models (Table1 and Fig.2). Those permeability values were input to soil models for analysis by SEEP/W and adopted by trial-and-error method. Thus, the completion of seepage analysis means the soil model presented the calculated flow rate and total head in the same range of the measured data obtained from seepage flow meter and from piezometers. This study used data of year 2007, and check the reliability of measurement.

The eight piezometers were compared with the water reservoir and with the elevation of their installation for checking the function as shown in Table 6. It remarked that there is no water pressure develop at random zone of the downstream, because the total head of P5, P7 and P8 are lower than those of installation elevation. It implied that designed chimney and blanket drains allowed all seepage flows through these path. On the other hand, these piezometers were installed in shallow depth which could not detect the water pressure at the downstream of Dike 1. In case these piezometers work well, it is the good sign for safety of the dam.

The five of piezometers installed in core zone and foundation show different value of water head compare with the elevation of reservoir water level. These piezometers work functionally. It noted that local officer read and recorded the data of piezometer, manual process, in 2009 the dam instruments had been gradually changed to the automation system. As water pressure plays role for earth dam, observation wells, OW5 and OW6 was used for calculation of the filed average hydraulics gradient of Dike 1. At downstream of Dike 1, calculated hydraulics gradients show about 0.12 to 0.14, which was smaller value than the critical hydraulic gradient about 7 to 8 times. Groundwater condition in OW5 and OW6 is clear. This evidence implies there was no erodible soil. Seepage flow meter is properly work which give the relationship between flow rate and reservoir water level as in

$$Q = 1.1088RWL - 92.98 \quad (8)$$

Where, Q is flow rate in m^3/day, RWL is reservoir water level in m. The coefficient of correlation (R^2) is 0.989.

Measured seepage flow rate was used as calibrated value with those computed from SEEP/W. The flow rate of Dike 1 from SEEP/W and from measurement was compared in Table 7.

Table 6 Total head of piezometers at certain time

Piezometer, EL, location	Total head, m msl		
	19/9/2007	5/12/2007	3/7/2009
P1, 59.940, c	79.107	80.395	76.810
P2, 70.000, c	83.032	82.291	79.221
P3, 85.000, c	88.247	87.738	85.718
P4, 60.079, f	70.726	70.885	67.164
P5, 85.079, r	84.402	84.691	84.886
P6, 58.000, f	69.327	69.646	65.557
P7, 75.000, r	73.751	73.639	72.912
P8, 75.059, r	74.594	74.841	74.063
RWL EL m msl	94.990	96.140	91.030

RWL = Reservoir Water Level, c = core, f = foundation, r = random

Table 7 Calibration of flow rate

Flow rate SEEP/W, m^3/day	Seepage Flow meter, m^3/day	Range m^3/day
6.323 (2.93×10^{-7} $m^3/s/m$)	6.740	5.7-7.0

After calibration of flowrate of the model which computed by SEEP/W. The calculated total head, from Seep analysis was correlated with measured total head of P1 as shown in Fig.4, for instance.

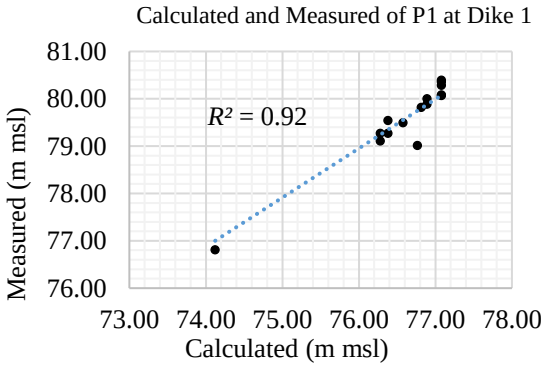

Fig.4 Calibration matching graph of P1 at Dike 1

The calibration graphs of P1, P 4 and P6 show linear correlation coefficient as 0.92, 0.82 and 0.60 respectively. Linear correlation coefficient of the calibration graphs of P2 and P3 are lower than 0.3. It probably due to the sensitivity of sensor and impervious core. Calibrations of total head data from SEEP/W and from piezometers are tabulated in Table 8. The requirements stated that the calculation value obtained by SEEP/W should be in the range value of the measured data. This soil model is accepted and established the permeability of soil and k-function, saturated water content, residual water and anisotropy ratio as shown in Table 9.

Table 8 Total head from piezometers and SEEP/W

Piezometer, location	Total Piezometer	Head, m SEEP/W	Range in meter
P1, Core	80.395	79.273	(79-81)
P2, Core	82.291	81.151	(80-83)
P3, Core	87.738	88.039	(87-88)
P4, Foundation	70.885	69.447	(69-71)
P5, Random	no water	84.604	-
P6, Foundation	69.646	68.964	(87-88)
P7, Random	no water	68.337	-
P8, Random	no water	73.859	-

Based on the computed results, installation of piezometers at the upstream of Dike 1 was recommended to the owner for calibration and for dam safety program. Calculated value of core zone's permeability shows 1×10^{-9} m/s which was verified by field permeability test, gravity method which showed the value as 0 to 7.9×10^{-9} m/s. Visual manual procedure defines those soil samples as Lean Clay (CL). Random zone, downstream of Dike 1 shows the filed permeability value 2.27×10^{-8} to 1.3×10^{-7} m/s from three locations. It is sandy clay, mainly.

Table 9 Calculated permeability by SEEP/W

Zone	Saturated WC	Residual Water	k, m/sec	k_y/k_x
Core	0.50	0.40	1.0×10^{-9}	0.20
Foundation	0.45	0.40	5.0×10^{-8}	0.25
Natural Ground	0.40	0.20	1.0×10^{-8}	0.40
Quarry Rock	0.30	0.01	5.0×10^{-3}	0.50
Random	0.40	0.05	1.0×10^{-7}	0.33
Chimney	0.35	0.01	1.0×10^{-6}	0.60
Selected	0.30	0.05	5.0×10^{-2}	0.60
Transition	0.35	0.10	1.0×10^{-6}	0.50
Grouting	0.60	0.10	7.0×10^{-10}	0.10

CONCLUSIONS

The study used SEEP/W software to generate seepage model of Dike 1 of Kang Krachan dam by assumed condition of foundation rock is homogeneous in 2-dimension with steady state of normal reservoir level. The trial-and-error method was adopted to calibrate the calculated total head and seepage flowrate vs the monitored by piezometers and seepage flow meter. Calculated permeability values of Dike 1 core and random materials presented the values in the reasonable range performed by gravity method of field permeability tests. In practice, there are limitation factors on homogeneous materials in the same zone and construction technology, for example, water spray, thick of compacted layer and compaction technique. Thus, there were various engineering soil properties in the same zone of dam. However, quality control of construction is processed as conceptual design and technical specification. SEEP/W was applied with clear understanding on hydraulics function of materials and seepage flow through dam. The result of the calculated models has plotted with implicated dam's instrument data to find out how similar it was, like calibration technique. This case shows the application of dam instruments and seepage analysis by SEEP/W, specified by the permeability values from the references and verified randomly by field tests.

ACKNOWLEDGMENTS

We would like to express our sincere gratitude to the Dam Safety Branch of Royal Irrigation Department for all supports.

REFERENCES

[1] Burt G. Look, Handbook of Geotechnical Investigation and Design Tables, Taylor & Francis, London, UK, 2007, pp. 93-96.

[2] Nassrin Jassim Hussien Al-Mansori , Thair Jabbar Mizhir Al-Fatlawi, Nariman Yahya Othman and Laith Shaker Ashoor Al-Zubaidi, Numerical Analysis of Seepage in Earth-Fill Dams, Civil Engineering Journal, Vol.6, No.7, 2020, pp. 336-1348.

[3] Royal Irrigation Department, Technical Record of ECI's reports, RID. Library, 1966.

[4] Department of Public Works and Town& Country Planning Petchaburi Province's soil report, 2007, 6 p.

[5] Department of Mineral Resource, Technical Seminar; Biostratigraphy and Karst Morphology of Satun Aspiring Geopark, 2017, 21 p.

[6] Matthew R. Broaddus, Performing in a Steady-State Seepage Analysis Using SEEP/W: a Primer for Engineering Students, Electronic Thesis, University of Louisville, 2015, 64 p.

[7] Al-Janabi, A. M. S., Ghazali, A. H., Ghazaw, Y. M., Afan, H. A., Al-Ansari, N., & Yaseen, Z. M. Experimental and numerical analysis for earth-fill dam seepage. In Sustainability (Switzerland) Vol. 12, 2020, pp. 1–14.

[8] Kamal Ganjalipour and Seyed Mahmod Fatemi Aghda, Calibration of seepage analysis sections based on observation well monitoring data: a case study on Darian dam abutments Kermansh-ah province, Iran, Modeling Earth Systems and Environment, 2019, 5: pp. 159–173.

[9] M. Javanmard, F. Amiri, S. M. Safavi, Instrumentation Readings versus Numerical Analysis of Taham Dam, International Journal of Engineering (IJE), IJE Transactions A: Basics Vol. 32, No. 1, 2019, pp. 28-35.

[10] Royal Irrigation Department, Work Manual of Soil Engineering Exploration, 2017, pp. 16-17.

11th Int. Conf. on Geotechnique, Construction Materials & Environment, Kyoto, Japan, 3-5 November 2021, ISBN: 978-4-909106063 C3051

PERFORMANCE OF REINFORCED BASE COURSES OF FLEXIBLE PAVEMENTS OVERLYING SOFT SUBGRADES: INSIGHTS FROM LARGE-SCALE MODEL EXPERIMENTS

Ramu Baadiga[1], Umashankar Balunaini[2], and Sireesh Saride[3]

[1]Doctoral Student, Indian Institute of Technology Hyderabad, India; [2,3] Faculty, Indian Institute of Technology Hyderabad, India

ABSTRACT

In this study, large-scale model pavement experiments (LSMPEs) were performed to assess the performance of geosynthetic-reinforced bases of flexible pavements overlying soft subgrades (with California bearing ratio equal to 1% and 5%). Two configurations of reinforcement were considered – (1) base layers reinforced with geocell (GC) alone, and (2) base layers reinforced with geocell and geogrid (GG) combinations (GC+GG). Model pavements were constructed inside the test chamber measuring 1.5m (length) × 1.5m (width) × 1.0m (height). Wheel loads on the pavements were simulated by applying repetitive load equivalent to the tire contact pressure of 550 kPa through an actuator on a rigid circular plate (diameter equal to 300 mm). The reinforcement combination with GC+GG was found to perform better than GC alone due to additional support offered by geogrid when used as a base or basal reinforcement underneath the geocell mattress. The performance was evaluated in terms of cumulative permanent deformations and Traffic Benefit Ratio (TBR) over 100,000 repetitive load cycles. TBRs of GC+GG combination showed values greater than 50 for test conditions considered. Furthermore, test results showed that the GC+GG combination reduced permanent deformation by up to 78%, while GC alone reduced it by about 52% compared to the unreinforced section. TBRs of geocell alone and geocell with basal geogrid combinations indicated extended service life of the pavement.

Keywords: Soft subgrade, Geocell, Geogrid, Permanent deformations, Traffic benefit ratio

INTRODUCTION

Pavements overlying soft subgrades cause excessive permanent deformation under repetitive loads. The subgrades associated with wetlands and heavy rainfall regions are a practical concern for improvement. Available conventional methods such as cement or lime stabilization or fiber reinforcement used to treat soft subgrades yield a good platform for the construction of pavement layers, but consume enormous time and money. Alternatively, geosynthetics are highly preferred due to their cost-effectiveness and ease of construction. Geosynthetic reinforcement materials, viz., geogrid, and geocell offer various benefits in flexible pavements such as lateral restrainment, load-carrying capacity, and membrane support [1-4]. Similarly, a three-dimensional honeycomb structure called geocell offers overall confinement and higher load carrying capacity [1, 5-7]. However, their benefit in terms of reduced deformations and improved pavement performance over soft subgrades is observed when reinforcement is placed near the loading region [8-11]. In most cases, when soft subgrades are encountered, single reinforcement such as geogrid or geocell placement in the base layers may not be adequate to control the pavement deformations. Hence, to overcome such problems generally, a geogrid reinforcement layer underlying a geocell mattress is placed to arrest downward deflections and provide extra support [8, 12, 13].

The geogrid basal reinforcement is used to increase the pavement's service life, decreasing base course thickness or arresting longitudinal cracks in the pavements [14]. The published studies suggest significant improvement in load-bearing capacity due to additional support with basal geogrid placed underneath geocell [8, 12]. The overall performance of the basal reinforcement accounts due to the tensile strength mobilization and membrane support [8, 13]. Previous researchers indicated the necessity of additional support with basal geogrid underneath the geocell mattress to increase the overall performance of the pavement [12, 13]. On the contrary, its benefit was reported to be marginal with an increase in the height of the geocell and was found to give superior performance when the limited size of geocell and appropriate geogrid is used [15]. The increase in height was reported to show buckling of geocell walls leading to a decrease in the load-bearing capacity [15].

The studies mentioned herewith have focused solely on evaluating the bearing capacity of reinforced foundations or pavements. However, studies have not focused on quantifying the overall

pavement performance of geocell and geogrid basal reinforcement, such as improved service life, especially when soft subgrades are encountered. The improved service life of the flexible pavement is generally quantified in terms of *Traffic Benefit Ratio* (TBR) [1]. TBR is defined as the ratio of number of load cycles sustained by base reinforced pavement at the defined permanent deformation to the number of load cycles sustained by the unreinforced pavement section at the same defined permanent deformation with the same material constitutions and thicknesses. Permanent deformation is also called cumulative permanent deformation or rutting. Thus, in this study, the influence of bases reinforced with geocell alone and combination of geocell and geogrid is evaluated in terms of cumulative permanent deformation and TBR of reinforced pavements overlying soft to relatively fair subgrades (with California bearing ratio (CBR) equal to 1% and 5%). The overall purpose of this study is to quantify the enhanced pavement performance in terms of increased service life by the inclusion of geosynthetics when soft subgrades with a CBR ≤ 5% are encountered.

MATERIALS AND METHODOLOGY

Subgrade soil, granular base and subbase, and asphalt layer

In this testing program, crushed aggregate, dense bituminous macadam, and clayey sand were used to prepare granular layers, asphalt layer, and subgrade, respectively. Similarly, geocell and geogrid made up of high-density polyethylene and polypropylene are selected for base reinforcement.

Locally available clayey sand was used as the subgrade material. The Standard Proctor test results showed a maximum dry unit weight of 19 kN/m^3 and an optimum water content of 14.5%. Soft and relatively fair subgrade conditions (CBR=1% and 5%) were simulated in the test chamber by varying water content and the compacted unit weight. Based on extensive calibration studies, targeted CBR =1% and 5% were achieved for the chosen subgrade when prepared at compacted dry unit weights and molding water contents of 16.55 kN/m^3 and 18.5%, and 17.40 kN/m^3 and 17.2%, respectively. The base and subbase layers were prepared following the gradation of wet-mix macadam with crushed stone aggregates, meeting the standard specifications mentioned in the American Society for Testing and Materials [16] and Ministry of Road Transportation and Highways [17], Government of India. Aggregates used for base and subbase layers had a maximum dry unit weight of 22.7 kN/m^3 and optimum water content of 5.5%. The asphalt material used in the study as a binder course had a compacted unit weight of 23.4 kN/m^3.

Geocell and geogrid

High-density polyethylene (HDPE) geocell (GC) of height equal to 100 mm with weld spacing of 356 mm and a seam peel strength of 1420 N was used. Geogrid (GG), made of polypropylene with peak tensile strength of 30 kN/m in biaxial directions and aperture size equal to 40 mm × 40 mm, was used as basal reinforcement placed right below the geocell mattress. The geogrid had a stiffness of 503 kN/m × 509 kN/m at 2% tensile strain in the biaxial directions. Figures 1 (a) and (b) show the geocell and geogrid used in the study.

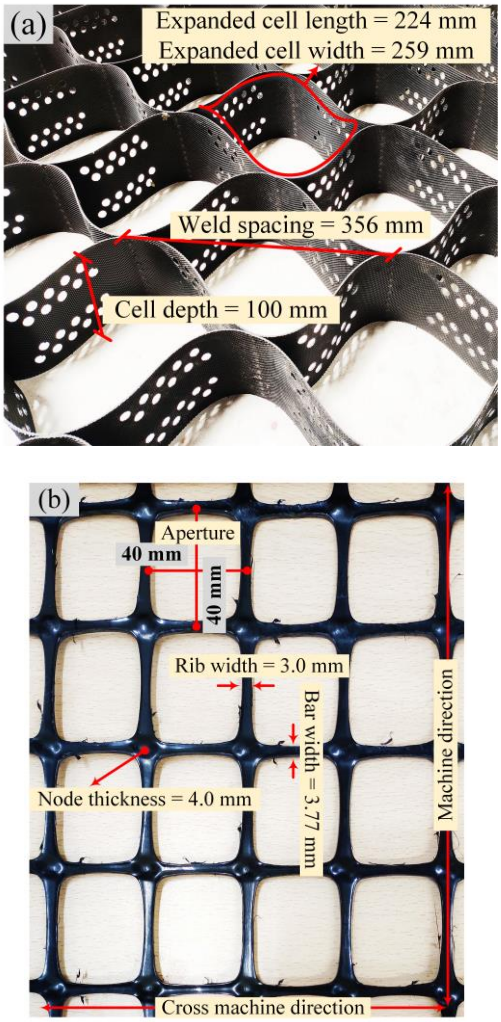

Fig.1 Photo snaps of geocell and geogrid used in the study (a) geocell and (b) basal geogrid used underneath the geocell mattress

EXPERIMENTAL PROGRAM

Pavement layers were prepared using a vibratory plate compactor inside the test chamber measuring 1.5 m × 1.5 m × 1.0 m [3]. The total thickness of granular layers (base plus subbase) and subgrade were maintained as 600 mm and 400 mm, respectively, overlying a soft subgrade of CBR=1%. In the case of pavements underlying relatively fair

subgrade with CBR=5%, a total thickness of granular and subgrade layer was selected as 440 mm and 500 mm, respectively. These thicknesses were finalized based on Indian Road Congress guidelines for design of flexible pavements [18]. Base layer thickness of 225 mm was maintained commonly for all the pavement sections. Over the prepared granular layer, a 50 mm thick asphalt layer was placed. Pavement layers were prepared to achieve 98% of their targeted densities. The expanded geocell mattress size equal to 1.45 m × 1.45 m in length and width was placed at 0.15*D* from the top of the base layer, where *D* is the diameter of the circular plate (i.e., 300 mm). In the case of basal reinforcement application, geogrid of size equal to 1.45 m × 1.45 m in length and width was placed right below the geocell mattress. Prepared testbed with complete instrumentation is shown in Fig. 2. In total, six large-scale model pavements were conducted. Two sections of unreinforced, two test sections with geocell alone, and two test sections with geocell and geogrid as a basal reinforcement were tested. The prepared testbed was ensured for proper consistency in unit weight and water content for all the test cases; the maximum deviation in the measured properties were within 3%. As shown in Fig. 2, repetitive load of haversine load pattern with 5 Hz frequency was simulated and applied over the prepared bed with a typical tire contact pressure of 550 kPa using 100 kN actuator on 300 mm rigid circular plate placed on the center of the testbed [2, 3]. Figure 3 presents the typical load pattern applied on the prepared testbed. The permanent deformation data was measured using an inline displacement transducer inbuilt with the actuator system (refer Fig. 2).

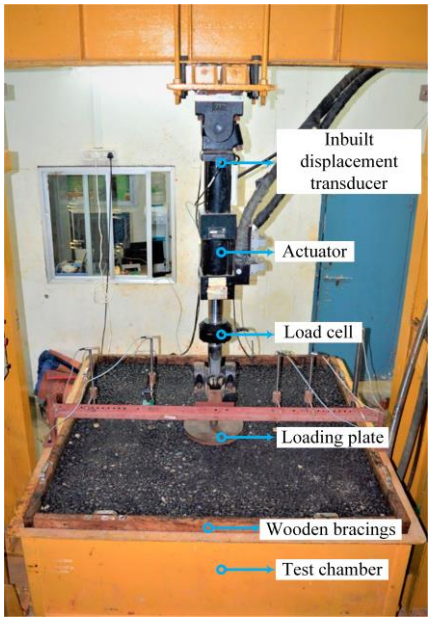

Fig. 2 Test setup showing prepared testbed system with actuator mounting

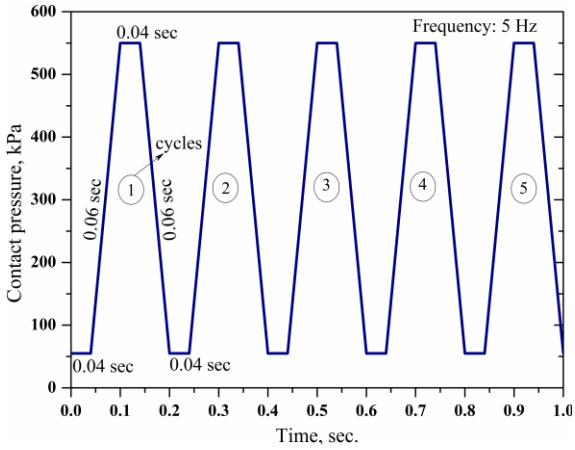

Fig. 3 Repetitive load pattern applied on the testbed

RESULTS AND DISCUSSION

Influence of single geocell and combination of geocell and basal geogrid on permanent deformations

Figures 4(a) and (b) present the permanent deformation *vs.* load cycles for geocell alone and geocell plus geogrid reinforced pavement bases overlying soft (CBR=1%) and relatively fair subgrade (CBR=5%), respectively. In all test cases, repetitive loads were applied up to 100,000 load cycles (N) due to test constraints related to the enormous amount of time it takes to apply repetitive loads. Figure 4(a) shows that the unreinforced section exhibits more than 20 mm of permanent deformation; thus exceeding the failure criterion in rutting. The relatively high permanent deformation of the unreinforced pavement section might have occurred to large vertical and lateral deformations of granular material overlying soft subgrade conditions under repetitive loads. During initial repetitive load cycles, reinforcement mobilization is low; however, as the load cycles increase further, deformations were drastically reduced for GC alone and GC+GG, as shown in Fig. 4(a). The superior benefit is witnessed for GC+GG combination. For example, at 100,000 load cycles, unreinforced section, GC, and GC + GG showed deformations of 24 mm, 11 mm, and 5 mm, respectively. Compared to an unreinforced section, a reduction in measured deformations were found to be about 54% and 73% corresponding to GC and GC+GG at the end of load cycles, respectively. In the case of pavement section reinforced with geocell alone, reduced deformation might have resulted due to overall confinement. In the case of GC+GG reinforcement combination, it is evident that due to the extra structural support offered through membrane and interlock action of basal geogrid, further reduction in permanent deformation was

observed. Beyond the 30,000 load cycles, a near constant permanent deformation was seen with the GC+GG reinforcement combination. Therefore, geocell with basal geogrid combination might be a viable solution to control deformation over very soft subgrades.

On the other hand, permanent deformations observed for pavements overlying relatively fair subgrade condition is presented in Fig. 4(b). In pavements underlying fair subgrade condition (CBR=5%), the resulting deformations were lower than those for a soft subgrade (CBR=1%) for a given applied load cycle. Between GC and GC+GG, the reinforcement benefit was found to be only marginal. Nevertheless, GC+GG reinforcement combination performed better showing lower deformations than the geocell alone. Almost consistent deformations were observed beyond 30,000 load cycles for geocell alone and a combination of geocell and basal geogrid. Based on the permanent deformations presented in Fig. 4(b), it can be inferred that the reductions were in the order of 51% and 66% for GC and GC+GG, respectively, over 100,000 load cycles. In the case of pavements encountered with relatively fair subgrade conditions, geocell alone might be used to reinforce the base layers as no significant improvement in reducing the deformations were observed for GC+GG.

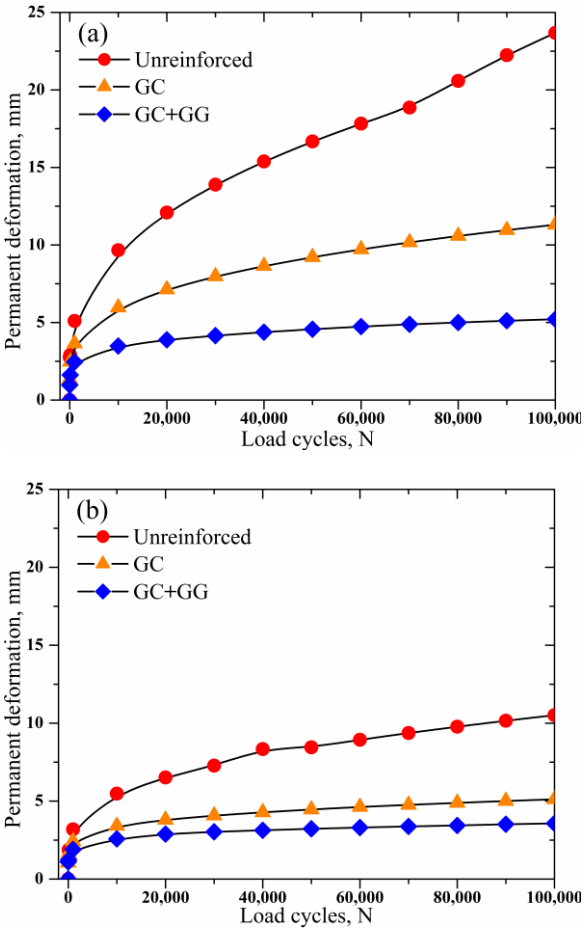

Fig. 4 Permanent deformation versus repetitive load cycles of unreinforced, GC reinforced base layer and GC+GG reinforced base layer for (a) pavement overlying CBR = 1%, and (b) pavement overlying CBR = 5%

Traffic benefit ratios (TBR) of reinforced base layers

TBR is also called traffic improvement life, which indicates the extended life of the pavement. Figures 5(a) and (b) show the TBRs of reinforced pavements overlying soft and relatively fair subgrade conditions. In this study, about 11 mm maximum permanent deformations were observed for reinforced sections. Hence, the TBRs were calculated within specified permanent deformation; however, to witness TBRs at higher deformation, it might require higher repetitive load cycles than those applied in the study. From Figs. 5(a) and (b), it can be noticed that pavements overlying soft and relatively fair subgrade conditions, GC reinforced base sections resulted in TBR as high as 12 and 8.3, respectively. Likewise, TBRs of bases reinforced with GC+GG combination was found to be as high as 150 and 38 over soft and relatively fair subgrade condition, respectively (refer to Fig. 5(b)). Initially, TBRs increase, and then with an increase in further permanent deformations, TBRs attenuates for GC reinforced section alone. However, this trend is expected as TBR is calculated as a ratio of reinforced cycles to unreinforced cycles at the same defined permanent deformation. In the case of GC+GG reinforced section, resulting load-carrying cycles were more, thereby leading to higher TBR than the GC alone. Higher TBRs were observed in the case of pavement overlying soft subgrades, and lower values were observed for fair subgrades. In the available literature, TBRs ranged as high as 670 for geosynthetic reinforced pavement bases [1]. However, TBRs recommended for design at failure deformations were reported between 1 to 4 [1].

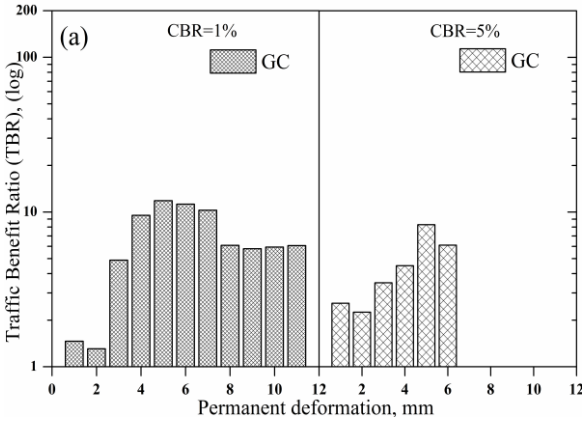

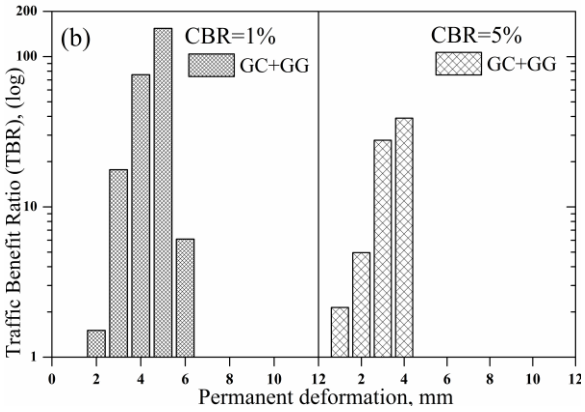

Fig. 5 TBR versus permanent deformations for (a) geocell alone for pavement overlying subgrades with CBR=1% and 5%, (b) combination of geocell plus basal geogrid for pavement overlying subgrades with CBR = 1% and 5%

Recommendations

The combination of geocell and geogrid placed below the geocell was found to be a viable solution over soft subgrades. The reinforcement benefit can be observed majorly in two ways. Firstly, the reduced cost due to a decrease in thickness of a granular layer, and secondly, increased service life and reduced maintenance cost if the same thickness of the pavement is maintained. On the contrary, the unreinforced pavement section frequently requires rehabilitation and asphalt overlays leading to huge cost incurrences; this activity might be minimal in the case of reinforced pavements. Over relatively fair subgrade conditions, geocell alone might help in improving pavement performance.

It can be noted that in the present study, reported TBR values ranged as high as 150 corresponding to low permanent deformation values (i.e., below 10 mm). However, this value may decrease further at higher permanent deformations (rutting) or at designated rutting failure criterion. For example, at a standard rutting criterion of 20 mm [18] of the pavement overlying subgrade with CBR=1%, the computed load cycles of unreinforced pavement and extrapolated load cycles at the same rut depth for GC [refer to Fig. 4(a)] alone resulted in about 76,593 and 1,014,862 cycles, respectively. Thus, the corresponding TBR is 13.25. Hence, it is recommended to adopt the TBR values pertaining to the rutting failure criterion. The design-related aspects that involve reducing base course and improving the pavement's service life can be found in Berg et al. [1] and Holtz et al. [19] studies.

CONCLUSIONS

In this study, essential insights obtained from large-scale model pavement experiments were discussed. The flexible pavement bases overlying soft (CBR=1%) to relatively fair subgrade (CBR=5%) conditions were reinforced with geocell alone (GC) and a combination of geocell plus geogrid (GC+GG) to witness the overall pavement performance. The repetitive load tests were conducted to evaluate the load-response of geosynthetic reinforced flexible pavements. The permanent deformation behavior versus the applied repetitive load cycles were evaluated for geocell alone, and geocell plus geogrid combination placed in the base layer of the flexible pavement overlying soft and relatively fair subgrades.

Further, the extended life of the pavement due to reinforcement is quantified in terms of traffic benefit ratio (TBR) by considering permanent deformation observed over 100,000 load cycles. The main conclusions obtained from the present study are discussed below.

- The reduction in pavement deformation due to geocell (GC) alone and geocell plus basal geogrid (GC+GG) ranged as high as 54% and 73%, respectively, over soft subgrades (CBR=1%). Likewise, the corresponding reductions were 51% and 66% for pavements over relatively fair subgrades (CBR=5%).
- Geogrid placed right underneath the geocell was found to arrest lateral movement of granular material effectively leading to higher reductions in deformations. In other words, the additional basal reinforcement right underneath the geocell mattress leads to sustain higher load cycles than the pavement base system supported with geocell alone for the same rut deformation.
- GC+GG combination was more effective than GC alone for pavements overlying soft subgrades (CBR=1%). However, no significant improvement of GC+GG compared to GC alone was observed for pavements overlying fair subgrades (CBR=5%).
- Higher TBRs were witnessed for a GC+GG due to extra support offered by geogrid underneath the geocell.
- Traffic Benefit Ratio (TBR) of GC alone ranged as high as 12 and 8.3, respectively, for pavements overlying soft and relatively fair subgrades.
- TBRs of geogrid placed underneath a geocell mattress (GC+GG) showed as high as 150 and 38 for pavement overlying soft and relatively fair subgrades, respectively. However, it may be noted that the reported TBR values correspond to relatively low permanent deformation values (i.e., within 12 mm).

ACKNOWLEDGEMENT

Authors would like to thank the National Highway Authority of India for the research grant under grant number: NHAI/TIC/R&D/108/2016.

REFERENCES

[1] Berg R.R., Christopher B.R. and Perkins S.W., Geosynthetic Reinforcement of the Aggregate Base/subbase Courses of Pavement Structures. Geosynthetic Materials Association White Paper-II, 2000, Roseville, Minnesota, USA.

[2] Baadiga R., Saride S., Balunaini U. and Madhira R. M., Influence of Tensile Strength of Geogrid and Subgrade Modulus on Layer Coefficients of Granular Bases. Transport. Geotech., Vol.29, 2021, pp.100557, https://doi.org/10.1016/j.trgeo.2021.100557

[3] Baadiga R., Balunaini U., Saride S. and Madhira R. M., Influence of Geogrid Properties on Rutting and Stress Distribution in Reinforced Flexible Pavements under Repetitive Wheel Loading, J. Mater. Civ. Eng., 2021, 10.1061/(ASCE)MT.1943-5533.0003972

[4] Saride S. and Baadiga R., New Layer Coefficients for Geogrid-reinforced Pavement bases. Indian Geotech. J., Vol.51, No.1, 2021, pp.182 – 196. DOI: 10.1007/s40098-020-00484-6

[5] Pokharel S.K., Han J., Manandhar C., Yang X., Leshchinsky D., Halahmi I. and Parsons R., Accelerated Pavement Testing of Geocell-Reinforced Unpaved Roads over Weak Subgrade. Transp. Res. Rec., J. Transp. Res. Board., Vol.2204, No.1, 2011, pp.67–75. https://doi.org/10.3141/2204-09

[6] Han J. and Thakur J. K., Sustainable Roadway Construction using Recycled Aggregates with Geosynthetics. Sustainable. Cities Soc., 14, 2014, pp.342–350. https://doi.org/10.1016/j.scs.2013.11.011

[7] Hegde A., Geocell Reinforced Foundation Beds-Past Findings, Present Trends and Future Prospects: A State-of-the-Art Review. Constr. Build. Mater., Vol.154, 2017, pp.658–674. https://doi.org/10.1016/j.conbuildmat.2017.07.230

[8] Dash S. K., Sireesh S. and Sitharam T. G., Model Studies on Circular Footing Supported on Geocell Reinforced Sand underlain by Soft Clay. Geotext. and Geomembr., Vol. 21, No.3, 2003, pp.197–219. https://doi.org/10.1016/S0266-1144(03)00017-7

[9] Sitharam T. G., Sireesh S. and Dash S. K., Model Studies of a Circular Footing Supported on Geocell-Reinforced Clay. Can. Geotech. J., Vol. 42, No.2, 2005, pp.693–703. https://doi.org/10.1139/t04-117

[10] Sireesh S., Mole P. A. F., Madhav M. R., and Kumar R. V., Non-linear Response of Geocell Reinforced Dense Granular Layer over Weak Soil Under Circular Loading. Int. J. Geotech. Eng., Vol.10, No.1, 2016, pp.23 – 30. https://doi.org/10.1179/1939787915Y.0000000014

[11] Thakur J. K., Han J. and Parsons R. L., Factors Influencing Deformations of Geocell-Reinforced Recycled Asphalt Pavement Bases Under Cyclic Loading. J. Mater. Civ. Eng., Vol.29, No.3, 2017, pp.1–12. https://doi.org/10.1061/(ASCE)MT.1943-5533.0001760

[12] Saride S., Sitharam T.G., and Puppala A.J., The Function of Basal Geogrids in Minimizing Rutting of Geocell Reinforced Subgrades. Geo-Frontiers Congress, 2011, pp.4645–4652. https://doi.org/10.1061/41165(397)475

[13] Hegde A., and Sitharam T. G., 3-Dimensional Numerical Modelling of Geocell Reinforced Sand Beds. Geotext. and Geomembr., Vol. 43, No.2, 2015, pp.171–181.https://doi.org/10.1016/j.geotexmem.2014.11.009

[14] Zornberg J. G., Reinforcement of Pavements over Expansive Clay Subgrades. In Proc. 17th Int. Conf. Soil Mech. Geotech. Eng., M. Hamza et al. (Eds.), 2009, pp. 765 – 768, doi:10.3233/978-1-60750-031-5-765

[15] Sitharam T. G. and Sireesh S., Effects of Base Geogrid on Geocell-Reinforced Foundation Beds. Geomech. Geoeng., Vol. 1, No.*3*, 2006, pp.207-216, *DOI:*10.1080/17486020600900596

[16] ASTM .2020. Standard Classification for Graded Aggregate Material for Bases or Subbases for Highways or Airports, ASTM D2940M-20, West Conshohocken, PA: ASTM.

[17] MORTH. Specifications for Road and Bridge Works, (5th Revision), Ministry of Road Transport & Highways, 2013

[18] IRC 37. Guidelines for the Design of Flexible Pavements, (3rd Revision), Indian Road Congress, 2012

[19] Holtz R.D, Christopher B.R. and Berg R.R., Geosynthetic Design and Construction Guidelines, Participant Notebook, FHWA Publication No. FHWA HI -07-092, Federal Highway Administration, Washington, D.C, 2008.

11th Int. Conf. on Geotechnique, Construction Materials & Environment,
Kyoto, Japan, 3-5 November 2021, ISBN: 978-4-909106063 C3051

EFFECT OF BENDING RIGIDITY OF PRECAST L-TYPE RETAINING WALL ON LATERAL PRESSURE CAUSED BY REPEATED WHEEL LOADING

Yukimine Otomo[1], Osamu Maruyama[2]

[1]Seikitokyu Kogyo Co., Ltd., Japan; [2]Department of Urban and Civil Engineering, Tokyo City University, Japan

ABSTRACT

The lateral earth pressure acting on the precast L-type retaining wall installed in the embankment section of the road is thought to be the result of the interaction between the retaining wall and the backfill soil. However, in dealing with earth-retaining concrete structures, few reports have clarified the mechanism of deterioration due to repeated loads of passing vehicles, and no diagnostic method for damage has been established. In this report, we focused on the bending rigidity of the wall and measured, by changing the bending rigidity of the wall, the lateral pressures that act when the test wheel is repeatedly loaded on the backfill soil. In the experiment, two types of walls were used; one was a wall of a box made of light gauge steel with its bending rigidity being three times that of the precast L-type retaining walls and the other a pseudo L-type retaining wall having almost the same bending rigidity. As a result, it was found that the magnitude of the lateral pressures depends on the bending rigidity of the precast L-type retaining wall.

Keywords: Precast L-type retaining wall, Repetitive loading, Lateral pressures, Bending rigidity

INTRODUCTION

Precast L-type retaining walls installed in the embankment section of the road are repeatedly exposed to various lateral pressures from passing vehicles through the backfill soil. These lateral pressures occur because of the interaction between the retaining wall and the backfill soil, and are thought to be affected by the bending rigidity of the stem [1]. However, few reports have clarified the mechanism of deterioration caused by repeated loads of passing vehicles, and no diagnostic method for damage has been established. In this paper, the bending rigidity of the wall was changed, and the lateral pressures and top displacements were measured when the backfill material was repeatedly loaded with test wheels. For the specimens, one was a 20cm high, 50cm wide wall made of light gauge steel with its bending rigidity being three times that of the precast L-type retaining wall. Another was a 20cm high, 15cm wide pseudo L-type retaining wall with its bending rigidity of 1.25 times the L-type's.

BENDING RIGIDITY OF PRECAST L-TYPE RETAINING WALLS

It is stated that in case the stem height of the precast L-type retaining wall is in the range of 0.91m to 2.06m, its thickness corresponds to 9cm to 19cm [2]. The design standard strength of the stem is 30N / mm^2 and the modulus of elasticity is 28000N/mm^2. And when the moment of inertia of area is calculated with the extension of 50cm, which is the same as the wall width of light gauge steel, the bending rigidity of the stem is in the range from 851kN-m^2 to 8002kN-m^2. The relationship between the stem height and bending rigidity is shown in Fig. 1, and Eq. (1) can be obtained by approximating with a cubic equation.

$$y = 771.36x^3 + 272.46x^2 + 51.031x - 1.8939 \quad (1)$$

Where, x is the height of the stem and y is the bending rigidity. From the approximate formula, the bending rigidity was estimated to be 25.4kN-m^2 when the wall height was 0.2m. The moment of inertia of area for the precast L-type retaining wall was also calculated with the extension of 15cm, which is the same as the wall width of the pseudo L-type retaining wall. The bending rigidity was obtained by taking into account the value of 25.4 abovementioned and the different widths between the two retaining walls as follows; 25.4 × 15 / 50 = 7.6kN-m^2.

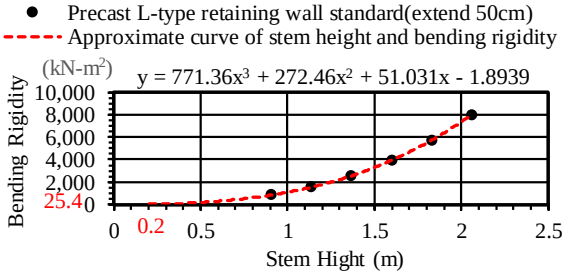

Fig. 1 Relationship between stem height and bending rigidity

METHOD OF REPETITIVE LOADING EXPERIMENT USING WALL SURFACE OF

LIGHT GAUGE STEEL

Bending Rigidity of Wall of Light Gauge Steel

Specimen is a box mostly made of light gauge steel. It is 50cm (25+25) wide, 25cm (11+14) long and 20cm deep (Fig. 2). The sidewalls as well as the 50cm wide wall and the bottom plate were fixed with M10 bolts. The bending rigidity of the wall, EI is obtained to be 76.0kN−m^2 by assuming the modulus of elasticity of the two light gauge steels, which form the wall, being 2.0×10^7N/cm^2, and calculating the moment of inertia of area around the weak axis as I=2×19=38cm^4. Therefore, the ratio of bending rigidity of the wall to that of the precast L-type retaining wall turns out to be 3.0 times (76/25.4=3.0).

Method of Measurement of Lateral Pressures and Top Displacement

Nine pressure gauges, with the diameter being 7.6mm, thickness 2mm and capacity 3MPA, were pasted on a thin metal plate. Then, a washer was placed around each of the pressure gauges to fix them on the metal plate. It was placed horizontally or vertically in the center of the box for the pressure measurement (Fig. 2). In this process, the pressure gauges and wires were covered with a 5mm thick NR sponge rubber. For the correlation of pressure with and without sponge rubber, a linear equation was obtained using a compression testing apparatus as is shown as Eq. (2), by which the measured pressure x (kN/m^2) was converted to the pressure y (kN/m^2) without sponge rubber. The measurement of lateral pressures and a top displacement started from the time of backfilling and continued until the specified number of loading was completed.

$$y = 1.042x + 34.3 \quad (2)$$

Backfill Material

Part of gradation-controlled crushed stone, which passed through a 5.6mm sieve, was used as backfill soil. The maximum dry density was 2.153g/cm^3, the optimum moisture content was 7.9%, and the soil particle density was 2.685g/cm^3. The backfill material was gravelly soil as seen from the grain size distribution (Fig. 3), and the angle of shear resistance was 35°. Generally, the optimum moisture content that maximizes the dry density is different from the moisture content that maximizes the strength.

It is said that the maximum strength is on the dry side of the optimum moisture content [3], leading to the selection of the moisture content of 6%. The backfill material was compacted with a tamper so that the compacted thickness of one layer was to be 5cm or less. The wet density after tamper compaction was 18.7kN/m^3 and the degree of compaction was 83%.

Loading Method and Loading Weight

The box was fixed so that the minimum horizontal distance from the pressure gauges to the center of the test wheel was to be 4cm (Fig. 2). For the repetitive loading test, a water-immersed wheel tracking machine was used. Its test wheel was of a diameter of 20cm and a width of 5cm. The moving distance of the wheel was set to be 35cm so that the test wheel could pass in front of, and cover, all the pressure gauges arranged in the lateral direction. The loads on the test wheel were 1472N, 1275N, 1079N, and 883N. The test wheel was manually operated and repeatedly moved in parallel with the wall.

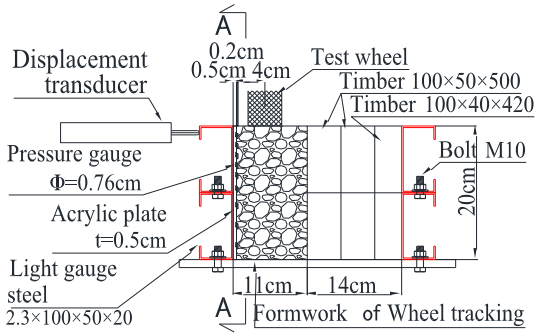

(b) B-B cross section

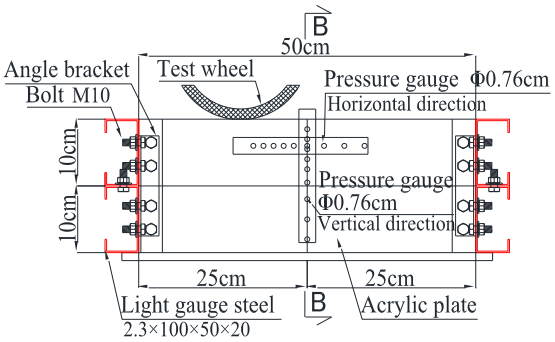

(a) A-A cross section

Fig. 2 Box with light gauge steel

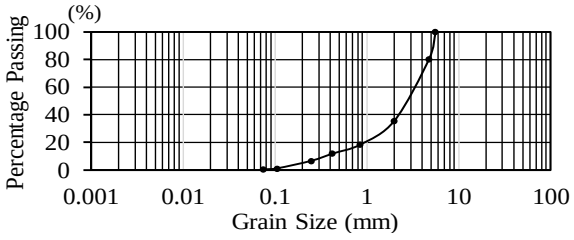

Fig. 3 Grain Distribution Curve

LATERAL PRESSURE ACTING ON WALL SURFACE OF LIGHT GAUGE STEEL AND DISPLACEMENT OF TOP

Lateral Pressures in Vertical Direction

The transition of the lateral pressures is shown in Fig. 4 as related to the time during which the wheel load of 1472N was manually and repeatedly loaded, 800 times in total. They were measured by the pressure gauges placed at specified depths. The figures with colored lines on the graph represent the depth at which the gauges were placed. It took about 34 minutes before the measurement for backfilling and compacting the backfill material. The combined lateral pressure due to the wheel load and the compaction using the tamper is the largest at a depth of 30mm, and the lateral pressures tend to decrease as the depth increases from 30mm. The peak of residual stress was 32 loadings at depths of 30 to 45mm (point A in Fig. 4) and 4 loadings at depths of 60 to 120mm.

It has been reported by Spangler and Mickle [4] that in case a wheel loading is statically acted on the backfill soil of the retaining wall, the lateral pressures acting on the stem after removing the loading is often larger than the lateral pressures before loading. In the repetitive loading test, it was confirmed as well at all the pressure gauges installed at each depth that the residual pressures increased and the values gradually decreased after reaching the maximum. The larger the initial residual pressures value, the more remarkable the decrease in the residual pressures. In addition, the difference between the maximum value of lateral pressures and the residual pressures (hereinafter referred to as the amplitude of pressures) tends to gradually decrease with each loading.

Granular soil becomes a particle structure corresponding to the applied load after repeated loading. It is stated that as the stress in the soil increases, plastic deformation occurs due to the change of the internal structure [5]. The experimental results showed that plastic deformation occurred from the start of repeated loading. In addition, the increase of residual pressures came to end when the plastic deformation converged. It is presumed that the magnitude of the amplitude of pressures is determined by the amount of plastic deformation. Both pressures after the convergence of plastic deformation seem to naturally decrease even if repetitive loading is applied.

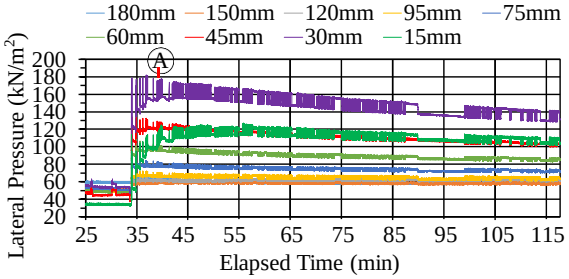

Fig. 4 Lateral pressures in vertical direction (wheel load 1472N, 800 loadings)

Lateral Pressures in Horizontal Direction and Displacement of Top

The transition of the lateral pressures and top displacement are shown in Fig. 5 and Fig. 6, respectively, as related to the time during which the wheel load of 1275N was repeatedly loaded, 120 times in total. The measurements were made at nine pressure gauges placed at a depth of 4cm. The legend above the graph in Fig. 5 shows the distance from the pressure gauge at the end. In the measurement, it took 10.4 minutes for backfilling and compacting the material. The numbers in the Fig. 5 represent the number of loadings. The lateral pressures at the beginning of repeated loading were solely the amplitude of pressures. The ratio of residual pressures gradually increased with repeated loadings. The residual pressures and the amplitude of pressures hardly increased at and after 37 loadings and gradually decreased after 69 loadings.

In addition, the displacement of top end increased by 0.45mm from 5.11mm to 5.56mm during the loading. It was confirmed that the increase rate of displacement at the top also changed with that of the residual pressures (Fig. 6).

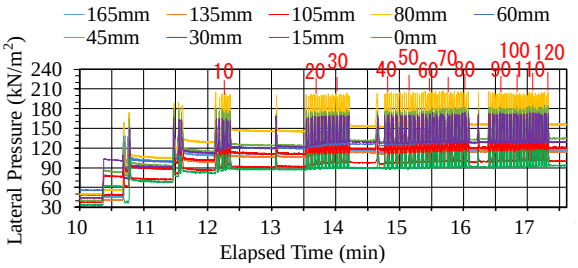

Fig. 5 Lateral pressures in horizontal direction (wheel load 1275N, depth 4cm, 120 loadings)

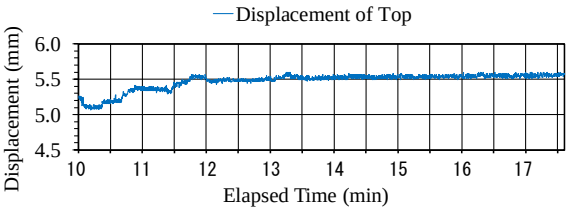

Fig. 6 Displacement of top (wheel load 1275N, depth 4cm, 120 loadings)

METHOD OF REPETITIVE LOADING EXPERIMENT USING PSEUDO L-TYPE RETAINING WALL

Bending Rigidity of Pseudo L-type Retaining Wall

Eight pseudo L-type retaining walls were made for the experiment from precast inlets of the following properties; internal dimensions were 30cm

× 30cm, 3cm thick and 15cm deep. The design standard strength was 30N/mm^2 and the maximum aggregate size was 20mm. The stem of the processed wall was 20cm high and the heel was 16cm wide. The pseudo-L-type retaining walls contained one normal iron wire with a diameter of 2.6mm.

The similarity between the pseudo L-type and real precast L-type retaining walls is confirmed as follows. The modulus of elasticity of the pseudo L-type retaining walls is 28000N/mm^2, and the bending rigidity of the stem and heel is 9.5kN-m^2. Therefore, the bending rigidity of the pseudo L-type retaining walls were considered to be 1.25 (9.5 / 7.6) times that of the real products.

Method of Measurement of Lateral Pressures and Top Displacement

The pseudo L-type retaining wall was placed in the box of light gauge steel, and square steel pipes were arranged linearly on both sides of the pseudo L-type retaining wall. Fig. 7 shows the layout and cross section of the pseudo L-type retaining wall. A metal plate with nine pressure gauges pasted on it was attached vertically on the stem, and the front surfaces of the pressure gauges and wiring were protected with 5mm thick NR sponge rubber. Measurements of lateral pressures and top displacement at two points continued from the backfilling to breakage of the pseudo L-type retaining wall. The pressures measured in repetitive loading experiment were converted to those pressures without sponge rubber using the Eq. (2).

Backfill Material

The backfill material used was the same as one that was used for the wall of light gauge steel. The thickness after compaction by tamper and the water content were the same, too.

Loading Method and Loading Weight

A pseudo L-type retaining wall was placed so that the minimum horizontal distance from the pressure gauges to the center of the test wheel was to be 4cm (Fig. 7). The wheel tracking tester was used for the repetitive loading test. The test wheel was a solid tire with its diameter of 20cm and width of 5cm. In changing and adjusting the load, steel plate of 18.1 to 95.6N per one piece was piled up above the test wheel. The moving distance was set to be 23cm so that the extension of the pseudo L-type retaining wall could be passed. The running speed was eight times/minute.

The bending moment at which the stem of the pseudo L-type retaining wall statically failed was estimated to be 135.4Nm from the static fracture test. The repetitive load, under which this bending moment was acting, was estimated to be 1875N using the bending moment that acted when the loadings 1472N to 883N were repeatedly loaded on the wall surface of the light gauge steel. And then, a set of proportional loads were selected and applied. Their ratios against 1875N were set to be in the range of 110.6% to 90.2% (2073N, 2019N, 1967N, 1911N, 1855N, 1809N, 1757N, 1692N).

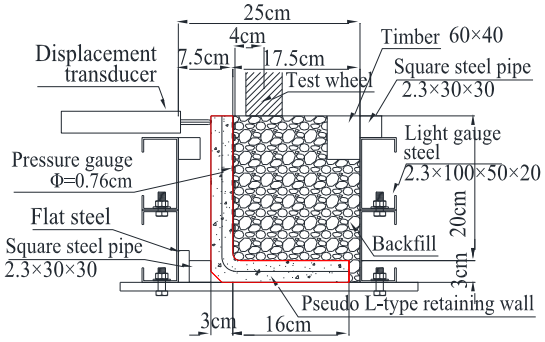

Fig. 7 Layout and cross section of the pseudo L-type retaining wall

RESULTS OF REPETITIVE LOADING EXPERIMENT ON PSEUDO L-TYPE RETAINING WALLS

Shape of Damaged Stem

In the repetitive loading experiments, cracks occurred at the end of the haunch only when the wheel load was 1692N. Cracks occurred at the haunch in the case of the remaining seven stems like when the wheel load was 2019N (Photo-1).


Wheel load of 1692N Wheel load of 2019N

Photo 1 Damaged shape after repetitive loading

Relationship between Top Displacement of Stem and Number of Loadings

When the wheel load of 1692N was repeatedly loaded, the wall failed at 69 loadings. The top displacement of the stem at that time is shown in Fig.8. The legend shows displacement No.1 and displacement No.2 representing the values measured by transducers installed at the top of the stem. It took 27.6 minutes for backfilling and compaction until the start of repetitive loading. The top displacement that

was 0mm before backfilling indicated 0.4mm on the average when loading was started.

When repetitive loading began, the top displacement gradually increased until the elapsed time reached 30 minutes, after which it increased to 1.6mm when the stem failed.

Relationship between Residual Pressures at Each Depth of Stem and Number of Loadings

The fluctuation of the lateral pressures by time at each depth of the stem when the wheel load 1692N was repeatedly loaded is shown in Fig. 9. The figure above the graph shows the depth from the ground surface, and the figures in the graph for the depth of 45mm indicate the number of loadings. The residual pressures at depths deeper than 60mm reached the maximum value after 8 loadings or so and then gradually decreased. The residual pressure at a depth of 45mm reached its maximum value at 11 loadings, and remained almost constant until it failed at 69 loadings. The residual pressures at depths shallower than 30mm reached the maximum value at 58 loadings, and then gradually decreased.

Relationship between Amplitude of Pressures at Each Depth of Stem and Number of Loadings.

Similarly, looking at the fluctuation in the amplitude of pressures in Fig. 9, the amplitude of pressures at depths of 60mm or more reached the maximum at two loadings. After that, it gradually decreased with each additional loading. The amplitude of pressure at a depth of 45mm reached its first peak at two loadings and then decreased. After reaching the minimum value at 30 loadings, it gradually increased until it failed. The amplitude of pressures at depths less than 30mm decreased after reaching the first peak at one loading. After reaching the minimum value at 11 loadings, it reached the maximum value at 66 loadings.

Increase of Lateral Pressure due to Difference of Displacements of Stem

In case the heel plate is fixed, the displacement of the stem increases as it approaches the top. And the displacement of the stem promotes the plastic deformation of the backfill material. What can be seen from Fig. 8 and Fig. 9 are as follows. At a depth of 60mm or more from the ground surface, the plastic deformation converged after 8 loadings, so it is considered that the residual pressures and the amplitude of the pressures naturally decreased even after repetitive loadings. At a depth of 45mm, it is estimated that the plastic deformation continued again due to the displacement of the stem after 11 loadings, and only the amplitude of pressures increased. At a depth of 30mm or less, it is presumed that the plastic deformation continued again due to the displacement of the stem after 8 loading, and the residual pressures and the amplitude of the pressures continued to increase.

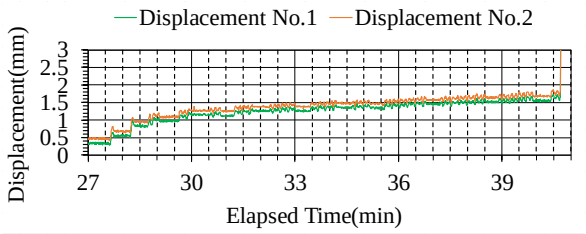

Fig. 8 Top displacement of the stem (1692N, 69 loadings)

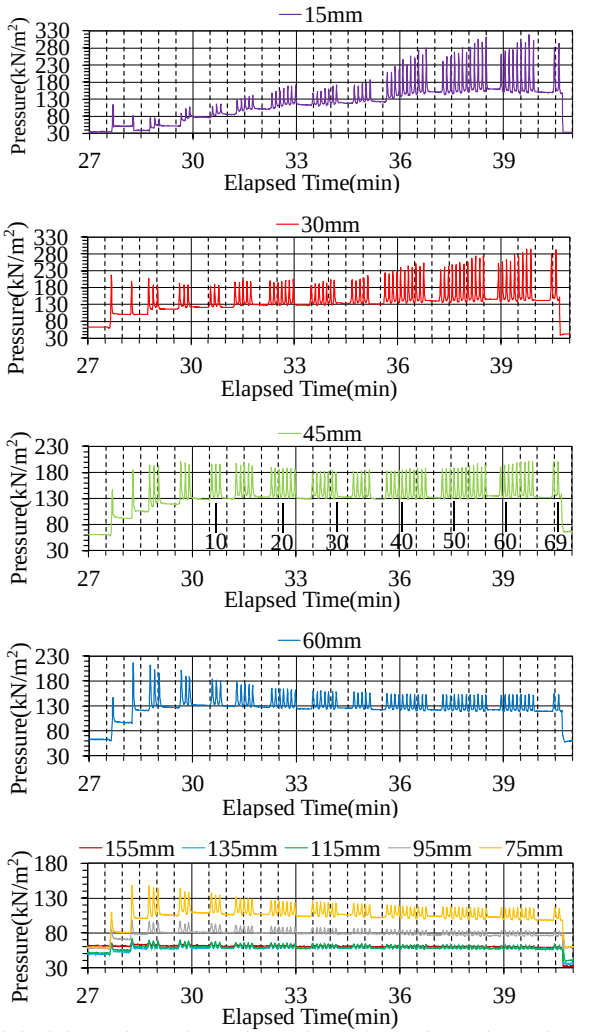

Fig. 9 Lateral pressures at each depth (1692N, 69 loadings)

Variations of Lateral Pressures Due to Difference in Bending Rigidity of Wall

Comparison was made between the wall surface of light gauge steel and the pseudo L-type retaining

wall, which revealed that the residual pressures and the amplitude of pressures increased at the depths 45mm or less after 30 loadings in the case of the latter. The difference was considered to be caused by the displacements of the stem. The reason for this is based on a laboratory experiment report that says that when the stem repeatedly undergoes minute displacement due to outside force, such as seasonal variation, its deformation tends to progress toward the active direction and the backside earth pressures gradually increases [6].

The bending rigidity of the real precast L-type and pseudo L-type retaining walls is almost similar. Therefore, it is considered that the stem is subject to higher residual pressures and amplitude of pressures acting on it and they increase more at points closer to the top affected by its displacement.

Relationship between Weight of Repetitive Loads and Number of Loadings Leading to Failure

Shown in Fig. 10 is the relationship between the repeated loads and the number of loadings to the failure in the repetitive loading experiment of the pseudo L-type retaining walls. The load is estimated to be 1875N that makes the stem to fail after 30 to 40 loadings. With some exceptions, the smaller the repetitive load, the greater the number of loadings required before failure.

By looking at the general tendency shown in Fig. 10, it would be possible to presume that the plastic deformation of the backfill material becomes main factor for the failure of the pseudo L-type retaining walls with repetitive loads larger than 1875N. In addition, it is considered that the pressures caused by the displacement of the stem is gradually added to the pressures due to the repetitive loading on the stem starting from 8 loadings or so. Therefore, it is considered that the smaller the repetitive loads are, the greater the ratio of lateral pressures due to the displacement of the stem gradually increases and fewer the number of repetitive loadings for failure becomes.

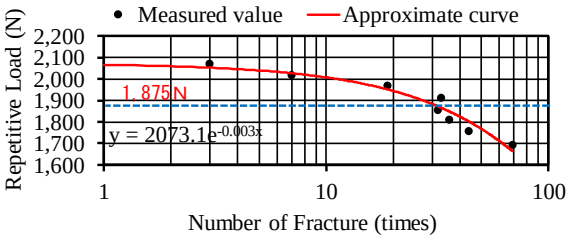

Fig. 10 Relationship between weight of repetitive loads and number of loadings leading to failure (stem height 20cm)

CONCLUSIONS

The magnitude of residual pressures and the amplitude of pressures was determined by that of the repetitive loading and the depth from the ground surface. In the case of the wall of the light gauge steel with high bending rigidity, the residual pressures and the amplitude of the pressures had peaks and then decreased even if the loading continued.

The smaller the repetitive wheel load on the pseudo L-type retaining wall was, the greater the number of loadings was required for failure. It failed even under the repetitive load of 1875N that was supposed to cause failure.

The lateral pressures acting on the stem depended on the bending rigidity of the stem. If the bending rigidity of the stem was low, the lateral pressures caused by the displacement of the stem were added to the lateral pressures due to the repetitive loading. In the case of the pseudo L-type retaining walls with low bending rigidity, plastic deformation of the backfill material increased the displacement of the stems, which in turn promoted plastic deformation of the backfill material. Both of them accelerated the failure of the stems by inducing the increase of residual pressures and amplitude of pressures. In this case, they became higher as they approached closer to the ground because of the effect of the displacement of top of the stem.

REFERENCES

[1] British Standards Institution, British Standard, Eurocode 7：Geotechnical design, Part 1: General rules, British Standards Institution, 2004, pp. 102-103.

[2] Shikoku Technical Office, Shikoku Regional Development Bureau, Ministry of Land, Infrastructure, Transport and Tourism, Design and Construction Manual for Precast L-Type Retaining Walls (Draft), Revised version, 2001, pp. 31-37. (Japanese).

[3] Japanese Geotechnical Society, Geotechnical Engineering - Practice Series No.30, Soil Compaction, Maruzen Publishing, 2012, pp. 7-17. (Japanese).

[4] Spangler, M. G., and Mickle, J. L., Lateral Pressures on Retaining Walls Due to Backfill Surface Loads, Highway Research Board Bulletin, 141, 1956, pp. 1-15.

[5] Hidetoshi Ochiai, Effect of Initial Density on Compressibility of Granular Soils, Journal of the Japanese Society of Soil Mechanics and Foundation Engineering, Vol. 15, No.2, 1975, pp. 89-95. (Japanese).

[6] Takashi Sumiyoshi, Behavior of U-type Retaining Wall Subjected to Cyclic Displacement, Annual Report I. C. E. of Tokyo Metropolitan Government, 2005, pp. 69-78. (Japanese).

11th Int. Conf. on Geotechnique, Construction Materials & Environment,
Kyoto, Japan, 3-5 November 2021, ISBN: 978-4-909106063 C3051

INVESTIGATION AND STABILITY ANALYSIS OF SLOPE FAILURE AT EXTREMELY SHALLOW LAYER AFTER SNOW MELT IN SNOWY COLD REGIONS

Naoki Miura[1], Dai Nakamura[2], Takayuki Kawaguchi[3] and Shunzo Kawajiri[4]

[1]Graduate School of Engineering, Kitami Institute of Technology, Japan
[2,3,4]Faculty of Engineering, Kitami Institute of Technology, Japan

ABSTRACT

In snowy cold regions such as Hokkaido, slopes can collapse owing to the frost heave phenomenon, freeze-thaw actions in winter, or snowmelt in spring. Kitami City in Hokkaido recently suffered from such slope failures when the extremely shallow layer eroded and slid after a snow melt in early spring of 2020. The depth of this slope failure was about 0.20 to 0.25 m, which was very shallow compared with general surface failures. In this research, we conducted a site investigation of the road slope, and collected undisturbed soil samples from a non-collapsed area near the slope failure to conduct a constant pressure direct shear test. For the direct shear tests, specimens with natural water content at the time of sampling and forcibly saturated specimens were used. The results of the slope stability analysis with the strength parameters obtained from the direct shear test showed that the slope failure was caused by snowmelt penetration, mainly due to a decrease in cohesion.

Keywords: Snowy cold region, Slope failure, Direct shear test, Slope stability analysis

INTRODUCTION

In snowy cold regions such as Hokkaido in Japan, slopes can collapse owing to the frost heave phenomenon, freeze-thaw actions in winter, or snowmelt in spring. Many incidents of slope failure along roadways of Hokkaido were reported (e.g. Subramanian et al. [1]). Such a slope failure also occurred in early spring of 2020 on a road slope in Kitami City, Hokkaido. The depth of this slope failure was about 0.20 to 0.25 m, which was very shallow compared with general surface failures. In this research, we conducted a site investigation of the road slope, and collected undisturbed soil samples from a non-collapsed area near the slope failure to conduct a constant pressure direct shear test. In addition, slope stability analysis of the infinite length assumptions without seepage was conducted using the strength parameters obtained from the direct shear tests, and the factors that led to the failure were discussed.

SITE INVESTIGATION OF THE ROAD SLOPE WHERE SURFACE FAILURE OCCURRED

Meteorological conditions before and after the day when the slope failure was observed

The slope failure was observed on April 3, 2020.

Figure 1 shows the overall appearance of the road slope where the failure occurred. Since the failure surface is a little dry, it is assumed that the slope failure occurred a little earlier than this date.

Figure 2 shows the daily mean temperature, snow depth, and daily precipitation around April 3, 2020, when the slope failure was observed. The meteorological data were observed at the AMeDAS Kitami station [2]. From this figure, it can be seen that the snow depth has been decreasing rapidly since mid-March, when the daily mean temperature became

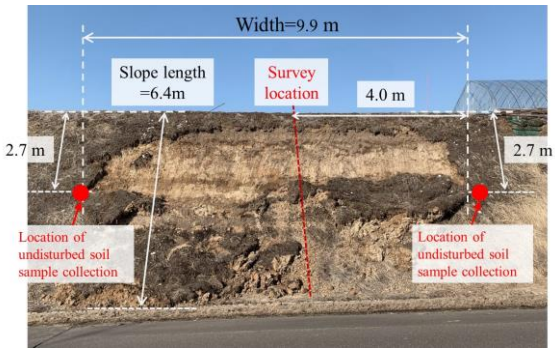

Fig. 1 Overall appearance of the road slope where the failure occurred

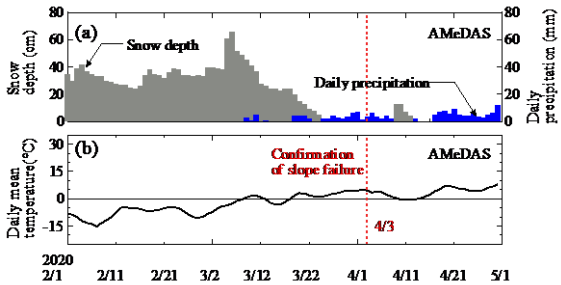

Fig. 2 Daily mean temperature, snow depth, and daily precipitation around April 3, 2021

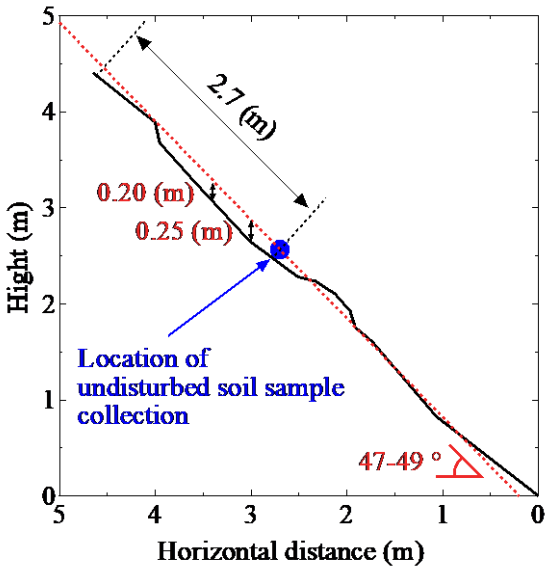

Fig. 3 Cross-sectional view of the slope failure obtained by surveying

positive. On the other hand, daily precipitation before the date of confirmed slope failure is low. Based on the above meteorological data, the trigger for this slope failure is thought to be the infiltration of snowmelt.

Overview of the investigated road slopes

The site investigation, including collection of undisturbed soil samples, was conducted from May 15 to June 5, 2020. The road slope is a cut slope facing south. The height is about 4.4 m, the angle is 47 to 49 °, and the upper part of the slope is flat and used as cultivated land. The surface of the slope was covered with vegetation work to prevent erosion, and a metal net was laid on top of it.

Figure 3 shows a cross-sectional view of the slope failure obtained by surveying. As shown in the figure, the depth of the failure surface (vertical depth) was about 0.20 to 0.25 m. This figure also shows the locations where the soil samples were collected.

Soil test results of collected soil samples

Figure 4 shows a vertical cross section of a non-collapsed area near the slope failure (2.7 m below the slope top). From site observations, it was confirmed that the soil layer from the slope surface to a depth of 0.5 m was slightly weathered sandy soil. The soil samples were collected from this section at intervals of 0.1 m in the vertical direction, and the grain size distribution, soil particle density, and water content were measured. All of the respective soil tests were conducted in accordance with the Japanese Geotechnical Society Standards [3-5].

Figure 5 shows the grain size accumulation curve of soil samples collected from the non-collapsed area.

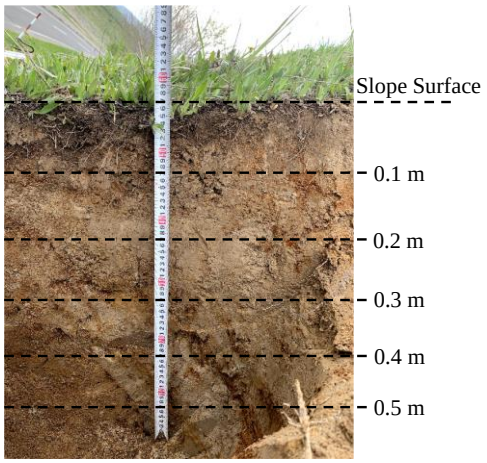

Fig. 4 Vertical cross section of a non-collapsed area near the slope failure

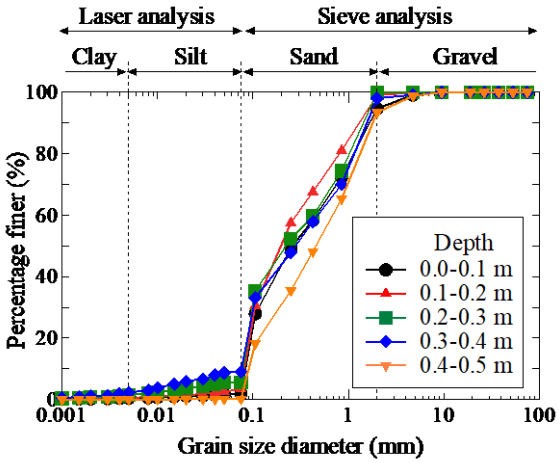

Fig. 5 Grain size accumulation curve

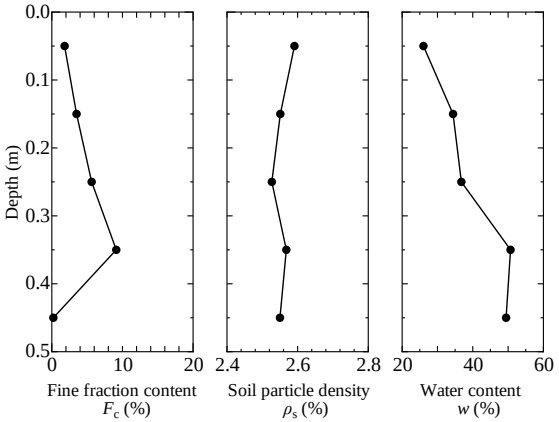

Fig. 6 Fine fraction content F_c, soil particle density ρ_s and water content w at each depth

In this study, the grain size distribution was determined by sieve analysis for grain sizes larger than 0.075 mm and by the laser diffraction method for smaller grain sizes.

Figure 6 shows the fine fraction content F_c, soil particle density ρ_s and water content w at each depth.

Table 1 Experimental conditions for the four cases conducted in this study

	Case 1	Case 2	Case 3	Case 4
Collection depth (m)	0.2	0.2	0.4	0.4
Moisture condition	Unsaturated	Saturated	Unsaturated	Saturated
Normal stresses (kN/m^2)	10, 30, 50	5, 10, 30, 50	15, 30, 50	15, 30, 50

The soil samples from 0.1 to 0.4 m depth contained a small amount of fine-grained material, while soil samples from 0.4 to 0.5 m depth contained no fine-grained material and a small amount of coarse-grained material.

Collection of undisturbed soil samples

The undisturbed soil samples for the constant pressure direct sheer test were collected from the non-collapsed area. An acrylic cylinder with an inner diameter of 60 mm attached to a sharp-edged shoe was used. Soil samples were collected undisturbedly by pressing this cylinder slowly and perpendicularly against the slope surface.

CONSTANT PRESSURE DIRECT SHEAR TEST

Specimens

In this study, the constant pressure direct shear tests were conducted to obtain the strength parameters (cohesion c, internal friction angle ϕ).

Table 1 summarizes the experimental conditions for the four cases conducted in this study. Two types of soil samples were used in the experiments: one was collected from a depth of 0.2 m near the failure surface, and the other was collected from a depth of 0.4 m, deeper than the failure surface. And also, two types of soil moisture conditions were used in the experiments: one was a natural water content state (unsaturated state), and other was a forcibly saturated state.

The specimens were prepared by the following procedure. First, the bottom surface of the undisturbed soil sample in the acrylic cylinder was cut and smoothed. Then, the sample was extruded from the acrylic cylinder using a piston and transferred directly into a shear box with the same inner diameter and a depth of 20 mm. Finally, the top surface of the specimen in the shear box was cut and smoothed. The size of the specimen was 60 mm in diameter and 20 mm in height, which is the Japanese Geotechnical Society Standards [6].

Some of the specimens were forcibly saturated using the following procedure. First, the specimen was placed in an acrylic cylinder, sandwiched between porous plates at the top and bottom, and submerged in a container filled with distilled water. Then, the container was placed in a separate pressure-resistant container and degassed with a vacuum pump. This degassing process took about 96 hours. Finally, the specimen was placed in distilled water for more than a week to increase the saturation.

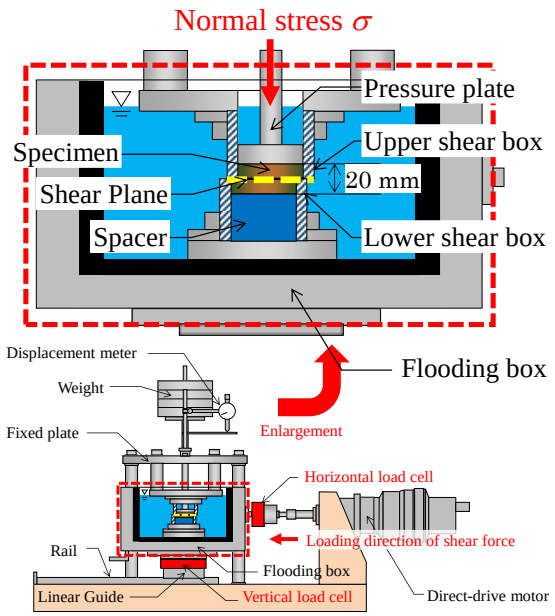

Fig. 7 Schematic diagram of the constant pressure direct shear test apparatus

Test apparatus and test method

Figure 7 shows the schematic diagram of the constant pressure direct shear test apparatus.

In this study, the change in normal stress on the shear plane due to frictional forces on the inner surface of the shear box was monitored by a vertical load cell. During the direct sheer test, the constant pressure was controlled by increasing or decreasing the weight to reflect the change in normal stress.

Table 1 also summarizes the vertical stresses established in the direct shear test. Normal stresses were applied to the specimens from the consolidation process until the end of the direct shear test. Among the specimens collected near the failure surface, the saturated specimens were tested with a small normal stress of 5 kN/m^2 because the change in normal stress due to an increasing friction force was small (Case 2). On the other hand, the minimum normal stress for the specimens collected deeper than the failure surface was 15 kN/m^2 due to the large change in normal stress due to the increase in frictional force (Case 3&4).

Shearing of the specimens was performed at a

Table 2 All direct shear test results conducted in this study

	Case 1			Case 2				Case 3			Case 4		
Normal stress σ (kN/m²)	10	30	50	5	10	30	50	15	30	50	15	30	50
Water content w (%)	30.1	31.6	32.3	64.4	49.4	51.3	44.3	39.0	38.1	36.0	55.9	49.4	50.1
Dry density ρ_d (g/cm³)	1.04	1.03	1.00	1.09	1.18	1.12	1.20	1.07	1.12	1.05	1.08	1.11	1.08
Wet density ρ_t (g/cm³)	1.35	1.35	1.33	1.78	1.76	1.70	1.73	1.49	1.60	1.42	1.68	1.66	1.62
Void ratio e	1.45	1.48	1.55	1.35	1.17	1.27	1.15	1.39	1.22	1.46	1.38	1.31	1.37
Degree of saturation S_r (%)	52.8	54.5	53.3	100.0	100.0	100.0	99.1	71.8	80.2	63.5	100.0	96.9	93.8
Maximum shear stress τ_{max} (kN/m²)	18.3	42.0	66.9	4.4	9.3	26.1	42.4	31.5	39.0	54.0	14.4	29.2	42.7

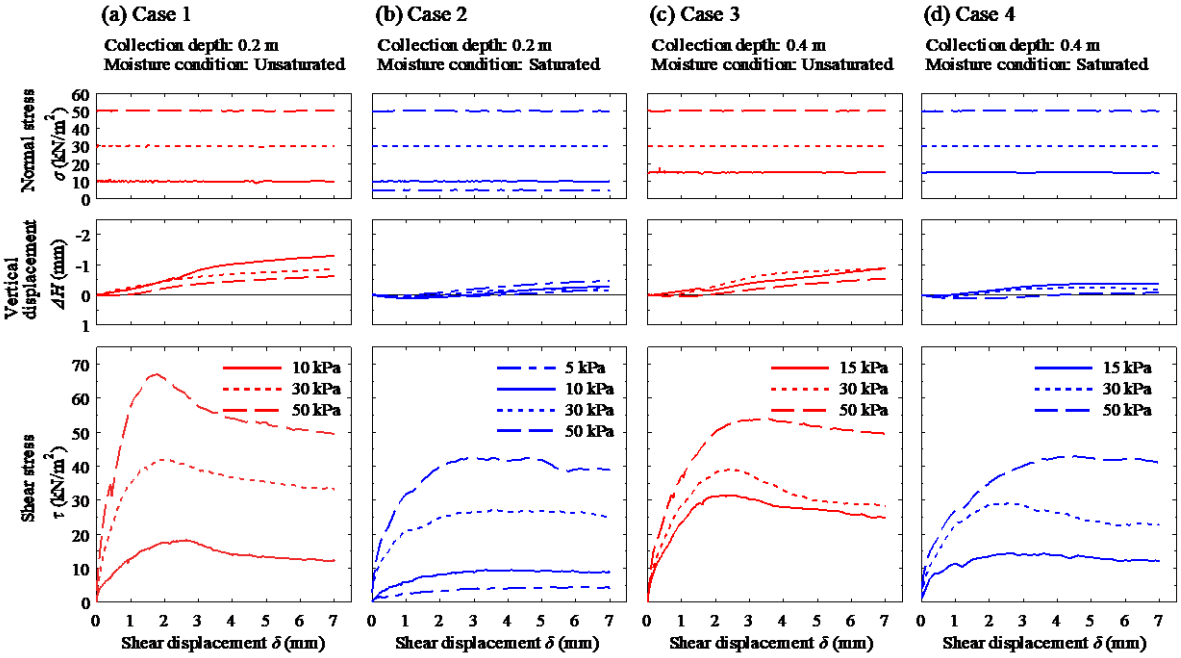

Fig. 8 Comparison of normal stress σ, vertical displacement ΔH and shear stress τ with shear displacement δ for each specimen under constant pressure direct shear test

constant speed by a direct-drive motor installed outside the flooding box. The volume change during the test was measured by a displacement meter attached to the vertical loading axis. The top and bottom shear box spacing was 0.2 mm, the shear displacement rate was 0.02 mm/min, and the maximum horizontal displacement was 7 mm. And the shearing position was set at 10 mm above the bottom of the specimen.

The shearing process was conducted after a consolidation process of about 24 hours. For the saturated specimens, the flooding box was filled with distilled water before consolidation.

Results and discussion of Constant Pressure Direct Shear Test

Table 2 summarizes the all test results conducted in this study.

Figure 8 shows the comparison of normal stress σ, vertical displacement ΔH and shear stress τ with shear displacement δ for each specimen under constant pressure direct shear test. It is confirmed that the normal stress σ during the direct shear test can be

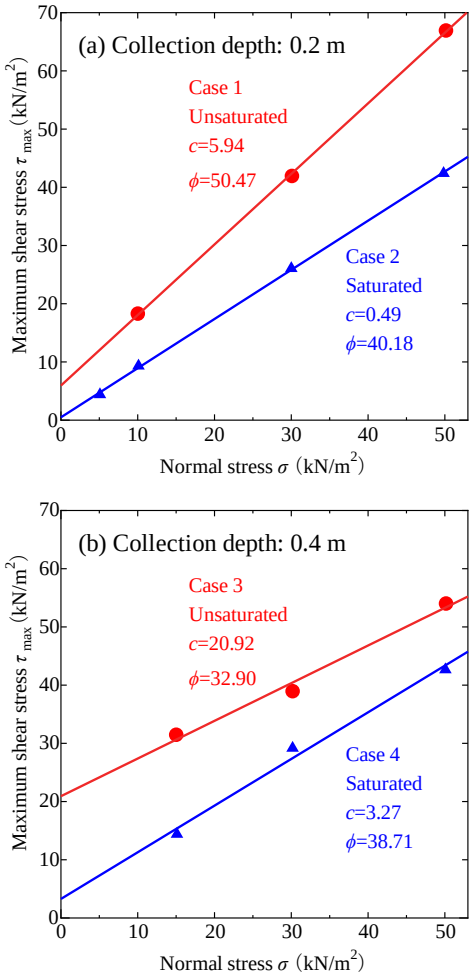

Fig. 9 Relationship between the maximum shear stress τ_{max} and the normal stress σ

controlled to be almost constant in all tests.

The comparison of the shear stresses τ in the unsaturated and saturated states of the specimens collected from near the failure surface (Fig. 8 (a), (b)) shows that the maximum shear stress τ_{max} decreases as the specimens become saturated. This is because the suction decreases and disappears as the specimen becomes saturated. Even for specimens collected from a depth deeper than the failure surface (Fig. 8 (c), (d)), the maximum shear stress τ_{max} decreases as the specimen saturates.

Comparing the shear stress τ in the saturation state of the specimens collected from near the failure surface and those collected from a depth deeper than the failure surface (Fig. 8 (b), (d)), it can be clearly seen that the maximum shear stress τ_{max} of the specimens collected from a depth deeper than the failure surface is higher.

Figure 9 shows the relationship between the maximum shear stress τ_{max} and the normal stress σ at that time for each test shown in Fig. 8. The figures also show cohesion c and the internal friction angle ϕ obtained from each specimen. For the specimens collected from near the failure surface, both cohesion c and the internal friction angle ϕ decrease with increasing saturation (Fig. 9 (a)). On the other hand, for specimens collected from a depth deeper than the failure surface, the internal friction angle ϕ increased slightly with saturation, but cohesion c decreased significantly (Fig. 9 (b)).

Table 3 Input conditions for the stability analysis

Cohesion c (kN/m²)	Case 1	5.94
	Case 2	0.49
	Case 3	20.92
	Case 4	3.27
Internal friction angle ϕ (°)	Case 1	50.47
	Case 2	40.18
	Case 3	32.90
	Case 4	38.71
Unit volume weight in a wet condition γ_t (kN/m³)	Case 1	13.17
	Case 2	16.91
	Case 3	14.72
	Case 4	16.23
Assumed slip surface angle α (°)	All cases	48

SLOPE STABILITY ANALYSIS OF THE INFINITE LENGTH ASSUMPTIONS WITHOUT SEEPAGE

In order to investigate the effect of changes in strength parameters due to snowmelt infiltration on the stability of the slope, stability analysis of the infinite length assumptions without seepage shown in Eq. (1) was conducted using strength parameters obtained from the direct shear tests.

$$F_s = \frac{c}{\gamma_t \cdot z \cdot \sin\alpha\cos\alpha} + \frac{\tan\phi}{\tan\alpha} \quad (1)$$

where F_s is the factor of safety, c is cohesion, ϕ is the internal friction angle, z is the assumed slip surface depth, and γ_t is the unit volume weight in a wet condition, α is the assumed slip surface angle. The infinite length assumptions are widely used to predict the slope failure probability (e.g. Haefeli. [7], Skempton and DeLory. [8]).

Table 3 shows the input conditions for the stability analysis. In this analysis, the average angle of this slope 48 ° was used as the assumed slip surface angle α.

Figure 10 shows the results of the slope stability analysis of the infinite length assumptions without seepage. It can be seen that the factor of safety F_s in the saturated state is clearly lower than that in the

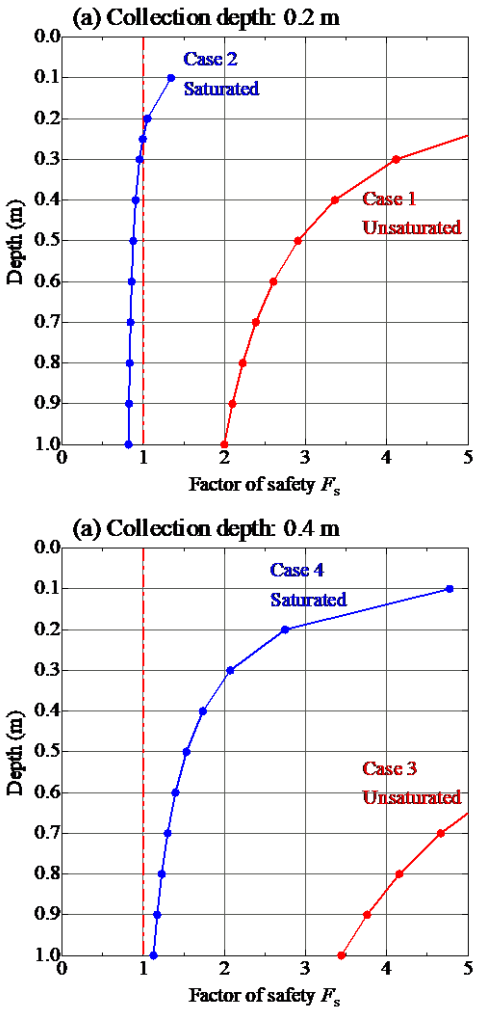

Fig. 10 Results slope stability analysis of the infinite length assumptions without seepage

unsaturated state for both specimens collected from the failure surface and specimens collected from a depth deeper than the failure surface. In particular, for the specimens collected from the failure surface in the saturated state, the factor of safety F_s is below 1 when the depth was deeper than 0.25 m (Fig. 10 (a)). This suggests that the surface layer of the slope was extremely unstable.

It can be understood that the decrease in cohesion c contributes significantly to the decrease in the factor of safety F_s due to the increase in saturation. These results suggest that the main cause of slope failure in this study is the decrease in cohesion c caused by the infiltration of snowmelt.

On the other hand, the factor of safety at a depth of 0.4 m for specimens collected from the failure surface in the saturated state is always greater than 1 (Fig. 10 (b)). This reason could be that the soil deeper than 0.4 m was not subjected to freezing and thawing history during the winter of 2019. Considering the fact that the slope failure occurred during the snowmelt season, the freezing and thawing history is considered to have had a significant influence. In the future, we would like to clarify the effects of frost heaving and other phenomena.

CONCLUSIONS

In this research, we conducted a site investigation of the road slope, and collected undisturbed soil samples from a non-collapsed area near the slope failure to conduct a constant pressure direct shear test. For the direct shear tests, specimens with natural water content at the time of sampling and forcibly saturated specimens were used. The results of the slope stability analysis with the strength parameters obtained from the direct shear test showed that the slope failure was caused by snowmelt penetration, mainly due to a decrease in cohesion.

We will continue to investigate slope failures and conduct soil tests to study the mechanism of slope failures at the extreme surface layer that occur in snowy cold regions.

REFERENCES

[1] Subramanian S. S., Ishikawa T. and Tokoro T. Stability assessment approach for soil slopes in seasonal cold regions, Engineering Geology, Vol. 221, 2017, pp.154-169.
[2] Japan Meteorological Agency, http://www.data.jma.go.jp/obd/stats/etrn/index.php
[3] Japanese Industrial Standards, JIS 1204:2020, Test method for particle size distribution of soils, 2020.
[4] Japanese Industrial Standards, JIS 1202:2020, Test method for density of soil particles, 2020.
[5] Japanese Industrial Standards, JIS 1203:2020, Test method for water content of soils, 2020.
[6] Japanese Geotechnical Society, JGS 0561-2020, Method for consolidated constant pressure direct box shear test on Soils, 2020.
[7] Haefeli R. The stability of slopes acted upon by parallel seepage, in Proc. 2nd Int. Conf. on Soil Mechanics and Foundation Engineering, Vol. 1, 1948, pp.57–62.
[8] Skempton A.W. and DeLory F.A. Stability of natural slopes in London clay. in Proc. 4th Int. Conf. on Soil Mechanics and Foundation Engineering, Vol. 2, 1957, pp. 378–381.

11th Int. Conf. on Geotechnique, Construction Materials & Environment,
Kyoto, Japan, 3-5 November 2021, ISBN: 978-4-909106063 C3051

ANALYTIC CONSIDERATIONS ON TWO-DIMENSIONAL MODELING OF PARTIAL FLOATING SHEET PILE METHOD

Nanase OGAWA[1], Kakuta FUJIWARA[2] and Kentaro NAKAI[3]

[1]GIKEN Ltd., Japan; [2]Department of Civil Engineering, Tokai University, Japan
[3]Civil and Environmental Engineering, Nagoya University, Japan

ABSTRACT

The partial floating sheet pile method is a steel sheet pile method combined of the end bearing sheet pile (long sheet pile) and the floating sheet pile (short sheet pile), which was developed as a countermeasure against land subsidence when constructing embankments on soft ground. The authors conducted a three-dimensional (3D) analysis to evaluate the usefulness of the PFS method during liquefaction and confirmed that it has the effect of decreasing the ground settlement. It has shown the behaviour of the ground movement beneath the floating sheet pile was also visualized in the 3D results. 3D analysis, its use is increasing with the spread of the software, but still more limited than 2D analysis, and it is not easy to carry out analysis. Therefore, 3D analysis and 2D analysis using the same program were performed, and the deformation state of the sheet pile wall was compared. As a result, it was confirmed that the average behavior of the 3D behavior can be grasped by averaging the rigidity of the steel sheet pile over the cross section in 2D analysis.

Keywords: Numerical analysis, Retaining wall, Partial floating sheet-pile method, Liquefaction

INTRODUCTION

The Partial Floating Sheet Pile Method

The steel sheet pile method has been developed as a construction method for temporary structures such as earth retaining walls and temporary coffering walls. But, in recent years, construction methods that are used for both temporary construction and permanent construction have been developed, and their use as permanent construction is increasing. One of them is the Partial Floating Sheet Pile Method (PFS meth-od).

The PFS method is also a stress shut off method, is a steel sheet pile method developed for the purpose of suppressing deformation of the surrounding ground that occurs when constructing an embankment structure on soft ground. Figure 1 shows a construction image of the PFS method. The structure is a combination of a long sheet pile "conventional sheet pile" that is embedded to the support layer and a short sheet pile "floating sheet pile" that is embedded only halfway through the soft ground. It's economical because the number of conventional sheet piles to be embedded up to the support layer is reduced, and the workability is improved that the interlocking length is also decrease by the floating sheet piles are increased.

Technical note for the PFS construction method was published by the PFS method association in 2005 [1], thereafter the number of construction cases is increasing mainly in the Kyushu region. Kasama et al. (2020) has reported that the subsidence of river embankments damaged by the 2016 Kumamoto earthquake, if an embankment does not liquefy, the subsidence due to the earthquake when reinforcement by the PFS method compared to the non-countermeasure embankment has been reduced [2]. Nakai et al. (2021) reported the PFS method using 2D numerical analysis assuming the actual ground, and reported the characteristics of ground deformation and the usefulness of a liquefaction countermeasure method by the PFS method [3, 4]. In Fujiwara (2021) [5], 3D analysis was carried out using the structural cross section constructed by the PFS method, and the behavior of the wall during an earthquake and the behavior of the ground under the floating sheet pile were confirmed.

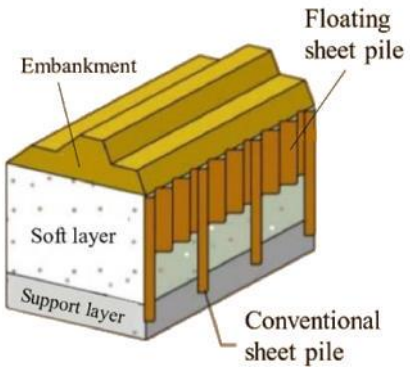

Fig. 1 Model of PFS method.

In this paper, we report the result of examining to reproduce the result of 3D analysis by 2D analysis. Chapter 2 explains the conditions of the analysis model. Chapter 3 shows the results of comparing the

results of 2D and 3D analysis, and Chapter 4 shows the summary of this paper.

NUMERICAL ANALIYSIS MODEL

The program used for the analysis is LIQCA2D17 [1, 6, 7]. Liqca is a numerical code developed based on the effective stress analysis method, and it is possible to determine the process of liquefaction and deformation of the ground due to an earthquake, as well as the dissolution process of excess pore water pressure after vibration. The program is provided in 2D and 3D, and this paper uses the 2D code.

Numerical model for the PFS method

The PFS method has a shape that combines a conventional steel sheet pile and a floating sheet pile. When creating an analytical model, the 3D model can reproduce the steel sheet pile as expected, but the 2D model cannot directly set the change in the length of the sheet pile in the depth direction. In this paper, the PFS method was reproduced by the following method.

Firstly, as a precondition, in order to compare the results of modeling the 3D analysis results under the same conditions, the steel sheet pile model also used a plane strain element and an elastic model. As same as the 3D analysis, the steel sheet pile was made into one steel sheet pile with two elements the embankment side and the free ground side as shown in Figure 2. The values averaged from Eq. (1) was adopted so that the physical property values of the steel sheet pile would be equivalent in the model cross section.

$$E_{sheetpile} I_{sheetpile} = E_{model} I_{model} \quad (1)$$

Steel sheet piles exist continuously in the depth direction up to the bottom of the floating sheet piles and the conventional sheet piles. The physical parameters for these sections were determined to be equivalent to the rigidity of the steel sheet pile in a cross section with a width of 0.2 m and a depth of 1 m. In the cross section from the bottom of the floating sheet pile to the conventional sheet pile, as shown in Figure 3, one element has been a steel sheet pile and the others have composed of the ground. In this paper, the idea of averaging in consideration of the depth direction (y-axis) has used, and the rigidity is reduced as the distance between the columns becomes wider.

The elastic modulus (E_s) of the steel material was 200G Pa. The I_{model} can be obtained from the equation ($BH^3/12$) in the case of the rectangular cross-sectional area, the E_{model} in the model was calculated from the equation 1.

A list of analysis conditions is shown in Table 1.

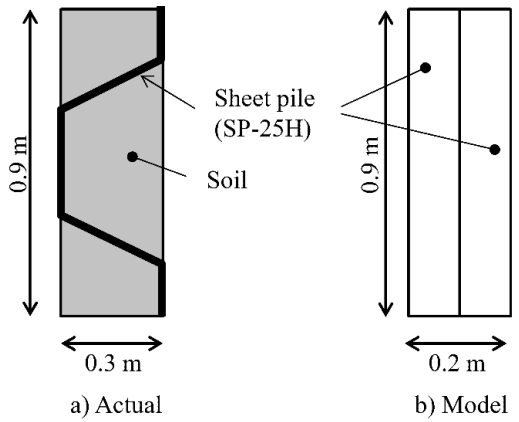

Fig. 2 Concept of cross section area of a sheet pile.

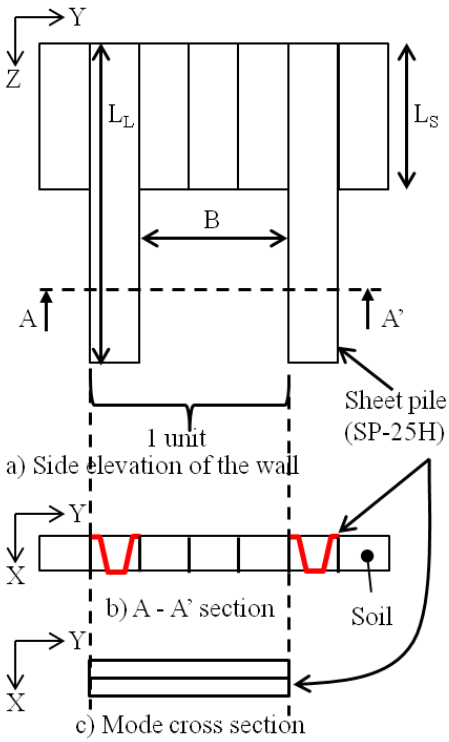

Fig. 3 Concept of cross section area of the PFS Method.

Table 1 Numerical cases.

	Counter-measure	Wall type	Sheet pile		Distance※
			L_L [m]	L_S [m]	B [m]
Case 0	×	—	—	—	—
Case 1	○	Supported	10	—	0
Case 2	○	Floating	—	4	0
Case 3	○	PFS	10	4	1
Case 4	○	PFS	10	4	2.5
Case 5	○	PFS	10	4	5
Case 6	○	PFS	10	4	10

Note: Distance between a long sheet pile and the next long sheet pile.

The length of the short sheet piles of the PFS method is set to 4 m, and which the number of short sheet piles placed between the long sheet piles are changed in 4 cases. In addition, with the conventional wall and without countermeasures are calculated 6 cases in total.

Table 2 Numerical parameters.

Liquefaction layer, D_r = 40%			
Cyclic elastic -plastic model			
Initial void ratio	e_0		0.833
Unit weight of soil	γ_t	kN/m^3	19.2
Satturated unit weight of soil	γ_{sat}	kN/m^3	20.2
Elements depth		m	1.0
Compression index	λ		0.018
Swelling index	κ		0.006
Normalized shear moduls	G_0/σ'_{m0}		873
Effective stress under OCR*		kN/m^3	1.0
Coefficient of earth pressure at rest under ODR*			1.0
Permeability cofficient/ Unit weight of water	k/γ_w	m/s/kN/m^3	2.17E-04
Gravity	g	m/s^2	9.81
Effective stress	σ'_v	kN/m^3	0.0
Coefficient of earth pressure at rest	K_0		1.0
Phase transformaion stress ratio	M^*_m		0.9090
Failure stress ratio	M^*_f		1.1220
Harding parameter	B^*_0		1800
Harding parameter	B^*_1		30
Harding parameter	C_f		0
Bulk modulus of water	K_f	kN/m^2	2.00E+06
Parameter of anisotropy	C_d		2000
Tentative overconsolidation ratio	OCR*		1.0
Dailatancy parameter	D^*_0		2.5
Dailatancy parameter	n		1.5
Reference strain parameter, Plastic	γ^{P*}_r		0.002
Reference strain parameter, Elastic	γ^{E*}_r		0.01
Yield criterion			Von Mises

Joint element			
Shear stiffness modulus	ks	kN/m^2	2.00.E+04
Normal stiffness modulus	kn	kN/m^2	2.00.E+08
Effective stress	σ'_v	kN/m^2	0
Coefficient of earth pressure at rest	K_0		0
Cohesion	c	kN/m^2	0
Friction angle	φ	deg.	0.27
Tension strength	-	kN/m^2	-1.0.E+08
Elements depth		m	1

Non Liquefaction layer, Dr =90%			
R-O model			
Unit weight of soil	γ_t	kN/m^3	18
Satturated unit weight of soil	γ_{sat}	kN/m^3	20
Paisson's ratio	ν		0.33
Effective stress	σ'_v	kN/m^2	50
Coefficient of earth pressure at rest	K_0		0.5
Parameter of shear elastic	a		33665
modulus	b		0.5
Cohesion	c		0.00
Friction angle	φ	deg.	42
R-O parameter	a		0.30
	b		2.30
Initial void ratio	e_0		0.6830
Permeability cofficient/ Unit weight of water	k/γ_w	m/sec/kN/m^3	6.73.E-07
Bulk modulus of water	K_f	kN/m^2	2.00E+06
Elements depth		m	1

Sheet pile			
Elastic model			
Effective stress	σ'_v	kN/m^2	0
Coefficient of earth pressure at rest	K_0		1.0
Permeability cofficient/ Unit weight of water	k/γ_w	m/sec/kN/m^3	0
Gravity	g	m/s^2	9.81
Unit weight of soil	γ_t	kN/m^3	34.8
Satturated unit weight of soil	γ_{sat}	kN/m^3	34.8
Initial void ratio	e_0		0.1
Bulk modulus of water	K_f	kN/m^2	2.00E+06
Elements depth		m	1
Lamé constants	λ		5.34.E+07
Lamé constants	μ		2.75.E+07

Lamé constants		
	λ	μ
case 1	5.3.E+07	2.8.E+07
case 2	5.3.E+07	2.8.E+07
case 3	1.3.E+07	6.9.E+06
case 4	4.4.E+06	2.2.E+06
case 5	1.5.E+06	7.6.E+05
case 6	4.4.E+05	2.3.E+05

※To change for the each cases.

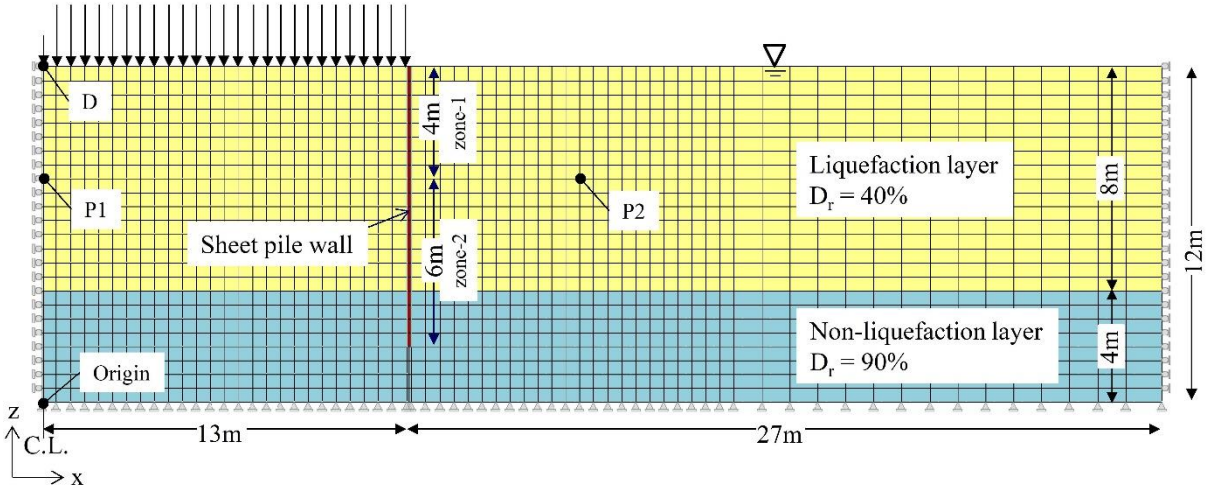

Fig. 4 Analysis cross section.

Soil conditions

The model ground consists of two layers, a liquefied layer with an upper layer of 8 m and a non-liquefied layer with a lower layer of 4 m as shown in Figure 4. The liquefied layer is used the repetitive elastoplastic model with a relative density of 40% of Toyoura sand, and the non-liquefied layer is used an RO model with a relative density of 90% of Toyoura sand. The physical parameters are shown in Table 2. These values were determined with reference to the results of the non-drainage triaxial compression test.

Load conditions

In the half-section model, the assumed embankment load is applied 3 m on the upper side, 13 m on the lower side, and 5 m in height, and the body volume weight is 1.8 kN / m3. In the analytical model, a more simplified and evenly averaged load (q) is applied as the nodal load. The model is a half-section, a load of 1/2q is applied to the central node.

Boundary conditions

The analysis cross section is shown in Figure 4. In the model, the origin (0,0) on the XY plane is set as the center point of the lower end of the half-section model. The nodes (0, Y) are the central surface of the embankment, and are used as the hinge fulcrum in consideration of line symmetry. The nodes (X, 0) are the lower end of the model and are the fixed point, and the nodes (40, Y) are the hinge fulcrum. These three sides are non-drainage boundaries. The water table is at the same depth as the ground surface, and the ground surface is a drainage boundary.

The boundary surface between the steel sheet pile element and the ground element is also a non-drainage boundary. A joint element is provided between the sheet pile element and the ground element in order to consider peeling and slippage.

Input motion

As shown in Figure 5, the wave with a maximum acceleration of 9 m/sec^2 at a frequency of 3 Hz is applied for 10 seconds. In the model ground, such a large load is applied in order to surely liquefy the ground and confirm the behavior of the steel sheet pile when an excessive force is applied.

For the dynamic analysis, the Newmark method is used, the coefficient β (0.3025), γ (0.6), the Reyleigh damping is initial stiffness dependence, and the coefficient is 0.003. The incremental time interval during analysis is 0.001 seconds.

In order to observe the extinction process of the excess pore water pressure generated by the vibration, the acceleration is maintained at 0 for 90 seconds after the vibration is performed for 10 seconds.

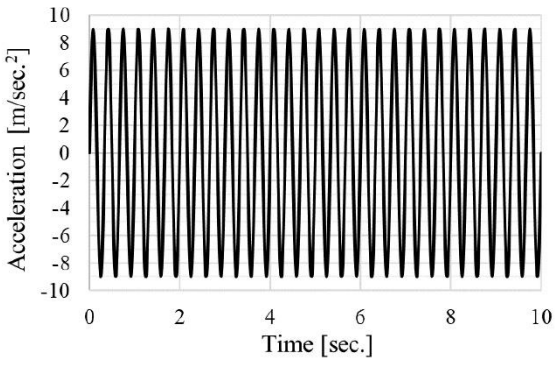

Fig. 5 Input motion.

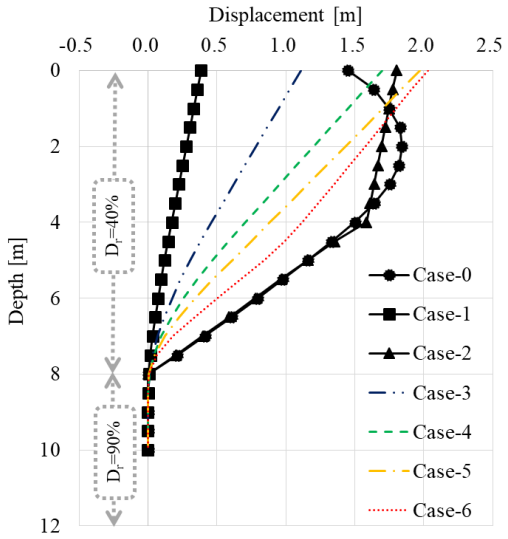

Fig. 6 Horizontal displacement in 2D.

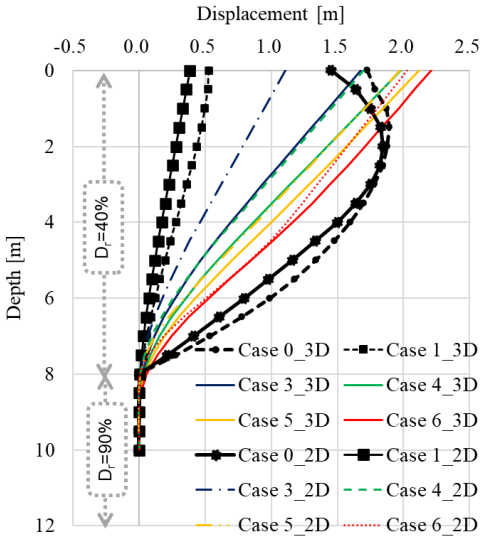

Fig. 7 Comparison of 2D and 3D PFS results.

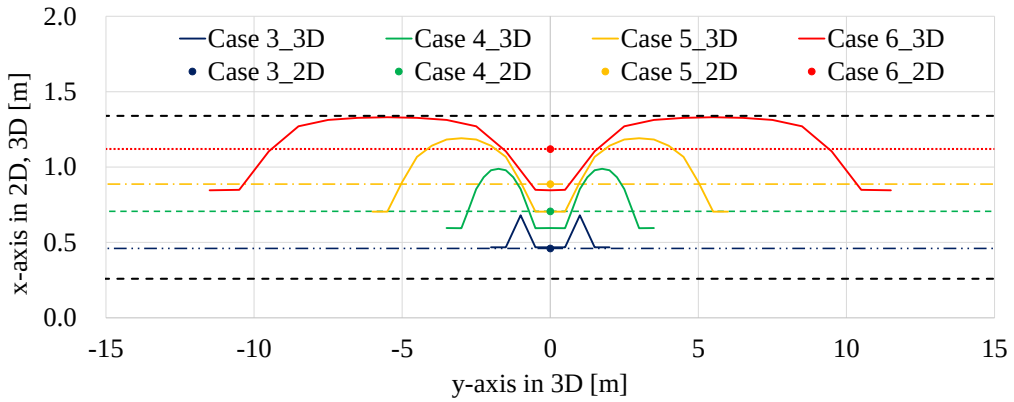

Fig. 8 Comparison of displacement of steel sheet pile on x-y plan at depth of 4m.

ANALYSIS RESULTS

Horizontal displacements

The horizontal displacement of the sheet pile element in each case is shown in Figure 6. In Case 0, where no countermeasure is taken, the maximum displacement occurs near a depth of 2 m. Case1 has consisted only a long sheet pile and has the smallest horizontal displacement. In Case 2 with only a short sheet pile, the displacement of the ground element deeper than 4 m without the sheet pile element is the same, but at shallower then 4m with the sheet pile element, the sheet pile shows rigid deformation, and the maximum horizontal displacement occurs on the ground surface. Cases 3 to 6 are PFS cases as a combination of long and as the distance between the long sheet piles increases, the deformation of Case 2 approaches.

Figure 7 shows the 2D analysis results of Cases 3 to 6 with broken lines and the 3D results with rigid line. It is confirmed that the deformations of Case 0 and Case 1 showed the same tendency, and PFS analysis is performed. The 2D results tended to approach the 3D results as the spacing between the long sheet piles increased. In this method, the deformation deeper than the short sheet pile in Case 6 was the same, but the other cases showed a tendency that the amount of deformation in 2D analysis was small overall.

One of the problems in 2D analysis is that it is not possible to express the slip-through of the ground under the short sheet pile. Figure 8 shows the result of this 2D analysis is superimposed on the deformation diagram [3] of the sheet pile at the bottom of the short sheet piles. At the boundary between the sheet pile and the ground, it is found that the values were equivalent to the average enemy behavior of one unit. Figure 9 shows the relationship between the deformation by 2D analysis on the

vertical axis and the average of the deformation by 3D analysis on the horizontal axis, at a depth of 4m. From the 2D analysis, the result with high correlation of the amount of deformation at the lower end of the short sheet pile was shown.

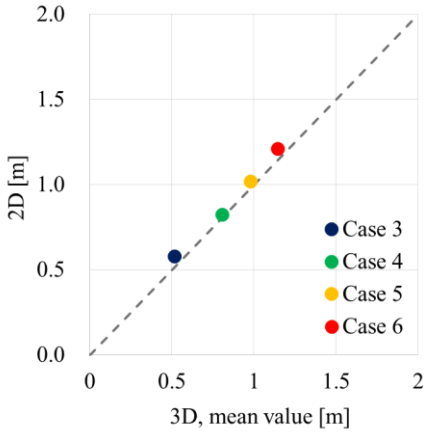

Fig. 9 Horizontal deformation distribution at the bottom of floating sheet pile.

CONCLUTIONS

Aiming at simplification of the design study of the PFS method, which is a wall body that combines a long sheet pile and a short sheet pile, we examined the reproduction by 2D analysis.

It was confirmed that the rigidity of the elements from the depth deeper than the short sheet pile to the lower end of the long sheet pile can be expressed by the method of averaging the rigidity of the sheet pile by the area to grasp the average behavior of the 3D behavior.

In this paper, the influence of the length of the short sheet pile is not considered. We would like to continue to study the effects of the ratio of long sheet piles to short sheet piles, consider the efficient application of the PFS method, and contribute to its widespread use.

ACKNOWLEDGMENTS

This research was supported by the IPA- TC3 (Chair: Prof. Jun Otani); Technical committee on expansion of applicability and assessment of seismic performance of PFS method. Authors express our deep appreciation for their advices and discussion.

REFERENCES

[1] PFS method association, Technical note for the PFS method, 2005, in Japanese.

[2] Kasama K., Yamamoto S., Ohno M., Mori H., Tsukamoto S. and Tanaka J., Seismic damage analysis on the river levees reinforced with steel sheet pile by the 2016 Kumamoto earthquake, Japanese Geotechnical Journal, Vol.15, No.2, 2020, pp395-404.

[3] Nakai, K., Noda, T., Taenaka, S., Ishihara, Y. and Ogawa, N., Seismic assessment of steel sheet pile reinforcement effect on river embankment constructed on a soft clay ground, Proceedings of the First International Conference on Press-in Engineering, 2018, pp.221-226.

[4] Nakai, K., Fujiwara, K. and Ogawa, N., Seismic performance evaluation of PFS method by soil-water coupled finite deformation analysis, Proceedings of 11th International Conference on Geotechnique, Construction Materials and Environment, GEOMATE 2021.

[5] Fujiwara K., Ogawa N. and Nakai K., 3-D Numerical Analysis of Partial Floating Sheet-pile Method as Countermeasure for liquefaction. Journal of JSCE, Vol. 9, 2021, pp.138-147.

[6] Oka F., Yashima A., Shibata T., Kato M and Uzuoka R., FEM-FDM coupled liquefaction analysis of a porous soil using an elasto-plastic model, Applied Scientific Research, Vol.52, 1994, pp.209-245.

[7] Oka F., Yashima A., Tauchi Y. and Yamashita A., A cyclic elasto-plastic constitutive model for sand considering aplastic-strain dependence of the shear modulus, Geotechnique, Vol.49, 1999, pp.661-680.

11th Int. Conf. on Geotechnique, Construction Materials & Environment,
Kyoto, Japan, 3-5 November 2021, ISBN: 978-4-909106063 C3051

USAGE LIMIT OF LUNAR SOIL SIMULANT

Keito Endo[1], Ryoichi Fukagawa[2] and Taizo Kobayashi[2]

[1] Graduate School of Science and Engineering, Ritsumeikan University, Japan;
[2] College of Science and Engineering, Ritsumeikan University, Japan

ABSTRACT

In recent years, lunar exploration has been given higher priority than other space exploration programs. To set up a base on the Moon, various countries have focused on grasping information on the geotechnical characteristics of lunar soil. The Moon surface is covered by lunar soil; it is called the "Lunar Regolith." The Lunar Regolith was brought back from the Moon in the Apollo program. However, soil samples are scarce and thus very precious; therefore, some researchers have developed several types of Lunar Regolith Simulants (RS). We used one of these simulants, FJS-1 [1], in our study, and we found that RS used often in experiments have different physical properties than those of the new RS. In this study, we clarified the following issues. The relationship between RS usage history and self-standing height was investigated by repeatedly compacting unused RS and measuring the change in self-standing height of specimens. In addition, we performed grain-sized analysis and shape measurements of RS to investigate the cause of the decrease in self-standing height. We estimated the apparent cohesion of RS particles using Rankine's earth pressure theory from the test results and proposed a usage limit for RS based on this value.

Keywords: Lunar Regolith Simulant, Apparent cohesion, Screw auger, Excavation, Self-standing height

INTRODUCTION

In recent years, the scope of human activity has expanded beyond Earth to include space. Among them, human interest in the Moon is high, and the possibility of building a lunar base for further research is increasing. As a result, it is becoming increasingly important to understand the mechanical properties of lunar surfaces. In the Fukagawa-Kobayashi laboratory, we developed a method to estimate the soil strength parameters from the excavation response of a screw auger. In this study, we used a lunar RS. We found that the usage history of RS had a significant effect on the reproducibility of the experiment. Figure. 1 shows the borehole formation after screw auger excavation. In the case of the old RS, the holes completely collapsed, but in the case of the new RS, the holes are still clearly visible. We attribute this difference to the scattering of fine particles and the change in particle shape during the process of model ground preparation. In this study, we examine the effect of RS usage history on the properties of RS and propose a usage limit for RS.

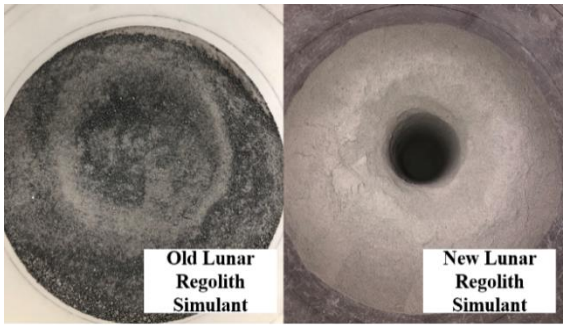

Fig. 1 Borehole formation after screw auger excavation for model RS grounds

LUNAR REGOLITH AND ITS SIMULANT

The lunar surface is covered with a deposit of fine, angular particles called the Lunar Regolith. The Lunar Regolith is formed by the continuous impact of large and small meteoroids and exposure of cosmic rays from the sun and stars [2]. Figure. 2 shows a microscopic photograph of the Lunar Regolith [3]. The Lunar Regolith is loosely deposited on the surface of the Moon, but the relative density rises sharply at a depth of approximately 5 cm. The relative density exceeds 90% at about 30 cm and remains the same at greater depths [4]. Since the Lunar Regolith brought back from the Moon by the Apollo program is rare and valuable, several kinds of RS, a simulated Lunar Regolith, have been developed. In our previous research, we also used RS (FJS-1[1]). Table 1 shows the chemical composition of the Lunar Regolith and its simulant [5], [6]. FJS-1 uses lava basalt as its main material, mixed with pulverized olivine and other materials to match its chemical composition and physical properties such as particle size and density.

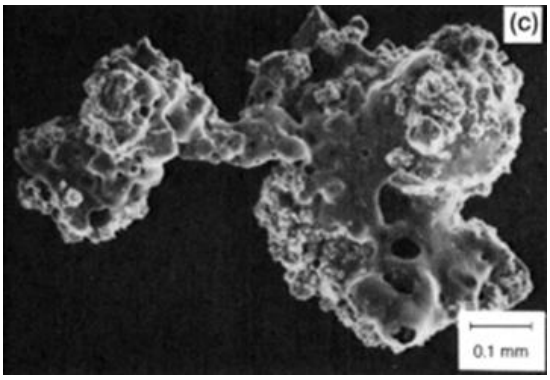

Fig. 2 Microscopic photograph of Lunar Regolith [3]

Table 1 Chemical composition of Lunar Regolith and its simulant[5], [6]

Chemical composition	Apollo 16 sample	Apollo 15 sample	FJS-1
SiO_2 (%)	45	46.8	46.8
TiO_2 (%)	0.54	1.4	1.6
Al_2O_3 (%)	27.3	14.6	17.8
Cr_2O_3 (%)	0.33	0.36	0
Fe_2O_3 (%)	-	-	3.8
FeO (%)	5.1	14.3	8.3
MnO (%)	0.30	0.19	0.3
MgO (%)	5.7	13.0	3.9
CaO (%)	15.7	10.3	11.2
Na_2O (%)	0.46	0.33	3.7
K_2O (%)	0.17	0.19	1.0
P_2O_3 (%)	0.11	0.19	0
Total (%)	99.9	99.4	98.4

COMPARISON OF THE PROPERTIES OF OLD AND NEW RS

In this section, we compare the properties of the old and new RS, as shown in Figure. 1. Although the old RS is a used RS, we can only express it qualitatively because we cannot quantitatively express its usage history. The old RS was repeatedly used for at least one year. To compare the old and new RS, we conducted grain-size analyses and excavation tests.

Grain-size analysis

For the grain-size analysis, we used a Shimadzu SALD-2300 laser diffraction particle size analyzer, as shown in Figure. 3. This analyzer is effective for testing rare and valuable materials such as RS because it can perform grain-sized analysis with a small amount of soil sample. The results of the grain-size analysis are presented in Fig. 4. The old RS lost the fine grain content contained in the new RS. This result indicates that fine particles were scattered gradually during the repeated compaction process.

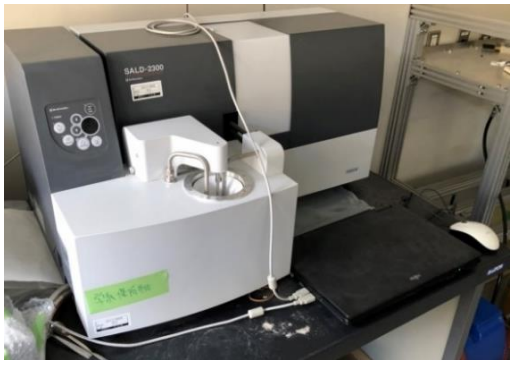

Fig. 3 Laser diffraction particle size analyzer SALD-2300

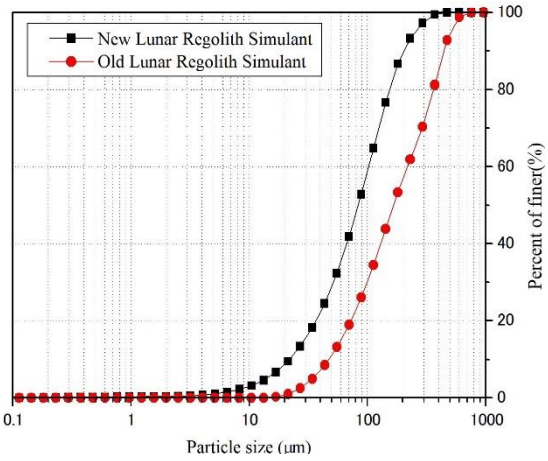

Fig. 4 Results of grain-size analysis for old and new RS

Excavation test

The model ground of the RS created in a circular soil bin was excavated using a screw auger. The excavation test was carried out in a specially controlled manner because we wanted to estimate the strength parameters of soil for every 25 mm depth. A cycle of excavation consists of 25 mm rotary excavation and 5 second rotation without excavation, which is the process of no-axial excavation and rotation. This cycle was repeated for the depth direction. Details of the test can be referred to within reference [7].

Figure. 1 shows the drilled hole after the excavation test. The other excavation conditions are as follows: Digging speed v=4 mm/s, rotational speed ω=0.5 (r/s). The model ground was prepared with 90% relative density to reproduce the lunar ground. The test results are shown in Fig. 5. From the test results, the excavation resistance of the new RS was higher than that of the old RS. This is thought to be due to the apparent cohesion. Apparent cohesion was also considered to have a strong effect on the shape of the borehole.

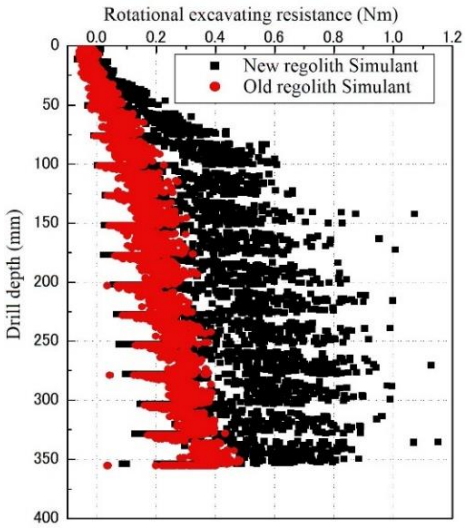

Fig. 5 Excavation resistance during controlled excavation for old and new RS

EXPERIMENTS TO INVESTIGATE THE EFFECT OF USAGE HISTORY ON BEHAVIORS OF RS

Self-standing test

Based on the results of the excavation tests, we hypothesized that the apparent cohesion of the RS would provide an indication of the usage history of the RS. In this section, we present a specimen of RS and compare its self-standing height with the physical properties of RS. Grain-size and particle shape analyses were used to evaluate the physical properties. For the above purposes, we conducted a series of self-standing tests using the two-split mold shown in Figure. 6. Matsushima and Ishikawa (2014) originally proposed the idea of self-standing height [8]. They made the self-standing condition of the specimen by pushing the sample out from the sampling tube upward. They investigated the relationship between the void ratio and self-standing height for new FJS-1 specimens. We believe the method to use the split mold is much better than the method of pushing the sample out from the sampling tube, because the former can avoid the influence of friction between the inner side of the sampling tube and the soil sample.

The mold in Figure 6 is 10 cm high and 5 cm in diameter, and we compact RS in this mold. An overview of the test method is shown in Fig. 7. If the specimen does not collapse at all, it is assumed to be self-standing. If the specimen collapses even slightly, it is assumed to have collapsed. The initial height of the specimen corresponded to the compaction height. If the specimen did not collapse after the mold was removed, the self-standing height was the same as the initial height of the specimen. Fig. 8(a) shows an example of a self-standing case, and Fig. 8(b) shows an example of a collapsing case.

A series of tests were conducted in the following manner. First, we compact the material in the mold at a height of 10 cm using a new RS. The relative density was found to be 90%. After that, we slowly removed the split mold to determine whether the specimen could stand on its own. The specimen was repeatedly made until it did not stand on its own at a compaction height of 10 cm. When it does not stand on its own, the compaction height is decreased by 1 cm, and the process is repeated until the compaction height is 1 cm. The relative density was set at 90% to simulate the lunar ground and to accelerate the degradation rate of the RS. A small amount of soil sample was taken at each self-standing height for grain-size analysis and particle shape measurement.

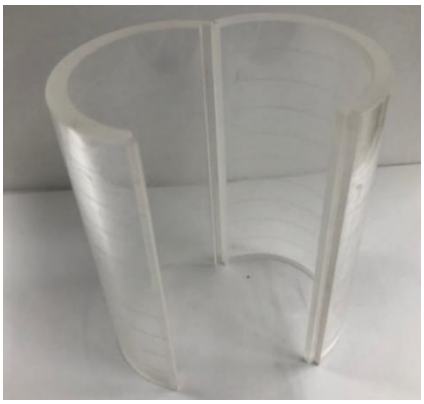

Fig. 6 Split mold for estimating self-standing height of RS specimens

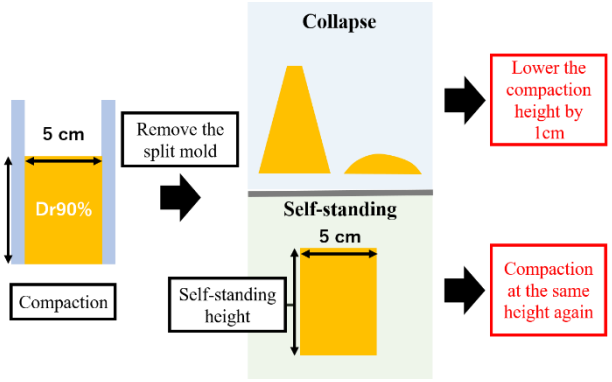

Fig. 7 Procedures of tests for definition of self-standing height

(a) Self-standing case (b) Collapsing case

Fig. 8 Definition of self-standing and collapsing conditions

Grain-size analysis

The results of the grain-size analysis are shown in Figure. 9. Some results on the self-standing height have been omitted from this figure for clarity. In addition, Fig. 10 shows the amount (%) of particles less than 10 μm that pass through. As the self-standing height decreased, the fine grain content in the RS decreased.

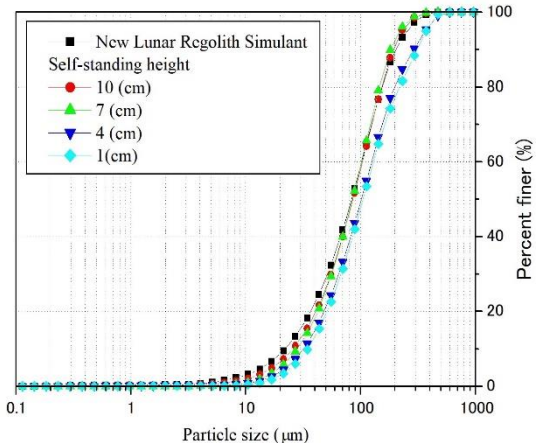

Fig. 9 Results of grain-size analysis

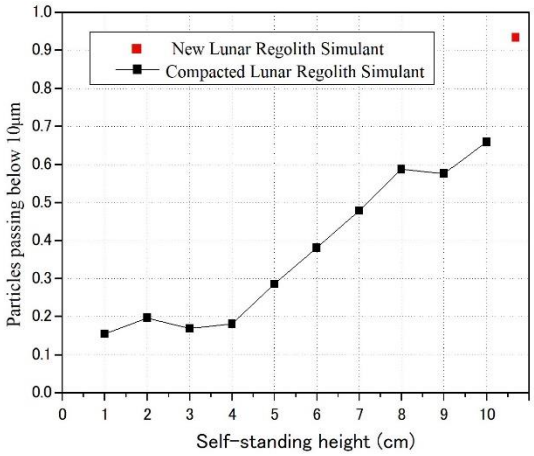

Fig.10 Relationship between Particles passing below 10μm and self-standing height

Particle shape measurement

Coefficient of form unevenness

To investigate the change in particle shape due to compaction, we measured the coefficient of form unevenness [9] and maximum length at each self-standing height. Magnified photographs were taken and measured using ImageJ software [10]. The enlarged photograph used in the analysis is shown in Figure. 11. Equation (1) shows the definition for the coefficient of form unevenness (*FU*) [8].

$$FU = \frac{4\pi A}{l^2} \qquad (1)$$

FU is calculated from area *A* and perimeter *l* ; using *FU*, the particle shape can be expressed as 0–1. The closer *FU* is to 1, the more the particle is a perfect **c**ircle, and the more uneven it is, the smaller the value. The smaller the particle, the less useful the value is; thus, *FU* was obtained by omitting particles with an area of less than 20 μm^2. The relationship between the number of samples and the average value of the coefficient of *FU* is shown in Fig. 12. It can be seen from this figure that the analysis based on more than approximately 100 samples gives a steady estimation result, so that the number of samples in this analysis is selected as 150 at each height. Fig. 13 shows the relationship between the mean and standard deviation of the coefficient from unevenness and each self-standing height. Both data fall within the small range, and there is almost no relationship with the self-standing height. This means that the coefficient of *FU* does not change significantly with repeated compaction.

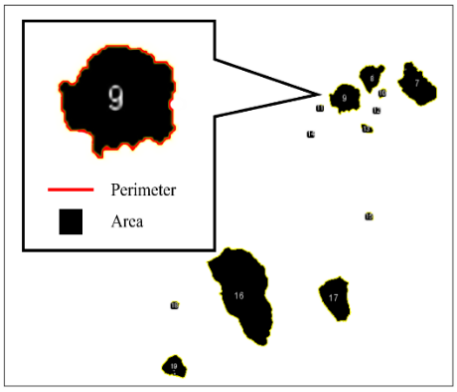

Fig. 11 Enlarged photo of RS

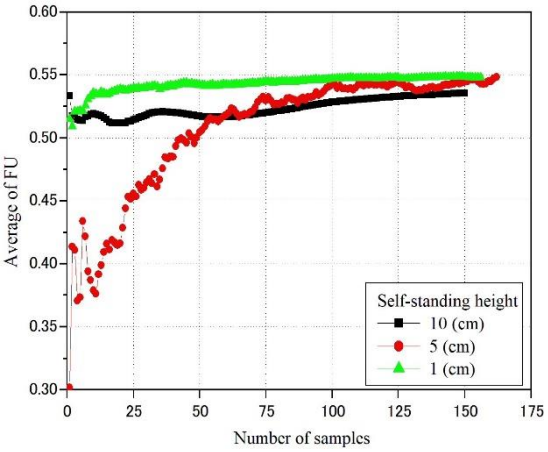

Fig. 12 Effect of sample numbers on coefficient of form unevenness

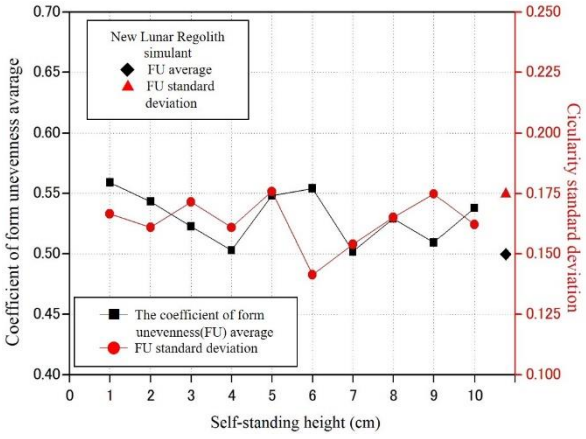

Fig. 13 Average and standard deviation of the coefficient form unevenness

Maximum length

Next, the maximum length was considered. The maximum length is the value of the longest side length of the rectangle circumscribed to each particle (see Figure. 14). The relationship between maximum length and self-standing height is shown in Fig. 15. This graph shows that the maximum length tends to decrease as the self-standing height decreases, except for the 10 cm self-standing height. This means that it is possible that repeated compaction results in the failure of soil particles.

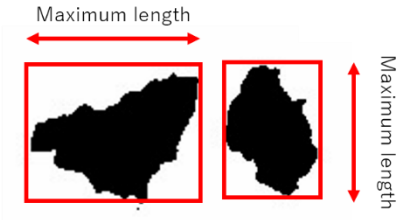

Fig. 14 Definition of maximum length of particle

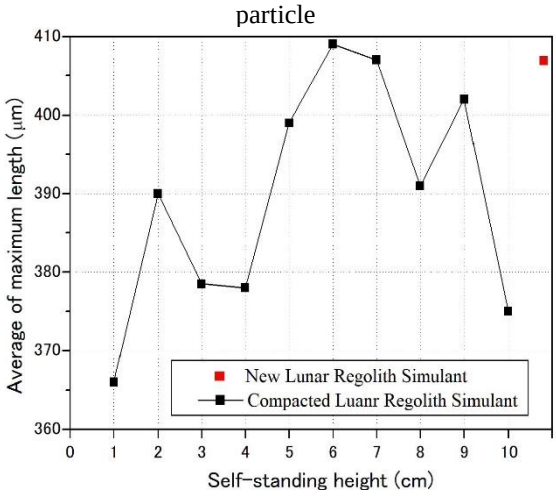

Fig. 15 Relationship between maximum length and self-standing height

RELATIONSHIP BETWEEN USAGE HISTORY OF RS AND SELF-STANDING HEIGHT

From the above test results, we can recognize the relationship between the self-standing height and the physical properties of RS. However, the influence of usage history on the self-standing height of RS has not yet been clarified. In this section, a series of tests using the two-split mold were performed again to investigate the relationship between the self-standing height and usage history. The number of times the specimen was made was used as an indicator of the usage history, and the relationship between the self-standing height and the number of times for making the specimen is shown in Figure. 16. As the number of times specimen-making increased, the self-standing height decreased almost linearly. This may be due to the poor interlocking of particles due to the scattering of fine particles caused by the compaction of RS, as shown in Figure 10.

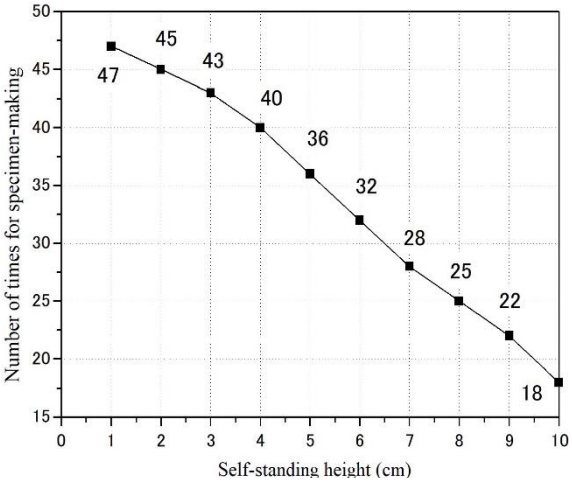

Fig. 16 Relationship between number of times for specimen-making and self-standing height

DISCUSSION

Causes of degradation of RS

As shown in Figures 1 and 5, the change in the mechanical properties of RS due to usage history has a significant effect on the reproducibility of the experiments. Let us consider the elements that cause the degradation of RS in this section.

As shown in Fig. 10, the fine grain content of RS decreased as the specimen was repeatedly formed by compaction. Dry and fine particles easily flew away during this compaction process. In addition, Figs 13 and 15 show that the coefficient of FU does not change significantly, and the particle size decreases with the progress of the degradation of RS.

Considering these results, the degradation of RS is mainly caused by the decrease in the fine grain content. The degradation of RS results in a decrease in self-standing height. The self-standing height is closely related to the apparent cohesion, "c." Therefore, let us consider the relationship between self-standing height and apparent cohesion of RS.

Estimation of the apparent cohesion of RS

The apparent cohesion of the RS can be estimated using Rankine's earth pressure theory. According to this theory, soil materials having "c" have self-standing height z_c expressed by Eq (2).

$$z_c = \frac{4c}{\gamma_t} \tan\left(45° + \frac{\phi}{2}\right) \qquad (2)$$

where c is the apparent cohesion, γ_t is the unit weight of the soil sample, and ϕ is the internal friction angle. The apparent cohesion, "c," can be obtained by substituting γ_t = 1.99 (gf/cm³), ϕ = 31.7 (deg) [11], and each self-standing height value z_c into Eq (2). The estimation results are presented in Figure. 17.

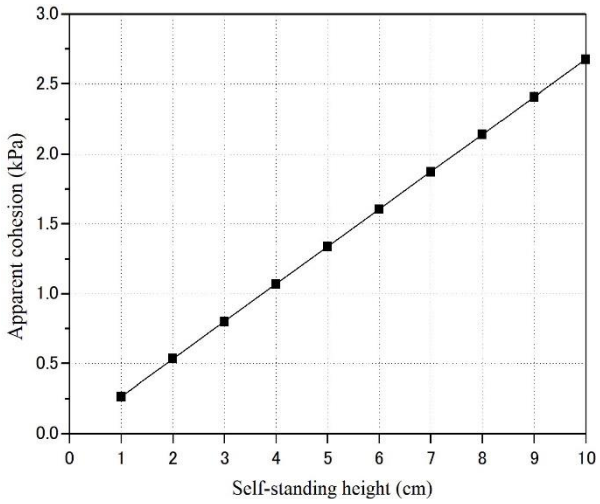

Fig. 17 Relationship between apparent cohesion and self-standing height

Proposal of the usage limit of RS

We compare the apparent cohesion of the Lunar Regolith brought back by past Apollo missions to suggest the usage limit of RS. The cohesion of the Lunar Regolith is expected to be 0.1-1 (kPa) [12]. Using this intermediate value as a reference, the apparent cohesion that RS should have is 0.55 (kPa).

From Figure. 17, the corresponding self-standing height against c=0.55 (kPa) is approximately 3 cm; however, we must consider the difference in gravity between the Earth and the Moon. If the gravity is one-sixth, z_c on the Moon surface becomes 6 times 2 cm, which is 12 cm. The number of times the specimen was made corresponding to the value of 12 cm was estimated by extrapolation to 10-12 cm, as shown in Fig. 16. Although we must consider the difference in the compaction process in self-standing tests and in other tests using model ground, we think that a self-standing height of 12 cm is an effective sign for the usage limit of RS.

CONCLUSIONS

In this study, we examined the effect of RS use history on the properties of RS and proposed a usage limit for RS. The main conclusions are as follows:

(1) First, we compared the grain-size analysis and excavation resistance of the RS with varying use histories. The results showed that the RS used had fewer fine grains and less excavation resistance than the new RS.

(2) To obtain quantitative data on use history, self-standing tests were conducted. As a result of the grain size analysis and particle shape measurement for each self-standing height, it was found that as the compaction was performed many times, the fine particles scattered and the particles became smaller while maintaining a certain shape, and the self-standing height (apparent cohesion) of RS decreased because of the poor interlocking of particles.

(3) To investigate the relationship between the self-supporting height and the number of times the specimen was made of, self-standing tests were conducted again. Consequently, a linear relationship was found between the two.

(4) From the results of the self-standing tests, we derived the apparent cohesion of the RS. The s y apparent cohesion of RS was compared with that of the Lunar Regolith, assuming a lunar surface, and we confirmed that RS can be used as a sample up to a self-standing height of 12 cm.

REFERENCES

[1] Kanamori, G., Udagawa, S., Yoshida, T., Matsumoto, S., and Takagi, K.: Properties of Lunar Soil Simulant Manufactured in Japan, Proc. of 6th Int. Conf. on Eng. Construction and Operations in Space, ASCE, pp. 462-468, 1998.

[2] Heiken. G. H., Vaniman. G. H. and French. B. M.: Lunar Sourcebook, A User's Guide to the Moon, New York, Cambridge University Press, p. 285, 1991.

[3] Heiken, G. H., et al.: op. cit., p. 297, 1991.

[4] Heiken, G. H., et al.: op. cit., p. 499, 1991.

[5] Heiken, G. H., et al.: op. cit., p. 349, 1991.

[6] Kanamori, G. and Shinoda, Y.: Basic Research on the Production of Construction Materials from Lunar Resources, Proc. 34th ISAS Space Energy Symposium, 6th March, 2015.

[7] Kurihara, K. and Fukagawa, R.: A Study on Estimation of Mechanical Properties of Soil Using Construction Information during Excavation by Screw Auger, p. 90, 2018.

[8] Matsushima, T. and Ishikawa, T.: Particle Grading Effect on Mechanical Properties of Lunar Soil Simulant FJS1, Proc. Earth & Space 2014, ASCE, pp. 60-68, 2014.

[9] Yoshimura, Y. and Ogawa, S.: A Simple Quantification Method of Grain Shape of Granular Materials Such as Sand, JSCE , pp. 95-103, 1993.

[10] Rasband, W.S., ImageJ, U. S. National Institutes of Health, Bethesda, Maryland, USA, http://rsb.info.nih.gov/ij/, 1997-2012.

[11] Kurihara, K. and Fukagawa, R.: op. cit., p.88, 2018.

[12] Heiken, G. H., et al.: op. cit., p. 506, 1991.

11th Int. Conf. on Geotechnique, Construction Materials & Environment,
Kyoto, Japan, 3-5 November 2021, ISBN: 978-4-909106063 C3051

MONITORING DEFORMATION WITH WIRELESS SENSOR NETWORK AND EVALUATION OF MECHANICAL STABILITY BY FDM SIMULATION FOR SLOPE

Satoshi Sugimoto[1] and Yoichi Ishizuka[1]

[1]Faculty of Engineering, Nagasaki University, Japan

ABSTRACT

In recent years, torrential rains have occurred frequently due to abnormal weather and the rainy season, and many slope failures have occurred accordingly. When it rains, the infiltration of rainwater and the inflow of groundwater from the upstream may reduce the shear resistance in the slope and the infiltration water pressure may lead to slope failure. In addition, the change in groundwater is large on the natural slopes, and the amount of groundwater inflow from the upstream increases, which may lead to slope failure. The purpose of this study is to reproduce and stabilize the groundwater level rise on the target slope by numerical analysis, and to consider the effect of the hydraulic conductivity on the groundwater level rise and the safety factor. And we proposed the method of observing the penetration of groundwater due to rainfall and the change of the groundwater depth using a wireless sensor network for sedimentation grounds Through the observation, we clarified the progress of the slope deformation and correlations between the rainfall, fluctuation of groundwater depth and the slope deformation.

Keywords: Wireless sensor network, Monitoring, Slope, FDM

INTRODUCTION

In recent years, due to the tight financial cost of local administration in Japan, there has been a need for unmanned management of local social infrastructure facilities. On the other hand, even with the recent development of infrastructure, many slope failures and landslide accidents caused by earthquakes and heavy rains have occurred in various regions. As a countermeasure against such slope disasters, it is thought to be effective to constantly monitor the signs of the disaster before it occurs in the predicted disaster area, and to implement countermeasures such as prioritizing high-risk areas for construction. However, most of the monitoring systems in use have been wired information collection systems, which are difficult to install in undeveloped areas such as slopes. In addition, high-precision and expensive sensors are often used for measurement, which limits the number of measurement points due to the cost of the system and the difficulty of installation. In addition, the difficulty of securing a power source to operate the system for a long period has been a major obstacle to monitoring in undeveloped areas such as slopes. As a result, the limitation of the amount of acquired measurement data and the localization of measurement locations have become problems for the data that are effective in determining the priority of proactive measures as described earlier.

In this study, slope deformation and changes in groundwater depth due to rainfall were observed using a wireless sensor network developed in previous studies [1]-[3] on an artificially reclaimed slope in Sasebo City, Nagasaki Prefecture, Japan. The purpose of this study is to quantitatively clarify the progression of slope deformation through continuous data collection and analysis and to clarify the correlation between rainfall, changes in groundwater depth, and the amount of ground deformation.

MEASUREMENT BY REMOTE MONITORING SYSTEM

Outline of Target Slope

The target slope shown in Fig. 1 is a former stable industrial waste disposal site located in Sasebo City, and consists of sediment-dominated industrial waste layers, talus deposit layers, and bedrock, in order from near the ground surface. Heavy rains in 2013 caused deformations from the middle to the lower part of the slope. In addition, a large-scale crack

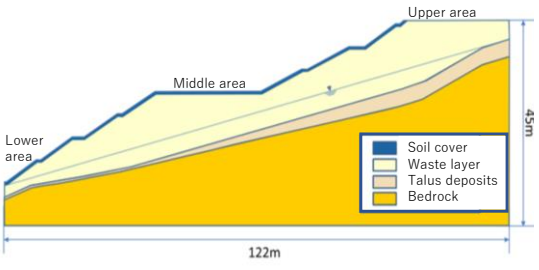

Fig. 1 Geological cross-section chart.

occurred near the middle section. As a result, the slope has been gently graded by cutting back the soil and intercepted by covering the surface layer with 0.5 m of soil. The current slope profile has a maximum slope gradient of about 35 degrees and a height of about 40m.

Overview of The Monitoring System

Figure 2 shows the various monitoring instruments and their installation locations. The structure of this monitoring system is as follows [4], [5]. (1) observation data is acquired by using observation devices such as a water level meter, rain gauges and tiltmeters, (2) data is collected by routers and a coordinator in the field through a wireless sensor network (hereinafter referred to as WSN), and (3) data is transmitted to the server through a mobile communication network. The monitoring can be carried out remotely, which enables to ensure the safety of the target slope and to analyze the current status in real-time by analyzing the sensing data. The water level meter used is measuring at a depth of about 10 meters from the ground surface. The water depth can be measured at a minimum depth of 0.01m and a maximum depth of about 20m. In addition, tiltmeters for detecting slope deformation are installed at 0.5 m below the ground surface at 13 locations (k-1 to k-13) on the target slope. The tiltmeter has a measurement range of -30 degree to +30 degree with a resolution of 0.02 degree.

Monitoring of Slope Surface Deformation by WSN

From the data of June 13, 2017, to January 31, 2021, the result of k-12 shown in Fig. 2, which has an especially large amount of deformation, was taken and analyzed during the period. Figure 3 shows the cumulative angle. Figure 4 shows the cumulative angle for each month. In the case of k-12, a large amount of deformation was observed in 2018 and 2020, and the amount of deformation increased over the years, indicating that the deformation in the direction perpendicular to the slope was large. The cumulative amount of deformation is represented by two-dimensional vectors for k-1 to k-13, and the visualization of the slope movement is shown in Fig. 5. From this figure, the relative size of the

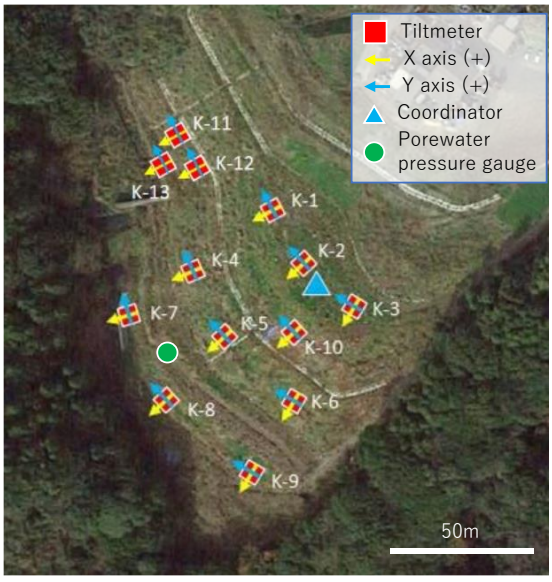

Fig. 2 Layout of installed instruments.

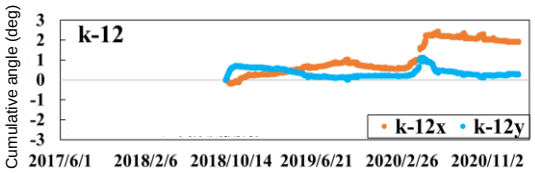

Fig. 3 Change in cumulative angle over time.

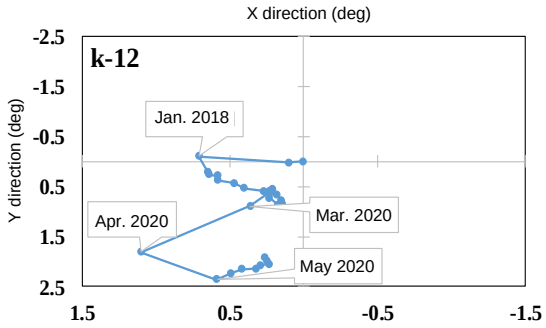

Fig. 4 Trajectory of cumulative angle by month.

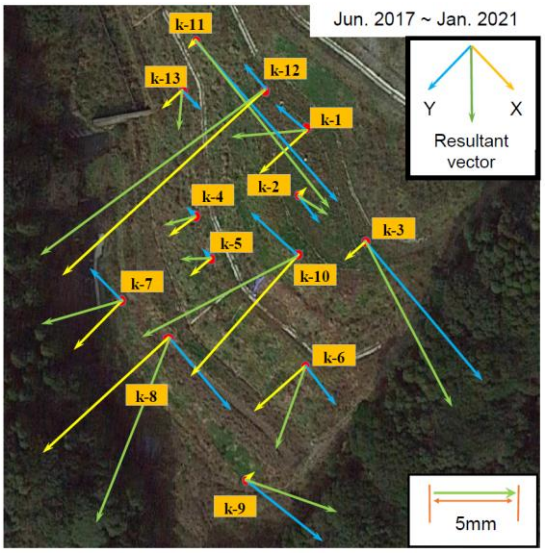

Fig. 5 Deformation vector estimated from measurement data.

deformation can be confirmed. It is considered that the downward deformation of the slope is linked to the mid-slope deformation. On the other hand, it is also possible that the lower part of the slope appears to be stationary due to the parallel movement of the slope, while the lower part is moving. A large amount of deformation in k-11 and k-12 can be explained by the fact that they are located near the slope where the failure is actually in progress. From these results, it is considered that the local deformation trend of the slope can be captured in a plane.

Variation of Groundwater Depth with Rainfall

The relationship between rainfall and groundwater depth was analyzed using the data from 2017 to 2020 for a water level meter installed at the lower part of the slope shown in Fig. 2. Figure 6 shows the relationship between rainfall and groundwater depth in 2020. Each color band in this figure means the period during which the increase and decrease of the groundwater depth due to one rainfall was confirmed. Figure 7 shows the relationship between rainfall and groundwater depth, and also shows the period from 2017 to 2020. The groundwater depth did not decrease every year, but it can be regarded as an overall decreasing trend during the four years from 2017 to 2020. This may indicate that the permeability of the layer where groundwater flows is increasing. It is also possible that some of the rainfall does not infiltrate into the ground but flows out to the surface. The relationship between the rainfall coefficient Cr [6] and the groundwater depth from the ground surface before rainfall is shown in Fig. 8. Cr is a parameter defined by Sugiyama et al. This is the percentage of the value obtained by dividing the amount of rainfall in a certain period by the amount of change in the groundwater depth. Figure 8 shows the results of the analysis of the relationship between Cr and the groundwater depth before rainfall. The rainfall coefficient Cr is the ratio of the amount of rainfall to the increase in the groundwater depth after the rainfall. In the descending curve, the higher the groundwater depth from the ground surface before rainfall, the smaller the rise in groundwater depth. In the rising curve, the rise in groundwater depth was small despite a large amount of rainfall. This may be since rainfall occurred before the water depth dropped to a steady state in response to the preceding rainfall, which may have affected the change in the rising water depth. It is expected that the correlation between rainfall and groundwater depth changes will be clarified by accumulating more data.

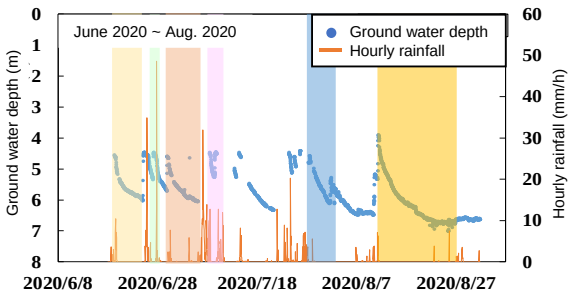

Fig. 6 Relationship between groundwater depth and rainfall.

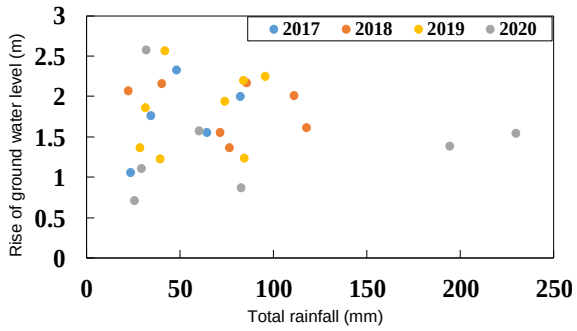

Fig. 7 Relationship between rainfall and water level rise.

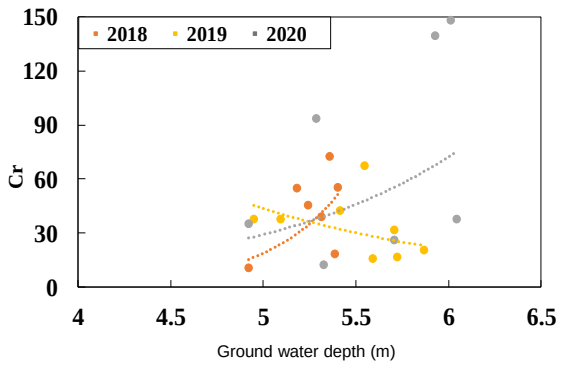

Fig. 8 Relationship between groundwater depth before rainfall and rainfall coefficient.

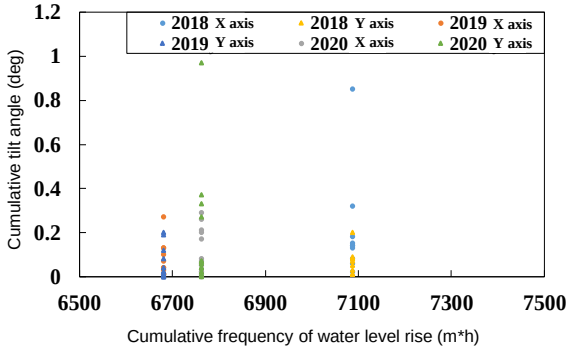

Fig. 9 Relationship between cumulative degree of water level rise and slope angle.

Relationship between Groundwater Depth Change and Slope Deformation

The relationship between the groundwater depth and the amount of slope deformation is shown in Fig. 9 which shows the cumulative frequency of water level rise and the inclination angles of x and y axes from June to August in the above period. The cumulative frequency of water level rise (m*h) is the frequency of water level rise by accumulating the groundwater depth from the basement rock for a certain period. The results show that the x-axis deformation was large in 2018 in the direction perpendicular to the slope, while the y-axis deformation was large in 2020. This indicates the tendency that the direction of easy movement differs from year to year. In addition, it was confirmed that the amount of deformation was excessive even if the value of the cumulative frequency of water level rise was relatively small.

EVALUATION OF SLOPE STABILITY BY NUMERICAL SIMULATION

The finite difference method and the finite element method are typical numerical analysis methods that consider the target ground as a continuum. The Finite Difference Method (FDM) is more advantageous than the Finite Element Method in performing stress-deformation calculations at each time increment based on explicit formulations because the constitutive laws are easier to formulate [7]-[9]. In this study, we used FLAC [10], a large-deformation finite-difference analysis code based on the explicit method developed by P.A. Cundall et al. FLAC has the capability of performing seepage analysis for porous media and can be used independently of stress-deformation analysis. FLAC can also perform coupled stress-osmosis flow analysis. A two-dimensional slope model was developed to perform elasto-plastic FDM analysis focusing on the conditions of slope deformation, rainfall and groundwater depth. Slope stability analyses based on the shear strength reduction method [7] were conducted under different conditions for the constituent geological features of the slope. The simulation flow can be divided into four major parts: (1) creation of the slope model and setting of physical properties, (2) reproduction of the steady-state of groundwater flow, (3) reproduction of rainfall and groundwater flow, and (4) determination of slope failure by gravity analysis.

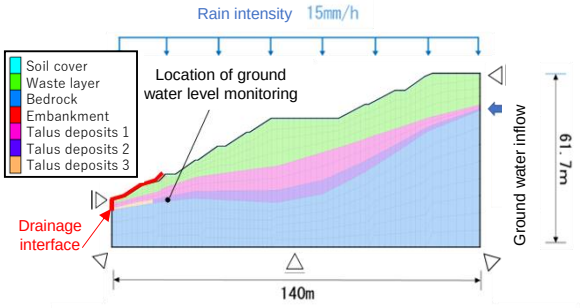

Fig. 10 Cross-section of the analysis model.

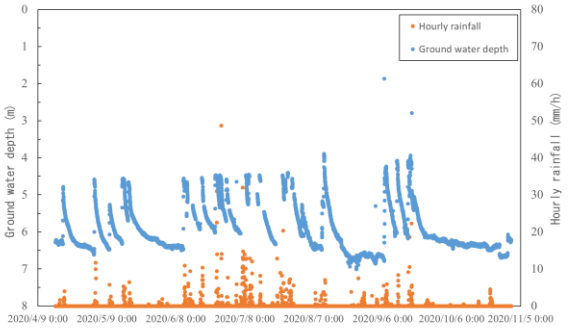

Fig. 11 Observation data of rainfall and groundwater depth.

Table 1 Physical properties.

Layer type	Dry density	Shear resistance angle	Cohiesion	Poisson's ratio	Deformation modulus	Coefficient of permeability		
						Case1	Case2	Case3
	ρ_d (kg/m^3)	ϕ (deg)	c (kN/m^2)	ν(-)	E(MN/m^2)	k (m/s)		
Bedrock	2300	-	-	0.15	1000	5.0×10^{-7}	5.0×10^{-7}	5.0×10^{-7}
Talus deposits 1	1700	35	0	0.3	300	5.0×10^{-5}	5.0×10^{-5}	5.0×10^{-5}
Talus deposits 2	1700	35	0	0.3	300	5.0×10^{-5}	2.5×10^{-2}	2.5×10^{-2}
Talus deposits 3	1700	35	0	0.3	300	5.0×10^{-5}	2.5×10^{-2}	1.0×10^{-2}
Waste layer	1400	37	8	0.3	200	3.0×10^{-5}	3.0×10^{-5}	3.0×10^{-5}
Soil cover	1400	15	10	0.3	200	5.0×10^{-7}	5.0×10^{-7}	5.0×10^{-7}
Embankment	2300	-	-	0.15	300	3.0×10^{-5}	3.0×10^{-5}	3.0×10^{-5}

Outline of The Slope Model

To reproduce the slope of interest, a numerical model with the same dimensions of 140 m in depth and 61.7 m in height (Fig. 10) was created. The physical properties used in the analysis were set based on previous studies [11], [12], as shown in Table 1. Figure 11 shows the groundwater depth and rainfall observed in the field shown in the previous section. It can be seen that the groundwater depth on the target slope rises by about 1 to 3 meters during a few tens of millimeters of rainfall down the slope. In addition, the groundwater depth fluctuates immediately after rainfall, indicating a sensitive response. To reproduce this situation, the following three analyses were conducted: Case 1: analysis of input conditions based on past geotechnical investigations, Case 2: analysis assuming that groundwater flowed more easily in the cliff cone sediment layer around the base surface, and Case 3: analysis assuming that permeability at the end of the slope became worse in addition to Case 2. The effect of the permeability of the cliff cone sediment layer on the groundwater level rise and the safety factor was examined.

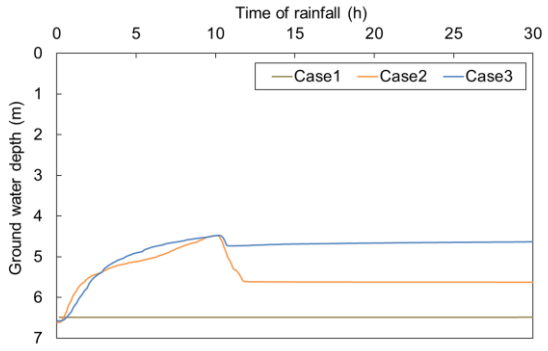

Fig. 12 Relationship between rainfall duration and groundwater depth.

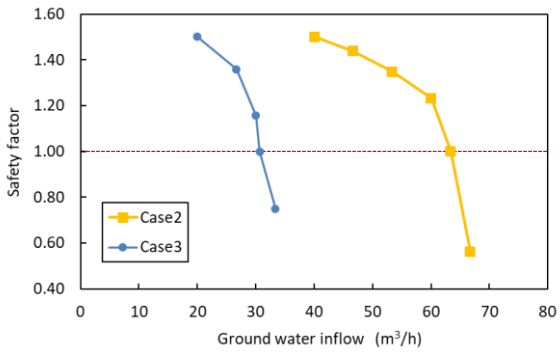

Fig. 13 Relationship between groundwater inflow and slope safety factor.

Reproduction of Steady Groundwater Flow and Rainfall

Groundwater flow was applied from the high side of the slope to simulate a steady groundwater surface. Then, rainfall intensity of 15 mm/h and total rainfall of 150 mm were applied from the slope surface to reproduce the slope with rainfall. The groundwater inflow from the high side of the slope was also increased with rainfall. Figure 12 shows the relationship between rainfall and groundwater depth. Comparison with Fig. 11 shows that the amount of groundwater level rise and the groundwater level rises immediately after rainfall was reproduced in cases 2 and 3.

Evaluation of Slope Stability by Gravity Analysis

In this study, the overall safety factor was calculated using the shear strength reduction method. The effect of the increase in groundwater inflow from the high side of the slope on the safety factor was also confirmed. Figure 13 shows that a slight decrease in the hydraulic conductivity at the end of the slope significantly reduces the amount of groundwater inflow required for the safety factor to fall below 1.0, which increases the risk of slope failure.

CONCLUSIONS

In this study, the ground deformation behavior of the slope was analyzed by monitoring the slope using WSN. In addition, it was clarified that the direction of slope deformation is not necessarily uniform even if the water depth changes to the same extent from year to year.

Numerical simulations based on the monitoring data reproduced the rapid rise of groundwater after rainfall due to the formation of localized high permeable zones in the layers forming the groundwater table. The results indicate that the groundwater depth is likely to rise and the safety factor is likely to decrease under 1.0, increasing the risk of collapse when the downstream permeability becomes poor in the future.

ACKNOWLEDGMENTS

The authors gratefully appreciate a lot of support and understanding for this research by Ryota ETO and Naoki YAMADA in their graduation theses. And this research was supported by a research grant from the Japan Construction Information Center Foundation (JACIC).

REFERENCES

[1] Nishikawa Y., Sasamura T., Ishizuka Y., Sugimoto S., Iwasaki S., Wang H., Fujishima T., Fujimoto T., Yamashita K., Suzuki T., Kurihara K., Design of Stable Wireless Sensor Network for Slope Monitoring, 2018 IEEE TOPICAL CONFERENCE ON WIRELESS SENSORS AND SENSOR NETWORKS, 2018, pp.8-11.

[2] Nishikawa Y., Sasamura T., Ishizuka Y., Sugimoto S., Fujishima T., Fujimoto T., Iwasaki S., Kurihara K., Yamashita K., Problems with independent power supplies in wireless sensor networks, IEICE technical report, Vol. 116, No. 429, EE2016-53, 2017, pp. 27-32. (in Japanese)

[3] Sugimoto S., Sasamura T., Ishida J., Ishizuka Y., Fujishima T., Fujimoto T., Iwasaki S., Yamashita K., Kurihara K., Basic research on the development and application of slope ground measurement systems using wireless sensor networks, Japan Society of Civil Engineers 2016 Annual Meeting, 2016, pp.27-28. (in Japanese)

[4] Ishida C., Sugimoto S., Jiang Y., Omine K., Ishizuka Y., Takaesu R., Iwasaki S., Basic research on the development of multi-point observation method for slope, Western Branch of Japan Society of Civil Engineers 2019 Annual Meeting, 2019, pp.347-348. (in Japanese)

[5] Nakamura T., Sugimoto S., Jiang Y., Omine K., Ishizuka Y., Takaesu R., Iwasaki S., Development of monitoring system for multi-point observation of slope, Western Branch of Japan Society of Civil Engineers 2020 Annual Meeting, 2020, pp349-350. (in Japanese)

[6] Sugiyama Y., Tsukuda E., Katoh K., Ikeda K., Analyses of groundwater data from observation wells for earthquake prediction in the Tokai District, Japan - An analysis of water level fluctuations (part 1)-, Geological Survey Monthly Report, Vol.32, No.3, 1981, pp.133-150. (in Japanese)

[7] Ishida J., Jiang Y., Omine K., Sugimoto S., Higashi Y., Ogata Y., Numerical study on slope stability in consideration of the influence of weathering by two-phase flow analysis, Proceeding of EUROCK 2015 – ISRM European Regional Symposium – the 64th Geomechanics Colloquy, 2015, pp.997-1002.

[8] Ishida J., Sugimoto S., Jiang Y., Seepage Flow Behavior in Slope Model Test and Verification of Reproducibility by Numerical Simulation, Proceedings of the 8th Asian Joint Symposium on Geotechnical and Geoenvironmental Engineering, 2016, pp.75-80.

[9] Sugimoto S., Jiang Y., Omine K., Ishida J., Higashi Y., Numerical studies on slope stability in torrential rainfall by using two-phase flow analysis, Proceeding of The 15th Asian Regional Conference on Soil Mechanics and Geotechnical Engineering, 2015, JPN-105(6 pages).

[10] Itasca Consulting Group, Inc., FLAC, Fast Lagrangian Analysis of Continua, Theory and Background, 2000.

[11] Chang H., Sugimoto S., Jiang Y., Omine K., Study on stability evaluation of slope ground with rainfall and groundwater flow, 2019, pp.335-336. (in Japanese)

[12] Nakamura M., Sugimoto S., Jiang Y., Omine K., Study on evaluation of mechanical stability of slopes with rainfall and groundwater flow, Western Branch of Japan Society of Civil Engineers 2020 Annual Meeting, 2020, pp.415-416. (in Japanese)

11th Int. Conf. on Geotechnique, Construction Materials & Environment, Kyoto, Japan, 3-5 November 2021, ISBN: 978-4-909106063 C3051

UNDERSTANDING THE EFFECT OF DEGREE OF SATURATION ON COMPRESSIVE STRENGTH BEHAVIORS FOR RECONSTITUTED CLAYEY SOIL OF DHAKA

Sultan Al Shafian[1], Sk. Abu Talha[2], Musaddik Hossain[3] and Hossain Md. Shahin[4]

[1]MSc Student, Islamic University of Technology, Bangladesh; [2]Phd Student, University of Cincinnati, USA; Faculty, Islamic University of Technology, Bangladesh; [3,4]

ABSTRACT

Using clayey soil to fill typical earthwork is a common practice in Bangladesh. Disturbed clayey soils at site are usually subjected under precompression load to achieve desired level of compaction for stabilization. Degree of saturation (DOS) affects the compressive behavior of clayey soil to a great extent. This study aims to investigate the effect of degree of saturation on unconfined compressive strength (UCS) of reconstituted clayey soil to imitate disturbed soil behavior. To this end, disturbed clay samples were collected from three different sites in Dhaka city. The collected soil samples had a liquid limit (LL) range of 28-41 and a plastic limit (PL) range of 18-25. The soil samples were reconstituted using slurry consolidation technique simulating a common practice carried out in Bangladesh to apply precompression on the subgrade layer of a pavement. USC tests were conducted on the reconstituted clay sample with varying degree of saturation. The considered range for degree of saturation in this study was 60-100%. From the test results, it was observed that the UCS increased with the decrease of degree of saturation. The relationship between the unconfined compressive strength and degree of saturation within the specified range was in agreement with the non-linear equation $y = ae^{-bx}$. The stress-strain relationship of the clay specimen also clearly indicated that the post-peak strain softening and ductility are largely dependent on the DOS of the specimens.

Keywords: Degree of saturation, Atterberg limit, Unconfined compressive strength, Clayey Soil

INTRODUCTION

Earthwork filling for civil engineering constructions (e.g foundation,embankment etc.) is the most essential task for any project.[1].In Bangladesh,specially in Dhaka ,mostly soils are cohesive (clayey soils)[2] and so for subgrade filling activities this soil has been used widely in various projects.To attain proper bearing capacity at site,necessary mechanically compaction is done is measured to ensure the quality at site.The compressive behaviour is affected by degree of saturation to a great extent.As this filling works are done usually disturbed soil and later compacted using mechanical forces,there is a scope to study the compressive behaviour of this kinds of soil.To understand and analyze the behaviour of the disturebd soils,reconsituted clay is an excellent option.

"A reconstituted clay is one that has been thoroughly mixed at between 1 and 1.5 times the liquid limit and preferably consolidated one-dimensionally":Burland[3]. Reconstituted clay is most commonly used processed clay that has been used for engineering infrastructures for decades due to the unavailability of undisturbed clay. So far, many researchers have conducted significant experiments to investigate the engineering properties of reconstituted clay. Graham et al. conducted an extensive study to compare among various soil properties like Critical state line, compressibilities, strengths and pore water pressure of natural and remolded clay through tri-axial test[4]. W Norhaliza et al in his study on shear strength of remolded samples using three different molding methods-proctor compaction method, hand operated method and miniature mold method concluded that all three methods conform to a desired shear strength though due to easiness and comfort hand operated method is more suitable[5]. Jianjun Ma et al. proposed an equation based on numerical models and experimental results to describe the intrinsic compressibility of reconstituted clay with different initial water contents[6]. Hong, Z. S et al [7], Liu, M. D [8], Sridharan, A et al [9] have notable works focusing the compressibility of reconstituted clay . To this end most of the studies mainly focused on the methods of reconstitution and compressibility of reconstituted clay but the unconfined compressive strength is a basic soil mechanical aspect to gain a first-hand information about the soil quality. This research aims to find a substantial relationship between compressive strength and degree of saturation of reconstituted clay. Besides, the behavior of stress-strain curve with respect to DOS will also be explored.

COLLECTION OF SOIL SPECIMENS

For this research, Dhaka soil has been selected for preparing reconstituted clay. The soil samples were

collected from three different location from a depth of 1.3-2.5m. The description of soil specimens collected for this study is summarized in Table 1. As presented in Table 1, the soil samples had specific gravity of around 2.6. The liquid limit (LL) and the plastic limit of the collected specimens were within the range of 30-41 and 19-24, respectively.

Table 1

Location	Sp	LL	PL	PI	USCS
Hatirpool(A)	2.6	41	24	17	CL
Ajimpur(B)	2.59	35	23	12	CL
Polashi(C)	2.61	30	19	11	CL

Note: Sp=Specific Gravity; LL=Liquid Limit, PL=Plastic Limit ;PI=Plasticity Index

RESEARCH METHODOLOGY

The research follows three steps: a) reconstitute the soil slurry by slurry-consolidation technique, b) preparation of soil specimen for UCS testing, and c) UCS testing.

The collected clay samples were first air dried and crushed into powdered form in the laboratory for testing. Laboratory tests were carried out to determine the physical properties such as liquid limit, plastic limit, plasticity index, and specific gravity. Later, all the samples were then reconstituted using K_o consolidation technique. Fig 1 shows the schematic setup diagram for the soil reconstitution process.

Reconstitution of Soil

Soil samples were reconstituted using the slurry-consolidation technique suggested by Sheeran and Krizek (1971). The reconstitution of the soil includes two major steps: preparation of slurry and Ko consolidation. The following subsections have a brief descriptions of these steps.

Preparation of Slurry

The soil was first air dried and crushed into powdered form. Then the soil was sieved through #40 sieve in order to remove any big chunk rocks or impurities which may affect the consolidation. The samples were then mixed with a water content equal to 1.15 times of liquid limits which was found as sufficient to yield uniform and homogeneous slurry.

K_o Consolidation

The soil slurry of each soil sample was then poured into three specific cylindrical molds one having diameter of 20cm and the others 26cm. Each mold containing the soil slurry has a drainage system to drain out the pore water to facilitate the consolidation.

Fig. 1 a) Ko-Consolidation of soil b) reconstituted soil specimen c) soil sample kept inside desiccator, and d) Failure plane after testing.

Each mold has perforated base plate below and top of the mold to bolster two-way drainage. The soil slurry was confined by Geo-textiles to prevent the particle migration. Lubrication was used on the inner wall to prevent any type of friction between soil and the wall of the mold. A schematic diagram showing various parts *K_o Consolidation* of have been shown in Figure 2.

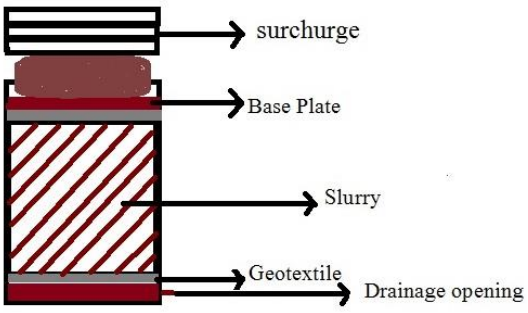

Fig. 2 Schematic diagram showing the set up for slurry- consolidation technique for sample preparation.

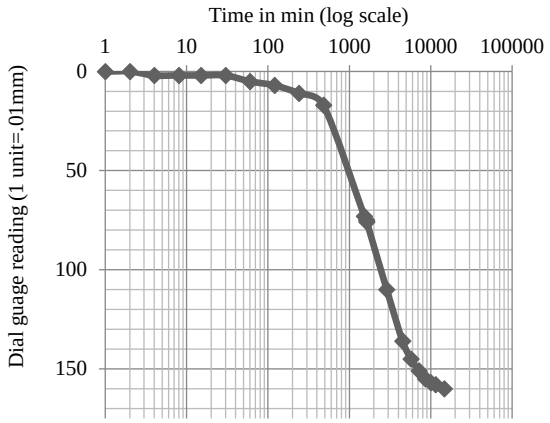

Fig. 3 A typical load-deformation curve

The prepared soil slurry was then poured inside the molds. Initially, the slurry was allowed to consolidate by the self-weight and the weight of the porous metal discs for about 48 hours. Then load was gradually applied with an increment of 50kpa. Each increment was held into position until the primary consolidation was fully completed. The time for primary consolidation was obtained from the deformation vs. time curve (Figure 3) for each incremental load. This process was repeated until pressure reached about 400kpa. It took almost 90 days for the soil samples to accomplish the primary consolidation. The time between each increment was delayed intentionally to prevent the instability of the soil structure.

Preparation of soil specimen for UCS

Once the primary consolidation was completed, the reconstituted soil sample was extracted from the mold and kept inside a desiccator for 24 hours. The soil sample was then cut and trimmed into smaller cylindrical samples for UCS test.

Determining DOS and UCS

The reconstituted soil specimen, after extracting from the mold, was kept initially in desiccator for 24 hours. Then the sample was divided into several smaller samples to facilitate the study. All the samples had height to diameter ratio greater than 2 (ASTM D2166-00). The sample was initially 100% saturated and degree of saturation decreased as the time went by and to foster the rate of decrease the lid of the desiccator was left open intentionally. For the first few samples unconfined compression test was conducted at 6 hours interval and later 24 hours. Every time after the unconfined compression test soil samples was oven dried to find the moisture content and hence degree of saturation was calculated.

To determine the unconfined compressive strength, unconfined compression test was performed in accordance to ASTM D2166 (2000). A typical stress strain curve obtained from UCS test is shown in Fig 4.

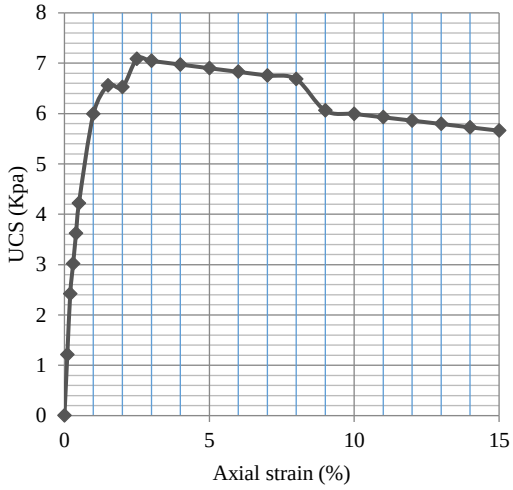

Fig. 4. A Typical stress-strain curve obtained in UCS test.

RESULTS AND ANALAYSIS

Influence of degree of saturation on UCS

Figure 5 shows the results of unconfined compressive tests under various degree of saturations for Sample A, sample B and sample C. It is apparent that the unconfined compressive strength increases with the reduction of degree of saturation for each of the sample. It is interesting to note that, for all three samples, initially the rate of increase of UCS are small. However, a drastic increase in UCS is observed once the degree of saturation drops below 90%. Therefore, care must be taken while measuring the UCS for samples having degree of saturation less than 90% since a slight decrease in degree of saturation may alter the UCS significantly. This phenomenon is more pronounced for sample B and C, where the plasticity indices were comparatively lower.

As mentioned earlier, in all three cases it was observed that initially the rate of increase is steady but when the degree of saturation is below 90% the UCS increases drastically. Based on this observation, relationships were developed between UCS and degree of saturation. The relationships for all the samples are summarized in Table 2.

As shown in Table 2, the relationship found between degree of saturation and UCS is exponential and can be expressed in the following form.

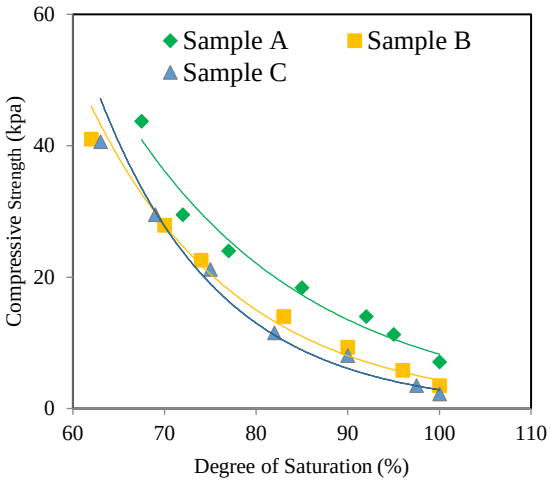

Fig. 5 Variation of UCS with respect to degree of saturation

$$UCS = ae^{-b*DOS} \quad (1)$$

Where 'a' and 'b' are the coefficient of the exponential equation. 'a' represents the shifting of the graph with respect to UCS axis and 'b' represents the rate of change of UCS with respect to DOS. It is interesting to note that the value of 'b' increases with the decrease of plasticity index. Lower plasticity index represents higher percentage of silt in clay. Therefore, the rate of increase in strength in clayey soil due variation of DOS may depend on the percentage of silt in the soil. From Table 2, it is also observed that the coefficient of regression varies between 0.95 to 0.98, indicating a very strong relationship between UCS and DOS.

Table 2

ID	PI	Relationship between UCS and DOS	Coefficient of regression (R^2)
A	17	$UCS = 4375\, e^{0.060*DOS}$	0.95
B	12	$UCS = 2188\, e^{0.062*DOS}$	0.98
C	11	$UCS = 5607\, e^{0.076*DOS}$	0.97

Shear stress-strain behavior

The stress-strain curves for all the specimens are shown in Fig 6. Each curve in the figure represents the stress vs strain curve for a particular DOS. As shown in Fig 6, the soil sample became brittle with the decrease in DOS for all three samples. In other words, the strain required to mobilize the peak shear stress dicreased with the decrease of DOS. In addtion, post-peak strain softening behavior was also observed as the DOS decreased. As indicated by Fig 6, the post

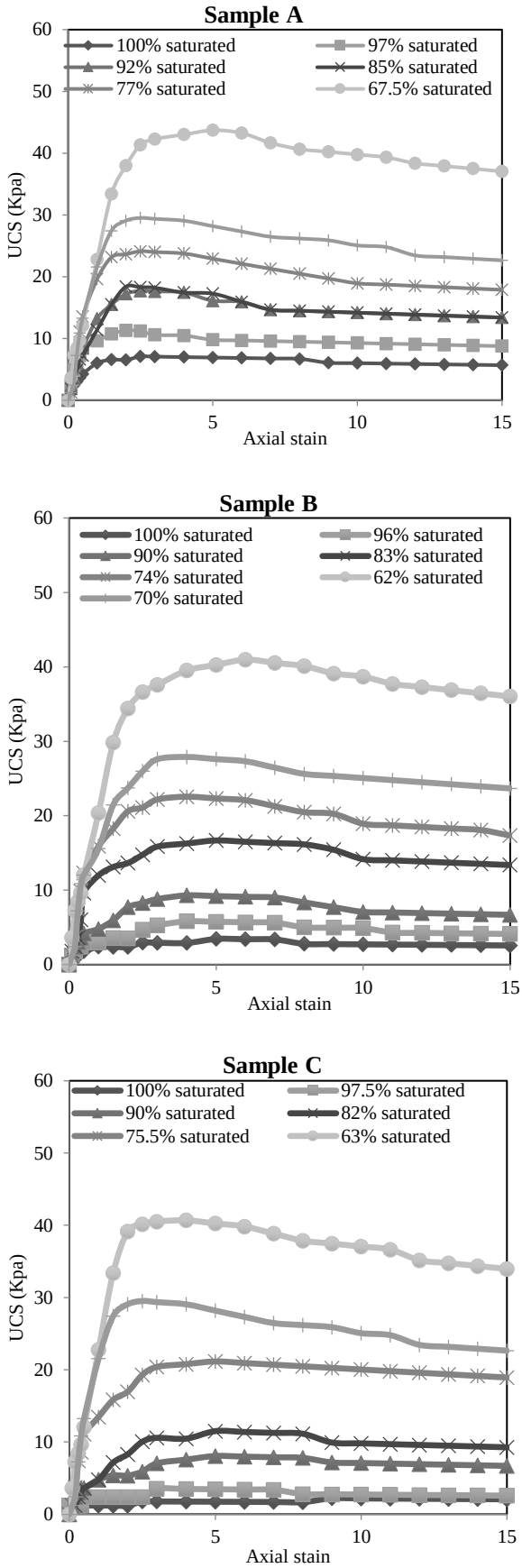

Fig. 6 Load vs strain curve for all DOS(Sample A,B,C)

peak behavior was observed once the DOS of the specimens were below 90%. However, it was more promiment when the DOS was below 80%. It is also worth mentioning that the distinct failure planes were observed of the clay samples when the DOS was below 80%, while the failure criteria observed for Specimens with higher DOS was bulging. In general, the results indicate that when the DOS of clay sample is below 90 %, it may start loosing its ductility and below 80% it may become brittle.

CONCLUSIONS

This study presented the results from the unconfined compressive strength test conducted on three different clayey soil samples with different DOS. The results of the study clearly indicated that the UCS of clay is significantly dependent on DOS and their non-linear relationship can be described with exponential equation. It was observed that the rate of increase in UCS is dependent on the PI of the clay samples. Sample with the lowest PI showed the highest rate of increase in UCS. Also, for all the soil samples, below 90% DOS, a steady increase in UCS was observed, whereas the rate of increase in UCS with the decrease of DOS was drastic for DOS below 90%. From the stress-strain curve, it was obvious that the post-peak strain softening of clayey soil is largely dependent on the DOS. The samples started showing post-peak strain softening once the DOS was below 90%. This behavior was more pronounced when DOS was lower than 80%. It was also obvious that below 80% DOS the clay soil specimens lost its ductility and behaved like a brittle material.

REFERENCES

[1] Mamat, R. C., Kasa, A., & Razali, S. F. M. (2019). A review of road embankment stability on soft ground: Problems and future perspective. IIUM Engineering Journal, 20(2), 32–56. https://doi.org/10.31436/iiumej.v20i2.996

[2] Abul Bashar, M. (2000). Geotechnical Characterization Of Dhaka Metropolitan Area. MSc thesis, Bangladesh University of Engineering and Technology (Buet). http://lib.buet.ac.bd:8080/xmlui/handle/123456789/1264

[3] Burland, John. (1990). Thirtieth Rankine Lecture: On the compressibility and shear strength of natural clays. Geotechnique. 40. 329-378. 10.1680/geot.1990.40.3.329. Graham, James & Li, E.. (1985). Comparison of Natural and Remolded Plastic Clay. Journal of Geotechnical Engineering. 111. 10.1061/(ASCE)0733-9410(1985)111:7(865).

[4] Graham, James & Li, E.. (1985). Comparison of Natural and Remolded Plastic Clay. Journal of Geotechnical Engineering. 111. 10.1061/(ASCE)0733-9410(1985)111:7(865).

[5] Norhaliza, W., Ismail, B., Azhar, A. T. S., & Nurul, N. J. (2016). Shear Strength of Remoulding Clay Samples Using Different Methods of Moulding. IOP Conference Series: Materials Science and Engineering, 136(1). https://doi.org/10.1088/1757-899X/136/1/012018

[6] Ma, J., Qian, M., Yu, C., & Yu, X. (2018). Compressibility Evaluation of Reconstituted Clays with Various Initial Water Contents. Journal of Performance of Constructed Facilities, 32(5),04018077.https://doi.org/10.1061/(asce)cf.1943-5509.0001221

[7] Hong, Z. S., Bian, X., Cui, Y. J., Gao, Y. F., & Zeng, L. L. (2013). Effect of initial water content on undrained shear behaviour of reconstituted clays. Geotechnique, 63(6), 441–450. https://doi.org/10.1680/geot.11.P.114

[8] Liu, M. D., Zhuang, Z., & Horpibulsuk, S. (2013). Estimation of the compression behaviour of reconstituted clays. Engineering Geology, 167, 84–94. https://doi.org/10.1016/j.enggeo.2013.10.015

[9] Sridharan, A., & Nagaraj, H. B. (2000). Compressibility behaviour of remoulded, fine-grained soils and correlation with index properties.

11th Int. Conf. on Geotechnique, Construction Materials & Environment,
Kyoto, Japan, 3-5 November 2021, ISBN: 978-4-909106063 C3051

SAFETY FACTORS VALUE OF ROCK MASS SLOPE AFTER DIFFERENT APPROACH OF ROCK FAILURE CRITERIA BY LIMIT EQUILIBRIUM METHOD

Arief Rachmansyah[1], Eko A Suryo[1], Hasyim Alhadar[2], Retno P Rini[2]

[1]Geotechnical Laboratory, Department of Civil Engineering, Brawijaya University, Indonesia
[2]Master's Program of Civil Engineering, Faculty of Engineering, Brawijaya University, Indonesia

ABSTRACT

Weathering zone, geological structures and discontinuities in the rock are weak areas and as groundwater infiltration pathways. The existence of these phenomena will reduce the stability of rock mass and the main implication is to increase the slope failure. The purpose of this study was to determine the type of rock failure, rock mass classification, and the stability of the rock slopes. The study was conducted on Miocene age of basaltic andesite lava and high discontinuity. After the kinematic analysis of rock failure this rocks failure can be categorized as planar rockslide. The value of Rock Mass Rating of andesitic rock is 53 and classified as medium rock mass. These characteristics show qualitative stability of rock slope. Slope stability analysis for andesite rock based on the generalized criteria Hoek - Brown failure was obtained a safety factor value of 1.55 with a slope angle of 60°, however analysis based on Mohr - Coulomb criteria obtained a safety factor value of 1.59 with a slope angle of 70°.

Keywords: *slope stability, kinematics analysis, rock mass rating, rock failure criteria, safety factor.*

INTRODUCTION

Road of Ponorogo to Pacitan on East Java Province Indonesia is known as a dangerous route, because the roads have been developed on the edge of a cliff. Rock and soil slides along the route occur often, especially during the rainy season. This paper will discuss the types of rockslides, and the application of rock mass classification system for different numerical analysis of the slope stability.

Base on Physiographic of East Java Island that proposed by Van Bemmelen (1949) Ponorogo – Pacitan Road located in the Southern Mountains Zone. In Miocene this zone is the east - west magmatic arch as a product of subduction of Indo-Australian to Eurasian Plates [1]. During the Late Miocene to Pliocene, it turned into a shallow sea that produced carbonate rocks. The tectonic setting causes this zone to be dominated by volcanic facies sediment, lava intrusive rocks, and dense geological structures. The plate collision from the south produces shear faults trending Southwest – Northeast, and Northeast - Southeast. Folded structures are also found in several places with a West – East axis. These conditions were also followed by mineralization of epithermal gold and porphyry copper in several places. [2].

Slope failure of rock and soil are generally influenced by conditions of inconsistency between the existence of the formation process in nature and the bond conditions between rocks that are identified as unconformity. The effect of non-conformity can affect the value of shear strength and the strength of the slope forming material [3]. Rock collapse usually starts and go along discontinuities of rock mass, such as joints, fractures, bedding planes, faults, and other types of cracks in the rock. According to, geological structures and discontinuities in rocks are weak areas and groundwater infiltration pathways [4]. The existence of geological structures and discontinuities will reduce the level of rock shear strength and the main implication is to increase the chance of landslides.

Type of Rock Failure

To determine the potential failure type in a rock slope, it is necessary to map the orientation of the discontinuity before and after the rock slope is exposed [5]. In general, the integration of rock discontinuity orientations

will form the main types of slides in rocks, namely:

- Plane failure, if the sliding plane is considered flat. The sliding area can be in the form of fractures, faults or rock layers.
- Wedge failure is happened when two or more weak planes intersect in such a way as to form a wedge against the slope. This wedge failure can be divided into 2 types of landslides, namely: single sliding and double sliding. For single landslides, the slide occurs in one plane, while the form of multiple landslides occurs at the intersection of the two planes.
- Toppling failure is generally occur on steep slopes and on massive rock masses where the weak areas are column shaped. Toppling failure occur because the weak areas on the slope are in the opposite direction to the slope direction. As a result of the opposite tilt direction, the material cannot support its own mass, resulting in toppling failure.
- Circular failure is the most common mass movement in nature, especially on soil and debris material., and high weathered rock mass so they almost resemble soil. As the name implies, the landslide field is arc shaped. In hard rocks, circular failure can be happened on the rock with has weathered and with very tight spacing fracture or discontinuous.

To determine the type of rockslide, it is analysis by drawing the surface plane of the slope and the discontinuity that acts as the cause of the failure on stereographic diagram. Currently, there are many software that can describe the position of the two planes on a stereographic.

Rock Mass Classification System

Rock Mass Classification is the process to determine rock masses into groups or classes in defined relationships and assigning a unique description (or number) to it based on similar properties / characteristics, so that the behavior of rock masses can be predicted [6]. Rock masses are called in situ rock material separated by rock discontinuities, mostly by joints, bedding planes, intrusions and faults, and other geology process.

Many experts propose rock mass classifications [7], including: Terzaghi (1946); Rabewicz, Muller and Pacher (1964); Patching and Coates (1968); Deere et al (1967), Wickham, et al (1972); Bieniewski (1973), Barton et al (1974), Hoek (1994), and Palmstorm (1995). Among the many classifications that have received much attention related to the numerical analysis of rock mass slope stability are Rock Mass Rating (RMR) proposed by Bieniewski, and Geological Strength Index (GSI) proposed by Hoek.

Rock Mass Rating

Rock Mass Rating (RMR) is used to determine the stability of rock mass empirically by providing an assessment of rock mass with weight and parameters based on geological conditions [8]. The RMR value is obtained by matching the results of field observations of rock mass characteristics on the table. The following five parameters are used to classify rock masses using the RMR system [9].

a. Uniaxial compressive strength (UCS)

The strength of intact rock in RMR is expressed by Uniaxial Compressive Strength (UCS). UCS is the strength of the intact rock obtained from the uniaxial compressive strength test results in the laboratory.

b. *Rock Quality Designation* (RQD)

The presence of discontinuity in the rock mass often adversely affects its mechanical properties so that the quantitative magnitude of the discontinuity plane needs to be known. Parameters that can indicate rock quality before excavation are Rock Quality Designation (RQD) that is obtained from core of exploration drilling.

To quantify the core of the box, the RQD must be calculated. RQD is calculated based on the percentage of core drill bits obtained with a minimum length of 10 cm and the number of core cuttings is usually measured at a 2 m long core. an example of RQD calculation of drill core. Cuts due to drilling handling must be ignored from the calculation and the core a soft and not good drill weight = 0 and the calculation is as follows.

$$\text{RQD} = \frac{\Sigma \text{ Length of core pieces} \geq 10 \text{ cm}}{\text{Total length of the core (cm)}} \times 100\% \qquad (1)$$

If core drills are not available, the RQD can be calculated indirectly by measuring the

orientation and distance between discontinuities in the rock outcrop. It is proposed an equation to determine the RQD from the line stretch data as follows [6].

$$\text{RQD} = 100\, e^{-0.1\lambda}(0.1\lambda + 1) \quad (2)$$

Where, λ is the ratio of the number of discontinuities per meter.

c. Discontinuity Distance

Discontinuity distance is determined from the average distance between rock fractures along the scanline measurement span.

d. Discontinuity Field Conditions

Discontinuity conditions are determined from the description of each discontinuity plane, in the form of weathering level, discontinuity plane surface roughness, continuity of the fracture plane, opening width, and discontinuity field fill material.

e. Groundwater Conditions

The presence of this water will reduce the shear strength between the two discontinuity surfaces. The weight of groundwater parameters can be determined in several ways, one of which is direct observation in the field by determining the general condition of groundwater.

Geologiy Strength Index

In 1995 Hoek et al included the concept of the Geological Strength Index (GSI) which provides an estimate of the reduction in rock mass strength due to differences in geological conditions. GSI was introduced and developed as tool for classification inability of Rock Mass Rating system to determine the rock quality with bad quality [10].

The GSI value is a rock strength index classification obtained in two ways, the first is by field observing the rock mass characteristics with the help of the GSI value estimation chart. The second is by reducing the RMR classification results through the following equation [11].

$$\text{GSI} = \text{RMR} - 5 \quad (3)$$

Rock Failure Criteria

Hoek and Brown introduced their failure criteria in an attempt to provide input data for the analyzes necessary for the design of underground excavation in hard rock. These criteria start from the properties of the intact rock and then introduce factors to reduce these properties based on discontinuity characteristics in a rock mass [12].

a. Hoek - Brown Generalized Failure Criteria

These criteria are derived from the results of research into intact rock collapse by Hoek and studies of rock mass behavior model by Brown. There are 2 rock collapse criteria based on Hoek & Brown's proposal. This criterion became known as the Generalized Hoek-Brown criterion with the equation [13]:

$$\sigma_1' = \sigma_3' + \sigma_{ci}\left(M_b \frac{\sigma_3'}{\sigma_{ci}} + s\right)^a \quad (4)$$

Where σ_1' and $\sigma_{3'}$ are the maximum and minimum effective stresses at failure, σ_{ci} is the compressive strength (UCS) of the intact rock. Meanwhile, M_b is the reduction factor of the rock type constant *mi*, and *s* and *a* are the rock mass constants obtained by the following equation.

$$\text{M}_\text{b} = \text{m}_\text{i}\exp\left(\frac{GSI-100}{24-14D}\right) \quad (5)$$

$$s = \exp\left(\frac{GSI-100}{9-3D}\right) \quad (6)$$

$$a = \frac{1}{2} + \frac{1}{6}\left(e^{-\frac{GSI}{15}} - e^{-\frac{20}{3}}\right) \quad (7)$$

The values of M_b, *s*, and *a* are used in determining the strength of rock mass, both for Hoek - Brown or Mohr-Coulomb criteria [14].

b. Mohr-Coulomb Criteria

Most geotechnical software still applicate the Mohr-Coulomb collapse criteria, so it is necessary to determine the inner shear angle and the cohesion value for each rock mass. The adjustment process requires a balance between the upper and lower areas on the Mohr-Coulomb plot, resulting in an equation to obtain the value of the inner shear angle and cohesion [15]:

$$c' = \frac{\sigma_{ci}[(1+2a)s+(1-a)m_b\sigma'_{3n}](s+m_b\sigma'_{3n})^{a-1}}{(1+a)(2+a)\sqrt{1+(6am_b(s+m_b\sigma'_{3n})^{a-1})/((1+a)(2+a))}} \quad (8)$$

$$\phi' = \sin^{-1}\left[\frac{6am_b(s+m_b\sigma'_{3n})^{a-1}}{2(1+a)(2+a)+6am_b(s+m_b\sigma'_{3n})^{a-1}}\right] \quad (9)$$

Determination of the value of σ_{3max} on different slopes and tunnels, for slopes the value of σ_{3max} is obtained based on the formula [15]:

$$\frac{\sigma'_{3max}}{\sigma'_{cm}} = 0.72 \left(\frac{\sigma'_{cm}}{\gamma H}\right)^{-0.91} \quad (10)$$

$$\sigma'_{cm} = \sigma_{ci} \frac{(mb+4s-a(mb-8s))\left(\frac{mb}{4}+s\right)^{a-1}}{2(1+a)(2+a)} \quad (11)$$

$$\sigma'_{3n} = \frac{\sigma'_{3max}}{\sigma_{ci}} \quad (12)$$

In the calculation of rock slope stability, this failure criterion is only suitable for circular failure types caused by very tight joints, but also can be used for planar type.

STUDY LOCATION AND METHOD

Location

The research location was conducted on Ponorogo - Pacitan road KM 232.5, administratively on Tegalombo District, Pacitan Region (Figure 1).

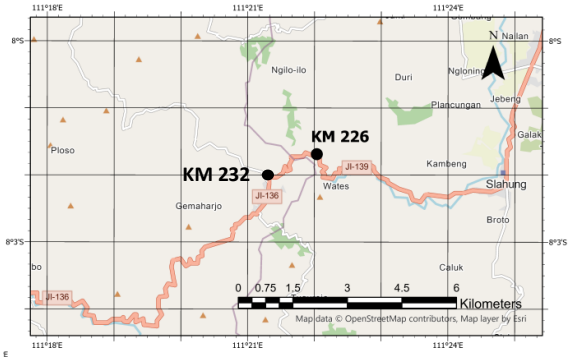

Figure 1 : Study Location

Method

The research steps include:

- Secondary data collection from difference institution
- Field survey which includes field observations and measurement of the orientation of geologic structure and other discontinuity.
- Laboratory tests for physical properties of rocks, and uniaxial compressive strength.
- Kinematic or stereographic analysis to determine the types of rockslides.
- Rock mass classification analysis using the Rock Mass Rating (RMR) and Geology Strength Index (GSI).
- Numerical modelling of rock slope stability by using limit equilibrium method with the help of software Rockplane.

RESULTS AND DISCUSSION

Geology

Based on the geological map sheet Pacitan scale 1:100000 the study location is composed of basaltic andesite lava which is part of the Watupatok Formation. This Miocene formation is composed of andesitic lava, volcanic breccia, and volcanic sandstone [16]. Basaltic andesite lava has a sheathing joint structure that has undergone a low to moderate weathering process. The soil formed is reddish brown and slightly plastic (Figure 2).

Figure 2: Slope failure on basaltic andesite rock with sheeting joint

Type of Slides

To identify the types of rockslides the field observation of rock mass and measurement of the orientation of joints was carried out. To determine the type of rockslide was carried out by kinematic analysis method using Dips software. The data obtained was a strike dip of slope of N154°E / 66°. Orientation of some strike and dip of joints is N138°E/48°.

It can be concluded that the type of rockslide that occurred was planar, because there is only 1 joint set, and the strike of planes is almost parallel to the slope. The difference between two planes is less than 20°. The results of stereographic analysis can be seen in Figure 3.

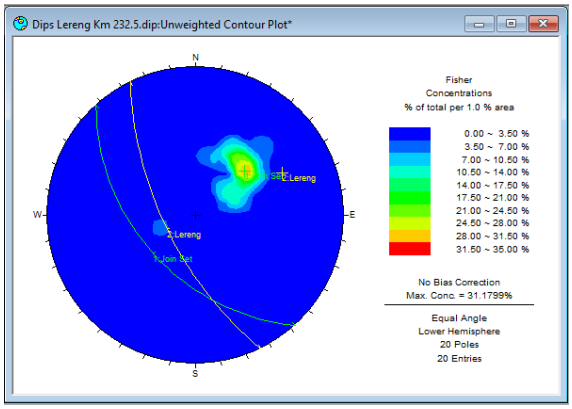

Figure 3. The results of the joint projection stereographic analysis using the Dips software.

Rock Mass Rating

Rock mass classification of slope is analyzed after Rock Mass Rating developed by Bieniawski (1989) using five parameters.

a. Intact rock strength

The intact rock strength parameters were carried out using laboratory testing, namely the Uniaxial Compressive Strength (UCS) test. In this case the rock type is andesite, the samples taken were tested by UCS, so the rock compressive strength for andesite rock types was 6.5 Mpa. So that the strength of the intact rock is obtained at 2.

b. RQD

The calculation of RQD is carried out by direct observation in the field by looking at the muscular structure on the slope. Observations were made on a slope span of 4 meters, in which observations obtained a total number of fractures along the length of 20 fractures, then the ratio of the average number of fractures (λ) can be calculated.

$$\lambda = \frac{20}{4} = 5 \text{ joint / meter}$$

Then the RQD can be calculated by using equation (2) of 90.87%. After this calculation weighting value of RQD is 20.

c. Distance Between Discontinuities

Determination of the distance between discontinuities was carried out using the scanline method, namely measuring the orientation of the rock mass in the field. Based on the measurement data of rock mass orientation, the average distance between discontinuities is 20 cm. It is known that the weight of the distance between discontinuities on the slope is 8.

d. Discontinuity Field Conditions

Based on field observations, the condition of the discontinuity plane is rather rough with the separation of discontinuities less than 1 mm and the rock conditions are very weathered. Based on RMR Table it is known that the weight of the discontinuity conditions on the slope is 13.

e. Groundwater Conditions

Groundwater parameters are directly observed in the field by observing the general condition that the slopes have found conditions on the slopes, namely humid. Based on the field observation there is springs water, and the rock mass is moist. The weighting of groundwater conditions is 10.

f. RMR total weight classification

Each result of the weighting of the five parameters that has been obtained is then added up to get the total RMR weight value that will be used to classify the rock mass class.

RMR value = 2 + 20 + 8 + 13 + 10 = 53

Based on the results of the total RMR weighting, then the rocks on the slope of KM 232.5 are included in the classification of class III rock masses (medium rocks). It can be concluded that the rock slopes belonging to the class III, and are susceptible to weathering, so they are classified as prone to landslides.

4.4. Slope Stability

Slope stability analysis is calculated by different rock failure criteria, namely Hoek - Brown's general criteria and Mohr - Coulomb criteria.

a. Hoek & Brown Failure

The general failure criteria of Hoek & Brown include several parameters, namely rock compressive strength (*σci*) from the compressive strength test results, the GSI value obtained from the RMR reduction (Bieniawski, 1989), rock mass constant (mi) based on rock type, and the value of the disturbance factor (D) based on stress relaxation.

The GSI value can be determined from the reduction in the weighting result of the RMR classification according to equation (3).

Previously, the RMR was obtained at 53, then the GSI value is 48.

As for several other parameters, namely M_b, s, and a which are calculated based on the value of mi, GSI and the disturbance factor (D) using the formulas (5), (6), and (7). Then the value of Mb = 0.609, s = 0.0002, and a = 0.507.

The data is inputted into the Rockplane software, and then slope modeling performed with this software. The results of slope stability analysis with this software are shown in Figure 4.

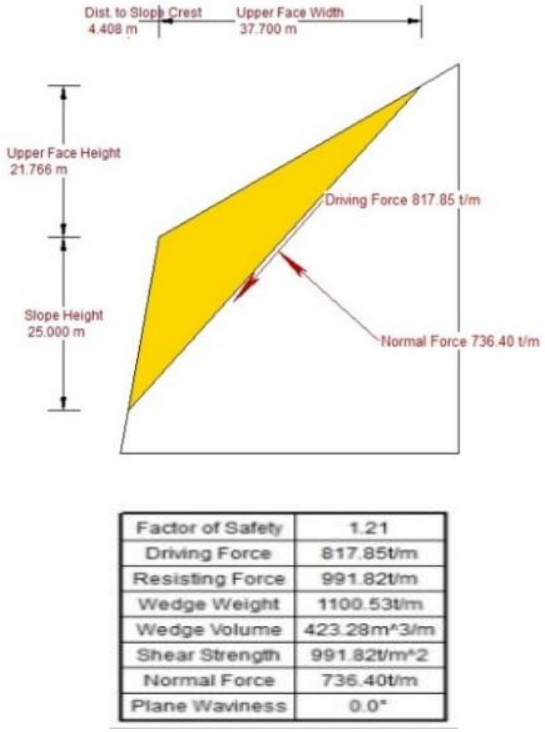

Factor of Safety	1.21
Driving Force	817.85t/m
Resisting Force	991.82t/m
Wedge Weight	1100.53t/m
Wedge Volume	423.28m^3/m
Shear Strength	991.82t/m^2
Normal Force	736.40t/m
Plane Waviness	0.0°

Figure 4. Analysis model of slope stability after Hoek – Brown criteria for slope angle of 80^o .

To make more stable slope it is necessary to reduce the slope angle. The slope angle was simulated until the safety factor more than 1.5, with the specified variation of 75°, 70°, 65°, 60°, and 55°. The safety factor of rock mass slope after simulation of the slope angle are shown in Table 1.

Based on these results, if the slope angle is reduced or smaller than the actual slope angle, the slope will approach a stable condition. At the specified slope angle variation, the slope becomes stable at an angle of 60° and 55° with the value of the safety factor that meets the standard, namely SF = 1.55 for the slope angle of 60° and SF = 1.79 for the slope angle of 55°.

Table 1. The safety factor value base on variations of the slope angle.

Slope (°)	Safety factor	Information
80	1.21	Not safe
75	1.26	Not safe
70	1.33	Not safe
65	1.42	Not safe
60	1.55	Safe
55	1.79	Safe

b. Mohr-Coulomb Criteria

The Mohr-Coulomb criterion parameters used in the slope stability analysis are cohesion (c') and inner shear angle (ϕ') determined by the equations of Hoek - Brown. The cohesion value is calculated using equation (8) of 0.098 Mpa and the inner shear angle is calculated using equation (9) of 32.25°.

The value of cohesion (c') and the inner angle of shear (ϕ') is then inputted into the Rockplane software for slope stability analysis. The results of the slope stability analysis are shown in Figure 5.

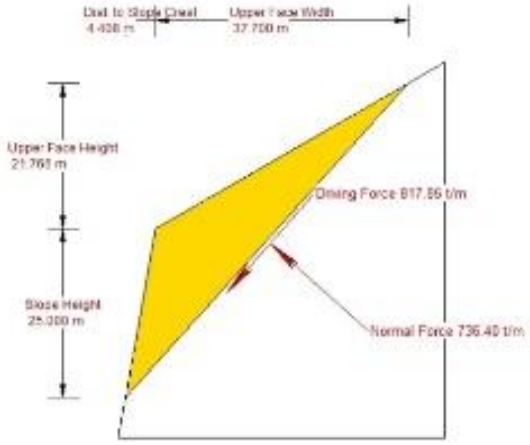

Factor of Safety	1.33
Driving Force	817.85t/m
Resisting Force	1086.76t/m
Wedge Weight	1100.53t/m
Wedge Volume	423.28m^3/m
Shear Strength	1086.76t/m^2
Normal Force	736.40t/m
Plane Waviness	0.0°

Figure 5. Analysis model of slope stability after Mohr - Coulomb criteria for slope angle of 80^o.

After the results analysis, the safety factor of slope is 1.33, it can be said that the slope is unstable. This is because the slope SF value is

smaller than the standard or does not meet the specified standards, namely SF ≥ 1.5.

To make the stable slope it is necessary to change the slope angle. Changes in the slope angle of the slope are made with several variations in the angle until the slope becomes stable, with the specified slope angle variation of 75°, 70°, 65°, 60°, and 55°. The results of the analysis of the safety factor of slope stability based on variations in the slope of the slope are shown in Table 2.

Based on these results, if the slope angle is reduced than the actual slope angle, the slope will approach a stable condition. At the specified slope angle variations, the slope becomes stable at an angle of 70° and 65° with the value of the safety factor that meets the standard, namely SF = 1.59 for the slope angle of 65° and SF = 1.83 for slope angle of 65°.

Table 2. The safety factor value base on variation of slope angle.

Slope (°)	Safety factor	Information
80	1.33	Not safe
75	1.44	Not safe
70	1.59	Safe
65	1.83	Safe
60	2.26	Safe
55	3.30	Safe

From the two methods used in analyzing the safety factor of slope stability, namely the Hoek & Brown collapse general criteria and the Mohr-Coulomb criterion, different safety factor values were obtained. The value of the safety factor of the two methods is shown in Table 3.

Table 3. The value of the safety factor is based on the general criteria for the failure of Hoek & Brown and the value of the safety factor is based on the Mohr-Coulomb criteria.

Slope (°)	SF Hoek - Brown's general criteria	SF Mohr-Coulomb criteria
80	1.21	1.33
75	1.26	1.44
70	1.33	1.59
65	1.42	1.83
60	1.55	2.26
55	1.79	3.30

Based on the table above, for the general criteria for Hoek - Brown failure the slope is said to be stable on a slope of 60° with the SF value = 1.55, while for the Mohr - Coulomb criteria the slope is said to be stable at a slope of 70° with the SF value = 1.59. With reference to the rock mass classification, the result of the safety factor is taken based on the general criteria for Hoek & Brown collapse with a slope angle of 60°.

CONCLUSIONS AND SUGGESTIONS

Conclusion

1. After stereographic kinematic analysis rock failure on study location can be classified as planar rockslides.
2. The weight value of Rock Mass Rating (RMR) of slope on site is 53 and can be classified as a medium rock class. The GSI value is 48.
3. Based on safety factor analysis with Hoek - Brown's general failure criteria rock mass will be stable, if SF is 1.55 and the slope angle is 60°. Meanwhile, based on the Mohr-Coulomb criteria the stability of rock mass can be reached if the SF value is 1.59 and the slope angle is 70°.

Suggestion

1. It is needed to more detailed geotechnical survey of the rock mass to obtain probability of hazard and its overcoming.
2. Periodic monitoring of slopes movement is necessary to detect other symptom of instability, so preventive efforts can be made immediately.

REFERENCES

[1] Purwanto, H.S. 1997. *Analisis Dan Genesa Pembenrukan Srruktur Geologi Pada Batuan Berumur Oligosen - Miosen Di Daerah Pacitan Dan Sekitarnya, Kabupaten Pacitan, Jawa Timur*. *Thesis Magister. ITB.*

[2] Sudrajat, A. and Jong-IK, 1993. *Report on The Join Mineral Exploration In The Pacitan Ponorogo Area, East Jawa, the Republic of Indonesia, Indonesian Geological Survey*. Unpublish.

[3] Priest, S. D. 1993. *The collection and analysis of discontinuity orientation data for engineering design, with examples.* In Rock Testing and Site Characterization (pp.167-192), Pergamon.

[4] Priest, S. D. 2012. *Discontinuity analysis for rock engineering*. Springer Science & Business Media.

[5] Hoek, E., & Bray, J. D. 1981. *Rock slope engineering*. 3rd. London: Institute of Mining and Metallurgy CRC Press.

[6] Bieniawski, Z. T., 1976. *Rock Mass Classification in Rock Engineering*. Proceeding Symposium of Exploration for Rock Engineering, 1, 97-106. Cape Town: Balkema.

[7] Palmstrom, A., 2000. *Rock Mass Classification Systems*. Proceedings Geo Eng. 2000.

[8] Romana, M. 1985. *New adjustment ratings for application of Bieniawski classifications to slopes. Proceeding of Rock Mechanics*. Zacatecas, Mexico, pp 49-53.

[9] Bieniawski, Z.T. 1989. *Engineering rock mass classifications*. New York: Wiley.

[10] Marinos, P., Hoek, E. & Benissi, M. 1998. *Applicability of the Geological Strength Index (GSI) classification for very weak and sheared rock masses. The case of the Athens Schist Formation*. Bulletin of Engineering Geology and the Environment, Vol 57 (2), pp 151-160.

[11] Hoek, E., Carter, T. G., & Diederichs, M. S., 2013. Quantification of the geological strength index chart. In *47th US rock mechanics/ geomechanics symposium*. American Rock Mechanics Association, January 2013.

[12] Hoek, E. and Brown, E.T. 1980. *Empirical Strength Criterion for Rock Masses*., Journal Geotech. Engineering Div., ASCE 106 (GT9), pp 1013-1035.

[13] Hoek, E. and Brown, E. T., 1988. The Hoek-Brown failure criterion - a 1988 update. *In Rock Engineering for Underground Excavations*, Proceeding 15th Canadian Rock Mechanics Symposium, (ed. J.C. Curran), 31-38. Toronto: Dept. Civil Engineering, University of Toronto.

[14] Hoek, E., Carranza-Torres C T., Corkum, B. *Hoek-Brown Failure Criterion, 2002 edition*. In*:* Proceedings of the 5th North American Rock Mechanics Symposium., Toronto, Canada, 2002: 1: pp 267–73.

[15] Cheng, Y. M., & Lau, C. K. 2014. *Slope stability analysis and stabilization: new methods and insight*. CRC Press.

[16] Samodra, H.; Gafoer, *S.;* dan Tjokrosapoetro, S. 1992. *Peta geologi lembar Pacitan*. Jawa. Sekala I : 100.000. Puslitbang Geologi. Bandung.

[17] Sophian, R. I., & Muslim, D. (2018). Pengaruh Geological Strength Index (GSI) Terhadap Nilai Faktor Keamanan Melalui Simulasi Kestabilan Lereng Tambang, Kecamatan Batu Kajang, Kabupaten Paser, Kalimantan Timur, Geoscience Journal, 2(6), 487-497.

11th Int. Conf. on Geotechnique, Construction Materials & Environment,
Kyoto, Japan, 3-5 November 2021, ISBN: 978-4-909106063 C3051

IMPACT OF UNDERGROUND DISPLACEMENT BEHAVIOR ON SLOPE FAILURE INITIATION DUE TO RAINFALL BASED ON EXPERIMENTAL STUDY

Xin Qin[1], Masamitsu Fujimoto[2] and Yoshifumi Masamitsu[3]

[1]Dept. of Civil Engineering, Ritsumeikan University; [2,3] Dept. of Civil Engineering, Ritsumeikan University

ABSTRACT

Rapid and intermittent soil movement due to precipitation events can occur within a matter of seconds. Even a single disaster of this type can cause heavy economic losses and casualties. However, studies of sliding initiation time are scarce, which are most relevant to the early warning of collapse. In this study, we conducted physical model experiments to discuss the deformation behavior due to displacement and slope collapse. This study is attempted to clarify the relationship between the two phenomena and the mechanism of the initial collapse, to improve the possibility of accurate prediction before the occurrence of the collapse. Three kinds of model slopes of a same shape with different densities were made under condition of the presence or absence of the weathered soil bedrock zone (low-permeability rock). We place a total of 12 accelerometer on two longitudinal line (left and right) with three points. The accelerometers were embedded at depths of 2 cm and 10 cm under the soil surface, to record the deformation of the model slope during rainfall. The accelerometer can detect significant displacement changes for low-density soil before the initial collapse. After the rainfall, the displacement was observed continuously. These results indicate that the possibility of predicting the collapse phenomenon can be improved by discussing underground displacement.

Keywords: Slope callops, Deformation behavior, Rainfall, Laboratory experiment

INTRODUCTION

Due to global climate change, the frequency and intensity of precipitation has recently increased in Japan, leading to severe sediment disasters caused by slope collapse and debris flow. More than 1,000 sediment disasters occur in Japan every year, with a fatality rate of 62% among those in the affected areas [1]. Sediment disasters are difficult to predict accurately and usually occur within a short period of time; they carry a risk of significant loss of life and property due to suboptimal evacuation times. Therefore, it is important to obtain accurate information about the vulnerability of different regions to sediment disasters, particularly in Japan, which has fragile geological conditions.

Slope collapse is influenced by various environmental factors, which in turn affect physical slope properties such as shear force and pore water pressure [2]. When the shear strength or water content of unsaturated soil changes slowly, it is possible to prevent the resulting progressive slope movement; however, rapid and intermittent soil movement can occur within seconds, without warning. Measuring the deformation behavior of slopes is considered to be one of the effective methods to assess the degree of slope stability [3]. Measurement of developing displacement to predict slope collapse has also been widely put into practical application in Japan [4]. Also, in Japan, disasters waring will be issued when heavy rain increases risk of sediment-relate disasters, the criteria of issue of the waring and advisory are based on rainfall intensity and soil water index. Although multiple measurement techniques and theories are constantly being refined, collapsing is still having a complex physical mechanical process. Excluding the intensity of rainfall, disaster warnings for slope failures are mostly established by measuring the changes in moisture or groundwater level in the soil and the displacement of the topsoil [5]. Slopes in natural environments have complex soil formations, and the distribution of groundwater is also influenced by these formations, showing great spatial variability. [6] These extreme criteria on current early warning systems are highly empirical. A better understanding of the processes during the collapse event can provide a correct assessment for treatment method and reduce the damage caused.

The objective of this study was to determine whether measured changes in slope acceleration are adequate for predicting collapse events. We performed laboratory experiments using a model slope of varying density, and placed accelerometers within the slope to record triaxial acceleration changes at multiple points. Then, we determined the effects of slope deformation on the early stages of

slope collapse.

METHODS

In this study, we used a slope model to simulate natural slope collapse due to rainfall (Fig. 1). The experimental setup consisted of an artificial rainfall device, a model slope, and sensors set at various points within the slope. Artificial rain was released from directly above the model slope at an intensity of 50 mm/h; the raindrops resembled fog particles. The model slope was composed of weathered granite, which is widely distributed on the mountains of Japan. The model slope was composed of dry soil, with a water content of only 5%. The total height of the model slope, including a 10-cm drainage layer, was 60 cm. The model slope had a width and length of 60 and 100 cm, respectively. The artificial rainfall device was set directly above the model slope, and the raindrops were in the form of mist with an intensity of 50m/h.

To reproduce the multi-layered structure of slopes in the natural environment, the model slope was composed of two layers, a surface layer, and an underlying permeable layer, which simulated the soil bedrock zone. For each experiment, we added soil onto the model vertically, in 10-cm layers, and compacted the soil evenly to ensure that the model would maintain uniform density. Six observation point were installed axis metrically at the right and left sides of the model slope, at distances of 25, 42, and 80 cm from its base (Fig 1). The accelerometers were embedded at depths of 2 cm (group A) and 10 cm (group B) under the soil surface, to record the deformation of the model slope during rainfall. We performed simulations for Cases 1–3, varying the density of the surface layer as 1.2, 1.4, and 1.6 g/cm³, respectively. The density of the internal bedrock zone remained constant at 1.8 g/cm³ in all experiments. A camera was placed at the front of the slope to record ground surface changes and evaluate the phase of the collapse during artificial rainfall.

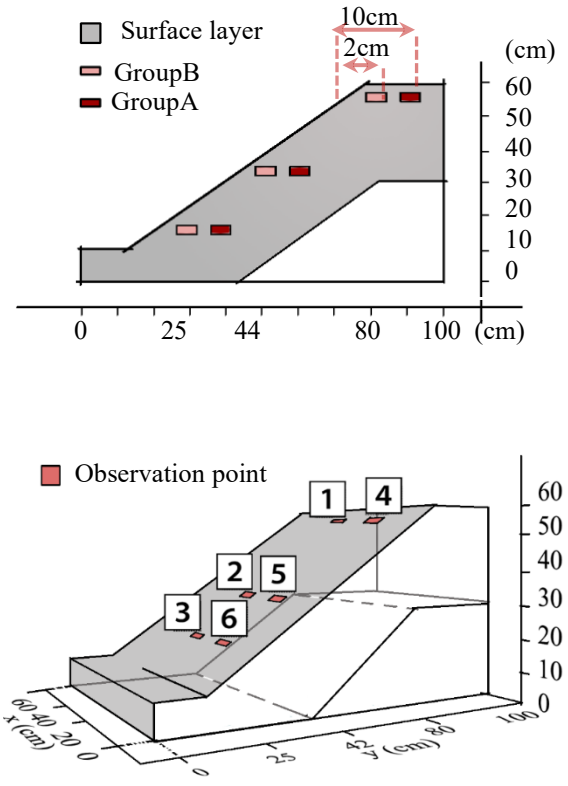

Fig. 1 Schematic of the model slope used in this study. Numbers indicate the positions of accelerometers placed axis metrically within the model slope, at distances of 25, 42, and 80 cm from the base, and depths of 2 cm (group A) and 10 cm (group B).

RESULTS AND DISCUSSION

Each laboratory experiment produced 12 set of soil deformation behavior observations for various locations and soil depths. Triaxial acceleration was measured at the onset of artificial rainfall, and throughout the experiment at a frequency of 24 times per second. Each measurement included both dynamic and static acceleration changes, where dynamic acceleration is caused by displacement and static acceleration by gravitational acceleration. Thus, if there was no change in acceleration between two measurements, the acceleration value of the axis did not return to zero; instead, the acceleration was stabilized due to projected intrinsic gravitational acceleration. Such acceleration changes caused by internal displacement produced a gradient that changed over time. The results for all experiments are shown in Fig.2-4.

Slope failure and deformation behavior

In Case 1, surface cracks were first observed 72 min after the start of rainfall. A long crack was observed at the top edge of the model slope near observation point 1. The crack developed gradually, and the surface soil slid downward from the crack. Accelerometers B3 and B6, at the front of the slope, showed significant deformation starting at 3 min after the onset of rainfall, and all accelerometers showed deformation within 15 min after the onset of rainfall. All shallow accelerometers (group A) showed clear changes in acceleration along the X-axis, with gradients approaching 90° at A1, A2, A3, A5, and A6. The deformation gradually stabilized as rainfall continued; a few minutes before the first crack formed, the X-axes of A1, A5, A6, B2, and B3; the Y-axes of A1 and B1, the X-axes and Y-axes of A6 and B6 underwent large acceleration changes.

In Case 2, the first crack was observed between observation points 5 and 6 at 75 min after the onset of

rainfall. A lateral crack developed gradually and cut off the entire sloping surface. The lower soil layer slid off, followed by the individual upper soil layers, eventually leading to collapse of the entire slope. Almost simultaneously with the rainfall, B4 began to record a sustained deformation behavior. Within 30 min after the onset of deformation, all accelerometers recorded deformation.

Among all cases, Case 3 showed the shortest time to initial cracking. A small part of the soil layer cracked near observation point 3, at the foot of the slope, followed by gushing of groundwater from the saturated soil. The cracks expanded upward from the initial crack, gradually leading to collapse of the entire slope. The crack and slope collapse in Case 3 occurred rapidly and abruptly. On the other hand, in Case 3, all accelerometers were constant at their initial values until the initial crack, except Y-axis of A1 and X-axis of A2 recorded subtle changes in the minutes before the initial cracking occurred. In a relatively loosely constructed soil layer such as in Case 1 (ρ =1.2g/cm^3) and Case2 (ρ =1.4g/cm^3), the deformation behavior can be observed continuously. On the contrary, in a soil layer with a hard structure as Case 3(ρ =1.6g/cm^3), the deformation behavior then becomes insignificant.

Comparison with deformation behavior in three cases

To summarize the experimental results for all

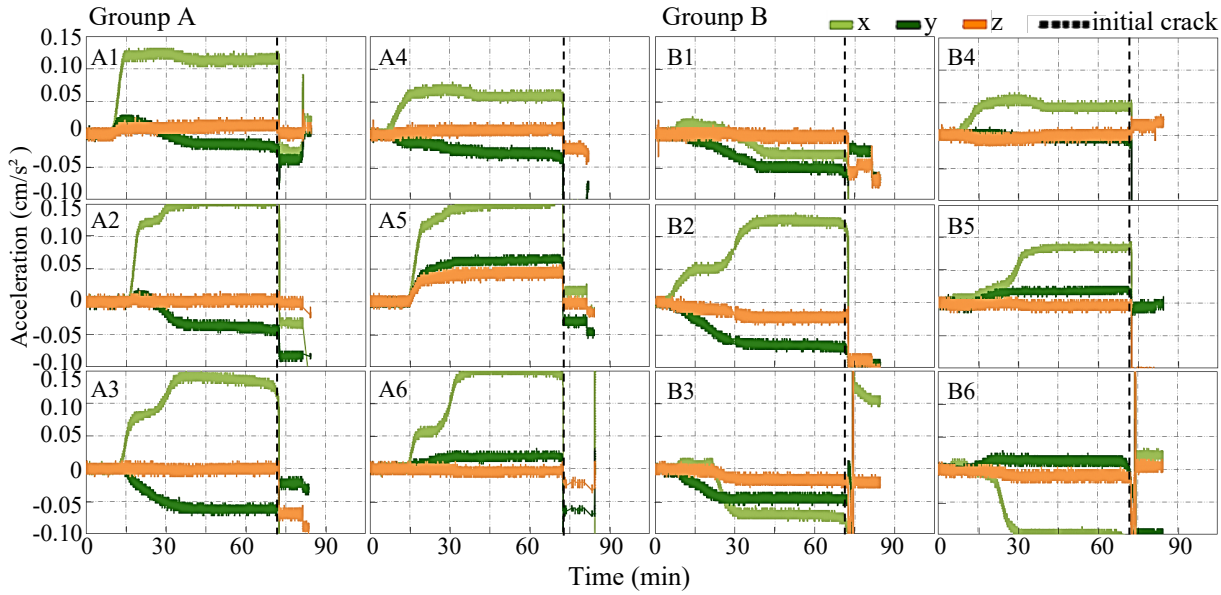

Fig. 2 Results of the internal deformation behavior of Case 1

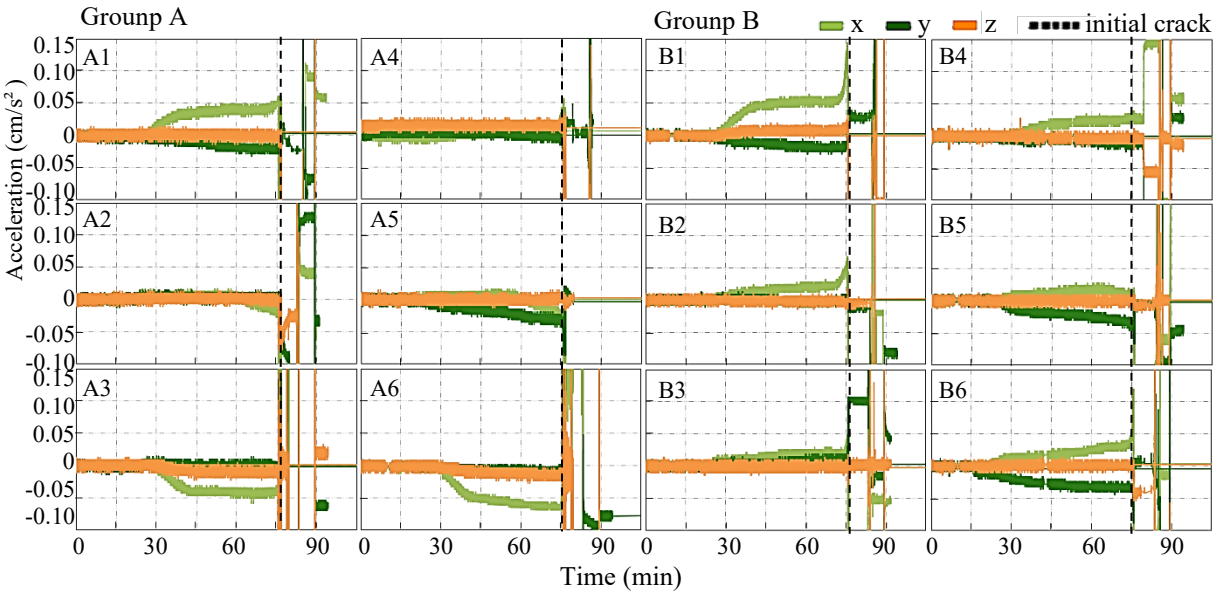

Fig. 3 Results of the internal deformation behavior of Case 2

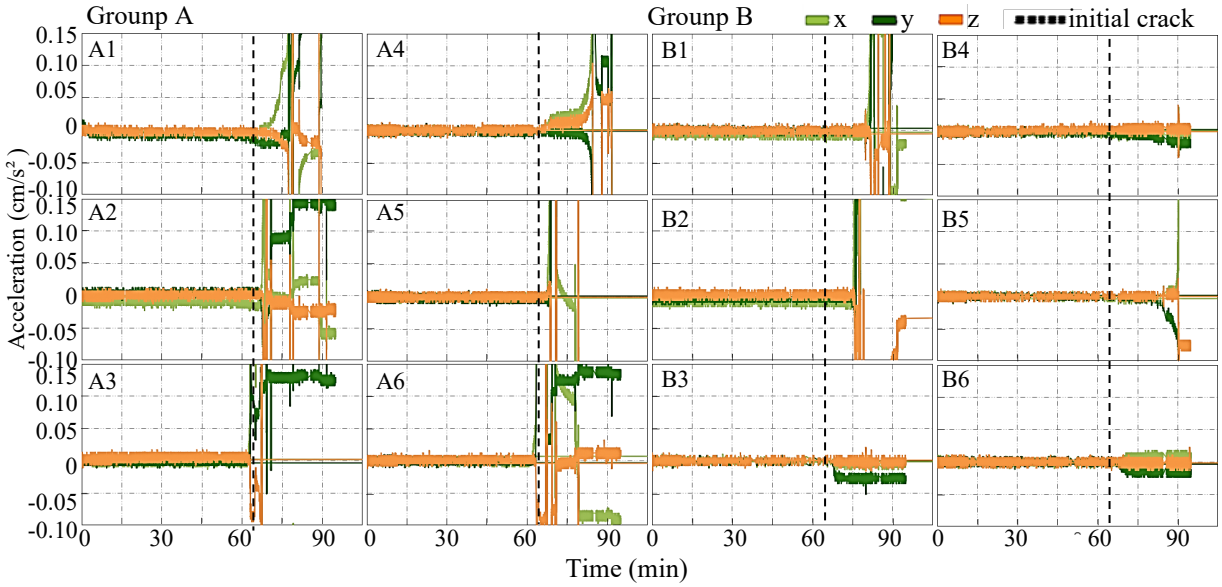

Fig. 4 Results of the internal deformation behavior of Case 3

three cases, the rate of change along the Z-axes was smaller than those along the X- and Y-axes. For example, in Case 1, Z-axis values at A3 and B1 were nearly constant with respect to the X- and Y-axes, whereas in Case 2, this contrast was more pronounced at observation points A1, A2, A4, A5, B2, B3, and B4. Thus, the deformation movements of the soil layer at these observation points resembled rotational rather than lateral movement.

For accelerometers installed at the same depth, we obtained similar trends but with different magnitudes at certain observation points. For example, in Case 1, the similar trends of variations were obtained for the X- and Y-axes at A1 and A2, the X-axes at A3 and A6 , etc. In Case 2, the similar trends of variations were obtained for the X-axes at A2 and A5 and X-axes at A3 and A6. Meanwhile, similar trend of variations was obtained at different depths for accelerometers at the same observation point. For example, in Case 1, the similar trend of variations was obtained for the Y-axes at A1 and B1, the X-axes at A4 and B4, etc. In Case 2, similar trends of variations were obtained for the X- and Y-axes at A1 and B1, A5 and B5 , etc. The deformation behavior showed it has a propagation range, the accelerometers which closer to the deformation point can recorded with larger variation. Therefore, for deformation behavior, it is not comprehensive to assess the stability of the whole slope by the measurements at a local point. In addition, for example, the deformation moves of A4 and B4, A2 and B2, located at different depths in the same location in Case 2, are more pronounced at depth than at shallow depths. These results show the measurement of deformation movements not only on the surface but also deep in the slope allows a better assessment of the stability of the slope. Also, the

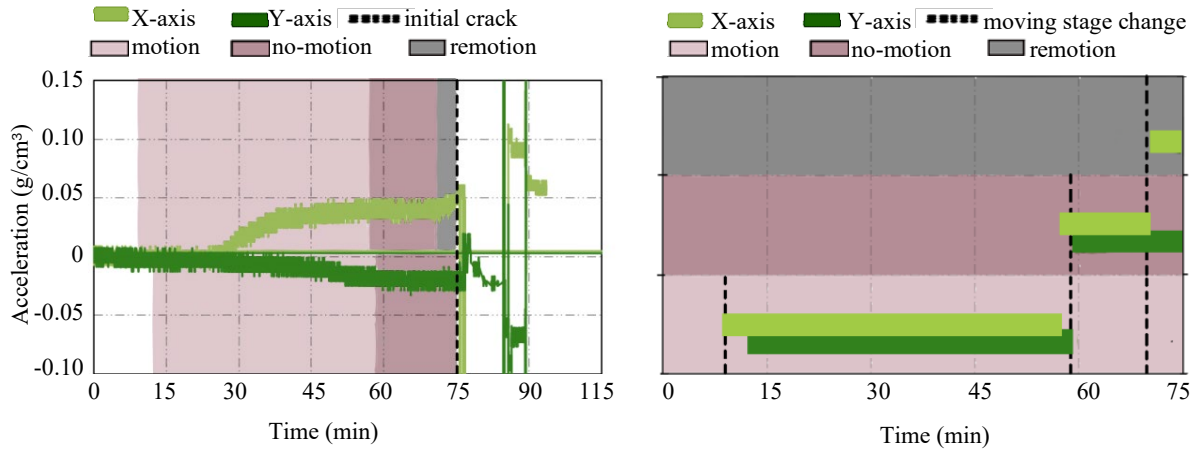

Fig.5 Examples of classification in the deformation stage.

measurement of multiple locations and multiple depths provides a better understanding of the changing conditions of the slope.

Moving stage classification of deformation behavior

When comparing the deformation behavior of each accelerator in the same case, it can be found that the deformation behavior can be divided into several different stages. We calculated the slope change of the measured values in the graphs of the experimental results of the deformation behavior, using the curve fitted to the average per unit time to assess whether the soil was moving or stationary at any given point in time.

The variation in three directions obtained by each accelerometer is not all the time in same state of motion. While the value in one direction is in a constant state, the value in the other direction could still be changing. When the value obtained in at least one axis does not stabilize and is still changing, the point where the accelerator is located is considered to be in motion.

As show in Fig.5, for example, in Case2-A1, the motion process of X axis can be divided into three-stage process: motion–stationary(no-motion)–remotion. The Y-axis, on the other hand, only goes through two phases: motion and stationery. The motion patterns of Case2-A1 can be classified as in the right side of Fig.5: The initial movement started 7 minutes after the rainfall and lasted until 59 min. 59 min to 71 min were stationary(no-motion) and after 71 min were observed to be in re-motion.

As mentioned above, the deformation behavior is more pronounced in soils possessing relatively loose structures, so we classify the results of the deformation behavior obtained in Case 1 and Case 2 in stages, that have a relatively low-density

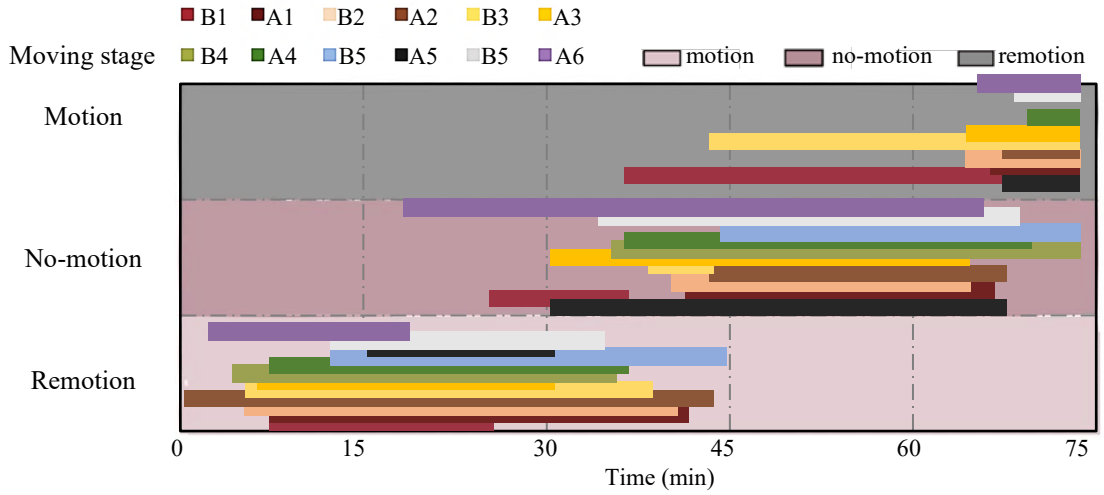

Fig.6 Classification of the deformation stage of Case1

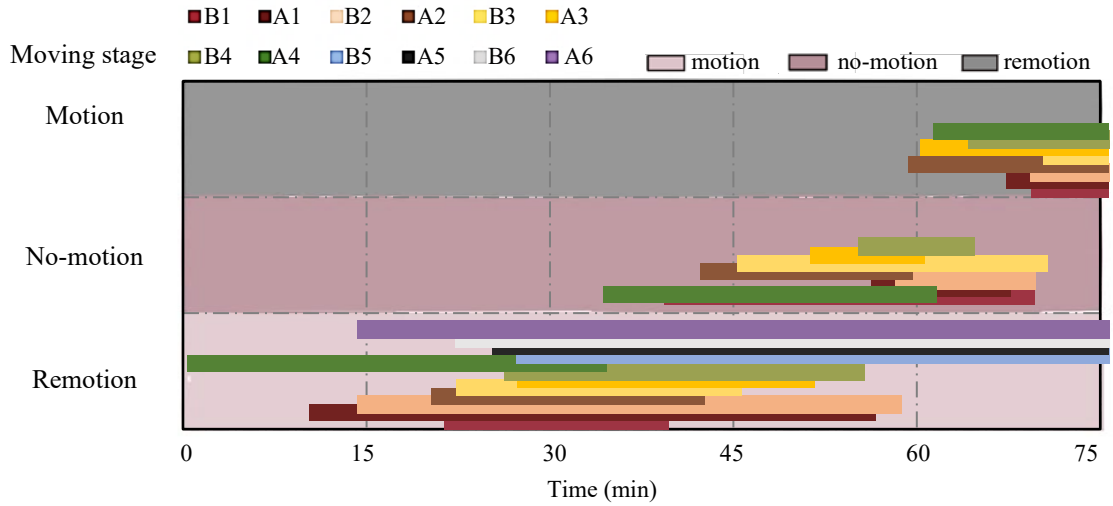

Fig.7 Classification of the deformation stage of Case1

soil.(Fig.6 ~ 7)

In Case 1, as rainfall proceeded, the recorded acceleration changes gradually stabilized, with less pronounced changes than those recorded during the previous phase. Except for B4 and B5, which stopped recording deformation behavior after stabilization at 36 and 37 min after the rainfall, respectively, all accelerators went through three-stage process: motion–stationary(no-motion). During the period of 45-65 minutes after the rainfall, almost all accelerators were in a stable state. On the other hand, and before this time, the deformation behavior of B1 located deep at the top of the slope and B3 at the foot of the slope were once again active. Near observation point 1, where accelerator B1 is located, we observed the occurrence of initial cracks.

In Case 2, all accelerometers observed deformation behavior 28 minutes after the onset of rainfall, and at A1, B1, A2, B2, A3, B3, A4, A5, B5, and A6 underwent a motion–stationary(no-motion)–remotion change as described above as the rainfall progressed. In, A5, B5, A6 and B6, at least one axis was observed to be continuously deforming until the initial crack occurred. Especially around the initial collapse, at the locations of observation points 5 and 6, the deformation behavior is continuously occurring.

It can be assumed that local changes will affect the overall force balance, and small-scale changes will cause a larger chain reaction. Therefore, local deformation appears to be an important trigger of overall slope collapse. It is also indicated that there is a higher probability of observing initial cracks in the vicinity of places where deformation is continuously occurring or where continuous deformation is observed again after settling down for a while.

Together, these results indicate that internal deformation movement reflected wide variation in the strength of the soil layers. In low-density soils structure, internal deformation behavior occurred after rainfall and before collapse; this was a continuous, readily observable process. Internal deformation behavior that spreads within a small distance. Deformation closer to the observation point had a greater impact and was more likely to alter the balance of forces within the soil layer at that point. Therefore, local deformation movement is an important factor that can trigger overall slope collapse. In low-density soils structure, deformation movement prior to initial cracking occurred in three stages. These stages can be used to estimate the potential collapse location for an unstable slope after the onset of rainfall.

CONCLUSION

In this study, we examined the characteristics of deformation behavior within a slope model during artificial rainfall. Our findings suggest that, in a low-density soil structure, deformation movement within the slope can serve as a criterion for predicting the location of initial slope collapse. These deformations are continuous, pronounced, and can be divided into several stages. The measurement of the deformation behavior inside the slope can be one of the initial criteria to determine the location of the initial cracking occurrence. The deformation has a certain propagation in distance, so the local deformation behavior can be considered as an important factor to trigger the overall collapse. In some instances, the deformation behavior at depth are more significant than those at the surface, and the measurement of deformation behavior at different depths can provide a better understanding of the stability of the slope.

The surface area of the experimental model used in this study was not large and accommodated a limited number of sensors. The detection of deformation movement at greater depths, and over a larger spatial scale, would be useful for designing more effective evacuation warning procedures to mitigate sediment damage from disasters.

REFERENCES

[1] Japan Ministry of Land and Transport Infrastructure, “Number of sediment-related disasters in 2018”, 2018.

[2] Muntohar Setyo Agus, “Rainfall infiltration: infinite slope model for landslides triggering by rainstorm”, Nat Hazards, vol.54, 2010, pp.967-984.

[3] Sasahara K. and Sakai N, “Shear Deformation Development and the Increase of Pore Pressure due to Rainfall Infiltration in Sandy Model Slope under Different Inclination”, Int. J. of GEOMAT, vol. 1, Oct. 2011, pp.64-70.

[4] Noki Sakai, “Advanced Trends in Slope Measurement”, National research institute for Earth science and disaster Prevention, 2016.

[5] Kazuhiko Nagata, “The Importance of Data Quality Control in Disaster Prevention and Mitigation”, Meteorological Agency Japan, 2010.

[6] Fujimoto, Masamitsu; Kosaki, Kenichiro; Baba, Nokia, “Flow characteristics of basement rock groundwater using tracers in weathered granite mountains.”, The Japanese Forest Society, 2013

11th Int. Conf. on Geotechnique, Construction Materials & Environment, Kyoto, Japan, 3-5 November 2021, ISBN: 978-4-909106063 C3051

THREE-DIMENSIONAL ANALYSIS OF GEOGRID REINFORCED FLEXIBLE PAVEMENT USING FINITE DIFFERENCE PROGRAM FLAC^{3D}

Rojimol J[1], Umashankar B[2]

[1]Department of Civil Engineering, IIT Hyderabad, India, [2] Department of Civil Engineering, IIT Hyderabad, India

ABSTRACT

India has the second-largest road network in the world after the United States. But most of the roads are less durable resulting in a large number of potholes, cracks, and ruts. In recent years, geosynthetics have created an impact on enhancing the life of the pavement. Numerous studies have been done on the application of geosynthetics on the flexible pavement to reduce rutting behavior and fatigue cracks. Laboratory and field studies have limitations such as cost and time constraints. These limitations can be overcome by making use of numerical models. This research focuses on the numerical analysis of biaxial geogrids in flexible pavement. Proper knowledge of geogrid-pavement layer interaction is essential to obtain an understanding of strains, stresses, and deflections in pavement layers. In this study, a three-dimensional model of the geogrid reinforced unpaved road is developed using the finite difference program - FLAC^{3D}. Appropriate constitutive models are selected for the pavement layers. Geogrid is modeled using a linear elastic 'geogrid' element in FLAC^{3D}. Pavement layer thicknesses in the analysis are taken as per the codal provisions of IRC: 37-2012. The study shows that geogrid is more efficient for settlement ratio (settlement under load with respect to width of loading) higher than 2% for weak subgrade. The optimal location of geogrid is proposed at one-third base thickness from the top of the surface of the pavement. This study is useful for construction sites where competent aggregates are not available and subgrade CBR is less than 5%.

Keywords Geogrids, optimal location, static loading, FLAC^{3D}

INTRODUCTION

Geosynthetics have been successfully applied in various civil engineering problems, especially to enhance the long-term performance of pavement. Construction sites where competent aggregates are not readily available, geosynthetic reinforcement technique can be a viable option. Commonly used geosynthetics in pavement applications include geotextiles, geogrids, and geocells. Researchers have examined the improvement in structural performance of pavement using these products via large-scale laboratory tests, full-scale field tests, and numerical modeling. Perkins [11] highlighted that geogrid when placed in base layer improved the performance of pavements. It was found that stabilization of pavements using geosynthetic reinforcement has led to a reduction in granular base layer thickness ([4], [6], [9], [11]), rutting and fatigue strains ([3], [14]), and reflective cracking ([1]), thereby increasing the pavement service life.

Laboratory and full-scale field tests are often preferred but are subjected to cost and time constraints. With the development of advanced computational facilities, numerical modeling of pavement can aid in calculating strains, stresses, and deflections occurring in pavement layers and properly study the geogrid-pavement layer interaction under wheel load. Consequently, time-consuming laboratory and field tests can be avoided. There are several numerical methods used by researchers such as Multilayer elastic theory, Finite difference methods (FDM), Finite element methods (FEM), Boundary element methods (BEM), etc., to estimate stress, strain and surface deformation in pavement.

Duncan [2] did pioneering work on the analysis of unreinforced flexible pavement using the FEM technique. He validated the model with elastic solutions and highlighted that this method is also capable of simulating the actual behavior of the pavement with inherent nonlinear material properties. Researchers have used FEM softwares, such as ANSYS, ABAQUS, ADINA, PLAXIS, etc., for numerical modeling of pavement. Wathugala [14] modeled reinforced pavement using finite element software ABAQUS by placing geogrid at the base-subgrade interface and found significant reduction in rut depth. Ling [7] used PLAXIS^{2D} to perform the analysis of reinforced pavement subjected to static, cyclic, and dynamic loading. Leng [6] used ABAQUS to conduct analysis of geogrid reinforced granular bases overlying soft subgrade. Saad [16] had used ADINA^{TM} for three-dimensional finite element analysis of geosynthetic reinforced flexible pavement subjected to dynamic loads. It was recommended that geogrid should be kept at the lower one-third of the

base layer thickness irrespective of subgrade strength. Ahirwar [13] conducted analysis of reinforced pavement using PLAXIS^{2D} and Mohr-Coulomb model was used for various pavement layers.

This study considers finite difference method for the analysis of unpaved road subjected to wheel loading. Finite difference method is one among the numerical methods used in the analysis of flexible pavement. Fast Lagrangian Analysis of Continua (FLAC3D), being an explicit FDM program, solves all equation of motion and has a variety of nonlinear constitutive models suitable for modeling nonlinear stress-strain characteristics of pavement materials. Goud [10] conducted numerical analysis of reinforced unpaved road using two-dimensional finite difference program FLAC^{2D}. Three dimensional analysis provides a better understanding of behavior of pavement under wheels of different configuration [16]. However, the present study focuses on the analysis of unreinforced and reinforced unpaved roads under stationary wheel loading. In this study, explicit finite difference program FLAC^{3D} is used to develop a three-dimensional comprehensive model of geogrid reinforced unpaved road. This study uses a simple constitutive material model- Mohr-Coulomb model -for modeling the nonlinearity of base and subgrade. The developed numerical model is subjected to static loading. The study also focusses on suggesting the optimal position of geogrid based on the load improvement factor and the effect of axial stiffness on efficiency of geogrid reinforcement. This study can be further used for analysis under various wheel configurations and moving wheel loads and considering more advanced material models for different pavement layers.

MATERIAL PROPERTIES

A typical unpaved road section consists of granular base course layer and subgrade layer. One of the challenges in constructing unpaved roads is the availability of competent aggregate for granular bases. In this study, typical marginal aggregate with elastic modulus of 50 MPa is taken. Thickness of aggregate layer is chosen as 250 mm, as recommended by Indian Road Congress [5]. According to [7], [11], geosynthetics have shown predominant effect in improving weak subgrade. Therefore, relatively soft subgrade with elastic modulus of 10 MPa with thickness 750mm is considered. The material properties of pavement layers and geogrid are chosen from a similar study [6]. Table 1 gives the properties of the pavement layers. Axial stiffness of geogrid is a major factor in finding the efficiency of geogrid application in pavement [13], [10]. Properties of various geogrid reinforcements used in the model are given in Table 2. Geogrid-soil interface properties are chosen based on Hedge [17] and Itasca [18].

Table 1. Properties of base course and subgrade

Property	Granular base	Subgrade
Material model	Mohr-Coulomb	Mohr-Coulomb
Mass density, ρ_d, (kg/m^3)	2100	1800
Elastic modulus, E, MPa	50	10
Poisson's ratio, ν	0.35	0.42
Cohesion, c, kPa	35	20
Friction angle, ϕ, degrees	40	4.9
Dilation angle, ψ, degrees	10	0

Table 2. Properties of various reinforcements

Properties	Reinfor-cement 1	Reinfor-cement 2	Reinfor-cement 3
Material model	Linear-elastic	Linear-elastic	Linear-elastic
Elastic modulus, E, MPa	1e8	4e8	8e8
Poisson's ratio, ν	0.35	0.35	0.35
Thickness, t, mm	3	3	3
Coupling spring cohesion, cs_coh, kPa	30	30	30
Coupling spring Friction angle, cs_fri, deg.	25	25	25

NUMERICAL MODELING

FLAC^{3D} is capable of modeling complex behavior of continuum models including non-linear material behavior, large displacements and strains. Considering the symmetry, one-fourth section of unpaved road is modelled. Boundary conditions are chosen so that fixed support is provided at the bottom and roller support at left and right boundaries. Lateral boundaries are kept at 0.75 m from center and bottom boundary is kept at 1.0m vertically down as in [6]. Fig. 1 shows the numerical model developed in FLAC^{3D}.

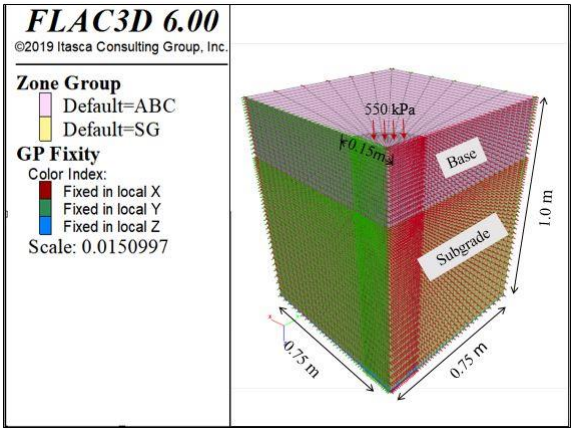

FIG.1 Numerical model in FlAC^{3D}

Granular base course and subgrade are modelled using the Mohr-Coulomb plasticity model. Modeling of biaxial geogrid is done using linear elastic 'geogrid' element available in FLAC^{3D}. Uniform loading of 550 kPa is applied. Large-strain mode is activated in order to account of the significant plastic deformations by unpaved road [12]. The convergence of the model in FLAC^{3D} is ensured by finer discretization of mesh and satisfying the criterion of reaching maximum unbalanced force ratio of 1e-6 for the equilibrium. In the analysis of reinforced pavement models, a refined mesh size around the interface equal to 0.8 times the mesh size of surrounding region is used in order to study the effect of geogrid. Vertical displacement contours for unreinforced and reinforced models are shown in Fig. 2 and 3. Unreinforced and reinforced pavement model developed is validated with available study in literature [6] by comparing the maximum surface displacements as given in Fig. 4.

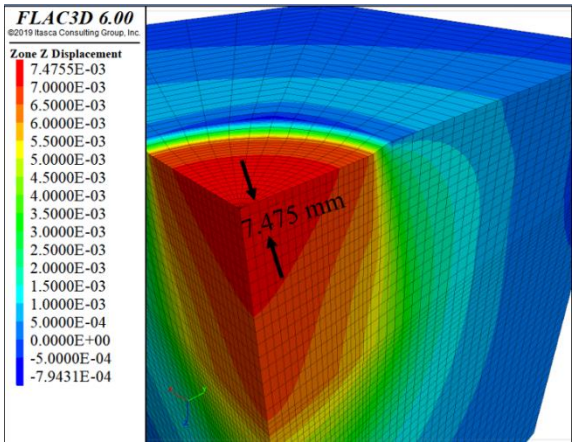

FIG. 2. Vertical displacement contours of unreinforced unpaved section

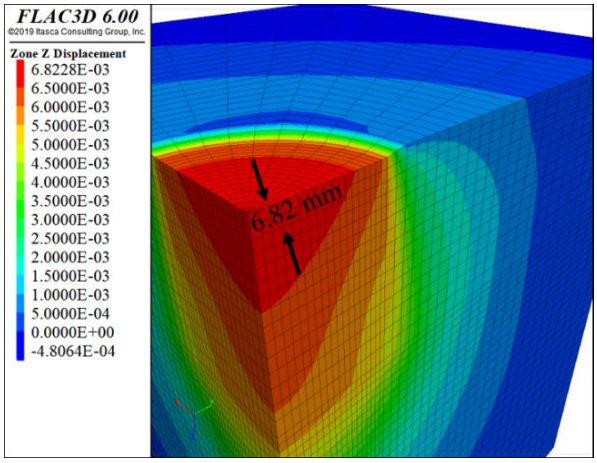

FIG. 3. Vertical displacement contours of reinforced unpaved section

Leng [6] has placed geogrid at the interface of the base and subgrade. Whereas this study focusses on placing the geogrid at various locations in base layer in order to study the optimal location at which maximum efficiency of geogrid is observed. This study is useful for pavements with thicker granular bases overlying soft subgrades [8]. In addition, reinforcement stiffness is varied to find the range of stiffness for which settlement reduces.

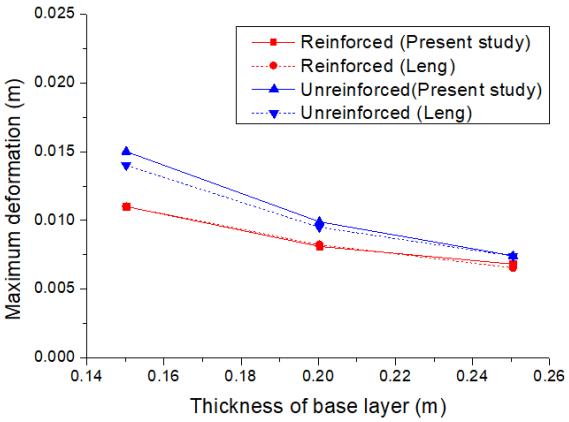

FIG. 4. Comparison of maximum surface displacement from this study with Leng [6].

RESULTS AND DISCUSSION

Analysis shows that geogrid reinforced unpaved section have lesser deformation compared to unreinforced unpaved sections for given base layer thickness under same loading. Fig. 5 shows the contour of vertical displacement of unreinforced and reinforced pavement section under 700 kPa. It is found that presence of geogrid has reduced maximum surface deformations by 12%.

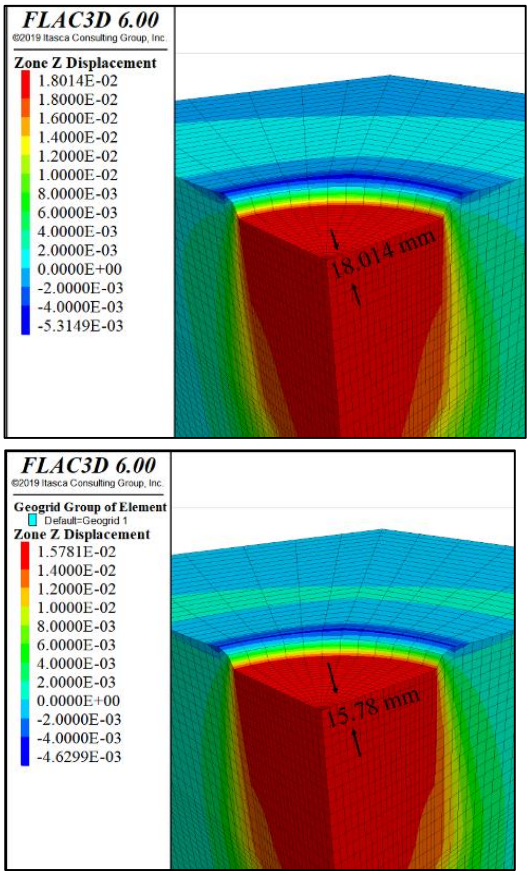

FIG. 5. Comparison of vertical displacements at 700 kPa for a) unreinforced and b) reinforced pavement model

Fig. 6 shows the bearing pressure *vs.* settlement ratio at various locations of geogrid in base layer. Inclusion of geogrid was found to reduce the surface deformations. It was observed that as load increases, the effect of geogrid was more significant. In addition, geogrid was more efficient at higher settlement ratio (greater than 2%). Geogrid was placed at three locations, viz., upper one-third base, mid depth base, and at the interface of base and subgrade. This was shown to improve the load-settlement behavior. The optimal location of geogrid in base layer is very important to assess the maximum benefit imparted by geogrid. In this study, placing the geogrid at upper one-third resulted in least deformations (Fig. 6).

Axial stiffness of reinforcement was varied by keeping geogrid at proposed location. As the axial stiffness of reinforcement increases, the load taken by the pavement for a given-settlement ratio was found to increase. Various geogrid stiffness were used for the study, viz., 300, 1200, 2400 kN/m. Fig. 7 shows load vs settlement ratio for varied geogrid stiffness. Stiffness above 1200 kN/m showed significant effect on load-settlement curve. Load improvement factor is defined as the ratio of the bearing pressure under footing of reinforced section to unreinforced section

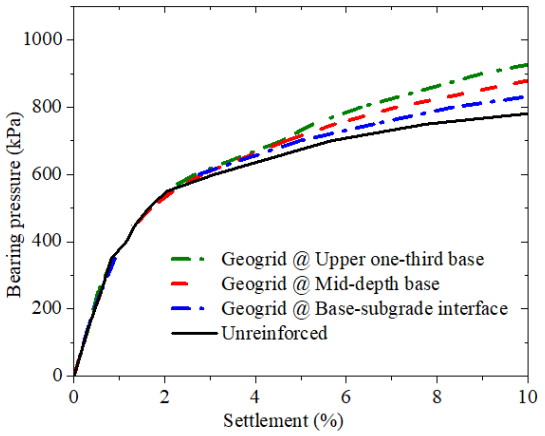

under for the same settlement.

FIG. 6. Load-settlement ratio curve for unreinforced and reinforced unpaved road

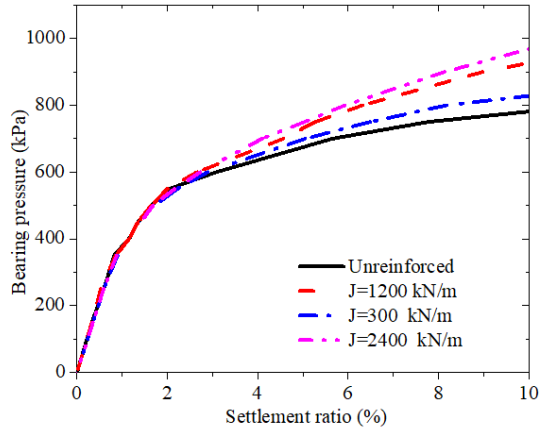

FIG. 7. Load-settlement ratio curve with various geogrid axial stiffness

Table 3 shows the load improvement factor for various reinforcement axial stiffness. Load improvement factor is more significant for settlement ratio higher than 2% as reported in [12]. For axial stiffness equal to 300 kN/m, the load improvement factor ranges from 1.03-1.06%. Goud [10] observed a load improvement factor of 1.06 for settlement ratio equal to 8% for the case of reinforcement with axial stiffness of 292 kN/m, which matches with present study. Whereas at higher stiffnesses of 1200 and 2400 kN/m, the load improvement factor varies from 1.05-1.19% and 1.11-1.25%, respectively. For unpaved roads, Goud [10] has reported load improvement factors ranging from 1.08 to1.28 for settlement ratios of 4-16% corresponding to geogrid axial stiffness ranging from 292-29,200 kN/m. Thus, a stiffness of 1200 kN/m give better performance and hence suitable for pavement with marginal aggregates.

Table 3. Load improvement factor for various reinforcement stiffness

Sl. No	Settlement ratio (%)	Load improvement factor		
		Reinforcement (J=300 kN/m)	Reinforcement (J=1200 kN/m)	Reinforcement (J=2400 kN/m)
1	4	1.03	1.05	1.10
2	6	1.05	1.12	1.15
3	8	1.06	1.15	1.19
4	10	1.06	1.19	1.25

CONCLUSIONS

Three-dimensional analysis of unreinforced and reinforced unpaved model was conducted using FLAC^{3D}. The reinforced unpaved section showed 12% lesser surface deformations in comparison with unreinforced section corresponding to a settlement ratio equal to 5%. The optimal location of geogrid in granular base layer is proposed as one-third depth from the surface. Another characteristic governing the reinforcement efficiency is choosing the appropriate axial stiffness of geogrid. As per the present study, reinforcement stiffness higher than 1200 kN/m was found to be more efficient than lower stiffness values. Judiciously choosing the optimal location and geogrid axial stiffness can save huge amount of construction cost and time. This study is relevant at places where competent aggregate material is not readily available and for soil subgrade of low CBR ranging between 2 and 5%. Also, the proposed research can be used for advanced material models and study the behavior under multiple wheel loads.

REFERENCES

[1] Khodaii A., Fallah S., and Nejad F.M., Effects of geosynthetics on reduction of reflection cracking in asphalt overlays, Geotext. Geomembr., Vol. 2, No.1, 2009, pp. 1-8.

[2] Duncan J.M., Monismith C.L., and Wilson E.L., Finite element analyses of pavements. Highway Research Record 228, Transportation Research Board, No.38, 1968, pp. 18–33.

[3] Giroud J.P., and Han J., Design method for geogrid-reinforced unpaved Roads. 1: Development of design method, J. Geotech. Eng., Vol. 130, No. 8, 2004, pp. 775-786.

[4] Haas R., Walls J., and Carroll R.G., Geogrid reinforcement of granular bases in flexible pavements, Transportation Research Record. 1188, No.1, 1988, pp. 19-27.

[5] IRC: 37-2012. Guidelines for the design of flexible pavements, Indian Roads Congress, New Delhi. 2012.

[6] Leng J., & Gabr M., Numerical analysis of stress-deformation response in reinforced unpaved road sections, Geosynthetics International, Vol. 12, No. 2, 2005, pp. 111-119.

[7] Ling H., and Liu H., Finite element studies of asphalt concrete pavement reinforced with geogrid. J. Eng. Mech., ASCE, Vol. 129, No. 7, 2003, pp. 801–811.

[8] Mousavi S.H., Gabr M.A. and Borden R.H. Optimum location of the geogrid reinforcement in unpaved road, Can. Geotech. J., Vol. 54, No. 7, 2017, pp.1047-1054

[9] Abu-Farsakh M.Y., Akond I., and Chen, Q., Evaluation of Performance of Geosynthetic-Reinforced Unpaved Roads using Plate Load Tests, 93rd TRB Annual Meet, 2014.

[10] Goud G.N., Mouli S. and Umashankar B., Numerical modelling of geosynthetic-reinforced unpaved roads using FLAC 2D, Proceedings of the 11th International Conference on Geosynthetics, South Korea, 2018.

[11] Perkins S.W., and Edens M.Q., Finite element and distress models for geosynthetic-reinforced pavements, Int. J. Pavement Eng., Vol. 3, No. 4, 2002, pp. 239-250.

[12] Benmebarek S., Remadna M.S., and Belounar L., Numerical modeling of reinforced unpaved roads by geogrid, Turkish Online Journal of Science and Technology, Vol. 3, No. 2, 2013, pp. 109-115.

[13] Ahirwar S.K., and Mandal J.N., Finite Element Analysis of Flexible Pavement with Geogrids, Transportation Geotechnics and Geoecology, Procedia Eng., 189, 2017, pp. 17-19.

[14] Wathugala G.W., Huang B., and Pal S., Numerical simulation of geogrid reinforced flexible pavements, Transportation Research Record 1534, Washington, D.C., 1996, pp. 58–65.

[15] Zornberg J.G., Advances in the use of geosynthetics in pavement design, Geosynthetics India, 2011, pp. 3-21.

[16] Saad B., Mitri H., and Poorooshasb H., Three-dimensional dynamic analysis of flexible

conventional pavement foundation, J. Transp. Eng., Vol. 131, No. 6, 2005, pp. 460-469.
[17] Hegde A., and Sitharam T.G., 2015a. 3-Dimensional numerical modelling of geocell reinforced sand beds. Geotext. Geomembr., Vol. 43, No. 2, pp. 171–181.
[18] Itasca Consulting Group, I., FLAC3D-Fast Lagrangian Analysis of Continua in Three Dimensions, Version 6.0 User's Guide. Minneapolis, USA. 2019

11th Int. Conf. on Geotechnique, Construction Materials & Environment,
Kyoto, Japan, 3-5 November 2021, ISBN: 978-4-909106063 C3051

NUMERICAL STUDY ON THE AXIAL AND RADIAL SWELLING BEHAVIORS OF UNSATURATED COMPACTED BENTONITE

Shinya Tachibana[1], Daisuke Hayashi[2], Tomoko Ishii[2], Tomohide Takeyama[3] and Atsushi Iizuka[1]

[1]Research Center for Urban Safety and Security, Kobe University, Japan
[2] Radioactive Waste Management Funding and Research Center, Japan
[3]Graduate School of Engineering, Kobe University, Japan

ABSTRACT

In this study, the swelling behavior with swelling limit of unsaturated bentonite specimen according to the direction of swelling, i.e. limited axial and radial swelling, is analytically investigated through unsaturated soil/water coupled finite element analyses. The results of the analysis, which includes changes in the distribution of dry density in the specimen formed in the direction of swelling and changes in swelling pressures generated not only in the same direction as the swelling direction that starts to generate after the gap is filled but also in the direction perpendicular to the swelling direction, are presented. The analysis results show that the distribution of dry density and swelling pressure in the specimen differs depending on the direction of swelling, even if the bentonite specimen reaches a saturated and equilibrium state after gap filling and has same average dry density and dimension. In the case of radial swelling, it is shown analytically that each of the three principal stresses forms a non-uniform distribution in the radial direction of the specimen.

Keywords: Bentonite; Swelling; Finite element Analysis; Elasto-plastic constitutive law

INTRODUCTION

Compacted bentonite is expected to be used as an engineered barrier or backfill in radioactive waste repositories and is part of a multi barrier system that slows the migration of radionuclides from the waste body. When blocks of compacted bentonite are installed as a buffer material and stacked around the waste body, gaps are created between the blocks or between the blocks and the surrounding host rock or waste body. Although such gaps, referred to as "technological voids", can become water channels allowing groundwater flow if they remain intact, one of the reasons to utilize bentonite as a buffer material is that it has a sealing function to close the gaps owing to its saturation-induced swelling with groundwater infiltration.

There has been considerable interest in quantitatively understanding the state changes of bentonite originating from the presence of gaps, and several experimental efforts have been reported [1-7]. These studies have focused on the changes in the dry density distribution within the bentonite, the associated permeability of the bentonite and the swelling pressure acting on the surfaces in contact with the bentonite, during the process of filling the gaps and afterwards until the bentonite reaches equilibrium. The results of these experimental studies have shown that the average dry density of bentonite decreases during the swelling process to close the gaps. It has also been measured that this reduction generally occurs first in the vicinity of the gaps, i.e. close to the seepage surface, resulting in the formation of a non-uniform dry density distribution within the bentonite. After the gap is closed, the excess pore water pressure (or suction) gradient in the bentonite dissipates and the dry density distribution becomes more uniform, but some inhomogeneity seems to remain even after the bentonite is saturated and the mechanical equilibrium is reached. The presence of gaps has been found to affect, at the same time, the mechanism of swelling pressure generation.

In this study, finite element simulations of problems related to saturation-induced swelling and gap filling of cylindrical unsaturated compacted bentonite specimens were carried out to investigate analytically the differences in the development of non-uniform distribution of dry density and the swelling pressure in each direction depending on the swelling direction of the specimen due to the position of the gap. Two types of boundary conditions were dealt with, i.e. both axial swelling with an upper gap and radial swelling with an outer side gap. In order to focus on the effect of swelling direction, the initial and geometrical conditions were set so that the initial volume and initial dry density of the bentonite specimens, as well as the specimen volume and average dry density after swelling, are common.

ANALYSIS METHOD OF UNSATURATED SOIL/WATER COUPLING PROBLEM

The finite element code DACSAR-I [8] was used to simulate the limited axial and radial swelling of unsaturated compacted bentonite specimens. The code is based on the theoretical framework of

unsaturated soil mechanics [9], capable of dealing with the coupling problem in which the soil deforms under the condition where its pore is partially saturated with water. In a general unsaturated coupling problem, the fields of pore-water and pore-air pressures are approximately obtained in addition to the displacement field by simultaneously solving the spatially discretized equations for the weak form of the equilibrium equation and the continuity equations for pore water and pore air. This study, however, assumes the fully drained condition for pore air where the pore-air pressure is always equal to the atmospheric pressure everywhere in the specimen, allowing us to disregard Darcy's law and the permeability coefficient, which govern the pore air flow, in carrying out the analysis. The following sections give an overview of the material models employed in the analysis.

Elasto-plastic constitutive model for unsaturated bentonite

The elasto-plastic constitutive model for saturated bentonite proposed by Tachibana et al. [10] was extended to describe the mechanical behavior of the unsaturated state and used in the analysis. The yield surface of the model which has an elliptical shape in the effective stress space, analogous to the modified Cam-clay model [11], can be formulated as

$$f\left(p', q, p'_{\mathrm{c}}, p'_{\mathrm{s}}\right) = \frac{q^2}{\tilde{M}^2} + \left(p' - p'_{\mathrm{c}}\right)\left(p' - p'_{\mathrm{s}}\right) = 0 \qquad (1)$$

where $\tilde{M}$ is a material parameter determining the ellipticity of yield surface, p' is an effective mean stress ($= \mathrm{tr}\boldsymbol{\sigma}'/3$), q is a stress deviator ($= \sqrt{3/2}\|\boldsymbol{s}\|$). $\boldsymbol{\sigma}'\left(=\boldsymbol{\sigma}^{net} + sS_{\mathrm{e}}\boldsymbol{1}\right)$ and $\boldsymbol{s}\left(=\boldsymbol{\sigma}' - p'\boldsymbol{1}\right)$ are the effective stress tensor and its deviatoric part, respectively, where $\boldsymbol{\sigma}^{net}$ is a net stress tensor (equivalent to the total stress $\boldsymbol{\sigma}$ in this study), s is a matric suction ($= p_{\mathrm{a}} - p_{\mathrm{w}}$; p_{a}: pore air pressure and p_{w}: pore water pressure), and S_{e} is an effective degree of saturation ($= \left(S_{\mathrm{r}} - S_{\mathrm{r0}}\right)/\left(1 - S_{\mathrm{r0}}\right)$; S_{r}: degree of saturation and S_{r0}: its residual value at the state where $s \to \infty$).

Adopting the idea of the model proposed by Ohno et al. [12] that the size of the yield surface depends on both plastic volumetric strain $\varepsilon_{\mathrm{v}}^{\mathrm{p}}$ and effective degree of saturation S_{e}, the following hardening law was formulated for the evolution of p'_{c} and p'_{s}:

$$p'_{\alpha} = p'_{\alpha}\left(\varepsilon_{\mathrm{v}}^{\mathrm{p}}, S_{\mathrm{e}}\right) = \bar{p}'_{\alpha}\left(\varepsilon_{\mathrm{v}}^{\mathrm{p}}\right) \times \xi_{\alpha}\left(S_{\mathrm{e}}\right);\ \alpha = \mathrm{c,s} \qquad (2)$$

In Eq. (2), $\bar{p}'_{\mathrm{c}}$ and $\bar{p}'_{\mathrm{s}}$ were formulated in a form similar to the Cam-clay model to describe the plastic volume change along the normal consolidation line (NCL) and plastic rebound line (PRL) shown in Figure 1, respectively, as follows:

$$\bar{p}'_{\alpha} = \bar{p}'_{\alpha 0} \exp\left(\frac{1 + e_{\alpha 0}}{\lambda - \kappa}\varepsilon_{\mathrm{v}}^{\mathrm{p}}\right);\ \alpha = \mathrm{c,s} \qquad (3)$$

where λ is a compression index denoting the slope of both NCL and PRL, κ is a swelling index denoting the slope of 'elastic' swelling line, $\bar{p}'_{\mathrm{c0}}$ and $\bar{p}'_{\mathrm{s0}}$ are initial values of $\bar{p}'_{\mathrm{c}}$ and $\bar{p}'_{\mathrm{s}}$, respectively. e_{c0} and e_{s0} are the reference void ratios corresponding to $\bar{p}'_{\mathrm{c0}}$ on the NCL and $\bar{p}'_{\mathrm{s0}}$ on the PRL, respectively.

ξ_{c} and ξ_{s} in Eq. (2) are parameters that control the expansion/shrink of the yield surface due to the contribution of effective degree of saturation, and are formulated by the following equations, respectively:

$$\xi_{\mathrm{c}} = \exp\left[\left(\beta\left(S_{\mathrm{e}}\right) - 1\right)\ln\frac{1+\zeta}{\theta+\zeta}\right];\ \left(\xi_{\mathrm{c}} \geq 1\right) \qquad (4)$$

$$\xi_{\mathrm{s}} = \exp\left[\left(\beta\left(S_{\mathrm{e}}\right) - 1\right)\ln\frac{\zeta}{\theta+\zeta}\right];\ \left(0 < \xi_{\mathrm{s}} \leq 1\right) \qquad (5)$$

where ζ is a material constant which determines the ratio of $\bar{p}'_{\mathrm{c}}$ to $\bar{p}'_{\mathrm{s}}$, i.e $\bar{p}'_{\mathrm{c}}/\bar{p}'_{\mathrm{s}} = (1+\zeta)/\zeta$. θ is also a material constant which determines the position of elastic swelling line as shown Fig. 1. It is noted that the elastic swelling line is defined as a straight line connecting the points of $\bar{p}'_{\mathrm{c}}$ on NCL and $\bar{p}'_{\mathrm{s}}$ on PRL in $e - \ln p'$ space at any time. Therefore, the swelling index κ is naturally modelled as a function of the degree of saturation and is required to satisfy the following relation, in the combination with Eqs. (4) and (5), as

$$\kappa = \kappa\left(S_{\mathrm{e}}\right) = \bar{\kappa}/\beta\left(S_{\mathrm{e}}\right) \qquad (6)$$

where the function β determines the slope of elastic swelling line depending on the effective degree of saturation. In order for κ to reduce $\bar{\kappa}$ at a fully saturated state, the function β has to satisfy the condition $\beta = 1$ at $S_{\mathrm{e}} = 1$. In addition, β is required to monotonously increase according to the decrease of S_{e} since the model assumes the expansion of yield surface due to desaturation. Thus, the function β was formulated as a candidate satisfying the above-mentioned requirement in the form

$$\beta = \beta\left(S_{\mathrm{e}}\right) = \alpha\left(1 - S_{\mathrm{e}}^{\,l}\right) + 1 \qquad (7)$$

where α and l are input parameters; the former determines the maximum magnification ratio of yield surface at a driest state ($S_e = 0$), while the latter controls the degree of influence of S_e on the swelling index κ .

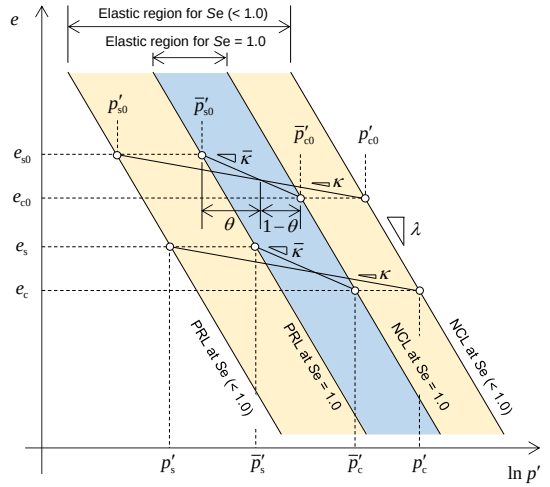

Fig. 1 Evolution of elastic region with change in saturation.

The following nonlinear elastic constitutive relationship, consistent with the elastic swelling line with the dependence of effective degree of saturation described above, was used.

$$\overset{\nabla}{\boldsymbol{\sigma}}' = \boldsymbol{D}^{\mathrm{e}} : \boldsymbol{d}^{\mathrm{e}} - K_{\mathrm{Se}} \dot{S}_{\mathrm{e}} \boldsymbol{1} \tag{8}$$

$$\boldsymbol{D}^{\mathrm{e}} = \left(K - \frac{2}{3} G \right) \boldsymbol{1} \otimes \boldsymbol{1} + 2G \boldsymbol{I} \tag{9}$$

$$K_{\mathrm{Se}} = -\frac{1}{\beta} \frac{\partial \beta}{\partial S_{\mathrm{e}}} p' \ln \frac{(1+\zeta)\, p'}{(\theta+\zeta)\, \bar{p}'_{\mathrm{c}}} \tag{10}$$

in which the elastic bulk modulus and the shear modulus are respectively given by

$$K = \frac{1+e_{\mathrm{c0}}}{\kappa} p' \quad \text{and} \quad G = \frac{3(1-2\nu')}{2(1+\nu')} K \tag{11), (12}$$

where ν' is Poisson's ratio.

In the elastic state, where the current stress is located inside the yield surface, Eq. (8) is used as the constitutive relation. On the other hand, in the elasto-plastic state, the elasto-plastic constitutive relation derived by imposing the consistency condition on the yield surface and applying the associated flow rule is used. The derivation of the constitutive relation is omitted for the sake of space, but it can be derived through the similar procedure to in the general framework of elasto-plasticity theory.

Permeability model for pore water flow

The flow of pore water is governed by the Darcy's law. In this study, we simply considered only the dependence of the void ratio and adopted the following permeability model proposed by Börgesson et al. [13].

$$k = k_0 \left(e / e_0 \right)^{\lambda_{\mathrm{k}}} \tag{13}$$

where k_0 is the hydraulic conductivity corresponding to the reference void ratio e_0 . λ_{k} is a material parameter that controls the dependence of the void ratio on the hydraulic conductivity.

Soil-water characteristic curve model

Among various models of soil-water characteristic curve (SWCC) which describe the relationship between the soil matric suction and the degree of saturation, the logistic curve model proposed by Sugii and Uno [14] was used. The curve is characterized by the following equation.

$$S_{\mathrm{r}} = S_{\mathrm{r0}} + \left(1 + S_{\mathrm{r0}}\right) \Big/ \left(1 + s^B \exp A\right) \tag{14}$$

where A and B are material parameters that determine a shape of SWCC. Since the present study basically deals with a monotonically increasing response of degree of saturation, the hysteresis of soil-moisture characteristics was not considered.

NUMERICAL SIMULATION OF LIMITED AXIAL AND RADIAL SWELLING

The simulation was carried out by setting ideal and well-defined boundary conditions in which water infiltration and deformation occur in either axial or lateral direction of a cylindrical unsaturated compacted bentonite specimen. The mixture of Na-bentonite (Kunigel V1) and silica sand, in a proportion of 70/30 in dry mass and with a specific gravity of 2.736, was assumed to be the material to be analyzed.

Analysis condition and input parameters

Fig. 2 show the geometric and boundary conditions for axial and radial swelling. In axial swelling, the diameter remains constant and the height changes, while in radial swelling, the height remains constant and the diameter changes. In both cases, the initial dry density of the bentonite specimen was set to 2.0 Mg/m^3, and the initial dimensions were set so that the swollen bentonite specimen was 25 mm high, 40 mm in diameter, and had the average dry

density of 1.6 Mg/m^3 after filling the gap. The friction with the inner wall of the container was not considered in the simulation. The permeable surface was set to be only on the top of the specimen for axial swelling and only on the side of the specimen for radial swelling. By setting the pore water pressure to zero on the permeable boundary, a hydraulic gradient is created and water infiltration is promoted as long as there is suction (negative pore water pressure) in the specimen. The state changes at the numbered locations in order of proximity from the permeable boundary will be of interest in the next section.

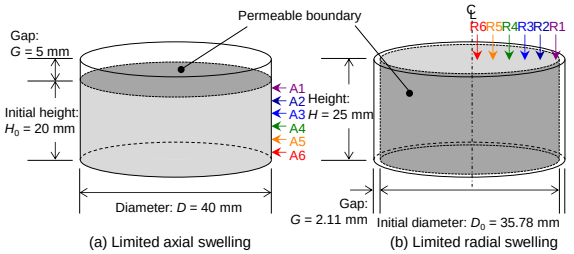

Fig. 2 Geometry and boundary conditions.

Table 1 summarizes the values of the material parameters used in the analysis. Among the parameters, those related to the elasto-plastic constitutive model were determined from the results of consolidation tests, undrained shear tests, and swelling pressure tests on the silica sand mixed bentonite to be analyzed. The parameters related to hydraulic conductivity and SWCC were also determined from the results of hydraulic conductivity and water retention tests on the materials, respectively.

The initial condition of the bentonite specimens is summarized in Table 2. The specimen was initially uniform and its stress state was assumed to be isotropic. The initial value of suction was determined based on SWCC, corresponding to the initial value of degree of saturation. Since a stress-free initial stress state was assumed ($p = p^{net} = 0$), the initial effective mean stress was calculated from the product of suction and effective degree of saturation from Eq. (1).

Numerical results

Fig. 3 shows the evolutions of the specimen height in axial swelling and the specimen radius in radial swelling. For reference, the results of the calculation without the swelling limit are shown in dashed lines. Comparing the time required for the bentonite specimen to close the gap, it can be seen that the radial swelling is shorter. Nevertheless, different results would be obtained if, for example, the aspect ratio of the specimen is changed.

Fig. 4 shows the isochrones of void ratio represented along the initial coordinate for both cases. The closer region to the permeable boundary of the specimen swells earlier until the gap is closed, resulting in non- uniformity of the void ratio. After closing the gap, the volume of the specimen remains constant, but the distribution is formed in such a way that the volume change between denser and looser regions is always balanced with respect to the average void ratio. In other words, the closer region to the permeable boundary is re-consolidated, while the region farther away continues to swell, resulting in the elimination of the non-uniformity. However, even after the entire specimen is saturated and reaches an equilibrium state, the non-uniform distribution of the void ratio remains without being completely eliminated.

Table 1 Material parameter input in the simulation

Notation and symbol	Value
Critical state parameter, $\bar{M}$	0.63
Compression index, λ	0.14
Swelling index at $S_e = 1$, $\bar{\kappa}$	0.028
Poisson's ratio, ν'	0.40
Reference void ratio on NCL, e_{c0}	0.350
Pre-consolidation pressure, $\bar{p}'_{c0}$	6.795 MPa
Plastic rebound parameter, ζ	0.45
Sizing parameter, α	6.37
Positioning parameter, θ	0.65
Se-Dependency adjustment, l	2.23
Reference void ratio for k, e_0	0.368
Hydraulic conductivity at e_0, k_0	1.18e-13 m/s
e-dependency adjustment, λ_k	2.15
Residual of S_r, S_{r0}	0.10
SWCC parameter, A	-3.00
SWCC parameter, B	4.85

Note: $\bar{M}^*$ in Eq. (1) can be obtained by $\bar{M}^* = (1+2\zeta)\bar{M}$. For A, the value corresponding to the suction unit MPa is shown.

Table 2 Initial condition of bentonite specimen

Notation and symbol	Value
Dry density, $\rho_{d,i}$	2.0 Mg/m^3
Void ratio, e_i	0.368
Water content, w_i	10.0 %
Degree of saturation, $S_{r,i}$	74.4 %
Matric suction, s_i	1.54 MPa
Mean total stress, p_i	0 MPa
Effective mean stress, p'_i	1.10 MPa

The swelling pressure generation in axial swelling is shown in Fig. 5. Due to the equilibrium of the axial forces in the specimen, the axial stress is always the same at all axial positions (black line). It only begins to increase when contact pressure is applied to the top surface of the specimen after the gap has been closed.

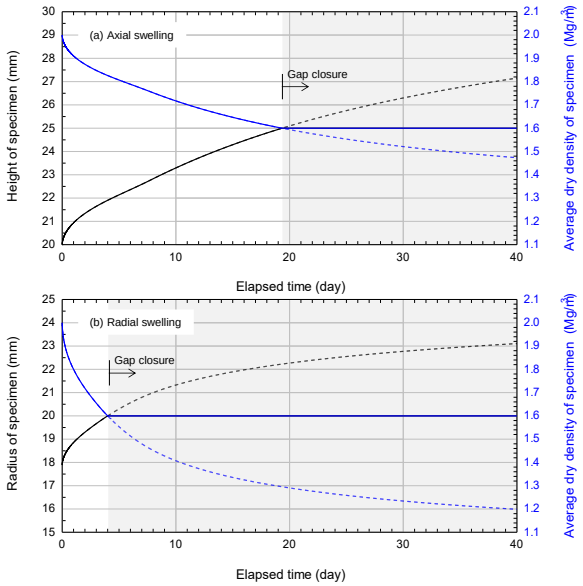

Fig. 3 Evolutions of (a) the height in axial swelling and (b) the radius in radial swelling.

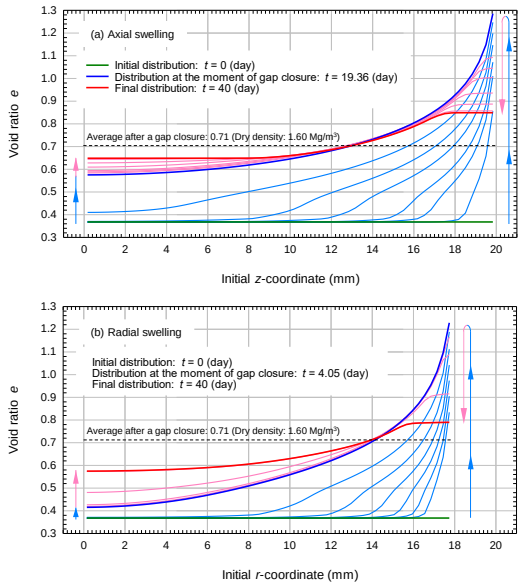

Fig. 4 Isochrones of void ratio in (a) axial swelling and (b) radial swelling.

The radial stress begins to generate immediately after the water infiltration, starting from the position where the saturation increases more quickly, i.e. closer to the permeable boundary, and rises to about 1.3 MPa before the closure of the gap, after which it turns to decrease. There is only a time lag in the axial response until the gap is closed. On the other hand, after closing the gap, it is found that the radial stress at the position where the swelling preceded the closing increases due to reconsolidation, while the radial stress at the position where the swelling occurs later decreases. The radial stress at equilibrium, as well as the void ratio, varies along the axial direction of the specimen, and the closer to the permeable boundary, the smaller the residual value. The values of axial and radial stresses at equilibrium are the same at a point slightly inside the top surface of the specimen, and the stress state reaches isotropic.

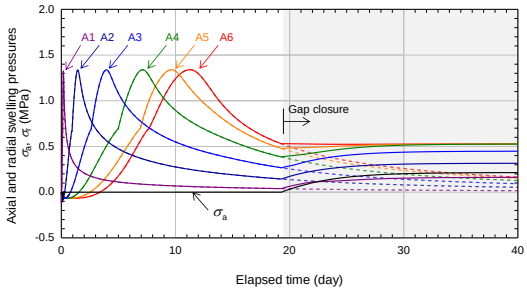

Fig. 5 Generation of swelling pressure along the axial direction in axial swelling

Fig. 6 shows the generation of swelling pressure along the radial direction in the radial swelling. In this case, even before the gap is closed, there is not only a time delay but also a difference in the magnitude of each stress component generated depending on the radial position. In this case too, the axial and circumferential stresses orthogonal to the swelling direction show peaks before the gap is closed, but the peak values become smaller as the position is further away from the permeable boundary. The only position where the radial stress is zero is R1, which is closest to the permeable boundary, and closer to the central axis, the greater the negative radial stress.

After closing the gap, the axial and radial stresses converge to larger values the closer the position is to the central axis. On the other hand, the residual value of the circumferential stress is still the largest at the position close to the central axis (R6), but it is the smallest at the position slightly inside the side of the specimen (R2). In the equilibrium state, the stress state is $\sigma_r > \sigma_a = \sigma_\theta$ at position R1 and $\sigma_a > \sigma_r = \sigma_\theta$ at position R6, which means the maximum and intermediate principal stresses seem to differ according to the radial position.

CONCLUSIONS

This study investigates analytically the differences in the development of non-uniform distribution of dry density and the swelling pressure in each direction depending on the swelling direction of the specimen due to the position of the gap, i.e. limited axial and radial swelling. For both axial and radial swelling, the analysis results show that the non-uniform distribution of dry density (or void ratio) in the specimen formed during the gap filling process becomes more uniform during the process of equilibrium after gap closure, but does not reach a perfect uniform distribution in both cases. The mechanism of generation of the swelling pressure orthogonal to the swelling direction differed between axial and radial swelling already in the swelling

process before the gap was closed. This seems to be related to the fact that in axial swelling the axisymmetric stress condition is maintained, i.e. the two principal stresses other than the axial stress are of the same value, whereas in radial swelling the three principal stresses are different from each other. The swelling pressure at the equilibrium state after the gap is closed is also non-uniform, and the radial swelling shows not only non-uniform distribution of axial pressure in the radial direction, but also non-uniform distribution of radial and circumferential pressure. As the degree of non-uniformity may vary depending on the initial and boundary conditions of the bentonite specimen, more comparisons and investigations are further needed.

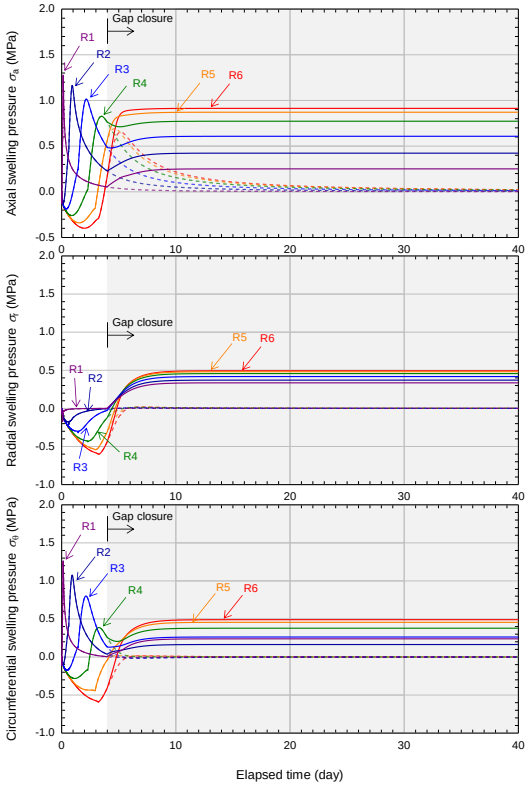

Fig. 6 Generation of swelling pressure along the radial direction in radial swelling

ACKNOWLEDGMENTS

This study was conducted in "The project for validating near-field system assessment methodology in geological disposal system (FY2020)" commissioned by Agency for Natural Resources and Energy in Ministry of Economy, Trade and Industry of Japan.

REFERENCES

[1] Komine H., Self-sealing capacity of some bentonite buffers in artificial seawater, In: Procs. of the 17th Int. Conf. on Soil Mechanics and Geotechnical Engineering, 2009, pp. 2495-2498.

[2] Gens A., Valleján B., Sánchez M., Imbert C., Villar M. V., Van Geet M., Hydromechanical behavior of a heterogeneous compacted soil: experimental observations and modeling, Géotechnique, Vol. 61 (5), 2011, pp. 367-386.

[3] Dueck A., Goudarzi R., Börgesson L., Buffer homoginization, status report 3. Technical Report TR-14-25. Swedish Nuclear Fuel and Waste Management Co., 2016.

[4] Wang Q., Tang A. M., Cui Y., Delage P., Barnichon J, Ye W., The effects of technological voids on the hydro-mechanical behavior of compacted bentonite-sand mixture, Soils and Foundations, Vol. 53, Issue 2, 2013, pp. 232-245.

[5] Bian X., Cui Y. J., Li X. Z., Voids effect on the swelling behaviour of compacted bentonite, Géotechnique, Vol. 69, (7), 2019, pp. 593-605.

[6] Jia L. Y., Chen Y. G. Ye W. M., Cui Y. J., Effects of a simulated gap on anisotropic swelling pressure of compacted GMZ bentonite, Engineering Geology, Vol. 248, 2019, pp. 155-163.

[7] Watanabe Y., Yokoyama S., Self-sealing behavior of compacted bentonite-sand mixtures containing technological voids, Geomechanics for Energy and the Environment, Vol. 25, 2021, 100213.

[8] Takeyama T., Tachibana S., Furukawa A., A finite element method to describe the cyclic behavior of saturated soil, Int. J. of Mater. Science and Engineering, Vol. 2, Issue. 1, 2015, pp. 20-25.

[9] Iizuka A., Tachibana S., Takeyama T., Sugiyama Y., Nomura S., Ohta H., Extension of unsaturated soil mechanics and its applications, Geotech. Research, Vol. 6, Issue. GR3, 2019, pp. 156-176.

[10] Tachibana S., Ito S., Iizuka A., Constitutive model with a concept of plastic rebound for expansive soil, Soils and Foundations, Vol. 60, 2020, pp. 179-197.

[11] Roscoe K. H., Burland J. H., On the generalized stress-strain behavior of 'wet' clay, In: Engineering Plasticity, Cambridge Univ. Press, 1968, pp. 535-609.

[12] Ohno S., Kawai K., Tachibana S., Elasto-plastic constitutive model for unsaturated soil applied effective degree of saturation as a parameter expressing stiffness, J. JSCE, Vol. 63, Issue. 4, 2007, pp. 1132-1141. (in Japanese)

[13] Börgesson L., Johannesson L. E., Sanden T., Hernelind J., Modeling of the physical behavior of water saturated clay barriers. Laboratory tests, material models and finite element applications, Technical Report TR-95-20. Swedish Nuclear Fuel and Waste Management Co., 1995.

[14] Sugii Y., Uno T, Modeling of hydraulic properties for unsaturated soils, Proc. Symp. Permeability of Unsaturated Ground, 1996, pp. 179-184. (in Japanese)

11th Int. Conf. on Geotechnique, Construction Materials & Environment,
Kyoto, Japan, 3-5 November 2021, ISBN: 978-4-909106063 C3051

INFLUENCE OF RICE HUSK ASH WITH MINIMAL DOSAGE OF CEMENT ON SHEAR STRENGTH AND MICROSTRUCTURE OF SOIL

Najmun Nahar[1, 2*], Sayful Kabir Khan[1, 3], Alex Otieno Owino[1], Zakaria Hossain[1] and Noma Tamaki[4]

[1]Graduate School of Bioresources, Mie University, Japan
[2]Life and Earth Science, Jagannath University, Bangladesh
[3]Directorate of Food, Dhaka, Bangladesh
[4]Make Integrated Technology Company, Osaka, Japan

ABSTRACT

Based on recent research, rice husk ash (RHA) is used as a secondary cementitious material for soil stabilization. Nominal dosage cement also can improve the engineering properties of soil. Usage of only RHA is unable to enhance the expected strength properties of soil. The present study attempted to investigate the effects of RHA with the nominal dosage of cement on shear strength and microstructure development of soil. In total, 10 combinations of soil-RHA-cement mixtures comprising of A-2-4 type soil with 5%, 10%, 15% of RHA, and 0.2%, 0.4%, 0.6% of cement were investigated. The Standard Proctor Test, Consolidated Drained Triaxial Test, and Scanning Electron Microscopy (SEM) were performed for study purposes. All specimens were moisture-cured for 1, 7, and 90 days. The test results revealed no significant shear strength of the admixtures was identified at specimens age one day and seven days due to slow chemical reaction. The highest strength was observed for the soil with 5% RHA and 0.6% cement at 90 days. The SEM test results also exhibited the best microstructural development by the chemical reaction among RHA, cement, and water after 90 days of curing for the same mix type, recommended as the optimum amount for practical purposes.

Keywords: Rice husk ash, shear strength; Calcium silicate hydrate; Scanning electron microscopy

INTRODUCTION

Rice husk ash (RHA) is an agricultural waste abundantly obtainable in many rice-producing countries globally [1]. It creates environmental pollution due to its being very lightweight after dumping in open places, roadsides, riversides and makes public health problems due to local air pollution [2]. RHA has the highest amount of amorphous silica (80%-95%) among all agro-wastes [3]. It can be substituted cement and used as a secondary cementitious material in ground improvement to improve soil strength properties and reduce project cost, waste disposal, and environmental contamination [4]. Using soil with RHA on its own does not give sufficient strength and stability to the soil as having a low pozzolanic substance [5]. Primarily, cement or lime additives are used with RHA for soil stabilization [6]. Cement is widely used with many soil types, but lime is appropriate for clay soil [7]. After mixing the RHA, cement, and optimum water with soil, calcium hydroxide is produced in the first step of the chemical reaction. Calcium Silicate Hydrate (CSH) and Calcium Aluminate Hydrates (CAH) gels are formed in the second phase of the reaction, which creates bonding within soil particles and gives the soil strength [8].

Many researchers have used RHA 5-15% and more with (2-10% cement) or more cement percentage of soil weight to improve soil properties [6,7, 9-14]. Hossain and Sakai [14] added less than 1% cement with clayey soil to improve soil strength, but that study used cement only, and no RHA was reported. Several studies were performed on the RHA and cement stabilized soil, but very little or no work was conducted on the RHA effects with minimal cement dosage. Technical and analytical study of soil, RHA with little cement, provides excellent benefits for the building the eco-friendly structure, e.g., roads, dams, paddy field ridges, and other agricultural construction. Therefore, the present study presents the effectiveness of RHA with the nominal dosage of cement, considering the curing periods on the shear strength and microstructure of the soil. All specimens were assessed by triaxial test and Scanning Electron Microscopy (SEM) test with the curing periods of 1, 7, and 90 days of moist curing. Results on the stress-strain relationship, shear strength, failure pattern, and microstructure development of soil mix with 5%, 10%, 15% of RHA, and 0.2%, 0.4%, 0.6% cement are described in the study.

MATERIALS AND METHODS

Materials

Soil, as-obtained RHA, and ordinary Portland cement were used in this study. The soil sample was collected from the Handa Area of Tsu City in Mie

Prefecture in Japan. The significant properties of soil are shown in Table 1. The particle size distribution curve of soil (Fig. 1) showed that the soil was well-graded.

Table 1: Major properties of soil

Parameters	Values
Specific gravity	2.70 g/cm^3
MDD	1.696 g/cm^3
OMC	17.50%
Sand (75 µm - 2 mm)	87.9%
Silt (5 - 75 µm)	8.9%
Clay < 5 µm	3.2%
Liquid Limit, LL	37.5%
Plastic Limit, PL	29.7%
Plasticity Index, PI	7.8%
Textural	Silty sand
USCS	SM
AASHTO classification	A-2-4

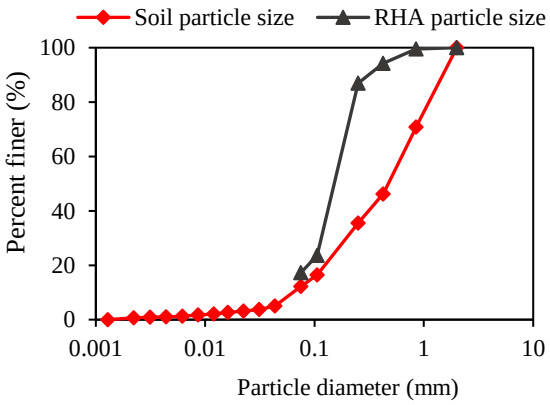

Fig. 1 Particle size distribution curve of soil and RHA

The readymade RHA was collected from Make Integrated Technology (MIT) company of Osaka City in Japan. The significant properties of RHA are presented in Table 2. The particle size distribution curve of RHA is shown in Fig. 1. It is noticed that about 86.97% of RHA particles passed through a 0.25 mm sieve, indicating an enormous number of fine particles in the RHA sample.

Table 2 Major properties of RHA [15]

Parameters	Values
Specific gravity	2.12 g/cm^3
Burning temperature	650°C-700°C
Burning time	27 hours
Average particle size	0.001-0.3 mm
Silica (SiO_2)	91.10%
Alumina (Al_2O_3)	0.03%
Lime (CaO)	0.57%
Magnesia (MgO)	0.16%
Carbon dioxide (CO_2)	4.35%

The ordinary Portland cement (OPC) was collected from the market in Japan. The specific gravity of OPC is 3.15 g/cm^3. Usually, the OPC is composed of 62.7% lime, 21.7% silica, 5% alumina, 2.9% magnesia, etc. [16].

Preparation of the Specimens with Mixed Design

As a part of soil sample preparation, the soil was dried at 25°C temperature in a room and sieved to eliminate the undesirable leaves and roots from the soil. In this investigation, 10 soil-RHA-cement combinations were made from the mixing proportions of soil with 0%, 5%, 10%, 15% RHA, and 0%, 0.2%, 0.4%, and 0.6% cement. The necessary amount of soil, RHA, and cement were gently mixed manually for 10 to 15 minutes in a large tray. About 2% water was reduced from OMC for ensuring better cement hydration and added the water content in the soil-RHA-cement mixtures. All triaxial and SEM test specimens were moist cured and reserved in a desiccator for 1, 7, and 90 days.

Experimental Method

Triaxial test method

The triaxial compression test is one of the most consistent techniques for determining soil shear strength [17]. The tests were performed following the standard of the Japanese Geotechnical Society (JGS 0520-0524) [18]. The triaxial test specimens of the soil-RHA-cement admixtures are manually compacted in a mold, with a height and diameter of 12.5 cm and 5.0 cm, respectively, using a hand-rammer with a 4.9 cm diameter, a mass of 1.0 kg, and a falling height of 30 cm. Three layers of the specimens were compressed, with each layer receiving 20 blows. The consolidated drained tests were demonstrated under three confining pressures (50 kPa, 100 kPa, 150 kPa). Both graphical and mathematical techniques were used to compute the cohesion (c) and angle of internal friction (φ) of triaxial test data. As a graphical technique, the Mohr-Coulomb failure criterion was used, in which specimens fail due to a critical combination of normal stress (σ_f) and shear stress (τ_f). The failure envelope line's equation is as follows:

$$\tau_f = c + \sigma_f \tan \varphi \qquad (1)$$

where, τ_f is the shear stress, and σ_f is the normal stress on the failure plane. The cohesion (c) and angle of internal friction (φ) were calculated using the following equation:

$$\sigma_a = \sigma_r \tan^2(45 + \varphi/2) + 2c \tan(45 + \varphi/2) \quad (2)$$

where, σ_a is the major, and σ_r the minor effective principal stress.

Scanning Electron Microscopy (SEM) Test Method

The SEM test specimens of soil-RHA-cement mix types were collected from compacted triaxial test specimens. All SEM images were captured at ×500 magnification and a scale of 60 µm to understand the microstructure development and changes of the particles in the specimens.

RESULTS AND DISCUSSIONS

Triaxial Test Results

Effects of RHA and cement with curing periods on the differential stress and axial strain curve of soil

The relationship between principal stress difference (σ_a-σ_r) and axial strain (ε_a) curves of control specimen, soil with 5%, 10%, 15 RHA with 0.2, 0.4, 0.6% cement mix type are shown in Table 3. These graphs also focused on the relationship between axial strain (Ɛa) and principal stress difference (σa-σr) of the combination types with 1, 7, and 90 days curing period. It was observed that the behavior of soil-RHA-cement specimens was significantly affected by the addition of RHA and cement percentage with the age of the specimens. The relationship between axial strain (ε_a) and principal stress difference (σ_a-σ_r) of all specimens showed that peak strength and brittleness behavior changed due to separate or combined effects of RHA and cement percentages. All the soil-RHA-cement specimens achieved peak value on 2-3% axial strain except for the control specimen (Fig. 2). The axial strain decreased after adding RHA and cement content compared to the control specimen (Table 3).

The ultimate principal stress difference was reduced with the increment of cement content for the same amount of RHA. All soil-RHA-cement specimens achieved the highest principal stress difference (σ_a-σ_r) under the confining pressure of 150 kPa. However, the maximum principal stress difference also diminished for all soil-RHA-cement combination types except the S+5R+0.6C specimen with the increase of the curing days. Perhaps below 0.6% cement and more than 5% RHA was unable to improve the shear strength of the soil. The surplus RHA with a minimal dosage of cement in the soil prohibited the cement hydration due to the water absorption by the microporous RHA with the time.

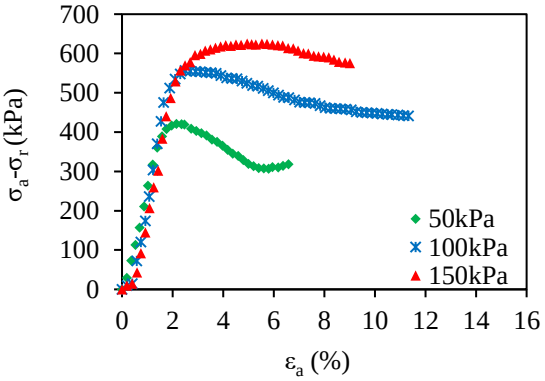

Fig. 2 The principal stress difference (σ_a-σ_r) and axial strain (ε_a) curves of control specimen

Table 2 The relationship between axial strain (ε_a) and principal stress difference (σ_a-σ_r) of various soil-RHA-cement combination types at 1, 7, and 90 days curing.

1 day	7 days	90 days
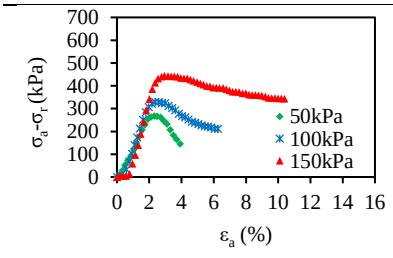	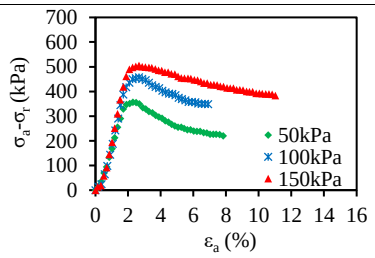	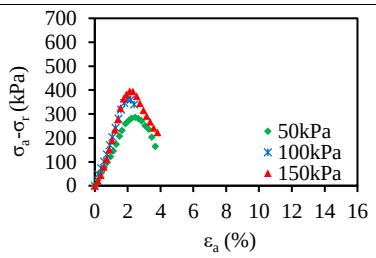
Soil + 5% RHA + 0.2% cement (S+5R+0.2C)		
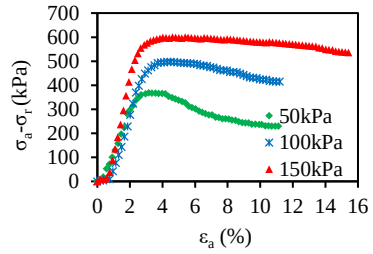	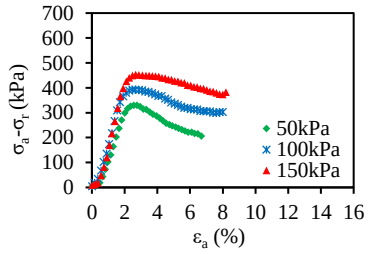	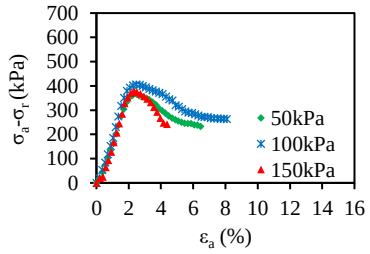

Table 2 Continued

1 day	7 days	90 days
Soil + 5% RHA + 0.4% cement (S+5R+0.4C)		
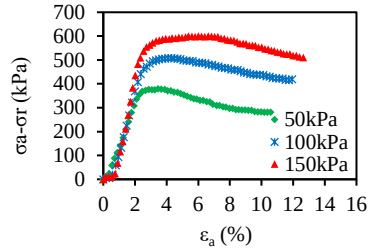	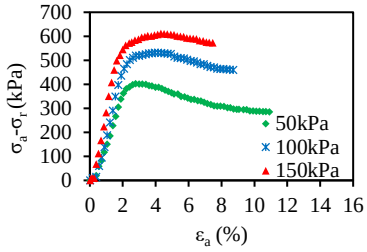	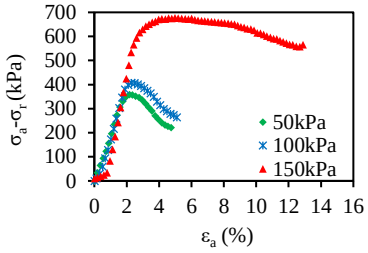
Soil + 5% RHA + 0.6% cement (S+5R+0.6C)		
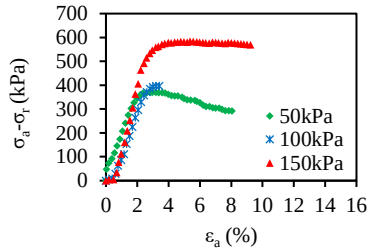	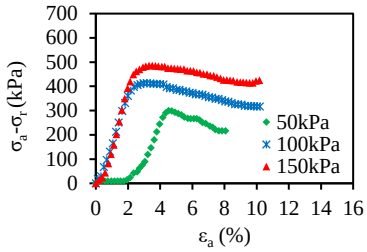	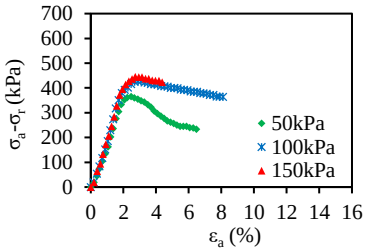
Soil + 10% RHA + 0.2% cement (S+10R+0.2C)		
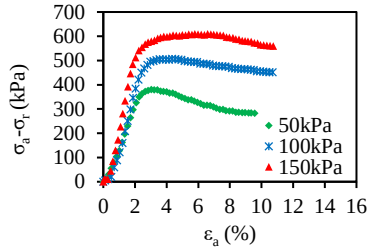	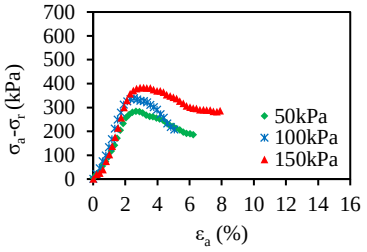	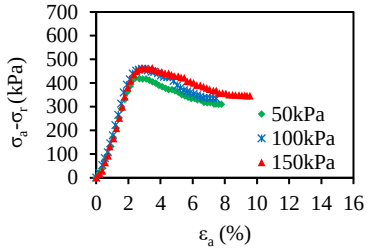
Soil + 10% RHA + 0.4% cement (S+10R+0.4C)		
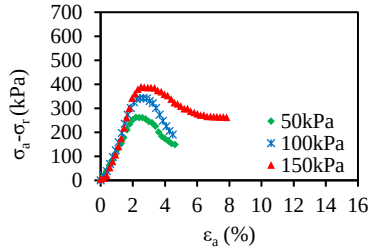	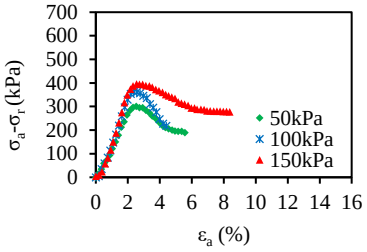	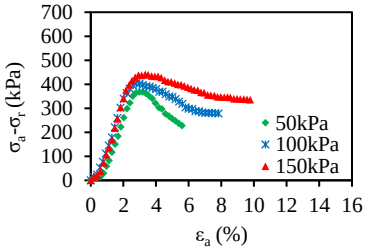
Soil + 10% RHA + 0.6% cement (S+10R+0.6C)		
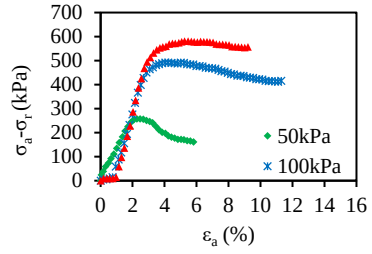	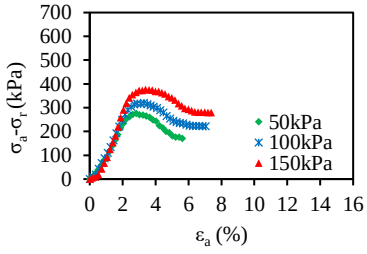	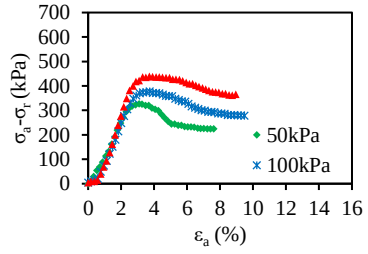
Soil + 15% RHA + 0.2% cement (S+15R+0.2C)		
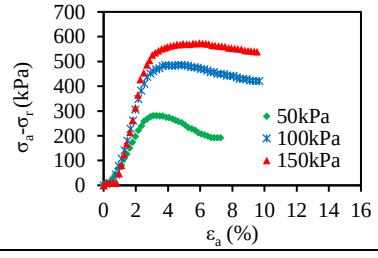	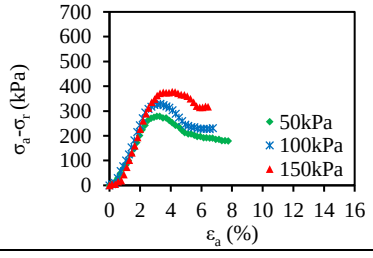	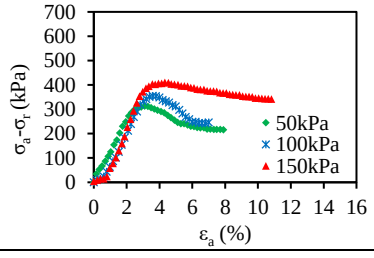

Soil +1 5% RHA + 0.4% cement (S+15R+0.4C)

Table 2 continued

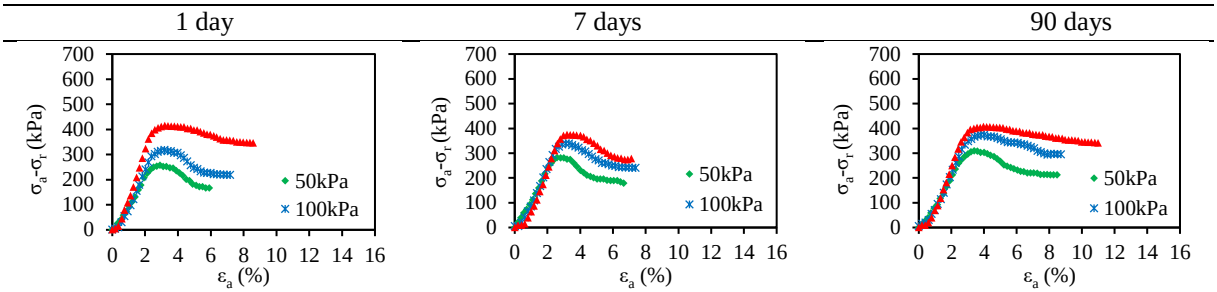

Soil + 15% RHA + 0.6% cement (S+15R+0.6C)

Effects of RHA and cement with the curing periods on cohesion and angle of internal friction of soil

Fig. 3 shows the cohesion of soil-RHA-cement mix types considering the curing periods (1, 7, 90 days). The cohesion of untreated soil was 76.0 kPa. It was noticed that there were significant effects of curing time on the cohesion of the soil-RHA-cement combination types. An improvement of cohesion was observed for all soil-RHA-cement combination types at 90 days. The mechanical interlocking among the soil, 5-10% RHA, and cement particles in the soil increased the cohesion value of the admixtures over time. However, 15% RHA content reduced the cohesion value compared to specimens consisting of 5-10% RHA due to less mechanical linkage of the particles by increasing the inter-particle distances among soil, RHA and cement particles.

Fig. 4 represents the angle of internal friction of all soil-RHA-cement combination types. The angle of internal friction of the control specimen was 32°, and it diminished with the increment of the curing days of the specimens. Perhaps the fine particles of RHA and cement particles decreased the angle of internal friction due to the anti-synergetic action between the angle of internal friction and cohesion over time [17,19].

Effects of RHA and cement with the curing periods on the microstructure of soil

The SEM images showed that soil microstructure was changed with the increment of RHA and cement content over time for all soil-RHA-cement mix types. The SEM images of the control specimen are shown in Fig. 5. It was observed from the figure that the air voids of the soil particles are reduced after compaction. Compared to the control specimen, significant microstructural changes and development were observed in the S+5R+0.6C combination 90-day (Fig. 6) curing. The mechanical joining of soil, RHA, and cement particles in that mixture changed the microstructure of soil. Moreover, 5% RHA and 0.6% cement content with water produced Calcium Silicate Hydrate (CSH) gel by the chemical reactions among SiO_2 and CaO in the soil through hydration process, which developed the microstructure of soil.

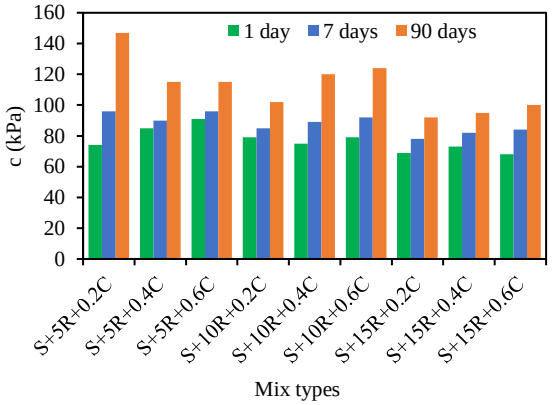

Fig. 3 Cohesion of soil-RHA-cement combinations

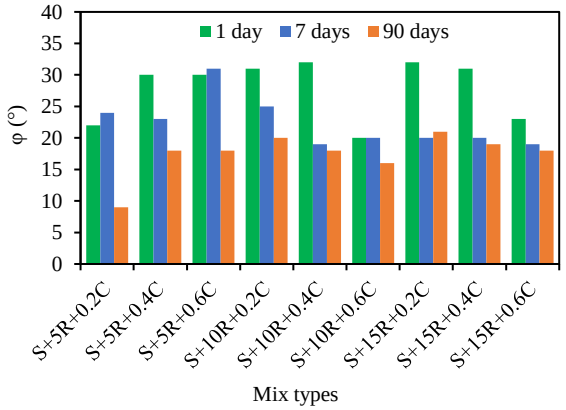

Fig. 4 Angle of internal friction of soil-RHA-cement combinations

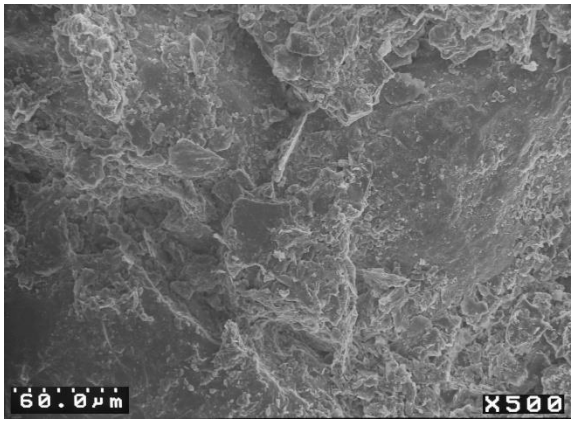

Fig. 5 SEM image of control specimen

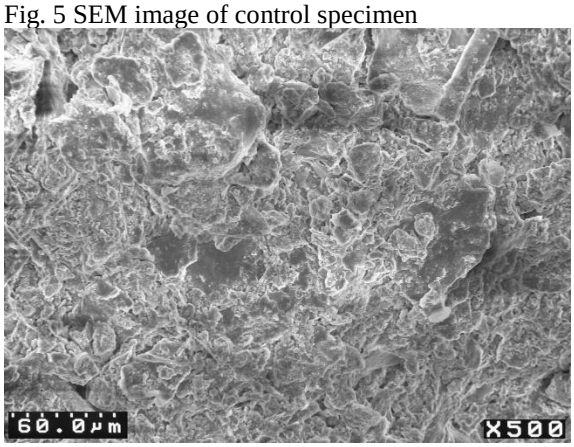

Fig. 6 SEM image of S+5R+0.6C at 90-day curing

CONCLUSIONS

The study investigated the effects of RHA with a nominal dosage of cement with the different curing days at A-2-4 type soil. The study can be concluded

- An improvement of shear strength was observed for the S+5R+0.6C combination at 90 days of curing.
- Cohesion values of all soil-RHA-cement combinations increased at 7 and 90 days.
- The angle of internal friction values of all combination types was decreased sharply also for 7 and 90 days.
- The SEM image on the S+5R+0.6C combination showed the best microstructural development for 90 days.
- S+5R+0.6C combination can be used for some applications of ground improvement considering the curing period.

REFERENCES

[1] Pode, R., Potential applications of rice husk ash waste from rice husk biomass power plant, Renewable and Sustainable Energy Reviews, Vol. 53, 2016, pp. 1468-1485.

[2] Kumar, A., Sengupta, B., Dasgupta, D., Mandal, T., and Datta, S., Recovery of value added products from rice husk ash to explore an economical way to recycle and reuse agricultural waste. Reviews in Environmental Science and Bio/Technology, Vol. 15, Issue 1, 2016, pp. 47-65.

[3] Ahmad, J., Rosli, M. I. F., & Rahman, A. S. A., The Effect of Rice Husk Ash (RHA) Mixtures on Geotechnical Properties of Soil. In Regional Conference on Science, Technology and Social Sciences (RCSTSS 2016) (pp. 345-352). Springer, Singapore.

[4] Xu, W., Lo, T. Y., and Memon, S. A., Microstructure and reactivity of rice husk ash. Construction and Building Materials, Vol. 29, 2012, pp. 541-547.

[5] Choobbasti, A. J., Samakoosh, M. A., and Kutanaei, S. S., Mechanical properties soil stabilized with nano calcium carbonate and reinforced with carpet waste fibers. Construction and Building Materials, Vol. 211, 2019, pp. 1094-1104.

[6] Basha, E. A., Hashim, R., Mahmud, H. B., and Muntohar, A. S. Stabilization of residual soil with rice husk ash and cement. Construction and Building Materials, Vol. 19, Issue 6, 2005, pp. 448-453.

[7] Hossain, A. S. M. M., Cement and cement-rice husk ash stabilization of selected local alluvial soils, 1986, A Masters dissertation in BUET, Dhaka, Bangladesh.

[8] Singh, B., Rice husk ash. In Waste and Supplementary Cementitious Materials in Concrete, 2018, pp. 417-460, Woodhead Publishing.

[9] Rahman, M. A., Effects of cement-rice husk ash mixtures on geotechnical properties of lateritic soils. Soils and Foundations, Vol. 27, Issue 2, 1987, pp. 61-65.

[10] Ali, F. H., Adnan, A., and Choy, C. K., Geotechnical properties of a chemically stabilized soil from Malaysia with rice husk ash as an additive. Geotechnical & Geological Engineering, Vol. 10, Issue 2, 1992, pp. 117-134.

[11] Alhassan, M., and Mustapha, A. M., Effect of rice husk ash on cement stabilized laterite. Leonardo Electronic Journal of Practices and Technologies, Vol. 11, 2007, pp. 47-58.

[12] Ahmad, J., Rosli, M. I. F., and Rahman, A. S. A., The Effect of Rice Husk Ash (RHA) Mixtures on Geotechnical Properties of Soil. In Regional Conference on Science, Technology and Social Sciences, 2016, pp. 345-352.

[13] Nguyen, D. T., and Nu, N. T., Effect of different types of rice husk ash on some geotechnical properties of cement-admixed soil. The Iraqi Geological Journal, 2020, pp. 1-12.

[14] Hossain, M. Z., and Sakai, T., The effectiveness of nominal dosage of ordinary cement on strength and permeability of clayey soil, Journal of the Japanese Society of Soil Physics, Vol. 110, 2008, pp. 25-35.

[15] MIT, What is plant-based (rice husk) silica? 2018, (in Japanese). Available at: https://www.mit-corp.biz/business/biosilica/.

[16] Lee, S. H., Hong, K. N., Park, J. K., & Ko, J. (2014). Influence of aggregate coated with modified sulfur on the properties of cement concrete. Materials, 7(6), 4739–4754.

[17] Rachmawati, S. H., Hossain, Z., and Shiau, J., Shear strength of soil by using clam shell waste as recycle aggregate. Journal of Agricultural Engineering, Vol. 51, Issue 3, 2020, pp. 155-160.

[18] JGS 0520-0524, Triaxial compression test of soil, Guidance and Basic - Soil Test (in Japanese), The Japanese Geotechnical Society, 2010, pp. 135-150.

[19] Hossain, M. Z., Narioka, H., and Sakai, T., Effect of Ordinary Portland-Cement on Properties of Clayey Soil in Mie Prefecture. Journal of the Japanese Society of Soil Physics, Vol. 130, 2006, pp. 31-38.

11th Int. Conf. on Geotechnique, Construction Materials & Environment,
Kyoto, Japan, 3-5 November 2021, ISBN: 978-4-909106063 C3051

EFFECTS OF BASALT FIBER ON STRENGTH AND PERMEABILITY OF RHA TREATED EXPANSIVE SOILS

Alex Otieno Owino[1], Najmun Nahar[1, 2], Saiful Kabir Khan[1, 3], Zakaria Hossain[1] and Noma Tamaki[4]

[1]Graduate School of Bioresources, Mie University, Japan
[2]Life and Earth sciences, Jagannath University, Bangladesh
[3]Directorate of Food, Dhaka, Bangladesh
[4]Make Integrated Technology Company, Osaka, Japan

ABSTRACT

The application of stabilized soil is in demand in construction works due to the improved geotechnical properties. This research focused on improving the compressive capabilities, and the permeability characteristics of RHA treated clayey soils using basalt fiber. Important variables included basalt fiber length (3mm, 6mm, and 12mm), RHA percentages (5% to 15%), and cement percentage (3%) in the stabilized soil matrix. The samples were prepared at optimum water content, OMC obtained from standard proctor compaction tests, and then subjected to unconfined compression strength (UCS) test, constant head permeability test, and scanning electron microscope (SEM) test. It was observed that the unconfined compression strength of the RHA treated clay increased with an increase in the length of the basalt fibers and significantly increased when the samples were allowed to wet cure for 28 days. Similarly, adding fibers into the soil improved the permeability coefficient, improving water flow in the soil. Scanning electron microscope (SEM) test showed the existence of a porous morphology that increased permeability. Furthermore, through SEM, the randomly oriented basalt fibers' meshing portrayed the reinforcing phenomenon related to improved compressive strength.

Keywords: Soil Stabilization, RHA, Basalt Fiber, Unconfined Compressive Strength, Permeability coefficient

INTRODUCTION

Ground improvement is a fundamental step in geotechnical engineering to improve the strength of naturally occurring soils. The application of such improved soils is in the rise in areas like the subgrade layers [1] and fill material [2] and stability for shallow foundations [3] [4]. Major parameters such as compressibility behavior, deformation coefficients, failure planes, permeability, and the soil microstructure interaction must be examined to support engineering structures. Several methods have been proposed to produce high-strength soils for engineering construction purposes within the last decade. Soil improvement can be through modification of the existing properties or by stabilization [5]. Stabilization methods include densification techniques using cement-rich mixtures, pozzolans to stabilize the soil chemically, and reinforcement techniques using different types of fibers. In most practices worldwide, the uses of densification practices by cement have been considered, but this has led to a tremendous increase in construction costs and environmental impacts associated with the manufacture of cement [6]. This encounter has led to the sustainable use of industrial wastes like RHA and fibers as potential replacements or reduction aggregates to conventional cement densification techniques, as described in the next section.

Pozzolanic stabilization technique

One of the predominant pozzolanic materials in engineering use today is rice husk ash (RHA). Rice husk is a by-product of the rice grain production process. Upon the controlled burning of rice husks, we obtain RHA, which is extensively used to improve soils' geotechnical properties due to its abundance and is superiorly inexpensive compared to other conventional stabilizing agents such as cement and lime [7]. Pozzolans are those materials that are rich in siliceous and aluminous compounds and which in themselves have very minimal cementitious properties until chemically reacted with calcium hydroxide from materials such as cement [8] [9]. Using the rice husk ask in soil stabilization is an advantageous method in terms of improved soil strength, durability, environmental impacts related to the uncontrolled disposal of agricultural waste, and a reduction in carbon dioxide emissions from uncontrolled burning in fields [6].

Rahman [11], in his research on the effects of rice husk ash alone on the UCS of stabilized soils, showed that with an increase of RHA to 20% increased the UCS of lateritic soils, after which they started to decrease. Noor [12] also examined the rice husk ash-cement ratios and how they positively influenced the proposed mix ratios, unconfined compressive strength, and durability. Muntohar [13] results showed that mixing rice husk ash with 6% lime significantly reduced swelling and increased

durability on such improved soils. The literature also showed that rice husk ash had an optimum percentage above which the UCS of improved soils decreased. Alhassan [14] showed that adding rice husk ash percentages between 0 to 4% to clay soils and lime specimens significantly increased the UCS value at specified lime contents. On the other hand, from the same research, increasing rice husk ash percentages from 6 to 8% decreased the UCS value considering the curing period in both cases.

Soil stabilization by rice husk ash involves a pozzolanic reaction between the $Ca(OH)_2$ rich cement or lime and the SiO_2 rich rice husk ash in an alkaline environment leading to the formation of calcium silicate hydrate (CSH) gel [15]. James [16] investigated the setting process for a lime-excess and a lime-deficient mixture, and the product of the reaction showed the CSH gel by a combination of thermal analysis, XRD, and electron microscopy. In a nutshell, the formation of CSH gel accounted for the strength of lime-rice husk ash and cement, as shown in Eq. (1).

$$Ca(OH)_2 + SiO_2 = CaO_{0.8\text{-}1.5}SiO_2(H_2O)_{1.0\text{-}2.5} + CaO_{1.5\text{-}2.0}SiO_{2.2}(H_2O) \quad (1)$$

Fiber stabilization techniques

Fibers inclusion in a soil matrix has proved to add more intensification in the compressive abilities of soils due to the reinforcing technique between the soil particles. Several pieces of research have been investigated considering different fibers and their applicability in enhancing soil strength from the literature. Kumar [17] investigated the UCS gain on the soil by mixing polyester fibers and soft clay and observed that the compaction degree affected the presence of fiber reinforcement, the unconfined compressive strength of clay increased with the addition of fibers, and it further increased when fibers were mixed in the clay-sand mixture.

Hossain [18] also examined the structural improvement on cement-based matrices using varied carbon fiber lengths, improving durability and compressive strength. With the diversity in the fiber available for soil stabilization, polypropylene and recycled carpet have also been used before. Where bender element tests on 126 cylindrical samples of cement-treated clay with various cement and fiber contents were analyzed to distinguish the relationships between fiber and cement content and the small-strain mechanical properties [19]. Park [20] further showed that compacting polyvinyl alcohol (PVA) fiber in different layers inside a cylindrical river sand specimen improved the compressive strength as the number of fiber layers increased. With fibers evenly distributed throughout the five layers, a reinforced specimen was twice as strong as a non-fiber-reinforced specimen. A more comparable study to this research was done by Cristelo [21], where the influence of discrete fiber reinforcement on the uniaxial compression response found out that sandy clay reinforced with polypropylene fibers and cement increased the stiffness, deformation coefficient, and compression strength of the mixtures for every cement content. Similar results were also determined by Maher [22] and Consoli [23]

Scope of the Study

This present study focused on stabilization by pozzolanic reactivity of rice husk ash and reinforcement method by randomly distributed basalt fiber in the proposed soil matrix. The inclusion of basalt fibers improved the strength of the soil RHA mixtures since, at low cement values, the compressive strength of RHA treated soils was reduced due to the limited catalytic $Ca(OH)_2$ elements for the pozzolanic reaction. Basalt fibers (lengths 3mm, 6mm, and 12mm), cement (3% of the dry weight of soil), and rice husk ash (5%, 10%, and 15% of the dry weight of soil) were added to clayey soils and mixed by hand to a homogenous matrix for the three sets of RHA percentages. Samples were then subjected to an unconfined compressive strength test (UCS), permeability test and microstructure examination by scanning electron microscope (SEM) to obtain the geotechnical properties for ground improvement, considering curing periods of 1 day, 7days and 28 days. The results presented in this study show a significant increase in the compressive strength and improved permeability in the new composite soil matrix.

MATERIAL AND METHODS

Material properties

The materials used in this research included soil, rice husk ash (RHA), cement, and basalt fiber (BF). Figure 1 is a pictorial representation of the engineering materials. A detailed explanation of the properties of the materials is as discussed below.

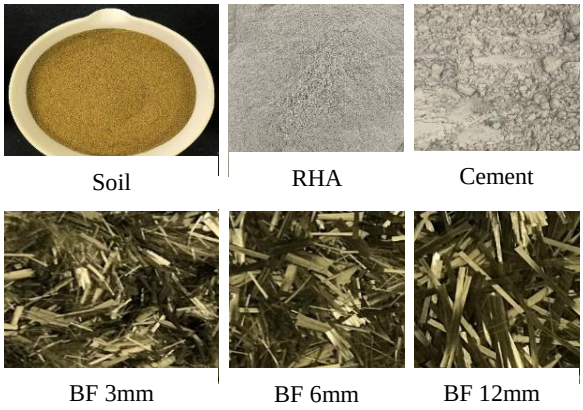

Fig. 1 Experiment materials

Soil

The soil used in this research was collected from Handa Area, Mie Prefecture, Japan. The soil was air-dried for 3weeks then sieved through the 2mm sieve, after which sieve analysis and hydrometer analysis were conducted on a 500 grams sample to classify the soil. According to the American Association of State Highway and Transportation Officials (AASHTO), the soil was classified as A-7-5 clayey soils with a composition of 6.2% coarse sand, 52.6% medium sand, 39.2% clay. More detailed properties are shown in Table 1.

Rice husk ash (RHA) properties

Rice husk ash (RHA) was obtained from Make Integrated Technology Co., Ltd, Osaka, Japan. The RHA was controlled-burned ash at 650-800 °C with high purity and high silica content of 91.10%. In this research, unground ash was used, keeping it in its natural particle size distribution of 0.07 to 0.3mm. The most dominant particles were between 0.07 and 0.106mm. Table 1 shows the detailed physical and chemical properties of the rice husk ash.

The particle distribution curves from sieve analysis and hydrometer analysis for soil and sieve analysis only for RHA are shown in Fig. 2.

Basalt Fibre (BF) Properties

Basalt fiber is made from basalt rock. The basalt rock is washed and melted, then extruded through small nozzles to produce the continuous filaments called basalt fibers [25]. Its application in engineering construction reinforcement works is derived from the high tensile strength of between 4100～4840 MPa, high elastic modulus ranging from 93.1～110GPa [26], durability, alkali resistance, and thermal stability compared to other fibers [27]. Table 1 illustrates the fundamental properties related to this study.Table 3 Basalt fiber (BF) properties

Properties	Parameters	Values
Soil Properties	Specific Gravity, (g/cm3)	2.751
	Dry Density, (g/cm3)	1.646
	Optimum water content, %	24.00
	Sand (75 μm - 2 mm), %	6.20
	Silt (5 - 75 μm), %	55.56
	Clay < 5 μm, %	39.22
	Liquid limit, LL, %	58.20
	Plastic limit, PL, %	31.05
	Plasticity Index, PI, %	27.15
	AASHTO classification	A-7-5
RHA Properties	Average Particle Size, mm	0.001-0.3
	Loss of Ignition, %	4-6
	Specific Gravity, g/cm^3	2.12
	Burning Temperature, °C	650-700
	Burning time, hour	27
	Silica (SiO_2), %	91.10
	Carbon dioxide (CO_2) %	4.35
	Potassium Oxide (K_2O), %	2.40
	Calcium Oxide (CaO), %	0.57
	Iron Oxide (Fe_2O_3), %	0.05
	Alumina (Al_2O_3), %	0.03
	Others, %	1.50
Basalt Fiber Properties	Fiber diameter, (μm)	6-30
	Density, (g/cm^3)	2.63-2.8
	Tensile strength, (MPa)	4100-4840
	Elastic modulus, (GPa)	93.1-110
	Fiber Lengths, (mm)	3, 6 & 12
	Fracture elongation rate, (%)	3.1

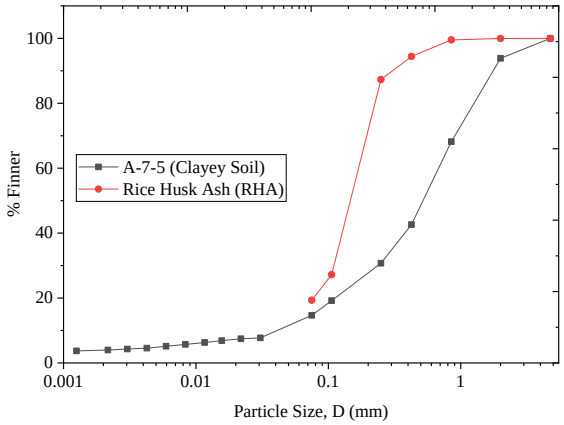

Fig. 2 Particle size distribution for Soil and RHA

Ordinary Portland Cement, OPC

OPC cement was chosen for this research due to its availability in the market.

Testing methods

Standard proctor compaction test

A standard proctor test was done following the JIS A 1210:2010 standards to evaluate the samples' dry unit weight (MDD) and the optimum water content (OMC). The soil samples (herein, sample refers to a mixture of soil, RHA, cement, and basalt fiber in varied ratios) were compacted in three layers inside the compaction mold measuring 10cm diameter and 12.68 cm height, using a 2.5kg rammer at a falling height of 30cm. A record of 25 blows was registered for each layer. A representative sample was taken and tested for moisture content, and the process repeated for all water increments.

The codes for the samples under study are explained in table 2:

Table 4 Mix ratios and codes.

Mix Code	Mix description
S	Soil (Control specimen)

S:5R	Soil+5%RHA
S:10R	Soil+10%RHA
S:15R	Soil+15%RHA
S:5R:3C:1BF3	Soil+5%RHA+3%cement+1% basalt fiber 3mm
S:10R:3C:1BF3	Soil+10%RHA+3%cement+1 %basalt fiber 3mm
S:15R:3C:1BF3	Soil+15%RHA+3%cement+1 %basalt fiber 3mm
S:5R:3C:1BF6	Soil+5%RHA+3%cement+1% basalt fiber 6mm
S:10R:3C:1BF6	Soil+10%RHA+3%cement+1 %basalt fiber 6mm
S:15R:3C:1BF6	Soil+15%RHA+3%cement+1 %basalt fiber 6mm
S:5R:3C:1BF12	Soil+5%RHA+3%cement+1% basalt fiber 12mm
S:10R:3C:1BF12	Soil+10%RHA+3%cement+1 %basalt fiber 12mm
S:15R:3C:1BF12	Soil+15%RHA+3%cement+1 %basalt fiber 12mm

Unconfined Compression Strength (UCS) Test

UCS test was done on a cylindrical sample with dimensions 5cm diameter and 12.5 cm height to examine the compressibility behavior of the mix ratios above. The samples were prepared using a cylindrical mold and a rammer weighing 1kg at a falling height of 30cm. All samples were prepared at the optimum moisture content obtained from compaction tests and wet cured for 1day, 7days, and 28days at a constant temperature of 25 degrees Celsius before testing. The data sets obtained from each sample were then analyzed for the stress-strain curve plots used to evaluate the compressive stress (q_u) and axial strain (ε) relationship and the deformation coefficient E50. The testing procedures were following Japan standards, JIS A 1216:2010.

Permeability test

In this study, a constant permeability test was carried out to examine the coefficient of permeability, k, for all the sample mix ratios considering curing periods 1day, 7days, and 28days. Each sample was compacted in three layers in the compaction mold (10.4 cm diameter and 6.3cm length) at 20 blows per layer to maintain constant compaction energy across all the samples in this study. The samples were wet cured while maintaining the water content at OMC, which allowed for enough hydration and pozzolanic activity in the samples. The constant water head was maintained at 45m, simulated by the air pressure of 0.45 MPa in the water chamber on top of the specimen. Water flowed through the sample until it was saturated before taking the first reading. Four readings were taken by measuring the volume of percolated water and the corresponding time taken for flow. Afterward, the average k of each flow was used to evaluate the final permeability coefficient (k). The experimental procedures followed Japan standards, JIS A 1218.

Scanning electron microscope

Microscopic examination was necessary to understand the microstructure interaction of the proposed composite ratios. A scanning electron microscope was used for all the samples, considering the curing periods and the percentages of the rice husk ash in the proposed mix ratios. A sample with dimensions 3mm by 3mm by 0.5mm was collected from the center of the cylindrical samples used in the UCS test. Soil-RHA mix ratios were examined at a magnification of x500, while the soil-RHA-C-BF mix ratios were taken at a magnification of x150 to provide a wider area for spotting the basalt fibers random distribution in the soil composite matrix.

RESULTS AND DISCUSSION

Compaction test

Compaction test refers to soil densification by removing air and rearranging the soil particles through mechanical energy. The degree of compaction is measured in terms of the maximum dry density, γ_{dmax}, and the optimum water content, OMC [28]. Figure 3 shows a plot of the compaction curves, emphasizing the maximum values for the optimum water content, OMC, and the dry unit weight γ_{dmax} for all the sample mix ratios.

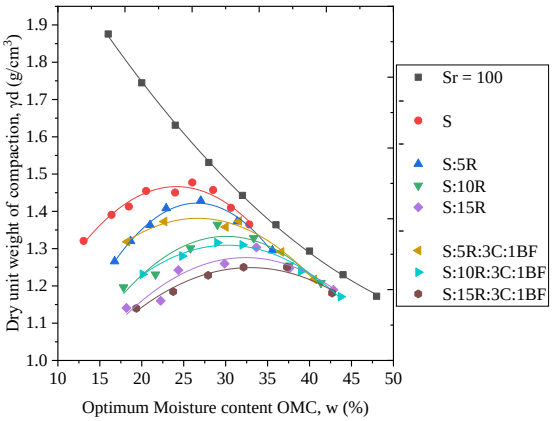

Figure 3 Compaction curves

The optimum water content increased with an increased percentage of rice husk ash. Similarly, upon adding cement into the mix ratios, there was a further increase in OMC.

On the contrary, the dry unit weight decreased with the addition of rice husk ash and cement. The increase in optimum water content was due to the high-water affinity by the increasing percentage of rice husk ash and the hydration effect with cement mixtures [29]. Furthermore, the decrease in dry

density was attributed to flocculation and cementitious compounds in the new composite soil mixtures.

Unconfined Compression Test, UCS

This section shows the relationship between compressive stress, q_u and axial strain, ε for 5%, 10%, and 15% RHA, and different basalt fiber lengths. In figure 4, the maximum compressive stresses, q_u were achieved with 5% RHA mix ratios at low axial strains, ε with mix ratio S:5R:3C:1BF12 giving the highest compressive stress than the control sample, soil only, S. In Figures 5 and 6, adding RHA to 10% and 15% respectively, reduced the compressive stresses with a slight increase in the axial strain. This increase in axial strain was due to the rearrangement of soil particles and the excess fine RHA particles filling the voids. Nevertheless, S:10R:3C:1BF12 and S:15R:3C:1BF12 samples produced significant stress-bearing characteristics compared to the soil only S sample.

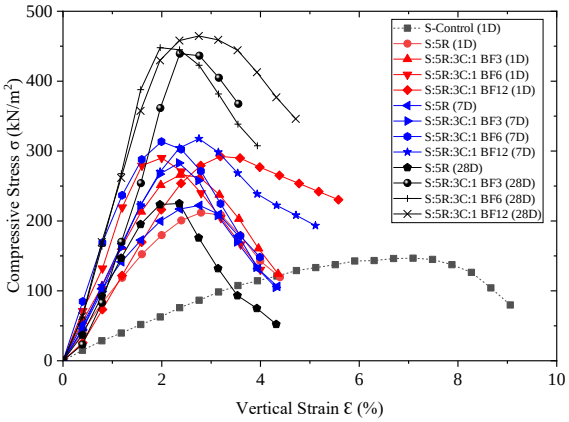

Fig. 4 Stress-Strain relationships for 5% RHA

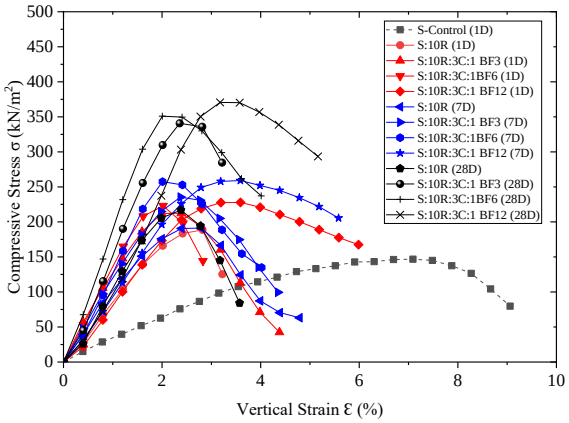

Fig. 5 Stress-Strain relationships for 10% RHA

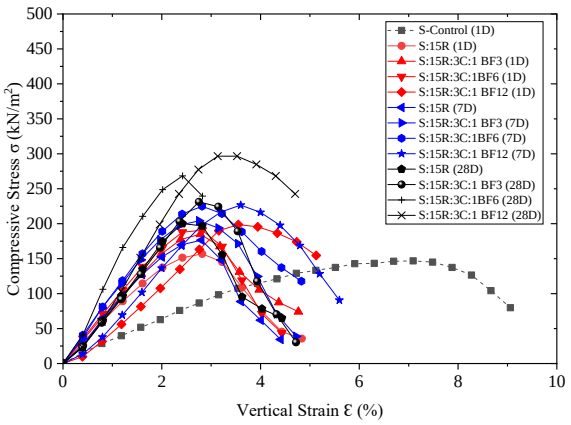

Fig. 6 Stress-Strain relationships for 15% RHA

For more reliability of the data sets obtained, curing period was considered for 1 day, 7days, and 28 days as shown in figure 7. From the graph, a slight improvement in q_u was observed for all the samples. For example, sample S:5R:3C:1BF12 had a qu of 292 kN/m^2 after one day, and the value increased to 318 kN/m^2 at 7 days of curing. After 28 days of curing, there was a significant increase in the UCS value for S:5R:3C:1BF3, S:5R:3C:1BF6 and S:5R:3C:1BF12 with values 438 kN/m^2, 453 kN/m^2 and 463 kN/m^2 respectively. The soil matrix also gained strength with an increase in the length of basalt fibers which enhanced the bonding of soil particles from the mesh generated by the fibers.

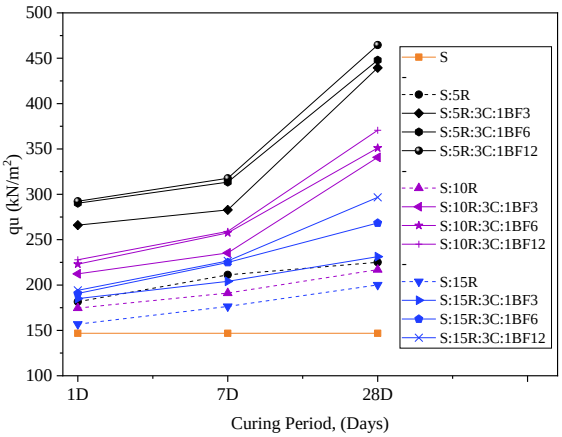

Fig. 7 q_u versus curing period

The high-strength samples in terms of basalt fiber length were those incorporated with 12mm long fibers. For example, for 5%, 10% and 15% RHA samples the highest qu's were obtained from S:5R:3C:1BF12 (463 kN/m^2), S:10R:3C:1BF12 (362 kN/m^2), S:15R:3C:1BF12 (297 kN/m^2), respectively. The qu increased due to fiber reinforcements and chemical reaction in the soil matrix, leading to silica gel formation [17] that aided in developing the cementitious properties compared to the control specimen S, which had compressive stress of 147 kN/m^2.

From this study, 5% RHA produced the most applicable compressive strengths for engineering construction works. Figure 10 summarises the failure planes for the 5% RHA samples; S, S:5R, S:5R:3C:1BF3, S:5R:3C:1BF6, and S:5R:3C:1BF12 . The first three samples experienced a simple shear failure upon maximum compression load, while the higher strength mix ratio S:5R:3C:1BF12 showed a tension failure as shown.

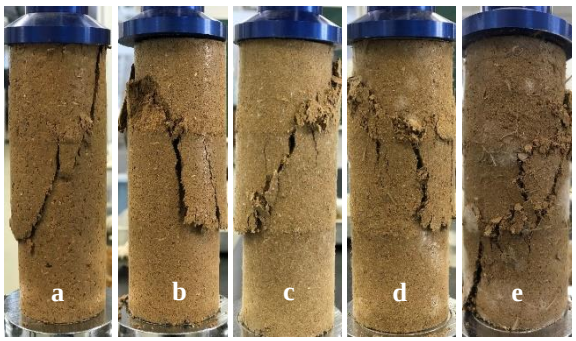

Fig 10 Failure patterns (a) S, (b) S:5R, (c) S:5R:3C:1BF3, (d) S:5R:3C:1BF6, (e) S:5R:3C:1BF12

It was observed that cracks occurred in the vertical plane for sample a at 7% strain, and this strain value reduced considerably to less than 3% for samples b, c, and d after adding basalt fibers. This reduction in axial strain is shown in Figures 8, 9, and 10 for 5%, 10%, and 15% RHA, respectively. Amongst the basalt fiber samples, 12mm long fibers had a 1% increase in axial strain compared to BF 3mm and BF 6mm. This increase was due to the slight extra deformations needed before the strengthening benefits were realized [30]. The axial strains reduced slightly after 28 days of curing, indicating shear strength development in the soil samples by adding fibers and cementation from the pozzolanic reaction.

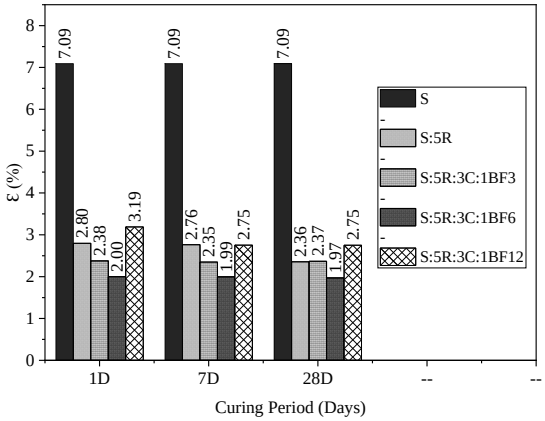

Fig. 7 Strain values for 5%RHA mixtures at different curing periods

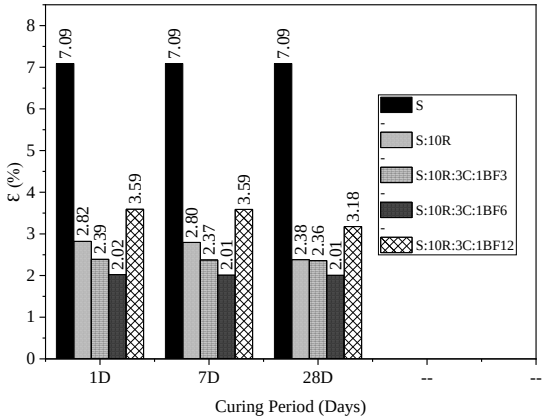

Fig. 8 Strain values for 10%RHA mixtures at different curing periods

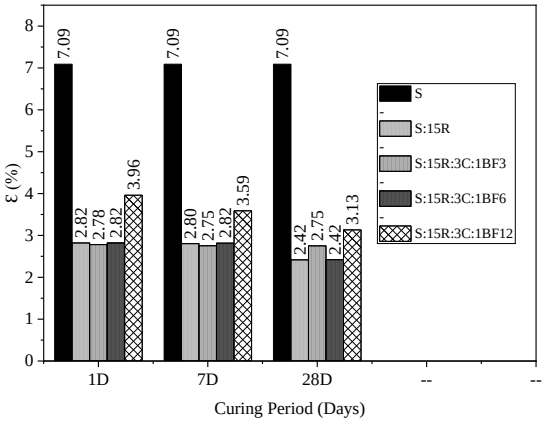

Fig. 9 Strain values for 15%RHA mixtures at different curing periods

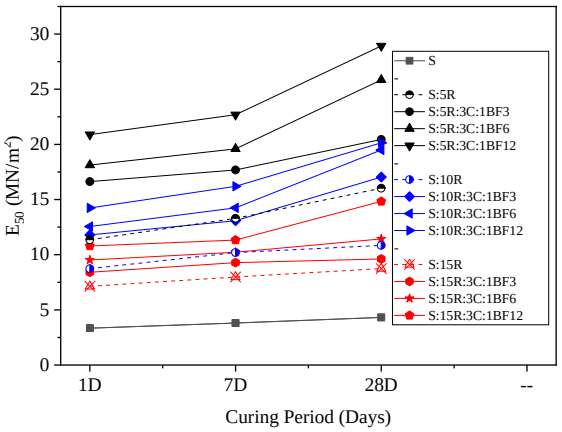

Fig. 10 Deformation coefficient E_{50} of different samples considering curing periods.

Lastly, deformation coefficients, E_{50} were also examined for all the samples considering curing period, basalt fiber length, and rice husk ash percentages, as shown in Fig. 10. Adding rice husk ash, cement, and basalt fiber had a tremendous influence on E_{50}. A significant increase was observed after 28 days of curing with 5% mix ratios giving the highest deformation coefficients. For mix ratios, 5R,

S:5R:3C:1BF3, S:5R:3C:1BF6, S:5R:3C:1BF12 the deformation coefficients were 16 MN/m^2, 20 MN/m^2, 26 MN/m^2, and 29 MN/m^2, respectively, which were much higher compared to control specimen S (3MN/m^2). S:5R:3C:1BF12 gave the highest value due to the intense interconnectivity of the longer fibers compared to the 3mm and 6mm.

Permeability test

Permeability test examines the water flow rate through a soil medium and is expressed as the coefficient of permeability, k. This water flow rate has a significant impact on soils' properties when it comes to drainage of subgrade material. In this study, the soil had a very low permeability of 7.1x10^{-6}, which was not considered suitable for subgrade or shallow foundation use. Adding basalt fibers into the soil increased the permeability coefficient, k to 10^{-5} for all 5% to 10%RHA samples and 10^{-4} for 15%RHA samples, as shown in figure 12. From 1 day to 7 days of curing, k increased due to the rapid flocculation of particles in the sample [31]. It was also evident that k declined at 28 days of curing due to the cementation effect that reduced the number of voids in the samples.

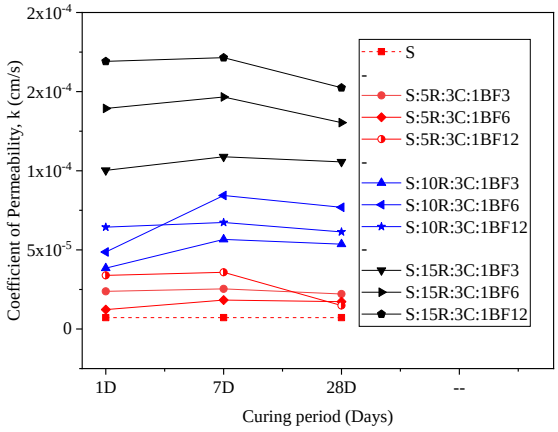

Fig. 11 Coefficient of Permeability, k of different mix ratios considering curing periods.

Scanning electron microscope

Figure 12 shows the meshing of basalt fibers at low resolutions of x150 and a scale of 200µm. Mesh joints in the S:R:C:BF matrix increased the compressive stresses in the sample due to the high tensile strength of the basalt fibers. In addition, fiber meshing also considerably reduced the axial strain within the sample, as explained earlier. The mixed chemical reaction between soil, rice husk ash, and cement and the reinforcing behavior of basalt fibers led to the production of a composite material inhibiting a porous morphology, as shown in Fig. 13 at a magnification of x500 and a scale of 60µm. This porous morphology and the fiber reinforcing points verified the significant increase in permeability coefficient, k

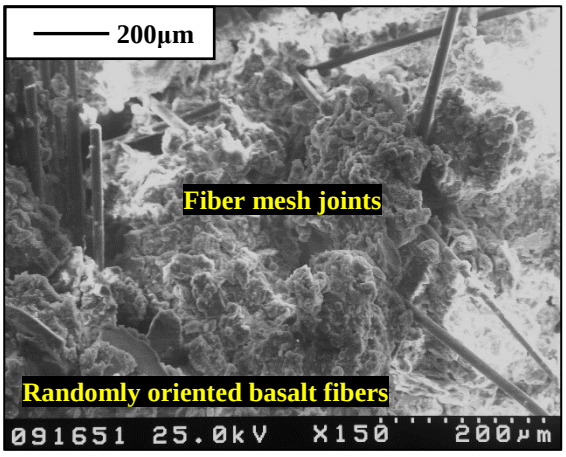

Fig. 12 Randomly oriented basalt fiber mesh in the improved soil matrix (Magnification x150)

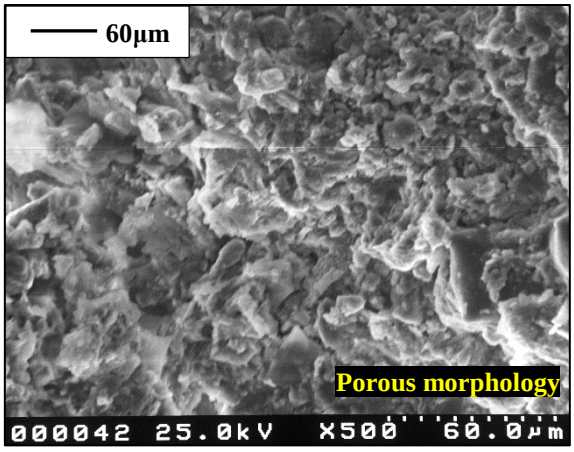

Fig. 14 Soil matrix showing a porous morphology

CONCLUSIONS

Unconfined compressive strength of compressible clay having 5% rice husk ash increased with the addition of basalt fibers from BF3mm to BF6mm to BF12mm. A similar increase in UCS value was evident for 10% and 15% rice husk ash but with lower values than the superior 5% rice husk mixtures.

Clay soil only had a, q_u of 146.79 (kN/m^2) and a Deformation coefficient E_{50} of 3.34 (MN/m^2), but upon improvement, the higher strength mixture, S:5R:3C:1BF12, showed a significant increase in both qu and E_{50} with values of 463 (kN/m^2) and 29(MN/m^2) respectively, after 28 days of curing at 25 ˚C. The axial strain within the soil sample during loading was reduced significantly by the addition of basalt fibers. This reduction demonstrated the tensile ability of the fibers to hold the sample particles together with minimal deformation.

This mix ratio, S:5R:3C:1BF12, SEM image confirmed the interconnected microstructure, enhanced by the basalt fiber (BF) mesh between the

soil particles and the cementitious soil mass, hence improved compressibility. The pozzolanic reaction that produced the cementitious matrix can be illustrated in equation 2 below, with $2Ca_2$ (SiO_3nH_2O) representing the CSH Gel.

$$(Si_2O_5,\ Al_2O_{2)} + 3Ca\ (OH)_2 + nH_2O = Ca_2(Al_2SiO_7,\ nH_2O) + 2Ca_2\ (SiO_3nH_2O) \quad (2)$$

Nevertheless, the inclusions of randomly oriented Basalt fiber into the soil, combined with the rapidly hardening CSH Gel, improved the geotechnical engineering behavior of the new material and can be proposed for use as a subgrade material for pavements and as fill material in shallow foundations.

ACKNOWLEDGMENTS

Sincere thanks to MEXT Scholarship and Mie university for according the chance to pursue this research journey.

REFERENCES

[1] Crockford, W.W., Grogan, W.P. and Chill, D.S.,. Strength and life of stabilized pavement layers containing fibrillated polypropylene,1993, (No. 1418).

[2] Festugato, L., Fourie, A. and Consoli, N.C., Cyclic shear response of fibre-reinforced cemented paste backfill. Géotechnique Letters, 3(1), 2013, pp.5-12.

[3] Ibraim, E., Diambra, A., Wood, D.M. and Russell, A.R., Static liquefaction of fibre reinforced sand under monotonic loading. Geotextiles and Geomembranes, 28(4), 2010, pp.374-385.

[4] Mitchell, J.K., Soil improvement-state of the art report. In Proc., 11th Int. Conf. on SMFE Vol. 4, 1981, pp. 509-565.

[5] Fattah, M.Y., Rahil, F.H. and Al-Soudany, K.Y., Improvement of clayey soil characteristics using rice husk ash. Journal of Civil Engineering and Urbanism, 3(1), 2013, pp.12-18.

[6] Alhassan, M., Potentials of rice husk ash for soil stabilization. Assumption university journal of technology, 11(4), 2008, pp.246-250.

[7] Aprianti, E., Shafigh, P., Bahri, S. and Farahani, J.N., 2015. Supplementary cementitious materials origin from agricultural wastes–A review. Construction and Building Materials, 74, pp.176-187.

[8] Malhotra V. M., and Mehta, P. K., Pozzolanic and cementitious materials. CRC Press, 2004.

[9] Basha, E. A., Hashim, R., Mahmud H. B., and Muntohar A. S., Stabilization of residual soil with rice husk ash and cement. Construction and building materials 19, no. 6, 2005, pp. 448-453.

[10] Ali, F. H., Adnan, A. and Choy, C. K., Geotechnical Properties of a chemically stabilized soil from Malaysia with rice husk ash as an additive. Geotechnical & Geological Engineering 10, no. 2, 1992. Pp. 117-134.

[11] Rahman, MD. A., The potentials of some stabilizers for the use of lateritic soil in construction. Building and Environment 21, no. 1, 1986, pp. 57-61.

[12] Noor, M. J. M. M., Aziz, A. A., and Suhadi, R. U. R., Effects of cement-rice husk ash mixtures on compaction, strength, and durability of Melaka Series lateritic soil. The Professional Journal of the Institution of Surveyors Malaysia 28, no. 3, 1993, pp. 61-67.

[13] Muntohar, A. S., Uses of RHA to enhanced lime-stabilized clay soil. In International Conference of Geotechnical Engineering, University of Sharjah, United Arab Emirate, 2004, pp. 356-357. 2004.

[14] Alhassan, M., Permeability of lateritic soil treated with lime and rice husk ash. Assumption University Journal of Thailand 12, no. 2, 2008, pp. 115-120.

[15] Rogers, C. D., and Glendinning S., Lime requirement for stabilization. Transportation Research Record 1721, no. 1, 2000, pp. 9-18.

[16] James, J., and Rao M. S., Reaction product of lime and silica from rice husk ash. Cement and Concrete Research 16, no. 1,1986, pp. 67-73.

[17] Kumar, A., Walia B. S., and Mohan, J., Compressive strength of fiber-reinforced highly compressible clay. Construction and building materials 20, no. 10, 2006, pp. 1063-1068.

[18] Hossain, M. Z., and Awal, A. A., Flexural response of hybrid carbon fiber thin cement composites. Construction and Building Materials 25, no. 2, 2011, pp. 670-677.

[19] Fatahi, B., Fatahi B., Le T. M., and Khabbaz H., Small-strain properties of soft clay treated with fiber and cement. Geosynthetics International 20, no. 4, 2013, pp. 286-300

[20] Park, S., Effect of fiber reinforcement and distribution on unconfined compressive strength of fiber-reinforced cemented sand. Geotextiles and Geomembranes 27, no. 2, 2009, pp. 162-166.

[21] Cristelo, N., Cunha, V.M., Dias, M., Gomes, A.T., Miranda, T. and Araújo, N., Influence of discrete fiber reinforcement on the uniaxial compression response and seismic wave velocity of a cement-stabilized sandy-clay. Geotextiles and Geomembranes 43, no. 1, 2015, pp. 1-13.

[22] Maher, M.H., and Gray D. H., Static response of sands reinforced with randomly distributed fibers. Journal of geotechnical engineering 116, no. 11, 1990, pp. 1661-1677

[23] Consoli, N.C., Prietto P. D., and Ulbrich L. A., Influence of fiber and cement addition on behavior of sandy soil. Journal of geotechnical and

geoenvironmental engineering 124, no. 12, 1998, pp. 1211-1214.

[24] Tavenas, F., Leblond, P., Jean, P. and Leroueil, S., 1983. The permeability of natural soft clays. Part I: Methods of laboratory measurement. Canadian Geotechnical Journal, 20(4), pp.629-644.

[25] Lopresto, V., Leone, C. and De Iorio I., Mechanical characterization of basalt fiber reinforced plastic. Composites Part B: Engineering 42, no. 4, 2011, pp. 717-723.

[26] Berozashvili, M., Continuous reinforcing fibers are being offered for construction, civil engineering, and other composites applications. Adv Mater Com News, Compos Worldwide 6, 2001, pp. 5-6.

[27] Sim, J. and Park, C., Characteristics of basalt fiber as a strengthening material for concrete structures. Composites Part B: Engineering 36, no. 6-7, 2005, pp. 504-512.

[28] Robert, W.D., Soil testing manual: procedures, classification data, and sampling practices. Press of Ohio, OH, USA, 2008.

[29] Anupam, A.K., Kumar, P. and Ransinchung, G.D., Permeability study on fly ash and rice husk ash admixes with subgrade soil for pavement construction. In Proceedings of International Conference on Advances in Architecture and Civil Engineering (AARCV 2012),Vol. 21, 2012 p. 489.

[30] Lawton, E.C., Khire, M.V. and Fox, N.S., Reinforcement of soils by multioriented geosynthetic inclusions. Journal of Geotechnical Engineering, 119(2), 1993, pp.257-275.

[31] Hossain, M.Z. and Sakai, T.,. The effectiveness of nominal dosage of ordinary cement on strength and permeability of clayey soil. Journal of the Japanese Society of Soil Physics, 110, 2008, pp.25-35.

11th Int. Conf. on Geotechnique, Construction Materials & Environment,
Kyoto, Japan, 3-5 November 2021, ISBN: 978-4-909106063 C3051

SEISMIC PERFORMANCE EVALUATION OF PFS METHOD BY SOIL-WATER COUPLED FINITE DEFORMATION ANALYSIS

Kentaro Nakai[1], Kakuta Fujiwara[2] and Nanase Ogawa[3]

[1]Faculty of Engineering, Nagoya University, Japan
[2] Faculty of Engineering, Tokai University, Japan
[3] Giken Ltd., Japan

ABSTRACT

The PFS method (Partially Floating Sheet pile method) has been frequently used as a countermeasure to reduce settlement during embankment construction due to the edge cutting effect. However, the aseismic effect has not yet been fully discussed. Therefore, to expand the applicability of the PFS method, seismic response analyses for river embankments on sand - clay alternating ground was conducted. As a result, it was shown that the PFS method can significantly reduce the earthquake damage compared to the floating sheet pile method, although it is not as good as the end-bearing sheet pile method. However, when the embedment depth of the floating sheet pile of the PFS method was short, the aseismic effect was reduced; that is not only the amount of settlement of the embankment increase but also the amount of lateral displacement of the soft clayey layer increases.

Keywords: PFS method, seismic response analysis, lateral displacement

INTRODUCTION

Steel sheet piles have been used for temporary construction to suppress lateral deformation of the ground and ensure stability. However, at present, it is also used as a permanent structure not only to prevent slip failure but also to reinforce embankments and suppress lateral flow and settlement in the soft ground under embankment construction. As for the settlement countermeasure method using steel sheet piles, the end bearing sheet pile method has been used so far, in which all the piles are embedded into the supporting layer. However, if the soft ground is thick, the pile length becomes very long and causes cost problem. In addition, the floating sheet pile method, which does not allow the piles to penetrate to the supporting layer, is economically effective and can be expected to have a certain effect on settlement countermeasures, but it also has the disadvantage of settlement of the pile itself. Based on these problems, the PFS method (Partially Floating Sheet pile method) shown in Fig. 1 has been developed.

The PFS method has many achievements in river embankments on the soft ground of the Kumamoto Plain. In the 2016 Kumamoto earthquake, there is a report that the PFS method, which was implemented as a countermeasure against settlement and lateral displacement, also suppressed the deformation during the earthquake. However, the aseismic effect has not yet been fully discussed for the PFS method. Therefore, to expand the applicability of the PFS method, seismic response analyses of river embankment on sand - clay alternating ground was conducted.

In this paper, a numerical investigation on the aseismic effect of the PFS method was conducted, as well as the effect of settlement and lateral displacement at the time of static loading due to embankment construction. The analysis code employed in this study was the soil-water coupled finite deformation analysis GEOASIA [1], which incorporates an elasto-plastic constitutive model, namely SYS Cam-clay model [2], that allows a description of the behavior of soils ranging from sand through intermediate soils to clay within the same theoretical framework. This analysis code can be applied to both ground deformation and failure and can be used to analyze co-seismic behavior over a time range of a few seconds to a few minutes and post-seismic behavior, in which case the time range is from a few years to a few centuries.

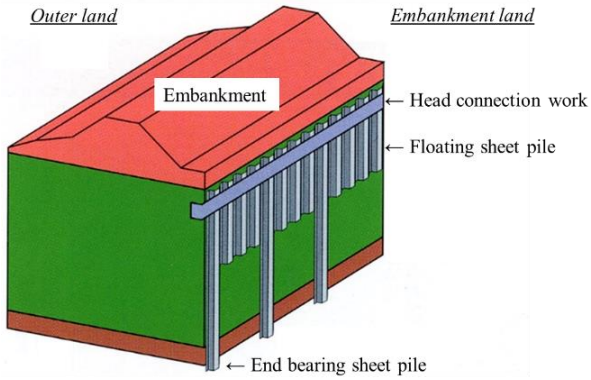

Fig. 1 Schematic figure of PFS method

ANALYSIS CONDITION

Figure 2 shows the finite element mesh used in this analysis. Target ground was soft sand-clay layer ground near the estuary of the Kikuchi river in Kumamoto plain. The ground was assumed to be initially horizontally layered, with an alternate layer of sand and clay. The hydraulic boundaries for the subsurface were designated as drained boundaries, and the bottom end and the two lateral faces were designated to be under undrained conditions. Periodic boundaries were realized by tying two nodes with the same height between both lateral ends.

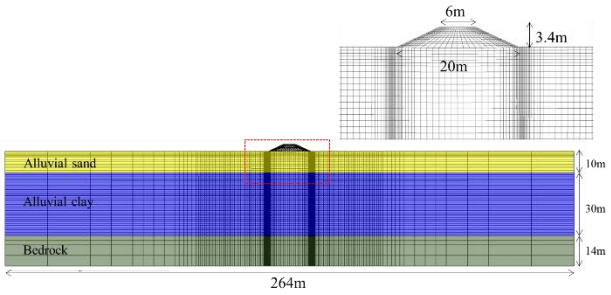

Fig. 2 Finite element mesh used in the analysis

Table 1 shows the elasto-plastic parameters (material constants and initial conditions) of the soils used in this analysis. These parameters were all determined based on the results of laboratory testing using undisturbed samples obtained from in-situ boring surveys. The elasto-plastic parameters were determined by replicating the results of these mechanical behaviors using the SYS Cam-Clay Model. Figures 3 and 4 show some examples of the reproduction results. The parameters were identified by reproducing the shear behavior to the compression behavior with a single set of material constants. For detail, please see reference [3].

Table 1 Elasto-plastic parameters of soils

	Emb	Sand	Clay	Bedrock
Elasto-plastic parameters				
Critical state index M	1.60	1.60	1.65	1.80
NCL intercept N	1.70	2.28	1.90	2.00
Compression index $\tilde{\lambda}$	0.05	0.165	0.243	0.05
Swelling index $\tilde{\kappa}$	0.005	0.025	0.020	0.005
Poisson's ratio ν	0.30	0.20	0.40	0.10
Evolution parameters				
Degradation index of structure a	1.00	1.00	0.60	0.01
Ratio of $-D_v^p$ to $\|D_s^p\|$ c_s	1.00	1.00	0.07	1.00
Degradation index of OC m	5.00	3.00	10.0	20.0
Rotational hardening index br	0.00	0.00	0.00	0.00
Limit of rotational hardening m_b	0.00	0.00	0.0	0.00
Initial conditions				
Specific volume v	-	-	-	-
Stress ratio η_0	0.545	0.545	0.545	0.545
Degree of structure $1/R^*_0$	1.0	1.05	20.0	1.00
Degree of overconsolidation $1/R_0$	200.0	30.0	1.80	500.0
Degree of anisotropy ς_0	0.00	0.00	0.00	0.00
Soil particle density ρ_s (g/cm3)	2.65	2.65	2.65	2.65
Mass permeability index k (cm/s)	1.0×10^{-5}	1.0×10^{-4}	1.0×10^{-6}	1.0×10^{-7}

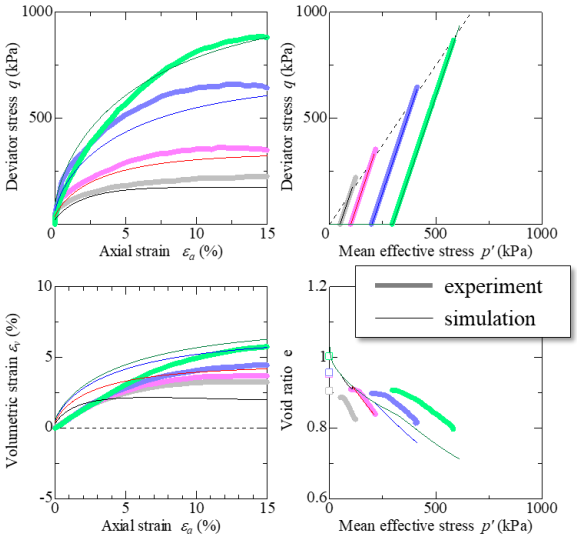

Fig. 3 Undrained shear behavior of clay

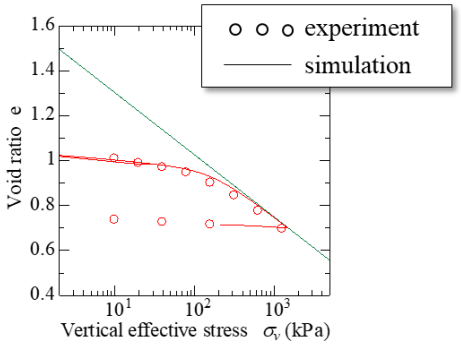

Fig. 4 One-dimensional compression behavior of clay

Table 2 shows the elastic parameters of sheet piles used in this analysis. The two-dimensional modeling of the PFS method was considered as follows [4, 5]. Although the sheet pile shows a complicated shape, it is considered as a mixture of the sheet pile and the surrounding ground and modeled as a one-phase elastic body so that the rigidity and weight per unit depth are equal. In addition, in the case of the PFS method under plane strain conditions, sheet piles and ground exist discretely in the same plane. Therefore, we considered the space between the end-bearing sheet piles as one unit and assumed average the rigidity within the unit. It was modeled as a two-phase elastic body and the hydraulic conductivity is assumed to equal to the ground.

Table 2 Elastic parameters for steel sheet pile

	Actual sheet pile	Sheet pile 1-phase mat.	Sheet pile 2-phase mat.
Density ρ (g/cm3)	7.80	1.80	1.80
Poisson's ratio ν	0.3	0.3	0.3
Young's modulus E (GPa)	200	43.15	7.2
Mass permeability index k (cm/s)	-	-	1.0×10^{-6}

Numerical analyses were carried out in the following steps.

1) A steel sheet pile was modeled by replacing the soil with a linear elastic material.
2) Embankments 3.4 m in height with slope gradients of 2:1 were constructed on the initial ground by adding finite element meshes.
3) The seismic waveform was input in the horizontal direction equally on all nodes of the bottom face of the ground. The seismic motion was the assumed Nankai trough earthquake prepared by the Cabinet Office. As you can see from Fig. 5, in addition to large acceleration, seismic motion contains many long-period components and has a long duration.
4) After the earthquake, consolidation has proceeded until the deformation converged.

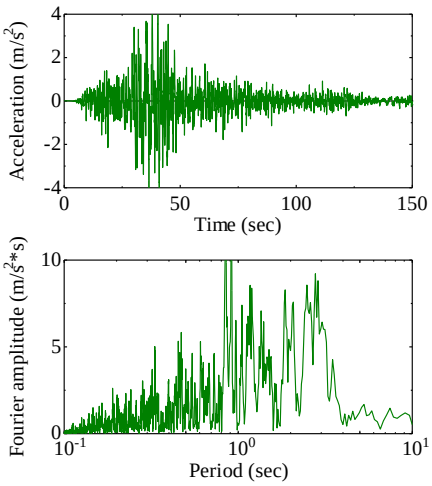

Fig. 5 Input seismic motion (expected Nankai trough earthquake by Cabinet Office)

ANALYSES CASES

Figure 6 shows the distribution of settlement in the depth direction during the embankment construction. The ground is the case of no countermeasures, and the measurement point of the settlement was at the embankment toe. According to the PFS method manual [6], the embedment depth of the floating sheet pile in the PFS method is calculated as the neutral point of the settlement distribution map. Therefore, the embedment depth of the floating sheet pile was determined as 20m in this research.

Figure 7 shows five analysis cases. The left side of the figure (assuming the outer land side of the embankment) is assumed to have end-bearing sheet piles in all cases. In addition to the (a) no countermeasure ground, (b) the end bearing sheet pile method, and (c) the floating sheet pile method was assumed. Moreover, two types of PFS methods with different floating sheet pile lengths were assumed.

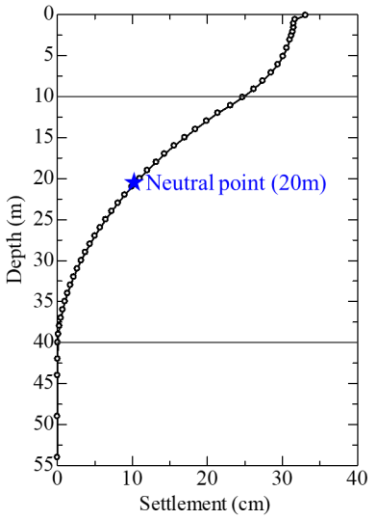

Fig. 6 Settlement distribution in the depth direction

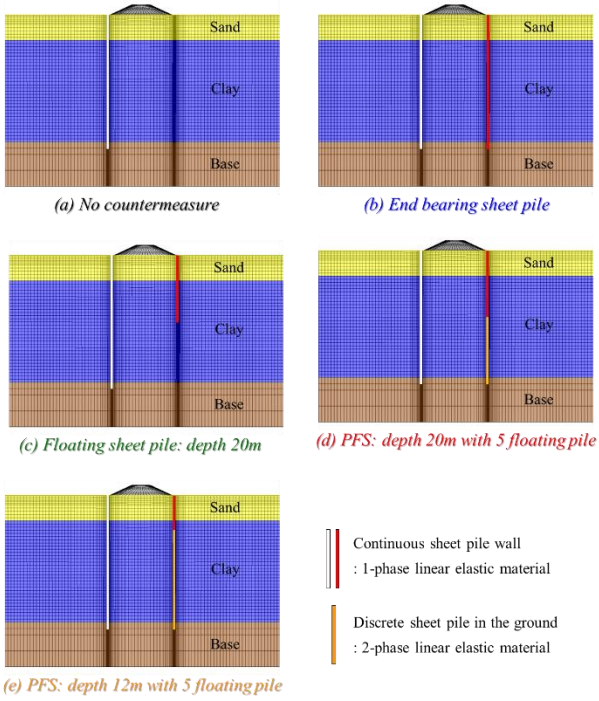

Fig. 7 Analysis cases (different countermeasures)

LATERAL DISPLACEMENT SUPPRESSION EFFECT DURING EMBANKMENT CONSTRUCTION

Figures 8 and 9 show the settlement at the embankment crown and lateral displacement at the embankment toe caused by the embankment construction.

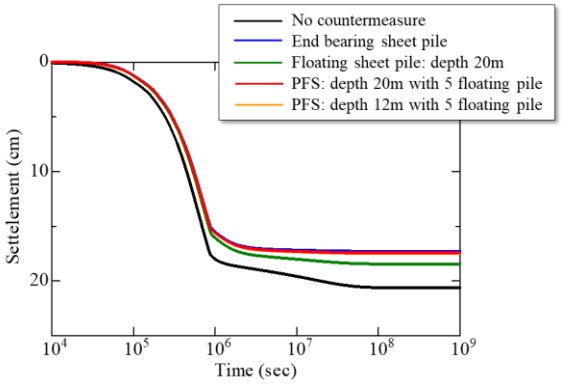

Fig. 8 Settlement at the embankment crown

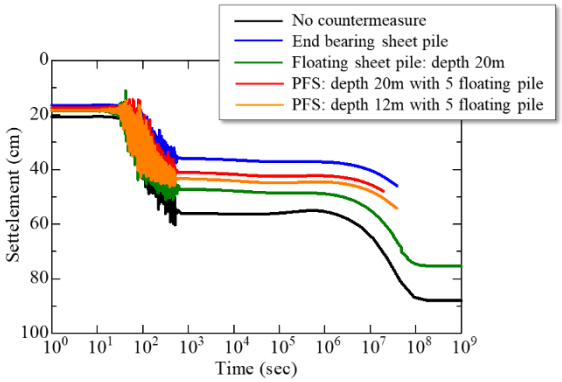

Fig. 10 Settlement during and after the earthquake at the embankment crown

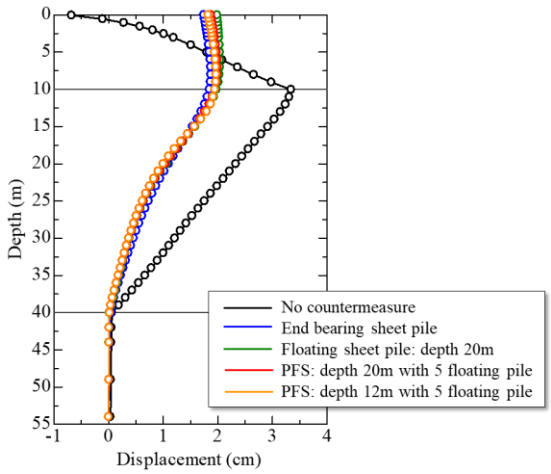

Fig. 9 Lateral displacement distributions to depth direction at the embankment toe

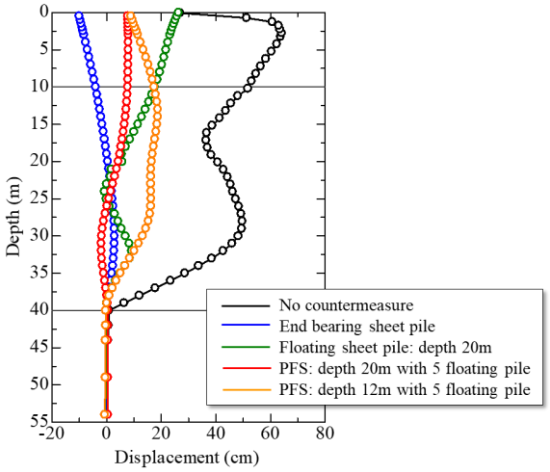

Fig. 11 Lateral displacement distributions to depth direction at the embankment toe 300 seconds after the occurrence of an earthquake

Compared to no countermeasures for both the settlement and the horizontal displacement, the amount of deformation can be suppressed in the order of the floating sheet pile method, the PFS method, and the end-bearing sheet pile method. This tendency is also consistent with the reference [7]. There is no significant difference in deformation depending on the type of countermeasure, but this is thought to be due to the large sand layer thickness of 10 m. This is considered to be due to the dispersing effect of the embankment load by the thick sand layer.

ASEISMIC EFFECT OF THE VARIOUS STEEL SHEET PILE METHODS

Figure 10 shows the settlement at the embankment crown during and after the earthquake. The initial settlement at time $t = 0$ is the displacement during the embankment construction shown in Fig. 8. Figure 11 shows lateral displacement distributions to depth direction at the embankment toe 300 seconds after the occurrence of an earthquake.

Unlike the static behavior during embankment loading, the dynamic deformation during an earthquake differs depending on the countermeasures. In the case of no countermeasures, the embankment will sink 90 cm and cause a lateral displacement of about 60 cm near the ground surface. However, in the case of the end-bearing sheet pile method, the amount of settlement will be reduced to about 2/3. Moreover, there is no lateral displacement at the embankment toe; it is pulled by the embankment settlement and causes a slight negative displacement. The floating sheet pile method and the PFS method are located between no countermeasures and end bearing sheet pile method. However, the floating sheet pile method has a larger amount of deformation and is close to no countermeasures. As can be seen from Fig. 12 below, in the case of the floating sheet pile method, the shear strain is concentrated at the tip of the sheet pile, and it can be seen that the clay layer near the tip was disturbed. The PFS method has a smaller amount of deformation than the floating sheet pile method and is close to an end-bearing sheet pile method. In particular, the effect of suppressing lateral displacement near the

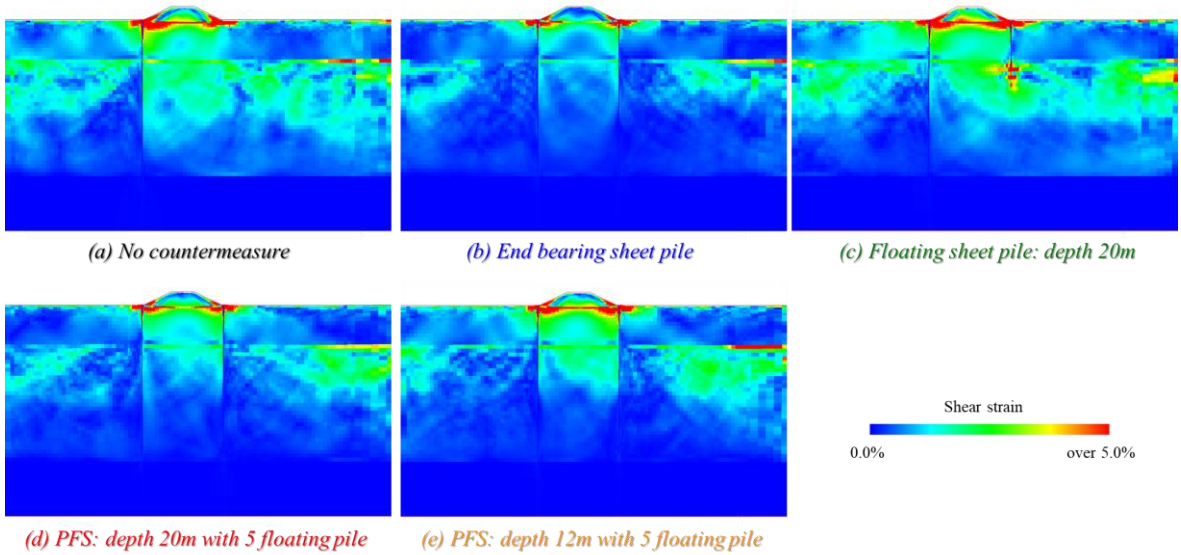

Fig. 12 Shear strain distributions 300 seconds after the occurrence of an earthquake

ground surface is great. It can be seen that when the depth of the floating sheet pile is shallow, lateral displacement (slip-through that occurs between the end bearing sheet piles) occurs in the deep part of the ground. However, when the embedment depth of the floating pile is 20 m, the amount of slip-through can be strongly suppressed.

Next, the influence area of seismic deformation was examined. Figure 12 shows shear strain distributions 300 seconds after the occurrence of an earthquake. In the case of no countermeasures or the floating sheet pile method, it can be seen that the shear strain spreads in the embankment land region on the right side of the figure. In the case of the PFS method, although it is not as good as the end-bearing sheet pile method, the shear strain growth to the embankment land was suppressed, and the deeper the depth of the floating sheet pile, the greater the effect.

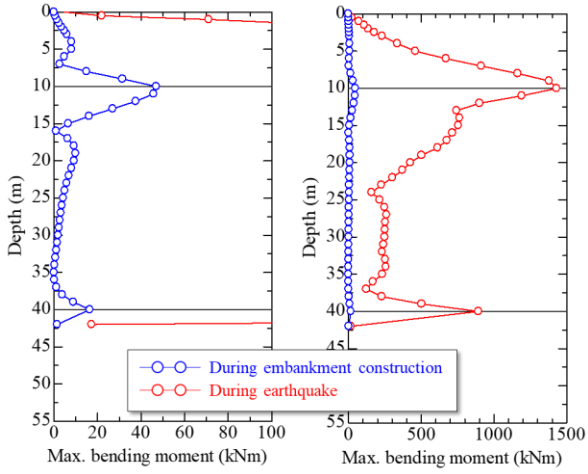

Fig. 13 Cross-section performance check of the sheet pile in case of PFS method with its floating pile 20m

Figure 13 shows the maximun bending moment acting on the sheet pile during embankment construction and earthquake. Comparing the bending moments acting on the sheet pile during embankment construction and during earthquakes, it can be seen that the bending moments during the earthquake are overwhelmingly larger than that of embankment construction. Since this research targeted a huge earthquake called the Nankai Trough earthquake, it means that there is a risk that a large moment will act during the earthquake and might exceed the yield and/or permissible values.

From the above discussions, the embankment deformation caused by the earthquake decreased in the order of no countermeasure >> floating sheet pile method> PFS method > end bearing sheet pile method, and the aseismic effect of the PFS method could be confirmed. In addition, the PFS method is considered to be more effective in suppressing lateral flow, especially near the ground surface, than the floating sheet pile method. In the case of the floating sheet pile method, the sheet pile itself flows together with the ground because the ground at the tip of the sheet pile was disturbed.

CONCLUSIONS

In this paper, a numerical investigation on the aseismic effect of the PFS method was conducted using soil-water coupled finite deformation analysis. Although the PFS sheet pile has a complicated three-dimensional structure, a simple two-dimensional plane strain model is derived by giving the average physical properties (equivalent rigidity and equivalent weight) of the steel sheet pile and the

ground per unit depth. The following conclusions were obtained.

1) Embankment damage (settlement of the embankment crown and horizontal displacement of the embankment toe) caused by the earthquake decreased in the order of no countermeasure >> floating sheet pile method> PFS method > end bearing sheet pile method, and the aseismic effect of the PFS method was confirmed.
2) PFS method was considered to be more effective in suppressing lateral flow, especially near the ground surface, than the floating sheet pile method. In the case of the floating sheet pile method, the sheet pile itself flows together with the ground because the ground at the tip of the sheet pile was disturbed.

Since this study was conducted under the condition that the sand layer thickness was relatively large. Therefore, it is necessary to investigate when the sand layer thickness was thinner, and when the soil layer conditions were different. In addition, since the seismic motion was very large as the Nankai trough earthquake, we should further work with different input seismic motion characteristics. Based on these additional studies, we would like to evaluate the aseismic performance of the PFS method and promote the expansion of the application of the PFS method.

ACKNOWLEDGMENTS

This research was supported by the International Press-in Association TC3 (Chair: Prof. Jun Otani). The authors express deep appreciation for the cooperation and useful discussion.

REFERENCES

[1] Noda, T., Asaoka, A., and Nakano, M., Soil-water coupled finite deformation analysis based on a rate-type equation of motion incorporating the SYS Cam-clay model, Soils and Foundations, Vol. 48, No. 6, 2008, pp. 771–790.
[2] Asaoka, A., Noda, T., Yamada, E., Kaneda, K., and Nakano, M., An elasto-plastic description of two distinct volume change mechanisms of soils, Soils and Foundations, Vol. 42, No. 5, 2002, pp. 47–57.
[3] Nakai, K., Noda, T., Taenaka, S., Ishihara, Y. and Ogawa, N., Seismic assessment of steel sheet pile reinforcement effect on river embankment constructed on a soft clay ground, Proceedings of the First International Conference on Press-in Engineering, 2018, pp.221-226.
[4] Fujiwara, K., Ogawa, N. and Nakai, K., 3-D numerical analysis for partial floating sheet-pile method under liquefaction, Journal of JSCE, Vol. 9, No.1, 2021, pp.138-147.
[5] Ogawa, N., Fujiwara, K. and Nakai, K., Analytic considerations on two-dimensional modeling of partial floating sheet pile method, Proceedings of 11th International Conference on Geotechnique, Construction Materials and Environment, GEOMATE 2021.
[6] PFS method association, Technical note for the PFS method, 2005. in Japanese.
[7] Kasama, K., Fujiyama, H. and Otani, J., 3D fem analysis of partial floating steel sheet piling method on two-layered ground, Proceedings of 2nd International Conference on Press-in Engineering (ICPE) 2021.

11th Int. Conf. on Geotechnique, Construction Materials & Environment,
Kyoto, Japan, 3-5 November 2021, ISBN: 978-4-909106063 C3051

STRENGTH EVALUATION OF CEMENT-TREATED SAND-EXPANDED POLYSTYRENE BEAD LIGHTWEIGHT FILL

Khola Iqbal[1], Hammad Siddique[2], Waleed Iqbal[2], Taro Uchimura[1] and Zain Maqsood[3]

[1]Department of Civil and Environmental Engineering, Saitama University, Japan; [2] Department of Civil Engineering, Mirpur University of Science and Technology, Mirpur, Pakistan; [3] School of Civil and Environmental Engineering, National University of Sciences and Technology, Islamabad, Pakistan

ABSTRACT

EPS (expanded polystyrene) is a light weight geo-synthetic material which can be utilized for various geotechnical applications including the desired compressive strength of soil, construction on the soft soils, reduction of the soil settlement, construction cost reduction, enhancement of slope stability and reduction in the lateral earth pressure. This study investigates the variation of physical and mechanical properties of the lightweight bulk filling material prepared with sandy soil mixed with different contents of Ordinary Portland Cement (OPC) and expanded polystyrene (EPS) beads. The influence of EPS beads and cement content on density and strength of this lightweight bulk filling material was examined by a series of laboratory tests including Modified Proctor Tests and Unconfined Compressive Strength (UCS) tests on cylindrical specimens. The test results showed that the inclusion of EPS beads in the mixture significantly reduces its density i.e. addition of 0.25% EPS beads reduces the density of the mixture by 10%. Further, the compressive strength of the mixture decreases with the increase in the EPS beads, however, the desired strength can be achieved by adding an optimum amount of cement content.

Keywords: Cement; Expanded polystyrene beads; Embankments; sand; Lightweight fill material.

INTRODUCTION

Excessive soil Settlement, bearing capacity failures, slope instability are some major challenges that are faced during the construction of infrastructure particularly during the construction of embankments on soft soils. Several ground improvement techniques are in practice in order to mitigate these problems including the haulage of good quality soil from considerable distances which greatly affect the cost of the projects. However, researchers nowadays are trying to develop light weight fill materials that would reduce the weight of the embankments to ensure that soft soils are not overloaded. This serves as major solution for mitigation of settlement problems in poor capacity soils.

From shredded tyres to geo-foam and air-foams various kinds of lightweight materials have been developed over the passage of time and have been used in my projects [1-6]. Engstrom and Lamb [7] came up with the idea of using the shredded tyres as a lightweight fill material in road construction to minimize and reduce the environmental issues because of waste tyres, this method was first adopted in Minnesota during 1985. They concluded that this kind of fill material not only proves to be beneficial for the environment but is also useful in construction. A research report was submitted by Stark et al. (2004) [8] to the Transportation Research Board highlighting the use of geo-foam (e.g. expanded polystyrene (EPS) blocks) as fill material in highway embankments and comparing the costs of this with that of general embankments. It was concluded that geo-foam proved to be a safe and economical method of dealing with the embankments on soft soil.

Expanded Polystyrene (EPS) is a lightweight material that has been used in recent years as a geo-foam to improve the properties of soft soils for constructing embankments. It has been noted to improve the bearing capacity of the stabilized soil, decrease permeability and lower the unit weight of the stabilized soil thus producing a lightweight composite material with better engineering properties [9]. Reference to EPS Industry Alliance (2012), EPS is approximately 1% of the soil weight, and is less than 10% the weight of other lightweight fill alternatives. This makes EPS embankments lighter compared with compacted soil embankments, and accordingly reduces the dead loads imposed on underlying soil. This in turn also allows to construct cost effectively and timely, and simplicity of construction as EPS blocks are easy to handle without the need for special equipment, and can be easily cut and shaped on site. Owing to the availability of EPS geo-foam in various densities, it can be selected by the designer depending on specific geotechnical application. As it retains its physical properties under various conditions, its durability and service span are comparable with various other construction materials [10].

However, the use of EPS geofoam is limited sometimes by its inability to fit irregular spaces. In such cases EPS- soil composite is an alternative. This

research was therefore conducted to investigate how the different properties of the sandy soil are affected by varying the contents of EPS beads and cement in regard to its suitability for a foundation material.

EXPERIMENTAL PROGRAM

Material Properties and Mixing Properties

The light weight material used in this research was made of sand, Portland cement, expanded polystyrene (EPS) beads, and water. The sand used was procured from Mangla, located in the State of Azad Jammu and Kashmir, Pakistan. Fig. 1 presents the physical properties and the particle-size distribution curve of this sand.

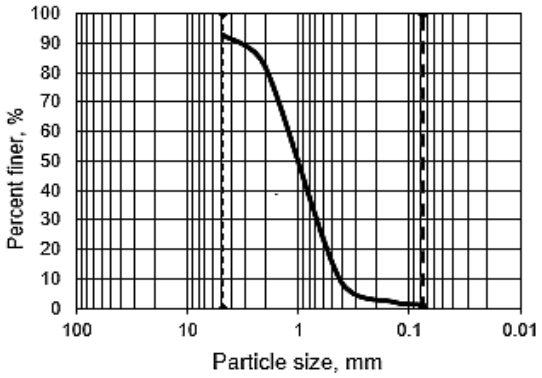

Fig. 1 Particle size distribution of sand used in the study

EPS beads are white, rounded particles with varying diameters depending on the manufacturing procedure. The EPS beads used in this study, shown in Fig. 2, were 2-5 mm in diameter having specific gravity of 0.044.

Fig. 2 EPS Beads used in study

Cement used was Ordinary Portland Cement to bind the cohesionless sand and EPS beads such that they would be easier to compact as well as stable and sufficiently strong to carry the required load after an appropriate curing time. Water was added for carrying out the hydration reaction and facilitate the mixing process.

The proportions of each material were taken by percentage weight. Varying contents of cement and EPS beads used in this study are presented in table 1. Based on the desired mixing ratio, the materials were weighed by electronic scale with an accuracy of 0.01 g. The mixing procedure used is presented as follows:

Dry sand and Portland cement were mixed first. Then water was added into the mixture and stirred properly; EPS beads were lastly added into the mixture and stirred to ensure the uniformity of the mixture. EPS beads had to be added after water was added in the soil and cement mixture for even distribution of water in the mixture since the EPS beads cover the mixture completely owing to their greater volume and adhesive nature. The whole mixing process took about 30 minutes.

Table 1 Mix proportions used in this study

EPS Beads (%)	Cement (%)
0, 0.25, 0.5, 1	5, 10, 20

Modified Proctor Tests

To obtain the optimum water content and the maximum dry density of the lightweight fill, modified Proctor tests [11] were undertaken. Besides determining OMC and MDD of each mix proportion for the sample preparation of unconfined compression tests, the effects of varying contents of EPS beads and cement on the soil composite were also examined.

Unconfined Compression Strength Tests

The unconfined compressive strength (UCS) tests [12] were conducted on cylindrical specimens with a diameter of 50 mm and height of 100 mm at the OMC and MDD condition determined earlier. The unconfined compression test device used is automatic and computer-controlled; the deformation rate was 0.5 mm/min.

Specimen Preparation

The moulds for the specimens were prepared manually by cutting the PVC pipes into the desired dimensions as shown in Fig. 3. The specimens were compacted with a metallic tamper in 5 layers. Each layer was given 25 blows. After preparation of specimen, it was wrapped properly, making it airtight. After the curing period, the specimens were removed from the moulds and tested.

(a)

(b)

Fig. 3 (a) Specimen during compaction (b) Prepared Specimen

RESULTS AND DISCUSSION

Modified Proctor Tests

Effect of EPS Beads Content

The effect of the varying content of EPS beads on OMC and MDD was investigated by conducting modified proctor tests. Four soil composites were prepared for this purpose with EPS beads content of 0%, 0.25%, 0.5% and 1% by weight of the composite.

The compaction behavior of the mixture in Fig. 4, indicates that increase in the EPS beads has no significant impact on the OMC, while it remarkably reduces the MDD of the samples. This is because firstly, the density of EPS is much less than the other materials and secondly, EPS beads are damping some of the compaction energy. The reduction is attributed to the EPS particles, of lower density, occupying the space that would have been occupied by the sand particles. Owing to the low volume mass ratio of EPS, the stabilised sample re-duces in the MDD (Illuri 2007)

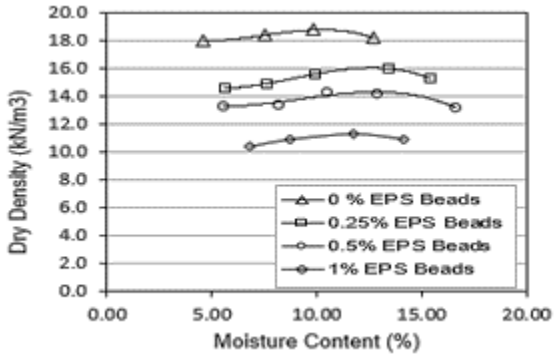

(a)

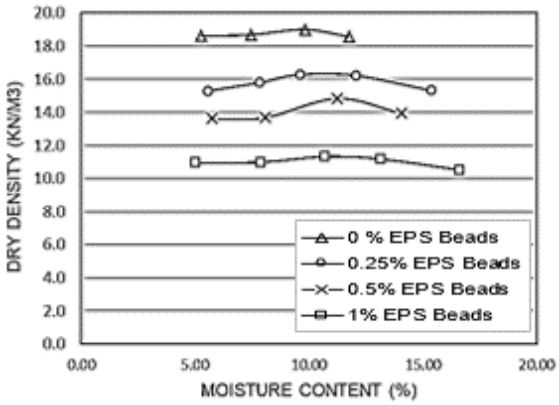

(b)

Fig.4 Effect of EPS Beads content on compaction parameters at cement content of (a) 10% (b) 20%

Effect of Cement Content

To investigate the effect of the cement content on the optimum water content and the maximum dry density of the lightweight fill, soil composites were prepared at cement contents of 5, 10 and 20% while keeping the EPS content constant and tested using the Modified Proctor test. The test results showed that the increase in cement content increases the maximum dry density while having no significant effect on the OMC of the composite as depicted in Fig. 5 which is in contradiction with the results of Brooks et al. (2010) which showed that the MDD and the OMC of the sample could be decreased and increased, respectively, when the amount of pozzolanic material is increased. However, bearing in mind that the compaction behavior of the mixture depends on different factors including the material type and composition.

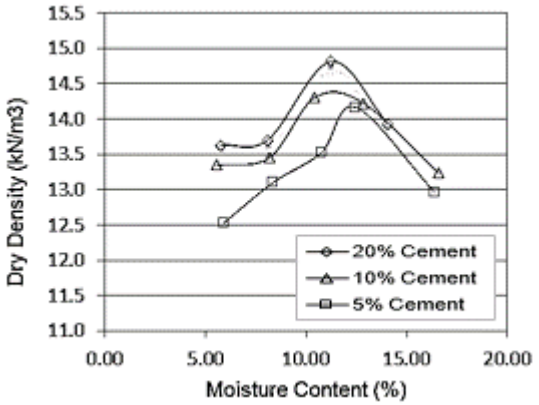

Fig. 5 Effect of cement content on compaction parameters at EPS Beads content of 10%

Unconfined Compression Strength Tests

According to the test results, increase in EPS beads content decreases the peak compressive stress, qu, of all samples Fig. 6. This can be due to the higher

compressibility of EPS beads compared to other constituents of the mixture. Moreover, EPS beads hinder the bond between the constituents due to its inability to absorb water.

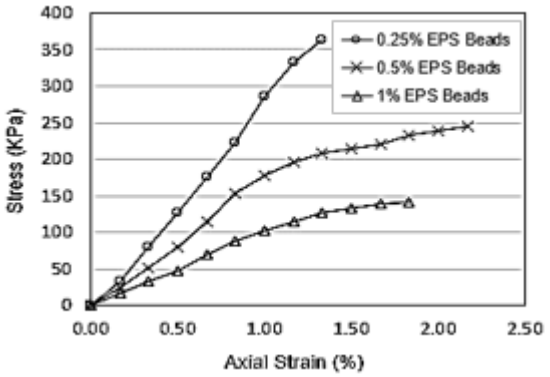

Fig. 6 Effect of EPS Beads on Compressive Strength of the composite having 10% cement content

CONCLUSIONS

This study investigated the suitability of using a lightweight fill material composed of sand, EPS beads and cement for construction of embankments over soft soils. Mechanical properties of the composite were evaluated with laboratory tests including the modified proctor tests and unconfined compression strength (UCS) tests. The main findings of the study are as follows:

• Increasing the amount of cement increased the MDD with no remarkable effect on OMC of the light weight fill

• During compaction tests, bleeding was observed with the increase in the amount of moisture content.

•An increase in the EPS beads content resulted in decline of compressive strength of the light weight fill which, however, can be compensated by an increase in cement content in optimum quantity.

ACKNOWLEDGMENTS

The authors wish to acknowledge Muhammad Kamran Attique and Munib Arif for their assistance in experimental work and interpretation of results.

REFERENCES

[1] Oh,W. S., Lee, J. K., Kwon, Y. C., and Lee, B. J. (2002). “Bearing capacity of light weight soil using recycled Styrofoam beads.” Proc., 12th Int. Offshore and Polar Engineering Conf., ISOPE, CA, 670–674.

[2] Tsuchida, T., and Kang, M. S. (2002). “Use of lightweight treated soil method in seaport and airport construction projects.” Proc., Nakase Memorial Symp., Soft Ground Engineering in Coastal Areas, Balkema, London, 353–365.

[3] Gan, C. H., and Tan, S. M. (2003). “Some construction experience on soft soil using lightweight materials.” Proc., 2nd Int. Conf. on Advance in Soft Soil Engineering and Technology, Universiti Putra Malaysia Press, Serdang Selangor Darul Ehsan, Malaysia, 1–8.

[4] Tsuchida, T., and Egashira, K. (2004). “The lightweight treated soil method: New geomaterials for soft ground engineering in coastal areas.” A. A. Balkema, London.

[5] Wang, F., and Miao, L. C. (2009). “A proposed lightweight fill for embankments using cement-treated Yangtze River sand and expanded polystyrene (EPS) beads.” Bull. Eng. Geol. Environ., 68(4), 517–524.

[6] Miao, L. C., Wang, F., Lv, W. H., and Li, J. (2010). “Study on cement-treated Yangtze hydraulic sand mixed with expanded polystyrenes (EPS) beads as backfill material in highway embankments.” Proc., GeoShanghai Int. Conf., ASCE, Shanghai, China, 372–378.

[7] Engstrom GM, Lamb R (1994) Using shredded waste tires as a lightweight fill material for road subgrades. Report MN/RD-94/10 to Minnesota Department of Transportation

[8] Stark, T. D., Horvath, J. S., and Leshchinsky, D. (2004). “Geo-foam application in the design and constructionof highway embankments.” TRB Project No. 24-14, TRB, Washington, DC.

[9] Stark, T. Bartlett, S. & Arellano, D. 2012. Expanded polystyrene (EPS) geofoam applications & technical data.EPS Industry Alliance.

[10] AbdelSalam, S.S., Azzam, S.A.: Reduction of lateral pressures on retaining walls using geofoam inclusion. ICE Geosynth. Int. 23(6), 395–407 (2016)

[11] ASTM (2012), Standard Test Methods for Laboratory Compaction Characteristics of Soil Using Modified Effort (56,000 ft-lbf/ft3(2,700 kN-m/m3)), ASTM D1557-12e1, West Conshohocken, Pennsylvania, U.S.A.

[12] ASTM (2016), Standard Test Method for Unconfined Compressive Strength of Cohesive Soil,ASTM D2166/D2166M-16, West Conshohocken, Pennsylvania, U.S.A.

Construction Material

11th Int. Conf. on Geotechnique, Construction Materials & Environment,
Kyoto, Japan, 3-5 November 2021, ISBN: 978-4-909106063 C3051

ADHESIVE FRACTURE MODES BETWEEN STEEL ANCHOR AND INJECTABLE MATERIAL AND CONCRETE IN CONSIDERATION OF WEDGE-SHAPED EFFECT

Tanaka Hidenori[1]
[1]National Institute of Technology (KOSEN), Gunma College

ABSTRACT

We have used some deformed steel anchors to install fans and steel columns on the concrete structures. There was significant problem that we couldn't precisely define the fracture modes between steel anchor and injectable material and concrete in structures such as interfacial, shear and bearing of steel anchor's node. They depended on the size of specimen and the treatment of surface with brush in injectable hole. In this research, the pushing out test method was adopted by universal testing machine. Changing the experimental factors such as wedge angle, surface treatment and specimen's diameter. As the result, there were effective wedge angles to improve adhesive resistance more than twice as much as that of normal case. And we could show the evolution of cracking from the steel anchor's node and along the interfacial surface between the straight-line of steel anchor and the concrete considering axisymmetric problem in two dimensions.

Keywords: Adhesive resistance, Wedge effect, Inorganic material, Fracture mode

INTRODUCTION

We have used organic material like epoxy and urethane resin to glue steel or plastic plates to concrete structures. Especially, epoxy resin is useful for cracking repair or injectable material. but, these materials have some flaws for example, deterioration by UV light, nonconformity under water construction and non-filling in case of the upward injection in hole.

Recently, the inorganic material has made up for the defects and has been used for injectable material to connect to a steel anchor and concrete structures in case of the thin thickness.

Adhesive resistance force has been easily defined by interfacial area of two materials or hypothesis of shear or diagonal fracture. However, these patters were within narrow limits. we have to consider other fracture modes like bond-splitting and mixed shear and bond-splitting. On top of that, some studies have considered the structures which was more than 400 (mm) thicknesses and never the ratio of span and shape of injectable hole [1], [2].

In this study, we conducted some experiments to clear the adhesive force between deformed steel anchor and injectable material, or injectable material and concrete block considering fracture modes by pushing out shearing test.

We already have recognized the effect of wedge-shaped injectable form to improve adhesive force in previous research [3]. Here, we showed the experimental results by the wedge - shaped injectable form compared with those of the normal cylindrical cases, Changing wedge angles, surface treatment of injectable hole and specimen's diameter.

As the results, the most effective angle was between 3 to 5 degrees. And the maximum effect as compared with that of normal cylindrical case became more than doubled. We found three mixed modes that were bond-splitting and shear in injectable material and interfacial between injectable material and concrete regardless of thin thickness.

EXPERIMENT

Experimental method

The pulling out test method was generally conducted to pull the top of anchor. In this case, it needs special steel jigs and tools [1], [2], [4]. And this method can't check the influence of structural size (thickness, support length), bending or shear deformation. For the above reasons, we adopted the pushing out test method. And then, we controlled constantly the displacement speed of specimen by universal testing machine at 2.0 (mm/min).

In this research, we used the cylindrical concrete specimens (diameter(D) = 150 and 300,500(mm)). the compressive strength is 40 (N/mm^2) of concrete and 50 (N/mm^2) of injectable material. The injectable length that was 70 (mm) that was equal to the specimen thickness and the wedge- angles(α) were changed from 3 to 5 and 7 (degrees). And then, the injectable topped diameter was equal to 48(mm). The steel anchor protrusion length from top or bottom surface of specimen was 20 (mm) respectively. One of the specimens and the concept of pushing out test

method were shown in Fig. 1.

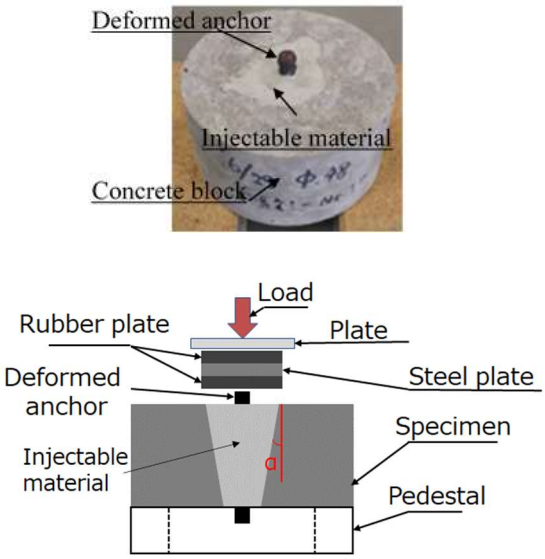

Fig.1 Typical of specimen and loading method

Material properties

We used almost same compressive strength concrete and injectable material. Because we would like to evaluate the effect of wedge-angle and treatment on side surface in injectable hole. The mix proportion of concrete and material properties were listed in Table 1 and Table 2.

Here, we set the air 7 (%) in concrete in order to keep the workability in fresh state and the durability against freezing and thawing in northern area of Gunma prefecture. And we set same value of mechanical properties both concrete and injectable material (refer to **NUMERICAL ANALYSIS**).

Table 1 Mix proportion of concrete

Gmax	Slump	W/C	Air	s/a
(mm)	(cm)	(%)	(%)	(%)
20	10	47	7	39
Quantity of material per unit of concrete volume (kg/m3)				
W	C	S	G	Sp
169	357	673	1183	2.86

Table 2 Mechanical properties

Young Modulus (kN/mm2)	Poisson's ratio
25	0.2

Experimental factors

The experimental factors were shown in Table3.

We set three experimental factors. The wedge-angle and the treatment by brush of injectable hole were expected to improve interfacial resistance between injectable material and concrete.

Next, the specimen's diameter has the influence on bending or shear fracture mode of specimen. Because the length from support point to loading point was important factor to evaluate shear capacity of concrete structure [5].

Table 3 Experimental factors

	Factor
Case1	wedge-angle (0,3,5,7 (degrees))
Case2	with or without treatment of side surface in injectable hole
Case3	specimen's diameter (150,300,500 (mm))

RESULTS OF EXPERIMENT

Effect of wedge-angle

We showed the maximum loads for all cases without treatment of side surface in hole in Fig.2.

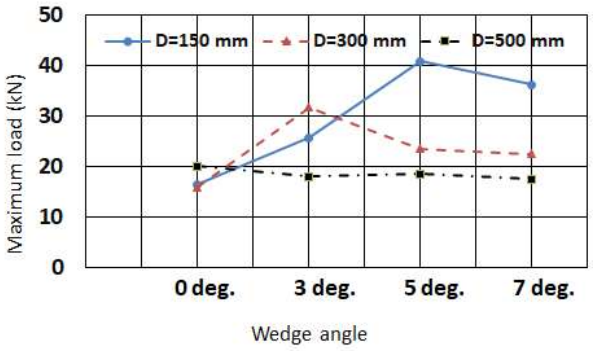

Fig.2 Relationship between max. load and angle

In the case of a diameter of 150 (mm), The maximum loads were proportion to wedge-angle. And there were the most effective angles for adhesive resistance between 5 and 7 degrees. And next, the fracture mode was radial tension due to circular tensile stress (refer to Fig.3). The bond-splitting fracture along deformed bar and the shear fracture in injectable material and the interfacial fracture were found for all cases from cut planes of specimen in detail (refer to Fig.4,5,6). We presumed that the bond-splitting fracture was occurred at first. And then, the shear and the interfacial fracture was occurred in sequence. Finally, they led to radial fracture mode. However, the interfacial fracture between injectable material and concrete was only occurred in 0 degrees (refer to Fig.7). We could determine the wedge-effect to build up the adhesive resistance without treatment.

Fig.3 Bottom of specimen (5 degrees)

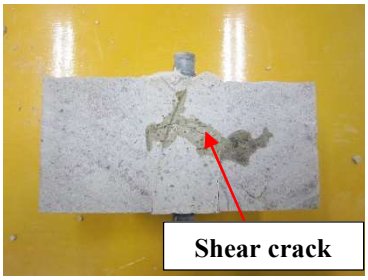

Fig.4 Cut plane of 3 degrees

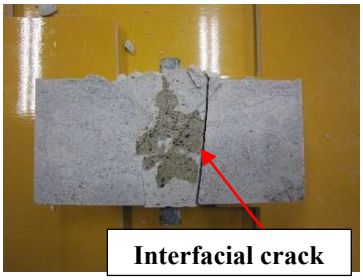

Fig.5 Cut plane of 5 degrees

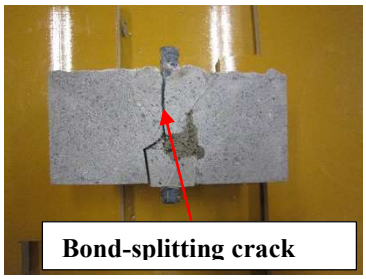

Fig.6 Cut plane of 7 degrees

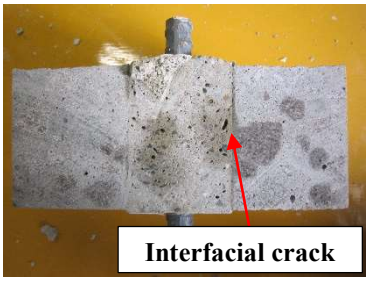

Fig.7 Cut plane of 0 degrees

In the case of a diameter of 300 (mm), The case of 3 degrees was the maximum load among others. As in the case of 150(mm), We presumed that the bond-splitting fracture was occurred at first. And then, the shear and the interfacial fracture was occurred in sequence (refer to Fig.4 and Fig.8).

Fig.8 Cut plane of 3 degrees

The cases of 5 and 7 degrees were almost same maximum load. It was considered that the radial tension fracture due to bending deformation was occurred before the shear and interfacial fracture. Therefor, the fracture mode would be shifted by wedge effect. We assumed that the wedge angle had little effect on the maximum load.

The bottom surface was shown in Fig.9.

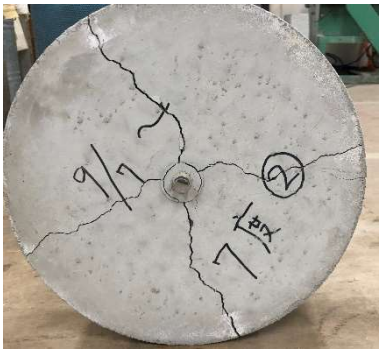

Fig.9 Bottom surface of 5 degrees

In the case of a diameter 500 (mm), there were not any effects on the maximum load due to wedge angle.

Effect of treatment by brush in hole

There was the relation between maximum load and wedge angle varying with or without treatment by brush in hole in Fig.10and Fig.11.

In the case of a diameter 300 (mm), the cases of 0 degrees and 3 degrees had significant effects on the maximum loads and fracture modes. At 0 degrees, the maximum load with treatment was 1.8 times bigger than that of without treatment. And the fracture mode without treatment was interfacial between injectable material and concrete. The other hand, with treatment was radial tension due to circular tensile stress. At 3 degrees, the maximum load without

treatment was 1.3 times bigger than that of with treatment due to wedge angle effect. And the fracture mode with treatment was radial tension due to circular tensile stress. Finally, at 5 and 7 degrees, there were little effect on the maximum load due to wedge angle. These cases were radial tension due to circular tensile stress. And, there were little effect on the maximum load due to wedge angle with treatment.

In the case of a diameter 500 (mm), regardless of whether there was a treatment or not, the maximum loads were almost same value due to wedge angle. The fracture modes were bending due to circular tensile stress (refer to Fig.12).

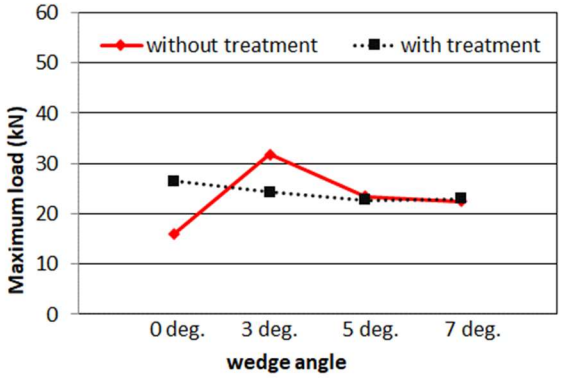

Fig.10 Max. load and wedge angle (D=300 mm)

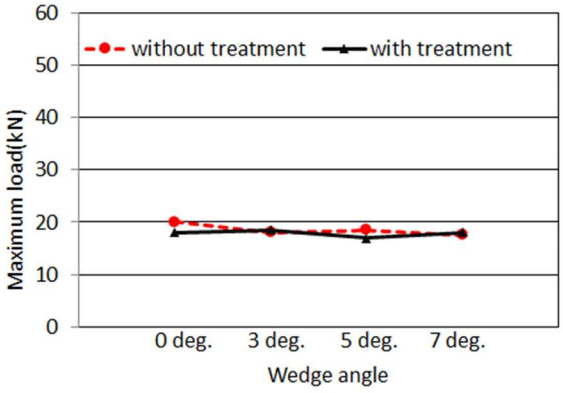

Fig.11 Max. load and wedge angle (D=500mm)

Fig.12 Bottom of specimen (without treatment)

Effect of diameter

We introduced the important parameter that so called the ratio of shear span to classify the fracture mode of the reinforced concrete structure [6]. In this section, we defined the parameter r/t. Here, r was a radius of specimen (75,150,250 (mm)) and t was a thickness (70(mm)).

The relation between the maximum load and ratio of shear span without the treatment in hole in Fig. 13.

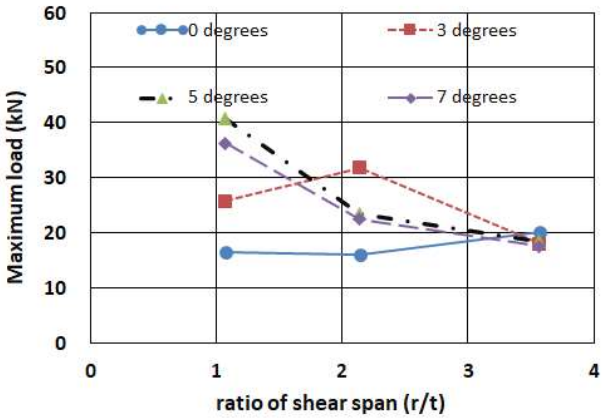

Fig.13 Max. load and ratio of shear span No.1

The wedge angle had effect on the maximum load from the case of ration of shear span 1.07 to 2.14. It showed the remarkable value at 1.07. The maximum load was almost same at 0 degrees because of interfacial fracture mode. All cases at 3.57 were bending fracture mode because of geometric shape.

The same graph with treatment was shown in Fig.14. We excluded the case of a diameter 150 (mm) because it has not been conducted yet.

There was little or no difference between any wedge angles. We recognized that the treatment by brush in hole was important factor to have an influence on the fracture mode of adhesive deformation.

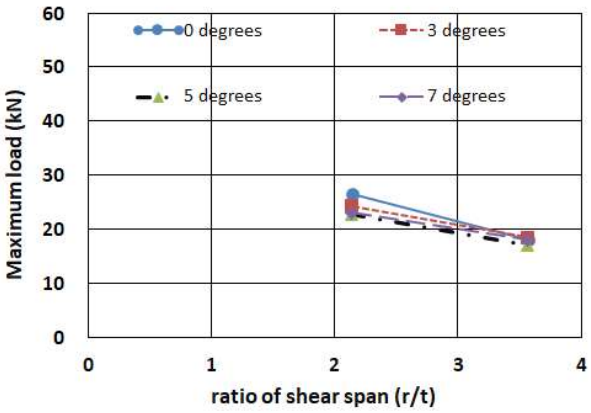

Fig.14 Max. load and ratio of shear span No.2

NUMERICAL ANALYSIS

Analysis case

In this section, we showed the numerical F.E analysis factoring in an axisymmetric problem in two dimensions by damage mechanics [7].

We selected the case of a diameter 150 (mm) and a wedge angle 5 degrees whether the bond-splitting, shear and interfacial fracture modes could be evaluated or not. The half size model with mesh division was shown in Fig.15.

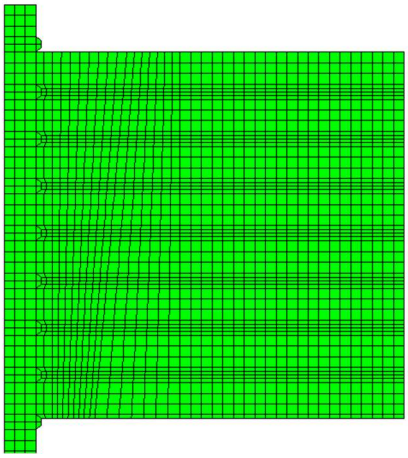

Fig.15 Model for analysis (5 degrees)

Constitutive equation

It was important to evaluate the equivalent stress and strain of material in numerical analysis. The constitutive equation was defined as followed [3].

$$F = F_p(\bar{\sigma}, \gamma, D) + F_D(Y, p, D)$$
$$= \overline{\sigma_{eq}} - \gamma - \sigma_Y + \frac{S_1}{(S_2+1)(1-D)}\left(\frac{Y}{S_1}\right)^{S_2+1} \quad (1)$$

Where F_p is the potential for growth of plastic strains, which is a function of the effective stress $\bar{\sigma}$, the plastic hardening parameter $\gamma(= Kp^n)$ and the scalar damage variable D.$F_D$is the potential for the evolution of damage, which is a function of strain energy release rate Y, material parameter S_1 , S_2 and the equivalent plastic strain p and scalar damage variable$D$. In the formulation of the constitutive equation and the yield function were assumed as follows.

$$f = \overline{\sigma_{eq}} - \gamma - \sigma_Y = 0$$
$$\overline{\sigma_{eq}} = \sigma_{eq}/(1-D)$$
$$\sigma_{eq} = \alpha I_1 + (J_2')^{1/2} \quad (2)$$

Where the following notations were used. $\overline{\sigma_{eq}}$; Effective Drucher-Prager's equivalent stress σ_Y; The yield stress, α; Material parameter I_1; The first invariant of stress , J_2'; The second invariant of stress deviator

$$dD = \left(\frac{Y}{S_1}\right)^{S_2} dp$$
$$Y = \frac{\sigma_{eq}^2}{2E(1-D)^2}$$
$$d\sigma = (1-D)d\bar{\sigma} - \bar{\sigma}dD = D_{epd}d\varepsilon$$
$$D_{epd} = \left[(1-D)C - \left\{(1-D)C\frac{\partial F_p}{\partial \bar{\sigma}} + \bar{\sigma}\frac{\partial F_D}{\partial Y}\right\}\frac{\left(\frac{\partial F_p}{\partial \bar{\sigma}}\right)^T C}{H+\left(\frac{\partial F_p}{\partial \bar{\sigma}}\right)^T C\frac{\partial F_p}{\partial \bar{\sigma}} - \frac{\overline{\sigma_{eq}}}{1-D}\frac{\partial F_D}{\partial Y}}\right] \quad (3)$$

D_{epd} meant elasto-plastic and damageable stiffness tensor, C is general elastic tensor.

The detail parameters were referred to the reference [3].

Results of analysis

The distribution of equivalent stresses was shown in Fig.16. The analysis was carried out to control the displacement at the top of deformed anchor.

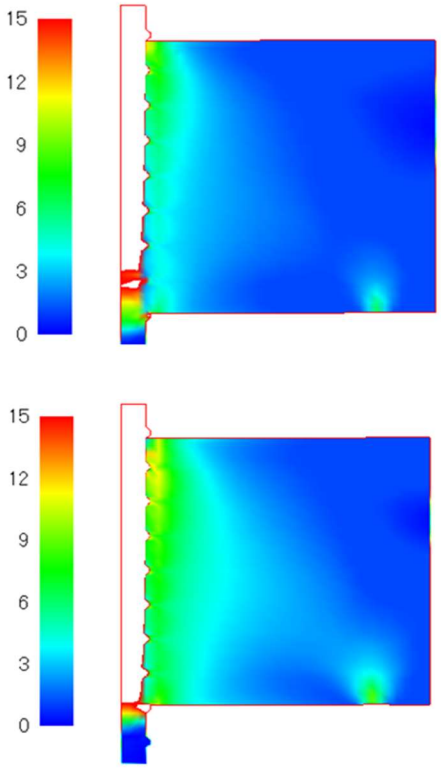

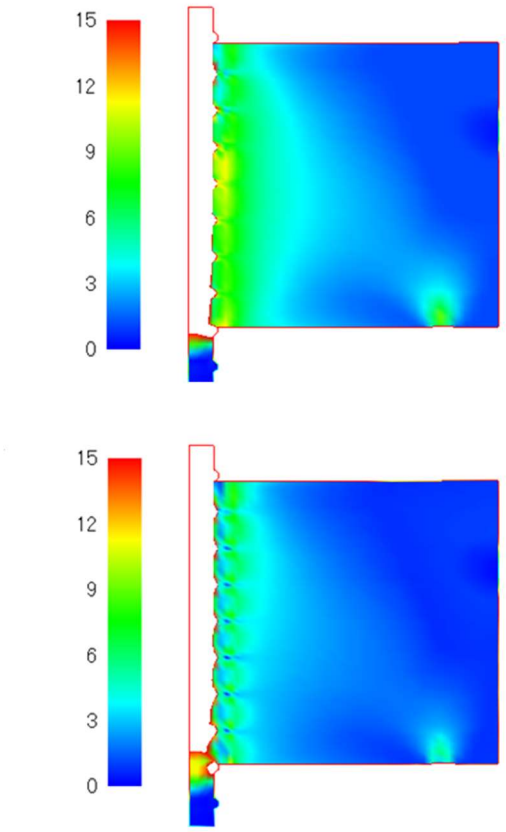

Fig.16 Distribution of equivalent stress (N/mm^2)

Firstly, the cohesive fracture was occurred at the top of interfacial area along the deformed bar. And next, the evolution of cracking from the deformed bar's node and along the interfacial surface between the straight-line of it in sequence. Finally, the bond-splitting fracture was found along the deformed bar.

In this analysis, we could not evaluate the shear fracture in injectable material and the interfacial fracture between injectable material and concrete.

CONCLUSIONS

The knowledge found in this research were as below.

(1) 5 degrees for the case of 150 (mm) or 3 degrees for 300 (mm) was the most effective wedge angle to enhance the adhesive force without treatment.

(2) At the case of 0 degrees, there were little effect on the maximum load for all specimens.

(3) The maximum loads for 5 or 7 degrees in a 300 (mm) were almost same with or without treatment.

(4) The wedge and treatment effects were little in the case of where the ratio of shear span was bigger than 3.57 due to bending fracture.

(5) We could define that the bond splitting crack was generated from the tip of deformed bar's node to injectable material as the results of experiments and numerical analyses.

(6) In case of normal case without treatment, the treatment was useful for adhesive resistance.

(7) We could not trace the shear crack in injectable material and the interfacial between interfacial material and concrete in analysis.

ACKNOWLEDGMENTS

Author appreciates Sumitomo Osaka Cement Co.,L.t.d. for providing the injectable inorganic material so called "Cemeforce anchor". And helping from Mr.Kurita, Mr.Yamanouchi, Mr.Kawahara and Mr.Nakamura who were mainly in charge of the experiments.

REFERENCES

[1] Andoh, S. Nakano,K. Tanuma,T.Yuki,K.. Relationship between crack width of concrete an retention ratio of ultimate load for cast-in-place anchor and inorganic post-installed anchor. Architecture of Technology and Design, 59(25), 2019, pp.51-54.

[2] Andoh, S. Nakano,K. Waranabe, K.,Influence od environmental and construction condition on the adhesive strength of post-install rapid hardening cement bonded anchor, Proceedings of the Japan Concete Institute,Vol.35,No.2,2013,pp.535-540.

[3] Hidenori Tanaka, ADHESION MECHANISM BETWEEN STEEL ANCHOR, INJECTABLE INORGANIC MATERIAL AND CONCRETE. Advanced in Construction Materials Proceedings of the ConMat'20, 2020, pp.372-382.

[4] Ministry of Land, Infrastructure, Transport and Tourism, Construction guideline of post-install anchor and continuous fiber reinforcement.2006.

[5] Japan Society of Civil Engineers, STANDARD SPECIFICATIONS FOR CONCRETE STRUCTURES-2012, Design, pp.180-187.

[6] Kobayashi Kazuo, Miyagawa Toyoaki et al, Concrete structural study, Morikita Publishing 2017,pp.80-90.

[7] EA de Souza Neto, D Peric, DRJ Owen, COMPUTATIONAL METHODS FOR PLASTICITY, Morikita Publishing, 2012.

11th Int. Conf. on Geotechnique, Construction Materials & Environment,
Kyoto, Japan, 3-5 November 2021, ISBN: 978-4-909106063 C3051

MODELING OF THE FLEXURAL BEHAVIOR OF CORRODED RC BEAMS STRENGTHENED BY CFRP SHEET

Hoai Anh Tran[1,2], Ngoc Tan Nguyen[1], Trung Kien Nguyen[1], Hoang Giang Nguyen[1]

[1]Faculty of Building and Industrial Construction, National University of Civil Engineering, Vietnam
[2] The South Agency, Ministry of Construction, Vietnam

ABSTRACT

In the present study, a series of numerical modeling is performed in order to investigate the structural behavior of corroded reinforced concrete beams externally strengthened to tension area with CFRP (Carbon Fiber Reinforced Polymer) with the aid of the finite element method adopted. A three-dimensional model employing the nonlinear characteristics of materials (e.g. elasto-plastic material model of steel reinforcement and damaged concrete model due to corrosion, bond stress-slip behavior between steel and concrete in good and deteriorated conditions) is created and validated. The numerical results obtained from the finite element analysis (FEA) are compared with the experimental results for six RC beams with different degrees of corrosion. The accuracy of the finite element models is based on comparison with the experimental curves of load-deflection. Results obtained from FEA showed a good correlation between the predicted residual flexural capacity and experimental results. The parametric study is then conducted to examine the capability of the FE model on assessing the structural behavior of the FRP-strengthened corroded RC beams in various strengthening conditions.

Keywords: Corroded beams, Steel corrosion, CFRP sheet, Strengthening, Modeling

INTRODUCTION

Steel corrosion is one of the main causes of deterioration in reinforced concrete (RC) structures. Many research works suggest that high durability requirements are not always achieved in practice due to corrosion of reinforcement [1]. The principal effects of corrosion on structural elements are loss of reinforcement cross-section and altering its mechanical properties, owing to the volumetric expansion compared to the base reinforcing bars, the generation of internal pressure induces splitting stresses. This stress-induced can lead to cracking and the reduction of compressive strength of the concrete cover when it reaches the tensile capacity of the concrete. As the splitting cracks develop, the confinement action of the concrete is rapidly decreased thereby reducing the bond strength at the interface between steel and concrete [2]–[4]. Therefore, deteriorated structures should be repaired to ensure proper functioning, to extend their service life, and to accommodate changes in increased loads.

As such, one alternative way to rehabilitate the deteriorated structures is to utilize fiber-reinforced polymer (FRP) composite materials, which are currently viewed by structural engineers as new and highly promising materials in the industry [1]. Advantages of FRP materials include a high strength-to-weight which is more applicable in confined space, excellent corrosion resistance, and high tensile strength. Regarding the application of FRP composites on corroded structures, several applications involve externally bonded composite fabrics, are significant in compressive, shear and flexural performances have been obtained. The overall performance of the RC beam under service load is slightly improved and the load-carrying capacity is remarkably increased when strengthening FRP sheets are used [5]–[8].

Furthermore, the finite element method (FEM) is extremely effective to solve the engineering problems especially structures having complex boundary conditions. It has been used widely for the structural analysis of reinforced concrete structures including FRP strengthened RC structures. Many previous numerical research works had demonstrated good agreement with experimental results [9]-[11].

However, from the literature, less attention has been paid to study the structural performance of corroded RC beams strengthened by FRP composites employing FEM. In this paper, the numerical results obtained from the FEA are compared with the experimental results for two non-corroded RC beams, two corroded RC beams and two corroded CFRP strengthened RC beams. The failure modes of the strengthened corroded beams are governed mainly by the bond between the CFRP sheet and concrete cover because it is the means for the transfer of stresses to develop composite action. The numerical analysis is then broadened, a parametric study is conducted considering the number of CFRP layers and the length of the CFRP sheets. Finally, the FEA confirmed the suitability of the model to predict the mechanical behavior of corroded RC members strengthened in flexure with the CFRP material considering many variables.

NUMERICAL MODELING

A three-dimensional nonlinear model is developed using DIANA FEA software. In analyses, the smeared crack concept was used with a rotating crack model based on total strain. The constitutive models of materials with element types applied in geometric modeling are used to develop the FE model with the validation from an experimental study with three sets of tested RC beams [11].

Finite Element Model (FEM)

In this study, the mesh size of concrete elements was investigated. Furthermore, the average mesh size corresponding to three times the diameter of maximum aggregates has been recommended [12]. The minimum mesh size is usually deemed the maximum size of coarse aggregates due to the heterogeneity of the concrete material. The three-dimensional (3D) analysis can be calculated with accuracy employing an acceptably large mesh size [13].

Hence, the load-deflection curves responded from FE analysis of non-corroded beams with different mesh sizes ranging from 20 to 100 mm were performed and illustrated in Fig. 1. Based on the computational time and accuracy of the obtained results, the mesh size of 50×50×50 mm has been selected for numerical modeling as in Fig. 2.

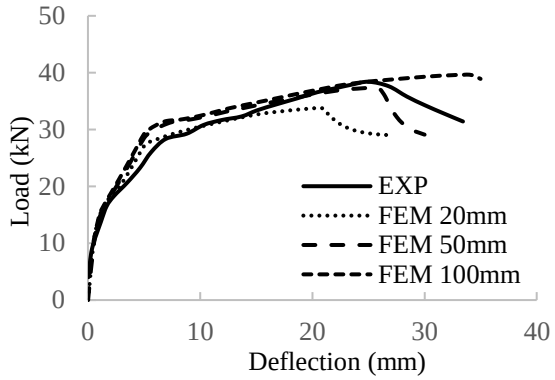

Fig. 1 Convergence study

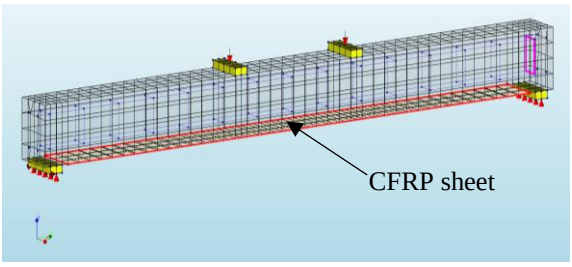

Fig. 2 Mesh discretization of the beam, CFRP sheet and the load, support conditions

Concrete, steel plates and CFRP sheet

Three-dimensional CHX60 element, a twenty-node isoparametric solid brick element, is employed for the concrete, CFRP laminates, support, and loading steel plates as illustrated in the DIANA FEA library [14]. Steel plates are added at support and loading locations in the finite element models (as in the actual beams) in order to avoid stress concentration problems.

Steel reinforcements

In the model of non-corroded RC beam, embedded bar elements are assigned for the longitudinal reinforcement and stirrups. They were embedded in the continuum element and their strains are calculated based on the displacement field of the surrounding continuum element.

When the failure mode is not governed by the bond between steel and concrete, the behavior of structural tested beams can be predicted using the perfect bond assumption. In case, the steel-concrete bond controlled the failure mechanism and structural performance of corroded RC beam as demonstrated in many previous experimental studies, the steel bars are modeled as bond-slip reinforcements. A line-solid interface element is employed to simulate the influence of bond stress-slip behavior.

Concrete-CFRP interface

A tie constraint is used to model the interaction between the different materials. The assumption that all materials had a perfect bond to one another is made.

Materials Modeling

Concrete

In the adopted rotating crack model, the concrete behavior in tension is described by the stress-strain curve of JSCE tension softening defined by the tensile strength and mode-I tensile fracture energy. The parabolic stress-strain curve in DIANA software is used for compression considering the reduction model due to lateral cracking and stress confinement model [14]. The post-peak response of this curve employing fracture energy and crack bandwidth as recommended [15]. The damaged concrete model due to corrosion was proposed by a reducing stress-strain relationship as suggested in [16].

Steel reinforcements and steel plates

The FEM employed linear elastic isotropic material to model steel plates at support and loading positions. An elasto-plastic material with linear strain

hardening was assigned to reinforcements. The tangent modulus in the plastic stage is set equal to one-hundredth of the modulus of elasticity. The appearance of pitting corrosion of reinforcements across their lengths has been shown to affect the strength and ductility of corroded reinforcement in previous studies [17], [18]. Since it is difficult to incorporate the actual variability of steel corrosion into a numerical model, an alternative method is to model the corroded steel bar over a length employing average cross-section loss.

CFRP sheet

Although the CFRP sheet is an orthotropic material that has higher modulus and strength in woven directions than through the thickness directions), it could be modeled as an isotropic material within the plane. This is because the loading on the CFRP sheet is spreading within the sheet plane.

Damaged steel-concrete interface

The bond between reinforcements and concrete covering plays a significant role in the mechanical response of the structures attacked by corrosion [2]-[4]. Moreover, pullout failure often seen in the structure where steel reinforcements embedded in well-confined concrete. Therefore, the bond stress-slip curve characterized pullout failure mode as shown in Fig. 3 from CEB-FIP Model Code 1990 [19] is adopted to model the bond between steel and concrete.

$$\tau = \tau_{\max}(\frac{s}{s_1})\alpha \qquad \text{for } 0 \le s \le s_1 \qquad (1)$$

$$\tau = \tau_{\max} \qquad \text{for } s_1 < s \le s_2 \qquad (2)$$

$$\tau = (\tau_{\max} - \tau_f)(\frac{s - s_2}{s_3 - s_2}) \qquad \text{for } s_2 < s \le s_3 \qquad (3)$$

$$\tau = \tau_f \qquad \text{for } s_3 < s \qquad (4)$$

The bond stresses between the reinforcing bar and concrete can be calculated as a function of the relative displacement (denoted *s*) as from Eq. (1) to Eq. (4). Where: τ_{max} is the maximum bond strength calculated as $\tau_{max} = 1.25\sqrt{f_c}$; τ_f is the residual bond strength $\tau_f = 0.4\tau_{\max}$; f_c is the characteristic value of the uniaxial compressive strength of concrete measured on cylindrical specimens. The parameters used in these equations are defined in CEB-FIP Model Code 1990 [19]. In the numerical study of Tørlen and Horrigmoe [20], in order to characterize the deterioration of bonds in corroded reinforcement, they proposed the deteriorated bond stress-slip curve by reducing maximum bond strength. Moreover, the assumption is made for the unchanged behavior along the deterioration region as illustrated in Fig. 3.

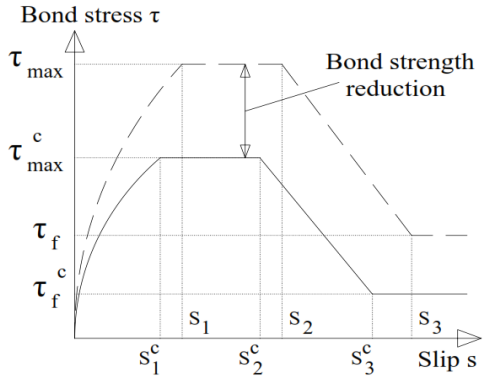

Fig. 3 Bond stress-slip behavior of CEB-FIP 1990 [19] and bond strength reduction model by Tørlen and Horrigmoe [20]

NUMERICAL VALIDATION

Details of Beam Specimens

The first set comprised the two non-corroded RC beams named S1-NC and S2-NC that were considered as control beams. The second set has two corroded RC beams named S3-C, S4-C with a corrosion degree of approximately 10%. Lastly, the third set also has two corroded RC beams named S5-CFRP, S6-CFRP subjected to a 10% degree of corrosion, the corroded beams are then sanded and spread with epoxy resin on the surface for covering corrosion cracks before strengthening. All tested beams, which are 2200 mm long are tested in a four-point-bending test as illustrated in Fig. 4. Six beams had the overall depth, the width of 200 mm, 150 mm, respectively. Each beam was reinforced in tension and compression with two ϕ12 mm longitudinal steel bars, whilst using ϕ6 mm stirrups with a spacing of 150 mm. The thickness of a single CFRP layer provided by the manufacturer was 0.111 mm, while the sheet width and length are 150 mm and 2000 mm, respectively [11].

Fig. 4 Four-point bending test on a typical beam specimen

The compression test of cubic specimens of 150mm obtained the average 28-day concrete

compressive strength of 40.9 MPa with a coefficient of variation of 1.6% from the average value. The tensile strength and elastic modulus of the CFRP sheet were 3400 MPa and 245000 MPa, respectively. Lastly, the elastic modulus of ϕ12 mm longitudinal steel bars is equal to 200 GPA, while the yield and ultimate tensile strengths are 374.3 and 543.2 MPa, respectively.

FEM Prediction

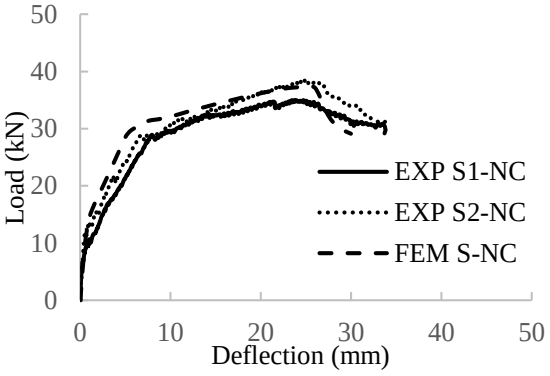

(a)

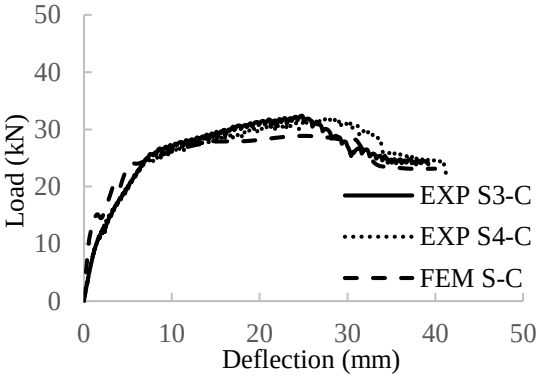

(b)

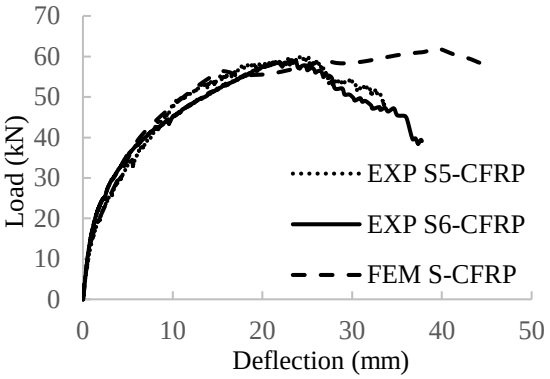

(c)

Fig. 5 EXP and FEA load-deflection curves

The experimental and numerical variations of maximum loading capacity with mid-span deflection under loading points for the tested beams are depicted in Fig. 5. The experimental (EXP) and FEA loading capacity are given in Table 1. As it can be seen, the stiffness of non-corroded specimens was close up to a load level of 28 kN both in experimental and numerical analysis. Similar nonlinear behavior was extended up to the maximum loading capacity of 38.5 kN of beam S2-NC and 35.0 kN beam S1-NC in the experiment compared with the value of 35.1 kN in finite element simulation. It shows the good agreement between the two results for the load-deflection curves as shown in Fig. 5(a).

Table 1 Experimental, FE-predicted maximum load

Beam notation	Maximum load (kN)		Deviation (%)
	EXP (Test)	FEA	
S1-NC	35.0	35.1	0.3
S2-NC	38.5	35.1	8.8
S3-C	32.4	28.9	10.8
S4-C	31.9	28.9	9.4
S5-CFRP	59.9	62.1	3.7
S6-CFRP	59.1	62.1	5.1

The experimental curves of load – deflection of corroded beams S3-C and S4-C are approximately linear up to crack formation at the corresponding load 25kN. Subsequently, the curves turned nonlinear as a result of stiffness deterioration due to corrosion cracking. The deterioration continued with increased loading until failure occurred with the maximum loading capacity of 32.1 kN on average. Fig. 5(b) clearly demonstrates that there is a very good match between the experimental and FEA load-deflection behavior from initial loading up to beam failure.

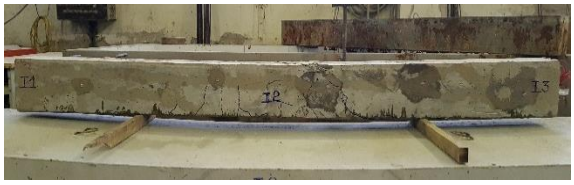

(a)

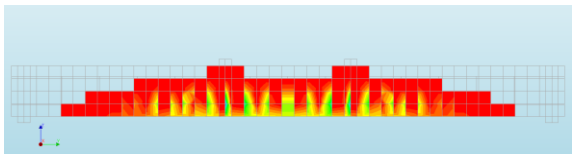

(b)

Fig. 6 Comparison of typical cracking patterns on S5-CFRP beam in (a) experiment and (b) FEA

Lastly, as the CFRP sheet bonded to the corroded beams C5-CFRP and C6-CFRP, higher yield loads and maximum loads were achieved. For example, the

maximum load for beam specimen S5-CFRP was 59.9 kN which approximately doubled the yield load of corroded beams S3-C and S4-C (32.4 kN and 31.9 kN). A similar trend was observed for the maximum capacity of 62.1 kN in the finite element simulation. It is reported in the experiment that the beam suffers from a bonding failure mechanism in the shear span. The crack due to cover separation between concrete and CFRP sheet propagates upwards until meeting the corrosion crack. It continues to travel up to the loading point forming the inclined crack as shown in Fig. 6. On the other hand, the failure mode obtained from FE analyses is a flexural failure with the crushing of concrete in the compression zone. These differences in failure mode were due to the smeared crack model of concrete used in FEM could not perfectly reflect the influence of localized cracking on laminates. Therefore, it is needed to extend the simulation by using a prescribed discrete crack model and bond-slip model between materials to achieve accuracy in simulating the debonding failure mechanism of strengthened CFRP beams.

FEM Parameter Analysis

In this section, the parametric study on the varying CFRP layers and the CFRP sheet length will be conducted to assess their influence on structural behavior. The FEM of specimen C5-CFRP and C6-CFRP are used with the assumption that the same material, geometry described in the experimental section.

Effects of CFRP layers

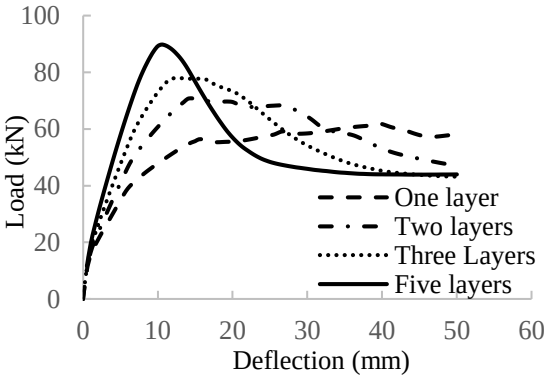

Fig. 7 Effet of the CFRP layers on the structural behavior of strengthened corroded beams

Fig. 7 indicates that the stiffness, yield load, the load-carrying capacity of the beam are enhanced with the increase of layers. The load-carrying capacity when using two, three, and five layers improved by 13.1%, 25.8%, and 44.8% in comparison with a single layer. The post-peak response in the load-deflection curve is becoming steeper as the number of FRP layers increased. That behavior indicates the considerable reduction of ductility in beams strengthened with more layers of CFRP sheets. This finding shares the same agreement with the research works on the multiple layers of FRP of RC beams conducted by previous experimental works [21].

Effects of CFRP sheets length

For the strengthened beams with different CFRP sheet lengths ranging from 1200 mm to 2000 mm, the development of the load-carrying before cracking is almost the same. In the case of a single layer, the length of the CFRP sheet has a slight effect on the change of load-carrying capacity as illustrated in Fig. 8. By reducing from 2000 mm to 1600 mm length of the strengthening sheet, the load-carrying capacity difference reported is around 3.24 kN. There is a more remarkable loss from the 1200 mm length CFRP sheet (800 mm shorter than the original) which is approximately 12.2 kN. As the length of the CFRP sheet decreases, the ductility of the beams decreases as well. This is because the cracking pattern is more evenly distributed over the area where RC beam is bonded with the CFRP sheet. Therefore, the overall sum of all crack widths is reduced and the ductility will be improved.

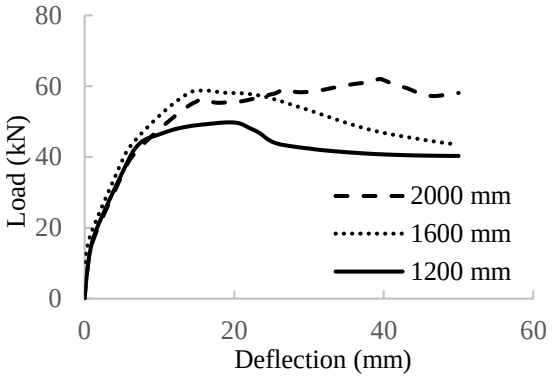

Fig. 8 Effect of CFRP lengths on the structural behavior of strengthened corroded beams

CONCLUSIONS

The paper contributes to a more understanding of the flexural behavior of RC beams with reinforcement corrosion strengthened with externally bonded CFRP sheets.

A FE model for RC corroded beams flexural-strengthened with CFRP sheets was successfully validated using published experiments to predict the load-carrying capacity of tested beams with relatively small deviation.

A parametric study is done to examine the capability of the applied FE simulation for many variables. It indicated that the predicted flexural strength enhancement was remarkably influenced by the increase of a limited number of CFRP layers while

it was smaller affected by the varying CFRP sheet lengths. The strengthened beams behave more ductile when externally bonded with more than one CFRP sheet and the ductility also increases along with the reduction of sheet length.

ACKNOWLEDGMENTS

The authors would like to thank Toray International, Inc., Japan for providing the materials of this research.

REFERENCES

[1] ACI 440.2R-17, Guide for the design and construction of externally bonded FRP systems for strengthening concrete structures, ACI Committee 440, 2017.
[2] Ahmadi M., Kheyroddin A. and Kioumarsi M. Prediction models for bond strength of steel reinforcement with consideration of corrosion, Materials Today: Proceedings, 2021.
[3] Yu X., Robuschi S., Fernandez I. and Lundgren K., Numerical assessment of bond-slip relationships for naturally corroded plain reinforcement bars in concrete beams, Engineering Structures, Vol. 239, 2021, 112309.
[4] Zhang Y., Bicici E., Sezen H. and Zheng S., Reinforcement slip model considering corrosion effects, Construction and Building Materials, Vol. 235, 2020, 117348.
[5] Abuodeh O.R., Abdalla J.A. and Hawileh, R.A., Prediction of shear strength and behavior of RC beams strengthened with externally bonded FRP sheets using machine learning techniques, Composite Structures, Vol. 234, 2020, 111698.
[6] Chen W., Pham T.M., Sichembe H., Chen L. and Hao H., Experimental study of flexural behaviour of RC beams strengthened by longitudinal and U-shaped basalt FRP sheet, Composites Part B: Engineering, Vol. 134, 2018, pp.114–126.
[7] Dong J., Wang Q., and Guan Z., Structural behaviour of RC beams with external flexural and flexural–shear strengthening by FRP sheets, Composites Part B: Engineering, Vol. 44, Issue 1, 2013, pp.604–612.
[8] McSwiggan C. and Fam A., Bio-based resins for flexural strengthening of reinforced concrete beams with FRP sheets, Construction and Building Materials, Vol. 131, 2017, pp.618–629.
[9] Godat A., Neale K.W. and Labossière P., Numerical modeling of FRP shear-strengthened reinforced concrete beams, Journal of Composites for Construction, Vol. 11, Issue 6, 2007, pp.640–649.
[10] Kishi N., Zhang G. and Mikami H., Numerical cracking and debonding analysis of RC beams reinforced with FRP sheet, Journal of Composites for Construction, Vol. 9, Issue 6, 2005, pp.507–514.
[11] Tran H.A., Nguyen H.G. and Nguyen N.T., An experimental study on the flexural strengthening of corroded RC beams using externally CFRP sheet, Journal of Science and Technology in Civil Engineering, Vol. 15, Issue 1V, 2021, pp.1–16 (in Vietnamese).
[12] Bažant Z. P. and Oh B.H., Crack band theory for fracture of concrete, Materials and Structures, Vol. 16, 1983, pp.155–177.
[13] Maekawa K., Pimanmas A. and Okamura H., Nonlinear mechanics of reinforced concrete, Spon Press, London, 2003.
[14] DIANA 10.3 User's manual, TNO Building and Construction Research, Delft, 2019.
[15] Nakamura H. and Higai T., Compressive fracture energy and fracture zone length of concrete, In: Modelling of inelastic behaviour of RC structures under seismic loads, Shing P. and Tanabe T-A., Ed.., American Society of Civil Engineers, 2001, pp.471-487.
[16] Coronelli D. and Gambarova P., Structural assessment of corroded reinforced concrete beams: modeling guidelines, Journal of Structural Engineering, Vol. 130, Issue 8, 2004, pp.1214–1224.
[17] Stewart M.G., Mechanical behaviour of pitting corrosion of flexural and shear reinforcement and its effect on structural reliability of corroding RC beams, Structural Safety, Vol. 31, Issue 1, 2009, pp.19–30.
[18] Chen E., Berrocal C.G., Fernandez I., Löfgren I. and Lundgren K., Assessment of the mechanical behaviour of reinforcement bars with localised pitting corrosion by Digital Image Correlation, Engineering Structures, Vol. 219, 2020, 110936.
[19] Fib. CEB-FIP model code 1990. London: Thomas Telford Services Ltd; 1993.
[20] Tørlen A. and Horrigmoe G., Modelling of bond between reinforcement and concrete for deteriorated and repaired beams, Report No. NTAS A98034, NORUT Technology, 1998, Narvik, Norway. (in Norwegian).
[21] Bsisu, K., Sargand, S., and Ball, R., The effect of width, multiple layers and strength of FRP sheets on strength and ductility of strengthened reinforced concrete beams in flexure, Jordan Journal of Civil Engineering, Vol. 9, Issue 1, 2015, pp.33-42.

11th Int. Conf. on Geotechnique, Construction Materials & Environment, Kyoto, Japan, 3-5 November 2021, ISBN: 978-4-909106063 C3051

SUCCESSIVE OVER RELAXATION METHOD FOR SOLVING HEAT EQUATION OF THERMAL CONDUCTIVITY OF CONCRETE

Dalal Adnan Maturi [1]

[1]Departement of Mathematics, Faculty of Science, King Abdulaziz University, Jeddah, Saudi Arabia

ABSTRACT

Any building regardless of its size always begins with development. The goal is to design not only the outward appearance of the future structure, but also the calculation of the main geometric letters. After all, the main task of construction is to build sturdy buildings that can help maintain a comfortable environment, without additional costs. Therefore, when choosing the raw materials used in the construction of buildings and structures, the thermal conductivity of the materials used in construction is taken into account, including all kinds of concrete. Concrete is a mixture of raw materials made up of sand, aggregate (or the tooth, which means breaking stones) and cement, with the addition of water to it. In this paper we will use the method of Successive Over Relaxation (SOR), to solve the two-dimensional heat equation with the thermal conductivity of concrete for the stable and unstable state. When comparing the results of the explicit and implicit methods, the explicit method converges faster and with less iterations. The explanation for this is that the implicit has more than one unknown, making it more difficult to solve, even though it is unconditionally stable at higher timer steps. Of the three iterative solvers (Jacobi, Gauss Seidel, and SOR), the SOR approach has the fastest convergence. Therefore, the use of iterative methods and numerical simulations allow us to choose suitable building materials depending on the thermal conductivity of the chosen material and this conductivity depends on the porous structure, density and humidity.

Keywords: Method of Successive Over Relaxation, Heat Equation, Thermal Conductivity of Concrete, Matlab.

INTRODUCTION

One of the most important methods for solving large linear system equations is successive over-relaxation (SOR). Fluid dynamics, mathematical programming, linear elasticity, and machine learning are just a few of the areas where it can be used. The study of steady heat conduction, turbulent flows, boundary layer flows, or chemically reactive flows are examples of SOR applications in Dynamics. As a result, both scholars and corporate policymakers should use the SOR method.

Time is always valuable in the real world, and no one wants to waste it; while solving systems of equations, it is sometimes preferable to have a near approximation of the solution rather than the precise solution for this reason, among others. The sequential over-relaxation approach (SOR) can help in this situation. Gaussian elimination, the industry standard for discovering accurate techniques, requires roughly n×n operations to solve the system, which becomes time demanding as n grows larger. While SOR just provides an approximation, it does so significantly faster than Gaussian elimination. David Young and H. Frankel created SOR in 1950 for use on digital computers.

FEATURES OF CONCRETE AND REINFORCED CONCRETE

These features can be summed up as follows:

1. Flexibility of use: Soft concrete is poured into molds to obtain different forms of concrete depending on the shape of the mold used.
2. Economical maintenance work: Metal structures need periodic painting works, and the connections of stone structures are usually affected by frost, while basic reinforced concrete structures do not need maintenance work.
3. Fire resistance: Concrete is a material with poor thermal conductivity, in addition to that it has less thermal expansion than other building materials such as clay and building stone. The low thermal expansion factor reduces the appearance of cracks when the concrete temperature rises, and the poor thermal conductivity prevents the heat of the fire from reaching the interior of the concrete block to reach the reinforcement steel. Experiments have shown that the exposure of the outer surface in a block of concrete to a high temperature in one hour does not lead to a noticeable rise in the surface layer temperature at a depth of about 2.5 cm in the mentioned surface, while the temperature rise is almost negligible in the layers at a depth of 7.5 cm. cm. Finally, the convergence of the thermal expansion factors of concrete and steel reinforcement allows reinvestment of the structure of reinforced concrete after surface repairs in cases of light or non-long-term fire, while the metal structure, for example, and in the same conditions can become uninvestable.
4. Resistance to emergency loads: Reinforced

concrete is less affected by the change in the application of live loads on it than the rest of the construction materials, due to its high self-weight. That is, the least resistant parts undergo sufficient deformations to transfer forces to the more resistant parts.

5. Possibility of obtaining prefabricated parts: The precast concrete parts can be implemented in the factory, and then they are assembled at the work site.

SUCCESSIVE OVER-RELAXATION (SOR)

The Gauss-Seidel iteration model was altered to create it.

1. Given $Ax = b$, where A and b are known and x, x_0, is a first estimate.

2. $L_* x_{k+1} = b - U x_k$ Where L_* denotes the matrix A's lower triangular components, U denotes the matrix $A's$ upper triangular components, and b denotes our $b\ x_{k+1}$is the next iteration of x, and x_{k+1} is the $x_{k+1} kth$ approximation of x. Hadjidimos [1] presented the accelerated Overrelaxation method as a two-parameter modification of the sequential Overrelaxation (SOR) approach for numerical solution. This is how the SOR technique works.

1. Given $Ax = b$ where A and b are known, x unknown, and an initial guess for x, x_0.

2. Let $A = D + L + U$ where D is the main diagonal of A, L the lower triangle components of A and U the upper triangle components of A.

3.

$$x_{k+1} = (1-w)x_i + \frac{w}{a_{i,i}}\left(b_i - \sum_{j<i} a_{i,j}\, x_{j(k+1)} - \sum_{j>i} a_{ij}\, x_{jk}\right) \quad (1)$$

Where x_k is the kth approximation of x, x_{k+1} is the next iteration of $x, a_{i,j}$ is the corresponding element of matrix A, b is our vector, and is our relaxation factor, and $a_{i,j}$ is the corresponding element of matrix A.

When we get to the following part, we'll discuss more about choosing an acceptable relaxation factor, but for now, remember that if $w = 1$, we get the Gauss-Siedel method. Because the value at a given iteration is made up of a mixture of the old value and the freshly calculated value, the convergence is improved.

$$x_i^{new} = w x_i^{new} + (1-w) x_i^{old} \quad (2)$$

The SOR method is similar to the Gauss-Seidel method, with the exception that it uses a scaling factor to reduce approximation error. Take a look at the equations below.

$$\sum_{j=1}^{n} a_{ij}\, x_j = b_i, \quad i = 1,2,\cdots,n \quad (3)$$

The values at the k iteration of the Gauss-Seidel method are provided by

$$x_i^{(k)} = \frac{1}{a_{i,i}}\left[b_i - \sum_{j=1}^{i-1} a_{ij}\, x_j^{(k)} - \sum_{j=i+1}^{n} a_{ij}\, x_j^{(k-1)}\right] \quad (4)$$

It's worth noting that when calculating x_i , the Variables with a lower index than $i$are iterated (k) times. while variables with indices greater than i remain unchanged the previous iteration $(k-1)$. The SOR equation is as follows: is offered as a method

$$x_i^{(k)} = x_i^{(k-1)} + w\left\{\frac{1}{a_{i,i}}\left[b_i - \sum_{j=1}^{i-1} a_{ij}\, x_j^{(k)} - \sum_{j=i+1}^{n} a_{ij}\, x_j^{(k-1)}\right] - x_i^{(k-1)}\right\} \quad (5)$$

The term in the bracket

$$\left\{\frac{1}{a_{i,i}}\left[b_i - \sum_{j=1}^{i-1} a_{ij}\, x_j^{(k)} - \sum_{j=i+1}^{n} a_{ij}\, x_j^{(k-1)}\right] - x_i^{(k-1)}\right\} \quad (6)$$

is just difference between the variables of the previous and present iterations for the Gauss-Seidel method

$$\left\{\frac{1}{a_{i,i}}\left[b_i - \sum_{j=1}^{i-1} a_{ij}\, x_j^{(k)} - \sum_{j=i+1}^{n} a_{ij}\, x_j^{(k-1)}\right] - x_i^{(k-1)}\right\} = \left[x_i^{(k)} - x_i^{(k-1)}\right]_{Gauss-Seidel} \quad (7)$$

APPLICATIONS OF SUCCESSIVE OVER-RELAXATION (SOR)

The staedy state equation for 2D heat conduction is by:

$$\alpha\left(\frac{\partial^2 T}{\partial x^2} + \frac{\partial^2 T}{\partial y^2}\right) + f = 0 \quad (8)$$

$\boldsymbol{\alpha}$ is thermal diffusivity, T is temperature, and f is the source term in the preceding equation. Because the source term is omitted for simplicity, the final equation is:

$$\boldsymbol{\alpha}\left(\frac{\partial^2 T}{\partial x^2} + \frac{\partial^2 T}{\partial y^2}\right) = \mathbf{0} \quad (9)$$

Finite difference equation is:

$$\frac{T_{i+1,j} - 2T_{i,j} + T_{i-1,j}}{(\Delta x)^2} + \frac{T_{i,j+1} - 2T_{i,j} + T_{i,j-1}}{(\Delta y)^2} = \mathbf{0} \quad (10)$$

The Unsteady state equation for 2D heat conduction is by:

$$\frac{\partial T}{\partial t} = \boldsymbol{\alpha}\left(\frac{\partial^2 T}{\partial x^2} + \frac{\partial^2 T}{\partial y^2}\right) + \boldsymbol{f} \quad (11)$$

Again, f is ignored, thus the equation is:

$$\frac{\partial T}{\partial t} = \boldsymbol{\alpha}\left(\frac{\partial^2 T}{\partial x^2} + \frac{\partial^2 T}{\partial y^2}\right) \quad (12)$$

Finite difference equation is:

$$\frac{T_{i,j}^{n+1}-T_{i,j}^{n}}{\Delta t}=\frac{T_{i+1,j}-2T_{i,j}+T_{i-1,j}}{(\Delta x)^2}+\frac{T_{i,j+1}-2T_{i,j}+T_{i,j-1}}{(\Delta y)^2} \quad (13)$$

Let $k_1=\alpha\Delta t/(\Delta x)^2$ and $k_2=\alpha\Delta t/(\Delta y)^2$

The number of grid points taken in both the X and Y directions along the square plate domain is 10 in the program. The time step size utilized in the explicit technique is 1e-2 and 1e-3 to see how the time step influences the solutions. To check the stability of the Implicit technique at higher time steps, 1e-2 is utilized as the time step size, and iterative solvers are utilized to converge the solutions so that the error falls within the stated tolerance requirements. Omega (scaling factor) is represented as an array of numbers in the Implicit SOR algorithm (0.8 to 1.2).

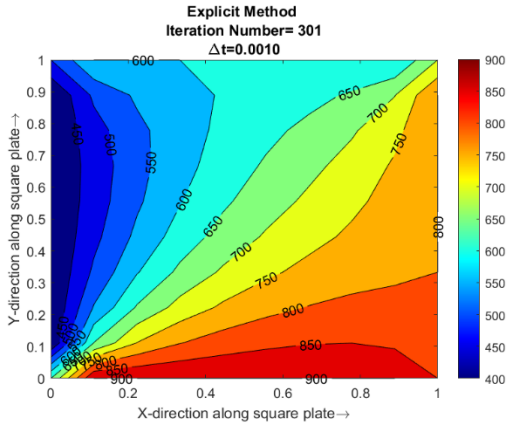

Fig. 1 This is the Explicit method at $\Delta t = 0.0010$.

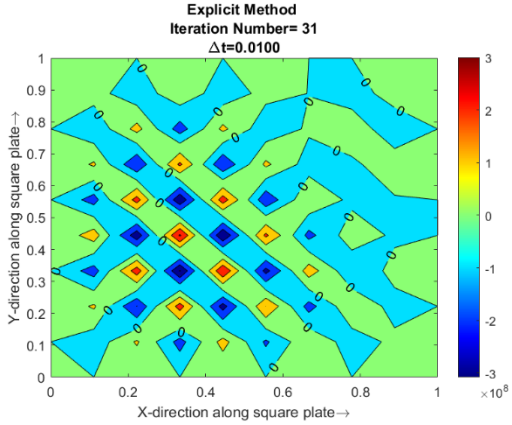

Fig. 2 This is the Explicit method at $\Delta t = 0.0100$

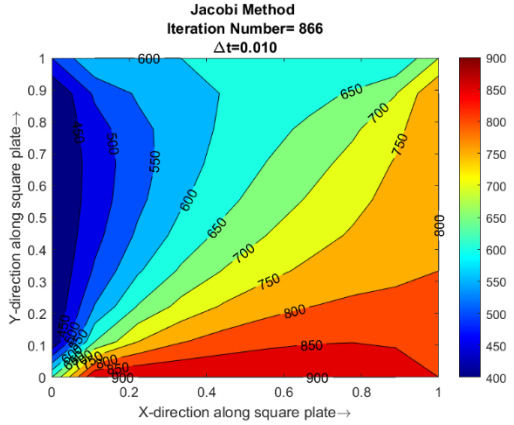

Fig. 3 This is the Jacobi method at $\Delta t = 0.010$

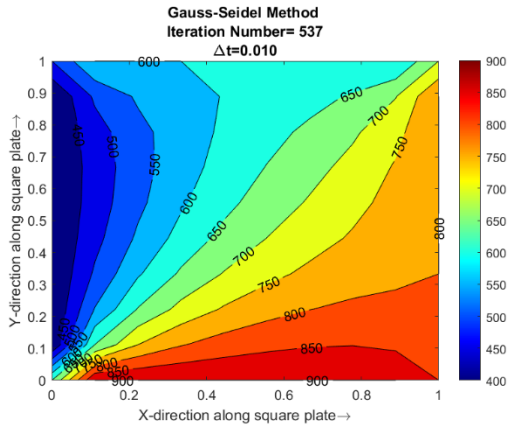

Fig. 4 This is the Gauss-Seidel method at $\Delta t = 0.010$

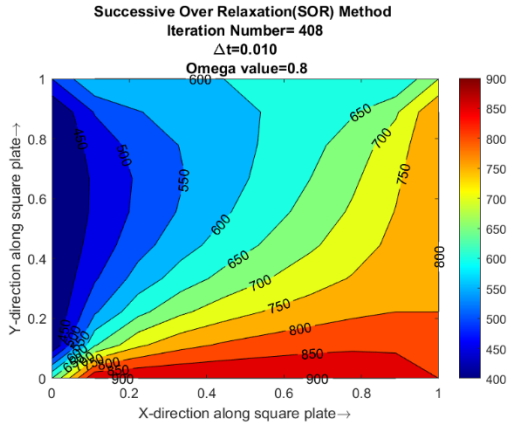

Fig. 5 This is the Successive Over Relaxation (SOR) method at $\Delta t = 0.010, \Omega = 0.8$

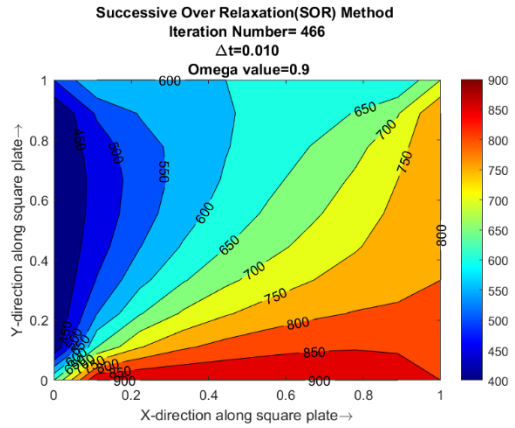

Fig. 6 This is the Successive Over Relaxation (SOR) method at $\Delta t = 0.010, \Omega = 0.9$

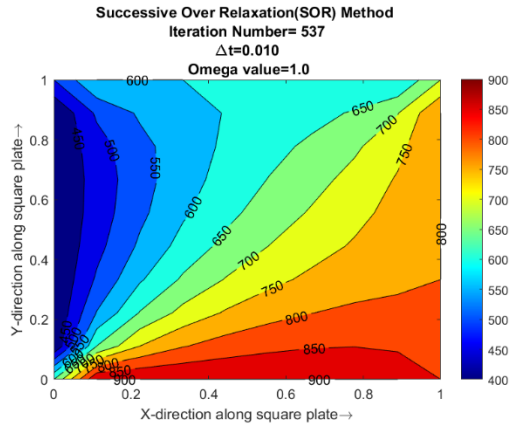

Fig. 7 This is the Successive Over Relaxation (SOR) method at $\Delta t = 0.010, \Omega = 1.0$

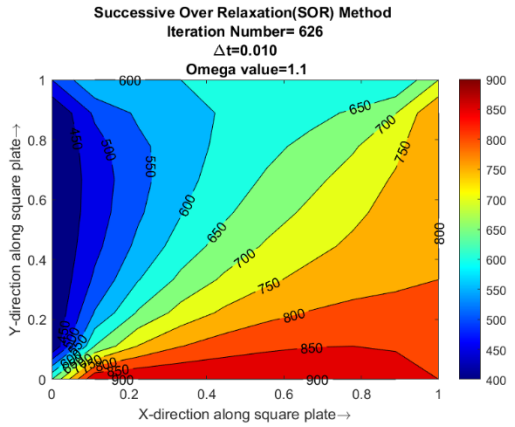

Fig. 8 This is the Successive Over Relaxation (SOR) method at $\Delta t = 0.010, \Omega = 1.1$

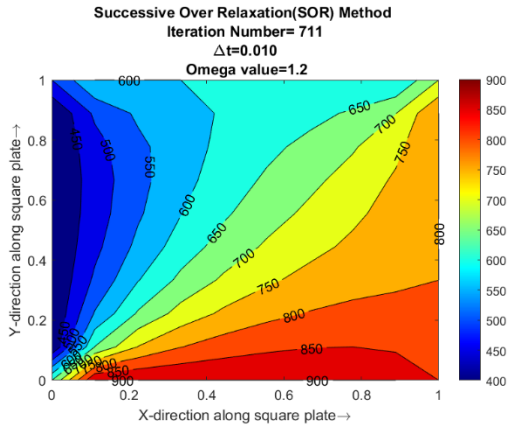

Fig. 9 This is the Successive Over Relaxation (SOR) method at $\Delta t = 0.010, \Omega = 1.2$

1. Steady-state conduction is a type of conduction in which the temperature differential that drives the conduction is consistent across time. In a transient-state condition, on the other hand, the temperature at the boundary fluctuate over time and finally settles into a steady state if the temperature isn't modified any further.

2. The solution is considered to be converged if the error term obtained is less than the tolerance value. We find an error term below the tolerance value(1e-4) for each case in the aforementioned issue, which is solved in steady and unsteady-state conditions, indicating that the solution is converged.

3.The answer is achieved utilizing three approaches in the implicit approach for steady-state and transient-state analysis, namely Jacobi(J), Gauss-Seidel (GS), and successive over-relaxation(SOR). SOR, the third of these three approaches, converges to the solution with less iterations than the other two approaches, assuming that the value of omega is acceptable. When compared to the other two methods, the Jacobi approach converges to the solution with the most iterations in both circumstances.

4. We may conclude that the sequential over-relaxation approach is the most effective approach since it converges the solution in fewer iterations and hence takes less time to solve than the Jacobi and Gauss-Seidel methods. This is mostly determined by the value of omega; if an adequate value is chosen, the solution will converge quickly; otherwise, it will take longer.

CONCLUSIONS

We have emphasized the relevance of using the SOR interactive solve method for expediting the solution of real-world problems in this study. It should come as no surprise that the SOR method is used to solve matrix systems $\boldsymbol{Ax} = \boldsymbol{b}$.

More research will be required to develop a SOR algorithm that produces better, more accurate outcomes.

However, the SOR technique excels in terms of speed and ability to solve any n x n system without the requirement for the coefficient matrix A to have an inverse or to store the matrix fully, saving both space and time.

ACKNOWLEDGMENTS

This paper was supported by the Deanship of Scientific Research (DSR), King Abdulaziz University, Jeddah.

REFERENCES

[1] Mayooran T., and Light E., Applying the Successive Over-relaxation Method to a Real-World Problems. Am. J. Appl. Math. Stat. 4, 2016 pp.113–117.

[2] Hadjidimos A., "Successive Overrelaxation (SOR) and related methods," Journal of Computational and Applied Mathematics, vol. 123, no. 1, pp. 177-199, 2000.

[3] Moitsheki R. J., and Harley C., Transient heat transfer in longitudinal fins of various profiles with temperature-dependent thermal conductivity and heat transfer coefficient; Pramana Journal of Physics 77,2011, pp.519-532.

[4] A.M. Wazwaz., The variational iteration method; a reliable tool for solving linear and nonlinear wave equations, Comput. Math. Appl., 54 (2007) 926–932.

[5] A.M. Wazwaz., A First Course in Integral Equations, World Scientific, Singapore, (1997).

[6] A.M. Wazwaz., Suheil A. Khuri, The variational iteration method for solving the Volterra integro-differential forms of the lane-Emden and the Emden-Fowler propblems with initial and boundary value conditions, DE GRUYTER Open Eng. (2015) ;5:31-41.

[7] D.A. Maturi., Numerical Solution of System of Two Nonlinear Volterra Integral Equations, International Journal of Computers & Technology, Vol12, No.10, pp.3967-3975,2014.

[8] D.A. Maturi., A.Z. Bajamal., B.M. AlGethami., Numerical Solution of Volterra Integral Equation of Second Kind Using Implicit Trapezoidal, Journal of Advances In Mathematics, Vol8, No.2, pp.1540-1553,2014.

[9] Dalal A. Maturi., Adomian Decomposition Method of Fredholm Integral Equation of the Second Kind Using Maple, Journal of Advances In Mathematics, Vol9, No.1, pp.1868-1875,2014.

[10] Dalal A. Maturi., Application of Adomian Decomposition Method for Solving of Fredholm Integral Equation of the Second Kind, European Journal of Science and Engineering, Vol9, No.2, pp.1-9,2014.

[11] H.H. Sorkun., S. Yalcinbas., Approximate solutions of linear Volterra integral equation systems with variable coefficients, Applied Mathematical Modeling, 34(2010) 3451-3464.

[12] Dalal A. Maturi., Honaida M. Malaikah., Numerical Solution of System of Three Nonlinear Volterra Integral Equation Using Implicit Trapezoidal, Journal of Mathematics Research; Vol. 10, No. 1; February 2018, ISSN 1916-9795doi:10.5539/jmr.v10n1p44URL: https://doi.org/10.5539/jmr.v10n1p44.

[13] Dalal A. Maturi., The Modified Decomposition Method for Solving Volterra Integral Equation Of The Second Kind Using Maple, International Journal of GEOMATE, Oct., 2019 Vol.17, Issue 62, pp. 23-28.

[14] Dalal A. Maturi., Amal I. Aljedani., Eman S. Alaidarous., Finite Difference Method For Solving Heat Conduction Equation Of The Granite, International Journal of GEOMATE, Sept., 2019 Vol.17, Issue 61, pp. 135 -140. ISSN: 2186-2982 (P), 2186-2990 (O), Japan.

[15] Dalal A. Maturi., Finite Difference Method For Solving Heat Conduction Equation Of The Brick, International Journal of GEOMATE, April, 2020 Vol.18, Issue 68, pp. 114-119.

[16] Dalal A. Maturi., Eman Ahmed M. Simbawa., The Modified Decomposition Method For Solving Volterra Fredholm Integro-Differential Equation Using Maple, International Journal of GEOMATE, March 2020 Vol.18, Issue 67, pp. 84-89.

11th Int. Conf. on Geotechnique, Construction Materials & Environment,
Kyoto, Japan, 3-5 November 2021, ISBN: 978-4-909106063 C3051

RESPONSE SURFACE MODELLING OF PERFORMANCE OF CONCRETE WITH BAUXITE LATERITE SOIL AND FLY ASH

Joenel Galupino[1], Mary Ann Adajar[1], John Jacob Abejuela[2],
Ernst Kenneth Alcantara[2], and Philippe Daniel Ebreo[2]

[1]Faculty, De La Salle University, Manila, Philippines
[2]Undergraduate student, De La Salle University, Manila, Philippines

ABSTRACT

The study investigated the use of waste materials such as fly ash and bauxite laterite soil in concrete in order to address the wastes' disposal issues and lower the cost of concrete products. Bauxite laterite soil is a byproduct of aluminum mining, whereas fly ash is a byproduct of coal power plants. To make bauxite laterite concrete, fly-ash was utilized as a partial substitute for cement in a 20% proportion and bauxite laterite soil was used as a fine aggregate substitute in 10%, 20%, 30%, and 40% quantities. We evaluated and compared the mechanical properties of bauxite laterite concrete to those of standard concrete. The test findings indicate that a 10% replacement of bauxite laterite soil is the optimal percentage substitution. The mixture attained 58 percent increase of the compressive strength compared to ordinary concrete after 28 days of curing. Additionally, bauxite laterite concrete displayed high early compressive strength and a unit weight reduction of approximately 6% to 8%. However, as bauxite laterite soil was increasingly substituted, the workability of the concrete mix decreased. A Response Surface Model was developed to forecast the compressive strength of concrete based on several parameters. It may be concluded that bauxite laterite soil and fly ash are both viable alternatives to fine aggregates and cement.

Keywords: Bauxite laterite soil, Fly-ash, Compressive strength, Response surface modelling

INTRODUCTION

Meyer (2009) [1] estimates that the world annual production of concrete is 10 billion tons. Concrete's huge demand necessitates vast volumes of raw resources and energy.

Fortunately, numerous researchers are investigating the use of other materials [2]-[21] and methods [23]-[27] to improve construction materials.

Consider the possibility of cement substitution. Cement is generally composed of limestone, clay, and shale. Silica, alumina, and lime are used as raw materials. They are calcined to make clinker in cement kilns. After that, the clinker is pulverized to an extremely fine powder. Cementitious or pozzolanic materials can be used in place of cement. Fly ash is an example of this; it is abundant in the Philippines. Fine aggregates are another component of concrete that is utilized in considerable quantities.

Fine aggregates are frequently obtained through river dredging and, in some situations, through the crushing of rocks. Substitute materials with comparable particle sizes and surface roughness can be used in place of fine aggregates. Due to its resemblance to sand, bauxite laterite soil is one of the materials that could be used.

Extraction of bauxite necessitates the clearance of enormous areas of land in order to reach the mineral beneath the ground. Surrounding ground surfaces are contaminated with mineral waste and are rendered useless following bauxite mining.

Both of the aforementioned materials were used as alternatives for components used in concrete manufacturing in the study. Due of the intrinsic pozzolanic and cementitious qualities of fly ash, it was used. The researchers' goal is to find a new purpose for things that are currently deemed garbage. Recycling is carried out in order to give an alternate source of raw materials, most notably cement and fine aggregates. While the relatively low replacement % may look inconsequential, when applied to large projects, significant savings might be achieved. The amount of waste that will be disposed of may reduce disposal issues. Additionally, it may eventually result in a reduction of pollutants produced by the mining and power generation industries.

One way of giving a relationship with the properties of these wastes and its subsequent results is to use modelling [28]-[32]. Response surface modelling will forecast or predict the causal relationship of using fly ash and bauxite laterite waste in this study, specifically its compressive strength and the days of curing. Thus, in this study, it is aimed to create a response surface model that will forecast the compressive strength of concrete given the percentage of fly ash and bauxite laterite used and its days of curing. Validation is important in a study [33]-[37], an equation for the compressive strength of concrete can be determined and used for estimating the concrete strength at a given percent substitution and days of curing.

METHODOLOGY

Design of Experiment

The experimental research approach established the causes and effects of partially substituting fly ash for cement and fine aggregates for bauxite laterite soil in the production of concrete on its mechanical properties. The experimental design considers a design mix containing a constant 20% cement replacement for fly ash and varied amounts of fine aggregate in place of bauxite laterite soil.

The compressive strength is the dependent variable in this study. The amount of bauxite laterite soil used as a partial fine aggregate substitution and the curing days affect all strength parameters. The study's control specimen is with the mix of Portland cement type 1b and fly ash class F (20 percent) to be used in place of cement.

The percentages of bauxite laterite soil substituted were 10%, 20%, 30%, and 40%, represented as LS0, LS10, LS20, LS30, and LS40. Laterite Soil (LS) and the number following it denotes the percentage replacement of fine particles.

Compressive strength of 25 MPa was used to calculate the design mix, shown in Table 1. A constant water cement ratio of 0.57 with a slump of 25mm-50mm was considered. Due to the specific gravity of fly ash class F being identical to that of cement, a partial substitution of cement was made in terms of weight. Due to the varying specific gravity of bauxite laterite soil and river sand, the fine aggregate replacement was done by volume at 10%, 20%, 30%, and 40%. Compressive strength specimens were made in cylindrical molds with a diameter and height of 150mm by 300mm, respectively.

Table 1 Design Mix

Mix (m^3)	LS0	LS10	LS20	LS30	LS40
Water	0.205	0.205	0.205	0.205	0.205
Cement	0.092	0.092	0.092	0.092	0.092
Fly Ash	0.023	0.023	0.023	0.023	0.023
LS	0.000	0.030	0.061	0.091	0.122
Gravel	0.358	0.358	0.358	0.358	0.358
Sand	0.303	0.270	0.240	0.210	0.180

Index Tests

The bauxite laterite soil was mined at Samar's aluminum mines. The mining locations are currently undergoing soil exploration, which has identified various layers of laterite soil.

The soil used in the study was extracted two meters below the earth to guarantee that it was free of contaminants. Visual examination revealed that the bauxite laterite soil is red in color and has a particle size distribution that is predominantly fine.

The soil underwent Atterberg Limit Test, Specific Gravity Test and Particle Size Distribution Curves in accordance with the ASTM Standards.

Concrete Works and Test

Concrete was cast and cured in accordance with ASTM C192 standards. The concrete mixes were conducted to the slump test, the concrete mix was carefully put to the pan. The slump test enables us to evaluate and quantify the workability of fresh concrete, allowing researchers to assess if the concrete mix has an adequate amount of water. The slump height was determined by measuring from the top of the mold to the top of the concrete.

The Compressive Strength of Concrete Test was performed on the concrete sample (based on ASTM C39). The test was designed to measure the sample's resistance to compressive forces up to the point of collapse. The concrete cylinder's two bases were covered and vertically positioned inside the Universal Testing Machine. The specimen was subsequently subjected to an axial compressive load till failure.

Table 2 Number of Specimen

Mix	Days of Curing			
	7	14	21	28
Control	5	5	5	5
LS0	5	5	5	5
LS10	5	5	5	5
LS20	5	5	5	5
LS30	5	5	5	5
LS40	5	5	5	5

Response Surface Modelling

Lastly, a response surface model was used to create a forecasting model to determine which variables have an impact on the compressive strength of the concrete mixed with Laterite Soil. An equality line was also used to validate the predicted versus the actual data.

RESULTS AND DISCUSSIONS

Index Tests

To determine the particle size distribution of the oven-dried specimen, sieve analysis was used. The bulk of particles, 96.85 percent, that passed through the #4 sieve and were retained on the #200 sieve were classed as sand and were used as a substitute for fine aggregate. Fines were identified as a very minor percentage of the 0.97 percent that passed through the

#200 sieve.

The soil is well-graded, as indicated by a uniformity coefficient, Cu, of 9.09. Additionally, the coefficient of curvature, Cc, value of 0.9, which is close to one, indicates that the delivered soil is well-graded sand. Due to the fact that our soil is well-graded, our sample contains particles of varied sizes. Which is great for substituting for fine aggregates since it aids in the interlocking of particles, which is necessary for concrete strength.

Bauxite laterite soil has a specific gravity of 2.05, which is lower than the specific gravity of fine particles. The liquid limit is determined to be 50.61 percent water, whereas the plastic limit is determined to be 35.92 percent water. The plasticity index for this soil sample is 14.69 percent, indicating that it is of medium plasticity. The soil's flexibility can be linked to the presence of clay particles in the sample.

Concrete Tests

Compressive, tensile, and flexural tests were performed on concrete samples to investigate the effect of bauxite laterite soil as a partial substitution for fine aggregates and fly ash as a 20% substitute for cement. Compressive strength development was determined on concrete sample after 7, 14, 21, and 28 days of curing.

The workability of bauxite laterite concrete decreases in direct proportion to the percentage substitution, as measured by the slump value. The concrete mix LS0 has the maximum slump due to the addition of fly ash as a plasticizer. On LS40, the lowest slump value was obtained. Due to the decreased workability of the concrete sample, shown in Figure 1, the researchers mixed fresh concrete manually. During the mixing process, it became apparent that the workability decreased due to the cohesiveness of the fresh concrete.

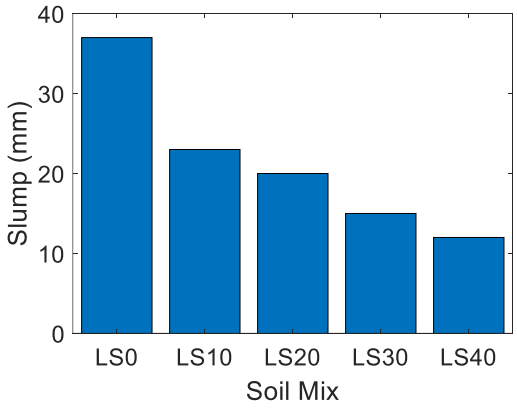

Figure 1 Workability of the Soil Mix

Clay is a form of soil that has a greater capacity for water retention than sandy soils [38]; this attribute of clay relates to the ability of laterite soil, which is rich in clay minerals, to retain more water than the ordinary sand used as fine aggregates in concrete. It was discovered during the mixing process that water is progressively absorbed by the bauxite laterite soil, drying portions of the concrete mix.

The control specimen failed in failure categories I and II, while the concrete specimen failed violently due to concrete's brittleness. The failure modes observed for LS0 and bauxite laterite concrete are Type II and IV.

The average compressive strength of concrete specimens was determined at various curing times. The control specimen has an average strength of 24.24 MPa, which meets the structural concrete minimum standards. The increased use of fine particles weakens the concrete specimen. LS0 has the maximum compressive strength when compared to bauxite laterite concrete, which has a compressive strength of 16.52 MPa. LS0 had a compressive strength of just 68% of that of the control specimen. The compressive strength of the LS10 specimen was marginally lower at 13.42 MPa. While the compressive strengths of LS20, LS30, and LS40 are decreasing at 12.65 MPa, 9.08 MPa, and 7.70 MPa, respectively. Additionally, it is worth noting that the early strength of LS10 and LS20 is greater than that of LS0, which increased strength through subsequent curing periods.

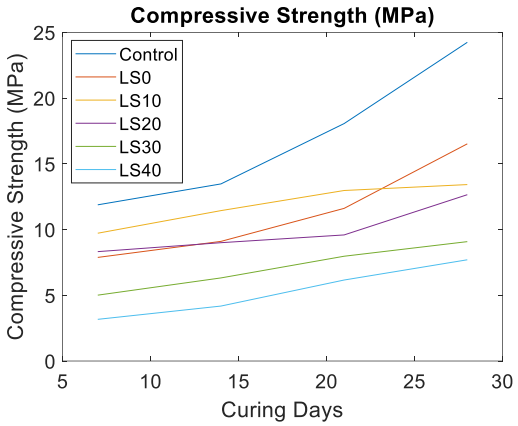

Figure 2 Compressive Strength vs. Curing Days

The control and LS0 specimens gained increasing amounts of strength over time, particularly during the later curing periods. As a result, both control and LS0 specimens demonstrated improved long-term strength. LS10 and LS20 build strength rapidly, attaining 69.37 percent and 65.77 percent strength after seven days, respectively. Although bauxite laterite concrete demonstrates a linear strength rise, this contributes to the material's poor 28-day compressive strength. On bauxite laterite concrete specimens, it is noted that the strength develops slowly.

Long-term strength can be linked to the hydration process, in which water causes concrete to harden by forming cementitious components. The chemical reaction between cement components and water produces hydration products, which are found in concrete [39]. Laterite soils are predicted to include clay, which has a better water holding capacity than sandy soils. Due to the low workability of laterite concrete, it is prone to include a large number of voids. While the curing process may have aided in the hydration of the specimen, due to water's incompressibility, it is unable to support loads, which may have resulted in the bauxite laterite concrete's decreased compressive strength.

The researchers noted that several concrete examples had uneven top and bottom surfaces. It was determined to be caused by air voids, settling, and moisture loss in the concrete. When the specimen was placed on the Universal Testing Machine, the specimen's uneven surface was seen. The initial focus of the applied force was on the partial cross-sectional region it impacted. Without having to optimize the strength, the top piece eventually failed. Side fractures occurred on either the top or bottom faces of these specimens.

Response Surface Modelling and Validation

A Response Surface Model for the compressive strength of concrete was used for estimating the concrete strength at a given percent substitution of the Laterite Soil and days of curing.

A Response surface model graph was used to illustrate the strength development curve for each percent substitution, shown on Figure 3.

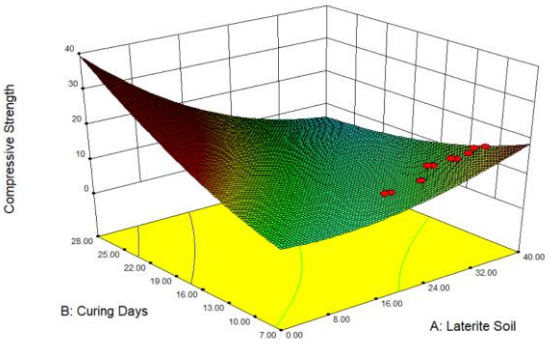

Figure 3 Response Surface Model Graph

The Response Surface Model has an R^2 value of 0.7542 which shows an agreement between the model and the observed parameters.

An equality line was also used to validate the predicted versus the actual data, shown in Figure 4.

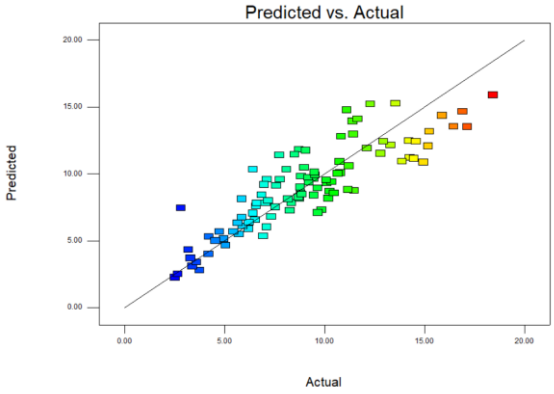

Figure 4 Equality Line for Validation

CONCLUSIONS

The parameters of the bauxite laterite soil, sand, gravel, fly ash, and cement were determined prior to the production of bauxite laterite concrete. After analyzing the index properties of bauxite laterite soil, it was determined that its sand-sized particles made it a good substitute for fine aggregate. The bauxite laterite soil is found to have uniform particle size distribution with a specific gravity of 2.05.

Increased partial substitution of bauxite laterite soil resulted in a decrease in the concrete's strength and workability. Thus, LS10 is the preferred % substitution specimen due to its superior combination of compressive, split-tensile, and flexural strength when compared to the other percentage substitution specimens. After seven days of curing, it regained 69.37 percent of its compressive strength. At 13.42 MPa, the compressive strength of LS10 was 57.80 percent that of the control sample. Due to the lower specific gravity of bauxite laterite soil compared to river sand, the unit weight of bauxite laterite concrete was up to 8% lighter than traditional concrete.

The study was able to create a Response Surface Model for the compressive strength of concrete for estimating the concrete strength at a given percent substitution of the Laterite Soil and days of curing. The Response Surface Model has an R^2 value of 0.7542 which shows an agreement between the model and the observed parameters.

REFERENCES

[1] Meyer, C. (2009). The greening of the concrete industry. Cement and Concrete Composites,31(8), 601-605.

[2] Ann Adajar, M., Galupino, J., Frianeza, C., Faye Aguilon, J., Sy, J. B., & Tan, P. A. (2020). COMPRESSIVE STRENGTH AND DURABILITY OF CONCRETE WITH COCONUT SHELL ASH AS CEMENT REPLACEMENT. International Journal of GEOMATE, 17, 183-190.

[3] Dungca, J. R., Galupino, J. G., Alday, J. C.,

Barretto, M. A. F., Bauzon, M. K. G., & Tolentino, A. N. (2018). Hydraulic conductivity characteristics of road base materials blended with fly ash and bottom ash. International Journal of GEOMATE, 14(44), 121-127. doi:10.21660/2018.44.7145

[4] Elevado, K. J. T., Galupino, J. G., & Gallardo, R. S. (2019). Compressive strength optimization of concrete mixed with waste ceramics and fly ash. International Journal of GEOMATE, 16(53), 135-140. doi:10.21660/2019.53.14268

[5] Galupino, J., Adajar, M. A., Uy, E. E., Koa, N. C., Lao, A. L., Lao, R. N., & Tan, J. C. M. (2020). Performance of concrete mixed with fly ash and plastic when exposed to fire. International Journal of GEOMATE, 19(74), 44-51. doi:10.21660/2020.74.9198

[6] Galupino, J. G., & Dungca, J. R. (2015). Permeability characteristics of soil-fly ash mix. ARPN Journal of Engineering and Applied Sciences, 10(15), 6440-6447.

[7] Uy, E. E. S., Adajar, M. A. Q., & Galupino, J. G. (2021). Utilization of philippine gold mine tailings as a material for geopolymerization. International Journal of GEOMATE, 21(83), 28-35. doi:10.21660/2021.83.9248

[8] Adajar, M. A. Q., Aquino, C. J. P., dela Cruz, J. D., Martin, C. P. H., & Urieta, D. K. G. (2019). Investigating the effectiveness of rice husk ash as stabilizing agent of expansive soil. International Journal of GEOMATE, 16(58), 33-40. doi:10.21660/2019.58.8123

[9] Adajar, M. A. Q., & Cutora, M. D. L. (2018). The effect of void ratio, moisture content and vertical pressure on the hydrocompression settlement of copper mine tailing. International Journal of GEOMATE, 14(44), 82-89. doi:10.21660/2018.44.7108

[10] Adajar, M. A. Q., de Guzman, E., Ho, R., Palma, C., & Sindico, D. (2017). Utilization of aggregate quarry waste in construction industry. International Journal of GEOMATE, 12(31), 16-22. doi:10.21660/2017.31.6511

[11] Adajar, M. A. Q., & Pabilona, W. N. K. (2018). Soil-structure interface behavior of cemented-paste backfill material mixed with mining waste. International Journal of GEOMATE, 14(44), 102-108. doi:10.21660/2018.44.7109

[12] Adajar, M. A. Q., & Zarco, M. A. H. (2014). An empirical model for predicting hydraulic conductivity of mine tailings. International Journal of GEOMATE, 7(2), 1054-1061.

[13] Adajar, M. A. Q., & Zarco, M. A. H. (2016). Predicting the stress-strain behavior of mine tailing using modified hyperbolic model. International Journal of GEOMATE, 10(3), 1834-1841. doi:10.21660/2016.21.5127

[14] Uy, E. E. S., & Adajar, M. A. Q. (2017). Assessment of critical-state shear strength properties of copper tailings. International Journal of GEOMATE, 12(32), 12-18. doi:10.21660/2017.32.6565

[15] Uy, E. E. S., Adajar, M. A. Q., & Dungca, J. R. (2019). Volume change behavior of sea water exposed coal ash using hyperbolic model. International Journal of GEOMATE, 16(58), 97-103. doi:10.21660/2019.58.8171

[16] Uy, E. E. S., Dadios, E. P., & Dungca, J. R. (2016). Preliminary assessment of liquefiable area in ermita, manila using genetic algorithm. Paper presented at the 8th International Conference on Humanoid, Nanotechnology, Information Technology, Communication and Control, Environment and Management, HNICEM 2015, doi:10.1109/HNICEM.2015.7393263

[17] Uy, E. E. S., & Dungca, J. R. (2018). A comparative settlement prediction of limestone blended materials using asaoka and hyperbolic method. International Journal of GEOMATE, 14(43), 63-69. doi:10.21660/2018.43.7170

[18] Uy, E. E. S., & Dungca, J. R. (2017). Constitutive modeling of coal ash using modified cam clay model. International Journal of GEOMATE, 12(31), 88-94. doi:10.21660/2017.31.6558

[19] Uy, E. E. S., & Dungca, J. R. (2018). Hyperbolic model parameters of philippine coal ash. International Journal of GEOMATE, 15(47), 95-102. doi:10.21660/2018.47.7171

[20] Dungca, J. R., & Dychangco, L. F. T. (2016). Strength properties of road base materials blended with waste limestones. International Journal of GEOMATE, 11(3), 2493-2498.

[21] Dungca, J. R., & Jao, J. A. L. (2017). Strength and permeability characteristics of road base materials blended with fly ash and bottom ash. International Journal of GEOMATE, 12(31), 9-15. doi:10.21660/2017.31.6508

[22] Adajar, J. B., Ubay, I. O., Alfaro, M., & Chen, Y. (2020). Discrete element model parameters to simulate slope movements. International Journal of GEOMATE, 18(65), 192-199. doi:10.21660/2020.65.9424

[23] Adajar, J. B., Ubay, I. O., Alfaro, M., & Chen, Y. (2020). Discrete element modelling of undrained consolidated triaxial test on cohesive soils. Paper presented at the Geotechnical Special Publication, , 2020-February(GSP 317) 172-182.

[24] Ubay, I. O., Alfaro, M., Alfaro, M., & Blatz, J. (2020). Stability assessment of an aging earth fill dam considering anisotropic behaviour of clay. International Journal of GEOMATE, 18(66), 84-91. doi:10.21660/2020.66.9462

[25] Dungca, J. R., Lao, W. D. T., Lim, M., Lu, W. D., & Redelicia, J. C. P. (2019). Radial flow permeameter: A proposed apparatus to measure horizontal hydraulic gradient of fly-ash based geopolymer-soil mix. International Journal of

GEOMATE, 16(58), 218-223. doi:10.21660/2019.58.4524

[26] Uy, E. E. S., & Boonyatee, T. (2016). Image processing for geotechnical laboratory measurements. International Journal of GEOMATE, 10(4), 1964-1970.

[27] Uy, E. E. S., Noda, T., Nakai, K., & Dungca, J. R. (2018). Monitoring the triggering of liquefaction using image processing. International Journal of GEOMATE, 15(51), 180-187. doi:10.21660/2018.51.02150

[28] Elevado, K. T., Galupino, J. G., & Gallardo, R. S. (2018). Compressive strength modelling of concrete mixed with fly ash and waste ceramics using K-nearest neighbor algorithm. International Journal of GEOMATE, 15(48), 169-174. doi:10.21660/2018.48.99305

[29] Elevado, K. J. T., Galupino, J. G., & Gallardo, R. S. (2018). Artificial neural network (ANN) modelling of concrete mixed with waste ceramic tiles and fly ash. International Journal of GEOMATE, 15(51), 154-159. doi:10.21660/2018.51.58567

[30] Dungca, J., Galupino, J., Sy, C., & Chiu, A. S. F. (2018). Linear optimization of soil mixes in the design of vertical cut-off walls. International Journal of GEOMATE, 14(44), 159-165. doi:10.21660/2018.44.7146

[31] Dungca, J. R., & Galupino, J. G. (2017). Artificial neural network permeability modeling of soil blended with fly ash. International Journal of GEOMATE, 12(31), 76-83. doi:10.21660/2017.31.6549

[32] Dungca, J. R., & Galupino, J. G. (2016). Modelling of permeability characteristics of soil-fly ash-bentonite cut-off wall using response surface method. International Journal of GEOMATE, 10(4), 2018-2024. doi:10.21660/2016.22.5173

[33] Galupino, E. J. G., Garciano, L. E. O., Paringit, M. C. R., & Dungca, J. R. (2017). Location based prioritization of surigao municipalities using probabilistic seismic hazard analysis (PSHA) and geographic information systems (GIS). Paper presented at the HNICEM 2017 - 9th International Conference on Humanoid, Nanotechnology, Information Technology, Communication and Control, Environment and Management, , 2018-January 1-7. doi:10.1109/HNICEM.2017.8269521

[34] Galupino, J. G., & Dungca, J. R. (2019). Quezon city soil profile reference. International Journal of GEOMATE, 16(58), 48-54. doi:10.21660/2019.58.8129

[35] Paringit, M. C. R., Cutora, M. D. L., Santiago, E. H., & Adajar, M. A. Q. (2020). Assessment of landslide susceptibility: A case study of carabao mountain in baguio city. International Journal of GEOMATE, 19(71), 166-173. doi:10.21660/2020.71.9261

[36] Dungca, J. R., Concepcion, I., Limyuen, M. C. M., See, T. O., & Vicencio, M. R. (2017). Soil bearing capacity reference for metro manila, philippines. International Journal of GEOMATE, 12(32), 5-11. doi:10.21660/2017.32.6556

[37] Uy, E. E. S., Paringit, M. C. R., Cutora, M. D. L., Galupino, J. G., Garciano, L. E. O., & Dungca, J. R. (2020). Characterization of cebu province municipalities using probabilistic seismic hazard assessment (PSHA) and geographic information system (GIS). Paper presented at the IOP Conference Series: Earth and Environmental Science, , 479(1) doi:10.1088/1755-1315/479/1/012001

[38] Tzu-Hsing Ko, "Nature and Properties of Lateritic Soils Derived from Different Parent Materials in Taiwan," The Scientific World Journal, vol. 2014, Article ID 247194, 4 pages, 2014. https://doi.org/10.1155/2014/247194.

[39] Kakali, G., Tsivilis, S., Aggeli, E., & Bati, M. (2000). Hydration products of C3A, C3S and Portland cement in the presence of CaCO3. Cement and Concrete Research, 30(7), 1073–1077. doi: https://doi.org/10.1016/S0008-8846(00)00292-1

11th Int. Conf. on Geotechnique, Construction Materials & Environment, Kyoto, Japan, 3-5 November 2021, ISBN: 978-4-909106063 C3051

NUMERICAL SIMULATION OF PERVIOUS CONCRETE PILE IN LOOSE AND SILTY SAND AFTER TREATING WITH MICROBIALLY INDUCED CALCITE PRECIPITATION

Hayder A. Hasan[1], Sabah H. Lafta[2], Muhannd W. Majeed[3], Hadi Khabbaz[4] and Mehdi Aghayarzadeh[5]

[1,2,3] Faculty of Engineering, Mustansiriyah University, Iraq; [4,5] School of Civil and Environmental Engineering, University of Technology Sydney, Australia

ABSTRACT

It is essential to provide a stable foundation system for construction projects to reduce the geotechnical risk of failure due to static or dynamic loads. Pile foundations are recommended to increase bearing capacity and decrease the dynamic oscillations of soils. Recently, soil stabilisation using microbially induced calcite precipitation (MICP) was widely used to increase shear strength parameters and reduce the hydraulic conductivity of sand. In this study, the technique of using MICP was reviewed based on previous studies and analysed using Plaxis 3D to evaluate the enhancement of a single pervious concrete pile under static, free vibration and earthquake stages of loose and silty sand. In the static stage, under the applying load to reach prescribed displacement 76 mm, the results of loose sand demonstrate that the static load capacity was increased from 470 kN of untreated loose sand to 582, 598 and 612 kN after treating by MICP along the shaft and tip of a concrete pile with 0.5,0.75 and 1 m, respectively. In earthquake stage, the result of treated loose sand such as vertical and lateral displacement were insignificant compared with untreated loose sand. The Plaxis 3D models were clarified the benefit of using MICP with pile foundation model.

Keywords: Soil improvement, Pervious concrete pile under static and dynamic load, Numerical analysis

INTRODUCTION

Post-grouting methods have been used to improve the load-carrying capacity of deep foundations by increasing shaft and/or tip resistances of the pile. Post-grouting was widely utilized to improve the tip resistance of drilled pile. However, the grouting process around the pile shaft is complex and difficult quality control [1], [2]. According to Suleiman [3], a pervious concrete pile is used as an injection point to improve the soil-pile interaction and capacity load. Lin [1], [2] has been used permeable pile (pervious concrete pile) to simplify the grouting procedure of MICP along the shaft and tip of foundation systems without applying pressure.

The results of [1] research demonstrated that the improving of pile capacity under axial compression was up to 2.5 times higher the amount of pile without bio-grouting. Moreover, a $CaCO_3$-cemented zone around the pile was extended from the effective pile diameter (76 mm) to approximately 165 mm. The pile length was increased roughly by 25 mm. Soil clumps were noted surrounding the pile tip, which pointed out the breaking and failure of the cemented soil around the pile tip. It could be concluded that the failure was occurring near the pile tip of the cemented soil.

Microbially induced calcite precipitation (MICP) is a biological process that uses to improve granular soils due to increasing shear strength parameters. MICP has emerged as a green, low cost, and sustainable technique for soil improvement [4]. Due to the urease enzyme activity of bacteria in existence of urea and calcium chloride, the calcite (calcium carbonate) is formed after a series of chemical reactions. Umar [5] clarified that the principle of MICP method is as follows: the reaction of hydrolysis of urea , $CO(NH_2)_2$, with water leading to the formation of ammonia (NH_3) and carbon dioxide (CO_2).

$$CO(NH_2)_2 + H_2O \longrightarrow 2NH_3 + CO_2 \quad (1)$$

The ammonium (NH_4^+) and hydroxyl ions (OH^-) induced by diversion of ammonia (NH_3) in the presence of water. Then, the carbon dioxide (CO_2) which generated by urease activity or respiration, decomposes rapidly to produce bicarbonate (HCO_3^-) and hydrogen ion (H^+) after reacting with water [6].

$$2NH_3 + 2H_2O \longrightarrow NH_4^+ + 2OH^- \quad (2)$$
$$CO_2 + 2H_2O \longrightarrow HCO_3^- + H^+ \quad (3)$$

The bicarbonate (HCO_3^-) combined with hydrogen and hydroxyl ions to create carbonate ions (CO_3^{2-}), which then combines with calcium ions Ca^{2+} (from dissolved calcium chloride) to precipitate calcium carbonate ($CaCO_3$).

$$HCO_3^- + H^+ + 2OH^- \leftrightarrow CO_3^{2-} + 2H_2O \quad (4)$$
$$Ca^{2+} + CO_3^{2-} \longrightarrow CaCO_3 \quad (5)$$

Calcium ions quickly combine with urea hydrolysis and water to produce calcium carbonate and ammonium.

$$CO(NH_2)_2 + 2H_2O \quad + \quad Ca^{2+} \longrightarrow \mathrm{NH_4^+} + CaCO_3 \qquad (6)$$

MICP processes are affected by many factors including bacterial species and strains, bacterial solution concentration, temperature, pH, cementation solution composition and concentration, grouting technology, and soil properties [7]. Bacillus and Sporosacina bacteria are commonly used in MICP-treated geotechnical technology due to having an excellent ability to create calcium carbonate. The best conditions for microbial to improve the geotechnical properties are temperature around 20 and 40 °C, pH ranges from 7 and 9.5 and the adequate grain size of soil particles ranging from 10 to 1000 μm [7].

Soon [8] used microorganism technique to improve shear strength and reduce hydraulic conductivity of two different soils under 85%, 90% and 95% of maximum densities. The first sample classified as Sandy Silt with high plasticity (MS), while the second sample classified as Well Graded Sand (WS). The research explored the bio-clogging and bio-cementation development depended on bacteria, cementation reagents (e.g., urea and calcium chloride) and soil densities. The best results of undrained shear strength parameter (c_u) and hydraulic conductivity (k) were under 95% densities of Sandy Silt specimen. The c_u improved from 26.2 kPa (untreated soil) to 69.2 kPa (treated soil with MICP). The k decreased from 1.0×10^{-7} m/s of untreated soil to 2.6×10^{-8} m/s of treated soil. The changing in parameters of c_u and k were inflicted by creating the calcite (1.711%) after treatment system. In sandy soil, the effective internal friction angle ($\emptyset'$) was 50° with treated soil while the $\emptyset'$ was 48.8° with untreated soil under 95% of maximum index density. In addition, hydraulic conductivity (k) decreased from 4.4×10^{-4} m/s of untreated soil to 6.7×10^{-5} m/s of treated soil. The reason for this change is that the calcite content is 2.935% because of MICP treated.

MICP technique suffers from some drawbacks when using with fine grains because of bacteria incapable of growth in very low permeability to oxygen and moving freely in tiny pore space [9]. Behzadipour [9] addressed the impacts of plastic and non-plastic fines on the bio-mediated soil improvement of shear strength parameters of sandy soils. The results presented that the presence of fine particles can decrease the efficiency of MICP treatment. The effect of created calcite on shear strength reduces as the fine content increases. The MICP efficiency to treat sandy soils was reduced more than with adding plastic fine compared with non-plastic fines.

The comprehensive experimental tests were carried out by [10]-[12] to investigate the influence of MICP technique on poorly graded sand treated with different percentage of silt. Zamani [10] studied the behaviour of monotonic and cyclic undrained direct shear tests of untreated and bio-cemented. Also, the change in permeability was examined on Nevada sand classifying as uniformly graded and Nevada sand containing 15% silt classifying as silty sand. A result of calcite precipitation due to MICP, the normalized shear strength increased from 0.15 to 0.38 for sand and from 0.23 to 0.38 for silty sand. Moreover, the reduction in permeability was reflected directly on excess pore water pressure. For example, the excess pore water pressure reduced about 75% when the permeability reduced from 5.04×10^{-5} m/s to 4.47×10^{-6} m/s of Sand. Also, the excess pore water pressure decreased 35% with reduction in permeability from 2.56×10^{-5} m/s to 2.45×10^{-6} m/s of silty sand.

The Seep/W and Sigma/W programs used to evaluate the changes in injection rate and the influence radius of MICP process progress [12]. The results of numerical modelling presented that the rates of injection could be increased of Nevada sand. However, it remains unchanged of Nevada sand with 15% silt content. In addition, the higher levels of pore water pressure were generated due to the presence of fines (silt) during the injection process, which requires higher strength enhancement to prevent the development of excessive plastic strains. The key parameter to determine the radius of treatment is to improve the shear strength and stiffness relative to the quantity of the hydraulic conductivity level and its change rate.

The purpose of this study is to focus on using Plaxis 3D program to assess the effect of MICP treatment on the ultimate loading capacity and the displacement of constant load under free vibration and earthquake. The research offers a promising way of using MICP as an eco-friendly stabiliser for treating a pervious concrete pile that is particularly embedded on loose sand.

CONSTRUCTION PARAMETERS AND FINITE ELEMENT MODEL SETUP

The dimensions of the model have been set with 40 m in X direction, 5 m in Y direction and 40 m in Z direction to minimize the boundary condition effect of dynamic steps that is assumed to have an effective action through the X direction.

The representative properties and model of soil and pile were constructed based on previous studies and recommendations. Tables 1 and 2 illustrate the properties of soils using in this study. The geotechnical properties of untreated and treated soils were gotten from [12]. The pervious concrete pile was modelled depending on reference [1] after scaling the

dimensions to 10 times. For example, the diameter of pile is 0.76 m while the length of pile is 10.7 m including an embedded length 9.16 m. The treated soil was assumed extending to 0.5, 0.75 and 1 m along the shaft and tip of a concrete pile.

Table 1 Soils properties*

Identification	Sand	Treated Sand	Silty sand	Treated Silty sand
Model	Mohr-Coulomb			
Drainage type	Drained			
Unsaturated Unit Weight, γ (kN/m^3)	17	17	17	17
Saturated Unit Weight, γ (kN/m^3)	19.25	20	19.25	20
Void ratio, e	0.709	0.647	0.709	0.650
Young's modulus (kPa)	5400	16200	8400	12900
Poisson ratio, ν	0.27	0.29	0.27	0.29
Friction Angle, $\phi°$	32.5	36	32	34.5
Permeability (m/day)	4.52	2.29	0.386	0.212

*The data were taken or derived from [12].

Table 2 The properties of concrete pile

Identification	Concrete pile
Model	Linear elastic
Drainage type	Drained
Unsaturated Unit Weight, γ (kN/m^3)	22
Saturated Unit Weight, γ (kN/m^3)	22
Void ratio, e	0.149•
Young's modulus (kPa)	20 x10^6
Poisson ratio, ν	0.1
Permeability (m/day)	1.04x10^6•

• The data were extended taken from [1].

To calculate the ultimate static load capacity to reach 76 mm prescribed displacement (10% of pile diameter) and dynamic states of untreated and treated soil, the design steps have been followed. The soil layer (sand or silty sand) was extended until -40 m. The untreated and treated soils were modelled as Mohr-Coulomb model with drain condition. The phreatic level assigns at the ground surface. The pile was modelled as half symmetric to reduce the calculation time. The interface elements were used to incorporate with interface strength reduction factor (Rinter) 0.8 to decrease the skin resistance of the interface that allows sliding between the pile and soil nodes. The geometry of treated soil with 1 m around the shaft and tip of a concrete pile is demonstrated in Fig. 1.

The earthquake was assumed as 0.5 m uniform prescribed displacement across the bottom boundary at X component with fixing Y and Z components. The data of earthquake, which is available in Plaxis, was used for the dynamic excitation under acceleration and drift correction options, as shown in Fig. 2.

The element distribution in Mesh mode was set to medium because of the calculation under dynamic taking more than one day to complete. The process of calculation includes the initial conditions phase, simulation of concrete pile with untreated and treated soil, prescribed displacement load under 76 mm, free vibration analysis and earthquake analysis. In prescribed displacement load and earthquake phases, the reset displacement was selected to zero.

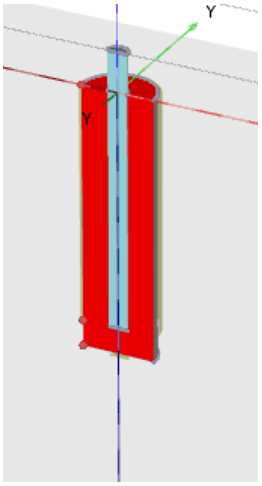

Fig. 1 The geometry of treated soil with 1 m around the shaft and tip of a concrete pile as half symmetric using Plaxis 3D.

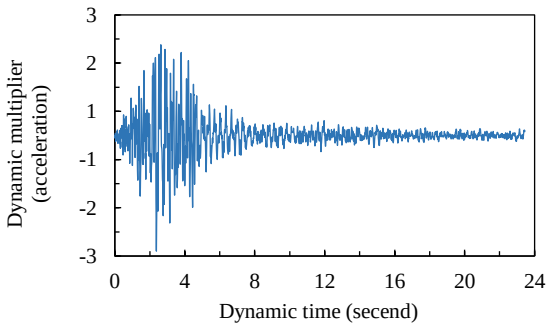

Fig. 2 Acceleration-time used in study (Plaxis program).

The free vibration or earthquake phases was started after completing prescribed displacement load. The free vibration analysed as dynamic option with 5 sec. time interval under boundary conditions in X directions and Z min as viscous while in Y directions and Z max as none. In earthquake phase, the dynamic option with 20 sec. time interval was selected. The boundaries were set to Free-field in the

X direction, to None in Y and Z max, and to Compliant base in Z min.

RESULTS AND DISCUSSION

Figure 3 illustrates the increase of half pile displacement due to the increasing load of untreated and treated loose sand with MICP. In untreated state, the load versus displacement curve is gradually decreased until the load is approximately reached 135 kN with a vertical displacement around 17 mm. The curve is then reduced sharply until reaching displacement 76 mm with a load 235 kN of half pile. The maximum load capacity of a complete pile is 470 kN. As you can see from the treated soil curves with 0.5, 0.75 and 1 m around the shaft and tip of a concrete pile, the gradient of the load-displacement graph is smaller than untreated soil. In addition, the curves of treated soil are reduced continuously up to approximately the load and displacement reaching 160 kN 13 mm, respectively. The curves of half pile are then dramatically decreased until reaching 76 mm displacement when load capacity of treated soil with 0.5, 0.75 and 1 m are 291, 299 and 306 kN, respectively. The enhancement ratio of treated soil with 0.5, 0.75 and 1 m is increased to 1.24, 1.27 and 1.3, respectively. In addition, the load capacity development is slightly increased after treatment with 0.5 m.

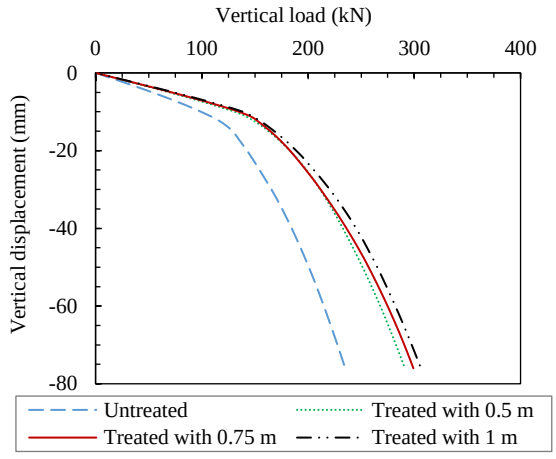

Fig. 3 Load – displacement relationship of untreated and treated loose sand.

The vertical displacement as shading of untreated and treated with 1 m loose sand is presented in Fig. 4. The displacement on the pile tip is more influence compared with the pile shaft. From another perspective, the intensity of displacement of treated loose sand around the pile shaft is higher than untreated sand. It could be because of more load (stress) requiring to attain 76 mm displacement.

Figure 5 presents the effect of MICP on the vertical pile load in silty sand. The maximum vertical load of untreated silty sand is 277 kN to extend 76 mm of displacement. As expected, the untreated silty sand exhibits a higher vertical load compared with untreated loose sand. It could be attributed to the higher contacts between silty sand particles. As shown in Fig. 5, the enhancement of load capacity is around 313 kN when the soil is treated with 0.5m along the shaft and tip of a concrete pile. However, the load capacity is insignificantly increased with 0.75 and 1 m treated.

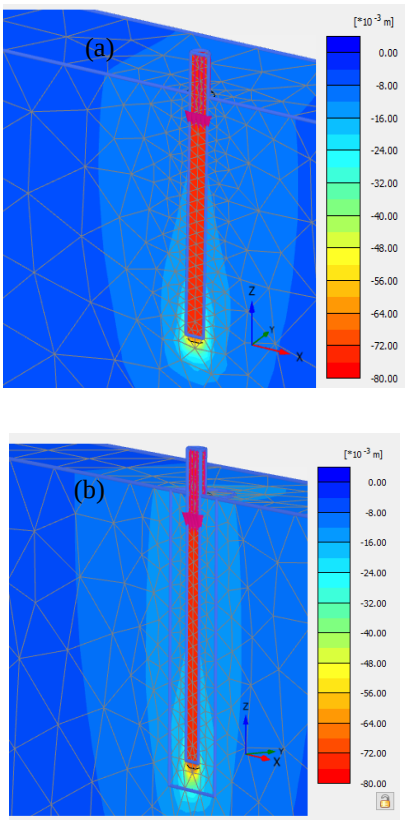

Fig. 4 Vertical displacements u_z to reach -0.076 m: (a) of untreated loose sand, (b) of treated loose sand with 1 m (scaled up 20 times).

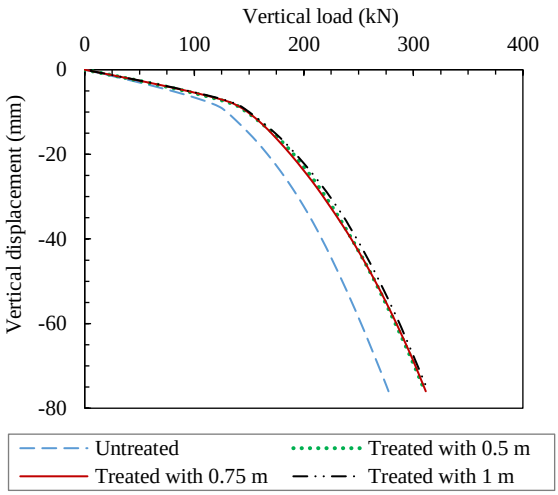

Fig. 5 Load – displacement relationship of untreated and treated silty sand.

Figure 6 shows the horizontal displacement (u_x) of free vibration versus time on the top of the pile centre (0, 0, 1.54). The greatest u_x of untreated sand is 7.798 x 10^{-1} mm at 0.955 sec. while the highest u_x of treated sand with 1 m along the shaft and tip of a concrete pile is 6.869 x 10^{-1} at 1.405 sec.

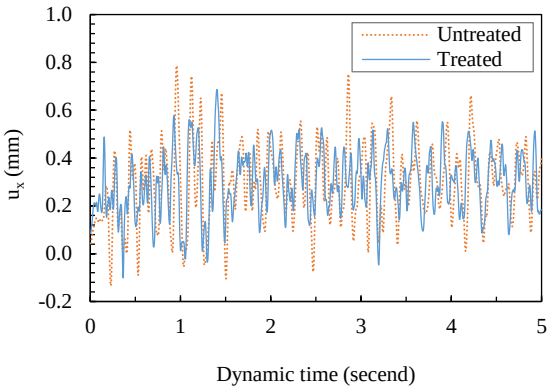

Fig. 6 Horizontal displacement (u_x) of free vibration versus dynamic time.

The vertical displacement (u_z) – dynamic time relationship under free vibration is illustrated in Fig. 7. The free vibration step calculated after reaching 76 mm prescribed displacement due to vertical load. The u_z of untreated sand is decreased to 117 mm at 0.73 sec while u_z of treated loose sand is reduced to 120 mm at 0.73 sec. It might be because the pile under-treated state was carried more load compared with the untreated state when obtaining 76 mm vertical displacement.

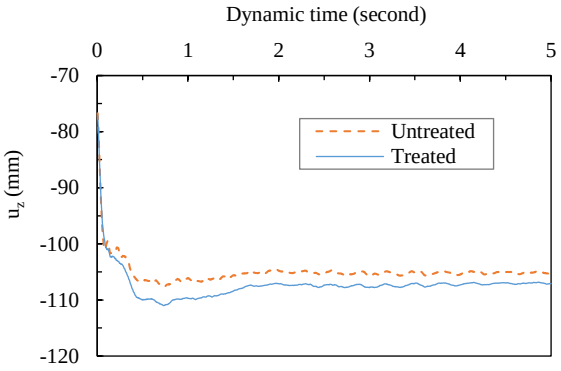

Fig. 7 Vertical displacement (u_z) – dynamic time relationship under free vibration.

Figure 8 illustrates the horizontal movement (u_x) with time on the top of the pile centre (0, 0, 1.54). It observes that the peak value of u_x of untreated and treated sand is an approximately close pattern.

The vertical displacement (u_z) versus time of untreated and treated loose sand under seismic condition is shown in Fig. 9. The displacement of the pile under earthquake condition determined after resetting the displacement to zero in Plaxis program. It appears that u_z is decreased to 35 mm after 1.3 sec. of untreated sand while u_z is reduced to 40 mm at 1.3 sec. of treated sand. It could be happened because of the same reason that mentioned at free vibration step.

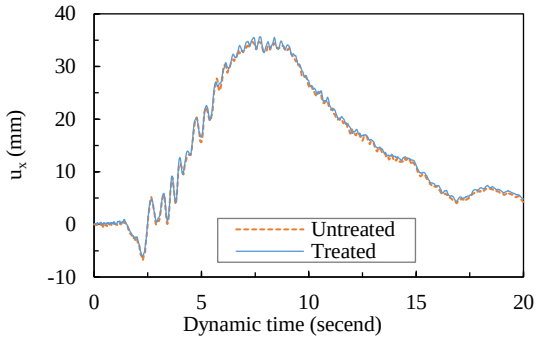

Fig. 8 Horizontal displacement (u_x) versus dynamic time on the top of the pile centre (0, 0, 1.54).

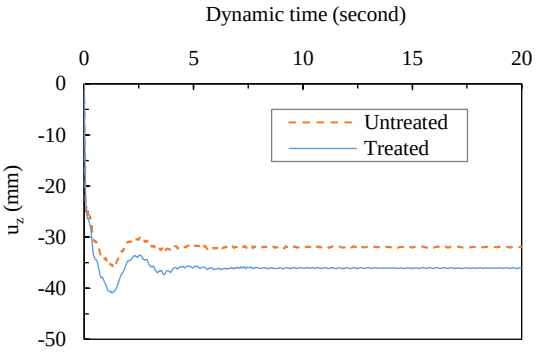

Fig. 9 Vertical displacement (u_z) – dynamic time relationship under earthquake.

CONCLUSIONS

This paper reports the outcomes of finite element modelling and analysis of a single pervious concrete pile in loose and silty sand before and after treated with MICP. The pile was subjected to free vibration and earthquake after evaluating the maximum vertical load. The following conclusions could be drawn as a result of this study.

The results reveal that using MICP has a significant effect on the pile bearing capacity of loose sand compared with silty sand. For example, the ultimate load capacity of the complete pile to displace 76 mm was increased from 470 kN to 582,598 and 612 kN when the loose sand treated with 0.5, 0.75 and 1 m, respectively. On the other hand, the maximum load was improved from 554 kN of untreated silty sand to 620 kN of treated silty sand with 0.5 m around the shaft and tip of the pile. Moreover, the enhancement of load capacity was insignificant increased after 0.5 m treated. The horizontal (u_x) and vertical (u_z) displacement were marginally changed

under free vibration and earthquake conditions of untreated and treated loose sand.

ACKNOWLEDGMENTS

The authors would thank Mustansiriyah University (www. uomustansiriyah.edu.iq) Baghdad-Iraq for its support in the present work.

REFERENCES

[1] Lin, H., Suleiman, M., Jabbour, H., Brown, D. and Kavazanjian, E., Enhancing the Axial Compression Response of Pervious Concrete Ground Improvement Piles Using Biogrouting. Journal of Geotechnical and Geoenvironmental Engineering, Vol. 142, Issue 10, 2016, p. 04016045.

[2] Lin, H., Suleiman, M., Jabbour, H. and Brown, D., Bio-grouting to Enhance Axial Pull-out Response of Pervious Concrete Ground Improvement Piles. Canadian Geotechnical Journal, Vol. 55, Issue 1, 2018, pp. 119-130.

[3] Suleiman, M., Ni, L. and Raich, A., Development of Pervious Concrete Pile Ground-Improvement Alternative and Behavior under Vertical Loading. Journal of Geotechnical and Geoenvironmental Engineering, Vol. 141, Issue 10, 2015, p.07015025.

[4] Mujah, D., Shahin, M. and Cheng, L., State of the Art Review of Biocementation by Microbially Induced Calcite Precipitation (MICP) for Soil Stabilization. Geomicrobiology Journal, Vol. 34, Issue 6, 2016. pp.524-537.

[5] Umar, M., Kassim, K. and Ping Chiet, K., Biological Process of Soil Improvement in Civil Engineering: A Review. Journal of Rock Mechanics and Geotechnical Engineering, Vol. 8, Issue 5, 2016, pp.767-774.

[6] Pakbaz, M., Behzadipour, H. and Ghezelbash, G., Evaluation of Shear Strength Parameters of Sandy Soils upon Microbial Treatment. Geomicrobiology Journal, Vol. 35, Issue 8, 2018, pp.721-726.

[7] Tang, C., Yin, L., Jiang, N., Zhu, C., Zeng, H., Li, H. and Shi, B., Factors Affecting the Performance of Microbial-Induced Carbonate Precipitation (MICP) Treated Soil: A Review. Environmental Earth Sciences, Vol. 79, Issue 5, 2020, p. 94.

[8] Soon, N., Lee, L., Khun, T. and Ling, H., Factors Affecting Improvement in Engineering Properties of Residual Soil through Microbial-Induced Calcite Precipitation. Journal of Geotechnical and Geoenvironmental Engineering, Vol. 140, Issue 5, 2014, p.04014006.

[9] Behzadipour, H., Pakbaz, M. and Ghezelbash, G. Effects of biocementation on strength parameters of silty and clayey sands. Bioinspired, Biomimetic and Nanobiomaterials, 2019, pp.1-9.

[10] Zamani, A. and Montoya, B., Shearing and Hydraulic Behavior of MICP Treated Silty Sand. Geotechnical Frontiers GSP 281. ASCE, 2017, pp.290-299.

[11] Zamani, A. and Montoya, B., Undrained Monotonic Shear Response of MICP-Treated Silty Sands. Journal of Geotechnical and Geoenvironmental Engineering, Vol. 144, Issue 6, 2018, p.04018029.

[12] Zamani, A., Montoya, B. and Gabr, M., Investigating Challenges of in Situ Delivery of Microbial-Induced Calcium Carbonate Precipitation (MICP) In Fine-Grain Sands and Silty Sand. Canadian Geotechnical Journal, Vol. 56, Issue 12, 2019, pp.1889-1900.

[13] Meena, N. and Nimbalkar, S., Effect of Water Drawdown and Dynamic Loads on Piled Raft: Two-Dimensional Finite Element Approach. Infrastructures, Vol. 4, Issue 4, 2019, p.75.

11th Int. Conf. on Geotechnique, Construction Materials & Environment,
Kyoto, Japan, 3-5 November 2021, ISBN: 978-4-909106063 C3051

AN EXPERIMENTAL STUDY ON THE CREEP OF CONCRETE MADE WITH RECYCLED COARSE AGGREAGES: CASE STUDY IN HANOI

Thanh Quang Nguyen[1,2], Hoang Giang Nguyen[1,*], Ngoc Tan Nguyen[1], Viet Cuong Tran[1], Ha Tan Nghiem[1]
[1] Faculty of Building and Industrial Construction, Hanoi University of Civil Engineering, Vietnam;
[2] Vietnam Paper Corporation, Hanoi, Vietnam

ABSTRACT

The properties of recycled coarse aggregates (RCA) from construction and demolition waste (CDW) depend highly on its source. Normally, the quality of RCA is lower than that of the natural aggregate, as it has lower particle density, lower resistance to fragmentation, and higher water absorption. The quality and proportion used of RCA can compromise the performance of recycled concrete. The deformation of recycled concrete is higher and more varied in comparison with ordinary concrete. This paper aims to determine creep and shrinkage evolution in time of recycled concretes that were made with RCA from CDW collected in an old-age reinforced concrete building in Hanoi, Vietnam. The substitution percentages of coarse natural aggregate by RCA were 0%, 50%, and 100%. The other compositions were remained constant in the mixture for all cases. The obtained results during 180 days of the measurements show that the creep coefficient of RC is about 1.32 - 1.45 times higher than that of NA, depending on the ratio of using RCA to replace NCA.

Keywords: Construction and demolition waste, Recycled coarse aggregate, Creep, Compressive strength, Modulus of elasticity.

INTRODUCTION

Demolition of old constructions is carried out during renovation and/or implementation of new construction projects and is especially common in large cities where urbanization is high. Every year, 850 million tons of construction and demolition (CDW) are generated in Europe, accounting for about 31% of the total waste generated. In the United States alone, the waste generated from the demolition of buildings is about 123 million tons per year [1]. Typically, CDW is transported to landfills, causing significant environmental impacts and health hazards. Furthermore, land shortages and increasing landfill costs are exacerbating environmental problems. Sustainable development is currently an important issue worldwide and now becomes a guiding principle in the construction sector [2]. The recycling and reuse of CDW is an inevitable trend and a feasible and potential technical solution to use waste as a renewable resource, thereby minimizing pressure on mining natural resources. Currently, the recycling of CDW contributes to the development of the construction engineering industry and plays an important role in regenerating the environment, as a new way to protect natural resources and reduce the amount of material discharged into landfills [3, 4].

In the world, many studies have been carried out to determine the mechanical properties of concrete made with recycled aggregates from CDW. Research by Tam et al. (2015) synthesized research results obtained from more than 26 studies that have been performed previously, it is showed that natural coarse aggregate (NCA) can be replaced by recycled coarse aggregate (RCA) which is often used with different rates of 30%, 50%, 70% and up to 100% [5]. The compressive strength of recycled concrete (RC) at 28 days of age is reduced by less than 35% when compared with natural aggregate concrete (NC). However, the strain of recycled concrete is usually higher and more variable than that of natural aggregate concrete. Similarly, the studies of Silva et al. (2014) [6, 7] also showed that the mechanical strength of RC depends on the quality and the content of the recycled aggregates used. Hansen (1986) [8] showed that the creep of concrete produced RCA is greater than concrete produced from NCA from 30% to 60%. This statement is also consistent with the results obtained from other studies that have been carried out [9-12]. These results are not surprising as recycled aggregate concrete has up to 50% more grout volume. The creep of concrete is directly proportional to the mortar content in the concrete [13]. However, Gomez-Soberon (2002) [14] indicates that with the test load corresponding to 40% of the compressive strength of concrete, the creep strain of RC is larger than NC from 35% to 51%, since the recycled aggregate particles contain old mortar, it is considered as a factor affecting the difference in creep between RC and NC. In which, the elastic modulus and characteristics of the old mortar are determined to be the decisive criteria for this difference. In fact, creep leads to stress relaxation of elastic strain and subsequent reduction of tensile stress in the case of limited shrinkage.

The properties and composition of RC affect the short-term and long-term mechanical behavior of concrete. In particular, the dry creep of RC is

significantly affected when the rate of replacing NCA with RCA is greater than 30%. The research results obtained on concrete samples of B20 and B35 compressive strength using 30% and 60% RCA indicate that the creep of RC increases compared to NC from 1.6 to 2.4 times. Meanwhile, the shrinkage of the RC is equal to or less than that of NC [15]. Therefore, it can be concluded that, when increasing the rate of replacement of recycled aggregate, the creep of concrete increases and increases more for dry creep when compared to basic creep.

CDW RECYCLING AND MANAGEMENT IN VIETNAM

In Vietnam, specific objectives on the management, collection, and recycling of CDW have been specified in the National Strategy [16]. Until now, there is only standard TCVN 11969:2018 [17] on RCA for concrete. However, the incompleteness of the system of technical standards related to recycled materials, as well as the habit of using natural materials leads to the application of recycled aggregates is very limited. In recent times, several studies on the current status of management and composition of CDW have been carried out [18–21]. Meanwhile, research studies on recycled materials and structures using recycled materials have not been interested. A number of studies have been carried out showing that local recycled aggregates derived from the demolition of old structures are a factor affecting the quality of concrete and the development of compressive strength, elastic modulus properties [22]. Therefore, an experimental study to investigate different content of RCA is essential.

In this study, block concrete waste was collected from an old building demolished in Hanoi, Vietnam. It is crushed at the factory to obtain RCA with a particle diameter of 10 - 20 mm. RCA is used to replace NCA in the aggregate composition, with ratios of 0%, 50%, and 100% respectively. In the laboratory, an experimental program was carried out to determine the compressive strength, modulus of elasticity, and the long-term compressive behavior of concrete. The obtained results allow determining the influence of the ratio of using RCA to replace NCA on the development of compressive strength, elastic modulus, and creep strain of RC with time.

EXPERIMENTAL PROGRAM

Materials

The materials used are Portland cement PC40 with the technical properties to ensure the requirements for properties and quality according to the standard TCVN 2682:2009 [23], river sand of size passing through 5 mm with the technical parameters of meet the standard TCVN 7570:2006 [24], NCA having the size ranging from 10 to 20 mm.

CDW is collected at a demolition site in Hanoi, Vietnam, then transported to the crusher system located in Dong Anh district (Fig. 1). The crushing line system allows obtaining recycled aggregate with a particle diameter of 0 - 20 mm, of which the recycled fine aggregate has a diameter of 0 - 5 mm, and the RCA has a diameter of 5 - 20 mm as shown in Fig. 2. In this study, only RCA particles with the diameter ranging from 5 – 20 mm were used.

Fig. 1. Crushing CDW materials at site

Fig. 2. RCA collected from crushing machine

The physical properties of RCA material such as water absorption, volumetric mass, specific gravity and dry density are done on RCA as per Vietnamese standards. The test results are shown in Table 1.

Table 1. Physical properties of RCA

Water absorption (%)	Volumetric mass (g/cm^3)	Specific gravity (g/cm^3)	Dry density (g/cm^3)
3.53	2.43	2.62	2.38

Concrete mix

In the laboratory, an experimental program was

carried out on three concrete mixtures that were named CP0 (control concrete), CP50, and CP100 (recycled concretes) corresponding to the RCA substitution percentage of 0%, 50%, and 100% for NCA replacement, respectively. Control concrete CP0 is designed to achieve compressive strength class C30/37 at 28-day. The compositions of each concrete studied are presented in Table 2 consisting of Portland cement (C), river sand (S), natural coarse aggregates (NCA), recycled coarse aggregates (RCA), water (W), and Superplasticizer Silka viscocrete 30M-2000 (A).

Table 2. Mix proportions (unit: kg/m^3)

Mix	W	C	S	NCA	RCA	A
CP0	190	490	700	1050	0	4.9
CP50	190	490	700	525	481	4.9
CP100	190	490	700	0	943	4.9

RESULTS

To determine the mechanical properties of concrete specimens with and without recycled coarse aggregates, cylinders of 150 mm diameter and 300 mm length were cast, cured and tested at 3, 7, 28, 60, 90 and 120 days after casting.

Compressive strength

The compressive strength of concrete cylindrical specimens was determined by conducting compression test. The maximum load was measured, and the compressive strength (f_c in MPa) was calculated by formula (1), with P (kN) being the maximum load, F (mm^2) being cross-sectional area.

$$f_c = \frac{P}{F} \quad (1)$$

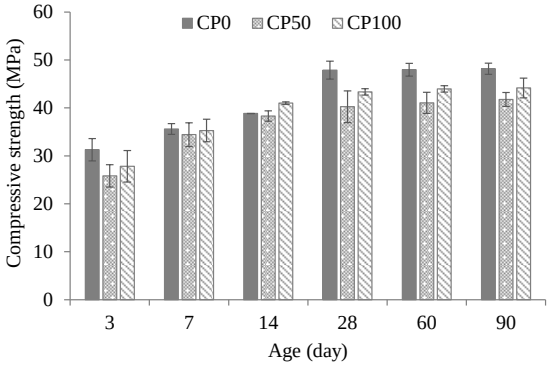

Fig. 3. Compressive strength of concretes with time

The results of the compression test are shown in Fig. 3 for three concretes CP0, CP50, and CP100. From 28 days of age, the compressive strength of control concrete CP0 has stabilized, not significantly increased, reaching the compressive strength R_{90} of 48.2 MPa. Meanwhile, two RC such as CP50 and CP100 have the compressive strength R_{28} values of 40.2 and 43.3 MPa, respectively, which decrease by 9.5 - 16.0% when compared to that of control concrete. Similar to the NA, the compressive strength of RC is stable and does not increase significantly after 28 days of age.

Modulus of elasticity

The test to determine the modulus of elasticity was performed on a 50-tonne hydraulic compressor combined with an electronic load-cell and a Data-logger TDS530, allowing continuous and automatic data recording during the experiment. The test piece is loaded to a compressive force equal to 30% of the specimen failure force. Elastic modulus tests were carried out according to the guidelines of RILEM CPC8 [25]. Each specimen is compressed for five cycles of loading and unloading at a constant speed. The modulus of elasticity at time t (day), denoted E_t (GPa), is determined by Eq. (2), with σ_t being the stress in the concrete, ε_τ being is the axial compressive strain.

$$E_t = \frac{\sigma_t}{\varepsilon_t} \quad (2)$$

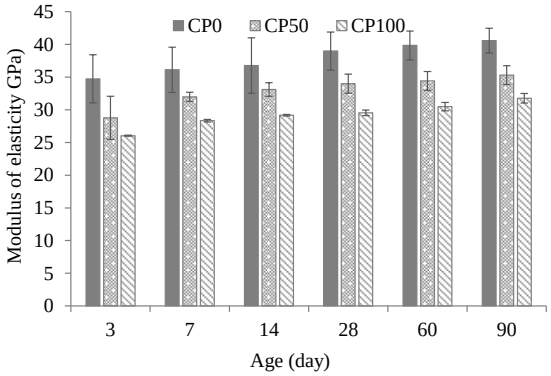

Fig. 4. Elastic modulus of concretes

The results in Fig. 4 show that, for each concrete used, the modulus of elasticity increases steadily with time. At 28 days, the elastic modulus of control concrete CP0 reached an average value E_{28} of 39.0 GPa. Meanwhile, the two recycled concretes CP50 and CP100 achieved the average E_{28} values of 34.0 and 29.5 GPa, respectively, which decrease by 12.8 - 24.2% compared to that of control concrete. After 28 days of age, the elastic modulus of all concretes tends to stabilize, increases by 4 - 8% at 90 days of age compared with the E_{28} value.

Creep of ordinary and recycled concretes

All test samples were stored and tested under identical indoor environmental conditions (temperature, humidity) of the laboratory. The load acting on the creep test specimens is taken as 30% of the compressive strength of each concrete at 28 days of age shown in Fig. 5.

Fig. 5. Set-up of concrete creep measurements

Fig. 6. Record of creep strain data in time

The creep rate is derived from Eq. (3) as follows:

$$\varepsilon = (1/E) + F(K)\log_e(t+1) \quad (3)$$

Where:

ε is the total load-induced strain per megapascal;
E is the instantaneous elastic modulus, in MPa;
$F(K)$ is the creep rate;
T is the time after loading, in day.

During the experiment, the temperature and humidity were regularly checked and recorded. The results show that the temperature varies from 18.7 to 27.6ºC with an average temperature of 24.8ºC. Meanwhile, the relative humidity is more variable, ranging from 42 to 81%, with an average value of 57.1%.

The dry creep deformation evolution of concretes used under compression has been calculated and shown in Fig. 7. For each concrete mixture, the measurements were carried out on a set of three cylinders with a diameter of 150 mm and a height of 300 mm, consisting of two loaded specimens and one unloaded specimen.

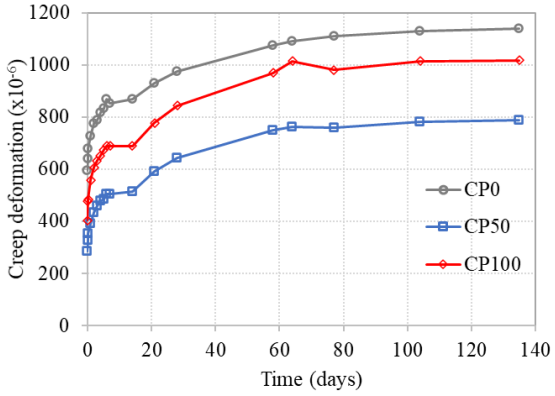

Fig. 7. Creep deformation of concretes used under long-term compression

The experimental results show that the creep strain of RC is smaller than NC. Even the creep strain of recycled concrete CP50 is only about 48 - 60% of the creep value of control concrete CP0. These results do not totally reflect the traditional argument when RC normally has a smaller elastic modulus than NC, so there will be a larger strain. The result can be explained by the presence of recycled coarse aggregates contain old mortar, which is considered as a factor affecting the difference in creep between RC and NC [14]. This result conforms to the instantaneous elastic modulus values shown in Table 4.

Table 4. Instantaneous elastic modulus

Mix	Compressive stress σ_c (MPa)	Instant strain ε (x10^{-6})	Instant elastic modulus E_i (GPa)
CP0	14,4	596	24,1
CP50	12,1	285	42,3
CP100	13,0	404	32,2

In this case, recycled concrete CP50 has the largest instantaneous elastic modulus, so it has the smallest compressive strain. In contrast, control concrete CP0 has the smallest instantaneous elastic modulus, so it has the largest compressive strain.

Characteristic creep and coefficient of creep

The characteristic creep and creep coefficient of concretes used have also been calculated and shown in Figs. 8 and 9. The results show that the creep coefficient of control concrete is usually smaller than those of recycled concretes. The creep coefficient of CP0 is determined as 1.91. The experimental values are completely consistent with the values specified in the Vietnamese design standard TCVN 5574:2018 [26]. Meanwhile, creep coefficients of recycled concretes CP50 and CP100 at 90 days of age were determined to be 2.77 and 2.52, respectively.

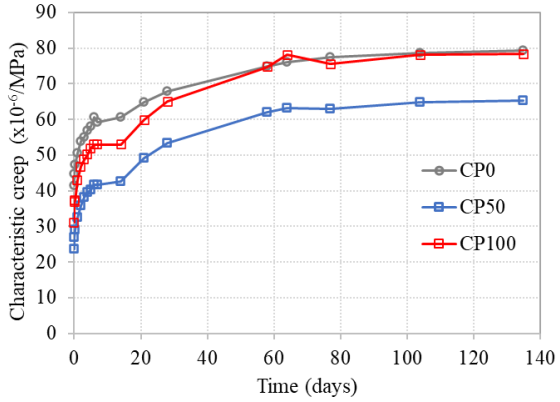

Fig. 8. Characteristic creep of concretes under long-term compression

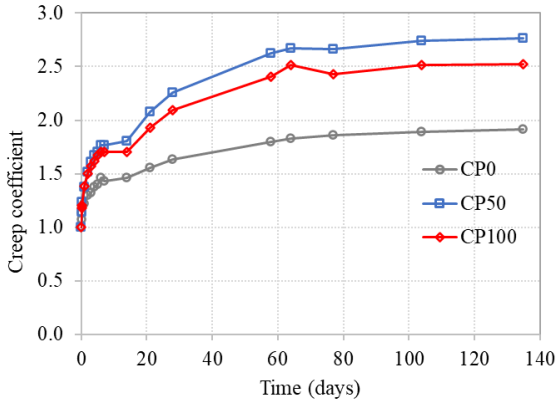

Fig. 9. Creep coefficients of concretes

CONCLUSIONS

Using RCA with good input quality, the strength development of RC is similar to that of NA. By the time, the compressive strength of RC reaches 80% to 100% of that of the NC. Moreover, the effect of RCA on compressive strength is less than that of elastic modulus.

The elastic modulus of RC decreases significantly, almost linearly with increasing RCA content in the concrete mix. Recycled concrete CP50 has a modulus of elasticity of 80-90% of the value of the NC. Meanwhile, for recycled concrete CP100, the modulus of elasticity is reduced to less than 80%.

The study determines creep deformation of concrete when subjected to compressive stress equal to 30% of the compressive strength over time. The obtained results show that the creep coefficient of RC is about 1.32 - 1.45 times higher than that of NA, depending on the ratio of using RCA to replace NCA.

The present results were obtained from a limited number of RCA concrete specimens. Thus, extending the experimental works in a vast program is necessary to comprehensively confirm the potential of concrete made with local CDW in Vietnam.

ACKNOWLEDGMENTS

This research was supported by the project of the Japan Science and Technology Agency (JST) - Japan International Cooperation Agency (JICA) on Science and Technology Research Partnership for Sustainable Development (SATREPS) (No. JPMJSA1701).

REFERENCES

[1] Malešev M., Radonjanin V., Marinković S., Recycled concrete as aggregate for structural concrete production, Sustainability 2, 2010,1204–1225.

[2] Limbachiya M.C., Koulouris A., Roberts J.J., Fried A.N., Performance of recycled aggregate concrete, in Proc. of RILEM International Symposium on Environment Conscious Materials and Systems for Sustainable Development, 2004, Koriyama, Japan, 127–136.

[3] Blengini G.A., Garbarino E., Resources and waste management in Turin (Italy): the role of recycled aggregates in the sustainable supply mix, J. Cleaner Prod., 18, 2010, 1021–1030.

[4] Rodrigues F., Carvalho M., Evangelista L.B., Physical-chemical and mineralogical characterization of fine aggregates from construction and demolition waste recycling plants, J. Cleaner Prod., 52, 2013, 438–445.

[5] Tam V. W. Y., Kotrayothar D., Xiao J., Long-term deformation behaviour of recycled aggregate concrete, Const. Build. Mat., 100, 2015, 262-272.

[6] Silva R.V., de Brito J., Ravindra Dhir, R.K., The influence of the use of recycled aggregates on the compressive strength of concrete: a review, Euro. J. Environ. Civil Engineer., 19 (7), 2014, 825-849.

[7] Silva R.V., de Brito J., Dhir R.K., Properties and composition of recycled aggregates from construction and demolition waste suitable for concrete production, Const. Build. Mat., 65, 2014, 201-217.

[8] Hansen T.C., Recycled aggregates and recycled aggregate concrete second state-of-the-art report developments 1945–1985, Materials and Structures, 19, 1986, 201–246.

[9] Gómez-Soberón J.M., Relationship between gas adsorption and the shrinkage and creep of recycled aggregate concrete, Cement, Concrete and Aggregates, 25, 2003, 42-48.

[10] Domingo-Cabo A., Lázaro C., López-Gayarre F., Serrano-López M.A., Serna P., Castaño-Tabares J.O., Creep and shrinkage of recycled aggregate concrete, Const. Build. Mat., 23 (7), 2009, 2545-2553.

[11] Fathifazl G., Ghani Razaqpur A., Burkan Isgor O., Abbas A., Fournier B., Foo S., Creep and drying shrinkage characteristics of concrete produced with coarse recycled concrete aggregate, Cement and Concrete Composite, 33 (10), 2011, 1026-1037.

[12] Marinkovic S., Radonjanin V., Life cycle assessment of concrete with recycled aggregate, In: Handbook of recycled concrete and demolition waste, Ed. Pacheco-Torgal F. et al., Woodhead Publishing, 2013.

[13] Lamond J.F., Campbell R.L. (Sr.), Campbell T.R., Cazares J.A., Giraldi A., Halczak W., Hale H.C. (Jr.), Jenkins N.J.T., Miller R., Seabrook P.T. (2001). Removal and Reuse of Hardened Concrete. ACI Committee 555.

[14] Gomez-Soberon J.M.V., Creep of concrete with substitution of normal aggregate by recycled concrete aggregate, ACI Material Journal, 209, 2002, 461-474.

[15] Waste and Resources Action Programme (WRAP). An investigation into the effects of recycled aggregates on the engineering properties of concrete, 104, 2007.

[16] Decision No. 491/QĐ-TTg, Approving adjustments to national strategy for general management of solid waste to 2025 with vision towards 2050, The prime minister of Vietnam, 2018. (in Vietnamese)

[17] Vietnamese standard TCVN 11969: 2018, Recycled coarse aggregate for concrete. (in Vietnamese)

[18] Hoang N.H., Ishigaki T., Kubota R., Tong T.K., Nguyen T.T., Nguyen H.G., Yamada M., Kawamoto K., Waste generation, composition, and handling in building-related construction and demolition in Hanoi, Vietnam, Waste Management, 117, 2020, 32-41.

[19] Nghiem H.T., Phan Q.M., Kawamoto K., Ngo K.T., Nguyen H.G., Nguyen T.D., Isobe Y., Kawasaki M., An investigation of the generation and management of construction and demolition waste in Vietnam, Detritus, 12, 2020, 135-139.

[20] Nguyen V.T., Tong T.K., Dang T.T.H., Tran T.V.N., Nguyen H.G., Nguyen T.D., Isobe Y., Ishigaki T., Kawamoto K., Current status of construction and demolition waste management in vietnam: challenges and opportunities, International Journal of GEOMATE, 15 (52), 2018, 23–29.

[21] Ngo K.T., Tran H.S., Le V.P., Nguyen X.H., Nguyen T.K., Vu V.H., Tran V.C., Study on current situation of construction and demolition waste management in Vietnam, Journal of Science and Technology in Civil Engineering 12(7): 107-116. (in Vietnamese).

[22] Tong T.K., Study on the use of construction waste in concrete manufacturing. PhD thesis, National University of Civil Engineering, 2017, Vietnam. (in Vietnamese).

[23] Vietnamese standard TCVN 2682: 2009, Portland cements - Specifications. (in Vietnamese).

[24] Vietnamese standard TCVN 7570: 2006, Aggregates for concrete and mortar - Specifications. (in Vietnamese).

[25] RILEM CPC8, Modulus of elasticity of concrete in compression, RILEM Recommendations for the testing and use of constructions materials, 1994, 25-27.

[26] Vietnamese standard TCVN 5574: 2018, Design of concrete and reinforced concrete structures. (in Vietnamese).

11th Int. Conf. on Geotechnique, Construction Materials & Environment,
Kyoto, Japan, 3-5 November 2021, ISBN: 978-4-909106063 C3051

INFLUENCE OF EACH MIXTURE PARAMETER ON FRESH PROPERTIES AND COMPRESSIVE STRENGTH OF GEOPOLYMER MORTAR

Takumi Osedo[1], Yoichi Mimura[2], Itaru Horiguchi[3]

[1]Advanced Course, Project Design Engineering, National Institute of Technology, Kure College, Japan;
[2, 3]Department of Civil Environmental Engineering, National Institute of Technology, Kure College, Japan;

ABSTRACT

Huge amount of Portland cement is manufactured as a binder of concrete. CO_2 emitted by manufacturing process of cement causes global warming, development of construction material with low CO_2 emissions is important issues for infrastructure engineers. Geopolymer (GP) is a relatively new generation construction material developed without using cement, and is hardened by the condensation polymerization of active filler based on industrial by-products and alkali solution instead of hydration of cement. Process of mixture design method of GP has not been established due to various mixture parameters, and its fresh properties are high viscosity and low workability. In this study, the effect of each mixture parameter on fresh properties and compressive strength of GP mortar was investigated. In this research, water glass and caustic soda solution were used as alkali solution, fly ash and blast furnace slag were used as active fillers, and high-performance AE water reducing agent and air entraining aid for fly ash were used as admixtures. The main mixture parameters of this study are alkali/water ratio (A/W), silicon/alkali ratio (Si/A), water/binder ratio (W/B), blast furnace slag substitution rate (BFS substitution rate) and admixture addition rate. Result of the mortar flow test indicates that the fluidity was increasing with higher W/B, and viscosity decrease with lower A/W and Si/A. However, GP mortar in this study was more viscous than cement mortar based on cement concrete with 8cm of slump. GP mortar had higher compressive strength by lowering W/B or increasing BFS substitution rate.

Keywords: Geopolymer, Fresh properties, Viscosity, Fluidity

INTRODUCTION

Global warming and reducing greenhouse gas emissions are worldwide issues. CO_2 is major greenhouse gas, and all industries should take action in reducing CO_2 emissions. Huge amount of Portland cement is manufactured as a binder of concrete. CO_2 emitted by the chemical decomposition of limestone and the consumption of energy in manufacturing process of cement. Geopolymer (GP), which contains no cement has been developed as an alternative construction material to cement concrete [1].

GP is a general term for a condensation polymer formed by reaction of alkali solution and active filler. By mixing active filler with alkali solution, metal ions of aluminum (Al) and silicon (Si) are eluted from active filler by alkali component. When the eluted metal ions come into contact with water glass in alkali solution, the metal ions cross-link the silicate ions (monomers) present in water glass to form a polymer. In this process, active filler particles are solidified with an inorganic adhesive, and sponge-like micropores characteristic of gels are generated. Generally, sodium silicate solution (Na_2SiO_3, water glass, WG) or sodium hydroxide (NaOH, caustic soda) is used as the alkali solution, and fly ash (FA) or blast furnace slag (BFS) is used as the active filler.

GP has various issues to be solved for wide usage as a construction material. The establishment of mixture design method is one of them [2]. This is because the effects of materials used in GP and each mixture parameter in the mixture design have not been clarified on fresh properties and mechanical properties of GP. In addition, viscosity of GP is higher than general concrete and its workability is inferior, so improvement of workability contributes more utilization of GP.

In this study, the effects of water/binder ratio (W/B) and BFS substitution rate and addition of admixture on fresh properties (fluidity and viscosity) and compressive strength of GP mortar were investigated after preliminary test on the effect of unit content of water glass for GP mortar.

MATERIALS AND METHOD OF TEST

Materials

Active fillers used in this study were FA (JIS II type), which is easy to obtain and widely distributed, and BFS (specific surface area: 4000 cm^2/g) in order to increase strength. Both materials are commercially available in Japan. Water glass and caustic soda solution (CS) were used as alkali solutions. For the

water glass, JIS No.1, which is generally used, was used in these tests. The caustic soda solution used in this study was prepared by adding caustic soda flakes to tap water. If the molarity of the caustic soda is low, large amount of caustic soda solution is required for GP and the water content of the alkali solutions can be exceed the unit content of water which is major mixture parameter. In the present study, the molarity of caustic soda solution was set to 15 mol/L. The water content of caustic soda solution and water glass may not reach unit content of water as a mixture parameter and the water content of GP was controlled by the additional water. Fine aggregate (S) was crushed sand with a density of 2.62 g/cm^3 and a fineness modulus of 2.71. A high-performance AE water-reducing agent (Ad1), which has main component of polycarboxylate-based dispersant, was used as admixture, and is generally adopted for cement concrete. Unburned carbon contained in FA prevents performance of Ad1, so an air entraining agent for FA concrete (Ad2) was also used for restraining the influence of the unburned carbon.

Method of Flow Test

A mortar mixer was used for mixing, and mixing volume for one batch was 1 L. First, FA, BFS, and S were mixed for 30 seconds, then an alkaline solution of water glass, caustic soda solution, and water was added, and the mixture was mixed for 1 minute. After mixing, the mortar flow test was immediately conducted.

The flow cone was placed on the center of the flow table, and 1/2 of the volume of the flow cone was filled with GP mortar. Then GP mortal was compacted 15 times with a tamping rod. This procedure was repeated for the second lift. After the flow cone was completely filled with mortar, top surface was leveled with cone top opening. After that, the flow cone was lifted vertically, and diameters of mortar were measured in 5 mm increments at the most spread and at right angle to it. The average of the measurement is the mortal flow in 0 bounce. Then, the flow table was bounced 15 times with one bounce per second, and diameters of mortal were measured again. The mortal flow in 15 bounce was evaluated from the average of diameters after bounces.

DETERMINATION OF A/W AND Si/A

Mixture

Mixture design of GP requires various mixture parameters, such as alkali/water ratio (A/W), silicon/alkali ratio (Si/A), unit water content (W), water/binder ratio (W/B) and BFS substitution rate. A/W (Na/H_2O) is a mole ratio of sodium to water in an alkaline solution. Si/A (Si/Na) represents a mole ratio of silicon to sodium in an alkaline solution. W is a unit content of water, and the mass of H_2O in the alkaline solution. W/B is the mass ratio of the unit water content to binder, the binder in the present study is an active filler included FA and BFS. BFS substitution rate (BFS sub rate) means a volume ratio of FA that is replaced by BFS.

Table 1 Mixture parameters and flow of GP mortar.

No.	A/W (mole ratio)	Si/A (mole ratio)	flow (mm)	
			0 bounce	15 bounces
M1	0.15	0.8	168	173
M2	0.1	0.4	170	213

Notes: W=240kg/m^3, W/B*=0.44, BFS sub rate=10%
* B=FA+BFS

Table 2 Mix proportion of GP mortar.

No.	kg/m^3					
	FA	BFS	WG	CS	water	S
M1	476	69	258	57	101	1244
M2	476	69	86	90	149	1328

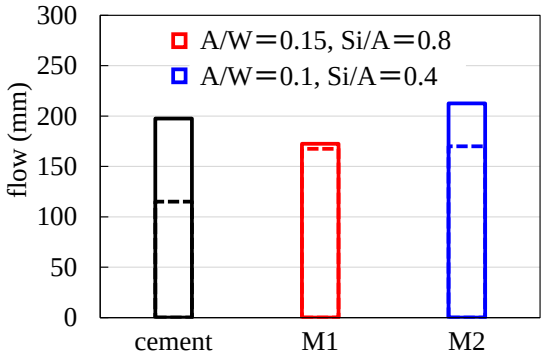

Fig. 1 Flow of GP mortal and cement mortal.

This paper investigates the effect of W/B and admixture on fresh properties and strength of GP mortal. First, control mix proportion of GP mortal was determined by the mortal flow test. Table 1 shows mixture parameters of GP mortal, and Table 2 shows mix proportion. A/W of M1 in this test was set to 0.15, because high A/W could cause fast setting and low workability of GP mortal due to its condensation property in high alkali region. Fresh properties of GP mortal with wide range of Si/A from 0.3 to 1.0 have reported by the technical committee report in JCI [2]. In this test, Si/A of M1 was set to 0.8. Increasing the unit water content induces to the improvement of fluidity of GP. However, water in GP has little contribution to the reaction of an alkali solution and an active filler, so increase in unit water content could cause the decrease in strength of GP. Therefore, the unit water content was set to 240 kg/m^3. W/B in this test was 0.44, referring to the previous

report [2]. BFS substitution rate was set to 10%, which is generally used in GP mortars.

GP mortal of M1 had high viscosity, this might be due to the viscosity of WG. A/W and Si/A of M2 were set to have lower unit content of WG than M1, each value was 0.1 and 0.4, respectively. The others of mixture parameters were the same as in M1: W=240 kg/m^3, W/B=0.44 and BFS substitution ratio =10%.

Result and Discussion

Result obtained from the mortar flow test is shown in Fig. 1. The mortar flow in 0 bounce and 15 bounces is demonstrated in as dotted and solid lines, respectively. For comparison with the GP mortar, the mortar flow test was also conducted with the cement mortar with 55% of water cement ratio. The concrete with this cement mortar has the targeted slump of 8 cm. While the 0 bounce flow of the cement mortar was 115 mm, the 0 bounce flow of M1 was 168 mm and the mortar of M1 had higher fluidity than the cement mortar. The 15 bounces flow of the cement mortar increased by 83 mm from the 0 bounce flow. Increase in mortar flow of M1 due to bounce of flow table was 5 mm, which was only 6% of cement mortar, and high viscosity of GP mortar of M1 could be visually observed. These results indicate little increase in mortar flow of M1 due to flow table bounce was caused by high viscosity in spite of high fluidity.

The 0 bounce flow of M2 with a smaller unit content of WG was 170 mm, which was almost equal to that of M1, and GP mortar of M2 had equivalent fluidity to M1. In addition, the 15 bounces flow increased from 173 mm of M1to 213 mm of M2 and the improvement of viscosity was confirmed by visual observation. Such results on mortar flow and visual observation indicate that reduction of WG by decreasing A/W and Si/A contributes to low viscosity of GP mortar. However, the flow increase of M2 due to flow table bounce was lower than that of the cement mortar, so GP mortar of M2 requires the improvement of viscosity.

In this study, the effect of W/B, BFS substitution rate and admixture on the flow and the compressive strength of GP mortar was investigated based on M2, which had lower viscosity than that of M1.

TEST ON W/B AND BFS SUBSTITUTION RATE AND ADMIXTURE

Mixture

Mixture proportions of GP mortar and amount of GP mortar adhered to flow cone in this study are shown in Table 3. The amount of GP mortar adhered to flow cone will be described in detail below. A/W, Si/A and W were determined as 0.1, 0.4 and 240 kg/m^3 based on preliminary flow test, respectively.

Table 3 Mixture proportion and adhesion amount of GP mortar.

No.	W/B (mass ratio)	BFS sub rate (vol%)	Ad1 (%)	Ad2 (%)	adhesion amount (g)
M1	0.33	10	0	0	0.8
M2			3	5	0.5
M3	0.35		0	0	0.7
M4			3	5	0.7
M5		20	0	0	14.7
M6			3	5	0.8
M7		30	0	0	1.1
M8			3	5	0.6
M9	0.37	10	0	0	1.6
M10			3	5	13.1
M11		20	0	0	115.0
M12			3	5	1.3
M13		30	0	0	9.0
M14			3	5	2.0
M15	0.44	10	0	0	5.5
M16			3	5	6.8
M17		20	0	0	19.0
M18			3	5	3.0
M19		30	0	0	64.7
M20			3	5	2.7

Nates: A/W＝0.1, Si/A＝0.4, W＝240kg/m^3

W/B was set to 0.33, 0.35, 0.37 and 0.44. In this study, A/W, which is related to the molarity of alkali solution, was set low, so GP with low molarity alkali solution could have lower strength than general concrete according to Uehara et al [3]. In order to increase strength of GP, the BFS substitution rate was increased from 10% to 20 or 30%. The rate of admixture was 3% or 5% by mass of active filler. These rates are the maximum of the manufacturer's standard usage. The mix proportion of M15 corresponds to that of preliminary flow test.

Method of Tests

In this study, mortar flow test with the same procedure of the preliminary experiment described above and compressive strength test were conducted. The flow cone, which inside is coated with fluorine resin, was used for mortar flow test in order to prevent excessive adhesion to flow cone inside due to high viscosity of GP mortar. In addition, the amount of GP mortar adhered to flow cone without inside coating was measured in order to investigate the viscosity of GP mortar. The adhesion amount of GP on flow cone was evaluated by the increase in its weight in mortar flow test.

In this study, three cylindrical specimens with 50 mm diameter and 100 mm height were used for each mixture in compressive strength test. GP mortar was

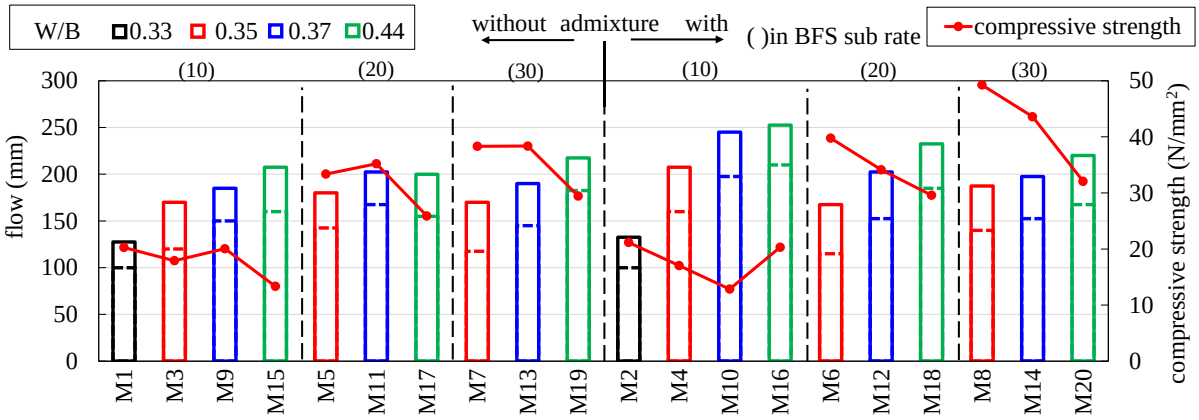

Fig. 2 Effect of W/B on mortar flow and compressive strength.

filled by two layers. Each layer was compacted five times by using a tamping rod with 9 mm of diameter, referring to JIS A 1132 on method of making concrete specimen. The compaction holes were closed by jigging. The top surface of specimen was leveled and sealed with plastic wrap to prevent from water evaporation. The specimen was cured in an electric furnace at 60 °C for 24 hours [4]. After that, curing temperature in an electric furnace was sustained at 20°C. The curing temperature was automatically controlled using a thermostat.

Compressive strength test in this study was conducted at the age of 2 days in accordance with JIS A 1149. Loading rate was set to 0.2 N/mm^2 per second. The compressive strength of the GP mortar was the average of results obtained from three specimens

Result and Discussion

Influence of fluorination on flow cone

The adhesion amount, which is evaluated by the mortar flow test using the flow cone without coating, is shown in Table 3. Most of GP mortar in this study had less adhesion amount obtained from flow test by using coated flow cone than that without coating. The GP mortar of M19 had the most difference due to coating, the adhesion amount with and without coating was 36.5 g and 64.7 g, respectively. This result indicates that the coating with fluorine resin is effective to restrain GP mortar adhesion to flow cone.

The effect of fluorine resin coating on mortar flow was also investigated by mortar flow test using the GP of M15. Although mortar flow at 0 bounce obtained from flow cone without coating was 170 mm, the mortar flow using coated flow cone was 160 mm. The coating inside with fluorine resin reduced the 0 bounce mortar flow by 10 mm. Decreasing GP mortar adhered to the flow cone due to coating was also visually observed. These results indicate that coating with a fluorine resin on flow cone is effective to

(a) M1 (W/B=0.33) (b) M3 (W/B=0.35)

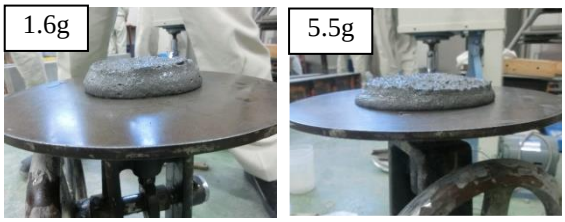

(c) M9 (W/B=0.37) (d) M15 (W/B=0.44)

Fig.3 GP mortar just after lifting the flow cone.

restrain GP mortar adhesion to flow cone and to evaluate fresh property of GP mortar with high viscosity.

Influence of W/B

The effect of W/B on mortar flow and compressive strength of GP mortar in this study is shown in Fig. 2. Mortar flow shown in Fig. 2 are results of mortar flow test using the fluorine-coated flow cone. As shown in Fig.2, GP mortar with higher W/B had more mortar flow at both bounces of 0 and 15 times except for M17. Figure. 3 shows GP mortar of M1, M3, M9, and M15 just after lifting flow cone. The adhesion amount of GP mortar on flow cone is also demonstrated in Fig. 3. As shown in Fig. 3, the GP mortar with higher W/B spread more just after lifting flow cone. This may be due to the decrease in the rate of powder (= FA + BFS) in GP mortar as W/B increases, and increase in W/B could cause higher fluidity. Increasing W/B by 0.02 from 0.33 to 0.37 was obviously more effective to fluidity of GP mortar than BFS substitution rate

and admixture, which will be described below. Although GP mortar with higher W/B had higher mortar flow, higher W/B caused the increase in the adhesion amount of GP mortar such as M1-M3-M9 at BFS substitution rate of 10% without admixture shown in Fig. 3, M7-M13-M19 at the BFS substitution rate of 30% without admixture, M6-M12-M18 at BFS substitution rate of 20% with admixture and M8-M14-M20 at BFS substitution rate of 30% with admixture.

Compressive strength was obviously dependent to W/B shown in Fig. 2 and increase in W/B caused decrease in compressive strength. This may be due to decrease in active filler, which is required for hardening of GP, to alkaline solution.

Influence of BFS substitution rate

The effect of BFS substitution rate on mortar flow and compressive strength of GP mortar is shown in Fig. 4 except for M1 and M2. The GP mortar without admixture had equivalent mortar flow, though BFS substitution rate was different. Before mortar flow test, it was expected that mortar flow would decrease as BFS substitution rate increased because BFS has a more non-uniform particle shape than FA spherical particles. However, mortar flow was similar, indicating that BFS substitution rate could cause little effect on mortar flow. Unburned carbon contained in FA absorbs admixture such as high-performance AE water-reducing agent and prevent performance of admixture. In GP mortar with the admixture, it was expected in advance that reduction in unit content of FA by substitution with BFS could lead to an increase in mortar flow. Contrary to expectations, the GP mortar with higher BFS substitution rate had lower mortar flow.

The effect of BFS substitution rate on the adhesion amount varied to W/B and admixture. The examples of results are shown below. In the GP without admixture, BFS substitution rate of 20% was the least effective to the reduction in the adhesion amount at W/B=0.35 (M3-M5-M7) and W/B=0.37 (M9-M11-M13), and the GP of W/B=0.44 (M15-M17-M19) had the most adhesion amount at BFS substitution rate of 30%. The GP mortar with admixture and 10% of BFS substitution rate had the most adhesion amount W/B=0.37 and 0.44. The adhesion amount was independent to BFS substitution rate at the GP mortar with W/B=0.35. These results indicate an appropriate BFS substitution rate for the adhesion amount differs in accordance with mixture parameters such as W/B and admixture.

Compressive strength of GP mortar obviously increased as BFS substitution rate increased. The compressive strength of the GP mortar with BFS substitution rate of 20% was from 46% to 164% greater than that of 10%, although the GP mortar with BFS substitution rate of 30% had 8-28% higher compressive strength than that with BFS substitution rate of 20%. In addition, compressive strength of the GP mortar with admixture had more strength development due to increase in BFS substitution rate, compared with the GP mortar without admixture.

Influence of admixture

The effect of admixture on mortar flow and the compressive strength is shown in Fig. 5. In some results of mortar flow test, mortar flow was increased by admixture. In particular, admixture was more effective to improvement of fluidity in the GP with BFS substitution rate of 10%. However, the maximum increase due to flow cone bounces was 53mm, and less than the result of 83 mm obtained with cement mortar shown in Fig. 1. GP in the present study had higher viscosity than cement mortar for concrete with the slump of 8cm.

The effect of admixture on the adhesion amount is shown in Fig. 6. The results in which the difference due to the admixture was less than 3g are not included in Fig. 6. Although the GP with W/B=0.37 and BFS substitution ratio of 20% had the adhesion amount of 115.0g, the adhesion amount was decreased to 1.3g

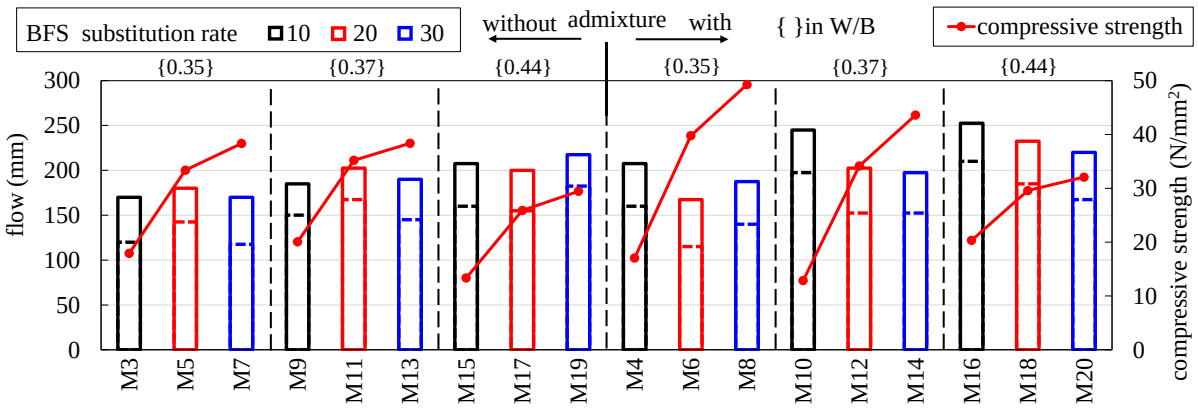

Fig. 4 Effect of BFS substitution rate on flow and compressive strength.

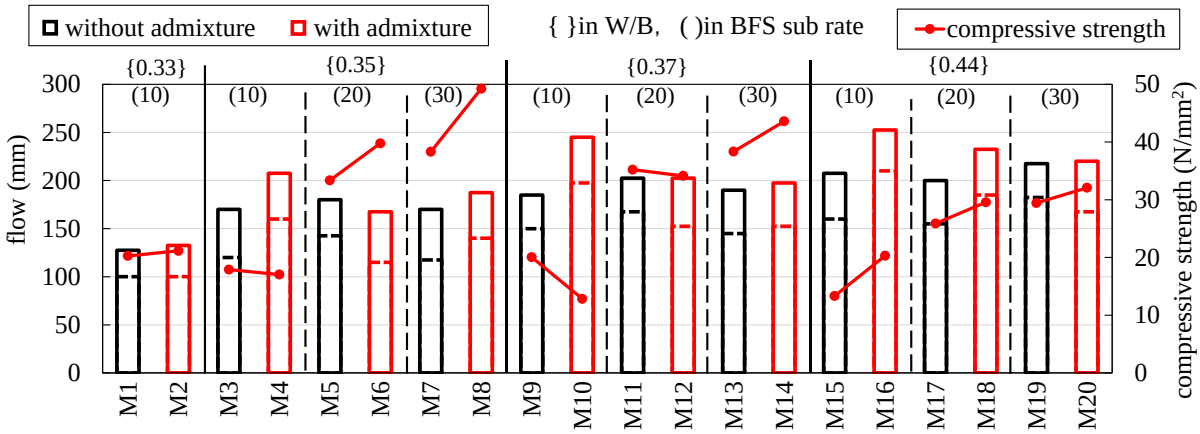

Fig. 5 Effect of admixture on flow and compressive strength.

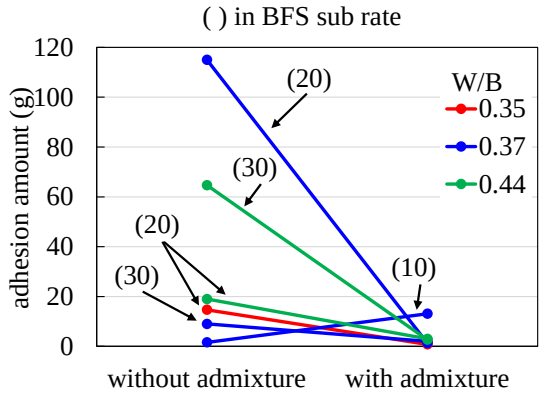

Fig. 6 Effect of admixture and adhesion amount.

by adding admixture. The GP with W/B=0.44 and BFS substitution ratio of 30% had also similar result. These GP (M11-M12 and M19-M20) had increase in mortar flow due to the bounce of flow table was improved by admixture. These results indicate that adding admixture to GP is effective restraining viscosity of GP mortar.

A high-performance AE water-reducing agent caused the increase in compressive strength in some GP as shown in Fig. 5. Although admixture was used for improvement of fluidity and viscosity in the present study, its effect was less than that of W/B and BFS substitution ratio.

CONCLUSIONS

GP, which has been developed as an alternative construction material with low CO_2 emissions, has various issues such as establishment of mixture design method. In this study, the effects of water/binder ratio (W/B) and BFS substitution rate and admixture on fresh and strength properties of GP mortar were investigated by the mortar flow test and the compressive strength test, after preliminary test on the effect of unit amount of water glass on GP mortar. Based on test results in this study, it can be concluded as follows:

(1) The GP mortar with higher W/B has more mortar flow. Some results indicate that fluidity of GP mortar can be increased by using high-performance AE water reducing agent for cement concrete.
(2) Although viscosity of GP mortar can be reduced by decreasing A/W and Si/A, viscosity of GP mortar in this study was higher than that of cement mortar.
(3) Compressive strength of GP mortar can be increased by lowering W/B or increasing BFS substitution rate. Some results indicate that compressive strength of GP mortar increased by using a high-performance AE water reducing agent.

REFERENCES

[1] Zhang Z., Provis J. L., Reid A. and Wang H., Geopolymer foam concrete: An emerging material for sustainable construction, Construction and Building Materials, Vol.56, 2014, pp.113-127
[2] JCI-TC155A, Technical Committee report on Application of Geopolymer Technology to Construction Field, Japan Concrete Institute, 2017 (in Japanese)
[3] Uehara M., Minami K., Hirata H. and Yamasaki A., Effect of mix proportions and production methods on hardened geopolymer, Proceedings of the Japan Concrete Institute, Vol.37, No.1, 2015, pp.1987-1992 (in Japanese)
[4] Zhang P., Zheng P., Wang K. and Zhang J., A review on properties of fresh and hardened geopolymer mortar, Composites Part B, Vol.152, 2018, pp.79-95

11th Int. Conf. on Geotechnique, Construction Materials & Environment,
Kyoto, Japan, 3-5 November 2021, ISBN: 978-4-909106063 C3051

TENSILE CREEP BEHAVIOR CONSIDERING STIFFNESS DEVELOPMENT OF HIGH STRENGTH CONCRETE AT EARLY AGE

Takuya Hara[1], Yoichi Mimura[2] and Itaru Horiguchi[3]

[1]Advanced Course, Project Design Engineering, National Institute of Technology, Kure College, Japan;
[2,3]Department of Civil Environmental Engineering, National Institute of Technology, Kure College, Japan;

ABSTRACT

High strength concrete has more unit cement content and higher temperature rise than ordinary concrete, therefore thermal crack is caused by the volume change by hydration of cement. The thermal crack affects long-term durability of concrete structures, so thermal stress is predicted by numerical analysis such as FEM. Numerical analysis (FEM) requires various thermal and mechanical properties of concrete. Accurate prediction of thermal stress including the relaxation due to the tensile creep at early age contributes effective control of thermal stress/crack. However, little researchers focus on the tensile creep behavior considering development of concrete strength and stiffness at early age. In this study, tensile creep tests by using high strength concrete with water cement ratio of 45% were carried out with 2 sets of loading stress. The tensile creep tests in the present study started loading at the age of 3 days and the loading was sustained for 14 days. The loading stresses were 30% or 40% of the splitting tensile strength at loading start. The test results of high strength concrete loaded 30% of strength indicate that each specific creep was in the range of ±25% of the average and the averaged specific creep was equivalent to that of concrete with ordinary strength (water cement ratio of 55%). On the other hands, most specific creeps with stress/strength ratio of 40% was equivalent to or greater than that of 30%, although some results with stress/strength ratio of 40%were smaller than that of 30%.

Keywords: High strength concrete, Thermal crack, Tensile creep, Water-cement ratio, Stress-strength ratio

INTRODUCTION

High strength concrete has been widely used for construction of structures with long span and large cross-section. Volume change due to hydration heat causes initial cracks in high strength mass concrete, which has more unit cement content. Such thermal crack occurs in a few weeks after casting and induces to degrade long term durability, so preventing the cracks or controlling the crack width is important issues for concrete engineers.

The finite element method (FEM) is generally conducted to analyze thermal stress in order to prevent thermal cracking due to temperature changes and temperature distribution. Accurate estimation of the thermal stresses contributes to appropriate selection of materials, mixture proportions and construction methods and to ensure the long term durability of concrete structures. Accurate FEM requires various input data which include mechanical properties such as strength, Young's modulus and creep. Effect of these properties development at early age should be considered for thermal stress analysis. This study focuses on the tensile creep behavior at early age in order to accurately predict tensile stress. The prediction of tensile stress without the relaxation due to the tensile creep might be overestimated than actual thermal stress, so the tensile creep behavior at early age is an essential factor to evaluate the stress relaxation in thermal stress prediction.

Basic creep of mature concrete based on experiments can be evaluate assuming a constant elastic strain during creep test with a constant load. However, the elastic strain in creep test at early age decreases due to stiffness development, so creep behavior evaluated by a constant elastic strain is differ to actual one. Little researchers have been reported on tensile creep behavior at early age considering developments of some mechanical properties such as concrete stiffness. In particular, there is even less research on tensile creep of high strength concrete with the low water cement ratio (W/C), although the low W/C increase the potential for cracking due to higher temperature rise at early age.

In this study, the tensile creep experiments at early age were carried out on high strength concrete with W/C = 45%, which has higher unit cement content and higher temperature rise than ordinary concrete with general strength. In the tensile creep test of the present study, the both ends of the dog-bone shaped specimen were connected to the loading apparatus with a pin in order to restrain of bending stress as possible. The tensile creep behaviors of concrete with different strength at early age are evaluated based on the experimental data obtained from the present study and the previous studies on the ordinary concrete with W/C = 55%. The tensile creep behaviors were investigated with the creep tests with different loading stress of 30% and 40% of the splitting tensile

strength at loading start.

MATERIALS AND TEST PROGRAM

Materials and Mixture Proportions

Table 1 shows the materials used for concrete and mix proportion in this study. The mix IDs of N and H represent the ordinary concrete mix with W/C =55% and the high strength concrete mix with W/C = 45%, respectively as shown in table 1. The targeted slump and targeted air content of high strength concrete is 8±2.5 cm, 4.5±1.5%, and they are the same level as that of ordinary concrete. An AE water reducing agent, which has the principal components of lignin sulfonate and oxycarboxylate was added at 1% of the cement mass for normal concrete and at 2% of the cement mass for high-strength concrete in order to ensure the targeted slump and air content.

Specimen

The dog-bone shaped specimen and loading apparatus used in the tensile creep test of this study are shown in Fig. 1. A jig is attached to the enlarged section of the dog-bone shaped specimen and connected to the loading apparatus. Both ends are connected with pins to minimize the bending stress due to eccentricity of the load. A small mold strain gauge having a temperature measurement function and a length of 50 mm was embedded in the center of the cross section of the dog-bone shaped specimen. In order to evaluate developments of the strength and the stiffness during the loading period of tensile creep tests, splitting tensile strength tests (conform to Japan Industrial Standards A 1113) and compression tests were conducted using a cylindrical specimen with 100 mm diameter and 200 mm height. For the strain measurement in compression tests, a strain gauge with length of 60 mm was attached at the center of both side faces of each specimen.

The temperature at mixing in this study was the outside air temperature. After casting, the specimens were carried into a curing room to be cured at a room

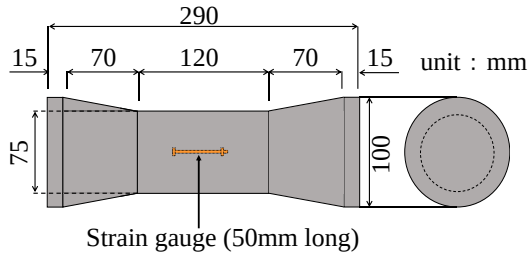

Fig. 1 Dog-bone shaped specimen

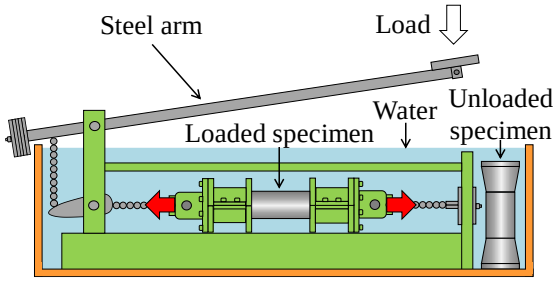

Fig. 2 Loading apparatus

temperature of 20 ± 1 degree Celsius for 24 hours before demolding. After that, the specimens were cured underwater in tank (16 ± 1 degree Celsius) installed in the curing room until loading.

Method of Tensile Creep Test

Figure 2 shows the loading apparatus used in the tensile creep test in this study. Tensile creep was loaded underwater, as shown in Fig .2. The loading apparatus was installed in the water tank in the curing room with the temperature remained at 20 ± 1 degree Celsius and the temperature in the water tank remained at 16 ± 1 degree Celsius. In this test, loading was carried out in water to eliminate the effect of drying shrinkage. Therefore, tensile creep in this study is targeted for basic creep without moisture transfer.

In this study, tensile creep experiments were conducted using two loading apparatus. Two dog-

Table 1 Materials and mix proportion

Property	Materials	Proportion		Density
		Ordinary concrete	High strength concrete	
Mix ID		N	H	
Water cement ratio		55%	45%	
Water (W)	Tap Water	165 kg/m^3	165 kg/m^3	1.00 g/cm^3
Cement (C)	Ordinal Portland Cement	300 kg/m^3	367 kg/m^3	3.16 g/cm^3
Fine aggregate (S)	Crushed rock sand	844 kg/m^3	812 kg/m^3	2.62 g/cm^3
Coarse aggregate (G1)	Crushed rock (20-15 mm)	499 kg/m^3	486 kg/m^3	2.67 g/cm^3
Coarse aggregate (G2)	Crushed rock (15-5 mm)	499 kg/m^3	486 kg/m^3	2.67 g/cm^3
Admixture (Ad)	AE water reducing agent	3.00 kg/m^3	7.34 kg/m^3	1.07 g/cm^3

bone shaped specimens were prepared for each loading apparatus. Loading specimen was subjected to constant and continuous loading, while the unloading specimen was installed in the same environment as the loaded specimen.

In this study, the tensile loading was started at the age of 3 days, because thermal stress changes from compression to tension around these ages. The loading period of 14 days was determined from the occurrence of the initial cracks in approximately two weeks after casting. According to Davis-Granville's principle, creep strain is roughly proportional to loading stress in the range of one-third of concrete strength. Therefore, the loading stress in this study was set to 30% (H30) and 40% (H40) of the splitting tensile strength at the loading-start age (3days). Tensile creep experiments were conducted once for H30 and twice for H40 (H40-a, H40-b). Table 2 shows the measured fresh properties of the tested concrete. As shown in Table 2, the tested concrete had equivalent fresh properties in the range of the targeted slump and air content. The strain and temperature of the loaded and unloaded specimens were automatically measured at one hour interval by a data logger during the tensile creep test, and the water temperature in each water tank was also measured as well as the strain and the temperature.

In this study, the stiffness of the concrete develops during the loading period of the tensile creep experiment due to active hydration at early age. Therefore, the elastic strain decreases with the development of stiffness though the load is sustained at a constant. The creep strain behavior at early age cannot be accurately evaluated unless such decreasing elastic strain is appropriately obtained. In order to measure the elastic strain during the tensile creep experiment, the strain was measured by temporary unloading every 24 hours.

In this study, tensile creep experiments were conducted in water, so the loading stress could not be measured by a load cell. The weight mass was calculated from the following equations related the weight mass placed on the steel arm tip and the tensile stress to the dog-bone shaped specimen, as shown in Equation (1) and Equation (2). Each equation is for each loading apparatus.

$$y = 12714x - 3280.7 \quad (1)$$

$$y = 17962x - 4357.0 \quad (2)$$

Where x is tensile stress loading to dog-bone shaped specimen (N/mm^2), y is weight of mass (g).

Mimura [1] have reported that the compressive Young's modulus calculated using the stress up to the tensile strength and the corresponding strain was equivalent to the tensile Young's modulus, even in the stress-strain relationship obtained by compression experiments. In this study, the compression test was conducted by the same method in the previous study [1] in order to obtain the compressive strength and

Table 2 Measured fresh properties

	H30	H40-a	H40-b
Slump (8±2.5 cm)	5.5 cm	5.5 cm	6.0 cm
Air content (4.5±1.5%)	3.5%	3.6%	3.3%

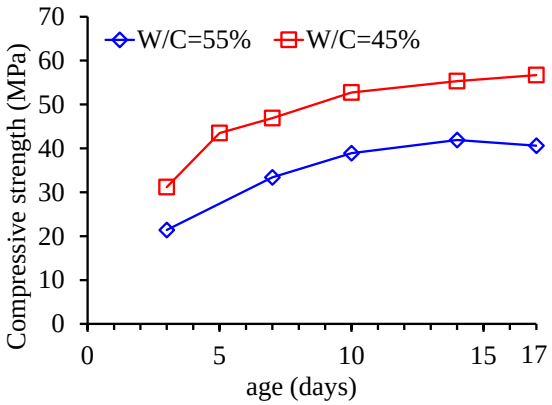

Fig. 3 Compressive strength during creep test

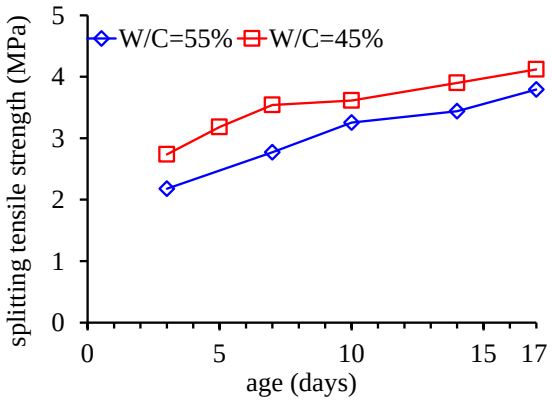

Fig. 4 Splitting tensile strength during creep test

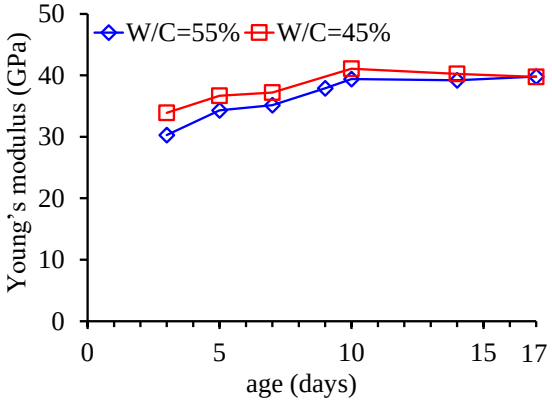

Fig. 5 Young's modulus during creep test

Young's modulus during the tensile creep test. The stress and the strain were measured ten times at the same stress interval until the loading stress reaches the splitting tensile strength at the tested age. The loading was temporally removed just after the measurement of the stress and the strain and the residual strains was also measured in order to consider the effect of inelastic strain in the stiffness evaluation. The Young's modulus was obtained by linear regression of the relationship between strain and stress obtained from the compression test. The splitting tensile strength test and the compression test were conducted at the age of 3, 5, 7, 10, 14, and 17 days. The compressive strength, splitting tensile strength and Young's modulus obtained from these tests are shown in Fig. 3, Fig. 4 and Fig. 5, respectively. In these figures, the results in the previous study [2] on the ordinary concrete with W/C=55% are also shown. As shown in Fig. 3, the compressive strength of the concrete with W/C=45% was greater than that of the ordinary concrete of W/C=55%, and the concrete had a high compressive strength more than 50 MPa at the age of 10 days. The splitting tensile strength was also greater than that of ordinary concrete, and had less difference between both the concretes than the compressive strength. The Young's modulus of the high strength concrete was less than 5% different from that of the ordinary concrete at the age of 5 days, and the difference gradually decreased. The Young's moduli of the high strength concrete and the ordinary concrete were almost equal at the age of 17 days. Table 3 shows the splitting tensile strength and loading stress at the age of 3 days when the tensile creep test was started. The loading tensile stresses in this study were set to 30% or 40% of the splitting tensile strength at age of 3 days, and were sustained for 14 days. As shown in Fig. 4, the splitting tensile strength develops during the tensile creep test in the present study, so the stress-strength ratio gradually decreases though the loading stress is a constant.

Table 3 Loading stress in tensile creep experiment

Mix ID	Age (days)	Splitting tensile strength (MPa)	Loading stress (MPa)
H30	3	2.57	0.770
H40-a		2.94	1.176
H40-b		2.70	1.081

RESULTS AND DISCUSSION

Tensile Creep Experiment results

The measured strains obtained from the tensile creep tests are shown in Fig. 6. The loaded strain and the unloaded strain shown in Fig. 6 are measured from the loaded specimen and the unloaded specimen, respectively. In H40-a, the measured strain from 12 days were obviously inappropriate due to the failure of the data logger, so such inappropriate strains in H40-a were removed for evaluation of tensile creep behavior. The measurement values of H40-b were also temporarily unavailable due to out of recording paper on the 3 days after the start of loading.

The loaded strain gradually increased with the sustained loading, and the unloaded strain also increased as shown in Fig. 6. The tensile creep test was conducted underwater, so the strain increase in the unloaded specimen might be caused by the expansion strain due to water absorption.

The elastic strains during the tensile creep test are shown in Fig. 7. The elastic strain in the present study was evaluated as the average of the difference between the strain at temporary unloading and the loaded strains before and after the unloading. The data between the loaded strain and unloaded strain are the strains at temporary unloading every 24 hours. As shown in Fig. 7, the elastic strains behaviors in H30 were almost equivalent, and the elastic strains of H40 had greater difference than that of H30. In all specimen, the decrease was significant up to 2 days after the start of loading, and the average decrease in elastic strain during the tensile creep test was 23% for H30, 27% for H40-a and 23% for H40-b. The

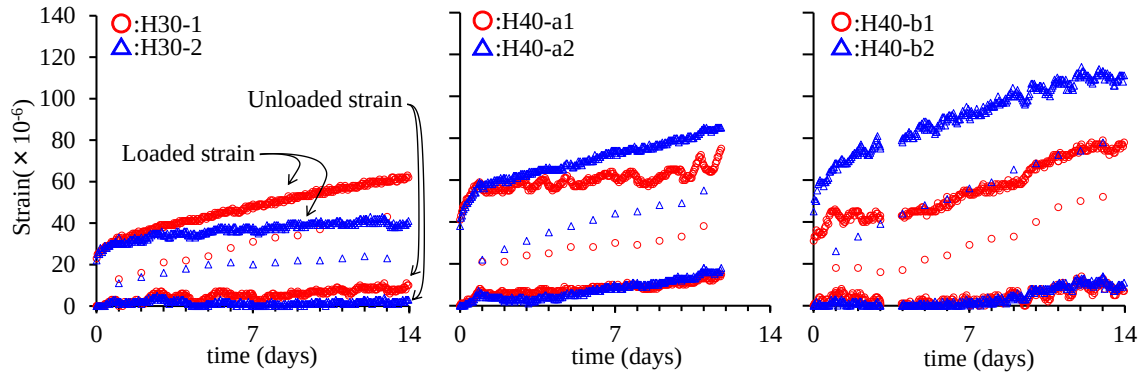

Fig. 6 Behaviors of loaded strain and unloaded strain.

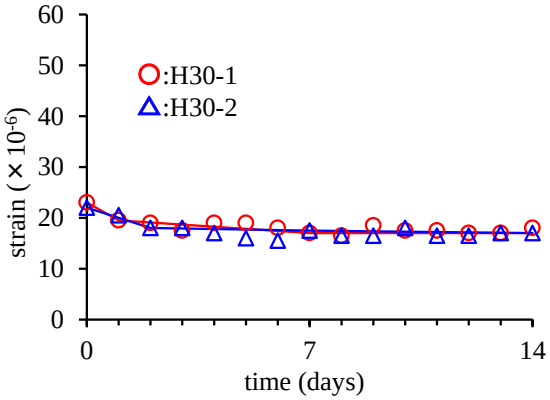

(a) H30

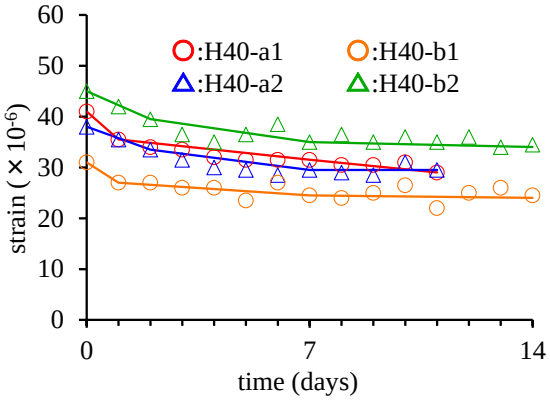

(b) H40

Fig. 7 Elastic strain behavior during tensile creep test.

decrease in elastic strain was approximately independent to the stress/strength ratio.

In this study, the measurement interval of the elastic strain was 24-hours, while the strains were measured every hour. The elastic strains every hour were required for hourly creep evaluation, and were estimated from the partially linear regression of the measured elastic strain.

Specific Creep Comparison

In this study, the creep strain was evaluated by subtracting the unloaded strain and the regressed elastic strain shown in Fig. 7 from the loaded strain. The specific creep of H30 obtained in this study is shown in Fig. 8. The specific creep is the creep strain per unit stress, which is calculated by dividing the creep strain by the loading stress. Specific creep is generally used for comparison of creep behaviors obtained from the experiments with different loading stresses, and is also required for the thermal stress estimation considering relaxation effect because thermal stress has time dependent. The specific creep behaviors of H30 shown in Fig. 8 were similar from loading to around 4 days. The specific creep of H30-1 had also increased since then and the specific creep

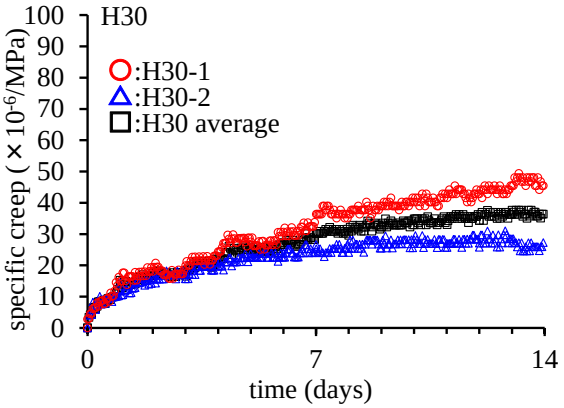

Fig. 8 Specific creep behavior of H30.

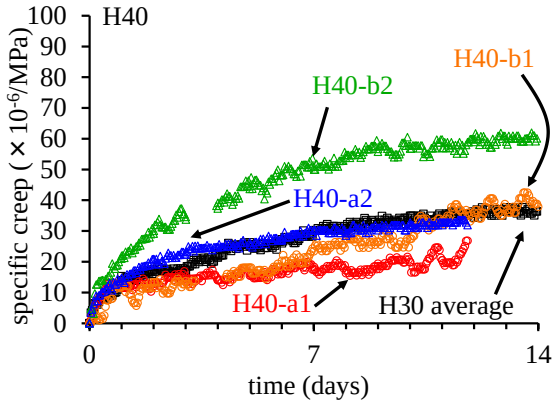

Fig. 9 Specific creep behavior of H40.

at 4 days was 51% of that at the end of loading, while the specific creep of H30-2 tended to converge. The averaged specific creep of H30-1 and H30-2 is demonstrated in Fig. 8, and each specific creep was in the range of ±25% of the average.

The specific creep behavior of H40 is shown in Fig. 9. The averaged specific creep of H30 is also shown in Fig. 9. The specific creep behavior of H40-a2 was similar to that of H30. The specific creep of H40-b1 was almost equivalent to that of H30 at the end of loading, though the behavior of H40-b1 differed to the result of H30 from loading to around 10 days. The specific creep of H40-a1 was obviously smaller than that of H30 through the loading period. The result of H40-b2 was obviously greater than that of the others and the specific creep at the end of loading was around 1.7 times greater than H30. The value of H40-a1 was obviously small, and the value of H40-b2 was large from the beginning of loading, and the specific creep at the end of loading was about 1.7 times larger than H30. Such specific creep of H40 had various behaviors. This may be due to over the linear range between loading stress and creep strain. Loading stress more than around 1/3 of concrete strength induces microcrack development, so nonlinear relationship between loading and creep

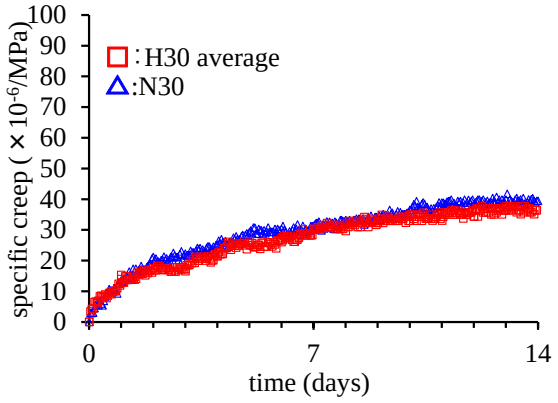

Fig. 10 Specific creep behavior of N30 and H30.

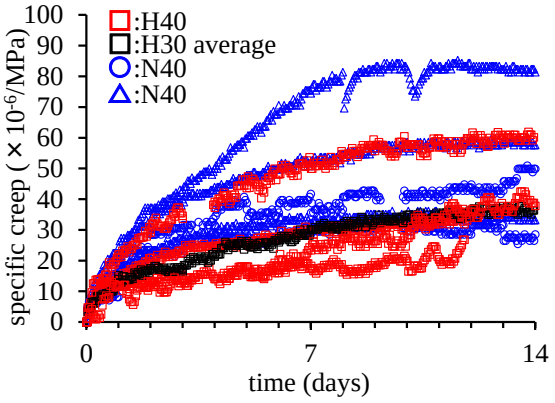

Fig. 11 Specific creep behavior of N40 and H40.

strain is caused by microcrack development. The microcrack development due to the loading stress with 40% of the splitting tensile strength could cause the different creep behavior, because the microcrack development is sensitive to a bit difference in the microstructure in concrete.

Figure. 10 shows the averaged specific creep behavior of H30 and N30 reported in the previous study [2]. Although the high strength concrete had the different strength development from the ordinary concrete as shown in Fig. 3 and Fig. 4, the averaged specific creep behavior of the high strength concrete with W/C=45% was almost equal to that of the ordinary concrete with W/C=55%. This result indicates that the specific creep behavior, which is caused by the loading stress with the stress/strength ratio of less than 30%, is independent to 10% difference of W/C and the specific creep of concrete with W/C from 45% to 55% can be represented by the same equation.

Figure. 11 shows the specific creep of N40 and H40 which were obtained from the tensile creep test with the stress/strength ratio of 40%. As mentioned above, the specific creep of H40 varied from specimens. As shown in Fig. 11, the specific creep behavior of each specimen with the ordinary concrete with W/C=55% also had significant difference. The averaged specific creep of H30 is shown in Fig. 11. Some results of H40 and N40 were smaller than H30, and most results of H40 and N40 were equivalent to or greater than that of H30. In particular, the specific creep of one of N40 [2] was more than twice of H30. These results indicate that the loading stress more than 1/3 of the concrete strength causes the nonlinear relationship between loading stress and creep strain due to microcrack development. Such microcrack development is so sensitive to microstructure of concrete in spite of concrete strength that the specific creep obtained from creep test can include large errors. Therefore, accurate evaluation of tensile creep behavior requires more experimental results.

CONCLUSIONS

This paper presents an investigation of the tensile creep behavior of high strength concrete with a consideration of the stiffness development at early age of concrete. The tensile creep tests using dog-bone shaped specimens were conducted to obtain tensile creep. Based on the test results in this study, it can be concluded as follows:

(1) Tensile creep which is caused by the loading stress with stress/strength ratio of 30% is similar in the range of W/C from 45% to 55%, although the strength development characteristics at early age are different, and the difference in water-cement ratio has little effect.
(2) Although the specific creep with a stress-strength ratio of 40% could be equal to or higher than that of 30%, the specific creep of high strength concrete loaded with a stress-strength ratio of 40% differed greatly among specimens. Such result was also obtained from ordinary concrete with W/C=55%. The difference among specimens in the tensile creep test loaded with a stress/strength ratio of 40% could be caused by microcrack development which is sensitive to a bit difference in microstructure in concrete.

REFERENCES

[1] Mimura Y., Yoshitake I. and Horituchi I., Experimental study on Young's modulus for crack analysis at early age, Proceedings of the Japan Concrete Institute, Vol.36, No.1, 2014, pp.400-405 (in Japanese)
[2] Mimura Y., Vimonsatit V., Horituchi I. and Yoshitake I., Tensile mechanical properties of fly ash concrete at early age for thermal stress analysis, Journal of Infrastructure Preservation and Resilience, Springer, Vol.1, No.14, 2020.11.

11th Int. Conf. on Geotechnique, Construction Materials & Environment,
Kyoto, Japan, 3-5 November 2021, ISBN: 978-4-909106063 C3051

EFFECTS OF POLYETHYLENE TEREPHTHALATE (PET) PLASTICS ON THE MECHANICAL PROPERTIES OF FLY ASH CONCRETE

Mary Ann Adajar[1] and Irene Olivia Ubay-Anongphouth[1]

[1]Civil Engineering, De La Salle University, Philippines

ABSTRACT

Concrete is a favored construction material for its high compressive strength and low maintenance cost. With the global interest on sustainable construction materials, continuous research is being done on alternative concrete materials. Research is geared towards the improvement of concrete properties as well as to contribute to waste utilization. A study was conducted by incorporating polyethylene terephthalate plastics (PET) into fly ash concrete to investigate the effects on compressive and flexural strengths. As the addition of fly ash as partial replacement of concrete is known to improve concrete strength, the addition of PET as partial substitute for fine aggregates could be advantageous. A constant of 30% fly ash was used in the concrete mix proportions for test specimens, while the amount of PET introduced varied from 5% to 15%. Specimens were prepared and tested in accordance with ASTM standards. It was observed that increasing the amount of PET in fly ash concrete mix also increased workability and decreased the unit weight of concrete. Compressive strength test results show that 5% to 10% PET plastic substitution increased the compressive strength of fly ash concrete. Test specimens containing 5% PET led to the increase of the flexural strength of fly ash concrete and further increase of PET content indicated a decrease in flexural strength. The results of this study show that the inclusion of PET in fly ash concrete could lead to increased workability, decrease in unit weight, and improved compressive and flexural strength without the use of admixtures.

Keywords: Concrete, Fly ash, Polyethylene terephthalate, Compressive strength, Flexural strength

INTRODUCTION

Concrete is one of the most common building material used worldwide. It is a favored construction material owing to its high compressive strength and low maintenance cost. Numerous research on alternative substitutable materials for cement as well as for both fine and coarse aggregates is continuously conducted in order to further improve concrete properties and contribute to waste utilization with the use of alternative concrete materials. Fly ash [1]- [3], palm oil fuel ash [4], and coconut shell ash [5] are some examples of viable substitute for cement. Recycled solid wates like wastes from aggregate quarries has been found as a possible replacement for conventional fine aggregates [6].

It was anticipated that there would be new coal power plants that will be constructed in the Philippines over the next five years to account for the electrical consumption needs of the country. The large demand for power would then increase the amount of fly ash produced annually. The abundance of fly ash motivated several researchers to investigate its effects on concrete properties. Studies have affirmed that the addition of fly ash can be beneficial to the mechanical properties of concrete. The incorporation of until 40% fly ash, as partial substitute to cement, can increase the compressive and flexural strength of concrete as well as improve its stress-strain behavior [1], [2].

Polyethylene terephthalate (PET) plastic is one of the most heavily produced waste materials. However, only a small percentage of these waste are recycled leaving the rest dumped in landfills, oceans, and the environment. Studies by Nikbin [7] and Jo et al. [8] indicated that PET plastics could be used as partial substitute for fine aggregates in concrete, which resulted in lightweight concrete due to the reduction in unit weight. Borg [9] stated that PET plastics could cause insignificant changes in the strength of concrete if used in small percentages. Borg [9] suggested that partial substitution of PET plastics up to 8% without contributing significant detrimental effects on the compressive strength of concrete.

A study on the combined effects of polyethylene terephthalate plastics (PET) and Class F fly ash (FA) as partial substitutes for fine aggregates and cement, respectively, on concrete strength was conducted. As initially stated, these waste materials continuously increase over time in landfills and bodies of water. With this study, not only will it provide additional information for the field of civil engineering, but also contribute to the reduction and utilization of the waste materials.

EXPERIMENTAL PROGRAM

To evaluate the combined effects of the substitution of PET plastics and Class F fly ash on its strength properties of concrete, alternative concrete

mix proportions were generated in accordance with ACI 211.1 [10]. The amount of fly ash used as a partial substitute to cement was constant at 30 percent. The amount of PET plastics used to substitute fine aggregates varied from zero to 15 percent. The mix design used for test specimens are shown in Table 1.

Table 1 Mix design used for tested samples

Component	0F-0P	30F-0P	30F-5P	30F-10P	30F-15P
Water, kg	184.0	184.0	184.0	184.0	184.0
Cement, kg	384.9	269.5	269.5	269.5	269.5
Sand, kg	722.7	672.8	639.1	605.5	571.8
Gravel, kg	930.0	930.0	930.0	930.0	930.0
Fly ash, kg	0	82.5	82.5	82.5	82.5
PET, kg	0	0	19.3	38.7	58.0

Note: F = Fly ash, P = PET

The compressive strength of concrete was investigated using cylindrical specimens of 150 mm in diameter and 300 mm in height and subjected to compression tests with a loading rate of 0.34 MPa/s in accordance with ASTM C39 [11]. The 7th, 14th, 21st, and 28th day compressive strengths were documented to compare the strength development between the different mix designs and to determine the effect of fly ash and PET plastics on the compressive strength of concrete. Beam specimens with dimensions of 150 mm x 250 mm x 500 mm were tested under the third-point loading condition following the procedure in ASTM C78 [11] to determine flexural strength. Strain gauges were attached unto beam specimens to observe the stress-strain behavior of the samples. The flexural strength of the samples was determined at the 28th day of curing to represent the theoretical maximum flexural strength of concrete. A total of 100 cylindrical specimens and 15 beam specimens were investigated.

Scanning Electron Microscopy (SEM) test was used to visually observe the chemical bonding of the materials used in the concrete mix. Samples for the aforementioned test were randomly taken from the pieces used from the strength tests performed.

EXPERIMENTAL RESULTS

Physical Properties

The physical properties observed in the study were the workability and unit weight of fly ash concrete as these properties have been noted to be affected by the incorporation of PET plastics. The results are summarized in Table 2.

The incorporation of fly ash slightly affected workability as seen in Table 2. Meanwhile, the addition of PET plastics could significantly increase the slump of concrete. PET plastics affected the slump of concrete due to its glassy and smooth texture. This caused less intergranular friction between the fresh concrete therefore causing the measured slump to increase.

Table 2 Workability and unit weight of concrete samples

Concrete Mix	Slump, mm	Unit Weight, kN/m^3
0F-0P	81.25	22.38
30F-0P	82.50	22.14
30F-5P	90.25	22.01
30F-10P	95.25	21.85
30F-15P	103.50	21.67

Another notable observation was that the unit weight was affected by the incorporation of PET plastics in the fly ash concrete mix. As shown in Table 2, the unit weight decreased insignificantly when fly ash was incorporated into the mix. However, a sudden change in unit weight was noted when PET plastics were introduced. The largest decrease in unit weight was 5.14% with 15% PET plastic substitution. Results indicated that the unit weights were less than the typical normal concrete unit weight of 22 to 24 kN/m^3 but were still greater than 18 kN/m^3, which is the typical value for lightweight concrete. The decrease in unit weight was due to PET plastics being lighter than sand. The specific gravity of PET plastics was determined to be 1.33 which was almost half of that of conventional sand used in concrete.

Compressive Strength

Table 3 presents the 28th day compressive strength of the different mix designs tested. The control samples (0F-0P) surpassed the target strength of 28 MPa. As exhibited in Table 3, the addition of fly ash reduced the compressive strength of concrete while the incorporation of PET plastics increased the compressive strength of concrete.

Table 3 Average 28th day compressive strength of tested samples

Concrete Mix	Compressive Strength, MPa
0F-0P	29.12
30F-0P	24.13
30F-5P	26.05
30F-10P	26.73
30F-15P	24.73

Fly ash concrete samples (30F-0P) manifested a decrease of 17.14% in strength with respect to the control samples. This was contradictory to previous studies stating that the incorporation of fly ash would

increase the strength of concrete [7]. The reduction of strength could be attributed to the cement used in the study having substances such as fly ash already incorporated, which caused the fly ash composition of the cement to have gone over the optimum of 30%. Thus, also reducing the strength of concrete. PET plastics were observed to increase the strength of concrete with respect to the samples with 0% PET plastics and 30% fly ash.

Fly ash concrete samples with 5% PET plastics manifested an increase of 7.96% and samples with 10% PET plastics displayed an increase of 10.77%, both with respect to the 0% PET plastics and 30% fly ash samples. Meanwhile, samples with 15% PET plastics exhibited a decrease of compressive strength. The decrease in compressive strength at 15% denotes that an increase in PET plastics would not contribute to a direct increase in strength. Rather, the trend suggests that PET plastics would be beneficial for compressive strength of concrete only to a certain amount. With the trend manifesting in the study, the optimum PET percentage suggested to be between 5% and 15% PET plastic partial substitution for sand.

Regression analysis on the compressive strength results returned a polynomial function with an R^2 of 0.976 as shown in Eq. 1,

$$y = -0.0392x^2 + 0.6376x + 24.058 \quad (1)$$

where: y is the compressive strength in MPa and x is the amount of PET plastics in percent. From Eq. 1, the amount of PET plastics that would generate optimum compressive strength of concrete with 30% fly ash was determined to be approximately 8.13%. Pearson correlation between theoretical and experimental compressive strength values per substitution of PET plastics up to 15% generated a linear relationship with an R^2 of 0.853 and R of 0.923. This indicated that the generated Eq. 1 was adequate to be used as a tool to estimate expected compressive strength up to 15% PET plastic substitution in concrete with 30% fly ash.

Figure 1 shows the strength development curve of the tested samples, which illustrated that PET plastics and fly ash do not significantly affect strength development as they simply manifest the same strength development trend as traditional concrete. The effect of PET plastics and fly ash on the compressive strength of concrete was seen to be significant through Analysis of Variance (ANOVA). The analysis was performed with an alpha (α) value of 0.05. The F value of 9.04954 was greater than the critical F value of 2.8661. This indicated that the two materials (PET and FA) significantly affect the compressive strength of concrete. A P value (0.0002) less than the alpha value further strengthened the claim that the addition of PET plastics and Class F fly ash has significant effect on the compressive strength of concrete compared to the typical concrete mix.

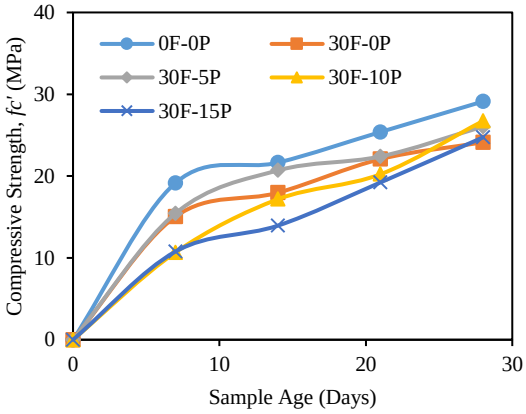

Fig. 1 Compressive strength development.

Flexural Strength

Table 4 shows the flexural strength of the samples tested in the study. As observed, the incorporation of fly ash reduced the strength of concrete likely because of the presence of fly ash in the cement powder causing a reduction in strength. On the other hand, the incorporation of PET plastics caused the concrete samples to have increased flexural strength. This result agrees with the observations made by Borg [9] in wherein PET plastics were observed to sustain larger peak loads than control samples.

Table 4 Average 28th-day flexural strength of tested samples

Concrete Mix	Flexural Strength, MPa
0F-0P	2.40
30F-0P	2.08
30F-5P	2.98
30F-10P	2.52
30F-15P	2.47

A trend similar to the results obtained from the compressive strength test was observed in which the flexural strength of the concrete beams increased for a partial substitution of 5% PET plastics. However, a drop was observed in flexural strength when partial substitution of PET reached 10%. Regression analysis on the determined flexural strength was also conducted. The analysis returned a third-degree polynomial equation with an R^2 of 0.887 as shown in Eq. 2,

$$y = 0.0024x^3 - 0.0626x^2 + 0.4342x + 2.0777 \quad (2)$$

where: y is the flexural strength in MPa and x is the amount of PET plastics in percent. From Eq. 2, it was determined that 4.78% PET plastics would produce

optimum flexural strength in concrete with 30% fly ash. Pearson correlation analysis between the theoretical and experimental flexural strength of samples with PET plastics until 15% gave a linear relationship with an R^2 of 0.891 and R of 0.944. Similar to compressive strength results, the Pearson correlation analysis has shown that Eq. 2 was acceptable as a tool to estimate expected flexural strength of concrete with 30 fly ash for PET plastic substitution of up to 15%.

Figure 2 illustrates the stress-strain graphs of the tested samples in the study. The incorporation of fly ash was observed to improve concrete stiffness, as the sample was able to sustain greater loads with less strain [12]. This was further supported by the modulus of elasticity values shown in Table 5 as samples with 0% PET and 30% fly ash having the greatest stiffness at approximately 30 GPa, as opposed to the control specimens with approximately 24 GPa. The result was in agreement with the result of the study of Uysal and Akyuncu [12] which claimed that fly ash may be used to improve the flexural performance of concrete due to its ability to increase the modulus of elasticity of concrete. In addition, fly ash concrete samples with PET plastics behaved like conventional concrete. However, the addition of PET plastics in fly ash concrete resulted to decreased stiffness. This can be attributed to the reduced frictional resistance between particles, as PET plastics are smooth and glassy in texture.

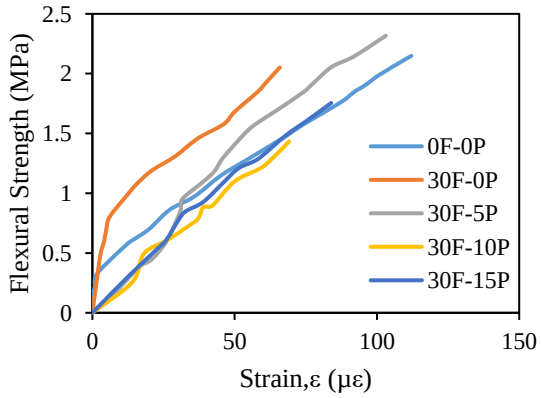

Fig. 2 Stress-strain curve of tested samples.

Table 5 Modulus of Elasticity of tested samples

Concrete Mix	Modulus of Elasticity, GPa
0F-0P	23.70
30F-0P	29.63
30F-5P	23.70
30F-10P	28.15
30F-15P	27.65

Results may show that PET plastics could be detrimental to the flexural behavior of concrete from the observed less desirable stress-strain behavior in the beams with PET plastics, in comparison to the samples with 0% PET and 30% fly ash. However, the detrimental effects were observed to be counteracted by the addition of fly ash. This compensation allowed samples with PET plastics to simply manifest similar deflection characteristics as the control samples. This indicated that the combination of PET plastics and fly ash can improve the flexural strength and without negatively affecting the flexural behavior of concrete.

Similar to the effect of PET plastics on the compressive strength of fly ash concrete, the effect on flexural strength of concrete was also proven to be significant using ANOVA. The F value of 19.908 was seen to be much greater than the critical F value, 3.478, which verifies that the two materials did significantly affect the flexural strength of concrete. A P value less (9.407×10^{-5}) than the alpha value of 0.05 further strengthens the claim that the addition of PET plastics and Class F fly ash has an effect on the flexural strength of concrete compared to typical concrete.

Concrete Microstructure

The micro-fabric structure of the concrete samples was observed with the use of the Scanning Electron Microscope (SEM). The microstructure of the concrete in the SEM photographs were merely composed of sharp, angular, and flakey surfaces with smooth or rough textures. Smooth textured surfaces were identified as PET plastics, while grainy surfaces were recognized as concrete [13].

Figures 3, 4, and 5 shows the microscopic view of fly ash concrete samples with 0%, 5%, and 15% PET plastics, respectively. Figure 3 shows the honeycomb-like pattern of plain concrete as well as the spherical particles, which indicate the presence of fly ash in the mix. The SEM image shown in Fig. 4 exhibits that the incorporation of PET plastics reduced the intergranular voids of concrete in comparison to fly ash concrete (Fig. 3). The reduction in intergranular voids manifests better bonding which then results into better strength. However, when the PET plastic substitution reached 15% (Fig. 5), the intergranular voids began to increase in size indicating weak bonding. Figure 5 also shows that some of the parts of the PET plastic are no longer bonded to fly ash concrete. This weaker bonding could be the reason for of the reduction of compressive and flexural strength in fly ash concrete with 10 to 15 percent PET plastics as was mentioned in the previous sections. It is possible that the increase in PET plastics (within the range of 10 to 15 percent) resulted in the reduction of calcium silicate hydrate (C-S-H) gel in the surrounding PET plastics within the concrete mix, thus leading to weaker bonding and reduced compressive and flexural strength.

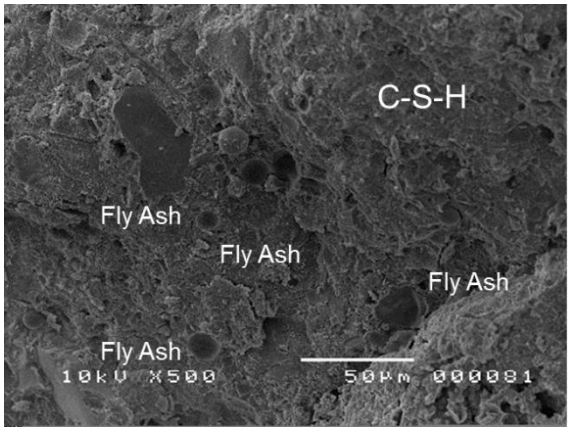

Fig. 3 SEM image of 30F-0P test sample.

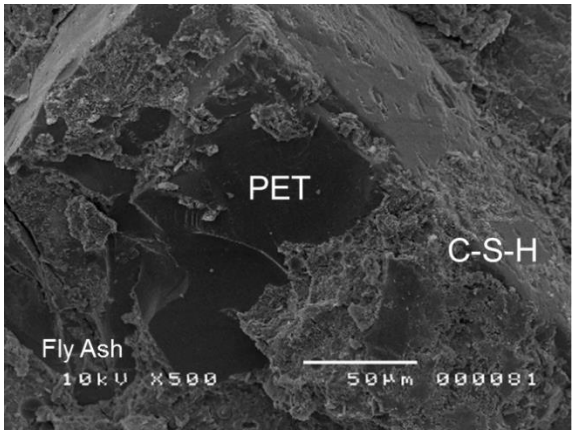

Fig. 4 SEM image of 30F-5P test sample.

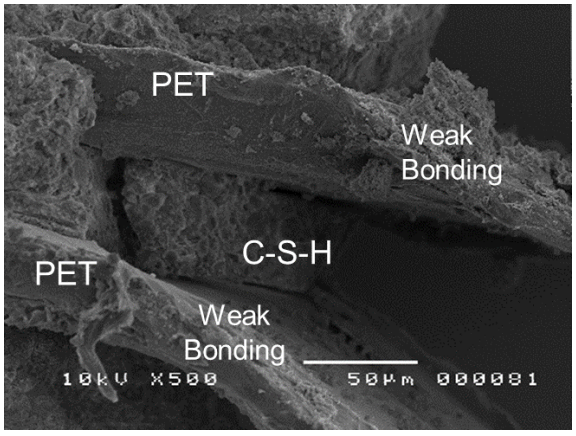

Fig. 5 SEM image of 30F-15P test sample.

CONCLUSIONS

The utilization of fly ash as partial cement substitute and PET plastics as partial fine aggregate substitute yielded noticeable effects on the performance of concrete and the following conclusions were made:

An evident increase in workability up to 27% was observed as PET plastic percentage increased. The incorporation of PET plastics into fly ash concrete also resulted to a 3.14% decrease in unit weight. Thus, PET plastics and fly ash produced concrete with higher workability with reduced unit weight.

Considering that the substitution of fly ash is constant within the other samples, it was observed that 5 and 10 percent of PET plastic substitution resulted to an increase in compressive strength of 8% and 11% from the control samples. Thus 5-10% of substitution of PET plastic promotes beneficial increase to the compressive strength of concrete. The flexural strength of concrete was observed to increase with a 5% PET plastic substitution as compared to a 0% PET plastic substitution. It was evaluated to manifest a 43% increase in flexural strength. Thus, addition of PET plastic will result to a noticeable increase to the flexural strength of the concrete.

Generated equations for predicting the compressive strength and the flexural strength of concrete with varying PET plastic percentage up to 15% was also verified to be valid and adequate with the use of external data obtained specifically for verification. Results indicate that a suggested amount of approximately 8.13% and 4.78% PET plastic substitution for fine aggregates in concrete with 30% fly ash would produce optimum compressive and flexural concrete strength, respectively.

The incorporation of both recyclable materials was observed to have no effect to the stress-strain behavior of concrete as well as the strength development of the concrete samples. With this, concrete with PET plastics and fly ash can be treated similarly to conventional concrete when used on site in terms of strength development and in observing deformation behavior due to applied loads. Therefore, PET plastics and fly ash may be used as materials to increase both the compressive strength and flexural strength of concrete without affecting its stress-strain behavior.

PET plastics is a viable substitute for fine aggregates up to 10% substitution with 30% fly ash as cement replacement in concrete mix without compromising the strength and quality of concrete products. However, it is recommended for further study the long term behavior of hardened concrete especially when it is expose to elevated temperature. It is also recommended to investigate the compressive and flexural strengths of concrete with fly ash at lower percentage and PET plastics higher than 10%.

ACKNOWLEDGMENTS

The experimentation of this research paper was made possible by the participation of De La Salle University – Civil Engineering students, Rafael Crisostomo, Steven Cruz, Cris Fernandez, and Benedict Imperial as part of their undergraduate thesis under the supervision of the authors.

REFERENCES

[1] Chandru, C., and A, D. C., Experimental Study on Effect of Addition of Flyash on the Properties of Plastic Fibers Reinforced Concrete. IJERT International Journal of Engineering Research and, Vol. 4, Issue 5, 2015.

[2] Thomas, M., Optimizing fly ash content for sustainability, durability, and constructability. Coventry University and The University of Wisconsin Milwaukee Center for By-Products Utilization, Second International Conference on Sustainable Construction Materials and Technologies, 2010, pp 1-11.

[3] Arifi E, Zacoeb A, and Shigeishi M, "Effect of fly ash on the strength of concrete made from recycled aggregate by pulsed power", Int. J. of GEOMATE, Vol. 7, No. 1 (Sl. No. 13), Japan, Sept. 2014, pp. 1009-1016.

[4] Awal A.S.M., Ibrahim M.H.W., Ali A.Z.M.A., and Hossain, M.Z., Mechanical Properties and Thermal Properties of Two-Stage Concrete Containing Palm Oil Fuel Ash, Int. Journal of GEOMATE, Vol. 12, Issue 32, 2017, pp. 166-175.

[5] Adajar, M., Galupino, J., Frianeza, C., Aguilon, J., Sy, J., and Tan, P., Compressive Strength and Durability of Concrete with Coconut Shell Ash as Cement Replacement, Int. Journal of GEOMATE, Vol. 18, Issue 70, 2020, pp. 183 - 190.

[6] Adajar, M., De Guzman, E., Ho, R., Palma Jr., C., and Sindico, D., Utilization of Aggregate Quarry Waste in Construction Industry, Int. Journal of GEOMATE, Vol. 12, Issue 31, March 2017, pp. 16-22.

[7] Nikbin, I. M., Feasibility study of waste Poly Ethylene Terephthalate (PET) particles as aggregate replacement for acid erosion of sustainable structural normal and lightweight concrete. Journal of Cleaner Production, Vol. 126, 2016, pp. 108 - 117.

[8] Jo, B., Park, S., and Park, J., Mechanical properties of polymer concrete made with recycled PET and recycled concrete aggregates. Construction Building Materials, Vol. 22, 2008, pp. 2281-2291.

[9] Borg, R., Early age performance and mechanical characteristics of recycled PET fibre reinforced concrete. Construction of Building Materials, Vol. 108, 2016, pp. 29 - 47.

[10] American Concrete Institute, ACI manual of concrete practice. Farmington Hills, MI: American Concrete Institute, 2013.

[11] American Society for Testing and Materials Annual, Annual Book of ASTM Standards. Philadelphia, PA, USA, 2010.

[12] Uysal, M., and Akyuncu, V., Durability performance of concrete incorporating class F and class C fly ashes. Construction and Building Materials, Vol. 34, 2012, pp. 170-178.

[13] Martin, L.H., Winnefeld, F., Tschopp, E., Müller, C. J., and Lothenbach, B., Influence of fly ash on the hydration of calcium sulfoaluminate cement. Cement and Concrete Research, Vol. 95, 2017.

11th Int. Conf. on Geotechnique, Construction Materials & Environment, Kyoto, Japan, 3-5 November 2021, ISBN: 978-4-909106063 C3051

GRINDING PROCESS INFLUENCES TO THE PHYSICAL AND MORPHOLOGICAL CHARACTERISTICS OF ULTRAFINE TREATED RICE HUSK ASH (UFTRHA) AS REACTIVE MINERAL ADDITIVE CONSTRUCTION MATERIAL

Siti Asmahani Saad[1], Aida Nabila Jamaluddin[1], Siti Aliyyah Masjuki[1], Salmia Beddu[3] and Nasir Shafq[2]

[1]Faculty of Engineering, International Islamic University Malaysia, Malaysia; [2]Faculty of Engineering, University of Technology PETRONAS, Malaysia; [3]College of Engineering, Universiti Tenaga Nasional, Malaysia

ABSTRACT

It is known that rice husk ash (RHA) contains high amount of silica that is beneficial in concrete strength development. Despite of numerous studies on conventional RHA were done since 1970's, usage of conventional RHA is still unfavourable in current concrete industry. This paper aims to extend the investigation of producing highly reactive additive material in ultrafine size, with particle diameter of less than 5μm through mechanical activation using planetary ball mill. In light of the mechanical activation process, most of studies were done to test materials such as metakaolin and fly ash. However, study on the mechanical activation effect via planetary ball mill to conventional RHA or treated RHA are limited. In this research, raw rice husk (RH) was treated using heated low concentration of acid, i.e. 0.01 - 0.1M hydrochloric acid (HCl). Then, the treated RH was combusted at 600 - 800ºC. The treated RHA was ground using planetary ball mill for 15 - 60 minutes. In terms of material average particle size, it was also observed that, burning temperature of 600ºC, treated at four hours, ground at 300rpm for 15 minutes had finest size of ultrafine treated RHA (UFTRHA) with value of 4.012μm. Largest specific surface area value was obtained at 222.9125 m^2/g with the similar treatment condition. In terms of the UFTRHA morphology, particle agglomeration was observed for samples with grinding duration more than 15 minutes. Therefore, grinding parameters involved in the process are proven to affect the physical and morphological attributes of UFTRHA produced.

Keywords: Ultrafine Treated Rice Husk Ash (UFTRHA), Mechanical Activation Process, Morphology of UFTRHA, Particle Size Distribution, Specific Surface.

INTRODUCTION

According to International Energy Agency (2015), steel and cement industry are responsible for 8% and 15% of total global energy consumption and total global anthropogenic carbon dioxide expose in 2012. As a consequence, the emissions hike from these sectors occurred rapidly between the 20 years of duration [1].

In this regard, most of researchers are currently working on the utilization of agricultural wastes as pozzolana to replace cement in concrete production. Pozzolana has cementitious property act as a binder and able to react with calcium hydroxide ($Ca(OH)_2$) formed from the hydration process of cement.

In light of incorporating rice husk ash (RHA) as an additive material into concrete production is regarded as one of them due to high silica content. Production of RHA is done via burning process of the rice husk from agricultural waste.

The mineral additive materials which possess pozzolanic behavior are favorable to be added into cement mixture due to its properties that promotes the concrete strength development. The usage of RHA in concrete is favorable in terms of material cost reduction. Thus, incorporation of RHA in concrete production promotes environmental and economic relief. It has greater reaction with $Ca(OH)_2$ in pozzolanic reaction, contributing towards increment in compressive strength value and durability of high performance concrete (HPC) and ultra-high performance concrete (UHPC) instead of fume and fly ash [2].

This paper is focused on the mechanical activation process to produce ultrafine size (<5μm) of RHA in order to achieve the maximum reaction of RHA as additive material in concrete production.

EXPERIMENTAL METHOD

In this study, the raw rice husk (RH) is acquired from a single local rice milling plant (BERNAS) in Sungai Ranggam, Perak. Then, the raw RH undergo several processes to produce ultrafine size of treated rice husk ash (UFTRHA) which are thermochemical pretreatment process, incineration, and mechanical activation process.

However, this study emphasizes the effect of using a planetary ball mill in the mechanical activation process as an important process to produce high quality and performance of UFTRHA.

Thermochemical Pretreatment Process

The thermochemical process includes treatment using diluted hydrochloric acid (HCl) and heating element at 0.01M, 0.05M and 0.1M. The soaking temperature are varied from 30 – 80ºC for 1 – 5 hours.

There is a significant difference between metallic impurities removal activities using HCl and distilled water (0M, denoted by DW) treatment was observed e.g. an increment of 400% potassium concentration removal using 0.1M HCl than DW treatment at 80ºC for 4 hours. This observation indicates that treatment process using acid is superior compared to the DW treatment process.

Incineration process

For the incineration process, the raw RH treated at 80ºC using 0.1M HCl was selected for incineration process. There are three different combustion temperatures used which are 600ºC, 700ºC and 800ºC from 1 up to 12 hours by using the laboratory furnace. Variation of burning period was introduced to observe the impact of prolonged combustion to SiO_2 content in both of the samples i.e., UFTRHA and non-treated rice husk ash (NTRHA).

From this process, it was evident that the sodium dioxide (SiO_2) content for UFTRHA were consistent than that of the NTRHA despite of extended burning period up to 12 hours. Overall, the UFTRHA produced at 600ºC for 1 hour burning period had yielded a maximum content of SiO_2 which is about 98.6%. Meanwhile, only the NTRHA sample prepared at 600ºC had only 70.1% of SiO_2 content at the same burning duration period.

This is again due to significant drop in the potassium oxide (K_2O) content for UFTRHA is anticipated that make SiO_2 much less susceptible to early crystallization during strong and prolonged combustions.

Mechanical Activation Process

Mechanical grinding is known as one of feasible method to be used in order to reduce average particle size and eventually increase the specific surface area (SSA) of a particle in powder form. Particle size reduction and large SSA value of UFTRHA is vital for excellent pozzolanic reaction and hence greater performance of the material as superior additive material in concrete application.

This mechanical activation mechanism is attainable using planetary ball mill. In this research, the UFTRHA-600℃ was ground at different grinding time i.e, 15, 30, 45 and 60 minutes using grinding speeds of 100, 200 and 300 rpm in order to identify the effect of the physical and morphological attributes of UFTRHA produced.

Overall, the UFTRHA was then mechanically activated by high energy planetary ball mill for 15 minutes at 300 rpm and ball-to-powder ratio (BPR) of 15:1 successively.

RESULT AND DISCUSSION

Mechanical Activation Process Influence to the Physical Characteristics of UFTRHA

The laser particle size analysis was employed in order to find the effect of grinding on the particle size distribution (PSD) of both NTRHA and UFTRHA

For PSD analysis, the most important information is D_{50} as this value give an indication of average particle size of the tested material in powder form. At Table 1, the observed trend of average particle size pattern for UFTRHA-600℃ at milling speed of 300rpm was contradicting to the other two speeds.

Table 1 PSD details of optimum UFTRHA-600℃ ground with BPR value of 15:1 at various speed and duration.

Grinding speed (rpm)	Grinding duration (Min)	Particle size (μm)		
		D_{10}	D_{50}	D_{90}
-	-	3.251	15.973	53.973
100	15	1.444	5.383	18.469
	30	1.514	5.300	15.959
	45	1.483	5.289	17.574
	60	1.603	5.044	14.074
200	15	1.285	5.071	20.791
	30	1.250	5.074	21.975
	45	1.323	5.044	17.881
	60	1.325	5.027	16.618
300	15	0.598	4.012	15.735
	30	1.393	4.380	14.144
	45	1.295	4.473	15.254
	60	1.460	4.676	14.768

However, the UFTRHA-600℃ at 300rpm for about 15 minutes has the lowest D_{50} value. The high speed of the grinding process has a greater velocity of the ball movements in the milling bowl. Therefore, shearing impact between grinding media (balls) and feed stock (UFTRHA) occurs vigorously in the system hence the smaller particle size obtained within short period of time. This is an evident that long milling duration at high speed lead towards particle agglomeration through excessive grinding process [3].

Compared to UFTRHA-600ºC powder sample, NTRHA-600ºC ground at 0rpm to 300rpm possessed a relatively larger D_{50} values at grinding duration of 15 minutes compared to UFTRHA-600ºC samples as shown in Table 2. The specific PSD of UFTRHA able to be achieved by either minimizing the grinding

speed and escalate the grinding duration or vice versa as reported elsewhere [4].

In addition, the UFTRHA-600℃ grain yielded was having smaller length than that of the NTRHA-600℃ ash. The metallic impurities presence on the surface of the NTRHA that caused difficulties of remaining carbon content in the NTRHA to be removed out during combustion process, hence define the colour difference. The trapped carbon content easily dissolved and remained in such ternary of Si–Na–O as well as Si–K–O oxides that melted on the surface of SiO_2 during the burning procedure [5].

Table 2 PSD details of optimum NTRHA-600℃ ground with BPR value of 15:1 at various speed and duration.

Grinding speed (rpm)	Particle size (μm)		
	D_{10}	D_{50}	D_{90}
-	3.213	28.002	194.82
100	1.115	7.807	26.17
200	1.442	5.951	24.471
300	1.339	5.158	18.704

Effect of Mechanical Activation Process on Specific Surface Area (SSA) of UFTRHA and NTRHA

The specific surface area (SSA) and pore characteristics of the porous structure of NTRHA and UFTRHA were assessed using the Brunauer Emmet Teller (BET) and Barret Joyner Halenda (BJH) techniques. The NTRHA and UFTRHA prepared with various combustion temperature at optimum grinding parameters (grinding at 300rpm speed with BPR 15:1 for 15 minutes).

From Table 3, it was evident that UFTRHA-600 possessed remarkably highest SSA value (222.9125 m^2/g) among all the samples due to the smallest particle size of this sample (D_{50} = 4.012μm). There is a huge difference of SSA values were recorded for both NTRHA and UFTRHA.

Table 3 Specific Surface Area (BET-SSA) of NTRHA and UFTRHA prepared with various combustion temperature.

Samples	Specific surface area (BET-SSA) (m^2/g)
NTRHA-600	4.8291
NTRHA-700	40.3132
NTRHA-800	28.1305
UFTRHA-600	222.9125
UFTRHA-700	205.1350
UFTRHA-800	219.5759

This phenomenon was due to higher unburnt carbon content in NTRHA that increased rigidity to the NTRHA structure, making it a harder material to be milled. However, based on BJH evaluation on pore characteristics in Table 4, all UFTRHA samples classified as mesoporous structured material since the average pore diameter recorded were less than 9 nm.

Mesoporous is defined as porous materials with pore size between 2 to 50nm. Usually, distribution of pore size for the mesoporous structured materials had a narrow range values i.e. between 2 to 22 nm with the average pore diameter value from 2 to 9 nm [6], [7].

Table 4 Pore features of NTRHA and UFTRHA prepared with various combustion temperature.

Samples	Pore features (BJH)		
	Adsorption cumulative pore surface area (m^2/g)	Adsorption cumulative pore volume (cm^3/g)	Adsorption cumulative average pore diameter (nm)
NTRHA-600	3.9110	0.0201	30.5403
NTRHA-700	34.2670	0.1456	12.5530
NTRHA-800	25.5360	0.1075	22.8062
UFTRHA-600	167.6350	0.2423	5.5593
UFTRHA-700	151.2060	0.2330	6.2720
UFTRHA-800	154.5550	0.2351	6.2203

Overall, the mesoporous UFTRHA-600 with an optimum grinding pramaters was identified to have the highest SSA, pore surface area, pore volume and lowest average pore diameter values.

Effect of Mechanical Activation Process on Morphology of UFTRHA and NTRHA

Based on the field emission scanning electron microscopy (FESEM) image of NTRHA ash as illustrated in Fig. 1, it had a corrugated, rough surface, rigid structure with cone-shaped protuberances. The outer surface of the RHA is dense and look like net-strip with arranged conical protrusion. Moreover, high content of unburnt carbon contributed towards rigidity of the NTRHA ash as well.

On the other hand, unground UFTRHA FESEM image in Fig. 2 gave an indication of soft structure of

the obtained ash. It was evident that the structure was already broke into small pieces even though no grinding aid had been introduced to the ash powder. The pore was already exposed, filled by agglomerated finely particles of UFTRHA even with no mechanical grinding imposed to the powder sample. This is due to the acid treatment process that successfully breaks the rigid structure of lignicellulosic material [8].

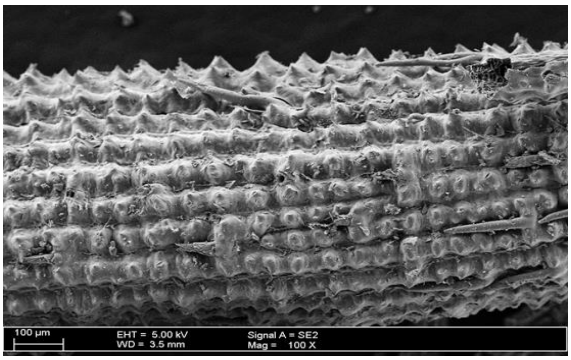

Figure 1 NTRHA-600 FESEM image captured 100X magnification

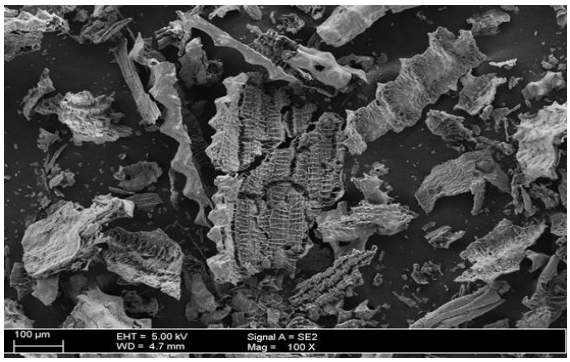

Figure 2 UFTRHA-600 FESEM image captured 100X magnification

In order to quantitatively analyze the effect of grinding duration to the morphology of UFTRHA, FESEM technique was used at high magnification of 1000X. The morphologies of the UFTRHA particles with respect to grinding duration variation are shown in the Fig. 3 to 5.

From the captured FESEM images, it can be seen that the powders have agglomerated particles with an irregular shape. Agglomeration of particles occurred due to excessive grinding aid. Therefore, extended duration of grinding process i.e. more than 15 minutes should be avoided.

Based on the explanation elaborated by Tanaka et al. (1999), amorphous is the state such a condition 'chaos just start to settle'. The word is derived from the Greek language which means 'without a definite shape'. According to this description it can be said that the amorphous material does not possess a fixed shape and the material arrangement form is undescribed [9].

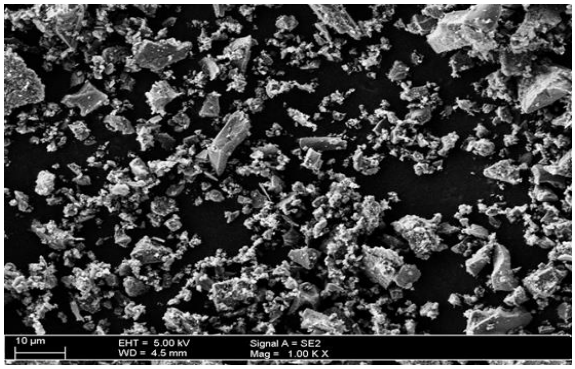

Figure 3 FESEM images UFTRHA-600 ground for 15 minutes, with grinding speed of 300 rpm and BPR value of 15:1

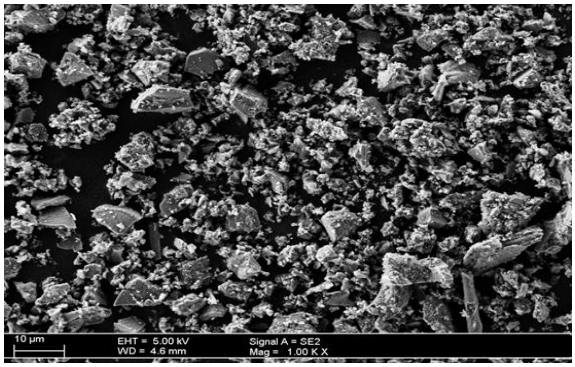

Figure 4 FESEM images of UFTRHA-600 ground for 30 minutes, with grinding speed of 300 rpm and BPR value of 15:1

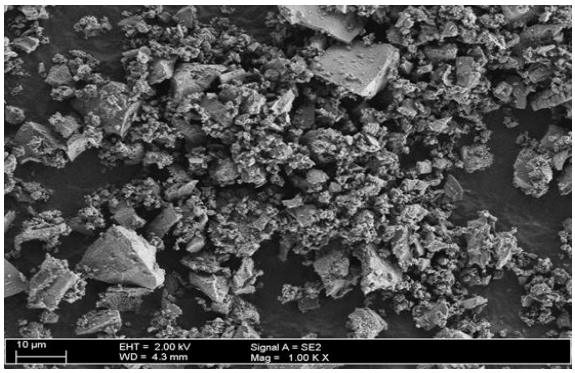

Figure 5 FESEM images of UFTRHA-600 ground for 45 minutes, with grinding speed of 300 rpm and BPR value of 15:1

CONCLUSIONS

In a nutshell, the mechanical activation process is proven to be an effective process to produce a highly reactive of UFTRHA. Based on the analysis conducted, the mechanical activation process reduce

the ultrafine sized particle (average particle size <5µm) with high BET-SSA value was obtained through grinding speed of 300 rpm, Ball-to-powder (BPR) ratio of 15:1 at only 15 minutes grinding duration. Extended grinding period caused particle agglomeration and hence larger particle size and lower BET-SSA value yielded.

ACKNOWLEDGMENTS

The author would like to express highest gratitude to the Ministry of Higher Education Malaysia (MoHE) under Fundamental Research Grant Scheme, project ID FRGS19-171-0780.

REFERENCES

[1] B. J. Van Ruijven, D. P. Van Vuuren, W. Boskaljon, M. L. Neelis, D. Saygin, and M. K. Patel, "Long-term model-based projections of energy use and CO2 emissions from the global steel and cement industries," *Resour. Conserv. Recycl.*, vol. 112, pp. 15–36, 2016, doi: 10.1016/j.resconrec.2016.04.016.

[2] N. Van Tuan, G. Ye, K. Van Breugel, A. L. A. Fraaij, and D. D. Bui, "The study of using rice husk ash to produce ultra high performance concrete," *Constr. Build. Mater.*, vol. 25, no. 4, pp. 2030–2035, 2011, doi: 10.1016/j.conbuildmat.2010.11.046.

[3] W. Xu *et al.*, "Effect of rice husk ash fineness on porosity and hydration reaction of blended cement paste," *Constr. Build. Mater.*, vol. 89, pp. 90–101, 2015, doi: 10.1016/j.conbuildmat.2015.04.030.

[4] H. K. Venkatanarayanan and P. R. Rangaraju, "Material Characterization Studies on Low- and High-Carbon Rice Husk Ash and Their Performance in Portland Cement Mixtures," *Adv. Civ. Eng. Mater.*, vol. 2, no. 1, p. 20120056, 2013, doi: 10.1520/acem20120056.

[5] J. Umeda and K. Kondoh, "High-purification of amorphous silica originated from rice husks by combination of polysaccharide hydrolysis and metallic impurities removal," *Ind. Crops Prod.*, vol. 32, no. 3, pp. 539–544, 2010, doi: 10.1016/j.indcrop.2010.07.002.

[6] Z. A. Alothman, "A review: Fundamental aspects of silicate mesoporous materials," *Materials (Basel).*, vol. 5, no. 12, pp. 2874–2902, 2012, doi: 10.3390/ma5122874.

[7] W. Wang, J. C. Martin, X. Fan, A. Han, Z. Luo, and L. Sun, "Silica nanoparticles and frameworks from rice husk biomass," *ACS Appl. Mater. Interfaces*, vol. 4, no. 2, pp. 977–981, 2012, doi: 10.1021/am201619u.

[8] H. V. Lee, S. B. A. Hamid, and S. K. Zain, "Conversion of lignocellulosic biomass to nanocellulose: Structure and chemical process," *Sci. World J.*, vol. 2014, 2014, doi: 10.1155/2014/631013.

[9] K. Tanaka, E. Maruyama, T. Shimada and H. Okamoto, *Amorphous Silicon*. Wiley, 1999.

11th Int. Conf. on Geotechnique, Construction Materials & Environment, Kyoto, Japan, 3-5 November 2021, ISBN: 978-4-909106063 C3051

REVIEW ON CURRENT SITUATION OF GENERATION AND MANAGEMENT OF COAL ASH IN VIETNAM

Tran Viet Cuong[1], Ken Kawamoto[2], Nguyen Hoang Giang[3]

[1] Department of Civil Engineering, National University of Civil Engineering, Hanoi, Vietnam.
[2] Saitama University, Japan.

ABSTRACT

Due to rapid industrialization and economic growth, the generation of coal ash from coal-fired thermal power plants is increasing in Vietnam. At present, the coal ash waste is mostly dumped at landfills and stored at stock yards, however, the capacity of landfilling and stock sites can be estimated to be insufficient in near future. In Vietnam, there are two main residential coal-burning technologies used in thermal power plants as pulverized combustion and circulating fluidizing bed (CFB) and 26 coal-fired power plants were generated 12.2 million tons of coal ash waste as of 2017. The generation amount can be expected to increase to up to 30 million tons according to the master plan for electricity development: 52 coal-fired power plants will be in operation by 2030. Therefore, the coal ash will be increased from 109 million tons in 2020 to 248 million tons in 2025 and 422 million tons in 2030. The coal ash impact on the environment problems while only 31% (~ 5 million tons) of the total is currently treated and recycled. Based on the survey results on legal framework and regulations, present treatment technologies, and management practice of coal ash, the major difficulties were summarized: i) there is no technical standards for handling, reuse and recycle of coal ash, ii) the thermal plants do not possess sufficient storage capacity of coal ash (especially, for small scale- and old plants that faces the risk of closure, iii) lack of collaborative system and framework among enterprises, government (central and local), and research institutes (including universities) to initiate actions for promoting an effective reuse and recycling of coal ash in Vietnam.

Keywords: *Coal ash, coal-fired power plant, reuse and recycling, Vietnam.*

INTRODUCTION

In 1993, less than half of Vietnamese households had use to electricity. By the end of 2015, more than 98% have been use it [1]. With the rapid growth of economic is parallel to the development of electricity has provided immense benefits to the economy and society. Besides these benefits came with effect environmental in recent year. According to the revised Seventh Power Development Plan of Vietnam, in 2017, 26 commercially operated thermal power plants generated 12.2 million tons of coal ash and is expected to increase to 30 million tons with 52 coal-fired power plants coming into operation by 2030 and the scale of coal in the structure of power resources for electricity production will gradually increase from 49.3% in 2020 to 56.4% in 2030. Most of this waste is disposed into the environment without any treatment and dumped in landfill sites even their capacity is overload [2].

The developed countries in the world always encourage the use of coal ash from coal-fired power plants if they have the standards used in construction materials. For instance, according to JCOAL, in Japan, the annual generation of coal ash is 12.35 million tons and effective use and recycling are achieving around 98% including 64 % of coal ash is used in cement and concrete field, and 14% of coal ash is used in the field of civil engineering including soil improvement. In Vietnam, at present, the most of coal-fired power plants even have measures to reuse and treatment coal ash yet. Only a little quantity of coal ash meets the input standards for use as cement, concrete and unburn construction materials while most of the rest is discharged directly to the dumping site. At the same time, the dust is arising during storage and transportation from coal-fired power plants to the dumping site by truck [3]. The trucks have not cover full truck crates and factories still not completed the transportation system, storage areas for ash have not met the requirements of environmental protection, polluting the environment around the plant [4]. Besides, many enterprises and localities need to use large amounts of coal ash to make construction materials and levelling but there are no standards and technical regulations that cannot be implemented [5].

COAL ASH FROM COAL-FIRED POWER PLANTS IN VIETNAM

Electricity from coal-fired power plants accounts for nearly 53.2% in total electricity production, consumed about 129 million tons of coal in 2030 [6]. Figure 1 show the map of coal-fired power plants in Viet Nam. Most focus along the beach and the economic centre in Vietnam.

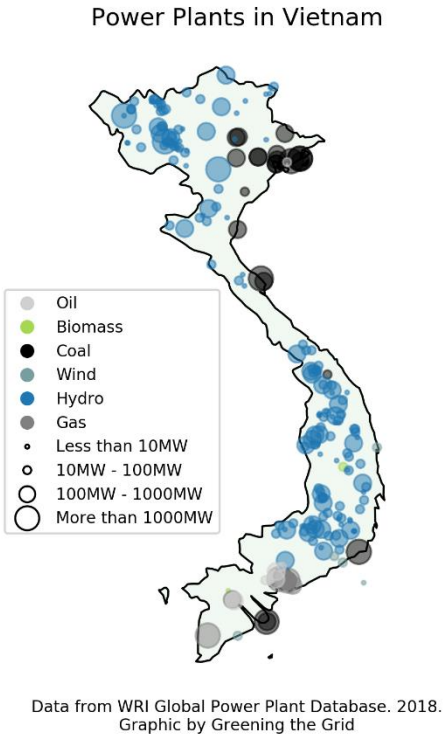

Fig. 1. Map on coal-fired power plants [7]

The process of burning coal to operate thermal power plants generates combustion product called coal ash. Coal ash consists of bottom and fly ashes. Bottom ash is also called slag, is coarse, large particles obtained at the bottom of the furnace; Fly ash is fine fly ash particles collected in dust filter. Normally, the amount of fly ash accounts for about 80 - 90%, while the slag accounts for only about 10-20%.

As of 2016, the total electricity capacity is 13,110 MW, the total amount of coal ash generated is about 15,784,357 tons [8]. The ratio of fly ash and bottom ash is shown in Fig. 2.

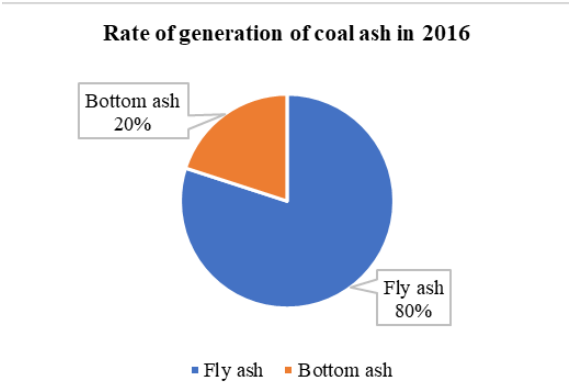

Fig. 2. Rate of generation of coal ash in 2016 [8]

Coal combustion technology

Currently, coal-fired thermal power plants in Vietnam use one of two types of burning technologies: pulverized combustion (PC) and circulating fluidizing bed (CFB).

PC technology

The coal is finely ground on crushing machine and dried to a particle size of less than 0.09mm then move to the storage tanks. The temperature in the furnace is about 1400ºC- 1600ºC for the purpose of heating to create the pressure feed the

power electricity. Burning coal leaves coal ash, part of the molten superheat turns into slag falling to the bottom of the furnace, cooled by water, most of the fine coal ash follows the flue wind to filter electric dust to retain, clean gas discharged into the environment [8].

CFB technology

This technology is used when the coal is low quality and high in sulphur. Coal and limestone are process on hammer crushing machine to a particle size is less than 10mm, stored in tanks has feeding and dosing at the bottom. Coal and limestone are fed into the circulating fluidized bed furnace to generate heat and feed the water into high-pressure steam to create electric. Fine ash into electrostatic dust filter to collect fly ash, clean gas discharged into the environment through the chimney. Large particles of coal ash and limestone, whether or not reactive will fall to the bottom of the kiln to form bottom ash. For plants using CFB technology, gypsum always mix with fly ash. Using CFB technology makes it difficult to separate gypsum from fly ash, it difficult to use as raw materials for construction materials production [8].

Properties of coal ash at thermal power plants in Vietnam

Properties of coal ash depend on the burning technology. Table 1 show the components of coal ash in some thermal power plants in Vietnam [8]. As for the coal ash of PC technology, coal ash composition of coal-fired power plants is similar; the slag obtained at the bottom of kiln has a loss of ignition less than 8%, it is match with the standard of TCVN 6882:2016 [9] for mineral additives for cement. As for the coal ash of CFB technology, coal ash from Cam Pha and Son Dong can be classified as Class F according to ASTM C618-19 [10]. Coal ash with high loss on ignition (LOI), CaO, $CaSO_4$ content is the cause

Table 1. The components of coal ash in some thermal power plants.

No	Thermal power plans	Capacity (MW)	$SiO_2 + Al_2O_3 + Fe_2O_3$ (%)	SO_3	CaO	LOI (%)
		PC Technology				
1	Uong Bi 1, Uong bi 2	735	85	0.58	<0.008	6-8
2	Pha Lai 1, Pha Lai 2	4x110, 2x300	64.5-71.3	0.12-0.06	<0.008	22.6-25
3	Quang Ninh 1, Quang Ninh 2	4x300	83-85.2	0.29	<0.008	6-8
4	Hai Phong 1, Hai Phong2	4x300	83-87.1	0.32	0.63	10-14
5	Ninh Binh	400	70	0.12-0.06	<0.008	22
6	Duyen Hai 1	2x622	84	0.32	0.63	12
7	Nghi Sơn 1	2x300	76.5			14-17
8	Vung Ang 1	2x600				<6
9	Vinh Tan 2	2x622				12
10	FMS Dong Nai	3x150	88.6	0.68		<6
		CFB Technology				
1	Na Duong	2x55	58.7	10.6	21.7	4-8
2	Cao Ngan	2x57.5	45.61	10.5	13.5	24-27
3	Cam Pha	2x340	78.0	2.4	5.5	8-12
4	Son Dong	2x110	85.6	1.1	1.3	10-14
5	Mao Khe	2x220	84.3	0.7	2.0	6-8
6	Mong Duong 1	2x540	72	1.87	7.42	11.0
7	An Khanh	2x58	83	0.7	1.96	6.6

of difficulty for their use in cement production as well as construction materials.

Current situation of coal-fired some thermal power plants

As the development of economic in recent years, the share of coal in the structure of power resources for electricity production will gradually increase from 49.3% in 2020 to 56.4% in 2030, according to the revised Seventh Power Development Plan of Vietnam [11]. It makes a large of coal ash exist at the dump site.

Table 2 show the total amount of coal ash exist if not reuse in the future.

Table 2: Total amount of coal ash exist if not reuse [8, 11].

No	Year	Total Coal Ash (Tons/year)	Total amount of Coal Ash exist if not reuse (Tons)
1	2016	15,784,357	22,705,558
2	2018	20,612,500	61,515,750
3	2020*	25,441,770	109,980,500
4	2025*	29,371,100	248,978,800
5	2030*	38,314,500	422,663,000

* *Estimated values.*

In Quang Ninh, there are 7 coal-fired power plants with total capacity of 4,150MW electricity (16% of the total electricity country). There are 2 more plants will operate in 2020 even through the dumping ground for coal ash is currently overloading. For instance, there are 2 plants in Cam Pha with total capacity of 600MW and spend 34 ha to dumping coal ash with 1 million tons per year. However, after 7 years of operation, the dumping ground has become nearly occupied for other purposes; Ha Long Bay are suffering from the 7 million tons of coal ash produced from the nearby coal-fired power plants, as shown in Figure 3. [12].

Fig. 3. A dumping site besides Ha Long Bay [12]

Mong Duong 1 thermal power plants operate at the end of 2015, is facing possible closure in near future due to overload of the coal ash problems. The capacity of plant is 1,080MW consumes about 3 million tons of coal per year and releases 1 million tons of coal ash. At the present, only 40% of coal ash could sale for cement manufacturing and concrete mixing, while fly ash meet difficulty to find buyer as well as treatment [13]. The dumping site of the plant

has a total volume of 2.25 million m^3 but it has already spent 1.8 million m^3.

EFFECT OF COAL ASH ON ENVIRONMENTAL POLLUTION AND POTENTIAL RISK TO HUMAN LIFE

The amount of coal ash remained currently is big problems such as: spending large dumping space, overloading the current dumping space leading to the closure of the plants, threatening to environment and people.

Monitoring by Ministry of Natural Resource and Environment (MONRE) [14] shows that at 100% of coal mining and processing facilities, the concentration of dust in the air is above the Vietnamese standard from 30 to 300 times [15]. Electricity generation from coal is responsible for producing airborne pollutants throughout its life cycle from coal mining, processing, and transportation to coal burning and coal ash handling (see Figure 4). Study in Mao Khe coal power plant shows concentrations of heavy metals and toxic in Gao Stream exceed Vietnamese standards. More than 75% of people interviewed around the Duyen Hai Coal Power Centre declared that they had to change their daily activities due to low air quality condition such as closing windows and sweeping the house more often.

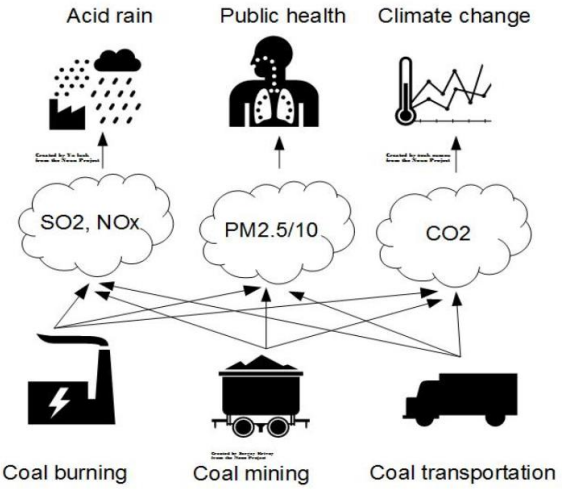

Fig. 4. Impact of coal to air quality from its whole life cycle [1]

Coal ash is affecting air quality by its transportation and storage. An example of poor coal ash management severely impact air quality is from Vinh Tan Coal Power Plant in Binh Thuan Province. Vinh Tan produces 4,000 tons of coal ash per day. Coal ash is transported to the dump site by trucks and piled up without any coverage (Figure 5). Dust is carried by strong winds causing air pollution that significantly impact local people [1].

Fig. 4. Coal ash transportation [3]

The Vietnamese standards on Ambient Air Quality (QCVN05:2013/BTNMT) [16] set the national standards for PM10 concentration at 50 $\mu g/m^3$ (measured as an annual mean) and 150 $\mu g/m^3$ (measured as a daily concentration). Standard for PM2.5 is 25 $\mu g/m^3$ and 50 $\mu g/m^3$, respectively. The concentration of PM2.5 is highest in the region where coal thermal power plants are concentrated [17].

CURRENT SITUATION AND SOLUTION OF RECYCLE AND MANAGEMENT OF COAL ASH

Current situation of recycle of coal ash in the world.

In the world, the total amount is estimated in 2001 to about 480 million tonnes. In Europe (EU25) about 95 million tonnes of coal ash were produced in 2003. In Europe, around 53% use in construction and underground mining, 36% are used for the restoration of open cast mines, quarries and pits. Only 12% of the total CCPs were temporarily stockpiled (8%) or had to be disposed of in disposal grounds (4%) [18]. In Japan, In 2016, thermal coal ash output of the country was about 12.35 million tons and its useful amount was 12.35 million tons, equivalent to 99.3%. Coal ash have been used in construction as raw material for cement, road pavement materials, ground-leveling materials or applied in the field of agriculture, forestry and fishery [19].

Current situation of recycle of coal ash in Vietnam.

Decision No. 1696/QD-TTg dated September 23, 2014 of the Prime Minister on a number of

solutions to treat and use coal ash from thermal power plants as raw materials for the production of building materials [20]. However, according to actual survey data and reporting units, the total amount of coal ash consumed is not large, only about 25% - 30% (around 5 million tonnes) of the total amount discharged annually. There are factories that have sold most of the coal ash discharged, while there are factories that have to discharge all to the site.

Vietnam government launched a program to use coal combustion residuals (CCR), a waste product from thermal power plants to make building materials. The program demanded that at least 25% of CCR must be recycled by 2015. However, only 18% of CCR was recycled at the end of 2015 according to the survey of the Building Materials Institute [21]. However, some of plants are doing well in recycling coal ash such as Cao Ngan plant. Each year, Cao Ngan coal-fired power plant discharges about 200,000 tons/year. Until the end of 2015, the Cao Ngan factory delivered nearly 32,000 tons of fly ash for the testing of cement production at the Quan Trieu Cement Plant. The average monthly amount was around 6500 to 7000 tons [2]. And, they can save about 2 ha (20,000 m^2) dumping area each year.

However, most of the coal-fired power plants are currently cannot find a solution for solving the coal ash problems [21]. In addition, some of new technologies such as the integrated gasification combined cycle (IGCC) and pressurized fluidized bed combustion (PFBC) will allow increases of 50% in efficiency rates in the future [22]. Ultra-clean coal (UCC) technology with new processing solutions will reduce fly ash to below 0.25%, and sulfur to a very low level [23]

Acts, regulation, strategies and official documents related to Coal ash in Vietnam

In recent year, Vietnamese government provide many laws and decisions to reused and recycled coal ash use in construction that shown in Table 3. The first law was published in 1993 on environmental management and the newest in 2018 has directives on the reuse of coal ash in construction.

Most prominent, decision No. 452/QD-TTg of the Prime Minister [24], dated 12th April 2017, approved a project which accelerates the treatment and reuse of ash slag and gypsum from power plants and fertilizer chemical factories as raw materials for construction. The goal of the Vietnamese government is to recycle at least 60% of ash released from power plants for building materials by 2020. This decision also states that the recycling of coal ash as a material for the production of building materials and in construction works must be aimed at protecting the environment, and reducing both the use of dump areas and mineral resources for building materials, to ensure sustainable development. Specifically, to make mineral additives for cement production about 14 million tons; replacing a part of clay to produce about 8 million tons of cement clinker; replacing a part of clay to produce baked clay bricks of about 7 million tons; as a mineral additive for the production of concrete and unburnt bricks, about 2 million tons; building levelling materials for works, reconstructing mines and making roads about 25 million tons.

Besides that, decision No. 452/QD-TTg encourages and funds research and development on using of coal ash, boiler slag, and gypsum for production of building materials. Basically, improve the treatment technologies and bring these technologies into operation ahead of June 2019. By 2020, ensure that an area of each dumping ground will not exceed the amount wastes released within two years of mean production. This regulation shall be specifically applied such as: (1) active plants from which proposals for treatment and use of ash, slag and gypsum produced have been submitted before December 31, 2018; (2) projects that are under construction, require modified proposals and submission of the accepted proposals before officially being put into operation; (3) projects that are at the stage of pre-investment arrangement, proposal formulation and submission of the request for approval of the proposal and the investment project. State-funded investment and construction projects must prefer to use ash, slag and gypsum or building materials made from ash, slag, FGD and PG gypsum provided these materials or products have the same economic and technical efficiency as other ones.

To promote the processing and consumption of ash, slag, and plaster, on December 28, 2018, the Ministry of Construction issued Document No. 3314/BXD-VLXD [25] on guiding the use of ash and slag as raw materials in construction and in construction works. Then Vietnamese's government promulgate TCVN 12249:2018: Coal ash of thermal power plant using as backfill material - General requirements [26].

Most recently, On 22 February 2021, the Ministry of Industry and Trade of Vietnam (MOIT) released the draft proposal for the national power development plan for the period of 2021-2030, with a vision to 2045 ("Draft PDP8") for public comments. This proposal focuses on some structural changes in the power industry especially coal power industry. In which,

Table 3. Acts, regulations, decisions related to treatment and recycled coal ash

Year	Type of document	Name of document	Remarks
1993	Law	Law on Environmental Protection	Environmental regulation shall consist in the review of natural and human elements and factors of the environment, observation and recording of their alterations, as well as the supervising of the causes of these alterations.
2005	Law	Law on Protection of the environment	Update from Law 1993
2007	Decree	No.59/2007/ND-CP. Decree on solid waste management	Initial guideline for managing solid waste
2009	QCVN	QCVN 07: 2009/BTNMT	National Technical Regulation on Hazardous Waste Thresholds
2009	Vietnamese Standard	Fly ash - Methods of chemical analysis	Prescribes chemical analysis methods for fly ash
2014	Decision	Decision No.1696/QD-TTg	Encouragement of recycling coal ash as building material (guideline, incentive, international cooperation)
2014	Vietnamese Standard	TCVN 10302:2014. Activity admixture - Fly ash for concrete, mortar and cement	To applies for mineral admixtures of fly ash (hereinafter referred to as fly ash) that have been through dry or wet sorting treatment technology for concrete, mortar and cement.
2017	Decision	Decision No.452/QD-TTg	Encouragement of recycling coal ash as building material (guideline, incentive, international cooperation)
2018	Vietnamese Standard	TCVN 12249:2018. Coal ash of thermal power plant using as backfill material	This standard applies to coal ash from coal-fired thermal power and is used for leveling for construction and technical infrastructure.
2018	Decision	Decision No.3986/QĐ-BNN-XD	Instructions for the use of fly ash in irrigation concrete

from 2020 to 2030, there will be no additional development of new coal-fired thermal power. The power capacity structure will be reducing coal-fired thermal power from 34% in 2020 to 27% in 2030 and the remaining 17-18% in 2045. The ratio of coal-fired thermal power will gradually be decreased from 40% in 2030 to about 30% in 2045 [27].

CONCLUSIONS

The Vietnam electricity has grown rapidly, reflecting the country's economic development. It is supposed to increase two to three times over the next two decades. The electricity peak requires growing an average of 12% annually. Currently, Vietnam's power industry is to be more heavily weighted toward coal-fired thermal plants as indigenous hydro resources become more limited. But the coal-fired power generation is accompanied by environmental protection challenges that are primarily caused by emissions and ash. Government needs to strongly promotes and solutions as well as supporting policies for recycling businesses of coal ash. At present, the use of coal ash from coal-fired power plants as construction materials to replace raw materials is one of the active solutions, bringing high efficiency to solve this issue.

Worldwide, renewable energy technologies such as solar and wind power are mature, commercial and expanding much more rapidly than fossil fuel generation technologies. Not yet in Vietnam. Energy efficiency and renewable energy sources should be given more attention, in terms of technology development and economic incentives.

- The government should step up its inter-ministerial efforts to organize the socioeconomic readiness conditions for a large-scale expansion of renewable energy.
- The development of renewable energy and higher efficient use of energy should be paid more attention by both direct and indirect subsidies and supports.

Basically, these mechanisms are necessary in the short run, especially when the full environmental costs of coal are not yet fully internalized.

ACKNOWLEDGMENTS

This research was supported by JST–JICA Science and Technology Research Partnership for Sustainable Development Program (SATREPS) project (No. JPMJSA1701).

REFERENCES

[1] Minh, H. D., An, H. T., And Hoang, A. T. N. (2016) *Synthesis Report on Socio-environmental Impacts of Coal and Coal-fired Power Plants in Vietnam.*

[2] Thriveni, T., Nguyen. T. M. N., Lai, Q. T., Trinh, H. S., Ho, H. H., Dang, T. N. T., Nguyen, T. T. T., Duong, T. T. T., Doan, T. N. H., Tran, T. V., Ramakrishna, C., and Ji, W. A. (2018) *Technological Solutions for Recycling Ash Slag from the Cao Ngan Coal Power Plant in Vietnam.*

[3] Le Truong (2015). "Live Together with Coal Ash and Dust." Nld.com.vn. April 6. *http://nld.com.vn/news20150406215144374.htm*

[4] Hoang Linh (2016). "Vinh Tan 2 Coal Power Plant Cause Pollution in Binh Thuan Province." Laodong.com.vn. January 26. *http://laodong.com.vn/chung-toi-len-tieng/nhiet-dienvinh-tan-2-treu-nguoi-tinh-binh-thuan-511896.bld*.

[5] Management solutions, using ash, coal slag in our country's thermal power system (2017), available at: *http://hoivlxdvn.org.vn/news/giai-phap-quan-ly-sudung-tro-xi-than-trong-he-thong-nha-may-nhiet-dien-nuoc-ta-40902.html*

[6] Decision No. 428/QĐ-TTg (2016). *The approval of revisions to the national power development plan from 2011 to 2020 with visions extended to 2030.*

[7] Report on Graphic by Greening the Grid (2018). *WRI Global Power Plant Database.*

[8] Le Van Quang (2019). Report on analysis technology. *Trends of application of coal ash in the production of building materials*.

[9] TCVN 6882:2001. *Mineral additive for cement.*

[10] ASTM C618-19. *Standard Specification for Coal Fly Ash and Raw or Calcined Natural Pozzolan for Use in Concrete.*

[11] Jongyeol, L., Taeyoon, K., Mina, S., Hong, H. T. Vu., Kyung, N. S., and Ji, W. A. (2020) *An Integrative Approach to International Technology Transfer for Recycling Vietnam Coal Ash with Consideration of the Technological, Legal, and Network Perspectives.*

[12] Ash & slag from thermal power plants threatens Ha Long Bay (2017), available at: *http://english.vietnamnet.vn/fms/environment/187712/ash---slag-from-thermal-power-plants-threatensha-long-bay.html.*

[13] Trang, V. (2017) $1.6-billion thermal power plant faces possible closure over ash problems. Available at https://www.vir.com.vn/16-billion-thermal-power-plant-faces-possible-closure-over-ash-problems-51889.html

[14] MONRE. (2014) National Environmental Report 2013 - Air Quality.

[15] Green ID. (2015) *Survey on some coal fired power plant in Vietnam.*

[16] QCVN05:2013/BTNMT (2013). *National Technical Regulation on Ambient Air Quality.*

[17] Koplitz, Shannon. (2015). "Burden of Disease from Rising Coal Emission in Asia." *presented at the International Symposium on Climate change and Coal, Tokyo, Japan, May 29.* Available at*: http://acmg.seas.harvard.edu/presentations/2015/koplitz_japan_symposium_20150529.pdf.*

[18] Report EN-10. *Residues from combustion of coal for energy production*

[19] The 2nd Japan – Viet Nam Coal Energy Working Group Conference, held in Hanoi in two days of 8 – 9 November 2018, by Viet Nam Electricity (EVN) and Japan Coal Energy Center (JCOAL). *https://en.evn.com.vn/d6/news/Japan-efficiently-reuses-over-99-thermal-coal-ash-6-12-1186.aspx*

[20] Decision No.1696/QD/TTg (2014). *Taking measures to treat ash, slag and gypsum from thermal power, chemical or fertilizer plants for the production of building materials.*

[21] Hong, H. T. V and Ji, W. A. (2018). *Overview of coal-fired power plant ash situation and cement industry in Vietnam. Journal of Energy Engineering, Vol. 27, No. 3, pp.57~62.*

[22] Global CCS Institute. (2017) Clean Coal Technologies, Carbon Capture and Sequestration. Available online: *http://www.world-nuclear.org/information-library/energy-and-theenvironment/clean-coal-technologies.aspx*.

[23] Rubiera, F., Arenillas, A., Arias, B., Pis, J.J., Suárez-Ruiz, I., Steel, K.M., Patrick, J.W. (2003). *Combustion behaviour of ultra clean coal obtained by chemical demineralization*. *Fuel 2003, 82, 2145–2151*.

[24] Decision No.452/QD-TTg. (2017) *Approving the proposal to boost treatment and use of ash, slag and gypsum discharged from thermal power plants, chemical and fertilizer plants for production of building materials and for use in construction projects.*

[25] No. 3314/BXD-VLXD. (2018). *Guidelines on the use of ash and slag as raw materials in construction and in construction works.*

[26] TCVN 12249:2018. (2018). *Coal ash of thermal power plant using as backfill material - General requirements.*

[27] Draft PDP8. "Key highlights of new draft of national power development plan". *https://www.globalcompliancenews.com/2021/03/13/vietnam-key-highlights-of-new-draft-of-national-power-development-plan-draft-pdp8-04032021-2/*

[28] Law on Environmental Protection (1993,2005).

[29] Decree No.59/2007/ND-CP (2007). *Decree on solid waste management.*

[30] TCVN 8262:2009. *Fly ash - Methods of chemical analysis Prescribes chemical analysis methods for fly ash.*

[31] TCVN 10302:2014. *Activity admixture - Fly ash for concrete, mortar and cement.*

[32] Decisions No.3986/QĐ-BNN-XD (2018). *Instructions for the use of fly ash in irrigation concrete.*

11th Int. Conf. on Geotechnique, Construction Materials & Environment,
Kyoto, Japan, 3-5 November 2021, ISBN: 978-4-909106063 C3051

POROSITY AND PERMEABILITY OF PERVIOUS CONCRETE USING CONSTRUCTION AND DEMOLITION WASTE

Kim Tuan NGO[1], Quang Minh PHAN[1], Hoang Giang NGUYEN[1], Tien Dung NGUYEN[1]
Ken KAWAMOTO[1,2]
[1] National University of Civil Engineering, Vietnam;
[2] Graduate School of Science and Engineering, Saitama University, Japan

ABSTRACT

The use of recycled aggregates (RA) from construction and demolition wastes to produce non-structural concrete is considered as a sustainable solution with dual environmental benefits. This paper aims to expand the potential use of RA to manufacture pervious concrete for permeable pavement systems. The ratio of concrete aggregates and clay brick aggregates, design porosity, and the mix design are chosen as the mix variables and evaluated their contributions in pervious concrete block. Porosity characteristics, hydraulic conductivity and mechanical properties of the pervious concrete were investigated in this study. The relationship between total and effective porosities and water permeability is also performed. Experimental results show that the mix using blended aggregate has lower mechanical properties than that containing concrete aggregate, while the clay brick aggregate leads to the lowest of compressive and flexural strength. However, the composition of the aggregate mixture has a negligible influence on the effective porosity and permeability of pervious concrete. The effect of the clay brick content on total porosity is significant. Increasing clay brick content in blended aggregate increases the total porosity of the pervious concrete and increases the water permeability coefficient. A relationship between permeability and effective pore characteristics over the total porosity and mechanical strength of pervious concrete was drawn.

Keywords: Pervious concrete, recycled aggregate, porosity, water permeability.

INTRODUCTION

Population growth, infrastructure, and housing construction activities generate large amounts of construction and demolition waste (CDW), and as a result, dire demand for recycling construction waste. Construction waste created during all phases of a building's life cycle: construction, renovation and demolition [1]. In many countries, the proportion of recycled aggregate used is very small, while the land for landfill becomes scarce and the world demand for aggregate reaches a massive 40 billion tons per year. Therefore, more solutions to this problem are needed. [2]. Japan and other developed countries are leading the way in recycling CDW, achieving 98% recycling, and the recycled CDW is used in many applications thanks to high taxes on natural aggregate and development techniques [3].

Recycled aggregate is commonly used as bulk backfill, in sub-base, base or surface material in road construction, sidewalk and hydraulically bound materials and in the manufacture of new concrete structure, fresh concrete [2][4]. Due to the weak mechanical characteristics and the high variability in quality, the use of recycled aggregates should be carefully considered in terms of applicability in proportion to the mechanical strength achieved. Pervious concrete is a potential application of recycled materials. It has a porosity and median pore diameter in the range of 0.15 – 0.3 and 2–4 mm, respectively [5]. Pervious concrete displays better water permeability characteristics due to its connected pore structure inside [6]. Further, pervious concrete is an environmentally friendly material that improves skid resistance, sound absorption, and reduces the ‘‘heat island effect” [7].

The experimental investigation shows that the hydraulic conductivity of any porous material is inherently dependent upon the pore features such as pore size, specific surface area of pores, porosity and the tortuous flow path [8]. However, the interconnected pore system (the main factor determining the drainage capacity) is most affected by the type of aggregate, not the size of the aggregate [9]. Pervious concrete using recycled aggregates with many angles often has porosity larger than the design porosity and higher than when using normal aggregates (from 2-3%) [10]. The pore system is enlarged and the water permeability of porous concrete using recycled aggregate is increased due to the thinner cement paste covering the aggregate particles. This phenomenon is due to the higher specific surface area of recycled aggregate than natural aggregate [11][12]. Another study showed that recycled concrete did not affect to porosity but reduced density and increased water permeability [13]. The water permeability of pervious concrete achieved range from 0.1 to 3.3 cm/s, it is perfectly suitable for making drainage water purposes [10]. The author [14] also obtained permeability coefficients up to 55 and 80 mm/s when using recycled aggregates to make concrete with large porosity. However, the compressive strength is only 3.5 MPa. In some cases, although the porosity is

equivalent to using natural aggregates, the drainage capacity is still increased [12]. Remarkable results when using 50% fine glass waste (2.36 – 5 mm) and 50% coarse aggregate from concrete, pervious concrete can be obtained that can meet both strength and drainage according to Japanese standards JIS A 5371 [15] for pedestrian road [16].

The available research results also have different views and results on the influence of recycled aggregates on the porosity and drainage characteristics. Further, the study of the influence of clay brick content in the recycled aggregate mix on the porosity and permeability properties as well as the strength of permeability concrete has not been mentioned by many studies. In this paper, the relationship between porosity, permeability, and strength of pervious concrete with different proportions of aggregate mixture of clay brick-recycled concrete will be clarified.

MATERIALS AND METHODS

Materials

There are three main materials in the fabrication of pervious concrete: cement, coarse aggregates, and water. Ordinary Portland cement with a specific gravity and specific surface area of 3.1 g/cm^3 and 3300 cm^2/g, respectively, was used for this investigation. The 28-day compressive strength of cement is 47 MPa. Two types of single-size coarse aggregates with 5–10 mm diameter were used in this study. The first was a recycled aggregate from crushed structural concrete (RC), and the last was a recycled aggregate from crushed broken clay brick (RB), two types obtained from a local construction site. No treatment was done on the RA to minimize the production cost of pervious concrete. Figure 1 shows the coarse aggregates used in this study and their properties are detailed in Table 1. The dry-rodded density of RC and RB were lower than that of NA (about 1550 kg/m^3) while the water absorptions were higher as expected.

Fig. 1 Coarse recycled aggregate

(a) RC aggregate (b) RB aggregate

Mix proportion

The process of design mixture proportions for pervious concrete according to the ACI 522R - 10. In general, the overarching philosophy of mixture proportioning for pervious concrete is to achieve balance between voids, strength, paste content, and workability [17]. The coarse aggregate size No. 8 (ASTM C33/C33M) was used in this study. The water-cementitious material ratio (w/cm) is an important consideration for obtaining desired strength and void structure in pervious concrete.

Table 1 Material properties of recycled aggregate from concrete and clay brick demolition waste

Properties	Recycled concrete (RC)	Recycled brick (RB)
Particle size (mm)	5.0 – 10.0	5.0 – 10.0
Specific gravity (g/cm^3)	2.60	2.55
Bulk density (kg/m^3)	1620	1280
24h water absorption (%)	5.5	14.6
Los Angeles abrasion (%)	38	46

Experience has shown that w/cm in the range of 0.26 to 0.45 will provide the best aggregate coating and paste stability. The w/cm was 0.33 in all mixture. To ensure that water will percolate through pervious concrete, the void content, both in the design of the mixture and measured as the percent air by ASTM C138/C138M (the gravimetric method) should be 15% or greater. The design porosity was in the range of 15%, 20% and 25% in this research. Base on void content and lightly compacted was used, the percentage of paste content was determined. Figure 2 shows the mix proportions of pervious concrete.

Testing methods

The compressive and flexural strengths of pervious concrete were determined at the age of 28 days. The porosity and water permeability coefficient of pervious concrete were tested using rectangular specimens of 210 x 100 x 60 mm, the reported values were the average of three specimens.

The pervious concrete porosity was calculated by taking the difference in weight of oven dry and saturated, submerged under water [18].

The total porosity, ϕ_T, can be determined by two methods. Assuming no isolated pores in the sample, the total porosity (%) was calculated using Eq.(1):

$$\phi_T = \left(1 - \frac{\rho_d}{G_s * \rho_w}\right) * 100 \quad (\%) \qquad (1)$$

If according to a water displacement method [18] [19], the ϕ_T can be calculated using Eq.(2):

$$\phi_T = \left(1 - \frac{M_d - M_{sub}}{V_T * \rho_w}\right) * 100 \ (\%) \qquad (2)$$

The effective porosity ϕ_{eff} represents the open

(connected) pores of the sample [20] [21]; and can be determined by using Eq.(3):

$$\phi_{eff} = (1 - \frac{M_{suf} - M_{sub}}{V_T * \rho_w}) * 100 \ (\%) \quad (3)$$

If it is assumed that the tested sample has a bimodal pore system consisting of inter-aggregate (outer-aggregate) and intra-aggregate pores [22] and absorbed water in the water adsorption test fills fully in intra-aggregate pores of aggregates and binders, the porosity of intra-aggregate pore ϕ_{intra} can be calculated using measured water absorption (%):

$$\phi_{intra} = (\frac{M_{suf} - M_d}{V_T * \rho_w}) * 100 \ (\%) \quad (4)$$

where ϕ_{eff} is the effective void (%), ϕ_{intra} is the inter-aggregate porosity, ϕ_T is the total porosity; M_{sub} is the weight of specimen under water (g), M_{suf} is saturated surface dried weight of the specimen (g), M_d is weight of dry sample; ρ_d is dry density (g/cm^3), and V_T volume of specimen (cm^3), G_s is the specific gravity, and ρ_w is the density of water

Hydraulic conductivity is calculated by the following equation, and et-up as shown in Fig. 2 (JIS A 5371-2016 of Japanese standard) [15].

$$K = \frac{t}{\Delta h} * \frac{Q}{A * 30} * \frac{1}{100} \ (\text{mm/s}) \quad (5)$$

where K is hydraulic conductivity (mm/s); t is the thickness of sample (mm), Q is the quantity of water (mm^3), Δ_h is water head difference (mm), A is area of sample (mm^2)

Table 2 Mix proportions of pervious concrete

Aggregate type	Design porosity (%)	Recycled concrete aggregate (RC) kg/m^3	Recycled brick aggregate (RB) kg/m^3	Cement (C) kg/m^3	Water (W) kg/m^3
100%RC	15 (RC15)	1519	0	414	138
	20 (RC20)	1519	0	337	112
	25 (RC25)	1519	0	270	89
100% RB	15 (RB15)	0	1121	414	137
	20 (RB20)	0	1121	337	112
	25 (RB25)	0	1121	268	88
50%RC + 50%RB	15 (M15)	754	565	414	137
	20 (M20)	754	565	337	111
	25 (M25)	754	565	268	88

Fig. 2 Test set-up of water permeability [15]

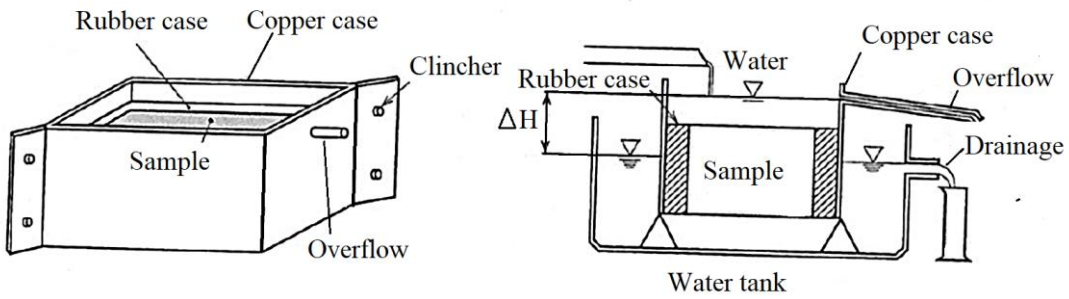

RESULTS AND DISCUSSIONS

Density, compressive and flexural strength

The results of density, compressive strength, and flexural strength tests of pervious concrete are shown in Figure 3. The density of pervious concrete depends on type aggregate and is directly related to the void content of a given mixture, were between 1394 and 1957 kg/m^3, which were lower than that of the conventional concrete (about 2400 - 2500 kg/m^3) due to the high void of pervious concrete. The smallest density of pervious concrete sample was 1394 kg/m3 which using 100% clay brick aggregate (RB) and 25% design porosity was 1394 kg/m^3. The highest density of 1957 kg/m^3 was determined in the sample using 100% concrete aggregate (RC) and 15% design porosity. As the design porosity increases, the density of pervious concrete decreases.

For a given porosity, the compressive strength of pervious concrete using clay brick aggregate (RB) were lower than that of concrete aggregate (RC). These results are also consistent with previous results [8][10]. The compressive strength of pervious concrete using RC and RB varies from 7.5 – 15.5 MPa and 3.5 – 7 MPa, respectively, depending on the design porosity. For example, at 20% designed porosity, the compressive strength of concrete using 100% concrete aggregate and 100% clay brick aggregate were 11.3 MPa and 5.2 MPa, respectively.

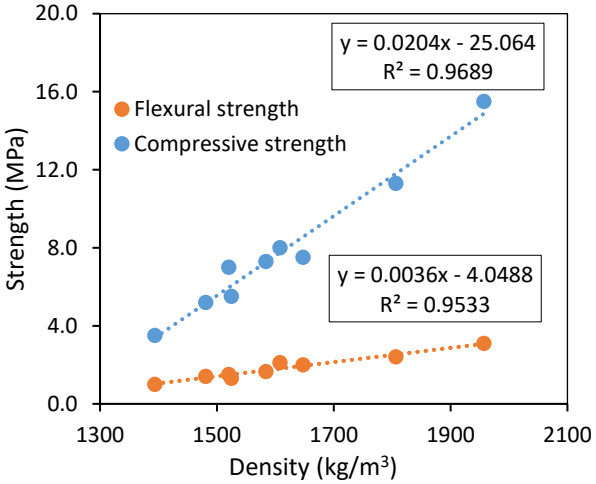

Fig. 3 Relationship between compressive and flexural strength and density.

The same trend was found at the other designed porosity. The highest compressive strength of 15.5 MPa was obtained with 15% designed porosity and using 100% RC, while the concrete sample used 100% RB and 25% designed porosity shows the lowest strength with 3.5 MPa. This result confirms that designed porosity is the most important factor affect to the compressive strength of pervious concrete [23] [24].

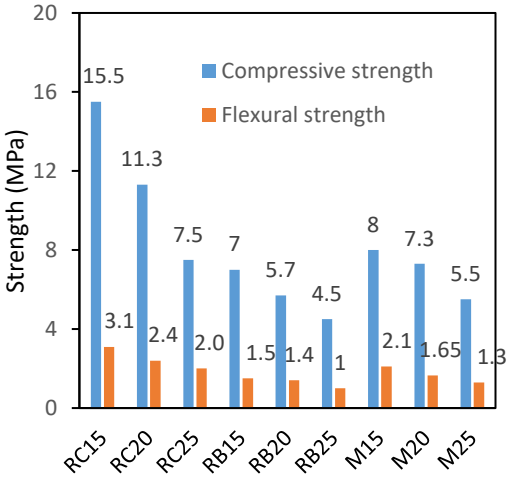

Fig. 4 Compressive and flexural strength of pervious concrete with difference designed porosity

The influence of design porosity on the compressive strength of concrete using brick aggregate is lower than when using concrete aggregate. Specifically, the design porosity increased from 15 to 25%, the compressive strength of concrete using RB decreased from 7 to 4.5 MPa respectively, equivalent to 36%. While that of pervious concrete using RC decreased from 15.5 to 7.5 MPa, equivalent to 52%. This phenomenon can be explained that, due to increasing porosity, the strength of concrete depending more on the aggregate strength and adhesion strength between aggregate and cement paste. With low strength characteristics of RB, almost failures undergo occur due to aggregate breakage. Meanwhile, the strength of pervious concrete using RC is larger than that using RB, and it relies on the adhesion strength of the cement paste and recycled aggregate, which is influenced by the design porosity and attached mortar in RC. The compressive strength of pervious concrete using 50%RB and 50%RC is higher than that of pervious concrete using 100%RB and lower than the case of using 100%RC. The strength of pervious concrete is directly related to the void content and the weakness of the attached mortar in recycled aggregate. Therefore, it leads to a reduction of strength of the pervious concrete. The relationship between density, compressive strength and flexural strength of all specimens is shown in Fig. 3. An increase in density enhanced the strength development of all mixes.

When comparing the effect of aggregate type and design porosity on the compressive strengths, flexural strength within each mix design were quite similar. As shown in Fig. 4, it is obvious that with the increase in the porosity, the flexural strength of the pervious concrete decreases. For example, the flexural strengths of RC15 and RB15 were 3.1 MPa and 1.5 MPa, while those of RC25 and RB25 were 2.0 and 1.0 MPa, respectively.

Void content

The method for determining the porosity of pervious concrete in this research involves a volumetric procedure in which the mass of water filling a sealed pervious concrete sample is converted to an equivalent volume of pores. As shown by the results in Fig. 5, 6, 7, three different porosities values were present: total porosity, effective porosity, and porosity of intra-aggregate pores. The relationship between designed porosity and measured porosity of all specimens is shown in Fig. 5. Thereby, it can be concluded that the total porosity and the effective porosity increase with the increase of designed porosity, while the intra-aggregate pores seem to be unaffected. Unlike smooth round aggregate, pervious concrete using RA often obtains a porosity value greater than the design porosity due to the shape and angles of aggregate [10]. The results show that measured effective porosity is higher than designed porosity (15%, 20% and 25%). In the case of using

brick aggregate RB and mixing aggregate M, the total porosity is significantly higher than the effective porosity and designed porosity. Meanwhile, when using RC aggregates, the total porosity is slightly higher than the design porosity (from 1 to 1.2%). After 24 h of water immersion, the voids in the aggregate have been filled with water due to the water absorption properties of the RC aggregate.

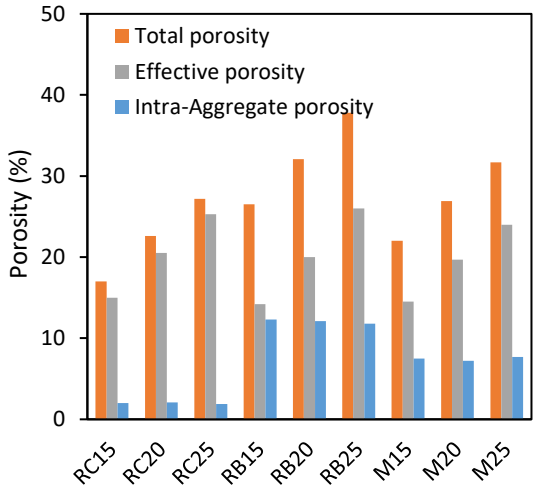

Fig. 5 Total porosity, effective porosity and intra-aggregate porosity with difference designed porosity

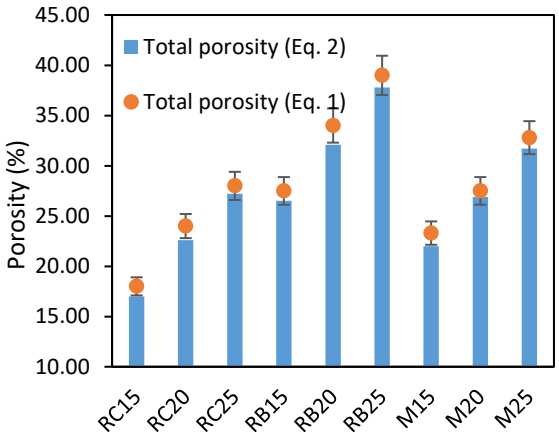

Fig. 6 Total porosity calculated by two different equations

The voids have been filled with water after 24h immersion in water contributing the total porosity. However, intra-aggregate porosity does not contribute to the water permeability properties. Effective porosity excludes intra-aggregate pore and closed voids. The RB25 mix had the highest total porosity of 39%, while the smallest total porosity was 16% for RC15. Samples using blended aggregates (50%RC-50%RB) have a total porosity of 22, 26.9 and 31.7% corresponding to 15%, 20% and 25% designed porosity.

From the experimental test results, Fig. 6 shows the total porosity calculated by two different equations. The total porosity determining by Eq. (1) larger than that of Eq. (2). For example, for a given design porosity of 20%, the total porosity of the pervious concrete samples using concrete aggregate, clay brick aggregate and blended aggregate corresponds to Eq. (1) were 24%, 34%, 27.5%, respectively, while these figures when applying Eq. (2) were 22.6%, 32.1%, 26.9%, respectively. The difference in the two calculation formulas is because Eq. (2) only calculates the total porosity when those voids are filled with water. In fact, after 24 hours of immersing the sample in water, there are still some isolated pores or small capillary tubes along with the air pressure in the pores preventing the water filling completely. Even in the case of soaking longer than 24 hours. With the increase in the porosity, the strength of pervious concrete is reduced.

Figure 8 shows the correlation between compressive strength, porosity and water permeability of pervious concrete. It displays the tendency of compressive strength to decrease when the void ratio increase.

Water permeability coefficient

The pervious concrete mixtures that were expected to have highest permeability rates were those constructed from single-sized aggregates. The permeability of the pervious concrete mixtures is shown in Table 3 and illustrated in Figs. 7 and 8. As with the effective porosity, the trends were opposite to those of the concrete strength.

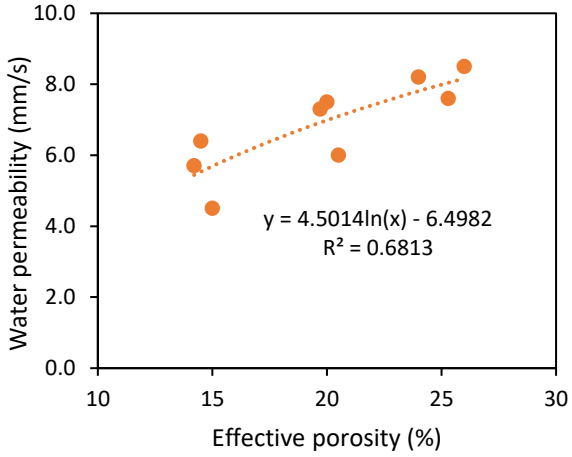

Fig. 7 Relationship between water permeability and effective porosity

The results confirm that the water permeability of pervious concrete rises with an increase in the void ratio. On the other hand, with the increase of total porosity and effective porosity, the compressive, flexural strength decreases. RC15 mixture (using concrete aggregate and 15% designed porosity) has significantly lower hydraulic conductivity than RC25 (25% designed porosity) with 3.5 mm/s and 6.6 mm/s, respectively.

The high values of water permeability coefficients of 5.7– 8.0 mm/s were achieved with pervious concrete using RB aggregate. The water permeability of RC aggregate was lower than that of RB aggregate with 3.5 – 6.6 mm/s. In general, using RB aggregate for pervious concrete can increase the drainage capacity, although the porosity is equivalent to the other aggregate as RC aggregate or mix aggregate. This point was confirmed by Gaedicke [12].

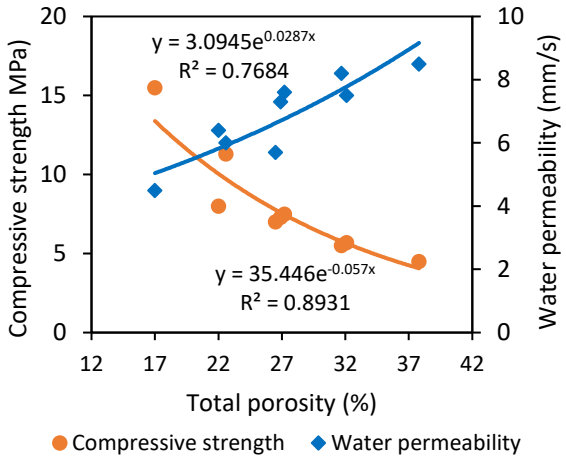

Fig. 8 Relationship among water permeability and compressive strength and total porosity

The explanation for such consequences can be given by the fact that the angular-sized aggregates possess larger shortest paths which have resulted in a higher water permeability coefficient. The level of porosity and permeability at all designed porosity illustrate a slightly decrease with a decrease in the percentage of clay brick content. Thank to light compaction, there is no tendency of brick aggregate was crushed into finer particles, which fills the available void spaces as well as provides better packing of aggregates [8]. For example, for a give designed porosity, water permeability of pervious concrete is 7.5, 7.3 and 6.0 mm/s corresponding to 100%, 50% and 0% clay brick were used.

From the experimental test results, it is understood the relationships among porosity, strength, and permeability for pervious concrete. It is used to estimate the void content needed for mixtures to satisfy the specification requirement for permeability and strength of concrete. By determining the void ratio, it could be possible to obtain proper permeability and compressive strength.

CONCLUSIONS

Based on the experimental investigation on the pervious recycled aggregate concrete, the effects of coarse aggregate types and designed porosity on pervious concrete properties were analyzed. From the test results, the following conclusions could be drawn:

-This study deals with the analysis of porosity and the permeability of pervious concrete using the recycled aggregate from crushed concrete waste (RC) and crushed clay bricks waste (RB). It is clear from the test results that the porous of pervious concrete with brick aggregate shows some different phenomena from that of the recycled concrete aggregate and conventional aggregate.

- The density of pervious concrete mixtures changes from 1394 kg/m^3 to 1957 kg/m^3 as total porosity decreases from 37.8% to 17% when clay brick content in the blended aggregate range from 100% to 0%. Density decreases with an increase of total porosity and decreasing strength of pervious concrete. However, the obtained compressive strengths of 3.5 –15.5 MPa were within the typical strength distribution reported [13] [8]. Linearity can be used to describe the relationship among density, compressive strength and flexural strength, the correlation coefficient reaches 0.97 and 0.95, respectively.

- Porosity is the most important factor determining pervious concrete properties (permeability, compressive strength, flexural strength). Higher porosity improves permeability but decreases the mechanical properties of the samples. The total porosity not only influences in the permeability of the mix, but also illustrating the characteristics of coarse aggregate. The clay brick aggregate and the attached mortar in recycled aggregate contributes significantly to total porosity thank to an intra-aggregate porosity.

- The water permeability, on the other hand, not be affected by intra-aggregate porosity. Effective porosity and shortest paths (connected pores) are a crucial factor to permeability. The use of recycled aggregate had slight effect on permeability depending on compacting method and aggregate angular. In this study, water permeability coefficients of 5.7– 8.0 mm/s and 3.5 – 6.6 mm/s were achieved with pervious concrete using RB and RC aggregate, respectively.

ACKNOWLEDGEMENT

This research was supported by JST-JICA Science and Technology Research Partnership for Sustainable Development (Satreps) project (No. JPMJSA1701) and National University of Civil Engineering (NUCE).

REFERENCES

[1] C. G. da Rocha and M. A. Sattler, “A discussion on the reuse of building components in Brazil: An analysis of major social, economical and legal factors,” Resources, Conservation and Recycling, vol. 54, no. 2, pp. 104–112, Dec. 2009, doi: 10.1016/J.RESCONREC.2009.07.004.

[2] V. W. Y. Tam, M. Soomro, and A. C. J. Evangelista, “A review of recycled aggregate in concrete applications (2000–2017),” Construction

and Building Materials, vol. 172, pp. 272–292, 2018, doi: 10.1016/j.conbuildmat.2018.03.240.

[3] P. Söderholm, "Taxing virgin natural resources: Lessons from aggregates taxation in Europe," Resources, Conservation and Recycling, vol. 55, no. 11, pp. 911–922, Sep. 2011, doi: 10.1016/J.RESCONREC.2011.05.011.

[4] A. M. Arisha, A. R. Gabr, S. M. El-Badawy, and S. A. Shwally, "Performance evaluation of construction and demolition waste materials for pavement construction in Egypt," Journal of Materials in Civil Engineering, vol. 30, no. 2, p. 4017270, 2018.

[5] M. S. Sumanasooriya and N. Neithalath, "Stereology-and Morphology-Based Pore Structure Descriptors of Enhanced Porosity (Pervious) Concretes.," ACI Materials Journal, vol. 106, no. 5, 2009.

[6] J. Huang et al., "Influence of porosity and cement grade on concrete mechanical properties," Advances in concrete construction, vol. 10, no. 5, pp. 393–402, 2020.

[7] A. Ferrari, A. Kubilay, D. Derome, and J. Carmeliet, "The use of permeable and reflective pavements as a potential strategy for urban heat island mitigation," Urban Climate, vol. 31, no. September 2019, p. 100534, Mar. 2020, doi: 10.1016/j.uclim.2019.100534.

[8] B. Debnath and P. P. Sarkar, "Permeability prediction and pore structure feature of pervious concrete using brick as aggregate," Construction and Building Materials, vol. 213, pp. 643–651, 2019, doi: 10.1016/j.conbuildmat.2019.04.099.

[9] K. Ćosić, L. Korat, V. Ducman, and I. Netinger, "Influence of aggregate type and size on properties of pervious concrete," Construction and Building Materials, vol. 78, pp. 69–76, 2015, doi: 10.1016/j.conbuildmat.2014.12.073.

[10] M. Aamer Rafique Bhutta, N. Hasanah, N. Farhayu, M. W. Hussin, M. B. M. Tahir, and J. Mirza, "Properties of porous concrete from waste crushed concrete (recycled aggregate)," Construction and Building Materials, vol. 47, no. February 2018, pp. 1243–1248, 2013, doi: 10.1016/j.conbuildmat.2013.06.022.

[11] M. S. Sumanasooriya and N. Neithalath, "Pore structure features of pervious concretes proportioned for desired porosities and their performance prediction," Cement and Concrete Composites, vol. 33, no. 8, pp. 778–787, 2011, doi: 10.1016/j.cemconcomp.2011.06.002.

[12] C. Gaedicke, A. Marines, L. Mata, and F. Miankodila, "Efecto del uso de materiales reciclados y métodos de compactación en las propiedades mecánicas e índice de reflectancia solar del hormigón permeable," Revista ingeniería de construcción, vol. 30, no. 3, pp. 159–167, 2015, doi: 10.4067/s0718-50732015000300001.

[13] Y. Zaetang, V. Sata, A. Wongsa, and P. Chindaprasirt, "Properties of pervious concrete containing recycled concrete block aggregate and recycled concrete aggregate," Construction and Building Materials, vol. 111, pp. 15–21, 2016, doi: 10.1016/j.conbuildmat.2016.02.060.

[14] P. W. Barnhouse and W. V. Srubar, "Material characterization and hydraulic conductivity modeling of macroporous recycled-aggregate pervious concrete," Construction and Building Materials, vol. 110, pp. 89–97, 2016, doi: 10.1016/j.conbuildmat.2016.02.014.

[15] Japanese Standards Association, "JIS A 5371:2016 - Precast Unreinforced Concrete Products," 2016.

[16] J. X. Lu, X. Yan, P. He, and C. S. Poon, "Sustainable design of pervious concrete using waste glass and recycled concrete aggregate," Journal of Cleaner Production, vol. 234, pp. 1102–1112, 2019, doi: 10.1016/j.jclepro.2019.06.260.

[17] ACI 522.R-10, Report on Pervious Concrete, no. March. 2010.

[18] F. Montes, S. Valavala, and L. M. Haselbach, "A new test method for porosity measurements of portland cement pervious concrete," Journal of ASTM international, vol. 2, no. 1, pp. 1–13, 2005.

[19] ASTM C1754/C1754M-12, "Standard Test Method for Density and Void Content of Hardened Pervious Concrete."

[20] A. A. Ramezanianpour and A. Joshaghani, "Mechanical characteristic of pervious concrete considering the gradation and size of coarse aggregates," Concrete - Innovation and Design: fib Symposium Proceedings, no. May 2017, pp. 152–153, 2015, doi: 10.19026/rjees.6.5255.

[21] H. Liu, G. Luo, H. Wei, and H. Yu, "Strength, permeability, and freeze-thaw durability of pervious concrete with different aggregate sizes, porosities, andwater-binder ratios," Applied Sciences (Switzerland), vol. 8, no. 8, 2018, doi: 10.3390/app8081217.

[22] W. Durner, "Hydraulic conductivity estimation for soils with heterogeneous pore structure," Water Resources Research, vol. 30, no. 2. pp. 211–223, 1994, doi: 10.1029/93WR02676.

[23] Z. Zhang, Y. Zhang, C. Yan, and Y. Liu, "Influence of crushing index on properties of recycled aggregates pervious concrete," Construction and Building Materials, vol. 135, pp. 112–118, 2017.

[24] E. Güneyisi, M. Gesoğlu, Q. Kareem, and S. İpek, "Effect of different substitution of natural aggregate by recycled aggregate on performance characteristics of pervious concrete," Materials and Structures, vol. 49, no. 1, pp. 521–536, 2016.

11th Int. Conf. on Geotechnique, Construction Materials & Environment,
Kyoto, Japan, 3-5 November 2021, ISBN: 978-4-909106063 C3051

ADSORPTION PROPERTIES OF MATERIALS ADSORBING SELECTIVELY ARSENIC FROM AQUEOUS SOLUTIONS CONTAINING MULTIPLE CHEMICAL SPECIES

Ayane Yanaka[1], Yuri Takeshita[2], Keiichiro Shibata[3], Yoshihiro Suenaga[4] and Hidenori Yoshida[4]

[1] Graduate School of Engineering, Kagawa University, Japan; [2] T-NET JAPAN CO., Ltd.; [3] Kajima Corporation, Japan; [4] Faculty of Engineering and Design, Kagawa University, Japan

ABSTRACT

Arsenic contamination has been confirmed in groundwater around the world. In particular, health hazard by arsenic occurs frequently in developing countries such as Bangladesh. In these countries, it is urgent to remove arsenic from water sources such as groundwater from the viewpoint of the security of safe and sufficient drinking water because the population growth is predicted in the future. Especially, inexpensive and simple technology for removing arsenic is required at arsenic-contaminated sites. As a simple method for removing arsenic, the adsorption method is mentioned. However, the adsorption method has two problems. One is that the cost required for the adsorption method is higher than that for other methods, and the other is that it is difficult to adsorb only arsenic selectively when arsenic is mixed with other chemical species. Thus, in this study, the inexpensive adsorbent (improving hydroxyapatite derived from fishbone [Patent No. 6351008 given by Japanese Patent Office], which has a low material cost) for the purpose of removing arsenic is developed, and the effect of other chemical species on the adsorption performance for the arsenic of the adsorbent is examined. In the case of no chemical species mixing (arsenic only), the case of mixing one or more kinds of chemical species, the adsorption test by the shaking test is carried out, and the adsorption performance is evaluated by the adsorption isotherm. From the test results, it is proven that arsenic is selectively adsorbed, even if the chemical species are mixed.

Keywords: Arsenic, Selectively adsorption performance, Chemical species, Adsorbent

INTRODUCTION

In recent years, arsenic contamination in groundwater has been frequently confirmed all over the world. For example, according to the research survey by Ohno et al. [1], it has been found that the arsenic concentration in all wells of the 10 sites in the central area of Nawabganji City in Bangladesh exceeded 0.01 mg/L which is the WHO guideline value (the guideline value) for drinking water quality. In addition, Bretzler et al. [2] reported that 14.6 % of drinking water wells in rural areas of Burkina Faso, West Africa, have arsenic concentrations exceeding the guideline value of 0.01 mg/L. According to this fact, about 560,000 people, one-fifth of 2.8 million people who live in areas with a high risk of arsenic contamination in the rural areas, may be exposed to arsenic-contaminated groundwater. Similarly, arsenic concentrations exceeding the guideline value have been detected in arsenic-contaminated groundwater of other developing countries in Asia and Africa. Additionally, in these countries, there are many patients with chronic arsenic poisoning such as keratosis and skin cancer due to continued intake of arsenic-contaminated groundwater as drinking water as described in [3], [4]. Furthermore, in these countries where the health hazard caused by arsenic contamination is serious, the population growth is predicted in the future, so it is essential to secure safe and sufficient drinking water. Therefore, it is urgent to remove arsenic from water sources such as groundwater.

There are mainly two methods in the current arsenic removal technologies, the aggregation method (coprecipitation method) and the adsorption method. According to Tonokai [5], the coprecipitation method has been used since the 1970s and is the arsenic removal technology generally adopted, since some flocculants used in the coprecipitation method are inexpensive and easily available. However, as shown in [6], a large amount of waste such as excess sludge is generated because a large amount of flocculant is required to reduce the arsenic concentration to the standard value depending on the flocculant used. That is why the disposal of the generated waste is costly. In addition, the coprecipitation method has many problems as follows: it is necessary to secure a large installation area in order to construct treatment facilities and it takes a lot of effort to manage them due to the complexity of the processing equipment, and so on. On the other hand, the adsorption method is a very convenient one compared with other methods for removing arsenic and the large-scale treatment

facilities are not required. However, depending on the adsorbent used, pretreatment such as pH adjustment may be required according to the past study [7]. Additionally, in the adsorption method, the manufacturing cost of the adsorbent is expensive, and the adsorption performance of the adsorbent is strongly affected by the substance (chemical species) which coexists with arsenic in the solution as an adsorption object. It is desirable to adopt a simple method for removing arsenic in addition to low material costs in developing countries in Asia and Africa where arsenic contamination is serious. When the adsorption method is selected with an emphasis on simplicity, the following three are required for the adsorbent. The first is that the adsorbent is cheap, the second is that the pretreatment is unnecessary in the adsorption treatment, and the third is that it has the adsorption performance which is not affected by other chemical species which coexists with arsenic. According to [1], [2], [8], [9], it is clarified that sodium (Na), magnesium (Mg), potassium (K), calcium (Ca), manganese (Mn), iron (Fe), bicarbonate ion (HCO_3), sulfate ion (SO_4) and nitrate ion (NO_3) are contained in a relatively high concentration as chemical species coexisting with arsenic in the groundwater of developing countries in Asia and Africa where arsenic contamination has been confirmed.

Therefore, in this study, an inexpensive adsorbent for the removal of arsenic is developed by improving low-cost fishbone hydroxyapatite [Patent No. 6351008 given by Japanese Patent Office]. At the same time, the effect of other chemical species (Na, Mg, K, Ca, Mn, Fe, HCO_3, SO_4, and NO_3) coexisting with arsenic on the adsorption performance for arsenic is investigated.

ADSORPTION TEST (SHAKING TEST)

The selective adsorption properties of the developed arsenic adsorbent (Functional Fishbone Powder, FFP) for arsenic in the solution containing not only arsenic but also other chemical species are verified. Therefore, the adsorption test by the shaking test is carried out in the case of no chemical species mixing (arsenic (As) only), the case of mixing one kind of chemical species, and the case of mixing multiple kinds of chemical species assuming the water quality in the actual arsenic contamination site. After that, the adsorption performance of the FFP for arsenic is evaluated based on the adsorption isotherm.

In the test, an arsenic standard solution (As_2O_3・NaCl (0.05%) ・HCl acidic solution) is used. First, the arsenic standard solution is prepared to seven initial concentrations (3 ppm, 4 ppm, 5 ppm, 6 ppm, 7 ppm, 30 ppm, 60 ppm), and the prepared solutions are mixed with a chemical species (one type or multiple types) set to a predetermined concentration. This prepares simulated solutions. Next, 10 mL of the simulated solution is poured into a centrifuge tube to which 20 mg of FFP is added. These are the specimens in the test. Then, these specimens are shaken for 24 hours at 200 rpm at a temperature of 20 °C. After that, the solutions are centrifuged at 2000 rpm for 3 minutes, and the residual concentration of arsenic in the solutions is analyzed by an ICP-AES.

Here, Table 1 shows the chemical species detected in the arsenic-contaminated areas of developing countries as mentioned above in Asia and Africa and their concentrations. Each concentration shown in Table 1 is the average value of the concentration in each chemical species listed in [1], [2], [8], [9]. In this study, 9 types of chemical species listed in Table 1 and their corresponding concentrations are adopted as test conditions. Regarding 9 types of chemical species, chloride-based solutions (sodium chloride solution, magnesium chloride solution, potassium chloride solution, calcium chloride solution, manganese chloride solution and iron chloride solution) are used for cation (Na, Mg, K, Ca, Mn, Fe), and sodium-based solutions (sodium bicarbonate solution, sodium sulfate solution and sodium nitrate solution) are used for anion (HCO_3, SO_4, NO_3). In addition, in the test with mixed multiple chemical species, a typical three types of water quality that have been confirmed in arsenic-contaminated areas of the developing countries in Asia and Africa are assumed. Table 2

Table 1 The concentration of each chemical species

Chemical species	Concentration (mg/L)
Na	491.7
Mg	30.9
K	5.5
Ca	56.1
Mn	241.7×10^{-3}
Fe	1.6
HCO_3	267.7
SO_4	1371.3
NO_3	19.3

Table 2 The combination of chemical species

Sample1	Sample2	Sample3
Mn, Fe, HCO_3	Na, Mg, K, Ca, HCO_3, SO_4, NO_3	Na, Mg, K, Ca, Mn, Fe, HCO_3, SO_4, NO_3

shows the combinations of chemical species in each water quality.

In the study, the adsorbed amount per unit mass of the FFP is employed as the evaluation of the test results. The adsorbed amount per unit mass of the FFP is defined by the following equation (1).

$$W_i(mg/g) = \frac{V(C_o - C_i)}{M_i} \quad (1)$$

where, "V" is the amount of the solution, "C_o" is the initial concentration of the solution, "C_i" is the residual concentration (equilibrium concentration) after the tests and "M_i" is the mass of the FFP. In order to ensure reproducibility, the mean value of three tests is adopted as a test result. In addition, the test results are applied to the Langmuir model so as to clarify the adsorption mechanism of the adsorbent for arsenic. The Langmuir model is typical adsorption equilibrium equations in liquid-phase adsorption. The Langmuir model is defined by the following equation (2).

$$\frac{C_i}{W_i} = \frac{1}{aW_s} + \frac{1}{W_s}C_i \quad (2)$$

where, "a" is the adsorption equilibrium constant and "W_s" is the amount of saturation adsorption.

ADSORPTION TEST RESULTS

In the case of mixing one chemical species, the adsorption isotherms plotted the test results obtained from the shaking tests are shown in Fig. 1 (cation, Na and K), Fig. 2 (cation, Mg and Ca), Fig. 3 (cation, Fe and Mn) and Fig. 4 (anion), respectively. In addition, Table 3 shows the coefficient of determination obtained by applying the results of shaking tests with one chemical species to the Langmuir model. The horizontal and vertical axes in Fig. 1 to Fig. 4 are the equilibrium concentration of As, and the equilibrium concentration divided by the adsorbed amount (C/W), respectively. The adsorption isotherm, as described in [10], indicates the relationship between the solute concentration in equilibrium under certain temperature conditions and the adsorbed amount at that time. The adsorption isotherm shows various types of curves depending on the combination of the adsorbent (refers to FFP in this study) and the adsorbate (a substance to be adsorbed, refers to As in this study). Its shape shows how As is adsorbed to FFP, i.e., the physical or chemical interaction between FFP and As. The adsorption isotherms obtained by plotting the residual concentration (equilibrium concentration) of the solute analyzed after the adsorption test on the horizontal axis and the adsorbed amount per unit mass of FFP on the vertical axis are in three patterns. One is that the adsorbed amount increases logarithmically as the equilibrium concentration increases, i.e., an upward convex curve, another is that the adsorbed amount increases exponentially as the equilibrium concentration increases, i.e., a downward convex curve, and the other is that a linear relationship exists between the equilibrium concentration and the adsorbed amount, i.e., a straight line which tends to rise to the right. The upward convex curve indicates that an attractive force acting between the FFP surface and As promotes adsorption of As by FFP, while the downward convex curve indicates that the attractive force which acts between the FFP surface and As is weak. Additionally, when a linear relationship is established between the equilibrium concentration and the adsorbed amount, it means the adsorption of As by FFP from a very dilute solution, which indicates the competitive adsorption of the solvent and As on the FFP surface. On the other hand, the Langmuir model expresses whether the adsorption mode is monolayer adsorption or not. The applicability of the Langmuir model depends on whether there is a linear relationship between the equilibrium concentration of As and the value of equilibrium concentration divided by the adsorbed amount of As.

Fig. 1 to Fig. 4 indicate that the adsorption isotherm shows an upward convex curve in mixing any one kind of chemical species, although the adsorbed amount is inferior to the case without chemical species. From this, it can be said that an attractive force acting between the FFP surface and As promotes adsorption of As by FFP. In addition, the coefficient of determination R^2 listed in Table 3 shows high values of 0.9 or more in each case. From these results, it is considered that the adsorption mode of FFP for As is monolayer adsorption and that As is chemically adsorbed on the FFP surface (such as chemical bonding), even when no chemical species (As only) or one kind of chemical species is mixed.

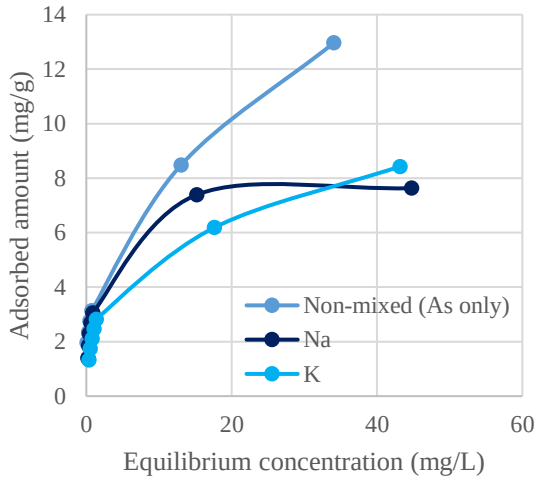

Fig. 1 Adsorption isotherm (Mixing one chemical species (Na, K))

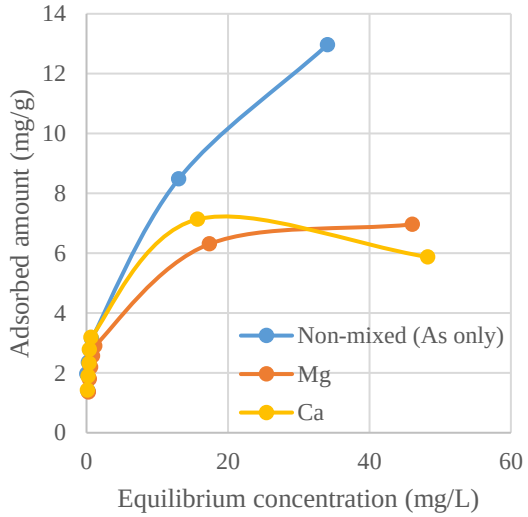

Fig. 2 Adsorption isotherm (Mixing one chemical species (Mg, Ca))

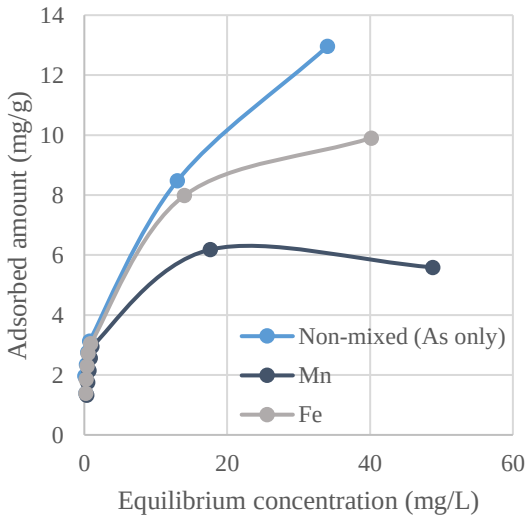

Fig. 3 Adsorption isotherm (Mixing one chemical species (Mn, Fe))

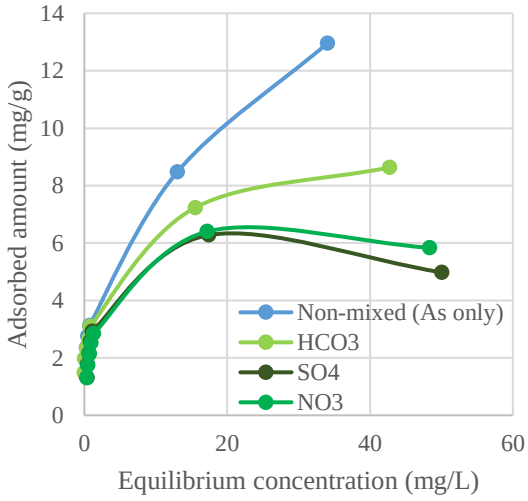

Fig. 4 Adsorption isotherm (Mixing one chemical species (Anion))

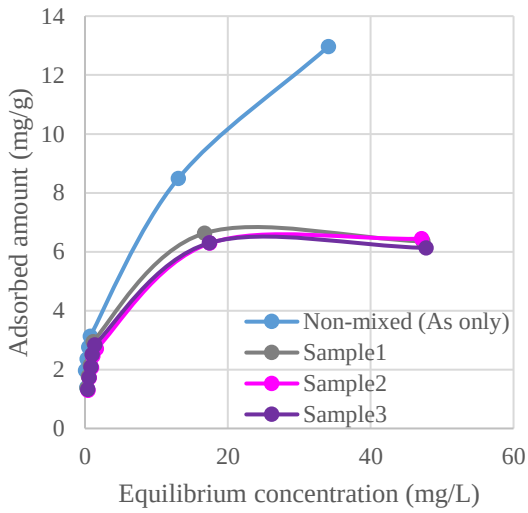

Fig. 5 Adsorption isotherm (Mixing multiple chemical species)

Table 3 Coefficient of determination obtained by appling test results to the Langmuir model (Mixing one chemical species)

Chemical species	R^2
Non-mixed (As only)	0.9977
Na	0.9699
Mg	0.9164
K	0.9176
Ca	0.9534
Mn	0.9019
Fe	0.9892
HCO_3	0.9641
SO_4	0.9064
NO_3	0.9193

Table 4 Coefficient of determination obtained by appling test results to the Langmuir model (Mixing multiple chemical species)

Chemical species	R^2
Non-mixed (As only)	0.9977
Sample1	0.9341
Sample2	0.9154
Sample3	0.9135

On the other hand, it can be seen that the coefficient of determination R^2 in the case of mixing K, Mg, Mn, SO_4 or NO_3 respectively is lower than that in the case of no chemical species mixing (As only) (< 0.95). These results suggest that the chemical species of Mg, K, Mn, SO_4 and NO_3 may affect the adsorption performance of FFP for As. Further examinations are needed to gain clearer insights into the effect of these chemical species on the adsorption performance of FFP for As.

In the case of mixing multiple chemical species, the adsorption isotherms plotted the test results obtained from the shaking tests are shown in Fig. 5, and the coefficient of determination obtained by applying the test results to the Langmuir model is shown in Table 4. The horizontal and vertical axes of Fig. 5 are the same as those of Fig. 1 to Fig. 4. Similar to Fig. 1 to Fig. 4, Fig. 5 indicates that the adsorption isotherm shows an upward convex curve in any combination patterns of chemical species, although the adsorbed amount is inferior to the case without chemical species. In addition, the coefficients of determination R^2 listed in Table 4 as well as those listed in Table 3 show high values of 0.9 or more in each case. However, it is found that the coefficient of determination R^2 in the case of mixing multiple chemical species is lower when more than one chemical species is mixed in any combination pattern of chemical species than when no chemical species is mixed (As only). Since the coefficient of determination R^2 decreases as the number of chemical species increases, the adsorption performance of FFP for As may be affected by the number of chemical species.

CONCLUSIONS

In this study, the selective adsorption property of FFP for arsenic was verified in the solution containing not only arsenic but also other chemical species (Na, Mg, K, Ca, Mn, Fe, HCO_3, SO_4 and NO_3). Concretely, the adsorption test by the shaking test was carried out in the case in which arsenic alone was mixed, the case in which one kind of chemical species was mixed except for arsenic, and the case in which multiple kinds of chemical species were mixed on the assumption of the water quality in an actual arsenic contamination field. The adsorption performance of FFP for arsenic was evaluated based on the adsorption isotherms obtained from the test results. The results obtained are as follows.

- In the case of mixing one or more kinds of chemical species, the adsorption isotherm showed an upward convex curve in mixing either kind of chemical species, though the adsorbed amount of arsenic was a little inferior to the case in which only arsenic was mixed.
- FFP has an adsorption performance for arsenic even without the addition of acid or alkali. Therefore, it can be an adsorbent which utilizable safely. In addition, it is an environmentally friendly adsorbent because FFP is developed using fishbone, which is food waste.
- From the value of the coefficient of determination R^2 obtained by applying the results of shaking tests to the Langmuir model, it is considered that the chemical species of K, Mg, Mn, SO_4 and NO_3 may affect the adsorption performance of FFP for arsenic. Further examinations are needed to gain clearer insights into the effect of these chemical species on the adsorption performance of FFP for arsenic.

From these results, in order to clarify the effect of the chemical species of K, Mg, Mn, SO_4 and NO_3 on the adsorption performance of FFP for arsenic, it is necessary to analyze the changes in the concentration of K, Mg, Mn, SO_4 or NO_3 respectively when the arsenic adsorption test is conducted in the case of mixing each chemical species and verify how much chemical species are adsorbed on FFP. Additionally, it is needed to carry out an adsorption test in which the concentration of mixed chemical species (K, Mg, Mn, SO_4 and NO_3) is changed.

ACKNOWLEDGMENTS

This work has been supported by JSPS KAKENHI Grant Number JP20K04684. Also, in carrying out this study, Nihon Kogyo Co., Ltd. provided FbP. We express our gratitude here.

REFERENCES

[1] Ohno K., Furukawa A., Hayashi K., Kamei T. and Magara Y., Relation between arsenic and other metals and ions in groundwater in Bangladesh, Environmental Engineering Research, Vol. 41, 2004, pp. 591-600.
[2] Bretzler A., Lalanne F., Nikiema J., Podgorski J., Pfenninger N., Berg M. and Schirmer M., Groundwater arsenic contamination in Burkina Faso, West Africa: Predicting and verifying regions at risk, Science of the Total Environment, Vol. 584-585, 2017, pp. 958-970.
[3] Ando M., Arsenic contamination of ground water in India and Bangladesh and its health effect, Journal of the National Institute of Public Hearth, Vol. 49, No. 3, 2000, pp. 266-274.
[4] Mazumder. D. N., Ghosh A., Majumgar K. K., Ghosh N., Saha C. and Mazumder N. R., Arsenic Contamination of Grand Water and its Health Impact on Population of Distinct of Nadia, West Bengal, India, Indian Journal of Community Medicine, Vol. 35, Issue 2, 2010, pp. 331-338.
[5] Tonokai K., Method of purification of arsenic contaminated groundwater, Global Environment,

Vol. 22, No. 1, 2017, pp. 91-98.
[6] Uyama H., Shan J. and Yano T., Development of Secure and Convenient Remediation Technology for Arsenic-contaminated Water, Manufacturing & Technology, Vol. 60, No. 3, 2008, pp. 81-84.
[7] Yanagida T., Jiang Y. and Nakamura M., Arsenic Adsorption Properties of New Iron Hydroxide, Journal of Japan Society on Water Environment, Vol. 36, No. 5, 2013, pp. 149-155.
[8] Berg M., Stengel C., Trang K. T. P., Hung V. P., Sampson L. M., Leng M., Samreth S. and Fredricks D., Magnitude of arsenic pollution in the Mekong and Red River Deltas – Cambodia and Vietnam, Science of the Total Environment, Vol. 372, Issue 2-3, 2007, pp. 413-425.
[9] Malana A. M. and Khosa A. M., Groundwater pollution with special focus on arsenic, Dera Ghazi Khan-Pakistan, Journal of Saudi Chemical Society, Vol. 15, Issue 1, 2011, pp. 39-47.
[10] Abe I., Chemistry of Adsorption, Oreo Science, Vol. 2, No. 5, 2002, pp. 275-281.

11th Int. Conf. on Geotechnique, Construction Materials & Environment,
Kyoto, Japan, 3-5 November 2021, ISBN: 978-4-909106063 C3051

EFFECT OF SCREW ON THE AXIAL PERFORMANCE OF COLD-FORMED STEEL

Desy Setyowulan[1], Eva Arifi[2], Devi Nuralinah[3], and Edwardo Pradana A.N.[4]

[1,2,3,4]Engineering, Universitas Brawijaya, Indonesia

ABSTRACT

Along with the development of the construction world in Indonesia, the use of cold-formed steel (CFS) as a construction material is also increasing. The connection is an important element that must be considered in this type of material. Structural elements that are joined experience stress concentration around the hole resulting in a change of the behavior of structure that becomes more complex. To predict the failure mode of the connection section, this study conducted an experimental test to study the capacity of cold-formed steel against tensile loads. The test specimens used in this study is canal type which is usually used as material construction, with three different configuration of screw positions. Effect of screw will be compared with original model without screw. Main failure modes for all types of screw connection are categorized by tilting and pull-out failure. Increasing space between screw will also increase the maximum load by 6.67% and 10.81% for connection with three and four screws, respectively. In addition, the specimens with one and four screw connection have an average extension which was 300% larger than that of without screw.

Keywords: *Axial Performance, Cold Formed Steel, Connection, Screw, Failure model*

INTRODUCTION

Nowadays, steel has become one of the most widely used construction materials around the world. The use of steel material will be effective in reducing the consumption of cement as the main binder of concrete. It means that the air pollution due to CO2 emissions will be reduced to realize the concept of green building and sustainable construction in Indonesia. Structural engineering applications of cold-formed steel is increasing steadily. Many advantages can be achieved by using this material in building construction, such as easily assembled into a wide range of structural and architectural forms, easily assembled and modified on site, Efficient use of material leads to competitive construction and to save in material costs, etc. However, the used of thin-walled sections and cold-forming manufacturing effects can results in special design problems, such as buckling strength (including local, global, distortional, shear), torsional rigidity, web crippling, ductility and plastic design, connections, fire resistance, and corrosion [1].

Many researches have been undertaken related to the behavior of cold-rolled steel in order to improve its design problem, such as numerical and experimental study related to the axial capacity, flexural capacity, and connection [2, 3, 4].

Connections are the critical components in cold-formed steel structures. Review on cold-formed steel connections is investigated [5]. The performance of screw connections, storage crack connections, welded connections, and bolted connection were discussed. From this review, it was concluded that screw is a common type of connections that is used due to the thinness of CFS sections. In addition, a review on CFS frame connection was also studied previously [6]. Based on the review assessment, the results highlighted that all types of connections except adhesive connections have shown the proper behavior that can trigger the change of any design codes.

The failure modes of connections were investigated by researchers. The results have shown that screwed CFS connections can be subjected to similar fracture and different moment–rotation capacities under loading [7]. An experimental investigation and FEA of CFS bolted connections with single and multiple bolts under shear loading were investigated [8]. The comparison results show that current AISI (2012) design provisions for the CFS provides the safe bearing resistances for the bolted connections with washers on oversized holes in single bolted, double bolted and quadruple bolted connections.

This study conducted an experimental test to study the axial performance of cold-formed steel connections with different screw configurations, including the capacity and failure modes of each model test. The results of this study will be used as the basis for analyzing whether the formulations in Indonesian Standard of 7971: 2013 are in accordance with the real conditions of using cold-formed steel profiles in the market.

METHODS

Experimental model of CFS connection with screw configurations are shown in Fig. 1. In this analysis, we used three different screw configurations. The block shear behaviors of double-shear screw connections fabricated with CFS were planned to investigated.

The common dimension for specimens is in the following; screw diameter *d* was 4 mm, thickness for each specimen of 0.6 mm, and space between each screw was determined by 4*d* and 5*d*. Each configuration has three specimens. The total length for specimen without connection as shown in Figure 1(a) was 200 mm, and for other specimens were 250 mm, as shown in Figure 1(b, c, d). The detail dimension for specimen without connection were 50 mm, 12.7 mm, 12.5 mm, 200 mm, 57 mm, 60 mm, and 20 mm for G, W, R, L, A, B, C, respectively. As shown in the configuration and assembly of test specimen of Figure 1, the specimen consist of two coupling CFS plate in the connection with length is adjusted to the space used between the plate.

The tensile strength test procedure was determined based on Indonesian National Standard (SNI 7971:2013), as shown in Fig. 2. The external tensile load was produced by Universal Testing Machine, which increased gradually until failure of each specimen. It indicated that the specimens cannot withstand the external load.

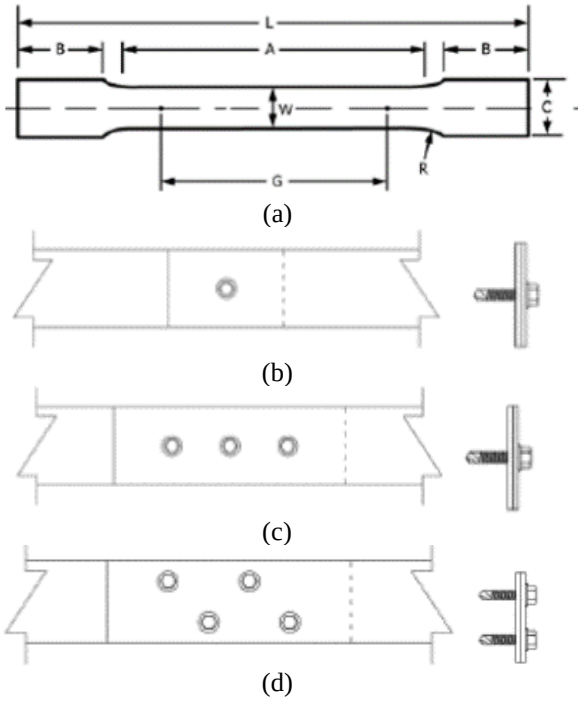

Fig. 1. Configuration and assembly of test specimen; (a) without connection, (b) 1 screw, (c) 3 screws, and (d) 4 screws.

RESULTS AND DISCUSSIONS

Tensile Testing Stages

The tensile testing stage for CFS with a screw connection is shown in Fig. 2. In this figure, the tensile testing stage can be seen clearly. These stages include the initial condition, balanced level before loading, tilting failure, and pull-out failure. When two materials of the same thickness are screwed together, or when the thicker material is against the screw head, tilting failure occurs [9]. Hancook [10] illustrates this shortcoming in Fig. 3.

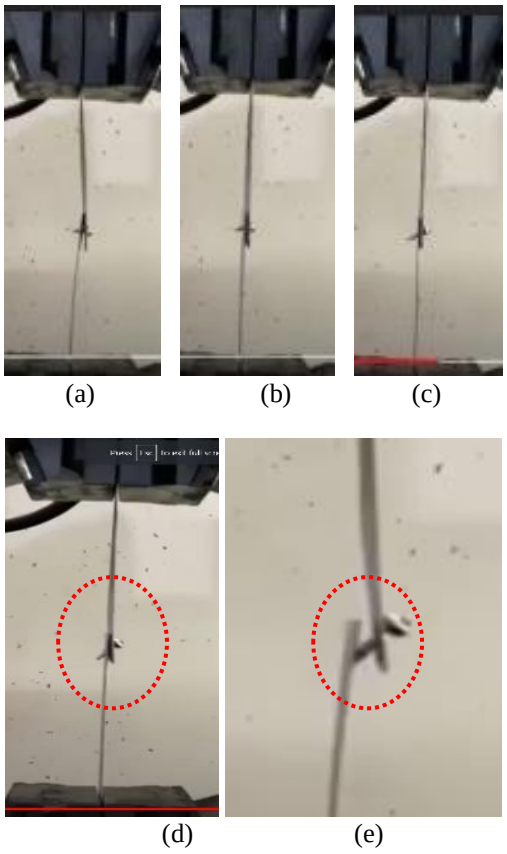

Fig. 2. Tensile testing stage for CFS using screw connections, including (a) initial condition, (b) balanced level, (c) and (d) tilting failure, (e) pull out failure
Source: Author's documentation, 2021

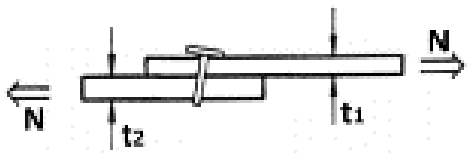

Figure 3. Tilting failure of screwed connections [10]

Failure Modes

Effect of edge distance and screw spacing to the failure modes of CFS connection were investigated, as shown in Fig. 4.

(a) Without connection

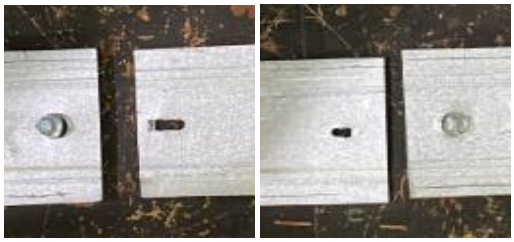

(b) One screw (4d) (c) One screw (5d)

(d) Three screws (4d)

(e) Three screws (5d)

(f) Four screws (4d)

(g) Four screws (5d)

Fig. 4. Failure modes for tensile specimens without connection

Previous study has shown that the end distance of 3d is enough to avoid the tear out failure for the stainless-steel bolted connections [11]. In this study, we used the space of 4d and 5d in accordance with SNI 7971:2013 with the minimum spacing should be ≥ 3d.

The main failure modes for all types of screw connection are categorized by tilting and pull-out failure. For the specimen without connection, fracture occur. This type of failure produces stretching of the hole on one side of the screw, while the plate is bunched together on the other side of screw. Because of the commonly thickness of CFS, Rogers and Hancook [12] demonstrated that using washers under the bolt head and nut can considerably boost a connection's resilience to bearing failure.

Maximum Load

Different variation for screw configuration number gives an impact to the maximum axial load, as shown in Table 1. From these results, it could be depicted that the average maximum load for tensile test without connections are similar with connection in one screw, shown as 6000 N. Increasing space between screw will also increase the maximum load by 6.67% and 10.81% for connection with three and four screws, respectively.

Table 1. Maximum load

No.	Specimens	Max Load (N)	Average Load (N)
Without connection	A	5.000	6.000
	B	7.000	
	C	6.000	
1 screw (4DF)	A	8.000	6.667
	B	8.000	
	C	4.000	
1 screw (5DF)	A	5.000	6.000
	B	7.000	
	C	6.000	
3 screws (4DF)	A	5.000	4.667
	B	5.000	
	C	4.000	
3 screws (5DF)	A	3.000	5.000
	B	6.000	
	C	6.000	
4 screws (4DF)	A	11.000	11.000
	B	10.000	
	C	12.000	
4 screws (5DF)	A	11.000	12.333
	B	12.000	
	C	14.000	

Load-extension Curve

Table 2 depicted the extension for each specimen. According to this data, connection with one screw and 4 screws have a similar result of 21 mm. Furthermore, minimum result occurs for specimen control without connection of 5 mm. The specimens with one and four screw connection have an average extension which was 300% larger than that of without screw. This capacity was limited by the shear capacity of the screw.

A load-extension curve for one screw connection is illustrated in Figure 5. The larger space (5d) shows a less ductile failure compared the smaller space (4d).

Table 2. Maximum extension for specimens

No.	Specimens	Max Extension (mm)	Average Extension (mm)
Without connection	A	4	5
	B	7	
	C	4	
1 screw (4DF)	A	25	20
	B	19	
	C	16	
1 screw (5DF)	A	23	22
	B	20	
	C	24	
3 screws (4DF)	A	19	16
	B	15	
	C	15	
3 screws (5DF)	A	15	18
	B	20	
	C	20	
4 screws (4DF)	A	18	21
	B	28	
	C	17	
4 screws (5DF)	A	21	21
	B	20	
	C	23	

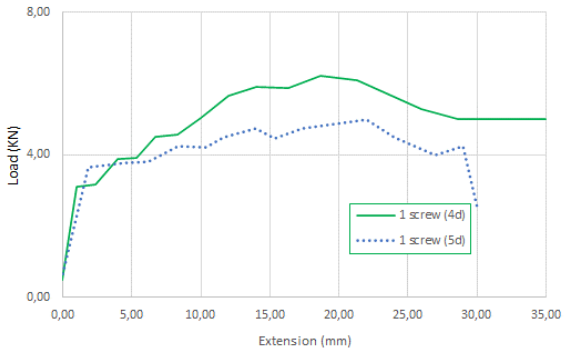

Figure 5. Load-extension curve

CONCLUSIONS

This study used an experimental test to determine the capacity of cold-formed steel against tensile loads in order to anticipate the failure mechanism of the connection section. The test specimens in this study were canal type, which is commonly utilized as a material construction, and had three distinct screw configurations. The screw's effect will be compared to the original model without the screw.

The following conclusions can be drawn from this research:

1. Tilting and pull-out failure are the most common failure modes for all types of screw connections.
2. For connections with three and four screws, increasing the spacing between screws increases the maximum load by 6.67% and 10.81%, respectively.
3. The specimens with one and four screws have an average extension that is 300 percent greater than the ones without screws.

ACKNOWLEDGMENTS

The authors greatly indebt to “BPPM FTUB” (Research and Community Service Agency, Faculty of Engineering, Universitas Brawijaya) for providing financial support through this research. Special thanks to the Civil Engineering Department, Universitas Brawijaya, for supporting this opportunity.

CITATION AND REFERENCE LIST

[1]. Dubina, D., Ungureanu, V., Landolfo, R. (2012). Design of Cold-formed Steel Structures, Eurocode 3: Design of Steel Structures, Part 1-3: Design of Cold-formed Steel Structures. Wiley-Blackwell, Ernst & Shon (A Wiley Company), Portugal.

[2]. Pandey, M., Young, B. (2020). Structural performance of cold-formed high strength steel tubular X-Joints under brace axial compression. Engineering Structures, Vol. 201.

[3]. Nandhakumar, C.S., Ramesh, R., Sreevidya, V. (2020). Investigation of cold formed steel beam subjected to torsion. Materials Today: Proceedings, Vol. 21, pp. 425-429.

[4]. Ye, J., Hajirasouliha, I., Becque, J. (2018). Experimental investigation of local-flexural interactive buckling of cold-formed steel channel columns. Thin-Walled Structures, Vol. 125, pp. 245-258.

[5]. Lee, Y.H., Tan, C.S., Mohammad, S., Tahir, M.Md., Shek, P.N. (2014). Review on Cold-

Formed Steel Connections. Hindawi, Article ID 951216, pp. 1-11.

[6]. Komara, I., Wahyuni, E., Suprobo, P. (2017). A Study on Cold-Formed Steel Frame Connection: A Review. The Journal for Technology and Science, Vol. 28, Issue 3, pp. 83-89.

[7]. Maali, M., Sagiroglu, M., Solak, M.S. (2015). Experimental Behavior of Screwed Beam-to-Column Connections in Cold-Formed Steel Frames. Arabian Journal of Geosciences, Vol. 11: 205.

[8]. Konkong, N. (2017). An Investigation of the Ultimate Strength of Cold-Formed Steel Bolted Connections. Engineering, Technology & Applied Science Research, Vol. 7, No. 4, pp. 1826-1832.

[9]. Zeynalian, M., Shelley, A., Ronagh, H.R. (2016). An experimental study into the capacity of cold-formed steel truss connections. Journal of Constructional Steel Reearch, Vol. 127, pp. 176-186.

[10]. Hancock, G.J. (1998). Design of Cold-formed Steel Structures: To Australian/New Zealand Standard As/NZS 4600: 1996. Australian Institute of Steel Construction.

[11]. Salih, E.L., Gardner, L., Nethercot, D.A. (2011). Bearing failure in stainless steel bolted connections. Engineering Structures, Vol. 33, Issue 2, pp. 549-562.

[12]. Rogers, C.A., Hancook, G.J. (1999). Screwed connection tests of thin G550 and G300 sheet steel. J. Struct. Eng., 125.

11th Int. Conf. on Geotechnique, Construction Materials & Environment,
Kyoto, Japan, 3-5 November 2021, ISBN: 978-4-909106063 C3051

PERFORMANCE OF INTERLOCKING BRICK WALLS AGAINST OUT-OF-PLANE EXCITATION

Aiko Furukawa[1], Johanes Jefry Prasetyo[2] and Junji Kiyono[1]

[1]Department of Urban Management, Kyoto University, Japan; [2]Pacific Consultants CO., LTD., Japan

ABSTRACT

Masonry structure is one of the most commonly used building types in developing countries due to its inexpensiveness and material availability. While masonry structure is intrinsically strong in resisting gravitational force, it is relatively weak in resisting lateral forces such as an earthquake. Therefore, reinforcement for masonry structures in earthquake-prone areas is necessary. This paper introduced an interlocking brick as one of the promising reinforcement methods for masonry structure as it does not require extra material and easy to implement. The performance of a lego-shaped interlocking brick in resisting dynamic lateral forces was investigated through 2-dimensional dynamic finite element analysis. The created lego-shaped interlocking brick wall was analyzed under the out-of-plane dynamic loading. Its performance was compared with the performance of the rectangular brick wall. The analysis results showed that the lego-shaped interlocking brick wall had better performance in resisting out-of-plane loading than the rectangular brick wall since the blocks interlock each other.

Keywords: Interlocking brick, Rectangular brick, Out-of-plane excitation, Dynamic finite element analysis

INTRODUCTION

Masonry structures are one of the most commonly used building types in developing countries due to their inexpensiveness and accessibility as construction material. While masonry structure is intrinsically strong under gravitational load, it is weak against lateral forces such as an earthquake. Historically, the collapses of structures due to earthquakes account for almost 75% of the earthquake fatalities [1], and the collapse of masonry structures accounts for a large number of fatalities among them [2]. Masonry structures are still commonly used in earthquake-prone areas in developing countries because they are inexpensive and easy to construct. To reduce causalities due to the collapse of the masonry structures in developing countries, reinforcing the masonry structure is deemed necessary.

The usage of steel reinforcing bars for masonry structures is one of the most commonly used reinforcement methods in developed countries. Its application, however, is not always easy in developing countries due to the lack of resources and knowledge [3]. Consequently, reinforcement methods for masonry structure which are cost-efficient and easy to implement are much preferable.

In the past several years, many kinds of research on the reinforcement of masonry structures have been conducted. Among them, reinforcement methods by utilizing vertical steel ties [4], fiber-reinforced plastic [5], tires [6] (as a tensioned material), and PP bands [7] are some of the examples which are easy to implement, and utilizing readily available materials, but require additional reinforcing material.

In this study, a reinforcing method that does not require reinforcing materials is considered for masonry structures. The method uses interlocking bricks instead of regular rectangular bricks. Interlocking bricks are bricks that utilize an interlocking system to reinforce against loading. When a joint failure occurs in a rectangular brick wall, the external force is resisted by only friction force (Fig.1(a)). In comparison, when a joint failure occurs in an interlocking brick wall, the external force is resisted by both friction force and the interlocking mechanism (Fig. 1(b)). By utilizing this concept, the interlocking brick is assumed to be able to reinforce masonry structures. Additional benefits of this method are that it does not require additional reinforcement material and easy to implement.

Researches on the performance of interlocking bricks against earthquake have been conducted [8-11]. Research [11] showed that interlocking bricks could reinforce masonry walls against the in-plane static lateral load. However, since earthquakes are dynamic loads, which also act in the out-of-plane direction, research on interlocking bricks' performance against dynamic lateral load in the out-of-plane direction is necessary. However, such researches have not been

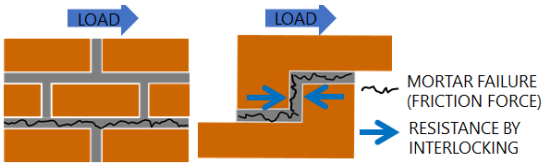

(a)Rectangular brick (b)Interlocking brick

Fig.1 Difference in the resistance mechanism against lateral load between rectangular and interlocking brick walls

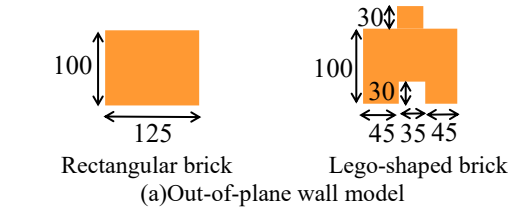

(a)Out-of-plane wall model

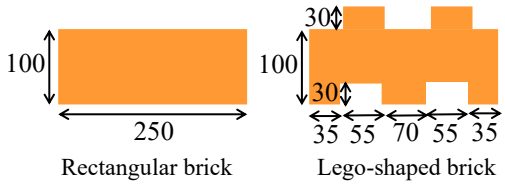

(b) Out-of-plane two-wall model

Fig.2 Assumed bricks (unit: mm)

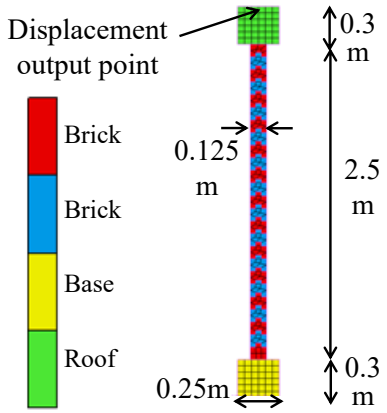

(a)Out-of-plane wall model

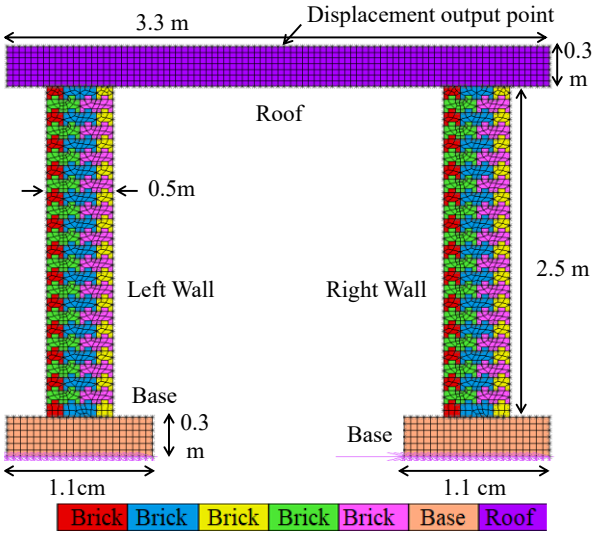

(b) Out-of-plane two-wall model

Fig.3 Wall models made of lego-shaped bricks

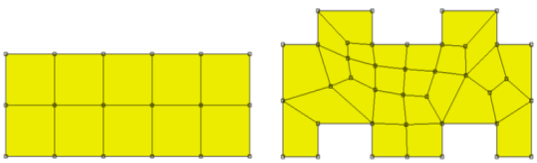

(a)Rectangular brick (b)Lego-shaped brick

Fig.4 Division of brick into elements

conducted yet. With this background, this paper aims to investigate the performance of interlocking bricks in resisting out-of-plane lateral excitation through the dynamic finite element analysis.

ANALYSIS CONDITIONS

Analysis models

In this study, two-dimensional dynamic analysis of masonry walls was performed using the general-purpose finite element analysis software, MSC Marc [12].

There are four analysis models, two one-wall models, and two two-wall models. Two one-wall models and two two-wall models are divided into a rectangular brick type and an interlocking wall type.

Dimensions of bricks for each model are shown in Fig. 2. Rectangular bricks and lego-shaped bricks are considered. In past research [8-11], I-shaped bricks and wave-shaped bricks were considered, which have the interlocking effect only in one direction. Since earthquake acts both in the in-plane and out-of-plane directions, the lego-shaped brick was considered since they have the interlocking effect in both directions.

Two-dimensional analysis models are shown in Fig.3. Analysis models in Fig. 3 are examples of the interlocking brick walls. Analysis models for the rectangular brick wall were also created similarly.

Fig. 3(a) is a thin wall model with only one brick in the horizontal direction, and Fig. 3(b) is a two-wall model with thicker walls. Assuming that the roof is supported more than two walls in actual buildings, Fig.3(b) is considered.

The lego-shaped bricks are only used for the wall part. The protrusions of bricks on top of the wall were neglected, and the top surface was smoothed. In the same way, holes for engaging with protrusions at the bottom of the wall are neglected.

Actual buildings have three-dimensional shapes and show three-dimensional behavior. However, this study used two-dimensional analysis to investigate the out-of-plane vibration since the wall is weak against the out-of-plane direction.

All nodes at the bottom are fixed in both horizontal and vertical directions. The horizontal inertia force was applied to all free nodes when inputting horizontal acceleration.

Fig. 4 indicates the example of how the rectangular and interlocking bricks are divided into elements. Plane strain 4-noded elements were utilized. The size of each element for the rectangular brick, roof, and steel elements is 5 cm × 5 cm. The lego-shaped brick was also divided into elements of a similar size.

Material properties are shown in Table 1(a). The base and roof are made of steel so that their deformation can be neglected.

Table 1 Analysis Parameters

(a)Material properties

Value	Brick	Base & Roof
Density (kg/mm^3)	1.9×10^{-6}	8.05×10^{-6}
Young Modulus (N/mm^2)	19,000	200,000
Poisson's Ratio	0.216	0.2

(b)Mortar properties

Value	Mortar
Tensile strength (N/mm^2)	0.3
Shear strength (N/mm^2)	0.3
Friction coefficient	0.463

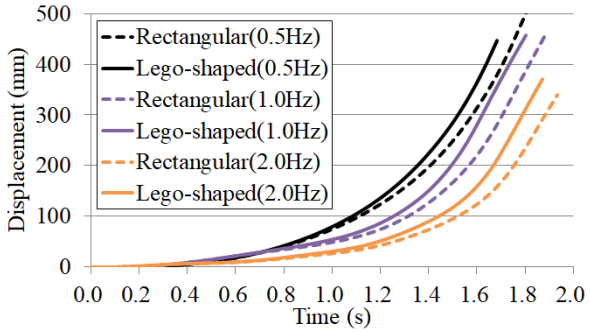

Fig.5 Horizontal displacement history of one-wall models

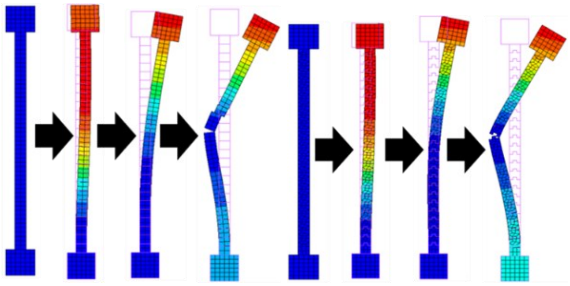

(a)Rectangular brick (b)Lego-shaped brick

Fig.6 Deformation process of one-wall models (1Hz)

Modeling of failure

It is considered that bricks are connected with mortar, and failure occurs at the mortar. Therefore, it was set that all bricks do not shear the nodes with other bricks. The bricks are glued with the adjacent bricks at the interface. The bricks move together with the adjacent bricks unless the glue does not get broken.

The mortar failure is modeled by the failure of the glue between elements. When the normal or shear stress at the interface between elements exceeds the tensile or shear strength, the glue is broken. After the failure, only compression and friction force acts between the elements. Mortar properties are shown in Table 1(b).

Input accelerations

Sinusoidal accelerations with the amplitude of 20gal and 120gal were input to the one-wall models and two-wall models in the out-of-plane direction. Three frequencies, 0.5Hz, 1.0Hz, and 2.0Hz, were used to investigate the performances under various frequencies.

The single-step Houbolt time integration method was used ($\gamma_1 = 1.5$ and $\gamma = -0.5$).

RESULTS OF NUMERICAL ANALYSIS

Overview

The analysis results of out-of-plane lateral excitation are discussed. The performance of the lego-shaped brick wall and the rectangular brick wall are compared concerning the displacement history and deformation process.

One-wall models

In one-wall models, sinusoidal accelerations of 20gal with the frequency of 0.5Hz, 1.0Hz, and 2.0Hz were input in the horizontal direction of Fig. 3(a).

The horizontal displacement history for all frequency cases is shown in Fig. 5. The walls are vulnerable, and both models collapsed by the sinusoidal acceleration of even 20gal irrespective of the frequency.

Since all models collapsed and showed similar behavior, the deformation process of the 1.0Hz case is shown in Fig. 6 as an example. The walls got fractured at the middle height and broken into two parts. The color contour of Fig. 6 indicates the horizontal displacement. The red color is the maximum displacement, and the blue color is the minimum displacement. The right side is the positive direction of the displacement. The top of the model has the largest displacement. After the walls are broken into two pieces, the middle part showed the minimum displacement since it moved to the left.

Since there is only one brick in the out-of-plane direction, the interlocking effect is small and could not resist the out-of-plane excitation.

Two-wall models

Dominant frequency

The one-wall model was too thin and got easily fractured even with a slight acceleration of 20gal. It was found the interlocking system does not work in such cases where the wall itself is vulnerable.

Next, two-wall models are analyzed. Their wall width is 50 cm, which is four times thicker than that of the one-wall models. Furthermore, the roof is supported by two walls, which means more stability. It is considered that the two-wall models are more realistic since the roof weight is usually supported by more than two walls in the actual buildings.

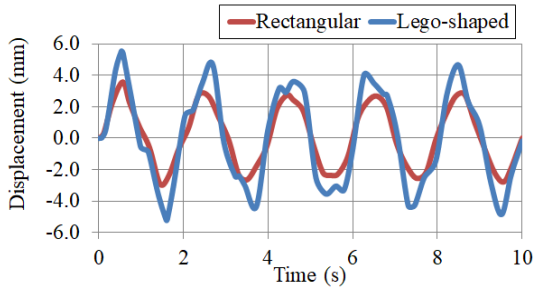

Fig.7 Horizontal displacement history of two-wall models (0.5Hz)

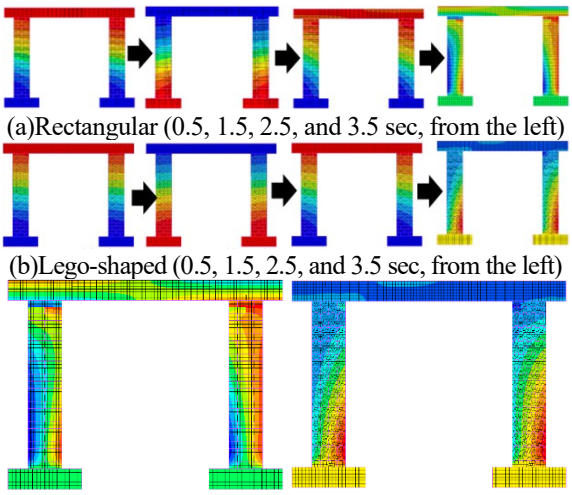

(a)Rectangular (0.5, 1.5, 2.5, and 3.5 sec, from the left)

(b)Lego-shaped (0.5, 1.5, 2.5, and 3.5 sec, from the left)

(c)Failure observed at the top of both walls of the rectangular brick wall (3.5 sec)

(d)No failure observed to the the lego-shaped brick wall (3.5 sec)

Fig. 8 Deformation process and horizontal displacement contour of two-wall models for 0.5Hz (red: maximum, blue: minimum)

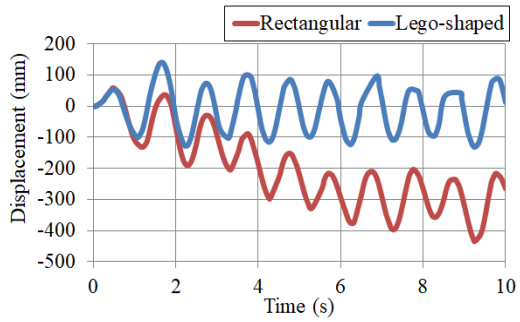

Fig.9 Horizontal displacement history of two-wall models for 1.0Hz

The dominant frequencies of the two-wall models were obtained from their free vibration responses. The models were excited by inputting an impulsive acceleration, where the acceleration amplitude for the first 0.01 sec is 1gal and that for the left 4.99 sec is 0 gal. Then the displacement histories at the top center of the roof were Fourier transformed, and the predominant frequencies were read. The dominant frequencies of both two-wall models were about 1.25 Hz.

Therefore, the input acceleration cases were divided into three categories, the case lower than the dominant frequency (0.5Hz), the case around the dominant frequency (1.0Hz), and the cases higher than the dominant frequency (2.0Hz).

When the sinusoidal acceleration of 20gal is input, both models experienced no failure. When no failure occurs, no difference is observed between the rectangular and lego-shaped brick models since there is no need for the interlocking system to work. Therefore, the lateral load was increased up to 120gal, where a noticeable performance difference between the two models was observed.

Result for 0.5 Hz

The horizontal displacement history for 0.5 Hz is shown in Fig. 7. The lego-shaped brick wall showed a slightly larger deformation than the rectangular brick wall, but its value is small.

The deformation process and displacement contour for 0.5 Hz are shown in Fig. 8(a)(b). Both models showed similar behavior until 2.5 sec, but the difference occurred at 3.5 sec. The enlarged figures at 3.5 sec are shown in Fig.8(c)(d).

Non-smoothness of displacement contour indicates the occurrence of failure. As shown in Fig. 8(c), the rectangular brick wall experienced failure around the top of both walls. In contrast, the lego-shaped brick wall shows a smooth displacement contour (Fig.8(d)), and no failure was observed. It was found that the interlocking system could avoid failure around the top of the walls.

Result for 1.0 Hz

The horizontal displacement history for 1.0 Hz is shown in Fig. 9. Compared to the result for 0.5 Hz, both models showed more significant horizontal displacement. The horizontal displacement of the rectangular brick wall model was gradually shifted to the negative direction, which means the roof moved to the left.

The deformation process and displacement contour for 1.0 Hz are shown in Fig. 10(a)(b). Fig. 10(a) shows that the sliding movement of the roof occurred in the rectangular brick wall since the horizontal cracks occurred on the upper walls. On the other hand, no sliding displacement occurred in the lego-shaped brick wall owing to the interlocking system (Fig. 10(b)).

The enlarged figures at 2.2 sec are shown in Fig.9(c)(d). As shown in Fig. 9(c), the rectangular brick wall experienced horizontal cracks at the top of both walls and diagonal cracks at the bottom of both walls. In contrast, the lego-shaped brick wall experienced no diagonal cracks at the bottom of the walls. Mortar failure occurred at the top of both walls, but no sliding between the walls and the roof occurred due to the interlocking system.

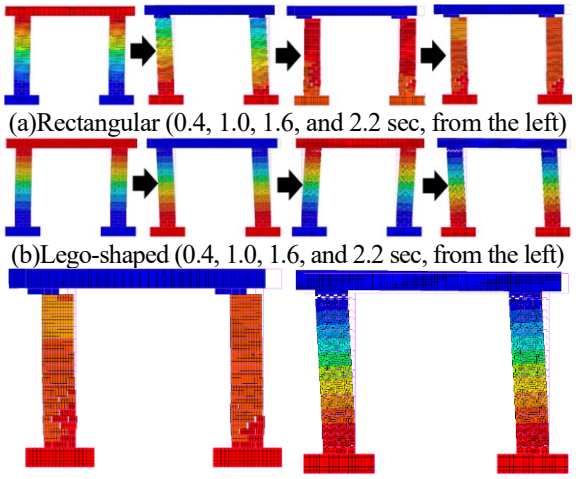

(a)Rectangular (0.4, 1.0, 1.6, and 2.2 sec, from the left)

(b)Lego-shaped (0.4, 1.0, 1.6, and 2.2 sec, from the left)

(c)Failure observed at the top of both walls of the rectangular brick wall (2.2 sec)

(d)No failure observed to the the lego-shaped brick wall (2.2 sec)

Fig. 10 Deformation process and horizontal displacement contour of two-wall models for 1.0 Hz (red: maximum, blue: minimum)

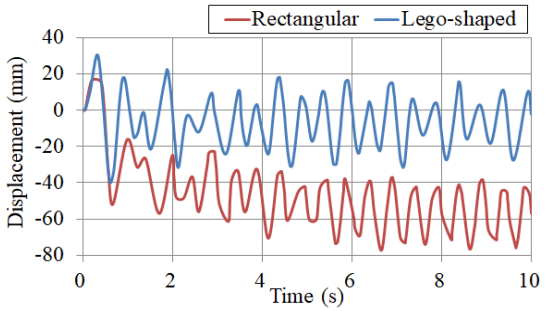

Fig.11 Horizontal displacement history of two-wall models for 2.0Hz

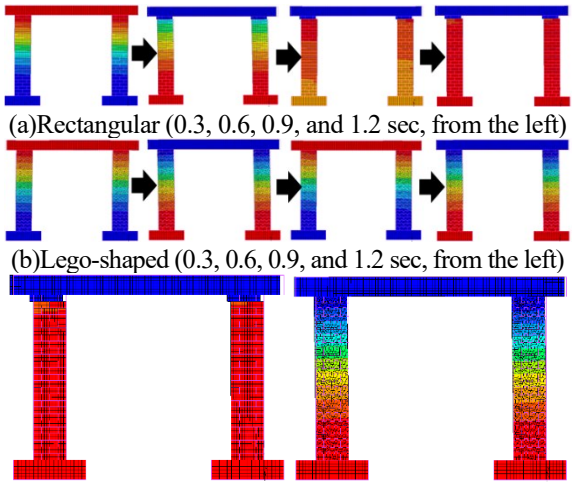

(a)Rectangular (0.3, 0.6, 0.9, and 1.2 sec, from the left)

(b)Lego-shaped (0.3, 0.6, 0.9, and 1.2 sec, from the left)

(c)Failure observed at the top of both walls of the rectangular brick wall (1.2 sec)

(d)No failure observed to the the lego-shaped brick wall (1.2 sec)

Fig. 12 Deformation process and horizontal displacement contour of two-wall models for 2 Hz (red: maximum, blue: minimum)

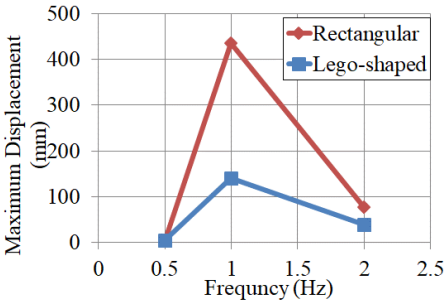

Fig. 13 Comparison of the maximum displacement for two-wall models

Result for 2.0 Hz

The horizontal displacement history for 2.0 Hz is shown in Fig. 11. They showed a similar tendency to the case of 1.0 Hz even though the horizontal displacement of 2.0 Hz is small. The horizontal displacement of 2.0 Hz is smaller since 2.0 Hz is farther from the dominant frequency of 1.25 Hz than 1.0 Hz.

The deformation process and displacement contour for 2.0 Hz are shown in Fig. 12(a)(b). Fig. 12(a) shows that the sliding movement of the roof occurred in the rectangular brick wall since the horizontal cracks occurred on the upper walls. On the other hand, no sliding displacement occurred in the lego-shaped brick wall, and horizontal displacement could be kept small due to the interlocking system (Fig. 12(b)).

The enlarged figures at 1.2 sec are shown in Fig.12(c)(d). In the rectangular brick wall model, the upper part of both walls got fractured. In the lego-shaped brick wall model, no failure occurred, and the model deformed as a united body.

Summary

The interlocking system did not work for thin one-wall models, while it worked for thick two-wall models.

The comparison of the maximum displacement for two-wall models is shown in Fig. 13. In all frequencies, the rectangular brick wall model showed larger displacement than the lego-shaped brick wall model.

The displacement suppression effect of the interlocking system was the largest at 1.0 Hz when both models had the largest displacement due to resonance, and the displacement of the lego-shaped brick wall was about 1/3 of that of the rectangular brick wall.

In the case of 2.0 Hz, the large displacement response and failure occurred to the rectangular brick wall. In contrast, no failure occurred, and displacement was kept small in the lego-shaped brick wall since the interlocking system worked.

In the case of 0.5 Hz, the displacement response was small and slight failure occurred to the

rectangular brick wall. Since there was not much room for the interlocking system to work, the displacement suppression effect of the lego-shaped brick wall was small. No damage occurred in the lego-shaped brick wall, and the interlocking effect was observed in damage prevention.

It could be concluded that the lego-shaped brick wall shows better performance in resting the lateral dynamic load even in the out-of-plane direction when the wall is not too thin.

CONCLUSION

In this study, the performance of the interlocking brick walls under lateral dynamic load in the out-of-plane direction was investigated using the 2-dimensional finite element analysis. The lego-shaped brick was chosen, and its performance was compared to the rectangular brick. Two models were compared. The first is a one-wall model of a single thin wall supporting a roof, and the second is the two-wall model of two thicker walls supporting the roof. Sinusoidal acceleration was input to the models with three frequencies of 0.5 Hz, 1.0 Hz, and 2.0 Hz.

In the one-wall models, both rectangular and interlocking brick wall models quickly got fractured and collapsed irrespective of the input frequencies. It was found that the interlocking system does not work for a thin wall subjected to the out-of-plane loading since the wall itself was vulnerable.

In the case of thick two-wall models, the interlocking system worked. The rectangular brick wall got failure, but the failure was avoided, and displacement response was kept small in the interlocking brick wall. When the displacement response is small, the effect of the interlocking system is small. As the displacement response larger, the interlocking system worked, and the displacement suppression effect was noticeable. The interlocking system caused the brick wall to deform together as a unit, eliminating the unwanted sliding movement due to failure.

It was confirmed that the lego-shaped brick walls showed a better performance in resisting the out-of-plane dynamic load due to the interlocking system if the wall is thick enough to exert the interlocking effect.

ACKNOWLEDGMENT

This work was supported by JST aXis Grant Number JPMJAS2020, Japan.

REFERENCES

[1] OCHA (Office for the Coordination of Humanitarian Affairs): www.unocha.org. [Accessed April 16, 2021].

[2] Coburn, A., and Spence, R., Earthquake protection 2nd Edition, Chichester, John Wiley and Sons, 2002.

[3] McWilliams, H., and Griffin, C.T, A critical assessment of concrete and masonry structures for reconstruction after seismic events in developing countries, Structures and Architecture: Concepts, applications, and challenges, Proceedings of the Second International Conference on Structures and Architecture, CRC Press, 2013, pp. 857-864.

[4] Darbhanzi, A., Marefat, S., and Khanmohammadi, M., Investigation of in-plane seismic retrofit of unreinforced masonry walls by means of vertical steel ties, Construction and Building Materials, Vol. 52, 2014, pp. 122-129.

[5] Marcari, G., Manfredi, G., Prota, A., and Pecce, M., In-plane shear performance of masonry panels strengthened with FRP, Composites: Part B, Vol. 38, 2007, pp. 887-901.

[6] Turer, A., and Golalm, M., Scrap tire as low-cost post-tensioning material for masonry strengthening, Materials and Structures, Vol. 41, 2011, pp. 1345-1361.

[7] Sathiparan, N., Sakurai, K., and Meguro, K., Experimental study of PP-band retrofitted masonry structure made of shapeless stone. SEISAN-KENKYU, Vol. 61, Issue 6, 2009, pp. 1051-1054.

[8] Sanada, Y., Nakamura, Y., Yamauchi, N., and Akano, Y., Seismic performance of masonry walls using interlocking units, Proceedings of the First European conference on earthquake engineering and seismology, Paper No. 508, 2006.

[9] Furukawa, A., Kimura, S., and Kiyono, J., Study on failure mechanism and strength increment effect of masonry walls made of interlocking bricks, Journal of Japan Society of Civil Engineers, Vol. 74, No. 4, 2018, pp. I_699-I_711 (in Japanese).

[10] Furukawa, A., Masuda, K., Daru, G.T.S., and Kiyono, J., Shape effect of interlocking blocks on force-displacement relationship and failure behavior of masonry wall, Journal of Structural Engineering, Vol. 64A, 2018, pp. 241-249 (in Japanese).

[11] Furukawa, A., Prasetyo, J.J., Kiyono, J., Failure process and load-displacement relationship of rectangular block and interlocking block walls during in-plane lateral loading, Journal of Japan Society for Natural Disaster Science, Vol. 38, 2019, pp.25-41.

[12] MSC Software Corporation: Marc, www.mscsoftware. com/product/marc. [Accessed April 16, 2021.]

11th Int. Conf. on Geotechnique, Construction Materials & Environment,
Kyoto, Japan, 3-5 November 2021, ISBN: 978-4-909106063 C3051

INFLUENCE OF FREEZING AND THAWING CONDITIONS AT INITIAL AGE ON THE STRENGTH DEVELOPMENT OF MORTARS

Peter Kaba[1], *Shushi Sato[2], Masahiro Yamamoto[3] and Keikichi Takahashi[4]

[1]United Graduate School of Agricultural Sciences, Ehime University, Japan; [1,2]Faculty of Agriculture, Kochi University, Kochi, Japan; [3]ASTON Company Limited, Japan; [4]KAIHATSU Concrete Company Limited, Japan.

ABSTRACT

Agricultural irrigation canals are widespread across Japan and extensively used in productive farming. There is an urgent need to extend the service life of these facilities to reduce their maintenance cost. Therefore, the purpose of this study is to experimentally explore the effect of low-temperature history on the long-term strength of polymer cement mortar, especially during the early stage of the mortar's life, thus, 3 days of age. In this study, two types of polymer cement mortar were used: powdered ordinary polymer cement mortar and powdered fast-hardening polymer cement mortar, thus 100P and 100PS respectively. The experimental results indicate that the compressive strength analysis of the polymer cement mortar is lower than the standard cured, whenever the initial curing process was subjected to rapid temperature changes (-10ºC to 5ºC) every 3 hours; subsequently, its purpose of extending the service life of agricultural canals cannot be fulfilled. We again noted that the compressive strength of the specimens subjected to low temperature during the initial curing period does not show positive strength on the 91st day, and depending on the timing of the repair work, the waterway may lack sufficient compressive strength. Finally, under a constant low-temperature environment where freezing and thawing do not occur (-10 ºC), the fast-setting polymer cement mortar shows sufficient strength up to 91 days. The results from this work will provide a reference to experimentally clarify the effect of low-temperature history on the long-term compressive strength of typical polymer cement mortar.

Keywords: Compressive strength, Polymer cement mortar, concrete, Freez-Thaw

1. INTRODUCTION

The first canals were built between the Middle Ages and the Renaissance to harness the driving force of water. Their development during the 18th and 19th centuries aimed to address the growing need for water in Mediterranean farming. Canals have aided the development of irrigated agriculture since the late 1800s, allowing for increased production, increased crop surfaces, and the introduction of new crops. [1].

Agricultural water use, as the largest form of water use, accounts for 70% of the total water consumption in the world and is a vital part of the social water cycle, and even in regions with relatively abundant water resources, the agricultural water demand cannot be met completely [2]. Intense water resource exploitation and utilization have resulted in severe changes in natural hydrological cycle processes in many agricultural watersheds.

As a result, irrigation canal scheduling is critical for achieving high crop yields and improved water use efficiency while lowering environmental impact. Concrete made of ordinary Portland cement has disadvantages such as slow hardening, large shrinkage, weak tensile and flexural strengths, lack of water tightness, and weak chemical resistance, although it also has some advantages, such as easy manufacturing and application in construction and high compressive strength [3].

To overcome the disadvantages of ordinary cement concrete and mortar with Portland cement, researchers have attempted over the last 60 years to develop a new type of concrete and mortar using polymer that demonstrates excellent performance [3, 4]. Today, various polymers are being tested to improve cement's properties as a binder; this new concept concrete or mortar has better physical properties and durability than ordinary cement concrete and is termed polymer-modified concrete/mortar or polymer cement concrete (PCC)/mortar (PCM).

Agricultural water utilization facilities, thus river canals in Japan were mainly constructed between the end of World War II and the period of rapid economic growth, and nearly 80 years have already passed. There is an urgent need to extend the service life of these facilities and to reduce their cost.

Agricultural open waterways are scattered throughout Japan[5]. Whenever there is a deterioration in the agriculture canal even if the

deterioration is of the same kind, it may be difficult to repair them using the same repair material due to various conditions such as environmental conditions, usage conditions, and location within the waterway. In addition, agricultural irrigation canals are often conducted during the off-season, that is winter, and the possibility of construction failure caused by low temperatures is considered to be high. Damage caused by frost expansion is a primary concern when designing concrete structures in cold weather regions.

Ordinary portland cement concrete has a range of benefits, including low costs, high compressive strengths, and flexibility in fabrication and casting, but its durability concerns are gaining more attention these days, as the majority of concrete structures are experiencing performance degradation. Concrete performance is affected by a variety of factors, including material composition, curing schemes and temperatures, hazard species, harsh conditions, and external loads [6].

Therefore, in this study, we focused on the repair of cracks in the concrete canal walls of agricultural canals as one of the aging problems of agricultural water utilization facilities.

Therefore, the purpose of this study was to experimentally elucidate the effect of low-temperature history on the long-term strength of polymer cement mortar, especially during the early stage of the mortar's life up to 3 days of age. The purpose of this study was to experimentally clarify the effect of low-temperature history on the long-term compressive strength of polymer cement mortar.

2. MATERIALS AND METHODS

Materials

In this study, two types of polymer cement mortar were used: powdered ordinary polymer cement mortar and powdered fast-hardening polymer cement mortar. The former will be referred to as 100P and the latter as 100PS. An electronic balance scale was used for measuring the cement powder. A CF 1033 table vibrator was used to level and release existing air in the mortar. Makita UT1305 cement mixer machine was used to mix the mortar in a bucket to control air bubbles that are entrained in the process of mixing. A Plamold plastic mold with a diameter of 50 mm and a height of 100 mm was adopted for casting. A concrete compression testing machine was used to measure the compressive strength employed in the fracture test at the final material age.

Methods

Firstly, grease was applied inside the plastic mold for easy removal of the made mortar. A 4kg of each polymer cement mortar, thus 100PS and 100P was measured using the electronic balance into the plamold cases. The water-cement ratio was the value recommended by the manufacturer, with a pH value of 7. A total of 90 mortal samples were prepared, which was subsequently subdivided, thus based on the properties of cement mortar used. All mortar specimens were prepared by hand-kneading using a stirrer.

The curing conditions of mortar specimens were all standard water curing after 3 days of material age except for intentional temperature change. An incubator capable of providing arbitrary low-temperature history was used to provide low-temperature levels up to 3 days of material age. Since the volume of the mortar was observed to expand with time, the top of the filled plamold case was sealed with plastic immediately after casting and the top load was applied to prevent any change from the predetermined volume.

In this experiment, the temperature history of the specimens during curing was set at 20°C (hereinafter referred to as control), which was recommended by the manufacturer, as the standard condition, and all other mortar specimens were subjected to low-temperature history immediately after curing. The minimum temperature was set at -10ºC and the maximum was set at +5ºC. The reason why the minimum value of the low temperature was set to -10°C is that it is the lowest temperature in cold regions in Japan, and the maximum value of the temperature history was set to +5°C based on the assumed daily difference.

Fig.1 workers repairing a deteriorated river canal in Kochi.

In general, freezing and thawing effects on hardened concrete cause volume expansion and contraction, which are the failure mechanisms in freezing damage. However, the effect of freezing and thawing immediately after casting on the long-term strength of cement hydrates has not yet been clarified. In this experiment, the temperature was repeatedly changed between -10°C and +5°C for 12 hours, 6 hours, and 3 hours with the aid of an incubator. The age of the specimens was set at 7, 28, and 91 days (365 days), and three specimens were prepared for each temperature history and age. The test results were basically the average of the three specimens. Table 1 below shows the temperature differences, duration, and the number of cycles for a cement mortar in an incubator.

Table 1.

Temperature (ºC)	Duration	Cycle
Standard 20ºC		
-10ºC	3 days	Keep in an incubator for 3 days at a controlled temperature of -10ºC
-10 ºC +5 ºC	12 hours, 3 days	+5ºC for 12 hours and -10ºC for 12hours (a cycle a day)
-10 ºC +5 ºC	6 hours, 3 days	+5ºC for 6 hours and -10ºC for 6 hours (4 cycles a day)
-10 ºC +5 ºC	3 hours, 3 days	+5ºC for 3 hours and -10ºC for 3 hours (9 cycles a day)

3. RESULTS AND DISCUSSION

Firstly, comparing the normal strength development characteristics of 100P and 100PS, it can be read that the compressive strength increases with time for both. However, the strength development characteristics were different, with the compressive strength of 100PS being greater at 7 days of age, but showing little change at 91 days of age.

In order to investigate the effects of freezing and thawing (freeze-thaw) cycles the specimens were subjected to a low-temperature history of -10°C for 3 days during initial curing as shown in. The compressive strength of 100P was very small (10.0 kN) at 7 days of age, and only about half of the compressive strength of the control specimen (20.0 kN) as shown in Fig 3(A). On the other hand, the difference between 100PS and the control specimen was minimal, and the strength of 100PS was about 3.7 times higher than that of 100P under the same condition as shown in Fig 3(B).

Fig. 2 A well repaired river canal repair in Kochi

Furthermore, as shown in Fig 3(A) and Fig 3(B), not much difference ware recorded for 100P and 100PS polymer cement mortars compared to the control specimen at 28 days of mortar age. This may be due to the constant temperature adopted during the initial curing process for 3 days of the mortar life.

At 91 days of age, the average compressive strength of both types of specimens for Fig 3(D) was 22.9 MPa, which was the least recorded among the specimens at the same mortar age. Both types of specimens that underwent freeze-thaw at 12 and 6-hour pitches showed an increase in strength with time, but the average compressive strength was lower in both conditions.

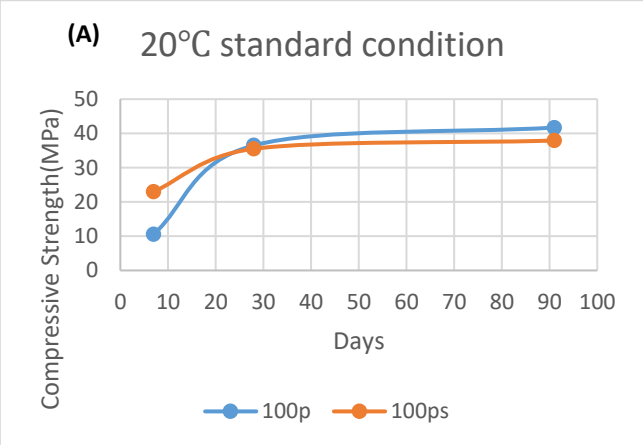

Fig. 3(A). 20 ºC standard condition in water

For the specimens subjected to freeze-thaw at a 3-hour pitch, both specimens showed relatively high compressive strength up to the 7th and 28th day, but

the compressive strength on the 91st day was lower than the compressive strength on the 28th day as shown in Fig 3(E).

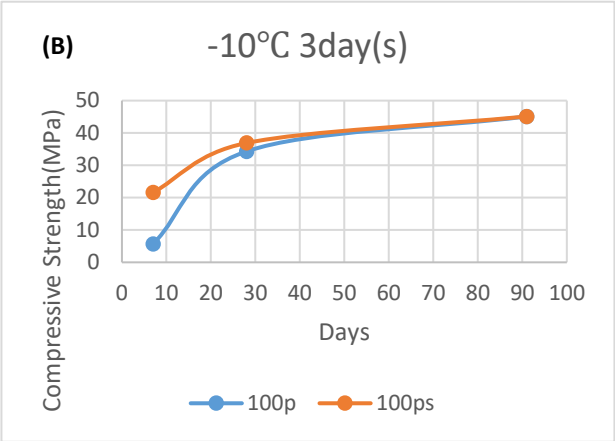

Fig. 3(B). Compressive strength of -10ºC for 3 days

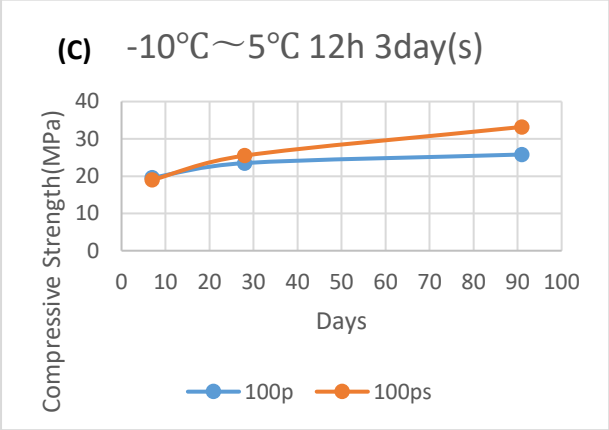

Fig. 3(C) Compressive strength of -10ºC~5 ºC for 3 hours

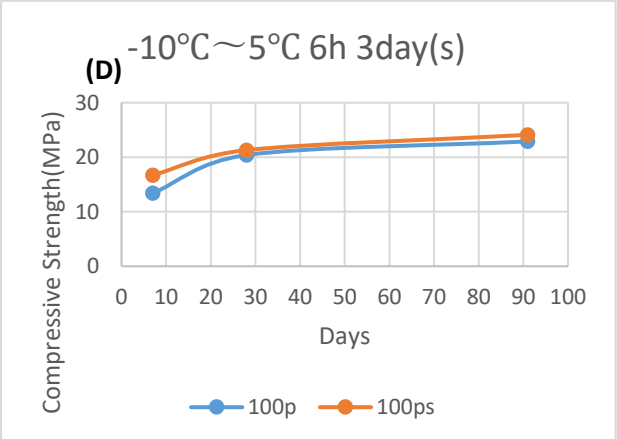

Fig. 3(D) Compressive strength of -10ºC~5 ºC for 3 hours

It was confirmed that 100PS, which is a fast curing type, has a larger initial strength development rate. According to the manufacturer's measurement, the compressive strength of 100P was higher than that of 100PS even at the age of 7 days. One possible reason for this is that the manufacturer recommended a water-mortar ratio (water/polymer cement mortar, weight %) in the range of 15.6~17.2% for 100P and 16~18% for 100PS.

In this study, the amount of water used for both is unified and set at 17%, which falls within the common range, and may have caused the difference between the strength expression in this experiment.

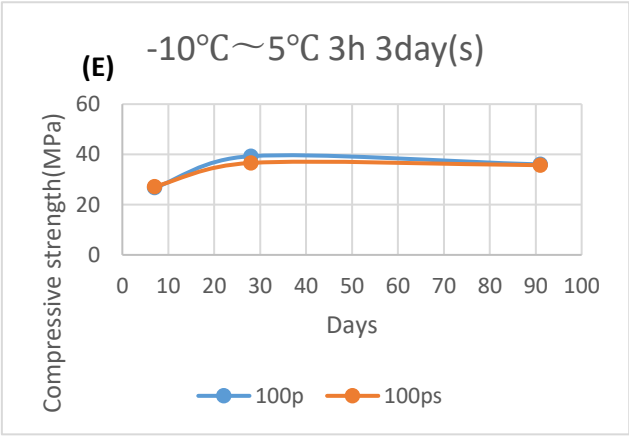

Fig. 3(E) Compressive strength of -10 ºC~ 5 ºC for 3 hours

We also confirmed that the freeze-thaw effect during the initial age of the specimens had a negative effect on the compressive strength, which was due to the increase in the volume of water in the specimens caused by freezing and the destruction of the hardened parts by fine cracks due to the hydration reaction. This suggests that the compressive strength of the specimens was not sufficient due to the increase in the volume of water in the specimens caused by freezing and the destruction of the hardened parts by fine cracks due to the hydration reaction.

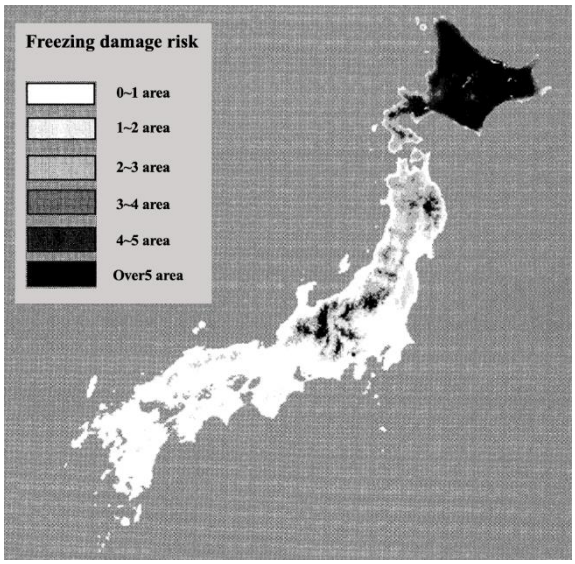

Fig. 4. Map of Japan showing freezing damage risk. *Source:*[7]

The decrease in compressive strength at 91 day(s) was caused by freeze-thaw action more times than the specimens with 12-hour and 6-hour pitches, indicating that freeze-thaw action after casting has a negative effect on long-term strength development, even for the mortars subjected to this study.

4. CONCLUSION

In this study, we focused on polymer cement mortar, one of the inorganic repair materials, in the cold climate of Japan, where the temperature sometimes drops below 0°C. The following three things were obtained by confirming the compressive strength of polymer cement mortar subjected to various low-temperature histories.

First, if the initial curing process is subjected to rapid temperature changes every three hours, the compressive strength tends to drop, and the purpose of extending the service life of agricultural canals cannot be fulfilled.

Secondly, the compressive strength of the specimens subjected to temperature changes during the initial curing period does not develop easily on the 91st day, and depending on the timing of the repair work, the waterway may be used without sufficient compressive strength.

Finally, under the low-temperature environment where freezing and thawing do not occur, the fast-setting polymer cement mortar shows sufficient strength up to the 91st day.

REFERENCES

1 Aspe, C., and Jacqué, M.: 'Agricultural Irrigation Canals in Southern France and New Urban Territorial Uses', Agriculture and Agricultural Science Procedia, 2015, 4, pp. 29-39

2 Wang, W., Hu, P., Wang, J., Zhao, J., Liu, H., and Yang, Z.: 'Scenario analysis for the sustainable development of agricultural water in the Wuyuer River basin based on the WEP model with a reservoir and diversion engineering module', Science of The Total Environment, 2021, 758, pp. 143668

3 Jo, Y.-K.: 'Adhesion in tension of polymer cement mortar by curing conditions using polymer dispersions as cement modifier', Construction and Building Materials, 2020, 242, pp. 118134

4 Huseien, G.F., Mirza, J., Ismail, M., Ghoshal, S., Hussein, A.A.J.R., and Reviews, S.E.: 'Geopolymer mortars as sustainable repair material: A comprehensive review', 2017, 80, pp. 54-74

5 Sakura, K.J.I., Society, and Glick, L.T.t.T.F.: 'The relationship between urban structure and waterways in Edo, old Tokyo', 2015, pp. 924-934

6 Peng, Y., Zhao, G., Qi, Y., and Zeng, Q.: 'In-situ assessment of the water-penetration resistance of polymer modified cement mortars by μ-XCT, SEM and EDS', Cement and Concrete Composites, 2020, 114, pp. 103821

7 Takeshi Narita, S.-i.K.a.H.M.: 'Frost Damage Risk Map Based on Local Climate Condition and Site Investigation', Concrete Research and Technology, 2008, Vol. 19, (1), pp. 29-38

Environment

11th Int. Conf. on Geotechnique, Construction Materials & Environment,
Kyoto, Japan, 3-5 November 2021, ISBN: 978-4-909106063 C3051

TEMPORAL CHANGES IN THE INDOOR RADON CONCENTRATION AS AN EARTHQUAKE PRECURSOR

Jae Wook Kim[1], Han Young Joo[1], Young Seo Kim[1], So Yun Jeong[1] and Joo Hyun Moon[1]

[1]Department of Energy Engineering, Dankook University, Gyeongju, Republic of Korea

ABSTRACT

This paper reviews the changes in indoor radon concentrations, measured in a university building in Gyeongju, Rep. of Korea, to find the relationship, if exists, between the indoor radon concentrations and the seismic activities in the area neighboring Gyeongju. The measurement period was from June 1, 2017 to May 31, 2019. During this period, numerous seismic activities occurred in the southeastern region of the Korean peninsula. Considering a magnitude and distances from our measurement place to epicenters, 11 earthquakes for analysis were chosen. Among this, nine earthquakes were found to have radon anomalies before their occurrences. Three earthquakes with magnitude greater than 4.0 were scrutinized for the correlation between radon anomalies. Effects of the environmental variables such as relative humidity, barometric pressure, rainfall and inlet temperature were also examined. Similar to those found in our previous study, spike-like patterns were also found in the indoor radon concentration distributions before the earthquakes.

Keywords: Indoor radon concentration, Gyeongju, Seismic activities, Pohang, Radon anomaly

INTRODUCTION

Radon is an inert radioactive gas generated by a series of the decay of uranium, and released to the air from the soil, groundwater, and cracks in buildings [1]. Due to cracks in the crust prior to seismic activity, radon gas emits highly than usual [2]. Using this phenomenon, lots of research have studied on radon concentrations as an earthquake precursor. Yasuoka et al. observed that, in the earthquake in Kobe, Japan, a rise in the atmospheric radon concentration was evident prior to the earthquake [3]. Sunarno et al. found that radon concentration increased 3 days before earthquake in Situbondo, Indonesia [4].

In general, radon concentrations in the atmosphere are affected by meteorological variables. Planinic et al. presented radon concentrations over four years along with the barometric pressure, rainfall, and air temperature, and investigated whether the weather variables affected changes in the environmental radiation [5]. Virk et al. measured the release of radon gas in the wake of an earthquake in the Himalayas' main boundary fault and explained that the soil, air temperature, rainfall, pressure, humidity, and wind speed were related to radon gas abnormalities [6].

Those studies focused on the outdoor radon concentrations in the air, soil or groundwater. However, unlike these previous studies, our previous studies investigated the relationship between the indoor radon concentration and earthquake occurred in Gyeongju and Pohang, Republic of Korea. In case of Gyeongju earthquake, we observed similar spike-like patterns between them: a sudden increase in the peak indoor radon concentration 1–4 days before an earthquake, gradual decrease before the earthquake, and sudden drop on the day of the earthquake if the interval between successive earthquakes was moderately longer, for example, 3 days [7]. In case of the Pohang earthquake, on the other hand, we observed no noticeable patterns between earthquake and indoor radon concentration due to the long distance between the epicenter and the measurement spot [8].

This study is an enlarged version of our previous studies. Our previous studies investigated the relationship between radon concentration and earthquake during specific period which main shock and its aftershocks occurred. However, this study investigated the changes in the indoor radon concentrations before and after earthquakes for two years from June 1, 2017 to May 31, 2019, to see if a similar pattern of indoor radon concentration is recurred prior to the earthquake, as in our previous study. We also scrutinized three earthquakes with magnitude 4 or greater and radon anomalies prior to each one.

MATERIALS AND METHODS

Measurement Device and Procedure

As shown in figure 1, we used a RAD7 detector to measure the indoor radon concentration continuously. The RAD7 can measure radon concentration in the range 0.1–20,000 pCi/L, with approximately 5% uncertainty [9]. The protocol of the U.S. Environmental Protection Agency was applied to measure indoor radon concentration [10]. The measurement place was the first floor of the

Engineering Hall at Dongguk University-Gyeongju, Rep. of Korea. Because the RAD7 was equipped next to the central entrance of the Hall, where hundreds of people come in and out the building a day, we assumed that there was no influence on ventilation. Measurements were made every 30 minutes, and the measurement data were collected and analyzed using the computer program for RAD7.

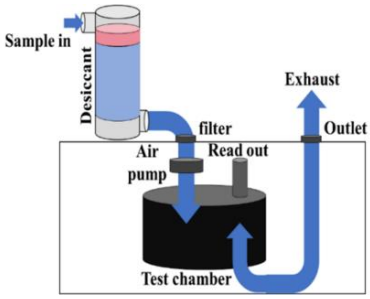

Fig. 1 Structure of a RAD7 detector.

Data Analysis Method

Gyeongju is located 360 km southeast of Seoul in Korean Peninsula, and Pohang is located 20 km north of Gyeongju. After a 5.8-magnitude quake (Gyeongju, September 12, 2016) and a 5.4-magnitude quake (Pohang, November 15, 2017) occurred, their aftershocks have still occurred in Gyeongju and Pohang. In order to identify the relationship indoor radon concentrations and the seismic activities, we investigated daily radon concentrations with seasonal average radon concentrations for two years from June 1, 2017 to May 31, 2019.

Earthquakes for analysis were screened by applying the following formula proposed by Hauksson and Goddard [11]:

$$M = 2.4 \log_{10} D - 0.43 \quad (1)$$

$$D_{MAX} = 10^{(M+0.43)/2.4} \quad (2)$$

Where
M = magnitude of earthquake (Richter scale)
D_{max} = maximum measurable distance from the epicenter (km)

D_{max} in equation (2) means the maximum distance from epicenter, which radon anomaly could be measured. It means that, if the M-magnitude quakes occurred and the measurement place is located within D_{max}, radon anomalies could be observed.

For analysis, we employed the value of 'seasonal average radon concentration + 2 × standard deviation (σ)' as a criterion to assume radon anomaly. That is, if radon concentration exceeded this value, we could consider it as effects of earthquakes not environmental impacts [12].

RESULTS AND DISCUSSIONS

Reviewing the Measurement Data and earthquakes

Table 1 shows the information of the earthquakes selected by using eq. (2). If the distance were equal to or less than D_{max}, that is, if the distance difference were 0 or higher, the radon anomalies could be found at the measurement place as a precursor of the earthquake. Magnitude of those earthquakes ranged from 2.5 to 5.4. There were 14 earthquakes from June 1, 2017 to May 31, 2019. In case of two or more earthquakes occurred on the same day, however, we regarded that only the largest magnitude earthquake occurred on that day. Finally, the 11 earthquakes were analyzed to identify the relationship between earthquake and radon concentrations.

Table 1 Information of the selected earthquakes using eq. (2)

Number	Date	Magnitude	Distance[b] [km]	D_{max} [km]	Distance Difference[c] [km]
1	17.06.11	2.5	13.5	16.6	3.2
2	17.10.16	2.5	11.8	16.6	4.8
3[a]	17.11.15	5.4	29.0	268.6	239.6
	17.11.15	3.6	28.0	47.8	19.8
	17.11.15	3.5	26.9	43.4	16.5
	17.11.15	4.3	30.1	93.5	63.4
4	17.11.16	3.6	30.1	47.8	17.7
5	17.11.19	3.5	30.1	43.4	13.3
6	17.11.20	3.6	32.2	47.8	15.6
7	17.12.25	3.5	29.0	43.4	14.4
8	18.02.11	4.6	25.9	124.7	98.8
9	18.04.09	2.4	14.3	15.1	0.8
10	19.01.10	2.5	8.1	16.6	8.5
11	19.02.10	4.1	71.5	77.2	5.7

[a] Regards that 5.4 magnitude earthquake occurred only on that day.
[b] Distance means the straight distance between the measurement point and the epicenter
[c] Distance difference = D_{max} – Distance

Because we are not able to show the measurements all together in one figure, we presented the measurements in the two figures: Fig. 2 and 3. In figure 2, we observed ten radon anomalies that reached or exceeded 'seasonal average + 2σ' and nine earthquakes. In figure 3, we found thirteen radon anomalies and two earthquakes. We observed 23 radon anomalies marked in small orange circle for our measurement period in total, and the details of the anomalies were summarized in Table 2. In Table 2, difference means how much the radon concentration exceed the seasonal average + 2σ. Next, we checked that if any anomalies occurred before seismic activities, and found that radon anomalies occurred before the nine among the eleven earthquakes as shown in Table 3. The earthquakes on November 19 and 20, 2017 were assumed to have the same radon anomaly because they happened over two consecutive days. It was interesting that no radon anomaly which exceed the value of 'seasonal average radon concentration + 2σ' was observed though the 5.4-magnitude earthquake occurred on November 15, 2017 and the distance between the epicenter and the measurement place was relatively short. We think that this was because radon released already due to a 2.5-magnitude quake on October 16, 2017, a month before the 5.4-magnitude quake.

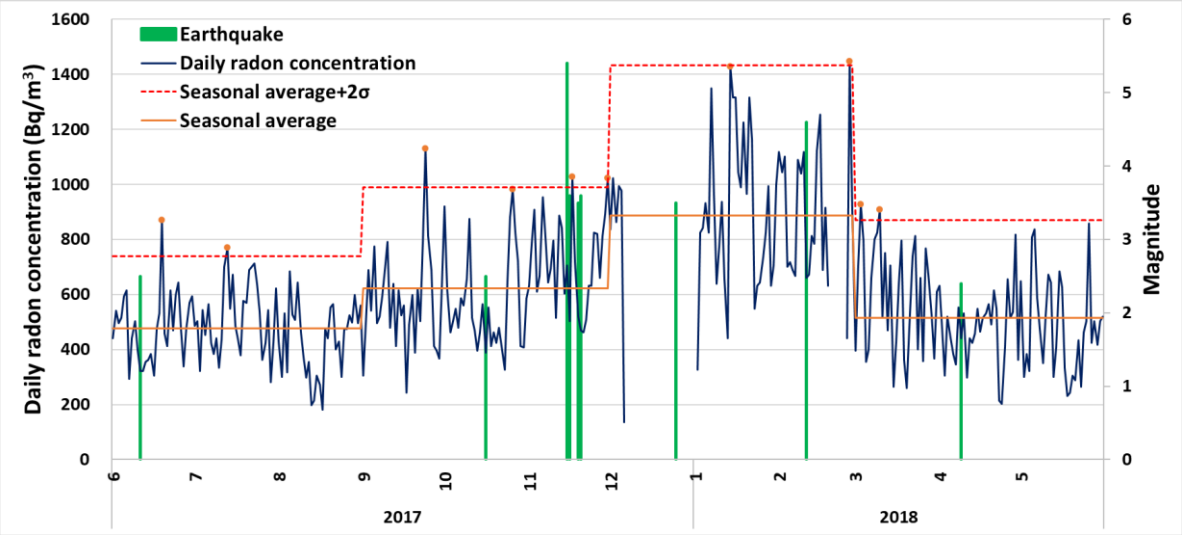

Fig. 2 Daily radon concentrations and earthquakes from June 1, 2017 to May 31, 2018.

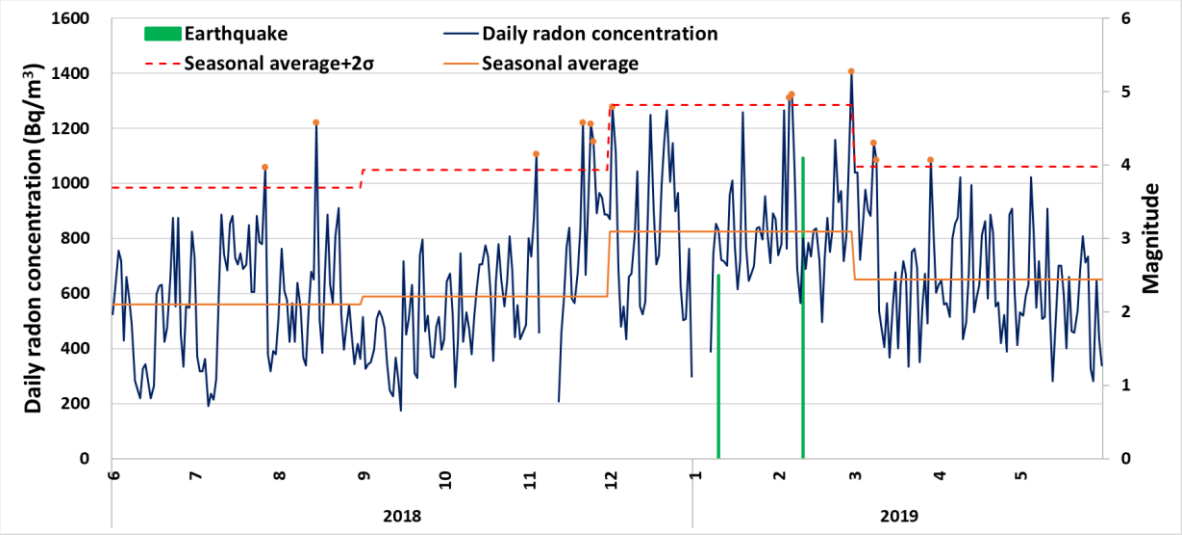

Fig. 3 Daily radon concentrations and earthquakes from June 1, 2018 to May 31, 2019.
Table 2 Radon anomalies which exceed or reached seasonal average radon concentrations + 2σ

Date	Radon anomaly concentration [Bq/m^3]	Seasonal average + 2σ [Bq/m^3]	Difference[a] [Bq/m^3]
17.06.19	869.7	739.4	130.2
17.07.13	768.7		29.2
17.09.24	1129.2		139.8
17.10.26	982.47	989.5	-7.0
17.11.17	1027.7		38.2
17.11.30	1022.0		32.6
18.01.14	1428.81	1433.5	-4.7
18.02.27	1445.9		12.4
18.03.03	926.2	870.7	55.6
18.03.10	909.2		38.5
18.07.27	1057.3	983.7	73.6
18.08.15	1221.1		237.4
18.11.04	1106.8		57.2
18.11.21	1219.7	1049.6	170.0
18.11.24	1214.2		164.6
18.11.25	1151.9		102.3
18.12.02	1276.2		-9.0
19.02.05	1310.2	1285.3	24.9
19.02.06	1321.6		36.3
19.02.28	1406.6		121.3
19.03.08	1146.3		85.5
19.03.09	1084.5	1060.8	23.7
19.03.29	1084.4		23.6

[a] Difference = Radon anomaly – (seasonal average + 2σ)

Table 3 Earthquakes that are accompanied by radon anomalies

Number	Earthquake occurrence date	Magnitude	Radon anomaly occurrence date	Radon anomaly concentration [Bq/m^3]	Time interval[a] [Day]
1	17.10.16	2.5	17.09.24	1129.2	22
2	17.11.15	5.4	17.10.26	982.47	20
3	17.11.19	3.5	17.11.17	1027.7	2
4	17.11.20	3.6			3
5	17.12.25	3.5	17.11.30	1022.0	25
6	18.02.11	4.6	18.01.14	1428.81	28
7	18.04.09	2.4	18.03.10	909.2	30
8	19.01.10	2.5	18.12.02	1276.2	39
9	19.02.10	4.1	19.02.05	1310.2	5
			19.02.06	1321.6	4

[a] Time interval between occurrence date of earthquake and that of radon anomaly

Scrutiny of Change in Indoor Radon Concentration

For three of the nine earthquakes with magnitude greater than 4.0, we scrutinized the indoor radon concentrations over 39 days including the day of the earthquake from 34 days before the earthquake to 4 days after it. Table 4 shows the indoor radon concentrations and environmental variables including relative humidity (RH), barometric pressure, rainfall and inlet temperature. Analysis periods were October 12–November 19, 2017, January 8–February 15, 2018, January 7–February 14, 2019, respectively.

Figures 4, 5, 6 show the daily indoor radon concentration and measurements of the environment variables such as barometric pressure, air temperature at inlet of the RAD7, rainfall and relative humidity (RH) inside the building. We checked if the fluctuation in the indoor radon concentration could have mainly resulted from variation of any environmental variables except seismic activity. Though the rainfall could potentially influence the indoor radon concentration, we measured the radon concentration inside the building using absorbents to avoid the effects of moisture and the rainfall had no significant impact.

As shown in figure 4, there were limited changes in the environmental variables measurements over the same period, from October 12 to November 19, 2017. The indoor radon concentrations for October 12–23, 2017 changed with small deviation, but it fluctuated after October 24 with a spike-like pattern that was also identified in our previous study [7].

Table 4 Indoor radon concentrations and environmental variables over 39 days for earthquakes of magnitude ≥4.0

Earthquake occurrence date	Analysis period	Average radon concentration [Bq/m^3]	Maximum/minimum				
			Daily radon concentration [Bq/m^3]	Air inlet temperature [℃]	Relative humidity [%]	Rainfall [mm]	Barometric pressure [mmHg]
17.11.15	17.10.12-17.11.19	631.7 ± 191.0	1027.7 / 327.5	21.3 / 11.4	4.0 / 2.0	24.0 / 0.0	1023.2 / 1006.4
18.02.11	18.01.08-18.02.15	903.1 ± 249.0	1428.8 / 440.5	12.8 / 7.5	2.6 / 1.0	9.5 / 0.0	1026.9 / 1005.2
19.02.10	18.01.07-18.01.14	823.1 ± 198.6	1321.6 / 389.6	14.8 / 10.6	3.9 / 1.4	6.5 / 0.0	1026.9 / 1010.2

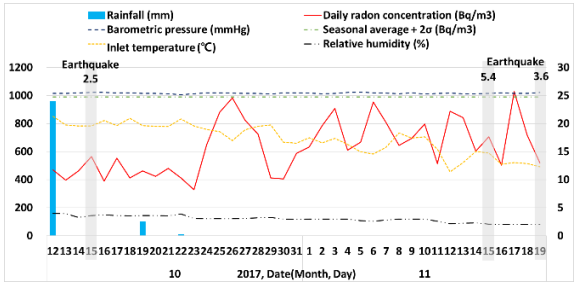

Fig. 4 Daily indoor radon concentration over 39 days October 12-November 19, 2017.

The temperatures at the inlet of the RAD7 gradually decreased overall throughout the same period since the measurement time was during a change of season from autumn to winter. In addition, radon concentrations were measured inside the building and the range of temperature fluctuations were limited. The temperature change trend did not synchronize with the indoor radon concentration change.

The RH was only 4%, even on the day when the rainfall was highest at 24 mm for the measurement period, which indicated that the rainfall did not impact the indoor radon concentration.

The barometric pressure was also relatively constant. Even though was observed an abnormal pattern in the indoor radon concentration patterns starting on October 24, it had changed little. Therefore, the abnormal pattern of the indoor radon concentration could not have resulted from a change in the barometric pressure.

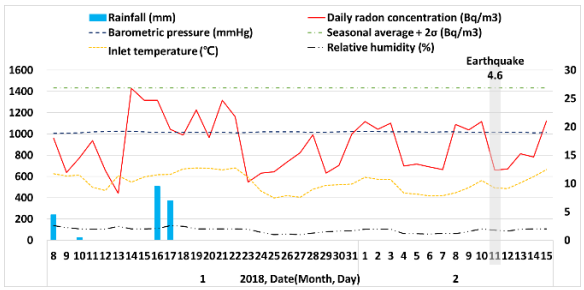

Fig. 5 Daily indoor radon concentration over 39 days January 8-February 15, 2018.

As shown in figure 5, on January 14 2018, peak of the indoor radon concentration reached 1428.8 Bq/m^3, just 4.7 Bq/m^3 lower than 'seasonal average + 2σ'. After that day, the indoor radon concentrations had kept low with a little deviation.

RH and barometric pressure were almost constant for this period. For the four days of this period, it rained, but it had no influence on the radon concentrations and radon fluctuation. In contrast, the inlet temperature seemed to synchronize with the daily radon concentration. However, that could not account for the peak and high radon concentrations during January 14-22, 2018.

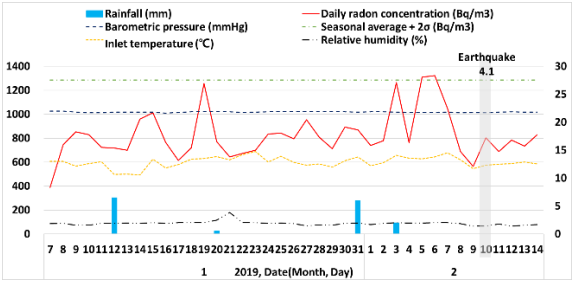

Fig. 6 Daily indoor radon concentration over 39 days January 7-February 14, 2019.

As shown in figure 6, three spike-like patterns were observed in this period, for January 7–February 14, 2019. On January 19, that was 21 days before the earthquake, the daily radon concentration remarkably increased and reached near the 'seasonal average radon concentration + 2σ'. Next, On February 3, the indoor radon concentration rose sharply to 1264.9 Bq/m^3 and it decreased to 762.2 Bq/m^3 on February 4. The next day, it increased again to 1310.2 Bq/m^3 and then gradually decreased to 564.6 Bq/m^3 on February 9, which was one day before the earthquake.

The temperature change trend did not synchronize with that of the indoor radon concentration change overall. The barometric pressure and RH changes were somewhat irrelevant to the indoor radon concentration.

The only notable difference between figs. 4, 5 and 6 was the occurrence time of the radon anomalies before earthquake. The daily indoor radon concentrations over 39 days for three earthquakes were compared in fig. 7. For the earthquake on November 15, 2017, the spike-like patterns were

observed on October 26, 2017, 20 days before the earthquake. The peak radon concentration was measured on January 14, 2018, 28 days before the earthquake on February 11, 2018. Finally, there were the four peaks measured before the earthquake on February 10, 2019. The first occurred 22 days before the earthquake, and others occurred seven, five, four days before the earthquake. For comparison, our previous study found that radon anomalies occurred a month before the 5.8 magnitude earthquake on September 12, 2016, in Gyeongju, and a few days before its aftershocks [7].

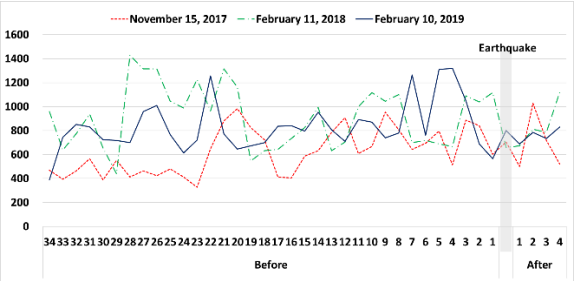

Fig. 7 Comparison of the daily indoor radon concentration over 39 days for the earthquakes of magnitude ≥4.0.

CONCLUSIONS

This study scrutinized the changes in the indoor radon concentrations that were continuously measured in a university building in Gyeongju, Rep. of Korea to see whether a similar pattern recurred in the indoor radon concentration prior to the earthquake or not, which was found in our previous study [7]. We analyzed the 11 earthquakes, and identified that, in nine cases of them, they have radon anomalies before they occurred. For three of the nine earthquakes with magnitude greater than 4.0, we checked what environmental variables mainly caused the fluctuation in the indoor radon concentration. From this, we could not find any environmental variable that seemed to have large influence on the indoor radon concentration. As in our previous study [7], we also identified similar spike patterns prior to earthquakes.

The recurring identifications imply that the indoor radon concentrations inside a building dozens of kilometers from the epicenter might have changed due to seismic activities prior to the earthquake, which could be a precursor and provide indications of an upcoming earthquake. We hope that our study could help identify a clearer relationship between them.

ACKNOWLEDGMENTS

This work is an enlarged version of our previous study [7], [8].

This work was supported by the National Research Foundation of Korea (NRF) grant funded by the Korean government (Ministry of Science and ICT). (No. 2020M2D2A2062436).

REFERENCES

[1] Timothy M.K., Geological Hazards: A Sourcebook, Greenwood Press, 2003.

[2] Sac M. M., Harmansh C., Camgoz B., and Sozbilir H., Radon Monitoring as the Earthquake precursor in fault line in western turkey. Ekoloji. Vol. 20, No. 79, 2011, pp.93–98.

[3] Yasuoka Y., Igarashi G., and Ishikawa T., Evidence of precursor phenomena in the Kobe earthquake obtained from atmospheric radon concentration. Applied Geochemistry, Vol. 21, No.6, 2016, pp.1064–1072.

[4] Sunarno, Firdaus H. L., Luckyarno Y. F., Waruwu M. M., and Wijaya R., Detection system for deterministic earthquake prediction based on radon concentration changes in Indonesia. Journal of Engineering science and technology, Vol. 15, No. 3, 2020, pp.1787-1798.

[5] Planinić J., Radolić V., and Vuković B., Radon as an earthquake precursor. Nuclear Instruments and Methods in Physics Research, Vol. 530, No.3, 2004, pp.568–574.

[6] Virk H. S., and Singh B., Radon anomalies in soil-gas and groundwater as earthquake precursor phenomena, Tectonophysics, Vol. 227, No. (1-4), 1993, pp.215–224.

[7] Kim J. W., Joo H. Y., Kim R., and Moon J. H., Investigation of the relationship between earthquakes and indoor radon concentrations at a building in Gyeongju, Korea. Nuclear Engineering and Technology, Vol. 50, No. 3, 2018, pp.512–518.

[8] Joo H. Y., Kim, J. W., and Moon J. H., Investigation of changes in indoor radon concentrations before and after seismic activities in Gyeongju and Pohang, Korea. International Journal of GEOMATE, Vol. 16, No. 56, 2019, pp.98–103.

[9] Durridge Company Inc., RAD7, Electronic Radon Detector User Manual, 2009.

[10] U.S Environmental Protection Agency (U.S.EPA), Indoor Radon and Radon Decay Product Measurement Device Protocols, Office of Air and Radiation, U.S EPA Publication, 402-R-92-004. 1992.

[11] Hauksson E., and Goddard J. G., Radon precursor studies in Iceland. Journal of Geophysical Research, Vol. 86, No. B8, 1981, pp.7037–7054.

[12] Gregorič A., Zmazek B., Deroski S., Torkar D., and Vaupotič J., Radon as an Earthquake Precursor – Methods for Detecting Anomalies, InTech, Rijeka, Croatia, 2012.

11th Int. Conf. on Geotechnique, Construction Materials & Environment, Kyoto, Japan, 3-5 November 2021, ISBN: 978-4-909106063 C3051

PARAMETRIC MODEL OF LINE TRANSECT SAMPLING FOR GROUPED DATA SET

Noryanti Muhammad[1,2] and Gamil.A.A.Saeed [1]

[1] Center for Mathematical Sciences, College of Computing and Applied Sciences, Universiti Malaysia Pahang, Lebuhraya Tun Razak, 26300, Gambang Kuantan Pahang, Malaysia;
[2] Centre of Excellence for Data Science & Artificial Intelligence, Universiti Malaysia Pahang,26300 Gambang, Malaysia.

ABSTRACT

The density (D) of certain object of the population is important for many areas such as biologists, ecologists and others. The line transect distance technique is used frequently by biometricians and researchers for estimating the population density of the wild population. In this research, we have restricted attention to considering a parametric model for the line transect sampling for grouping data set. The maximum likelihood estimation method is used to estimate the density function $f(0)$ and the interested object. The parametric model has been applied to Laake Stakes real data as the grouped data set. Then, the performance of the proposed estimator is investigated. The result shows that the proposed estimator performance is quite well, but further research should be considered.

Keywords: Grouped data, Line transect sampling, Parametric model.

INTRODUCTION

There are several methods to estimate the population abundance. One of the methods used is the line transect sampling. This technique is an ideal technique to estimate the wild population density due to its advantages. In the line transect sampling technique, the density D of the interested objects on certain area relies upon on the measured of the distances $y_1,...,y_n$ between the detected objects and the line of transect, L. The main assumptions for line transect distance sampling are the detectabilty of the objects on the line transect should have a perfect probability and the observed objects should be detected at their original place. The distance sampling (DS) provides an unbiased estimator for population abundance if these two assumptions are valid as mentioned in Buckland et al. [3]. This lead to define that the concept of detectability function plays the main part of the line transect sampling which can be represented as

$$g(y) = P(\textit{observing object / its perpendicular distances } y). \quad (1)$$

The detectability function $g(y)$ is assume to be a decreasing function on $[0,\infty)$. The probability of detection should close to one as the distance from the line increases from zero, which means that the detection function satisfied the shape criterion $(g(0)=1)$. Let $y_1,...,y_n$ denoted to the grouped observed perpendicular distances which selected randomly and independently from the line transect. Then, the density function $f(y)$ is defined on $[0,w)$ given by Burnham and Anderson [5] as

$$f(y) = \frac{g(y)}{\int_0^w g(u)du} \quad (2)$$

By assuming that all objects present on the line and have perfect probability, Burnham and Anderson [5] proved that the density D of the observed objects in surveyed area is related to the probability density function (pdf) $f(y)$ which determined at $y=0$ as

$$D = \frac{E(n) f(y=0)}{2L} \quad (3)$$

where $E(n)$ is the expected value of observed objects. The density D is estimated by $\hat{f}(0)$ due to the density D depends to $f(0)$. According to Burnham and Anderson [6] and Buckland et al. [2], [4], the density D is estimated by

$$\hat{D} = \frac{n}{2L}\hat{f}(0) \quad (4)$$

Several parametric models have been proposed to estimate $f(0)$, for example in Gates et al. [7], Hemingway [8], Ababneh and Eidous [1] and Saeed et al. [10].

The Model

Let $y_1,...,y_n$ random variables and identically and independent distributed (iid) of size n observed perpendicular distances which have probability density function (pdf) $f(y)$ and detection function $g(y)$. Saeed et al. [10] introduced a detection function,

$$g\left(y;\sigma^2\right)=\left(2-e^{-y^2/2\sigma^2}\right)e^{-y^2/2\sigma^2};y\geq 0,\sigma^2>0. \quad (5)$$

and the corresponding pdf is given by Saeed et al. [10] as

$$f\left(y;\sigma^2\right)=\frac{2}{\left(2\sqrt{2}-1\right)\pi\sqrt{\sigma^2}}\left(2-e^{-y^2/2\sigma^2}\right)e^{-y^2/2\sigma^2} ;y\geq 0,\sigma^2>0 \quad (6)$$

The model in Eq. (6) has been studied by Noryanti et al. [9] to fit the ungrouped line transect data.

MATERIAL AND METHODS

Parametric Model and Grouped Data

Grouped data is distances of detected objects which has been organised in group. Distances usually are grouped which been binned with intervals defined by cut points. Rounding errors in measurements often cause the data to be grouped to some degree, but it must be analysed either it had been recorded accurately or grouped further, in attempt to reduce the effects of rounding on bias. Distances are often assigned to be predetermined distance intervals, therefore must be analysed using an appropriate method developed for frequency grouped data. Burnham et al. [6] gave two reasons for considering to analysis of the grouped data. First, line transect data are sometimes recorded in a grouped. Second, the grouping is sometimes necessary to achieve robustness due to problems during data recording or inaccurate field measurements.

Assume that the perpendicular distances were taken in the field only by intervals, or for some reasons, the perpendicular distances must be analysed as grouped data. Consider n perpendicular distances are grouped into intervals (or bins) corresponding to whether it independently falls into one of the intervals. The number of perpendicular distance counted in distance interval i is $m_i\ i,i=1,...,k$ and $n=\sum_{i=1}^{k}m_i$ where n is the total sample size. Assume that each distance independently falls into one of the intervals with probability $P_i;i=1,...,n$, then the distribution of m_i is multinomial with probabilities $P_i;i=1,...,k$. For such a scheme it is natural, at least in large samples, to use the unbiased estimator of P_i , the relative frequency is given as

$$\hat{P}_i=\frac{m_i}{n}. \quad (7)$$

For grouped line transect data using maximum likelihood estimator (MLE), Burnham and Anderson [6] stated that if $f(y)$ is follows any pdf(s) for the ungrouped perpendicular distances data, an estimator of $f(y=0)$ can validly be based on the model using grouped data.

Let the perpendicular distances be grouped into k intervals by cut points, $a_0<a_1<...<a_k$; the i^{th} intervals is $\left(a_{i-1},a_i\right)$ with $a_0=0$ and $a_k=w$, w may be chosen to be larger than the largest perpendicular distance. Each detection object will fall into one of the k mutually exclusive intervals, then the probabilities satisfy the condition

$$\sum_{i=1}^{k}P_i=1. \quad (8)$$

Consider the perpendicular distances as a grouped data, then, the multinomial likelihood function given by Buckland et al. [3] as

$$P\left(m_1,m_2,...,m_k\right)=\frac{n!}{m_1!m_2!...m_k!}\prod_{i=1}^{k}P_i^{m_i}, \quad (9)$$

where m_i is the number of objects counted in the distance interval $i,i=1,...,k$, $n=\sum_{i=1}^{k}m_i$, and

$$P_i=\int_{a_{i-1}}^{a_i}f\left(y\right)dy=F\left(a_i\right)-F\left(a_{i-1}\right), \quad (10)$$

where $a_0=0,a_1,...,a_k=w$ are the cut points between bins and $F\left(y\right)$ is the cumulative distribution (CDF) of the pdf $f\left(y\right)$. In this case, the proposed model $f\left(y\right)$ is fitted to the grouped data by linking the model in Eq. (6), P_i has been expressed as function of σ^2 .

The Maximum Likelihood Estimator

For a given data set, the log likelihood function is given by Buckland et al. [3] as

$$\ln L\left(\sigma^2\right) = \ln\left(\frac{n!}{m_1!m_2!...m_k!}\right) + \sum_{i=1}^{k} m_i \ln P_i, \qquad (11)$$

In this case, each cell probability P_i has been expressed as

$$P_i = \int_{a_{i-1}}^{a_i} f\left(y;\sigma^2\right)dy = F\left(a_i\right) - F\left(a_{i-1}\right), \qquad (12)$$

where $F\left(y\right)$ is the CDF of the corresponding density function $f\left(y;\sigma^2\right)$ which is given in Equation (6). The MLE of the σ^2 is the solution of the following equation,

$$\frac{d\ln L\left(\sigma^2\right)}{d\sigma^2} = \sum_{i=1}^{k} \frac{m_i}{P_i}.\frac{P_i}{d\sigma^2} = 0. \qquad (13)$$

The MLE of the σ^2 is obtained numerically in order to estimate the $\hat{f}(0)$ by differentiate the Eq. (11) with respect to σ^2 and solve the Eq. (13). Hence, the MLE estimator of $\hat{f}(0)$ and the density of the interested object D based on the parametric model in Saeed et al. [10] are given as

$$\hat{f}\left(0\right) = \frac{2}{\left(2\sqrt{2}-1\right)\pi\sqrt{\hat{\sigma}^2}}, \qquad (14)$$

and

$$\hat{D} = \frac{n}{2L}\hat{f}(0). \qquad (15)$$

Data Description

The Laake stakes data set which is given in Burnham and Anderson [6] is reanalyzed in this study by applying the parametric model in Saeed et al. [10]. The data were collected by using line transect technique to estimate the density of the stakes. These data are the perpendicular distances (in meters) of detected stakes from the line transect. In this experiment, the investigator was placed 150 stakes at random in an area of $L = 1000$ meters long. Out of 150 stakes, 68 stakes were detected. The true pdf $f\left(y\right)$ for the perpendicular distances is unknown, but the true density $\left(D\right)$ of stakes is known and equals to $0.00375 stakes/m^2$, which gives the true value of $f\left(0\right) = 0.110294$. The value of $f\left(0\right)$ can be obtained by using the following equation

$$D = \frac{n}{2L} f\left(0\right)$$

The perpendicular distances for the 68 stakes found are reproduced in Table 1.

Table 1 Laake Stakes Data. Note: The data shown are perpendicular distances in meters and appear on page 62 of Burnham et al. [6].

No	y_i	No	y_i	No	y_i	No	y_i
1	2.02	18	1.61	35	3.79	52	8.49
2	0.45	19	31.31	36	15.24	53	6.08
3	10.40	20	6.50	37	3.47	54	0.40
4	3.61	21	8.27	38	3.05	55	9.33
5	0.92	22	4.85	39	7.93	56	0.53
6	1.00	23	1.47	40	18.15	57	1.23
7	3.40	24	18.60	41	10.05	58	1.67
8	2.90	25	0.41	42	4.41	59	4.53
9	8.16	26	0.40	43	1.27	60	3.12
10	6.47	27	0.20	44	13.72	61	3.05
11	5.66	28	11.59	45	6.25	62	6.60
12	2.95	29	3.17	46	3.59	63	4.40
13	3.96	30	7.10	47	9.04	64	4.97
14	0.08	31	10.71	48	7.68	65	3.17
15	11.82	32	3.86	49	4.89	66	7.67
16	14.23	33	6.05	50	9.10	67	18.16
17	2.44	34	6.42	51	3.25	68	4.08

RESULTS AND DISCUSSION

The stakes data set has been grouped to find the value of the proposed estimator $\hat{f}(0)$ as in Eq. (13). The Stakes data pooled into six intervals, each interval with group width is equals to 3.195. The corresponding frequency of intervals is demonstrated in Table 2. Based on the table, the frequency histogram of the perpendicular distances which were grouped into six intervals is shown in Fig.1.

Table 2 The interval boundaries of six intervals for perpendicular distances of Stake data and the corresponding number of observations.

Interval Number	Boundaries of intervals	Number of observations
1	0.000-3.195	23
2	3.195-6.295	19
3	6.295-9.395	14
4	9.395-12.495	5
5	12.495-15.595	3
6	15.595-31.31	4

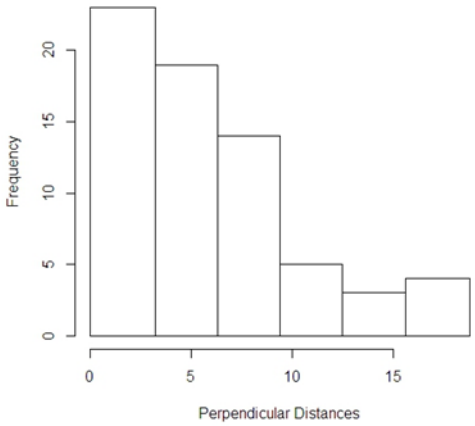

Fig. 1 The frequency histogram of Stakes data which grouped into six equally intervals.

The MLEs of D and $f(0)$, and the corresponding $\hat{D}$ and $\hat{f}(0)$ respectively, based on the proposed model in Saeed et al. [10], using Eq. (14) and (15) are computed depending on $\hat{\sigma}^2$. Table 3 shows the values of the estimators $\hat{\sigma}^2$, $\hat{f}(0)$ and $\hat{D}$. Based on the table, the values of the proposed estimators $\hat{f}(0)$ and $\hat{D}$ quite close to the true parameters. However, after remove the cut point of $w_k = 31.31$, the values of the proposed estimators $\hat{f}(0)$ and $\hat{D}$ are improve to 0.097654 and 0.00327 stakes/hectare, respectively.

Table 3 The MLE of $\hat{\sigma}^2$, $\hat{f}(0)$ and $\hat{D}$ for grouped data.

Number of observed distances		$\hat{\sigma}^2$	$\hat{f}(0)$	$\hat{D}$
Actual	68	na	0.110294	0.00375
Proposed	68	44.9659	0.092031	0.00313
	67	39.9371	0.097654	0.00327

CONCLUSIONS

As conclusion, the concept and the essential role of distance sampling (DS) is important in the estimation of the population densities has been presented. Based on the results, the proposed estimators perform better in case of $n = 67$ compared to $n = 68$, this due to outlier which has been removed. Overall, the values of proposed estimators $\hat{f}(0)$ and $\hat{D}$ are quite close to the true values of $f(0)$ and D for both sample size. However, in this paper, the work has been restricted to use the parametric model to fit the line transect by only considering a grouped data set. Currently, the other estimation methods and different interval are considered.

ACKNOWLEDGMENTS

We gratefully thanks to Ministry of Higher Education of Malaysia (FRGS Grant RDU 1901190) (FRGS/1/2019/STG06/UMP/02/11) and Universiti Malaysia Pahang for financial support under Doctoral Research Scheme (DRS). We also thanks Ministry of Yemen Higher Education for sponsor this research study.

REFERENCES

[1] Ababneh, F. and Eidous, O. M. 2012 A weighted exponential detection function model for line transect data. Journal of Modern Applied Statistical Methods. Vol. 11, No. 1, 144-151.

[2] Buckland, S. T., Anderson, D. R., Burnham, K. P. and Laake, J. L. 1993 Distance sampling Chapman and Hall, London.

[3] Buckland, S. T., Anderson, D. R., Burnham, K. P., Laake, J. L. Borchers, D.L., and Thomas, L. 2001. Introduction to distance sampling Oxford university Press, Oxford.

[4] Buckland, S. T., Rexstad, E. A., Marques, T. A. and Oedekoven, C. S. 2015 Distance sampling: methods and applications Springer.

[5] Burnham, K. and Anderson, D. (1976). Mathematical models for nonparametric inferencesfrom line transect data. Biometrics, pages 325–336.

[6] Burnham, K. P., Anderson, D. R., and Laake, J. L. (1980). Estimation of density from line transect sampling of biological populations. Wildlife monographs, (72):3–202.

[7] Gates, C. E., Marshall, W. H., and Olson, D. P. (1968). Line transect method of estimating grouse population densities. Biometrics, pages 135–145.

[8] Hemingway, P. (1971). Field trials of the line transect method of sampling large populations of herbivores. The scientific management of animal and plant communities for conservation, pages 405–411.

[9] Noryanti Muhammad, Gamil.A.A. Saeed and Wan Nur Syahidah binti Wan Yusoff 2018 ASM Sci. J. Special Issue 2018(1).

[10] Saeed, G. A. A., Muhammad, N., Liang, C. Z., Yusoff, W. N. S. W. and Salleh, M. Z. 2017 J. Phys.: Conf.Series 890 IOP Publishing (p. 0121

11th Int. Conf. on Geotechnique, Construction Materials & Environment,
Kyoto, Japan, 3-5 November 2021, ISBN: 978-4-909106063 C3051

SEDIMENT ACCUMULATION ASSESSMENT DURING WET AND DRY SEASONS IN FISH CAGE CULTURE AREA: A CASE STUDY OF THE RANGSIT CANAL 13 IN THAILAND'S PATHUM THANI PROVINCE

Boontarika Thongdonphum[1], Kittima Vanichkul[1], Sangob Srimueang[1] and Adun Bunchaleamchai[2]

[1]Faculty of Agricultural Technology, Rajamangala University of Technology Thanyaburi, THAILAND
[2]Faculty of Medical Technology, Rangsit University

ABSTRACT

This research investigates the sedimentation rate for assessment of sediment accumulation in fish cage culture area, Rangsit canal 13 in Thailand's central province of Pathum Thani. Water and sediment qualities were conducted during September 2017 (rainy season) and March 2018 (dry season). The temperatures, dissolved oxygen, and pH ranged between 30.5-31.5 ^{O}C, 5.54-7.78 mg L^{-1}, and 7.7-8.1, respectively. The results revealed that the dissolved oxygen varied from season to season ($p \leq 0.05$). The results indicated that the water qualities varied in response to the seasonal variability and alarmingly higher than Thailand's minimum threshold for aquaculture. In term of sediment qualities, variations in water content, total organic matter, and sedimentation rate ranged between 37.4-62.4%, 67.6-97.6 mg g-dry weight^{-1}, and 438.8-3,768.8 g $m^{-2}day^{-1}$, respectively. The results revealed that water content and total organic matter had not different significance ($p > 0.05$) while sedimentation rate varied significantly ($p \leq 0.05$) with seasons. Such levels of total organic matter and sedimentation rate were highly in the area, especially in the rainy season. The finding also showed that mass transfer and water inflow in the area, especially in the rainy season, influenced on the sediment output in the water system, indicating the adequate of sediment input-output balance. The water mass transfer will require consideration for the assessment of sediment accumulation and water resource management in the study area.

Keywords: Sedimentation rate, Accumulation, Fish cage culture

INTRODUCTION

The south Rangsit canal is located in Thailand's central province of *Pathum Thani*, about 50 km north of the capital Bangkok [1] . The canal is on the east of the *Chao Phraya River* and approximately 54 km in length [2]. Land utilization along the canal is categorized into four main categories: urban areas, agriculture, aquaculture, and industry [3]. The Rangsit canal 13 is one of the main canal's branch. In fact, water resources are used in more than 1,000 cages for fish farming, such as raising tilapia, catfish, and other freshwater fish throughout the year [4]. Aquaculture using the natural systems saves the financial cost on water preparation and improvement [5]. By the way, in the event of a flood, this could have an impact on production risks. The sediment in the water, as well as pollution from human activities, causes cloudiness. and fish disease epidemics [6]. The canal's deteriorating biochemical composition, including excessive nutrient loadings, is a result of increased area utilization [7].

The process of sedimentation from the surface water to the bottom. It can reflect the area's activity and physical condition, as well as the effects of precipitation on the sediment's chemical quality. The occurrence of anaerobic conditions in the soil, as well as the continuous accumulation of sulfides, which are toxic to benthic organisms [8]. As a result, one of the most important factors affecting the quality of fishery production is the problem of sediment quality in the culture area.

Fish cage culture's impact on sediment quality. It's necessary to monitoring and assess the sediment quality at a level that does not have an impact on water resources. Thus, this current research aims to comparatively investigate the effects of seasonal variability (the rainy and dry seasons), the sediment quality and sedimentation rate in the fish cage area. The findings are expected to avoid any negative impact on the ecosystems of water resources, which will be used for aquaculture and the production of fishery products for farmers in the future.

MATERIALS AND METHODS

Sampling sites

In this research, eight localities with along the Rangsit canal 13 were selected as the sampling stations (Fig.1) and were clustered in a 'fish cage area' (Stn. 1, 4, 7, and 8), and 'without fish cage' (Stn. 2, 3, 5, and 6) in sampling site. The water and sediment sampling were conducted in two separate

time periods to take account of the effects of seasonal variability: September 2017 (rainy season) and March 2018 (dry season). Under the influence of monsoon winds, Thailand has three seasons: rainy season (May-September), winter season (October-February) and dry season (March-April) [9]. In addition, the Rangsit canal 13 is under the jurisdiction of the North Rangsit Irrigation Office, which is responsible for management and maintenance of the canal water for local demand [10]. Here, water management depending on the situation and agricultural activities. During the dry season, for example, the water discharge level was 64.8x10^6 m^3/month under normal conditions. When wastewater is present, the water discharge rate can be increased to 181.4x10^6 m^3/month.

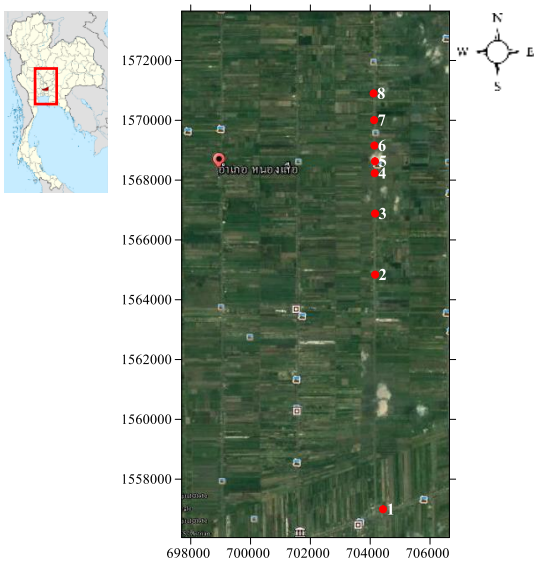

Fig. 1 Sampling stations (UTM; 47P) from the satellite image of the Rangsit canal 13 with the eight sampling stations (St.1-8)

Sample collection and analysis

The temperatures, dissolved oxygen (DO), and pH of the water samples were measured with a multi-parameter probe (YSI-6600 Sonde instrument) at the sampling sites (st.1-8). In the nutrient analysis, surface water samples (30 cm deep) were collected and pre-filtered using GF/F (Whatman) and retained at 4 ^{o}C for further analysis. The ammonium (NH_4^+), nitrite and nitrate (NO_2^-+NO_3^-) and orthophosphate (PO_4^{3-}) concentrations were determined using a SKALAR segmented flow analyzer, given the corresponding detection limits of 0.70-57.14; 0.70-14.28 and 0.03-3.87 µmol L^{-1}. Samples to determine the levels of chlorophyll a and total suspended solids (TSS) were collected and placed in polyethylene bags that were kept away from direct light and heat. The samples were filtered through pre-weighed GF/F. Chlorophyll a and TSS measurements were analyzed according to a spectrophotometric method and a freeze-dried technique, respectively.

The sedimentation rates were determined using sedimentation traps, including two attached cylinders (30 cm height and 10 cm diameter) and made up of two cylinders with an open top and a closed bottom. Each cylinder was placed at the bottom and was taken through after 24 hours. The particulate matter generated during the investigation was measured in samples collected in sedimentation chambers installed below all the net cages. Sedimentation trap samples were collected and placed in polyethylene bags that kept frozen at -20 ^{o}C for no longer than two months before being defrosted for analysis. The sedimentation rates were perform using the gravimetric method, consists of measuring the weight loss of components. The sedimentation rate was given in g m^{-2} day^{-1}. The water content was determined using an oven-drying method at 110 ^{o}C for 48 hours. After heating the dried sediment at 660 ^{o}C for 3 hours, the organic matter content was measured by weight difference.

Data analysis

Physicochemical properties of the water and sediment samples associated with both sampling periods September 2017 (rainy season) and March 2018 (dry season) were determined using descriptive statistics and presented as means ± standard deviations (SD). T-test was used to verify statistical differences between the two study periods, with $p \leq 0.05$.

RESULTS

Table 1 shows the physicochemical characteristics of the water samples for both study periods (rainy and dry seasons). Results revealed that water temperature and pH varied minimally from season to season ($p > 0.05$). Sampling locations (st.1-12) and seasonal variability had no significant impact on pH levels which remained relatively constant throughout (Fig. 2c).

Table 1 Physicochemical properties of water samples (mean±SD)

Parameters	Study period	
	September 2017 (rainy)	Match 2018 (dry)
Temp (^{o}C)	30.8±0.2^a	30.9±0.3^a
DO (mg L^{-1})	4.9±0.4^a	5.9±0.8^b
pH	7.9±0.1^a	7.8±0.1^a
NH_4^+ (µmol L^{-1})	7.6±4.3^a	4.0±1.7^b
NO_2^-+NO_3^- (µmol L^{-1})	5.6±1.5^a	6.5±0.6^a
PO_4^{3-} (µmol L^{-1})	0.7±0.3^a	1.0±0.1^b
Chlorophyll a (µg L^{-1})	9.2±1.9^a	20.2±5.7^b
TSS (mg L^{-1})	59.0±15.7^a	19.8±6.0^a

Note: The values in the same row with different superscript letters are significantly different ($p \leq 0.05$).

The DO varied from 4.5 to 5.6 and 5.1-7.8 mg L^{-1} in rainy and dry season, respectively, and showed in response to seasonal variability ($p \leq 0.05$) at alarmingly higher than Thailand's minimum threshold of 4 mg L^{-1}. Average levels of NH_4^+ varied significantly ($p \leq 0.05$) with the season. Maximum concentrations of NH_4^+ found in rainy season. Observations also revealed that $NO_2^- + NO_3^-$ and PO_4^{3-} were high during the dry season ($p \leq 0.05$).

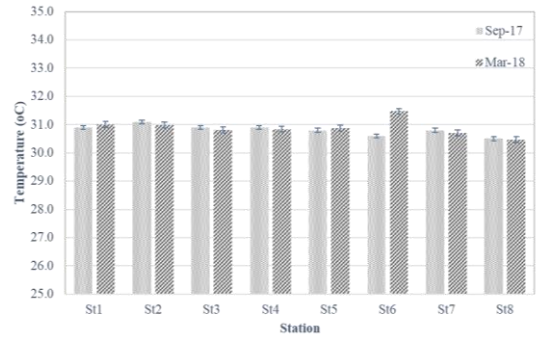

(a)

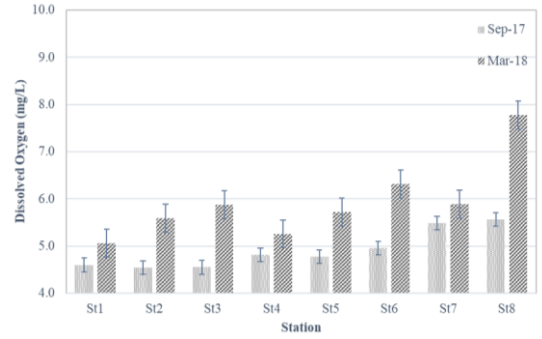

(b)

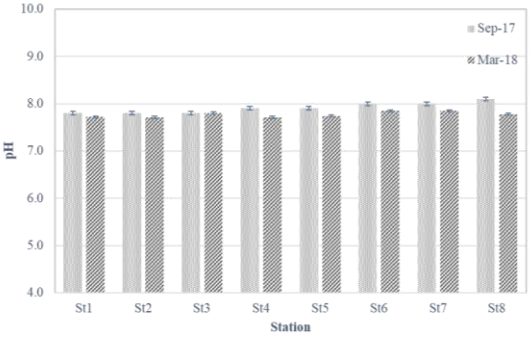

(c)

Fig. 2 Distribution of (a) water temperature (°C), (b) dissolved oxygen (mg L^{-1}) and (c) pH in the Rangsit canal 13 surveyed during September 2017 and March 2018

Levels of chlorophyll a varies from 7.8 to 13.6 μg L^{-1} and 8.4 to 25.4 μg L^{-1} in rainy and dry season, respectively. Chlorophyll a varied significantly ($p \leq 0.05$) by season. High levels were apparent at St. 2 (>10 (μg L^{-1}) in rainy season, where somewhat high, which may have been a result of this sampling point being situated just near an urbanization. In addition, the average levels of chlorophyll a showed higher than 10 μg L^{-1} in dry season. Such levels reflected signs of plankton blooming and the watercolor was visibly changed.

High concentrations of TSS were found during the rainy season and varied from 39.6 to 91.5 mg L^{-1}. Higher TSS concentrations in the st.3 area reflected greater anthropogenic particulate loads from canal dredging. Sediment overloading as a result of land and stream erosion has serious consequences for the environment.

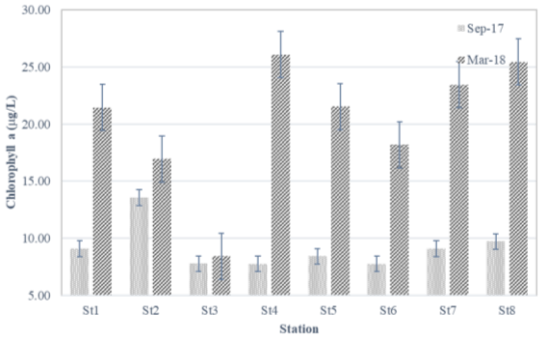

(a)

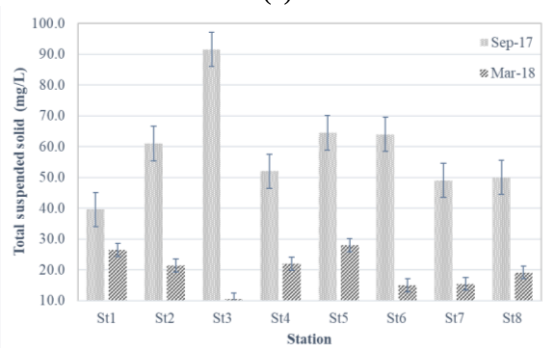

(b)

Fig. 2 Distribution of Chlorophyll a (μg L^{-1}) and TSS (mg L^{-1}) in the Rangsit canal 13 surveyed during September 2017 and March 2018

Table 2 shows the physical characteristics of the sediment samples for both study periods (rainy and dry season). Water content could be defined texture and structure of sediment, such as soil, rock, clay. WC varied from 37.4 to 59.8% and 41.7 to 62.4% in rainy and dry season, respectively ($p > 0.05$). High levels were apparent at Stn. 8 in both seasons.

TOM shows high levels, varied from 70.2 to 97.6 and 67.6 to 97.0 mg g-dry $weight^{-1}$ in rainy and dry season, respectively. Sedimentation rate varied from 1,031.3 to 3,768.8 and 438.8 to 1,699.4 g m^{-2} day^{-1} in rainy and dry season, respectively.

Table 2 Physical properties of sediment samples (mean±SD)

Parameters	Study period	
	September 2017 (rainy)	Match 2018 (dry)
WC (%)	46.6±9.4[a]	48.8±8.3[a]
TOM (mg g^{-1} dry-weight)	86.9±10.1[a]	84.0±9.3[a]
Sedimentation rate (g m^{-2} day^{-1})	2,719.6±1,068.1[a]	1,133.6±469.5[b]

Note: The values in the same row with different superscript letters are significantly different (p≤0.05).

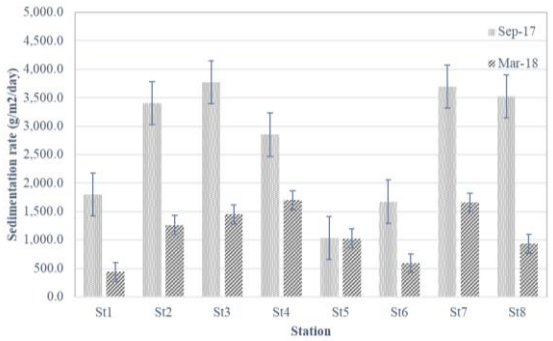

Fig. 2 Distribution of Sedimentation rate in the Rangsit canal 13 surveyed during September 2017 and March 2018

DISCUSSIONS

Research showed that the temperature of the channel water varied minimally for seasons, while the pH was consistent throughout the entire period. The findings revealed the alarmingly higher than Thailand's minimum threshold of 4 mg L^{-1}, rendering it unfit for the aquatic animals [11]. In water quality assessment, NH_4^+ is an important indicator of the water quality [11]. The NH_4^+ levels in water bodies should be below 1 mg L^{-1} (or 71.4 μmol L^{-1}) [12], and the PO_4^{3-} levels below 1 μmol L^{-1} to avert eutrophication [13]. The PO_4^{3-} levels in the *Rangsit* canal 13 were in excess of the limit during dry season. In addition, land use could contribute to nitrogen enrichment in the river [14], while phosphorus emission from wastewater is prevalent in highly populated areas [15]. Nutrients, particularly nitrogen and phosphorus, are directly related to the eutrophication of waters [16]. The wastes from fish farming can cause problems due to the high sedimentation load of total dissolved solids and nutrients such as nitrogen and phosphorus [17]. When the flow is less than $40x10^6$ m^3 $month^{-1}$, the water quality is poor [18].

Chlorophyll a showed higher than 10 μg L^{-1} in dry season. Such levels reflected signs of plankton blooming and the watercolor was visibly changed. Higher TSS concentrations could be reflected greater anthropogenic particulate loads in those areas [13] and freshwater inflow and precipitation-induced drainage influenced the TSS level. Fish cage culture, along with other activities such as agriculture, pond aquaculture, livestock, paddy fields, and household sewage discharge, all contributed to changes in the canal's water quality [18]. Excessive release of this nutrient into the aquatic environment can cause eutrophication and a variety of conflicts related to the use of affected ecosystems [17].

Solid waste, also known as particulate organic matter, is frequently composed of feces or uneaten food. Organic wastes are present in the recirculation system in three forms: settled solids, which accumulate on the tank's bottom; suspended solids, which float in the water column and will not settle out of water; and fine and dissolved solids, which float in the water column and can cause gill irritation and health damage to fish [19]. The potential for sedimentation rate may be greatly enhanced by the discharge of large pulses of water. According to [10], During the dry season, the water discharge level can be increased to control wastewater and support agricultural areas. The water's homogeneity could be a result of the canal's shallowness of 2.5-4.0 meters and the water flow that flushed solid waste downstream via the sluice gate [18]. The accumulated water in reservoirs disrupts the river's hydro-morphodynamic continuity, accumulating not only water but also sediment transported by the river [20]. Fish farming contributes the organic matter to the environment. The finding indicated the high level of total organic matter in the area. The tilapia cultivation in net cages increased the sedimentation rates of nutrients and particulate matter [17]

CONCLUSIONS

Effects of seasonal variability (rainy and dry seasons) and sediment accumulation patterns on the fish farming**,** the Rangsit canal 13 in Thailand were investigated. The DO showed in response to seasonal variability at alarmingly higher than Thailand's minimum threshold of 4 mg L^{-1}. Average levels of NH_4^+ varied significantly (p≤0.05) with the season and lower than NH_4^+ limitation in water bodies. The PO_4^{3-} levels were in excess of the limit during dry season. The levels of total organic matter and sedimentation rate were highly in the area. Sedimentation rates was high during the rainy season. The sediment accumulation was found to be season-dependent. The results revealed that the amount of

water that flows through the system during the rainy season is higher than the dry season. This increases the likelihood of water bodies sediment erosion. The water release level of the area is controlled compared to the dry season.

ACKNOWLEDGMENTS

The authors would like to extend their deep gratitude to the Research Institute and Faculty of Agricultural Technology, Rajamangala University of Technology Thanyaburi (RMUTT) for financial support.

REFERENCES

[1] Pathum Thani Office Center, Development Plan of Pathum Thani Province, assessed : http://www2.pathumthani.go.th/551017.pdf, (April 3, 2019)

[2] RIO 11, Data Project, South Rangsit Irrigation Project, Regional Irrigation Office 11, Royal Irrigation Department , Ministry of Agriculture and Cooperatives, assessed : http://ridceo.rid.go.th/pathum/rangsits/Data.html, (Aug 22, 2012)

[3] Thongkumpow J. and Sumpanpanit P., Water Use Patterns of the Irrigation Area in Klong Rang Sit Tai, Environmental research institute, Chulalongkorn university intellectual repository, 1997.

[4] Pathum Thani Provincial Fisheries office. (2016). Number of Farmers. Department of Fisheries. Assessed : http://www.fisheries.go.th/fpo-pathumtani/t052.html, (April 28, 2016).

[5] Kasamesiri, P. and Thaimuengphol, V., Trophic status of Nile Tilapia Cage Culture Areas in the Central Part of Chi River. Burapha Science Journal, Vol 20, Issue 2, 2015, pp. 48-55.

[6] Lebel, P., Leudpasuk, S., Lebel, L. and Chaibu, P., Fish Cage Culture in Upper Part of Ping River. Journal of Fisheries Technology Research, Vol 1, Issue 2, 2007, pp. 160-170.

[7] Thongdonphum B., Meksumpun S., Meksumpun C., Sawasdee B. and Kasemsiri P., The Predictive Model for Biochemical Component of Phytoplankton in the River and Estuary System of the Mae Klong River, Thailand, International Journal of Environmental and Rural Development, Vol. 4-1, 2013, pp. 13-18.

[8] Faculty of Fisheries, Final report on Bang Pakong Electricity Generating Authority of Thailand on the Impact of Drainage from the Cooling System of the Bang Pakong Power Plant on Water Quality, Sediment, and Biological Resources in the Bang Pakong River, Kasetsart University, Bangkok, Thailand, 2003.

[9] TMD, Climate of Thailand, Thai Meteorological Department, Thailand, assessed : https://www.tmd.go.th/info/info.php?FileID=53 (April 15, 2021)

[10] North Rangsit Irrigation Office, Water Resources Management. accessed : http://ridceo.rid.go.th/pathum/rangsitn/about/abouthead.html, (April 5, 2019)

[11] Pollution Control Department, Water Quality Standard, assessed : http://www.pcd.go.th/info_serv/reg_std_water06.html (March 20, 2021)

[12] PHILMINAQ, Water Quality Criteria and Standards for Freshwater and Marine Aquaculture, Mitigating Impact from Aquaculture in Philippines, assessed: https://www.researchgate.net/file.PostFileLoader.html?id=571b93653d7f4b012861d0a1&assetKey=AS%3A354056255098880%40146142499773 9. (Mar 2, 2016)

[13] Thongdonphum B., Meksumpun S. and Meksumpun C., Nutrient Loads and their Impacts on Chlorophyll a in the Mae Klong River and Estuarine Ecosystem: An Approach for Nutrient Criteria Development. Water Science and Technology, Vol. 64, Issue 1, 2011, pp. 178-188.

[14] Li R., Liu S., Zhang G., Ren J. and Zhang J., Biogeochemistry of Nutrients in an Estuary Affected by Human Activities: the Wanquan River Estuary, eastern Hainan Island, China, Continental Shelf Research, Vol. 57, 18-31.

[15] Mockler E.M., Deakin J., Archbold M., Gill L., Daly D. and Bruen M., Sources of Nitrogen and Phosphorus Emission to Irish Rivers and Coastal Waters: Estimates from a Nutrient Load Apportionment Framework, Science of the Environment, Vol. 601-602, 2017, pp. 326-229.

[16] Júlio César da Silva Cachoa, Rodrigo Sávio Teixeira de Mourab, Gustavo Gonzaga Henry-Silva., Influence of Nile tilapia (*Oreochromis niloticus*) Fish Farming in Net Cages on the Nutrient and Particulate Matter Sedimentation Rates in Umari Reservoir, Brazilian semi-arid, Aquaculture Reports, Vol 17, 2020, pp. 1-7.

[17] Montanhini R.N. and Ostrensky A., Nutrient Load Estimation in the Waste of Nile Tilapia Oreochromis niloticus (L.) Reared in Cages in Tropical Climate Conditions, Aquaculture Research, Vol 46, 2015, pp.1309-1322.

[18] Ingthamjitr S., Paankhao N., Lueangtongkham W. and Oopariktatipong K., The Impact of Fish Cage Culture on Water Quality of Taasarn-Bangpla Canal, Nakhon Pathom Province, Thailand, Journal of Fisheries and Environment, Vol 41 (1), 2017, pp. 37-44.

[19] Cao L., Wang W., Yang Y., Yang C., Yuan Z., Xiong S. and Diana J., Environmental Impact of Aquaculture and Countermeasures to Aquaculture Pollution in China, Environmental Science Pollution Research, Vol 14 (7), 2007, pp. 452-462.

[20] Reisenbüchler M., Bui M.D., Skublics D. and Rutschmann P., Sediment Management at Run-of-River Reservoirs Using Numerical Modelling, Water, Vol 12, pp. 3-17.

11th Int. Conf. on Geotechnique, Construction Materials & Environment, Kyoto, Japan, 3-5 November 2021, ISBN: 978-4-909106063 C3051

WATER POLLUTION OF THE JYUSHI-GAWA RIVER IN YOKKAICHI-CITY

Yukimasa Takemoto[1], Masaaki Takahashi[1], Maki Ooyagi[1], Shigeaki Inagaki[2], Atsushi Suzuki[3]

[1]Faculty of Environmental and Information Sciences, Yokkaichi University, Japan; [2]Tomida-Chiku Machizukuri Kyougikai, Jyushi-Gawa to Kankyou wo Mamorukai, Japan; [3]Mie Prefecture Environmental Conservation Agency, Japan

ABSTRACT

The Jyushi-Gawa river is a very short river, which flows down through the northern part of Yokkaichi-City to Ise-Bay. Recently, around the catchment area, many factories and stores have been constructed, and water pollution is concern. In order to confirm the influences of these factories and stores, investigations on the water quality of the river were carried out for 10 years. In the middle of the river, inflow of the wastewater is obvious, and many pollutants (Nutrients; COD, NO_3-N, PO_4-P) were found.

Key words; Jyushi-Gawa, domestic water, water pollution, Yokkaichi

INTRODUCTION

The Jyushi-Gawa river is a small river (length about 4 km) which flows down through the northern part of Yokkaichi city. Many cherry trees are planted on the bank, and the river attracts many citizens. The catchment area of the river is located near the Higashi-Meihan Highway Interchange. Around the upstream and midstream of the river, waste disposal sites, factories and stores are constructed. From those developments, water pollution of the river is considered serious [1] [2]. In order to confirm the level of the pollution, investigations were carried out for 10 years [3].

FEATURE OF THE CATCHMENT AREA OF JYUSHI–GAWA RIVER

Almost all of the catchment area is spread around the upstream (around St5, in Fig.1) and midstream (St3 to St4 in Fig.1) of the river. On the contrary, the downstream (St1 to St3 in Fig 1) has very small catchment area because of the river structure (raised bed). In order to prevent floods, bank and river bed are covered with concrete. The flow rate of the river (based on the data of this research show in Fig.2) apparently increases at St3 mainly in autumn and winter. The increase in flow rate is due to the introduction of the Asake-Yousui irrigation.

The upstream side of the river is located around the hillside (about 40m height), and is covered with fields or forests. Near here the Oyachi-Heizu waste disposal site was constructed about 40 years ago, but to now closed. For over 10 years, many factories and warehouses have been built on the upstream side. In this area, a public sewage system is not provided, and factories are treating their wastewater using own water treatment facility. The reservoir (space 8336m^2, volume: 20325 m^3) was constructed in 2009 between St5 and St4, and rain water is stored there during heavy rain fall, but its effect on improving water quality is not clear.

At the midstream of the river, supermarkets, restaurants and many houses were constructed, and the sewage system is not provided, so each store is treating the domestic wastewater using the private water treatment equipment. However, some residents in this area that do not have the private sewage tank, discharge wastewater directly into the river. Around the area (between St3 to St4) a sewage system is currently under construction.

At the downstream of the river, a sewage system has already been provided for many years, and also, the drains of the streets are not connected to the river for the above reasons.

METHODS

Investigation Period and Sites

The investigations were carried out from Jul. 2011 to Nov. 2020 twice a year. For 2 years (2015, 2016) it was 4 times. The investigations were carried out on the 5 sites (St1 to St5) shown in Fig.1. The features of the every site are described as follows.

St 1: Houei-Bashi bridge, near of the mouth of the river. The current of the river is very slow, and depth of the river is influenced by the tidal change.

St 2: Near Yokkaichi-High School. Cherry trees

are planted around the bank. St 3: Higashikawara-Bashi bridge (Ikaruga-chou district). St 4: Upstream of the Itsuki-Bashi bridge. The width of the river is wide, and usually the depth of the river is very shallow. St 5: Upstream of the Hokusei-Bypath road, and the width of the river is very narrow.

.

Parameters and the Analytical Methods

The outline of the survey items, method and investigation period is shown in Table 1.

Table 1 Parameters and Analytical Method

Item	Analytical method	Investigation period (year)	Remarks
pH	Glass-electrode	2011 to 2020	
DO	Winkler method	2011 to 2020	
EC	Platinum electrode	2011 to 2020	
COD	Acidic potassium per manganese method	2011 to 2020	
NO_3-N	UV light absorption method	2016 to 2020	
NH4 ion	Indo Phenol method	2016 to 2020	
PO_4-P	Molybdenium Ammonite method	2011 to 2020	
Cl ion	Silver nitrate titration	2014 to 2020	
SS	Glass filter method	2014 to 2016	
Flow rate	Current meter	2011 to 2020	Except for St1

Flow rate was calculated by current velocity, depth and width.

Fig. 1 Map around the investigation site (Yahoo Map)

Flow rate (m3/s)

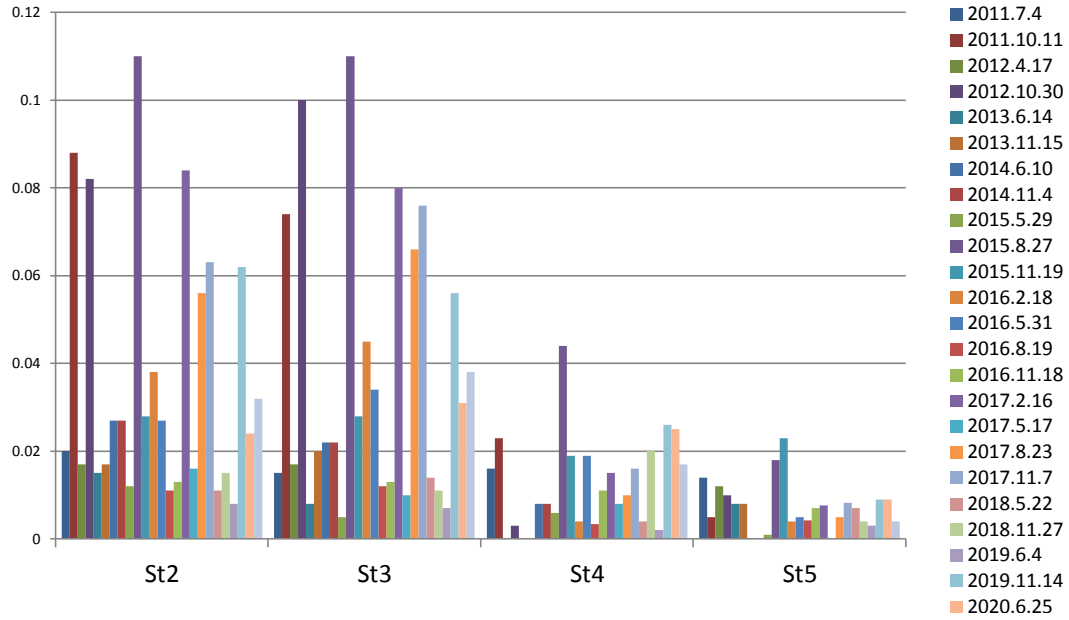

Fig.

Fig. 2 Flow rate of the river

RESULTS AND DISCUSSION

Temperature: The water temperature became higher at St4, and the inflow of relatively hot wastewater and the riverbed structure are considered to be the cause. The temperature gets lower as it goes downstream.

pH: At St5, the pH value is about 8, and tends to increase from St4 to St2, because of the influence of the aquatic plants of the river [4].

EC: EC tend to be lower from St5 toward downstream. This is considered to be due to that the factories discharge salty wastewater, and EC decreases with dilution. At St1 sometimes high EC value was found, which is thought to be the influences of the sea.

DO: DO tend to become higher toward the downstream especially at St2, which is thought to be due to the influence of the aquatic plants. However, it became low at St1 which is considered to be the influence of the sea (Fig.3).

COD: COD became high at St4, which is considered due to the inflow of the wastewater around St4, and it gets lower toward downstream by dilution (Fig.4).

NO_3-N: At St4, relatively high values were found, and it gradually decreased toward the downstream. This is considered to be the influence of the wastewater (Fig.5).

PO4-P: At St4 a high value was found, and it decreases toward the downstream (Fig.6). The reason is considered to be the influence of the wastewater.

Flow rate: At St5, the flow rate was very low, and it has increased at St3 due to the introduction of the Asake-Yousui irrigation.

Cl ion: Some times, high values are found at St1, and this may be due to the influence of the sea same as EC.

SS: At St4 and St5, a relatively high value was found, which shows the influence of the water discharged from the factories.

Relation between flow rate and COD: In order to confirm the effect of the introducing water from Asake-Yousui irrigation, the relation between the COD value and the flow rate at St3 was investigated. The result shows (Fig.7) that COD tends to decrease sharply with the higher flow rate.

The outstanding pollution caused by nearby the Ooyachi –Heizu waste disposal sites was not found.

DO (mg/L)

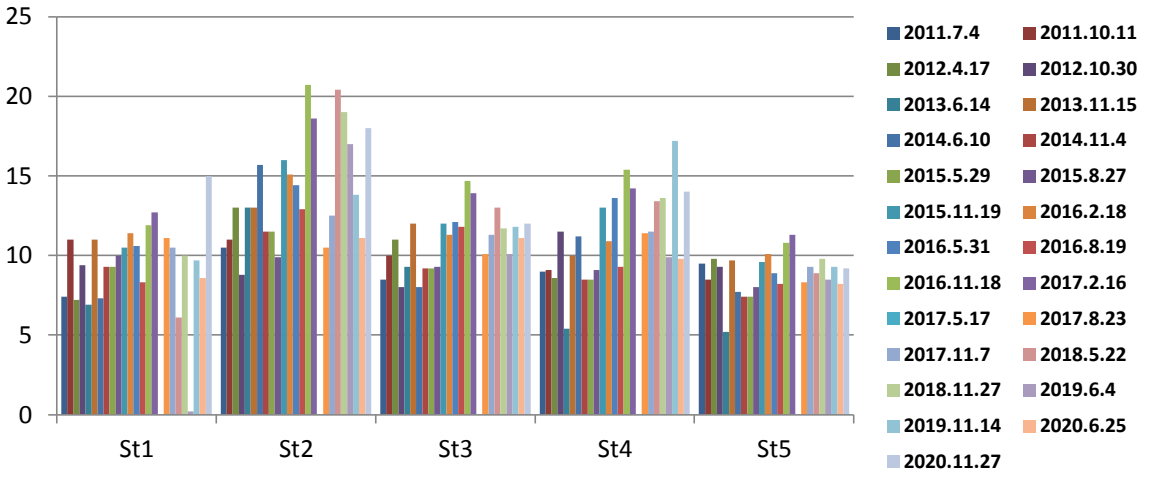

Fig.3 DO of each site

COD (mg/L)

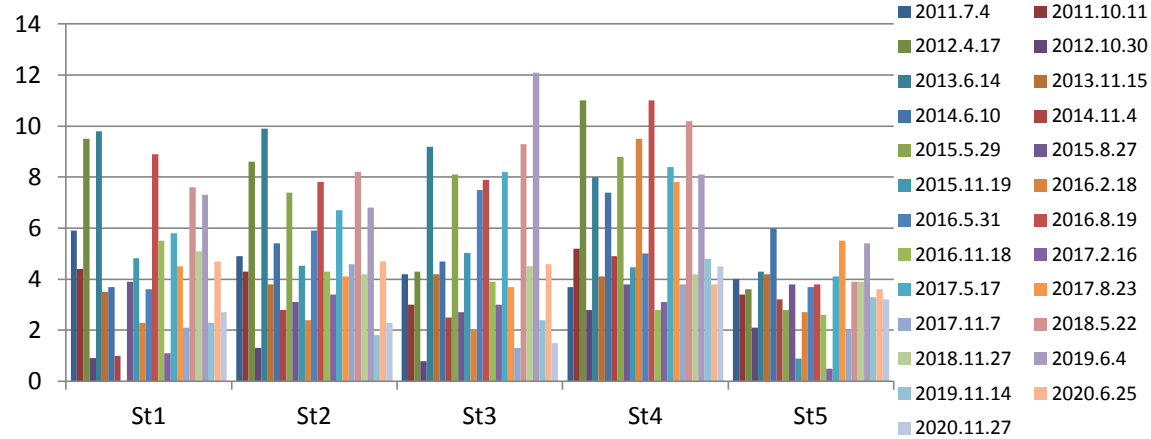

Fig.4 COD of each site

NO_3-N (mg/L)

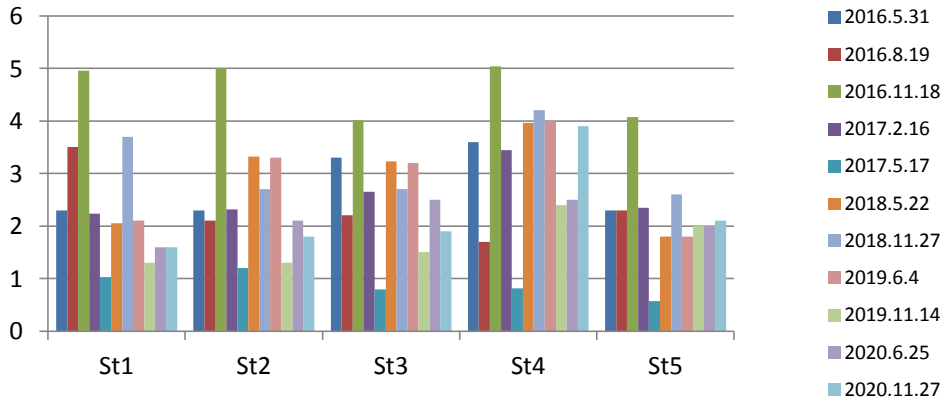

Fig. 5 NO_3-N of each site

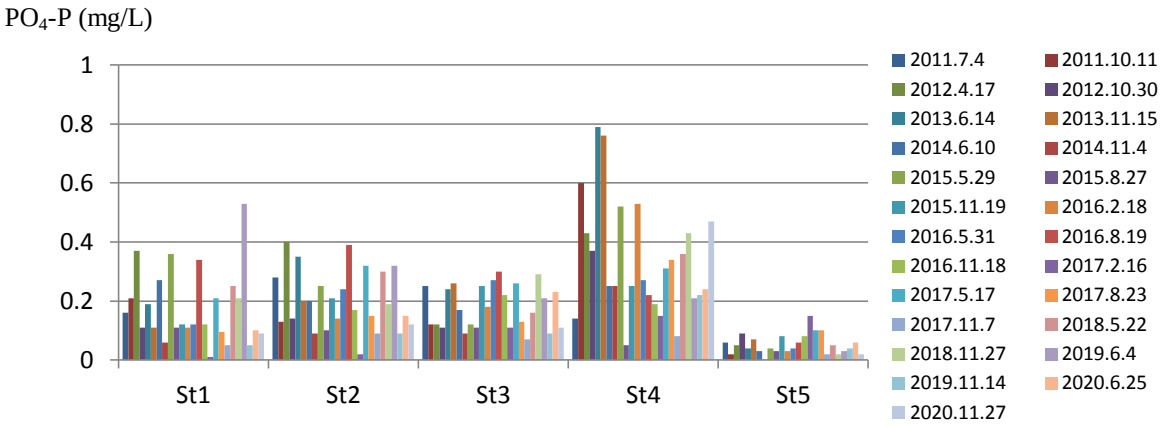

Fig. 6 PO_4-P of each site

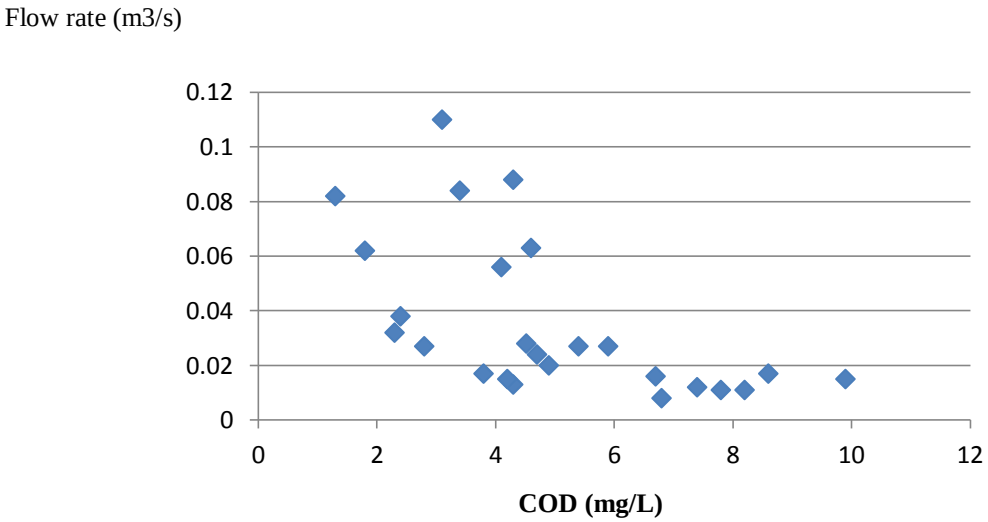

Fig. 7 Relation between flow rate and COD (St3)

CONCLUSIONS

In order to determine the environmental influence caused by the development around the Jyushi-gawa river, ten years of the investigations were carried out. On the upstream side, significant pollution was not found. Typical pollutants ((Nutrients; COD, NO_3-N, PO_4-P) were found in the middle of the river, which were caused by the waste water of the surrounding area. The pollution gradually decreases as it flows down downstream. The introduction of the irrigation water is considered particularly effective in improving the water quality. At St1, which situates near the mouth of the river, the influence of sea water was observed. Outstanding pollution caused by the Ooyachi-Heizu waste disposal sites was not found.

Some pollution was found at the Jyushi-Gawa river, however, the pollution is less serious than in other rivers in Yokkaichi city [5][6], and water quality is improving due to the construction of the sewage system.

ACKNOWLEGEMENT

The authors wish to express their appreciation to Dr. Eric Bray (Professor of Yokkaichi University) for his advice on making this article.

REFERENCE

[1] Masaaki Takahashi, Kayoko Awaya, Mikihiro ioka, Yukimasa Takemoto: Water and soil pollution near Ohyachi-heizu Waste Disposal Site, The Journal of Yokkaichi University, Vol. 11, No. 2, 2008, pp.27-31

[2] M. Takahashi, Y. Tkemoto, K. Awaya, M. Ioka and P. Guo: Water pollution around the Ohyachi-heizu District of Yokkaichi City, The Journal of Yokkaichi University, Vol. 15, No. 2,2012, pp.83-89

[3] Yukimasa Takemoto, Masaaki Takahashi, Maki Ooyagi, Shigeaki Inagaki, Reigirou Hashimoto, Kazuo Hirata and Tadamichi Hattori, Water pollution of the Jyushi-Gawa river, The Journal of Yokkaichi University, Vol. 30, No. 2, 2018, pp.153-174

[4]Dissolved Oxygen (DO) Kankyou Chousa Butyou Okano Takeshi, https://www.dir.co.jp/research/report/esg/keyword/20130918_007694.html, Accessed Apr. 2021

[5] Sachie Takeuchi, Masaaki Takahashi, Yukimasa Takemoto, Maki Oyagi, Satoshi Chiba, Yuzou Morikawa, Jia Zhou, Kunihide Miyaoka, Kaoru Ito, Takanori Terazawa: WATER POLLUTION of KAMATANI-RIVER BASIN in YOKKAICHI, Seventh International Conference on Geotechnique, Construction Materials and Environment, Mie, Japan, Nov 2017, pp. 21-24

[6] Yukimasa Takemoto, Masaaki Takahashi, Maki Ooyagi, Seiji Iwasaki, Masashi Sakakibara, Jirou Ito, Naoki Shimomura, Takanori Terazawa and Tadashi Kobayashi: Water pollution of the Kaizo-Gawa river, 9th International Conference on Geotechnique, Construction Materials and Environment, Tokyo, Japan, November, 2019, pp20-22

11th Int. Conf. on Geotechnique, Construction Materials & Environment,
Kyoto, Japan, 3-5 November 2021, ISBN: 978-4-909106063 C3051

EXPERIMENTAL STUDY ON GROUND STRENGTHENING AND ELECTRIC POWER GENERATION WITH USING RECYCLED ASPHALT PAVEMENT MATERIAL

Shoji Yokohama[1]

[1]Faculty of Engineering, Hokkaido University, Japan

ABSTRACT

In order to secure a safe living environment against frequent natural disasters, mechanical strengthening the ground and stable supply of electric power are required. Reusing resources is essential for developing a sustainable social living system. In this study, a total system that realizes ground strengthening and electric power generation by using recycled asphalt pavement material is proposed. In the proposed total system, newly made T-shaped unit is the core tool for both of improving the bearing capacity and generating the electric power. T-shaped unit is inserted into the ground and the ground surface is covered by recycled asphalt pavement material (RAP). Bearing capacity of the ground is improved and deformation of the ground is restrained by T-shaped unit and RAP laid on the on the surface of ground. On the other hands, Peltier elements are built into the T-shaped unit. The electric power can be generated by Thermoelectric effect by converting the temperature difference between the ground surface and underground. In this study, the bearing capacity of the strengthened ground and power generation behavior are investigated by the laboratory tests and field monitoring, respectively. It is shown that the bearing capacity of the ground is improved by the RAP laying and inserting the T-shaped unit by the results of laboratory tests. The electric power generation can be recognized from the result of field monitoring. Based on these experimental results, the feasibility of a total system for ground strengthening, power generation and construction waste material reusing will be discussed.

Keywords: Recycled asphalt pavement material, Ground protection, Power generation, Electromagnetic force

INTRODUCTION

In recent years, damages caused by natural disasters have become enormous and prolonged due to both the occurrence ground collapse and stopping the supply of energy required for daily life by damage to the various infrastructure. In order to deal with such a situation, it is beneficial for engineering that significance to suggest and to research for practical use a method that achieves both ground protection and stable energy supply. In addition, it is important to make effective use of construction materials in the field of civil engineering in order to build a sustainable social system.

In this study, a concept to realize ground protection and power generation at the same time while reusing the recycled asphalt pavement material is suggested and its feasibility is tried to discuss through the experimental studies. Regarding ground protection, a method to improve the bearing capacity of the ground by inserting a reinforcing tool into the ground and generating a magnetic force around the reinforcing tool is proposed in present study. The bearing capacity of the ground inserted the reinforcing tool were examined by the laboratory tests. In this study, a power generation unit built in thermoelectric elements was also prepared. The effectiveness of a power generation method of the prepared unit utilizing the ground temperature was investigated by field monitoring. Based on the results of the laboratory tests and the field monitoring, the feasibility of a system that realizes both ground protection and power generation by utilizing recycled asphalt pavement materials and ground surface temperature are discussed.

Fig.1 Protecting ground surface by RAP

APPLICATION OF RECYCLED ASPHALT PAVEMENT MATERIAL FOR GROUND SURFACE PROTECTION

Before starting this study, investigating the construction case where the recycled asphalt

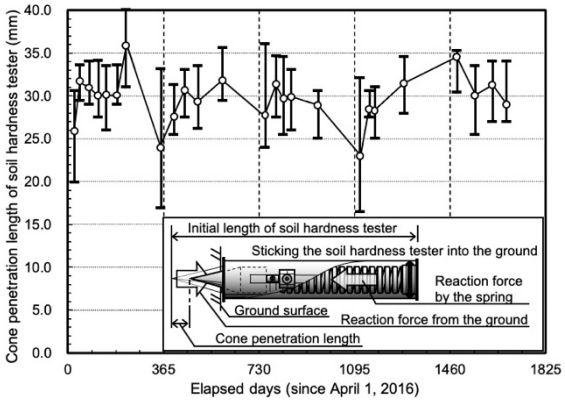

Fig.2 Soil hardness at the protected ground surface by RAP

pavement material (hereinafter referred to as RAP) is used as a ground surface protection material have been performed. Fig.1 shows the situation of the protection of the ground surface, including the slope, using recycled asphalt pavement material, which was carried out in Uryu-cho, Hokkaido, JAPAN. The figure was taken in September 2020. The whole of ground surface was covered by RAP material. It is seen the ground surface was kept on stable from this figure. This ground protection work was carried out in June 2009 to prevent mud situation on the ground surface when the water content is high and to facilitate passage of vehicle for construction work. The compaction control at the RAP layer was not planned.

Fig.2 shows the value of soil hardness on the surface of slope (see the area of dotted line in Fig.1) covered with RAP. The soil hardness was measured by using a soil hardness tester. When the soil hardness tester was sticked into the ground surface, the cone was moving into the tester and the cone penetration length could be read by the scale. The high value of the cone penetration length could be read if the ground surface was hard. From this figure, it was found that the soil hardness value in each spring season was slightly lower than the value in other seasons, but the soil hardness value was around 30 mm from 2016 to 2020. This result suggests that the long-term protection of ground surface is possible by utilizing recycled asphalt pavement material.

CONCEPT OF SYSTEM FOR GROUND PROTECTION, POWER GENERATION AND REUSING RECYCLED ASPHALT PAVEMENT MATERIAL

Fig.3 illustrates the concept of total system for ground protection - power generation - construction waste material reusing. In the proposed system, the ground surface is covered with RAP, and T-shaped unit (PG unit) is inserted into the ground to reinforce

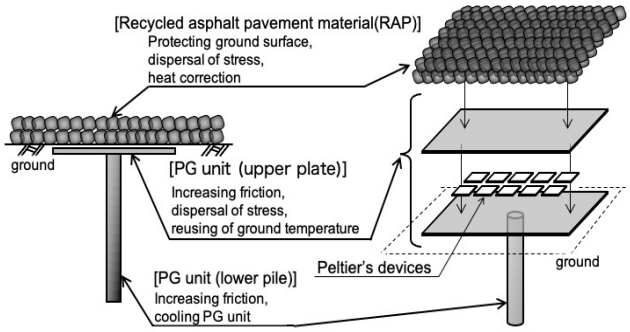

Fig.3 Concept of ground protection and power generation by using RAP

and protect the ground. RAP has several mechanical advantages [1]. The advantages are as follows;

1. The cyclic strength of sandy soil mixed with RAP is higher than that of the plain sandy soil.
2. The bonding occurs between soil particles when the RAP specimen is compressed with a low confining pressure at the triaxial compression test.

RAP is adopted as the testing material in this study because these advantages are effective in realizing the suggested system [1], [2]. In this study, the tool used for the proposed system that realizes ground reinforcement and power generation is called PG unit. The PG unit has a shape in which plate and pile are connected. It is thought that ground reinforcement is realized by inserting the PG unit into the ground and exerting friction between the PG unit and the ground. On the other hand, the PG unit, which is a built-in Peltier element [3] attempting to generate the electric power using the temperature difference between ground surface and underground. RAP covering the ground surface is exposed to sunlight irradiation and plays a role in increasing the temperature difference on surface of the PG unit.

MECHANICAL PROPERTIES OF THE PROTECTED GROUND

The ground behavior protected by the PG unit and recycled asphalt waste material (RAP) was examined by a laboratory test. Fig. 4 illustrates the test apparatus. The test apparatus mainly consists of an acrylic cylindrical cell with an inner diameter of 200 mm, a loading plate, and a loading frame. Toyoura sand (T sand) was used as the testing material, and a ground with a height of about 200 mm was prepared by the multiple sieves pluviating method (MSP method) [4]. A loading plate with a diameter of 54 mm was placed in the center of the ground surface, and a vertical force was loaded on it. The vertical loading was carried out by increasing the vertical force by about 23 N in 10 minutes. The vertical force and the displacement of load plate were measured with a load cell and dial gauge connected to the test

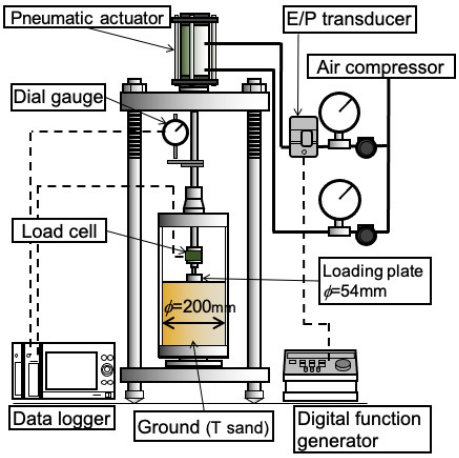

Fig.4 Test apparatus for bearing capacity of the protected ground

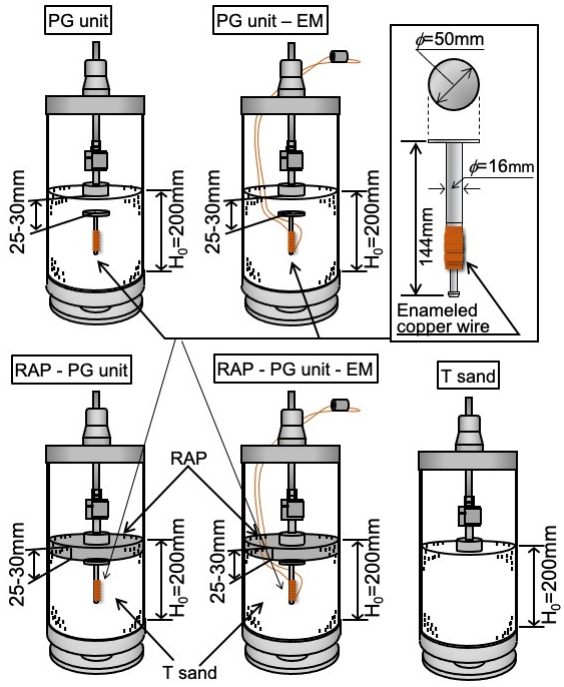

Fig.5 Test conditions in the laboratory test

equipment.

Fig. 5 shows the test conditions adopted in the study. In this study, the T-shaped reinforcing tool (called the PG unit) made of iron was inserted into the ground. Enameled wire with length of 30 m and diameter of 1.6 mm was wound in a coil around the lower pile of the PG unit. At PG unit case, the PG unit was inserted into the testing ground. At PG unit-EM case, the electric current was passed through the enameled wire of the inserted PG unit. The conditions that the ground above the PG unit was replaced with recycled asphalt pavement material (RAP) are referred to RAP-PG unit case and RAP-PG unit-EM case. The ground behavior was observed without any strengthening at T sand case. The electric current to

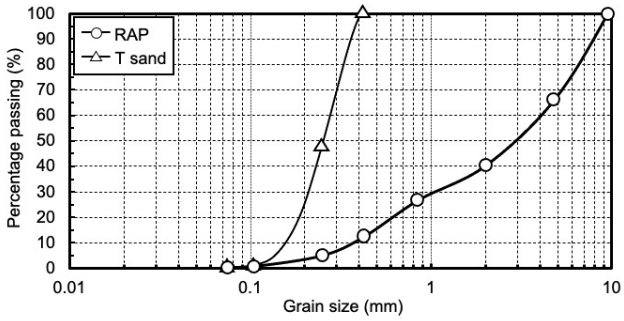

Fig.6 Grain size distributions of RAP and T sand

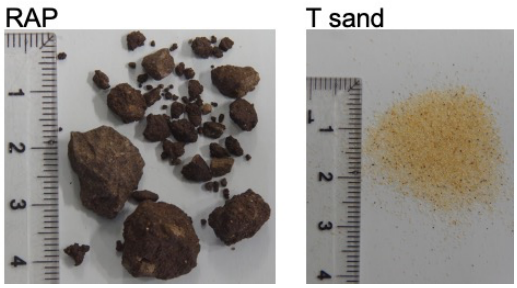

Fig.7 Appearance of RAP and T sand

Table 1 The index of physical properties of samples

		ρ_s (g/cm^3)	ρ_{dmax} (g/cm^3)	ρ_{dmin} (g/cm^3)
Recycled asphalt pavement material	(RAP)	2.366	1.607	1.412
Toyoura sand	(T sand)	2.649	1.636	1.344

the PG unit was supplied from a power source in which six nickel-metal hydride batteries (6500 mAh, 1.2 V) were connected in series. The purpose of supplying the electric current to the PG unit is to generate a magnetic force from the PG unit and attract the iron sand in T sand to the PG unit to improve the friction with the ground. Fig.6 and Fig.7 show the particle size distribution and appearance of the samples (RAP and T sand) used in the study. From these figures, it can be seen that T sand is fine sand with a uniform particle size, while RAP has a black surface and a uniformity coefficient of 10 or more. The RAP was a sample collected from a plant in Sapporo City in August 2014, and the maximum particle size was adjusted to 9.5 mm for this study. The index of physical properties of each sample are shown in Table 1. It has been confirmed in advance that the iron sand content of T sand used in this study is about 0.43 % of the total mass of T sand.

Fig. 8 shows the relationship between the loading stress σ_v and the normalized settlement of the loading plate $\Delta H/H_0$ in PG unit, PG unit-EM, and T sand cases. Where, ΔH and H_0 are the settlement of loading plate

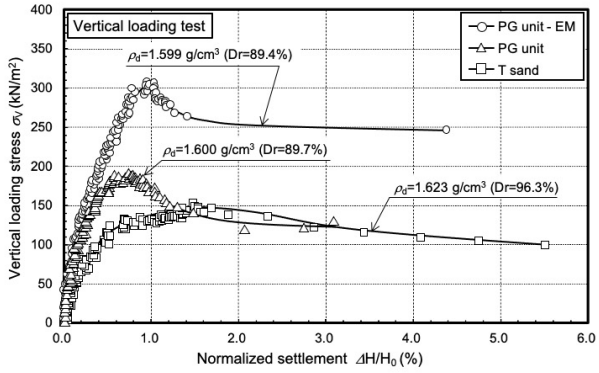

Fig.8 Bearing capacity for T sand ground protected by PG unit

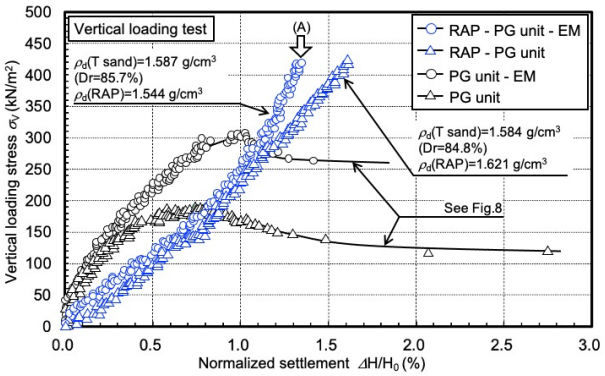

Fig.9 Bearing capacity for T sand ground protected By PG unit and RAP

and the initial ground thickness, respectively. The relative density D_r of the ground is around 90 %. It can be found that the maximum load stress in the PG unit and PG unit–EM cases is higher than that in the T sand case, and the maximum load stress in the PG unit–EM is highest of the all. From the result, it can be inferred that in addition to the effect of inserting the PG unit, the magnetic force generated around the PG unit exerted an effect of contributing to the improvement of the bearing capacity in the sandy ground.

Next, the residual state after the maximum value of the loading stress appears is being focused. It is seen that the loading stress in the residual state in the PG unit-EM reaches about twice the value in the T sand and PG unit cases. This fact indicates that the magnetic force generated around the PG unit affected the stress distribution in the ground due to the effect of attracting iron sand in the ground and the value of the loading stress in the residual state became higher than in the case without magnetic force. From these results, it was clarified that the friction between the sand ground and the PG unit was increased by the insertion of the PG unit and the magnetic force generated around the PG unit, and the bearing capacity was improved.

The behavior of the sand ground protected by RAP layer is examined. Fig. 9 shows the relationship between the loading stress σ_v and the normalized settlement $\Delta H/H_0$ obtained in the RAP-PG unit and RAP-PG unit-EM cases. In both cases, the relative density of the T sand ground D_r is about 85 %. For comparison, the results of PG unit and PG unit–EM case (see Fig. 8) are also shown in Fig.9. From the figure, it is found that in the RAP-PG unit and RAP-PG unit-EM cases, the increase in loading stress at the stage where the normalized settlement $\Delta H/H_0$ is small is slower than in the test cases without the RAP layer (PG unit and PG unit–EM case), and when $\Delta H/H_0$ becomes about 1.1% or more, a higher loading stress value is exhibited compared to PG unit and PG unit–EM cases. In the results of RAP-PG unit and RAP-PG unit-EM, it could not be possible to measure the peak value of the loading stress clearly due to the measurement capacity of the load cell mounted on the test apparatus, but a tendency for increasing the bearing capacity of the ground by using RAP layer is described.

POWER GENERATION BY USING RAP AND GROUND TEMPERATURE

Fig.10 shows the configuration of the power generation equipment (referred to as the PG unit for power generation) used in the field monitoring of power generation behavior in this study. The PG unit for power generation is mainly composed of an upper plate made by sandwiching a Peltier element between aluminum plates (thickness 0.3 mm, width 300 mm, length 200 mm) and a group of members for cooling the back surface of the upper plate. Inside the upper plate of the PG unit for power generation, 30 Peltier elements are connected in series and arranged side by side. The Peltier element is a square with a side of 40 mm and a thickness of 4 mm, its maximum heat absorption is 51 W, and the maximum voltage that can be input to the Peltier element from the outside is 15.4 V. Thermometers were attached to the front and back surfaces of the upper plate of the PG unit to get the temperature data.

On the surface of the upper plate of the PG unit for power generation, a heat collecting box made of a heat insulating material with a thickness of 20 mm and an aluminum plate was attached, and recycled asphalt pavement material (RAP) was spread inside the heat collecting box to raise the surface temperature. A cooling agent (a commercially available product containing a highly water-absorbent resin, etc.) was attached to the back surface of the upper plate, and two brass fixing bases were attached to cool the PG unit for power generation. When setting the PG unit outdoors, two stainless steel tumblers filled with tap water were prepared and

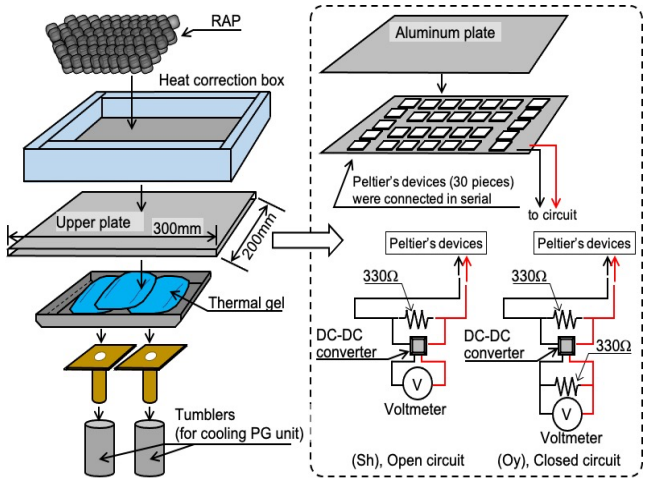

Fig.10 Configuration of the PG unit for power generation

Fig.11 Situation of field monitoring at [Oy] and [Sh]

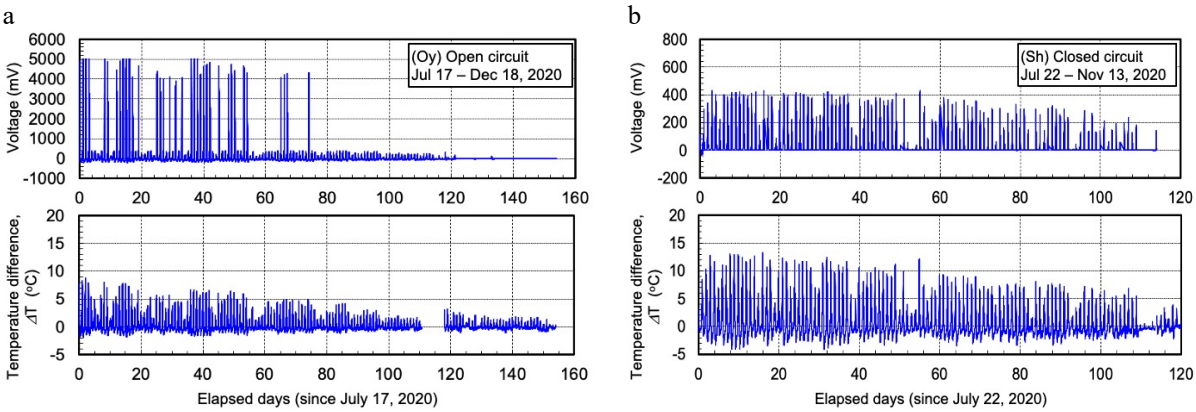

Fig.12 Voltage and temperature difference of PG unit, (a) : [Oy](Open circuit), (b) : [Sh](Closed ciicuit)

buried in the ground so that the protrusions of the fixed base attached to the PG unit could be inserted. In this study, two types of electric circuits were prepared. In each circuit, a 330 Ω resistor and a step-up DC-DC converter (maximum output 5V) were connected to the wiring from the Peltier's element. One of them is to connect a voltmeter with the circuit from the step-up DC-DC converter as an open type (referred to open circuit) in order to confirm that whether the step-up DC-DC converter operates. On the other hand, a 330 Ω resistor and a voltmeter were connected to the output circuit from the step-up DC-DC converter, and the power generation behavior was investigated (referred to as a closed circuit).

Field monitoring were carried out at two locations of Oyachi (denoted as [Oy]) and Shinoro (denoted as [Sh]) in Sapporo city, JAPAN. In [Oy], PG units with open circuit was used. In [Sh], the PG unit with closed circuit was used. Fig. 11 shows the set-up situation of the PG unit in [Oy] and [Sh]. A tumbler filled with tap water is buried near the ground surface, the PG unit is put on it. The recycled asphalt pavement material is spread with a thickness of about 50 mm inside the heat collection box.

Fig.12 (a) and (b) show the measured voltage and temperature difference of PG unit ΔT at [Oy] and [Sh]. The temperature difference ΔT is defined as the difference between the temperature on front surface and that on back surface of the upper plate of the PG unit. From Fig.12 (a), it was seen that the output voltage was corresponding to the fluctuation of the temperature difference ΔT, and the voltage sometimes could reach 5000 mV. Such voltage behavior indicates that the step-up DC-DC converter can be run by the output electric power from the PG unit when the temperature difference can be secured. From Fig.12 (b), it was found that the temperature difference ΔT reached a maximum of 13 °C, and the voltage at the resistor of 330 Ω connected to the circuit reached 400 mV. Although the voltage output behavior depends on the season and time, according to the suggested method in this study, it is possible to secure the temperature difference of about 10 °C for the PG unit, and the electric power can be generated by running the step-up DC-DC converter.

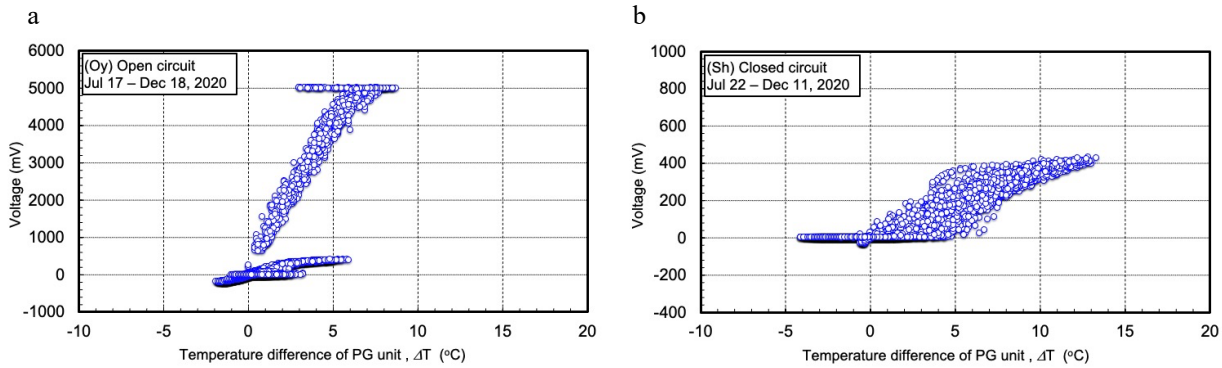

Fig.13 Relationship between voltage and temperature difference, (a) : [Oy](Open circuit), (b) : [Sh](Closed circuit)

The relationships between the output voltage and the temperature difference ΔT are shown in Fig.13 (a) and (b). According to the results of [Oy] (see Fig.13 (a)), when the temperature difference ΔT was 3 °C or higher, the step-up DC-DC converter was activated and the output voltage of about 5 V was observed. On the other hand, there were cases that the output voltage was 400 to 500 mV even when the temperature difference ΔT was 5 °C or higher in Fig. 13 (b). From these results, it is recognized that the electric power required for the running of the step-up DC-DC converter can be produced when the temperature difference ΔT could be larger than a certain value. But it is also noted that the other factor from the temperature difference ΔT should be considered for the stable running of the step-up DC-DC converter.

CONCLUSIONS

In this study, the concept for the implementation of ground reinforcement and power generation by using recycled asphalt pavement material was suggested. In order to confirm embodying the concept, the laboratory tests on ground reinforcement and field monitoring on power generation were carried out. The main results obtained from the study are as follows;

1. It was shown that when recycled asphalt pavement material is laid on the ground surface and a reinforcing tool is inserted into the ground, the bearing capacity of the ground can be improved. It was also shown that the bearing capacity can be further improved by generating a magnetic force around the reinforcing tool inserted in the ground.
2. The output of electric power could be seen by using the power generation unit with built-in the thermoelectric devices. The power generation unit was put on near the ground surface and its surface of the power generation unit was covered with recycled asphalt pavement material. It was also clarified that it is necessary for achieving stable power generation to take keeping the temperature difference between the front and back surfaces of the power generation unit larger.

From the above results, if a reinforcing tool that is equipped with a thermoelectric element and will not be damaged by acting some stresses can be manufactured, it may be possible to embody the system for ground protection and power generation by utilizing the recycled asphalt pavement material.

ACKNOWLEDGMENTS

Author received generous support of the field monitoring for the ground protection and the electric power generation from Mr. Juichi Hatakeyama in Uryu-cho, Hokkaido, Japan. This study was supported by JSPS KAKENHI Grant Number JP18K04341.

REFERENCES

[1] Yokohama S. and Sato A., Cyclic mechanical properties of sandy soil by mixing recycled asphalt pavement material, International Journal of GEOMATE, Vol.16, Issue 58, 2019, pp.41-47.
[2] Soleimanbeigi, A. Tuncer B. Edil, and Craig H. B., Creep response of recycled asphalt shingles, Canadian Geotechnical Journal, Vol.51, 2014, pp.103-114.
[3] Ahiska R. , Mamur H., A review :Thermoelectric generators in renewable energy, International journal of Renewable Energy Research, Vol.4, No.1, 2014, pp.128-136.
[4] Miura S. and Toki S., A sample preparation method and its effect on static and cyclic deformation-strength properties of sand, Soils and Foundations, Vol. 22, No.1, 1982, pp.61-77.

11th Int. Conf. on Geotechnique, Construction Materials & Environment,
Kyoto, Japan, 3-5 November 2021, ISBN: 978-4-909106063 C3051

STUDY ON CHANGES OF PUBLIC TRANSPORT USE AND CONSCIOUSNESS DURING THE COVID-19 INFECTION PERIOD

Ryotaro Kinoshita[1], Tetsuo Morita[1], Tomohiro Miyazaki [1] and Shinya Tsukada[2]

[1]Maebashi Institute of Technology, Japan; [2]Maebashi City Municipality, Japan

ABSTRACT

People who stay indoors are increasing with the COVID-19 and the spread of computers. We analyzed changes in the public transport and consciousness and behavior during the COVID-19 infection period, using the results of surveys in May and October in 2020, and January 2021, for perceptions on the risk of coronavirus, attitude towards public transportations and activities. First, we analyzed the chronological relationship between the subjective risk of infection when using public transportation and the announcement of the state of emergency by the Japanese government. The state of emergency announcement reduced trips by people and raised the awareness of infection risk. It was also found out that people tend to overestimate the risk when using public transportation. Next, Factor analysis showed the potential factors behind the results of respondents' attitudes toward lifestyle and the government measures. Furthermore, changes in scores of extracted factors were analyzed according to gender, place of residence, and time series.

Keywords: COVID-19, transportation choices, living consciousness, factor analysis, quantification method Ⅱ

INTRODUCTION

During the state of emergency due to the spread of the new coronavirus infection, the Japanese government called for people to avoid three Cs (Crowded, Close contact, Confined and enclosed space), and recommended online homecoming and working from home. As a result, people have the tendency to aware of infection risk when going one place to another. This led to the decrease of public transportation users, and the utilization rate of public transportation services such as railway, bus, ship, aviation is much lower than usual [1].

The Purpose of the Study

The purpose of this study is to clarify shifts in public transportation use and living consciousness during the period of the COVID-19 pandemic concerning the relationship between personal attributes, place of residence, consciousness.

RESEARCH SIGNIFICANCE

Kawakami, Sugita, Morio and Morita studied traffic behavior by cohort analysis and concluded that the share of automobile use by women was on the rise and that the baby boomer generation for men and the bubble generation for women peaked and the net generation intensity began to decrease [2]. Ishii, Mori, and Aono analyzed characteristics of the traffic behavior and concluded that the frequency of going out and the number of trips differ depending on occupations, annual income, and access to traffic services [3]. Yanagihara, Shimada and Daito showed that among elderly or handicapped people who need assistance when going out, those who frequently go out and men are more likely to use public transportation, and women and the older generation were less likely to understand the use of public transportation [4].

Yabusaki, Morishige and Morimoto analyzed changes in bicycle usage trends from the 1960s to the 2000s regarding the shifts of transportation choices. They showed that the number of municipalities which have a high proportion of use of bicycles as the major means of transportation, decreased in suburban areas and increased in urban areas from the 1980s to the 2000s. They also showed that the number of municipalities where citizens use bicycles frequently for trips over long distances increased from the 1990s to the 2000s [5]. Imai, Okushima and Kondo analyzed from an environmental point of view and showed that self-sacrifice intention to prevent global warming was a factor related to the shifts of commuting means [6].

Regarding the relationship between COVID-19 pandemic and frequency of going out, Hiroi showed that despite the state of emergency in April 2020 had the effect of reducing the trips for commuting purposes, it made little change in trips for meals and sightseeing purposes. Hiroi also clarified that the higher the frequency of going out of the person, the higher the face-to-face rate [7]. In addition, Li, Ko, Chang, Yen and Chen showed that there was a positive correlation between risk perception for coronavirus infection and the degree of countermeasure implementation [8]. In addition, Moriwaki, Hiyoshi and Murota analyzed an opinion survey conducted in November 2020 and concluded

References for transportation choices and lifestyle consciousness before the pandemic
the 2015 National Survey of Urban Traffic Characteristics,
the 2015 NHK National Living Time Survey

References for transportation choices and lifestyle consciousness in May, 2020
the 1st Behavior / Awareness Survey on Coronavirus (by the Committee of Infrastructure Planning and Management)

References for transportation choices and lifestyle consciousness in October, 2020
the 2nd Behavior / Awareness Survey on Coronavirus

References for transportation choices and lifestyle consciousness in January, 2021
the 3rd Behavior / Awareness Survey on Coronavirus

Comparison for transportation choices and lifestyle awareness based between 3 surveys

Fig. 1 Research procedures

that decrease in life satisfaction was seen in many respondents, and the cause was decrease in the frequency of going out [9].

It is clear that the means of transportation and frequency of trips change depending on individual attributes (gender, car ownership, family type), the purpose of travel, and health consciousness, but hygiene have not been considered as a change factor. There are mainly two characteristics of this research: The first is to consider unprecedented infectious disease as the factor of shifts of modal choices and frequency of trips. The second is social significance since this research dealt with shifts in transportation and now is an important turning point in changing attitudes towards transportations in the future.

RESEARCH METHODS

In this study, The COVID-19 infection period is defined as the term starting from January 16, 2020 to the last day when the infection case was not confirmed for two consecutive weeks.

We studied the relationship between transportation choices and lifestyle consciousness before the infection period, based on the results of the 2015 National Survey of Urban Traffic Characteristics (by Ministry of Land, Infrastructure, Transport, and Tourism) and the 2015 NHK National Living Time Survey (NHK, Japan Broadcasting Corporation). Then, we analyzed the

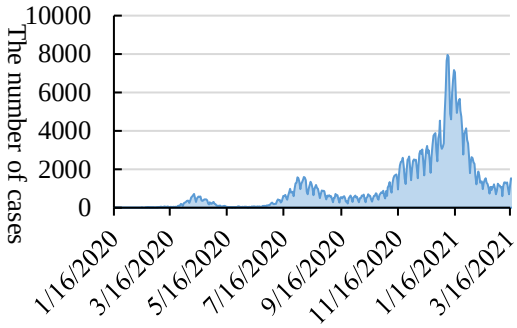

Fig. 2 The number of COVID-19 cases in Japan

relationship between transportation choices and lifestyle consciousness during the pandemic as of May 2020 and October 2020, based on the results of the 1st, 2nd and 3rd Behavior / Awareness Survey on Coronavirus (by the Committee of Infrastructure Planning and Management) [10]. (Fig. 1)

CHANGES OF THE COVID-19 CASES AND MEASURES BY THE GOVERNMENT

The number of COVID-19 cases

The number of COVID-19 cases in Japan has changed as shown in Fig. 2.

The first wave (March to May last year), the second wave (July to September last year), the third wave (December to February last year), the fourth wave (March to May this year) The time was divided by comparing the increase and decrease in the number of infected people to a wave. We also use the terms of the 1st to 4th waves in this research.

The state of emergency by the government

The Japanese government has announced a state of emergency in line with the increase in the number of infected people. (See Table 1) The state of emergency is an emergency measure based on the Act on Special Measures against Novel Influenza, etc. The first announcement was in April, 2020, and it covered seven prefectures where cases were rapidly spreading. Along with this, the government designated four prefectures as requiring special caution due to their large number of infections. As the number of the cases have increased nationwide, the government increased the coverage of prefectures, and the government eventually applied the state of emergency nationwide. In contrast, the 2nd state of emergency was aimed at particular prefectures. Note that there was no state of emergency during the second wave.

In this research, prefectures are classified at the time of the announcement of the state of emergency, and the prefectures corresponding to (1), (2), and (3) in Table 1 are designated as Area1, Area2, and Area3, respectively. (See Fig. 3)

Table 1 Government measures and state of emergency

State of emergency (Announcement / lifting date)	Applicable prefectures
Announcement (1) (April 11, 2020)	Saitama, Chiba, Tokyo, Kanagawa, Osaka, Hyogo, Fukuoka (Area 1)
Prefectures requiring special caution	the prefectures in (1), Hokkaido, Ibaraki, Ishikawa, Gifu, Aichi, Kyoto (Area 2)
Additional announcement (April 16)	(Area 1), (Area 2), The rest of the Prefectures (Area 3)
lifting (May 14)	39 prefectures other than Hokkaido, Saitama, Chiba, Tokyo, Kanagawa, Osaka, Kyoto, and Hyogo
lifting (May 21)	Osaka / Kyoto / Hyogo
lifting (May 25)	Saitama, Chiba, Tokyo, Kanagawa, Hokkaido
Announcement (January 7, 2021)	Saitama, Chiba, Tokyo, Kanagawa
Additional announcement (January 13)	Tochigi, Gifu, Aichi, Kyoto, Osaka, Hyogo, Fukuoka
Lifting (February 2)	Tochigi
Additional Lifting (February 26)	Gifu / Aichi / Osaka / Hyogo / Fukuoka
Additional Lifting (March 8)	Saitama, Chiba, Tokyo, Kanagawa

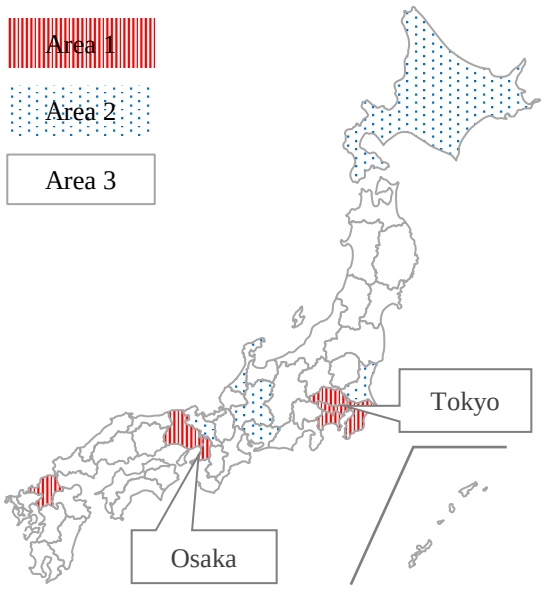

Fig.3 The classification of prefectures

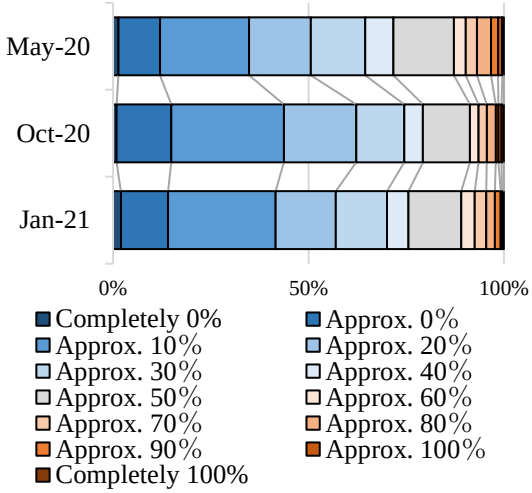

Fig. 4 Temporal difference in subjective infection risk during travel

TEMPORAL DIFFERENCES IN SUBJECTIVE INFECTION RISK OF USING PUBLIC TRANSPORTATION

In 3 surveys, there were questions to fill in the perception of the probability of infection while taking bus, train, or taxi. The response results are shown in Fig. 4. In the 2nd survey in October 2020, the rate of respondents who estimated that the risk of infection was lower increased compared to the 1st survey in May. Then the rate of respondents who estimated infection risk higher increased again in the 3rd survey in January 2021. This shows that the state of emergency announcement not only reduces trips by people but also has a psychological effect of raising the awareness of infection risk. However, the actual value was 1% [10], which was significantly different from the subjective risk of infection among the people.

ANALYSIS OF CONFORMITY AND POLICY SUPPORT

Extraction of Factors

We conducted a factor analysis on the questions and answers that were asked to evaluate going out for private purpose and the announcement of the state of emergency. At this time, it was judged that the number of factors was 2 based on the screen plot and the materials of the Committee of Infrastructure Planning and Management [10]. The factor estimation method was the maximum likelihood method. The rotation method was oblique rotation (Promax rotation), and the analysis targets were 10 variables common to the 1st to 3rd times. The results are shown in Table 2.

Table 2 The result of factor extraction

variables	1st survey May-20		2nd survey Oct-20		3rd survey Jan-21	
Do you think private meetings are bad?	0.871	0.025	0.941	0.162	0.948	-0.007
Do you think it is bad when you see people who go out for private purposes?	0.842	0.028	0.886	0.173	0.788	0.079
Do you think going out for private purposes is bad?	0.842	0.058	0.927	0.167	0.948	-0.003
Do you think it is bad when you see people who meet for private purposes?	0.835	0.025	0.880	0.155	0.781	0.080
Do you think going out on business is bad?	0.517	-0.144	0.767	0.019	0.675	-0.135
Should shops that do not comply with self-restraint requests be blamed?	0.415	0.140	0.469	0.328	0.490	0.179
Should people who infected coronavirus be blamed?	0.391	-0.073	0.642	0.088	0.505	-0.081
Do you support guidelines that contact with people should be reduced by 80%?	0.064	0.886	0.189	0.673	0.007	0.714
Do you support the extension of the state of emergency by the end of May nationwide?	-0.041	0.811	0.138	0.943	-0.047	0.947
Do you support announcement of the state of emergency in Tokyo, Osaka, and Fukuoka?	-0.077	0.730	0.105	0.911	0.016	0.877
Characteristic value	3.96	1.56	4.67	2.11	4.39	1.86
Contribution ratio	39.6%	15.6%	46.7%	21.2%	43.9%	18.6%
Cumulative Contribution	39.6%	55.2%	46.7%	67.8%	43.9%	62.5%
Name of factor	Cnfr.	Pol. Sup.	Cnfr.	Pol. Sup.	Cnfr.	Pol. Sup.

Note: Abbreviations: Cnfr. = Conformity, Pol. Sup. = Policy Support

The Results of Factor Analysis

There were no variables that linearly combine. Factor 1 included items such as "Do you think private meetings are bad?" "Do you think it is bad when you see people who go out for private purposes?" "Should shops that do not comply with self-restraint requests be blamed?", thus we named the factor "Conformity". Factor 2 was named "Policy Support" because it contained variables related to "guidelines that contact with people should be reduced" and "the state of the emergency". Since the cumulative contribution rate after factor extraction also exceeded 50%, we judged the approximate accuracy was maintained.

As shown in Table 2, the contribution rate of pressure to private meetings and going out was high in May 2020. In contrast, in October 2020 and in January 2021, the contribution rate of fear to private meetings and going out was high.

Therefore, it can be seen that the proportion of consciousness for private behavior was raised under the sense of conformity.

The Relationship between the Extracted Factors and Gender and Place of Residence

The relationship between the extracted factors and individual attributes was calculated by the average score for each attribute, and the time-series changes were analyzed. At this time, it was pooled once and factor analysis was performed. The higher the factor score, the stronger the conformity or the more supportive the policy.

Also, Fig.4 shows that women have higher conformity than men and were more likely to support policy. In chronological order, it was found that October 2020, when no state of emergency was announced, had the weakest conformity for both men and women among the three points.

According to Fig. 5, it was Area 2 residents who had strong conformity in their place of residence and they were likely to support the policy. The prefectures in Area 2 include many prefectures with

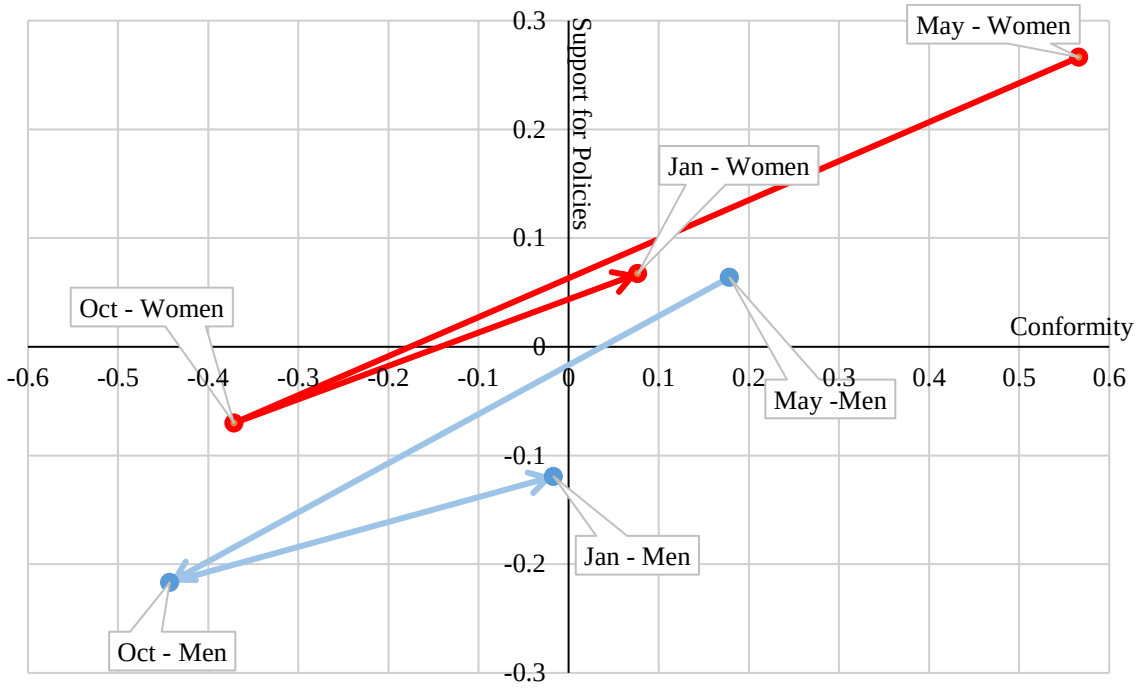

Note: May=May 2020, Oct=October 2020, Jan=January 2021.

Fig. 4 Extracted factors and Gender

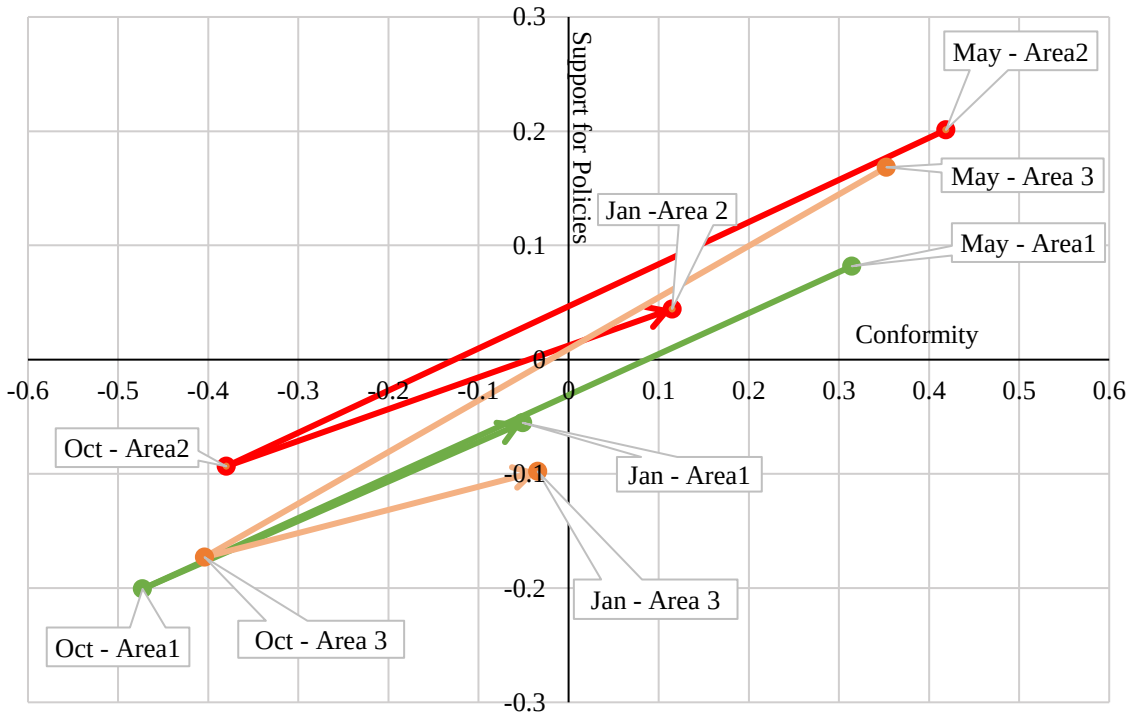

Note: May=May 2020, Oct=October 2020, Jan=January 2021.
Prefectures in each Area are shown in Fig.3.

Fig. 5 Extracted factors and Place of residence

a smaller population, and the state of emergency was applied later than prefectures in Area 1. Due to the rapid spread of infection, measures similar to those in Area 1 were taken, and as a result, awareness for others and policies became stronger.

As for chronological changes, as with gender, respondents had the strongest sympathetic pressure and supports the policy in May. It can be judged that the declaration of the state of emergency raised the conformity.

CONCLUSION

We analyzed the means of transportation and changes in consciousness as of May 2020, October of the same year, and January 2021, according to the open data of the Infrastructure Planning Research Committee.

As a result, the following 2 points were found.

First, the subjective risk of infection when using public transportation was the highest in May and January when the state of emergency was announced, and it was thought that the risk of infection tends to be overestimated due to the increase in the number of infected people and the announcement of the state of emergency.

Second, the potential factors of sympathetic pressure and policy support were extracted, and scores of each factor change according to gender, place of residence and time series. Moreover, and the sympathetic pressure that affects subjective risk perception was the lowest in October among the three points in time.

Furthermore, it was found that the state of emergency influences subjective risk perception and changes in the frequency of going out. We will look into changes in frequency of activities such as commuting, shopping, or entertainment, before self-restraint, in May and October 2020, and in January 2021.

We showed the attributes and ideas that lead to estimate the higher infection risk when using public transportation, the characteristics of people who are likely to switch to automobiles, and who continue to use public transportation in the future. As a result, when a company plans an event, it is possible to effectively narrow down the target customer. For example, automobile companies can narrow down their new target customers to women, young people, and the elderly are more likely to switch their means of transportation to automobiles. On the other hand, operators for public transportations would be able to plan for trains or buses departing from and arrive in populated areas (Area 1, in this study) targeting men and people who have a higher tendency of non-daily activities. Thus, this study can be used as a tool in the urban economy.

Although the number of trips has decreased in general, it remained to be clarified in terms of the ratio of transportation modes in this study. Thus, we would like to work on changes in transportation use in each Area. It will also be necessary to analyze how subjective risk perception changes depending on the number of the announcement of the state of emergency.

REFERENCES

[1] The Research Institute for Local Public Transport, The Public Transport Management Report, 2021 [in Japanese]

[2] Kawakami S., Sugita H., Morio J., Morita T., Analysis on Changes in Travel behavior characteristics Focused on Life Stage, Period and Generation -Based on the Five Time Data of Tokyo Metropolitan Area PT Survey-, Journal of Traffic Engineering, Vol.55, No.2, pp.174-181, 2020.

[3] Ishii R., Mori Y., Aono S., Study on Traffic Behavior Characteristics Focusing on Transportation Service and Personal and Household Attributes Using Web Questionnaire Survey in Tokyo Metropolitan Area, Journal of Traffic Engineering, Vol.5 , No.2, 2019, pp. B_49-B_58.

[4] Yanagihara T., Shimada M., Daito T., Consideration About the Special Quality between the Going out Frequency and Travel Behavior of the Elderly or People with Restricted Mobility, Journal of Japan Society of Civil Engineering D3, Vol.3, No.5, 2017, I_761-I_769.

[5] Yabusaki R., Morishige Y., Morimoto A., Analysis of long-term Changes in the Bicycle Use by Use of the PT Survey Data, Journal of Traffic Engineering, Vol.6, No.2, 2020, pp. A_97-A_104.

[6] Imai Y., Okushima M., Kondo A., Structural Analysis of Environmental Consciousness with Social Interaction Related to Modal Shift of Commuting Trip, Vol.68, No.5, 2012, I_607-I_614.

[7] U H., A Study on the Effect of Japanese-style Lockdown on Self-restraint Request for COVID-19, Journal of the City Planning Institute of Japan, Vol.55, No.3, 2020, pp.902-909.

[8] Dian-Jeng Li, Nai-Ying Ko, Yu-Pimg Chang, Cheng-Fang Yen, Yi-Lung Chen, Mediating Effects of Risk Perception on Association between Social Support and Coping with COVID-19: An Online Survey, International Journal of Environmental Research and Public Health, Vol.18, No.4, 2021

[9] Moriwaki Y.,Hiyoshi N., Murota M., A study on changes in going out behavior, outdoor space usage and life satisfaction with COVID-19, Reports of the City Planning Institute of Japan, No.19, pp.435-438.

[10] Japan Society of Civil Engineering, the Committee of Infrastructure Planning and Management, the Behavior / Awareness Survey on Coronavirus [in Japanese]

[11] Hirayama N., Factors that influence on the infection prevention measures during pandemic period, Journal of Society for Environmental Economics and Policy Studies, Vol.14, No.1, 2021, pp_43-pp_46 [in Japanese]

11th Int. Conf. on Geotechnique, Construction Materials & Environment,
Kyoto, Japan, 3-5 November 2021, ISBN: 978-4-909106063 C3051

THE ISO DESIGN GUIDE FOR GEOSYNTHETIC BARRIERS AND THE USE FOR SAFE AND ECONOMIC BARRIER SOLUTIONS

Kent von Maubeuge[1] and Jake Stoyle[2]

[1]NAUE GmbH & Co. KG, Germany; [2]NAUE Geosynthetics Ltd., UK

ABSTRACT

Over the past 40 years, the advantages in utilising geosynthetic barriers versus traditional barrier materials have been well documented, e.g., greater project economy, extended service lives, enhanced environmental protection, and greater site safety. Achievements such as conserving water resources and enabling beneficial site reuse have even given geosynthetic engineering a level of importance. As such, the use of geosynthetic barriers has increasingly been required. However, there are regions and applications in which the use of these barrier technologies should be more widely adopted. This paper highlights the principles and practices of design using geosynthetic barriers and takes into account a number of different parameters. An ISO design guide aims to assist the process by identifying the various characteristics of barrier types and comparing them with the requirements of a variety of different applications. It also offers design advice to professionals involved in the design of civil engineering and construction solutions using geosynthetic materials. Overall, the intent is to encourage appropriate selection of materials and design methods to suit particular applications, rather than to redesign projects to suit predetermined materials. This paper will describe both the process and outcomes of a new ISO design guide for barrier systems, some of the challenges and make recommendations how it can be used to improve regulations. Further, an example of successful use of barrier systems for encapsulation of debris from Fukushima with an innovative barrier system is described.

Keywords: Geosynthetic clay liner, Barrier, Multicomponent, Guideline, Liner

INTRODUCTION

Geosynthetic barriers are an established product group in the geo-environmental industry. They include factory-made polymeric geomembranes (e.g., HDPE), bituminous barriers (bitumen attached to geotextile), and geosynthetic clay liners (with clay/bentonite core). These geosynthetic materials are accepted as barrier solutions for landfill caps and base liners, under roadways and railways, and with various containment structures such as dams, canals, ponds, rivers, and lakes. They are also used for waterproofing of buildings and similar structures. Advantages of geosynthetic barrier systems vs. traditional designs include:

- More economical to produce, transport, and install (quicker and simpler)
- Enable predictability designs
- Reduced excavation required (e.g., less fill required, less land disturbed)
- Clear, established quality controls from production through installation
- More homogeneous than soil and aggregates
- Less environmentally sensitive and lower environmental impact
- Improved performance and durability
- Better sustainability
- Better resilience

The use of geosynthetic barriers continues to grow internationally, but more regulatory support is needed and also a better understanding of the limitations when designing with these types of geosynthetic barriers as a wrong design can cause a risk to the design without the geosynthetic being the pulling trigger.

BRIEF HISTORY OF GEOSYNTHETIC BARRIER SYSTEMS

Geomembranes (ASTM D4439 [1] definition: an essentially impermeable geosynthetic composed of one or more synthetic sheets) can be either smooth or textured on the surface, are essentially impermeable and are used as fluid barriers. Textured surfaces provide an enhancement of frictional characteristics, which allows designs on steeper slopes or where shear stress occurs. Geomembrane liner materials belong to the group of geosynthetic polymeric barriers (GBR-P) and the terminology of these types of products are defined by ISO 10318 [2] as follows: Factory-assembled structure of geosynthetic materials in the form of a sheet in which the barrier function is fulfilled by polymers other than bitumen.

Geosynthetic clay liners (GCL) (according to ASTM 4439: a manufactured hydraulic barrier consisting of clay bonded to a layer or layers of geosynthetic materials) also known as geosynthetic clay barrier (GBR-C) according to ISO 10318 [2] are:

Factory-assembled structure of geosynthetic materials in the form of a sheet in which the barrier function is fulfilled by clay.

Most recently, multicomponent GCLs (Fig. 1) are introduced to the market and enable to challenge particular site conditions (prevent desiccation, perform against critical chemical fluids, reduce root penetration, under extreme hydraulic gradients, etc.) where the use of GCLs has previously been limited. The following definition proposals are currently being used in ASTM D35 standards: multicomponent GCL, a GCL with an attached film, coating, or membrane decreasing the hydraulic conductivity or protecting the clay core or both.

BARRIER APPLICATIONS

With the increasing number of geosynthetic barriers and the increasing potential of barrier applications, geosynthetic barrier systems are becoming a very important part of the construction industry. Geosynthetic barriers provide a number of benefits and it is these benefits that are attracting more clients and construction professionals to their use. Geosynthetic barriers can often reduce the amount of excavation and fill material. They also provide a number of design benefits both technical and aesthetic. These benefits can have an effect on the cost of a project, and many solutions using geosynthetic barriers as opposed to more traditional methods have resulted in reduced costs. In addition to cost, sustainability of a construction solution is also very important. Hopefully with government targets and legislation, designers, owners, operators and manufacturers are being driven towards reducing their carbon footprint and carbon emissions (Fig. 2). And besides the design benefits provided by geosynthetic barriers, they have also been shown to reduce the carbon footprint of a number of construction projects [3]. Geosynthetic barriers are widely used in all types of applications where liquid or fluid tightness is required to prevent any kind of inflow or outflow. In the following the most known applications are described.

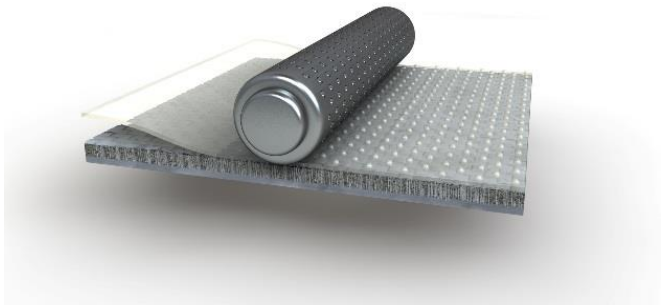

Fig. 1 Multicomponent geosynthetic clay liner – attaching an extruded polymer coating to the GCL

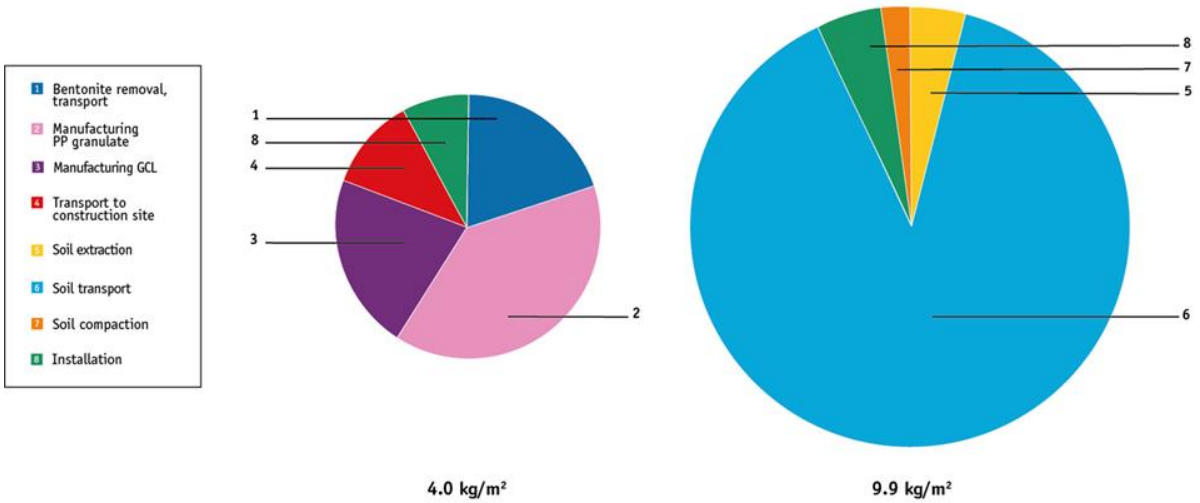

Fig. 2 Comparison of CO_2 emissions of a GCL (left) and a compacted clay liner (right) in a 36,000 m² large landfill cap [3]

Landfill Barrier Systems

Many modern landfills constructed over the past decades are performing very well and this is due to the fact that the content of landfills is considered hazardous for the environment and that landfills are typically located in cities or at least nearby to them, so that the effect on the environment is noticeably in an early stage.

Further regulations have been developed in the last decades, ensuring proper design and proper requirements to ensure that the geosynthetic barrier system in the base or as a cap will last far beyond the estimated design life of the landfill structure. There are several factors which contribute to the protection of the environment, but one key factor is the use of a polymeric geomembrane and/or a geosynthetic clay liner (GCL).

Surface Impoundments

Numerous national regulatory bodies have passed wide-reaching clean water legislation. Many of these regulations require the use of geomembrane liner systems in treatment lagoons at publicly operated wastewater treatment plants. These are also being used in potable water reservoirs (e.g., liners and floating covers). Here, these materials and systems have helped conserve water annually by minimising water seepage.

Also, storm water retention and detention management increasingly require smart lining solutions and include geomembranes, geosynthetic clay liners (GCLs) and multicomponent lining systems.

Geosynthetic products can also be used for practical or decorative pond liners at golf courses, amusement parks, and resorts, as well as in agriculture and aquaculture to create healthier, more efficient, and cost-effective systems.

Mining Applications

The daily mining rates, scale of single-site operations, and costs associated with mining in-crease every year. Advances in extraction technologies have greatly increased recovery rates from ore bodies. Geomembranes and GCLs under the large leach pads prevent the loss of valuable metal-laden chemical solutions while protecting soils and groundwater.

Geosynthetic barriers are also used to recapture and recycle harmful chemicals on site and in secondary containment applications.

Geosynthetics can aid in channelling surface water run-off and in preventing rainwater intrusion into heap leach pads, thus minimising solution dilution. In general, few regulations govern mining usage of geosynthetic barriers. Basic environmental laws apply, country by country; but the mining industry is unique in that it increasingly adopts geosynthetic barriers primarily for economic advantages.

Environmental Protection in Infrastructure Applications

Groundwater protection is generally required where a road enters a groundwater sensitive area, to avoid damage from winter maintenance with de-icing salt, everyday pollution arising from motor vehicles, and to protect the area from accidents with the possible release of polluting substances [4]. This German Guideline of the RiStWag [5] was one of the earlier guidelines on this topic (first publication 1982). The guideline describes, among other things, geomembranes and GCLs for environmental protection (Fig. 3).

Encapsulation of Contaminated Soils

Road noise and view-blocking barriers along roads and railway lines can be built with lightly contaminated soils or recycling material [6]. This may include slag, ash, contaminated soils from remediated sites, and residue from construction waste recycling or industrial processing. These wastes must meet certain environmental-chemical requirements and must be provided with a surface sealing cap (Fig. 4) to prevent water penetration and any contaminant transport. Suitable sealing materials for these purposes include GCLs and geomembranes.

Water Conveyance in Canals

Government agencies such as the United States Bureau of Reclamation (BuRec) indicate that seepage from unlined irrigation canals and waterways may be substantial and costly; and that geosynthetic barriers offer economically flexible and highly effective performance enhancement for canals. They are effective alternatives to concrete, asphalt or compacted clay soils. Stark and Hynes [7] summarised numerous geosynthetic barrier installations in canal systems, including single geomembranes (various polymers), exposed and buried installations, and composite systems, such as geomembrane with geotextile protection or concrete cover.

In Germany, all important technical information on waterway lining systems has been collated in the new guideline, “Recommendations for the use of lining systems on beds and banks of waterways.” The guideline, taking into account local boundary conditions, provides liner system selection information to be used by agencies. The focus is primarily on the underwater installation of GCL.

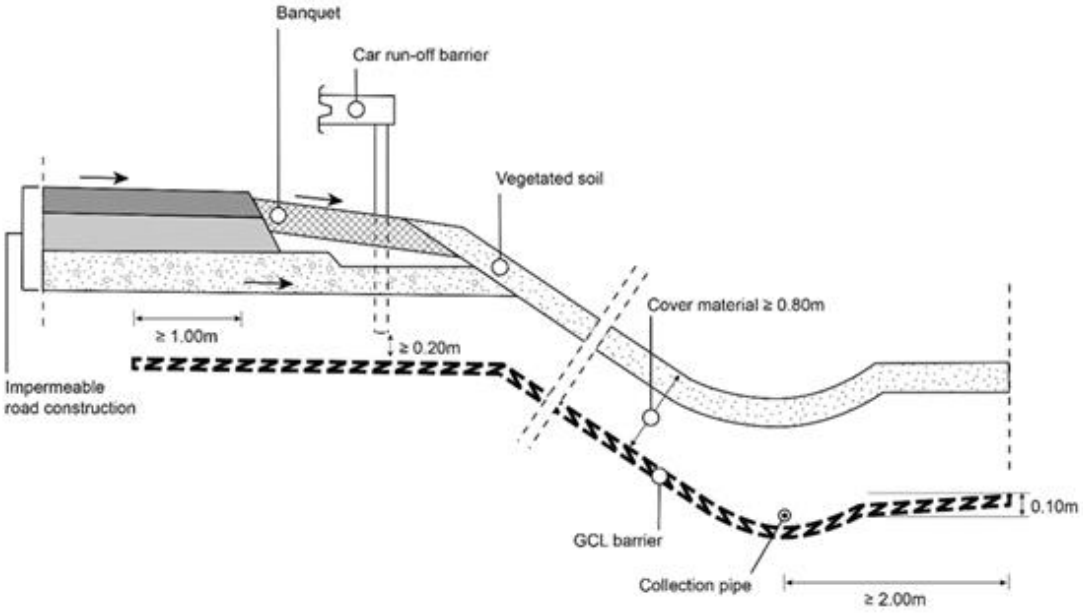

Fig. 3 Groundwater protection for a road dam construction [according to 5]

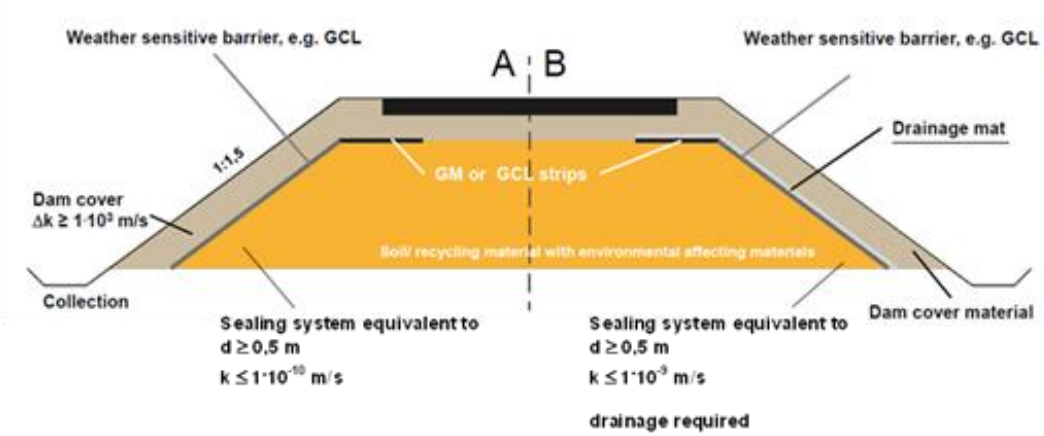

Fig. 4 Typical cross section of geosynthetic barrier system for the encapsulation of contaminated soils in road constructions

Dams – Levees – Dykes

Geosynthetic barriers provide easy-to-implement solutions for dams and flood defences, with project records extending back 40 years or more. When waters rise in a levee system, the integrity of the levee itself may be at risk. If water permeates the earthen structure, it weakens the dam stability and precipitates failure. Geosynthetic barriers resolve threats like this, often in ways that can be adapted easily to the local conditions. For flood protection and dam designs (Fig. 5), geosynthetic barriers (geomembranes and GCLs) provide long-term sealing performance, prevent permeation through the earthen construction and may reduce the dam or levee stability.

Fig. 5 Geosynthetic clay liner as hydraulic barrier in a water storage dam

Coal Ash Storage

In recent years, there have been several tragic failures of coal ash storage facilities worldwide and in many documented cases groundwater contamination at or nearby coal ash storage facilities. This contributed to the US EPA's issuance of new regulations for the storage of coal ash which require the use of geosynthetic materials. The US EPA regulations for coal ash storage propose the most efficient and effective barrier system as a composite liner system using a primary geomembrane (GM) liner, in combination with a compacted clay liner (CCL), approx. 500mm thick, or a needle-punched geosynthetic clay liner (GCL).

THE ISO DESIGN GUIDE

This new design guide ISO/DTR 18228-9 [8] is intended to offer advice to designers as to what to consider when using geosynthetics in a particular civil engineering or construction design [9]. As such it needs to cover a range of applications, material types, climatic and geological issues. Further, it covers installation and site preparation / completion recommendations. The emphasis is on choosing the most appropriate type(s) of material(s) for the application rather than changing the design to suit a particular material.

A possible whole process (Fig. 6) is organised into a basic flow chart to guide designers through the process of choices which need to be considered when designing with a geosynthetics barrier and the possible actions are described below.

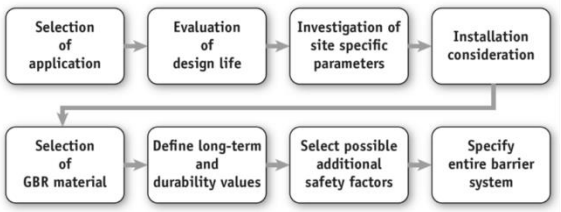

Fig. 6 Organised basic flow chart for designers when considering a geosynthetic barrier

- Selection of application: The first part of the process asks to select the application. With that it is necessary to check local regulations and requirements.
- Evaluation of design life: During this evaluation process, it is necessary to find out what the life time expectations should be, knowing that no construction method lasts forever. Realistically, they can be 5 (e.g., temporary solutions), 25 (e.g., secondary containment), 50 (e.g., containment non-landfills) or 100 years (e.g., landfills).
- Investigation of site-specific parameters: This is a very important part, as all site-specific conditions need to be evaluated and they have influence on the performance of the barrier system. It includes soil types on site, inclinations, weather conditions, vegetation, burrowing animals, etc.
- Installation considerations: Geosynthetic barrier systems are likely to be less sensitive to installation than traditional barrier systems like compacted clay liners, but they are still considered as relatively thin elements. Therefore, the installation process as well as the surrounding soil types need to be considered as well.
- Selection of barrier system: Balancing the combination of often conflicting performance criteria and different GBR materials to the proposed installation is always a complex matter. This inevitably comes down to professional judgement which geosynthetic barrier system suits best for the selected application.
- Define long-term and durability values: For a few applications there are well federal regulated geosynthetic barrier requirements. This process ensures national consistency and minimum standards while providing flexibility to states in implementing rules. It should be noted that the baseline of known requirements is pretty strict in material properties (e.g., GRI-GCL-3 [10] and GM-13[11]) and design selections are also sometimes available (e.g., GRI-GCL5 [12]).
- Select possible additional safety factors: Areas such as subgrade preparation, slope stability, climatic conditions, protection and hydraulic uplift, installation parameters and types of CQA are also considered as to what effect these may have on the design as well as what additional factors of safety they may offer.
- Specify entire barrier system: Obviously, a well prepared and written complete specification will avoid issues and questions on site.

One topic which the standard does not address is costs, not because these are not important but they can vary enormously according to the availability of types of materials, transport distances and costs, installation expertise etc. Good quality design needs to consider the cost effectiveness of any solution but must first qualify and meet all technical and service expectations of the stakeholders in the end use.

Additionally, as not mentioned yet, a good quality control and assurance plan from the manufacturing to the installation is also required. One set of good guide specifications and quality control on the manufacturing side is documented in the GSI specifications and they have seen worldwide implementation and use. The test methods include ASTM and ISO standards and have harmonised ASTM and ISO tables. The specifications are under

constant review and are updated frequently (http://geosynthetic-institute.org/specs.htm).

GEOSYNTHETICS NEED TO BE INCLUDED IN REGULATIONS

There is every reason to believe that geosynthetics will continue to be adopted into regulations around the world. No other field of engineered materials has developed as rapidly or gained such wide-spread acceptance as geosynthetics. This has much to do with the innovation and quality control measures in manufacturing and care of handling in the field. It also has much to do with geosynthetics being used in two primary situations: to perform better and/or more economically than traditional geotechnical designs. With a large record of data in support of cost and performance measures, and with secondary benefits such as decreased project carbon footprints with geosynthetics, the field's growth is assured.

It is absolutely necessary that regulations include application accepted geosynthetics in their regulations to allow cost-effective and high-performing solutions as they are already state-of-the-art and state-of-practice.

ISO DESIGN GUIDE AS THE BASIS FOR REGULATIONS

In many parts of the world, landfills are very well regulated by the federal government agencies through the process known as rulemaking. Such processes should also be introduced in other application regulations to ensure national consistency and minimum standards while providing flexibility to states in implementing rules. In general, following the approach of the ISO design guide is a good start what the expectations are.

Designers, authorities or other involved parties should recognize that geosynthetics cannot be specified purely on properties. It is important to see the big picture and consider all facts of the project, such as the German RiStWag guideline indicates in Fig. 7.

CASE STUDY: FUKUSHIMA NUCLEAR WASTE STORAGE

In March 2011, the Fukushima Nuclear Power Plant was severely damaged by an earthquake and tsunami. The subsequent radioactive leakage at the site led to the event being classified as a Level 7 on the International Nuclear Event Scale (INES). To date, the only other disaster to equal this radioactive threat to a population was the 1986 Chernobyl disaster. The epicentre of the earthquake was 72 km from the area in the Pacific Ocean. At 9.0 – 9.1, it ranks as the most powerful earthquake ever recorded in Japan. The tsunami waves produced by the quake were up to 40 m high.

The waves that reached the Fukushima Nuclear Power Plant were roughly 14 m high, which allowed them to overtop the seawall around the plant. Four reactors were flooded and the emergency generators failed, shutting off the coolant circulation pumps. With the cores not being cooled, the plant experienced nuclear meltdowns and hydrogen explosions in three of the four reactors that had suffered flooding. Radiation was released over a series of days. More than 154,000 people were evacuated from the area.

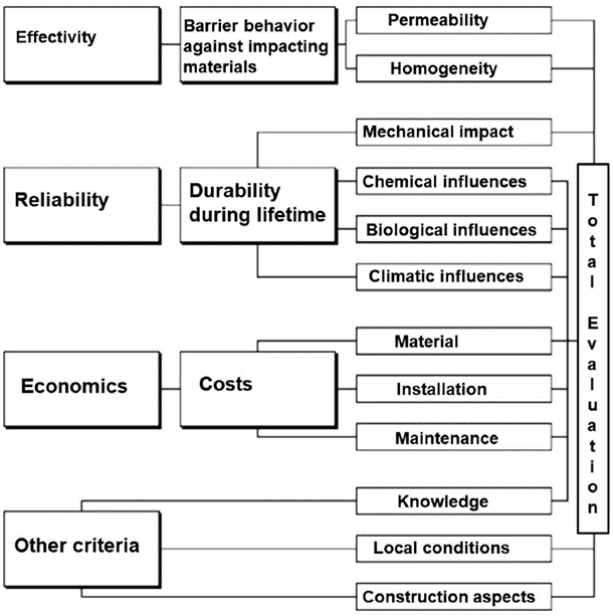

Fig. 7 Additional aspects for barrier systems requested by the German RiStWag guideline for groundwater protection in infrastructure projects [5]

In the years since the disaster, engineers have worked to design temporary and final disposal sites for the contaminated soils and waste from Fukushima. Geosynthetic containment has been a key part of the Interim Storage Facility (ISF) plan to enable waste to be stored without negatively impacting the soils beneath the ISF itself.

The primary ISF, which is in operation, will ultimately house 14.1 million m³ of contaminated material until a final disposal site is finalised. The contaminated material arrives at the initial soil separation facility in flexible bulk bags. A series of conveyor belts feeds the bag through a bag opener, sieving machine, soil improvement, removal of bag waste, a secondary sieving machine, removal of plant-based material, and finally the separated soil piles that are ready for interim storage.

In the soil storage area, the separated soil is deposited from trucks onto covered conveyor belts that deposit the waste in the lined disposal cell. A leachate collection system controls seepage and transports any leachate to a special treatment facility. Due to the importance of the barrier function, the ISF disposal cell is lined with a geosynthetic clay liner (GCL). Approximately 20,000 m² of a multicomponent GCL material was supplied in March 2018 (Fig. 8).

This particular GCL is one of the newer types within this barrier class. It is a multicomponent GCL that utilises an extruded, polyethylene coating on one side to enhance the material's performance against risks of desiccation, cation exchange, gas emission, and bentonite erosion. The special coating ensures that the GCL's ability to perform its impermeable barrier function is optimised. For a highly sensitive waste disposal site requiring long-term containment, it is a strong design strategy. The ISF is expected to receive all planned soils and waste by the end of 2021.

The ISF project is not the first use of geosynthetic clay liners in the management of contaminated soils from the disaster. In 2013, one of the early projects involved the installation of a GCL cap over contaminated soils. That project used a needle-punched GCL that has additional bentonite powder in the entire cover nonwoven to create self-sealing overlaps for a quicker, even more secure overlap sealing.

The use of GCL for lining the base and slopes of the contaminated soil storage facility and for capping contaminated soils to prevent the migration of polluted material emphasises how much trust engineers and environmental regulators have in these barrier systems.

Fig. 8 Installation of the PE extrusion-coated multicomponent geosynthetic clay liner

CONCLUSION

In many parts of the world governmental agencies have mandated the use of geosynthetics in many applications. The strongest sector seems to be landfills.

It is essential that their use is made mandatory in regulations in order to have efficient solutions with large potential on cost savings, safety of the designed structures and a minimum of environmental pollution including large reduction of the use of natural resources.

Most regulations describe material properties in detail or refer to existing specifications. However, some regulations show a shortage on other relevant design parameters, such as design issues, external effects, durability issues, installation considerations and/or quality control/assurance. The current version of the ISO design guide (approved and ready for publication) ISO/DTR 18228-9 "Design using geosynthetics — Part 9: Barriers" is an international standard containing recommendations and guidance for the design of geosynthetic barriers in geotechnical applications. It provides design guidance over various applications, design lives, material types, parameters and site-specific conditions. Obviously professional judgement is still needed in all designs and this guide will not substitute that as the document is intended only to assist in the process by identifying parameters which are relevant.

Good quality design needs to consider the cost effectiveness of any solution but must first qualify and meet all technical and service expectations of the stakeholders in the end use. All engineers must have a current working knowledge of the sort of costs incurred by their designs but the view was taken that to try and incorporate such parameters into the standards would be virtually impossible and almost certainly inaccurate.

REFERENCES

[1] ASTM D4439. Standard Terminology for Geosynthetics, ASTM International, West Conshohocken, PA, United States, 2020

[2] ISO 10318, Geosynthetics – Part 1: Terms and definitions, 2015

[3] Egloffstein, T. A., Heerten, G., von Maubeuge, K. P., Comparative life cycle assessment for clay geosynthetic barriers versus clay liners and other sealing systems used in river dykes, canals, storm water retention ponds and landfills. GBR-C 2K10; 3rd International Symposium Geo-synthetic Clay Liners, Germany, 2010

[4] von Maubeuge, K. P., and Post, A., Regulated groundwater protection in roads with geosynthetic barriers, Proceedings of the 17th African Regional Conference on Soil Mechanics and Geotechnical Engineering. 7, 8 & 9 October 2019 – Cape Town

[5] RiStWag FGSV Nr. 514, Richtlinien für bautechnische Maßnahmen an Straßen in Wasserschutzgebieten (translated: Guidelines for Construction Projects in Waterways of Protected Areas), Forschungsgesellschaft für das Straßen- und Verkehrswesen, Germany, 2016

[6] MTSE FGSV-Nr. 559, Merkblatt über Bauweisen für technische Sicherungs-maßnahmen beim Einsatz von Böden und Baustoffen mit umweltrelevanten Inhalts-stoffen im Erdbau (Recommendation on construction methods for technical safety measures when using soils and building materials with environmentally relevant substances in earthworks). Forschungs-gesellschaft für das Straßen- und Verkehrs-wesen, Germany, 2017

[7] Stark, T.D. and Hynes, J.M., Geomembranes for Canal Lining. Proceedings of Geosynthetics 2009, Industrial Fabrics Association International, Roseville, Minn., USA

[8] ISO/DTR 18228-9, Design using geosynthetics — Part 9: Barriers, 2021

[9] von Maubeuge, K. P., Geosynthetic barriers in regulations and recommendations in line with the ISO design guide? Innovative Infrastructure Solutions, Springer Nature Switzerland AG 2018

[10] GRI-GCL3, Standard Specification for Test Methods, Required Properties, and Testing Frequencies of Geosynthetic Clay Liners (GCLs), Geosynthetic Institute, Folsom, PA, USA, 2016

[11] GRI-GM13, Test Methods, Test Properties and Testing Frequency for High Density Polyethylene (HDPE) Smooth and Textured Geomembranes, Geosynthetic Institute, Folsom, Pennsylvania, USA, 2021

[12] GRI-GCL5, Test Methods, Required Properties, and Testing Frequencies of Geosynthetic Clay Liners (GCLs). Geosynthetic Institute, Folsom, Pennsylvania, USA, 2013

11th Int. Conf. on Geotechnique, Construction Materials & Environment, Kyoto, Japan, 3-5 November 2021, ISBN: 978-4-909106063 C3051

STUDY ON THE RELATIONSHIP BETWEEN THE CHANGE OF RIVER MOUTH SANDBAR AND RIVER DISCHARGE AND OCEAN WAVE AT THE OMONO RIVER

Junya Taniguchi[1], Kazuya Watanabe[1] and Noritoshi Saito[1]

[1,2,3]Graduate School of Engineering Science, Akita University, Japan

ABSTRACT

The sandbar exists at the river mouth of the gentle flow river. The river mouth sandbar topography was affected by combined forces, such as river discharge, sea waves, and wave direction, etc. River mouth sandbar interrupts salt and wave intrusion and affects the navigation of cruisers and fishing vessels. Field investigation was carried out for change of a river mouth sandbar in Omono River which locate on Akita Prefecture in Japan. The topographic surveys using UAV were conducted. Then, analysis of the sandbar change process was conducted on how sandbar area and river mouth width were calculated from reconstructed topography by the SfM technique. Moreover, an investigation of a relationship between sandbar area and river mouth width and river discharge, cross-shore, and longshore direction waves were carried out. As a result, the following results were confirmed from this study. (1) Right side sandbar has the sand spit which faced the south or left side sandbar develop very much in winter. (2) Sandbar area and river mouth width have a positive interrelation between river discharge and cross-shore waves. (3) Sandbar area has a strong negative interrelation between river mouth width.

Keywords: Omono River, Sandbar area, River mouth width, River discharge, Ocean wave

INTRODUCTION

Sandbar repeatedly develops or reduces at river mouth of gentle flow river [1]. Developing sandbar prevents ocean waves and salinity from intruding and affects the navigation of cruisers and fishing vessels. On the other hand, these kinds of reasons, the behavior of river mouth topographic change was required to understand for river management. There is a seasonal characteristic at the river on the Sea of Japan coast. Sandbar was grown up in winter because river discharge was decreased, and ocean wave was developed by the monsoon from Northwest. Sandbar was decreased in spring, summer, and Autumn because river discharge was increased by snowmelt or heavy rain [2].

In previous studies, sandbar area, recovery of river mouth sandbar on Nanakita River were researched to take aerial photographs and analytical solution of one-line model [3]. Variation of sandbar on Yura River was studied to observe shape and sandbar area and conducted flume experiment and numerical simulation [4]. Reformation of sandbar at Tenjin River after a typhoon event was studied by field investigation on sandbar topography using UAV (Unmanned Aerial Vehicle) and RTK-GNSS [5].

Sandbar was grown up from both sides at the river mouth on the Omono River. So, few studies were carried out about the river mouth sandbar on the Omono River. Dynamics of sand movement between river mouth terrace and river mouth was studied using aerial photographs, sandbar shape, and submarine topography map [6]. Recovery process of sandbar after a flood was monitored using UAV and was carried out experiences [7]. However, it is necessary for understanding the change of sandbar in detail to increase the frequency of the field observation and study quantitatively relationship between sandbar and external force which river discharge and ocean wave.

In this study, first, sandbar was reconstructed conducting UAV survey and using SfM (Structure from Motion) technique. Second, change of river mouth sandbar topography was observed and sandbar area and river mouth width were calculated. Finally, it was studied about the relationship between sandbar which change of sandbar shape, sandbar area, and river mouth width and external force which river discharge and ocean wave.

STUDY AREA

Omono River is located in Akita prefecture in Japan. Figure 1 shows the location of Omono River and investigated points of data. The size of the catchment area is 4710 m^2 and the channel extension is 133 km. The channel bed profile in the downstream area is 1/4000~1/5000, so Omono River is the gentle flow river. Estimated high water discharge on the river mouth is 9300 m^3/s. This river flows towards the Sea of Japan and there is long sandy coast on both sides of the river mouth.

River discharge, significant wave height, and wave direction were observed by Ministry of Land, Infrastructure, Transport and Tourism. River discharge was observed for every 1 hour at Tsubakigawa station which was located at the upper

13.1 km, significant wave height $H_{1/3}$ and wave direction were observed for every 20 minutes at Akita Port. Anyway, the wave of 1-188 degrees from the north clockwise toward the sea from land because wave which toward the land from sea was considered [8]. Cross-shore wave $H_{1/3}^2 cos\theta$ and longshore wave $H_{1/3}^2 sin\theta$ were calculated because the square of wave height is proportional to wave energy. Figure 2 shows definition of cross-shore wave and longshore wave.

STUDY METHOD

First, UAV surveying that aerial photographs of sandbar were taken to overlap 80% horizontal and vertical from ground to 150 m height were carried out [9].

Second, sandbar topography was reconstructed using SfM technique from taken aerial photographs. Figure 3 shows the reconstructed sandbar. Anyway, sandbar area A, sandbar area at the right side A_R, sandbar area at the left side A_L, and river mouth width B were calculated from the reconstructed sandbar. Also, shoreline was not modified considering sea level because tidal range is small on seashore on the Sea of Japan [10].

Finally, to examine the influence that sandbar area and river mouth width were affected by river discharge, cross-shore wave, and longshore wave, a comparison was carried out between sandbar data and external force.

RIVER DISCHARGE, CROSS-SHORE WAVE, AND LONGSHORE WAVE

Figure 4 shows river discharge, longshore, and cross-shore wave 2017-2020 year. River discharge was used data for every 1 hour. Cross-shore wave and longshore wave were used data averaged for 24 hours. Regarding longshore waves, the positive number shows wave direction from south to north, negative number shows wave direction from north to south.

River discharge decreased 100-500 m^3/s in winter every year. After that, river discharge was increased 700-1500 m^3/s by snowmelt in spring and greatly increased by heavy rain in summer and autumn.

Cross-shore waves were excelled in comparison with longshore waves. Cross-shore waves tended to decrease from spring to summer. It was increased from autumn to winter and grew up most strongly in winter. Longshore waves tended to become strongest in winter and go ahead to north from south mainly.

CHANGE OF SANDBAR

Figure 5 shows change of shape of sandbar from 2017 to 2020. In winter, sand spit was formed toward south from the right side sandbar and river toward south from right side sandbar and river channel was

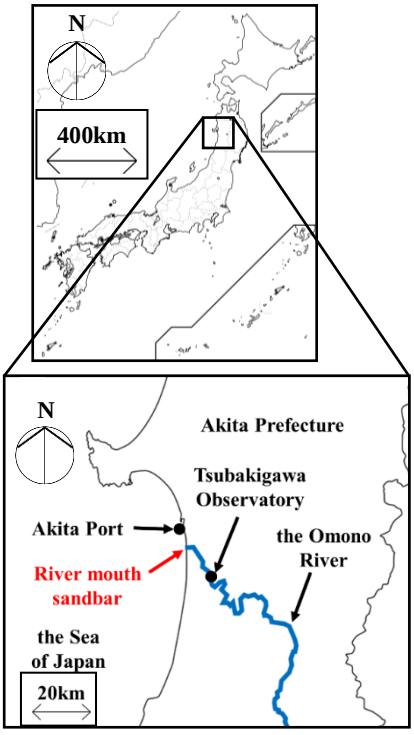

Fig. 1 Location of Omono River and investigated places of data.

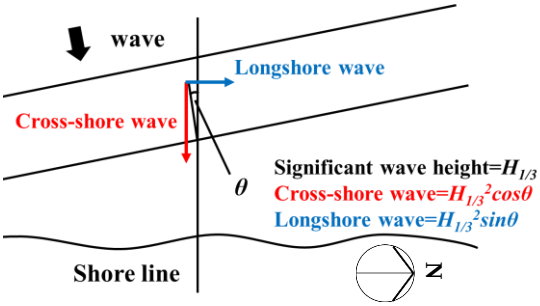

Fig. 2 Definition of longshore wave and cross shore wave.

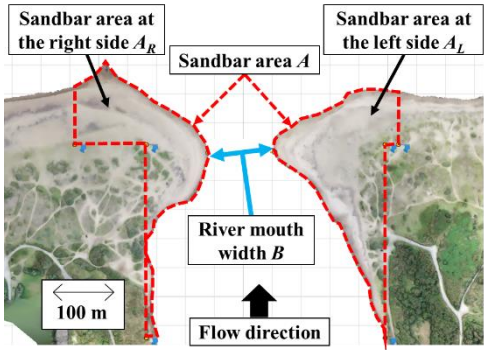

Fig. 3 River mouth sandbar.

curved to southwest in winter. River discharge was decreased most in winter and cross-shore wave was increased most from autumn to winter as indicated in Figure 4. Therefore, it was considered that sand spit toward south was formed because cross-shore wave

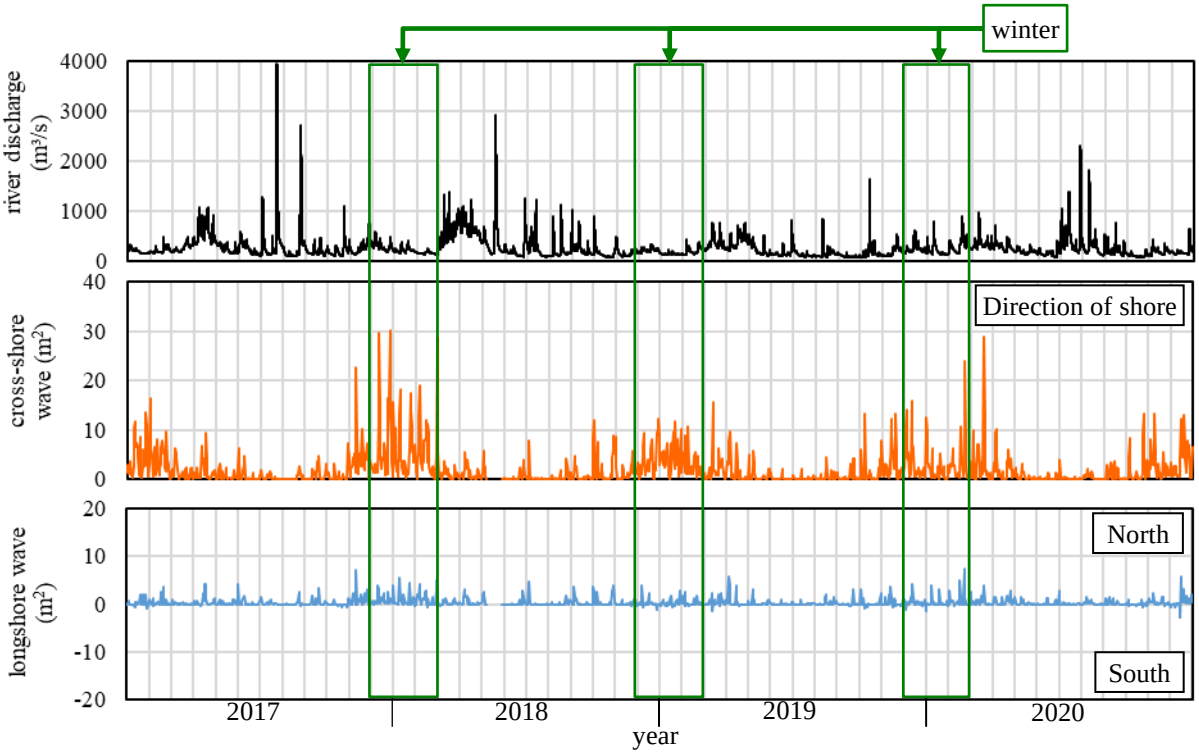

Fig. 4 River discharge, cross-shore wave, and longshore wave.

and river flow was balanced and sand transported from offshore was deposited.

River discharge was increased caused by snowmelt and cross-shore wave was decreased. Hence, sand spit was reduced or disappeared, and river mouth width was extended in spring.

River mouth width was extended more because river discharge was sometimes increased greatly by heavy rain in summer and autumn. In particular, river mouth width was extended greatly on July 29, 2017, after river discharge was increased July 24, 2017, and on May 21, 2018, after river discharge was increased 2904 m³/s on May 19, 2018.

Furthermore, it was found out that developed sandbar from right side or left side toward offshore was bent to north on September 4, 2017, May 21, 2018, June 1, 2018, and November 19, 2020, as illustrated in Figure 5 and longshore wave go-ahead to north. These show that sandbar was affected slightly by longshore waves toward north.

Shoreline was repeated advancing and retrograding both sides. To focus on winter, it was found out that shoreline was very different every year. Thus, it was not able to find relationship between shoreline and season.

CHANGE OF SANDBAR AREA AND RIVER MOUTH WIDTH

Sandbar Area and River Mouth Width

Figure 6 shows change of river mouth sandbar area, river mouth width, sandbar area at the right side, and sandbar area at the left side 2017-2020 year. Sandbar area was increased from autumn to winter and arrived at the maximum, approximately 80000 m^2, in winter. It was begun to decrease from spring, then arrived at the minimum in summer or autumn. Therefore, it was considered that sandbar area was decreased because sand was drained from sandbar by river flow when river discharge was increased caused by snowmelt in spring or heavy rain in summer and autumn. Moreover, it was decreased because sand was carried by cross-shore waves from offshore and deposited on sandbar. It was found out that sandbar area change is similar to topographic change. Thus, it was proved that topographic change of sandbar was able to evaluate quantitatively to monitor using UAV and SfM technique.

River mouth width was begun to increase from spring, then reached the maximum in summer or autumn. It was decreased from autumn to winter and reached the maximum, approximately 50 meters in winter. These results show that sand was drained from sandbar caused by river flow in spring, summer, and autumn. Furthermore, river mouth width was got narrow because sand was carried from offshore and deposited on sandbar. According to this result, river mouth sandbar on Omono River was found to have the characteristic like other rivers which flow to the Sea of Japan [11], [12].

Sandbar area on the right side was similar to sandbar area as illustrated in Figure 6 that these were increased from autumn to winter and reached

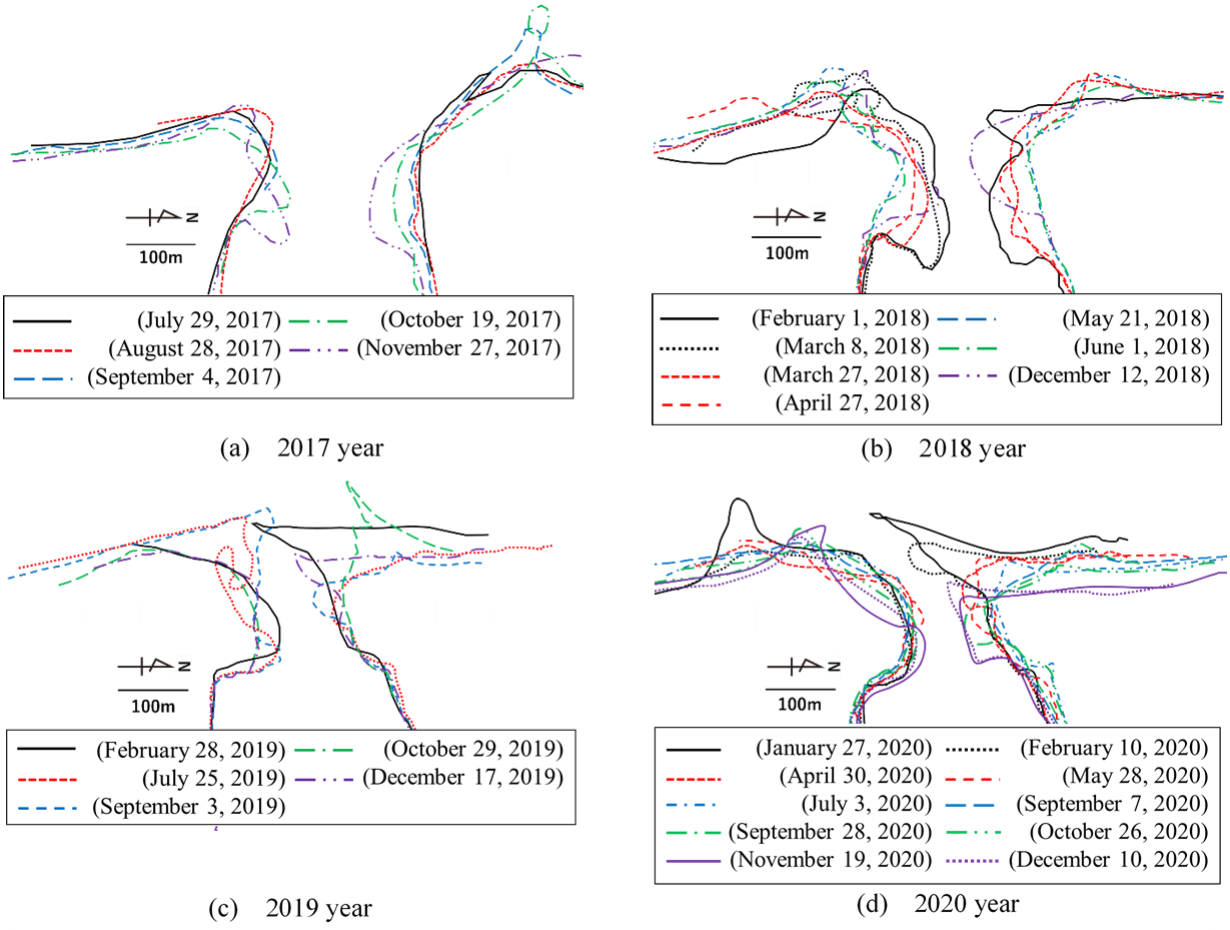

Fig. 5 Change of shape of river mouth sandbar.

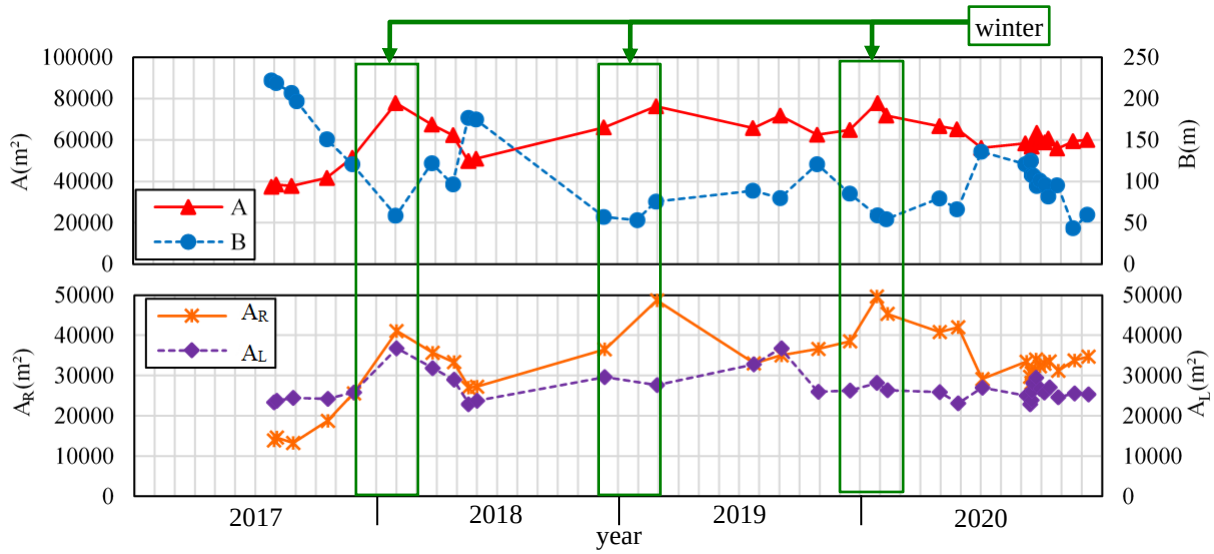

Fig. 6 Change of sandbar area, river mouth width, sandbar area at the right side, and sandbar area at the left side.

maximum in winter. After that, it was decreased from spring and reached a minimum in summer or autumn. The factor which sandbar area on the right side became greatly big in winter was that sand spit was formed on the right side. On the other hand, sandbar area on the left side was not similar to sandbar area and was not able to confirm seasonal characteristics. Moreover, the right side sandbar is important for the management of the river mouth sandbar because the right side sandbar was changed more intensely than the left side.

Recovery of Sandbar

Recovery of sandbar was examined by studying change of sandbar after the flood. It was defined as the flood when river discharge was exceeded 1500 m³/s. Figure 7 shows change of sandbar area after the flood. Anyway, when the flood has happened was set with 0 days and sandbar area in the observation day immediately after the flood was set of 0 m³/s. Explanatory notes in Figure 7 show the maximum river discharge in the flood and the day when the flood has happened. Sandbar area was not suddenly increased just after the flood regardless of season and was increased gently until 60 days later. By the change after August 25, 2017, and October 13, 2019, sandbar area was suddenly grown up after about 90 days.

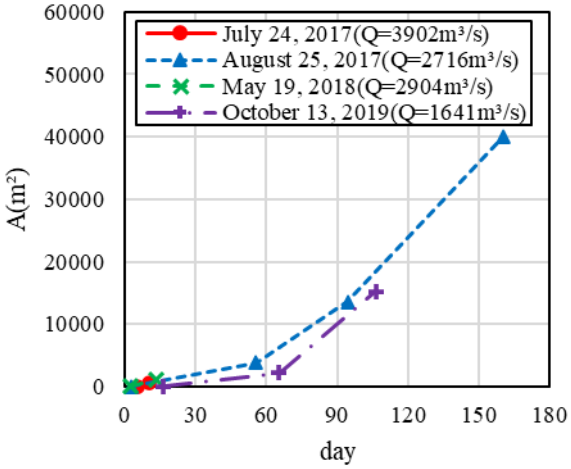

Fig. 7 Change of sandbar area after the flood.

RELATIONSHIP BETWEEN VARIATION OF SANDBAR AREA AND RIVER MOUTH WIDTH WITH WAVE

Variation of sandbar area per day from *x* to *y* was defined as *dA/dt* and river mouth width per day from *x* to *y* was defined as *dB/dt*. Equation (1) is variation of sandbar area per day.

$$\frac{dA}{dt} = \frac{A_y - A_x}{y - x} \quad (1)$$

Equation (2) is river mouth width per day.

$$\frac{dB}{dt} = \frac{B_y - B_x}{y - x} \quad (2)$$

Mean of cross-shore wave from x to y that $H_{1/3}{}^2 cos\theta_{Ave}$ and mean of longshore wave from x to y that $H_{1/3}{}^2 sin\theta_{Ave}$ were calculated. Furthermore, relationship between variation of sandbar area and river mouth width with wave was studied. Figure 8 shows relationship between variation of sandbar area

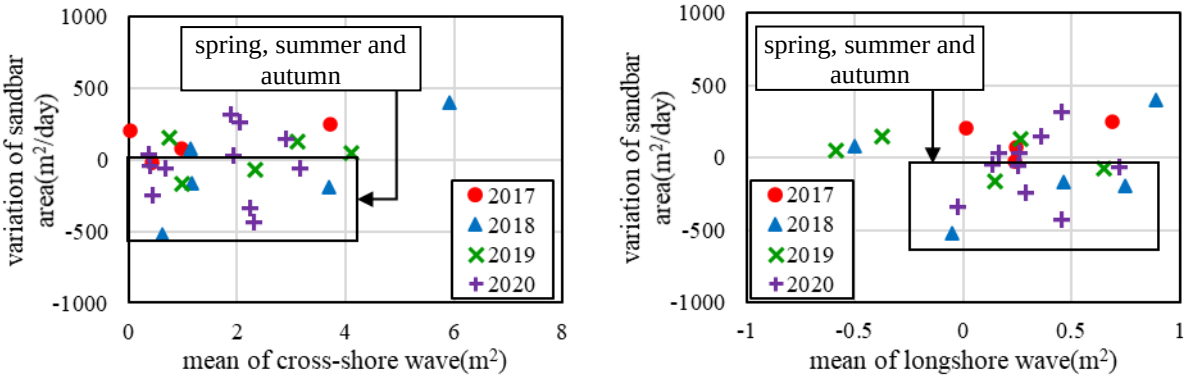

Fig. 8 Relationship variation of sandbar area with mean of cross-shore wave and longshore wave.

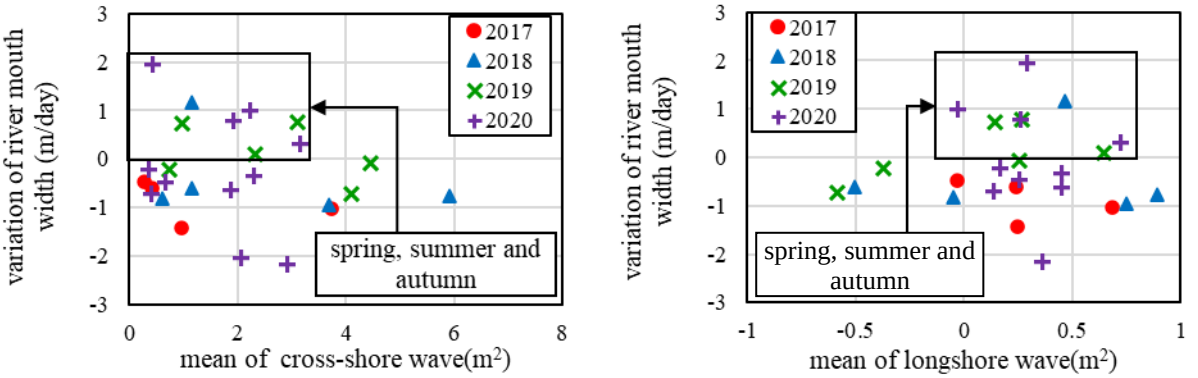

Fig. 9 Relationship variation of river mouth width with mean of cross-shore wave and longshore wave.

with cross-shore wave and longshore wave. Figure 9 shows relationship between variation of river mouth width with cross-shore wave and longshore wave. Anyway, data within six days were removed that the days of the interval on an observation day because it was considered the sudden change of area and river mouth width.

Variation of sandbar area per day was -500-+400 m², and variation of river mouth width was -2-+2 m. On the other hand, it was not able to confirm relationship between variation of sandbar area and river mouth width with cross-shore wave and longshore wave.

Being plus in winter and minus in spring and summer, sandbar area was confirmed that was increased in winter and decreased in spring and summer.

Variation of river mouth width was positive in spring, summer, and winter. However, it was negative regardless of season. According to these results, river mouth width was extended by strong river flow in spring, summer, and autumn, just after that, sand was deposited on river mouth sandbar.

CONCLUSIONS

It would be concluded as follows.

1) The cycle in Omono River was confirmed that sandbar was eroded by strong river flow caused by snowmelt in spring and heavy rain in summer and autumn. After that, sand was carried from offshore and deposited on sandbar by cross-shore waves in autumn and winter like other rivers on the Sea of Japan.
2) Sandbar area was grown up mostly in winter and decreased most in summer or autumn. However, river mouth width was got narrow in winter and extended most in summer or autumn.
3) Sandbar area was changed -500-+400 m^2 per day. River mouth width was changed -2-+2 m per day.

ACKNOWLEDGMENTS

The author would like to thank Ministry of Land, Infrastructure, Transport and Tourism for their contributions to this study.

REFERENCES

[1] Shimatani H., Sasamoto M., Kasai S., Ohba K., Fuse Y. and Sakai S., River Mouth Fluctuation of Yoneshiro River, Proceeding of Coastal Engineering, JSCE, Vol. 44, 1997, pp. 571-575. (in Japanese)

[2] Nishikawa K., Sasaki M., Maekawa K., Uda T. and Kunimatsu H., River Mouth Topography Changes at the Mogami River, Proceeding of Coastal Engineering, JSCE, Vol. 37, 1990, pp. 374-378. (in Japanese)

[3] Hoang C. V., Tanaka H. and Mitobe Y., Morphological Evolution of Beach Adjacent to the River Mouth After the 2011 Tsunami, Proceeding of the 36th IAHR World Congress, 2015, pp. 4379-4385.

[4] Miwa H., Kanda K., Ochi T. and Kawaguchi H., Dynamic state of river-mouth bar in the Yuragawa River and its control under flood flow conditions, Proceedings of the 13rd International Symposium on River Sedimentation, 2016, pp. 710-718.

[5] Katayama T., Kuroiwa M., Kajikawa Y. and Kurasige H., Field Investigation for Morphodynamic of River Mouth Bar Using UAV and RTK-GNSS, Proceedings of the 10th International Conference on Asian and Pacific Coasts, Vol. 74, No. 2, 2018, pp. 793-798.

[6] Uda T. and Matsuda H., Relation between the Formation and Disappearance of a River Mouth Bar and a River Mouth terrace in the Omono River, Proceedings of Coastal Engineering, JSCE, Vol. 42, 1995, pp. 566-570. (in Japanese)

[7] Watanabe K., Dinh V. D., Noguchi K. and Tanaka H., Study on Recovery Process of Sediment Deposit and Mechanism in the Formation of River Mouth Terrace, Proceedings of Coastal Engineering, JSCE, Vol. 74, issue 2, 2018, pp. 787-792. (in Japanese)

[8] Matsutomi H. and Fujita M., Verification of Correspondence of Long-term Trend of Shoreline Position and Wind Wave Height Changes on the Akita Southern Coast, Journal of Japan Society of Civil Engineer, Ser. B2 (Coastal Engineering), Vol. 70, No. 2, 2014, pp. 731-735. (in Japanese)

[9] Taniguchi J., Watanabe K. and Saito N., Study on the Behavior of Sandbar in a River Channel at the Babamegawa River, International Journal of GEOMATE, Vol. 20, issue 78, 2021, pp.115-120.

[10] Matsutomi H. and Kondo Y., Kimura T. and Tanaka H. Long- and Short- term Trends of Shoreline Position Change near the New Mouth of the Omono, Proceedings of Coastal Engineering, JSCE, Vol. 55, 2008, pp. 636-640 (in Japanese)

[11] Maekawa K. and Kon A., On Change in the Topography at the Mouth of the Aka River, Bulletin of the Yamagata University. Agriculture science, Vol. 11, No. 4, 1993, pp. 891-898.(in Japanese)

[12] Ochi T., Kanda H., Miwa H., and Nakamura F., Research on the Dynamic State of River-Mouth Bar under Flood Conditions in the Yuragawa River, E-proceedings of the 36th IAHR World Congress, 2015, pp. 2428-2439.

11th Int. Conf. on Geotechnique, Construction Materials & Environment,
Kyoto, Japan, 3-5 November 2021, ISBN: 978-4-909106063 C3051

PREDICTION ACCURACY OF RETRAINED SELF-ORGANIZING MAP BASED SURROGATE MODEL FOR A REAL COASTAL AQUIFER

Dushyantha Wagale[1], Bithin Datta[2]

[1,2]College of Science & Engineering, James Cook University, Australia

ABSTRACT

Salinity intrusion is an issue in coastal aquifers around the world. It can be controlled through appropriate management strategies, and optimal sustainable pumping strategy for groundwater use is always preferred due to high demand and scarcity of freshwater sources in coastal areas. Search based simulation optimization algorithms used in formulation and development of such prescriptive management strategies require surrogate models in place of computationally expensive numerical flow and transport simulation models. This ensures computational feasibility. This study evaluates the prediction accuracy of Retrained Self-Organizing Map (SOM) based surrogate model. The surrogate model is developed for a real life coastal aquifer – Rita Island in North Queensland, Australia. It is a deltaic island in Burdekin River with an approximate area of 60 square kilometers. Sugarcane farming has been carried out in the area since early nineteenth century and utilizing groundwater pumping for irrigation. Monitoring well readings have indicated presence of saline waters in certain parts of the aquifer. The developed hydraulic simulation model for the aquifer was calibrated and validated and found to be in good agreement with filed data. It was used to generate training and testing data for Retrained SOMs. Several SOMs were created during the training process under different training parameters to understand the effect of these parameters on prediction accuracy of the saltwater intrusion process. Analysis of results indicate that prediction errors are in the order of 10^{-6}.

Keywords: Coastal aquifers, Self-Organizing Maps, Surrogate models, saltwater intrusion, Burdekin River

1. INTRODUCTION

The management of coastal aquifers have been given substantial attention in recent years due to the increased environmental consciousness and their economic importance. The coastal aquifers are vital for economic activities all over the world as they provide water for human needs and 50% of the world's population do live within 60 km narrow strip of land from sea shore[1]. Costal aquifers are different from other aquifers as they have hydraulic connection with the sea. In costal aquifers the lighter fresh water is flowing towards the sea through upper layers; while dense saline water encroaches towards the land in lower layers of the aquifer. The density difference of the saline water and the freshwater governs the configuration of the aquifer. This configuration requires groundwater modelers to model the aquifer by means of density dependent flow and transport models to achieve accurate predictions. Though, in return these density dependent flow and transport simulation models are computationally expensive especially when used in optimization algorithms utilizing search methods using linked simulation optimization. Use of surrogate models are unavoidable in formulation of prescriptive management strategies for coastal aquifers due to the extreme computation burden inherited by hydraulic simulation models. When surrogate models are employed in place of hydraulic models, the efficiency of the optimization process increases significantly [2] [3].

The use of replacement models significantly reduce the calculation burden during the optimization process and, if not, the optimization process is uneconomical in terms of calculation time to converge into an optimal solution [4]. One such potential replacement model is Retrained Self-organizing Maps (RSOM). Once properly trained and tested, SOM can be used to predict unknown variables[5] [6]. In this study a calibrated and validated real aquifer model has been built for a real coastal aquifer – Rita Island, a deltaic island in Burdekin River delta in North Queensland, Australia. The data generated from this model was used to train and test the prediction accuracy of RSOM based surrogate model.

2. RETRAINED SELF-ORGANISING MAPS (RSOM) AS A SURROGATE MODEL

SOMs are neural networks with the ability of spatial adaptation [7]. The training process of SOM is a recursive non-parametric iteration process. SOM is a low order representation of higher order

dimensional data enabling better visualization, clustering and analysis [8][9][10][11]. Exploitation of SOM's prediction capabilities are not common, but in past it has been used successfully for prediction of unknown variables.

A Retrained Self-Organizing Map is obtained through repeating the training process over and over again but with different training parameters to ensure that the topology of the training data is well transferred to the SOM.

The use of RSOM as a surrogate model is feasible once properly trained and tested. To train a RSOM, a properly selected data set has to be used in order to obtain reliable and robust RSOM based surrogate model. Training data set must be beyond the upper and lower bounds of the interested constraint variables to ensure there is no effect due to the bounds under which RSOM has been trained on the predication capability. The mathematical approach for the use of trained RSOM as a replacement models for a general case for an aquifer management period with pumping patterns with *n* elements for a and resulting concentration values at *n* monitoring locations is discussed below.

Let the vectorial representation of neurons in a SOM, which has *m* number of vector points that carry pumping at different wells and resulting concentration at monitoring locations as their vector elements be denoted as:

$\overline{\boldsymbol{W}}_1, \overline{\boldsymbol{W}}_2, \overline{\boldsymbol{W}}_3, \ldots, \overline{\boldsymbol{W}}_i, \ldots, \overline{\boldsymbol{W}}_m$, and a representative neuron in this SOM can be expressed as:

$$\overline{\boldsymbol{W}}_i = \left({}_i\boldsymbol{x}_{p1}, \ldots, {}_i\boldsymbol{x}_{pn}, {}_i\boldsymbol{x}_{c1}, \ldots, {}_i\boldsymbol{x}_{cn} \right) \quad (1)$$

Where,
$\overline{\boldsymbol{W}}_i$ = i^{th} vector in SOM
${}_i\boldsymbol{x}_{pn}$ = n^{th} element of the pumping pattern in $\overline{\boldsymbol{W}}_i$
${}_i\boldsymbol{x}_{cn}$ = n^{th} element of concentration in the $\overline{\boldsymbol{W}}_i$

Let the input pumping realization for which the corresponding concentration values are required to be;

$$ {}^I\boldsymbol{X}_p = \left({}^I\boldsymbol{x}_{p1}, {}^I\boldsymbol{x}_{p2}, \ldots, {}^I\boldsymbol{x}_{pn} \right) \quad (2)$$

The ${}^I\boldsymbol{X}_p$ pumping realization is checked against all the SOM point vectors, only taking into consideration vector elements of pumping, to find the best matching unit (BMU) following the argument in Eq. (3).

$$\arg\min_i \left\| \sqrt{\sum_{n=1}^{N} \left({}^S_i x_{pn} - {}^I x_{pn} \right)^2} \right\| \quad (3)$$

for i = 1,2,3,…,m

Where;
${}^S_i x_{pn}$ = n^{th} pumping element in $\overline{\boldsymbol{W}}_i$
${}^I x_{pn}$ = n^{th} element of the input pumping realization

Once the BMU corresponding to the pumping elements on the SOM is known, then the remaining elements of the BMU vector-concentration values are directly read from the SOM.

To investigate the predication capability of RSOM as a replacement model instead of a numerical flow and transport simulation model, a coastal aquifer model was developed to generate training and testing data for the evaluation.

3. RITA ISLAND AQUIFER MODEL

To train and test the RSOMs two separate data sets were generated; training and testing data set. These data sets were generated by running a hydraulic simulation model for a real aquifer, the Rita Island. It is a portion of larger lower Burdekin alluvium, in North Queensland Australia [12].

Rita Island is a deltaic island with an area of 6000 ha (60 km^2). Rita Island carries clear hydraulic and transport boundaries. The eastern hydraulic boundary of the aquifer is the Coral Sea. The southern boundary is Burdekin River and the northern boundary is Anabranch. The disjunction of the Anabranch and the Burdekin River lies approximately 10 km inland to the Coral Sea. In the Burdekin area, sugar cane farming has been continuing since early 19th century and ground water has been used to irrigate the sugarcane fields since the commencement of farming[13]. The deltaic island has encountered salinity issues and at present some of the monitoring wells indicate higher level of salinity in ground water with reading over 1200 mg/L. Figure 1 shows a 3-dimensional image of Rita Island and its surroundings.

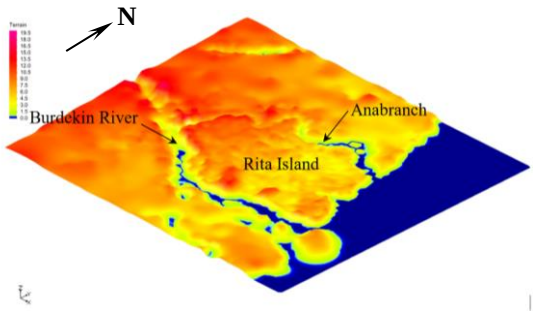

Fig.1 Rita island 3D representation of terrain and water bodies around it

The area receives annual average rainfall of 993mm and is located within the dry tropics region

of Northern Queensland. By analyzing borehole data [14], it was concluded that the average thickness of the aquifer varies between 60-80m. It was also concluded that it is reasonable to represent the aquifer by two material layers, the upper layer similar to sandy loam and the lower layer similar to gravelly sand. Aquifer material was assigned to be homogeneous, although the hydraulic conductivity had been taken to be transversely anisotropic. Horizontal components of hydraulic conductivity (Kx and Ky values) were taken to be the same while the vertical component of hydraulic conductivity (Kz) were selected to be less than that of horizontal values. To simulate the hydraulics and contaminant transport, a three-dimensional density dependent flow and transport simulation model; FEMWATER [15] was used. A finite element model was generated to represent the aquifer, with sufficient number of elements with appropriate size, shape and orientation in such a way that results would be reliable.

The upper layer of the aquifer was sub divided in to two layers of elements while the underlying layer was subdivided into three layers of elements. Along the aquifer boundaries the vertices were distributed in such a way that the element size is being maintained close to but less than 500 m. Around the wells the element were refined to have size of 350m or 200m depending on the location of the well. The finite element model had 3525 grid elements with 2250 nodes. Figure 2 illustrates the finite element mesh used in the model.

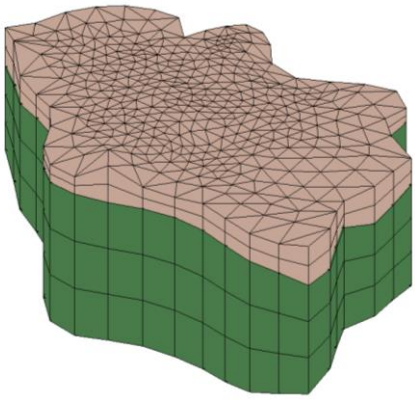

Fig. 2 material layers and finite element mesh used in the model

The model's boundary conditions were determined based on the physical characteristics of the aquifer and hydrological features around it. Logically, the upper bound of the aquifer was chosen to be the terrain. Terrain elevation data was extracted from google maps. The lower bound of the aquifer material was derived from the bedrock elevation derived from borehole data. The Coral Sea is the eastern boundary of the aquifer. It was assigned to be a specific head boundary at mean sea level, the transport boundary condition, along it was set to be at a saline concentration of 35,000 mg/L. The Northern boundary, Anabranch and the southern boundary, the Burdekin River, were modelled as varying specific head boundary. Head at the disjunction of the Anabranch from the Burdekin River was assigned to be at 3m based on the topography of the area. The transport boundary conditions for the freshwater bodies were defined based on conductivity readings of the Burdekin River. After a conversion of conductivity to salinity [16] the fresh water was adopted to be at a salinity concentration of 160 mg/L. The salinity value was incrementally increased for the freshwater bodies, from 160 mg/L to 35,000 mg/L downstream to the sand barriers which are constructed across the Burdekin River and Anabranch. This was to accommodate influence of tidal effects. The vertical recharge was modelled as an influx (infiltration) over a polygon. Aquifer recharge was assumed to be 20% of the rainfall and daily recharge averaged over 3 month periods were used in the model calculations.

4. MODEL CALIBRATION

The model was calibrated using available geo-hydrological, meteorological and crop data. The pumping from the aquifer was assigned to the aquifer as a negative flux as there are over a hundred wells within the aquifer. The pumping demand was calculated based on the soil water balance. Daily water balance was calculated using the daily evapotranspiration and rainfall combined with crop coefficient, root zone depth and soil type. It was assumed that the irrigation is carried out each time the readily available water reaches 25% of the total available water. The pumping was taken to be a negative flux. The resulting value after combining the positive recharge flux and negative pumping flux was applied to the model. When selecting the hydraulic conductivity values for testing the trial range was kept within prescribed values for Burdekin Delta, 25-100 m/d [1]. For the calibration run the initial conditions were generated following a two-step process. The first step was to generate the pre irrigation conditions. The pre irrigation condition represents the steady state conditions of the aquifer prior to the commencement of irrigation. The total simulation period adopted for the first step was 120 years. Generated results, head and concentration values were used as the initial condition for step two. The second step was to generate the resulting head and concentrations under pumping which was carried out for 120 years. The rainfall influx was combined with the pumping requirement and was applied as a resultant flux over

the aquifer. Resulting water levels were checked against the field observations for early 2012. Rita Island has network of monitoring locations with a continuous record of well head and conductivity readings over the past several decades. Figure. 3 shows the monitoring location with monitoring well numbers. Field observed values and adopted values in the model were in good agreement. It was observed that the max deviation is 2.6m over an approximately 75m ground water column except for one outlier.

Fig.3 Monitoring locations in Rita Island

The filed observed concentrations in early 2012 were interpolated to the finite element mesh and was used as the initial conditions. Analysis of interpolated values showed, that the monitoring locations identified as MW3 had high observed concentrations compared to the distributed value.

Considering the location of the M3 (Fig. (3)), it was concluded that observed salinity concentrations at this location are not resulted by salinity intrusion. It is also noted that the monitoring locations to the east of MW3 have less concentration readings. Hence, it was concluded that this anomaly is due to connate water resides deep in the fissures as the location of the monitoring locations and the salinity concentrations does not go hand in hand.

In Fig. 4 calibration run results are compared with the observed head at the end of the 3 year period from 2012 January to 2015 January. It is noted that field observed and model run results for concentration at M3 are not in good agreement. But the difference of head values at this location is only 0.466 m and considered to be acceptable calibration results. The maximum difference between calibration run results and filed observations for hydraulic head is 2.63 m. This difference is over a ground water column of 76.586 m at monitoring location M8. The average error is 1.515 m, which as a percentage is 2.0%. The maximum error is 3.4%. Hence, it is concluded that the calibration run for the heads is acceptable.

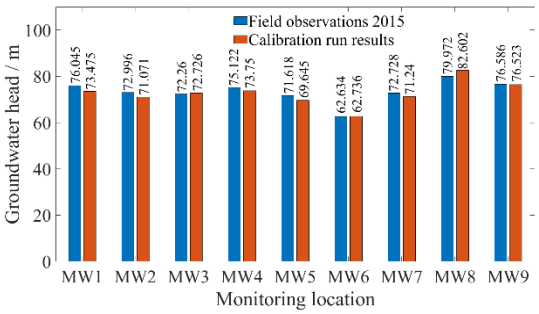

Fig.4 Calibration results for monitoring locations groundwater heads

Figure.5 provides comparison of calibration run results with the field observed concentration values. Monitoring location MW3 has been given for completion of data but in the analysis it was removed. According to the analysis the maximum deviation is 252 and it is 37%. The second largest deviation is 184 which is 18% deviation from the observed values. The maximum percentage error is observed at MW9 where the observed values are small – 95 mg/L. The average percentage error is 21%. This is accepted to be good as the match between the hydraulic heads are good.

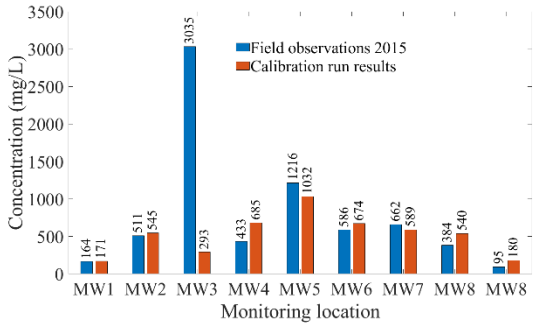

Fig. 5 Calibration results for monitoring locations – saline concentrations

5. MODEL VALIDATION

Model validation was carried out in the same manner that the calibration was done, except the adopted time period was 2013 to 2016. The validation run results are given in Fig. 6 and Fig. 7. In Fig. 6 it is clear that the match between the field observed head and the validation run results have a good match with very little variation. The maximum deviation is 2.66m and the average deviation of head is 0.874m; as a percentage error it is 1.2%.

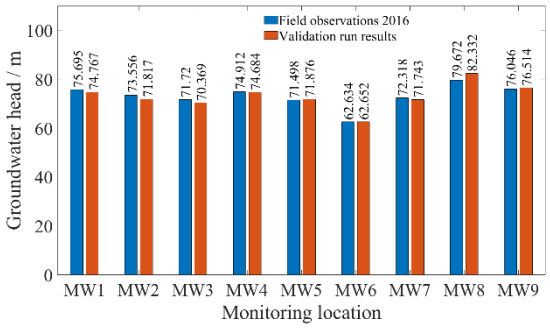

Fig. 6 Validation results heads

Figure 7 shows the validation results for concentration values. When comparing the concentration values simulated and observed at the end of validation period, it is noted that the average difference is 107 mg/L, and as a percentage it is 23%. The comparison is accepted as four of the monitoring locations have differences less than or equal to 40 mg/L, while another two are under 185 mg/L and the remaining two under 245 mg/L. The validation results are concluded to be very good given that the match of heads are very good and the concentration values are acceptable.

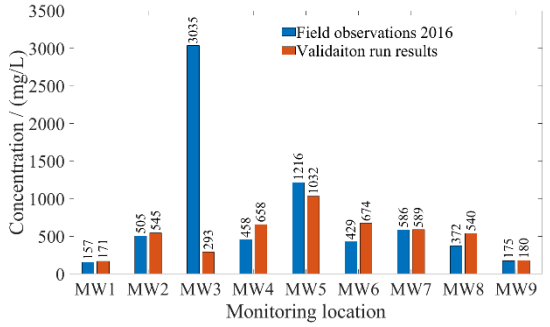

Fig.7 Validation results concentrations

The Table 1 provides the adopted parameter values in the model. Some of them are adopted from past literature.

Table 1 Parameters used in the model

Parameter	Value	
	Upper layer	Lower layer
Hydraulic conductivity (m/day)		
K_{xx}	35	55
K_{yy}	35	55
K_{zz}	3	4
Lateral dispersivity (m)	0.5	0.5
Longitudinal dispersivity (m)	2.5	2.5
Molecular diffusivity (m^2/s)	10^{-9}	10^{-9}
Bulk density of the soil (kg/m^3)	1600	1600
Effective porosity (%)	41	41
Density reference ratio		7.14×10^{-7}

6. DATA GENERATION FOR TRAINING AND TESTING RETRAINED SOM BASE SURROGATE MODEL

The farming area within Rita Island was divided in to approximately fourteen equal areas, with a well assigned for each area. These fourteen wells were assigned random pumping in between 2500 to 15000 m3/day. Five monitoring wells were chosen within the aquifer along the eastern boundary of the cultivated area. The adopted monitoring well configuration allows for establishment of the maximum allowable pumping, and if the salinity front moves towards the arable area, monitoring wells will pick this change and remedial measures can be implemented. Hence, these locations are best to assign constraint values for a management model. During salinity intrusion, the saline waterfront which migrate from coastline to inland will be picked up by these monitoring wells prior to the pumping wells being affected by saline water, and any adverse impacts on aquifer can be avoided. Fig. 8 provides the pumping wells (Well 1 – 14) field along with the monitoring wells (M1 – M5).

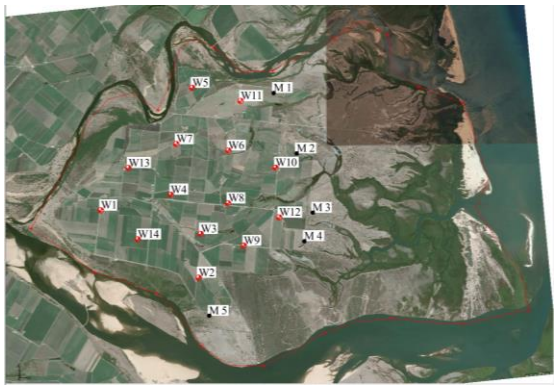

Fig.8. Pumping wells (W1 to W14) and monitoring well (M1 to M5) for the regional aquifer model

An individual management scenario was taken to be spanning over a three-year period. A pumping season was assumed to be three months, resulting in 12 pumping seasons over the management period. For 1 management scenario, a random pumping pattern with 168 pumping values was required as there were 14 pumping wells. To train the SOM, some 2000 of such patterns were used. Pumping patterns were generated by sampling from Halton sequence[17] by using MATLAB. Halton sampling can generate unbiased samples [18]. These pumping values are fed to the FEMWATER aquifer model and resulting concentration values are read. Similarly, a separate test data set, with 250 pumping patterns, was generated using the same process.

7. GENERATION OF RETRAINED SELF ORGANIZING MAPS BASED SURROGATE MODELS

Six RSOMs were created to evaluate the prediction capability. Created maps were of different size. Table 2 provides basic information on generated maps.

Table 2 Retained SOMs generated

Map	Number of vector points in the SOM
25 by 25	625
50 by 50	2,500
75 by 75	5,625
100 by 100	10,000
150 by 150	22,500
200 by 200	40,000

While training the maps some of the training parameters were kept constant within the similar training step (for e.g. training step 1) for all the maps. But these parameters were changed from one training step to the other, for example the number of iterations and Alpha – the learning rate parameter. Table 3 provides the number of iterations and Alpha adopted in training. Table 4 provides the radius of neighborhood adopted for different maps in respective training steps.

Table 3 Number of iterations and Alpha values

Training Step	Number of iterations	Alpha
Training Step 1	10,000	0.5
Training Step 2	10,000	0.5
Training Step 3	10,000	0.5
Training Step 4	100,000	0.05
Training Step 5	1,000,000	0.05
Training Step 6	1,000,000	0.05
Training Step 7	1,000,000	0.05

The generated SOMs were used in prediction of concentration values at monitoring locations for pumping realizations in test data by using equation 4. These predictions were used to calculate the prediction error by using Eq. (4).

$$RE = \frac{1}{N}\sum_{n=1}^{N}\left(\frac{\left|{}^{S}x_{cn} - {}^{T}x_{cn}\right|}{{}^{S}x_{cn}}\right) \qquad (4)$$

Where:

RE = relative error

$^{S}x_{cn}$= predicted concentration by RSOM

$^{T}x_{cn}$= simulated concentration results in test data

Table 4. Radius of neighborhood adopted in the training of different SOMs

Map	Training Step 1	Training Step 2	Training Step 3	Training Step 4	Training Step 5	Training Step 6	Training Step 7
25 by 25	25	12	6	4	3	2	2
50 by 50	50	25	12	6	4	3	2
75 by 75	75	40	20	10	5	3	2
100 by 100	100	50	25	12	6	3	2
150 by 150	150	75	35	17	8	4	2
200 by 200	200	100	50	25	12	6	2

8. RESULTS

It is noted that 25 by 25 map carries 625 vector points, which is less than that of the number of training data. On the other hand the largest map 200 by 200 had 40,000 vector points in it.

Figure 9 shows variation of relative error for prediction against the map size and training step. In this figure it is clear that the errors are large for maps 25 by 25, 50 by 50 and 75 by 75 regardless of how much they were trained. On the other hand for maps 100 by 100, 150 by 150 and 200 by 200 the prediction accuracy increases with retraining. This is significant after training step 4.

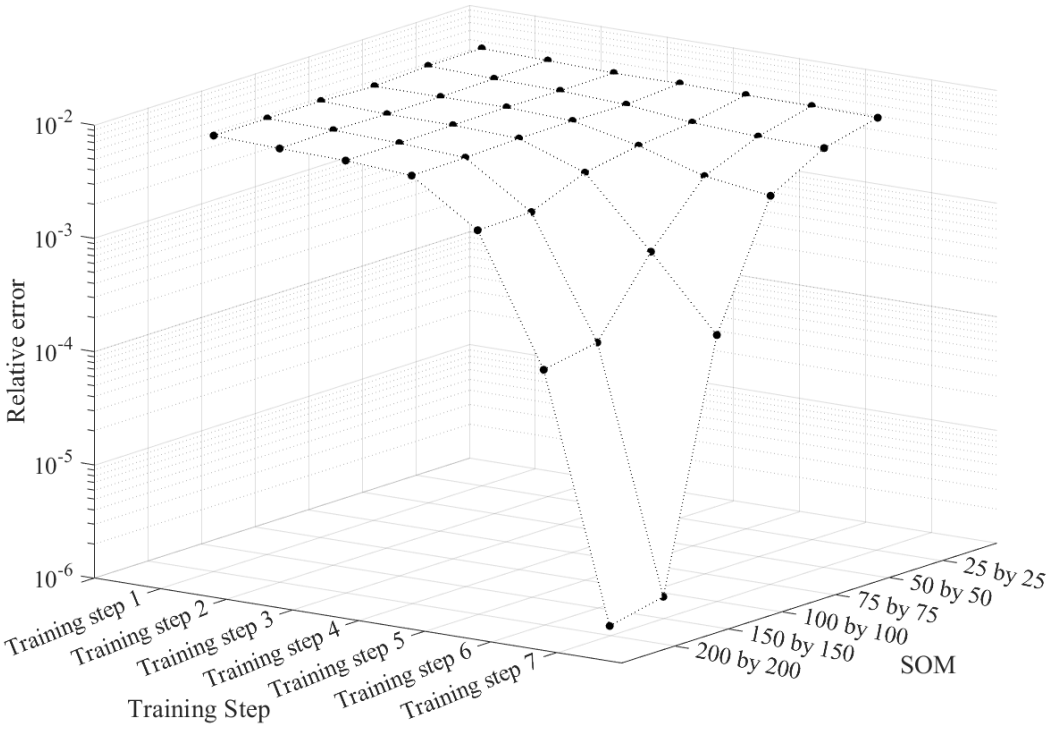

Fig. 9 Variation of relative prediction error with map and training step

It is also noted that for the 100 by 100 RSOM's errors are better than that of 75 by 75 RSOM though not as good as 150 by 150 after training step 4. But the difference between the errors in 150 by 150 and 200 by 200 RSOMs are more or less similar to each other at corresponding training steps. The 200 by 200 RSOM at the end of training step 7 has an average error of 1.2×10^{-6}, while for the same training step the 150 by 150 map carries an average error of 1.6×10^{-6}.

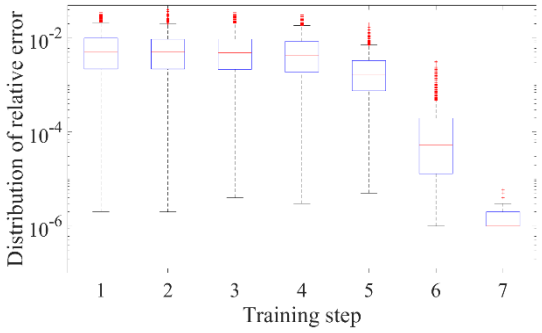

Fig. 10 Box plot for distribution of prediction error for 200 by 200 map for each training step

Figure 10 shows the box plot of prediction error distribution for 200 by 200 RSOM. By analyzing Fig. 10 it can be concluded that there is an improvement in the error after training step 4. In Table 3 it is clear that training step 5 and above had 1,000,000 iterations compared to training step 4 which had only 100,000 iterations. This improvement in prediction can be attributed to the number of iterations. In the figure it is also noted that at the seventh step there is only three outliers and all of them are in the rage of 10^{-5}.

9. CONCLUSION

A finite element based density dependent coupled flow and transport simulation model was implemented for a real aquifer – Rita Island in Burdekin River delta in North Queensland Australia. This model was calibrated and validated against hydraulic head and salinity levels at nine monitoring wells within the island. Validated model was used to generate training and testing data to generate retrained self-organizing map based surrogate models of different sizes to understand the effect of map sizes, and extent of training on prediction accuracy. It was concluded that RSOMs with vector points 10 times the data set can retain the topology of the training data set for the aquifer model. It is also concluded that prediction accuracy increases with the number of iterations in the training process.

10. ACKNOWLEDGMENTS

Authors would like to thank the Department of Natural Resources and Mines, Ayr office staff and Burdekin Water Board staff for their support while collecting data for the aquifer model.

11. REFERENCES

[1] Narayan, K., et al., Effects of Groundwater Pumping on Saltwater Intrusion in the Lower Burdekin Delta, North Queensland. MODSIM 2003 International Congress on Modelling and Simulation 2003. Vol. 2: p.224-229.

[2] Rao, S., et al., Planning groundwater development in coastal aquifers. Hydrological Sciences Journal, 2004. 49: p. 155-170.

[3] Dhar, A. and B. Datta, Saltwater Intrusion Management of Coastal Aquifers. II: Operation Uncertainty and Monitoring. Journal of Hydrologic Engineering, 2009. 14(12): p. 1273-1282.

[4] Sreekanth, J. and B. Datta, Multi-objective management of saltwater intrusion in coastal aquifers using genetic programming and modular neural network based surrogate models. Journal of hydrology (Amsterdam), 2010. 393(3-4): p. 245-256.

[5] Hazrati, S. and B. Datta, Self-organizing map based surrogatemodels for contaminant source identification under parameter uncertainty. Int J Geomate, 2017. 13(36): p. 11-18.

[6] Xia, X., et al., Identification of transient contaminant sources in aquifers through a surrogate model based on a modified self-organizing-maps algorithm. Hydrogeology Journal, 2019. 27(7): p. 2535-2550.

[7] Kohonen, T., Self-organizing Maps. 3 ed. 2001: Springer.

[8] Sinha, P., et al., Downscaled rainfall projections in south Florida using self-organizing maps. The Science of the total environment, 2018. 635: p. 1110-1123.

[9] Hsu, K.-C. and S.-T. Li, Clustering spatial–temporal precipitation data using wavelet transform and self-organizing map neural network. Advances in water resources, 2010. 33(2): p. 190-200.

[10] Farzad, F., et al., Performance Enhancement of Rainfall Pattern – Water Level Prediction Model Utilizing Self-Organizing-Map Clustering Method. Water Resources Management, 2017. 31(3): p. 945-959.

[11] Farsadnia, F., et al., Identification of homogeneous regions for regionalization of watersheds by two-level self-organizing feature maps. Journal of Hydrology, 2014. 509: p. 387-397.

[12] McMahon, G.A., Reading, L., Foy, Z., Wang, J., Bajracharya, K., Corbett, N., Gallagher, M., Lenahan, M.J., Gurieff, L. , Development of a hydrological modelling toolkit to support sustainable development in the Lower Burdekin groundwater system: Conceptualisation of the Lower Burdekin aquifer. 2012, Brisbane: Department of Science, Information Technology, Innovation and the Arts, Queensland Government.

[13] Kumar A. Narayan, C.S., Keith L. Bristow,, Modelling seawater intrusion in the Burdekin Delta Irrigation Area, North Queensland, Australia. Agricultural Water Management, 2007. Volume 89(Issue 3): p. 217-228.

[14] Wiebenga, W.A., Polka, E.J., Andrew, J.T.G., Wainwright, M., Kevi, L., Burdekin delta underground water investigation, North Queensland 1962-1963. 1966: Department of National Development, Bureau of Mineral Resources, Geology and Geophysics

[15] Lin, J., et al., FEMWATER : A Three-Dimensional Finite Element Computer Model for Simulating Density-Dependent Flow and Transport in Variably Saturated Media. 1997.

[16] UNESCO, Unesco technical papers in marine science 37, Background papers and Supporting data on the practical salinity scale 1978. 1981, France: United Nations Educational, Scientific and Cultural Organization.

[17] Halton, J. Algorithm 247: Radical-inverse quasi-random point sequence. 1964. Volume 7, p. 701-702. DOI: 10.1145/355588.365104.

[18] Roy, D.K., and B. Datta, Modelling and management of saltwater intrusion in a coastal aquifer system*:* A regional-scale study. Groundwater for sustainable development, 2020. 11: p. 100479.

11th Int. Conf. on Geotechnique, Construction Materials & Environment,
Kyoto, Japan, 3-5 November 2021, ISBN: 978-4-909106063 C3051

EFFECT OF PACLOBUTRAZOL CONCENTRATIONS OF FOLIAR APPLICATION ON FLOWERING OF 'MAHACHANOK' MANGO

Yaowarat Wongsrisakulkaew[1], Unaroj Boonprakob[1] and Lop Phavaphutanon[1]

[1]Faculty of Agriculture at Kampang Saen, Kasetsart University, Thailand

ABSTRACT

Paclobutrazol (PBZ) is a growth regulator, has been widely marketed throughout to stimulate mango flowering. In the recent years, many reports showed that application of PBZ by soil drenching can cause permanent stunting of flushes, vegetative and root growth was reduced. 'Mahachanok' mango trees were used in this study. The experimental design was CRD (completely randomized design) with 10 treatments and 4 replications. Mango trees received two and three PBZ foliar applications, applied at 15 days after shoot pruning with 0, 1,000 2,000, 3,000 and 4,000 mg/L. and repeated at 30 and 45 days with PBZ 2,000 mg/L. The results showed that PBZ could stimulate earlier flowering and higher percentage of flowering shoots than the control trees. Significantly differences were obtained on the time to flowering, percentage of flowering shoots and panicle length. Phyto toxic symptoms of shoots and panicles were observed on the PBZ treatments at 4,000 mg/L.

Keywords: Paclobutrazol, Foliar application, 'Mahachanok' mango

INTRODUCTION

Mango is a commercially important tropical fruit crop in Thailand. The cultivation of mango trees is highly popular among growers in all regions of the country, since there are lots of mango varieties being cultivated for different consuming purposes depending on variety some of them are grown for ripe fruit production and others are used for pickled fruits and edible fresh fruits like apple fruits, its annual production of fruits plays an important role in the Thai economy. The well known commercial cultivar is Mahachanok.

Mango flowering is a physiological process that onset the fruit production [1] and it is the first of several events that set the stage for mango production each year. It also influences the quality and quantity of fruits [2]. Mango trees flower in response to the age of the last vegetative flush in the tropical conditions. Synchronization of the vegetative of tree canopies is a necessary first step in the flowering management program. Synchronization growth is best accomplished by tip pruning all of the stems on the tree [3]. The next step is to decide whether to use Paclobutrazol (PBZ) or not. PBZ has been used with considerable success to induce flowering in several fruit crops such as apple [4], pummelo[5], apricot [6] and mango [7]. PBZ inhibits gibberellin biosynthesis reduces vegetative growth and induces water-stress tolerance as well as increases total non-structural carbohydrates (TNC) [8]. PBZ has been widely marketed throughout the tropics to stimulate mango flowering. Soil application of PBZ has been found to be more responsive in regard to suppressing the vegetative growth and enhancing the reproductive growth in mango [9]. Studies have shown that PBZ is needed to be applied annually to increase mango fruit yields [10]. In the recent years, many reports showed that application of PBZ by soil drenching produced uneven distribution of the chemical throughout the plants as noticed by the uneven size of the panicles in the lower versus the upper part of tree. Overdose may cause undesirable effects such as stunting of flushes, panicle malformation, vegetative and root growth of mango was reduced [11]. In areas where PBZ is applied regularly, there may be risk of environmental contamination due to its residues persisting in soil for a very long time [12].

Then, the aim of this work was to determine the effects of PBZ on flowering of Mahachanok mango. Foliar application was used in this study to insure uniform flowering and reduce the detrimental side effects.

MATERIALS AND METHODS

Experimental details

This experiment was carried out at Tropical Fruit Research and Development Center Kasetsart University, Kamphaeng Saen Campus Nakhon Pathom Province, Thailand. Mango trees (cv. Mahachanok), at the age of 6 year-old, were selected. Tip pruning has been done to induce new flush from all the stems on the tree (Fig.1). Foliar application at 15 days after pruning with PBZ at 0, 1,000, 2,000, 3,000 and 4,000 mg/L and it was repeated at 30 days after pruning with 0 and 2,000 mg/L. and repeated again at 45 days after pruning with 0 and 2,000 mg/L.

(a)

(b)

(c)

Fig.1 New flush at 15 days (a), 30 days (b) and 45 days (c) after pruning in Mahachanok mango.

Experimental design and data analysis

Completely randomized design (CRD) was used in this study. There were four replications with ten treatments: T1) control; T2) spray with 2,000 mg/L of PBZ at 30 days; T3) spray with 1,000 mg/L of PBZ at 15 days and repeated at 30 days with 2,000 mg/L of PBZ; T4) spray with 2,000 mg/L of PBZ at 15 days and repeated at 30 days with 2,000 mg/L of PBZ; T5) spray with 3,000 mg/L of PBZ at 15 days and repeated at 30 days with 2,000 mg/L of PBZ; T6) spray with 4,000 mg/L of PBZ at 15 days and repeated at 30 days with 2,000 mg/L of PBZ; T7) spray with 1,000 mg/L of PBZ at 15 days and repeated at 30 days with 2,000 mg/L and repeated again at 45 days with 2,000 mg/L of PBZ; T8) spray with 2,000 mg/L of PBZ at 15 days and repeated at 30 days with 2,000 mg/L and repeated again at 45 days with 2,000 mg/L of PBZ; T9) spray with 3,000 mg/L of PBZ at 15 days and repeated at 30 days with 2,000 mg/L and repeated again at 45 days with 2,000 mg/L of PBZ; and T10) spray with 4,000 mg/L of PBZ at 15 days and repeated at 30 days with 2,000 mg/L and repeated again at 45 days with 2,000 mg/L of PBZ. Ten shoots per tree are randomly tagged around the canopy of each tree and monitored for flower in determination after foliar application of PBZ. The parameters measured were percentage of flowering shoots, time taken from shoots pruning to flower emergence, panicle length (panicle length was measured at 50% bloom) and phenological changes of shoots. The data were subjected to analysis of variance and the means were separated by Duncan's new multiple range test (DMRT) at $P < 0.05$.

RESULTS

The results showed that the use of PBZ could stimulate higher percentage of flowering shoots than the control trees. Trees receiving 1,000 mg/L at 15 days and repeated at 30 days with 2,000 mg/L of PBZ had the highest percentage of flowering shoots of 72.5%, whereas those control trees showed the lowest flowering percentage of 0% (Table 1, Fig.2).

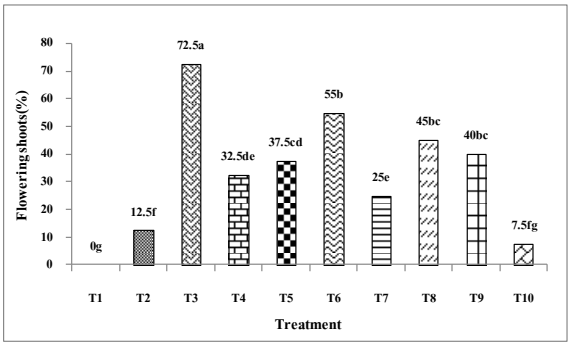

Fig.2 Percentage of flowering shoots of Mahachanok mango.

PBZ could stimulate earlier flowering. Time taken from application to flower mergence was highly significant among the PBZ treated trees. Trees receiving 1,000 mg/L at 15 days and repeated at 30 days with 2,000 mg/L of PBZ had earliest flowering at 106.5 days from application (Fig.3 and Table 1).

There was a significant difference on the length of panicle. Trees treated with PBZ at the rate of 2,000 mg/L and above had a significant shorter panicle compared with the control. However, the higher concentration of PBZ gave shorter panicle. Panicles from the trees receiving with 2,000 mg/L of PBZ at 15 days and repeated at 30 days with 2,000 mg/L and repeated again at 45 days with 2,000 mg/L of PBZ had the shortest panicle of 15.5 cm (Table 1, Fig.4).

Table 1 Effect of PBZ on percentage of flowering shoots, time to flowering and length of panicle of Mahachanok mango after foliar application of PBZ at different rate.

Treatment	Flowering shoots (%)	Time to flowering (days)	Length of panicle (cm)
T1	0.00 g	172.75 a	42.13 a
T2	12.50 f	111.25 c	33.00 c
T3	72.50 a	106.50 d	37.75 b
T4	32.50 de	107.25 d	28.63 d
T5	37.50 cd	107.75 d	28.50 d
T6	55.00 b	107.50 d	16.28 f
T7	25.00 e	107.25 d	24.65 e
T8	45.00 bc	107.75 d	15.50 f
T9	40.00 cd	107.50 d	26.65 de
T10	7.50 fg	162.25 b	25.50 e
F-test	*	*	*
cv.(%)	22.28	1.26	4.81

Means followed by the same letter at the same column were not significantly different at the 5% level by DMRT.
* = significantly different at $P < 0.05$

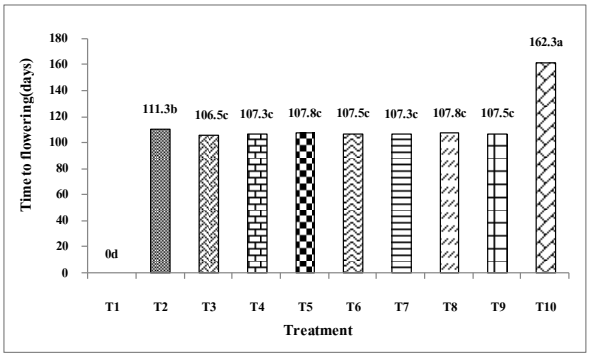

Fig.3 The time to flowering of Mahachanok mango.

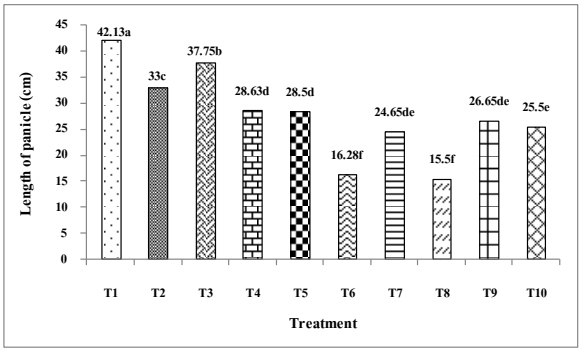

Fig.4 The length of panicle in Mahachanok mango.

The trees receiving the PBZ application showed its effect by decreasing shoot and panicle length significantly (Table 1).

In this study, the phyto toxic symptoms of shoots and panicles were observed on the PBZ treatments at 2,000 mg/L. The trees receiving the PBZ at 2,000 mg/L were stunting of flushes and panicle malformation (Fig.5, Fig.6).

DISCUSSION

Application of PBZ affected vegetative growth and reproductive growth of Mahachanok mango. The vegetative growth of mango trees was observed 2 wks after treated with PBZ. Shoot number was not different but shoot length showed significant differences among treatments. In the present study, PBZ application was effective in reducing shoot length since the PBZ inhibits GA biosynthesis by blocking the step in the oxidation of ent-kaurene to ent-kaurenoic acid [13] resulting in unelongated shoots, even though cell division still occurs. Triazoles compounds are anti-giberellic could alter the levels of gibberellins in shoot buds. Paclobutrazol application increased the number of flowering shoots due to lower vegetative growth and higher reserves in the tree. Similar results were also obtained by Silva et al., [14] in mango cv. Kent. Alphonso is a variety often enters in to alternate bearing habit it can be possible with break that alternate bearing with growth retardants. The triazole products help to shift the vegetative phase into flowering in 'Tommy Atkins' a cultivar difficult to change the phase [3]. Similar results have been reported in apple [4]. In addition, PBZ could also induce flowering in mango trees because it reduced vegetative growth. The

involvement of the GA in mango was also demonstrated by Yamashita *et al*.[14] who reported that GA acts as a flowering inhibitor. The use of PBZ could stimulate higher percentage of flowering shoots than the control trees. This result was supported by Yeshitela *et al*. [8] who found that PBZ produced the highest number of flowers per panicle in mango. The trees receiving the PBZ at 2,000 mg/L by foliar application were stunting of flush and panicle malformation.

CONCLUSIONS

The study of using paclobuctrazol applying as foliar spray to mango trees cv. Mahachanok could stimulate earlier flowering and higher percentage of flowering shoots than the control trees. Significantly differences were obtained on the time to flowering, percentage of flowering shoots and panicle length.

ACKNOWLEDGMENTS

This research was supported by a grant from the program Strategic Scholarships for Frontier Research Network form the Higher Education Commission, Thailand.

(a) (b) (c) (d)

Fig. 5 The control tree (a) and phyto toxic symptoms of shoots (b)- (d) in Mahachanok mango.

(a) (b) (c)

(d) (e) (f)

Fig. 6 The control tree (a) and phyto toxic symptoms of panicles (b)- (f) in Mahachanok mango.

REFERENCES

[1] Ramírez, F. and Davenport, T.L., Mango (*Mangifera indica* L.) flowering physiology, Scientia Hort. Vol. 126, Issue 2, 2010, pp. 65-72.

[2] Tiwari, D.K., Patel, V.B. and Pandey, K., Floral induction in mango: physiological, biochemical and molecular basis, Int. J. Chem. Studies. Vol. 6, Issue 1, 2018, pp. 252-259.

[3] Davenport, T. L., Reproductive physiology of mango, Brazz. J. Plant Physiol. Vol.19, 2007, pp. 363-376.

[4] Zhu, L.-H., A. Peppel, X.-Y. Li and M. Welander. Changes of leaf water potential and endogenous cytokinins in young apple trees treated with or without paclobutrazol under drought conditions. Scientia Hort. Vol.99, 2004, pp. 133–141.

[5] Phadung, P., K. Krisanapook and Phavaphutanon, L. Paclobutrazol, Water Stress and Nitrogen Induced Flowering in 'Khao Nam Phueng' Pummelo. Kasetsart J. (Nat. Sci.) Vol.45, No.2, 2011, pp. 189 – 200.

[6] Arzani, K. and H.R. Roosta. Effects of paclobutrazol on vegetative and reproductive growth and leaf mineral content of mature apricot (*Prunus armeniaca* L.) trees. J. Agric. Sci. Technol. Vol.6, 2004, pp. 43–55.

[7] Wongsrisakulkaew Y., B. Boonprakob, R.Sethpakdee, and N. Juntawong., Effect of paclobutrazole concentrations and time of foliar application on flowering of 'Namdokmai-Sitong' mango. International Journal of GEOMATE. Vol. 12 Issue 30, 2017, pp. 23–27.

[8] Yeshitela, T., P. J. Robbertse and P.J.C. Stassen. Paclobutrazol suppressed vegetative growth and improved yield as well as fruit quality of 'Tommy Atkins' mango (*Mangifera indica*) in Ethiopia. NZ J. Crop Hort. Sci. Vol. 32, 2004, pp. 281–293.

[9] Singh, D. K. and Ram, S. Level of paclobutrazol residues in shoot and fruit of mango Indian J. Plant Physiol. Vol.5, 2000, pp. 186-188.

[10] Yadava, R.B.R., Singh, V.K. Long term effects of paclobutrazol (PP 333) on yield and quality of Dashehari mango (*Mangifera indica* L.). Ind. J. Plant Physiol.Vol.3, No.2, 1998, pp.166–167.

[11] Singh, Z. Effect of (2RS, 3RS) paclobutrazol on tree vigour, flowering, fruit set and yield in mango. Acta Hort. Vol. 525, 2000, pp. 459–462.

[12] Debi Sharma and Mahesh D. Awasthi. Uptake of soil applied paclobutrazol in mango (*Mangifera indica* L.) and its persistence in fruit and soil. Chemosophere. Vol. 60, 2005, pp. 164-169.

[13] Sterrett, J.P. Paclobutrazol: A promising growth inhibitor for injection into woody plants. J. Amer. Soc. Hort. Sci. Vol.110, No.1, 1985, pp. 4–8.

[14] Silva, G. J. N., E. M. Souza, J. D. Rodrigues, E. O. Ono and Mouco, M. A. C., Uniconazole on mango floral induction cultivar 'Kent' at submediosaofrancisco region, Brazil. Acta Hort., Vol. 884, 2010, pp. 677- 682.

[15] Yamashita, K., K. Kitazono and S. Iwasaki. Flower bud differentiation of Satsuma Mandarin as promoted by soil-drenching treatment with IAA, BA or paclobutrazol solution. J. Japan. Soc. Hort. Sci. Vol.66, No.1, 1997, pp. 67–76.

11th Int. Conf. on Geotechnique, Construction Materials & Environment, Kyoto, Japan, 3-5 November 2021, ISBN: 978-4-909106063 C3051

THE RELATIONSHIP BETWEEN AQUATIC ORGANISMS AND ENVIRONMENTAL PARAMETERS IN URBAN RIVER WITH IMPROVEMENT

Michiko Masuda[1], Koichi Takada[2] and Fumitake Nishimura[3]

[1,2]Faculty of Engineering, Nagoya Institute of Technology, Japan; [3] Faculty of Engineering, Kyoto University, Japan

ABSTRACT

Many habitat models about organisms have been constructed by many researchers. Most of the models are constructed using only a year data. We collected over 5 years data about organisms and environmental factors in the Yamazaki River, an urban river in Nagoya city at the center of Japan. Using the data, we constructed a general linear model at each year. It was revealed that the river improvement at every year affected the distribution of the alien species, especially the vegetation cover changing. The model of shrimps with low ability of moving was very predictable of the distribution. But in the model of the species with high ability of moving, it occurred the good model was made by chance. It was revealed that the distribution of the river species is always changing therefore so the good model will be made by chance. In order to predict the distribution of the species, we must investigate for some years.

Keywords: General linear model, Alien species, Native Species, Year fluctuation

INTRODUCTION

In Japan, at the maintenance of the river the target species has been set up from the viewpoint of environment by local public entity [1]. The Ministry of Land, Infrastructure, Transport suggested that the river management should be done not only for the safety of people life but also the natural environment.

The Yamazaki River is an urban river in Nagoya city, in the center of Japan, with many fishes, *Plecoglossus altivelis* (native species), *Oryzias latipes* (endangered species). But some alien species live in the river, for example *Zacco platypus*, *Lepomis macrochirus* and *Cyprinus carpio* [2]. And the target species of the river is *Rhinogobius* spp. But few numbers of the species were observed, nevertheless Nagoya city managed the river maintenance with the environmental factors, such as the water flow rate, the depth of the river and the materials of the river bottoms which were controlled for the species. Perhaps other environmental factors are needed for *Rhinogobius* spp.

From the factor of the living species, the maintenance of the river system should be done in order to conserve the native species. What were environmental factors needed for the native species? The maintenance of the Yamazaki River, i.e. excavation of sandbanks, the riverbank reinforcement and deforestation, has been done for past 5 years. Continuous maintenance affects seriously damages to habitat of living things in the river.

Generally, the number of the species is always changing among years, especially migratory fish species [3] because of r-strategy of the fishes [4]. Fishes and other species with low survival rate at juvenile are always fluctuate the population, because the increasing rate (r-strategy). On the other hand, the species with high survival rate at juvenile is always stationary (K-strategy). But there are few reports about the year fluctuation about the number of juvenile fishes. Is the fluctuation of the fish population among years caused by environmental changing or r-strategy of fecundity? Then, we collected the environmental factors and the number of fishes for 4 years. Finally, we realized the ideal environmental condition for native species, and make the guideline in order to maintenance the rivers.

First, we made some habitat prediction model using General Linear Models (GLM) to further define the environment of each native and alien fish species habitat. Second, for past 5 years river maintenance changed the environmental factors, then we analyze between the influence of the environmental changing and the fish population changing with each GLM among years.

MATERIALS AND METHODS

Study site

The place of the investigation was the Yamazaki River, located in east side of Nagoya City at center of Japan (Fig. 1). The river is 13.6km, the size of a catchment area is 26.6km^2. At the mouth of the river, the sea water goes up to 5km from the mouth of the river. This river level and width are always controlled by the gate of pond at the source of the river.

From the source of the river to the mouth of the

river, 9 stations were set up for the investigation. Each station has 100m length with 5m x 5m quadrat. St.1 is narrow river, so the 20 quadrats were set up. The width from St.2 to St.8 was almost 10m, so the 40 quadrats were set up at each station. The width of the St. 9 was 15m, 60 quadrats were set up. We investigate at a total of 360 quadrats along the river.

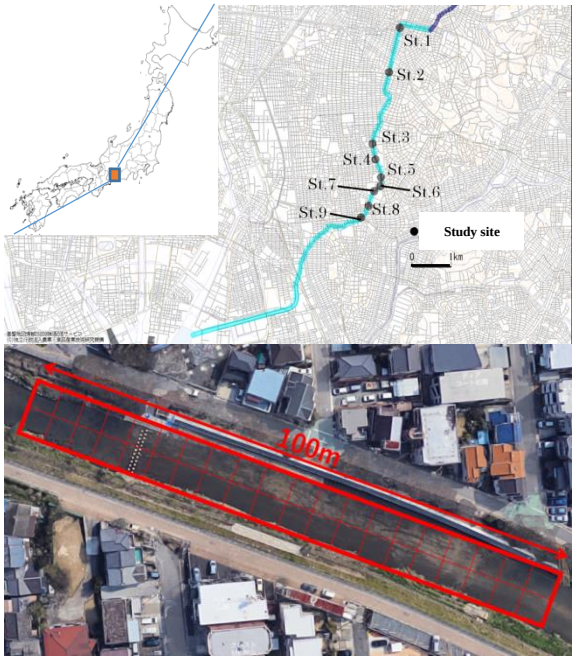

Fig. 1 The map of study site, and quadrat at St.2.

Population Research

In order to know the population of each species in the Yamazaki River, we conducted rough investigation with rectangle fish capture net (40cm x 25cm) with 5mm mesh. At each quadrat one person chased from the edge of quadrat and other person received fishes. The investigation was done 6 times (from June to November) at each year (2013, 2017-2020). We collected all the fishes and benthos in the water tank after catch, we distinguished species and counted.

Environmental Factor Measurement

We measured each environmental factor at each quadrat once a year in Fall in 2013, from 2017 to 2020. Eight environmental parameters, the velocity of a flowing fluid (*v*), the depth of the river (*D*), the closed area rate over the water surface (*N*), vegetation cover degree (*P*), materials of river bottom (*RB*), materials of riverbed (*RS*), dissolved oxygen (*DO*) and loss on ignition (*HL*) were measured in each quadrat. The velocity of a flowing fluid was measured by the current meter (Kenek Co. VE10). The depth of the river was measured using pole for leveling (Myzox Co. N-150) at three points at center line at quadrat. The length and the width of the cover at the closed area by vegetation or concreate block or somethings were measured by tape measure. The vegetation cover degree was 4 levels. 0 degree is no vegetation, 1 degree is 0-20%, 2 degree is 20-40% and 3 degree is over 40%. Materials of the river bottom were observed by eyes, C: concrete, M: main gravel, S: sub gravel, T: transit gravel, D: mud. Materials of river bed was observed by eyes, c: concrete, r: rock, s: sand, n: no river bed. The dissolved oxygen was measured by a portable meter (Hanna Instruments Japan Co. HI914N). Loss on ignition was measured by sampling river bottom materials. After sampling the materials was into an incubator at 120^{o}C for 2days in order to loss the water. After pretreatment, the weight was measured and they were burned in a muffle furnace (800^{o}C 1day) to measure loss on ignition.

Statistical Analysis

We performed analysis using GLM (using quick-R: correspondence analysis program) to elucidate the habitation density of each fish species and its relationship to environmental factors in each year. The environmental parameters used in this study assumes eight kinds of measurement data. The population of each species at each quadrat was used as the distribution research data.

The environmental factors should be standardized in order to compare with each factor, standardization is used for easily comparing among different average, distribution and units. The multicollinearity is confirmed by the value of variance inflation factors (VIF>10: there is the multicollinearity). We confirm the possibility of VIF.

The response is the population density of each species in the study. Thus, we supposed that the probability distribution of the response obeyed negative binomial distribution. Then the link equation is the logarithm equation. To explain the distribution of density, our model assumes the main effect term. The environmental factors are two types, one is a linear numeric factor and the other is factor type. We must exchange the factor type to numeric factor. The number of numeric factor is N, then we prepare N-1 dummy variable.

$$\begin{pmatrix} \mathbf{1} \\ \mathbf{2} \\ \mathbf{3} \\ \vdots \\ \mathbf{N-1} \\ \mathbf{N} \end{pmatrix} = \begin{bmatrix} \mathbf{0} & \mathbf{0} & \mathbf{0} & & \mathbf{0} & \mathbf{0} \\ \mathbf{1} & \mathbf{0} & \mathbf{0} & \cdots & \mathbf{0} & \mathbf{0} \\ \mathbf{0} & \mathbf{1} & \mathbf{0} & & \mathbf{0} & \mathbf{0} \\ & \vdots & & \ddots & \vdots & \\ \mathbf{0} & \mathbf{0} & \mathbf{0} & & \mathbf{1} & \mathbf{0} \\ \mathbf{0} & \mathbf{0} & \mathbf{0} & \cdots & \mathbf{0} & \mathbf{1} \end{bmatrix} \quad (1)$$

The left side is the level of factors, and the right side is the dummy variable. Interaction terms in the case, we performed centration for 2 variables beforehand and incorporated it as an explanatory variable. In addition on the main effect variable without dummy variable. As a standard to evaluate the good model, we used Akaike's information criterion (AIC).

Evaluation of Biodiversity

To evaluate the biodiversity, the species diversity index is mainly used. The Simpson index (2) reflects not only the number of species, the amounts of species. We used the Simpson index to evaluate the biodiversity in the Yamazaki River.

$$Sindex = 1 - \sum_{i=1}^{S} p_i^2 \qquad (2)$$

$$p_i = \frac{n_i}{N} \qquad (3)$$

S: the number of species, species *i* priority degree is p_i, p_i is brought to equation (3). *N* is the number of total organisms, n_i is the number of species *i*.

RESULTS

Field census

The population size of each species varied among 5 years. The result of each year is compiled in Table 1. In 2017, 2018, 2020, over a half of the population is alien species. The habitat of the Yamazaki River is occupied by alien species. The number of *Cyprinus carpio* was stable for years. There was over twice fluctuation at the number of each species, especially in *Gambusia affinis* where eight times difference was observed.

Table 1 The number of each genus from 2013 to 2020

Genus	2013	2017	2018	2019	2020
Cyprinus	270	401	256	230	241
Gambusia	4194	32598	8873	6841	6469
Palaemon	2028	8400	4129	4422	3049
Zacco	8598	1296	1466	2295	2751
Pseudorasbora	32	54	218	422	164
Gymnogobius	331	313	1585	185	99
Oryzias	46	112	93	130	106
No. of total	15897	46717	17004	14703	13100
Total No. of alien	11301	10468	7722	7755	6214
Total No. of native	4596	36249	9282	7151	6886
Total No. of species	22	21	25	26	25

There were some differences among years in each St. For example, Fig. 2 and 3 showed the distribution of each station in 2013 and 2020. The velocity of St. 1-3 was faster than the other stations, and the velocity at St. 9 was the slow stream. Except St. 4 there is no clear difference between the years. The maintenance of the river changed the velocity at St. 4. The upper river flow was faster than that of the end of the river.

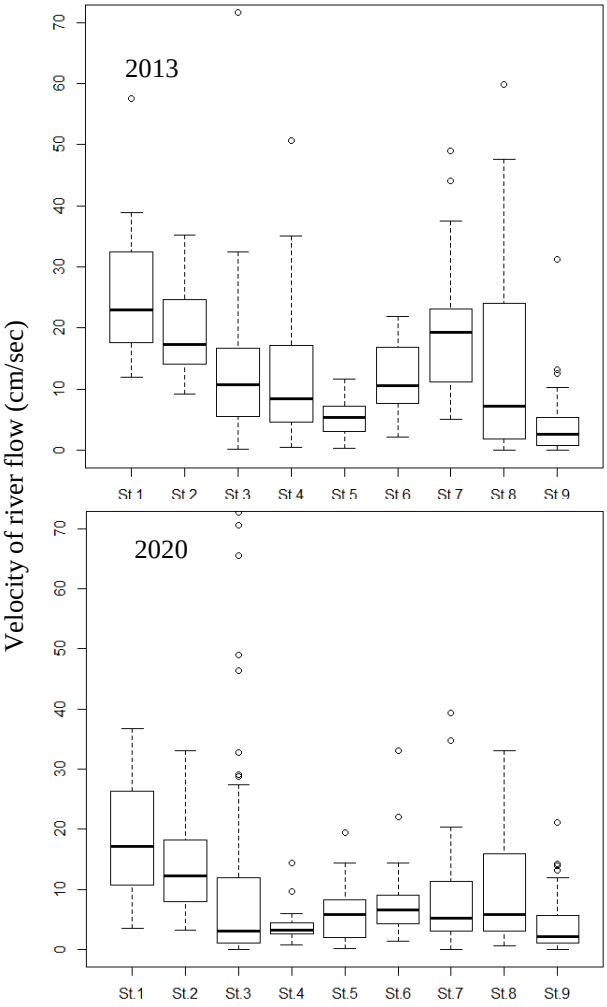

Fig. 2 The distribution of velocity of river flow at each Station in 2013 and 2020

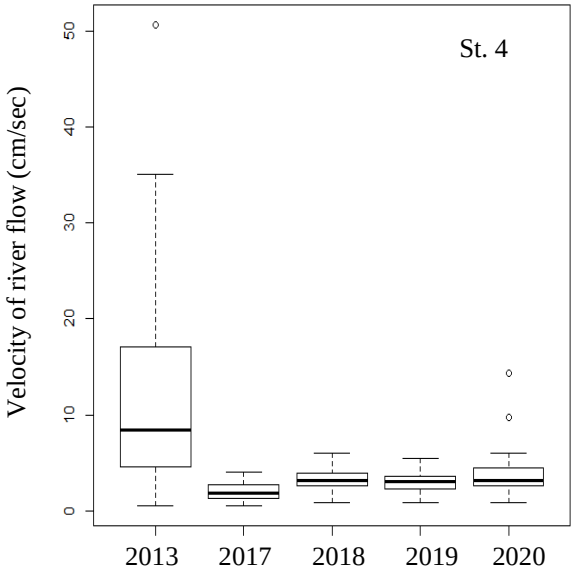

Fig. 3 The distribution of the velocity of river flow at St. 4 from 2013 to 2020.

Appendix showed the summary of the parameter data from 2013 to 2020.

The Habitation Model

From the data of field census, the population size of 6 species was sufficient to create new models, two alien species, *Cyprinus carpio* and *Gambusia affinis*, four native species, *Palaemon* sp., *Zacco platypus*, *Pseudorasbora parva* and *Gymnogobius petschiliensis*.

The habitation model of *C. carpio* was shown in Table 2. Only parameters that have the significant difference were shown in Table 2. And RSC, RSR and RSS mean the dummy variable from equation (1). There were few differences among 5 years. The species chooses deep and likes rock, concrete and sand river bed materials area, and don't chooses fast stream in both all seasons and all years. *C. carpio* likes the habitat where the slow stream and deep area, therefore we can control the population of the species.

Table 2 The habitation model of *C. carpio* of each parameter

		Parameter						
Year	Season	V	D	N	RSC	RSR	RSS	HL
2013	Summer	**	**		*	**	*	
	Autumn	***		***				
2017	Summer	***						
	Autumn	**	***					
2018	Summer		***			***		
	Autumn	*	***					
2019	Summer		***			**		
	Autumn	**	***			**		
2020	Summer		***				***	***
	Autumn		***	**		***		

***: P <0.001, **: P <0.01, *: P <0.05, if the coefficient is minor, the star is red.

The second habitation model of *Gambusia affinis* was shown in Table 3. The prediction of the species was not stable, because of the fluctuation of the significant value among years. From 2013 to 2017 the species liked shallow with no stream. After 2018 there was no significant preference observed. In 2019 and 2020 new parameter, dissolved oxygen was measured. The preference of the high dissolved oxygen area was observed. And the mass of the population in 2017 was very high, therefore the model of the 2017 reflects the high number population preference. In autumn the species likes the surface of the river or shallow area, in summer the species likes no stream area.

The third habitation model of *Palaemon* sp. was shown in Table 4. The preference of the species depends on the vegetation cover. The *Palaemon* sp. is very important to the food web because of the feed of higher carnivore. The model provides the bottom up of the food web of the ecological network.

Table 3 The habitation model of *G. affinis* of each parameter

		Parameter									
Year	Season	V	D	N	RBS	RBT	RSR	RSS	RSN	P	DO
2013	Summer	***	***		***	***	***	*			
	Autumn	***	***		***	***	***	*			
2017	Summer	***					*	***	***		
	Autumn		***					***	***	*	
2018	Summer	***									
	Autumn	*		***	*			***		***	
2019	Summer	*				**	***		***		
	Autumn	*					***	**	***	***	**
2020	Summer							**			*
	Autumn						***		***		***

***: P <0.001, **: P <0.01, *: P <0.05, if the coefficient is minor, the star is red.

Table 4 The habitation model of *Palaemon* sp. of each parameter

		Parameter												
Year	Season	*V*	*D*	*N*	*RBS*	*RBT*	*RBD*	*RBM*	*RSS*	*RSN*	*RSR*	*HL*	*P*	*DO*
2013	Summer	**			**	**								
	Autumn	***	**			*								
2017	Summer						**						***	
	Autumn								***	***			***	
2018	Summer		***	**					**	*			***	
	Autumn		***	**						***	**		***	
2019	Summer		***		*				*	**			***	
	Autumn		***				***	**		***			***	***
2020	Summer		***	*			***	**					**	
	Autumn		***	**						***	***	**	***	

***: *P*<0.001, **: *P*<0.01, *: *P*<0.05, if the coefficient is minor, the star is red.

The fourth habitation model of *Zacco platypus* was shown in Table 5. The population of species was not stable among years. In 2017 at autumn there was no significant data about the population. The significance of the parameter was not stable, it was always changing. And the preference of the species was not stable. We cannot predict the habitat of the species beside of the categorized seasonality parameter.

The fifth habitation model of *Pseudorasbora parva* was shown in Table 6. *P. parva* generally lived in pond for the agricultural water supply. The preference of the species would be estimated low velocity area. Sometimes the preference of the low

velocity was observed at summer in 2017 and 2018, but in the other season that was not observed.

Table 5 The habitation model of *Zacco platypus* of each parameter

		Parameter										
Year	Season	*V*	*D*	*N*	*RBS*	*RBT*	*RBD*	*RSS*	*RSN*	*RSR*	*P*	*DO*
2013	Summer	**			***	***						
	Autumn	**			***	***						
2017	Summer	-	-	-	-	-	-	-	-	-	-	-
	Autumn	***	***	***				***		***	***	
2018	Summer	**										
	Autumn	***	*	**					*			
2019	Summer						**	*			*	
	Autumn									***		***
2020	Summer			**	**	*				***	**	
	Autumn	***	***	***								

***: $P<0.001$, **: $P<0.01$, *: $P<0.05$, if the coefficient is minor, the star is red.

Table 6 The habitation model of *Pseudorasbora parva* of each parameter

		Parameter								
Year	Season	*V*	*D*	*N*	*RBM*	*RSS*	*RSN*	*RSR*	*P*	*DO*
2013	Summer	-	-	-	-	-	-	-	-	-
	Autumn	-	-	-	-	-	-	-	-	-
2017	Summer	*					**		*	
	Autumn	-	-	-	-	-	-	-	-	-
2018	Summer	*					**		*	
	Autumn			*						
2019	Summer									**
	Autumn		***	*	**	**	***	*		
2020	Summer						***			**
	Autumn	-	-	-	-	-	-	-	-	-

***: $P<0.001$, **: $P<0.01$, *: $P<0.05$, if the coefficient is minor, the star is red.

The last habitation model of *Gymnogovius petschiliensis* was shown in Table 7. This species is always lived in the mouth of the river with vegetation cover and low loss of ignition. Then they like low velocity area. There was no significant parameter observed through 5 years. The habitation model is not suitable for the species.

Biodiversity of the Yamazaki River

The biodiversity was shown in Fig. 4. The biodiversity was changing seasonally at each study site.

Table 7 The habitation model of *Gymnogobius petschiliensis* of each parameter

		Parameter										
Year	Season	*V*	*D*	*N*	*RBS*	*RBT*	*RSS*	*RSN*	*RSR*	*HL*	*P*	*DO*
2013	Summer	*		***								
	Autumn	***	**			*						
2017	Summer		***					*	*			
	Autumn		***	*								
2018	Summer								*			
	Autumn			*								
2019	Summer									*	**	**
	Autumn	-	-	-	-	-	-	-	-	-	-	-
2020	Summer						*					*
	Autumn	-	-	-	-	-	-	-	-	-	-	-

***: $P<0.001$, **: $P<0.01$, *: $P<0.05$, if the coefficient is minor, the star is red.

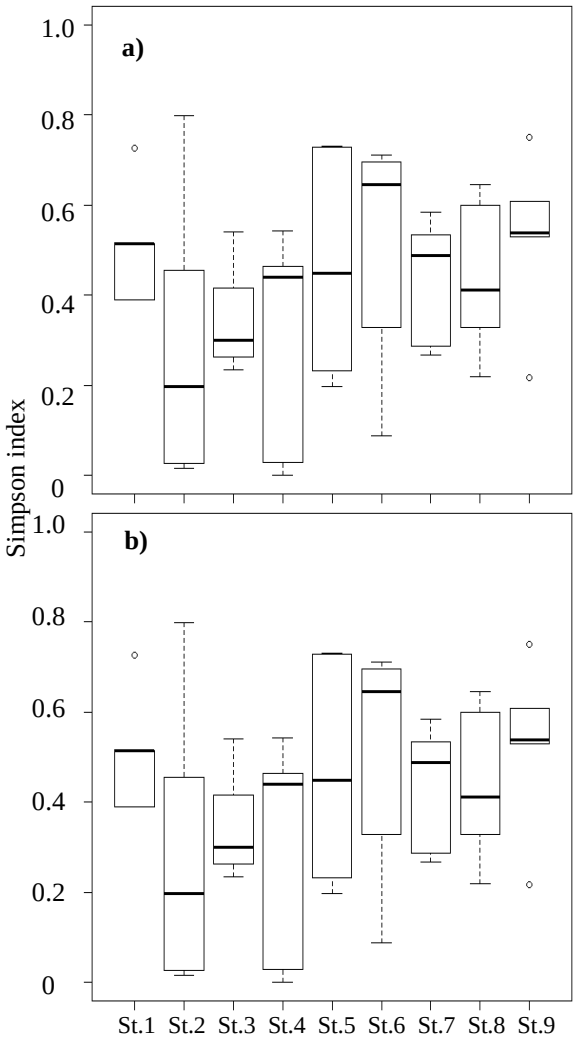

Fig. 4 The distribution of Simpson index in each station from 2013 to 2020, a) summer b) autumn

DISCUSSION

Some Habitation Model of river biology by GLM were existed ever [5]-[8]. Every model was able to be predictive for the habitat of each species. But all studies were conducted using only a year data. There was no study about GLM model with long-term data. Then we made habitation models each year by GLM and compared each model among years at same species. The result of that, the prediction of the number of species with low moving ability could be predicted by GLM models through years. For the species with high ability of migration, there were cases where it was possible to create a valid model that matched the original ecology by focusing only on one year. However, multi-year comparisons of such species distribution have revealed that GLM models can sometimes produce seemingly appropriate models. From the fact, it can be said that when creating a habitat model using GLM, it is necessary to avoid erroneous model creation by comparing over multi years.

About *C. carpio* habitation models, there was few differences about the tendency of habitation model among years. Especially St.4 provide good habitat for the species. *C. carpio* has been selected as one of the 100 worst invasive alien species in the world and causes problems such as competition with native fish [9]. The habitation model of the species is appropriate because the tendency of the habitat did not change among years. It is possible to reduce the population by creating an environment in which the species is difficult to stay.

The habitation model of *G. affinis* was not stable through 5 years. This alien species are sometimes found in shallow area with no flow and sometimes in gentle streams. The habitat of the species was not clear. The species affect the population of *Oryzias laties* (endangered species), therefore conservationists want to clean up the species. But the habitation was not clear by GLM models, we must look for other environmental factors affecting the habitat of the species.

According to the habitation model of *Palaemon* sp. it was shown that the riverbank material, river bed material and vegetation degree had a great influence. The population of *Palaemon* sp. has a life cycle with low moving ability. The presence of plants that thrives in water is considered important for *Palaemon* sp. [10]. *Palaemon* sp. is important species that feeds large organisms in the ecosystem [4], the presence of the species is desirable. By improving the habitat of the species, a network of river ecosystem can be constructed.

As *Z. platypus* grows, it expands its habitat from shallow areas near the shore to open areas with no obstruction [11]. It is said that an environment where the flow is slow is suitable for habitation and these cases where this species increases after river improvement and other species decrease accordingly [12]. As a result of the field census and GLM model, the results were different from the character of the species, which prefers a gentle flow velocity. In addition, the difference in selection characteristics from year to year becomes clear, and although a model that fits well in every year could be created, it was not possible to create a consistent habitat model that differs from year to year.

P. parva lives a wide range of freshwater areas such as lakes, downstream areas of rivers, irrigation canals, reservoirs, and paddy fields, and lives in groups in shallow bottoms with abundant aquatic plants and gentle flow [13]. Then the species was expected that the model would be negative at the flow velocity, and positive at mud river bed and vegetation. But only 2 years model has followed the fact. Due to its alert nature, it may have been captured in a different location than its habitat.

There was wide variation of habitation models of *G. petschiliensis* among years. The number of the species in the Yamazaki River is declining, especially in early summer. In early summer the juvenile fishes swim down to the mouth of the river, therefore the population of the species is expected to increase. Maybe the reproduction of the species does not succeed in the Yamazaki River.

Using GLM has the advantage that important environmental factors for the target species are likely to be highlighted. Therefore, as shown in the model for each species, we were able to clarify the environmental materials that the Yamazaki River lacks. However, it was found that the correlation of the models varies from year to year, and although it is a simple method, it does not lead to an absolute evaluation.

CONCLUSIONS

The following conclusions are drawn from the study.

1) The GLM model is effective to more fully understand the habitation area of river species easily.
2) However, it is necessary to take the data some years because there is a year variation in the habitat situation.
3) From the predictive model with consistent data among year, we can create the good habitat for native species.
4) Using the GLM, it is possible to predict the increase or decrease of the population from the river improvement for some years.

ACKNOWLEDGMENTS

We send thanks to Prof. T. Kitano who advised the analysis of statistical method. We also thank to the colleague at our laboratory and the group of ‘the

Clean Up Yamazaki River', they helped the field census.

REFERENCES

[1] The Ministry of Land, Infrastructure, Transport, the report 'Development to the making of multi-nature river'. 2006. https://www.mlit.go.jp/kisha/kisha06/05/050530/00.pdf

[2] Nagoya City, The living species and environmental factors in River in Nagoya city, 2016, https://www.city.nagoya.jp/ryokuseidoboku/cmsfiles/contents/0000080/80159/sinaikasenn(1).pdf

[3] Shimada K., Goto K., Yamamoto K. and Wada Y., Forecasting ascending population sizes of amphidromous juvenile ayu *Plecoglossus altivelis* in the Nagara River. Nippon Suisan Gakkaishi, Vol. 73, Issue 4, 2006, pp. 665-672.

[4] Begon M., and Townsend C.R., Ecology: from individuals to ecosystems, Wiley, 2021.

[5] Inui R., Hitotsumatsu A., Akamatsu Y., and Kono T., Development of model prediction for fish biomass in Saba River, Japan. Journal of Japan Society of Civil Engineers ser. BI Hydraulic engineering, Vol. 72, Issue 4, 2016, pp. 997-1002.

[6] Hirayama T., Endo T., Kanou K., Usui S., and Kaneko S., Invasion of channel catfish into small rivers connected to Lake Kitaura, Ibaraki Prefecture, Japan. Nippon Suisan Gakkaishi, Vol. 84, Issue 1, 2018, pp. 136-138.

[7] Sugiyama Y., Nakamura M., Senda S, and Masuda M., Environmental parameters controlling the habitat of the brackish water clam *Corbicula japonica* identified by predictive modelling. International Journal of GEOMATE, Vol. 17, Issue 59, 2019, pp.68-73.

[8] Masuda M., Morioka T., and Nishimura F., The environmental parameters controlling the habitat of invasive alien species, Spartina alterniflora identified by predictive modeling. International Journal of GEOMATE, Vol. 20, Issue 79, 2021, pp. 62-67.

[9] IUCN, 100 of the world's worst invasive alien species, ISSG office, 2000.

[10] Kawaguchi Y. Saiki M., Mizuno T., and Kayaba Y., Evaluate the function of waterfront vegetation for aquatic organisms in experiment river. Conference of Japan Society of Civil Engineering, Vol. 59, 2004, pp. 543-544.

[11] Takamura K., Utilization of habitat by young pale chub, Zacco platypus (Temminck et Schlegel). Japanese Journal of Ecology, Vol. 29, Issue 3, 1979, pp. 295-306.

[12] Shimatani Y. Oguri S., and Kayaba Y., Impact of stream modification on habitat component and fish in Tagawa River. Vol. 38, 1994, pp 337-344.

[13] Jackson M.C., Britton J.R., Variation in the rophicoverlap of invasive *Pseudorasbora parva* and sympatric cyprinid fishes. Ecology of Freshwater Fish, Vol. 22, Issue 4, 2013, pp. 654-657.

Appendix Environmental parameter of each station from 2013 to 2020, the number if the mean of each station

year	parameter	St.1	St.2	St.3	St.4	St.5	St.6	St.7	St. 8	St.9
2013	*V*	23.00	17.25	10.75	8.4	5.35	10.65	19.3	7.25	2.6
	D	24.60	19.65	33.05	20.6	44.2	22.45	14.05	22.15	50.25
	N	0.02	0.12	0.06	0.14	0.03	0.12	0.05	0.11	0.06
	RB	M-S	M-S	S-T	S	T	S	S	S	S-T
	RS	C-R	C	R-S	C	C	C-S	S	S	S-C
2017	*V*	15.8	13.38	7.18	3.1	4.13	6.68	2.15	6.38	3.16
	D	23.5	21.5	53.2	83.67	59.87	48.83	36.2	15.33	45.00
	N	0.19	0.1	0.17	0.04	0.05	0.05	0.09	0.13	0.11
	P	0	1.25	0.53	0.45	0.5	0.98	0.68	0.73	0.80
	RB	M-S	S	S-T	T	S-T	T-S	S-T	S	M-D-S
	RS	R	C	R	C	C	C-S	C-S	S	S-C
2018	*V*	18.68	14.57	4.47	3.12	4.02	5.65	7.78	6.22	2.42
	D	13.17	14.83	35.17	83.83	46.33	34.33	21.50	15.33	42
	N	0.17	0.12	0.16	0.04	0.04	0.04	0.09	0.12	0.11
	P	0.09	1.78	0.83	0.38	0.5	0.45	0.68	1.15	0.82
	RB	M-S	S	S-T	T	S-T	T-S	S-T	S	M-D-S
	RS	R	C	R	C	C	C-S	C-S	S	S-C-R
2019	*V*	16.75	19.45	5.47	1.87	2.78	3.25	19.43	13.38	2.02
	D	18.83	12.33	37.67	88.17	61.67	57.00	30.00	23.83	48.67
	N	0.17	0.09	0.16	0.04	0.01	0.06	0.07	0.11	0.08
	P	0.00	0.00	0.60	0.20	0.00	0.60	1.15	1.15	0.88
	RB	M-S	S	S-T	T	S-T	T-S	S-T	S	M-D-S
	RS	R	C	R	C	C	C-S	C-S	S	S-C-R
	HL	1.25	0.99	0.77	0.74	0.73	0.71	0.77	0.79	0.75
	DO	9.65	9.40	10.20	10.20	10.20	10.05	8.70	8.20	9.50
2020	*V*	17.13	12.50	7.68	3.87	6.90	8.82	7.03	9.70	3.95
	D	19.5	17.00	41.00	85.3	45.33	45.45	29.00	20.50	27.83
	N	0.22	0.10	0.17	0.03	0.05	0.06	0.09	0.14	0.14
	P	0.15	1.18	0.68	0.40	0.53	0.35	0.33	1.40	0.13
	RB	M-T	S	S-T	T	S-T	T-S	T-S	S	M-D-S
	RS	R	C	R	C	C	C-S	C-S	S	S-C-R
	HL	1.05	1.07	1.08	1.13	1.14	1.09	1.13	1.13	1.16
	DO	9.40	9.15	9.10	9.15	8.80	8.80	9.20	8.80	9.00

11th Int. Conf. on Geotechnique, Construction Materials & Environment,
Kyoto, Japan, 3-5 November 2021, ISBN: 978-4-909106063 C3051

EVALUATION OF THE VISIBILITY OF STAIRCASES IN UMEDA UNDERGROUND STREET BY USING DEPTHMAP

Yuanhang SONG[1], Akira TAKAHASHI[2], Kensuke YASUFUKU[2] and Hirokazu ABE[2]

[1] Global Architecture, Osaka University, Japan; [2] Cybermedia Center, Osaka University, Japan

ABSTRACT

When an earthquake occurs, the tsunami caused by the earthquake can threaten people's lives. Especially for low-lying terrain and densely populated areas, it is necessary to evacuate people to a safe place as soon as possible. The predicted water level of the Osaka Umeda Underground Street during the tsunami flood will reach 0.5-1.0 meters. And people inside the underground street need to reach the ground through stairs or evacuate from the exits connected to the surrounding buildings. There are a large number of stairs distributed inside the Umeda Underground Street. This study uses spatial syntax theory and depthmapX software to quantitatively analyze and organize the visibility of the staircases, so as to evaluate whether the stairs at different locations are easy to be discovered by the crowd during evacuation. And then lay the foundation for further evacuation research. In this paper, the following conclusions can be drawn: The visibility of staircases under different radius 。 restrictions is different. On the whole, the stairs near the integration center and the square nodes have better visibility, and those stairs which require multiple turns and have deeper visual depth are more difficult to find and use.

Keywords: Tsunami, Staircases, Visibility, Integration

INTRODUCTION

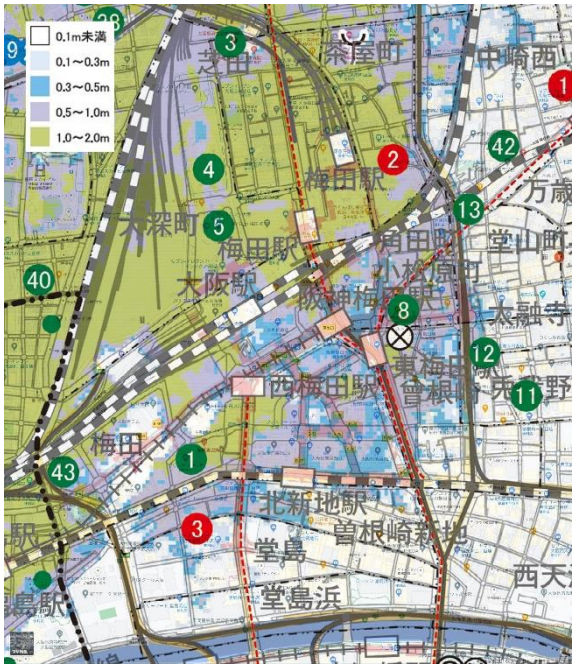

Fig. 1 Flooding in the Umeda area of Osaka at the time of the tsunami

When a huge earthquake occurs, the accompanying tsunamis often threaten the lives of people in the city. When a disaster occurs, people located in an underground shopping street need to use the shortest route to reach a safe place which they can evacuate as quickly as possible. According to the flood hazards issued by the Osaka City Hall, it can be seen that in the Umeda area, the depth of water caused by the tsunami was about 0.5-1.0 meters when the earthquake occurred (Fig. 1). And the tsunami refuge building directly connected to the underground street is only one, the Osaka Fukoku Life Hall (No. 8).[1]

Therefore, the most important thing during a disaster is to let people in the underground street find the nearest exit to the ground or the surrounding building. This leads to the analysis and evaluation of the staircases in the underground street.

Accessibility theory

Accessibility refers to how easy it is to reach a location in space. In 1980, William. H. Whyte described the relationship between the accessibility of urban space and the communication activities that occur in urban space in his book "The Social Life of Small Urban Spaces". Among them, accessibility is listed as the most important feature of a successful space. [2]

Firstly, accessibility has a visual meaning. At the level of visibility, only the "visible" space has the possibility of "reachable". Secondly, accessibility has spatial significance. Accessibility reflects the ease of communication between spaces and expresses the logical relationship between spaces. [3] In addition, accessibility is also affected by people's psychology, and the psychological guidance and hints to people in some spaces will also affect accessibility.

RESEARCH BACKGROUND PURPOSE AND SIGNIFICANCE

Research background

As Japan is one of the countries with frequent earthquakes, disasters such as tsunamis caused by earthquakes have always been important issues for researchers. How to minimize the loss of people's lives and property caused by natural disasters is a task that researchers should continue to study and think about.

The 2011 earthquake of the Pacific coast of Tōhoku occurred on March 11, 2011, the magnitude of the earthquake reached 9.0 and was the fifth largest earthquake in history. The huge tsunami triggered by the earthquake caused devastating damage to the coastal areas of northeastern Japan and also caused heavy casualties. Now in 2021, 10 years have passed since this huge earthquake. While commemorating and mourning the victims of the earthquake, it's also meaningful for us to take this as a topic to study the evacuation plan in the case of an earthquake or a tsunami, and to deal with similar problems in the future.

When a tsunami occurs, low-lying and densely populated areas are more susceptible to disasters and face greater evacuation pressure. Especially as the density of cities is increasing and the three-dimensional transportation system is greatly developed today, the commercial street around the underground station is the area where the evacuation problem should be addressed. The Umeda area in Osaka is one of such typical areas.

And in recent years, the Space Syntax theory proposed by Bill Hillier of the University of London has entered the vision of more people. As a new method of describing and analyzing space, Space Syntax believes that "space itself is not important, but more important is the relationship between spaces." [4] This theory, which studying space logic with mathematical methods, is gradually becoming widely used in the study of road systems in cities and neighborhoods.

The purpose and significance of the research

The Umeda area is in danger of being damaged by floods due to its low altitude in the case of tsunamis. In addition, the Umeda Underground Street is connected to the subway system and there are also many shops located in the Umeda Underground Street. It can be imagined that there's always a large number of people here. This research aims to evaluate and simulate the location of stairs and exits in the underground streets by analyzing the visual integration of the Umeda underground area, and then find the dangerous parts, thereby obtaining evacuation inspiration.

The significance of this research is to evaluate the distribution of the staircases by summarizing and analyzing the overall passable roads inside the Underground Street. To predict the stairs that are prone to be crowded in situations of disasters, and formulate targeted evacuation plans and response measures when necessary. It also lays the foundation for further research on disaster simulation.

RESEARCH OBJECTS AND METHODS

Research object and scope

The research area is located in the Umeda Underground Street, Kita Osaka, around JR Osaka Station and Hankyu Umeda Station. It mainly analyzes the visual accessibility of the underground passable parts except for stations and shops (Fig. 2). And it also analyzes the staircases and exits that can reach the ground or surrounding buildings.

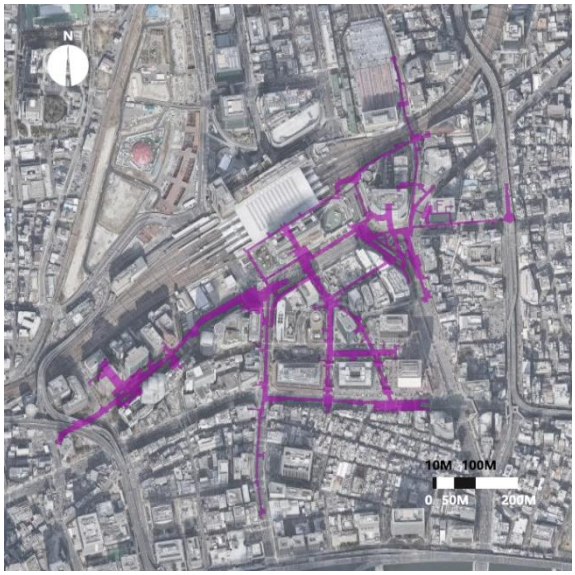

Fig. 2 The scope of the Umeda Underground Street of the research

In the Fig.2, The purple part is the scope of research in this paper. In this research, I believe that within these parts of the underground street, the sight of people can travel through the space without obstruction theoretically. Therefore, the parts with a large height difference, which need to be traversed through multiple stairs, and the shop area with a clear sense of spatial separation are not considered as research objects.

To study the visibility of stairs and exits in the entire underground street, and to compare and evaluate them, firstly mark all the stairs and exit positions inside the underground street to facilitate subsequent discussion. [5] (Fig. 3)

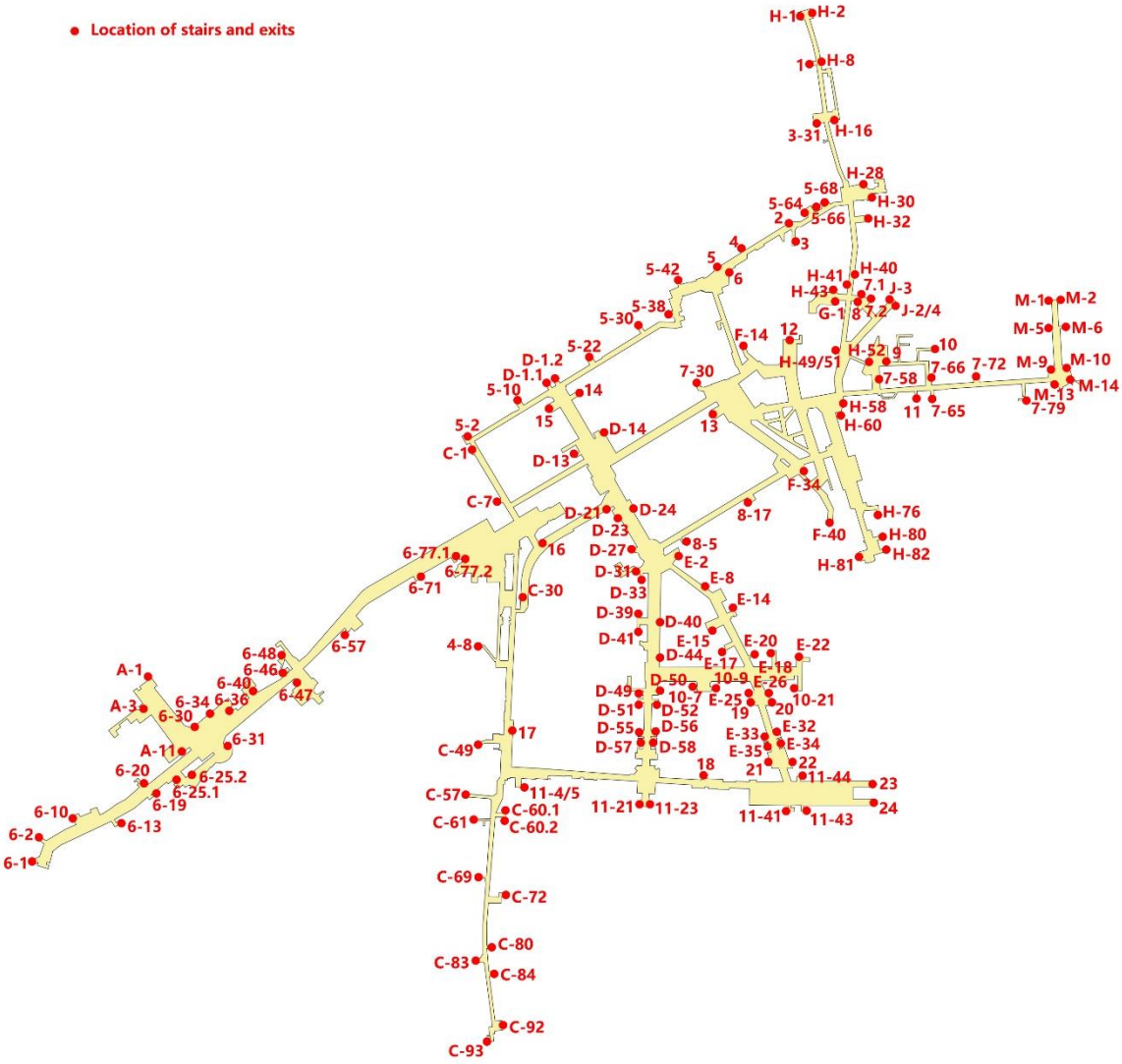

Fig. 3 The locations of all the stairs and exits

Space Syntax Theory

The space syntax theory was first proposed in the 1970s by Bill Hillier of UCL, England. Now a relatively complete and mature theoretical system and methodology, as well as technologies and software for spatial analysis, have been formed. Based on the analysis of spatial accessibility at the theoretical level, it is also further researching various indicators of spatial accessibility from a quantitative perspective.

In this article, depthmapX software is used to quantitatively analyze the research area from the aspect of visual reachability. Visual accessibility is the attribute of whether things can be seen in sight. It can be studied from the perspective of spatial connectivity and isovist area.

The analysis of the visibility in the space is to examine the distribution of the depth of the sight in a space.

As for the definition of the depth of sight, we can set it on a straight street. If point b can be directly seen from point a, then from a to b is the distance of one depth of sight. However, when the street turns, point e cannot be seen directly from point c. If you want to reach point e from c, you must first go to point d. In this case, the distance between c and e is two sight depths. (Fig. 4)

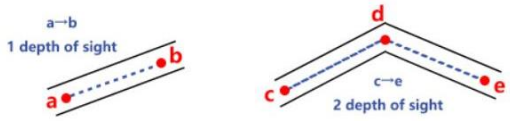

Fig. 4 Definition of the depth of sight

Besides, we can also set the maximum distance that the sight can reach. For example, if the farthest visible distance in space is 150 meters, and the distance from a to b is already 200 meters, then a to b

is already 2 sight depths distance.

Convex Map model

The convex map model is to understand the architectural space as a system composed of convex spaces. Convex space means that within a space, any two points can see each other. In the research and calculation of space syntax, we transform the space that is not convex space into a system composed of several convex spaces. The convex space involved in the calculation is the "element". In the following research, an infinitely subdivided square grid will be used to replace the original spatial system. [6]

RESULTS

The convex space analysis method is used to study the interior of the Umeda Underground Street, starting from the analysis of the connectivity, and further analyzing the isovist area. Then use the depthmapX software to compare the visual integration under different radius, and find out whether each staircase can be seen by the crowd under different visual ranges.

Result of connectivity and isovist area

Use an infinitely subdivided convex space grid to replace the spatial plan. This is the first step "set grid" process. In this study, the grid scale is set to 1000. And then set the farthest range of sight on this basis, I set 10 meters here. After the calculation is performed, the connectivity of the space will be obtained. (Fig. 5)

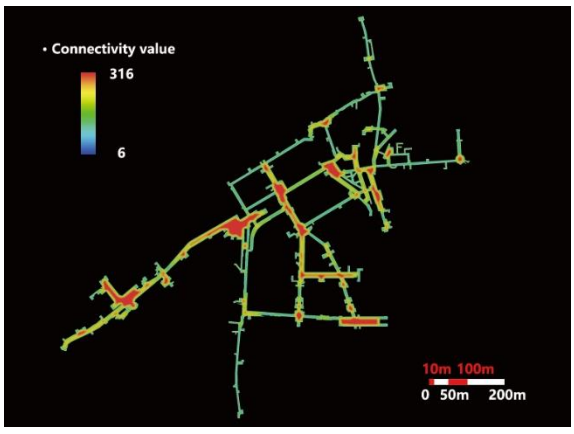

Fig. 5 Connectivity in the area

The connectivity generated based on the grid means that from a certain element in the space, a total value of several other elements can be seen is added up, and then fed back to that element. After each element has a value, these values are regarded as a sequence of numbers, and the interval of the sequence is a closed interval of $[n_1, n_2]$. Take $\frac{n_2-n_1}{10}$ as the width, divide this value segment into ten equal parts, and assign red to the highest value segment, blue to the lowest value segment, and the middle-value segment from top to bottom from warm to cold. It can be seen that the closer the position to the center of the wide space, the higher the connectivity value. These positions are usually similar to nodes and small squares in the space.

Based on the numerical feature distribution of connectivity, a spatial isovist feature map can be generated. The isovist map means that looking out from an element a, the value of the area that can be seen is fed back to a. At this time, if point b and point a are in different positions, but their value is in the same value range, then a and b will show the same color. (Fig. 6)

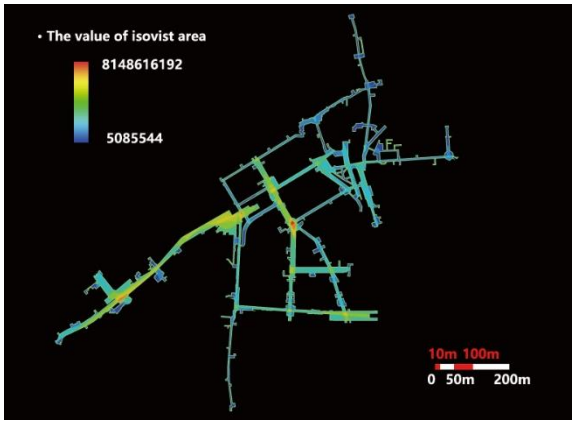

Fig. 6 Isovist area map

Because the Isovist area map calculates the visible area, the Umeda Underground Street we studied is greatly affected by the spatial shape and road width, and the results displayed by the Isovist area and connectivity are quite different. For squares and roads in a wider area, the visible range of sight in the isovist map tends to be wider.

Result of Visual Integration

Using the depthmapX software to analyze and calculate the spatial visibility relationship. In this study, the numerical distribution of the spatial sight integration degree is mainly calculated. Visual integration, that is, "accessibility of sight". It describes how many turns people need to make one point to another. And in space designing and planning, the "shortest distance" is always one of the most meaningful contents to think about. That is why I choose the Visual Integration [HH] value to get the result.

Visual Integration [HH] means the global visual depth after removing all the influencing factors in

topology. The higher the value, it means that this element only needs fewer turns to see other elements in the entire system. The lower the value, it indicates that starting from this element, if you want to see other elements, you need more turns. Simply say, the higher the value of Visual Integration [HH], the easier it is to attract people's attention, and the easier it is for people to use that place.

When analyzing, the first step is to set the radius of the analysis, that is, how many sight depths our analysis is limited to. For different space systems, the appropriate range is also different. Here I choose R3, R5, R7, R9, R11 (corresponding to the range of 30 meters, 50 meters, 70 meters, 90 meters, and 110 meters), these situations for analyzing. (Fig. 7-11)

It can be seen that under the conditions of different radius restrictions, the results obtained are not the same. From R3 to R11, with the gradual expansion of the radius, some nodes with better views in the space gradually become obvious, and the possibility of each staircase being discovered by people also changes.

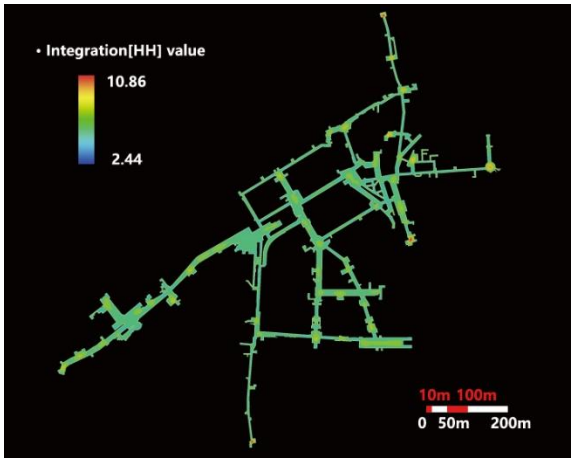

Fig. 7 Visual Integration [HH] R3

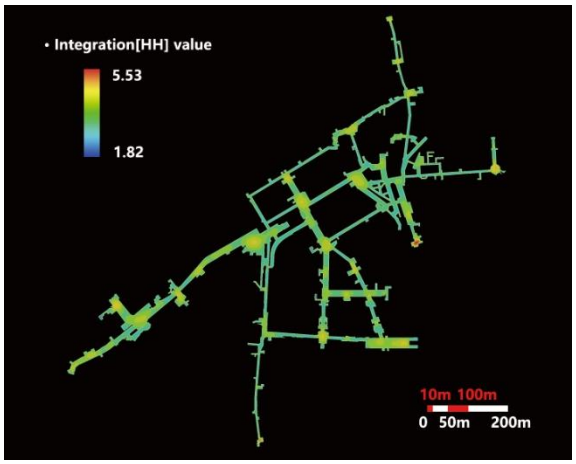

Fig. 8 Visual Integration [HH] R5

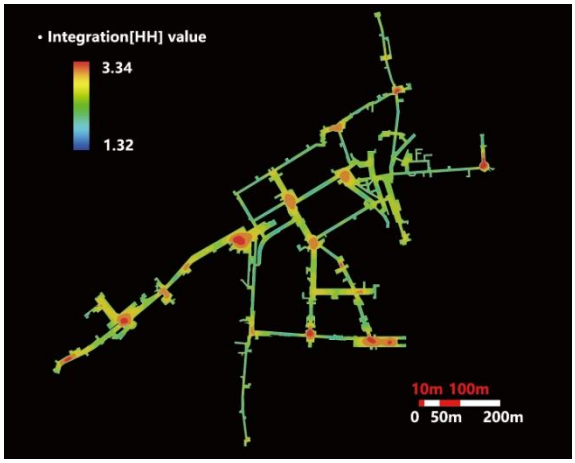

Fig. 9 Visual Integration [HH] R7

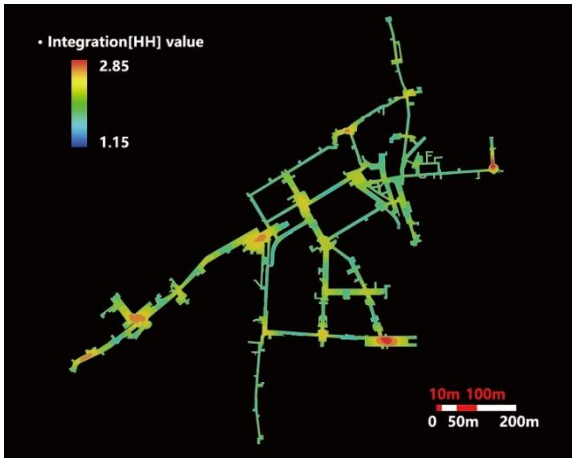

Fig. 10 Visual Integration [HH] R9

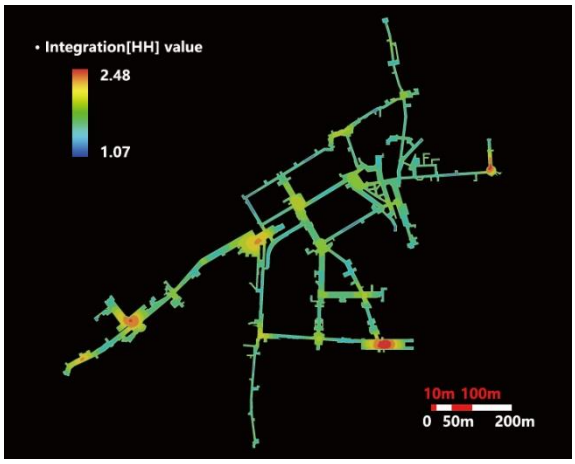

Fig. 11 Visual Integration [HH] R11

Then count the visual integration value of all the stairs and exits. And draw charts and statistics on the results obtained. (Fig. 12-15)

On the whole, the visual integration value of the staircases decreases from R3 to R11, which also shows that the larger the range, the lower the

probability that the stairs will be discovered by people. As a result, it is necessary to ensure that within a certain range, there are enough stairs to meet the evacuation needs.

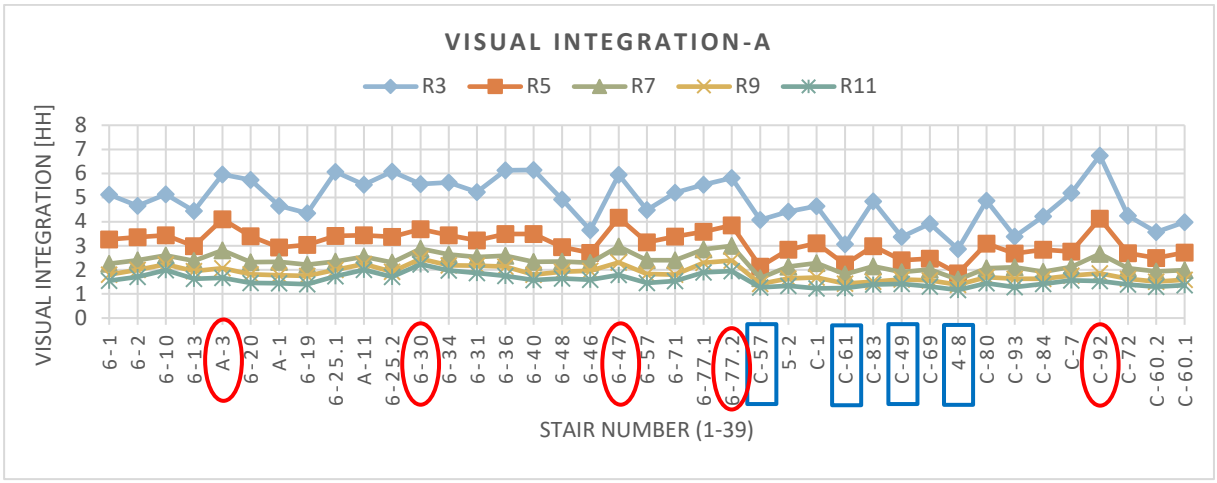

Fig. 12 Comparison of Visual Integration-Part A

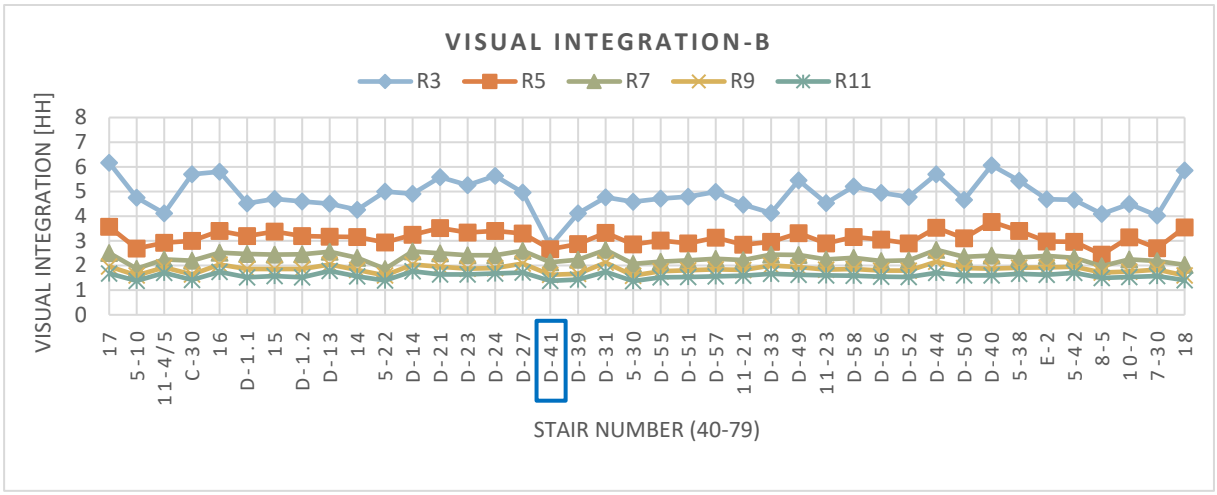

Fig. 13 Comparison of Visual Integration-Part B

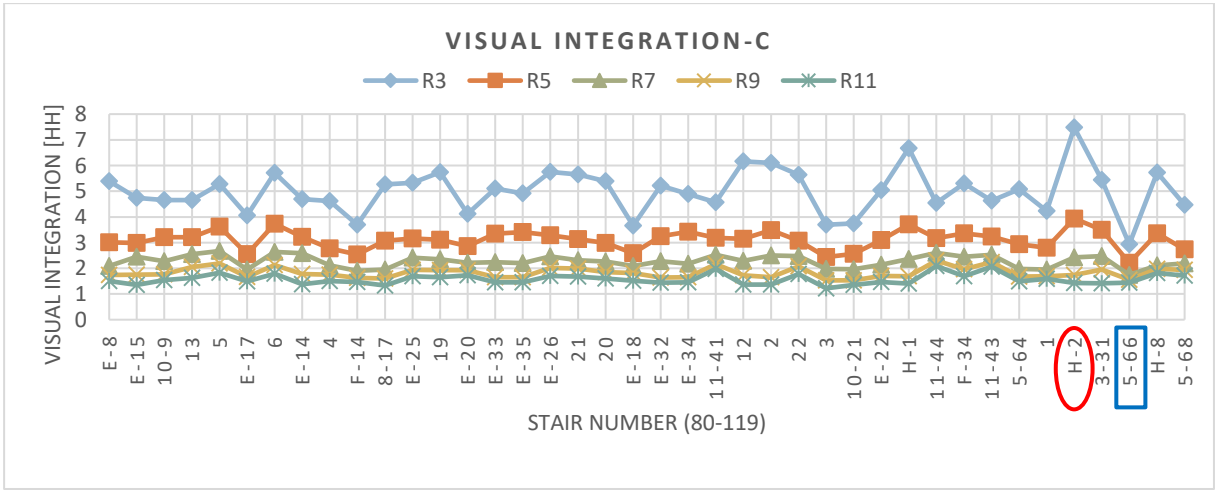

Fig. 14 Comparison of Visual Integration-Part C

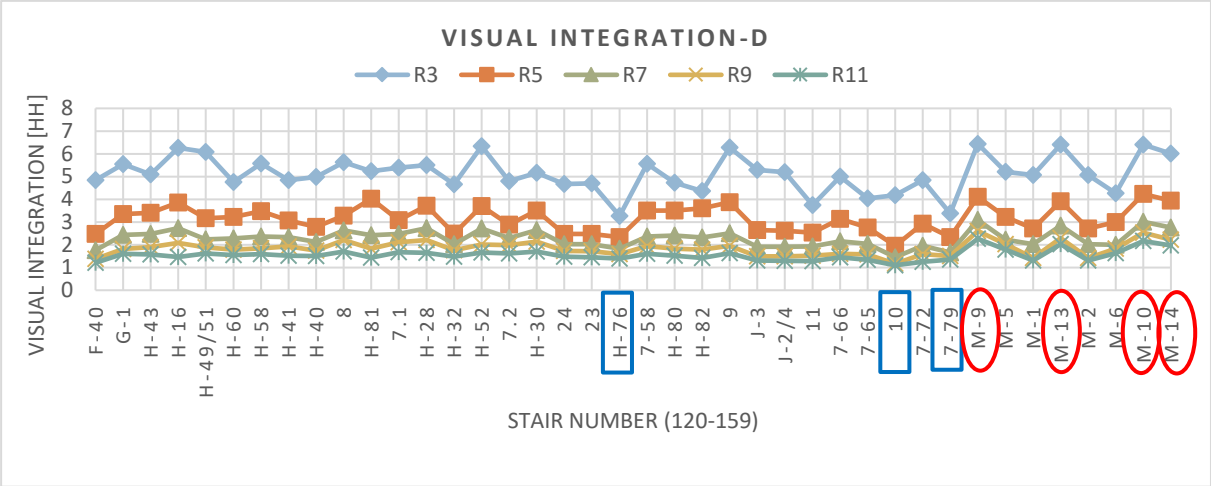

Fig. 15 Comparison of Visual Integration-Part D

From the overall trend, with the expansion of the sight radius, the trend of the integration value distribution of each staircase is gradually regular, however, under the radius of R3 (small range), the value of the integration degree of the staircases fluctuates greatly.

DISCUSSION

In addition, from the obtained data results, some distinctive staircase positions can also be found and show that it is necessary to pay attention to them.

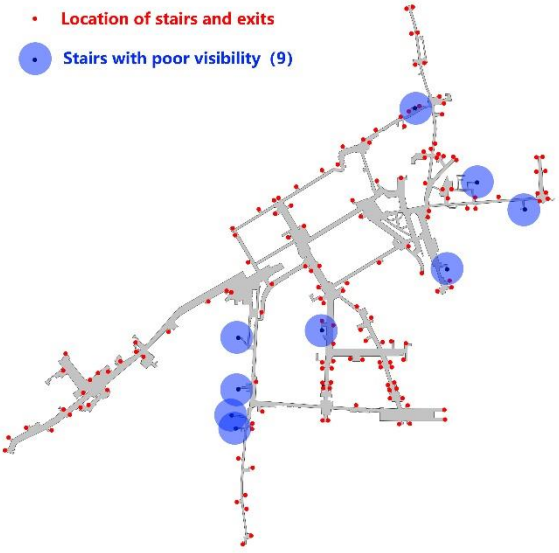

Fig. 16 Distribution of stairs with poor visibility

Firstly, there are some stairs, even though they are within the radius of 30 meters, their visibility is still very low. It means that these stairs are still not easy to find in a small area. Inspecting its specific distribution location, it can be found that most of these stairs with poor visibility are located in branch roads with more turns from the main roads, such as stairs No. 4-8, C-61, 10, 5-66, 7-79, H-76, C-57, D-41 and C-49. (Fig. 16) This suggests that people are more prone to choose staircases that are easier to reach from the main road, for the reason that these stairs have better visibility.

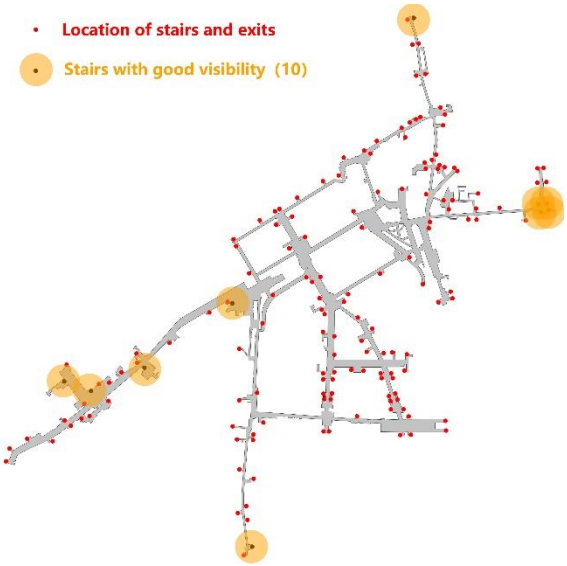

Fig. 17 Distribution of stairs with good visibility

Next, there are some stairs with higher integration values under different radius ranges, such as M-9, M-10, M-13, 6-47, H-2, 6-77.2, C-92, M-14, 6-30, A-3 (Fig. 17). By analyzing the map, the locations of these stairs are very close to the small centers of integration, such as the intersections or the vicinity of small squares. But correspondingly, it's important to note that in the process of evacuation, it may be easier to cause congestion at the locations of these stairs.

CONCLUSION

This study analyzed the visibility of the staircases inside the Umeda Underground Street and got the following conclusions:

1. From the perspective of connectivity, the connectivity between open road intersections and square nodes is higher than that of narrow and terminal roads. Correspondingly, from the isovist area map, the value of connectivity plus the area value within the visual range of the location also shows that the area of sight on squares and wide roads is larger than that of narrow places, that is to say, narrow roads are not only more likely to be crowded, but also more difficult to find safe exits within sight.

2. From the perspective of visual integration, under different limits of the radius, the visual integration center, and the visual integration value at the location of each staircase are different, but the overall integration center distribution trend is similar. With the enlargement of the sight radius, the center of integration becomes more obvious and concentrated.

3. Through the analysis of the specific values of the staircase locations, it is possible to find and locate some stairs that are difficult to find, and some stairs that are easier to be found - the stairs that are close to the square and nodes and can be reached without many turns are easier to use; and the stairs with many turns and far away from the main roads have low visibility in people's vision.

In general, most of the stairs' visibility can be seen to be relatively average, and that guides me to do the simulation of the crowd to find more patterns in specific evacuation situations in future research.

ACKNOWLEDGMENTS

In writing this paper, I have benefited from the presence of my teachers and my friends. They generously helped me collect the materials I needed and made many invaluable suggestions. I hereby extend my thanks to them for their kind help, without which the paper would not have been what it is.

Particularly, I am deeply indebted to my Professor, Hirokazu ABE, who guided me throughout my writing of this thesis. And teachers Akira TAKAHASHI and Kensuke YASUFUKU, also gave me a lot of help.

REFERENCES

[1] Osaka City, "To protect lives from tsunami and flood damage" Flood hazard map, 2021.4.19.

[2] William. H. Whyte. The Social Life of Small Urban Spaces. Washington D.C.: Conservation Foundation, 1980.

[3] Jijing Liu, Research On Design Strategies of the Contact Spacein Architectural Department Hall for the Coordination Innovation Education, 2015.6.28.

[4] B. Hillier, Space is the machine: fabric construction theory, January, 2008.

[5] Osaka City Osaka Station Area Underground Space Inundation Countermeasure Plan Ver.1 (Material-Second Half), 2017.11.4.

[6] Space Syntax: a very short introduction, July, 2013. pp.9–42.

[7] Rina Uogashi, Aimi Itokawa, Yuichi Yamaguchi, Analysis of evacuation behavior in Umeda underground shopping center, Osaka.

[8] Junpei Ueno, Tatsuya Kishimoto, An analysis of pedestrian movement in multilevel complex by Space Syntax theory – In the case of Shibuya station, Journal of the City Planning Institute of Japan, No.43-3, October, 2008, pp.49–54.

[9] Fumiko ITO, Yoshifumi FUJIKI, Analysis of the Relation between Complexity and Impression of Street Network, Journal of the City Planning Institute of Japan, Vol.48 No.3, October, 2013, pp.327–332.

[10] Eiji Nakamura, Koike Norimitsu, Prediction of residents and proposals for evacuation guidance from evacuation simulations based on visitor surveys in underground malls -Nagoya • Central Park as an example-, JSCE Proceedings F6 (Safety Issues), Vol.74 No.2, 2018, pp.93–100.

[11] Toshiyuki KANEDA, Akira OTA, Junya KOBAYSHI， A STUDY ON FACTOR ANALYSES OF PEDESTRIANS' SPATIAL DISTRIBUTION IN KANAYAMA DISTRICT, NAGOYA – By applying Agent Analysis in Space Syntax studies, J. Archit. Plann, AIJ. Vol.85 No.767, Jan., 2020, pp.121–129.

[12] Kei YASUDA, Ken MIURA, PLANNING OF SHARED SPACE IN SENIOR CITIZENS' LIVING FACILITY USING VISIBILITY ANALYSIS – Case study on elderly housing with supportive services, J. Archit. Plann, AIJ. Vol.86 No.781, Mar., 2021, pp.727–737.

[13] Hu Bin, Ni Zhenjie, Lyu Yuan, Optimization Design for Transfer Space Orientation in Subway Station Based on Depthmap, Metropolitan Rail Transit, Vol.29 No.1, Feb., 2016, pp.30–34.

[14] MA Chenxiao, SUN Yi, PENG Fangle, Space Syntax Based Space Analysis of Wujiaochang Underground Pedestrian System, Shanghai, MODERN TUNNELLING TECHNOLOGY (S2), Vol.55 (S2), Nov., 2018, pp.1255–1262.

[15] Rongrong Yuan, Michael J. Ostwald, Spatio-visual experience of movement through the Yuyuan Garden: A computational analysis based on isovists and visibility graphs, Frontiers of Architectural Research (2018) 7, pp.497–509.

[16] Hou Xiana, Zheng Lipeng, Simulation of Pedestrian Flow in Traditional Commercial Streets Based on Space Syntax, Procedia Engineering 205 (2017), pp.1344–1349.

11th Int. Conf. on Geotechnique, Construction Materials & Environment,
Kyoto, Japan, 3-5 November 2021, ISBN: 978-4-909106063 C3051

THE OCCURRENCE OF MICROPLASTICS ON THE START-UP PROCESS OF AN ANOXIC BIOFILM BATCH REACTOR

Ansiha Nur[1], Mhd Fauzi[2], Prayatni Soewondo[3], Ahmad Soleh Setiyawan[3], Katharina Oginawati[3]
[1] Environmental Engineering Doctoral Program of Institut Teknologi Bandung, Indonesia; [2] Environmental Engineering Master Program of Institut Teknologi Bandung, Indonesia; [3] Environmental Engineering of Institut Teknologi Bandung, Indonesia

ABSTRACT

Activated sludge from several sources is often used to initiate bacterial growth on the start-up of the biological treatment system and it contains microplastic impurities. Currently, there is no information regarding the presence of microplastics in a biological reactor during the start-up process. The aim of this study was to investigate the occurrence of microplastics during the start-up process in an anoxic fixed-biofilm batch reactor. Three units of 42 L laboratory-scale reactor fed with synthetic biodegradable substrates was inoculated with activated sludge from fecal sludge of residential areas. Each unit filled with PET media with three different specific surface ara (SSA). The results showed that the stable biofilm formation rates were associated with removal of COD after 75 days. The source of microplastics in the reactors during the start-up process comes from fecal sludge ($\bar{x}$ ± SD, n = 3) 7.666,67 ± 513.16 MP/kg (w/w). Approximately 7.96 – 9.24% of microplastics were adsorbed on the biofilm. No PET as secondary microplastic was found during 75 days of the start-up process. Two types of microplastics found in the reactor were fibers and fragments with the amount of 80.87 ± 44.8% and 19.13 ± 10,1%, respectively. The types of polymers detected by the ATR-FTIR spectroscopy were PES, PE, PET and PS. SSA affects the adhesion of microplastics on PET media. In a larger SSA, more microplastics are adsorbed on the biofilm.

Keywords: Anaerobic, Fecal sludge, Fixed-biofilm batch reactor, Microplastics, Start-up process

INTRODUCTION

In recent years, the biological wastewater treatment process is still the most widely used method to remove organic pollutants and nutrients because of high treatment efficiency and cost-effectiveness [1]–[2]. The use of attached growth systems, such as fixed-bed biofilm reactors (FBBRs) or moving bed biofilm reactors (MBBRs), has a promising alternative to remove organic and nutrient from wastewater, such as domestic wastewater [3].

Seeding is the initial biofilm adhesion to supporting media in attached growth systems during the start-up of process. The start-up process is defined as the biofilm development rate period to reach a stable value, it can vary 1 – 6 weeks [4]–[5]. Fecal sludge from residential is potential used for seed sludge because of a high VSS value. Behind the advantages, the occurance of microplastic on start up process in a reactor are still unknown. Most studies are still focused on the bacteria accumulation, biomass adhesion, biofilm growth to support media in order to reducing the start-up duration within reactor.

Currently, publications on microplastics raised concerns in the food chain as potential intake by humans and harm health [6] – [7]. Estimation of microplastics consumption within food and beverage range 39.000 to 52.000 particles annually by human in America [6]. Schwabl [8] have been investigated microplastics in human stool was 20 particles per 10 g of stool in median concentration. The abundance of microplastics in human feces found 1 particle/g to 36 particles/g (size 20 – 800 µm) in Beijing, China [9].

Microplastics, a type of an emerging environmental pollutant, are small particles less than 5 mm in size [10]. Based on the origin, the microplastics classified as primary and secondary. Primary microplastics were originally manufactured in very small sizes, such as microbeads (facial scrub cleansers), industrial ‘scrubbers’ used to blast clean surfaces aand plastic powders used in molding [11]. Secondary microplastics are the result of decomposed, degraded, and fragmented of larger plastics into sizes smaller than 5 mm due to environmental mechanical, photo-oxidative, physicochemical, and biotic factors [12].

To date, there have been limited studies on the occurrence of microplastics during the start-up of fixed attached growth systems. The purpose of this study was to identify the occurance of microplastics in the fixed-bed reactor during the start-up process as a result of the use of fecal sludge as inoculum. This research uses PET plastic bottles as support material. This is based on its advantages such as lightweight, inertness, large surface area, does not rot, and can attach bacteria [13] – [15]. Despite its advantages, the potential solubility of PET as a microplastic during the start-up process was investigated in this study. PET scraps have the potential as microplastics [16] in the reactor.

MATERIAL AND METHODS

Reactor and biofilm media

This study was carried out in a lab-scale fixed-bed circulating batch reactor (CBR), made from transparent acrylic material with a working volume of 42 L (Fig. 1). The CBR reactor was equipped with a recirculation pump to make the substrate and activated sludge mixed well, in order to make the biomass attached to the PET surface during seeding process. The experiment used three units of CBR under anoxic condition. Each reactor was filled with PET modules with three different specific surface area (SSA); Anx-1 (SSA-1; 555.78 m^2/m^3), Anx-2 (SSA-2; 444.53 m^2/m^3), and Anx-3 (SSA-3; 374.68 m^2/m^3) as shown in Fig. 2.

To obtain anoxic conditions in the CBR, the DO level in the wastewater was artificially removed by injecting N_2 gas into the reactor for 15-20 minutes [17]. The N_2 gas injection pressure was set at ± 4.5 lbf/in^2. Measured DO less than 1 mg O_2/L to 0.2 mg O_2/L. During the experiment period, the operating temperature kept in a constant temperature room. After the reactor was run, to determine the presence of microplastics in the reactor, the microplastics mass balance was calculated in the initial liquid (day 0) and at the end of seeding (day 75). The initial liquid sample (0 day) was taken at the beginning of the seeding process when the activated sludge and wastewater were completely mixed after the pump was turned on. At the end of seeding (75 day), liquid and biofilm samples were taken.

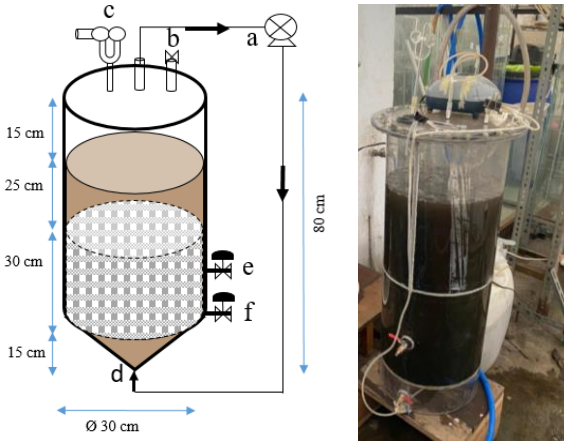

a = resirculation pump, b = feeding valve, c = siphon tube, d = aerator, e = sampling point, f = discharge valve

Fig. 1 Anoxic Circulating Batch Reactor

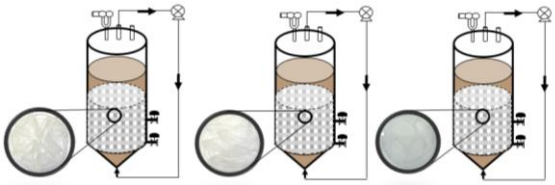

Fig. 2 Different SSA on CBR. a) Anx-1, b) Anx-2, c) Anx-3

Synthetic wastewater

Synthetic wastewater consisted of glucose as a source of carbon, NH_4Cl as a source of nitrogen, and KH_2PO_4 as a source of phosphate, and tap water of the Water Quality Research Laboratory, Environmental Engineering Institut Teknologi Bandung (ITB) as mixing water was used. Before use, the characteristics of tap water are checked for organic and nutrient content. The result showed that tap water was free from organic and nutrient content and its characteristics are relatively constant. Microplastic content is also checked.

Seeding

Activated sludge in this study taken from a septic tank of one household, Bandung City. The C:N:P substrate ratio used for optimum bacterial growth conditions, 100:5:1 for anoxic [18]. To monitor bacterial growth, VSS and COD were measured routinely according SMEWW (Standard Methods for Examination of Water and Wastewater) 2540 E and 5220 I. During the seeding process, the optimum pH for bacterial growth was maintained at 6.5 – 7.5 [19] by checking the pH periodically and operating the reactor at room temperature, 25 – 27 ^{0}C. DO conditions under anoxic conditions were maintained not to exceed 2 mg/L

Identification and quantification of microplastics

There is no standard method for the quantification and identification of microplastics in a sample. However, various sample processing for identification and quantification methods for microplastics were employed. There are 3 types of samples processing for microplastics; artificial wastewater, sludge, and biofilm. To remove natural organic from samples, 30% H_2O_2 solution was added to the samples, digest using a magnetic stirrer under heat 60^{0}C until H_2O_2 fully evaporated [20]. Artificial wastewater filtered using a glass microfiber filter Whatman GF/C and dried in an oven heat 60 ^{0}C for 30 minutes [21]. Different processing from artificial wastewater, before sludge and biofilm samples digest with 30% H_2O_2, the samples were dried in an oven heat 60 ^{0}C over 24 h [22]. When it dried, mixed with distilled water. The next step was using density separation by using $ZnCl_2$ 1,5 mg/cm^3 [23] for 24

hours. The supernatant of both, was filtered under vacuum onto a glass microfiber filter paper (Whatman GF/C).

Filter papers were observed by visual observation using an Olympus CX-21 light binocular microscope with 100x magnification coupled with Optilab Viewer 3.0 software. Observations on the surface of the filter paper in a zigzag manner [24]. The measurement of particle by using Image Raster 3.0 software. To ensure that the particle was microplastic, then the chemical structure was identified using the Attenuated Total Reflection-Fourier Transform Infrared (ATR-FTIR) at the Environmental Engineering Instrument Laboratory, ITB. ATR-FTIR (Bruker Alpha II Platinum ATR).

RESULTS AND DISCUSSION

Activated sludge as a source of microplastics in the reactor

Although fecal sludge was a source of bacterial seeds needed during seeding, microplastics derived from activated sludge are the largest contributor to the presence of microplastics in the seeding process in an anoxic batch reactor. The average of microplastics in the activated sludge ($\bar{x}$ ± SD, n = 3) was 7,666.67 ± 513.16 MP/kg (w/w). No microplastics were found in artificial wastewater.

Figure 3 shows the distribution of size, shape, polymer, and color of microplastics in the activated sludge used. The dominant of microplastic characteristics were microplastics with less than 300 µm in size, in the form of fibers (80.87 ± 44.8 %), transparent (55%) in color, and polyester (PES) polymer (39%). PES types are mostly found in this activated sludge, then polyethylene terephthalate (PET) and polystyrene (PS) types. This was because its density was greater than water, so a lot of it settled in the sludge. Density of PS 1.04 – 1.1 g/cm^3, Polyethylene (PE) 0.92 – 0.97 g/cm^3, PET 1.37 – 1.45 g/cm^3, PES 1.24 – 2.3 g/cm^3 and water 1.0 g/cm^3.

Feces is a waste product of the human digestive. One of the potential routes of microplastics into the human body is through the ingestion process, consumption of food and beverages [6], [7], [25]. The food chain is strong evidence of the transfer of microplastics to humans [26]. The presence of microplastics found in human feces in Beijing 1 – 36 particles/gr (20 – 800 µm), PET (83.3%), polystyrene (PS) (50%), polyethyelene (50%) [27], human feces in Europe and Asia, an average of 20 particles/10 g (50 – 500 µm) [8]. Schwabl [8] found sizes 50 – 500 µm and polypropylene (PP) (62.8%), PET (17%) polymers were the most commonly found. Its similar size with microplastics obtained in this study, less

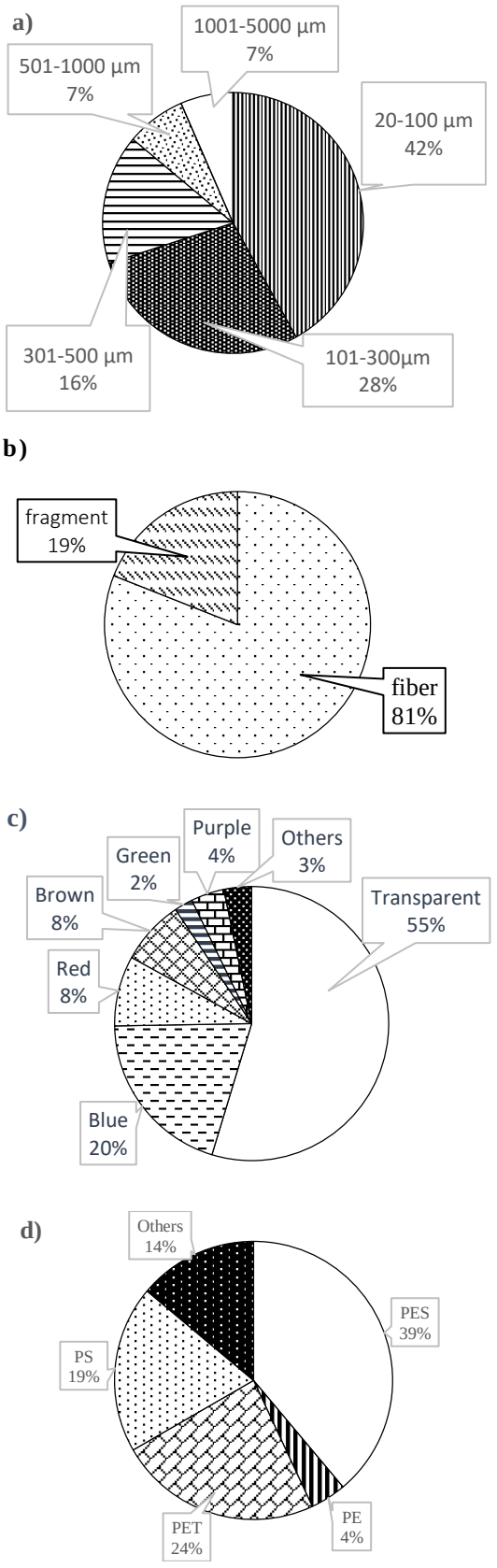

Fig. 3 Distribution of microplastic characteristics in activated sludge. a) size, b) shape, c) color, d) polymer

than < 500 µm. Also similar size of the human stool found by Schwabl [8] and Zhang [27]. Comparing with the previous study, the differences in polymers that were found in this study, as an effect of the difference in food and beverage consumption in a country.

Several studies on investigating the potential sources of microplastics from various types of food and beverage have been reported. Microplastics were found in foods and beverages commonly consumed by humans such as sea salt, lake salt [28], seafood [29], fish [27] [30], vegetables and fruit [31]-[32], piped water [33], [27], drinking water [34], mineral water from various countries, such as Indonesia, Thailand, China, India, Mexico, Brazil, USA, Thailand, Lebanon [35]. Microplastics found in PET bottled water was < 10 m [36]-[38].

Mass balance microplastics in the reactor

The presence of PET as secondary microplastic as long as the start-up period was detected from the mass balance of the presence of microplastics in the reactor (Table 1).

Tabel 1 Mass balance of micoplastics in the reactor (MP/L)

Reactor	Time	Liquid	Biofilm
Anx-1	Day 0	1190	0
	Day 75	1080	110
Anx-2	Day 0	1304	0
	Day 75	1200	104
Anx-3	Day 0	1130	0
	Day 75	1040	90

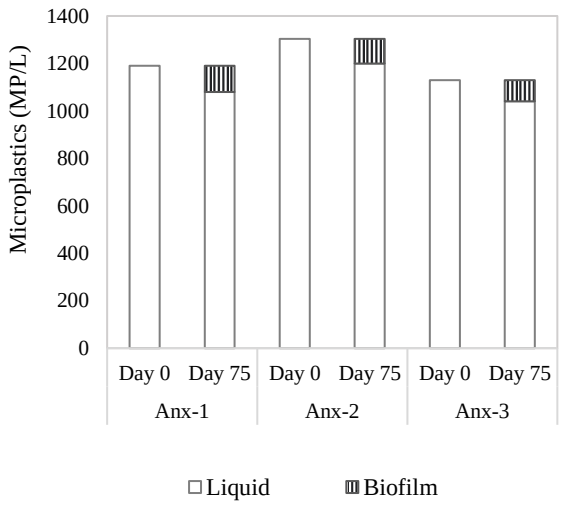

Fig.4 The occurence of microplastics during seeding process

In Fig. 4 can be seen that there were no microplastics added at the end of the start-up process. It means that there is no addition of secondary microplastic from PET media in a short period (75 days. Figure 4 and Table 1 show SSA affects the adhesion of microplastics to PET media. In larger SSA, more microplastics are adsorbed on the biofilm. At the beginning of seeding, all microplastics are suspended and completely mixed in the artificial wastewater. At the end of seeding, 7.96 – 9.24% of microplastics were adsorbed on the biofilm growing on PET.

Identification of PET polymer

Even though from the mass balance known that there was no addition of microplastics during the seeding process, identification of PET from bottles using ATR-FTIR was still carried out by matching it with the standard spectrum of PET from plastic bottles. For this purpose, a standard spectrum of PET bottles was made, then stored in a spectrum library, making it easier to identify PET polymers from samples of microplastic particles that were read by ATR-FTIR. The sample spectra were matched with the spectrum library, as well as the information that appeared on the monitor screen showing the molecular formula and images of the PET functional groups. The PET functional groups that appear on the monitor screen are adapted to the PET functional groups described by Crawford and Quinn, 2017 and Andardy, 2017.

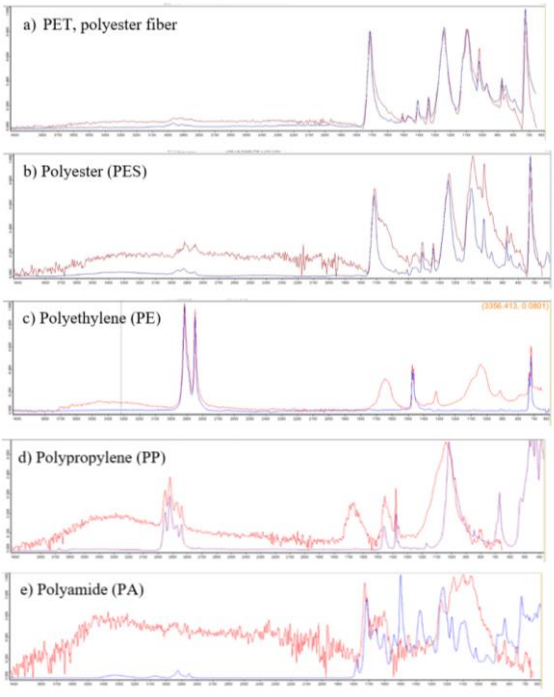

Fig. 5 Types of microplastic sample polymer found by the ATR-FTIR

Figure 5 shows the types of microplastic polymers found in ATR-FTIR. The types of microplastic polymers identified by ATR-FTIR in the seeding reactor samples are PE, polystyrene (PS), polyester (PES), and PET. In addition, other types of polymers such as polypropylene (PP), polyamide (PA) were also found in small amounts. The red spectrum graph shows the sample spectrum and the blue one shows the standard spectrum in the library. Figure 6 shows the polymer distribution in the anoxic reactor during the seeding process in the liquid phase and biofilm. Differences in density, shape, and size of each particle in the sludge affect their presence in the reactor during the seeding process.

PET polymer was found 17.38 ± 5.72% in the anoxic reactor, less abundant than PES and PE polymers. The difference in particle density affects its distribution in the liquid and biofilm. PE polymer found in biofilms more dominant than others, because its density is smaller than water, so it's easier adsorbed on biofilms.

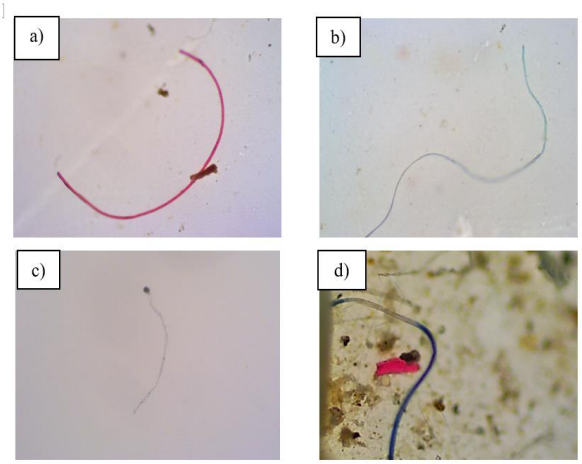

Fig. 6 Size, shape and color of microplastics in the reactor; a) red fiber, b) blue fiber, c) transparent fiber, d) red fragment and blue.

CONCLUSIONS

The source of microplastic in the anoxic reactor for 75 days of start-up process came from fecal sludge taken from housing with a concentration of 7,666.67 ± 513.16 MP/kg (w/w). At the end of seeding, around 7.96-9.24% of microplastics were adsorbed on the biofilm. The most identified types of microplastics by the ATR-FTR were PES and PET polymers. Based on the mass balance calculation, there was no microplastics addition at the end of seeding, meaning that no PET was dissolved as secondary microplastics during the seeding process.

ACKNOWLEDGMENTS

This work was supported by Riset Unggulan ITB, 2021.

REFERENCES

[1] Zhang, Y., Zhao, X., Peng, S., A Review of Different Drinking Water Treatment for Natural Organic Matter Removal. Water Sci. Tech. Water Supply, Vol 15, 2015, pp. 442-455.

[2] Xu, S., Jiang, Q., Surface modification of carbon fiber support by ferrous oxalate for biofilm wastewater treatment system. Journal Cleaner Production, Vol 194, 2018, pp. 416-424.

[3] Vandith, V, Setiyawan, A. S dan Soewondo, P., Kinetics of Nutrient Removal in an On-site Domestic Wastewater Treatment Facility, SIBE 2017, MATEC Web of Conferences, Bandung, Indonesia, Vol.147, 2018, 04004.

[4] Dong, Y., Fan, S.-Q., Shen, Y., Yang, J.-X., Yan, P., Chen, Y.-P., Li, J., Guo, J.-S., Duan, X.- M., Fang, F., Liu, S.-Y., A Novel Bio-Carrier Fabricated Using 3D Printing Technique for Wastewater Treatment. Sci. Rep. Vol. 5, 2015, pp.1–10.

[5] Leyva-Díaz, J.C., Martín-Pascual, J., Muñío, M.M., González-López, J., Hontoria, E., dan Poyatos, J.M., *Comparative kinetics of hybrid and pure moving bed reactor-membrane bioreactors.* Ecological Engineering, Vol. 70, 2014, pp. 227-234.

[6] Cox, K.D., Covernton, G.A., Davies, H.L., Dower, J.F., Juanes, F., Dudas, S.E., Human Consumption of Microplastics. Environ. Sci. Technol. Vol. 53, 2019, 7068–7074.

[7] Revel, M., Châtel, A., Mouneyrac, C., Micro(nano)plastics: A Threat to Human Health? Curr. Opin. Environ. Sci. Health, Vol. 1, 2018, 17–23.

[8] Schwabl, P., Kppel, S., Knigshofer, P., Bucsics, T., Liebmann, B., Detection of Various Microplastics in Human Stool: A Prospective Case Series. Ann. Intern. Med. Vol. 171, 2019, pp. 453–457.

[9] Zhang, N., Li, Y. B, He, H. R, Zhang, J. F, Ma, G. S., You Are What You Eat: Microplastics in The Feces of Young Men Living in Beijing. Science of the Total Environment, Vol. 767, 2021, 144345.

[10] Eerkes-medrano, D., Thompson, R.C., Aldridge, D.C., Microplastics in Freshwater Systems: A Review of the Emerging Threats, Identification of Knowledge Gaps and Prioritisation Of Research Needs. Water Res. Vol. 75, 2015, pp. 63–82.

[11] Napper, I.E., Bakir, A., Rowland, S.J., Thompson, R.C., Characterization, Quantity and Sorptive Properties of Microplastics Extracted from Cosmetics. Mar. Pollut. Bull. Vol. 99, Issue 1–2, 2015, pp.178–185.

[12] Penalver, R, Natalia Arroyo-Manzanares, Ignacio Lopez-García, Manuel Hernandez-Cordoba., Review: An overview of microplastics

characterization by thermal analysis. Chemosphere, Vol. 242, 2020, pp. 125170.

[13] Ahn, K.H., Hwang, J. H., Song, K. G., Jung, H.Y., Cho, E. S., Lim, B. R., Dezotti, Kim, K. S., Nitrogen Removal Using Recycled Polystyrene Bottles as Biofilm Media. Metals and Materials International, Vol. 10, 2004, pp. 167-170.

[14] Espinoza, K., Fernandez, C., Perez, J., Benalcazar, D., Romero, D., Lapo, B., Support Materials of Fixed Biofilm Based on Solid Plastic Wastes for Domestic Wastewater Treatment. Rev. Tec. Ing. Uviversitas Zulia, Vol. 42, Issue 2, 2019, pp. 67-75.

[15] di Biase, A., Maciej S. Kowalski, Tanner R. Devlin, Jan A. Oleszkiewicz., Moving Bed Biofilm Reactor Technology in Municipal Wastewater Treatment: A Review. Journal of Environmental Management, Vol. 247, 2019, pp. 849–866.

[16] Moharir, R.V., Kumar, S., Challenges Associated with Plastic Waste Disposal and Allied Microbial Routes for Its Effective Degradation: A Comprehensive Review. Journal of Cleaner Production, Vol. 208, 2019, pp. 65-76.

[17] Butler, I. B., Schoonen, M. A. A., Rickard, D. T., Removal of Dissolved Oxygen from Water, A Comparison of Four Common Techniques, Vol. 41, Issue 2,1993, pp. 211-215.

[18] Tchobanoglous, G., Stensel, H.D., Tzuchihashi, R., dan Burton, F., Wastewater Engineering – Treatment and Resource Recovery, fifth edition, McGraw-Hill, New York, 2014.

[19] Reynold, T.D., Unit Operations, and Process in Environmental Engineering. B/C Engineering Division, Boston.1982.

[20] Ziajahromi, S., Peta A. Neale, Llew Rintoul, Frederic D.L. Leusch., Wastewater Treatment Plants as A Pathway for Microplastics: Development of A New Approach to Sample Wastewater-Based Microplastics. Water Research, Vol. 112, 2017, pp. 93-99.

[21] Alam, F., Sembiring, E., Muntalif, B. S., Suendo, V. (2019): Microplastic distribution in surface water and sediment river around slum and industria area (case study: Ciwalengke River, Majalaya distric, Indonesia). Chemosphere, 224, 637 – 645.

[22] Copper, D. A Corcoran, P.I., Effects of mechanical and chemical processes on the degradation of plastics beach debris on the island of Kauai, Hawaii. Mar. Pollut. Bull. Vol. 60, 2010, pp. 650-654.

[23] Coppock, R.L., Cole, M., Lindeque, P.K., Queiros, A. M., Galloway, T. S., A Small-Scale, Portable Method for Extracting Microplastics from Marine Sediments. Environmental Pollution, Vol. 230, 2017, pp. 829-837.

[24] Hidalgo-Ruz, V., Gutow, L., Thompson, R.C., Thiel, M., Microplastics in The Marine Environment: A Review of the Methods Used for Identification and Quantification. Environmental Science & Technology, Vol. 46, 2012, pp. 3060-3075.

[25] Danopoulos, E., Jenner, L., Twiddy, M., Rotchell, J.M., Microplastic Contamination of Salt Intended for Human Consumption: A Systematic Review and Meta-Analysis. SN Applied Sciences, Vol. 2, Issue 12, 2020.

[26] Lwanga, E. H., Vega, J. M., Quej, V. K., Chi, J. de los A., Sanchez del Cid, L., Chi, C., Escalona Segura, G., Gertsen, H., Salanki, T., van der Ploeg, M., Koelmans, A. A., Geissen, V., Field Evidence for Transfer of Plastic Debris Along a Terrestrial Food Chain. Sci. Rep. Vol. 7, 2017, pp. 1–7.

[27] Zhang, N., Li, Y. B, He, H. R, Zhang, J. F, Ma, G. S., You Are What You Eat: Microplastics in The Feces of Young Men Living in Beijing. Science of the Total Environment, Vol. 767, 2021, pp. 144345.

[28] Dongqi, Y., Huahong, S., Lan, L., Jiana, L., Khalida, J., Prabhu, K., Microplastic Pollution in Table Salts from China. Environ. Sci. Technol. Vol. 49, 2105, pp. 13622.

[29] Cho Y, Shim WJ, Jang M., Abundance and characteristics of microplastics in market bivalves from South Korea. Environ Pollut. Vol. 245, 2019, 1107-16.

[30] Fareza, A. A, and Sembiring, E., Occurence of Microplastics in Water, Sediment and Milkfish (Chanos chanos) in Citarum River Downstream (Case Study: Muara Gembong). E3S Web of Conference, Vol. 148, 2020, 070005.

[31] Beriot, N., Peek, J., Zornoza, R., Geissen, V., Lwanga, E. H., Low Density-Microplastics Detected in Sheep Faeces and Soil: A Case Study from The Intensive Vegetable Farming in Southeast Spain, Science of The Total Environment, Vol. 755, 2021, 142653.

[32] Conti, G. O., Ferrantea, M., Banni, M., Favara, C., Nicolosi, I., Cristaldi, A., Fiore, M., Zuccarello, P., Micro- and nano-plastics in edible fruit and vegetables. The first diet risks assessment for the general population. Environmental Research. Vol. 187, 2020, pp. 109677.

[33] Mary, K., Mason, S.A., Wattenberg, E.V., Zhi, Z., Anthropogenic Contamination of Tap Water, Beer, and Sea Salt. PLoS One 13, 2018, 0194970.

[34] Eerkes-Medrano, D., Leslie, H.A., Quinn, B., Microplastics in Drinking Water: A Review and Assessment of an Emerging Concern. Curr. Opin. Environ. Sci. Health, Vol. 7, 2018, pp. 69–75.

[35] Mason, S. A, Welch, V. G. Neratko, J., Synthetic Polimer Contamination in Bottled Water. Frontiers in Chemistry, Vol. 407, Issue 6, 2018.

[36] Zuccarello, P., et al., Exposure to Microplastics (< 10 Mm) Associated to Plastic Bottles Mineral Water Consumption: The First Quantitative Study. Water Res. Vol. 157, 2019a, pp. 365–371.

[37] Zuccarello, P., et al., Reply for Comment On "Exposure yo Microplastics (< 10 mm) Associated to Plastic Bottles Mineral Water Consumption: The First Quantitative Study by Zuccarello et al. Water Res. 157 (2019) 365-371]". Water Res. Vol. 166, 2019b, pp. 115077.

[38] Welle, F., Franz, R., Microplastic in Bottled Natural Mineral Water – Literature Review and Considerations on Exposure and Risk Assessment. Food Addit. Contam. Part A Chem Anal Control Expo Risk Assess, Vo. 35, Issue 12, 2018, pp. 2482–2492.

11th Int. Conf. on Geotechnique, Construction Materials & Environment,
Kyoto, Japan, 3-5 November 2021, ISBN: 978-4-909106063 C3051

CHANGES IN RIVER ENVIRONMENT AT THE DOWNSTREAM AREA DUE TO MAINTENANCE FLOW DISCHARGE FROM THE HIRAIDE DAM LOCATED ON KATASHINA RIVER

Naoki Miyazato[1], Yuko Kakegawa[2], Keiji Nakajima[2], Hiroyuki Aizawa[3], Yuya Saito[4],Yuishi Yagi[5], Akihiro Horio[1], Toru Aoi[1] and Yoshikatsu Yamamoto[1]

[1]National Institute of Technology (KOSEN), Gunma College, Japan
[2]Organization-Kawagera-no-kai, Japan
[3]2-7-3, Bunkyo-cho, Maebashi, Gunma, Japan
[4]Yaritanago restoration project team, Japan
[5]Branch office of JASHA, Japan

ABSTRACT

In 2011, a new hydroelectric power station was built by Gunma Prefecture to improve the river environment. The water of river maintenance flow is used by the new hydroelectric power station.

In this study, water quality, diatoms, aquatic insects, and freshwater fish in the low flow section in 2010 and the maintenance flow discharge section at Katashina River in 2015 were examined. The results are summarised, First, Nitrogen concentrations of Katashina River water were as high as 0.15mg-N/l at all sampling sites. Second, The amount of *Melosira varians* in the maintenance flow discharge section was decreased comparing that in the low flow discharge section. Third, the most amount of freshwater fish was *Tribolodon hankonesis* at Katashina river. These results indicated that Katashina River environments were improved slightly.

Keywords: decreased flow rate section, water quality, diatoms, aquatic insect, freshwater fish

INTRODUCTION

Until 2010 in winter seasons, the Katashiina River, a tributary of Tone River (Gunma Prefecture, Japan) has suffered a decreased flow rate section of 2.7 km due to flow diversion to the hydroelectric power station of Hiraide Dam, resulting in deterioration of the river environment as a wildlife habitat. In 2011, a new hydroelectric power station (Shin-Tonami electric power station) was built by Gunma Prefecture to improve the river environment. The water of river maintenance flow is used by the new hydroelectric power station [1]-[3].

Conversely, diatoms are widely used for the biological assessment of rivers, along with aquatic insects and fish [4]-[7]. Diatoms are used in a variety of ways to show the impacts of environmental disturbance. Effects of dams on diatom communities along the Katsuura River were investigated to understand the relationship between the environmental factors and the characteristics of diatom communities [8].

In this study, water quality, diatoms, aquatic insects, and freshwater fish in the low flow section and the maintenance flow section in Katashina River were examined. The purpose is to investigate the aquatic organisms and water quality at the Katashina River for five years, after the construction of the Shintonami Power Station and the start of maintenance flow discharge, and to grasp and evaluate the improvement status of the river environment.

MATERIAL AND METHOD

Katashina River and sampling sections

Figure 1 shows that Katashina River is located in the northern part of Gunma Prefecture. Figure 2 shows that five survey areas were selected on the Katashina River. The river water was sampled from the Katashina River occasionally. The water surface width and water depth in the figure are the conditions when the Gunma Prefectural Enterprise Bureau conducted the test release [1]. However, in this survey,

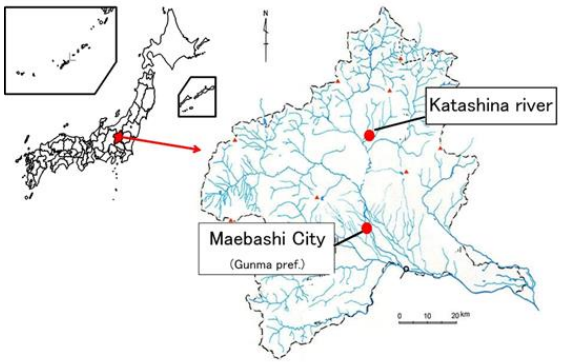

Figure 1 Katashina River was located in northern of Gunma prefecture, Japan

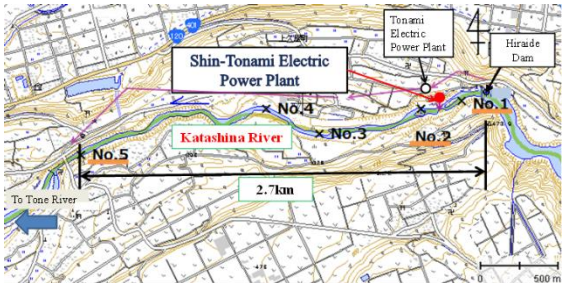

Figure 2 Five sampling sites, number 1 to 5 on Katashina River

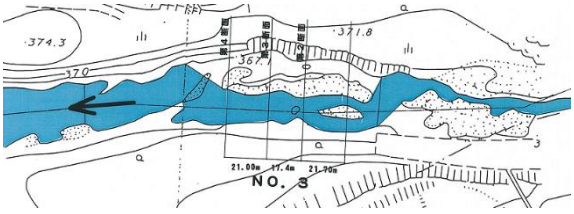

Figure 3 survey site No.3

it was predicted that there would be danger in collecting samples at survey site No. 3 (Figure 3) due to changes in riverbank conditions (effects of gravel, weeds, etc.), so we abandoned the survey.

Biological survey

Diatom survey

Analyze the diatom community attached to the gravel at survey sites No. 1 and 2 and 4 to 5 to clarify the type and composition of diatoms at the survey points. The diatom survey will also be conducted when a fish survey was conducted. In this survey, diatoms adhering to the gravel will be collected at the site and stored in 70% ethanol. After that, we will take it back to our laboratory and investigate the composition of diatoms. After treating the sample with concentrated sulfuric acid, seal it with proof flux to prepare a permanent preparation. The samples were examined under an optical microscope (using an oil-immersion lens) and made a 2000x photograph. The diatom list was created by counting each sample.

Habitat survey of aquatic insects

This survey will be conducted at survey sites No.1-2 and 4-5. At each survey site, aquatic insects will be collected at 4 locations (4 times) at 1 site using a 25 cm x 25 cm square frame and nylon net. The 0.25 m2 quantitative survey will be conducted. The collected aquatic insects are taken out from the nylon net using tweezers. They are soaked in 70% ethanol and stored in a 25 ml glass bottle. The wet weight was measured to take out aquatic insects soaked in ethanol, wipe the surface using Kimwipe, and measure by species and family.

Fish survey

Fishes were collected at each survey site No.1-2 and 4-5 using a scoop net with a diameter of about 30 cm. In addition, electric shockers, cast nets, and fishing were also used. The number of fish obtained was counted for each species, the total length was measured, and then the fishes were released on the spot.

Water quality survey

The water temperature (°C) and electrical conductivity (EC: mS/m) at survey points No. 1 to 2 and 4 to 5 were measured. 1 liter of river water was collected. In our laboratory, pH was measured using pH meter. Ammonia nitrogen (NH^4-N), nitrite nitrogen (NO^2-N), oxidized nitrogen (NO^x-N), phosphate phosphorus (PO^4-P) were analyzed using an autoanalyzer (BLtec, Quattro-II).

RESULTS AND DISCUSSION

Biological survey

Diatom survey results

The diatom survey was conducted on June 21, 2015, October 25, November 15, and December 6, 2015. The diatoms observed in this survey are 30 species in a total of 15 families.

Table 1 shows the observed diatom species.

At all survey sites, the main species that appeared were Achnanthes minutissima, Achnanthes japonica, Encyonema minutum, and Navicala cryptotenella.

Achnanthes minutissima belonging to eurysaprobic taxa and Achnanthes japonica belonging to saproxenous taxa showed at survey sites.

The number of confirmed saprophilous taxa, eurysaprobic taxa, and saproxenous taxa at each survey site are shown in figure 4. At each survey site, it was confirmed that there were a large amount of eurysaprobic taxa. Furthermore, the abundance ratios of the confirmed diatom species were determined for aprophilous taxa, eurysaprobic taxa, and saproxenous taxa. Figure 5 shows the abundance ratio compared Furthermore, the abundance ratios of the confirmed diatom species were determined for aprophilous taxa, eurysaprobic taxa, and saproxenous taxa.

Table 1 Diatom in survey site No. 1 to 5

month/day/year		6/21/15				10/15/15			11/15/15				12/6/15				taxa
species / site No.		No.1	No.2	No.4	No.5	No.1	No.2	No.5	No.1	No.2	No.4	No.5	No.1	No.2	No.4	No.5	
Achnanthes	convergens	48	60	48	28	108	33	108	12	5	63	21	24	6	36	21	Saprophilous taxa
	minutissima	38	154	94	68	243	99	246	159	66	120	222	174	114	84	59	Eurysaprobic taxa
	japomica	52	112	120	48	144	96	18	108	144	162	24	216	84	300	76	Saproxenous taxa
	exigua		4	3	16	18		3	0								Eurysaprobic taxa
	clevei	6	20					81									Saprophilous taxa
Encyonema	minutum	33	184	63	32	201	135	225	150	24	75	15	75	126	96	54	Saproxenous taxa
	lange-bertalotii	21	96	42	24	48	84	168	84	48	30	18	30	48	30	41	Saproxenous taxa
Fragilaria	capitellata		128	28	60	111	9	8	24	24	3		27		24	12	Eurysaprobic taxa
	capucina	29	56	39	56	15	3	0		6		6					Saprophilous taxa
Nitzschia	dissipata	10	148	60	60	69		12	9	18	12		9	12	42	15	Saprophilous taxa
	inconspicua		16	6	12	3	45	0	57	96	99	96	30	72	81	138	Eurysaprobic taxa
	foutica	4	28	15	16	12	3	12		12	3	6			18		Eurysaprobic taxa
Synedra	inaequalis	4	20			33	12		39	24	9	9	15	24	6	6	Saprophilous taxa
	angusta	2															
	ulna			3	3												Saprophilous taxa
Asterionella	formosa	58	60	48	33	3	0		3								Saprophilous taxa
Novicala	cryptotenella	22	116	66	24	252	72	33	240	108	180	87	78	132	132	57	Eurysaprobic taxa
	angusta		4		3		33		36	36	30	39	39	18	18	24	Saprophilous taxa
cyclotella	stelligera	3	8	3	9	108	39	18	51	18	24	12	15	18	36		Eurysaprobic taxa
Diploneis	boldtiana		12	9	3	9	3	3	6	24	15	6	9	6	18	12	Saprophilous taxa
Cocconcis	placentula		12	15	47	24	3	32	6	18	42	6	24	24	6		Eurysaprobic taxa
Diatoma	kuetzingii		8	6		6		20	12	42	24	18	12	24	30	18	
	mesodon	1	4														Saprophilous taxa
Cymbella	mexicana		12		6	21	3	12	6	18	87	57	3		36	31	Saprophilous taxa
	turgidula var.nipponia		8				3		3								Saprophilous taxa
Melosira	varians	3	12	6			0	4	6	45	6	12	69	24		27	Eurysaprobic taxa
Gomphonema	angustatum	1	4				0			6							Eurysaprobic taxa
	parvulm	17															Eurysaprobic taxa
	clevei	11															Saprophilous taxa
Rhoicosphenia	abbreviata	20		21	6	18	12	36	9	48	12	6	6	6		3	Saprophilous taxa

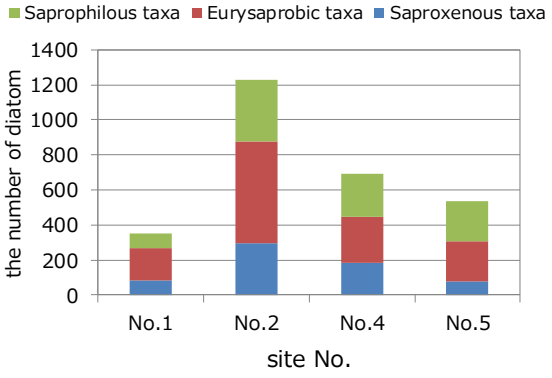

Figure 4 the comparison of results that species of Saproxenous taxa (blue), Eurysaprobic taxa (green), Saprophilous taxa (red) are shown at all survey areas in 2010 and 2015

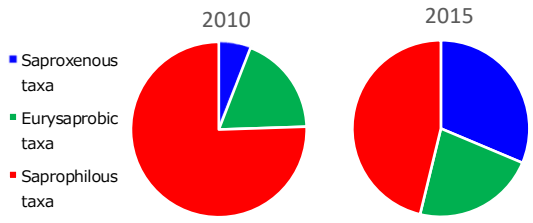

Figure 5 the percentage of species that are Saproxenous taxa (blue), Eurysaprobic taxa (green), Saprophilous taxa (red) are shown at all survey areas.

Figure 4 shows the abundance ratio compared with the results of the 2010 survey and the 2015 survey. In the 2015 survey, it was confirmed that the number of eurysaprobic taxa, which accounted for about 75% before the start of maintenance flow in 2010, has decreased. In addition, saproxenous taxa (this species that can be confirmed mainly in the upstream area) increased, accounting for about 30%. It was considered that this result was largely due to the decrease in *Melosira varians* belonging to eurysaprobic taxa, and the increase in *Achnanthes japonica* belonging to saproxenous taxa. It was suggested that the maintenance flow discharge may have improved the water quality of the Katashina River.

aquatic insects survey

Comparison with the results of the preliminary survey (2010/12/02) conducted before the start of maintenance flow

The results of this survey are shown in figure 4. Compared with the results of the 2010 survey before the start of maintenance flow, it can be confirmed that the number of species and individuals increased in site No. 1 and No. 2. However, the number of species and individuals decreased in site No. 4 and No. 5. Aquatic insects were probably washed away in No. 4 that occurred in 2015.

This result suggests that it was not possible to and confirm the increase of aquatic insects due to the maintenance flow discharge. The increase in aquatic insects was confirmed in survey site No. 1 where the

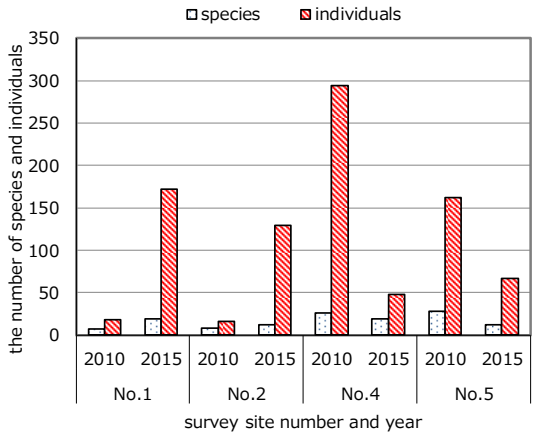

Figure 6 the number of species and individuals at survey sites in Katashina river

No. 5 due to the large impact of Typhoon No. 18. The discharge was released from the dam due to the influence of the typhoon. The survey site No. 2 where the flow was slow and the dam was not easily affected due to the typhoon. It was suggested that the number and population of aquatic insects increased due to the maintenance flow discharge.

Comparison due to the Japanese version average score method (number of departments) MWP (Bilogical Monitoring Working Party) for japanese ver.

In the Japanese version of the average score method, the scores given to the appearance departments are added to calculate the total score, and the average score per taxon (ASPT) is divided by the number of appearance departments to evaluate.

ASPT indicates that the upstream environment is in good condition at a score 10-8 and that the downstream river environment is polluted below score 4.

The collected aquatic insects were scored by the Japanese average scoring method and compared. The scoring value is based on [11]. The results are shown in Table 1. The average score (ASPT) was 6.55 in the 2010 survey. However, the score in the 2015 survey is 7.03. The result suggests that the river environment is improving in the upstream area.

Comparison due to EPT value (species number)

Table 2 shows the results of comparison by EPT value (species number)[10]-[11]. The total number of species belonging to the order *Ephemeroptera*, the order *Plecoptera*, and the order *Caddisfly Trichoptera* is used as the EPT value. *Ephemeroptera*, Stoneflies,

Table 1 Comparison appling Bilogical Monitoring Working Party for japanese version

class / family		score
Ephemeroptera	Dipteromimidae	10
	Ameletidae	8
	Isonychiidae	8
	Heptageniidae	9
	Baetidae	6
	Ephemerellidae	8
	Ephemeridae	8
Plecoptera	Nemouridae	6
	Perlodidae	9
	Perlidae	9
Neuroptera	Corydalidae	9
Trichoptera	Stenopsychidae	9
	Hydropsychidae	7
	Rhyacophilidae	9
	Leptoceridae	8
Diptera	Tipulidae	8
	Simuliidae	7
	Chironomidae	6
	Ceratopogonidai	7
Opisthopora	Oligochaeta	4
Hirudinea		24
	family number	198
	TS	25
	ASPT	7.92

MWP(Bilogical Monitoring Working Party) for japanese ver.
TS:Total Score
ASPT:Average Score Per Taxon)

Table 2 Comparison EPT value

class, MM/dd/year	12/2/2010	12/6/2015
Ephemeroptera	9	17
Plecoptera	0	5
Trichoptera	13	11
TPT	22	33

*the number of species

and *Caddisflies* are benthic organisms that live in clean waters, and these species are abundant in clean waters.

The results are shown in Table 2, the EPT value was 22 in the 2010 survey, but it was 33 in the 2015 survey. The EPT value indicates that the aquatic insects are diversified in Katashina rever environment.

Fish survey in Katashina river

Outline of each survey site for fish

Two *Lethenteron* spp. and eleven *Tribolodon hakonensis* were confirmed at 3-time surveys in site No.1. The survey points are generally low in gravel and the bedrock is exposed, and there are few suitable places for fish. The two species were obtained from a

small amount of gravel in the slow stream and accumulated fallen leaves.

Rhinogobius sp. was confirmed at 3-time surveys in site No.2. A large pool was developed, and the place where it could be collected by the net was only a small part near the shore.

Two *Lethenteron* spp., five *Opsariichthys platypus*, five *Phoxinus lagowskii steindachneri*, 39 *Tribolodon hakonensis*, a peace of *Gnathopogon elongatus elongatus*, two *Misgurnus anguillicaudatus*, six *Cobitis* sp. BIWAE type C, 2 two *Rhinogobius* sp., and *Gymnogobius urotaenia* were confirmed at site No.4. The center of the stream at site No.4 is a state in which about 50 cm of boulders is piled

A total of 6 *Lethenteron* spp., one *Phoxinus lagowskii steindachneri*, two *Tribolodon hakonensis*, six *Cobitis* sp. BIWAE type C, two *Rhinogobius* sp. OR, and four *Gymnogobius* sp. 1 were confirmed at three time surveys in site No.5.

Fish survey consideration

The scientific names of fish based on Sekine, K., et. al. [12] and Hosoya, K., and Uchiyama, R., [13] were applied. Ten species belonging to four families of fish and jawless fish were confirmed on surveys (11 times in 2015) at four survey sites. *Lethenteron* spp., *Phoxinus lagowskii steindachneri*, *Tribolodon hakonensis*, *Cobitis* sp. BIWAE type C, *Rhinogobius* sp. OR are major fish at rivers in Gunma Prefecture. They were confirmed at a few sites at this time.

These fish inhabited widely in this area and various sizes (young fish and adult fish) fish were confirmed. These results suggest that they were also breeding. In addition, it seems that breeding for *Opsariichthys platypus* and *Misgurnus anguillicaudatus* is possible to consider the river morphology.

On the other hand, *Gnathopogon elongatus elongatus*, *Gymnogobius urotaenia* and *Gymnogobius* sp.1 are originally fish that live on the sandy mud bottoms of small and medium-sized rivers, agricultural waterways, and ponds. This result suggests that outflow from the Hiraide-dam lake carried these species.

In this survey, ten species were confirmed, but this number of each individual was not large. It is inferred that these results are related the situations that few slow-flowing parts of the gravel bottom are favorable for fish habitat.

Table 3 Water quality at surve site in Katashina river

y/m/d	sait No.	pH	EC	NH_4-N	NO_2-N	NOx-N	Inorg-N	PO_4-P
2015.6.21	No.1	9.86	9	0.017	0.010	0.870	0.887	0.042
	No.2	8.75	5	0.017	0.010	1.127	1.144	0.045
	No.4	8.30	9	-	-	-	-	-
	No.5	7.31	6	0.017	0.011	1.305	1.322	0.032
2015.10.25	No.1	8.28	14	0.072	0.016	0.944	1.016	0.022
	No.2	8.12	12	0.299	0.011	1.007	1.306	0.066
	No.4	-	-	-	-	-	-	-
	No.5	7.19	21	0.037	0.015	1.401	1.438	0.061
2015.11.15	No.1	8.76	11	0.000	0.016	0.979	0.979	0.227
	No.2	8.54	11	0.027	0.016	0.869	0.896	0.036
	No.4	8.11	10	0.017	0.015	0.950	0.967	0.028
	No.5	8.06	10	0.017	0.015	1.272	1.289	0.025
2015.12.7	No.1	8.27	11	0.016	0.005	1.01	1.026	0.016
	No.2	8.48	10	0.033	0.005	0.97	1.003	0.000
	No.4	8.59	10	0.017	0.004	1.07	1.087	0.083
	No.5	8.43	11	0.020	0.004	1.41	1.430	0.000

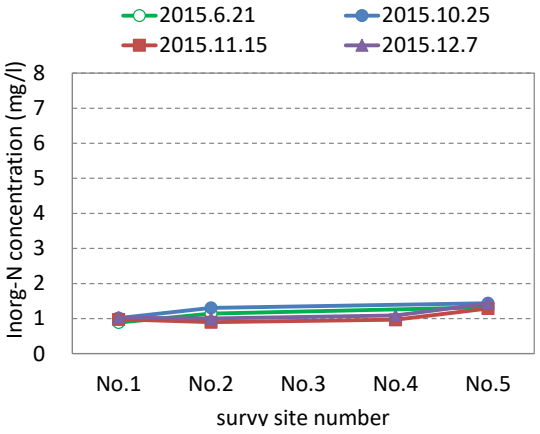

Figure 7 Inorganic nitrogen concentration at survey site 1 ~ 5 in Katashina river on 2015

River- water quality survey

Table 4 shows the results of water quality analysis at each survey point in this survey.

In addition, figure 7 shows the concentration of inorganic nitrogen at each survey site.

However, at survey points No. 4 on June 21 and October 25, water sampling was difficult due to the condition of the river, and the analysis was not possible. The results showed that the nitrogen concentration was high at all the survey points where water could be sampled. The inorganic nitrogen concentration was about 1.0 mg/L at all survey sites. In the northern part of Gunma prefecture, it has been reported that one of the causes is that nitrogen oxides contained in the exhaust gas emitted from cars running in the metropolitan area are carried by the wind and are poured down by rainfall [9]. That effect is also suggested in the Katashina River basin. In addition, the value of inorganic nitrogen

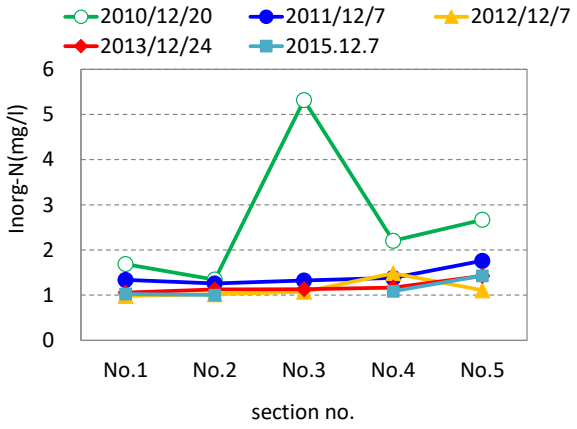

Figure 8 Inorganic nitrogen concentrationat survey site 1 ~ 5 in Katashina river on 2010 ~ 2013[1]-[3], 2015

concentration of 1.0 mg / l or more is higher than T-N=0.15 mg/L, which is the standard for eutrophication.

According to the reports of Katashina river water quality written by Gunma prefecture Oze high school[10], the water quality of the Katashina River from Ozenuma is not artificially affected, and the nitrogen concentration is low. The results previously reported (Figure 8,[1]-[3]) and these results suggest that there is almost no effect of the inflow of domestic wastewater in the survey area of Katashina River.

CONCLUSIONS

Five years have passed since the completion of the Shintonami Power Plant, and the start of maintenance flow discharge in 2015. These results in the survey suggest that the environmental condition of the Katashina River with a sufficient amount of water is enriched mainly due to the ecosystem of diatoms and aquatic insects in the winter season. Although we have not conducted a thorough survey, the Katashina River has few slow-flowing areas with gravel bottoms, and the results of this survey suggest that the amount of water has not improved the habitat for fish.

The river water quality data suggest that the river environmental condition is favorable. It is necessary to investigate the habitat for fish due to long-term continuous surveys in the future.

ACKNOWLEDGMENTS

The authors wish to express their thanks to graduate students at National institute technology (KOSEN), Gunma college, and Gunma prefecture for their technical assistance.

REFERENCES

[1] Miyazato, M., Kakegawa, Y., Nakajima, K., Yagi, Y., Aoi, T., and Yamamoto, Y., Research of river environments comparing the low flow section and the maintenance flow section in Katashina Rive, Proceeding of 5nd IWA-ASPIRE Conference and Exhibition in Daejeon, 2013, oral-11C2-4 in USB

[2] Miyazato, M., Ajisawa, Y., Kakegawa, Y., Nakajima, K., Yagi, Noguchi, K., Aoi, T., and Yamamoto, Y., Effects of maintenance flow water for river environmental at Katasina river, the 48th annual conference of japan society on water environment in 2014, p.4, in Japanese

[3] Miyazato, M., Ajisawa, Y., Y., Kakegawa, Y., Nakajima, K., Yagi, Y., Aoi, T., and Yamamoto, Y., The effect of maintenance flow for water quality and aquatic organisms in Katashina river, the 49th annual conference of japan society on water environment in 2015, p.4, in Japanese

[4] Amisah, S., Cowx, I,G., Response of the fish population of the River Don in South Yorkshire to water quality and habitat improvements, Environmental Pollution Vol.108, No.2, 2000 , pp.191-199

[5] Delgado, C., Pardo, I., Garcia, L., Diatom communities as indicators of ecological status in Mediterranean temporary streams (Balearic Islands, Spain), Ecological Indicators, Vol.15, Issue 1, 2012, pp.131–139

[6] Growns, I., Is genus or species identification of periphytic diatom required to determine the impacts of river regulation?, Journal of Applied Phycology, Vol.11(3), 1999, pp.273-283

[7] Matsuno, T., Ohkubo, M., Toriiminami, Y., Tsushima, M., Sakaguchi, S., Minami, T., Maoka, T., Carotenoids in food chain between freshwater fish and aquatic insects, Vol.124, Issue 3, 1999, pp.341-345.

[8] Shiratori, M., Kozuki, Y., Kurata, K., Haseda, M., Kofuji, M., Murakami, H., Characteristics and colonising processes of periphytic diatom communities downstream of dam sites along the Katsuuta River, Tokushima Prefecture, Environmental Engineering Research, Vol. 40, 2003, pp.117-126. in Japanese.

[9] Aoi, T. Nitrogen pollution in the upper basin of Tone river without artificial sources, Global Environmental Research, Vol. 15(2), 2010, pp.145-152, in Japanese

[10] Ministry of Land, Infrastructure, Transport and Tourism, https://www.mlit.go.jp/common/000046619.pdf June.11. 2021, in Japanese

[11] Nozaki, T., Biological Assessment Based on Macroinvertebrate Communities : Average Score System for Japanese Rivers, Journal of Japan Society on Water Environment 35(4), 2012, pp.118-121, in Japanese

[12] Sekine, K., Gunma-ken no doubutsushi, Gunma high school education and research association, 1985, in Japanese

[13] Hosoya, K., Uchiyama R., Nihon no Tansuigyo, 2019, Yama-kei Publishers co.,Ltd. in Japanese

[14] http://www.oze-ic.gsn.ed.jp/data/H18-katashinagawa.pdf, June.10. 2021, in Japanese

11th Int. Conf. on Geotechnique, Construction Materials & Environment, Kyoto, Japan, 3-5 November 2021, ISBN: 978-4-909106063 C3051

DEVELOPMENT OF ANFIS MODEL FOR AIR QUALITY FORECASTING IN DHAKA CITY

A. A. Abeer, J. Farzana and M. T. Rahman

Civil Engineering Department, Military Institute of Science & Technology, Bangladesh

ABSTRACT

This study aims to forecast the daily concentrations of PM_{10} and $PM_{2.5}$ in the atmosphere of Dhaka city using the Adaptive Neuro-Fuzzy Inference System (ANFIS). In Dhaka, particulate matter (PM) is the most harmful air pollutant to public health. So, to forecast the concentration of PM in the atmosphere is important for the development of cost-effective control strategies to alert and protect the population. In this study, the ANFIS model predictor considers five meteorological factors (pressure, temperature, relative humidity, wind speed, and rainfall) and the previous day's pollutant concentration in different combinations as the inputs to predict the same day and 1-day advance air pollution concentration. In order to reduce the computational cost and time, the collinearity tests and forward selection (FS) technique are applied to remove the dispensable input variables and select the different combinations of input variables, respectively. Root mean square error (RMSE), Coefficient of determination (R^2), Normalized Mean Square Error (NMSE), Index of Agreement (IOA), and Fractional Bias (FB) are applied for the performance testing of the model. Since ANFIS is a combination of neural and fuzzy logic is capable of representing knowledge acquired from human experts and which further improves the prediction. From this study, considering the better values of the indices the PM2.5-PDPM2.5-T & PM10-PDPM10-P model performed well for prediction.

Keywords: ANFIS Model, Forward search, Collinearity, Computational cost, Air pollutants

INTRODUCTION

Air, the most essential aspect of the living world gradually losing its quality due to anthropogenic practices all over the world. In Bangladesh, the air pollution situation is getting aggravated with the rapid growth in urbanization and industrialization. Dhaka-the center of all administrative, economic and cultural activities of Bangladesh was the second most air polluted city in 2020 as the majority of processing plants in two industrial towns on the periphery do not follow emission requirements. The problem is exacerbated further by transport mega-projects such as a metro rail system and an elevated expressway, which generate massive quantities of pollution, leading to pollution from old cars, private building sites, and open garbage burning. Particulate matter with an aerodynamic diameter of less than 10 μm can deeply penetrate the human lung and cause diseases such as bronchitis, impaired lung function, and cardiopulmonary problems [1], [2]. Hence it is necessary to create air monitoring networks and develop air quality management strategies (which include measurements, forecasting, regulations, etc.). A neural network modeling scheme provides an efficient computational tool for mapping input-output or cause-effect relationships and establishes intelligent what-if scenarios based on robust learning mechanisms. One such example is the Adaptive Neuro-Fuzzy Inference System (ANFIS), which has a hybrid algorithm and was proposed by Jang et al. (1997) [3].In the ANFIS model, crisp input series are converted to fuzzy inputs by developing a membership function for each input series [4]. The membership function can be any shape but it depends on the data set. Many researchers used the FS method to develop proper prediction models [5]. The ANFIS model with a reduced input combination lowers computational cost and predicts with less errors. It seems that timely forecasting of air quality lets authorities alarm the residents and helps them manage its detrimental effects. Thus, the present study aims to develop an ANFIS model for forecasting of daily air quality of Dhaka city.

OBJECTIVES

The study aims to find out the best combination of weather parameters to develop an ANFIS model, to forecast air quality based on the best combination and to evaluate developed hybrid models with all input variables to show that FS techniques reduce not only the output error but also computational complexity and cost due to less number of inputs.

METHODOLOGY

Input & Output Parameter Selection

In the present study, five meteorological parameters (temperature, pressure, wind speed, relative humidity, and rainfall) along with the

previous day's pollutant concentration were considered as input variables.

Multi-collinearity test

A multi-collinearity test was conducted to eliminate the redundant input variables [6]. Collinearity means that two or more of the independent/ explanatory variables in a regression have a linear relationship. The close relationship of the variables makes the isolation difficult. A multi-collinearity diagnosis was conducted through regression analysis using SPSS software version 25. Multi-collinearity can be diagnosed based on two factors. These are variance inflation factors (VIF) and tolerance. If the VIF values of the independent variables are more than 10 and tolerance is less than 0.1, then we can say that the model is suffering from multi-collinearity [7].

Forward search method

As the number of variables is high, the number of combinations will require high computation cost. Step-by-step algorithms such as forward search (FS) can be extremely beneficial in terms of lowering computing costs. FS method has been successfully used by many researchers in order to build robust prediction models. A linear regression model is the basis of this approach. Ordering of the explanatory variables according to their correlation with the dependent variable (from the most to the least correlated variable). Then, the explanatory variable, which is best correlated with the dependent variable, is selected as the first input. All remained variables are then added one by one as the second input according to their correlation with the output and the variable which most significantly increases the correlation coefficient (R^2) is selected as the second input [8].

Assigning Membership Function Type & Number

Expressing linguistic values in the form of fuzzy sets is the first thing to do for generating a FIS system. The membership functions can be constructed from several basic functions such as piecewise linear functions, the sigmoid curve, the Gaussian distribution function, quadratic and cubic polynomial curves. The range of input and output variables can be divided into several linguistic values. In this study, the function computes fuzzy membership values using a generalized bell-shaped membership function.

Data Normalization

To increase the accuracy of the results and decrease the range of data the normalization method is utilized. This normalization process brings the values of variables in between 1 and -1. The normalization of data was done using the following formula:

$$X = [(2((A - Amin)/(Amax - Amin))) - 1] \quad (1)$$

Where, X=Normalized Value & A=Observed value.

Model Training & Testing

The data sets are divided into two parts (training data set and testing data set) after normalization. Training data contain 70% of the data and the testing data set contains 30% of the data. Both the training data sets & testing data sets are loaded in the ANFIS toolbox of MATLAB software version 8.3. After data loading, membership number and type for each input and output variables were assigned to generate the FIS system. After that, the models are trained for each input combinations as described above and the performance of the models are tested using the testing data sets.

Performance Test of Models

The deviation of the predicted data (FIS output) from the observed value is determined for the performance evaluation of models. Five statistical indices- Fractional Bias (FB), Root Mean Squared Error (RMSE), Coefficient of determination (R^2), Normalized Mean Square Error (NMSE), and Index of Agreement (IOA) were used for performance evaluation of the model.

Best Model Selection

Based on the statistical performance tests, the best models were chosen having the highest index of agreement and good performance test output.

RESULTS

Description of Analysis & Data Source

The method explained for the development of the ANFIS model in methodology is applied for air quality forecasting in Dhaka city, Bangladesh. The daily ambient air pollutant concentrations PM_{10} (24-

hrs average) and $PM_{2.5}$ (24-hrs average) are used for the study. Air pollutant data have been collected from the Department of Environment (DoE) and the US Embassy, Bangladesh. The daily mean values of meteorological data (temperature, pressure, relative humidity, wind speed & rainfall) are obtained from Bangladesh Meteorological Department (BMD). The annual average of PM_{10} concentration in 2014, 2015, 2016 & 2017 are respectively 160.03 µg/m^3, 149.88 µg/m^3, 142.37 µg/m^3 and 144.95 µg/m^3 .This indicates that the annual average concentration of PM_{10} has been decreased from 2014 to 2016 and slightly increased in 2017. The annual average of $PM_{2.5}$ concentration in 2016, 2017, 2018 & 2019 are respectively 85.27 µg/m^3, 80.11 µg/m^3, 87.48 µg/m^3 and 85.75 µg/m^3. This indicates that the annual average concentration of $PM_{2.5}$ has been decreased from 2016 to 2017 and increased during 2018. Figures 1 and 2 represent the daily variation of PM_{10} and $PM_{2.5}$ respectively.

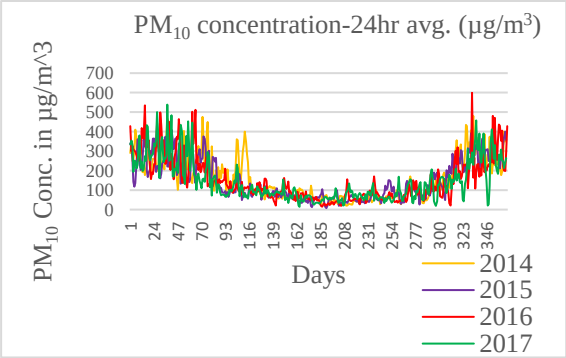

Fig. 1 Daily variation of PM_{10} concentration

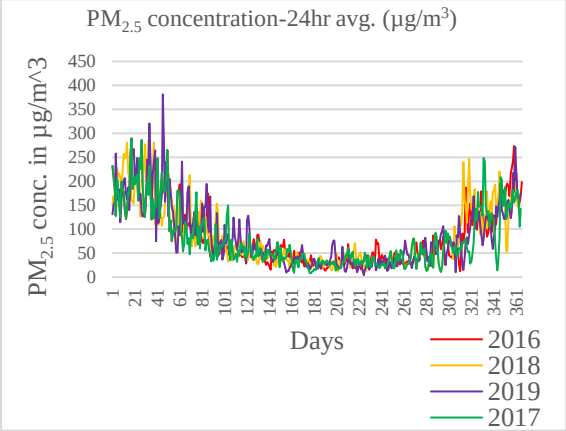

Fig. 2 Daily variation of $PM_{2.5}$ concentration

Descriptive statistics of $PM_{2.5}$, PM_{10} are shown in Tables 1 and 2 respectively.

Table 1 Descriptive Statistics of Air Pollutant conc. ($PM_{2.5}$)

$PM_{2.5}$ in µg /m^3	
2016	
Maximum	289.417
Minimum	12.46
Mean	85.271
Standard Deviation	62.768
2017	
Maximum	289.417
Minimum	8.2
Mean	80.107
Standard Deviation	61.7058
2018	
Maximum	285.7
Minimum	10.7
Mean	87.475
Standard Deviation	66.016
2019	
Maximum	381.25
Minimum	4
Mean	85.752
Standard Deviation	65.157

Table 2 Descriptive Statistics of Air Pollutant conc. (PM_{10})

PM_{10} in µg /m^3	
2014	
Maximum	480.313
Minimum	19.963
Mean	160.033
Standard Deviation	110.328
2015	
Maximum	420.603
Minimum	7.176
Mean	149.881
Standard Deviation	104.070
2016	
Maximum	599
Minimum	15.056
Mean	152.367
Standard Deviation	114.983
2017	
Maximum	538.501
Minimum	14.065
Mean	144.946
Standard Deviation	105.847

The multi-collinearity was diagnosed using the two factors (VIF and tolerance level). The results of the multi-collinearity test are represented in table 3 indicating there is no collinearity problem in these variables.

Table 3 Collinearity Statistics

Air Pollutant	Parameters	Tolerance	VIF
$PM_{2.5}$	Rainfall (R)	0.84	1.18
	Temperature (T)	0.38	2.61
	Relative Humidity (H)	0.65	1.53
	Pressure (P)	0.29	3.38
	Wind Speed (WS)	0.96	1.04
PM_{10}	Rainfall (R)	0.82	1.21
	Temperature (T)	0.35	2.83
	Relative Humidity (H)	0.62	1.61
	Pressure (P)	0.26	3.72
	Wind Speed (WS)	0.93	1.07

Correlation analyses were done for the determination of correlation coefficients between air pollution concentration and each input variable including the previous day's pollution concentration. The result of correlation analysis is represented in Table 4.

Table 4 Correlations among Pollutant and Meteorological Parameters

Air pollutants	Rainfall	Temperature	Relative Humidity
$PM_{2.5}$	-0.257	-0.743	-0.518
PM_{10}	-0.295	-0.677	-0.499
Air pollutants	**Pressure**	**Wind Speed**	**PDPM**
$PM_{2.5}$	0.734	-0.191	0.88
PM_{10}	0.729	-0.249	0.863

Input parameter subsets for different models are shown in Table 5. The ANFIS model results in different input combinations are shown in Table 6. The scatter plots between observed and predicted values of PM_{10} & $PM_{2.5}$ conc. are indicated in Figs. 3 and 4 respectively.

Table 5 Input Parameter Subset for Different Models

PM_{10}	Model 1	PM_{10}-$PDPM_{10}$,P,T,H,R,WS
	Model 2	PM_{10}-$PDPM_{10}$,P,T,H,R
	Model 3	PM_{10}-$PDPM_{10}$,P,T,H
	Model 4	PM_{10}-$PDPM_{10}$,P,T
	Model 5	PM_{10}-$PDPM_{10}$,P
	Model 6	PM_{10}-$PDPM_{10}$
$PM_{2.5}$	Model 1	$PM_{2.5}$-$PDPM_{2.5}$,T,P,H,R,WS
	Model 2	$PM_{2.5}$-$PDPM_{2.5}$,T,P,H,R
	Model 3	$PM_{2.5}$-$PDPM_{2.5}$,T,P,H
	Model 4	$PM_{2.5}$-$PDPM_{2.5}$,T,P
	Model 5	$PM_{2.5}$-$PDPM_{2.5}$,T
	Model 6	$PM_{2.5}$-$PDPM_{2.5}$

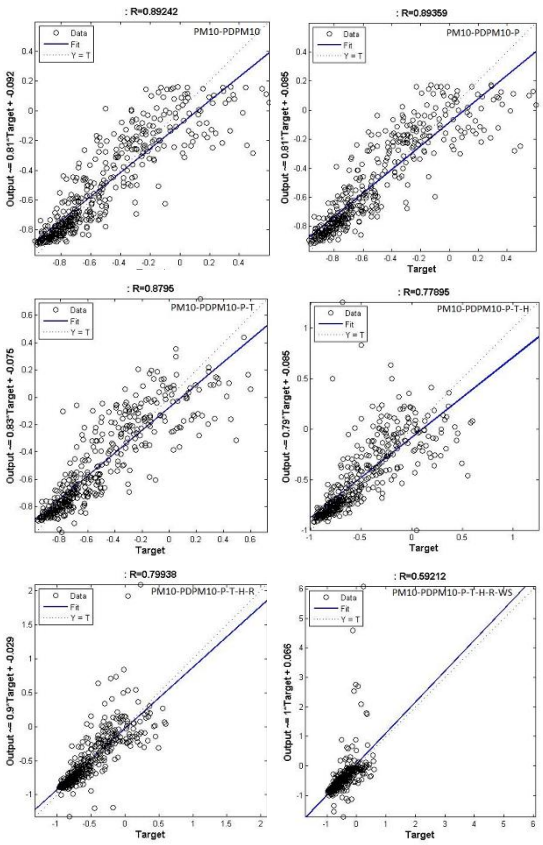

Fig. 3 Scattered Plots for Correlation (R) for same-day forecasting of PM_{10}

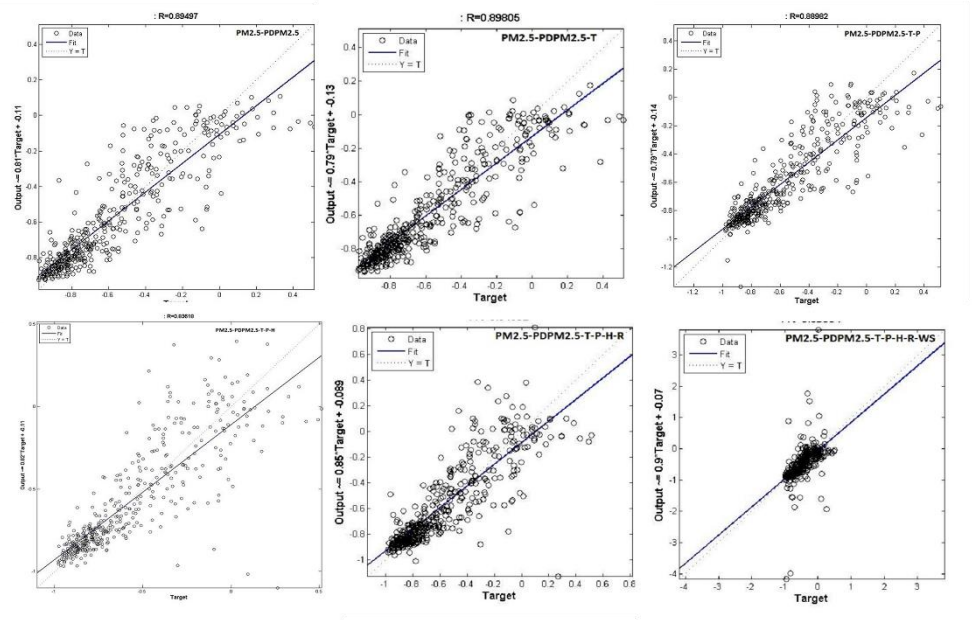

Fig. 4 Scattered Plots for Correlation (R) for same-day forecasting of $PM_{2.5}$

Table 6 ANFIS model results in different input combinations

It is seen that Model 01 with input variables

Same Day Forecasting PM_{10}						
INDICES	Model-06 (PM_{10}-PDPM$_{10}$)	Model-05 (PM_{10}-PDPM$_{10}$,P)	Model-04 (PM_{10}-PDPM$_{10}$,P,T)	Model-03 (PM_{10}-PDPM$_{10}$,P,T,H)	Model-02 (PM_{10}-PDPM$_{10}$,P,T,H,R)	Model-01 (PM_{10}-PDPM$_{10}$,P,T,H,R,WS)
RMSE	0.1590	0.1585	0.1695	0.237	0.2421	0.5032
R^2	0.7928	0.7948	0.77	0.604	0.6361	0.3490
NMSE	0.0970	0.0972	0.1111	0.2221	0.2311	1.0433
FB	-0.0143	-0.0220	-0.0214	-0.0424	-0.0417	-0.0854
IOA	0.9860	0.9862	0.9844	0.9700	0.9693	0.8831
INDICES	Model-06 ($PM_{2.5}$-PDPM$_{2.5}$)	Model-05 ($PM_{2.5}$-PDPM$_{2.5}$,P)	Model-04 ($PM_{2.5}$-PDPM$_{2.5}$,P,T)	Model-03 ($PM_{2.5}$-PDPM$_{2.5}$,P,T,H)	Model-02 ($PM_{2.5}$-PDPM$_{2.5}$,P,T,H,R)	Model-01 ($PM_{2.5}$-PDPM$_{2.5}$,P,T,H,R,WS)
Same Day Forecasting $PM_{2.5}$						
RMSE	0.1484	0.1471	0.1536	0.1887	0.1825	0.4133
R^2	0.7973	0.8028	0.7881	0.6960	0.7173	0.3465
NMSE	0.0691	0.0662	0.0711	0.1101	0.1042	0.5216
FB	0.0012	0.0266	0.0410	0.0155	0.0044	0.0279
IOA	0.9891	0.9892	0.9883	0.9828	0.9839	0.9274
One Day Advance Forecasting $PM_{2.5}$						
RMSE	0.1759	0.1698	0.1750	0.2025	0.1941	0.2840
R2	0.7113	0.7305	0.7165	0.6431	0.6607	0.4664
NMSE	0.0942	0.0868	0.0929	0.1241	0.1139	0.2518
FB	-0.0087	0.0027	-0.0051	-0.0023	-0.0010	-0.0336
IOA	0.9847	0.9857	0.9851	0.9805	0.9819	0.9636

$PDPM_{10}$, P, T, R, and WS for forecasting same day PM_{10} has RMSE of 0.5032 which is not close to 0, R^2 was only 34.90% which is not that satisfactory and IOA is 0.8831 which is not that much close to 1. On the other hand, it is observed Model 05 with input variables $PDPM_{10}$, P for forecasting same day PM_{10} had RMSE of 0.1585 which is much closer to zero, R^2 is 79.48% which indicated quite excellent result and IOA is 0.9862 which is much closer to 1.For same day forecasting $PM_{2.5}$ it is observed that Model 05 with input variables $PDPM_{2.5}$, T for forecasting same day $PM_{2.5}$ had RMSE of 0.1471 which is much closer to zero, R^2 is 80.28% which indicates quite excellent result and IOA is 0.9892 which is much closer to 1. Again for 1-day advance forecasting for $PM_{2.5}$ Model 5 performs better. All other models' values were in between those two models. For all models, NMSE & FB were calculated to check the models' condition and values came out quite satisfactory.

DISCUSSION

The input combination used in MODEL 5-PM_{10} & MODEL 5-$PM_{2.5}$ can be selected for optimal forecasting. It is observed that with the data of previous day's $PM_{2.5}/PM_{10}$ concentration, current $PM_{2.5}/PM_{10}$ concentration and with only one environmental parameter among five different parameters (Temperature for $PM_{2.5}$ & Air pressure for PM_{10}), a better forecasting can be done. This process saves computational time. By plotting of real PM ($PM_{2.5}/PM_{10}$) concentration data and predicted PM ($PM_{2.5}/PM_{10}$) concentration for best model, a similar trend is seen. In case of PM_{10}, it was notable that only with input parameter previous day PM_{10} and pressure value prediction of PM_{10} came out well whereas in case of $PM_{2.5}$, input parameter- previous day $PM_{2.5}$ and temperature value prediction of $PM_{2.5}$ showed better output. In both cases previous day's particulate matters value were needed but because of difference in particulate matter size second input might be varying. FS method successfully reduced the computational complexity and output error. There are a few limitations of this forecasting model. For example, weather parameters are considered here only but $PM_{2.5}/PM_{10}$ concentration can fluctuate because of urbanization (construction work), industrialization (brick kilns) & traffic emission etc.

CONCLUSION

Neuro-fuzzy logic is a probabilistic approach used for forecasting purposes providing a good alternative to existing models based on time series like ANN. This technique can analyse and interpret any kind of information. It seems that timely forecasting of air quality lets authorities alarm the residents and helps them manage its detrimental effects.The ANFIS model predictor considers the value of meteorological variables like pressure, temperature, relative humidity, wind speed, rainfall and previous day's pollutant concentration in different combinations as the inputs for the prediction of the same day air quality concentration. Collinearity tests and FS techniques reduced input combination that lowers computational complexity and predicts with less errors.

ACKNOWLEDGEMENTS

Authors are thankful to US Embassy, Dhaka, Bangladesh for making air pollution data available on the website for public use.

REFERENCES

[1] Dockery D.W., Pope C.A., 3rd Acute respiratory effects of particulate air pollution. Annual Review of Public Health 1994, Vol.15, pp.107-132.

[2] Xing Y. F., Xu, Y. H., Shi M. H.,& Lian Y. X.,The impact of PM2.5 on the human respiratory system. Journal of thoracic disease, Vol.8 (1), 2016, E69-E74.

[3] Jang J.S.R., Sun C.T., Mizutani E., Neuro-fuzzy and soft computing: a computational, approach to learning and machine Intelligence, IEEET Automat Control, Vol.42, No.10, 1997.

[4] Tektas M.,Weather Forecasting Using ANFIS and ARIMA- A Case Study for Istanbul, Environmental Research, Engineering and Management, Vol. 1 (51), pp. 5–10, 2010.

[5] Cerioli A., Farcomeni A., Riani M., Strong consistency and robustness of the Forward Search estimator of multivariate location and scatter. Journal of Multivariate Analysis, Vol.126, 2014.

[6] Chen G. J., A simple way to deal with multi-collinearity, Journal of Applied Statistics, Vol.39, Issue.9, 2012, pp.1893-1909.

[7] Hair, J., Black, W. C., Babin, B. J., & Anderson, R. E. (2010). Multivariate data analysis (7th ed.). Upper saddle River, New Jersey: Pearson Education International.

[8] Prasad K., Gorai A.K., Goyal P., Development of ANFIS models for air quality forecasting and input optimization for reducing the computational cost and time, Atmospheric Environment, Vol. 128,2016,pp. 246-262.

11th Int. Conf. on Geotechnique, Construction Materials & Environment, Kyoto, Japan, 3-5 November 2021, ISBN: 978-4-909106063 C3051

THE RECYCLING WASTE FROM SUGAR INDUSTRY: THE OPTIMALIZATION OF CO2 ADSORPTION CAPACITY ON SUGARCANE BAGASSE-BASED BIOCHAR AND ZEOLITE

Ambar Pertiwiningrum[1], Margaretha Arnita Wuri[2], Widyawati Luhur Pambudi[3], Andang Widi Harto[4], Alva Edy Tontowi[5] and Rachmad Nur Besari[6]

[1,3,6]Faculty of Animal Science, Universitas Gadjah Mada, Indonesia; [2]Center for Energy Studies, Universitas Gadjah Mada, Indonesia; [4,5]Faculty of Engineering, Universitas Gadjah Mada, Indonesia

ABSTRACT

The recycling of biomass waste for CO_2 adsorption in biogas purification is still rare. This study was investigated the CO2 adsorption capacity by sugarcane bagasse-based biochar and natural zeolite with a volume ratio of 50%:50%. The CO_2 adsorption test carried out using biogas purificator in the difference adsorption time (10, 15, 20 and 25 minutes). The biogas was purified by adsorbing CO_2 in the mixture gases. Adsorption CO_2 on sugarcane bagasse-based biochar and zeolite have been investigated at a room temperature and gas pressure ranging from 6-8 bar. The CO_2 adsorption capacity was further reduced by increasing adsorption time. The combination of sugarcane bagasse-based biochar and zeolite exhibited a high CO_2 removal capacity of 78.49% at 10 minutes of adsorption time. The CO_2 adsorption capacity was saturated by the increase in time adsorption. The lowest CO_2 adsorption capacity was performed at 25 minutes adsorption time with CO_2 removal capacity of 12.34%.

Keywords: Adsorption, Biochar, Carbon dioxide, Sugarcane bagasse, Zeolite

INTRODUCTION

Based on Indonesia Energy Outlook [1], Indonesia has biomass energy potential of 32,654 MW that comes from animal, edible and non-edible plants. These resources can be converted to biogas energy for supplying national energy. Biogas becomes an alternative energy that substitute to LPG (liquid petroleum gas). In Indonesia, LPG demand is expected increase from 7.2 million tons in 2017 to 17.4 million tons in 2050 [2], whereas currently LPG production only 2 million tons. The increasing import of LPG is feared to burden Indonesia's current trade balance so that to meet the demand, it needs other alternative energies. Therefore, an alternative energy like biogas for cooking in households needs to be encouraged.

One of the large potentials of biomass in Indonesia is waste from sugarcane industries. Sugarcane industries are one of acro-based industries that produce huge quantity of waste during sugar production. Until 2016, Indonesia has 63 sugar mills owned by 18 companies with a total running capacity of 245,900 tons per cane per day [3]. In 2019, a total running capacity in sugarcane industries in Indonesia of 278,411 tons per cane per day [4]. It means waste from sugary industries will increase with the increase in production capacity of sugar in Indonesia.

First step sugar production from sugarcane is juice extraction or cane crushing using crushing rollers. After extraction of the juice, the fibrous material is known as bagasse [5]. Nelson et al. [6] reported that bagasse yield in every 1000 tons sugarcane is 27%. Munagala and Yogendra [7] also reported that one ton of sugarcane yields 0.3 tons of bagasse. The bagasse is composed of 40-50% of cellulose, 30-35% hemicellulose, 20-30% lignin and small percentage other material [8]. Utilization of bagasse usually for producing energy, paper, and cattle feed [5]. Lignocellulosic feedstock in bagasse also can be used for energy [7] or the other application like adsorbent. Valorization of bagasse as adsorbent can be used in biogas purification by carbonization process. This conversion leads to implement circular bioeconomy concept for sustainable management in sugary industries. Conversion of waste from sugary industries is revealed reduced carbon dioxide emissions [9].

Wojciech [10] explained that adsorption is one of methods in biogas purification the efforts in. By adsorption biogas produces high methane and calorific value. Himjyoti and Charu [11] explained that natural zeolite and clay are nature-based materials that can be used as CO_2 absorbing adsorbents. In addition, activated carbon, biochar, and flying ash from biomass waste have been widely developed as alternative adsorbent.

Bagasse can be used as precursor of biogas adsorbent because of its abundant commodity in the environment so that it can reduce production. The converting bagasse to biochar aims to increase the adsorption ability [12]. Rizkyarief [13] stated that the

advantage of biochar is its good capacity in adsorption, biochar has pore structure and chemical functional groups on the surface. Therefore, biochar can absorb carbon levels well.

Many factors effect on biogas purification performance. Difference in the physical properties of adsorbent generate differences in the adsorption performance [14]. The carbon dioxide adsorption undergoes a physical and chemical adsorption at the surface of adsorbent. The important factors influencing on carbon dioxide adsorption are the basicity and pore size of adsorbent [15]. Beside internal factors, external factors like temperature, air pressure and contact time also influence on carbon dioxide adsorption. According to A, Boonpoke et al. [10], for the temperature range of 30-150ºC, carbon dioxide adsorption capacity on activated carbon decreased as adsorption temperature and air pressure increased. The same results also reported by Masoud and Fatemeh [16]. Masoud and Fatemeh and Diogo *et al*. [17] are reported that the optimum pressure for carbon dioxide adsorption at range of 5-7 bar. For contact time, Anne *et al*. [18] observed that the kinetic carbon dioxide adsorption process occurred very quickly in the first ten minutes and slowed down after ten minutes and flattened at 60 minutes. It means that the equilibrium has been reached at 60 minutes contact time. The same phenomenon also reported by Lalhmingsanga and Pinakeswar [19] and Xiaoyun *et al*. [20].

In this study, we investigated the influence of adsorption contact time on biochar-based sugarcane bagasse. The investigation conducted for finding the optimal contact time in biogas purification.

METHODOLOGY

Biochar-based Sugarcane Bagasse

Sugarcane bagasse that collected from the surrounding environment was still in a wet condition so it needs to be dried under sunlight for several days. Then sugarcane bagasse pyrolyzed at a temperature of 255°C for 3 hours.

Biogas Purification – Carbon Dioxide Adsorption

Carbon dioxide adsorption was conducted at room temperature and pressure range of 5-7 bar. Adsorption column type that used in this study is packed second-level bed column with a column length of 20 cm and a diameter of 3 cm. Every column filled adsorbent with the formulation in Table 1. The column directly connected with biodigester and biogas holder. Biogas mixture will be passed through the column for carbon dioxide adsorption process by air compressor. The

Table 1 The composition of adsorbents in every column (%volume)

Items	Biochar-based sugarcane bagasse (%)	Zeolite (%)
ZZ	0	100
ZB1	25	75
ZB2	50	50
ZB3	75	25
ZB4	100	0

The results of the best composition adsorbent that seen from the highest decrease in carbon dioxide is used for contact time variation treatment. The variation of contact time was carried out for 10, 15, 20 and 25 minutes.

RESULTS AND DISCUSSION

Carbon Dioxide Adsorption in The Difference Composition of Adsorbent

The level of carbon dioxide as impurity gas in biogas is an important indicator to determine the quality of the biogas. The lower level of carbon dioxide shows that a better quality of biogas produced. In this study, the results of carbon dioxide decreasing in the difference compositions (Table 2) will be used as a reference in the difference contact time experiment.

Table 2. The decrease carbon dioxide in the difference composition of adsorbents

Items	Before adsorption (ppm)	After adsorption (ppm)	The reduction of CO_2 (%)
ZZ	214,700	229,000	-6.00
ZB1	261,360	213,540	17.33
ZB2	178,720	38,445	77.66
ZB3	221,020	203,720	7.33
ZB4	180,830	212,020	-17.00

Note: - means an increase in carbon dioxide composition.

The results that presented in Table 2 indicate that the highest decrease in carbon dioxide level was performed by the adsorbent composition of 50% sugarcane bagasse-based biochar and 50% of natural zeolite (ZB2) with the decrease level of 77,66% and the lowest decrease was in the treatment performed by 100% sugarcane bagasse-based biochar (ZB4) with the decrease level of -17,00%. A balanced combination of zeolite and biochar will maximize the carbon dioxide adsorption because they have

different properties in its absorption but complement each other. Abdul and Masrukhil [21] state that zeolite is hydrophilic and polar which is able to bind oxygen while biochar is hydrophobic and nonpolar which is able to bind carbon, so that the combination of the two absorbents will maximize absorption. A. Alonso-Vicaro [22] stated that natural zeolites and biomass-based absorbents need to be further activated in order to have wider pores so that they can more maximize in carbon dioxide adsorption.

Carbon Dioxide Adsorption in The Difference Contact Time

Many reports showed that the difference of adsorption contact time influenced on adsorption capacity. In this study, the influence of contact time on biochar-based sugarcane bagasse was investigated. The aim of this study is finding the optimal condition for biogas purification using biochar-based sugarcane bagasse. In this study, the highest carbon dioxide adsorption capacity in the previous study was used for next experiment, the difference of contact time. Based on the results on Table 2 showed that the using of combination of 50% volume of zeolite and 50% of biochar (ZB2) performed the best carbon dioxide adsorption capacity of 77.66%. The combination of 50% volume of zeolite and 50% of biochar (ZB2) used for next experiment in the variation of contact time of 10, 15, 20 and 25 minutes.

After the experiment, gas samples before and after adsorption were analyzed by gas chromatography. The results of gas chromatography analysis were showed in Table 3.

Table 3 The decrease carbon dioxide in the difference adsorption contact time

Time (minutes)	Before adsorption (ppm)	After adsorption (ppm)	The decrease in CO_2
10	178,715.98	38445.64	78.46
15	219,024.58	113,079.69	48.28
20	289,014.54	191,709.38	33.13
25	287,056.84	251,638.30	11.19

Results in Table 3 presents that the variation contact time effected on the decrease in carbon dioxide. The highest carbon dioxide adsorption performed by combination of 50% volume of zeolite and 50% of biochar (ZB2) with adsorption contact time for 10 minutes. It can be concluded that the longer adsorption time, the lower level of carbon dioxide decreasing. It occurred due to the maximal adsorption capacity in first ten minutes. The contact time more than 10 minutes, carbon dioxide adsorption capacity decreased. With the increasing time of adsorption, the pores were filled with more carbon dioxide molecules so that the adsorption capacity decreased. This condition can even reach the saturation point [15-16]. Investigation to find the saturation point in adsorption time need to be inspected at the next research.

CONCLUSION

The results of this study, on optimizing carbon dioxide adsorption with sugarcane bagasse-based biochar and zeolite, concluded that the highest decrease in CO_2 occurred in the use of 50% sugarcane bagasse-based biochar and 50% zeolite (ZB2) with a decrease carbon dioxide level of 77,66% and was used as an indicator of time variation treatment. This study also revealed that contact time of adsorption effected on the decrease carbon dioxide level. The longer adsorption time resulted more saturated point in carbon dioxide adsorption. The use of 50% sugarcane bagasse-based biochar and 50% zeolite (ZB2) in carbon dioxide adsorption in biogas purification has saturation point at 25 minutes of adsorption time.

So, in general, this study states that differences in the composition of the adsorbent and the contact time affect the carbon dioxide adsorption capacity. The longer in the adsorption contact time, the lower the carbon dioxide adsorption capacity.

ACKNOWLEDGMENTS

We gratefully acknowledge the support from BRIN - Ristek Grant through the Research Directorate of Universitas Gadjah Mada with a contract number of 2134/UN1/DITLIT/DIT-LIT/PT/2021. We also thank the Center of Agro Technology Innovation for contribution in this research and college students of Faculty of Animal Science Universitas Gadjah Mada for helping in collecting the data.

REFERENCES

[1] Secretariat General National Energy Council, Ministry of Energy and Mineral Resources, 2019, pp.1-75.
[2] Center of Assessment of Process Industry and Energy, Agency for the Assessment and Application of Technology, 2019, pp.1-90.
[3] Aris T. and Triantarti., An Overview of Sugar Sector in Indonesia. Sugar Technology, Vol.18, 2016, pp.636-641.
[4] Garret M. and Sugiarti M., Indonesia Sugar Annual Report 2019, USDA Foreign Agricultural Service, 2019, pp.1-10.
[5] Amit B., Kavindra K.K. and Narasinha S.,

Multidisciplinary Approaches to Handling Wastes in Sugar Industries. Water Air Soil Pollution, Vol.227, Issue 11, 2016, pp.1-30.

[6] Nelson L.N., Franklun J.A., Franklin A. and Frank P.A., International Thomson Publishing Company, 1998, pp.1-748.

[7] Munagala M. and Yogendra S., Sustainable Valorization of Sugar Industry Waste: Status, Opprtunities, and Challenges. Bioresource Technology, Vol.303, 2020, pp.1-10.

[8] Harish M.N., Nagendra M.S. and Amaresh P., Utilization of Sugar Industry Wates in Agriculture. Agriculture and Food e-Newsletter, Vol.2, Issue 1, 2020, pp.14-23.

[9] Fateme M., Anne R., Mohammad A.A., Majid A. and Hossein V., Life Cycle Assessment (LCA) of The Energetic Use of Bagasse in Irianian Sugar Industry. Renewable Energy, Vol.145, 2020, pp.1870-1882.

[10] Wojciech M.B., A Review of Potential Innovations for Production, Conditioning and Utilization of Biogas with Multiple-Criteria Assessment. Renewable and Sustainable Energy Reviews, Vol.54, Issue 2, 2016, pp.1148-1171.

[11] Himjyoti D. and Charu L.M., Traditional Parboiled Rice-Based Products Revisited: Current Status and Future Research Challenges. Rice Science. Vol.21, Issue 4, 2016, pp.187 – 200.

[12] Ade A., The Used of Sugarcane Bagasse Charcoal as An Adsorbent of Metal Ions Cd, Cr, Cu and Pb in Wastewater. Syarif Hidayatullah State Islamic University Jakarta, 2010.

[13] Rizkyarief E., The Use of Carbon Active Bagasse for Reducing Concentration of Metal Pb In Aqueos Solution, University of Semarang, 2017.

[14] A. Boonpoke, S. Chiarakorn, N. Laosiripojana, S. Towprayoon and A. Chidthaisong, Synthesis of Activated Carbon and MCM-41 from Bagasse and Rice Husk and Their Carbon Dioxide Adsorption Capacity. Journal of Sustainable Energy and Environment, Vol.2, 2011, pp.77-81.

[15] Danielle B., Mourad K., Patrick N., Murielle M., and Robert H., Advances in Principal Factors Influencing Carbon Dioxide Adsorption on Zeolites. Science Technology Advanced Materials, Vol.9, 2008, pp.1-7.

[16] Masoud M. and Fatemeh G., Gas Adsorption of CO_2/CH_4 System using Zeolite 5A. Microporous and Mesoporous Materials, Vol.200, 2014, pp.1-10.

[17] Diogo P.B., Ronan S.O., Rodrigo S.V., Celio L.C.Jr., and Diana C.S.A., Adsorption of CO_2 on Nitrogen-enriched Activated Carbon and Zeolite 13X. Adsorption, Vol.17, 2011, pp.235-246.

[18] Anne E.C., Bin G. and Ming Z., Carbon Dioxide Capture using Biochar Produced from Sugarcane Bagasse and Hickory Wood. Chemical Engineering Journal, Vol.249, 2014, pp.174-179.

[19] Lalhmingsanga H. and Pinakeswar M., Carbon Dioxide Adsorption on Zeolites and Activated Carbon by Pressure Swing Adsorption in a Fixed Bed. International Journal Energy Environment Engineering, Vol.5, 2014, pp.349-356.

[20] Xiaoyun X., Yue K., Ling Z. and Xinde C., Chemical Transformation of CO2 during Its Capture by Waste Biomass Derived Biochars. Environmental Pollution, Vol.213, 2016, pp.533-540.

[21] Abdul M.R. and Masrukhi M., Optimalization of Methane Biogas from Cow Manure by Using Difference Absorbents. Journal of Agricultural Engineering, Vol.10, Issue 2, 2017, pp.8-17.

[22] A. Alonso-Vicar, Jose R.O., S.G. Gil-Rio, O. Gomez-Jimenez-Aberasturi, C.A. Ramirez-Lopez, J. Torrecilla-Soria and A. Dominguez, Purification and Upgrading of Biogas by Pressure Swing Adsorption on Synthetic and Natural Zeolites. Microporous and Mesoporous Materials, Vol. 134, 2010, pp.100-107.

11th Int. Conf. on Geotechnique, Construction Materials & Environment,
Kyoto, Japan, 3-5 November 2021, ISBN: 978-4-909106063 C3051

REPRODUCTIVE ECOLOGY OF THE ENDANGERED *PYRUS CALLERYANA* DECNE IN URBAN PARKS

Naoya Motoori[1]and Michiko Masuda[2]

[1,2]Faculty of Technology, Nagoya Institute of Technology, Japan

ABSTRACT

Recently urban development has invaded conservation-important biotic communities, including the endangered Pyrus calleryana Decne, which exists in urban parks, in the Center of Japan. The condition of urban parks is not suitable for the species so the number of the species is decreasing in most habitat. In order to conserve the species, the reproductive elements, the number of flowers, fruits and seeds, and survival rate of the seeds were measured in some parks for 10 years. Then the reproduction is not successful in the half of the parks. The number of the flower and fruit were fluctuating among years. And the half of the seeds was not useful for the survival rate. The result of that, the seedlings of the species were not produced. For the self-incompatibility of the species prevent the production of seeds. The absence of the pollinators was expected because of the agriculture chemical is used in urban parks for the people.

Keywords: Pyrus calleryana Decne, Number of flowers, Number of fruits, Year fluctuation

INTRODUCTION

In recent years, attention has been focused on the importance of biodiversity. In October 2010, the 5th Conference of the Parties to the Cartagena Protocol on Biosafety of the Convention on Biological Diversity (COP-MOP5) and the 10th Conference of the Parties to the Convention on Biological Diversity (COP10) were held in Nagoya City, Aichi Prefecture. At COP10, the new global goal "Aichi Targets (Strategic Plan 2011-2020)" by 2020 was formulated, and the "Nagoya Protocol", which is an international framework for ABS (acquisition of genetic resources and profit sharing) adoption was raised.

In the Tokai region, including Aichi prefecture, many spring swamps are distributed and endemic flora exists. This endemic flora is called the "Tokai Hill Element" [1]. It has been reported that the number of existing Tokai hill elements is small due to the development of hills [5]. Due to the recognition of the importance of the environment in which the above flora grows, various conservation groups are currently giving conservative consideration. On the other hand, these floras are often designated as protected areas because of their rarity. For this reason, it is difficult to investigate, there is a lack of ecological knowledge, and even if transplanted, it often dies.

Pyrus calleryana Decne, which was the subject of this study, is a type of Tokai hill element that is distributed only in Aichi, Gifu, and Mie prefectures.It is designated as Critically Endangered IA (CR) in Aichi Prefecture and Endangered IB (EN) in Mie Prefecture.Critically Endangered IA (CR) is at extremely high risk of extinction in the wild in the very near future, Endangered IB (EN) is not as dangerous as IA, but is at risk of extinction in the wild in the near future is extremely high [4]. In addition, this species, along with Vaccinium sieboldii Miq, is the most critical of the plants that characterize Aichi Prefecture, and requires systematic protection measures [6].

The *Pyrus calleryana* Decne population, which is large enough for breeding, is distributed in Inuyama, Owariasahi, Kuwana, and Komaki. *Pyrus calleryana* Decne has different ecological characteristics and flower scents depending on the local population. Therefore, it is highly possible that they are ecologically differentiated. Understanding the unique ecological characteristics is important in considering genetic diversity.Therefore, the purpose of this study is to create a foundation for conservation activities suitable for the habitat by conducting a counting survey of the number of flowers and fruiting in the habitat of Callery pear in Komaki City and clarifying the characteristics of the habitat.

MATERIALS AND METHODS

Study Plant

The subject of this study is Callery pear, which belongs to the subfamily Rosaceae and subfamily Pear (Fig. 1). It is closely related to Pyrus pynifolia Decne. It is a deciduous small tree that branches well and has a height of 8-10 m. The bark is gray-purple-black with vertical cracks. Leaves alternate on long branches or mostly bundled on short branches, broad-ovate, oval or oval oblong, sharp-pointed at the tip, usually round at the base, 4-9 cm long, 3-6 cm wide, has fine blunt serrations on the edges, and initially has

white vellus hair, but later becomes hairless. The flowering season is from March to April, the flowers are white and about 2.5 cm in diameter, with 5 petals, 2-3 styles, and 6 ovules.

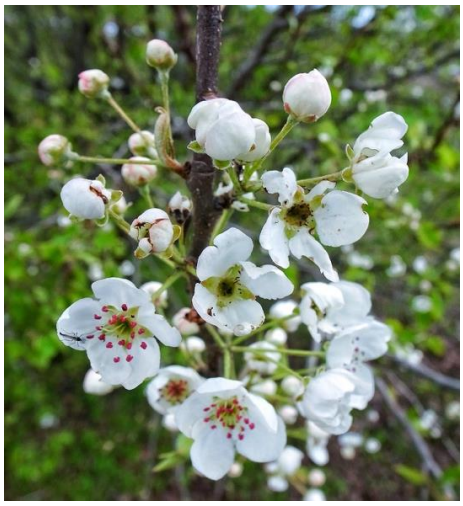

Fig. 1 Photo of *Pyrus calleryana* Decne

The fruit is almost spherical, about 1 cm in diameter, yellowish brown with many small round lenticels, and is a thorny tree, so it may be cut down as an obstacle [6] (Fig. 2).

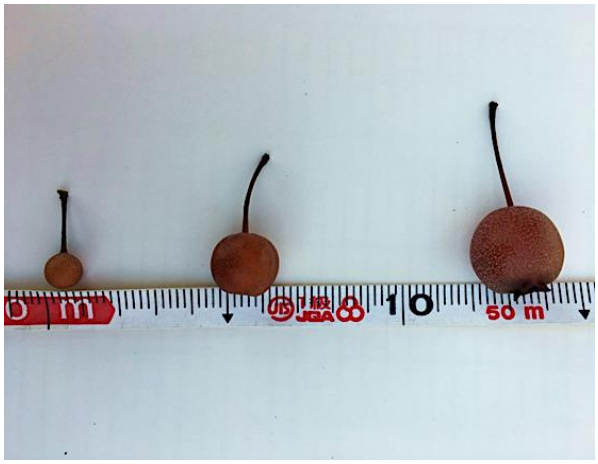

Fig. 2 From left: *Pyrus calleryana* Decne, intermediate species, callery pear fruit

Pyrus calleryana Decne has the property of self-incompatibility. Self-incompatibility is a general term for several types of genetic properties that prevent self-pollination in order to maintain genetic diversity. Self-incompatibility can be divided into three levels. First, even if pollen of the same strain is attached to the pistil, the pollen tube does not be extend and pollination does not occur. Next, pollen of the same strain is attached to the pistil and pollinated, but the reaction is such that no fruit is produced. Finally, pollen of the same strain is attached to the pistil and pollinated to produce fruits, but the seeds do not function normally. It is known that seeding is difficult in populations that have lost genetic diversity.

It is known that *Pyrus calleryana* Decne has different ecological characteristics depending on the population. Therefore, it is highly possible that they are ecologically quite differentiated. As for the polyneta, the population of Nagoya City has the largest number of honeybees, and the population of Komaki City has the largest number of honey fly. About the same number of honeybees and honey fly were found in the population of Kuwana City. The presence of pollinators is important because of the nature of self-incompatibility. It is thought that the range of gene flow by pollen is 5 km in the case of Western honeybee and about 100 m in the case of honey fly. Seed dispersal was expected to be carried out by birds, but it was pointed out that it was not eaten frequently. For this reason, it is thought that many of them are transported by free fall or water flow. In recent years, spraying by raccoon dogs has been confirmed, and it is known that a large amount of seedlings are germinated from raccoon dog droppings (Fig. 3). The seed dispersal range is considered to be about 5 km from the raccoon dog's range of action. It is thought to be about 10 km when sprayed by bulbuls and starlings.

Fig. 3 Seedlings germinating from raccoon dog droppings

Predation by bulbuls and starlings is relatively common in Moriyama and Seto, and the spraying style varies from region to region.

Study Site

The survey site is Komaki City, which is located in the northwestern part of Aichi Prefecture (Fig. 4).

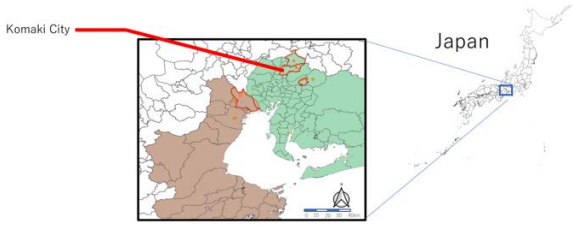

Fig. 4 Komaki City

The survey site in Komaki City is the habitat of *Pyrus calleryana* Decne, a large grass on the east coast of the Dairakami pond (Fig. 5).The Daira pond is one of the largest agricultural ponds in the city. The pond on the north side is called the Dairakami pond, the south side is called the Shimodaira pond, and there are paddy fields in between. In the hills of Daira pond, which is dotted with agricultural land, residential land, and thickets, a factory complex has been constructed on the east side since 2010. In addition, there is Toukadai New Town on the west side, and development projects have been carried out from 1972 to 1999.

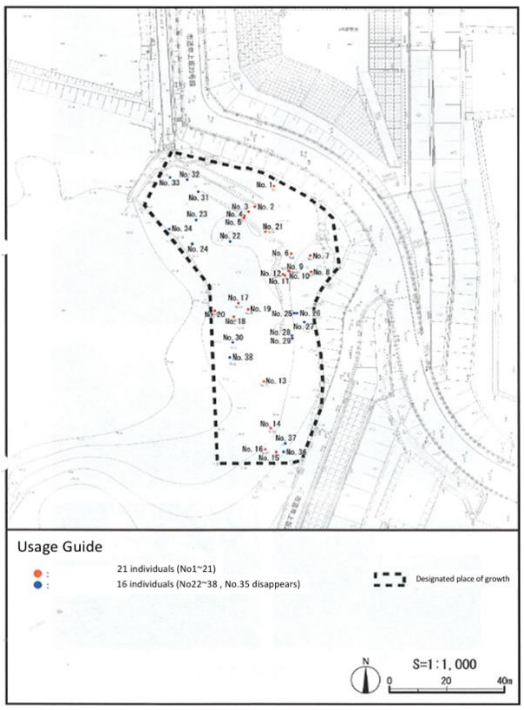

Fig. 5 Position of the individual in the Dairakami pond, which is the survey site of Komaki City.

The habitat of *Pyrus calleryana* Decne is often located at the edge of the pond, suggesting that it may be maintained in relation to humans.

Method

Flowering number, Fruiting number survey

The survey period is 2013-2020. The number of flowers was measured for flowering individuals from March to May, which is the flowering time of *Pyrus calleryana* Decne. In addition, the number of fruit set was measured for all fruiting individuals from October to November, which is the fruiting time of *Pyrus calleryana* Decne.

The measurement method is rough because the number of measurements is enormous. Count the reference 100 sets and count how many of them there are. Count with 2-3 people, and let the average value be the number of flowers and the number of fruits.

RESULT

Flowering Number, Fruiting Number Survey

Table 1 shows the number of flowers per individual in 2013-2020, and Table 2 shows the number of fruit set per individual in 2013-2020.

Table 1 Flowers number for each individual in 2013-2020

No.	2013	2014	2015	2016	2017	2018	2019	2020
0	0	1200	6500	2200	1100	500	1920	120
1	157	20000	15000	6000	12000	15000	13500	39760
2	126	10000	13000	5500	9500	10000	9800	17760
3	235	40000	15000	6100	11000	10000	19100	16450
4	17	1000	1200	15	-	-	-	-
5	111	60000	25000	19000	12500	60000	54200	66370
6	173	20000	20000	5150	12000	10000	44700	6960
7	470	33000	25000	14000	13000	20000	50550	51230
8	159	22000	22000	21000	19000	25000	61100	26260
9	4	35000	8000	11500	12000	20000	57000	12400
10	-	10000	100	370	320	1000	1200	250
11	-	20	1000	320	5	5000	440	580
12	-	0	30	0	-	-	-	-
13	4080	60000	60000	31000	15000	50000	30600	41850
14	2600	20000	23000	8100	2800	15000	9350	13780
15	4850	17000	20000	2800	230	400	230	220
16	2400	24000	20000	460	250	300	400	190
17	1260	30000	25000	19200	5500	500	34100	2190
18	1720	24000	25000	16500	16000	25000	20450	17710
19	0	0	550	350	100	500	390	400
20	3450	16000	20000	24000	16000	15000	15100	13430
21	1730	50000	28000	14000	15000	50000	395400	65380
22	1030	800	5000	1500	400	25000	62380	27640
23	1550	15000	18000	3650	600	20000	5175	9890
24	460	1000	9000	5100	1800	500	13490	10580
25	670	650	1200	720	2500	20000	9660	21580
26	2340	780	2500	1100	2500	25000	12750	27500
27	0	840	2000	320	400	5000	2150	1950
28	0	10	10	50	0	500	10	0
29	620	2000	2500	80	0	1000	60	490
30	-	10	50	0	0	300	550	1510
31	-	500	5500	830	400	50	3890	4480
32	-	20000	6000	1600	800	20000	8230	12890
33	-	55	2000	410	320	10000	500	460
34	-	30	50	60	0	0	20	30
35	-	750	0	-	-	-	-	-
36	-	-	-	-	-	-	-	-
37	-	-	-	-	-	-	-	-
38	-	-	-	-	-	-	-	-

Table 2 Fruit number for each individual in 2013-2020

No.	2013	2014	2015	2016	2017	2018	2019	2020
0	-	20	40	5	450	0	20	1
1	10	2500	240	90	10000	500	4000	25000
2	0	3000	160	160	9000	250	2500	2100
3	0	32000	200	40	9500	0	4500	3500
4	0	50	10	-	-	-	-	-
5	30	40000	1300	1700	7000	300	6000	12000
6	20	20000	250	100	10000	400	2000	950
7	100	200	400	50	8500	50	6500	5500
8	0	20000	100	50	12000	0	4000	8000
9	0	3000	1300	300	4000	50	14000	500
10	-	150	30	50	50	0	250	50
11	-	10	10	40	4	0	100	100
12	-	-	-	-	-	-	-	-
13	3100	30000	4000	200	2500	500	4500	15000
14	800	18000	2500	190	520	250	5500	5000
15	1800	10000	400	800	200	0	0	200
16	200	100	80	0	120	0	70	0
17	270	22000	500	2000	4500	0	5000	1000
18	120	22000	2500	450	7800	200	3000	2500
19	0	0	60	50	45	100	150	200
20	450	12000	7000	1200	15000	3000	6000	8500
21	50	22000	500	240	13500	3000	10000	15000
22	50	100	60	140	350	400	4500	3000
23	850	1100	280	220	550	150	250	500
24	120	220	420	270	1650	50	1250	700
25	20	50	40	0	2300	300	300	150
26	160	80	30	100	1200	200	300	800
27	0	30	30	0	350	50	300	450
28	0	0	10	0	0	0	10	0
29	0	200	20	0	0	0	50	50
30	-	1	5	0	0	0	50	500
31	-	100	20	80	360	0	550	750
32	-	300	50	140	770	300	2000	1200
33	-	50	25	40	300	300	50	50
34	-	5	0	0	0	0	10	0
35	-	25	0	-	-	-	-	-
36	-	-	-	-	-	-	-	-
37	-	-	-	-	-	-	-	-
38	-	-	-	-	-	-	-	-

In 2013, the number of flowers per individual was 0-4850, and the number of fruits was 0-3100. In 2014, the number of flowers per individual was 0-60000, and the number of fruits was 0-40000. In 2015, the number of flowers per individual was 0-60000 and the number of fruits was 0-7000. In 2016, the number of flowers per individual was 0-31000 and the number of fruits was 0-2000. In 2017, the number of flowers per individual was 0-16000 and the number of fruits was 0-15000. In 2018, the number of flowers per individual was 0-60000, and the number of fruits was 0-3000. In 2019, the number of flowers per individual was 10-395400, and the number of fruits was 0-14000. In 2020, the number of flowers per individual was 0-66370, and the number of fruits was 0-25000. The number of individuals that did not produce fruit despite flowering was 3 in 2013, 1 in 2014, 1 in 2015, 2 in 2016, 0 in 2017, 9 individuals in 2018, 1 individual in 2019, 2 individuals in 2020. The value obtained by dividing the number of fruits by the number of flowers was used as the fruiting rate, and the ratio of fruits produced among the flowers that bloomed was shown. Table 3 shows the fruiting rates for each individual in 2013-2020. The number of individuals with a fruiting rate exceeding 50% is 2 in 2013, 12 in 2014, 1 in 2015, 0 in 2016, 20 in 2017, 0 in 2018, 4 in 2019, 3 in 2020.

Table 3 Fruiting rate for each individual in 2013-2020

No.	2013	2014	2015	2016	2017	2018	2019	2020
0	-	1.7	0.6	0.2	40.9	0.0	1.0	0.8
1	6.4	12.5	1.6	1.5	83.3	3.3	29.6	62.9
2	0.0	30.0	1.2	2.9	94.7	2.5	25.5	11.8
3	0.0	80.0	1.3	0.7	86.4	0.0	23.6	21.3
4	0.0	5.0	0.8	-	-	-	-	-
5	27.0	66.7	5.2	8.9	56.0	0.5	11.1	18.1
6	11.6	100.0	1.3	1.9	83.3	4.0	4.5	13.6
7	21.3	0.6	1.6	0.4	65.4	0.3	12.9	10.7
8	0.0	90.9	0.5	0.2	63.2	0.0	6.5	30.5
9	0.0	8.6	16.3	2.6	33.3	0.3	24.6	4.0
10	-	1.5	30.0	13.5	15.6	0.0	20.8	20.0
11	-	50.0	1.0	12.5	80.0	0.0	22.7	17.2
12	-	-	-	-	-	-	-	-
13	76.0	50.0	6.7	0.6	16.7	1.0	14.7	35.8
14	30.8	90.0	10.9	2.3	18.6	1.7	58.8	36.3
15	37.1	58.8	2.0	28.6	87.0	0.0	0.0	90.9
16	8.3	0.4	0.4	0.0	48.0	0.0	17.5	0.0
17	21.4	73.3	2.0	10.4	81.8	0.0	14.7	45.7
18	7.0	91.7	10.0	2.7	48.8	0.8	14.7	14.1
19	0.0	0.0	10.9	14.3	45.0	20.0	38.5	50.0
20	13.0	75.0	35.0	5.0	93.8	20.0	39.7	63.3
21	2.9	44.0	1.8	1.7	90.0	6.0	2.5	22.9
22	4.9	12.5	1.2	9.3	87.5	1.6	7.2	10.9
23	54.8	7.3	1.6	6.0	91.7	0.8	4.8	5.1
24	26.1	22.0	4.7	5.3	91.7	10.0	9.3	6.6
25	3.0	7.7	3.3	0.0	92.0	1.5	3.1	0.7
26	6.8	10.3	1.2	9.1	48.0	0.8	2.4	2.9
27	0.0	3.6	1.5	0.0	87.5	1.0	14.0	23.1
28	0.0	0.0	100.0	0.0	0.0	0.0	100.0	0.0
29	0.0	10.0	0.8	0.0	0.0	0.0	83.3	10.2
30	-	10.0	10.0	0.0	0.0	0.0	9.1	33.1
31	-	20.0	0.4	9.6	90.0	0.0	14.1	16.7
32	-	1.5	0.8	8.8	96.3	1.5	24.3	9.3
33	-	90.9	1.3	9.8	93.8	3.0	10.0	10.9
34	-	16.7	0.0	0.0	0.0	0.0	50.0	0.0
35	-	3.3	0.0	-	-	-	-	-
36	-	-	-	-	-	-	-	-
37	-	-	-	-	-	-	-	-
38	-	-	-	-	-	-	-	-

Table 4 shows the number of flowers, the number of fruits, and the rate of fruits in the entire habitat for each year. The number of flowers, the number of fruits, and the rate of fruits in the entire habitat vary from year to year. Of the eight years, the highest number of flowers was reached in 2019, and the highest number of fruits was reached in 2014. In 2013, both the number of flowers and the number of fruits were the lowest. Regarding the fruiting rate, the maximum value was 66.9% (2017) and the minimum value was 2.2% (2018).

Table 4 Number of flowers, fruits and fruiting rate of the entire habitat in 2013-2020

	2013	2014	2015	2016	2017	2018	2019	2020
Flowers	30212	535645	427190	222985	183025	460550	938395	512290
Fruits	8150	259291	22570	8705	122519	10350	87710	113251
Fruiting Rate	27.0	48.4	5.3	3.9	66.9	2.2	9.3	22.1

Table 5 shows the comparison results of the number of fruits set by year. It was found that there was a significant difference (Steel-Dwass. Test P <0.05) in the number of fruits in 2013 compared with 2017, 2019 and 2020. It was found that there was no significant difference (Steel-Dwass. Test N.S.) in the number of fruits in 2013 compared with 2014, 2015, 2016 and 2018.It was found that there was a significant difference (Steel-Dwass. Test P <0.05) in the number of fruits in 2014 compared with 2016 and 2018.It was found that there was no significant difference (Steel-Dwass. Test N.S.) in the number of

fruits in 2014 compared with 2015, 2017, 2019 and 2020.It was found that there was a significant difference (Steel-Dwass. Test P <0.05) in the number of fruits in 2015 compared with 2017, 2019 and 2020.It was found that there was no significant difference (Steel-Dwass. Test N.S.) in the number of fruits in 2015 compared with 2016 and 2018.It was found that there was a significant difference (Steel-Dwass. Test P <0.05) in the number of fruits in 2016 compared with 2017, 2019 and 2020.It was found that there was no significant difference (Steel-Dwass. Test N.S.) in the number of fruits in 2016 compared with 2018.It was found that there was a significant difference (Steel-Dwass. Test P <0.05) in the number of fruits in 2017 compared with 2018.It was found that there was no significant difference (Steel-Dwass. Test N.S.) in the number of fruits in 2017 compared with 2019 and 2020.It was found that there was a significant difference (Steel-Dwass. Test P <0.05) in the number of fruits in 2018 compared with 2019 and 2020.It was found that there was no significant difference (Steel-Dwass. Test N.S.) in the number of fruits in 2018 compared with 2020.

Table 5 List of p-values (Steel-Dwass. Test P <0.05) by comparing the number of fruits in 2013-2020

	2013	2014	2015	2016	2017	2018	2019	2020
2013		N.S.	N.S.	N.S.	0.0047	N.S.	0.0021	0.0048
2014	N.S.		N.S.	0.2333	N.S.	0.1120	N.S.	N.S.
2015	N.S.	N.S.		N.S.	0.0331	N.S.	0.0343	0.0399
2016	N.S.	0.2333	N.S.		0.0040	N.S.	0.0033	0.0054
2017	0.0047	N.S.	0.0331	0.0040		0.0017	N.S.	N.S.
2018	N.S.	0.1120	N.S.	N.S.	0.0017		0.0026	0.0020
2019	0.0021	N.S.	0.0343	0.0033	N.S.	0.0026		N.S.
2020	0.0048	N.S.	0.0399	0.0054	N.S.	0.0020	N.S.	

CONSIDERATION

The purpose of this study is to clarify the characteristics of the habitat of *Pyrus calleryana* Decne in Komaki City and to lay the foundation for conservation activities suitable for the habitat.

Regarding the number of flowering, there is a concern that the results of the number of flowering in each year cannot be compared correctly because the survey method is not unified between the years. However, the method of conducting the survey is also slightly different. In 2017, 2019, and 2020, we conducted a flowering number survey and a flowering phenology survey in parallel, so we were able to count evenly during the flowering period. On the other hand, in 2013, 2014, 2015, 2016 and 2018, the flowering phenology survey was not conducted, so the flowering number survey was conducted only on a few days of the flowering period. Since the time of full bloom differs depending on the individual, not all individuals can be counted at the time of full bloom. Therefore, there is a possibility of underestimation in the counting result of the number of flowers. In the future, in order to correctly compare the counting results of the number of flowers in the continuous survey, it is necessary to establish a unified survey method. From the results of this study and the feelings of the investigators involved in the survey, it is considered that the degree of flowering in the entire habitat varies from year to year. In order to recognize the significant difference from year to year, we thought that it would be useful to establish a unified survey method and to grasp the cycle of the year when the number of flowers is rich and the year when the number of flowers is poor, which will help to lay the foundation for future conservation activities.

It can be judged that the number of fruit set varies from year to year because a significant difference is often observed in the yearly comparison results. It is said that all species of plants have biennial bearing, and biennial bearing is the property of repeating abundant and poor harvests of fruits. No such report has been made on *Pyrus calleryana* Decne, and it has been considered a so-called "yearless species". However, this study found 8150-259291 annual variations in the number of fruits, revealing that *Pyrus calleryana* Decne has years that produce significantly more fruit. In general, if the biennial bearing is strong, a good harvest and a poor harvest are repeated every other year, but the cycle of the year of birth is unknown in the 8-year survey, and it is considered that continuous survey is necessary in the future.

The average annual fruiting rate was 2.2-66.9%, and in 2017, more than half of the habitat populations showed a fruiting rate of 50% or more. Therefore, compared to the average fruiting rate of 0.0-21.8% in the habitats of Inuyama City, Owariasahi City, and Kuwana City in 2020, the habitat of Komaki City has a large number of fruiting relative to the number of flowers. [11]. Summarize the current status and future prospects of each habitat learned through this research. Individuals in the habitat of Komaki City have a large number of flowers and fruit set, showing a high fruit set rate. As the investigation progressed, the seedlings and the growth of young trees were confirmed, so it is considered that the environment is suitable for the growth of *Pyrus calleryana* Decne.

Conservation groups, local governments, and neighboring companies are gradually working to protect *Pyrus calleryana* Decne's habitat. However, it is unclear whether there are any scientifically-based conservation activities suitable for *Pyrus calleryana* Decne. It is considered that conservation activities based on the survey are necessary. As a future policy,

we would like to continue the survey so far, consider new survey items, and build a foundation for conservation activities suitable for each habitat.

REFERENCES

[1] Kunihiko Ueda, Phytogeography of Tokai hill elements I. Plant Taxonomy, Geography Vol. 40, 1989, pp. 190-202.
[2] Kunihiko Ueda, Magnolia stellata, Planter Volume 7, 1990, pp. 77-81.
[3] Kunihiko Ueda, Natural History of Plants, Hokkaido University Book Publishing Association, 1994, pp. 3-8.
[4] Richard B, Primack and Hiromi Kobori, Recommendation of conservation biology, Bunichi Comprehensive publishing, 2008.
[5] Shozo Hiroki, Satoyama Ecology, Nagoya University Press, 2002, pp. 42-96.
[6] Aichi Prefectural Environmental Research Center, Endangered wildlife in Aichi Prefecture, Plant Edition, Red Data Book Aichi 2009, 2009, pp. 94.
[7] Aichi prefecture, 2011 Environmental, White Paper, 2011, pp. 1-2.
[8] Mikio Watanabe, evening edition on March 12, Chunichi Shimbun, 2013.
[9] Niki Tanaka, Interrelationship between conservation activities and endangered plants, Master's thesis, Nagoya Institute of Technology, 2018.
[10] Wataru Ueda, Ecological characteristics of endangered callery pear in Owariasahi, Komaki, and Inuyama, Graduation thesis, Nagoya Institute of Technology, 2019.
[11] Naoya Motoori, Comparative ecology in all Callery pear distribution areas, Graduation thesis, Nagoya Institute of Technology, 2020.

11th Int. Conf. on Geotechnique, Construction Materials & Environment,
Kyoto, Japan, 3-5 November 2021, ISBN: 978-4-909106063 C3051

CONSIDERATION ON THE DYNAMICS OF PARK USERS UNDER COVID-19 CRISIS; TAKING SHIKISHIMA PARK IN MAEBASHI CITY AS AN EXAMPLE

Shinya Tsukada[1], Xingyu Tao[2], Tetsuo Morita[3]and Toshikazu Nishio[4]

[1]Maebashi City Office, Japan; [2,3]Maebashi Institute of Technology, Japan;
[4] Takasaki Technical High School, Japan

ABSTRACT

This study considers the dynamics of park users under COVID-19 crisis taking Shikishima Park in Maebashi City, Gunma Prefecture as an example. In this study, we analyzed the traffic volume of users measured by installing a camera in the parking lot of Shikishima Park. An analysis of user behavior during each infection period showed that the number of pedestrians increased in the second wave period despite the spread of infection. The mask wearing rate of park users has been stable at 60% to 80%, and it is considered that the habit of wearing masks has become more common. In addition, despite the spread of infection, the number of pedestrians increased during the consecutive holidays in May and the summer vacation. As mentioned above, the dynamics of park users under COVID-19 crisis were obtained. We believe that the research results will be useful as an archive of the actual state of park use in under COVID-19 and for the park management plan of the "With COVID-19 pandemic era".

Keywords: COVID-19, urban park, number of pedestrians, constant observation survey

INTRODUCTION

The new coronavirus (COVID-19), which was reported in Wuhan City, Hubei Province, China in December 2019, has spread all over the world and has not subsided even now. In Japan, the infection has spread rapidly since the first infection was reported in January 2020. In April 2020, a state of emergency was issued due to the spread of COVID-19, and it was requested to refrain from going out unnecessarily. It is presumed that the spread of this infectious disease has significantly changed people's lifestyles and behavior patterns. Therefore, it is possible that the usage pattern of the park, which is a familiar green open space, will change.

RESEARCH SIGNIFICANCE

As the infection spread, the national and local governments took measures against infectious diseases through press conferences and websites.

Hiroi showed that despite the state of emergency in April 2020 had the effect of reducing the trips for commuting purposes, it made little change in trips for meals and sightseeing purposes [1]. In addition, Li, Ko, Chang, Yen and Chen showed that there was a positive correlation between risk perception for coronavirus infection and the degree of countermeasure implementation [2]. In addition, Moriwaki, Hiyoshi and Murota analyzed an opinion survey conducted in November 2020 and concluded that decrease in life satisfaction was seen in many respondents, and the cause was decrease in the frequency of going out [3].

Under such circumstances, it is meaningful to know how the use of parks has changed in considering the future of parks. To date, much research has been done on COVID-19 crisis and park use. Takeyama et al. analyzed the actual number of park users during the period of infectious disease control implemented by Hyogo Prefecture and other periods using big data collected from the location information of smartphones [4]. Takeuchi et al. analyzed the actual usage of large-scale parks in Tokyo by conducting hearing surveys and grasping the number of park users using line census data [5].

Hashimura et al. clarified the relationship between preschoolers and their mothers' use of parks and child-rearing stress under COVID-19 crisis from a questionnaire survey in Tokyo [6]. Osamura et al. conducted a questionnaire survey of university students in Tokyo to understand the changes in sports implementation and usage space during the COVID-19 expansion period [7].

Fig. 1 Location of Maebashi City, Gunma Prefecture

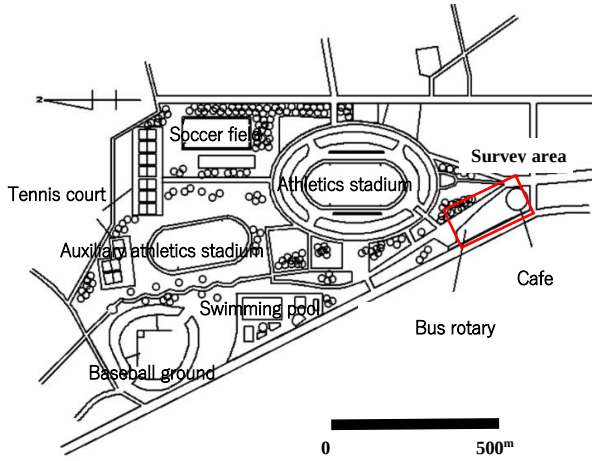

Fig. 2 Facility overview of Shikishima Park

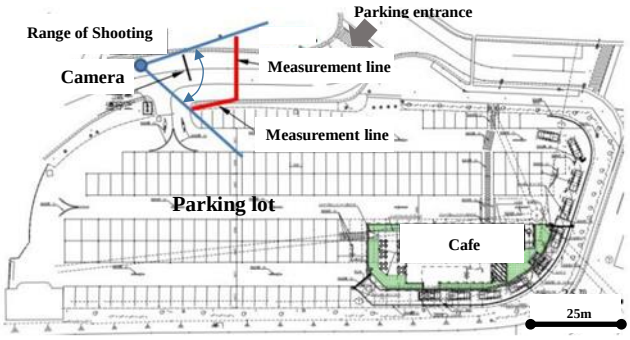

Fig .3 Survey point

All of the above studies were conducted on the use of parks in large cities such as Tokyo and Hyogo prefectures. But there are not many studies conducted on local cities such as Gunma prefecture. Therefore, the originality of this study is to capture the traffic dynamics of COVID-19 by grasping the traffic volume of park users through constant observation surveys in Maebashi City, Gunma Prefecture. The location of Maebashi City, Gunma Prefecture is as shown on the previous page (Fig. 1).

Here, we will grasp the changes in pedestrian traffic volume in city parks during the COVID-19 expansion period in local cities. The purpose of this study was to obtain basic materials useful for archiving the actual state of park use under COVID-19 crisis and for the park management plan of the "With Corona era".

RESEACH METHODS

Maebashi City is the prefectural capital of Gunma Prefecture. Maebashi has a population of 334,204 and a total of 152,466 households (as of 2021.6.30). The population ratio of Maebashi City by industry is 1.2% for agriculture and forestry, 21.9% for industry, and 76.9% for service.

Fig. 4 Picture of Survey location (Shooting range from the camera, see Fig. 3)

Table 1 Survey outline

Investigation period	March 30, 2020～ September 27, 2020
Survey method	Capture changes in traffic volume during COVID-19 period in still images taken with a camera
Totalization	(i)Hourly pedestrians, bicycles, cars (ii)Mask wearing status of pedestrians and cyclists

It is known that the citizens of Maebashi City have a great relationship between water and greenery [8]. In addition, Maebashi citizens are interested in park management [9]. There are 425 city parks in Maebashi City, Gunma Prefecture, with a total area of 395.78 ha, which is 11.8 m2 in terms of park area per capita. There are two large-scale parks in Maebashi City, Maebashi Park and Shikishima Park. Open garden activities were taking place around Shikishima Park [10].

In this study, we focused on Shikishima Park, which was the most well-known in the citizen questionnaire. Shikishima Park is an athletic park (area 36.6ha) that serves as the backbone park of the city. The facility scale and facility contents are the same as those of the Komazawa Olympic Park (area 41.1ha, athletic park) in Tokyo, which was the subject of previous research [4].

Shikishima Park is a city park with a long history that was established in 1922 by the Maebashi City Council as a park around the river site called Koidegawara. It is an athletic park located about 3km northwest of the center of Maebashi City and bordering the Tone River on the west side. Full-scale athletic facilities such as a baseball field, including a 400m track and field stadium, are installed. Gunma Prefecture manages the park facilities (Fig. 2).

The survey was conducted on a record of cross-sectional traffic volume of park users by installing a camera in the parking lot of Shikishima Park (Fig. 3).

Differences could be seen depending on the surface on which the target pedestrians, motorcycles, buses, and automobiles pass. Therefore, we measured two cross-sections, one(roads) for pedestrians, bicycles and buses and the other (parking lot entrances and exits) for automobiles and motorcycles (Fig. 4).

By installing an automatic measurement camera, we photographed pedestrians, bicycles, buses, cars, and motorcycles entering the shooting area. It was verified whether it was possible to grasp the cross-sectional traffic volume in the captured still image. It was also found that it is possible to grasp the wearing situation of the mask in the still image.

We also tried to determine the age of the users and whether or not they were wearing masks by checking the captured still images. As a result, it was impossible to determine age. However, it was difficult to determine the age of an individual by wearing a mask.

Table 1 shows the outline of the survey. We thought that the use of the park under COVID-19 crisis was influenced by three factors: the infection situation, government measures, and the press.

In this study, the traffic volume was defined as the number of pedestrians and the number of park facility users. In addition to the traffic volume of pedestrians and bicycles, the wearing status of masks was also tabulated. In advancing the research, the analysis period was set as follows.

In Japan, the "First Wave" of COVID-19 is from mid-March to mid-May 2020 (Red line in the fig.). In Japan, the "Second Wave" of COVID-19 is from late June to September 2020 (Yellow line in the fig.).

In this study, the analysis period was set from March 30 to September 30, 2020, including the first and second waves (Other than Blue line in the fig.).

DYNAMICS OF PARK USERS UNDER COVID-19 CRISIS

The Relationship between The Number of PCR-Positive People

Fig. 5 show the relationship between the number of PCR-positive people (Japan) on the X-axis and the number of pedestrians in the park observed by the camera on the Y-axis. From the figure, the relationship between the number of PCR-positive people and the number of pedestrians showed that the number of pedestrians increased from July to August when the second wave of infection was spreading.

Fig. 6 show the relationship between the number of PCR-positive people (Japan) on the X-axis and the mask wearing rate of pedestrians on the Y-axis.

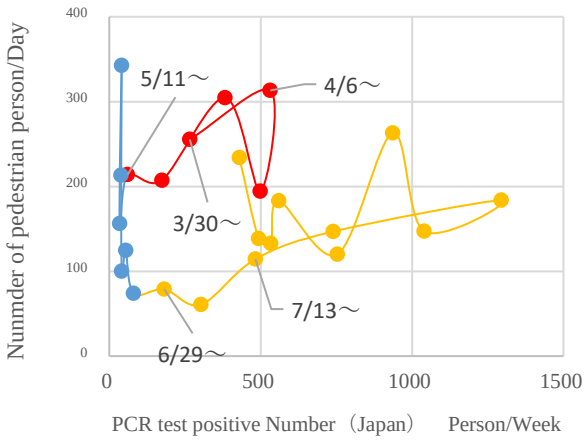

Fig. 5 Relationship between the number of PCR-positive people and the number of pedestrians

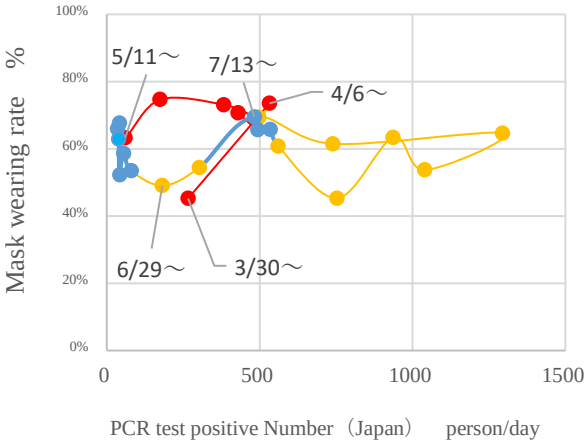

Fig. 6 Relationship between the number of PCR-positive people and the wearing rate of masks

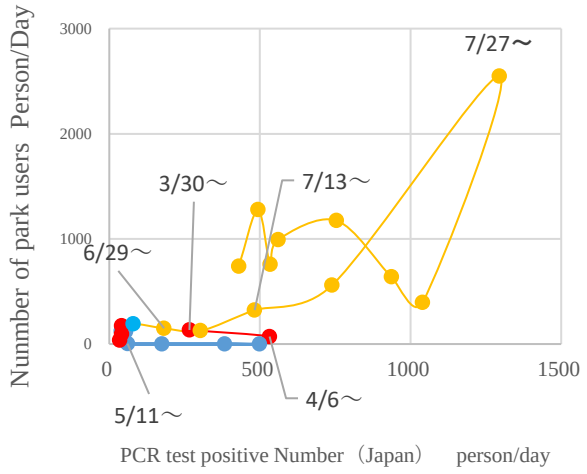

Fig. 7 Relationship between the number of PCR-positive people and the number of park users

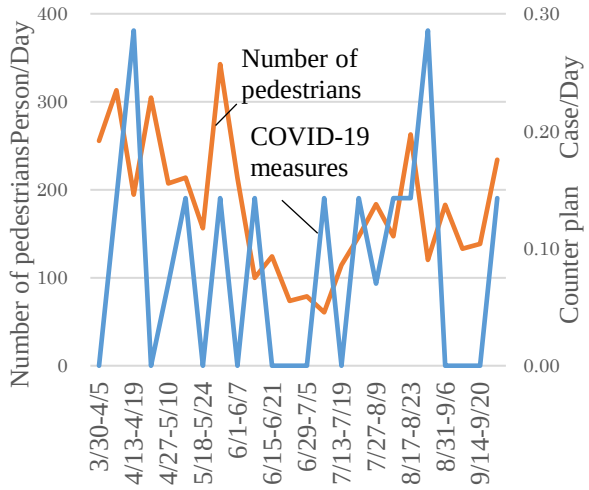

Fig. 8 Relationship between COVID-19 measures and the number of park users in Gunma Prefecture

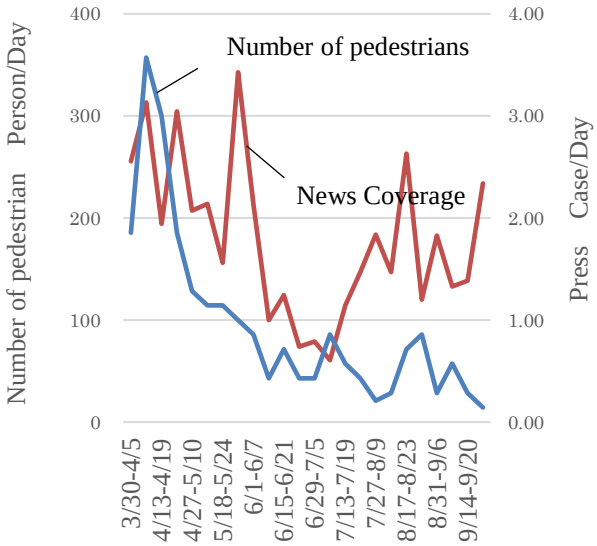

Fig. 9 Relationship between News Coverage and the number of park users in Gunma Prefecture

From the figure, regarding the relationship between the number of PCR-positive people (Japan) and the mask wearing rate of pedestrians, the mask wearing rate of pedestrians increased from March to early April in the first wave period. After that, it declined after the cancellation of the state of emergency on May 13. In addition, it was flat during the second wave period of infection spread.

Fig. 7 show the relationship between the number of PCR-positive people (Japan) on the X-axis and the number of park facility users provided by the manager of Shikishima Park on the Y-axis. From the figure, regarding the relationship between the number of PCR test positives and the number of park users, while the infection spread in the second wave, the number of park facility users increased from July to August. From the above, it is considered that the reason why the number of park users from July to August increased despite the spread of infection in the second wave is that many people used the park during the summer vacation. Regarding the pedestrian mask wearing rate, the pedestrian mask wearing rate increased from March to early April of the first wave. However, with the cancellation of the state of emergency on May 13, it was found that the rate of pedestrians wearing masks decreased. In addition, the rate of pedestrians wearing masks remained at about the same level after the end of June, the period of spread of the second wave of infection.

The Relationship between The Number of park users

Fig. 8 show the relationship between the number of measures taken by Gunma Prefecture and the number of pedestrians [11]. The number of COVID-19 crisis countermeasures issued by Gunma Prefecture was grasped by three types: "Declaration," "Request," and "Policy." Regarding the measures taken by Gunma Prefecture, we searched the "Gunma Prefecture Homepage" on the Internet and extracted it from the "Summary of Coronavirus Infectious Diseases" page.

In addition, the measures against COVID-19 crisis taken by Maebashi City were not included in the number of extractions because they were included in the measures taken by Gunma Prefecture. Among them, there are "state of emergency", "request for self-restraint", and "policy to prevent the spread of COVID-19", and each of the extracted items is counted as one case. It was found that measures were taken by Gunma Prefecture during each of the first and second waves of infection. However, during the Golden Week holidays in May, the number of pedestrians around the park was increasing.

Fig. 9 show the relationship between the number of pedestrians and the number of news articles on COVID-19 by the Jomo Shimbun, a local newspaper in Gunma Prefecture. To extract news articles, I searched the local newspaper "Jomo Shimbun" in Gunma prefecture on the Internet, opened the homepage, and entered "Gunma Corona" in the search word [12]. The number of reports on COVID-19 in the Jomo Shimbun during the second wave period was decreasing. On the other hand, the number of pedestrians increased during this period.

CONCLUSIONS

This study uses an observation camera to investigate the actual traffic conditions of park users, taking Shikishima Park in Maebashi City as an example. The results of the study are as follows.

(1) We analyzed the walking behavior of city parks during COVID-19 infection period. The number of users of Komazawa Olympic Park, which is similar in scale and facility, decreased significantly in May and continued to decrease after June (previous study [2]).However, in the second wave of the infection, the number of pedestrians increased despite the spread of the infection.

(2) It is considered that the reason why the number of pedestrians and users of the park increased during the Golden Week holidays in May and from July to August was that many people used the park on long holidays such as summer vacation. In addition, as for the pedestrian mask wearing rate, it was found that the rate decreased with the cancellation of the state of emergency on May 13.

Behind the results, there are many "public transportation such as trains" as the means of access to parks in Tokyo. It was thought that the access to the park in Maebashi City was "private car", and that the self-control over the use of the park was looser in Maebashi City than in Tokyo (previous study [7]).

In the use of parks in After COVID-19, the time will come when we will consider equalizing the use of parks. In that case, it is effective for us to think about the park usage plan while grasping the actual conditions of the park access means and the number of park usage. However, after the second wave, the pedestrian mask wearing rate was stable at 60% to 80%.From this, it is considered that pedestrians have become accustomed to wearing masks after the second wave. Furthermore, in order to understand the impact of information management on park users, we analyzed the announcement of measures against COVID-19 infectious diseases in Gunma Prefecture and the coverage of the Jomo News paper. As a result of the analysis, the measures taken by Gunma Prefecture and the coverage of COVID-19-related news by the Jomo Shimbun increased during each of the first and second waves. However, despite the measures taken in Gunma Prefecture and newspaper reports, the number of pedestrians around the park tended to increase during the Golden Week holidays in May. In the future, it will be necessary to carry out a more detailed analysis and understand the usage status of the park in relation to other urban facilities.

REFERENCES

[1] U H., A Study on the Effect of Japanese-style Lockdown on Self-restraint Request for COVID-19, Journal of the City Planning Institute of Japan, Vol.55, No.3, 2020, pp.902-909.

[2] Dian-Jeng Li, Nai-Ying Ko, Yu-Pimg Chang, Cheng-Fang Yen, Yi-Lung Chen, Mediating Effects of Risk Perception on Association between Social Support and Coping with COVID-19: An Online Survey, International Journal of Environmental Research and Public Health, Vol.18, No.4, 2021

[3] Moriwaki Y.,Hiyoshi N., Murota M., A study on changes in going out behavior, outdoor space usage and life satisfaction with COVID-19, Reports of the City Planning Institute of Japan, No.19, pp.435-438.

[4] Takeyama H., Wakai S., Yamamoto S. , Yakushiji T. and Nakase I., A Study on the Use of Urban Parks Using Location-Based Big Data under the Coronavirus Crisis, Japanese Institute Landscape Architecture, Vol. 84, No. 5, 2021, pp. 475-478.

[5] Takeuchi T. and Kuma A., Analysis of Changes in the Number of Park Users and the Facility Usage Restrictions in Tokyo Metropolitan Parks under the COVID-19 Pandemic, Japanese Institute Landscape Architecture, Vol. 84, No. 5, 2021, pp. 479-484.

[6] Hahimura C., Amemia M., Hata N. and SHIMADA T., The Relationship between Changes in Park Use by Mothers with Preschool Children and Parenting Stress of those Mothers under the COVID-19 Pandemic, Japanese Institute Landscape Architecture, Vol. 84, No. 5, 2021, pp. 485-490.

[7] Osamura Y., Fukuoka T., Study of Changes in University Students' Exercise Routine and Locations pre and during COVID-19 Outbreak, Japanese Institute Landscape Architecture, Vol. 84, No. 5, 2021, pp. 491-494.

[8] Tetsuo M., Shinya T., Yoshihito K., Hiroshi S., Tsuyoshi B., Shinya T., Naoki M., A Study on Evaluation of Quality of Life in Consideration of Water/Green Environment, Int. Journal of GEOMATEVol.2(2), 2011, pp.241-246

[9] Shinya T., Tetsuo M., A Study of Public Opinion on Green Spaces using data from Free-Text Descriptive Responses- A Case Study of Regional City in Japan, Int. Journal of GEOMATE Vol.14(46), 2018, pp.21-25

[10] Shinya T., Kazuya T., Tetsuo M., Residents' Evaluation and Continuity in The case of Shikisima Open Garden in Maebashi City**,** Int. Journal of GEOMATE Vol.18(68), 2019, pp.108‑113

[11] https://www.pref.gunma.jp/

[12] https://www.jomo-news.co.jp/

[13] Shinya T., May K., Tetsuo M. and Akira Y., A study influence by Quality of life captured from Travel valued of Shikishima park, Japanese Institute Landscape Architecture, Vol. 81, No. 5, 2018, pp. 495-500.

11th Int. Conf. on Geotechnique, Construction Materials & Environment,
Kyoto, Japan, 3-5 November 2021, ISBN: 978-4-909106063 C3051

CONVERSION OF BLAST FURNACE SLAG INTO HYDROGARNET FOR HUMIC ACID REMOVAL

Takaaki Wajima[1]

[1]Graduate School of Engineering, Chiba University, Japan

ABSTRACT

The discharge of humic acid in aqueous environments is a key health and esthetic issue. In this study, blast furnace (BF) slag, a byproduct of iron- and steel-making plants, is converted into a hydrogarnet product under a hydrothermal reaction for humic acid removal. The BF slag is pulverized and passed through sieves of four different sizes, i.e., 100, 100–300, 300–500, and 500–1000 μm. Subsequently, these BF slags are added to NaOH, KOH, and LiOH solutions with 1–4 M NaOH solution/BF slag (= 20, 10, and 4 mL/g) and heated at 80, 120, and 160 °C for 24 h, with or without $Al(OH)_3$ addition. In the absence of $Al(OH)_3$, portlandite is synthesized in alkali solutions, and the highest crystallinity of portlandite in the product is obtained in 3 M NaOH at 160 °C. With the addition of $Al(OH)_3$, katoite, which is a hydrogarnet, as well as tobermorite and hydroxysodalite are synthesized from BF slag. As the NaOH solution/BF slag ratio increases, the peaks of hydroxysodalite and tobermorite increase, whereas those of katoite decrease. As the BF slag size decreases, the peaks of katoite increase because of the increase in Ca supply from the BF slag. The product, including katoite, can remove humic acid.

Keywords: Blast furnace slag, Hydrogarnet, Humic acid removal, Alkali hydrothermal synthesis

INTRODUCTION

Humic acid (HA) is a ubiquitous natural organic polyelectrolyte formed by the breakdown of animal and vegetable matter in aqueous environments. The presence of significant amounts of HA in water is indicated by a yellowish to brown color, and the chlorine used during water purification reacts with HA to form carcinogenic materials [1]. Therefore, the discharge of HA in water is a major environmental and health concern.

Several methods, including membrane separation and coagulation techniques, have been used to remove HA from effluents [2, 3]. Furthermore, HA can be removed from aqueous solutions via adsorption using micropores and functionalized substrate filters, which serve as adsorption sites. In activated carbon, the pores can be obstructed by the adsorption of HA [4]; therefore, carbon filters with mesopores were prepared to overcome this problem [5]. Meanwhile, kaolinite exhibits higher adsorption for HA than montmorillinite, although their surface functional groups (Al–OH and Si–OH) are similar [6]. The adsorption of HA on Mg/Al-layered double hydroxides occurs via a ligand exchange reaction with surface groups [7]. Therefore, it is believed that the binding energies of the surface functional groups significantly affect HA adsorption properties.

HA contains various organic functional groups such as hydroxyl, carboxylic, and phenolic groups, resulting in reaction sites with different potential energies. It is difficult to achieve a complete removal of HA from aqueous environments because of its complex structure. Increasing the number of interactions between HA and the material surface is key to improving the adsorption properties of HA removal systems. To manipulate various adsorption sites for HA at the material surface, the hydroxyl groups must have a diverse range of binding energies. It is expected that these groups can be easily tunable as sites for reaction with HA. The hydrogarnet series $Ca_3Al_2(SiO_4)_{3-x}(OH)_{4x}$ ($0 < x < 3$) is a solid solution comprising grossular ($x = 0$) and katoite ($x = 3$). The increased substitution of $(SiO_4)^{4-}$ in this structure causes a decrease in the lattice constants, resulting in disorder in the cation-centered polyhedral [8], and a hydrogarnet with a number of hydroxyl groups on the surface being able to adsorb HA from aqueous solutions [9].

Hydrogarnets are known as the primary hydration product in solidified cement pastes [10-12]; they can be synthesized by the hydrothermal treatment of byproducts such as coal ash or molten slag [13, 14]. Blast furnace (BF) slag is the dominant byproduct of iron- and steel-making processes, and more than 23 million tons of BF slag is generated annually in Japan [15]. Although BF slag is widely used for cement production, road construction, and as a concrete aggregate, the capacity for the use of recycled BF slag in these fields has become saturated, and the development of value-added products from such waste slag has become an important issue for sustainability. Therefore, various recycling processes have been investigated recently [16, 17].

In this study, hydrogarnets were synthesized from BF slag using hydrothermal treatment to remove HA from aqueous solutions. Hydrogarnets were synthesized from BF slag using an alkali

hydrothermal reaction, and the ability of the product to remove HA from aqueous solution was analyzed for its possible application in wastewater treatment.

EXPERIMENTAL

Sample

BF slag can be classified into air- and water-cooled slags, based on the cooling method. The slags contain crystalline and amorphous phases, respectively. To ensure that the phases in the slag were converted into functional phases by alkali fusion, the BF slag used in this study (received a steel-producing plant in Japan) was water cooled. The BF slag was gently ground using a mill and sieved to less than 2 mm. The chemical and mineralogical compositions of the raw slag were obtained via X-ray fluorescence spectrometry (Shimadzu, XRF-1700) and X-ray diffraction (XRD) (Rigaku, RINT-2500), respectively, as shown in Table 1 and Fig.1. The raw slag was composed primarily of CaO (42.9%), SiO_2 (34.5%), and Al_2O_3 (13.7%) in the amorphous phase and minor crystalline phase, and gehlenite ($Ca_2Al_2SiO_7$). Other oxides, such as MgO, SO_3, Fe_2O_3, TiO_2, K_2O, and MnO, were present in lower amounts.

Table 1 Chemical composition of BF slag.

	Content (wt.%)
CaO	42.9
SiO_2	34.5
Al_2O_3	13.7
MgO	6.1
SO_3	1.1
Fe_2O_3	0.6

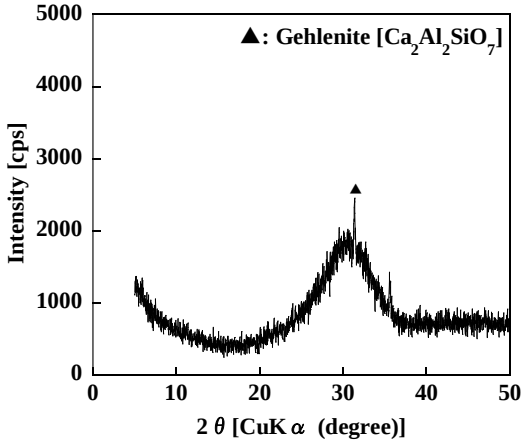

Fig. 1 XRD patterns of BF slag.

Synthesis

The raw slag was first ground in a mill and sieved into four slags of different sizes: S-1, 100–250 μm; S-2, 250–500 μm;, S-3, 500–1000 μm; and S-4, 1–2 mm. The slag (0.5, 1, and 2.5 g) with or without $Al(OH)_3$ (Wako) was added to 10 mL of 1–4 M NaOH, KOH, and LiOH solutions in 50 mL pressure vessels, and heated at 80 °C, 120 °C, and 160 °C for 24 h in an electric oven. After heating, the solid was filtered, washed with distilled water, and dried in an oven at 60 °C overnight to obtain the product. The product phases and morphologies were analyzed using XRD. The change in the amount of mineralogical phases in the product was represented as a relative crystallinity (RC) by calculation using the intensity of the major XRD peaks in the product at specified diffraction faces, i.e., portlandite (0 0 1), as follows:

$$RC = \frac{(\text{Intensity of major peaks in the product})}{(\text{Intensity of major peaks in the standard})} \times 100 \quad (1)$$

Commercial $Ca(OH)_2$ (Wako) were used as the standard.

Adsorption

The HA adsorption capacity of the product was evaluated using 0.25 g/L of product. The HA solution was prepared using a method first reported by Moriguchi et al. [18]. Briefly, HA was dissolved in a diluted NaOH solution, and the solution was filtered using a membrane filter with 0.45 μm pores. Subsequently, the solution was added to a diluted HCl solution for precipitation and centrifuged to obtain HA. After the dissolution of the resultant HA in diluted NaOH, diluted HCl was added to shift the pH of the HA solution to 7 to simulate real natural water. The product was soaked in HA solution at 0–30 mg/L for 24 h, and the supernatant obtained by centrifuging the slurry solution was analyzed via UV/Vis spectroscopy by monitoring the change in absorbance at 400 nm. Blank samples without a product were measured for each adsorption test as a reference. The adsorption amount of HA (q_e) was calculated using the following equation:

$$q_e = \frac{(C_0 - C) \times V}{w} \quad (2)$$

where C_0 (mg/L) and C (mg/L) are the initial and measured concentrations, respectively; V (L) is the

volume of the solution; *w* (g) is the weight of the added sample.

RESULTS AND DISCUSSION

Hydrogarnet Synthesis

The effects of the alkali species, concentration, and temperature on the product were investigated. It is noteworthy that 2.5 g of raw slag (< 2 mm) was treated with 10 mL of 1–4 M NaOH, KOH, and LiOH solutions at 80 °C, 120 °C, and 160 °C for 24 h. All obtained products contained portlandite ($Ca(OH)_2$) without hydrogarnets. The typical XRD patterns of the product are shown in Fig. 2.

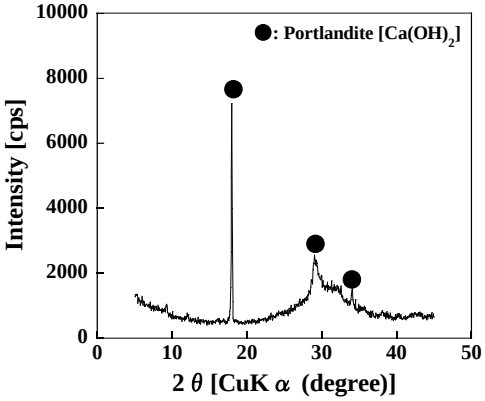

Fig. 2 XRD patterns of product from BF slag in 3 M NaOH solution at 160 °C.

Figure 3 shows the RC of the portlandite phase of the product. The abscissa is the concentration of the solution, and the ordinate is the heating temperature. The white zone indicates the high crystallinity of portlandite in the product, and the black zone indicates no portlandite phase in the product. The crystallinity of portlandite in the product using NaOH solution was higher than that using KOH and LiOH solutions. As the NaOH solution and heating temperature increased (from bottom left to top right), the crystallinity of portlandite increased, and the product with the highest crystallinity of portlandite was synthesized in 3 M NaOH solution at 160 °C for 24 h.

The effect of the solid/solution ratio on the product was determined. It is noteworthy that raw slag (0.5, 1, and 2.5 g) was treated with 3 M NaOH solution (10 mL) at 160 °C for 24 h. The XRD patterns of the product when the solution/slag ratios were 20, 10, and 5 mL/g are shown in Fig. 4. As the solution/slag ratio increased, tobermorite appeared in the product with portlandite, but hydrogarnet peaks were not observed.

The effect of the particle size on the product was investigated. The slag (2.5 g) with various particle sizes was treated with 3 M NaOH solution (10 mL) at 160 °C for 24 h. The XRD patterns of the product from the slag with various particle sizes are shown in Fig. 5. As the particle size, tobermorite appeared in the product synthesized from the slag with particles measuring less than 500 μm, and katoite, one of the hydrogarnets, appeared in the product from the slag with particles measuring less than 100 μm.

These results indicate that hydrogarnets can be synthesized from slag with particles measuring less than 100 μm in 3 M NaOH solution at 160 °C for 24 h. It is noteworthy that the insufficient Al content in the solution rendered the synthesis of hydrogarnets difficult.

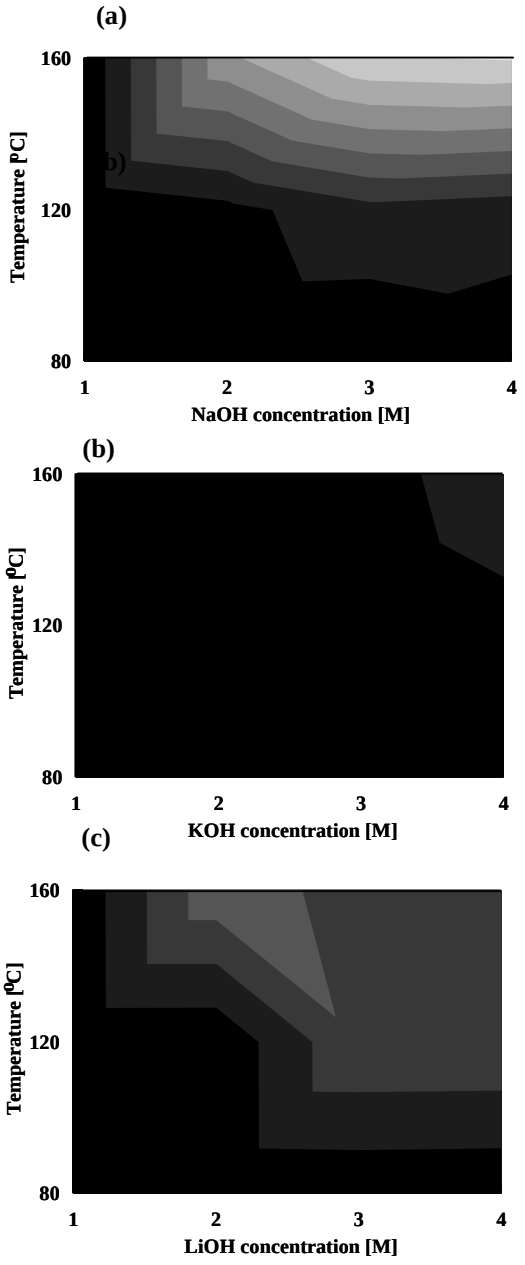

Fig. 3 Crystallinity of portlandite synthesized from BF slag in (a) NaOH, (b) KOH, and (c) LiOH solution at various temperatures.

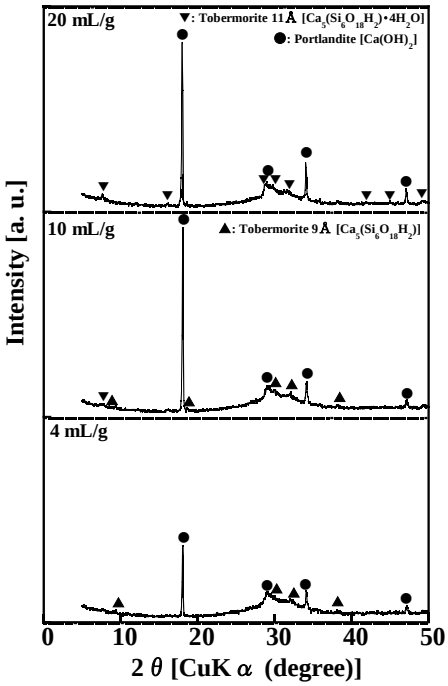

Fig. 4 XRD patterns of product from BF slag in 3 M NaOH solution at 160 °C when solution/slag ratios were 20, 10, and 5 mL/ g.

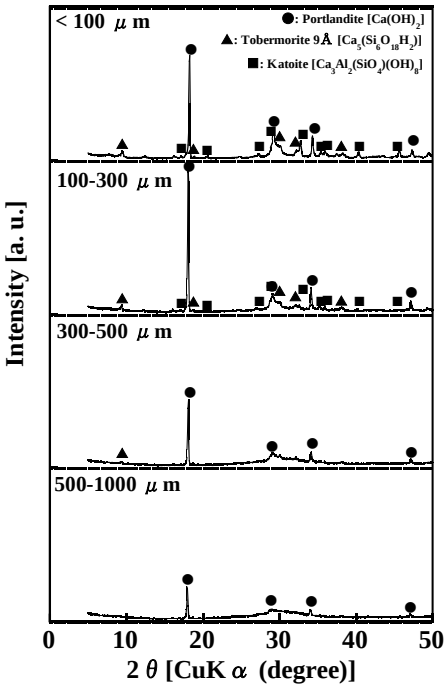

Fig. 5 XRD patterns of product from BF slag with various particle size in 3 M NaOH solution at 160 °C.

For hydrogarnet synthesis, 2.5 g of slag (< 2 mm) and 1 g of $Al(OH)_3$ were added to a 1–3 M NaOH solution (10 mL) at 160 °C for 24 h. The XRD patterns of the product synthesized from the slag with $Al(OH)_3$ added are shown in Fig. 6. Portlandite was synthesized in the absence of $Al(OH)_3$. With the addition of $Al(OH)_3$, katoite can be synthesized in the product. The peaks of katoite and bohemite were confirmed in the product synthesized in 1 M NaOH solution, and as the NaOH concentration increased, the peak intensity of bohemite decreased. The product containing katoite and hydroxysodalite can be synthesized from the slag in 3 M NaOH solution.

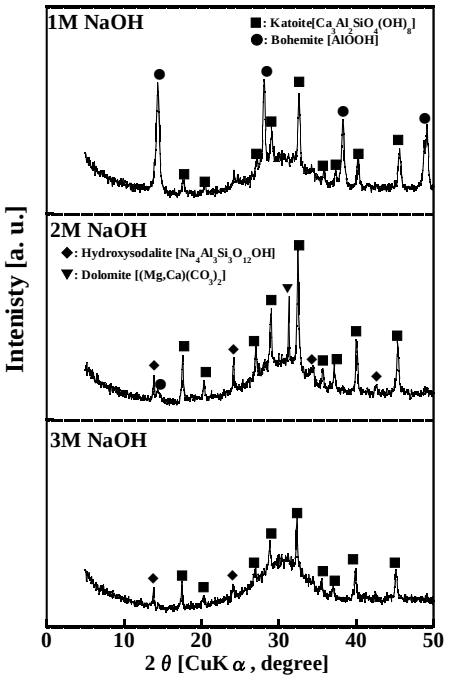

Fig. 6 XRD patterns of products synthesized from BF slag in 1–3 M NaOH solution at 160 °C for 24 h with $Al(OH)_3$ added.

The effect of the solution/slag ratio on the product synthesized with $Al(OH)_3$ added was investigated. The slag (5 g) and $Al(OH)_3$ (2 g) were mixed, and the mixture (0.6, 1.2, and 3.5 g) was treated with 3 M NaOH solution at 160 °C for 24 h. The XRD patterns of the product synthesized from the slag $Al(OH)_3$ added at various solution/slag ratios are shown in Fig. 7. All products contained katoite, and as the solution/slag ratio increased, the peaks of katoite decreased, whereas those of hydroxysodalite and tobermorite increased. It was assumed that the synthesis of hydrogarnets at 4 mL/g would yield better results than those at 10 and 20 mL/g.

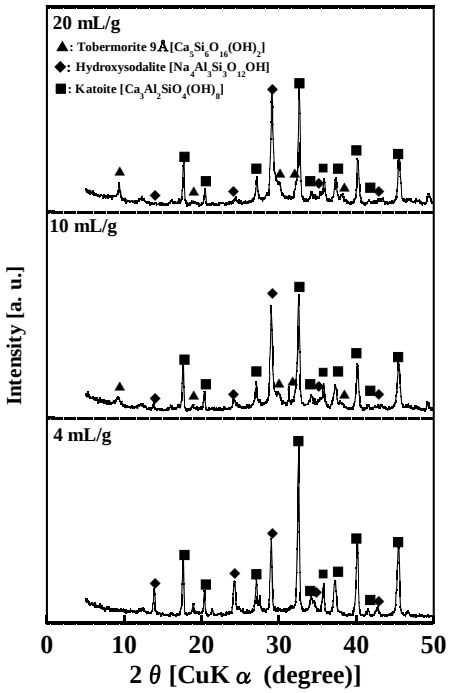

Fig. 7 XRD patterns of product from BF slag with $Al(OH)_3$ in 3 M NaOH solution at 160 °C for solution/slag ratios of 20, 10, and 4 mL/ g.

The effect of particle size on the product synthesized with $Al(OH)_3$ added was investigated. The slag (2.5 g) and $Al(OH)_3$ (1 g) were mixed, and the mixture was treated with 3 M NaOH solution at 160 °C for 24 h. The XRD patterns of the product synthesized from the slag of various particle sizes with $Al(OH)_3$ added are shown in Fig. 8. All products contained katoite, and as the particle size decreased, the peaks of katoite and hydroxysodalite increased. It was assumed that the synthesis of hydrogarnets from slag with smaller particles would yield better results, due to the higher supply of Ca to mineral phases from smaller particles, as shown in Fig. 5.

These results suggest that the product, including hydrogarnets, can be synthesized from slag with particles measuring less than 100 m by adding $Al(OH)_3$ in 3 M NaOH solution at 160 °C for 24 h.

HA Removal

The HA adsorption of the product is shown in Fig. 9. The product was synthesized from 2.5 g of the slag (< 100 μm) with $Al(OH)_3$ addition (1 g) in 3 M NaOH solution (10 mL) at 160 °C for 24 h. As the HA concentration increased, HA adsorption increased gradually.

The HA adsorption of the product was determined based on isotherm models. Several isotherm models can be used to describe the equilibrium sorption distribution, in which two models are used to fit the experimental data, i.e., Langmuir and Freundlich models.

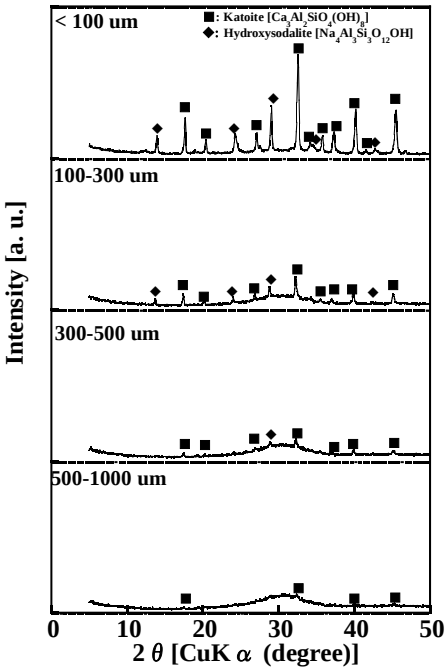

Fig. 8 XRD patterns of product from mixture of BF slag of various particle sizes and $Al(OH)_3$ in 3 M NaOH solution at 160 °C.

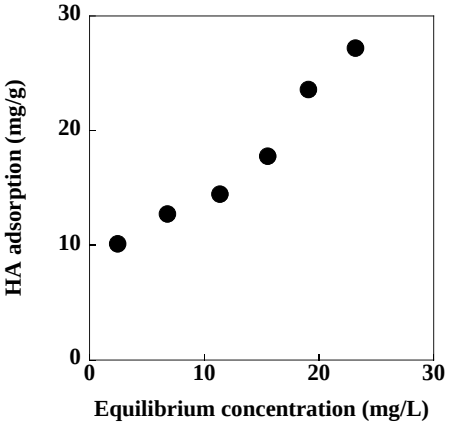

Fig. 9 Isotherm of HA adsorption for product.

The linear forms of the Langmuir and Freundlich models are expressed as follows:

$$\frac{C_e}{q_e} = \frac{1}{q_{\max} \times K_L} + \frac{C_e}{q_{\max}} \quad (3)$$

$$\ln(q_e) = \ln(K_F) + \frac{1}{n}\ln(C_e), \quad (4)$$

where q_e is the HA adsorption amount at equilibrium (mg/g); q_{max} (mg/g) and K_L (L/mg) are Langmuir constants related to the maximum adsorption capacity corresponding to the complete coverage of available adsorption sites and a measure of adsorption energy (equilibrium adsorption constant), respectively. K_F and n are Freundlich constants.

The results of the isotherm analysis are presented in Table 2. Our experimental results indicate a correlation regression coefficient (R^2), which is the

measure of goodness-of-fit, of 0.975 and 0.978 when the Langmuir and Freundlich models were used, respectively. The Freundlich model indicated a better fit than the Langmuir model, as the former had a higher R^2 than the latter.

Table 2 Parameters and correlation regression for Langmuir and Freundlich models

Langmuir			Freundlich		
q_{max}	K_L	R^2	n	K_F	R^2
192.3	0.006	0.975	1.09	1.50	0.978

CONCLUSIONS

BF slag was converted into a product that included hydrogarnets to remove HA from the aqueous solution. The results are summarized as follows:

·BF slag with smaller particles can be converted into a product including hydrogarnets via hydrothermal treatment with 3 M NaOH solution at 160 °C for 24 h with $Al(OH)_3$ addition, when the solution/slag ratio was 4 mL/g.

·The product can remove HA from an aqueous solution.

·The HA adsorption of the product was fitted to the Freundlich isotherm model.

This study demonstrated that a novel hydrogarnet-containing adsorbent capable of removing HA from aqueous solutions can be synthesized from BF slag through an alkali reaction with $Al(OH)_3$ addition. These results suggested that new recycling technology for steel making and new adsorbent for HA removal in water treatment.

REFERENCES

[1] Tang W. Z. and Tassos S., Oxidation Kinetics and Mechanisms of Trihalomethanes by Fenton's reagent, Water Res., Vol. 31, 1997, pp.1117-1125.

[2] Jucker C. and Clark M. M., Adsorption of Aquatic Humic Substances on Hydrophobic Ultrafiltration Membranes, J. Membr. Sci., Vol. 97, 1994, pp. 37-52.

[3] Wei J., Gao B., Yue Q., Wang Y., Li W. and Zhu X., Comparison of Coagulation Behavior and Floc Structure Characteristic of Different Polyferric-Cationic Polymer Dual Coagulants in Humic Acid Solution, Water Res., Vol. 43, 2009, pp. 724-732.

[4] Chen J. P. and Wu S., Simultaneous Adsorption of Copper Ions and Humic Acid Onto an Activated Carbon, J. Colloid Interface Sci., Vol. 280, 2004, pp. 334-342.

[5] Libbrecht W., Verberckmores A., Thybaut J. W., Voort P. V. D. and Clercq J. D., Tunable Large Pore Mesoporous Carbons for the Enhanced Adsorption of Humic Acid, Langmuir, Vol. 33, 2017, pp. 6769-6777.

[6] Feng X., Simpson A. J. and Simpson M. J., Chemical and Mineralogical Controls on Humic Acid Sorption to Clay Mineral Surfaces, Org. Geochem., Vol. 36, 2005, pp. 1553-1566.

[7] Vreysen S. and Maes A., Adsorption Mechanism of Humic and Fulvic Acid Onto Mg/Al Layered Double Hydroxides, Appl. Clay Sci., Vol. 38, 2008, pp. 237-249.

[8] Mercury J. M. R., Turrillas X., Aza A. H. and Pena P., Calcium Aluminates Hydration in Presence of Amorphous SiO_2 at Temperatures Below 90 °C, J. Solid State Chem., Vol. 179, 2006, pp. 2988-2997.

[9] Maeda H., Kurosaki Y., Nakayama M., Ishida E. H. and Kasuga T., Adsorption Behavior of Hydrogarnet for Humic Acid, R. Soc. Open Sci., Vol. 5, 2018, 172023.

[10] Kobayashi S. and Shoji T., Infrared Analysis of the Grossular-Hydrogrossular Series, Mineral. J., Vol. 11, 1982, pp. 331-343.

[11] Passaglia E. and Rinaldi R., Katoite, A New Member of the $Ca_3Al_2(SiO_4)_3$-$Ca_3Al_2(OH)_{12}$ Series and a New Nomenclature for the Hydrogrossular Group of Minerals, Bull. Mineral., Vol. 107, 1984, pp. 605-618.

[12] Sacerdoti M. and Passaglia E., The Crystal Structure of Katoite and Implications Within the Hydrogrossular Group of Minerals, Bull. Mineral., Vol. 108, 1985, pp. 1-8.

[13] Fujita S., Suzuki K. and Shibasaki Y., The Mild Hydrothermal Synthesis of Hydrogrossular from Coal Ash, J. Mater. Cycles Waste Manage., Vol. 4, 2002, pp. 41-45.

[14] Fujita S., Suzuki K., Shibasaki Y. and Mori T., Synthesis Hydrogarnet from Molten Slag and its Hydrogen Chloride Fixation Performance at High-temperature, J. Mater. Cycles Waste Manage., Vol. 4, 2002, pp. 70-76.

[15] Nippon Slag Association (NSA), The Annual Report of Statics of Iron and Steel Slag 2018, http://www.slg.jp/statistics/report.html

[16] Wajima T. and Munakata K., Synthesis of 11A Tobermorite from Blast Furnace Slag Using EDTA, J. Ion Exch., Vol. 21, 2010, pp. 171-174.

[17] Wajima T., Oya K., Shibayama A., Sugawara K. and Munakta K., Synthesis of Hydrocalumite-like Adsorbent from Blast Furnace Slag Using Alkali Fusion, ISIJ Int., Vol. 51, 2011, pp. 1179-1184.

[18] Moriguchi T., Yano K., Tahara M. and Yaguchi K., Metal-modified Silica Adsorbents for Removal of Humic Substances in Water, J. Colloid Interface Sci., Vol. 283, 2005, pp. 300-310.

[19]

11th Int. Conf. on Geotechnique, Construction Materials & Environment,
Kyoto, Japan, 3-5 November 2021, ISBN: 978-4-909106063 C3051

INTEGRATED APPROACH BASED ON FLUID PHENOMENA FOR BENTONITE SUBJECTED TO THERMAL ACTION

Tomoyoshi Nishimura[1]

[1]Department of Civil Engineering, Ashikaga University, Japan

ABSTRACT

Thermal characterization of geotechnical materials is essential for many applications to mechanical prediction such as deformation, seepage and strength capacity, which is possible to reflect to safety design associate environmental structure consist of soils. Interprets to thermal characterization have been supplied and computed to ecosystem service recently. Focusing on the computation of thermal properties, analyzing the effect, which is important for solution of environmental geotechnical problems. This study conducted out some experimental tests using developed apparatus to compacted unsaturated sodium bentonite, and it is most important to represent thermal characteristic for material related to geotechnical environmental practice. Thermal characteristic parameters consist of strength, occurrence of fluid pressure, hydro-conductivity such as air/liquid flow. Sodium bentonite has been widely used for thermal-hydro-mechanical-chemical properties to barrier system in radioactive disposal waste facility, which is constructed at quite deep underground. Some experimental works have contributed to interpret of thermal properties such as decreasing strength and developing of hydro conductivity (i.e. coefficient of permeability). The strength properties have indicated only as thermal proletaries. Producing fluid pressure in void structure such as macro-micro aggregate is required for establishing mathematical models in order to predict safe design to barrier system. This study verifies increment of fluid pressure due to heating under isotropic conductivity for temperature range is from 20 C to 80 C. Increment of fluid pressure induced that absorbing performance offer reduction, as well as decreasing of strength resistance.

Keywords: Bentonite, Heating, Volume change, Pore pressure, Unconfined compressive strength, Relative humidity

INTRODUCTION

Thermal characterization of a bentonite such as geotechnical materials is essential necessary to evaluate maintaining of safety for high level radio active waste disposal facility constructed at further deeply underground [1]. This study conducted out some experimental tests, in which were callibration test in order to define relationship between temperature and relative humidity associate to modified vapor pressure technique, decision of pore pressure at undrained condition, investigation of increasing for pore pressure through absorbing water process, deformations properties induced by heating and observations of reduction to shear resistance.

TESTING PROCEDURE

This testing programs composite that thermal-hydration-mechanical properties for unsaturated-saturated bentonite is mainly investigated in various measurement using some test apparatus. All of specimens are Na type bentonite (Sodium bentonite) mixture with sand. Soil materials, and modified apparatus demonstrated, and testing process is verified as following below sections.

Soil materials used in this study

Kunigel V1 was used in this testing program which was sodium bentonite, and is product by Kunimine Co. Ltd. Mechanical properties for Kunigel V1 was measured as one of representative materials consist of artificial barrier system in previous many works. Having high content of montmorillonite on chemical properties, a bentonite had absolutely fined content larger than 95 %. measured density of soil particles was 2.733 Mg/㎥.

Moreover, SiO_2 occupied 62 % as chemical components. For mixture, silica sand, named Iitoyo No.4, was used as compositing testing specimen, which had highly unique grain size distribution obtained from grain size analysis test. Maximum size was evaluated as 2.0 mm. The mixture ratio of sand and bentonite was 7:3 in dry weight.

Subsequently the bentonite-sand was adjusted to a required water content of 17.0 %, specimens was compacted statically in the stiffness steel mold. Sizes of specimens were a diameter of 3.8 cm and a height of 7.6 cm, respectively with creating a ratio of 2.0 to diameter against height. Initial specimens had a dry density of 1.600 Mg/m^3, void ratio of 0.710 and degree of saturation of 65.61 % as physical variables.

Measurement of temperature and relative humidity

To measure temperature and relative humidity surrounding bentonite is necessary to consider the effort to mechanical properties for deformation while heating process. A small temperature & humidity logger (Product by KN-Labs Co. Ltd), in which had a diameter of 17.0 mm, thickness of 6.0 mm and a weight of 3.3 g. Instructions are exhibited as followings; temperature range is from minus twenty C to positive eighty C and relative humidity is permitted from zero % to 95 % depending on environmental temperature. Each physical quantity is enough accuracy that 0.1 C in temperature and 0.5 % in relative humidity. Various chemical substances are located with a small temperature & humidity logger into steel chamber, which have a subjection to create specialized relative humidity, and relative humidity against chemical substance is indicated into testing code: JGS 0151-2009 corresponding to vapor pressure technique for Test method for water retentivity of soils. Subsequently, the logger was place into specimen, and it was composed two separated specimens. Decision of relative humidity for void structure revealed with processing increment temperature.

Measurement of pore pressure under isotropic heating conductivity

Radioactive waste in packing induced significant high heating due to chemical reaction, which is made in high carbon steel, has quite strong stiffness. It is predicted that some efforts applied to bentonite within barrier system. This study conducted out that pore pressure in further small void structure are measured using developed pore pressure sensor (PHL-A-3MPA-A, Product by KYOWA Co. Ltd). Instruction for the sensor provided that capacity is 3.0 MPa, permitted temperature range is from minus 40 C to 150 degrees Celsius and accuracy is less than 0.3 % RO. Tow sensors were prepared and installed into upper and lower portion on steel mold. A steel mold with the developed pressure sensors locate in thermostat oven, and atmospheric temperature controlled from twenty degrees Celsius to eighty degrees Celsius with step by step. Require temperatures are 20, 40, 60 and 80 C, and the difference is 20 C.

Measurement of deformation due to heating and changing of relative humidity

It is often found out that interpretations of shear strength for unsaturated compacted bentonite have been moderated on previous experimental works corresponding to difference heating methodology as thermal properties in couple phenomena. Almost of

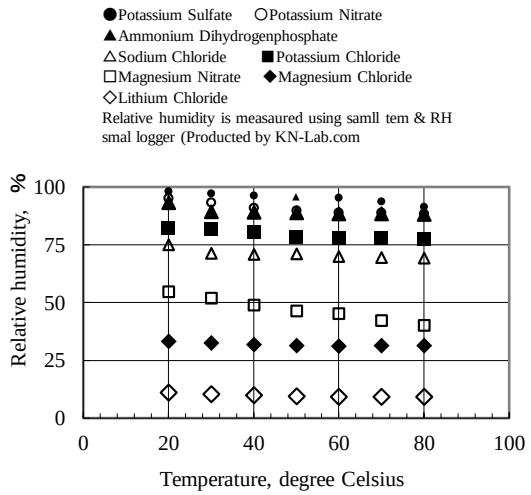

Fig. 1 Calibration of relative humidity corresponding to temperature.

all mechanical tests associated to heating efforts have focused on resistance reduction and translation of stress-strain behavior which many cracks in bentonite caused by heating at least in common. Thermal efforts not only caused producing cracks, but also significant deformations for bentonite is observed that is obviously influence to changing of shear resistance or stability. This testing program prepared to conducted out applying heating and controlling relative humidity that unsaturated bentonite placed into a steel mold with difference chemical substance above mentioned in order to control relative humidity based on vapor pressure technique as one of representative suction controlling methods.

TEST RESULTS

Test results provide calibration of relationship between temperature and relative humidity using a temperature & humidity small logger up to 80 C. Producing increment of relative humidity in specimen with temperature observed, and pore pressure in specimen increased due to isotropic conductivity heating. Deformations for unsaturated bentonite induced by both heating and relative humidity alternation obviously verified, and unconfined compressive strength properties described according to heating efforts.

Calibration for relative humidity variation with increment temperature using temperature & humidity small logger

A steel mold was prepared that some chemical substances were put in order to investigate relative humidity changing. The mold was placed in

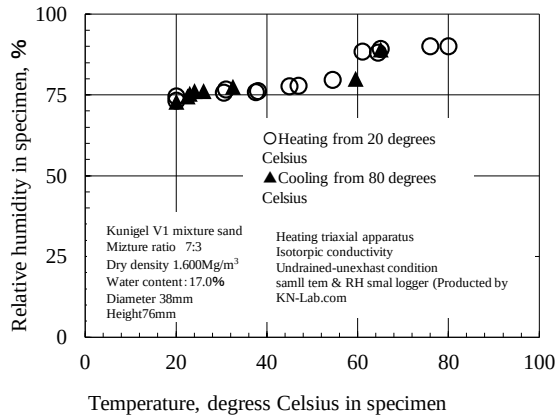

Fig. 2 Changing of relative humidity in unsaturated bentonite with temperature increment and decrement.

thermostat oven, in which permitted a range from twenty degrees Celsius to eighty degrees Celsius. Eights difference chemical substances were used to verify relative humidity corresponding to changing of temperature that obtained result was described as shown in Fig. 1. Determined relative humidity has a range from 95 % to 9.0 %. All of chemical substances have common tendency which is reduction with increment of temperature regardless of relative humidity at twenty degrees Celsius. Much reduction of relative humidity was indicated in such tendency when Magnesium Nitrate was placed in the mold, which showed 54.7 % - 40.2 % reduction in relative humidity. Calibrated results are considerable useful to predict or evaluate relative humidity on heating process.

Changing of relative humidity in unsaturated bentonite increment and decrement in temperature

Beyond establishing calibration relative humidity above mentioned, measuring relative humidity in a specimen simultaneously that illustration was shown in Photo. 1, and consist of two mass and small logger, and they was covered by membrane with a thickness of 2.5 mm. Subsequently, the specimens were put on a pedestal carefully, and membrane covered them. Heating controlling apparatus applied heating to specimens at isotropic thermal conductivity up to eighty C. To measure relative humidity according with increasing the temperature in specimen is significant procedure, and it promoted to convey physical factor corresponding to thermal-hydration phenomena for bentonite. Initially, relative humidity measured a 75 % in rough, and subsequently, slight increment of temperature had produced insignificant increasing of relative humidity till 54.5 C as shown in Fig. 2. Relative humidity of 88.4 % was measured at 61 C beyond 54.5 C that it was distinct increasing. It found out that small growing was remained during

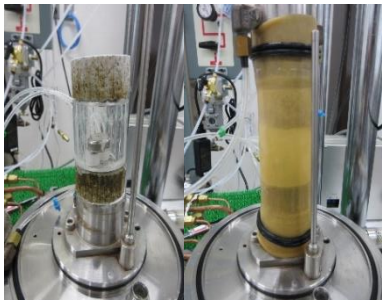

Photo. 1 Measurement of relative humidity in specimen using a small tem & RH logger.

achievement to maximum temperature of eighty degrees Celsius. While cooling process as opposite process, relative humidity was measured, and it had determined that decreasing for relative humidity was confirmed such as opposite behavior comparison to heating process. A few differences are identified though heating process and cooling process, and existing a reversibility for relative humidity associated to change the temperature is applicable on experimental measurement. Finally, when back to twenty C, relative humidity of 75.0 % was determined, and it was coincident to initial relative humidity before heating.

Process of pore pressure due to isotropic conductivity heating for unsaturated bentonite

It is generally that investigation and interpretations for swelling pressure properties of unsaturated bentonite have been studied on experimental works, establishing mathematical models and suggesting further parameters to prediction with safety aspects. Thus, swelling properties is possible to applicable to prediction correct of safety for artificial barrier system as one of thermal-hydration-mechanical-chemical coupling constitutive behavior. Other hands, investigation of evaluation the pore pressure in bentonite due to high heating is necessary to achieve completely understanding scientific phenomena to bentonite associated to various influence factors. This testing programs included that directly measurement was adopted using a developed steel mold, in which had two pressure sensors was install on the lateral surface. The developed steel mold was placed into a thermostat oven as shown in Photo. 2, which had an oven space of 154 liters (i.e. a wide of 600 mm, a length of 600 mm and a height of 430 mm), and a temperature controlling range 60 C to 260 C in possible. A distance is 19.0 mm from each top and bottom of the mold extremity that equipped pressure sensor was correct. The mold had supplied isotropic conductivity heating in the oven. An inspection hall was produced carefully, and two electrical codes having coating connected to pressure sensor, water supply nylon tube having heat resistance are though

Photo. 2 Installed pore pressure sensors at steel mold, thermostat oven and burette for measurement of absorbed water.

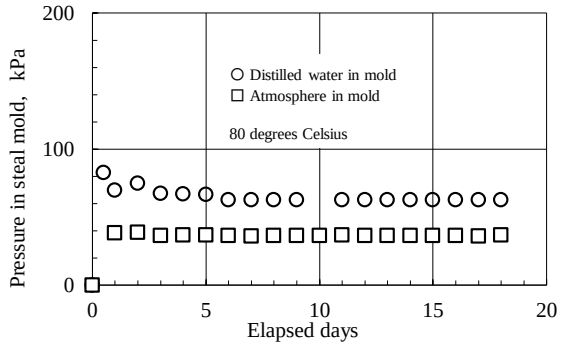

Fig. 3 Occurrence of pressure in mold at 80 C.

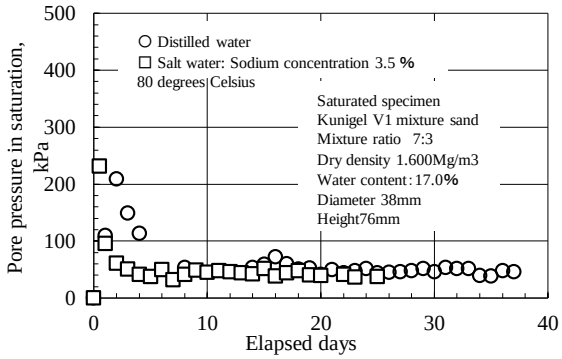

Fig. 4 Occurrence of pressure for saturated bentonite at 80 C.

the surface of wall in thermostat oven.

Firstly, two cases were prepared that distilled water was full up into mold, and other one was empty (i.e. atmospheric only) in order to measure each producing pressure to two difference fluids. Beginning of heating had practice from steady twenty degrees Celsius that it clearly found out increment at once as shown in Fig. 3, and it was easy to consider pressure phenomena for obviously growing the pressure. Comparison two pressure behavior with elapsed day that distilled water was rapidly growing, and had a remaining large pressure than that of atmospheric (i.e. data sets distribution is indicated to atmospheric data sets.). The difference pressure maintained 26 kPa at least while a testing. Then, decision pore pressure in saturated bentonite was adopted that two differences saturated bentonite were

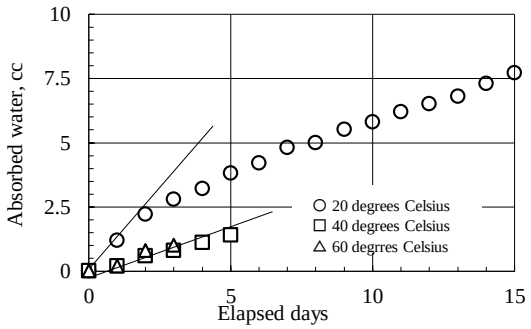

Fig. 5 Deference of absorbed water behavior with various temperature.

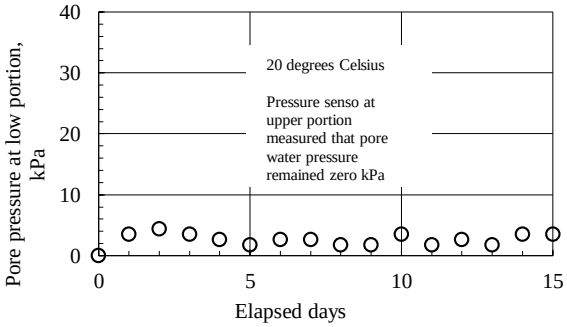

Fig. 6 Changing of pore pressure at 20 degrees Celsius.

prepared in the mold, in which absorbed water was variance in fact. One is distilled water and other one was salt water with 3.5 % of salinity concentration, in which is similar to that of nature sea water. It was causing that eighty degrees Celsius produced excess pore pressure to two saturated specimens as shown in Fig. 4. Further increments of pore water pressure was provided to both containing and no containing in salinity components as comprehension. Maintained pore pressure of 36 kPa was determined at end of test for two saturated bentonites, and it was similar. two saturated bentonites, and it was similar.

Producing pore pressure with accompanying of adsorbed water

It is very interesting to see pore pressure with absorbing of water as swelling properties under isotropic conductivity heating. Heating was applied to unsaturated bentonite in steel mold as shown in Fig. 2, and water supply was adopted from bottom of specimen through nylon tube with temperature resistance. The tube connected to burette installed a difference voltage sensor, in which placed outside of thermostat oven. Magnitude of absorbed water into specimen was automatically measured, and two pressure sensors as explained above measured pore pressure accuracy to each temperature (i.e. 20, 40 and 60 degrees Celsius). Well, adsorbed water changing was indicated under difference temperatures with swelling as shown in Fig. 5. Large absorbing that

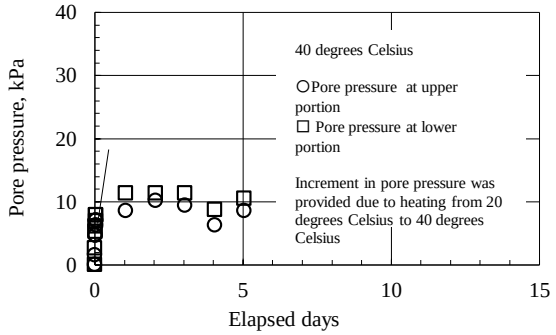

Fig. 7 Changing of pore pressure at 40 degrees Celsius.

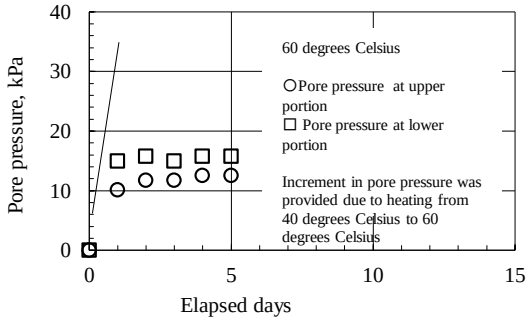

Fig. 8 Changing of pore pressure at 60 degrees Celsius.

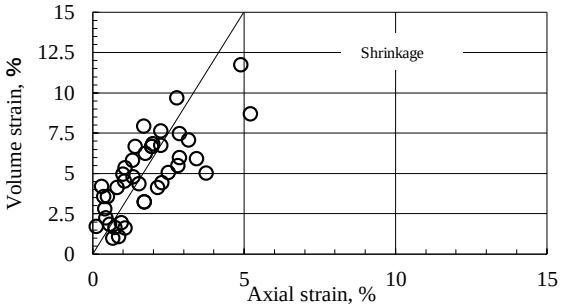

Fig. 9 Relationship between axial strain and volume strain.

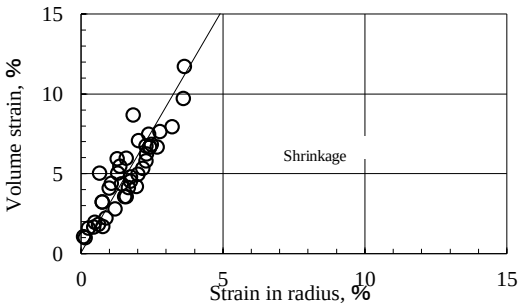

Fig. 10 Relationship between strain in radius and volume strain.

decline was rapidly at twenty degrees Celsius, and subsequently increments were smoothly when commencement at 40 degrees Celsius. Similarity, specimen with 60 degrees Celsius described smooth increment, and tow absorbed phenomena was closely. Simultaneously, pore pressures at two measurement points were measured that pore pressures indicated variation with elapsed day at lower portion of specimen as shown in Fig. 6. Neglection that no measurement was at upper potion at twenty degrees Celsius. Also, pore pressures were observed at tow portions (i.e. upper potion and lower potion) as shown in Fig. 7. Pore pressures grew rapidly at beginning of heating approaching to 40 degrees Celsius. Pore pressures approached to 11.0 kPa as maximum pressure, and it was steady phenomena during five days. Moreover, temperature increased to 600 degrees Celsius as shown in Fig. 8, and pore pressure increased to 16 kPa, and pore pressure at lower portion was larger comparison to pressure upper portion. It was common tendency with limitation in 20, 40 and 60 degrees Celsius.

Volume shrinkage for unsaturated bentonite induced by heating and changing of relative humidity

General speakers have often demonstrated that unmatured benitoite subjected to heating is significant reduction in shear resistance, changing stress-strain properties, decreasing yield stress (i.e. pre-consolidation pressure) and modulus rigidly (i.e. stiffness). It is however few investigations that deformation for unsaturated bentonite due to thermal effort verified on experimental works and solve using prediction mathematical models [2]. It is lack to suggest some parameters associated to volume shrinkage tendency and volume shrinkage index. This study realized through volume change test for unsaturated bentonite, which both heating and relative humidity changing applied to all specimens in a steel mold place in a thermostat oven. Three difference chemical substances were put into the steel mold, that were Magnesium Chloride, Sodium Chloride and Ammonium Dihydrogen phosphate. Each relative humidity was corresponding to 55.0 %, 75.0 % and 93.0 % at twenty degrees Celsius. As above mention (Fig. 1), each relative humidity varies depending on temperature. After equilibrium each temperature and relative humidity, a diameter and height were collected, and calculated strain to radius way and axial way. In addition to compose each strain to estimate total volume shrinkage strain. To better find some tendency regard to producing deformation for unsaturated bentonite is so interesting and is further effectively to understanding bentonite properties deeply. Volume shrinkage strains corresponding to each axial strain and strain in radius way are shown in Figs. 9 and 10. Strain in radius exhibit to be close to volume shrinkage strain compare to axial strain, and it was 3 times to strain in radius way. It has been moderated the producing

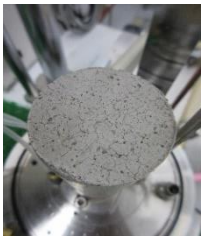

Photo. 3 Observed cracks on surface for unsaturated bentonite subjected to heating.

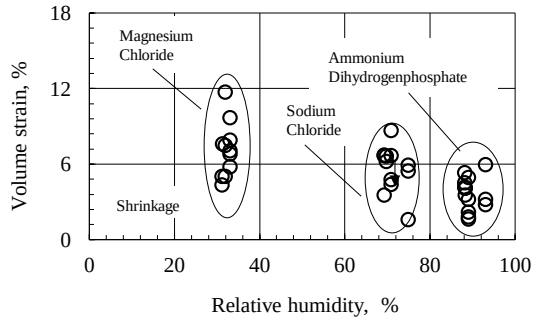

Fig. 11 Increment of shrinkage with decreasing of relative humidity.

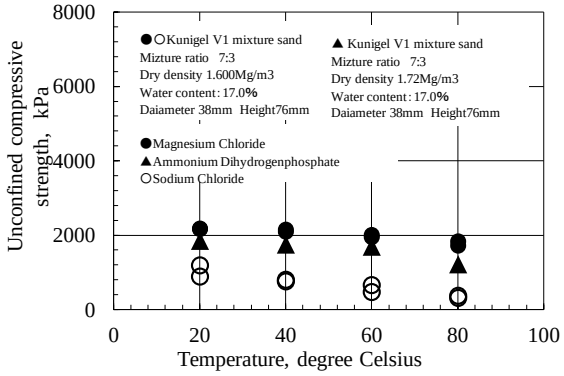

Fig. 12 Reduction of unconfined compressive strength due to heating.

cracks for unsaturated bentonite subjected to heating or increment of temperature, and significant cracks are confirmed in this study with similar to previous investigation as shown in Photo 3. Many cracks are widely sprayed on the surface of specimen, and they are either continuous distribution or discontinuous distribution. Volume shrinkage strain is discussed like a thus cracks distribution. Relationship between relative humidity and volume shrinkage strain was verified with three groups used in Magnesium Chloride, Sodium Chloride and Ammonium Dihydrogen phosphate as shown in Fig. 11. It is seemed to be reduction in volume shrinkage strain with increasing of relative humidity that has widely scatter, and it is difficult to establish applicable trend.

Discussion for shear resistance subjected to heating and changing of relative humidity

As mechanical component, unconfined compression test conducted out for unsaturated bentonite subjected to heating and developed relative humidity, and all specimens had further cracks as shown in Photo. 3. All specimens were applied required temperatures using a heating triaxial compression triaxial apparatus, while temperatures were 20, 40, 60 and 80 degrees Celsius. Reductions of unconfined compressive strength was provided through four difference temperatures as one tendency as shown in Fig. 12. Volume shrinkage and much cracks are significant factor to decrease the resistance of unsaturated bentonites.

CONCLUSIONS

This study conducted out some experimental tests that the subjections were to realize thermal properties for bentonite, and some developed tests revealed important characters including heating efforts. The obtained resukts are summaried as following: Growing of pore pressure was induced by heating for saturated bentonite, that is confirmed to both distilled water and salinity water. Pore pressure accomplishing with absorbed water through sweing process obvioulsy increased according to incremant of temperature. Further volume shrinkage was derived due to heating and changing of relative humidity, that relationship between volume shrinkage strain and strain in radius way verified as one unique tendency. Fiinally, the unsaturated benotite subjected to heating effort and chnaging relative humisity exhibited reduction to unconfined cmompressive strength.

ACKNOWLEDGMENTS

The author is grateful to Dr. Shuichi YAMAMOTO (Obayashi Corporation, Japan) for supporting to establish pore pressure measurement system using developed pressure sensor. Also, this study has been supported by a Grant-in-Aid for Scientific Research (No. 21K04259) from JSPS.

REFERENCES

[1] Bucher, F. and Müller-Vonmoos, M., Bentonite as a containment barrier for the disposal of highly radioactive wastes, Appl. Clay Sci. 4, No. 2, 157–177, 1989.

[2] Lloret, A. and Villar, M., Advances on the knowledge of the thermo-hydro-mechanical behaviour of heavily compacted 'FEBEX' bentonite. Phys. Chem. Earth, Parts A/B/C 32, No. 8, 701–715, 2007.

11th Int. Conf. on Geotechnique, Construction Materials & Environment,
Kyoto, Japan, 3-5 November 2021, ISBN: 978-4-909106063 C3051

STUDY OF SOIL ERODIBILITY UNDER THE POTATO FARMING SYSTEM IN THE UPSTREAM LEMBANG WATERSHED

Aprisal[1], Bambang Istijono [2], Irwan Darpis[1], Mimin Harianti[1], and Teguh Huria Aditia[3].

[1] Soil science of Agriculture Faculty Andalas University, Padang Indonesia
[2] Hydrology laboratory technique Faculty of Andalas University Padang Indonesia
[3]Postgradute of Soil Science of Agriculture Faculty Andalas University Padang, Indonesia

ABSTRACT

Farmers cultivate potatoes intensively in the upper Lembang watershed, i.e. cultivate the land every planting season. The soil management system does not apply soil conservation methods, so it is suspected that there has been a decline in soil fertility. The purpose of this study was to examine the soil properties of potato farming in several land forms. The method used is the land survey method. Soil sampling was done by purposive random sampling and descriptive. Soil samples taken were disturbed soil samples for analysis of soil physical properties (texture, bulk density, total pore space, permeability) while direct measurements in the field were effective soil depth and infiltration rate. Meanwhile, undisturbed soil samples were used to analyze the chemical properties of C-organic soil. Soil analysis was carried out in the laboratory of the Department of Soil, Faculty of Agriculture, Andalas University. To determine the soil characteristics of the landform is to analyze the soil parameters using Minitab 17 software. The results showed that the value of soil erodibility in the production center area is strongly influenced by c-organic variables, dust, bulk density, total pore space, fine sand fraction, fraction clay and soil permeability. The value of soil erodibility includes low to moderate criteria. It was concluded that the soil condition was still quite good.

Keywords. Potato farming, soil erodibility, soil degradation, conservation

INTRODUCTION

Intensive land use in agricultural land, causes changes in soil properties, such as soil resistance to the destructive power of rain kinetic energy or also known as rain erosivity energy. Soil resistance to the destructive power of raindrop energy greatly influences soil erosion or erosion of the soil surface, causing the soil surface layer, especially the tillage layer to become thinner. This is because erosion carries parts of the soil from one place to another, especially on lower slopes. According to the soil loss equation, the rate of soil erosion can be more influenced by rainfall characteristics, land slope and slope length, land cover, and management than soil properties. However, some soils erode more easily than others despite the similarity of the factors of the soils. This difference, influenced by the properties of the soil itself, is called soil erodibility [1]. Soil erodibility is strongly influenced by soil properties such as: soil texture (very fine sand, silt, and clay), soil structure, organic matter content, and permeability [2].

The shape of the land cultivated by farmers now is wavy, so this causes a variety of soil properties. The cause is the effect of erosion on land with sloping slopes and accumulation of erosion material on lower or flatter slopes transported by surface runoff. The soil is easily eroded by surface runoff due to its height. Varied landforms and intensive use will cause soil erodibility values to also vary. Land that has a gentler slope will cause the erodibility of the soil to be higher. This will causethe amount of fine soil particles carried by surface runoff [3].Therefore, soil erodibility is the sensitivity of the soil to erosion, the higher the erodibility value of a soil, the easier the soil is to erode. Soil erodibility is influenced by soil texture, soil structure, organic matter, and permeability [4]. Soil erodibility factor shows the resistance of soil particles to peeling and transport of soil particles by the kinetic energy of rainwater [5]. Furthermore, it was found that the average soil loss was negatively correlated with clay content but positively correlated with very fine sand and silt plus very fine sand content [6]. Soil physical and chemical properties are often influenced by organic matter content, by building aggregations, soil organic matter affects soil erodibility.

This study aims to study the dominant factors that affect the value of soil erodibility in potato production centers in the upstream sub-watershed of Lembang.

MATERIALS AND METHODS

Research sites

This research was conducted in a potato production center located in the upstream of the Lembang sub-watershed. More precisely in the villages of Kampung Batu Dalam and Batu Bajanjang with a geographical position of 100º42'0" E - 100º44'0"E and 1º0'0"S-1º0'2"S (Figure 1), Solok district, West Sumatra, Indonesia.

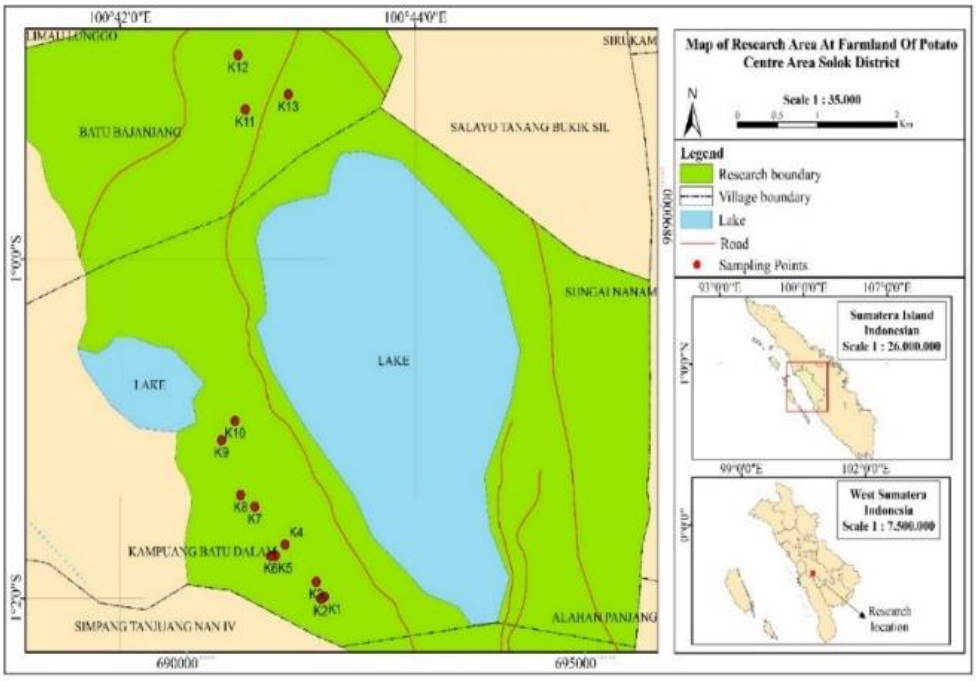

Figure 2. Map the research location.

Research methods

Soil sampling.

This research was conducted by means of a field survey in the potato production center area in the Upper Lembang sub-watershed. Samples were taken

Figure 2. Photos of potato fields in the research location.

based on five groups of land units (Table 1). Based on the soil map, the potato production center area is dominated by two soil orders, namely Andisol and Inseptisol (Table 1). The study was conducted on V groups of farmers based on the physiography of the land, the groups are; groups I, II, III, IV and V. Group I is flat, II is slightly sloping, III is sloping, IV is flat, V is sloping. Therefore, it is the center of potato production. Soil samples taken are undisturbed soil samples with a ring sample for analysis of soil physical properties. For analysis of soil chemical properties, disturbed soil samples were taken using a Belgian soil drill.

Table 1. Groups, soil types and sampling points

Location	Type of soil	Soil sampling	plan type
I	Andisol	3	Potatoes
II	Andisol	2	Potatoes
III	Inceptisol	4	Potatoes
IV	Inceptisol	2	Potatoes
V	Inceptisol	2	Potatoes

Soil analysis in the laboratory.

Soil samples from the field were analyzed in the soil laboratory, for analysis of soil physical properties for variables; texture and permeability, bulk density, total pore space. The variable soil chemical properties analyzed were organic matter.

Soil Variable Calculation

Soil erodibility.

Soil variable data from the results of laboratory analysis is used to calculate the value of soil erodibility using the soil erodibility formula [1]. Soil Erodibility (K) The calculation, soil erodibility is obtained from the results of field observations and laboratory analysis. The soil properties tested were organic matter content, texture, structure, soil permeability, which were then calculated using the equation 1:

$$K = \frac{2{,}71\, M^{1{,}14}\,(10^{-4})(12-a)+3{,}25(b-2)+2{,}5(c-3)}{100}$$

description: M = value of (% dust + % very fine sand) (100 - % clay)
a = organic matter (% C organic x 1.724)
b = soil structure value
c = value of permeability

Table 2. Criteria for soil erodibility value

No	Class	Criteria
1	Very low	0.00 – 0.10
2	Low	0.11 – 0.20
3	Currently	0.21 – 0.32
4	A bit high	0.33 – 0.43
5	Tall	0.44 – 0.55
6	Very high	0.56 – 0.64

The erodibility value obtained from the calculation of the soil properties in each land unit is compared with the criteria for the erodibility value of the soil (Table 2).

Principle component analysis

Analysis of the main components of the soil from the erodibility characteristics of the soil. Principal Component Analysis (PCA), is used to: determine what factors most influence the value of soil erodibility. The researcher also uses this method to determine the main factors that affect the value by using PC with an eigenvalue of more than 1 as the independent variable. Therefore, this value is highly correlated with the independent value in PC, [7]. Researchers used Minitab 17 to analyze data variables.

RESULTS AND DISCUSSION

Soil properties

From the soil analysis in the laboratory, soil variables were obtained to calculate the soil erodibility value (Table 2). The results of the analysis of the physical and chemical properties of the soil at the research site (Table 2) indicate that the soil in this area is dominated by soil with a dusty loam texture and crumb soil structure, so that potatoes are very suitable to grow in this area. The soil is quite crumbly and plants can grow and develop well. In this soil condition, potato roots and tubers can develop optimally, so that potato yields are optimal. Soils that have loose properties are usually easily dispersed by the kinetic energy of rainfall.

Soil Erodibility

Based on the variable data of soil properties (Table 3), the soil erodibility value was calculated using the formula. From the calculation results of the soil erodibility value, the soil erodibility value is obtained as shown in Table 4. This soil erodibility value is compared with the criterion value (Table 2). It turns out that the value of soil erodibility in this potato production center area is dominated by very low and low criteria. This means that the soil in the potato production center area has a fairly good ability to withstand the threat of soil erosion. This is due to the high influence of organic matter on the soil so that it can become a cemented agent for soil fractions. Further research [6]. in Iran also stated that organic matter by coating soil particles and creating a water-repellent layer that prevents soil release and keeps soil particles flocculated, thereby reducing erodibility and soil erosion. In addition, the factor seen from the relationship between organic matter and erodibility has a negative correlation, meaning that increasing organic matter will reduce the value of soil erodibility..

Further research [8] showed that soil organic matter and clay content were the main factors affecting soil anti-erodibility in the Loess Plateau and the percentage of stable aggregate to water was the best indicator.

Table 3. Soil properties from the location of the potato production center area in the upstream sub-watershed of Lembang.

Location of The sampling	C-org %	Sand %	Dust %	Clay %	Bv g/Cm3	Permeability (cm/hour)	Total Pore %
1	6.94	6.1	68.86	24.84	0.53	24.79	80
2	7.08	12.87	70.1	16.7	0.54	2.86	76.02
3	4.45	20.25	57.87	18.26	0.7	7.31	73.58
4	6.99	4.29	62.94	26.1	0.66	7.54	75.09
5	8.31	5	62.48	22.23	0.65	26.18	75.47
6	9.26	5.78	57.83	33.25	0.85	1.95	67.92
7	7.56	5.68	61.52	23.9	0.46	0.35	82.64
8	9.9	5.68	51.51	23.9	0.65	12.51	75.47
9	10.18	7.67	66,48	8.02	0.78	4.44	70.57
10	9.4	13.79	67.44	15,17	0.56	21.85	78.87
11	11.59	6.62	51.13	24.21	0.97	2.14	63.4
12	11.74	5.26	44.73	42.07	0.92	10.96	65.28
13	8.62	6.75	47.38	17.92	0.91	21	65.66

Table 4. Soil properties and soil erodibility values in the potato production center area in the upstream Lembang sub-watershed

Location sampling	fine sand %	Dust %	Clay %	a	b	c	M	K
1	6.1	68.86	24.84	6.94	3	1	5634.0	0.15 r
2	12.87	70.1	16.7	7.08	2	3	6911.4	0.13 r
3	20.25	57.87	18.26	4.45	2	2	6385.5	0.19 r
4	4.29	62.94	26.1	6.99	2	2	4968.3	0.12 r
5	5	62.48	22.23	8.31	3	1	5247.9	0.12 r
6	5.78	57.83	33.25	9.26	2	4	4246.0	0.09 SR
7	5.68	61.52	23.9	7.56	2	5	5113.9	0.15 r
8	5.68	51.51	23.9	9.9	3	1	4352.2	0.07 SR
9	7.67	66,48	8.02	10.18	2	3	6820.3	0.05 SR
10	13.79	67.44	15,17	9.4	3	1	6890.7	0.09 SR
11	6.62	51.13	24.21	11.59	2	3	4376.9	0.01 SR
12	5.26	44.73	42.07	11.74	3	1	2895.9	0.02 SR
13	6.75	47.38	17.92	8.62	3	1	4443.0	0.11 r

Description: K = erodibility, M = value of (% dust + % very fine sand) (100 - % clay) a = organic matter (% C organic x 1.724) b = soil structure value c = permeability value, SR = very low, r = low

Table 5. The eigenvalues from the analysis of soil variables with PCA

Eigenvalue	4,7864	1,2779	1,1122	0,9514	0,4367	0,3426	0,0749	0,0109	0,0070
Proportion	0,532	0,142	0,124	0,106	0,049	0,038	0,008	0,001	0,001
Cumulative	0,532	0,674	0,797	0,903	0,952	0,990	0,998	0,999	1,000

Table 6. The loading matrix value from analysis of soil biophysical properties

Variable	PC1	PC2	PC3	PC4	PC5	PC6	PC7	PC8	PC9
Location	-0,375	0,098	-0,356	0,086	0,512	-0,267	0,605	-0,038	0,123
K	0,401	0,057	0,265	0,317	0,040	-0,351	0,286	0,503	-0,454
C-org	-0,395	-0,174	-0,301	-0,273	0,099	0,308	-0,167	0,501	-0,515
Sand	0,213	0,670	-0,034	0,205	0,326	0,594	-0,029	0,004	-0,047
Dust	0,366	-0,064	-0,264	-0,384	-0,407	0,311	0,618	-0,007	-0,001
Clay	-0,209	-0,425	0,634	0,122	0,194	0,461	0,323	-0,029	0,048
Bv	-0,402	0,280	0,107	0,185	-0,416	-0,032	0,163	-0,462	-0,548
Permebility	0,066	-0,376	-0,461	0,748	-0,181	0,216	-0,037	-0,011	0,045
Total Pore	0,392	-0,323	-0,123	-0,140	0,459	-0,024	-0,098	-0,530	-0,454

Principle Component Analysis (PCA)

Eigenvalues

The determining factor based on the eigenvalue greater than 1 is retained, but if it is less than 1 then the factor is excluded from the model. An eigen value shows the contribution of the factor to the variance of all original variables. Only factors with variance greater than 1 are included in the model. Factors with a variance of less than 1 are not good because the original variables have been standardized, which means the average is 0 and the variance is 1 (Table 5).

Main component

To determine which soil properties are more dominant, the soil erodibility factor is determined based on the results of the principle component analysis (PCA) and can be seen in table 6. From the PCA analysis, there are three main components that determine the diversity of soil erodibility, namely PC1, PC2 and PC3. . Table 6 shows that there are three factors (PC) having eigenvalues greater than 1, namely PC1, PC2 and PC3. Of the three factors, it is able to explain the variation of the total data that more influences the value of soil erodibility in the potato production center area in the upstream Lembang sub-watershed. From the extract of many data variables, PC1 with an eigen value of 4.78 gives the proportion of influence of 53.2 percent. Then PC2 with an eigen value of 1.27 gives a proportion of 14.2 percent, and PC3 with an eigen value of 1, 11 contributed a proportion of 12.4 percent. These three components cumulatively contribute to explaining the diversity of the total data by 79.7 percent. This means that these three components are representative for all variations that affect the value of soil erodibility in the potato production center area. The first factor (PC1) is a variable of soil properties, namely c-organic, and dust. The second factor (PC2) is sand, and clay. While the third factor (PC3) is the rate of permeability. His previous research [9]. This means that these three components are representative for all variations that affect the value of soil erodibility in the potato production center area. The first factor (PC1) is a variable of soil properties, namely c-organic, and dust. The second factor (PC2) is sand, and clay. While the third factor (PC3) is the rate of permeability. His previous research [9]. This means that these three components are representative for all variations that affect the value of soil erodibility in the potato production center area. The first factor (PC1) is a variable of soil properties, namely c-organic, and dust. The second factor (PC2) is sand, and clay. While the third factor (PC3) is the rate of permeability. His previous research [9]. stated otherwise, sand content has a negative relationship with erodibility and sediment load. Because the mass of the sand particles is greater, runoff cannot transport them. On the other hand, the presence of sand particles in the soil causes an increase in macro pores, water infiltration, and consequently a decrease in susceptibility to erosion.

CONCLUSION

Based on the results of the study, several conclusions can be drawn;

1. That the resistance of the soil to the erosion of rain erosion is strongly influenced by several variables of soil properties, namely c-organic, fine sand, dust, clay and soil permeability.
2. The value of soil erodibility in the corn production center area is still in very low to low criteria. This means that the soil in this area is not easily damaged by the erosive energy of rain.

ACKNOWLEDGMENTS

The researcher wishes to express his profound gratitude to the rector of Andalas University for the support and providing all the facilities needed to carry out this study. This research was funded by Andalas University under Research Grant No SP DIPA 023.017.2.677513/2021, 23 Novemver 2020

REFERENCES

[1]. Wischmeier, W., Johnson, C., Cross, B. A land of the nomograph erodibility for farmland and

construction sites. Journal of Soil and Water Conservation Vol.26,No.3,1971, pp.189-193

[2]. Bhandaria, KB, Charles P. Westa, Veronica Acosta-Martinezb, Jon Cottonb, and Amanda Cano. 2018. Soil health indicators as affected by diverse forage species and mixtures in semi-arid pastures. Applied Soil Ecology 132 (2018) 179–186

[3].. Aprisal, Istijono. Taifur, WD, Indradwipa. 2020 Study effect of land management of horticultural on soil erodibility at the upstream of sumani watershed. International Journal of GEOMATE, March, 2020, Vol.18, Issue 67, pp. 175-181 ISSN: 2186-2982.

[4]. Arsyad, S. 2000. Soil and water conservation. IPB Press. Bogor.

[5]. Asdak, Chay. Hydrology and river basin management. Yogyakarta: Gadjah Mada University Press.2004.pp1-61

[6]. Mazllom, U., Emami, H., Hossain, G., Haghnia. 2016. Prediction the soil erodibility and sediments load using soil attributes. Eurasian J Soil Sci 2016, 5 (3) 201 - 208

[7]. Santoso, S. 2002 "SPSS Multivariate Statistics", Jakarta: PT. Elex Media Kompitundo

[9]. Wang, YM, Guo, PC, Gao, WS, 1994. A study on soil anti-erodibility in Loess Plateau. Journal of Soil Erosion and Water Conservation 8(4): 11-16 [in Chinese].

[10]. Santos, FL, Reis, JL, Martins, OC, Castanheira, NL, Serralheiro, RP, 2003 Comparative assessment of infiltration, runoff and erosion of sprinkler irrigated soils. Biosystem Engineering 86(3): 355-364

11th Int. Conf. on Geotechnique, Construction Materials & Environment,
Kyoto, Japan, 3-5 November 2021, ISBN: 978-4-909106063 C3051

A STUDY ON APPLICATION OF DEEP LEARNING TO WATER ENVIRONMENT PLANNING

Shengping Zhang[1] and Jie Qi[2]

[1]Professor, Meijo University, Japan; [2]Professor, Utsunomiya University, Japan

ABSTRACT

The water environment of the most important watersheds has generally not been improved upon in a considerable manner in the last two decades although the Japanese government has made significant management and improvement efforts, such as increasing sewerage system coverage rates nationwide and installing advanced wastewater treatment systems. The marginal effects of these direct efforts have been diminishing. This study seeks to discover the most effective water environment improvement measures in a wider range other than those direct measures. An artificial intelligence (AI) model has been constructed with Deep Learning technology by applying the watershed information from the 104 watersheds as the teacher data to train the AI model. The well-trained AI model is used to identify the effectiveness of all the direct and indirect water-environment-related factors, ranging from geological/geographical factors, hydrological/hydraulic factors to socio-economic factors. This study concludes by pointing out that Deep Learning is able to reveal and simulate the complicated relationships between river management goals and diverse water environment factors and it is also able to make the sensitivity analysis and the selecting of effective water environment improvement measures much more convenient and reliable. The aim of this study is to establish a more reliable river environment planning and management methodology.

Keywords: Water Environment Evaluation, Artificial Intelligence (AI), Deep Learning, Sensitivity Analysis

INTRODUCTION

Water environment evaluation and planning have been mainly depended on 1) mathematic models that simulate all the physical, chemical and biochemical processes leading to water environment changes over time and space and 2) expertise of planners on a specific river [1]. Mathematic models connect all direct water environment factors to management goals, and the final evaluation and decision-making are usually based on the expertise of planners. In this planning process, most of the indirect environment factors have not been taken into consideration in a reasonable and proper manner, and expertise tends to put much more weights on characters of a specific river and ignore the common characters of all the other rivers in the same region. How to evaluate and apply the experiences and lessons all the rivers with some common characters can provide has been remained to be answered. This study approaches this problem by applying the water environment big data to environment planning.

In Japan, a water quality survey of public water areas focusing on items that are used in environmental quality standards (EQSs) for the prevention of water pollution has been performed since 1971 under the provisions of the "Water Pollution Control Law" (enacted in December 1970). This survey has been conducted by local governments (including prefectures and designated cities) under the Water Pollution Control Law and also, in the case of direct-administrative-control areas of Class-A rivers.

The survey has shown that the requirements of the environmental quality standards for human health have been achieved in almost all monitoring sites for the last thirty years, and the achievement rate was 99.1% in 2018 [2]. As for the environmental quality standards for conservation of the living environment, their achievement rate of BOD had improved significantly in the first three decades after the survey started, and compliance rate reached 90% in 2004 for the first time since the survey started [3].

However, the compliance rate of the environmental quality standards for conservation of the living environment was still 94.1% in 2018 [2], and the water environment of the most important watersheds, almost all of which are designated as the direct-administrative-control areas of Class-A rivers, generally has not been improved in a considerable manner in the last two decades, although the Japanese government has made significant management as well as improvement efforts, such as increasing sewerage system coverage rates nationwide, installing advanced wastewater treatment systems. It is believed that the marginal effects of these direct efforts have been diminishing [4]. This study seeks to discover the most effective water environment improvement measures in a wider range outside of these direct measures. An artificial intelligence (AI) model has been constructed with Deep Learning technology by applying the watershed information from the 104 Class-A watersheds as the teacher data to train the AI model.

ARTIFICIAL INTELLIGENCE MODEL

An artificial intelligence model, specifically a neural network model has been adopted to compose a water environment evaluation method for evaluation or prediction problems due to the suitability of neural network models [5], [6].

Structure of A Neural Network [6]

A neural network is a network system constructed artificially by idealizing the neurons (nerve cells), and consists of a number of nodes and lines that are called *units* and *connections* (or *links*) respectively. Based on the differences in network structures, neural networks generally are classified into two types: layered networks and interconnected networks. It has been shown that a layered network is suitable for evaluation/prediction problems due to its abilities in learning (self-organization) and parallel processing of information.

A typical layered neural network, which has a layer of input units at the top, a layer of output units at the bottom, and a number of hidden layers between the input layer and the output layer. Connections exist only between the units in the adjacent layers, and connections within a layer or from higher to lower layers are forbidden.

Modelling A Neural Network

For the sake of simplicity, consider a neural network consisting of three layers.

Let the unit numbers of the input layer, hidden layer and output layer be N, M, and 1, respectively. When an input $\{I_i,\ i = 1,2,\cdots,\ N\}$ is given to the units of the input layer, the inputs and outputs of the hidden layer units as well as the output layer units are represented as follows.

$$Y_j = f(X_j),\ \ j = 1,2,\cdots,M \tag{1}$$

$$X_j = \sum_{i=1}^{N} w_{ij} I_i + \theta_i \quad ,\quad j = 1,2,\cdots,M \tag{2}$$

$$O = f(Z) \tag{3}$$

$$Z = \sum_{j=1}^{M} w_j Y_j + \theta \tag{4}$$

Where Y_j : output from the unit j of the hidden layer.
X_j : input the unit j of the hidden layer.
$f(\cdot)$: unit output function.
w_{ij}: connection weight between the input layer unit i and hidden layer unit j.
θ_j : threshold value of the hidden layer unit j
O : output from the output layer unit.
Z : input to the output layer unit.
w_j: connection weight between the hidden layer unit j and the output layer unit.
Θ : threshold value of the hidden layer unit j

For the unit output function $f(\cdot)$, some expressions have been proposed. The following Sigmoid function has been applied frequently. However, it is not necessarily the best one in terms of learning efficiency. A testing process for different output functions is strongly suggested. In this studied this Sigmoid function has been finally adopted after careful tests.

$$f(x) = \frac{1}{1 + e^{-x}} \tag{5}$$

Theoretically, the neural network model expressed by Eqs. (1) through (5) is able to approximate any non-linear relationship between inputs and outputs with any degree of accuracy by using enough hidden layer units and setting connection weights and thresholds to be appropriate through proper learning processes [6]. The potential of this model has been verified with similar problem to this study [4].

Learning Process of Neural Network Model

For a neural network model, the process of setting the connection weights unit thresholds is called *learning*. The term *learning* here means the self-organization process through which the neural network model automatically adjusts all the parameters (i.e. all the connections and thresholds) to the appropriate values, when a series of samples of input-output data (called teacher data or teacher signals) are shown to the model. If we consider the information processing in a neural network model as a transformation of input data to output data, then model learning can be considered to be a process through which the neural network model gradually becomes capable of imitating the transforming patterns represented by the teacher data.

A lot of learning algorithms have been proposed, and among them the Error Back Propagation Algorithm is the most widely used and most successful algorithm. The following is the summary of the Error Back Propagation Algorithm [7].

Suppose T sets of teacher data are given.

$$\left\{I_1^{(t)}, I_2^{(t)}, \cdots, I_N^{(t)}, O^{(t)};\ t = 1,2,\cdots,T\right\} \tag{6}$$

Notice that the teacher data consists of two parts: the input part $\left\{I_1^{(t)},\ I_2^{(t)}, \cdots,\ I_N^{(t)};\ t = 1,2,\cdots,T\right\}$ and the output part $\left\{O^{(t)};\ t = 1,2,\cdots,T\right\}$.

Now consider an initial value

$$w_{ij}^{[k]}, w_j^{[k]}, \theta_j^{[k]}, \theta^{[k]} \ , \ k = 0 \tag{7}$$

for each of the connection weights and threshold values, respectively. Notice that the superscript [k] indicates the number of learning iterations and [k=0] means the initial values for all the parameters directly preceding the start of the learning process. Then the outputs corresponding to the inputs of the teacher data $\left\{I_1^{(t)}, I_2^{(t)}, \cdots, I_N^{(t)}; \ t = 1, 2, \cdots, T\right\}$ can be obtained from Eq. (1) ~ Eq. (5). Let these outputs be $\left\{U^{[k](t)}; \ t = 1, 2, \cdots, T \ and \ k = 0\right\}$. Clearly, $\left\{U^{[k](t)}; \ t = 1, 2, \cdots, T \ and \ k = 0\right\}$ are different from the outputs of the teacher data $\left\{O^{(t)}; \ t = 1,2, \cdots, T\right\}$, and an error function can be defined with the two different kinds of outputs as follows.

$$R^{[k]} = \sum_{t=1}^{T} \left(O^{(t)} - U^{[k](t)}\right)^2, \ k = 0 \tag{8}$$

Obviously, $R^{[k]}$ is a function of connection weights and threshold values because $\left\{U^{[k](t)}; \ t = 1, 2, \cdots, T \ and \ k = 0\right\}$ are calculated after all $w_{ij}^{[k]}$, $w_j^{[k]}, \theta_j^{[k]} \ and \ \theta^{[k]}$ are given.

The Error Back Propagation Algorithm makes use of the connection weights and threshold values that minimize the above error function $R^{[k]}$. Usually a non-linear programming method is required to solve the optimization problem along with an iteration process in order to obtain the optimal (but possibly suboptimal) connection weights and threshold values. The final iteration procedures derived from a non-linear programming method known as the Method of Gradient Descent are as follows.

$$w_j^{[k+1]} = w_j^{[k]} - \eta \cdot \sum_{t=1}^{T} \left(\delta^{[k](t)} \cdot Y_j^{[k](t)}\right) \tag{9}$$

$$\theta^{[k+1]} = \theta^{[k]} - \eta \cdot \sum_{t=1}^{T} \delta^{[k](t)} \tag{10}$$

$$w_{ij}^{[k+1]} = w_{ij}^{[k]} - \eta \cdot \sum_{t=1}^{T} \left(\delta^{[k](t)} \cdot w_j^{[k+1]} \cdot \gamma_j^{[k](t)} \cdot I_i^{(t)}\right) \tag{11}$$

$$\theta_j^{[k+1]} = \theta_j^{[k]} - \eta \cdot \sum_{t=1}^{T} \left(\delta^{[k](t)} \cdot w_j^{[k+1]} \cdot \gamma_j^{[k](t)}\right) \tag{12}$$

where the superscript [k] indicates the number of learning iterations as mentioned earlier, and η is a small positive number that indicates the step size of the Method of Gradient Descent for optimization iteration process, and we have set $\eta = 0.25$ in this study. The other variables which occurred in the final learning procedures are defined as follows.

$$\delta^{[k](t)} = (O^{(t)} - U^{[k](t)}) \cdot O^{(t)} \cdot (1 - O^{(t)}) \tag{13}$$

$$\gamma_j^{[k](t)} = Y_j^{[k](t)} \cdot \left(1 - Y_j^{[k](t)}\right) \tag{14}$$

In order to avoid the overfitting (or over-learning) problem, a criterion is usually required to make a judgement when the iterative learning process should be terminated. In this study the learning process will be stopped when the Mean Relative Error (MRE) of the outputs is less than a specified relative error expectation for prediction/evaluation results, which is a common treatment for a learning process of teacher data with random errors (i.e. white noise). Needless to say, this error expectation should be set according to the required accuracy of the problem which is being dealt with. In this study we have set the error expectation to 2%, which is considered an accuracy that is good enough for the expected result.

TRAINING OF NEURAL NETWORK MODEL

Teacher Data

In order to apply the neural network model proposed above to a water environment evaluation problem, the model has to be trained appropriately through a deep learning process by using water-environment-related data.

In this study, the data obtained from the water quality survey conducted for the 109 Class-A rivers of Japan are used for the deep learning process [8].

After a careful data verification process, only 104 rivers out of 109 are chosen to be included in the teacher data set for deep learning because there are quite a few of data missing for the other 5 rivers. For each river the data includes 58 water environment items as shown in Table 1. The data records used in this study are from 1998 to 2018 with a duration of 21 years long.

The 58 environment items are divided into two parts to form a teacher data set, evaluation goal variables and explanation variables. The evaluation goal variables include the five environment items that are used to define The Water Environment Standards for Rivers as shown in Table 2 [9], which are pH, BOD, SS, DO and Total coliform. All the environment items are used to explain how the achievement of water environment standards are impacted.

The achievement of water environment standards has been scored with an effort to make the final scores for different standard classes that are corresponding to different water use purposes a uniform distribution, which is expected to maximize the score distance between different standard classes. The results are shown in Table 3.

Table 1 Water environment items included in the teacher data for deep leaning

Category	Water Environment Item	Number of Items
Time of Sampling	Year/Month/Day/Hour	4
River/Flow Conditions	Place of Sampling Weather Water Level Quantity of Flow Total Water Depth Water Depth of Sampling Temperature Water Temperature Visual Appearance: 1) Water Color 2) Flow Strength 3) Turbidity (Muddiness) 4) Floating Waste/Garbage Water Smell Vertical Visibility Horizontal Visibility Time of Low Tide of Sampling Day Time of High Tide of Sampling Day	17
Watershed Conditions	Length of Main Stream Catchment Area Catchment Population Number of Tributaries Annual Average Stream Flow Number Of Dams Number Of Hydraulic Power Plants	7
Water Quality Indexes For The Living Environment	pH BOD COD SS DO Saturation Degree of DO Total Coliform The Amount of N-Hexane Extract(Oil) Total Nitrogen Total Phosphorus	10
Water Quality Indexes About Human Health	Cadmium Cyanogen Lead Hexavalent Chromium Arsenic Total Mercury Alkyl Mercury PCB Dichloromethane	9
Water Quality Index For Inflow Of Domestic Wastewater;	Ammonium Nitrogen	1
Others	Chromaticity Turbidity Evaporation Residues Total Hardness Potassium Permanganate Consumption Sodium Iron Manganese Aluminum Residual Chlorine	10
		Total: 58

Table 2 Water environment standards for rivers [9]

Item class	Water use	Standard value				
		Hydrogen-ion concentration (pH)	Biochemical oxygen demand (BOD)	Suspended solids (SS)	Dissolved oxygen (DO)	Total coliform
AA	Water supply class 1, conservation of natural environment, and uses listed in A-E	6.5 ≤ pH ≤ 8.5	≤ 1 mg/L	≤ 25 mg/L	≥ 7.5 mg/L	≤ 50 MPN/100mL
A	Water supply class 2, fishery class 1, bathing and uses listed in B-E	6.5 ≤ pH ≤ 8.5	≤ 2 mg/L	≤ 25 mg/L	≥ 7.5 mg/L	≤ 1,000 MPN/100mL
B	Water supply class 3, fishery class 2, and uses listed in C-E	6.5 ≤ pH ≤ 8.5	≤ 3 mg/L	≤ 25 mg/L	≥ 5 mg/L	≤ 5,000 MPN/100mL
C	Fishery class 3, industrial water class 1, and uses listed in D-E	6.5 ≤ pH ≤ 8.5	≤ 5 mg/L	≤ 50 mg/L	≥ 5 mg/L	—
D	Industrial water class 2, agricultural water, and uses listed in E	6.0 ≤ pH ≤ 8.5	≤ 8 mg/L	≤ 100 mg/L	≥ 2 mg/L	—
E	Industry water class 3 and conservation of environment	6.0 ≤ pH ≤ 8.5	≤ 10 mg/L	Floating matter such as garbage should not be observed.	≥ 2 mg/L	—

Remarks: 1. Standard values are based on daily average values. The same applies to the standard values of lakes and coastal waters.
2. At intake for agriculture, pH shall be between 6.0 and 7.5 and DO shall be more than 5mg/l. The same applies to the standard values of lakes.

Notes: 1. Nature conservation: Conservation of sightseeing and other environments
2. Water supply class 1: Purify water using filters and other simple means
Water supply class 2: Purify water using sedimentation filters and other ordinary means
Water supply class 3: Purify water using pre-treatment and other advanced methods
3. Fishery class 1: For such oligosaprobic members of the Salmonidae (salmon/trout) species as Salmo masou and Salvelinus leuconmaenisu, and marine products for fishery class 2 and 3
Fishery class 2: For such alpha-oligosaprobic marine products as the Salmonidae (salmon/trout) species, sweetfish, and marine products for fishery class 3
Fishery class 3: For such beta-oligosaprobic marine products as carp and crucian
4. Industrial water class 1: Water purified using sedimentation and other ordinary means
Industrial water class 2: Purify water using chemical additives and other advanced means
Industrial water class 3: Purify water using special means
5. Environmental conservation: Limit of not disrupting the day-to-day lives of the population

Table 3 Scoring of achievement degree of the environment quality standards

Water quality class ranked with the environmental quality standards for conservation of the living environment	Score
AA Class	0.9
A Class with indexes ranked in AA	0.8
A Class	0.7
B Class with indexes ranked in A or higher	0.6
B Class	0.5
C Class	0.4
D Class	0.3
E Class	0.2
Below E Class	0.1

Training of Neural Network Model

The neural network model has been trained (put under a learning process) with the collected teacher data explained above. The training process is based on the learning procedures as described prior, but it is still a process of trial and error because there are still many details that remain undecided, such as a suitable step size of optimization, a suitable output function, an efficient order to present the teacher data to the neural network model, and a proper initial network size (layers and units in each layers). The learning process was stopped after the trained neural network model is able to reproduce the entire teacher data with an acceptable error, which was set in this study to be below 2% in mean relative error.

WATER ENVIRONMENT EVALUATION

Sensibility Analyses of Variables

The well-trained neural network model has been used to carry out a sensibility analysis for all the variables to identify how much each variable impacts on the achievement of water environment standards. The sensibility coefficient of a variable is defined as the partial derivative of the achievement score regarding each variable as follows.

$$S_i = \frac{\partial O(X_1, X_2, \cdots, X_N)}{\partial X_i}\Big|_{at\ a\ given\ variable\ value\ set} \quad (15)$$

where S_i is the sensitivity coefficient of variable X_i at a given variable value set.

For all the variables, the sensitivity coefficients have been evaluated for the average variable value of the last data year 2018. This sensitivity analyses have identified 7 variables that have the most significant and meaningful impacts on the achievement degree of water environment standards as shown in Table 4. As for all the other variables, the sensitivities were not great enough to treat them as variables with a considerable impact in terms of average variable values.

Needless to say, the sensitivity is defined as the differentiation of the evaluation function with respect to each factors at a given time(the final year of the data records in this study), and just means how sensitive the evaluation function is to the change in each factor. It is reasonable to view the sensitivity as a relative index to compare different factors, but it is not designed to make a sense in terms of absolute impacts of each factor on the evaluation function.

Discussions

The environment items with the greatest impacts on the achievement degree of water environment standards can be classified into three categories: natural factors, human factors and mixed factors.

Natural factors include month of sampling and annual average stream flow. The fact that the month of sampling has great impacts means that water environment has a clear tendency of seasonal change. This is because of the subtropical climate pattern in Japan with a clear rainy season and a typhoon season. The seasonal rainfall change is considered the main cause for the seasonal change tendency in river water

Table 4 The environment items with the greatest impacts on achievement of water environment standards

Environment Item	Sensitivity	Descriptions
Month of Sampling	0.16	It means that water environment has a clear tendency of seasonal change.
Annual Average Stream Flow	0.09	It is reasonable and expected that water quantity has a tremendous impact on water quality.
Catchment Population	0.07	This just reconfirmed that human activity is one of the main factors that are able to make a great difference on water environments.
Visual Appearance: Turbidity (Muddiness)	0.04	Visual turbidity usually gets remarkably worse right after storms that cause landslides or debris flow in mountain areas, soil erosion in farmland and sewage overflow in urban areas.
Total Nitrogen	0.03	Total nitrogen in water environment is mainly contributed by sewage inflow and agriculture drainages.
Dichloromethane	0.02	Dichloromethane is almost entirely from industrial wastewater.
Number Of Hydraulic Power Plants	0.01	Power plants can change river flow, and consequently water environments

environment. This is consistent with the fact that the annual average stream flow is ranked as the second most important factor to water environment. This is also a reasonable result expected from the common sense that water quantity has a tremendous impact on water quality.

Human factors include catchment population, total nitrogen, dichloromethane and number of hydraulic power plants. Catchment population implies that human activity is one of the main factors that can make a significant difference on water environments. Total nitrogen in water environment is mainly contributed by sewage inflow and agriculture drainages (overuse of fertilizers), and Dichloro-methane is almost entirely from industrial wastewater. Power plants are the most controversial factor. The conflicts between power generation and conservation of river environment have been problems in most basins and a priority problem of river flow for different purposes is remained to be resolved.

The only mixed factor is turbidity or muddiness in terms of visual appearance. Visual turbidity usually gets remarkably worse right after a heavy storm that causes landslides or debris flow in mountain areas, soil erosion in farmland and sewage overflow in urban areas. Both catchment natural condition and farming or urban human activities are contributing indirectly to river flow turbidity during rainy time.

CONCLUSIONS

With the purpose of developing a better methodology for water environment evaluation and management of rivers, a neural network model has been proposed for water environment evaluation in this study.

The neural network model was trained through a deep learning process with the water environment data of 104 Class-A rivers that are under the direct administrative control for 58 environment items from 1998 to 2018.

The well-trained neural network model was applied to a sensitivity analysis of environment items. The sensitivity analysis results have identified 7 variables that have the most significant and meaningful impacts on the achievement degree of water environment standards, of which there are natural factors (season and annual average stream flow), human factors (catchment population, total nitrogen, dichloromethane and number of hydraulic power plants) and a mixture of both (Visual turbidity). These results are reasonable and are consistent with the expectation derived from common knowledge.

It is more meaningful and important that the above analysis results have shown that an artificial intelligence model with a deep learning technology can treat both numerically continuous variables such as annual average stream flow and categorical variables such as visual turbidity with the discrete values yes/no without substantial effort or hinderances. This implies a significant potential application of the artificial intelligence model to the water environment management area.

With this well-trained neural network model, the next step is to identify the most influential environment factors for each river, and find the most effective combination of water environment improvement measures.

The biggest difference between a traditional water environment model and an artificial intelligence model is the difference of the knowledge base used in environment evaluations. Traditional models are mainly based on the knowledge and experiences (or expertise) with regard to a specific target river. Artificial intelligence models, however, are using the full knowledge and experiences that are hidden in the environment survey data of all rivers with similar characters. More analyses are required to show what kind of differences this character of artificial intelligence model can make in water environment evaluation and management in the future. These results combined together in their entirety will demonstrate that artificial intelligence is an effective and efficient tool for water environment evaluation.

REFERENCES

[1] Hagihara Y. and Hagihara K. ed., Planning of Urban Water and Green Space, Kyoto University Press, 2010.

[2] Ministry of The Environment of Japan, Results of the FY 2018 Water Quality Survey of Public Water Areas, 2019.

[3] Ministry of The Environment of Japan, Results of the FY 2004 Water Quality Survey of Public Water Areas, 2005.

[4] Zhang S. P. and Kido Y., A Study on the Environment Evaluation method for Aise River and the Effectiveness of River Environment Improvement Measures, Urban Science Studies, No. 21, 2016, pp. 45-56.

[5] IPA, WHITE PAPER Artificial Intelligence 2019, Kadokawa publisher, 2018.

[6] Asou H., The Information Processing by Neural Network Models, Sangyo Publisher, 1988.

[7] Rumelhart D. E., Hinton G. E., and Williams R. J., Learning Representations by Back-propagating Errors, Nature, Vol. 323, No. 9, 1986, pp. 533-536.

[8] Ministry of Land, Infrastructure, Transport and Tourism of Japan, Water Information System, http://www1.river.go.jp/ (an Online Open Source Database).

[9] Ministry of Environment of Japan, Environmental White Paper, 2020.

11th Int. Conf. on Geotechnique, Construction Materials & Environment,
Kyoto, Japan, 3-5 November 2021, ISBN: 978-4-909106063 C3051

ESTIMATION OF USEFUL SPECIES OF BENTHIC ANIMALS AND WATER PLANTS FOR AN INDEX OF AL AND CR CONTAMINATION FOR RIVER IN THE KINOKAWA RIVER CATCHMENT

Takuma Kubohara[1] and Hiroyuki Ii[2]

[1]Kinokawa City Office, Japan; [2]Faculty of Systems Engineering, Wakayama University, Japan

ABSTRACT

Useful species for an index of Al and Cr contamination for river were estimated in the Kinokawa River catchment because there are few studies on whether benthic animals and water plants are useful for an index of Al and Cr contamination for river. Al concentrations of crane fly larva and bryophyte at the closed Cu mine were high (260 to 5,260 and 640 to 20,000 mg/kg-dry for crane fly larva and bryophyte). Cr concentrations of dragonfly larva and bryophyte at the serpentinite were high (3 to 30 and 3 to 91 mg/kg-dry for dragonfly larva and bryophyte). Crane fly larva for Al (260 to 5,260 mg/kg-dry) and dragonfly larva for Cr (0.6 to 30 mg/kg-dry) in benthic animals and bryophyte for Al and Cr (220 to 20,000 and 2 to 91 mg/kg-dry for Al and Cr) in water plants had high and a wide range of metal concentrations. Therefore, it was thought that crane fly larva for Al, dragonfly larva for Cr and bryophyte for Al and Cr were useful species for an index of metal contamination. Moreover, bryophyte had the highest and a wide range of Al and Cr concentrations among benthic animals and water plants. Therefore, bryophyte was useful species for an index of Al and Cr contamination among benthic animals and water plants.

Keywords: Al, Cr, Bryophyte, Crane fly larva, Dragonfly larva

INTRODUCTION

To investigate the influence of heavy metals for aquatic life in river, metal concentration of river water and river sediment are measured. Generally, metal concentration of river water is always very low. Moreover, it is changeable depending on the change of flow rate. And then, heavy metal concentration of river sediment does not represent the heavy metal mass transferring in river (soluble only) because heavy metals of river sediment are soluble and insoluble. Therefore, the metal concentrations of river water and river sediment were not always useful for an index of the influence of heavy metals for aquatic life in river. On the other hand, it is reported that the metal concentration of benthic animal and water plant is useful for investigating the influence of heavy metals for aquatic life in river [1]-[6]. However, there are few studies on whether benthic animals and water plants are useful for an index of Al and Cr contamination for river. Therefore, Al and Cr concentration of benthic animals and water plants were measured in the Kinokawa River catchment and then useful species for an index of Al and Cr contamination for river were estimated. Useful species as an index of Al and Cr contamination needs a high concentration for Al and Cr in a contaminated area and a low concentration for them in a non-contaminated area. Moreover, it needs a high and a wide range of their concentration and also common.

STUDY AREA

Figures 1 and 2 show study area. The Kinokawa River is located in the center of Kinki district and is classified into A river based on the Ministry of Land, Infrastructure, Transport and Tourism of Japan. The length and total area of the Kinokawa River are 136 km and 1,750 km^2 [7]. It flows into the Kii Channel through the Kii plain from South Nara. The Izumi Group composed of sedimentary rocks, sandstone, mudstone and conglomerate is distributed in the northwest part of the catchment. The Sanbagawa Belt composed of metamorphic rocks, serpentinite and crystalline schist is distributed in the southwest part

Fig.1 Location of study area.

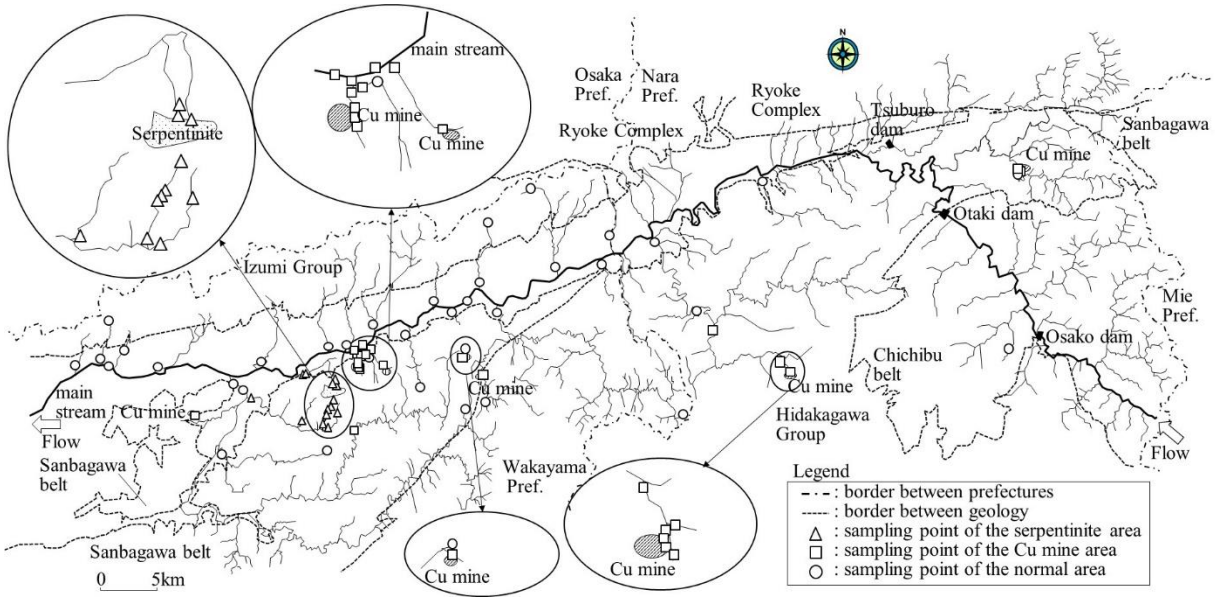

Fig.2 Kinokawa River catchment.

and the northeast part of the catchment. The Hidakagawa Group composed of sedimentary rocks, sandstone and shale is distributed from the southern part to the northeast part of the catchment. The Chichibu Belt composed of sedimentary rocks, sandstone, mudstone, limestone and chert is distributed in the eastern part of the catchment [8]. The Ryoke Complex composed of plutonic rocks, granite and gneiss is distributed in the northeast part of the catchment. In the Kinokawa River catchment, there are the closed Cu mines and serpentinite. The closed Cu mine produced a lot of Cu and Fe sulfide ore and the waste water was low pH and high concentration of sulfate with metal. The chemistry of serpentinite is quite different from the other rocks and in particular Mg, Ni, Cr concentrations of serpentinite are high.

STUDY METHOD

Benthic animals and water plants in the river bed were sampled in the Kinokawa River catchment. Sampling points were shown in fig.2. The number of sampling points was 73 points. Investigation period is July 2013 to April 2016. The kinds of sampled benthic animals were Japanese freshwater crab, caddice-worm, dobsonfly larva, dragonfly larva, stonefly larva, crane fly larva, mayfly larva and corixidae. The kinds of sampled water plants were reed, fern, bryophyte, Japanese knotweed and coix. Sampling points were classified into three groups, the serpentinite area, the Cu mine area and the normal area. The serpentinte area is a sampling point around the serpentinite. The Cu mine area is a sampling point around the Cu mine. The normal area is a sampling point excluding those areas. Crane fly larva and reed were not sampled in the serpentinite area. Moreover, Japanese knotweed was not sampled in the normal area.

In the laboratory, the sampled benthic animals and water plants were rinsed with ultrapure water at first. Secondly, they were desiccated by dryer. After drying, they were dissolved with concentrated nitric acid and it was filtered with the membrane filter with 0.45 micrometer of pore size. After filtering, Al and Cr concentrations of benthic animals and water plants were measured by ICP-OES (AMETEK, Inc., SPECTRO ARCOS) in the laboratory of Wakayama University. The actual detection limit of ICP-OES is 0.01ppm for Al and Cr. Water plants excluding bryophyte were divided into leaf, upper part stem, middle part stem, lower part stem and root and each part was separately analyzed.

RESULTS AND DISCUSSION

Al Concentration of Benthic Animals and Water Plants

Figures 3 and 4 show Al concentrations of benthic animals and water plants. Al concentrations of dragonfly larva and crane fly larva in the Cu mine area were 151 to 3,100 and 260 to 5,260 mg/kg-dry, respectively. Al concentrations of dragonfly larva and crane fly larva in the other areas were 88 to 1,100 and 530 to 3,100 mg/kg-dry, respectively. Al concentrations of reed root, leaf and root of fern, bryophyte, upper and middle part stem and root of Japanese knotweed and coix root in the Cu mine area were 610 to 1,600, 260 to 3,200, 640 to 20,000, 270 to 3,000 and 380 to 500 mg/kg-dry, respectively. Al concentrations of reed root, leaf and root of fern, bryophyte, upper and middle part stem and root of Japanese knotweed and coix root in the other areas

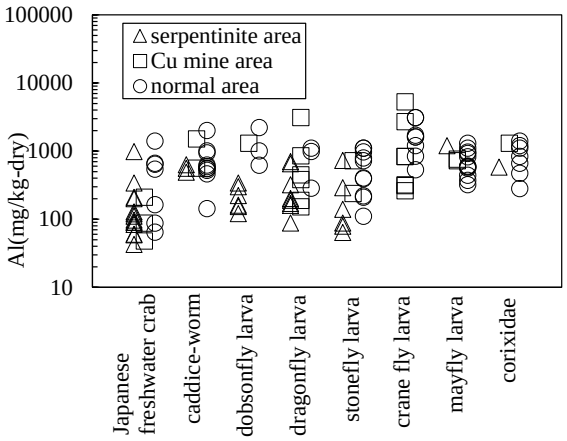

Fig.3 Al concentrations of benthic animals.

were 440 to 590, 180 to 1,600, 220 to 13,000, 190 to 1,300 and 340 mg/kg-dry, respectively. Therefore, their Al concentrations in the Cu mine area were higher than those in the other areas. Aluminum is widely distributed as feldspar and clay minerals in rocks in the crust, where it is the third most abundant element following oxygen and silicon. The solubility of aluminum silicate and aluminum hydroxide in rocks is large in low or high pH condition. The closed Cu mine produce low pH waste water. Chemical equations of aluminum silicate and aluminum hydroxide with water in low pH condition are shown as below [9].

$$Al_2Si_2O_5(OH)_4 + 6H^+ = 2Al^{3+} + 2H_4SiO_4 + H_2O \quad (1)$$

$$Al(OH)_3 = Al^{3+} + 3OH^- \quad (2)$$

Therefore, it was thought that high Al concentrations of dragonfly larva, crane fly larva, reed root, leaf and root of fern, bryophyte, upper and middle part stem and root of Japanese knotweed and coix root in the Cu mine area were caused by waste water from the closed Cu mines.

On the other hand, Al concentrations of corixidae, lower part stem of fern, lower part stem of Japanese knotweed and middle and lower part stem of coix in the Cu mine area were 1,300, 450 to 690, 200 to 260 and 420 to 710 mg/kg-dry, respectively. Al concentrations of corixidae, lower part stem of fern, lower part stem of Japanese knotweed and middle and lower part stem of coix in the other areas were 280 to 1,400, 250 to 610, 250 and 470 to 720 mg/kg-dry, respectively. Therefore, their Al concentrations in the Cu mine area were almost the same as those in the other areas. Al concentrations of Japanese freshwater crab, caddice-worm, dobsonfly larva, stonefly larva, mayfly larva, reed stem, middle part stem of fern and upper part stem of coix in the Cu mine area were 48 to 210, 560 to 1,500, 1,300, 237 to 720, 720 to 760,

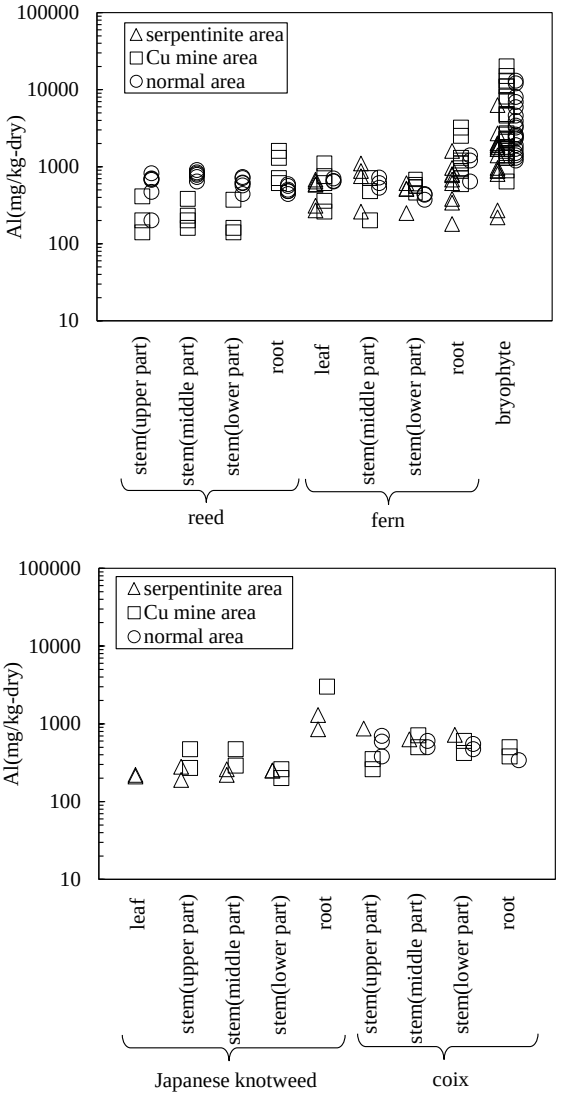

Fig.4 Al concentrations of water plants.

140 to 410, 200 to 710 and 260 to 350 mg/kg-dry, respectively. Al concentrations of Japanese freshwater crab, caddice-worm, dobsonfly larva, stonefly larva, mayfly larva, reed stem, middle part stem of fern and upper part stem of coix in the other areas were 43 to 1,400, 142 to 2,000, 121 to 2,200, 64 to 1,100, 320 to 1,300, 200 to 900, 260 to 1,100 and 380 to 870 mg/kg-dry, respectively. Therefore, their Al concentrations in the Cu mine area were not higher than those in the other areas.

Al concentrations of Japanese freshwater crab, caddice-worm, dobsonfly larva, dragonfly larva, stonefly larva, crane fly larva, mayfly larva and corixidae were 43 to 1,300, 142 to 2,000, 121 to 2,200, 88 to 3,100, 64 to 1,100, 260 to 5,260, 320 to 1,300 and 280 to 1,400 mg/kg-dry, respectively. Therefore, crane fly larva had the highest and a wide range of Al concentration among benthic animals. Al concentrations of reed, fern, bryophyte, Japanese knotweed and coix were 140 to 1,600, 180 to 3,200, 220 to 20,000, 190 to 3,000 and 260 to 870 mg/kg-

dry, respectively. Therefore, bryophyte had the highest and a wide range of Al concentration among water plants.

From the above results, crane fly larva had the highest and a wide range of Al concentration among benthic animals. Bryophyte had the highest and a wide range of Al concentration among water plants. Moreover, Al concentrations of crane fly larva and bryophyte were high in the Cu mine area and were low in the other areas. Therefore, crane fly larva and bryophyte were useful species for an index of Al contamination.

Cr Concentration of Benthic Animals and Water Plants

Figures 5 and 6 show Cr concentrations of benthic animals and water plants. Solid mark indicates Cr concentration of benthic animal and water plant under the detection limit, 0.01 ppm of concentration for sample solution.

Cr concentrations of caddice-worm, dragonfly larva and mayfly larva in the serpentinite area were 9 to 19, 3 to 30 and 20 mg/kg-dry, respectively. Cr concentrations of caddice-worm, dragonfly larva and mayfly larva in the other area were 0.3 to 10, 0.6 to 9 and 1 to 5 mg/kg-dry, respectively. Cr concentrations of bryophyte and Japanese knotweed root in the serpentinite area were 3 to 91 and 27 to 60 mg/kg-dry, respectively. Cr concentrations of bryophyte and Japanese knotweed root in the other area were 2 to 53 and 26 mg/kg-dry, respectively. It is known that the serpentinite contains a large amount of Cr. It is reported that Cr concentrations of the serpentinite were 400 to 31,300 ppm [10]-[11]. Therefore, it was thought that high Cr concentrations of caddice-worm, dragonfly larva, mayfly larva, bryophyte and Japanese knotweed root in the serpentinite area were caused by the serpentinite.

On the other hand, Cr concentrations of Japanese

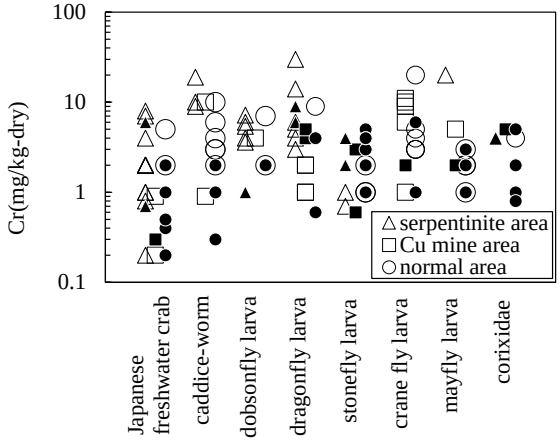

Fig.5 Cr concentrations of benthic animals.

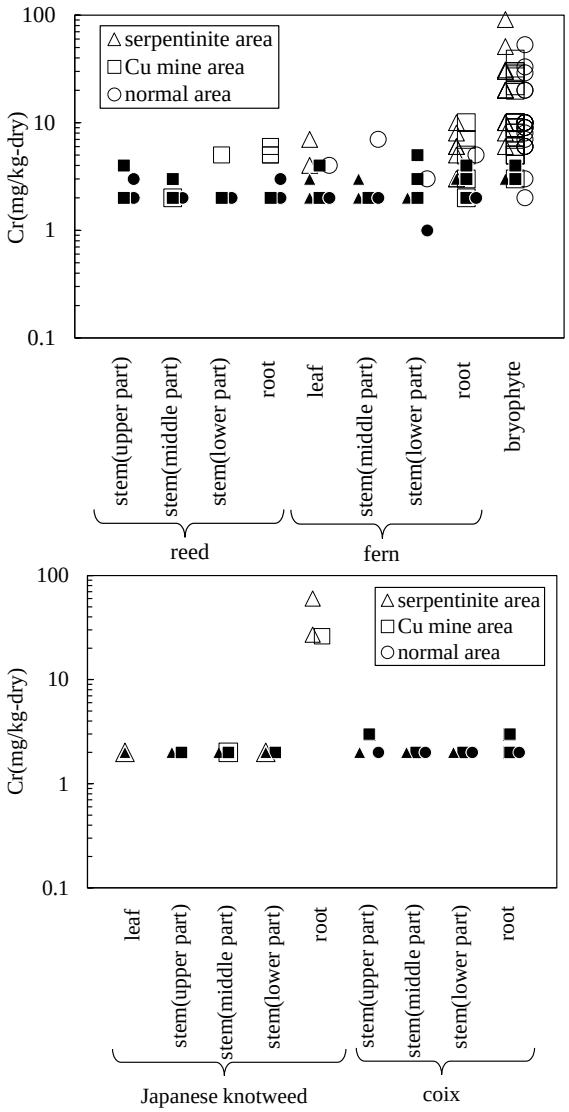

Fig.6 Cr concentrations of water plants.

freshwater crab, dobsonfly larva, stonefly larva, corixidae, fern, Japanese knotweed stem and coix in the serpentinite area were 0.2 to 8, 1 to 7, 0.7 to 4, 4, 2 to 10, 2 and 2 mg/kg-dry, respectively. Cr concentrations of Japanese freshwater crab, dobsonfly larva, stonefly larva, corixidae, fern, Japanese knotweed stem and coix in the other areas were 0.2 to 5, 2 to 7, 0.6 to 5, 0.8 to 5, 1 to 10, 2 and 2 to 3 mg/kg-dry, respectively. Therefore, their Cr concentrations in the serpentinite area were almost the same as those in the other areas.

Cr concentrations of Japanese freshwater crab, caddice-worm, dobsonfly larva, dragonfly larva, stonefly larva, mayfly larva and corixidae were 0.2 to 8, 0.3 to 19, 1 to 7, 0.6 to 30, 0.6 to 5, 1 to 20 and 0.8 to 5 mg/kg-dry, respectively. Therefore, dragonfly larva had the highest and a wide range of Cr concentration among benthic animals. Cr concentrations of fern, bryophyte, Japanese knotweed

and coix were 1 to 10, 2 to 91, 2 to 60 and 2 to 3 mg/kg-dry, respectively. Therefore, bryophyte had the highest and a wide range of Cr concentration among water plants.

From the above results, dragonfly larva had the highest and a wide range of Cr concentration among benthic animals. Bryophyte had the highest and a wide range of Cr concentration among water plants. Moreover, Cr concentrations of dragonfly larva and bryophyte were high in the serpentinite area and were low in the other areas. Therefore, dragonfly larva and bryophyte were useful species for an index of Cr contamination.

Most Useful Species for Al and Cr contamination of River

From figs.3 and 4, Al concentrations of benthic animals, bryophyte and other water plants were 43 to 5,260, 220 to 20,000 and 140 to 3,200 mg/kg-dry, respectively. From figs.5 and 6, Cr concentrations of benthic animals, bryophyte and other water plants were 0.2 to 30, 2 to 91 and 1 to 60 mg/kg-dry, respectively. Therefore, bryophyte had the highest and a wide range of Al and Cr concentrations among benthic animals and water plants. Moreover, Al concentrations of bryophyte in the Cu mine area were higher than those in the other areas. And then, Cr concentrations of bryophyte in the serpentinite area were higher than those in the other areas. It is known that bryophyte absorbs heavy metals from the whole surface of the body [12]. Therefore, it is thought that bryophyte is easy to absorb heavy metals compared with benthic animals and other water plants. Moreover, it is thought that bryophyte is little metal consumption because the growth rate of bryophyte is generally slow [13]. From the above reasons, it was thought that bryophyte had the highest and a wide range of Al and Cr concentrations among benthic animals and water plants. Therefore, bryophyte was useful species for an index of Al and Cr contamination among benthic animals and water plants.

CONCLUSIONS

Al and Cr concentration of benthic animals and water plants in the Kinokawa River catchment were investigated in order to estimate useful species for an index of Al and Cr contamination for river. Useful species as an index of Al and Cr contamination needs a high concentration for Al and Cr in a contaminated area and a low concentration for them in a non-contaminated area. Moreover, it needs a high and a wide range of their concentration and also common.

Al concentrations of crane fly larva and bryophyte in the Cu mine area were higher than those in the other areas. Cr concentrations of dragonfly larva and bryophyte in the serpentinite area were higher than those in the other areas. Moreover, crane fly larva for Al and dragonfly larva for Cr had the highest and a wide range concentration among benthic animals. Bryophyte had the highest and a wide range of Al and Cr concentrations among water plants. Therefore, crane fly larva for Al and dragonfly larva for Cr were useful species for an index of metal contamination among benthic animals. Bryophyte was useful species for an index of Al and Cr contamination among water plants.

Bryophyte had the highest and a wide range of Al and Cr concentrations among benthic animals and water plants. Therefore, bryophyte was useful species for an index of Al and Cr contamination among benthic animals and water plants.

REFERENCES

[1] Hatakeyama S., Satake K., and Fukushima S., Flora and Fauna in Heavy Metal Polluted Rivers I Density of Epeorus latifolium (Ephemeroptera) and Heavy Metal Concentrations of Baetis spp. (Ephemeroptera) Relating to Cd, Cu and Zn Concentrations, Research Report from the National Institute for Environmental Studies, No.99, 1986, pp.15-33.

[2] Ii H., and Nishida A., Effectiveness of Using River Insect Larvae as an Index of Cu, Zn and As Contaminations in Rivers, Japan, International Journal of Geomate, Vol.12, No.33, 2017, pp.153-159.

[3] Kubohara T., and Ii H., Cu Co and Ni Contamination Index for River Using River Insects and River Plants, International Journal of GEOMATE, Vol.11, Issue 26, 2016, pp.2651-2658.

[4] Kubohara T., and Ii H., Evaluation of Metal Contamination for River using Bryophyte in the Kinokawa River Catchment, International Journal of GEOMATE, Vol.12, Issue 37, 2017, pp.135-142.

[5] Kubohara T., and Ii H., Zn and Fe Contamination Index for River using River Insects and Water Plants in The Kinokawa River Catchment, International Journal of GEOMATE, Vol.19, Issue 75, 2020, pp.76-83.

[6] Satake K., Elemental Composition of Water and Aquatic Bryophytes Collected from the Central Part of Kyushu (Mt. Kuju, Mt. Aso and the City of Kumamoto), Proceedings of the Bryological Society of Japan, Vol.3, No.9, 1983, pp.137-140.

[7] Ministry of Land, Infrastructure, Transport and Tourism, https://www.mlit.go.jp/river/toukei_cho

usa/kasen/jiten/nihon_kawa/0604_kinokawa/0604_kinokawa_00.html
[8] Wakayama City Children's Science Museum, Wakayama no Ishi, 2002, pp.7-13.
[9] Ii H., Hirata T., Matsuo H., Tase N. and Nishikawa M., pH and Chemistry of Nitrogen, Phosphate, Sulfar and Aluminum in Surface Water near Tea Plantation, Doboku Gakkai Ronbunshu, No.594, 1998, pp.58-63.
[10] Mizuno N., Studies on Chemical Characteristics of Serpentine Soils and Mineral Deficiencies and Toxicities of Crops, Report of Hokkaido Prefectural Agricultural Experiment Stations, No.29, 1979, 87p.
[11] Bamba T., Genetic Study on the Chromite Deposits of Japan. Based on Ultra-Basic Rocks and Chromite Deposits of Hokkaido, Chugoku and Shikoku Districts, Reports, Geological Survey of Japan, No.200, 1963, 68p.
[12] Yoshio H., Okayama University of Science, http://had0.big.ous.ac.jp/thema/moss/moss.htm
[13] Graduate School of Agricultural and Life Sciences, The University of Tokyo, https://www.a.u-tokyo.ac.jp/topics/2018/20180327-3.html

11th Int. Conf. on Geotechnique, Construction Materials & Environment, Kyoto, Japan, 3-5 November 2021, ISBN: 978-4-909106063 C3051

FLOATING AUTOMATED FACTORY SYSTEM FOR EFFECTIVE UTILIZATION OF SEABED RESOURCES AND REDUCTION OF CO_2 EMISSIONS

Shinji Sato[1] and Ryo Deyama[2]

[1]Department of Oceanic Architecture and Engineering, College of Science and Technology, Nihon University, Japan; [2]NIHON SEKKEI, INC., Japan

ABSTRACT

The economy of Japan is growing to become the third-largest in the world by 2020 in terms of GDP. Japan is one of the world's largest consumers of electrical energy. However, Japan's self-sufficiency rate of energy resources, excluding nuclear power, is only 9.6%; thus, they currently rely on importation for more than 80% of their energy demands.

On the other hand, under the seabed of Japan's exclusive economic zone, there are methane hydrates, nearly 100 times larger than Japan's annual consumption of natural gas. Methane is a clean energy source with CO_2 emissions 30% lower than that of oil and about 45% lower than that of coal.

In the current development of submarine resources, the deeper the water depth, the higher the cost for extracting resources. To minimize cost, from the extraction to the processing of submarine resources, it is most efficient to set up a base directly above the sea area where the resources are located, and power can be generated after the extraction and conversion to energy. In the future, it would be possible to reduce the overall cost, from product processing to finished product manufacturing, by siting various factories around the base of the resources as floating structures.

Here, we propose a floating structure that can consolidate the movement of people, products, and logistics from the seabed to the sea and its surroundings for the effective use of energy resources and reduction of CO_2 emissions.

Keywords: Energy resources, Methane Hydrates,Marine Space, Vertical production city, Floating structure

INTRODUCTION

Following the period of high economic growth in the 1970s, Japan has grown into a wealthy country. With this social development, power consumption has grown dramatically, and today, Japan is the third highest consumer of energy in the world. However, the energy resources self-sufficiency rate of Japan is below 9.6%, and the country relies on importation for more than 80% of its energy resources.

With the Fukushima Daiichi Power Plant accident during the Great East Japan earthquake, Japan faces a turning point in energy policies. In the future, there would be a need for less dependence on imported resources and the securing of safe and clean domestic energy sources. Thus, currently, seabed resources around Japan have attracted attention.

Methane hydrates, the most representative seabed resources, are natural gas resources called "fire ice." Compared to conventional fossil fuels, CO_2 emissions during methane combustion is about half. Thus, it is a potential clean energy source. About 6 trillion cubic meters of methane reserve in the waters of the Nankai Trough were also reported [1].

Based on this survey, to commercialize methane hydrates as a new domestic energy resource, the Ministry of Economy, Trade, and Industry established the "Methane Hydrates Development Plan in Japan" in July 2001. This development plan was a long-term plan that covered the period from 2001 to 2018. In March 2013, the Agency for Natural Resources and Energy conducted a gas production experiment with methane hydrates and recorded the first success in the world. With this experiment, the transition to commercial production of methane is anticipated in the 2020s [2].

In this paper, we propose an island city of a floating automated factory system using methane hydrates as the main energy source. It is anticipated to be the new domestic energy resource.

PLAN BACKGROUND

Energy In Japan

While Japan is a major energy consumer, its self-sufficiency rate of energy resources, excluding nuclear power, is only 9.6%; thus, the country depends on importation for the majority of its energy needs (Fig. 1, 2).

From the energy resource explorations to energy production in Japan, consider oil as an example; Oil accounts for half of Japan's energy needs.

The process is as follows: exploration overseas → primary refining process → loading on ships at a port → transport by sea → unloading at a port → final

refining process at a petrochemical complex → production at each factory → cities and consumers.

Shipping oil from the Middle East, where 90% of oil supply comes from, involves risks as ships must pass through the Persian Gulf, which has unstable political situations, and the narrow Strait of Hormuz and Strait of Malacca. In addition, since the ships travel a long distance of 12,000 km, the cost of logistics is quite high. It takes about 45 days to make a round trip, during which a large amount of greenhouse gases are emitted (Fig. 3).

Outlook Of Domestic Energy Production

In Japan, which depends on importation for most of its energy resources, such as oil and coal, it has been a challenge to find new energy resources that can replace the limited resources. Following the Fukushima Daiichi nuclear power plant accident, the world demands a stop to the dependence on nuclear power, and there is increasing anticipation for renewable natural energy, such as solar and wind power. Natural energy has many challenges, such as varying output by climate conditions, the low energy density per area, and high cost. In Japan, the solutions to these challenges would take much time; thus, the hope is currently put on the seabed resources buried in the oceans around Japan.

Methane Hydrates As An Energy Resource

Methane hydrates have recently gained attention as next-generation energy resource. It has been reported that there is a rich reserve of methane hydrates in the oceans surrounding Japan. This potential is suggested by what is known as bottom simulating reflector (BSR). As the deep seafloor has low temperature and under high pressure, methane hydrates are stable. Since the lower limit of the stable range for methane hydrates can be estimated using BSR, the location of the reserves can be explored once the existence of methane hydrates is confirmed.

Marine production tests confirmed BSR along the shoreline of Shikoku to Kyushu, south of Hokkaido,

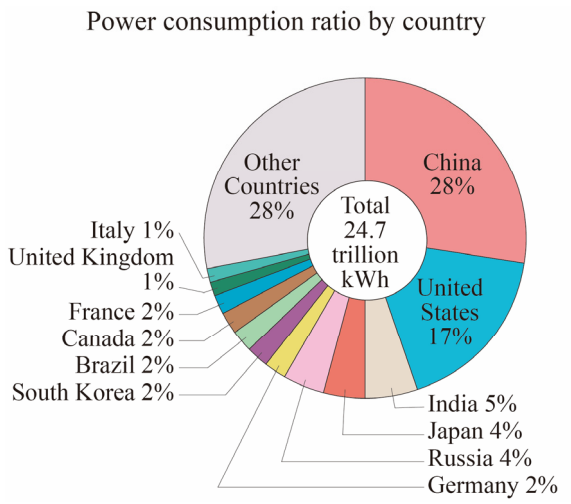

Fig. 1 Power consumption rate by country [3].

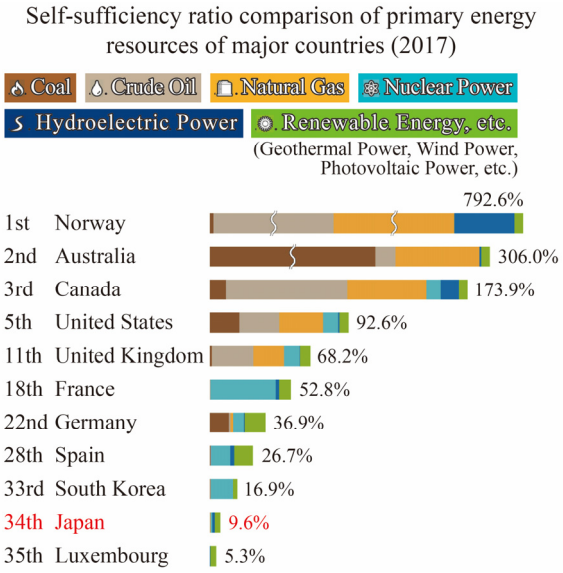

Fig. 2 Self-sufficiency rate of energy resources by country [2].

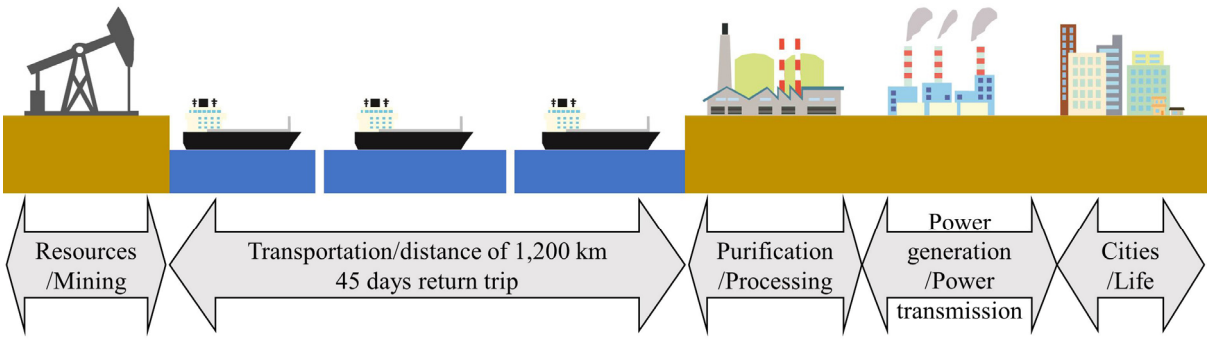

Fig. 3 Process of oil resource mining to production for Japan

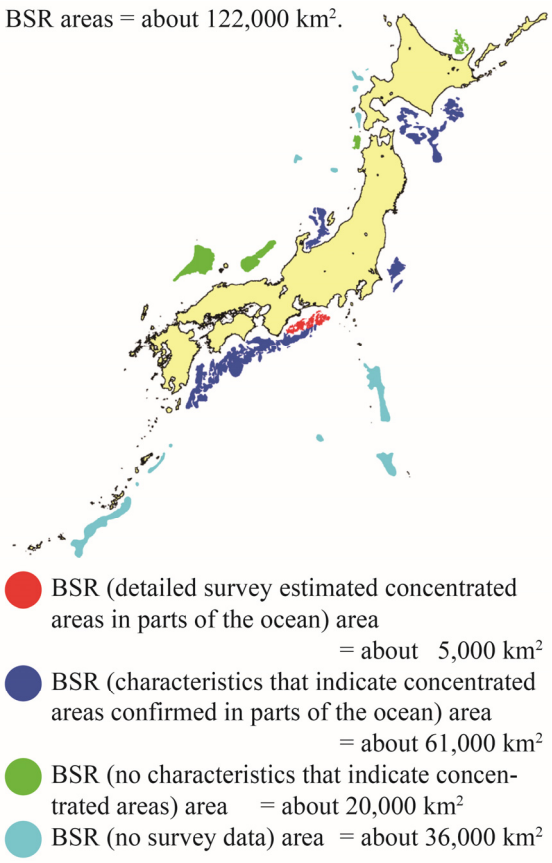

Fig. 4 BSR distribution in oceans around Japan [4]

and offshore of Boso and Noto Peninsulas. The estimated amount of methane gas contained in the methane hydrates found at the seafloor of "the eastern Nankai Trough," located offshore of Aichi and Mie Prefectures, is equivalent to 10 years' worth of natural gas imported. If other locations are added, the resource is anticipated to exceed 100 years (Fig. 4).

Though Japan relies on imports for the majority of natural gas, the successful commercialization of methane hydrates makes it possible for Japan to become the next-generation energy resource powerhouse [5], [6].

Uses Of Methane Hydrates

Methane gas obtained from methane hydrates is the main component of liquid natural gas currently imported to Japan. It emits less sulfur oxide, nitrogen oxide, and CO_2 compared to oil and coal, and it is predicted to be an environmentally friendly resource. Methane gas can be used as an energy source in various applications, such as city gas, fuel for power generation, natural gas vehicles, and fuel cells.

The steam-reforming method, in which methane reacts with water, is widely used in the industry. This method allows easy manufacturing of hydrogen as a new energy for the 21st century, and its diverse use is anticipated [7].

Use Of Marine Space

Japan has the 6th widest exclusive economic zone on the world, which is 10 times the land area, it is filled with potential for marine development. Thus, to create space on water, a very large floating structure, mega-float, is being developed. The Technological Research Association of Mega-Float, established in 1995, advanced technological development, and during the Great East Japan earthquake, a mega-float was used as a floating disaster prevention base for Muroran. Thus, mega-floats are used for various facilities [8].

Preparation Against Disasters

Japan is one of the most earthquake-affected countries in the world, and has experienced many major earthquakes, such as the Great Hanshin–Awaji and Great East Japan earthquake. Earthquakes that are predicted to have more than 60% probability of occurrence in next 30 years include Tokai/Tonankai earthquake, the earthquake directly below Tokyo, the Tokachi earthquake, and the Miyagi Offshore earthquake. Specifically, the Nankai Trough earthquake is estimated to be M8 or larger, and various measures are being taken to prepare for it. During the Great East Japan earthquake, tsunamis stopped the operation of several power plants along the shoreline, which led to a large-scale power shortage. With such experiences, a base with disaster prevention function on the sea, which is less likely to suffer disaster damage, would be vital in recovery.

FLOATING PRODUCTION FACILITY

Characteristics And Plans For A Floating Structure

Here, we propose a floating marine production facility that is mainly supplied with methane hydrates, which is anticipated to be widely used as a domestic energy resource in the future. The plan will fully utilize the properties of a floating structure [9].

1. A floating structure does not require land and can be placed in an area with the likely presence of rich marine resources in order to obtain a stable supply.
2. Methane and hydrogen gases require completely sealed space. Thus, gas tanks can utilize the internal space of a mega-float.
3. A floating structure is easy to relocate, move, and process; thus, it can accommodate the expansion of a project.
4. Expansion through floating structures, such as mooring of production facilities, factories, and hotels, is easy.

Plan With Power Generation Function

By combining a floating structure and power generation function in a plan, the following advantages are anticipated (Fig. 5).

1. Independent production and operation on the ocean become possible, allowing for long-term activities.

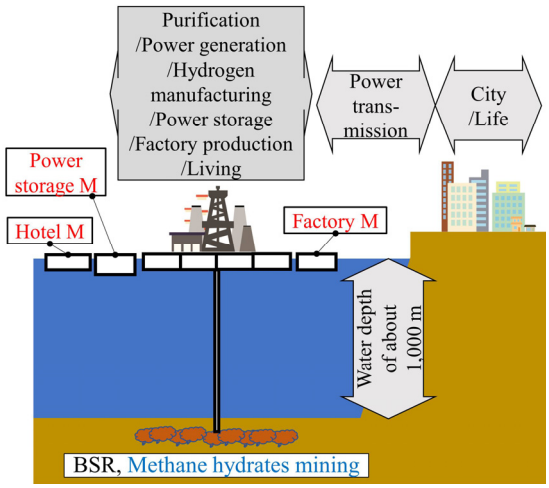

Fig. 5 Functional configuration diagram of a floating production facility

2. Majorities of the automotive industry located on the shoreline anticipate exports. Cooperating and linking with a floating structure, it would be possible to share power and produce on the ocean.
3. It is possible to manufacture hydrogen through the methane-steam-reforming method.
4. Combining with lithium in the seawater, lithium-ion batteries can be manufactured, providing a power storage function.
5. A floating structure is not vulnerable to earthquakes. Therefore, during a disaster, it can play a role of the recovery base by providing power to the affected area, and so on.

BASIC PLAN

Site Selection

Based on the abovementioned plans and policies, the following site selection criteria are proposed: the sea is in a calm condition; the area is rich with resource reserve to provide a stable supply.

Planned Marine Area

With these selection criteria, the seabed of "eastern Nankai Trough," located offshore of Aichi and Mie Prefectures (Fig. 6), was selected. This area

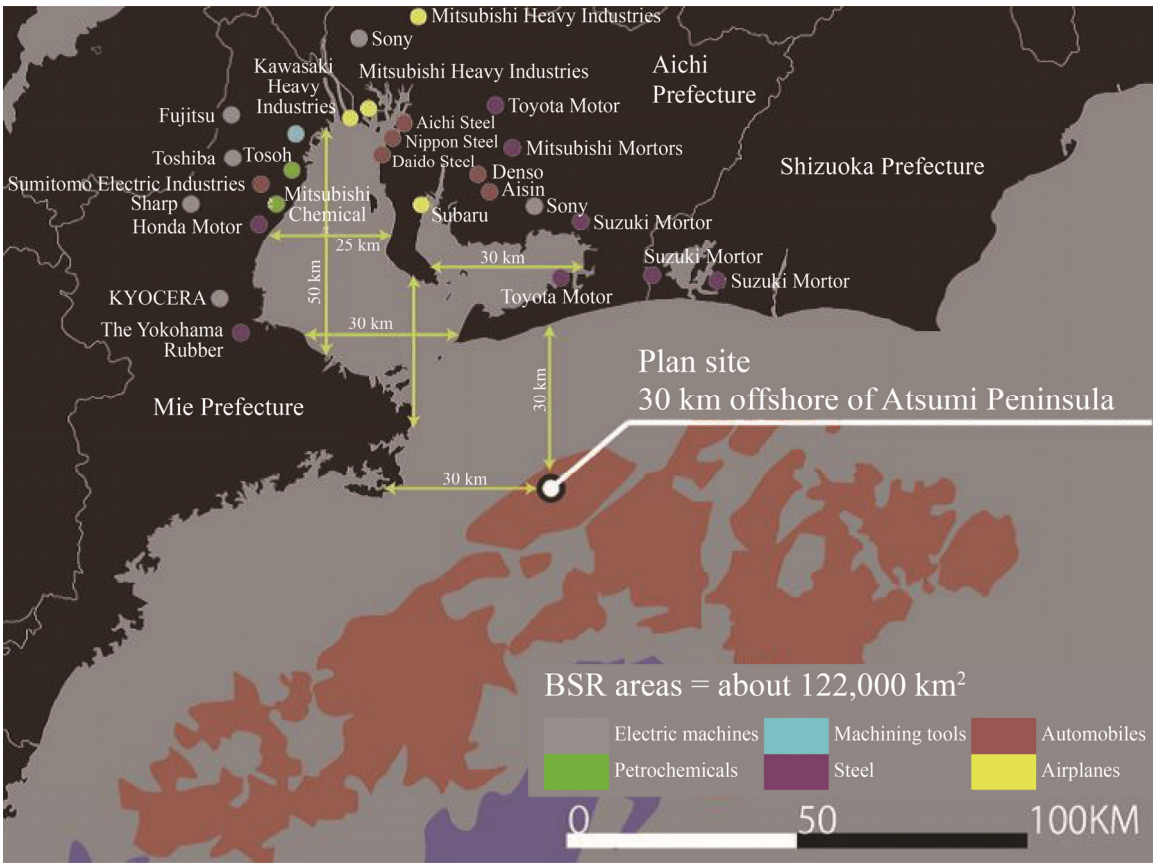

Fig. 6 Plan site: Eastern Nankai Trough at 30 km offshore [4], [5].

is not affected by the Kuroshio Current throughout the year, and it is located 30 km from Atsumi Peninsula where the Chūkyō Industrial Area is situated.

Produced methane gas is used to generate power within the facility, converted and processed as secondary energy media, such as lithium-ion batteries and hydrogen, and shipped to surrounding floating factories or the Chūkyō Industrial Area.

Selection Of A Floating Structure- FPSO

A floating production, storage, and offloading system (FPSO) is a facility where oil and gas are produced on the sea and stored in a tank located in the facility. Then, they are loaded in transport tankers. It is the most popular type of production facility (60% or more of floating marine oil/gas production facilities). Today, there are about 160 FPSO bases in operation around the world. These facilities are built inside a mega-float.

Drilling For Methane Hydrates

We employ the CO_2-in-Water Emulsion Injection method, which is also used to extract natural gas resources. The CO_2-in-Water Emulsion Injection method involves drilling to a methane-hydrate layer at around 1000 m below the seafloor, which breaks down methane hydrates into methane gas and water, which the gas is collected. It can provide a stable supply under various conditions [10].

CONSTRUCTION PLAN

Introduction Function/Scale Calculation

Following the plan background and basic policies, we perform the introduction function and scale calculation. As the major function of the proposed facility, four functions, including residence/activity department, power generation department, production department, and storage department, are introduced.

Facility Plan That Makes Life Comfortable On The Sea

Infrastructure maintenance is performed for a long-term life on the sea. Based on the above introduction and scale calculation, we proposed to install five facilities with the residences at the core where 270 staff resided.

The plan has five facilities with residences at the core. It includes food production building, in which exhaust heat and CO_2 from the power generation facilities are effectively utilized for cultivation in the plant factory. It also includes accommodation building, where researchers and workers can stay and work temporarily, leisure building for workers on break, and sport building dedicated to indoor sports (Fig. 7).

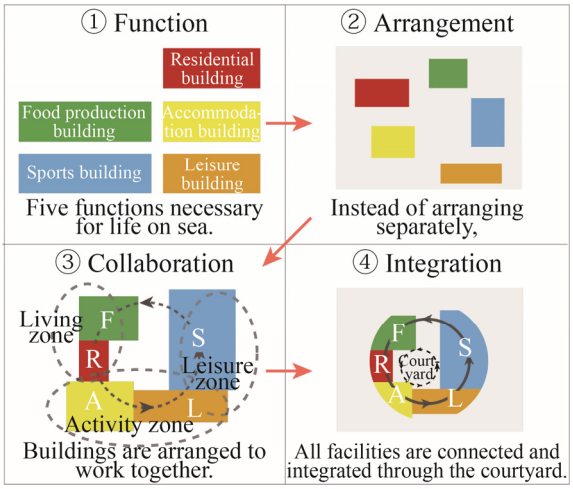

Fig. 7 Overall facility configuration

CONCLUSIONS

Reviewing Renewable Resources

Energy resources in Japan are extremely limited; thus, much of the energy resources used are imported. The dependence on overseas is, directly and indirectly, attributed to the increased cost of production and other costs. In a country like Japan, which is highly dependent on imports, this is a severe issue that demands urgent solutions.

Thus, we propose a system that vertically integrates the process of mining the seafloor energy resource in the nearby ocean, followed by purification and distribution as energy instead of long and horizontal movement of energy resource.

Energy-Producing Island City

The highest advantage of the proposed system is the extremely low production cost and absence of risk usually incurred when moving resources. Since a mega-float is a floating structure, its position can be changed according to the mining conditions of the seabed resources. Furthermore, it can be combined with a manufacturing factory, power storage, hotel, residential building for workers, and so on, as modules above or near the floating structure. Such a system with limited movements of energy resources, objects, and people can be called a vertical production city.

The advantages of this city include extremely low cost for production and processing, low CO_2 emission, and less time required for administrative procedures to perform environmental assessments of the plant site. Furthermore, by preparing various facilities as modules, the facilities can be extended or reduced,

depending on the function.

The disadvantage of floating structures is that they are costly because they are not currently mass-produced. However, since it is not premised on moving, it does not require equipment such as steering, engine, and fuel like ships, so it is expected that the cost will decrease if it is mass-produced.

Island City Prepared For A Disaster

In the proposed facility, located 20–30 km offshore of Japan, the impact of earthquakes and tsunami would be extremely small; thus, the advantages of the facility during disasters, such as earthquakes and tsunamis are significant. In other words, the module design of such a floating structure can be called a novel 21st-century disaster preventative city.

Notes:

[Note 1] The survey conducted by the Ministry of Economy, Trade, and Industry was implemented in 2006. The resource reserve in the oceans surrounding Japan was evaluated.

[Note 2] The methane-hydrate development plan in Japan: 1) clarification of the theoretical reserve and characteristics of methane hydrates in the oceans surrounding Japan; 2) estimate of potential methane gas reserve in the areas with theoretical methane-hydrate reserves; 3), selection of the methane-hydrate field from the candidate reserves and examination of its economic potential; 4) marine production experiment in the selected methane-hydrate field; 5) updates to technologies for commercial production; 6) establishment of a system that considers environmental protection.

REFERENCES

[1] Agency for Natural Resources and Energy, Natural Resources and Fuel Department, Promotion of Resource Development in Oceans Around Japan, 2017, https://www.meti.go.jp/shingikai/enecho/shigen_nenryo/pdf/021_04_00.pdf, May 2017, pp.13-19.

[2] Agency for Natural Resources and Energy, Energy in Japan 2018, https://www.enecho.meti.go.jp/about/pamphlet/energy2018/html/001/#section1.

[3] The Federation of Electric Power Companies of Japan, https://www.fepc.or.jp/enterprise/jigyou/shuyoukoku/index.html.

[4] MH21-S R&D consortium, The distribution map of BSRs related to methane hydrates, offshore Japan, 2009, https://www.mh21japan.gr.jp/pdf/BSR_2009.pdf.

[5] Fujii T., Suzuki K., Tamaki M., Komatsu Y., and Takayama T., Reservoir properties and heterogeneity of turbidite sediment revealed from the exploration of methane hydrate in the eastern Nankai Trough, Japan. Journal of the Japanese Association for Petroleum Technology, Vol. 8, Issue 1, 2016, pp.84-95.

[6] Tanaka S., Brief mention of the first phase of Japan's Methane Hydrate R&D Program. Journal of the Japanese Association for Petroleum Technology, Vol. 74, Issue 4, 2009, pp.265-269.

[7] Hirata K., Katagiri K., Maeda T., Shinoki T., and Funaki J., Hydrogen Production by Ethanol-Steam Reforming Using $Cu/ZnO/Al_2O_3$ Catalyst. Transactions of the Japan Society of Mechanical Engineers. B, Vol. 79, Issue 808, 2013, pp.2587-2591.

[8] Sato C., Principal Characteristic of Mega-Float and It's Structure Planning Flow. Journal of the Japan Welding Society, Vol. 69, Issue 4, 2000, pp.304-308.

[9] Sato C., and Kawamura A., A Study of Ultra-large Floating Marine Structure and the Result (Part 3): Floating Structure Design Techniques, A Study of Durable Technologies: Chapter 4 A Study of Floating Structure Design Techniques. Techno Marine, Vol. 841, 1999, pp.512-529.

[10] Tanaka Y., Sasaki T., Miyake S., Masuda Y., Naganawa S., and Nagano J., Experimental Study on CO_2-in-Water Emulsion Injection Method for Enhanced Methane Hydrate Recovery, CSMH-5 2013 (5th Comprehensive Symposium on Methane Hydrate). Methane Hydrate Research Center, AIST, 2013, pp.1-4.

11th Int. Conf. on Geotechnique, Construction Materials & Environment,
Kyoto, Japan, 3-5 November 2021, ISBN: 978-4-909106063 C3051

THE EFFECT OF POROUS CONCRETE HANDLING ON EROSION REDUCTION IN SLOPED SOIL AND SANDY CLAY CONDITIONS

Bimo Brata Aditya[1)], Putranto, Dinar DA[2], Anis Saggaff[2)], Hanafiah[2)]

[1] Doctor degree program, Faculty of Engineering, Sriwijaya University; [2] Department of Civil Engineering and Planning, Faculty of Engineering, Sriwijaya University, Jl. Raya Inderalaya Km. 32, Inderalaya District, South Sumatra, Indonesia

ABSTRACT

Erosion is the process of eroding the surface of the topsoil caused by the intensity of the rainfall that occurs and causing splashes due to the working kinetic energy (J/m2), coupled with runoff due to the slope factor, which is influenced by soil type and land cover. The characteristics of soil type and topography cause damage to the topsoil and push the sedimentation volume to increase from time to time. Therefore Road safety infrastructure buildings, such as cliff protection on a slope, irrigation building walls, and so on, require good security to avoid collapse or loss of slope stability. Reducing the occurrence of kinetic energy in the topsoil surface layer and reducing erosion can be done by making a surface layer with a porous concrete pavement structure. However, first, it necessary to analyze the amount of kinetic energy acting on the soil surface. The positive effects of porous concrete layers on slope stability are discussed using: i) geo-mechanical effects, namely soil reinforcement with shaft concrete; ii) soil hydrological effects, namely the suction regime of the soil, which is influenced by the absorption of water flowing through the concrete shaft. A one-dimensional vertical groundwater dynamics model is assumed to simulate the soil suction regime, representing soil covered with shaft concrete on slopes with various gradients. It was found that in various soil types and different slopes, in the case of sandy loam soils, geo-mechanical effects tend to be more relevant than soil hydrological effects during the rainy season.

Keywords: porous concrete, kinetic energy, geo-mechanical, rain intensity, slope

INTRODUCTION

In the development of human civilization, the decline in the socio-economic conditions of society is primarily due to the unwise exploitation of environmental resources [1].

In the development of the industry to date, human activity can be said to be an essential agent in ecological change. According to a 2005 study by Wilkinson, human activity is the most critical agent of geomorphic change, compared to natural processes that gradually work on the land surface.

Furthermore, Price, Ford, Cooper, and Neal [2] stated that the annual change in sediment caused by human activities exceeds that carried by river flows. In the treatment process carried out by humans in mining activities, many topographic trimmings with a reasonably extreme slope have caused many topographic changes, resulting in an erosion process in the area [3]. Likewise, in infrastructure development such as roads, dams, and so on [4], much topography is trimmed to increase erosion in the area, which will increase the incidence of sedimentation. On this basis, it is essential to reduce the increase in ecological damage in infrastructure development such as roads, built areas, and dams. Therefore, it is necessary to engineer a layering of the basic soil structure with special treatment, to minimize the stripping of the soil layer due to erosion caused by water flow

The topographical modelling approach for erosion and deposition is illustrated using the upstream Lematang Sub-watershed, South Sumatra Province, Indonesia. Geographically, the research area is located at 2º 45 '- 4º 20' South Latitude and 103º 05 '- 104º 20' East Longitude. The upper Lematang watershed consists of steep undulating hills, with slope angles of between 30% - 50%. To meet the irrigation water needs for the Lematang Irrigation Area in center Dempo District Pagar Alam City, South Sumatra Province, the Lematang Weir has been built, which is located in the hilly area of the upstream Lematang sub-watershed. Meanwhile, the hillsides that tilt towards the river flow in some places form steep slopes (the angle is almost 50%), such as the pedestal hill to the left of the weir, while the right pedestal hill is formed gentler slopes [5].

The most important thing in looking at the study of weir construction in the hill area is the need to calibrate the characteristics of the river in the watershed (DAS) of the study area. This is very important considering that the shape and magnitude

of the flood hydrograph are highly dependent on the characteristics of the watershed. The watershed features become the basis for reducing the scour rate at the bottom of the channel [6].
In a study conducted by Sulaeman et al [4], the numerical analysis uses 3D Delft to predict patterns, flow velocity, and morphological changes upstream and downstream of the weir. The results showed a trend of change at the bottom of the river, namely degradation of the outer bend channel upstream of the weir and a decrease in the left side of the riverbed, while sedimentation occurred on the right downstream of the riverbed the weir.

METHOD

The approach used is first to compare the distribution of sediment transport values, erosion, and soil deposition with different parameters: a) only paying attention to topographic factors, b) topography and soil erosion, and c) topography, water seepage, and layering experiments. Second, a general assessment of watershed stability in terms of the mutual interaction between erosion and deposition is carried out by comparing the contribution of sediment from the Upper Lematang watershed.

RESULTS

Figure 1 presents the distribution of erosion and deposition in the Upper Lematang sub-watershed for four different combinations of factors using the USPED decline and deposition model [7]. Initially, the analysis was carried out only paying attention to topographical factors, then combined with soil erosion factors and land cover factors. They were analyzed simultaneously. Thus, there are three factors used in conducting analysis using the erosion mechanism of the runoff model for comparison purposes. Overall (see Table 1), the classification of the magnitude of the erosion distribution is minus (0 -100) tons/ha/year, spreading over an area of approximately 1,331.35 Km^2 in a room with a land slope of around 17^o – 34^o [8].

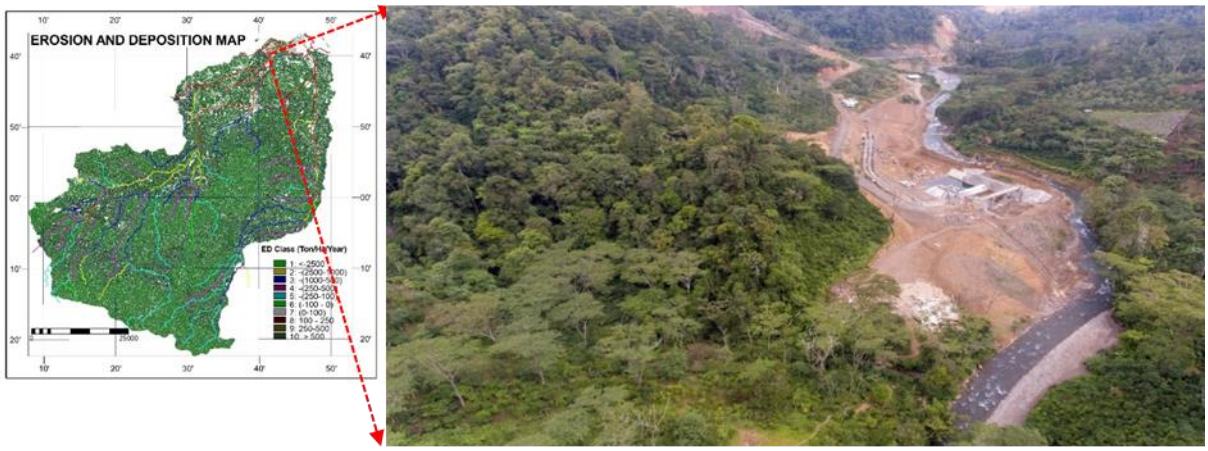

Fig. 1 The upper Lematang sub-watershed and the location of the Lematang Dam

Meanwhile, the amount of deposition is between +(0-100) tons/Ha/Year spreads over an area of approximately 1,278.41 Km^2, with a land slope of around 0^o-17^o. Meanwhile, sheet erosion of more than 500 tons/ha/year occurs on an area of approximately 71.26 Km^2. This magnitude of the erosion and deposition processes with high intensity is relatively low. The distribution also changes with the addition of topographic factors into the model. With a topographic slope of more than 34o, the amount of erosion is more than 500 tons/ha/year, occurring on an area of 33.54 Km^2. If the vegetation factor is removed, the erosion rate will increase significantly up to 0.5% [9].

River Channel Change Analysis

Based on speed distribution

Changes in the river bed upstream and downstream of the Lematang weir can occur due to the high flow velocity during drainage, of 2.3 m/s at a 5-year return period discharge downstream of the weir with an average river bed material around the downstream of the weir of 2 mm [5]. Based on the Hjulstorm graph, namely the relationship between the diameter of the material grains and the flow velocity (Figure 2), the tendency for scour to occur results in a decrease in the riverbed (blue line).

Table 1 Erosion classification and deposition of erosion rates in the upper Lematang sub-watershed

Classification (Ton/Ha/Year)	Area (Ha)	Area (Km2)	%
< - (2500)	273.75	2.74	0.09
-(2500-1000)	1,576.31	15.76	0.50
-(1000 – 500)	3,354.00	33.54	1.07
-(500 – 250)	7,125.50	71.26	2.28
-(250 –100)	15,693.13	156.93	5.02
(100 - 0)	133,134.75	1,331.35	42.62
(0 – 100)	127,840.88	1,278.41	40.93
(100-250)	13,411.19	134.11	4.29
(250-500)	5,599.94	56.00	1.79
> 500	4,364.25	43.64	1.40
Total		2,123.74	100.00

With the shape of the river that bends sharply upstream and downstream of the weir, it is possible for scouring to occur at the foot of the outer river bank. When depicted on the Hjulstorm graph, with a 5-year return period discharge and a flow velocity of 0.9 m/s, the grain size of the D50 material is 0.8 mm. At the upstream of the weir (red line), with a speed of 1.4m/s, at the downstream bend with a material diameter of D50 (2 mm), it is predicted that riverbed scour (green line) will occur (Figure 2).

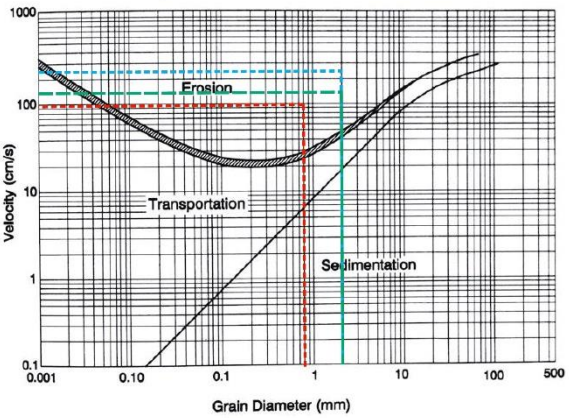

Fig. 2 Graph of the relationship between flow velocity and the grain diameter of the river bed material (0.8 mm)

Based on the flow shear stress

One of the parameters to predict scouring is the flow shear stress parameter (τo). By comparing the flow shear stress (τo), that occurs and the critical grain shear stress (τcr), the prediction of scouring or deposition will occur. From the results of plotting the flow shear stress on the graph of the relationship between the diameter of the sediment material and the shear stress in Figure 3, it is found that the shear force that occurs at the five-year return discharge, in the position after leaving the stilling pond, to the right of the downstream channel of the weir, has a shear force value of 43 N/m2 with a material diameter of 2 mm D50 (red line). This explains that with a 5-year return period, discharge of 26.3 m3/s can erode the riverbed downstream of the weir.

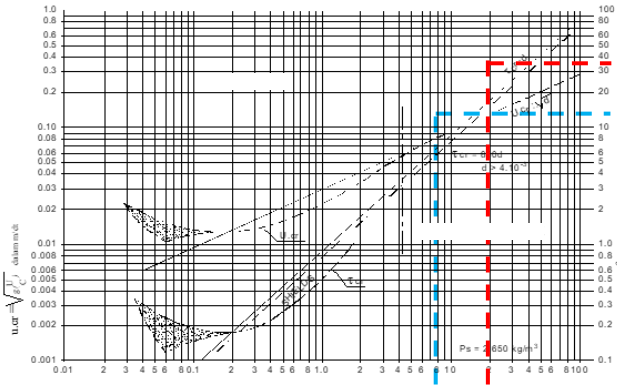

Fig. 3 Graph of critical shear stress relationship with riverbed grain diameter (2mm)

Similarly, upstream of the dam, the water flow from the left upstream hitting the cliff to the right upstream has a shear force value of 15 N/m2 with a material diameter of D50 is 0.8 mm shown in the blue line. This explains that the 5-year return discharge of 26, 3 m3/s can erode the riverbed upstream of the weir. The sheer force of the flow increases with the increase in release at the return period, and it will also increase the potential for greater scouring of the riverbed [5]

Discussion

Sediment transport rate and spatial distribution of erosion and sediment affected by topographical functions

In reducing the sediment transport capacity for the upstream Lematang sub-watershed, terrain geometry plays the most critical role. In addition, there is a fixed pattern underlying the sediment transport capacity, which is controlled by topographical conditions. When modified by vegetation cover conditions and soil type distribution, topographical geometrical properties (slope) determine the spatial distribution of sediment transport capacity in the sub-watershed [10]. Sheet flow is usually characteristic of areas with good vegetation cover. However, it can occur in very compacted soils, where soil detachment and the formation of natural flow can be prevented by compaction. The increasing contribution to the slope area, combined with high local slope values, is indicated by high levels of sediment transport. Areas with high sediment transport rates associated with concave slope profiles and valleys will accelerate convergent sediment transport rates. Comparing sediment transport rates between sheet erosion and

natural erosion shows that the actual flow is turbulent. As a result, it can carry sediment further in the flow and be more concentrated along the valley and in the concave part of the hillside than if the flow was dispersed by vegetation in sheet flow.

Sediment transport rate divergence (qs) can be identified in areas where the sediment transport rate increases in the direction of flow (leading to erosion), decreases (leads to deposition), or remains constant (no corrosion or deposit). It is essential to emphasize the difference between the quantities calculated using the Erosivity Index (E) and Transport Capacity (T) equations, i.e., sediment transport rates and erosion and deposition rates: which can detect areas of high mass-carrying capacity. While the second allows the detection of erosion and deposition patterns determined by the distribution of incoming sediment supply to local transport capacity [11].

The resulting erosion/deposition map (based on topography only) shows that the estimated high-risk erosion areas are located at the top of the hillside, in basins and valley centers with concentrated flows. The depositional area usually occurs in the lower part of the hillside and the concave portion of the valley. This situation is consistent with previous results showing that the highest erosion rates correlate with divergent elements and deposition with convergent avalanche elements [12]. Maximum soil loss occurs on slopes with a slope degree of more than 34^{o}, and total soil erosion occurs on both sides of the traversed pitch.

Sediment transport rate and spatial distribution of erosion and sediment as a function of topography and soil erosion

Overall, by including the K-factor in the analysis, the spatial pattern of sediment transport shows the influence of areas with high erosion. However, because the distribution of soil types is highly correlated with topography, the design is strongly dominated by topography. Thus sediment flows will have lower values over a more prominent location across the landscape than they would have very high values concentrated in high-sloping sunken areas[13].

The inclusion of soil erosion patterns also modified the spatial distribution of erosion and deposition. This will increase the area of the area that is at greater risk of decline. Although the percentage of sites with erosion/deposition values is less than or equal to the case where the topography is the only triggering factor (42.62%). It should be noted the distribution of erosion and deposition values for both. Erosion and deposition cases were analyzed by taking into account the soil erosion factor, and the erosion percentage ranged from 5.02% to 4.29%. At the same time, the topographic factor has a much more significant influence on erosion (40.93 to 42.62) %. The corresponding erosion range from (-0 to 100) covered 9.92% of the study area (Table 1). Regions with maximum erosion risk are concentrated along steep slopes (42.62%), which also have large soil erosion values, while deposition occurs in areas with lower pitches and occurs along valleys [8].

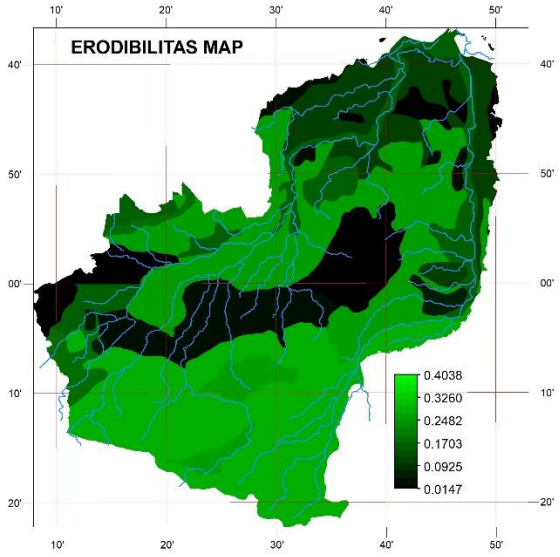

Fig. 4 Erosion and Sedimentation as a function of topography and soil erodibility

Reducing the effect of water seepage, which can reduce the amount of erosion

Experiment using a pond in a different case to test water seepage in a watercourse [14][15]. Six ponds with a capacity of 100 m3 observed the rate of seepage during the rainy season and after the rainy season. During the rainy season, surface water is kept at the pond's bottom, limiting the vertical flow of water and sometimes damaging seepage. One of the ponds was coated with a low-density polyethylene film to see the effect of the absence of seepage. The result provides the lowest level of seepage compared to pools lined with broken brick material or pools lined with a mixture of soil and cement.

Meanwhile, Wang et al conducted a study on seepage loss in channels with various coating materials [16]. The seepage loss analyzed by the Inflow-Outflow method varies from 0.225 to 0.315 ft3/ft2/hour. At the same time, the process of observing the water level in the pond obtained results ranging from 0.1954 ft3/ft2/hour to 0.2584ft3/ft2/hour. The rate of constant seepage loss over 200 ft in the earth channel was found to vary from 12 to 18 percent of the inflow to the outlet, i.e., 0.23 to 0.41 ft3/ft2/hr [17].

By conducting a semi-field trial using the following composition, [18] : (1) Cement-gravel-sand-gravel concrete (0.58 : 0.15 :5:10); (2) Cement – fly ash-sand-gravel concrete (0.8: 0.2: 5: 10); (3) A layer of sand – asphalt – cement on the soil base (0.85: 0.1: 0.05); (4) Sand-bitumen – cement layer on the

cement mortar base (0.85: 075: 0.075) and (5) without treatment. The results obtained are that the maximum seepage occurs in the uncoated channel, which is 45 m3 per 1000 m2. While the minimum seepage in treatment No. 2 is 2.76 m3 per 1000 m2.

On this basis, to reduce water seepage due to the flow process in areas that significantly influence slopes and high erosion potential due to cliff erosion, it is necessary to design using coatings. It is recommended that infrastructure development, which can lose water or reduce surface erosion in general, should be equipped with a layer in all future projects.

Zhang et al [19] experimented on seepage loss through experiments with field conditions coated with different coating materials. The seepage of various coating specifications varies from almost nil to 0.3 m3/Mm2 in a double layer tile layer with a layer of 1:3 cement sand plaster on the slope side and single layer bricks on the base 6.8 cm thick asphalt concrete on the side—each layer. The seepage loss through the precast beams of single-layer cement mortar 1:3 bricks ranged from 0.04 to 0.16 m3/Mm2.

Preliminary laboratory tests have been carried out on a layer of asphalt concrete consisting of pea jelly, quarry dust, fine aggregate, rock dust (20: 40: 25: 10), and 60/70 asphalt 9 percent by weight and cement concrete 1:4:8 with 13 percent bentonite. Furthermore, it concluded that the asphalt concrete layer could function as a suitable coating material.

Experimentally Mclaughlin et al [20] proved that emulsified asphalt mixed with soil had shown promise as a coating material, reducing the level of erosiveness in a topsoil layer.

Worstell [21] conducted tests on various coating materials to study the seepage loss and found the range of seepage loss through different coating materials as below : (1) Concrete (0.009-0.29) m/day); (2) Compacted soil (0.003 to 0.29 m/day); (3) Asphalt cement (0.003 to 0.92 m/day; (4) Soil cement (100 : 5) with (0.009 to 0.06 m/day; (5) Chemical Sealant (0.1-2.53 m/day); (6) Sediment Seal (0.12 to 0.40 m/day); (7) Unlined (0.003 to 5.37 m/day).

The Maharashtra Engineering Research Institute Nasik [22] develop an inexpensive channel coating material in mortar-stabilized soil tile and fly ash concrete. It has been observed that flash has uniform properties except for its fineness, although the coal used has very variable properties.

It was observed that cement could be replaced by fly ash up to 10 percent for 1:3 and 1:5 mortars, and sand could be replaced by fly ash up to 20 percent for 1:3 and 1:5 mixtures. The study was made based on the strength criteria, and it was found that if 90 days is a strength criterion, then 20 percent of cement will be replaced for significant works such as dams, and if 28 days is a strength criterion, 15 percent of glue can be replaced with fly ash. Fly ash has been used in stable soils as support for tiles. This technique has been adopted in the Jaikwadi and Girna Command Areas.

CONCLUSIONS

1. Comparison of USLE, LS and topographic factors and the erosion/deposition index shows that a water-based destructive power approach is more appropriate for erosion modelling on a landscape scale. Especially when the location of both regions is at risk of erosion and with potential deposition, it is very likely to occur
2. With this analysis has improved the approach based on water damaging power units by increasing DEM calculations using smaller pixel sizes and by perfecting the flow direction using vector-grid algorithm
3. Retaining walls to hold the soil on the cliff from scouring due to flow patterns and flow velocity as well as natural collapse caused by water scouring and slope slope
4. It is recommended that infrastructure development, which can lose water or reduce surface erosion in general, should be equipped with a layer in all future projects.

ACKNOWLEDGMENTS

Thank you to Sriwijaya University, through the Institute for Research and Community Service, through funding for innovation research. Which is intended to increase the role of Sriwijaya University in supporting climate change monitoring in the Musi River Basin. And Increasing Independent Learning of the Independent Campus..

REFERENCES

[1] L. P. B. McNeill, Cameron L. David A Burney, “Evidence disputing deforestation as the cause for the collapse of the ancient Maya polity of copan, Honduras.” pp. 1017–1022, 2009.

[2] N. Haregeweyn *et al.*, “Comprehensive assessment of soil erosion risk for better land use planning in river basins: Case study of the Upper Blue Nile River,” *Sci. Total Environ.*, vol. 574, 2017.

[3] A. L. Yuono and D. D. P. Sarino, Sarino, “Analisis Spasial Kondisi Lingkungan dan Hidrologi Sub DAS Komering Hulu Kaitannya dengan Penurunan Ketersediaan Air,” no. September, pp. 978–979, 2019.

[4] F. Sulaeman, A., Harianto., Kaharudin, H. K., Pramana, “Kajian morfologi sungai akibat perletakan bendung Lematang,” in *Seminar Nasional Teknik Sumber Daya Air*, 2016, pp. 1–8.

[5] F. Pramana, A. Saggaff, and F. Hadinata, “AN ANALYSIS OF A DESIGN FLOOD

DISCHARGE IN THE DEVELOPMENTAL," vol. 9, no. 03, 2020.

[6] N. Mulatu, Atshushi, "Exploring land use_land cover changes, drivers and their implications in contrasting agro-ecological environments of Ethiopia _ Enhanced Reader.pdf." pp. 1–15, 2019.

[7] a Pistocchi, G. Cassani, and O. Zani, "Use of the USPED model for mapping soil erosion and managing best land conservation practices," *Proc. First Bienn. Meet. Int. Environ. Model. Softw. Soc. Integr. Assess. Decis. Support*, vol. 3, pp. 163–168, 2002.

[8] D. D. A. Putranto, Sarino, and A. L. Yuono, "Spatial distribution level of land erosion disposition based on the analysis of slope on Central Lematang sub basin," in *AIP Conference Proceedings*, 2017.

[9] Sarino, A. L. Yuono, and D. A. Putranto Dinar, "Spatial pattern of sediment transport for analysis of precipitation direction and magnitude in the upper Lematang river sub-basin," *IOP Conf. Ser. Earth Environ. Sci.*, vol. 389, no. 1, 2019.

[10] P. R. I. Putranto Dinar DA, Titis Pratami, "ASSESSMENT OF SPATIAL DISTRIBUTION OF LAND BASED ON ANALYSIS OF SLOPE AND WATER CONSERVATION PROGRAMS," in *International Conference on suitainaible agriculture (ICOSA)*, 2017, pp. 1–9.

[11] X. C. J. Zhang and Z. L. Wang, "Interrill soil erosion processes on steep slopes," *J. Hydrol.*, vol. 548, 2017.

[12] V. Belton and T. Stewart, *Multiple Criteria Decision Analysis: An Integrated Approach*. 2002.

[13] A. Jordán *et al.*, "Wettability of ash conditions splash erosion and runoff rates in the post-fire," *Sci. Total Environ.*, vol. 572, 2016.

[14] B. Tian, T., Balzer, D., Wang, L., Torizin, J., Wan, L., Li, X., . . . Tong, "N Landslide hazard and risk assessment Lanzhou, Province Gansu, China - project introduction and outlook. In Mikos M., Tiwari B., Yin Y., & Sassa K. (Eds.), Advancing culture of living with landslideso Title," *Adv. Cult. living with landslides*, vol. 2, pp. 1027–1033, 2017.

[15] M. Tibebe, "Low cost and Efficient Lining Material for Seepage Lose Control on Water Harvesting Structures at Holetta Catchment , Ethiopia," no. May, 2019.

[16] C. and F. Xudong, Wang, Zhu, Huang, Yang, "An Experimental Study on Concrete and Geomembrane Lining E ff ects on Canal Seepage in Arid," *Water*, vol. 12, pp. 1–21, 2020.

[17] A. A. Kulkarni and R. Nagarajan, "Conveyance Loss Modelling and Conservation Planning for Irrigation Canals – A Geo-Spatial Approach," vol. 0869, no. 01, pp. 384–389, 2018.

[18] Z. Shah, S. Haider, and T. Jafri, "Analysis of seepage loss from concrete lined irrigation canals in Punjab , Pakistan †," no. July, 2020.

[19] Q. Zhang, Junrui, Zenguang, "Investigation of Irrigation Canal Seepage Losses through Use of Four Different Methods in Hetao Irrigation District, China," *J. Hydrol. Eng.*, vol. 22, no. 3, 2016.

[20] McLaughlin N.B.; Dyck F.B.; Sommerfeldt, "An asphalt incorporator and packer for lining irrigation ditches," *Trans. ASAE*, vol. 19, pp. 1085–1088, 2012.

[21] Robert V. Worstell, "ESTIMATING SEEPAGE LOSSES FROM CANAL SYSTEMS," *J. Irrig. Drain. Div.*, vol. 1190, no. irrigation, pp. 137–147, 1976.

[22] G. of M. Water Resources Department, "Reservoirs & Enroute Storages," in *Water Resources*, 2012, pp. 246–283.

11th Int. Conf. on Geotechnique, Construction Materials & Environment,
Kyoto, Japan, 3-5 November 2021, ISBN: 978-4-909106063 C3051

PROPOSAL OF ISOLATION MEASURES FOR MOUNTAIN VILLAGES BASED ON ANALYSIS OF DISASTER PREVENTION DRILLS

Zhijun Tang [1,2], Takeyasu Suzuki[1]

[1] The University of Yamanashi, Japan
[2] Chuo Kaihatsu Corporation, Japan

ABSTRACT

As measures against the isolation of mountain villages, it is the mainstream to enable two-way communication between residents and the local government by installing satellite mobile phones and answer back function of disaster prevention radio, that is, to secure information transmission means. However, due to sediment-related disasters, isolation may occur even within the village, the heavy snowfall or sediment may prevent the installation of satellite mobile phones and disaster prevention radios. Therefore, we propose to arrange a wireless communication network and an information terminal that has a WiFi function and is easy to operate and to proceed with the construction of a wireless communication network (public assistance) along with the safety confirmation (mutual assistance) by the residents of the village, and confirmed by a practical disaster prevention drill.

Keywords: Isolation measures, Mutual assistance, Public assistance, Safety confirmation , Mountain village

INTRODUCTION

Many types of natural disasters occur in Japan such as tsunamis, earthquakes, typhoons, and landslides. More than 17,000 villages may be stranded due to these natural disasters in national land, for example, in Yamanashi Prefecture, 493 villages may be isolated due to road blockages caused by earthquakes[1].

Disaster Countermeasures for being stranded are not only hard measures but also soft measures like early warning evacuation. When a sudden disaster occurs, it should be aiming to evacuate to a safe community center. Living in an unfamiliar shelter can be stressful, especially for the elderly. It is better If can evacuate to the village public hall, because it can easily get the supplies from the home nearby, and if the home is not damaged, it is possible to live at home. In addition, the life of the village public hall is not so stressful because it is a neighbor who is acquainted with each other. If someone is injured, or suddenly ill, it needs to be taken to a hospital. if there is a shortage of supplies such as food and medicine, support must be requested.

Local governments are promoting the introduction of satellite mobile phones to villages that may be isolated to secure communication means in the event of a disaster. Since satellite mobile phones communicate via satellites, unlike fixed-line phones and mobile phones, they have the advantage of being less susceptible to line congestion and power outages. However, satellite mobile phone has some demerits, firstly, it must point their antennas in the direction of the artificial satellite to capture the radio signal. Secondly, it cannot be used in a room without a window unless taken outdoors, and it is impossible to make a call on a cloudy day. finally, since satellite mobile phones are generally installed in public halls, it is necessary to go there to use them.

Therefore, we setup local wireless network and information system, examined the effects of differences in information transmission means such as mobile phones, landlines, satellite mobile phones, and disaster prevention administrative radios on disaster response such as safety confirmation and rescue requests in disaster prevention drills.

SURVEY SITE

The survey sites are located at Hachinoshiri district, Ichikawa Misato Town, Yamanashi Prefecture, shown in Fig.1. It is a mountain village and a landslide area, if a large earthquake occurs, the road may be blocked by the landslide and the village may become isolated. The evacuation center is in the gymnasium of Elementary School and Junior High School in the Kurosawa area at the foot of the mountain.

In January 2014, a practical disaster prevention drill in these sites was conducted on the condition that

the district was isolated and mobile phones could not be used due to line congestion. "Safety confirmation using ICT, rescue request" was executed in "Safety confirmation system derived by residents themselves". Risk Communication using the CAUSE Model has been conducted in disaster isolation measures, to make the residents get the consensus of evacuating from the village when a disaster occurs.

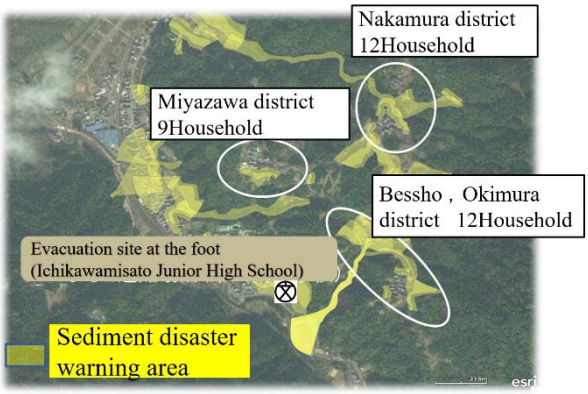

Fig.1 The survey site in Yamanashi Prefecture

RISK COMMUNICATION

Risk Communication, in general, means that accurate information on the risks surrounding society is shared among governments, experts, companies, and citizens to communicate with each other.

Risk Communication is required when regarding problems that involve certain risks such as fostering public understanding of disasters and environmental problems and still require sharing of awareness among related parties, and when it is necessary to recognize safety measures and share cooperative relationships.

Risk Communication in disaster prevention shares information on disaster risk among stakeholders such as the government and citizens, and mutually understands the information provided by residents to the government and the information and service contents provided by the government to the residents. It is a process of working together to promote and mitigate risks as much as possible. In this process, the parties concerned do not hide the information, share all the good and bad information, and discuss and solve the bad things.

By communicating with each other and building a cooperative system through Risk Communication even before a risk arises, it is possible to mitigate the risk when it occurs.

Along with improving self-help and mutual assistance, building disaster countermeasures in collaboration with residents and the government will lead to the improvement of regional disaster prevention capabilities. "Workshop on home evacuation as an isolation measure" was held as an initiative to carry out Risk Communication using the CAUSE Model.

The CAUSE model is a method proposed by Professor Rowan of George Mason University in the United States for Risk Communication education for regional crisis managers. CAUSE is an acronym for Confidence, Awareness, Understanding, Satisfaction with proposed Solutions, and Enactment arranged in the order of C, A, U, S, E[2].

Targeting the Hachinoshiri area of the mountain village, the local community and the government collaborated to form a consensus on evacuation at home[3]. First, we built a relationship of trust with university teachers, students, municipal disaster prevention officers, and residents (Confidence).

Next, make people aware that they have the option of evacuating at home in the event of a disaster (Awareness). Finally, make people understand the advantages and disadvantages of staying in a village in the event of an earthquake disaster (Understanding).

If the problem is solved, stay in the village depending on the degree of damage (Solution). The residents discussed by themselves and took out the solutions also conducted.

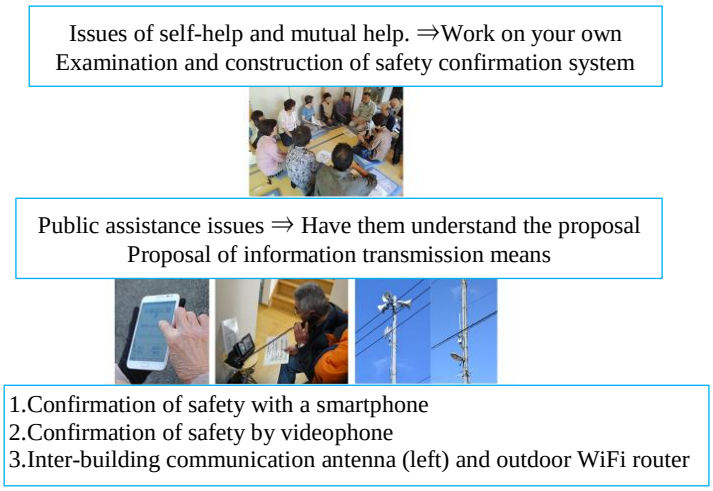

Fig.2 safety confirms by communication means

WIRELESS NETWORKS AND INFORMATION SYSTEMS

Considering the characteristics of mountainous areas, it is considered that a wireless network that builds a wireless connection by radio waves instead of cables in the event of a disaster is applicable. It is

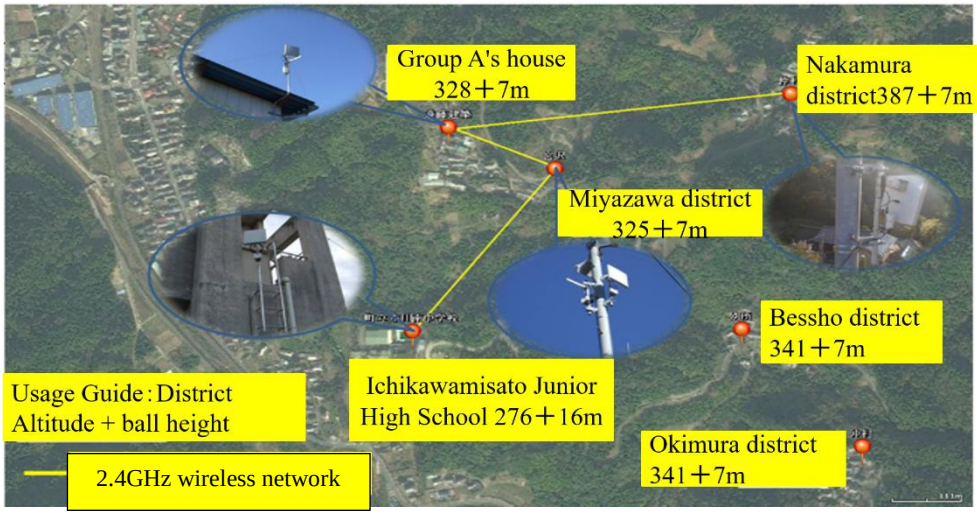

Fig.3 Wireless network built in the villages

expected that fixed-line phones will gradually be replaced by mobile phones (smartphones), and wireless communication will be carried out by anyone anywhere.

It is indispensable to build a wireless network as a countermeasure against the isolation of mountain villages instead of satellite mobile phones. But the wireless network has not been constructed in the Bessho area and the Okimura area, because of many radio obstacles in this mountainous area.

Professor Suzuki proposed a method of designing a wireless network in advance on a desk that reflects topographical conditions to build a wireless network as a countermeasure against the isolation of mountain villages[4]. Group the mountain villages, obtain and prepare the necessary data in advance for the wireless network of the mountain villages where it is difficult to conduct on-site reconnaissance and radio wave surveys, and then limit the number of relay stations to two between base stations and use GIS. So, we proposed an algorithm for designing a wireless network using it, shown in Fig.3.

Then, the wireless network design method was applied to 29 isolated villages in Ichikawamisato Town. As a result, we were able to construct a wireless network that connects nine villages by installing three relay stations and a wireless network that connects six villages by installing one relay station. In particular, regarding the wireless network of the group including the Hachijiri area, the wireless network could be constructed in Okimura and Bessho, which could not be constructed even if the telecommunications carrier examined it locally, and the user could be proved.

PHONES IN THE VILLAGE

Before the actual disaster prevention drill, we visited all households one by one in the Hachinoshiri district, in order to understand the means of information transmission for each household. Hachinoshiri district consists of Miyazawa, Nakamura, Bessho / Okimura, and the number of households in each district is 10, 15, and 12 households.

On November 17, a survey on information and communication methods for residents conducted home visits to 34 households in the Hachinoshiri area, only 3 households could not visit at home(Table 1).

Regarding the results of the survey, among all Hachinoshiri households, 7 households have 15

Table 1 Households in the Hachinoshiri area

Total	Visited	Absent
37	34	3

Table 2 Ordinary mobile phone in 23 households

Total	docomo	au	softbank
38 units	23 units	13 units	2 units

Table 3 Smart mobile phone in 7 households

Total	docomo	au	softbank
16 units	4 units	10 units	2 units

Table 4 About the fixed-line phone

All fixed-line phone	31
Use of mobile mail function	10
Don't use email at all	10
Terminals that can receive Earthquake Early Warning Area Mail	21

smartphones, and 23 households have 38 ordinary mobile phones. Regarding the contracted mobile phone companies, DoCoMo has 27 cases, au has 20 cases, and SoftBank has 2 cases. For model types, see DoCoMo's MicroSD, f-10a, f88ies, f-08c. There were au MicroSD, Koos, sony Xperia, sol21, etc, shown in Table 2 and Table 3.

We checked from the homepages of the three carriers and found that only 21 units could receive the Earthquake Early Warning Area Mail. It was also confirmed that 31 households have 31 fixed-line telephones as another means of communication. It is shown in Table 4.

Before the actual disaster prevention drill, the residents of Hachinoshiri used four smartphone phones and five videophones borrowed from Yamanashi University to register their safety and report the damage situation and found out the schedule.

RESULTS OF DISASTER PREVENTION DRILLS

On January 11, 2014, a practical disaster prevention drill started at 9 o'clock in the Hachinoshiri district of Ichikawamisato Town, Yamanashi Prefecture, shown in Fig.4 and Fig.5. The occurrence of an earthquake and the issuance of evacuation advisories were communicated by the voice from the disaster prevention radio. At the same time, emergency earthquake messages were transmitted by mail and SNS.

Since we registered the information on the establishment of the disaster countermeasures headquarters and the issuance of evacuation advisories, it could be started to confirm the safety of residents. The safety of the residents was confirmed by the system decided by each village and reported to the government office by IP phone, SNS, videophone, and satellite mobile phone.

After the training starts, the residents implemented the safety confirmation system for each group and promptly confirmed the safety. Some residents in the group have a videophone or smartphone, and when they confirm their safety, they register the safety information on the Ichikawamisato SNS and inform the town of the safety information. In addition, the injured residents and the residents whose houses have collapsed and whose safety is unknown are found, and a rescue request is made to the town.

The precondition is that the mobile phone call function cannot be used due to line congestion or the destruction of the base station due to an earthquake.

Fig.4 Disaster prevention drill in Bessho

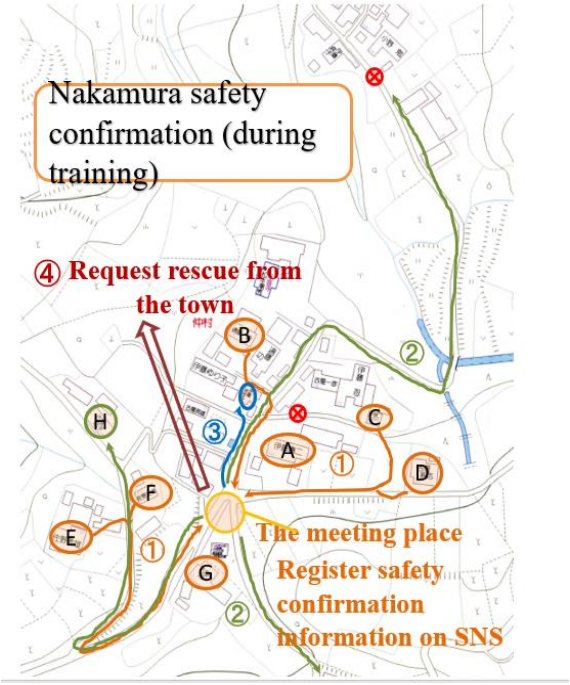

Fig.5 Disaster prevention drill in Nakamura

In addition, a simulated disaster was generated in the district according to the scenario.

Signs, traffic cones, and people closed the road to block the passage of residents. It was assumed that all the roads leading to the outside of the area were cut off and the Hachinoshiri area was isolated. A practical disaster prevention drill using ICT (Information and Communication Technology) was conducted for the residents of Hachinoshiri. Planned for the first time so that information can be exchanged smoothly in the event of a disaster. Residents used smartphone phones and other devices to register their safety and report on the damage situation using the information sharing system being developed by the University of Yamanashi.

It was confirmed that the safety confirmation based on the safety confirmation system was carried out (Enactment) in each group from the behavior observation and questionnaire survey of each inhabitant. It was confirmed that 95% of the residents carried out the safety confirmation.

(1) All the residents were not aware of the voice speakers of the disaster prevention radio, emergency bulletin mail, IP phones (videophones, smartphones), and SNS, and the certainty was not satisfied. By adding a call (safety confirmation), it was found that all the residents in the Yanojiri area were able to be aware of the evacuation information.

(2) As a result of investigating all mobile phone types owned by residents in the Hachinoshiri area and sending an Earthquake Early Warning Area Mail, in areas where the radio waves of mobile carriers are relatively weak, it is also within the area. However, it turned out that the Earthquake Early Warning Area Mail could not be received.

(3) When evaluated in the entire Yanojiri area, in the case of calls using IP phones and response actions using SNS, safety confirmation in the village, information transmission to the town hall, information sharing between the town hall and the fire department, safety information on SNS, It was confirmed that the input of damage information was effectively achieved.

EVALUATION OF INFORMATION TRANSMISSION MEANS

From the questionnaires conducted in the Yanojiri district practical disaster prevention drills, these means can be used for disaster response such as safety confirmation/rescue requests. The evaluation of communication means as a disaster isolation measure in mountainous villages is described as the following indexes.

(1) "Time" from the disaster to the time when the government office contacts the fire department

The total time taken for the response action in the process of the government office contacting the fire department from the disaster for each condition of the communication means is defined as the "time" from the disaster until the government office contacts the fire department.

The time required for response actions using ICT and mobile phones was set based on the results of the training survey. The time required for a walk visit was calculated using the time required for walking (80m / min). Landline phone that could not be investigated in the Hachinoshiri district practical disaster prevention drill. The time required for response actions using satellite mobile phones and disaster prevention administrative radio, and the time required for rescue requests from the government office to the fire department is set as table 5 and Fig.6.

Table 5 The time required in different methods

Methods	Time
Calls using ICT	3 Minutes
Enter safety information and damage information into SNS	1 Minute
Calls using mobile phones	3 Minutes
Calls using landlines	3 Minutes
Calls using satellite mobile phones and disaster prevention administrative radio	5 Minutes
Based on SNS information, the government office requests the fire department to rescue the residents	1 Minute
Based on the report by telephone, the government office requests the fire department to rescue the residents	5 Minutes

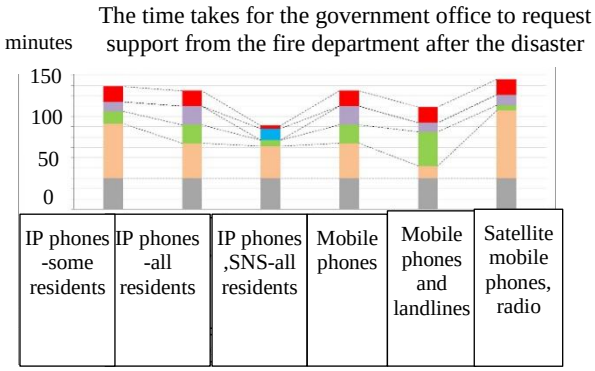

Fig.6 Time of different communication means

(2) "Number of activities" from the disaster to the time when the government office contacts the fire department

The latest route from the disaster to the office contacting the fire department is extracted, and it is defined as the "number of activities" from the disaster to the office contacting the fire department. The types of activities are shown below.

1.Gather at the meeting place, confirm the safety
2.Visit on foot, confirm the safety
3.Use communication equipment to confirm safety
4.Enter safety information by SNS
5.Resident's report safety to the government office
6.Rescue from the fire department

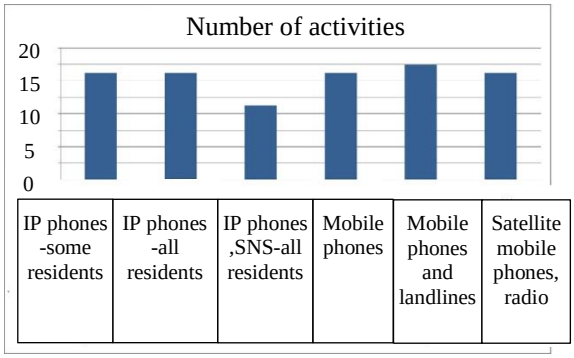

Fig.7 Number of activities

(3) The "stage" from the disaster to the time when the government office contacts the fire department

The contents of the response actions at each stage, which are color-coded, are organized, and the evaluation index is whether the government office is surely performing the rescue request to the fire department, shown in Fig.8.

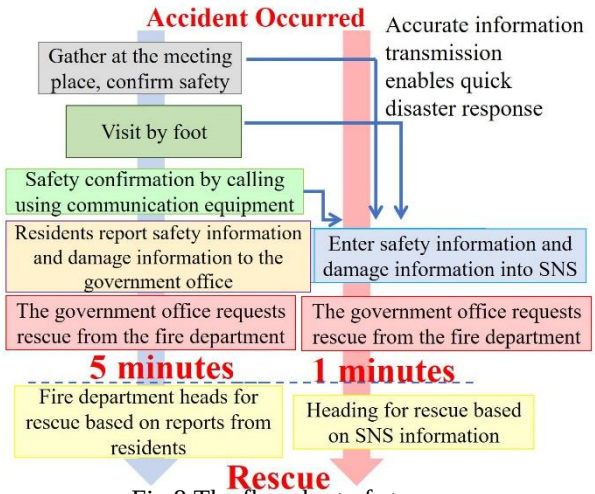

Fig.8 The flowchart of stage

Using the three evaluation indexes of "time", "number of activities", and "stage" from the time of the disaster until the government office contacts the fire department, the impact of the differences in the five information transmission methods on disaster response was confirmed.

When evaluated in Miyazawa, Nakamura, Bessho / Okimura, and Yanojiri district, in the case of calling using IP phones and responding actions using SNS, safety confirmation in the village, information transmission to the town hall, It was found that the three stages of information sharing between the government office and the fire department were integrated into one stage of inputting safety information and damage information into SNS.

Under the preconditions of residents who do not have phones. Therefore, in the case of calls using IP phones and response actions using SNS, isolated households could not be confirmed the safety.

In "Calls using mobile phones and landlines," all residents in the Yanojiri area were able to confirm their safety. Therefore, if the usability of software such as IP phones and SNS is improved, the safety confirmation of all residents will be confirmed. It is thought that the "time" from the disaster to the government office requesting support from the fire department can be shortened and the "number of activities" can be reduced.

From the above, a system in which residents and governments collaborate in a WiFi environment built on a local area network using wireless is effective as a communication means for disaster isolation measures in mountain villages.

SUMMARY

A practical disaster prevention drill in the Hachinoshiri area was conducted. As a measure against the isolation of mountain villages, it was clarified that it is important to establish a safety confirmation system and secure a means of communication between the government office and the village by wireless communication.

To reduce the damage to people caused by disasters, different communication means are necessary, and local area network using wireless is effective as a countermeasure for the isolation of mountain villages on disaster response such as safety confirmation and rescue requests.

REFERENCES

[1] "Cabinet Office of Japan.Disaster Management in Japan. Available online:," 2015, http://www.bousai.go.jp/1info/pdf/saigaipamphlet_je.pdf.

[2] K. E. Rowan, "Why Rules for Risk Communication Are Not Enough: A Problem-Solving Approach to Risk Communication," *Risk Anal.*, vol. 14, no. 3, pp. 365–374, 1994, doi: https://doi.org/10.1111/j.1539-6924.1994.tb00253.x.

[3]T. Suzuki, T. Watanabe, and S. Okuyama, "Facilitating community risk communication for wide-area evacuation during large-scale floods," *Int. J. Environ. Res. Public Health*, vol. 16, no. 14, 2019, doi: 10.3390/ijerph16142466.

[4] T. Suzuki, "Influence of Communication Tools on Transmission Characteristics based on the Evacuation Information Transmission Test," *J-STAGE*, no. 13, pp. 48–56, 2015, doi: https://doi.org/10.24709/jasdis.13.0_48.

11th Int. Conf. on Geotechnique, Construction Materials & Environment, Kyoto, Japan, 3-5 November 2021, ISBN: 978-4-909106063 C3051

SPATIAL STATISTICAL ANALYSIS OF THE POROUS MEDIUM EXTRACTED FROM VIRTUAL PACKED GRAINS WITH RANDOM SIZES

Yu Song[1], Junichiro Takeuchi[1], Yuto Takeuchi[1] and Masayuki Fujihara[1]

[1] Graduate School of Agriculture, Kyoto University, Japan

ABSTRACT

Hydraulic properties such as water retention properties and permeability, which are macro characteristics of porous media, are determined in a bottom-up manner by pore properties including pore shape, pore-size distribution, and pore connectivity. Hydraulic properties could be reproduced from local physical phenomena such as capillarity in the pores using a pore-network model. Spatial distribution of pores could affect these hydraulic properties. In this research, global and local Moran's indexes, which are spatial statistics, are used to analyze the spatial distribution of pores in porous media packed with both single-size and various-size grains. The obtained results of global Moran's indexes show that pore distribution has positive autocorrelation in all the media we packed, and those of local Moran's indexes show that larger pores tend to be formed around larger pores, and that those form large-pore clusters. These results imply that hydraulic properties of porous media could be affected by the spatial distribution of pores.

Keywords: Water retention property, Pore-network, Spatial statistics, Global and local Moran's indexes

INTRODUCTION

It is well known that soil water relations are an important aspect of the soil environment of the plant. The hydraulic properties of soils such as water retention properties and permeability, which are macro characteristics of porous media, play an important central role in determining the movement and storage of water in soil and thus have a large influence on crop growth.

Soil water retention and transport properties are altered in response to changes in pore properties including pore shape, pore-size distribution, and pore connectivity [1]. Pore-network models could be utilized to reproduce the hydraulic properties from local physical phenomena such as capillarity in the pores [2,3]. It was presented that the water retention property of the original pore-network model extracted from a porous medium model is different from that of pore-network models generated randomly based on the same pore-size distribution, which suggests that pores have a certain spatial structure in the porous medium [4].

In this research, we used the spatial statistics called global and local Moran's indexes [5] to analyze the spatial pore-size distribution of porous media packed with both single-size and various-size grains, to find the global spatial autocorrelation in the pore distribution.

SPATIAL AUTOCORRELATION

Spatial autocorrelation can be defined in the phenomenon that occurs when the spatial distribution of the variable of interest exhibits a systematic pattern. Moran's I statistics are one of the statistical and computational methods for examining spatial autocorrelation on a network, that is, the correlation between attribute values of the same kind at different locations on a network or on different subnetworks (including line segments and links) forming the network [6]. Moran's I statistics include two types: global Moran's I statistic and local Moran's I statistic. The former shows the average level of spatial autocorrelation over the whole network; the latter examines the correlation between the attribute value of a specific network and those of its surrounding network points.

Global Spatial Autocorrelation

The global Moran's I statistic on a network, network global Moran's I statistic, is used for global spatial autocorrelation, which is defined as:

$$I = \frac{\sum_{i=1}^{n}\sum_{j=1}^{n} w_{ij}\left(x_i - \bar{x}\right)\left(x_j - \bar{x}\right)}{m_2 S_0}, \tag{1}$$

where n is the number of the data, x_i is the attribute value that denotes the value taken on by the variable x of interest at location i and $\bar{x}$ denotes the mean of these values, which is defined as follows:

$$\bar{x} = \frac{1}{n}\sum_{i=1}^{n} x_i, \tag{2}$$

m_2 and S_0 are defined as:

$$m_2 = \frac{1}{n}\sum_{i=1}^{n}\left(x_i - \bar{x}\right)^2 , \quad (3)$$

$$S_0 = \sum_{i=1}^{n}\sum_{j=1}^{n} w_{ij} . \quad (4)$$

In the present study, x_i is the diameter of the pore body (PB) whose index is i, and n is the number of all PBs in the interest pore-network.

Spatial autocorrelation statistics deal with the correlation between nearby attribute values. w_{ij} denotes the elements of the spatial weights matrix W corresponding to the location pair (i, j) and can formalize the nearness mathematically. In this research, $w_{ij} = 1$ if network points are adjacent; otherwise, $w_{ij} = 0$.

When I is positive, it suggests a positive autocorrelation; when I is negative, it suggests a negative autocorrelation. Statistical test is based on Z_I values, computed by subtracting $E[I]$ from I and dividing it by the standard deviation of I, which is given by:

$$Z_I = \frac{I - E[I]}{\sqrt{Var(I)}} \sim N(0,1) . \quad (5)$$

The expected value and variance of I under the null hypothesis of the normal variate spatial randomness are derived as:

$$E[I] = -\frac{1}{n-1} , \quad (6)$$

$$Var(I) = \frac{n^2 S_1 - nS_2 + 3S_0^2}{\left(n^2 - 1\right)S_0^2} - \left\{E[I]\right\}^2 , \quad (7)$$

$$S_1 = \frac{1}{2}\sum_{i=1}^{n}\sum_{j=1}^{n}\left(w_{ij} + w_{ji}\right)^2 , \; S_2 = \frac{1}{2}\sum_{i=1}^{n}\left(w_{i*} + w_{*i}\right)^2 , \quad (8)$$

$$w_{i*} = \sum_{j=1}^{n} w_{ij} , \; w_{*i} = \sum_{j=1}^{n} w_{ji} . \quad (9)$$

Local Spatial Autocorrelation

The local Moran's I statistic can examine the correlation between the attribute value of a specific network point and those of its surrounding network points, which is defined as follows:

$$I_i^L = \frac{\left(x_i - \bar{x}\right)}{m_2}\sum_{j=1}^{n} w_{ij}\left(x_j - \bar{x}\right) . \quad (10)$$

This equation can express both the deviation from the average of the point's own value and that of the surrounding points'. That means, I^L is positive when both of them are greater than or less than the average, and I^L is negative if either one is greater or smaller than the average.

In terms of the network global Moran's I statistic, this equation is written as:

$$I = \sum_{i=1}^{n} I_i^L / S_0 . \quad (11)$$

This equation shows that the global Moran's I statistic is proportional to the average of network local Moran's I statistics over all network points.

The same as those of the global Moran's I statistic, the expected value and variance of I^L under the null hypothesis of no global spatial autocorrelation, which can be utilized for identifying statistically significant points, are derived as:

$$Z_{I_i^L} = \frac{I_i^L - E\left[I_i^L\right]}{\sqrt{Var\left(I_i^L\right)}} \sim N(0,1) , \quad (12)$$

where

$$E\left[I_i^L\right] = -\frac{w_{i*}}{n-1} , \quad (13)$$

$$Var\left(I_i^L\right) = \frac{w_{i(2)}\left(n - b_2\right)}{n-1} + \frac{2w_{i(kh)}\left(2b_2 - n\right)}{\left(n-1\right)\left(n-2\right)} - \left\{E\left[I\right]\right\}^2 , \quad (14)$$

and

$$w_{i(2)} = \sum_{j=1}^{n} {w_{ij}}^2 , \; w_{i(kh)} = \frac{1}{2}\sum_{k=1}^{n}\sum_{h=1}^{n} w_{ik} w_{ih} , \quad (15)$$

$$b_2 = \frac{m_4}{m_2^2} , \; m_4 = \frac{1}{n}\sum_{i=1}^{n}\left(x_i - \bar{x}\right)^4 . \quad (16)$$

Moran Scatter Plot

Spatial distribution of the attribute values can be visualized through classification by the scatter plot with the original attribute values on the horizontal axis and the surrounding values on the vertical axis [7].

In the Moran scatter plot, the attribute values are divided into four quadrants, each of which represents a different kind of spatial association: Spatial categories in the upper right (HH, high-high) and lower left (LL, low-low) quadrants, and spatial categories in the lower right (HL, high-low) and upper left (LH, low-high) quadrants.

NUMERICAL EXPERIMENTS

Pore-network Models

Pore-network models extracted from porous media are utilized to conduct the numerical experiments in this research. The virtual porous media are prepared by using the discrete element method, which are composed of various kinds of spherical grains packed randomly in the cubic containers. The method used for pore network extraction is known as the watershed segmentation algorithm, which has been popular these days due to the effectiveness in working with porous media images of any porosity and its easier implementation [8]. In this research, we put SNOW algorithm [9], an efficient algorithm for extracting networks using only standard image analysis techniques, into implementation. Details on network extraction using this method can be found in the reference [9].

A pore-network consists of pore bodies (PBs) and pore throats (PTs). PBs are relatively large, however, PTs that connect two PBs are relatively small. To make networks sufficiently large that exceed the representative element volume (REV), we tried packing spherical grains from 1000 to 7000 and extracted the pore networks under the conditions of the voxels from 200^3 to 700^3. By observing histograms of the frequency distributions of pore sizes and coordinate number, the number of PTs that a single PB connects, we find that when the number of grains is larger than 2000 and the voxels exceed 500^3, packed porous media and the extracted networks are sufficiently large and resolved for numerical experiments.

In this research we packed porous media with four grain size distributions (A-D) and three different samples were made in each grain size distribution: Sample A1-3 are packed with single-size spherical grains; the others are packed with uniformly distributed spherical grains. The numbers of grains all exceed 3000, and we choose voxels of 600^3 to get more delicate models. The sample holders (mm) of them are A-44.1^3, B-32.6^3, C-45.1^3 and D-48.1^3.

Table 1 shows the properties of packed porous media and the extracted pore networks. Figure 1 shows the virtual porous media and pore-networks of A1 and D1. The former is packed with single-size spherical grains; the latter is packed with uniformly distributed spherical grains. To eliminate the influence of boundary PBs and PTs, we make the frequency distributions of pore-sizes and coordinate number of the internal pore-network models D1-3, which are shown in Fig. 2, and it was confirmed that similar pore-size and coordinate number distributions were obtained from different grain-packing in the cubic container. Moreover, the following numerical experiments are all applied on the internal pore-network models.

Table 1 Properties of porous media and pore-networks

NAME	Size of grains (mm)	No. of grains	No. of PB-internal/ PB-all	No. of PT-internal/ PT-all
A1	3	3615	9720/11441	34255/35976
A2	3	3603	9693/11450	33893/35650
A3	3	3619	9753/11551	34256/36054
B1	1.77-2.57	3728	9765/11530	33956/35721
B2	1.77-2.57	3725	9749/11484	34111/35864
B3	1.77-2.57	3714	9663/11422	33727/35486
C1	2-4	3557	9280/11054	32103/33727
C2	2-4	3525	9204/10907	31592/33293
C3	2-4	3549	9336/11000	32009/33823
D1	1-5	3342	7949/9417	27468/28652
D2	1-5	3301	7787/9304	26782/28299
D3	1-5	3311	7857/9505	27092/29024

Results

The global Moran's I of internal pore-network models are shown in Table 2 as well as the $Z-score$ and $P-value$ of them. When the results of I distribute around 0, it indicates the normal variate spatial randomness and shows that pore-size distributions are random ones and that those has no global spatial autocorrelation.

The global Moran's I of A1-3, B1-3, C1-3, and D1-3 shows strong spatial autocorrelations, and the null hypothesis that there is no spatial autocorrelation was rejected at a significant level of 1%, which indicates that there are same clusters of larger and/or smaller PBs in the porous media.

Regarding the local Moran's I, the numbers of significant PBs at the 5% statistically significant level in each category are shown in Table 2. Figure 3 denotes the Moran scatter plots of A1, B1, C1 and D1; Figure 4 shows the spatial distributions of categories for both all PBs and significant PBs of A1 and D1.

As we can see in Fig. 3, the numbers of statistically significant PBs in HH region are obviously higher than LH, LL and HL, and the numbers of significant PBs in LL and HL regions are extremely small, which indicates that large PBs tend to distribute around large PBs.

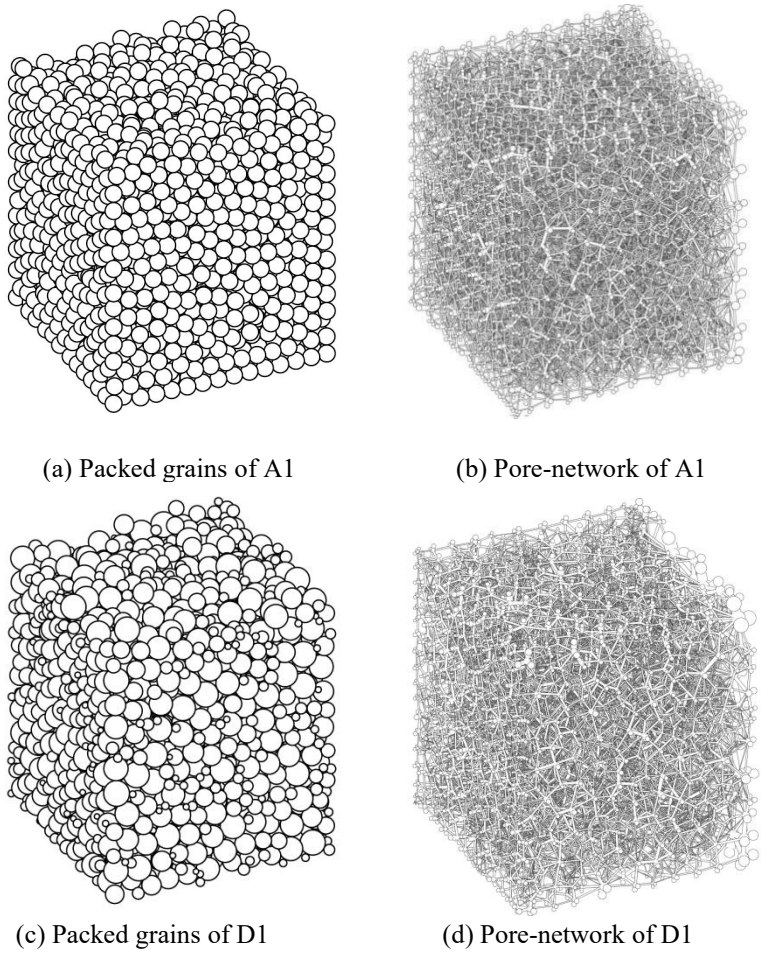

(a) Packed grains of A1 (b) Pore-network of A1

(c) Packed grains of D1 (d) Pore-network of D1

Fig. 1 Virtual porous media and pore-networks (A1, D1)

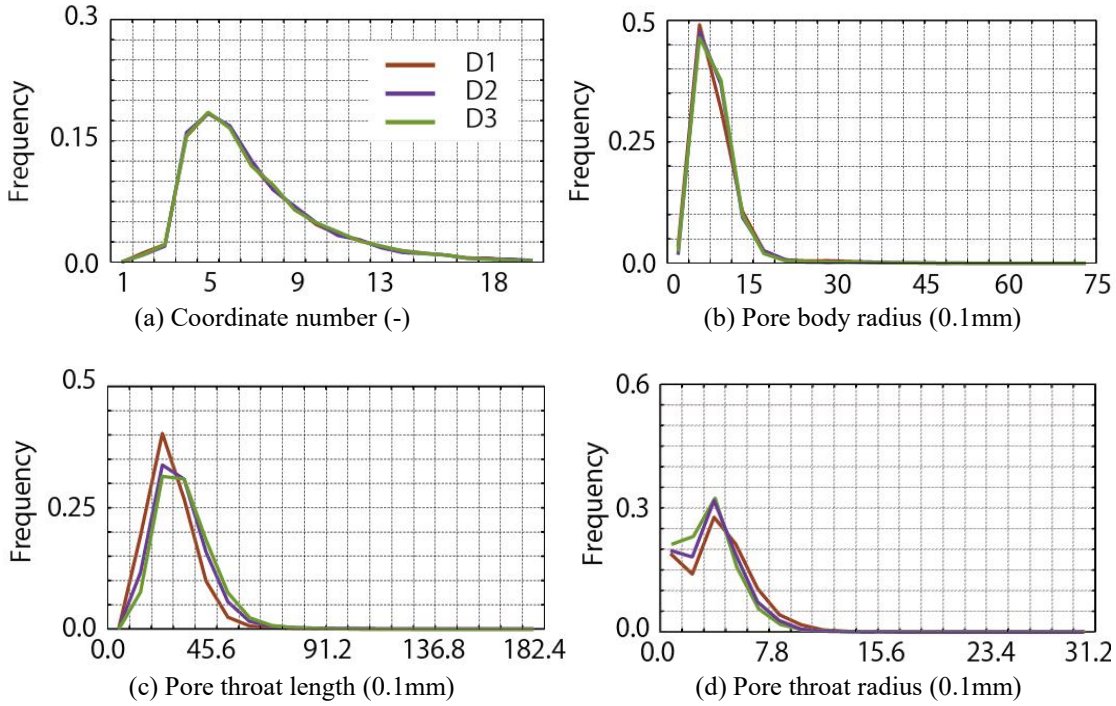

(a) Coordinate number (-) (b) Pore body radius (0.1mm)

(c) Pore throat length (0.1mm) (d) Pore throat radius (0.1mm)

Fig. 2 Frequency of coordinate number and pore-sizes (D1-3, Internal)

Table 2 Global Moran's I and number of significant/all PBs-Internal in each category

Pore-networks	I	$Z-score$	$P-value$	HH	LH	LL	HL
A1	0.473	29.77	Neary 0	996/2677	104/2379	11/3563	1/1101
A2	0.488	30.57	Neary 0	920/2700	91/2346	2/3566	2/1081
A3	0.482	30.30	Neary 0	942/2807	89/2321	4/3501	0/1124
B1	0.498	31.57	Neary 0	1058/2706	107/2311	12/3624	6/1124
B2	0.489	30.89	Neary 0	1030/2744	105/2250	7/3632	2/1123
B3	0.495	31.18	Neary 0	1022/2769	91/2250	31/3601	2/1043
C1	0.474	29.32	Neary 0	999/2642	88/2159	12/3411	1/1068
C2	0.474	29.22	Neary 0	1055/2640	110/2067	7/3482	3/1015
C3	0.506	31.45	Neary 0	967/2551	81/2031	6/3696	1/1058
D1	0.483	27.69	Neary 0	877/2351	119/1976	10/2832	1/790
D2	0.494	28.09	Neary 0	808/2277	111/1799	10/2975	2/736
D3	0.478	27.31	Neary 0	844/2301	110/1830	16/2940	0/786

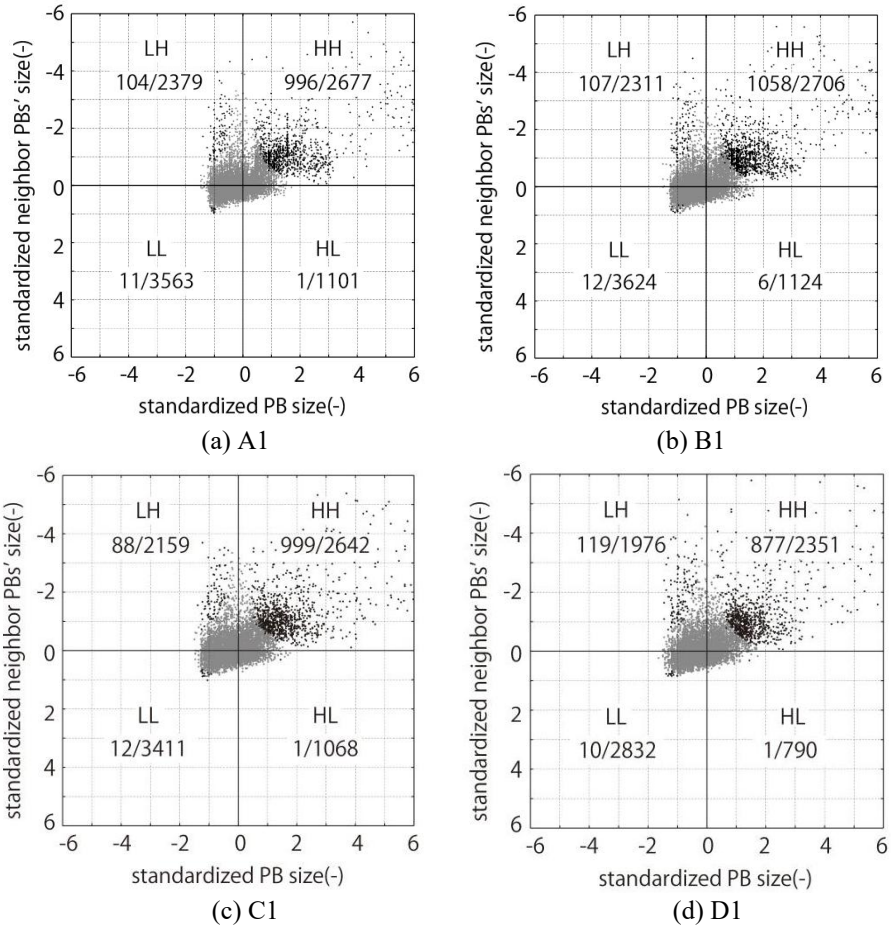

Fig. 3 Moran scatter plot

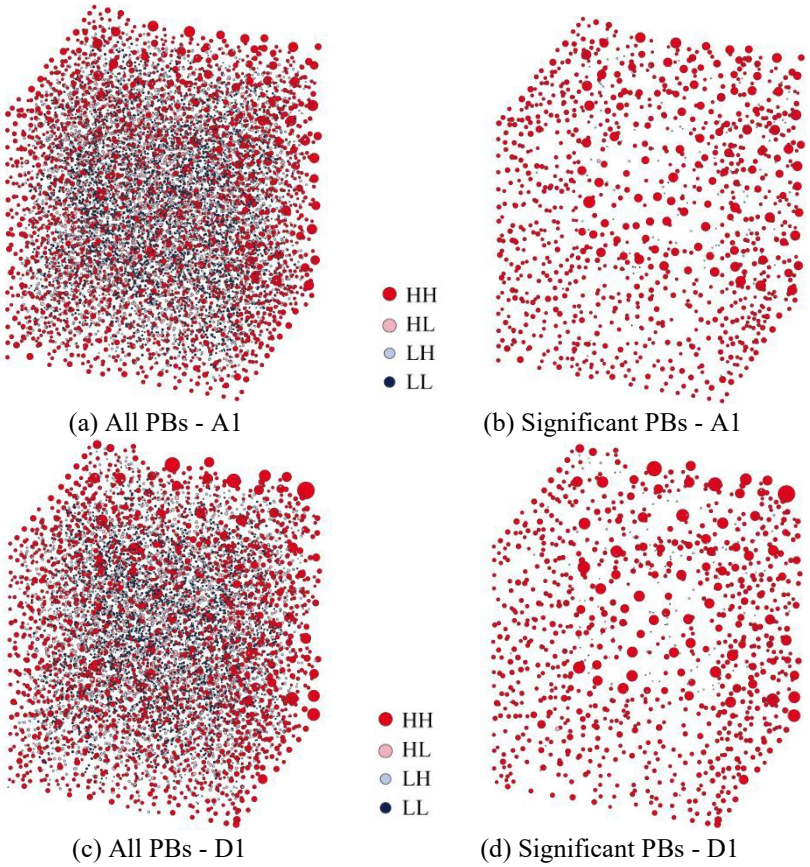

(a) All PBs - A1 (b) Significant PBs - A1

(c) All PBs - D1 (d) Significant PBs - D1

Fig. 4 Spatial distributions of categories for PB-Internal

CONCLUSIONS

In this research, global and local Moran's indexes, which are spatial statistics, are used to analyze the spatial distribution of porous media packed with both single-size and various-size grains. The obtained results of the spatial statistics show that there is a spatial autocorrelation in the pore distribution, both in the porous media packed with single-size spherical grains and uniformly distributed spherical grains. In addition, the numbers of significant PBs at the 5% statistically significant level that distributed in HH category are obviously higher than LH, LL and HL regions, which indicates that large PBs tend to distribute around large PBs. All of these imply that hydraulic properties of porous media could be affected by the spatial structure of pores.

REFERENCES

[1] Horton, R., M. D. Ankeny, and R. R. Allmaras, Effects of compaction on soil hydraulic properties, Developments in Agricultural Engineering, Vol. 11, 1994, pp.141-165.

[2] Takeuchi, J., Sumii, W., and Fujihara, M., Modeling of fluid intrusion into porous media with mixed wettabilities using pore-network, International Journal of GEOMATE, Vol. 10, 2016, pp.1971-1977.

[3] Takeuchi, J., Sumii, W., Tsuji, H., and Fujihara, M., Estimation of permeability of porous media with mixed wettabilities using pore-network model, International Journal of GEOMATE, Vol. 11, 2016, pp.2241-2247.

[4] Takeuchi J. and Fujihara M., Spatial Statistical Analysis of Pores in Single-size Grains Packing, Proceedings of JRCSA 2017 Annual Congress, 2017, pp.18-21 (in Japanese).

[5] Moran, P. A., Notes on continuous stochastic phenomena, Biometrika, Vol. 37(1/2), 1950, pp.17-23.

[6] Okabe, A., and Sugihara, K., Network spatial autocorrelation, Spatial analysis along networks: statistical and computational methods. John Wiley and Sons, 2012, pp.137-151.

[7] Pisati, M., sg162: Tools for spatial data analysis, Stata Technical Bulletin, Vol. 60, 2001, pp.21-37.

[8] Rabbani, A., Jamshidi, S., and Salehi, S., An automated simple algorithm for realistic pore network extraction from micro-tomography images. Journal of Petroleum Science and Engineering, Vol. 123, 2014, pp.164-171.

[9] Gostick, J. T., Versatile and efficient pore network extraction method using marker-based watershed segmentation, Physical Review E, Vol. 96(2), 2017, p.02330.

11th Int. Conf. on Geotechnique, Construction Materials & Environment,
Kyoto, Japan, 3-5 November 2021, ISBN: 978-4-909106063 C3051

GROUNDWATER FLUORIDE HAZARD ZONATION IN THE VOLCANOGENIC POLLUTED AREA, EAST JAVA, INDONESIA

Dhandhun Wacano[1,2], Lutfia Isna Ardhayanti[2], Suphia Rahmawati[2], Ihsan Diyahulhaq Fadhlurahman[2], Mawarti Sekar Ratri Nastiti[2], Auniatul Aulia[2], Minoru Yoneda[1]

[1]Department of Environmental Engineering, Graduate School of Engineering, Kyoto University, Japan;
[2]Department of Environmental Engineering, Universitas Islam Indonesia, Yogyakarta, Indonesia

ABSTRACT

Volcanic activity can release numerous hazardous contaminants, including toxic elements such as fluoride. Despite the relevance of fluorine to human nutrition, the ingestion of excessive doses can have adverse health effects such as fluorosis disease. Asembagus, Banyuputih and Jangkar (ABJ) subdistrict in East Java Indonesia have been polluted by fluoride, where the Asembagus subdistrict is known as a fluorosis endemic area in Indonesia. The high groundwater fluoride concentrations in this area were reported from effluent of hyper-acid water lake of Kawah Ijen volcano. In order to prevent and mitigate severe chronic effects of prolonged exposure of fluoride in ABJ subdistrict, the zonation of polluted area was developed. Spatial multi criteria evaluation (SMCE) approach and geospatial analysis technique was applied to visualize fluoride hazard zone. Moreover, spatial hazard model with 5x5 m^2 grid resolution showed that 56 % area in very low zone, 12% area in low zone, 21 % area in high zone, and 11 % area in very high zone respectively. Cross operation technique also revealed that 9 villages were in the high hazard zone with potential for dental fluorosis and 5 villages were in the very high hazard zone with potential for skeletal fluorosis chronic effect. Based on the condition of drinking water source, development of clean water networks and groundwater quality improvement in accordance with standards of drinking water is needed. Furthermore, risk communication about fluoride exposure hazard should be addressed to reduce and mitigate fluoride pollution risk in Asembagus, Banyuputih, and Jangkar subdistrict.

Keywords: Asembagus, Groundwater fluoride pollution, Risk mitigation, Kawah Ijen volcano

1. INTRODUCTION

Kawah Ijen volcano in East Java, Indonesia, is the largest hyper-acid volcanic crater lake in the world. The effluent of hyper-acid water from crater lake through Banyupahit-Banyuputih river channel is reported as the source of natural pollution in the northern part of Kawah Ijen volcano [1]. The polluted areas are Asembagus, Banyuputih, and Jangkar (ABJ) subdistrict. This acid water is entering polluted areas not only from the watershed system, but also via irrigation channel that loading toxic element including fluoride.

In the Banyupahit-Banyuputih river, the fluoride concentration is in the range between 5.5 and 14.2 mg L^{-1} and near this area, the concentration of fluoride in groundwater reached 4.2 mg L^{-1} [2]. The high fluoride concentration in the water of the study area is originated from Kawah Ijen crater lake which the pH of the water is lower than 0.3 and the concentration of fluoride is up to 1500 mg L^{-1}.

The water from Banyuputih river is also used for irrigating agriculture field in Asembagus and Jangkar area. The irrigation practice is carried out during the dry season. Approximately 2800 kg of fluoride is discharged per day into the soil in this area during the irrigation process [3]. The long-term application of this highly acid and fluoride-polluted water for the irrigation process has been changed the agriculture soil [4] and groundwater quality [1]-[2].

Fluoride is an essential micronutrient need by the human body, especially for teeth and bones. A certain amount of fluoride is found in drinking water within the permissible limit of concentration between 0.5 to 1.5 mg L^{-1} as prescribed by the World Health Organization (WHO) [5]. Even so, fluoride contamination in water becomes a significant problem globally. Some article states that there will be a negative impact on the human body when exposed with higher fluoride intake. Most of them reported dental and skeletal fluorosis as the impact of the higher fluoride intake [6]-[7].

Even though fluoride health is still well controlled in some countries, many dental fluorosis cases have been reported [6]. Zuo [8] reportedly that accumulation of fluoride in the environment could affect health risk for plants, animals, and humans. In the study area, the total daily F intake exceeds the possible limit that can be causal factor for dental and skeletal fluorosis [2]. Furthermore, the groundwater is used for the drinking water source by the local residents. This practice has caused many health problems especially dental and skeletal fluorosis to the local residents.

Due to the potential health risk that caused by the high concentration of fluoride in groundwater, this study presents hazard map from groundwater fluoride in ABJ subdistrict. Spatially, hazard quotient analysis in Asembagus was calculated by [2] and showed based on the point of well samples and village community. However, this study used different approach and technique to complement the previous study. The spatial pattern of fluoride concentration is explained using drainage system approach, while spatial analysis with multi criteria parameter has been used in order to develop fluoride hazard index.

2. MATERIALS AND METHODS

2.1. Study Area and Samples Location

The study area is located in the Situbondo Regency, in the northern part of Kawah Ijen volcano, East Java province, Indonesia Fig.1. This area consists of three subdistricts namely Asembagus, Banyuputih and Jangkar which will be abbreviated as ABJ subdistrict for convenience. Morphologically, the ABJ subdistrict is coastal plain with the volcanic soil as dominant surface material. Five watershed systems are bordered in the study area i.e., Sokmaelang watershed, Jangkar Watershed, Banyuputih watershed, Leket watershed and Klompret watershed with drainage networks are categorized as acid river of Banyuputih, acid irrigation channel mostly in Asembagus subdistrict, neutral irrigation channel and neutral river stream.

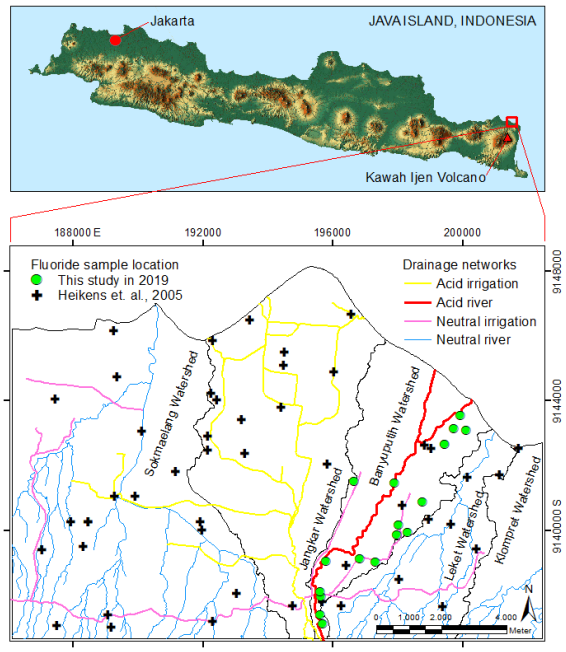

Fig. 1 Map of study area and sample location.

Groundwater fluoride samples are divided into two categories based on the data sources. A total of 49 groundwater samples is selected from [2] in dry season of 1999 and 2000. During dry season 2019, 17 water wells were sampled in this study to compare and validate the previous samples. It is clear that the temporal difference between the two types of groundwater samples is about 20 years. The 2019 samples were taken mostly within Banyuputih watershed as the main sources of high fluoride concentration in the river water from Kawah Ijen crater lake. The consideration of the sample location is based on the information that acid river is more potential as the pathway of fluoride pollution in the study area.

2.2. Samples Analysis

Fluoride samples concentration from [2] was measured with a Dionex DX120 ion chromatograph combine with Pulse Electrochemical Detector. In order to analysis 17 samples of 2019, SPADNS Spectrophtometric Method was applied. The principle of this method based on the process of reaction between fluoride and zirconium. Fluoride will react with Zr-SPADNS and resulting coloured complex then measured in a spectrophotometer at 570 nm.

2.3. Spatial Analysis

Geographic information system (GIS) was used to develop fluoride hazard index. ArcGIS 10.8 and ILWIS 3.3 Academic software packages were combined in order to analyze both of type vector and raster data set. Vector based analysis was applied mostly for index parameter preparation steps. A georeferenced corner was created to determine the relation between row and column numbers in a raster map and XY-coordinates, along with the 5x5 m^2 grid resolution are generated.

A total of 49 groundwater fluoride samples from [2] was interpolated using inverse distance weighted (IDW) interpolation to show the general spatial pattern of fluoride concentration distribution in the study area. This interpolation technique was chosen due to their easy and merely show the factual data pattern. This result of interpolation then classified with chronic health effect concentration following [9]-[10].

Drainage networks were analyzed using distance calculation technique. This process is crucial to identify the correlation of groundwater fluoride concentration with drainage networks both acid and neutral channel.

Spatial multi-criteria evaluation (SMCE) is a technique for supporting stakeholders to make decision. The complexity of parameters in the decision process is simplified by the systematic hierarchy. Parameter maps as input for SMCE were grouped, standardized, and weighted in a criteria tree Fig 2.

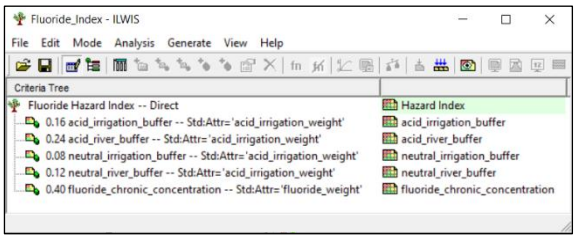

Fig. 2 The criteria tree of fluoride hazard index

3. RESULTS AND DISCUSSION

3.1. Groundwater Fluoride Pattern

Cross correlation between groundwater fluoride concentration and irrigation distance shows a negative correlation Fig. 3. The correlation is relatively weak that indicated not clear influence of acid irrigation to fluoride concentration in groundwater. Moreover, many samples with concentration of 0.1 mg L^{-1} are present at almost every distance from closest to farthest. This data condition explained unclear correlation that acid irrigation is the main source of groundwater fluoride concentration in study area.

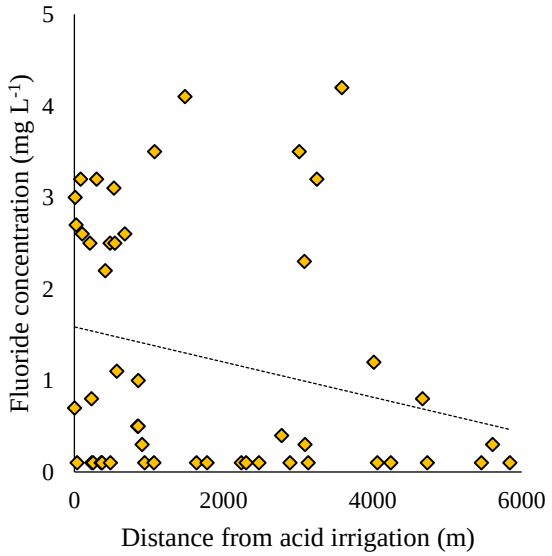

Fig. 3 Graphic plot F concentration versus distance of acid irrigation

Different from the previous cross correlation in Fig 3, the graphic at Fig. 4 shows relatively a strong negative correlation. Despite the low groundwater fluoride with concentration of 0.1 mg L^{-1} is also present in every distance, strong negative correlation indicates that acid river has a strong influence to contribute fluoride concentration in the groundwater. This condition may be affected by the base characteristic of acid channel. Base of acid irrigation channel usually constructed by cement concrete that will protect the acid water from infiltration process.

The acid river base is naturally from soil or surface lithological condition. This characteristic of material drives the acid water more easily to infiltrate into groundwater. The other explanation is period time of exposure between acid river and irrigation river. The acid river has flowed for more than a hundred years [3], while the acid irrigation is shorter period of time. This clear indication that fluoride exposure will intensively occurring with duration time of exposure from the acid river.

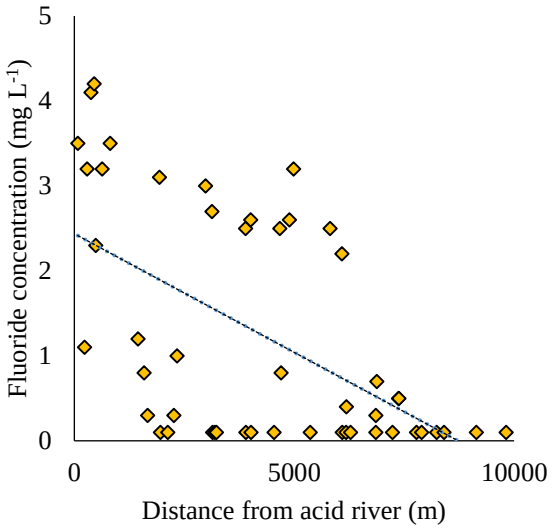

Fig. 4 Graphic plot F concentration versus distance of acid river

The groundwater fluoride pattern also can be explained by the drainage length (Dl) and drainage density (Dd) characteristic. Drainage length calculation in the Table 1 shows comparison between acid drainage length and neutral drainage length within every watershed system. The result of calculation shows Jangkar watershed has the longest acid drainage length, followed by Banyuputih and Sokmaelang watershed. The longest acid drainage length will affect the range of fluoride dispersion in the soil surface and into groundwater. Klompret and Leket watershed will not be polluted by fluoride since the acid drainage does not flow in these two watersheds, showed in zero value of drainage length.

Table 1 Drainage length in watershed system

Watershed	Acid length (km)	Neutral length (km)
Banyuputih	14.18	9.91
Jangkar	55.34	3.53
Klompret	0	10.06
Leket	0	42.58
Sokmaelang	12.16	116.23

Drainage density calculation in the Table 2 shows comparison between acid drainage density and neutral drainage density within every watershed system. The result of calculation shows Jangkar watershed has the highest acid drainage density, followed Banyuputih and Sokmaelang watershed. The highest drainage density will affect the concentration of fluoride dispersion from the soil surface into the groundwater. Otherwise, the highest neutral drainage density will contribute to the dilution process of fluoride becoming lower its concentration before reach groundwater aquifer system.

Table 2 Drainage density (Dd) in watershed system

Watershed	Acid-Dd	Neutral-Dd
Banyuputih	0.00065	0.00046
Jangkar	0.00142	0.00009
Klompret	0	0.00094
Leket	0	0.00261
Sokmaelang	0.00019	0.00183

3.2. Parameter and Sub-parameter map

Parameter and sub-parameter maps are used to generate fluoride hazard index. In this study, five-parameter maps were prepared Fig 5. Buffer map is a parameter that give information about classified distance from the drainage both acid and neutral, with the 6 class sub-parameter Fig. 5a-d. These buffer map including acid river buffer, acid irrigation buffer, neutral river buffer and neutral irrigation buffer.

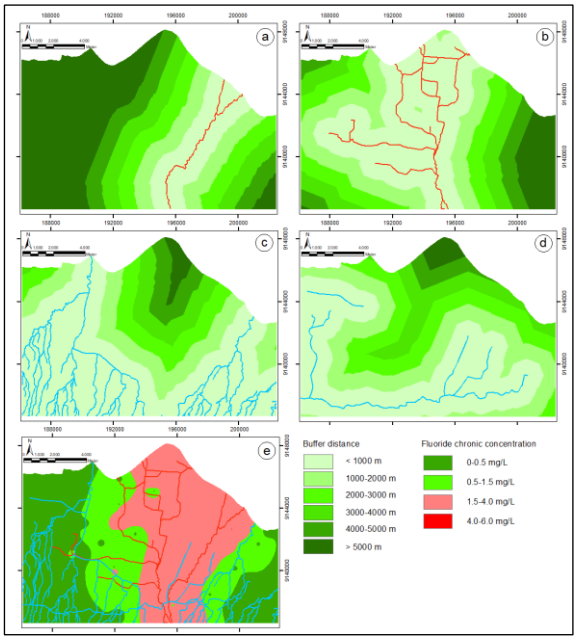

Fig. 5 Parameter map (a) acid river buffer, (b) acid irrigation buffer, (c) neutral river buffer, (d) neutral irrigation buffer, (e) fluoride chronic concentration

The groundwater fluoride concentration in the study area varied from 0.1 to 4.2 mg L^{-1} with a mean concentration of 1.9 mg L^{-1} from [2] data, and between 1.4 - 3.3 mg L^{-1} with a mean concentration of 2.4 mg L^{-1} from survey data in 2019. Based on the chronic health effect concentration of groundwater fluoride, the study area samples were classified into four pollution zones Fig. 5e: low category (0-0.5 mg L^{-1}), medium category (0.5-1.5 mg L^{-1}), high category (1.5-4.0 mg L^{-1}), and very high category (4.0-6.0 mg L^{-1}). Analysis of samples revealed that 26 % concentration in the range of dental caries suffer, 12 % in the recommended health range, 56 % in the fluorosis-mottled teeth potential health chronic effect, and 6 % in dental fluorosis and skeletal fluorosis potential chronic health effect.

Fluoride concentration increases with the mean of increasing is 0.7 mg L^{-1} and cover about 47 % of samples Fig. 6. In the other hand, decreasing of fluoride concentration cover 53 % of total samples with the average of decreasing concentration is 0.6 mg L^{-1}. The condition of change concentrations in groundwater indicates that after 20 years interval time, there is a fluctuation of fluoride concentration in the groundwater.

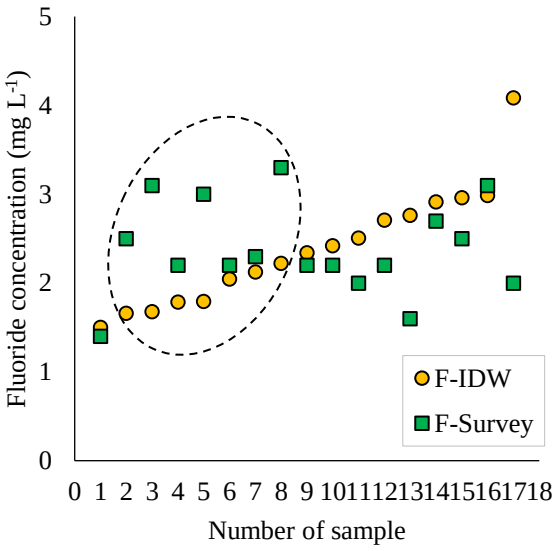

Fig. 6 Graphic plot of F-IDW and F-Survey

3.3. Fluoride Hazard Index and Zonation

Fluoride hazard index result shows that the range index is from 0.0 to 1.0 Fig. 7a. Small value index indicates the low hazard potential and the highest value is in the high hazard potential. The hazard zonation was classified into four pollution zones: very low category (<0.51), low category (0.51-0.67), high category (0.67-0.84), and very high category (>0.84). The hazard map was crossed with the settlements area to analyze the number of villages in ABJ subdistrict that potentially polluted by groundwater fluoride. Village number 1-10 is in Asembagus subdistrict,

number 11-13 is in Banyuputih subdistrict and village number 14-20 is in Jangkar subdistrict Fig 7b.

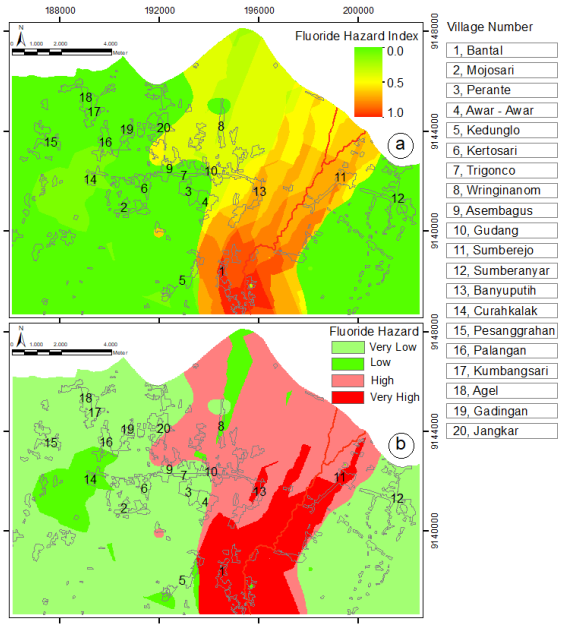

Fig. 7 Map of (a) fluoride hazard index and (b) fluoride hazard category zonation

3.4. Fluoride Hazard and Risk Mitigation

Cross correlation analysis revealed that 26 % concentration is potentially make dental caries suffer which is not correlated with fluoride concentration in drinking water [2] but strongly related to dental fluorosis. This is proven with 56 % of samples is in the fluorosis-mottled teeth potential health chronic effect, while about only 12 % in the recommended health range. The skeletal fluorosis also potentially occurs in ABJ subdistrict due to 6 % samples is in skeletal fluorosis potential chronic health effect.

Table 3 Hazard category area in the villages

Village	High area (km^2)	Very high (km^2)
Bantal	-	507.08
Perante	38.88	-
Awar – Awar	191.33	41.43
Kedunglo	-	0.35
Trigonco	260.30	-
Wringinanom	885.70	-
Asembagus	212.58	-
Gudang	356.45	-
Sumberejo	311.85	936.78
Banyuputih	624.98	222.25
Palangan	82.13	-

The percentage of fluoride concentrations in drinking water and its chronic health effects supported dental caries and dental fluorosis-mottled teeth as the result of fluoride groundwater polluted in ABJ Subdistrict Table 3. Very high hazard category is Sumberejo village followed by Bantal village and Banyuputih village. All of village in Table 3 is confirmed previous information that a total 14 village receive polluted water from Banyuputih river, whereas 3 villages are not including in hazard map resulted in this study.

Unfortunately, the problem of confidence among the local people to consult their health condition in Health Clinic lead the lack of fluorosis data in ABJ Subdistrict. This situation makes the validation of model becoming more difficult. The condition become severe when the municipality in 1990 failed to solve this drinking water problem in ABJ subdistrict [11]. Most of the inhabitants Fig. 8 preferred to drink water from their own well because taste feeling and economically reasons.

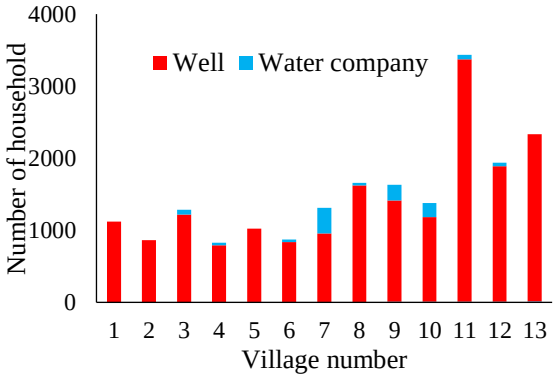

Fig. 8 Daily water source of household (1-10 in 2018 and 11-13 in 2017)

Dry season also enhances the risk of fluoride pollution in water [12]. Age also becomes the role play in the fluoride-health problem as children have a higher risk of the fluoride-health problem than adults. For children, the high amount of fluoride in the body will impact neurodevelopment than for an adult, the higher amount of fluoride will affect the dental and skeletal problem [13].

4. CONCLUSIONS

Groundwater fluoride hazard zonation in the study area was classified into four categories namely very low (<0.51), low (0.51-0.67), high category (0.67-0.84), and very high category (>0.84). Spatial model showed that 56 % of study area in very low category, 12% area in low category, 21 % area in high category, and 11 % area in very high category. Furthermore, spatial analysis also revealed that 9 villages were in the high category with potential for dental fluorosis and 5 villages were in the very high

category with potential for skeletal fluorosis chronic effect. Based on the condition of drinking water source, development of clean water networks and groundwater quality improvement in accordance with standards of drinking water is needed. Moreover, risk communication about fluoride exposure hazard should be addressed to reduce and mitigate fluoride pollution risk in Asembagus, Banyuputih, and Jangkar subdistrict.

ACKNOWLEDGMENTS

Authors would like to thank the Department of Environmental Engineering Kyoto University, and Department of Environmental Engineering Universitas Islam Indonesia for supporting this research. The author would also like to thank students from the Kawah Ijen volcano group for their support during the survey campaign in 2019.

REFERENCES

[1] Löhr, A.J., Bogaard, T.A., Heikens, A., Hendriks, M.R., Sumarti, S., Van Bergen, M.J., Van Gestel, C.A.M., Van Straalen, N.M., Vroon, P.Z., Widianarko, B., Natural pollution caused by the extremely acidic crater Lake Kawah Ijen, East Java, Indonesia. Environmental Science and Pollution Research, Vol. 12, Issue 2, 2005, pp.89–95.

[2] Heikens, A., Sumarti, S., van Bergen, M., Widianarko, B., Fokkert, L., van Leeuwen, K., Seinen, W., The impact of the hyperacid Ijen Crater Lake: risks of excess fluoride to human health. Science of the Total Environment, Vol. 346, Issue 1–3, 2005, pp.56–69.

[3] Delmelle, P., Bernard, A., Downstream composition changes of acidic volcanic waters discharged into the Banyupahit stream, Ijen caldera, Indonesia. Journal of Volcanology and Geothermal Research, Vol. 97, Issue 1 –4, 2000, pp.55–75.

[4] van Rotterdam-Los, A.M.D., Heikens, A., Vriend, S.P., van Bergen, M.J., van Gaans, P.F.M., The effect of naturally acidified irrigation water on agricultural volcanic soils. The case of Asembagus, Java, Indonesia. Journal of Geochemical Exploration, Vol. 96, 2008, pp.53 –68.

[5] WHO, Guidelines for drinking-water quality: Fourth edition incorporating the first addendum. Geneva, 2017, pp.370-373.

[6] Ali, S., Thakur, S.K., Sarkar, A., and Shekhar, S., Worldwide Contamination of Water by Fluoride. Environmental Chemistry Letters, Vol. 14, 2016, pp.291-315.

[7] Dasaiah S., Kurakalva R.M., and Pindi P.K., Data on fluoride concentration profile in groundwater of rural habitats in Mahabubnagar district, Telangana, India. Data in Brief, Vol. 32, 2020, pp.1-6.

[8] Zuo H., Chen L., Kong M., Qiu L., Lu P., Wu P., Yang Y., and Chen K., Toxic Effects of Fluoride on Organisms. Life Sciences, Vol. 198, 2018, pp.18-24.

[9] Dissanayake, C.B., The fluoride problem in the ground water of Sri Lanka: environmental management and health. International Journal of Environmental Studies Vol. 38, Issue 2-3, 1991, pp.137–156.

[10] Edmunds W.M., Smedley P.L. Fluoride in Natural Waters. in Essentials of Medical Geology, 2013, pp 311-336.

[11] Budiparmana E.S., Hapsoro A., Irmawati E.S., and Kuntari S., Dental Fluorosis and Caries Prevalence in the Fluorosis Endemic Area of Asembagus, Indonesia. International Journal of Paediatric Dentistry, Vol. 12, 2002, pp.415-422.

[12] Zhang Q., Xu P., Qian H., and Yang F., Hydrogeochemistry and Fluoride Contamination in Jiaokou Irrigation Subdistrict, Central China: Assessment based on multivariate statistical approach and human health risk. Science of the Total Environment, Vol. 741, 2020, pp.1-15

[13] Liu J., Peng Y., Li C., Gao Z., and Chen S., A Characterization of Groundwater Fluoride, Influencing Factors and Risk to Human Health in the Southwest Plain of Shandong Province, North China. Ecotoxicology and Environmental Safety, Vol. 207, 2021, pp.1-10.

11th Int. Conf. on Geotechnique, Construction Materials & Environment,
Kyoto, Japan, 3-5 November 2021, ISBN: 978-4-909106063 C3051

TRANSITION TOWARDS SUSTAINABLE ENERGY IN THAILAND: DRIVERS, BARRIERS AND CHALLENGES OF SOLAR ENERGY INITIATIVE AT KRABI PROVINCE

Chariya Senpong[1] and Dawan Wiwattanadate[2]

[1]Environment, Development and Sustainability, Interdisciplinary Program Graduate School, Chulalongkorn University, Bangkok, Thailand; Faculty of Engineering
[2]Chulalongkorn University, Bangkok, Thailand

ABSTRACT

Solar energy investment initiative is a leading pathway of renewable energy transition towards sustainable energy in Thailand. This study conducted a survey for potential barriers and drivers for solar energy initiatives at Krabi province. The study found that the potential of solar rooftops in Krabi province is more than a thousand MW and the highest portion compared with others like biomass, biogas and waste to energy. However, Krabi has land limitations for solar farm development, except shifting of most lands of rubber and palm oil tree plantation. While a solar rooftop potential of a thousand MW was observed, which is the highest portion of renewable energy potential in the province. To prioritise solar rooftop investment is experienced on some success projects and drives the relevant barriers to reach the target, including unlocking the national solar energy policy, the price of solar energy purchasing agreement and motivative measures for investment, such as financial start-up for solar energy's loan for solar rooftop prosumers and the new framework of its contribute to the cooperative's members to enhance the solar rooftop on their residential. However, supporting policy for solar energy from the government is still necessary. The following key factors to challenge solar energy initiatives at Krabi province needed to be considered: political, legal, economic transition and disruptive phenomenon.

Keywords: Solar energy, Energy transition, Krabi province, Renewable energy, Success and barrier

INTRODUCTION

The renewable energy transition has also occurred in Krabi province as one of the top tourism destinations and earns high income from those relevant businesses. The average of electricity consumption has been continuously increasing annually following the data of tourism seasonal peak. Green tourism is the priority to reach out the quality of natural conservation serving the tourism industry and people's life. How to win green tourism and energy is challenging the province's planning and implementation for long term development. This article will illustrate the study of Krabi energy transition which is a part of Thailand's renewable energy initiatives.

Drivers, barriers as well as drivers to achieve Krabi's sustainable energy will be described in this paper. The renewable energy transition trend has grown rapidly in the power sector in recent years in local communities, urban, peri-urban and rural areas. The total capacity of more than 200 gigawatts globally power sector was 26.4 percent of renewable share of total final energy consumption [1] and the expectation for solar PV growth is to reach approximately 107 gigawatts in 2020 even with the uncertain energy policy in ASEAN country [2]. The largest increase in renewable energy installation mostly solar PV in many countries adopted policies encouraging the measurement of feed-in-tariff for the long term power producer agreement (PPAs), the net metering for the solar rooftop, public utility policy and the intensive regulatory for decentralized system pathway.

Corporates and prosumers are driving the energy storage technologies. Renewable energy plays an important role protecting the environment and mitigating climate change [3] including reducing air pollutants in the energy sector [4]. That implement innovation and investments support the pillars of sustainable development goals (economic, social and environmental development [5] including the impact of job creation. To achieve the goals, the systematic policy development plan and financial support planning are the initiative and essential program for driving the country's ambitious scenario [6] and the dynamics of social behaviors, the role of social innovations, community involvement and social acceptance [7].

RESEARCH METHODOLOGY

The research aims to study the electricity demand and supply of Krabi province and its

potential for electricity generation from renewable resources, drivers, and barriers for the renewable energy transition towards Krabi's sustainable energy related to national and provincial levels. Drivers as well as barriers and challenges taking part in renewable energy transition were investigated in this study by using the qualitative method. Potential as well as the existing solar energy investment was collected from the secondary data from the energy agencies including the provincial and national level and seeking the relevant studies. Qualitative method applied the case study theory [8] as the single case focusing to explain the phenomenon of solar energy transition and point to the significance of time and past events since the beginning of solar energy was emerging.

Barriers and drivers were collected by in-depth interviews as well as onsite-observation. The researcher used the explanatory method for the thoughts, views and perceptions of interviewees of Krabi solar energy transition, applied the descriptive approach from the open-ended questions, grouping the interview's wording, analysis to the typical information by considering of each word and specific relational or what it is called and diversity of relationship and convert the the frequency wording to the success factors, barriers and challenges and describe how people participate in energy transition.

RESULT AND DISCUSSION

Thailand's Renewable Energy Transition

The first solar energy investment in Thailand was installed in 1987 by the governmental policy support Later, an adder scheme was applied to encourage renewable energy investment during 2007-2013, since then a feed-in-tariff scheme has been applied instead.The earlier phase of the development adder program applied in 2007 to benefit the start-up renewable energy investor in a country and the systematic model would attract the solar farm streamline application generating electricity to the grid. This initiative program was drafted by the Ministry of Energy (MoE) and proposed to the National Energy Policy Commission (NEPC) [9].

The attractive adder rate raised the capacity in the pipeline and targeted a country to further establish the formulation and regulation of renewable energy. The National Energy Policy Commission (NEPC) continually promoted solar energy purchasing policy in 2007 with a total target of 500 MW according to the Alternative Energy Development Plan (AEDP) and planned for the next 10 years, to reach the total target 3,000 MW under the Alternative Energy Development Plan (AEDP) [10, 11, and 12]. The price of energy purchasing in 2013, was high at the beginning of solar energy development at 8 baht (+-$0.26) per unit for VSPP and SPP for the long term support of 7 years and extended to 10 years. In 2010, the adder deduction policy was forced down to 6.50 baht (+-$0.21) per unit by NEPC and transmitted to FiT policy. Adder intensive policy was distributed with a huge budget as the beginning to encourage the new international and national solar energy investors and at the turning point, when the solar energy's market was competitive reflecting the dropped solar energy cost.

The later adopted policy in 2013 was feed-in tariff (FiT) for solar PV rooftop and the effectiveness of this program depended on the rate of energy price, design and implementation details [13]. In 2014, the business model of solar power was growing capacity mainly from utility-scale installation of the solar farms investment [14] distributed location in the central and northeast of a country with a high concentration factor. Price of its purchase was 5.66 baht (+-$0.18) per unit within the 25 years contract period for governmental agencies and agricultural cooperatives [15]. Moreover, the specified price for the household sector was 6.96 baht (+-$0.22) per unit, 6.55 baht (+-$0.21) for small businesses and 6.16 baht (+-$0.20) for medium and large business scale.

The country's pilot phase of solar rooftop applied during 2019 officially opened the quota for 100 MW household sector [16] and the additional 100 MW for the business and industrial sector with the FiT long term contract. A pilot project of solar rooftop had mainly created the household target to self-energy generating supporting their consumption and sold the left to the grid system, the total installation capacity not exceeding 10 kilowatts per each and totally less than 100 MW across the country and reaching a 10 years purchasing agreement of net billing measurement [17]. In 2019, Solar for All projects [18] were announced by the Energy Regulatory Commission of Thailand, ERC opening the quota of solar rooftop for the household sector for the 10 years power purchasing contract under the net billing measurement, separately the quota 30 and 70 MW for Metropolitan Electricity Authority (MEA) and Provincial Electricity Authority (PEA) respectively.

In late 2019, Thailand Solar Fund [19] had solidarity with the 15 wider networks including environmental, consumer and green development groups raising crowdfunding across the country to support the solar rooftop installation as the initiative solar hospital and technician schools projects. Although a country could deliver the generated solar energy on grid the remaining barriers [20] of solar power purchasing agreement (PPA) was uncleared status of a third-party developer could sell electricity to the consumer as a scale up business model, the sizing of solar rooftop system

was limited and not allowing the excessing energy production flow to the grid, the potential policy of net metering regulatory has not been yet implemented even the customer's bill saving are loading benefits [21], the financial scheme and business model had less support to motivate solar rooftop market and prosumers and the mindset of solar e-waste and requires the plan to offset environmental burden [22] even solar energy created the less impact compared to fossil fuel based electricity life cycle assessment [23].

Krabi's Renewable Energy Transition

The research found that Krabi's renewable energy transition had been implemented since 2007 by investing in biomass energy, later growing the potential of biogas from the left of biomass fuel source and the latest was solar energy. The target was to fulfill the energy consumption of Krabi province and was expected to be increased continually every year. Considering the last ten years in 2010, the peak load reached 111 MW annually and gradually growing approximately 5 to10 MW in each year. In 2019, the peak load significantly increased to 159 MW as the historical record [24]. During the recovery of the covid-19 epidemic for some period the consumption in province became nearly up to the usual rate of consumption and the main factor was related to the tourism season of the province as the priority energy consumption and income growing.

The potential of Krabi's solar rooftop was studied in 2018 [25] to install on the rooftop of the residential, hotel and business building prioritise reducing electrical bill and transition loss for the long distance and to benefit the ownership of the decentralisation system. The study calculated the capacity of Krabi's rooftop for the household sector, business SMEs and large building sectors with a total capacity of 1,125 MW. The 91,362 households in the province were calculated with the roof area at average 20 sq.m. and the result with the housing potential was 634 MW and the small, medium and specialised businesses were for the average 50 kW per unit with the potential total of 468 MW The large building sector averaged 1,000 kWh per place and 23 MW potential. However, as of 2020 the installed grid connected solar rooftop reported by PEA was found to be totally 2.23 MW. In addition, solar street lights have been installed by Krabi Provincial Administrative since 2019. Total Krabi's renewable energy is COD at 59.06 MW, 44.4 MW of which are biomass and biogas from rubber and palm oil industry, and the rest (nearly 15 MW.) are solar energy [26].

According to the data from Provincial Electricity Authority of Thailand (PEA) in June 2020, the highest potential of renewable energy in the province was biomass and biogas as the majority areas of palms and rubber trees. Since 2014, the initiative of solar rooftop on the grid was from the household sector by Wanna Chaideker's home with 0.0068 MW in Krabi province and rapidly growing in 2018 with the capacity of solar farms for agricultural cooperation, total installation almost 15 MW. Furthermore, local governmental administration and private sectors continually generated electricity from solar energy including schools, marine tourism port, governmental building, and supermarket in fig1. And the latest solar energy development was under the hundred street lights projects of Krabi Provincial Administrative authority. Even though the potential of solar energy was high, especially in rooftop investment, its purchasing policy had not motivated the electrical consumers enough to shift supply. The capacity of accessing technology transfer affected their mindset to invest in solar rooftop for households and business. During the beginning of solar investment, communities were concerned about solar cell reflection as vision and healthy impact and the proof of the potential of solar production at day time.

National solar energy policy was the obstacle of its development at the provincial level as well, especially the price of selling back to grid transmission much lower than buying. Saving money from solar energy installation was thought first for the business sector and led to duplicate investment for general prosumers across a province. Transition pattern of solar energy was initiated by the private sector who had capacity for financial support and imported its technology. Tourism sector and local governmental agencies were the front line of the renewable energy transition that followed the green concept of green tourism and green energy to promote and conserve gross income growth.

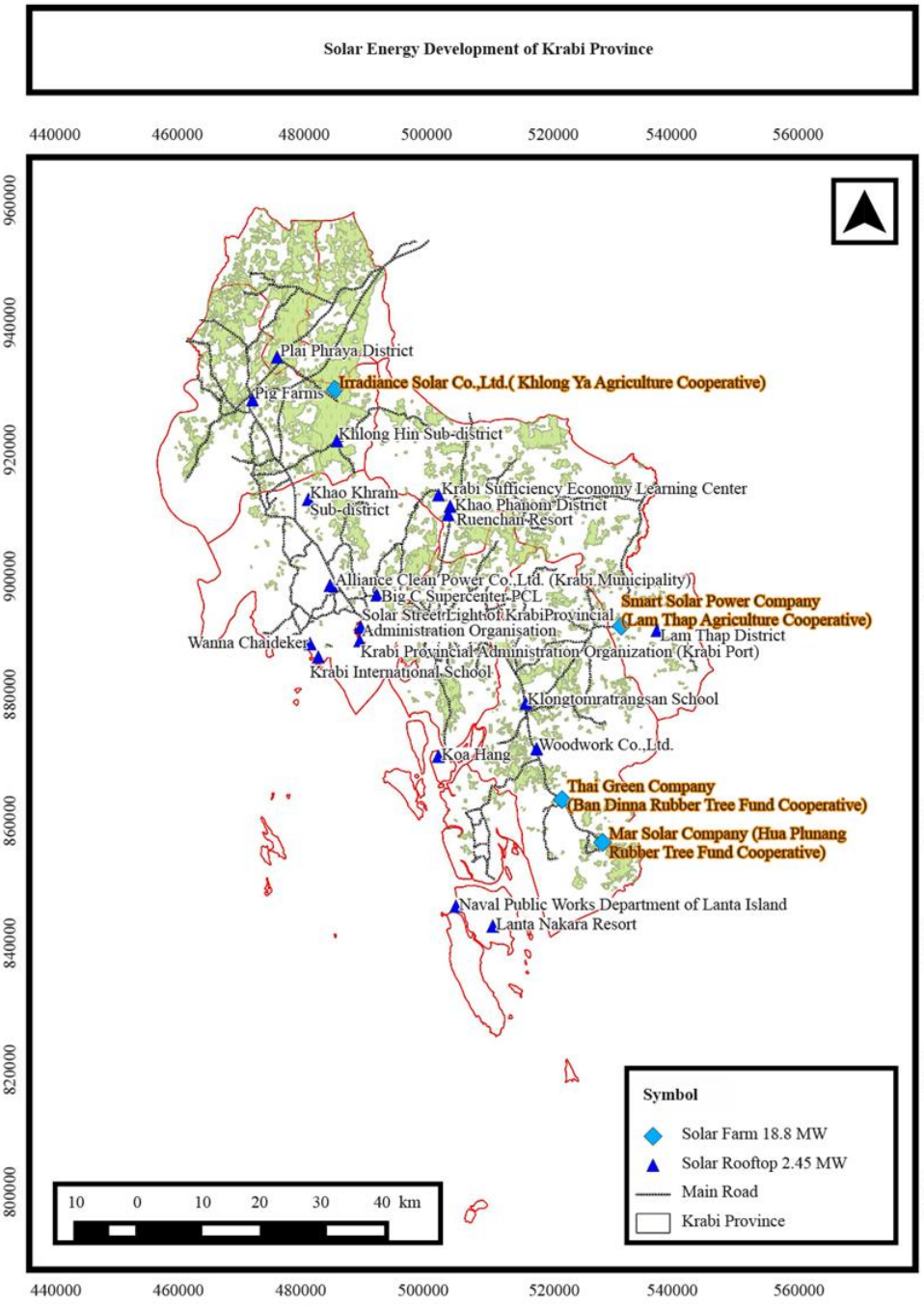

Fig.1 Solar Energy Development of Krabi Province, 2020

In 2018, solar farms for agricultural cooperation have been prioritized for joint venture investment between the Ministry of Energy, Ministry of Agriculture and Cooperative and solar energy business sectors. This phenomenon concretely changed solar energy investment in Krabi province and people's mindset when benefits sharing was the priorities proposing. The selected projects gained land use for solar farm installation, the income of electricity purchasing was agreement between the investors and each cooperatives, and the right to sell electricity and the fines if the investors break the contract was under the cooperative authorized under the 25 years feed-in-tariff long term agreement. Two main regulatory enforcement to manage the solar farm projects were the cooperative management fund and cooperative welfare fund. And the additional qualification for solar farm cooperatives was under the conditions of ERC regulation. In table1, the capacity of solar energy production has been quite stable and slightly decreasing during the heavy raining season in May-September as usual.

Table 1 Krabi's VSPP Solar Farm in 2018-2020, Provincial Electricity Authority of Thailand, 2020

Name	Year	COD (kWh/Month)			
		Jan	Feb	Mar	Apr
Mar Solar Company (Hua Plunang Rubber Tree Fund Cooperative)	2018	-	-	-	-
	2019	877,680	944,580	986,280	840,240
	2020	928,980	866,040	1,040,460	844,440
Smart Solar Power Company (Lam Thap Agriculture Cooperative)	2018	-	-	-	-
	2019	653,985	661,185	732,060	703,665
	2020	787,815	739,800	874,215	661,725
Thai Green Company (Ban Dinna Rubber Tree Fund Cooperative)	2018	-	-	-	-
	2019	636,840	678,360	764,220	690,840
	2020	741,840	667,680	790,020	620,100

Name	Year	COD (kWh/Month)			
		May	Jun	Jul	Aug
Mar Solar Company (Hua Plunang Rubber Tree Fund Cooperative)	2018	-	-	-	-
	2019	781,860	710,820	751,020	660,600
	2020	790,740	643,200	700,620	729,780
Smart Solar Power Company (Lam Thap Agriculture Cooperative)	2018	-	-	-	-
	2019	631,485	600,885	648,720	592,740
	2020	627,615	557,910	589,905	633,330
Thai Green Company (Ban Dinna Rubber Tree Fund Cooperative)	2018	-	-	-	-
	2019	622,800	551,280	565,620	555,060
	2020	583,140	492,720	535,440	552,900

Name	Year	COD (kWh/Month)			
		Sep	Oct	Nov	Dec
Mar Solar Company (Hua Plunang Rubber Tree Fund Cooperative)	2018	-	-	-	95,760
	2019	694,200	683,520	697,080	807,300
	2020	-	-	-	-
Smart Solar Power Company (Lam Thap Agriculture Cooperative)	2018	-	-	-	93,105
	2019	567,630	541,665	545,940	653,040
	2020	-	-	-	-
Thai Green Company (Ban Dinna Rubber Tree Fund Cooperative)	2018	-	-	-	134,520
	2019	602,100	572,940	591,540	664,500
	2020	-	-	-	-

Key Drivers and Barriers

The qualitative research studied the key stakeholders of solar energy transition of Krabi province including political, environmental, economic, technological and social aspects. The researcher had an in-depth interview with the stakeholders of each aspect and sought the relevant solar energy data, and momentum event analysis covering the connection of key solutions, barriers and challenges in fig 2.

Key drivers

The present study found that energy policy and strengthening of the private sector in the province were significantly driving renewable energy investment even though it took more than 10 years of investment and movement across the province. In 2014, Krabi was the first province of a country collaborating with the Krabi vision 2020 [27,28] they were working together with different stakeholders in a province such as local governmental agencies, tourism associations, fishery groups, agricultural networks and other communities. Driving the master plan of the province was conducted for years with the eight accreditation of provincial committees in the different responsibilities and roles. Head of the province was the leader of the plan and was responsible for the direction of the long term vision. The first draft of the plan was signed by more than 200 organizations and networks under the Declaration of Green Tourism and completed the full vision of Krabi 2020 to lead the economy, environment and the quality of life. From the green tourism plan to Krabi vision 2020 plan, Krabi had also studied the feasibility of renewable energy of

the province and during the opposition of the new coal power plant project since 2012.

Aside from the driving of provincial policy planning and people's movement to derail the new plant, the market trend was a disruptive phenomenon that pushed the challenge to a province to make a decision of energy demand and supply shifting. Linked to technological factors, when solar energy had been installed across a country the trend of citizens in the province was interested so the first local solar company was established in 2015. The potential of solar energy proved energy security and the return of investment shortly at the present within 5-6 years so the household sector, especially tourism business and supermarkets were escalated to save their electricity consumption and the cost of electricity bills. And the governmental agencies projects such as building, schools, tourism pier and street lighting transferred their budget to invest more solar energy. The company also created job opportunities for young graduates from technician schools and people from the local communities by training and knowledge sharing. Political aspect was the important part of the solar energy transition in Krabi province and lifting the potential of its installation to approximately 15 MW. in the present.

The collaboration between the Ministry of Energy and Ministry of Agriculture and Cooperatives initiated the solar energy project that benefited the grid supply. When the national energy policy unlocked the capacity of solar energy production, the flow of the implementation plan in the province continually drove to achieve the plan and naturally supported the vision of local governmental agencies and boosting the private sector and investors deciding to agree on the plan. And in the depth of power analysis, the strong vision and relationship of the leaders, key influencers and private investors in the province motivated the followers to be on a track of the policy implementations. The legal factors had also been released to respond to the energy policy movement, the power purchasing agreement addressed the price per unit of solar energy, the amount of quota in each timeline and feed-in-tariff measurement. In the case of solar energy for cooperatives, the qualification of them was essential to be considered joining a project across the country, especially the transparency management which identified the grade of each cooperatives by internal checks with the Ministry of Agriculture and Cooperatives agencies.

Economic factors impacted as a majority subject could build the income and domestic growth in the province. Creating direct and indirect jobs from solar energy investment such as construction, solar cells installation, technician and engineering, gardening, cleaning and security guards. Benefit sharing encouraged the members of cooperatives to make a decision to accept the solar energy project. Those income would be distributed to the cooperative's funding for hundreds members' welfare in each, including the land rental of the project regulated to rent from the members of its cooperatives in the long term period following the solar project contract. The fast track of solar energy investment required the financial support that the party of contract had capacity to deal with.

Social aspect was much mentioned in the process of energy transition and the way to move the vision of the province to be real practice on the ground. Public participation was the vital process of solar energy investment especially solar farm projects of cooperatives. The process had not just only to know its details but also the members of the cooperative had a right to make their own decision to approve the project. The ownership of the solar farm joint investment would change people's mindset and be aware of their concerns of its impacts during the process of public hearing held by governmental agencies, companies and cooperatives in the community. And the transparency process of bidding that was implemented after the public hearing was important to them because of the benefits and income for the 25 years energy purchasing agreement.

The last one was the environmental aspect, the mindset and acceptance of renewable energy were avoiding the opposition to new projects. Solar energy had less impact and green energy, both reasons had been integrated to the vision of the province that prioritizes on green tourism. At the stage of project consideration, the environmental agencies in the province were required to approve the solar farm project covering the impact assessment, city planning and the risk management such as landslide, water management and land use authority.

Key barriers

Krabi province had a capacity to increase more solar energy supply to the grid according to the relevant studies as mentioned above. The quota system was one of the national solar energy policies that blocked the investment potential of both cooperative institutions and the household sector. This policy significantly limited the potential of the cooperative's solar energy projects and solar rooftop because the opening round of promotion was fixed by the number of solar projects and installation's capacity. The limited supply affected the selection process of solar energy for the cooperative group as well, that means the qualified would be eliminated by the randomness process.

A solar farm project to support the cooperative investment required the review of land use permission policy because there was one project of

solar energy farm that has been sued to the administrative court. The potential of a solar farm, about 5 MW has not been supplied to the national grid even though the project has been completely installed on the land of cooperative settlement. The loss of energy supply to the grid system and benefits to a company and cooperative was an unexpected policy that significantly impacted the investment. This problem was a conflict between the agencies of the Ministry of Energy and Ministry of Agriculture and Cooperatives. And the unlocked cooperative enforcement was able to grow the potential of solar energy investment for example, the cooperative, as the owner of the project had authority to borrow the money from the financial institution to invest in their own project.

Financial sector has opened the limited opportunities for the customers such as the household sector and cooperative institutions to apply for any financial support implementing solar energy projects. There are some banks exploring the new policy of solar energy loan and mostly service for the private sector such as property owners and tourism associations. Lacking financial flowing, the solar energy investment in both solar rooftop and solar farm has not been growing fast. Finally, the limited internal experts forced the province to seek and import the solar energy professional from the outside and took time to share the relevant knowledge and the effective investment. The growth of prosumer and the potential of solar investment still require fast development and respond to the consumer demands.

Key challenges

Krabi is a tourism province of Thailand having continuously invested in electricity generated from renewable sources since 2007. Key drivers for the renewable investment are "electricity demand increasing" to fulfill the tourism sector and the province's Krabi Goes Green vision. While facing various barriers such as the extension of solar farm projects is the challenge and will have a potential effect on the capacity of biomass and biogas energy production because of the collapse of land use management, the requirement of internal grid system extension and management require support for energy security supply and demand sides, the need of smart grid and decentralization implementation plan to invest more budget to feeding the renewable energy production and consumption.

Key factors	Drivers	Barriers	Challenges
Social	Bidding process	Limited internal experts	Technological knowledge exchanging
	Joint ownership		Grid system extention and investment
	Mindset		Decentralisation system
	Public participation		Energy storage
Techological	Local solar company		
	Solar energy potential		
	Knowledge sharing		
	Energy security		
Economic	Job creation	Lacking financial/bank support	Land use management
	Benefit sharing		Solar for cooperative's member
	Community land rental		
	External financial support		
Environmental	Green energy		Carbon credit
	Water management		
	City planning		
Policy			
National level	Govemmnetal agencies collaboration	Quota system	
	Energy policy support	Randomness process	
Provincial level	Key influencers and business relationship		
	Vision of local governmental agencies		
Legal	Power purchasing agreement	Land use permission	Intensive cost of solar purchasing
	Cooperative transparency management		Cooperative's investment legislation
	Feed-in-tariff		
Disruptive	Solar energy cost reduction		
	Return on investment		
	Krabi Goes Green		

Fig. 2 Drivers, barriers and challenges of Krabi's solar energy transition, 2021

CONCLUSION

The study found that solar rooftop tends to be the highest potential and some drivers like supporting the household's potential and the pathway of the cooperative's members that urges them to install solar cells reducing the cost of

electricity bill and agricultural production cost, wider prosumers will lead the technology knowledge exchanging in the southern and also across the country as the golden opportunity, regulate the intensive cost of solar energy purchasing will be the one factor to fill the gap of renewable energy investment and motivate the internal economy from selling the electricity energy across the province especially in the area of Andaman tourism provinces to value the green tourism and energy, support the decentralization and energy storage will be a priority for the future solar energy transition both on land and the island, must be well considered.

ACKNOWLEDGMENTS

This study is partly funded by the Doctorate Scholarship Program "The 100th Anniversary Chulalongkorn University Fund for Doctoral Scholarship", in the Environment, Development and Sustainability international program, Graduate School of Chulalongkorn University.

REFERENCES

[1] REN21, Renewable Energy Policy Network for the 21st Century, renewable 2020 global status report. Available at https://www.ren21.net/wp-content/uploads/2019/05/gsr_2020_key_findings_en.pdf.

[2] Renewables 2020: Analysis and forecast to 2025 report, International Energy Agency. Available at https://www.iea.org/reports/renewables-2020.

[3] Simionescu M.Wadim S. and Manuela T., Renewable energy in final energy consumption and income in the EU-28 countries, Journal of Energies Vol.13, 2020 pp. 1-18.

[4] Shahsavari A. and Akbari M., Potential of solar energy in developing countries for reducing energy-related emissions, Renewable and Sustainable Energy Reviews Journal, Vol.106,2018, pp. 275-291.

[5] United Nations, 2030 Agenda for Sustainable Development. Available at https://sustainabledevelopment.un.org/content/documents/21252030%20Agenda%20for%20Sustainable%20Development%20web.pdf.

[6] Gorjian S. Zadeh N. B.Eltrop L.Shamshiri R.R. and Amanlou Y.,Solar photovoltaic power generation in Iran: Development, policies, and barriers, Renewable and Sustainable Energy Reviews Journal, Vol. 106, 2019, pp.110-123.

[7] Marquardt J.and Delina L. L.,Reimaging energy futures: Contributions from community sustainable energy transitions in Thailand and the Philippines, Energy Research and Social Science Journal, Vol.49, 2019,pp. 91-102.

[8] Yin R. K., A Book of Case study research: Design and methods (4th Ed.), Thousand Oaks, CA: Sage, 2009, pp. 1-219.

[9] Tongsopit S. and Greacen C., An assessment of Thailand's feed-in tariff program, Renewable Energy Journal, Vol. 60, 2013, pp. 439-445.

[10] Thailand PV Status Report 2016 -2017, Department of Alternative Energy Development and Efficiency, Ministry of Energy. Available at http://webkc.dede.go.th/testmax/sites/default/files/Book%20TPSR%20Eng.pdf.

[11] Alternative Energy Development Plan: AEDP2015. Department of Alternative Energy Development and Efficiency, Ministry of Energy. Available at https://www.dede.go.th/download/files/AEDP2015_Final_version.pdf.

[12] Chaitusaney S.Limmanee A. Kittner N. and Hoontrakul P.,Scaling Up Solar PV: A Roadmap for Thailand, Department of Alternative Energy Development and Efficiency, Ministry of Energy, 2015, pp. 1-65. Available at https://www.dede.go.th/download/files/1_ScalingUpSolarPV.pdf.

[13] Tongsopit S.,Thailand's feed-in tariff for residential rooftop solar PV system : Progress so far, Energy for Sustainable Development Journal, Vol.29, 2015, pp.127-134.

[14] Tongsopit S, Moungchareon S, Aksornkij A. and Potisat T., Business models and financing options for a rapid scale-up of rooftop solar power system in Thailand Energy Policy Journal Vol. 95, 2016, pp. 447-457.

[15] Solar energy development for the governmental sector and cooperative of agricultural projects, 2017-2019.Energy Regulatory Commission, Available at http://www.erc.or.th/ERCWeb2/Front/News/NewsDetail.aspx?rid=23719&CatId=1&&muid=36.

[16] Solar rooftop for household sector project,Energy Regulatory Commission, 2019, Available at http://www.erc.or.th/ERCWeb2/Front/News/NewsDetail.aspx?rid=23719&CatId=1&&muid=36.

[17] Thongsopit S. Junlakarn S. Wibulpolprasert W. Chaianong A. Kokchang P. and Hiang V.N.,The economics of solar PV self-consumption in Thailand,Renewable Energy Jounal, Vol.138,2019,pp. 395-408.

[18] Solar Energy for All projects, Energy Regulatory Commission, 2019, Available at https://www.erc.or.th/ERCWeb2/Front/News/NewsDetail.aspx?rid=85397&CatId=1&&muid=36.

[19] Thailand Solar Fund, 2019, Available at https://thailandsolarfund.org.

[20] Potisat T. Tongsopit S. Aksornkij A. and Moungchareon S.,To buy the system or to buy the service: the emergence of a solar service model in thailand, Renewable Energy Focus Journal, Vol.21,2017,pp. 1-10.

[21] Chaianong A. Tongsopit S. Bangwiwat A. and Menke C.,Bill saving analysis of rooftop PV customers and policy implications for Thailand,Renewbale Energy Journal,Vol.131,2019,pp. 422-434.

[22] Eskew J. Ratledge M.Wallace M.Gheewala H.S. and Rakkwamsuk P., An environmental Life Cycle Assessment of rooftop solar in Bangkok,Thailand,Renewable Energy, Vol.123,2018, pp. 781-792.

[23] Kittner N. Gheewala H.S. and Kamens M.R.,An environmental life cycle comparison of single-crystalline and amorphous-silicon thin-film photovoltaic systems in Thailand,Energy for Sustainable Development, Vol.17,2013, pp.605-614.

[24] Krabi's Energy Peak Load from 1998-2021, Provincial Electricity Authority of Thailand, June 2020.

[25] Very Small Power Producer and Small Power Producer (COD) of Southern Thailand, Provincial Electricity Authority of Thailand, June 2020. Available at http://www.erc.or.th/ERCSPP/default.aspx?x=0&muid=23&prid=41.

[26] Krabi Goes Green: Towards A Model Town, With More Than 100% Renewable Energy Report,Krabi Goes Green Network,2018.

[27] Krabi Vision 2020, Krabi Provincial Administration, 2014, pp.1-48.Available at http://www.krabi.go.th/krabi2015/m_file/KrabiVision2020.pdf.

[28] Senpong C. and Wiwattanadate D.,Challenge of Renewable Energy Transition towards Krabi's Sustainable Energy City,Earth and Environmental Science Jounal, Vol.385,2019,pp. 1-16.

11th Int. Conf. on Geotechnique, Construction Materials & Environment,
Kyoto, Japan, 3-5 November 2021, ISBN: 978-4-909106063 C3051

CLIMATE VARIABILITY'S IMPACT ON RAINFED-SUGARCANE PRODUCTION IN THAILAND'S NORTHEAST

Piyapong Wongkhunkaew[1], Supasit Konyai [2] and Vichai Sriboonlue [3]

[1] Graduate Student of Agricultural Engineering, Faculty of Engineering, Khonkaen University, Thailand;
[2] Associate Professor of Agricultural Engineering, Faculty of Engineering, Khonkaen University, Thailand;
[3] Associate Professor of Agricultural Engineering, Faculty of Engineering, Khonkaen University, Thailand.

ABSTRACT

Sugarcane is one of Thailand's most valuable cash crops. However, besides being used for sugar production, sugarcane can also be used to manufacture biofuel, resulting in increase in demand for sugarcane. Although Northeast's Thailand has the most sugarcane production and cultivation areas, but it receives less yield than other parts. The climate fluctuation has both direct and indirect effects on sugarcane yields. It aimed to investigate the effects of climate variability on sugarcane yields and productivity in northeastern Thailand. Actual evapotranspiration is mechanism that occurs during plant transpiration and soil surface water evaporation, its causes plants to absorb nutrients and water from the soil, which results in plant growth. The study relied on ENSO index data, meteorological data, and sugarcane cultivation data from 2008 to 2017.

The results showed that ONI and SEaI's return period were 3.3 and 4-10 years, respectively and ENSO events happen 3-4 months before SEaI events, according to spectrum analysis. The fluctuation in SEaI will occur more rapidly than the ENSO. For comparison, SEaI 1, 3, 6, and 12 months were implemented. The best time scale of SEaIs with yields is 6 and 12 month time scale. The highest yield was in correlation with SEaI at 6 months at 0.78 on Nakhonphanom station, with an increase in yield with SEaI for every station, but the production and harvested area were inconsistent with SEaI. It has been shown that yield depends on amount of soil moisture and the rainfall. However, sugarcane production and the harvested area also depend on other factors, etc. political, prices, farm management.

Keywords: Climate variability, Standardized actual Evapotranspiration Index, Sugarcane production and yield.

INTRODUCTION

Thailand is the world's fifth largest producer of sugarcane and the world's second largest exporter of sugar, dropping only Brazil. Sugarcane is one of Thailand's most important economic crops. There are 57 sugar mills in Thailand, except the southern region. Other parts of sugarcane can be used for other purposes, such as biomass from bagasse and ethanol from cane leaves, in addition to producing granulated sugar. As a result, the demand for sugar and cane grows year after year. This demonstrates the sugar cane and sugar industry's continued growth. For a long time, climate variability has had a direct and indirect impact on sugarcane and sugar production. For example, severe drought events in 1997/1998 and 2015/2016 resulted in a significant decrease in sugarcane production, which was caused by climate variability. The relationship between climate variations, cane production, and sugar production in Thailand should be studied. Understanding trends and directions, including the effects of climate variability on cane and sugar production, and using this information to develop policy planning strategies for appropriate cane production. Because it receives a lot of rain during the wet season, Southeast Asian countries have one of the best climates for sugarcane cultivation. During the months of May to October, the northeast of Thailand receives a lot of rain from two sources: the southwest monsoon from the Indian Ocean and tropical cyclones from the Pacific Ocean. The upper part of the Northeast is unique in that the Phetchabun, Dong Phaya Yen, and Sankambeng mountain ranges have an orographic effect that postpones the flow of the Southwest monsoon into the region. Before reaching the northwestern region, tropical cyclones from the Pacific must pass through Vietnam, Laos, Cambodia, and the eastern part of the Northeast. When the southwest monsoon is weak and there are no tropical cyclones, the region typically receives less rainfall than the rest of Thailand. During a year with a strong summer monsoon and a large number of tropical cyclones, however, the area can be flooded. El Nino Southern Oscillation has indicated that these dry and wet years are the result of atmospheric and Pacific Ocean interaction (ENSO). These lowland rainfed cane fields get their water from rainfall and runoff, and they lose it to

evapotranspiration, which is a combination of evaporation and crop transpiration. Actual evapotranspiration, or standardized actual evapotranspiration index, is a moisture availability indicator for sugarcane crops (SEaI). The SEaI index outperforms other indices in detecting both wet and dry soil extremes. Our aims and objectives are to compare and correlate the cane production and yields of the eight upper provinces in Thailand's northeast with their SPEIs and then with ENSO..

STUDY AREA AND DATA COLLECTION

Our study area is in Thailand's upper northeast, between 15 31' and 18 21' north latitude and 100 83' and 103 66' west latitude. The eight provinces covered are NongKhai, Nongbualamphu, Khonkaen, Udonthani, Sakonnakhon, NakhonPhanom, Mukdaharn, and Loei. The Northeast region is a high-level plain and one of the large sub-basins of the Khorat plateau on the Mekong River's right bank. The Phu Phan mountain range, which runs northwest-southeast, separates the northeastern region into two basins. The Sakonnakhon Basin, a large high-level plain in the west and Khorat Basin, which is smaller and slopes toward east, is another. Interestingly, our research area covers both basins: Khonkaen is in the Khorat Basin, while Udonthani, NongKhai, Sakon Nakhon, Nakhon Phanom, Mukdaharn, and Loei are in the Sakol Nakhon Basin. Nongbualamphu, however, covers both basins.

Hydro-meteorological, ENSO index, and sugarcane cultivation data are the three types of data that will be used. The Thai Meteorological Department provided hydro-meteorological data from 2008 to 2017. (TMD). Daily maximum temperature, daily minimum temperature, daily dew point temperature, daily solar radiation, daily maximum relative humidity, daily minimum relative humidity, daily wind speed, and daily precipitation are all needed for SETaI evaluation. The ETa must be calculated using the Morton CRAE formula (Eq. (6)), which requires a variety of meteorological data.

METHODOLOGY

We reasoned that actual evapotranspiration should be proportional to the amount of soil water available for crop growth. Crop water supply determines the timing and quantity of evapotranspiration. Drought was exacerbated by excessive evapotranspiration. Crop production and yield are affected by the drought. The Standardized actual Evapotranspiration Index (SEaI), which is a function of actual evapotranspiration calculated using the Morton CRAE method, is calculated using ETa. We also believe SEaI is a new drought index that is fully dependent on the variability of ETa estimates calculated using the complementary relationship (CR) method.

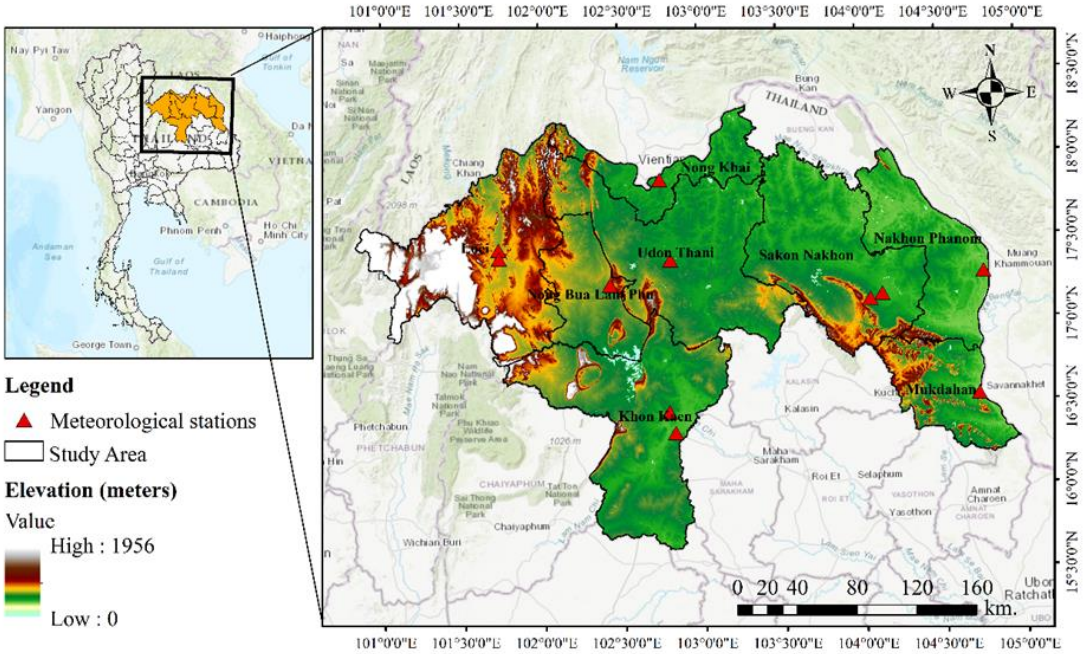

Fig. 1 Topography area of the eight-province study region in Thailand.

Calculation Procedure of Standardized Actual Evapotranspiration Index

The SEaI is a classification system for climate variables based on hydrometeorological data. It was developed by replacing rainfall with actual

evapotranspiration in the same case that the standardized precipitation index (SPI) was developed [1], [2]. Monthly actual evapotranspiration is used as the input data for the SEaI. The Morton CRAE method is used to calculate the ETa, which is difficult due to the involvement of numerous parameters such as daily temperature, daily dew point temperature, daily solar radiation, daily maxi-min relative humidity, daily wind speed, and daily precipitation [3]. The probability distribution function is calculated from the long-term data by fitting a function to it, which is then transformed to a normal distribution with a mean of zero and standard deviation of one using equal probability, resulting in SETaI values that are truly in standard deviations.

Morton CRAE (Complementary Relationship Areal Evapotranspiration)

The CRAE model consists of three components: potential evapotranspiration, wet environment areal evapotranspiration and actual areal evapotranspiration [4],[5].

Estimating potential evapotranspiration (ET_p)

The potential evapotranspiration by Morton CRAE's model for a catchment or a large vegetated surface is to solve the energy-balance and the vapor transfer equations respectively for potential evapotranspiration and the equilibrium temperature (Eq. 1 and 2):

$$ETp = \frac{1}{\lambda}\{R_n - [\gamma p f_v + 4\varepsilon_s \sigma (T_e+273)^3](T_e - T_a)\} \quad (1)$$

$$ETp = \frac{1}{\lambda}\{f_v(v_e^* - v_D^*)\} \quad (2)$$

Where ETp is potential evapotranspiration (mm. day^{-1}), λ is the latent heat of vaporization (Wdaykg^{-1}), R_n is net radiation for soil/plant surfaces at air temperature (Wm^{-2}), γ is the psychrometric constant (mbar°C^{-1}), p is the atmospheric pressure (mbar), f_v is the vapour transfer coefficient (Wm^{-2}mbar^{-1}) and is a function of atmospheric stability, ε_s is the surface emissivity, σ is the Stefan–Boltzmann constant (Wm^{-2}K^{-4}), T_e and T_a are the equilibrium temperature (°C) and air temperature (°C) respectively, v_e^* is saturation vapour pressure (mbar) at Te and, v_D^* is the saturation vapour pressure (mbar) at dew point temperature.
f_v is given by (Eq. 3):

$$f_v = \left(\frac{p_s}{p}\right)^{0.5} \frac{f_z}{\xi} \quad (3)$$

Where p_s is the sea-level atmospheric pressure (mbar), p is at-site atmospheric pressure (mbar), fZ is a constant (W m-2 mbar-1) and ξ is a dimensionless stability factor estimated from (Eq. 4):

$$\xi = \frac{1}{0.28\left(1+\frac{v_D^*}{v_a^*}\right)+\frac{R_n \Delta}{\left[\gamma p\left(\frac{p_s}{p}\right)^{0.5} b_0 f_z (v_a^* - v_D^*)\right]}} \quad \text{noting that } \xi \geq 1 \quad (4)$$

where v_D^* is the saturation vapour pressure (mbar) at dew point temperature, v_a^* is the saturation vapour pressure (mbar) at air temperature, Δ is the slope of the saturation vapour pressure curve (mbar°C^{-1}) at air temperature and, $b0$ = 1.0 for the CRAE model

Estimating wet-environment areal evapotranspiration (ET_{wet})

The conventional definition of potential evapotranspiration is the same as the wet-environment areal evapotranspiration. To account for atmospheric advection, a term (b1) was added to the Priestley–Taylor equation to estimate wet-environment areal evapotranspiration from Eq. 5:

$$ETwet = \frac{1}{\lambda}\left\{b_1 + b_2 \frac{R_{ne}}{\left(1+\frac{\gamma p}{\Delta_e}\right)}\right\} \quad (5)$$

Where ET_{wet} is the wet-environment areal evapotranspiration (mm.day^{-1}), Rne is the net radiation (Wm^{-2}) for the soil/plant surface at the equilibrium temperature T_e (◦C), γ is the psychrometric constant (mbar ◦C^{-1}), p is atmospheric pressure (mbar), Δ_e is slope of the saturation vapour pressure curve (mbar ◦C^{-1}) at T_e, b_1 and b_2 are the empirical coefficients (Wm^{-2}) for Morton's procedure.

Estimating actual areal evapotranspiration (ETa)

The actual areal evapotranspiration (*ETa*) (mm day^{-1}), one uses the results from the complementary relationship method as follows Eq. 6 and Eq. 7 [6]:

$$ETa = 2ETwet - ETp \quad (6)$$

$$ETa = \frac{1}{\lambda}\left[2\left\{b_1 + b_2 \frac{R_{ne}}{\left(1+\frac{\gamma p}{\Delta_e}\right)}\right\} - \{f_v(v_e^* - v_D^*)\}\right] \quad (7)$$

Where ET_{wet} is the wet-environment areal evapotranspiration (mm.day^{-1}) and ET_p is potential evapotranspiration (mm.day^{-1})

Accurate temperature and relative humidity estimates from a representative land-based location are required to calculate the Morton CRAE model, which suggested a 5-day limit as the minimum time step for analysis.

Correlation Coefficient

The statistical metrics were used to quantify and compare the performance of the SEaIs with that of other drought indices. The Pearson correlation coefficient, which was calculated as Eq. 8, was used to test the correlation between the drought indices SEaIs, SPIs, and SPEIs in different months.

$$P_{x,y} = \frac{Cov(X,Y)}{\sqrt{Var(X)}\sqrt{Var(Y)}} \quad (8)$$

where X, Y represent two variables for comparison; *Cov* represents the covariance of X and Y; and *Var* represents the variance of X or Y.

RESULT AND DISCUSSIONS

The data from Nongkhai are the only ones we have, although the results from the other eight provinces are remarkably comparable. The ONI fluctuates slowly over time, but the ETa fluctuates rapidly. In Fig 2, the EL Nino condition is represented by a positive ONI (dry condition), whereas the La Nina condition is represented by a negative ONI (wet condition) (La Nina years in 2010-2011 and El Nino year in 2015-2016). The wet soil is represented by a positive ETa, whereas the dry soil is represented by a negative ETa. When the ETa values from 2015-2016 were compared to the El Nino event, they were found to be inconsistent. This suggests that when ONI is strong, the value of ETa decreases, meaning that if ETA falls, drought or low soil moisture conditions will occur. On the other hand, if there is a lot of rain or a lot of soil moisture, the ETa value will be high too though. As a result, ETA values could be used to predict soil moisture content based on meteorological conditions [7], [8].

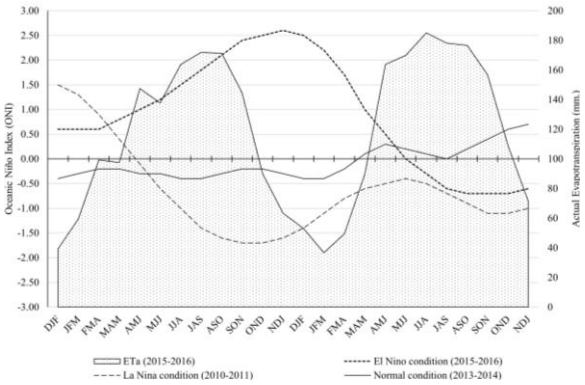

Fig 2. Time series of climate variability 3 condition and actual evapotranspiration value in Nongkhai.

Because the ENSO index and the drought index are both time series with sinusoidal forms, both require time-series analysis in both the time and frequency domains to completely appreciate them. Every time series is the result of the addition of numerous frequencies. The technique of separating the spectrum in the frequency domain in order to determine the time series' dominant frequency is known as spectral analysis.

To see the dominating spectrums, spectral analyses were performed on the time series of ONI and SEaIs, as shown in Fig. 3. The dominating return periods of ONI and SEaIs of the eight provinces are provided in Table 1 and the maximum peak curves are shown as wavelengths (Fig. 3 a)). Table 1 shows that the ONI recurrence time should be around 3.3 years, which is similar to the SEaIs for Nongkhai, Sakon Nakhon, and Loei, which are 4 - 5 years, and Udonthani, NakhonPhanom, KhonKaen, Mukdaharn, and NongBuaLamPhu, which are 9-10 years.

Table 1 The spectral analysis results of agricultural drought indices.

		Highest Spectrum	Frequency	Return Period	
				Month	Year
ENSO Index	ONI	0.392	0.025	40	3.3
SEaI	NK	0.198	0.019	52.6	4.4
	L	0.163	0.016	62.5	5.2
	UD	0.256	0.009	111.1	9.3
	SK	0.163	0.017	58.8	4.9
	NP	0.170	0.008	120.5	10.0
	KK	0.204	0.008	120.5	10.0
	MD	0.180	0.008	126.6	10.5
	NB	0.237	0.008	120.5	10.0

In Table2 and Fig 3 b), we found that the strongest correlations occur in the h-negative region, indicating that a higher average value of ONI is likely to lead to a lower average value of "SEaI" in Nongkhai, Loei, Sakolnakhon, Nakhonphanom, and Mukdahan about 4 months earlier. And, approximately 4 months later, a lower average of ONI is related to a likely higher-average SPEI value. The higher average value of ONI in Udonthani, Khonkaen, and Nongbualamphu is likely to lead to a lower average value of "SEaI" about 3 months earlier.

A distinguishing feature of important SEaIs is the time scale format. Pearson's correlation coefficient was used to investigate the relationship between sugarcane production, harvested area, and yield in Thailand and SEaIs. Nongkhai, Sakol Nakhon, Udonthani, Nakhonphanom Mukdahan, and Loei are all in the Sakol Nakhon Basin, but Khonkaen is in the Khorat Basin, and Nongbualamphu is in both basins [9].

Table 2 The cross-correlation results of ENSO and SEaI in 1-month time scale in Upper-Northeast Thailand during 2008-2017.

	Highest Cross Correlation	Lag (months)
NK	-0.36	-4
L	-0.43	-4
UD	-0.38	-3
SK	-0.29	-4
NP	-0.40	-4
KK	-0.20	-3
MD	-0.33	-4
NB	-0.34	-3

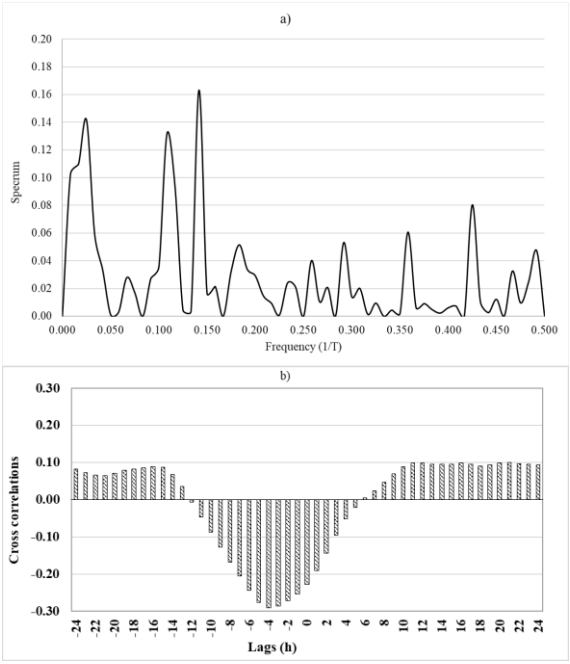

Fig. 3. The a) spectrums of SEaI in 1-month time scale and b) cross correlation between ONI and SPEI 1-month time scale on Nongkhai from 2008-2017 period.

Table 3 The Pearson's correlation coefficients of SPEIs with rice production and yield at several time scales.

	Time scale	NK	L	UD	SK	NP	KK	MD	NB
Production (ton)	1	-0.27	-0.17	0.05	0.21	0.37	-0.10	-0.26	0.00
	3	-0.11	0.00	-0.16	0.26	0.36	-0.23	0.05	0.00
	6	-0.04	-0.03	0.25	**0.59**	**0.41**	-0.10	**0.33**	**-0.10**
	12	**-0.28**	**-0.27**	**-0.28**	0.46	0.18	**-0.29**	0.01	0.07
Yield (ton/ha)	1	0.16	0.39	0.01	0.60	0.71	-0.09	0.02	0.36
	3	-0.01	0.46	0.10	0.60	0.71	-0.20	0.02	0.39
	6	0.28	0.51	0.23	**0.68**	**0.78**	-0.08	**0.28**	0.34
	12	**0.28**	**0.56**	**0.34**	0.44	0.67	**0.20**	0.16	**0.39**

The optimal time scale for sugarcane production and yield for the same period (t) was a 12-month time scale, with the best yield correlations of 0.28, 0.56, and 0.34 for Nong Khai, Loei, and Udonthani, respectively, and the best sugarcane production correlations of -0.28, -0.27, and -0.28 for Nong Khai, Loei, and Udonthani, respectively. At a 6-month time scale, the best correlation for yields was 0.68, 0.78, and 0.28 for Sakol Nakhon, Nakhonphanom, and Mukdahan, respectively, and production was 0.59, 0.41, and 0.33. At the 12-month time scale, the best correlations for Khonkaen's production and yield are -0.29 and 0.20, respectively.Only the cane yield of Nongbualamphu corresponds with SEaI at 0.39 of a 12-month time scale, but not the production.

5. CONCLUSIONS

The sugarcane is the most important economic crops in Thailand. The sugarcane productions and yields from 8 provincial regions of upper-northeast, Thailand. Correlation between SEaI and ONI using Pearson's correlation coefficient. It was found that the two variables had opposite relationships. It shows that when ONI is positive (El Nino), SEaI will have negative value, on the contrary, if La Nina (heavy rain) occurs, SEaI value will be positive (high soil moisture. When using spectrum analysis to find the correlation, ONI's return period was 3.3 years and SEaI's return period was 4-10 years. The best time scale of SPEIs and found that the yields were agreeable with SEaI-12 nicely especially in NK, L, UD, KK and NB. SK, NP and MD were agreeable with 6-month time scale. However, production and harvested area value did not follow all time. The findings will help the stakeholders of sugar production to understand, plan, and manage sugarcane farming accordingly to obtain better yields.

ACKNOWLEDGMENTS

The authors would like to thank the Graduate School and Applied Engineering for Important Crops of North East Research Group, Khon Kaen University for providing facilities, the Water Engineering Group, Faculty of Engineering, Khon Kaen University for funding and data supporting.

REFERENCES

[1] McKee, T.B., Nolan, J., Kleist, J., The relationship of drought frequency and duration to time scales. Proceedings of the 8th Conference on Applied Climatology, California, 1993, pp.179-184.

[2] Labudova, L.; Labuda, M. and Takae, J. (2017) Comparison of SPI and SPEI applicability for drought impact assessment on crop production in

the Danubian Lowland and the East Slovakian Lowland. Theoretical and Applied Climatology, Vol. 128, 2017, pp. 491-506.

[3] Guo, D.; Westa, S. and Maier, H.R., An R package for modelling actual, potential, and reference evapotranspiration. Environmental Modelling and Software, Vol. 78, 2016, pp 216-224.

[4] Mcmahon, T.A.; Peel, M.P.; Lowe, L.; Srikanthan, R. and McVicar, T.R., Estimating actual, potential, reference crop and pan evaporation using standard meteorological data: a pragmatic synthesis. Hydrology and Earth System Sciences, Vol. 17, 2013, pp. 1331-1363.

[5] Kim, D. and Rhee, J., A drought index based on actual evapotranspiration from the Bouchet hypothesis. Geophysical Research Letters, Vol. 43, 2016, pp. 10277-10285.

[6] Kim, D. and Rhee, J., A drought index based on actual evapotranspiration from the Bouchet hypothesis. Geophysical Research Letters, Vol. 43, Issue 19, 2016, pp. 10277-10285.

[7] Ohba, K and Ponsena, P., Evapotranspiration in the Northeast District of Thailand as estimate by Morton method. Journal of Agricultural Meteorology, Vol. 42, Issue 4, 1987, pp. 329-336.

[8] Zhang, L.; Song, W. and Song, W., Assessment of agricultural drought risk in the Lancang-Mekong region, South East Asia. International Journal of Environmental Research and Public Health, Vol. 17, 2020, pp. 6153.

[9] Ray, D.K.; Gerber, J.S.; MacDonald, G.K. and West, P.C., Climate variation explains a third of global crop yield variability. Nature Communications, Vol. 6, 2015, pp. 5989.

11th Int. Conf. on Geotechnique, Construction Materials & Environment,
Kyoto, Japan, 3-5 November 2021, ISBN: 978-4-909106063 C3051

IMPLEMENTATION OF GREEN CAMPUS AT UNIVERSITIES IN INDONESIA

Any Eliza[1], Dinda Fali Rifan[2], Lindrianasari[3], Nur Wahyu Ningsih[4]

[1,2,4] Faculty of Economic and Islamic Business, Islamic State University of Raden Intan, Lampung, Indonesia
[3] Faculty of Economics and Business, University of Lampung, Indonesia

ABSTRACT

This study aims to describe the implementation of green campus for universities in Indonesia. Using the ranking of the Most Sustainable University category at the national level UI GreenMetric World University Rankings, three universities were selected as samples. This type of research is field research and uses the results of interviews and documentation from sustainability reports and university website. The implementation of Green Campus is measured based on 4 instruments, namely Environmental Awareness, Environmental Involvement, Environmental Reporting, and Environmental Auditing. The findings of this study indicate that three universities have met the stages of environmental awareness, environmental involvement, and environmental reporting, but have not met the stages of environmental auditing. The university's participation in UI Green can be an indication that the university has awareness in the university and its surroundings about the importance of sustainability issues. University X has the highest percentage of achieving 4 green campus implementation instruments. The theory of legitimacy can explain that an organization must be able to adapt to the value system that has been implemented by society and the environment because the more forms of responsibility it takes to its environment, the better the image and reputation of the organization will be.

Keywords: green campus, universities in Indonesia, environmental management accounting

INTRODUCTION

The Sustainable Development Goals (TPB/SDGs) prioritize the implementation principle with inclusiveness, which involves both government and non-government elements such as business actors, philanthropists, community organizations, as well as academics and universities so that more people are involved. Universities play a very important role in achieving TPB/SDGs and must be able to become a center of excellence in the field of science in accordance with their core competencies, prioritize SDGs in the education/teaching process, become a partner of the central and regional governments and other stakeholders in monitor and evaluate the implementation of the SDGs, as well as provide recommendations. The university is strategically positioned to make agreements on key areas for actual action, in line with the "triple bottom line" or "3 Es" concept of equality, economy, environment, green buildings and education for sustainable development.

In 2010, the University of Indonesia (UI) initiated a World University Ranking which became known as the "UI GreenMetric World University Rankings" to determine the university's sustainable efforts. The UI GreenMetric world university ranking was created as a tool for universities to address sustainability issues facing the world today. Universities can work together to reduce the impact of environmental problems and UI GreenMetric is a non-profit organization so all universities can participate free of charge. In general, UI GreenMetric uses the concept of a sustainable environment which has 3 components, namely environmental, economic and social. Environmental aspects include the use of natural resources, environmental management and pollution control where the economic aspects include profit and efficiency. While the social aspects include education, community and social involvement. These three aspects are used as UI GreenMetric criteria. Currently the UIN GreenMetric network consists of 719 universities from Asia, Europe, Africa, Australia, and Oceania as well as 1,997,294 teaching staff, 16,413,522 students with US$ 7,529,29,073 research funds for environment and sustainability [1].

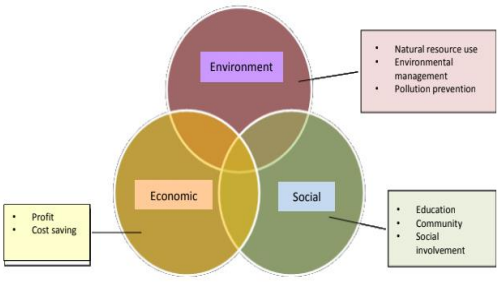

Fig. 1 UI GreenMetric Criteria

The university's participation in UIGM can help raise awareness in the university and its

surroundings about the importance of sustainability issues. UI GreenMetric uses the important role of higher education institutions to raise awareness by assessing and comparing the efforts made by the world of education towards sustainable development, sustainable research, greening campuses and their social impact.

Disclosure of the role of universities in realizing a sustainable campus can be seen through sustainability reporting and information presented on the university website. Research results in various countries show that some universities have not focused on environmental reporting with almost no economic and social disclosures [2] [3] [4] [5] [6]. UI GreenMetric encourages Universities to create and publish Sustainability Reporting which is reflected in questionnaire questions, which can be an evaluation for the university, Make it easier for other universities to get information and to adapt existing policies at the university, Make it easier for UI GreenMetric Assessors to clarify answers and evidence provided in the questionnaire. Universities that are members of the UIGM ranking Publish Sustainability Reporting through the disclosure of indicators in UI GreenMetric: Arrangement and Infrastructure, Energy and Climate Change, Waste, Water, Transportation, Education and Research.

However, until now in Indonesia, there is no regulation that requires universities to disclose social information related to the activities carried out, especially the responsibility of universities to the environmental impact of the activities carried out, while the benefits for the ethics of institutional sustainability are enormous. Disclosure of the role of universities in realizing a sustainable campus is voluntary and has been carried out by universities that are members of the UI GreenMetric World University Rankings. Based on this, the research objective is to analyze the implementation of Green Campus at universities in Indonesia.

LITERATURE REVIEW

Legitimacy and stakeholder theory state that organizations must be able to adapt to the value system that has been applied by society and the environment. Among other things, the company's business is realized through social disclosure. This is carried out with the aim that the activities and activities of the organization are legitimized in the eyes of the community. The more forms of responsibility an organization undertakes to its environment, the better the image and reputation of the organization will be. Ahadis et.al. [7] argued that mining regulations issued by the government improve community welfare and confirm regulatory theory, especially the theory of public interest.

The term *green campus* can be defined as an ethical quality policy in the activities of the university community (students, lecturers, administrative staff), through responsible management of the educational, cognitive, workforce, and environmental impacts of the university, in participatory dialogue with the community to promote human development. sustainability in four steps: (1) commitment, (2) self-diagnosis, (3) compliance, and (4) accountability [8]. Green campus can be considered as a university philosophy as an ethical approach to developing and engaging with local and global communities in order to sustain social, ecological, environmental, technical, and economic development. Green campus can be implemented well if the campus can implement environmental management accounting correctly. Environmental management accounting is limited in use and fragmented in organizations at the reactive and preventive stages except for using environmental management accounting for cost savings and efficiency improvements. However, the findings suggest that and when organizations progress into higher levels of cleaner production strategy development, there is a relatively high level of use of environmental management accounting in terms of integrative tools, and for control and stewardship purposes [9].

The practice of social responsibility of universities or green campuses has also attracted the attention of the Asian region. The Association of Southeast Asian Nations Network (ASEAN) proposes a conceptual framework for AUN University Social Responsibility and Sustainability with the following main components: (1) teaching and learning, research and academic services, (2) university governance and administration, (3) community involvement, and (4) campus life to promote green campus practices and address social, economic, and environmental challenges faced in the ASEAN Community.

Research of Chen et.al. [10], found that most of the actual practice and strategic plans were focused on achieving academic service. Thus, further investigation of green campus components, practices, and how exactly to create such a green campus impact should be examined in the future. The process of implementing environmental management accounting at the University of Bologna has been able to implement its main concepts, namely academic autonomy and freedom, as a new form of social responsibility. This accountability to the whole of society involves personal improvement in the interest of society and for its main concerns: climate change, global injustice, environmental protection and recycling [11]. Lindrianasari et.al [12] found that the theory of regulation (particularly for public

interest theory) can clearly explain the reasons why the four variables research have increased after the environmental regulations issued. Their research found similar results in all companies listed on stock exchanges in three developing countries, namely Indonesia, Malaysia and Thailand, related to new policies on social and environmental responsibility.

An organization can be categorized as taking part in protecting the environment if it has *Environmental Awareness, Environmental Involvement, Environmental Reporting, and Environmental Auditing*. Therefore, it can be concluded that at least four factors are needed in terms of organizational responsibility for the environment, namely environmental awareness, environmental involvement, environmental reports, and environmental audits [13] [14] . Evana et.al [15] said that public acceptance of mining companies is influenced by several factors, including the cost of living, quality of the environment, community involvement, improved infrastructure, the impact of other industries, and public welfare.

RESEARCH METHODS

This research is a *field research*. The population in this study are universities in Indonesia which are included in the top 50 greenest campuses in Indonesia according to the UI Green Metric in 2019. The universities sampled in this study are the University of Indonesia, Raden Intan State Islamic University, Lampung, Muhammadiyah University of Yogyakarta, and State University Yogyakarta. The considerations are representatives of higher education institutions that are included in the category of the greenest campus in Indonesia according to the 2019 UI Green Metric version which are willing to be used as research samples.

Data collection techniques used interviews and documentation of leaders, lecturers, education staff, and students from universities that were sampled. The measurement of data is based on the respondent's tendency towards 4 indicators of the stages of higher education in implementing Green Accounting, namely *Environmental Awareness, Environmental Involvement, Environmental Reporting, and Environmental Auditing*. After the data collected, then they are processed systematically according to the problem formulation as well as analyzed in a qualitative descriptive manner.

DISCUSSION

The university's participation in the UI GreenMetric World University Rankings can be an indication of the university to realize a Green Campus. Universities that are members of the UIGM ranking publish Sustainability Reporting through the disclosure of categories and assessment indicators for the UI GreenMetric World University Rankings: Arrangement and Infrastructure, Energy and Climate Change, Waste, Water, Transportation, Education and Research. The categories and weights of points in the UI GreenMetric World University Rankings are as follows

Table 1 Categories and Their Weighting Used in UI GreenMetric World University Rankings

No	Categories	Percentage of Total Points (%)
1	Setting and Infrastructure (SI)	15
2	Energy and Climate Change (EC)	21
3	Waste (WS)	18
4	Water (WR	10
5	Transportation (TR)	18
6	Education (ED)	18
	TOTAL	100%

Source: UI GreenMetric Guidelines, 2019

Based on information of the table above, category of Energy and Climate Change (EC) has the highest score in the UI GreenMetric World University Rankings assessment, followed by the category of Waste (WS), Transportation (TR), Education (ED), Setting and Infrastructure (SI), and Water (WR).). UI GreenMetric World University Rankings is managed by a team under the Rector of Indonesia University. The team members come from various academic backgrounds and experiences, such as Environmental Sciences, Engineering, Architecture and Urban Design, Computer Engineering, Dentistry, Public Health, Statistics, Chemistry, Physics, Linguistics and Cultural Studies.

Based on the 2019 UI GreenMetric Guidelines, the Setting and Infrastructure (SI) category provides an overview of campus tendencies towards a green environment and aims to trigger participating universities to provide more green open spaces for reforestation and protecting the environment as well as sustainable energy. The Energy and Climate Change (EC) category provides an overview of the use of energy-efficient equipment, implementation of smart building/automation building/intelligent building, policies on the use of renewable energy, total use of electrical energy, energy conservation programs, elements of green building, adaptation to climate change and mitigation programs, policies for reducing greenhouse gas emissions and carbon footprints. The Waste (WS) category is related to waste treatment and recycling activities

in creating a sustainable environment. The Water (WR) category is related to water conservation programs, water recycling programs, the use of water-saving equipment, and the use of treated water. The Transportation (TR) category is related to the transportation system that plays an important role in carbon emissions and pollution levels on campus. The Education (ED) category relates to the availability of sustainability-related courses offered on campus, research funding for sustainability research, indexed scientific publications related to environment and sustainability published annually, campus events/activities (e.g. conferences, workshops, awareness raising , training, etc.) related to environmental and sustainability issues, student organizations at both the faculty and university level related to environmental sustainability, university sustainability websites, and the availability of university sustainability reporting. Several stages that can be carried out are through the four stages, namely *Environmental Awareness, Environmental Involvement, Environmental Reporting,* and *Environmental Auditing*. The stages of the Environmental Awareness Indicators are as follows

Table 2 Stages of Environmental Awareness Indicators in Planning for Green Campus Implementation in Indonesia

Indicators Environmental Awareness	X	Y	Z
There are regulations regarding the environment	v	v	x
Philosophy of university leadership	v	v	v
The support of Human Resources (HR) and Economic Resources (SDE)	v	v	v
Support for research master plan and community service	v	v	v

The Environmental Awareness stage is to build awareness and commitment to the importance of preserving the environment. The University leadership strongly supports the existence of the university as an environmentally friendly campus. University leaders generally have a philosophy about the environment. Based on the results of an interview with one of the managers of the university's green campus Z, the leadership's commitment to building environmental awareness is manifested in the form of:

1. Place the UI green metric ranking as one of the performance indicators of university leaders and use the UI GreenMetric World University Rankings form as a green campus document;
2. Build infrastructure and facilities that refer to green building standards;
3. Build facilities by prioritizing reforestation;
4. There is a recycling program in the treatment of waste, water, plastic, glass;
5. Provide zero emission transportation;
6. Organize community service activities and environmental-based research designs;

Efforts to build environmental awareness are carried out through posters, campaign activities and appeals. To foster a sense of environmental concern, the campus has socialized the call for no smoking, maintaining cleanliness, an appeal to save light and air conditioning when not in use, a carbon reduction campaign, a plastic waste reduction campaign and other non-binding appeals throughout the campus area. However, University Z has not yet had a written rule issued by the university leadership which includes obligations and sanctions related to violations of these appeals.

In general, based on the presentation of the results of interviews, study documentation on the Sustainability Report and information available on the special green campus website, as well as the awards that have been achieved in recent years including the acquisition of the UI Green Metric World University Ranking, it can be stated that the leadership of University Z has high commitment to build environmental awareness and become a sustainable campus. At university X according to the facts on the ground with the proven commitment of the university to uphold good governance of the university and the new jargon at the university "Greening Your Campus, Greening Your Life". This jargon is in line with the university's vision as stated in the statute, namely the realization of the university as an international reference in the development of integrative-multidisciplinary Islamic science with an environmental perspective in 2035. In addition, the campus also held a "Car Free Day". In order to improve the management of green campuses and accelerate the realization of the Vision, the university gives awards to study programs and faculties related to environmental management. This award is known as the Environmental Management Awards (EMA). At university Y, the university leadership has a high commitment to making the university an environmentally friendly campus. This is evidenced by a university issuing a Rector's Regulation on green campuses. The stages of the Environmental Involvement Indicators are as follows

Table 3 Stages of Environmental Involvement Indicators in Planning for Green Campus Implementation in Indonesia

Indicators	X	Y	Z

Environmental Involvement			
The existence of environmental units in universities	v	x	x
Availability of funds for environmental protection	v	v	v
Availability of programs or procedures that reduce consumption of natural resources	v	v	v
Availability of environmental safety studies if the entity uses machines in its operational activities	v	v	v

Environmental involvement can be seen through the existence of a special team that is formed directly under the supervision of the appointed university leadership and evaluates the implementation and measures the effectiveness of green campus implementation. University Z does not yet have a special division/work unit that is specifically responsible for handling green campus implementation, but it is attached to related bureaus/units, such as:

- The General Bureau regulates water, green space cleanliness, bicycles, electricity, and others; Bureau of Information Systems makes programs/applications for paperless office ;
- Special activities regarding green campuses are carried out by ad hoc bodies or committees, for example carbon reduction campaigns, plastic waste reduction campaigns, etc;
- Infrastructure development refers to green building standards designed by a special team;
- Activities related to green campus rankings are carried out by the Strategic Data and Information Center, the Planning and Development Agency under the coordination of the Vice Chancellor for Governance, Cooperation and International Affairs.;
- Routine activities related to environmental regulation are adjusted to the appropriate organizational structure and governance;
- Temporary activities are also adjusted to the appropriate organizational structure and governance.

Fig. 2 The Implementation of Solid Waste Management in Y University

Work governance regarding the implementation of green campus refers to the Decree (SK) of the appropriate bureau officials as well as the Decree (SK) and duties for ad hoc bodies or special committees. At university Y the team is still ad hoc and the team coordinates directly with the Vice Chancellor for Division 2 regarding funding and infrastructure development.

The campus provides a special budget or funding for the green campus program as stated in the University RKT. The university's budget for infrastructure, facilities, personnel costs, including Research Funds Dedicated to Sustainability Research is disclosed in the university's Sustainability Reporting and is one of the fillings in the questionnaire in the UI Green Metric World University Rankings.

Since 2011, Z University has special programs in the context of conserving natural resources and the environment, such as setting most of its open space area with trees growing, constructing more smart buildings, paperless behavior and efficient energy appliances (Air conditioning with the VRV technology, LED lighting in most buildings), recycling program in the management of waste, water, plastic, glass, Providing zero emission transportation.

Regarding education and curriculum design, the University through several study programs has opened several courses related to the environment. The trend of data on environmental involvement shows that the indicators of environmental involvement are in the high category because many components or environmental conditions at University Z are already good. In 2019, University X formed a Sustainable and Environmentally Insight Campus Development Team (TPKBBL) through the Chancellor's Decree. The Stages of Environmental Reporting Indicators are as follows

Table 4 Stages of Environmental Reporting Indicators in Planning for Green Campus Implementation in Indonesia

Indicators Environmental Reporting	X	Y	Z
Environmental performance report	v	x	v
Performance reports are reported continuously	v	x	v
Performance report published	v	x	v
The environmental performance report is attached with publication	v	x	v

Environmental reporting is required for the decision-making process as well as for the purpose of disclosing material and relevant information about the university. Activities in order to support the implementation of the green campus are contained in the Sustanability Report which

generally contains the achievements/indicators of the UI Green Metric World University Ranking. The Sustainability Report is published by Universities X and Z every year on the relevant green campus web. Documentation is carried out on videos stored on YouTube, social media, and the university's green campus web. The Stages of *Environmental Auditing Indicators* are as follows:

Table 5 Stages of Environmental Auditing Indicators in Planning for Green Campus Implementation in Indonesia

Indicators Environmental Auditing	X	Y	Z
There is an audit report regarding the implementation of a green campus at the university	x	x	x
There is an internal supervisory unit (SPI) that audits the implementation of the green campus at the university	x	x	x

The Environmental Auditing stage is carried out to ensure whether the performance of environmental conservation programs run by universities has been carried out effectively and efficiently is the existence of environmental performance audits. This is measured based on answers to the availability of environmental performance audit reports or university green campus implementations. Until now, the Internal Audit Unit or the University's Internal Supervisory Unit does not yet have a special program related to auditing programs, funds, and environmental performance carried out by the University. In other words, there has never been an audit of the performance of the green campus implementation, both from internal and external parties.

Based on 4 stages, universities in their planning to implement Green Campus have met the stages of environmental awareness, environmental involvement, and environmental reporting. All universities have not met the environmental auditing stage. The following is a graph of the percentage of achievements in the stages of implementing green campus in Indonesia:

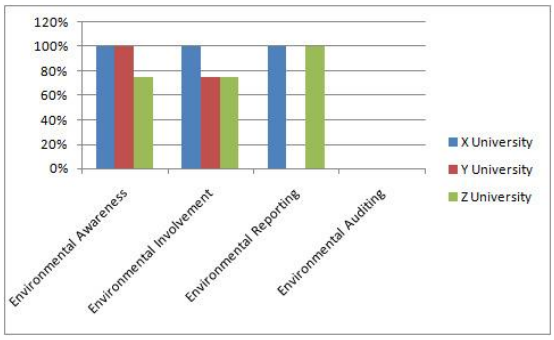

Fig. 3 graph of the percentage of achievements in the stages of implementing green campus in Indonesia

The university's participation in UI Green can be an indication that the university has awareness in the university and its surroundings about the importance of sustainability issues. University X has the highest percentage of achieving 4 green campus implementation instruments. Based on the graph above, at the environmental awareness stage, University X and Y have a higher percentage than University Z. At the environmental involvement stage the highest percentage value is owned by University X. At the environmental reporting stage, University Y has not yet done At the environmental awareness stage, environmental reporting, but universities X and Z have done environmental reporting. Meanwhile, no university has implemented environmental auditing yet.

CONCLUSION

The implementation of Green Campus is measured based on 4 instruments, namely Environmental Awareness, Environmental Involvement, Environmental Reporting, and Environmental Auditing. The findings of this study indicate that three universities have met the stages of environmental awareness, environmental involvement, and environmental reporting, but have not met the stages of environmental auditing. The university's participation in UI Green can be an indication that the university has awareness in the university and its surroundings about the importance of sustainability issues. University X has the highest percentage in achieving 4 green campus implementation instruments. The theory of legitimacy can explain that an organization must be able to adapt to the value system that has been implemented by society and the environment because the more forms of responsibility it takes to its environment, the better the image and reputation of the organization will be.

Through the implementation of a green campus, universities must pay attention to economic, social, and environmental aspects so that their existence and environmental sustainability will be maintained. Legitimacy

theory can explain that organizations must be able to adapt to the value system that has been applied by society and the environment because the more forms of responsibility that are carried out on their environment, the better the image and reputation of the organization will be.

ACKNOWLEDGMENTS

This research can be done well due to the funds provided by the government of the Republic of Indonesia through a research grant scheme at the Islamic State University of Raden Intan, Lampung. We would like to thank for the financial support of this research. In addition, we would also like to thank our colleagues at Universities in Indonesia to access the data. Participant feedback and suggestions in The 11th International Conference on Geotechnique, Construction Materials and Environment (GEOMATE), Kyoto, Japan, Nov. 3-5, 2021.

REFERENCES

[1] UI Green Metric, *UI GreenMetric World University Rankings 2019*. Jakarta, 2019.

[2] L. Dagilienė and V. Mykolaitienė, "Disclosure of Social Responsibility in Annual Performance Reports of Universities," *Procedia - Soc. Behav. Sci.*, vol. 213, 2015, doi: 10.1016/j.sbspro.2015.11.454.

[3] I. Ferrero-Ferrero, M. Á. Fernández-Izquierdo, M. J. Muñoz-Torres, and L. Bellés-Colomer, "Stakeholder engagement in sustainability reporting in higher education: An analysis of key internal stakeholders' expectations," *Int. J. Sustain. High. Educ.*, vol. 19, no. 2, 2018, doi: 10.1108/IJSHE-06-2016-0116.

[4] Y. An, H. Davey, and H. Harun, "Sustainability reporting at a New Zealand public university: A longitudinal analysis," *Sustain.*, vol. 9, no. 9, 2017, doi: 10.3390/su9091529.

[5] B. Yasbie and Z. Barokah, "Sustainability Reporting By Universities In Indonesia Abstract," *Indones. J. Account. Res.*, vol. 21, no. 03, 2018, doi: 10.33312/ijar.400.

[6] R. Lozano, J. Llobet, and G. Tideswell, "Developing a university sustainability report: Experiences from the university of leeds," in *Sustainability Assessment Tools in Higher Education Institutions: Mapping Trends and Good Practices Around the World*, 2013.

[7] H. Ahadis, W. A. Zakaria, I. S. Banuwa, and Lindrianasari, "Mining regulation and it's impact on public welfare," *Int. J. GEOMATE*, vol. 19, no. 72, 2020, doi: 10.21660/2020.72.9404.

[8] J. L. Vázquez, A. Lanero, and O. Licandro, "Corporate social responsibility and higher education: Uruguay university students' perceptions," *Econ. Sociol.*, vol. 6, no. 2, 2013, doi: 10.14254/2071-789X.2013/6-2/13.

[9] N. Gunarathne and K. H. Lee, "Corporate cleaner production strategy development and environmental management accounting: A contingency theory perspective," *J. Clean. Prod.*, vol. 308, 2021, doi: 10.1016/j.jclepro.2021.127402.

[10] S. H. A. Chen, J. Nasongkhla, and J. A. Donaldson, "University social responsibility (USR): Identifying an ethical foundation within higher education institutions," *Turkish Online J. Educ. Technol.*, vol. 14, no. 4, 2015.

[11] R. Vasilescu, C. Barna, M. Epure, and C. Baicu, "Developing university social responsibility: A model for the challenges of the new civil society," in *Procedia - Social and Behavioral Sciences*, 2010, vol. 2, no. 2, doi: 10.1016/j.sbspro.2010.03.660.

[12] Lindrianasari, M. Kufepaksi, Y. Asmaranti, and A. Komalasari, "Social and environmental responsibility in developing countries: A theoretical approach to regulation," *Int. J. GEOMATE*, vol. 15, no. 49, 2018, doi: 10.21660/2018.49.3684.

[13] Y. F. Jahamani, "Green accounting in developing countries: The case of U.A.E. and Jordan," *Manag. Financ.*, vol. 29, no. 8, 2003, doi: 10.1108/03074350310768418.

[14] A. S. Dunk, "Product quality, environmental accounting and quality performance," *Accounting, Auditing & Accountability Journal*, vol. 15, no. 5. 2002, doi: 10.1108/09513570210448975.

[15] E. Evana, Lindrianasari, H. Ahadis, and Y. Asmaranti, "Public acceptance of mining companies in Indonesia," *Int. J. GEOMATE*, vol. 19, no. 72, 2020, doi: 10.21660/2020.72.9148.

11th Int. Conf. on Geotechnique, Construction Materials & Environment,
Kyoto, Japan, 3-5 November 2021, ISBN: 978-4-909106063 C3051

METALAXYL RESISTANCE, PATHOGENICITY, AND CROSS-INFECTIVITY OF *PHYTOPHTHORA PALMIVORA* FROM DURIAN AND PARA-RUBBER DISEASES IN SOUTHERN THAILAND

Pornprapa Kongtragoul[1] and Thammanoon Phelawan[1]

[1]Management Technology for Plant Production, Department of Agricultural Technology,
King Mongkut's Institute of Technology Ladkrabang, Prince of Chumphon, THAILAND

ABSTRACT

Durian and para-rubber are the economic crops of Southern Thailand. The serious pathogen of both is *Phytophthora palmivora.* Metalaxyl has been commonly used to control this pathogen. The objectives of this study were to detect the metalaxyl resistance of *P. palmivora*, their pathogenicity test and cross-infectivity test. Ten isolates of parental isolate [PI] were successfully isolated from para rubber cv. RRIM600 and durian cv. Monthong by tissue transplanting technique. The metalaxyl-resistant assay was conducted on V8 agar amended with metalaxyl by poisoned food method. The results showed that 8 isolates of PI were highly resistant to metalaxyl [Met^{HR}], which they were able to grow at > 500 µg/ml, and 2 isolates of PI were sensitive to metalaxyl [Met^{S}], which they were able to grow at ≤10 µg/ml. Moreover, the hyphal tips isolate [HI] derived from PI isolates 6-month preservation showed the results indicated that all Met^{HR} isolates of PI were still Met^{HR} phenotype. All HI isolates were studied for pathogenicity and cross-infectivity by the detached leaves technique. The results showed that the lesion diameters of all isolates from durian disease were significantly wider than all isolates from para-rubber disease after inoculation for 4 days. All isolates from durian disease were pathogenic to un-wounded host leaves, but all isolates from the para-rubber disease were not pathogenic to un-wounded host leaves. The isolates of DF03-Met^{HR} and DS07-Met^{S} showed the highest percent infection after inoculation for 4 days at 16.66% and 13.88%, respectively. However, all isolates were pathogenic to wounded cross-host leaves, and the PRS01-Met^{HR} isolate showed the widest lesion diameter after inoculation for 4 days at 23.16+3.36 mm. On the other hand, all isolates were not pathogenic to un-wounded cross-host leaves.

Keywords: Fungicide resistance, Phenylamides, Plant disease, Durian, Para rubber

INTRODUCTION

Durian and para-rubber are the important economic crops of Thailand. They have the most plantations in Southern Thailand, and Chumphon province is ranked among both production areas [1]. However, the most serious pathogen of both crop production is the genus *Phytophthora*. It causes fruit, stem, and root rot diseases in durian; black strip and leaf fall in para-rubber [2]. They are the key limiting factors of durian and para-rubber production. Fungicides are still important for plant production. Some fungicides were used to reduce the Phytophthora diseases because almost farmers believed that fungicides could successfully control the plant pathogen better than other methods. They applied the systemic fungicides such as metalaxyl for controlling this pathogen. It has been widely used for many years ago in durian and para-rubber orchard. Therefore, its long term may induce mutant isolates in the field.

Metalaxyl is the most active of the phenylamides fungicides, and it has curative as well as protective activity, and rapid uptake and translocation to new growth. The mode of action is so specific at RNA polymerase I of nucleic acids metabolism that oomycetes have developed resistance to this group of compounds. Fungicide resistance action committee (FRAC) reported that metalaxyl is a high-risk resistance in various Oomycetes but mechanism unknown [3], [4]. However, using fungicides may be the acquired appearance of resistant strains in the durian and para-rubber orchard. It may be one of the significant limiting factors for poor disease control because of pathogen resistance development. This resistance is transferrable to descendants. Moreover, the side effects of fungicides cause risks to humans, animals, and the environment. Resistance had occurred in some fungi because metalaxyl was used intensively before the dangers of resistance were understood. Therefore, knowledge of fungicide resistance, pathogenicity, and cross-infectivity is important for effective pathogen control. The resistance of *Phytophthora* spp. to metalaxyl has been reported in many regions of the world [5]-[11]. However, limited information is available on the sensitivity of *P. palmivora* to metalaxyl in Thailand.

The objectives of this research were to [i] determine the occurrence of metalaxyl-resistant *P. palmivora* vegetative reproduction causing durian

and para-rubber diseases and [ii] their pathogenicity of *P. palmivora* on the host plant and [ii] cross-infectivity of *P. palmivora* on durian and para-rubber.

MATERIALS AND METHODS

Isolation and identification pathogen causing para-rubber and durian diseases

The disease samples of durian cv. Monthong and para-rubber cv. RRIM600 that showed infection naturally were collected from orchards in Chumphon provinces, Thailand. PAR[PH]-V8 selective medium was made for purification purposes by adding antibiotics and fungicides and cooled clarified V8 juice medium followed Jeffers [12].

The diseased plant tissue was cut into pieces and surface sterilized by soaking in 10% Clorox®, rinsed in sterile distilled water, and blotted dry on sterile paper. The dried tissues were placed on PAR[PH]-V8 selective medium and incubated at room temperature [RT] of approximately 28-30ºC. The parental isolates [PI] were cut from the hyphal tip of a 4-days-old culture after isolated from single discrete lesions and transferred onto clarified V8 juice agar for 6 months.

Three isolates [PRS01, PRS02, and PRS03] were isolated from black stripe symptoms on the naturally infected para-rubber stem [Figure 1a]. Five [DS02, DS03, DS06, DS07, and DS10] and two [DF01, DF03] isolates were isolated from stem and fruit rot symptoms on naturally infected durian, respectively [Figure 1b, 1c].

[a] [b] [c]

Fig. 1 Symptoms of black stripe disease [a] in para-rubber, stem rot disease [b], and fruit rot disease [c] in durian.

Metalaxyl-resistance assay

The resistance to metalaxyl was studied for all isolates of *P. palmivora* by phenotypic assay. The resistibility of each isolate to metalaxyl was observed from the growth of the colony. For each isolate, the parental isolate [PI] was cut from the margin after isolated from infected tissue. The hyphal tips isolate [HI] derived from PI isolates were kept on V8 agar for 6 months for metalaxyl-resistance assay. The fungicides applied for *P. palmivora* control in durian and para-rubber diseases were metalaxyl for 40g/ 20 l water [25% w/v]. Resistant reaction to metalaxyl [25%WP w/v] of PI and HI isolates was determined through in vitro comparison of each isolate's mycelial growth on the final concentrations of metalaxyl at 0.1, 1, 10, 100, 500 [field-use recommended rate], and 1,000 a.i. µg/ml amended V8 agar and un-amended V8 agar with the growth of the same isolate on medium. Metalaxyl was added to V8 agar after autoclaving, and the plates were incubated at RT. The mycelial plugs of 5 mm diameter were cut from the margin of a 5 day old culture and placed with the mycelium in contact with the test medium [5 replicates for each isolate at each concentration].

The response of resistance to metalaxyl was categorized which modified from Kongtragoul et al. [13] as follows:

- sensitive to metalaxyl [Met^S]: the culture was able to grow at ≤10 µg/ml
- resistant to metalaxyl [Met^R]: the culture was able to grow at $10 < EC_{50} \leq 100$ µg/ml
- highly resistant to metalaxyl [Met^{HR}]: the culture was able to grow at > 500 µg/ml

Pathogenicity and Cross-infectivity in vivo test

Pathogenicity test on a host

All HI isolates of *P. palmivora* were pathogenic on host leaves. The healthy leaves were detached without applying the fungicide orchard in KMITL Chumphon campus, Thailand. The healthy leaves were washed thoroughly under running tap water before being surface sterilized with 10% Clorox® and blotted slightly on paper towels to remove excess moisture. The base of each detached leaf was cover with a piece of moist cotton to reduce leaf desiccation. Wound and un-wound inoculation were performed for pathogenicity tests on the leaves of the 'Monthong' durian and 'RRIM600' para-rubber. Then they were placed in a plastic box. A circular inoculation site, with a 5 mm diameter, was marked on the leaf surface. The Mycelium disc of each isolate was cut at the peripheral colony and transferred to the wounded and un-wounded area. Moistened paper towels were placed in the plastic box containing the inoculated leaves and incubated at RT. The lesion diameters were measured after four days of incubation on wounded inoculation. For un-wounded inoculation were observed the number of the lesion and calculate the percentage of infection.

Cross-infectivity

The determination of the cross-infection of *P. palmivora* isolates from durian and para-rubber was used to inoculate each of the above host combinations. The isolates from durian diseases were inoculated by mycelium disc on wounded and non-wounded para-rubber leaves, and the isolates from para-rubber diseases were inoculated by mycelium disc on wounded and non-wounded durian leaves.

RESULTS AND DISCUSSION

Isolation and identification pathogen causing para-rubber and durian diseases

Ten isolates were isolated from para-rubber and durian diseases. The colony of all isolates was white [Figure 2a]. Mycelia were branched, non-septate, and hyaline [Figure 2b]. They formed sporangium with papilla by growing on clarified V8 agar for 7 days [Figure 2c]. These morphological characteristics were identified as *P. palmivora* [12]. This situation is similar to that in other durian and para-rubber producing countries such as Malaysia, Vietnam, and Indonesia, etc., where the fungus, *P. palmivora*, has been reported to cause both crops [2].

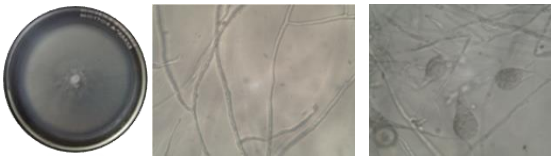

[a] [b] [c]

Fig. 2 Morphological characterization of Phytophthora palmivora; colony color on V8 agar [a], hypha [b], and sporangium [c].

Metalaxyl-resistance assay

The results showed that three isolates were classified as the Met^{HR} phenotype, of which 3 [PRS02, PRS01, PRS03] and 5 [DS02, DS03, DS06, DF01, DF03] were obtained from para-rubber and durian, respectively. All Met^{HR} isolates were obtained from treated fungicide orchards. All PI isolates, 2 isolates from durian [DS07, DS10], were classified as the MetS phenotype, of which both isolates were obtained from untreated fungicide orchards. After kept PI isolates for 6 months on V8 agar, the mycelium of all isolates was repeated the resistibility to the metalaxyl test. The result shows that all PI Met^{HR} isolates could still grow on metalaxyl at the field-use recommended concentration. All Met^{HR} of PI were classified as the Met^{HR} of HI after kept mycelium for 6 months [Table 1]. In other reports, metalaxyl resistance has been almost found on *P. infestans* in Northern Thailand [14] and other countries such as; China [5, 6], Mexico [10], USA [15], Uganda [7], Morocco [8], Cameroon [9], Russia [16], Estonia [17], and Poland [18]. This result is one of the reasons for increasing difficulties in disease control. Furthermore, the information on fungicide resistance of *P. palmivora* must be study in the molecular level. It may help in understanding in the fungicidal mechanism.

Table 1 Metalaxyl-resistant assays of *Phytophthora palmivora,* causing durian and para-rubber diseases on V8 agar amended with metalaxyl.

Isolate code		Percentage growth						Resistant levels
		Metalaxyl concentrations [mg/l]						
		0.1	1	10	100	500*	1,000	
PRS01	PI	100	100	97.78	58.45	38.66	17.34	Met^{HR}
	HI	100	100	95.55	62.22	41.48	20.74	Met^{HR}
PRS02	PI	100	100	96.76	66.67	36.78	16.77	Met^{HR}
	HI	100	100	98.14	78.14	40.74	23.70	Met^{HR}
PRS03	PI	100	100	98.54	66.76	34.16	16.86	Met^{HR}
	HI	100	100	95.5	70.37	44.81	22.77	Met^{HR}
DS02	PI	100	100	100	71.48	33.33	17.70	Met^{HR}
	HI	100	100	100	77.77	36.38	25.00	Met^{HR}
DS03	PI	100	100	100	61.38	29.16	28.33	Met^{HR}
	HI	100	100	100	77.77	40.00	22.66	Met^{HR}
DS06	PI	100	100	100	57.77	26.94	13.05	Met^{HR}
	HI	100	100	100	71.33	34.4	22.66	Met^{HR}
DS07	PI	98.34	10.00	7.7	0	0	0	Met^{S}
	HI	98.44	14.40	0	0	0	0	Met^{S}
DS10	PI	97.77	13.55	7.7	0	0	0	Met^{S}
	HI	98.00	12.44	0	0	0	0	Met^{S}
DF01	PI	100	100	100	68.16	33.88	16.38	Met^{HR}
	HI	100	100	97.50	76.39	44.81	27.40	Met^{HR}
DF03	PI	100	100	100	73.3	34.44	23.61	Met^{HR}
	HI	100	100	94.81	70.84	40.37	22.96	Met^{HR}

*Field-use recommended rate, parental isolates [PI], hyphal tips isolate [HI]

Pathogenicity and Cross-infectivity in vivo test

The pathogenicity test and cross-infection confirmed that the vegetative reproduction of *P. palmivora* after kept for 6 months was pathogenic to both the durian and para-rubber on wounded leave. However, all isolates from durian disease were pathogenic to un-wounded host leaves, but all isolates from the para-rubber disease were not pathogenic to un-wounded host leaves. The lesion diameters of all isolates from durian disease were significantly wider than all isolates from para-rubber disease after inoculation for 4 days. DS02-Met^{HR}, DF03-Met^{HR}, and DS07-Met^{S} showed the widest lesion diameter after inoculation for 4 days at 18.61+0.88, 18.52+1.24, and 17.94+2.38, respectively. The isolates of DF03-Met^{HR} showed the highest of percent infection after inoculation for 4 days at 16.66%.

Moreover, all isolates were pathogenic to

wounded cross-host leaves, and the PRS01-Met^{HR} isolate showed the widest lesion diameter after inoculation for 4 days at 23.16+3.36 mm. On the other hand, all isolates were not pathogenic to un-wounded cross-host leaves [Table 2, 3]. This implies that the wound is a significant factor in pathogenic to host and cross-host of *P. palmivora*. Moreover, the metalaxyl response group is not significant to infection.

Table 2 Lesion diameters of host leave after inoculation with *Phytophthora palmivora* on wounded leaves for 5 days and percent of infection on host leaves after inoculation on un-wounded leaves for 4 days.

Isolate code	Lesion diameter on host [mm ± standard deviation][1/]	Percent of infection
on 'RRIM 600' para-rubber leaves		
PRS01-Met^{HR}	7.87±0.15d	0.00b
PRS02-Met^{HR}	7.90±0.37d	0.00b
PRS03-Met^{HR}	11.81±2.59c	0.00b
on 'Monthong' durian leaves		
DS02-Met^{HR}	17.94±2.38a	8.33ab
DS03-Met^{HR}	17.23±0.85ab	5.55ab
DS06-Met^{HR}	16.75±1.01ab	9.72ab
DS07-Met^{S}	18.52±1.24a	11.10ab
DS10-Met^{S}	17.52±0.43ab	9.72ab
DF01-Met^{HR}	15.27±1.28b	4.16b
DF03-Met^{HR}	18.61±0.88a	16.66a

[1/]Average of four replications [18 sub-replications]. The mean followed by the same letter is not signification different by least significant difference [LSD].

Table 3 Lesion diameters and cross-host leave after inoculation with *Phytophthora palmivora* on wounded leaves for 4 days.

Isolate Code	Lesion diameter on host [mm ± standard deviation][1/]	Percent of infection
on wounded 'Monthong' durian leaves		
PRS01-Met^{HR}	16.66±2.14a	0
PRS02-Met^{HR}	5.84±0.95e	0
PRS03-Met^{HR}	14.29±1.70abc	0
on wounded 'RRIM 600' para-rubber leaves		
DS02-Met^{HR}	12.35±2.99bcd	0
DS03-Met^{HR}	10.18±1.29d	0
DS06-Met^{HR}	11.47±1.40cd	0
DS07-Met^{S}	13.37±1.33abcd	0
DS10-Met^{S}	12.91±1.46bcd	0
DF01-Met^{HR}	15.22±1.54ab	0
DF03-Met^{HR}	10.93±1.22d	0

[1/]Average of four replications [18 sub-replications]. The mean followed by the same letter is not signification different by least significant difference [LSD].

CONCLUSIONS

This study demonstrated that *P. palmivora* vegetative reproduction is highly resistant to metalaxyl. All tested isolates from durian were pathogenic to host leaves and not pathogenic to un-wounded para-rubber leaves. We conclude that the application of metalaxyl fungicide should be carefully planned for durian and para-rubber disease management.

ACKNOWLEDGMENTS

We express my sincere thanks to King Mongkut's Institute of Technology Ladkrabang, Prince of Chumphon Campus, Thailand for support.

REFERENCES

[1] Office of Agricultural Economics Department of Agriculture Thailand, Quantity and value of imports of agricultural hazardous substances, 2018, (Online) Available http://oldweb.oae.go.th/economicdata/pesticides.html

[2] Drenth, A., and Guest D. I., Diversity and Management of Phytophthora in Southeast Asia, Canberra Australia Australian Centre for International Agricultural Research, 2004, pp.1-238.

[3] Fungicide Resistance Action Committee, List of Resistant Pathogenic Organisms Resistant to Disease Control Agents, 2018, (Online) Available http://www.frac.info/docs/default-source/publications/list-of-resistant-plant-pathogens/list-of-resistant-plant-pathogenic-organisms_may-2018.pdf

[4] Hollomon D. W., Fungicide Resistance: Facing the Challenge, Plant Protection Science, Vol. 51, Issue 4, 2015, pp. 170-176.

[5] Wang W., Liu X., Han T., Li K., Qu Y., and Gao Z., Differential Potential of *Phytophthora capsici* Resistance Mechanisms to the Fungicide Metalaxyl in Peppers, Microorganisms, Vol. 8, Issue 2, 2020, pp. 1-17.

[6] Cui L., Yin W., Tang Q., Dong S., Zheng X., Zhang Z., and Wang Y., Distribution, Pathotypes, and Metalaxyl Sensitivity of *Phytophthora sojae* from Heilongjiang and Fujian provinces in China, Plant Disease, Vol. 94, Issue 7, 2010, pp. 881-884.

[7] Mukalazi J., Adipala E., Sengooba T., Hakiza J. J., Olanya M., and Kidanemariam H. M., Metalaxyl Resistance, Mating Types and Pathogenicity of *Phytophthora infestans* in Uganda, Crop Protection, Vol. 20, Issue 5, 2001, pp. 379-388.

[8] Hammi A., Msatef Y., Bennani, A., Ismaili A. E. L., and Serrhini M. N., Mating Type

Metalaxyl Resistance and Aggressiveness of *Phytophthora infestans* (Mont.) de Bary in Morocco, Journal of Phytopathology, Vol. 150, Issue 4-5, 2002, pp. 289–291.

[9] Fontem D. A., Olanya O. M., Tsopmbeng G. R., and Owona M. A. P., Pathogenicity and Metalaxyl Sensitivity of *Phytophthora infestans* Isolates Obtained from Garden Huckleberry, Potato and Tomato in Cameroon, Crop protection, Vol. 24, Issue 5, 2005, pp. 449-456.

[10] Grünwald N. J., Sturbaum A. K. and Montes G. R., Selection for Fungicide Resistance within a Growing Season in Field Populations of *Phytophthora infestans* at the Center of Origin. Phytopathology, Vol. 96, Issue 12, 2006, pp. 1397–1403.

[11] Earnshaw D. M., and Shattock R. C., Sensitivity of Progeny of *Phytophthora infestans* to Fungicides, Asian Journal of Agricultural Sciences, Vol. 4, Issue 3, 2012, pp. 213-224.

[12] Jeffer S. N. Identifying Species of *Phytophthora*, Clemson University (Online) 2006, Available https://fhm.fs.fed.us/sp/sod/misc/culturing_species_phytophthora.pdf

[13] Kongtragoul P., Nalumpang S., Miyamoto Y., Izumi Y., and Akimitsu K., Mutation at Codon 198 of TUB2 Gene for Carbendazim Resistance in *Colletotrichum gloeosporioides* Causing Mango Anthracnose in Thailand, Journal Plant Protection Research, Vol. 51, Issue 4, 2011, pp. 377–383.

[14] Chiampiriyakul P., Sopee J., and Mekmok T., Evaluation of Metalaxyl Sensitivity Among *Phytophthora infestans* by Poisoned Food Technique Using Corn Agar, Proceeding of 49th Kasetsart University Annual Conference Plants 1-4 February 2011, pp. 480-487.

[15] Parra G., and Ristaino J. B. Resistance to Mefenoxam and Metalaxyl Among Field Isolates of *Phytophthora capsici* Causing Phytophthora Blight of Bell Pepper, Plant Disease, Vol. 85, Issue 10, 2001, pp. 1069-1075.

[16] Elansky S., Apryshko V. P., Milyutina D. I., and Kozlovsky B. E., Resistance of Russian Strains of *Phytophthora infestans* to Fungicides Metalaxyl and Dimethomorph, Moscow University Biological Science Bullatin, Vol. 62, Issue 1, 2007, pp. 11-14.

[17] Runno-Paurson E., Fry, W. E., Remmel, T. Mänd, M. and Myers K. L., Phenotypic and Genotypic Characterisation of Estonian Isolates of *Phytophthora infestans* in 2004–2007, Journal of Plant Pathology, Vol 92, Issue 2, 2010, pp. 375–384.

[18] Sobkowiak S., Śliwka J., Chmielarz M., Lebecka R., and Zimnoch-Guzowska E., Resistance to Metalaxyl of *Phytophthora infestans* Isolates Occurring in Poland in 2006-2010, Plant Breeding and Acclimatization Institute – National Research Institute Research Division at Młochów Młochów Poland, Phytopathologia, Vol. 61, pp. 29-35.

11th Int. Conf. on Geotechnique, Construction Materials & Environment, Kyoto, Japan, 3-5 November 2021, ISBN: 978-4-909106063 C3051

3D NUMERICAL ANALYSIS OF TSUNAMI-INDUCED FLOW AND TOPOGRAPHY CHANGE IN AN ABRUPT EXPANSION AREA WITH DIFFERENT SHORELINE CONDITIONS

Yuki Kajikawa[1] and Masamitsu Kuroiwa[2]

[1,2] Faculty of Engineering, Tottori University, Japan

ABSTRACT

The purpose of this study is to clarify the applicability of a three-dimensional numerical model to predicting flow and topography changes induced by tsunamis in an abrupt expansion area with different shoreline conditions of overflow and reflection. In the numerical model, the tsunami flow was calculated using the three-dimensional Reynolds-averaged Navier–Stokes equations with the shear-stress transport k–ω turbulence model using the Cartesian coordinate system. The topography change was estimated by the sediment continuity equation considering the nonequilibrium bed-load and suspended-load transport. Moreover, the fractional area–volume obstacle representation method was introduced into the governing equations. To investigate the applicability of the model to the phenomena, it was applied to laboratory experiments conducted by Arimitsu and Kawasaki (2017). By comparing the calculated results and the experimental data, it was clarified that it is critical to set the appropriate side wall roughness to accurately reproduce the tsunami flow in the abrupt expansion area using three-dimensional numerical models. Moreover, the model developed in this study was found to reproduce the flow and topography changes in an abrupt expansion area with different shoreline conditions.

Keywords: Tsunami, Abrupt expansion area, Shoreline condition, 3D numerical analysis, Topography change

INTRODUCTION

From the perspective of disaster prevention, it is extremely important to predict flows and topography change induced by a tsunami in an inland sea leading from a narrow pass to an abrupt expansion area, such as a harbor. Therefore, numerous studies on the prediction of the phenomenon have been conducted experimentally [1], [3], [4] and numerically [1]–[3], [5]. Arimitsu et al. [3] experimentally clarified that the circulation flow formed in the abrupt expansion area will be the same scale regardless of the depth of the area behind the expansion area. Furthermore, they also clarified, using the shallow water equations based on the zero-equation turbulence model, that setting the eddy viscosity coefficient is very important in accurately reproducing the flow and topography change in the abrupt expansion area.

Incidentally, inside the circulation flow formed in the abrupt expansion area, the flow near the bed is known to be more inclined to the vortex center than near the water surface due to the development of the Ekman layer. This flow near the bed transports sand to the vortex center and prompts sediment accumulation. Therefore, a three-dimensional (3D) numerical model is essential to predicting the flow with vertical distribution and topography change induced by the circulation flow accurately. However, in the 3D numerical model based on the Reynolds-averaged Navier–Stokes (RNAS) equations, a turbulence model that can appropriately predict the phenomenon has not yet been elucidated, although various turbulence models have been proposed. Additionally, in turbulence models in which the model constants are determined almost uniquely, such as the k-ε model, it is preferable to maintain the constants so that the phenomenon can be reproduced. Therefore, it is necessary to aim at reproducing the phenomenon by setting other conditions. However, the conditions to be set have not been clarified, and the applicability of 3D models to this phenomenon is still unclear.

Accordingly, the purpose of this study is to clarify the applicability of a 3D RANS numerical model to the prediction of flow and topography change induced by a tsunami in an abrupt expansion area with different shoreline conditions of overflow and reflection. Specifically, the authors first developed a 3D RANS numerical model and conducted the tsunami flow analyses with the side wall roughness changed for the experiments conducted by Arimitsu and Kawasaki [4]. Then, after determining the side wall roughness, analyses for the movable bed experiments were performed.

NUMERICAL MODEL

Governing Equations for Tsunami flow

In the tsunami flow model, 3D RANS equations using the Cartesian coordinate system was adopted. Furthermore, the fractional area–volume obstacle representation (FAVOR) method [5], [6], which can smoothly impose boundary conditions at complex

boundaries, was introduced into the governing equations. The momentum and continuity equations based on 3D RANS equations are as follows:

$$\frac{\partial u_i}{\partial t}+\frac{1}{V}\left\{\frac{\partial A_{(j)}u_j u_i}{\partial x_j}\right\}=-g\delta_{3i}-\frac{1}{\rho}\frac{\partial P}{\partial x_i}+\frac{1}{V}\frac{\partial}{\partial x_j}\left\{A_{(j)}\left(\nu+\nu_t\right)\left(\frac{\partial u_i}{\partial x_j}+\frac{\partial u_j}{\partial x_i}\right)\right\} \quad (1)$$

$$\frac{\partial}{\partial x_j}\left\{A_{(j)}u_j\right\}=0 \quad (2)$$

where t is time; i = 1, 2, 3; j = 1, 2, 3; (x_1, x_2, x_3) = (x, y, z) in the Cartesian coordinates (x, y, and z denote the horizontal, cross, and vertical coordinates, respectively); u_i is the velocity in the x_i direction [(u_1, u_2, u_3) = (u, v, w)]; V is the fractional volume rate occupied by the fluid in an calculation grid; $A_{(j)}$ is the fractional area rate occupied by the fluid on the grid boundary surface in the x_j direction [($A_{(1)}$, $A_{(2)}$, $A_{(3)}$) = (A_x, A_y, A_z)]; g is the gravitational acceleration; δ is the Kronecker's delta; ρ is the fluid density; $P = p + 2/3k$; p is the pressure; ν is the kinematic viscosity of fluid; k is the turbulent kinetic energy; and ν_t is the eddy viscosity coefficient.

In this model, the shear-stress transport (SST) k–ω turbulence model [7] was adopted for the evaluation of the eddy viscosity coefficient ν_t to accurately reproduce the circulation flow in the abrupt expansion area.

Governing Equations for Topography Change

In the topography change model, both the bed-load and suspended-load transport were considered. The bed-load transport rate was estimated from the following nonequilibrium bed-load transport model proposed by Uchida and Fukuoka [8]:

$$\frac{\partial q_{Bi}}{\partial t}+\frac{1}{S}\left\{\frac{\partial L_{(j)}u_{Bj}q_{Bi}}{\partial x_j}\right\}=\frac{q_{Be}u_{Bei}}{\zeta_e}-\frac{q_B u_{Bi}}{\zeta}+m_* h_B\left(\gamma_{ei}-\gamma_i\right) \quad (3)$$

$$\begin{cases} u_B/\sqrt{sgd}=3.3(q_{B*})^{1/3}, u_{Be}/\sqrt{sgd}=3.3(q_{Be*})^{1/3} \\ h_B/d=0.3(q_{B*})^{2/3} \\ \zeta_e/d=600(q_{Be*})^{2/3}, \zeta/d=600\max(q_{Be*},q_{B*})^{2/3} \end{cases} \quad (4)$$

where q_{Bi} is the bed-load transport rate in the x_i direction ($q_B^2 = q_{Bi}q_{Bi}$); S is the fractional area rate occupied by the movable bed on a two-dimensional horizontal (2DH) calculation grid; $L_{(j)}$ is the fractional line rate occupied by the movable bed on the 2DH grid boundary in the x_j direction; u_{Bj} is the sediment particle velocity of bed load in the x_j direction ($u_B^2 = u_{Bj}u_{Bj}$); q_{Be} is the equilibrium bed-load transport rate; ζ is the spatial lag distance; ζ_e and u_{Bei} are the ζ and u_{Bi} for equilibrium condition, respectively; $m_* = \mu_k s g \cos\theta_b/(s+1+C_M)$; μ_k is the dynamic friction coefficient of sediment; s is the specific gravity of sediment in water (= σ/ρ – 1, σ is the density of sediment); θ_b is the maximum bed angle; C_M is the coefficient of added mass (= 0.5); $h_B = q_B u_B$; $\gamma_i = q_{Bi}/q_B$; $\gamma_{ei} = q_{Bei}/q_{Be}$; $q_{B*} = q_B/(sgd^3)^{0.5}$; $q_{Be*} = q_{Be}/(sgd^3)^{0.5}$; and d is the sediment diameter.

The equilibrium bed-load transport rate, q_{Be}, in Eq. (3) was calculated using the following formula proposed by Ashida and Michiue [9]:

$$\frac{q_{Be}}{\sqrt{sgd^3}}=17\tau_*^{3/2}\left(1-\frac{K_c\tau_{*c}}{\tau_*}\right)\left(1-\sqrt{\frac{K_c\tau_{*c}}{\tau_*}}\right) \quad (5)$$

where τ_* and τ_{*c} are the non-dimensional and critical bed tractive forces [10], respectively; and K_c is the correction factor attributed to the influence of bed inclination on sediment motion [11].

Moreover, the suspended-load transport rate per unit area q_{su} was defined using the following formula proposed by Itakura and Kishi [12]:

$$q_{su}=K\left(\alpha_*\frac{\sigma-\rho}{\sigma}\frac{gd}{u_*}\Omega-w_f\right) \quad (6)$$

$$\Omega=\frac{\tau_*}{B_*}\frac{\int_{\alpha'}^{\infty}\xi\frac{1}{\sqrt{\pi}}\exp\left(-\xi^2\right)d\xi}{\int_{\alpha'}^{\infty}\frac{1}{\sqrt{\pi}}\exp\left(-\xi^2\right)d\xi}+2\frac{\tau_*}{B_*}-1 \quad (7)$$

where w_f is the settling velocity of the sediment given by Rubey's formula [13]; $\alpha' = B_*/\tau_* - 2$; $\alpha_* = 0.14$; $K = 0.008$; and $B_* = 0.143$.

The advection and diffusion processes of the suspended load were calculated using the following suspended-sediment transport equation, into which the FAVOR method was introduced:

$$\frac{\partial c}{\partial t}+\frac{1}{V}\left\{\frac{\partial A_{(j)}u_j c}{\partial x_j}-\frac{\partial A_{(3)}w_f c}{\partial x_3}\right\}=\frac{1}{V}\frac{\partial}{\partial x_j}\left\{A_{(j)}D_t\frac{\partial c}{\partial x_j}\right\} \quad (8)$$

where c is the concentration of the suspended load; D_t is the eddy diffusion coefficient (= ν_t/σ_t); and σ_t is the turbulent Schmidt number (= 0.8).

The topography change was calculated using the following continuity equation of sediment transport into which the FAVOR method was introduced:

$$\frac{\partial z_b}{\partial t}+\frac{1}{S(1-\lambda)}\left\{\frac{\partial L_{(j)}q_{Bj}}{\partial x_j}+S\left(q_{su}-w_f c_b\right)\right\}=0 \quad (9)$$

where z_B is the bed elevation; λ is the porosity of the bed material; and c_b is the near-bed concentration of

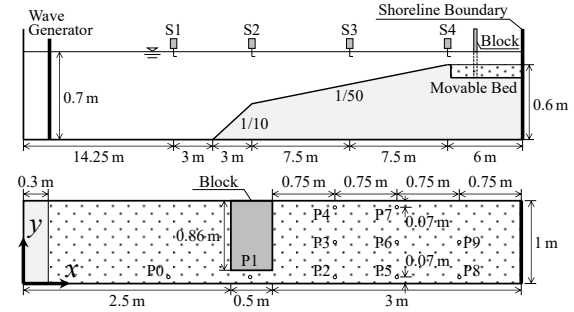

Fig. 1 Experimental setup (Top: Elevated view; Bottom: Top view of movable bed area).

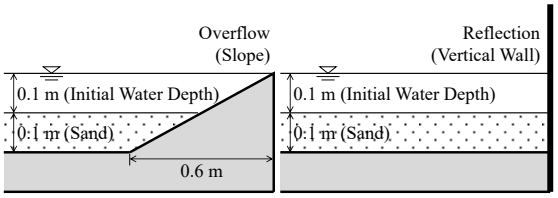

Fig. 2 Boundary conditions of shoreline (Left: Overflow; Right: Reflection).

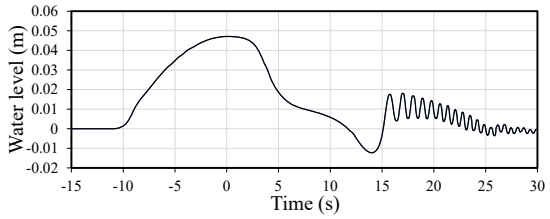

Fig. 3 Wave profile at the offshore boundary.

the suspended load.

Numerical Method

A collocated grid system was adopted for the computational grids of the tsunami flow. The fifth-order weighted essentially non-oscillatory (WENO) scheme [14] was applied to discretize the advection terms of the momentum equation in Eq. (1), and the hybrid scheme [15] was applied to discretize the SST k–ω equations and the suspended-sediment transport equation in Eq. (8). The velocities at the grid boundaries and the pressure in the grid center were calculated using the highly simplified mark-and-cell method on the collocated grid system (C-HSMAC) [16].

As boundary conditions, frictional resistance was considered according to the logarithmic law at the vertical wall and bed boundaries. The turbulent quantities were given by the wall functions at the bed boundary and by the slip condition at the vertical wall. Moreover, the time variation of the wave profile measured in the experiment was provided at the offshore boundary.

MODEL APPLICATION AND DISCUSSION

Outline of Targeted Experiments

Numerical analyses were performed for the laboratory experiments with an abrupt expansion area; the different shoreline conditions from the experiments conducted by Arimitsu and Kawasaki [4] were used. The experimental setup is shown in Fig. 1. Uniform sand with grain diameter d = 0.064 mm was used in the movable bed area. The boundary conditions of the shoreline is illustrated in Fig. 2. The experiments were performed under two types of boundary conditions: overflow and reflection. The generated wave profile measured at S2 (indicated in Fig. 1) is shown in Fig. 3. The time on the horizontal axis in this figure was set to 0 s when the water level reached its maximum at S2. This wave profile was given at the offshore boundary in the calculations.

As the calculation conditions, the horizontal grid sizes (Δx and Δy) and the vertical grid size (Δz) were set to 0.02 m and 0.005 m, respectively. The calculation time step Δt was set to 0.0025 s, and Manning's roughness coefficient at bed n_b was fixed at 0.010 s/m$^{1/3}$.

Discussion on Reproducibility of Tsunami Flow

First, the numerical analyses with different side wall roughness n is performed for the experiment of overflow condition with fixed bed. Fig. 4 and Fig. 5 show the comparison of measured and calculated water levels and flow velocities at each station indicated in Fig. 1, respectively. Here, the measured and calculated velocities are given for 0.04 m height from the bed. Regarding the water level, the calculated results generally replicates the measured ones regardless of the side wall roughness. However, in terms of velocities at P5 and P8, the calculated results with the small side wall roughness n = 0.014 are considerably different from the measured data. In contrast, the results with the large side wall roughness n = 0.019 are in good agreement with the measured results. In other words, it is very important to set appropriate side wall roughness to accurately reproduce the tsunami flow in the abrupt expansion area.

Next, the analysis with the fixed side wall roughness n = 0.019 was conducted for the experiment under reflection condition. Fig. 6 and Fig. 7 show the comparisons of measured and calculated water levels and flow velocities at each station indicated in Fig. 1, respectively. The calculated results for both the water levels and flow velocities are in good agreement with the measured results. Thus, the developed numerical model was found to sufficiently reproduce the tsunami flow in the abrupt expansion area by setting the side wall roughness appropriately, even if the conditions of the shoreline

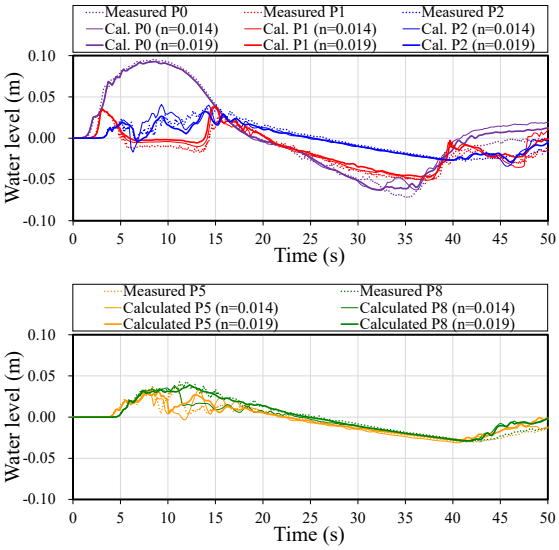

Fig. 4 Comparison of measured and calculated water levels at each station under overflow condition (Top: P0, P1, P2; Bottom: P5, P8).

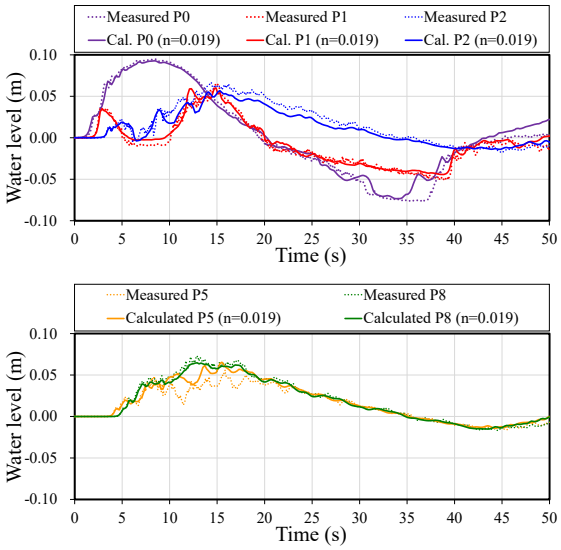

Fig. 6 Comparison of measured and calculated water levels at each station under reflection condition (Top: P0, P1, P2; Bottom: P5, P8).

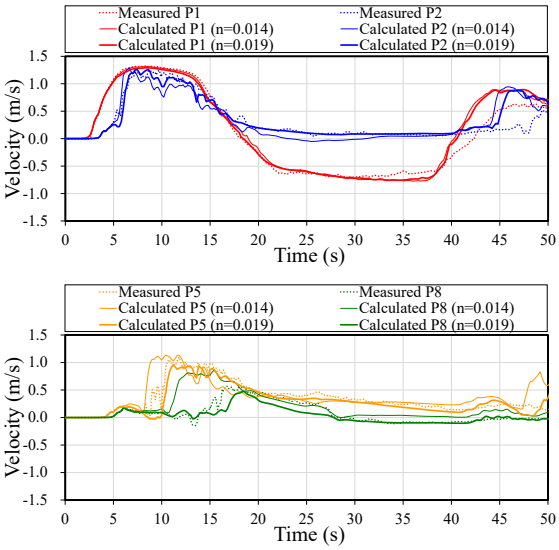

Fig. 5 Comparison of measured and calculated velocities at each station under overflow condition (Top: P1, P2; Bottom: P5, P8).

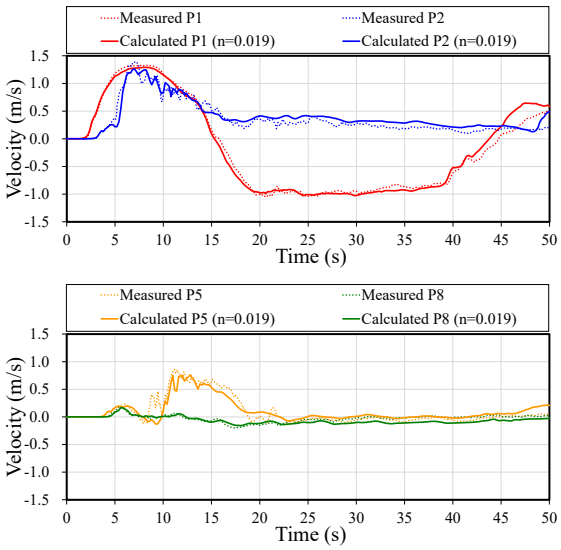

Fig. 7 Comparison of measured and calculated velocities at each station under reflection condition (Top: P1, P2; Bottom: P5, P8).

boundary change.

The horizontal flow velocity vectors at a height of 0.04 m from the bed at time t = 15 s is illustrated in Fig. 8. The eddy viscosity coefficient contours are also shown. Here, the eddy viscosity coefficient ν_t is dimensionless for the kinematic viscosity $\nu = 1.01 \times 10^{-6}$ m^2/s. By comparing the results of n = 0.014 and n = 0.019 under the same shoreline condition of overflow, it was found that the position of the circulation flow center was quite different. In the case of the small side wall roughness n = 0.014, the circulation flow is formed at the back of the abrupt expansion area, and the eddy viscosity coefficient ν_t indicates a large value—800 times greater than the kinematic viscosity ν along the side wall from the narrow pass. Conversely, in the case of n = 0.019, the position of the circulation flow is almost at the center of the abrupt expansion area, and the situation is in good agreement with that observed in the experiment [4]. Thus, it was clarified that the reproducibility of the circulation flow in the abrupt expansion area greatly differs depending on the influence of the side

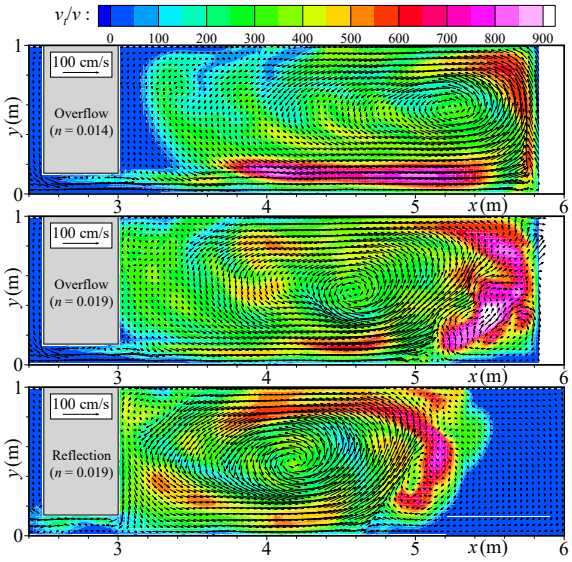

Fig. 8 Calculated flow velocity vectors with eddy viscosity coefficient contours (Top: n = 0.014 with overflow; Middle: n = 0.019 with overflow; Bottom: n = 0.019 with reflection).

wall roughness. Moreover, comparing the results for the overflow and the reflection conditions under the same roughness n = 0.019, the position of the circulation flow under the reflection condition is found to be closer to the block than that under the overflow condition. These situations are also in good agreement with those observed in the experiments, thereby confirming the validity of the model.

Discussion on Reproducibility of Topography Change

Topography change analyses under the movable bed condition were performed with the side wall roughness fixed at n = 0.019. Fig. 9 and Fig. 10 show the comparison of measured and calculated bed variation contours under the overflow and reflection conditions, respectively. In the experiments, salient erosion was observed in the narrow pass where a high flow velocity occurs under both shoreline conditions. Additionally, although severe sedimentation and erosion occurred on the shoreline side from the block in the case of overflow condition, they occurred on the offshore side from the block for the reflection condition. The calculated results are found to reproduce these phenomena well. However, in the calculations, erosion not observed in the experiments occurred near x = 4 m on the opposite side of the narrow pass. The cause of this erosion has not yet been clarified. Therefore, we intend to investigate the cause of this erosion in the future by introducing a new estimation method of the bed shear stress or another sediment transport formula.

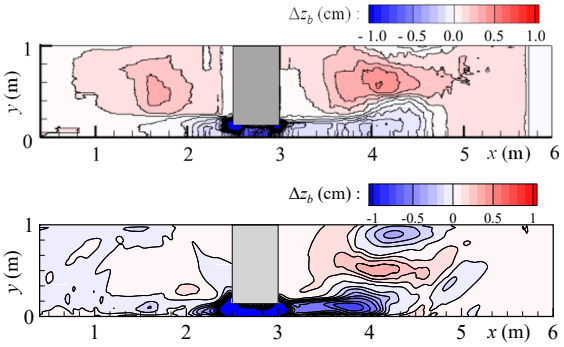

Fig. 9 Comparison of measured and calculated bed variation contour under overflow condition (Top: Measured; Bottom: Calculated).

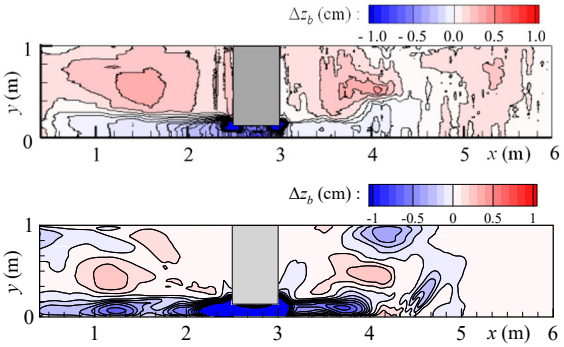

Fig. 10 Comparison of measured and calculated bed variation contour under reflection condition (Top: Measured; Bottom: Calculated).

CONCLUSIONS

In this study, the authors investigated the applicability of a 3D RANS numerical model for the prediction of flow and topography changes induced by tsunamis in an abrupt expansion area with different shoreline conditions of overflow and reflection. In the developed model, the SST k–ω turbulence model was adopted to accurately evaluate the circulation flow in the abrupt expansion area, and the nonequilibrium bed-load and suspended-load transport were considered in the topography change model. The model was applied to the laboratory experiments conducted by Arimitsu and Kawasaki [4]. Consequently, the importance of setting the appropriate side wall roughness to accurately reproduce the tsunami flow in the abrupt expansion area using 3D RANS models was clarified. Moreover, the developed numerical model was found to reproduce the tsunami flow and topography changes in an abrupt expansion area with different shoreline conditions. However, in the calculated results, erosion was noted on the opposite side of the narrow pass, which was not observed in the experiments. In

our next work, we intend to clarify the cause of this erosion by modifying the model.

ACKNOWLEDGMENT

The authors appreciate the valuable comments from the reviewers. This work was supported by JSPS KAKENHI Grant Number JP21K04274.

REFERENCES

[1] Yoshii, T., Ikeno, M., Matsuyama, M. and Fujii, N., Pick-up rate of suspended sand due to tsunami, Coastal Eng. Proc., Vol. 1, No. 32, 2010, https://doi.org/10.9753/icce.v32.sediment.12

[2] Kihara, N., Fujii, N. and Matsuyama, M., Three-dimensional sediment transport processes on tsunami-induced topography changes in a harbor, Earth, Planets and Space, Vol. 64, No. 10, 2012, pp. 787-797.

[3] Arimitsu, T., Kawasaki, K. and Takahashi, T., Numerical simulation of bottom topography change due to tsunami in coastal sea area with abrupt expansion region, Journal of Japan Society of Civil Engineers, Series B2 (Coastal Engineering), Vol. 72, No. 2, 2016, pp. I_607-I_612. (in Japanese with English abstract).

[4] Arimitsu, T. and Kawasaki, K., Tsunami-induced topography change in coastal sea area with narrow pass and influence of shoreline condition, Ann., Journal of Japan Society of Civil Engineers, Series B3 (Ocean Engineering), Vol. 33, No. 2, 2017, pp. I_666-I_671. (in Japanese with English abstract).

[5] Kajikawa, Y. and Kuroiwa, M., Numerical simulation of 3D flow and topography change in harbor caused by tsunami, Proc. 10th int. conf. on Asian and Pacific Coasts, 2019, pp. 183-190.

[6] Hirt, C. W. and Sicilian, J. M., A Porosity technique for the definition obstacle in rectangular cell meshes, Proc. 4th int. conf. on Numerical Ship Hydrodynamics, 1985, pp. 1-19.

[7] Menter, F. R., Kuntz, M. and Langtry, R., Ten years of industrial experience with the SST turbulence model, Turbulence, Heat and Mass Transfer, Vol. 4, 2003, pp. 625-632.

[8] Uchida, T. and Fukuoka, S., Numerical calculation for bed variation in compound-meandering channel using depth integrated model without assumption of shallow water flow, Advances in Water Resources, Vol. 72, 2014, pp. 45-56.

[9] Ashida, K. and Michiue, M., Study on Hydraulic resistance and bed-load transport rate in alluvial stream, Proceedings of the Japan Society of Civil Engineers, Vol. 206, 1972, pp. 59-69. (in Japanese).

[10] Iwagaki, Y., Fundamental study on critical tractive force (I), Hydrodynamical study on critical tractive force, Trans. Japan Soc., Civil Engineer, Vol. 41, 1956, pp. 1-17.

[11] Takebayashi, H. and Okabe, T., Geometric characteristics of braided channel on non-uniform sediment bed, The Int. Cong. INTERPRAVENT, 2002. in the Pacific Rim, Congress Publication, 1, 2002, pp. 79-89.

[12] Itakura, T. and Kishi, T., Open channel flow with suspended sediments, J. of Hydraulic Division, ASCE, Vol. 106, No. 8, HY8, 1980, pp. 1325-1343.

[13] Rubey, W. W., Settling velocity of gravel, sand, and silt particles, American Journal of Science, Vol. s5-25, No. 148, 1933, pp. 325-338.

[14] Shu, C.-W., High-order finite difference and finite volume WENO schemes and discontinuous Galerkin Methods for CFD, International Journal of Computational Fluid Dynamics, Vol. 17, No. 2, 2003, pp. 107-118.

[15] Patankar, S. V., Chapter 5, Numerical heat transfer and flow, McGraw-Hill, New York, 1980.

[16] Ushijima, S. and Nezu, I., Computational method for free-surface flows on collocated grid with moving curvilinear coordinates, J. of Japan Society of Civil Eng., Vol. 698, No. II-58, 2002, pp. 11-19. (in Japanese with English abstract).

11th Int. Conf. on Geotechnique, Construction Materials & Environment, Kyoto, Japan, 3-5 November 2021, ISBN: 978-4-909106063 C3051

EVALUATION OF UNDERGROUND SPACE FOR TSUNAMI EVACUATION SAFETY BY AGENT-BASED SIMULATION

Akira Takahashi [1], Kensuke Yasufuku [1] and Hirokazu Abe [1]

[1] Cybermedia Center, Osaka University, Japan

ABSTRACT

This study quantitatively evaluates the safety of an evacuation guidance plan created for a large underground facility in preparation for the flooding that would result from earthquake-related tsunamis and examines the effects of evacuation route obstacles via simulations. The main findings are as follows:

1. In some scenarios, the occurrence of evacuation route obstructions will cause delays in evacuation completion times due to evacuee congestion on stairways.
2. By comparing the results of each scenario with the evacuation safety plan prepared by the facility management company, the impacts on safety could be evaluated quantitatively.
3. When considering evacuation route obstacles, evacuation efficiency impacts differed depending on which stairways and/or corridors became unavailable.
4. The scenarios in this study showed that evacuation time impacts were more severe in cases involving blocked corridors than in cases involving blocked stairways.

Keywords: Evacuation simulation, Large-scale underground mall, Flooding, Evacuation guidance plan, Tsunami

INTRODUCTION

In Japan, many large cities have constructed extensive underground facilities in areas below sea level, and such spaces now cover widespread areas. These developments have resulted in a need for social and economic risk management plans to prevent or minimize human casualties and damage to infrastructure in underground facilities such as subways in the event of large-scale flooding caused by torrential rains and earthquake-related tsunamis.

For example, in the Great East Japan Earthquake that occurred on March 11, 2011, a massive tsunami that exceeded predictions caused extensive flooding damage over a widespread area, thereby forcing a fundamental review of previous disaster prevention measures [1].

The resulting Act on Development of Areas Resilient to Tsunami Disasters 2011 requires the managers of underground facilities such as basement shopping malls, etc., in areas designated as Tsunami Disaster Prevention Zones to prepare and publish evacuation safety plans detailing measures that will ensure smooth and rapid evacuations from their facilities in the event of a tsunami. However, when attempting to verify whether all affected persons can evacuate safely in the case of a major earthquake-related tsunami, it is necessary to consider various route obstacles that may result when the disaster first strikes. For example, evacuation routes may be blocked by falling shelves or damage to glass windows, walls, or ceiling materials, which would affect evacuation safety and efficiency.

With the above points in mind, it is crucially important to prepare alternative evacuation routes in anticipation of cases where the optimal evacuation routes are no longer available during a disaster.

However, evacuation routes are often determined empirically, and various conditions impose limitations on the ability of facility managers to evaluate their evacuation safety plans. To assist such efforts, multi-agent simulation systems, which are increasingly being used to evaluate the evacuation safety of buildings, can quickly be adapted to predict the evacuation properties of underground facilities under various conditions [2].

For example, using a multi-agent crowd simulator, Yamada et al. (2013) reported on human behaviors during the evacuation of an underground facility directly connected to an anonymous terminal station after an earthquake disaster [3]. However, that study did not consider inflows from connected underground malls that may host numerous commercial facilities. Separately, Kiyono et al. (2001) and Nakamura et al. (2018) conducted detailed traffic surveys of actual underground malls and used the collected data to conduct evacuation simulations [4],[5]. However, these studies did not consider flood damages that would result from tsunamis or torrential rains.

In other studies, Takizawa (2015) and Goda (2014) estimated the evacuation capacity of connected buildings in their target areas and the number of pedestrians during rush hour periods for a large-scale underground shopping mall. They then used that information in basic simulations of vertical

evacuations to the connected buildings under assumed flooding conditions. Their results showed severe evacuee congestion on certain staircases, which delayed evacuation completion times, and that the number of evacuees would exceed the capacities of some connected buildings [6],[7].

Yamamoto (2019) proposed a mathematical programming problem to minimize the evacuation completion time of an underground shopping mall in Osaka City, along with a workflow to convert general geometric spatial data into graphical data. Ultimately, the accuracy of the proposed method was confirmed by multi-agent simulations [8]. In another study, in order to verify the evacuation safety of buildings in the event of a major earthquake, Yasufuku (2017) proposed an evacuation analysis method that uses a multi-agent system to consider multiple path obstructions caused by damage to non-structural materials [9].

However, the abovementioned studies did not evaluate evacuation cases using surface-level exits and specific evacuation safety plans prepared by facility management companies.

Accordingly, this study quantitatively evaluates the safety of the evacuation guidance plan of a large underground facility prepared by the facility management company in anticipation of the flooding hazards that can result from earthquake-related tsunamis and examines the effects of evacuation route obstacles via simulations.

RESEARCH OBJECT

Underground mall

Our study object is an underground mall (Whity Umeda) located near JR Osaka Station in Osaka City, Japan, which is part of an even larger underground complex called the Osaka Umeda Underground Mall. The subject underground mall is connected to the main stations of two Osaka Metro Co., Ltd. subway lines and serves approximately 400,000 daily users, which is the highest number of all the underground malls and underpasses in Osaka City. However, in the event of the long-predicted Nankai Trough Earthquake, the area around this underground mall is expected to be inundated by floodwater up to two meters deep [10].

Figure 1 shows the floor plan and outline of the subject facility, which has a 31,336 m^2 total floor area, two basement levels, 25 stairways to the surface level, 27 building connections, and 182 stores and restaurants. The nine areas in Fig. 1 show how the floor area was divided by the facility management company for the purpose of estimating the number of people in the underground mall.

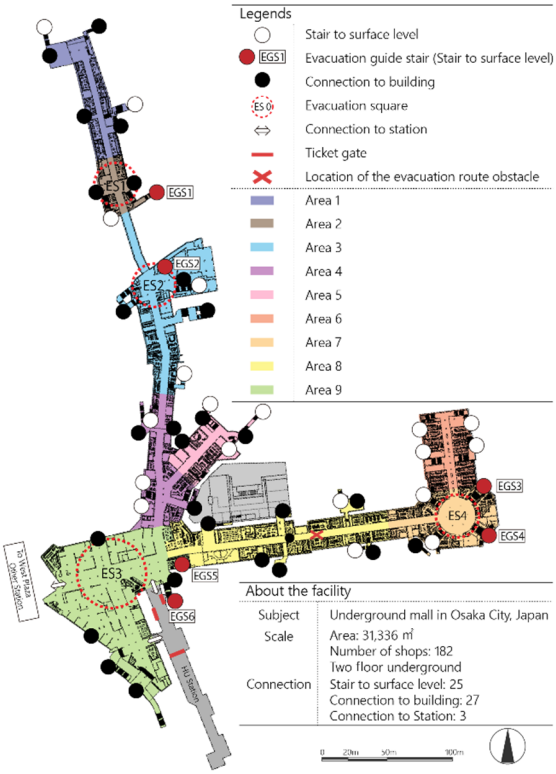

Fig. 1 Floorplan of underground mall

Evacuation Safety Plan

The evacuation safety plan prepared and published by the facility management company has been revised several times to improve evacuation safety and efficiency [11]. According to the newest version, the evacuation locations in the event of a tsunami disaster include the surface area to the east of the underground shopping mall that is outside the expected flooding zone and the second or higher floors of mall-connected buildings. The primary routes to these evacuation sites are, in principle, via the nearest evacuation stairways.

However, the Osaka City Underground Flooding Prevention Council has estimated that the maximum number of people that could be evacuated from the target underground mall and surrounding stations to the second and higher floors of connecting buildings at 18:00 on weekdays at approximately 1,700 people, which would make it difficult to evacuate all the affected visitors and commuters to connecting buildings [12].

As for the guidance method, although the facility evacuation safety plan states that when the plan is in effect, evacuees are to be led to the nearest safe stairways and persons outside are to be prevented from entering the underground mall, the plan does not provide a detailed description of the evacuation guidance method. However, according to a facility management company official interviewed in conjunction with this study, even though the

evacuation safety plan does not contain a specific evacuation guidance method, it is expected that the evacuation will proceed in accordance with the Evacuation Timeline that was prepared in the event of a major earthquake.

In that timeline, evacuation to connecting buildings is not anticipated because the estimated number of people that can be accommodated in those buildings is likely to be too small in relation to the number of people in the mall requiring evacuation. Therefore, in principle, the tsunami evacuation will proceed based on horizontal movements that lead people to the east side of the underground mall, which is outside the anticipated flooding area.

Figure 2 shows the depth of anticipated flooding in the vicinity of JR Osaka Station, including the underground mall, in the event of a major Nankai Trough earthquake. The target line for horizontal evacuation is the area more than 300 m east of Shin-Mido-Suji street, which is indicated by the black dotted line in the figure. Here, it should be noted that physically challenged and injured persons who have difficulty walking will be evacuated to connected buildings, but this matter is outside the scope of this paper.

One of the purposes of the timeline under consideration here is to simplify evacuation guidance. This is because such guidance is primarily expected to be provided by personnel who normally perform daily security and facility management duties, and the number of such persons is limited. This, in turn, imposes a limit on their ability to check the safety of the evacuation stairways, including those to surface level, in a limited amount of time. After considering stairway widths, access to the horizontal evacuation target line, the underground mall structure, and available human resources, the number of evacuation guidance

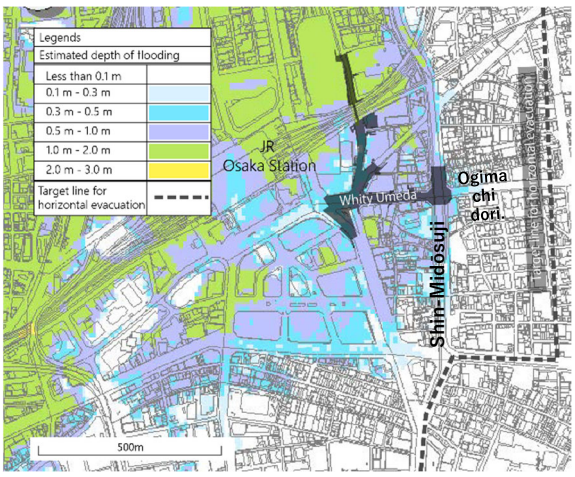

Fig. 2 Map of assumption of flooding [12]
Note: This figure was added and modified by the author from the figure in Ref. 12.

stairways (EGSs) in the timeline was limited to six (Table 1).

Once an evacuation has been announced, evacuees are first expected to gather and wait at the four evacuation squares (ESs), established by the facility management company, shown by the red dotted circles in Fig. 1. Then, after facility management personnel have confirmed the safety of the evacuation stairways and the surface level exits, they will be directed to evacuate to the EGS sequentially while following the specific evacuation instructions provided.

Table 1 Width of each EGS

	EGS1	EGS2	EGS3	EGS4	EGS5	EGS6
Width(mm)	3000	1800	5400	5400	1850	3585

Evacuation Timeline

Figure 3 shows the specific steps in the Evacuation Timeline. After a disaster occurs, evacuees will first act to protect themselves (Act 01). Next, they are expected to move to the nearest ES while following instructions provided by store staff members and public address system announcements given by underground mall facility managers (Act 02). Simultaneously, facility managers will confirm the safety of the EGSs and divide the areas with ropes to prevent the evacuation flow from crossing into Area 9 (Fig. 4). This is to ensure smooth evacuation guidance in Area 9, where the largest concentration of evacuees is expected.

Next, the managers place staff members at each ES to handle crowd control. Because it will take management staffers approximately eight minutes to confirm the safety of each EGS and its surface area exit after the disaster starts, the evacuation to surface level will begin when this process is complete. The evacuees will then be guided from each ES to the surface level exits via the EGSs.

More specifically, evacuees in ES1 and ES2 will use EGS1 and EGS2, respectively (Act 05), while evacuees in ES3 and ES4 will use EGS3 and EGS4 (Act 06). Evacuees in ES3 on the south side, which will be divided by ropes, will use EGS5 and EGS6 (Act 07) (Fig. 4). Evacuee inflows are expected from the West Plaza and Higashi Umeda station (HU station), which are connected to Area 9. West Plaza inflowing evacuees (Act 03) will be directed to follow the path of Act 06 evacuees, and evacuees from HU station (Acts 04, 08, and 09) will follow the path of Act 07 evacuees.

After evacuees arrive on the surface (Act 10), they will be instructed to horizontally evacuate (walk) until they pass the target line into areas where flooding is not expected (Act 11). In this study, the evacuation simulation concludes with Act 10. Since

the expected arrival time of a tsunami in the JR Osaka Station area is estimated to be 150 minutes after the Nankai Trough Earthquake occurrence, the target time for Act 11 completion is 140 minutes.

The distance from the furthest EGS to the target line for horizontal evacuation is about 500 meters, which is the distance an average person can normally be expected to walk in about 10 minutes. However, considering the enhanced need for safety and the potential for confusion on the surface due to the earthquake, we assume that the travel time will be about 20 minutes. Therefore, the target time to complete the Act 10 evacuation is 120 minutes after the earthquake occurrence.

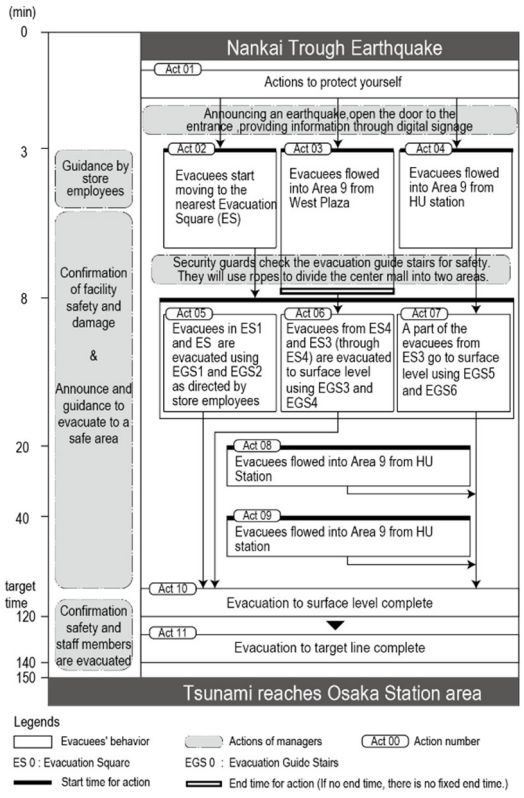

Fig. 3 Evacuation timeline flowchart

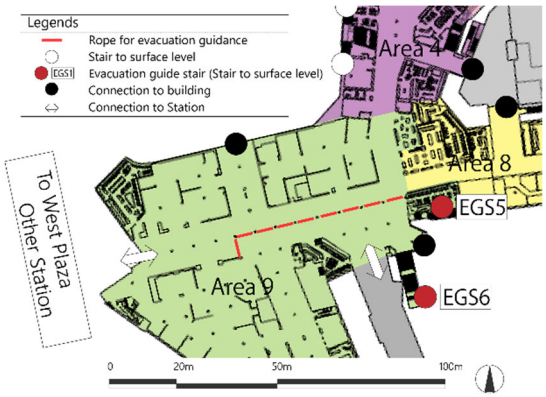

Fig. 4 Division of Area 9 (ES3)

SIMULATION SOFTWARE

Pathfinder simulation software (Thunderhead Engineering Consultants, Inc., Manhattan, KS) is used in this study [13], [14]. Pathfinder is an agent-based simulation software that can create model structures with two-dimensional navigational geometry. This navigational geometry is based on simulating the flow of motions in a room and is suitable for reproducing complex shapes.

In the simulation, navigation geometries are grouped by rooms, and adjacent rooms are connected by doors and stairways. To assign individual behaviors to each occupant, attributes called profiles are used. When setting up an individual profile, various characteristics such as body size, movement speed, and collision behavior can be defined. Behavioral patterns can also be used to define various instructions to the occupants. Thus, occupants can be classified by profiles and behavior patterns.

Simulator algorithm

When an occupant in the simulation moves to a specific destination, the process involves three steps: path planning, path generation, and path following.

Path planning is the process of determining the path to a destination. Each occupant has cost information for local and global targets and the expected waiting times. Since the shortest route is not necessarily the fastest, cost calculations are made for each occupant's route to their destination. In other words, by calculating the route to the room exit and the route to the destination after exiting the room separately, the optimum route can be selected based on cost. In addition, the door queue cost is also calculated, after which a path to that door that the occupant can follow is generated.

Once a local target is selected by path planning, a path to the target is needed. To produce it, the Pathfinder application uses the A* search algorithm and a triangulated navigation mesh [15]. The resulting path is represented by a series of points on the triangular edges of the mesh. In order for the occupants to move smoothly along the resulting path, they proceed to points on the mesh called waypoints (Fig. 5) [16].

Path following is conducted using a combination of inverse steering [17] and collision handling algorithms. These algorithms enable occupants to deviate from the path in order to avoid obstacles while still heading in the correct direction toward their goal [14]. The inverse steering method evaluates several discrete directions of movement based on the cost factors between the old and new paths.

Potential new paths are calculated by various cost factors, including velocity, acceleration, and

waiting time until the path with the lowest cost factor is identified and set as the alternative path. While moving, each occupant tries to maintain a predetermined behavior pattern with regard to distance from walls and other occupants, walking speed, obstacle avoidance, and turning.

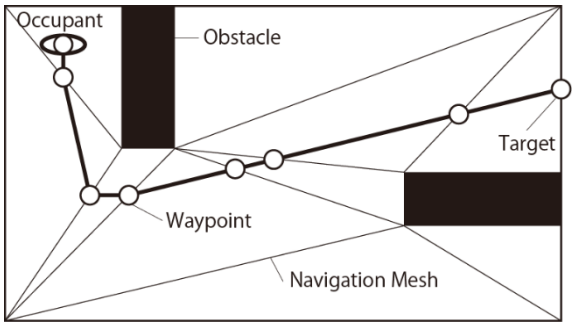

Fig. 5 An occupant's path and a waypoint on the mesh

In this experiment, referring to the evacuation safety verification method supported by the Ministry of Land, Infrastructure, Transport and Tourism (MLIT), the maximum walking speed was set to 1.0 m/s for level surfaces, and 0.45 m/s was set the maximum speed for traveling up stairways [18]. For the other required path selection parameters, the initial Pathfinder software values were used. For more details, please refer to the Pathfinder Technical Reference Manual [14].

Simulation data

The underground mall data modeled in our simulation was created from the overall floor plan of the facility, the floor plans of each store, and stairway data provided by the facility management company.

The input data was the number of people in the facility, which was calculated from a pedestrian-traffic volume survey conducted by the facility management company. That pedestrian-traffic volume survey was conducted on two weekdays and two holidays in 2020, and the average survey value of those days was selected as the traffic volume. The number of visitors and commuters was calculated by dividing the underground mall into nine areas based on the points surveyed in the pedestrian-traffic volume survey, as shown in Fig. 1.

The input data for the number of evacuees were taken at 18:00 on weekdays when the number of people in the underground mall is normally the highest, and the initial positions of each evacuee were randomly assigned, as shown in Fig. 6. Table 2 shows the input values for each area and the inflow numbers of evacuees used in the simulation. The primary evacuee inflows are expected to come from two locations.

The first is the inflow from HU station, which is expected to come in two waves. The primary wave (beginning 20 minutes after the earthquake) is assumed to be people temporarily stopped in the station concourse and platforms, and the second wave (beginning 40 minutes after the earthquake) will consist of passengers evacuating from trains that stopped between stations after the earthquake.

The second inflow, which will be people from the West Plaza connected to Area 9, is calculated based on the number of people staying in the plaza and the number of people coming from the stations. This inflow is assumed to consist of about 3,898 people in five minutes. West Plaza is connected to many of Osaka City's major stations, including Metro and private railway terminal stations, as well as large department stores, making it a major crossway of the extended Osaka underground mall area.

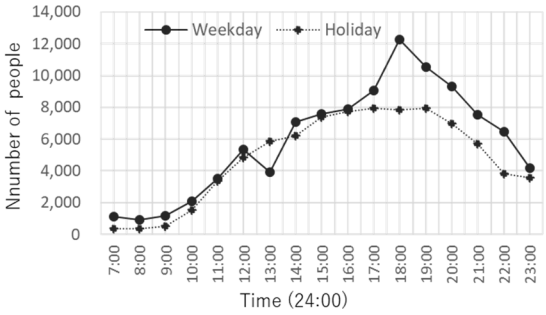

Fig. 6 Numbers of mall visitors by time

Table 2 Number of people in simulation (Weekday/18:00)

Number of People in Areas	Area 1		158
	Area 2		73
	Area 3		1,089
	Area 4		1,149
	Area 5		1,122
	Area 6		577
	Area 7		517
	Area 8		764
	Area 9		6,823
		total	12,272
Number of People inflow from HU Station	on the platform		114
	1 st inflow(after 20 min)		647
	2 nd inflow(after 40 min)		1,296
		total	2,057
Number of People inflow from West Plaza (in 5 minutes)			3,898

Evacuation route obstructions

Figure 3 shows Scenario 0, which is the baseline of the Evacuation Timeline. The following two

conditions are considered in each of the five scenarios shown below: situations in which the EGSs cannot be used due to a blocking obstacle such as a collapsed ceiling, and situations in which the corridors that serve as evacuation routes cannot be used because they are partially blocked. Scenarios 1 through 5 are set as shown below:

- Scenario 0 (S0): Evacuation Timeline baseline (no incident)
- Scenario 1 (S1): EGS4 blocked by an obstacle
- Scenario 2 (S2): Route in Area 8 partially blocked by an obstacle
- Scenario 3 (S3): Route in Area 8 blocked by an obstacle
- Scenario 4 (S4): EGS5 blocked by an obstacle
- Scenario 5 (S5): EGS6 blocked by an obstacle

The Area 8 corridor width is about 5000 mm, and in Scenario 2, it is assumed that a 2500 × 3500 mm area is no longer passable (Fig. 1).

RESULTS AND DISCUSSION

Table 3 shows the evacuation completion time, average evacuation time, and average congestion time for each scenario. The evacuation completion time indicates the time when the last evacuee exited the facility. The average evacuation time indicates the average time it took for each evacuee to exit the facility, while the average congestion time indicates the average of the total time during which the walking speed of each evacuee was less than 0.25 m/s.

Table 3 shows that, in completion time comparisons, S0 and S4 were almost the same; S1 and S2 increased 7% and 10% over S0, respectively; while S3 and S4 increased significantly to 62% and 55% over S0, respectively. However, for all scenarios, the evacuations were completed within the target evacuation time of 120 minutes after the earthquake occurrence.

Both the average evacuation time and the average congestion time generally showed the same trends as the evacuation completion time, but for S5, the ratio of increase in the evacuation and congestion completion time averages were smaller than the increase ratio in the evacuation completion time. When compared to S0, S3 showed an increase of more than three times in the average congestion time.

Figures 7 and 8 show the total number of evacuees by time and EGSs for each scenario, respectively. The slope in the figures indicates the evacuation efficiency, with a steeper indicating a more efficient evacuation. These figures indicate that some evacuation routes suffered more unavailability impacts than others. For example, compared with S0, the largest impact on evacuation efficiency is seen in S3, and the slope in Fig. 7 becomes shallower shortly after the start of evacuation.

In Figure 8, it can be seen that in S3, evacuee congestion occurs in the vicinity of EGS5 and EGS6. Hence, in order to more efficiently distribute the evacuees, it might be advisable to direct a portion of the EGS5 and EGS6 evacuees to EGS1 and EGS2. In the case of S4, where EGS5 was not available, it can be seen that the Fig. 7 slope was almost unaffected. In contrast, in the case of S5, where EGS6 was not available, the Fig. 7 slope rapidly became shallow around 2000 seconds after the disaster onset.

From the number of evacuees processed via EGS5 and EGS6, it can be seen that EGS6, which is 3585 mm wide, was able to provide a sufficient throughflow. In contrast, EGS5, which is the narrowest of the evacuation stairways (1850 mm), was considered to have insufficient flow capacity for S4 and S5, as shown in Fig. 8. Therefore, if EGS6 becomes unavailable, a flexible response such as redirecting evacuees to EGS3 and EGS4 will be required.

Comparing S2 (where the corridor is partially blocked) and S3 (where the corridor is completely

Table 3 Results of the evacuation simulation each scenario

	Completed time for evacuation		Average time for evacuation		Average time for congestion	
	(sec)	/S0 (%)	(sec)	/S0 (%)	(sec)	/S0 (%)
Scenario 0 (S0)	2,875		1,248		436	
Scenario 1 (S1)	3,092	108	1,606	129	761	175
Scenario 2 (S2)	3,254	113	1,597	128	766	176
Scenario 3 (S3)	4,666	162	2,029	163	1,343	308
Scenario 4 (S4)	2,875	100	1,356	109	536	123
Scenario 5 (S5)	4,475	156	1,590	127	767	176

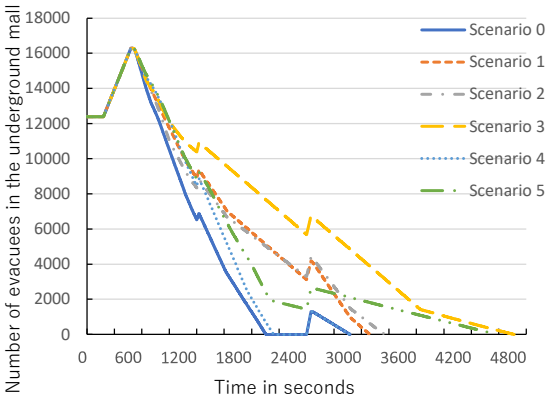

Fig. 7 Number of evacuees by time

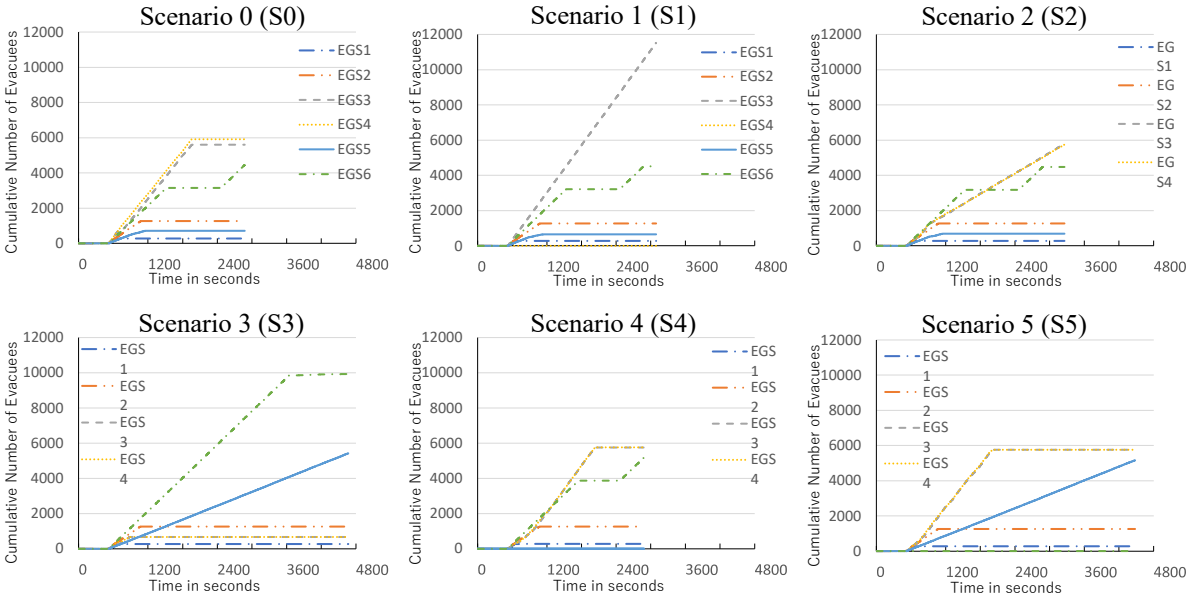

Fig. 8 Number of evacuees by stairways in each scenario

closed), it can be seen that the S3 evacuation completion time was 1.4 times longer. In the simulation, the evacuation efficiency rates of EGS3 and EGS4 were strongly affected by the flow rate congestion that resulted from a bottleneck at the end of the corridor connecting Area 9 to Area 8.

Therefore, when only half the corridor width is available, the evacuation efficiency of EGS3 and EGS4 is approximately 50%. In S2, the final evacuees were in the direction of EGS3 and EGS4, so if the passageway flow rate of Area 8 is reduced due to a larger blockage area, the impact is expected to be more severe.

CONCLUSIONS

This study was conducted to quantitatively evaluate the safety of evacuation plans for the inundation hazards in large underground spaces that might result from earthquake-related tsunamis and to examine the effects of evacuation route obstacles. The main findings are as follows:

1. In some scenarios, evacuation route obstructions caused delays in evacuation completion times due to stairway congestion in areas where evacuees were most concentrated.
2. By comparing the results with the evacuation safety plan prepared by the facility management company and the results of simulation each scenario, we could evaluate safety impacts quantitatively.
3. When considering evacuation route obstructions, the impact on evacuation efficiency differed depending on the stairways and corridors that became unavailable.
4. The scenarios in this study showed that impacts on evacuation time were more severe in cases involving closed corridors than in cases of closed stairways.

When considering evacuation route obstacles, we found that the impact on the evacuation guidance plan differed significantly depending on which stairways and corridors became unavailable. Therefore, when route obstacles appear, it is imperative to consider redirecting evacuees away from congested stairways and towards other stairways in order to improve evacuation safety.

However, in this experiment, the most severe impact was seen in the scenario in which the corridor was blocked, thus indicating that the possibility of blocked corridors requires more attention, primarily because the number of stairways to which evacuees can be redirected will be limited.

ACKNOWLEDGMENTS

This work was supported by the Japan Science and Technology Agency (JST) Future Society Creation Project JPMJMI20D1 and Osaka Chikagai Co., Ltd., to whom we would like to express our sincere gratitude.

REFERENCES

[1] Cabinet Office, Government of Japan: Disaster Management in Japan, DIRECTOR GENERAL FOR DISASTER MANAGEMENT CABINET OFFICE, GOVERNMENT OF JAPAN, 3. 2015 http://www.bousai.go.jp/1info/pdf/saigaipamphlet_je.pdf (accessed 23. 3. 2021)

[2] Urban Transport Facilities Division of City Bureau of Ministry of Land, Infrastructure, Transport, and Tourism: Guideline for Safety Evacuation Measure for Underground Malls, 2020. 3 (in Japanese)
[3] Yamada, T., Ohmori, T., Hiroi, U., Fukui, K.: Study of Evacuation from the Underground Space around a Large-Scale Station Using the Crowd Simulation, Proceedings of the Symposium on Underground Space, Vol. 18, pp. 137-144, 2013. 1 (in Japanese)
[4] Kiyono, J., Toki, K., Inukai, N., Takeuchi, T.: Evaluation of Safety of Evacuation Behavior from an Underground Space during an Earthquake, Proceedings of JSCE 689, pp. 31-43, 2001. 10 (in Japanese)
[5] Nakamura, E., Koike, N.: Crowd Congestion Estimation and Evacuation Planning Based on Real Number of Underground Mall Visitors – Case Study of Central Park in Nagoya, Journal of Japan Society of Civil Engineers, Ser. F6 (Safety Problem), Vol. 74, No. 2, pp. 93-100, 2018 (in Japanese)
[6] Takizawa, A., Takagi, N., Taniguchi, Y.: A Multi-Agent Based Simulation of Evacuation from the Umeda Underground Malls to Connected Buildings at the Time of Flooding, Summaries of Technical Papers of Annual Meeting, Architectural Institute of Japan, E-1, pp. 749-750, 2015. 7 (in Japanese)
[7] Goda, S., Taniguchi, Y., Yoshinaka, S., Takizawa, A.: Study on Tsunami Evacuation Plan at the Underground Mall in front of Osaka Station, Summaries of Technical Papers of Annual Meeting, Architectural Institute of Japan, B-2, pp. 147-148, 2014. 7 (in Japanese)
[8] Yamamoto, R., Takizawa, A. Partitioning Vertical Evacuation Areas in Umeda Underground Mall to Minimize the Evacuation Completion Time. Rev Socionetwork Strat 13, 209–225 (2019). https://doi.org/10.1007/s12626-019-00037-1
[9] Yasufuku K and Nagano Y, Evacuation Analysis of Several Impassable Routes by Using Multi-agent System, Summaries of Technical Papers of Annual Meeting, Architectural Institute of Japan, pp. 387-388, 2017. 7 (in Japanese)
[10] Osaka City Underground Flooding Prevention Council: Osaka City Underground Flooding Prevention Guidelines, 2018. 3 (in Japanese)
[11] Osaka Chikagai Co.,Ltd.: Umeda Underground Space Evacuation and Flooding Prevention Plan, 2006.12 (2017.7 revision) (in Japanese)
[12] Osaka City Underground Flooding Prevention Council: Flooding Prevention Plan for Underground Spaces around Osaka Station Ver. 1, 2016. 3 (in Japanese)
[13] Thunderhead Engineering Consultants Inc.: Pathfinder User Manual https://support.thunderheadeng.com/docs/pathfinder/2020-3/user-manual/ (accessed 2021. 6. 3)
[14] Thunderhead Engineering Consultants Inc.: Pathfinder Technical Reference Manual https://support.thunderheadeng.com/docs/pathfinder/2020-5/technical-reference-manual/ (accessed 2021. 6. 3)
[15] Hart P, Nilsson N, Raphael B: A formal basis for the heuristic determination of minimum cost paths. IEEE Trans Syst Sci Cybern 4:100–107, 1968 https ://doi.org/10.1109/TSSC.1968.300136
[16] Geraint Johnson: Smoothing a Navigation Mesh Path, AI Game Programming Wisdom 3, ed. S. Rabin. pp. 129-139, 2006.
[17] Heni Ben Amor, Jan Murray, and Oliver Obst: Fast, Neat, and Under Control: Arbitrating Between Steering Behaviors, AI Game Programming Wisdom 3, ed. S. Rabin. pp. 221-232, 2006
[18] Ministry of Construction: Ministry of Construction Notification, No. 1441, 1-4, 2000. 5. 31 (in Japanese)

11th Int. Conf. on Geotechnique, Construction Materials & Environment,
Kyoto, Japan, 3-5 November 2021, ISBN: 978-4-909106063 C3051

ON GEOGRAPHIC INFORMATION MAP BY THE SPATIAL ATTRACTIVENESS

Ami Hasegawa[1], Kazunari Tanaka[1]

[1] Osaka Institute of Technology, 5-16-1, Omiya, Asahi-ku, Osaka, Osaka, Japan

ABSTRACT

Currently, various districts have been redeveloped in Japanese cities to make the city comfortable. However, this change sometimes reduce the spaces and playgrounds that children can freely use. Creating a city that is easier and more enjoyable for children to live in is an issue for future urban development. In order to address this, it is necessary to understand the image of the city that children will find attractive. The purpose of this study is to clarify the elements and shapes of the cityscape that influence the image of the city by comparing the spatial cognition between children and adults in the town where they live. As for the research method, we conducted a paired comparison method using photographs of roads that actually exist and a cognitive map survey of elementary school students on spatial cognition of the streets that they use on a daily basis, and analyzed the results. In the paired comparison method, it found that the path preferred by children and the path preferred by adults tended to be different. In the children's cognitive maps, the places where direction changes, such as curves and intersections, were drawn disproportionately larger than they actually are. And the lively spaces where shops are grouped close together, such as shopping streets, are drawn proportionately wider and shorter than actual street width and length.

Keywords: Cognitive Map, Color, Image, Street

INTRODUCTION

In modern times, various areas and districts in Japan have been redeveloped in cities and suburbs to make our life comfortable. However, the alteration sometimes reduce the spaces and playgrounds that children can freely use. We think that children can gain a lot from interacting with nature, people, and various physical spaces and things in their childhood. By thinking and playing around for themselves, the children make new discoveries and grow. Changes in the environment centered on public spaces have a strong impact on the physical and mental health of children. In order to solve such problems in the future, we should investigate the differences in objects and places that adults and children find attractive, and propose urban space designs that both adults and children find attractive.

PURPOSE AND METHOD

Creating a city that is easier for both children and adults to live in and enjoy is an issue for future urban development. In order to create them, we need to understand the image of a city that children will find attractive.

The purpose of this study is to clarify the elements and shapes of the cityscape that influence the image of the city by comparing the spatial cognition between children and adults in the town where they live.

The research method will be divided into two for children and adults according to their purpose. One is to conduct a route selection experiment via the paired comparison method using photographs of actual roads, extract the components of each photograph, and compare them with the results of the psychological experiment. We will then find if they like them or not. The second is to conduct a cognitive map survey using the basic drawing method, to examine the distortion between the elements of extraction and actual elements, with the difference between the drawn cognitive space and the actual space. We will find what kind of place they usually see and what elements you can easily remember.

The Developmental Stage according to the study of J. Piaget is 12 years and over. In the experiment in this study, 18 years old and over are the subjects as adults. The children, 10 to 12 years old are targeted in consideration of the specific investigation stage and formal operation period. Regarding the image of the city, we conducted research based on Chapter 2 Cognitive Space and Research Targets from the study of urban distortion in children's spatial cognition conducted by Sakai et al [1].

Research on children's cognitive space has been conducted for a variety of purposes and methods [2][3][4][5]. In this study, these results are also referred to.

ROUTE SELECTION EXPERIMENT

Experiment Contents

A paired comparison method was performed with the cooperation of 150 adults aged 18 and over and 184 children in grades 5 and 6 from two elementary schools, using 13 photographs of actual roads. From

the 13 photographs, the ratio of the area occupied by spatial components such as plants, buildings, and roads in the photographs was calculated, and experiments were conducted by comparing the results of the paired comparison method with adults and children. Furthermore, based on the results of the comparison, the photographs were visually analyzed.

Experimental result

Comparison of selectivity and each component

Fig.1 and Fig.2 shows the area ratio occupied by each spatial component in the photographs from the 13 photographs, and compares them between adult and child together with the results of the paired comparison method.

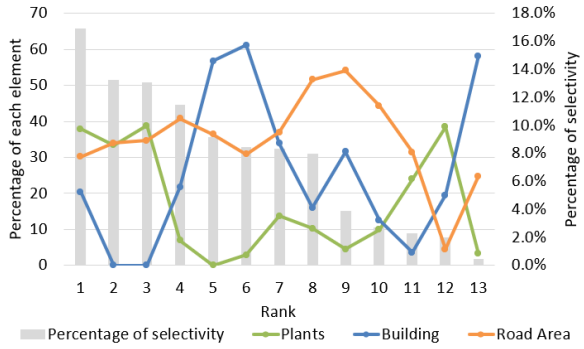

Fig. 1 Results of paired comparison method of adults

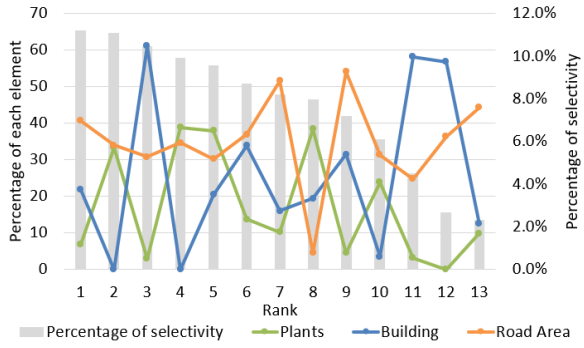

Fig. 2 Results of paired comparison method of children

For adults, the top three rated photos comprised of about 40% plants, and the 4th to 10th ranks are 15% or less. Regarding roads, the top half from 1st to 7th comprised of 30-40%. Regarding the ratio of plants to road, the top three are close to 100% (Fig. 1). Next, for children, the bottom three had less than 30% plants. The top six photos had 30 to 40% roads. In addition, although it is not shown in the graph, when paying attention to the actual road width, it was found that the bottom three were around 2 meters wide (Fig. 2).

Also, regarding the comparison of the spatial components between adults children, overall the adult graph shows a cohesiveness in each item, while the child graph does not. Regarding the proportion of buildings, there was no tendency for either adults nor children.

Visual analysis of photographs

Next, from the results of visual analysis of the photos, we observed that what the top three rated photos had in common for adults was that greenery and plants were manicured and maintained (Fig. 3). On the other hand, the bottom three had unmaintained greenery. In other words, the streets were not organized and there was a lack of cleanliness (Fig. 4).

Fig. 3 The top three photos for adults

Fig. 4 The bottom three photos for adults

The top three for children were ones where the sky is visible and unobstructed (Fig. 5). The bottom three were where the sky was obstructed or not visible, and not open space (Fig. 6).

Fig. 5 The top three photos for children

Fig. 6 The bottom three photos for children

Consideration

From the results, we conclude that children are attracted to roads with good visibility, and adults are attracted to roads that are manicured. In addition, adults had a tendency in the upper ranks, but children tended to have a tendency in the lower ranks, so I think that the selection criteria for choosing a path may differ between adults and children.

COGNITIVE MAP SURVEY

Experiment Contents

In the cognitive map survey, we conducted it with children aged 10-12 going to school A or school B and adults aged 20 and over who attended a university. Children drew a map of the road they take to school and its surroundings on an A2 size blank piece of paper and 12 colored pencils. (Fig. 7, 8) Urban elements were extracted and analyzed for each zone of the elementary school. For the Adults, we asked them to draw a map of the university surroundings on a A2 size blank piece of paper and 12 colored pencils. Urban elements were extracted and analyzed. For the elements, what was drawn on the cognitive map was extracted by dividing it into letters and pictures.

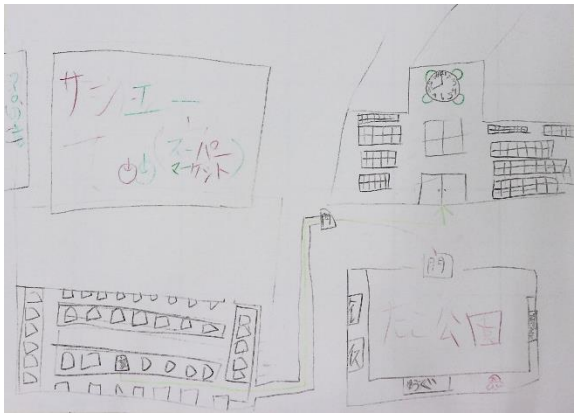

Fig. 7 Cognitive map of elementary school A

Fig. 8 Cognitive map of elementary school B

Experimental result

Analysis of elements

First, we compared the number of elements on the cognitive map with the average number per person. Fig. 9 shows the number and ratio of the average elements of the characters and pictures drawn on the cognitive map. From the results, the number of elements that had a combination of pictures and letters was 12.67 per adult, 6.43 for children at School A, and 8.63 for children at school B, 1.5 to 2 times more for adults. Next, when comparing the number of picture elements, the results were 4.11 per adult, 1.88 at school A, and 3.11 at school B. Comparing the number of character elements, the results were 8.56 per adult, 4.55 at school A, and 5.53 at school. (Fig. 9)

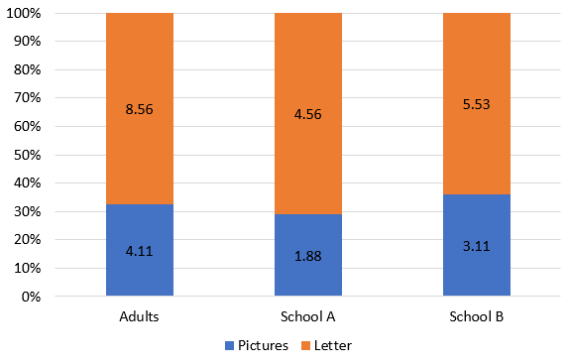

Fig. 9 Percentages and averages of elements on the cognitive map

Both adults and children had more letter drawn elements than pictures, as about 30% of the elements were pictures. Fig.10, Fig.11, and Fig.12 show the proportions of all the elements drawn on the cognitive map by item and by adult and elementary school.

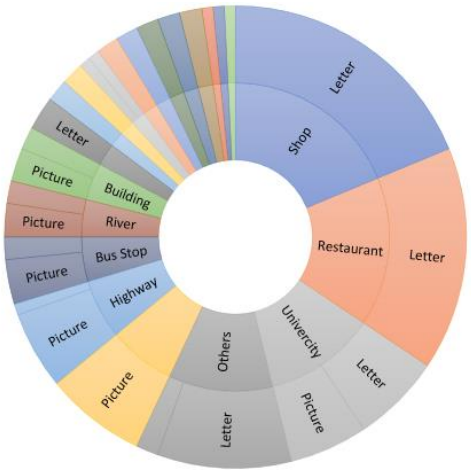

Fig. 10 Percentage of elements on the adult cognitive map

Fig. 11 Percentage of elements on the school A cognitive map

Fig. 12 Percentage of elements on the school B cognitive map

For adults, it can be seen that the ratio of shops and restaurants is large when excluding the university because they drew the area surrounding the university. For children, if we exclude the elementary school and home because they drew the road to the school, the ratio of parks and apartments is large in school A located in the suburbs, while many traffic lights, road markings, and roads were drawn at school B located in the city.

Focusing on the results of adults, it was found that most of the shops and restaurants in particular were drawn in letters. On the other hand, in the painting, it was found that many highways, banks, and stairs on the banks were drawn. Focusing on the results of children, most of the parks, which had a high proportion in elementary school A, were drawn in letters. The proportion of parks in the text elements and the proportion of parks in the picture elements were almost the same. All apartments, which also had a high proportion, were drawn in letters. It was found that most of the traffic lights and road markings, which were common in elementary school B, were drawn with pictures, and the roads were drawn with about half pictures and half letters.

In addition, it was found that plants were 100% drawn with pictures, and most of the shops and restaurants were drawn with letters. From the results, what elementary school A and B have in common is that about half of the pictures and letters are written for their homes, and that the elementary school has both pictures and letters. It turns out that the number of elementary schools drawn as letters is nearly double that of elementary schools drawn as pictures. In addition, while many children drew only the site when drawing an elementary school, most adults drew each school building on the site when drawing a university. While no traffic lights, pedestrian crossings, traffic signs, etc., were drawn on the adult cognitive maps, most children drew traffic lights, pedestrian crossings, traffic signs, etc., on their cognitive map. In the elements drawn in letters for both children and adults, there were many places where the usage was clear, such as restaurants, shops, and schools.

On the other hand, many of the elements depicted in the drawings had a characteristic shape. For example, for adults, these were large structures such as highways and banks, and for children, they were traffic lights and roads with "stop" signs, pedestrian crossings and other symbols and patterns, plants and fences. Comparing the places that block the view such as buildings and plants with the places that can open such as parks and vacant lots, for adults about 70% of the drawings were things that block the view, and only about 15% were the open spaces. On the other hand, it was found that about 50% of the children's drawings in both elementary schools were objects that obstruct the view, and 25% were open spaces.

Consideration

The differences in the number of elements drawn between adults and children is thought to be due to the difference in the number of places they normally use. While the top elements drawn on the adult cognitive maps were shops and restaurants, the top elements drawn on the child cognitive maps were not shops and restaurants. We think it may be the difference in frequency and interests. Also, while most children draw traffic lights and road markings, adults almost did not draw these at all, so it is possible that children are more interested in objects relative to their body size than adults. For both adults and children, there are many places where the usage of the elements drawn as letters is clear, and many of the elements drawn as pictures are large objects, shapes, patterns, etc. I think that large structures are memorized in form, and children may memorize things that exist in illustrations and shapes.

CONCLUSION

From the results of the paired comparison method, there was an overall tendency in the results from adults, but it was difficult to see the tendency in the children's results. Although the route is selected, it is considered that the child selects the route by focusing on the part that is not a component of the road.

In the cognitive map survey, many restaurants were drawn by adults, and for children, many places to play with friends, such as parks and friends' houses, were drawn. Regarding the cognition of the street space, we think that the difference in the place that they usually use with their friends is reflected in the difference between adults and children. Also, while the adults drew large structures, the children' did not draw many large structures, and even if they were drawn, the structures were not drawn in great detail. This is probably attributed to varying line-of-sight from height differences between adults and children. With large structures being harder to see, children are attracted by things that are drawn on the ground, such as road markings that adults do not pay attention to, and things that are displayed with patterns such as signboards. We think that this is because attention is paid to the shape close to the size and athletic ability of one's body.

As a result of the above, it goes without saying that buildings with various functions and uses in town development have a great influence on the image of the city. In addition to that, it can be seen that the height and display are important, for example, on familiar roads where children walk. In the future, it is necessary to look at the composition and classification of such elements.

REFERENCES

[1] T. Sakai, On the Relationship Between the Spatial Elements and Perceptual Space of Children, 6th Int. Conf. on GEOMATE, 2016.

[2] H. Tsukaguti and K. Matsuda, Pedestrian route selection behavior analysis, Japan Society of Civil Engineers Papers, Vol. 2002, Issue 709, 2002, pp. 117-126.

[3] J. Zhang and H. Imada, A Study on City Landscape Based on Free Description Written about "My Favorite Scenery" by Children, Social information science: journal of the Faculty of Social Information Science, Hiroshima Bunka Gakuen University 22, 45-52, 2017

[4] E. Kumazawa and T. Awahara, A Study on 'Children's play space' through the Analysis of Hand Drawn Maps V: On effects by Geographical Conditions2, Urban Plannning (2013), 247-248 (7124), Architectural Institute of Japan, 2013

[5] K. Umekawa, H.Yokoyama and Y. Miyagishi, A study on the playgrounds for the children and the space cognition in the city, Conf. on Architectural Institute of Japan Kinki (49), 365-368 (7020), Architectural Institute of Japan, 2009

11th Int. Conf. on Geotechnique, Construction Materials & Environment, Kyoto, Japan, 3-5 November 2021, ISBN: 978-4-909106063 C3051

ON EVALUATION OF ENVIRONMENTAL SOUND BY DEGREE OF HUMAN CONCENTRATION

Haru Kanda[1], Kazunari Tanaka[2]

[1]Architecture, Civil Engineering and Urban Design, Graduate School of Engineering, Osaka Institute of Technology, 5-16-1, Omiya, Asahi-ku, Osaka, Osaka, Japan
[2]Osaka Institute of Technology, 5-16-1, Omiya, Asahi-ku, Osaka, Osaka, Japan

ABSTRACT

Currently, COVID-19 is changing the learning environment of students and the working environment of office workers. They spend more time at home. In this study, we focused on the environmental sound, clarifying the difference in the environment of residential areas, which is different from educational districts and office areas, from the viewpoint of concentration. We applied two methods of psychological experiment and physiological experiment. In the psychological experiment, five grades were used to evaluate how concentrated the collected environmental sounds were. As for the physiological experiment, an electroencephalogram measuring device (EMOTIV EPOC X) was used to detect concetration. Testers were requested to answer 12 simple arithmetic operations by mental arithmetic, while they were under the specific sound stimuli for each question. As a result, the difference in concentration due to the difference in sound was extracted. The data obtained in the physiological experiment and the psychological experiment were compared. Of the four, the one that hindered concentration most was the human voice. We also found that the sound of turning paper and the chirping of clocks and birds do not interfere with concentration. There was some differences between the psychological and physiological experiments. Both experiments detected human voice as an adverse effect on concentration.

Keywords: Sound, pollution, brain waves, concentration

INTRODUCTION

There are many studies from the viewpoint of soundscape, but there are very few studies on the comfort of space (especially focusing on concentration) from the type of sound. Therefore, the comfort of the space will be examined based on the type of environmental sound.

Background

Today, there are seven typical pollutions in Japan. Out of the complaints received for pollution, noise pollution, which is one of these, is the highest received. [1] The definition of noise is ambiguous, and noise is often referred to as unwanted sound rather than volume. In other words, noise exists in our daily lives and is always present as environmental sounds surrounds us.

The world has been disrupted by the influence of COVID-19, and changes in the environment are occurring for many Japanese people. This means that work and study have switched to online and more people are working and studying in unusual environments. In other words, the sound environment changes as the environment changes, and many people are not accustomed to working in a different space than usual. We investigated what kinds of sounds have adverse effects and what kinds of sounds have positive effects in order to build a comfortable sound environment. When evaluating "comfort" with regards to, working environment, we focused on whether or not the concentration was improved.

PURPOSE AND METHOD

Purpose

The purpose of this study is to clarify the noise that affects our concentration in various environments. In addition, it is to find indicators to get the level of the noise. Ultimately, we aim to improve the healthy environment of the city and create a good urban space.

Method

As a research method, after conducting a preliminary survey, we conducted research from two points, psychological and physical aspects.

Preliminary Survey *Method*

Before conducting the psychological experiment, a questionnaire was conducted for undergraduate and graduate students as a preliminary survey. [3] In the questionnaire, we asked two questions, "What is the sound you hear when you are in the house, and at school?" We collected as much as possible from the experiments under same situation.

Psychological Experiment Method

The psychological experiment presents environmental sounds and asks the subject to evaluate whether or not the environmental sounds can be concentrated in five stages. At this time, the subject is not actually asked to listen to the sound [4], but rather asked if he-/-she would likely be able to concentrate. The environmental sounds evaluated by the subjects were classified by the author and used in the physiological experiment. The environmental sounds were divided into a total of seven sounds: natural sounds, sounds emitted from humans, human movement sounds, animal sounds, mechanical sounds, external sounds, and other sounds. Since there are a considerable number of classified environmental sounds and it is difficult for the subjects to evaluate all of these sounds, representative sounds were selected in these seven types and used in psychological experiments. In psychological experiments, these environmental sounds are evaluated on a five-point scale as to whether or not they are likely to be prevalent at university or home.

Physiological Experiment Method

In this chapter, unlike the psychological aspect performed in Psychological Experiment, the subject is actually given a sound stimulus, and the concentration is verified from their physical reaction.[5]

In the physiological experiment, the concentration was evaluated using an electroencephalograph. In the evaluation, the intensity of the frequency band such as α wave and β wave is observed from the electroencephalogram spectrum measured by the electroencephalograph, and the degree of concentration is analyzed from the activity level. [2]

The one used for this experiment was EMOTIVE POCX, and the analysis software was EMOTIV PRO. In FIG. 1, the upper half of the waveform is a Fourier transformation of the measured brain wave, and the lower half shows the band power for each frequency band from the waveform.

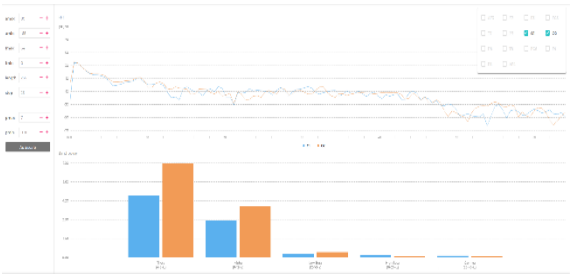

Fig. 1 Measured Brain Wave and Fourier Transform

The sound source used was a sound stimulus created from free materials existing on the Internet. However, I couldn't find a specific sound source such as the sound of "a mechanical pencil" falling in my search, so I recorded those myself. [6] As for the types of environmental sounds, the same 12 types of environmental sounds used in the psychological experiment are used. First, each sound is played at the same time, and only one sound is set louder. Using PowerPoint, ask them to perform a simple four arithmetic operation problem that appears on the display during the time when the sound is being heard. The time required for each question was set to 10 seconds, and the response time was set to 2 seconds. A total of 157 seconds of brain waves were measured, including the resting time. Since the electroencephalograph picks up a weak electric current and affects the waveform, we did not have subjects use their hands to fill in the answer, and tried to keep body movement to a minimum. In addition, when determining concentration, it is generally suggested that when low β waves and α waves appear, they are concentrated, so brain waves in O1 and O2, where α waves and β groups are likely to appear, are measured. Then, Fourier analysis was performed using EMOTIV PRO, and the maximum values of brain waves for each problem were compared.

RISULTS AND DISCUSSION

Results and Considerations of Preliminary Survey

The respondents were 21 males (55.3%) and 17 females (44.7%), for a total of 38 respondents. As a result, there were 106 types of environmental sounds in the house and 70 types of environmental sounds in the university.

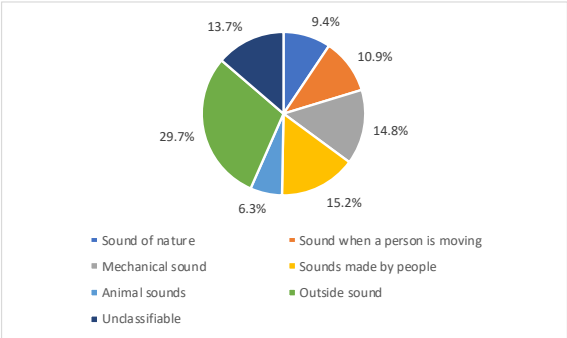

Fig. 2 Percentage of each group of home environmental sounds

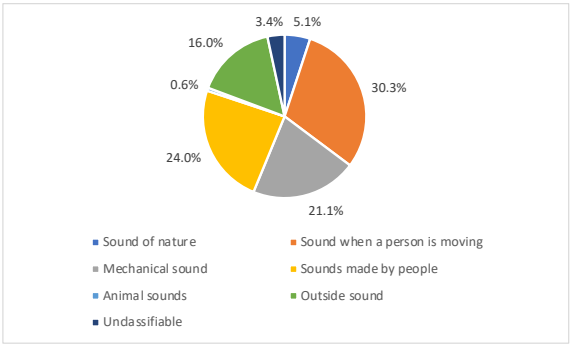

Fig. 3 Percentage of each group of university environmental sounds

The ratios of the seven sounds-classifications are shown in Fig. 2 and 3. As a result, in the houses, 26.1% of the total were sounds emitted from people and the sound of human movement, and 54.3% at the university, and the result was that the university recognized more environmental sounds for people. Another major difference is the external sound. The outside sounds at the university were 16.0%, while the outside sounds at home were 29.7%, which was about twice the difference. From this result, it was found that the house is more conscious of outside sounds.

It is thought that the way of thinking about space is different between the university and the house. At university, the range of personal space is narrow, and it is easy to focus on the surrounding sounds. Therefore, it is easy to hear sounds that are relatively close to oneself, such as sounds emitted from humans. On the other hand, at home, because the range of personal space is bigger, the sound inside the personal space is not a concern, and the outside sound is easier to hear. In other words, it is easy to hear external sounds that are considered to be outside the personal space.

Since it was found that the recognizable ranges are different, the next step is to investigate the effects of auditory image on concentration.

Results and Considerations of Psychological Survey

Tables 1 and 2 below show the average value and standard deviation of the five-grade evaluation for each environmental sound.

Table 1 Value of Environmental Sounds in House

Environmental sound	average	standard deviation
Thunder	2.82	1.27
Rain	3.79	1.28
Cough	2.92	1.09
Human voice	2.89	1.02
The sound of turning paper	3.89	1.17
The sound of writing letters with a mechanical pencil	3.79	1.15
Clock	3.61	1.14
Air conditioner	3.66	0.98
Car running noise	3.24	1.29
The sound of a mechanical pencil falling	3.16	1.09
Bird chirping	3.74	1.23
Crow barks	3.32	1.28

Table 2 Value of Environmental Sounds in University

Environmental sound	average	standard deviation
Thunder	2.65	1.21
Rain	3.76	1.01
Cough	2.54	1.14
Human voice	2.19	1.15
The sound of turning paper	3.68	1.16
The sound of writing letters with a mechanical pencil	3.76	1.14
Clock	3.97	1.07
Air conditioner	3.41	1.04
Car running noise	2.89	1.02
The sound of a mechanical pencil falling	3.11	1.33
Bird chirping	3.84	1.01
Crow barks	3.14	1.23

From this data, a t-test was performed by one-sided test. In the t-test, when the P value was less than 0.05, it was considered statistically significant. From Table 3, it was found that the environmental sound of less than 0.05 corresponds to the human voice.

Table 3 The P Value in the T-test

Environmental sound	P value
Thunder	0.2821
Rain	0.4516
Cough	0.0733
Human voice	0.0034
The sound of turning paper	0.2097
The sound of writing letters with a mechanical pencil	0.4513
Clock	0.0778
Air conditioner	0.1431
Car running noise	0.1028
The sound of a mechanical pencil falling	0.4303
Bird chirping	0.3505
Crow barks	0.2687

From the results of the questionnaire, there are sounds in which the groups were divided into two high and low evaluation. They are the "bird chirping" and the "paper-turning sound" heard from house, and the "rain sound" heard at university. Hereafter, the "bird chirping" is referred to ①, the "paper-turning sound" in the house is-_ ②, and the "rain sound" at university is-_③. The correlations between the evaluations of the three sounds and the other sounds are as follows. The subjects who gave high marks in ① selected sounds best able to concentrate most on rain (80.0%), the sound of turning paper (60.0%) and the sound of writing with a mechanical pencil (60.0%). On the other hand, - the subjects who did not evaluate well in ① evaluated that they could not concentrate with cough (73.0%), mechanical pencil falling sound (54.7%), and crow calls (63.7%). Subjects who gave high marks in ② tend to give high marks to the sound of writing letters with a mechanical pencil (81.2%), rain (62.5%), chirping of birds (56.3%), clocks (50.1%). Conversely, subjects who did not evaluate ② well were coughing (60.1%), human speaking (50.2%), writing with a mechanical pencil (50.2%), air conditioner (50.2%), bird chirping (50.2%) and the crow calling (50.2%). There were no clear tendencies.

Subjects who highly evaluated ③ tended to highly evaluate the clock (63.6%), the chirping of birds (63.6%) and the sound of writing letters with a mechanical pencil (54.5%). - Subjects who rated ③ low, rated the cracking of lightning (53.3%), air conditioners (53.3%), and crow calls (53.3%).

From the above results, it can be seen that there may be differences in these three types of sounds imaged from words depending on the subject.

The group with a high evaluation of the three sounds regards these sounds as continuous sounds. It is considered a sound that can be heard continuously at a volume that does not bother you. On the contrary, the subjects had negative images of unexpected sounds such as sounds that cannot be continuously heard, that is, sudden coughing and falling mechanical pencils. We can imagine the sudden loud call of a crow and the voice of a person as a sudden sound. From this, it is possible that these subjects perceive the sounds of birds chirping and paper-turning expressed in letters as exceptions.

③ is considered to have the same tendency. Another way to look at it may be whether the subject can concentrate or not, depending on whether the sound of rain at the university is perceived as if it were from inside the house or as a loud sound heard in the classroom.

Results and Considerations of Physiological Survey

According to the results of the α waves in Fig. 4, it was observed that the sounds of the mechanical pencil falling and the car running detected a large amount of the α wave. In addition, it was confirmed that all the subjects had a decrease in alpha waves when the human voice became louder. Further, FIG. 5 shows the result of the Low β wave. There was a reaction to three points: the sound of turning paper, the sound of a car running, and the chirping of birds. Similarly, it can be seen that the value of human speech is low.

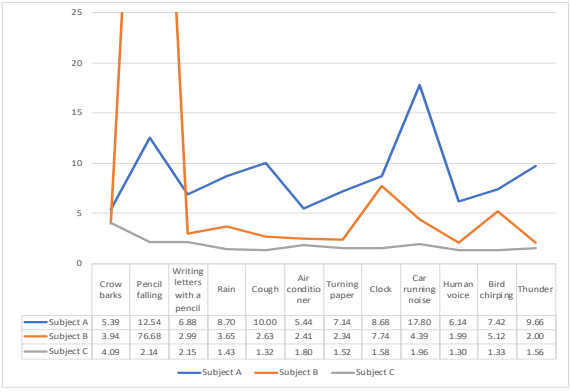

Fig. 4 Comparison of the highest value of alpha wave

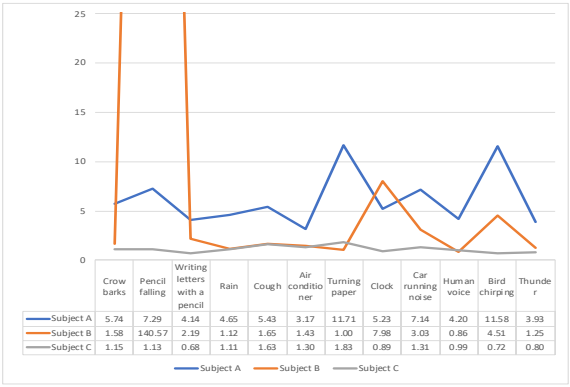

Fig. 5 Comparison of the highest values of Low β waves

When a lot of α waves and Low β waves appear, it can be said that they are in a concentrated state, so the sound of driving a car, the sound of a mechanical pencil falling, the sound of turning paper, the chirping of birds, clocks- etc, have some commonality for the subjects. It can be said that it is in a state of being seen and concentrated. However, in general, the running noise of a car is often regarded as noise pollution, so there are still some doubts about this result. The running sound of the car used this time was the sound of only one car running without making such a loud noise, so this may have been a factor. In addition, there was an opinion from the subject that the sound of the car running and the sound of waves were very similar after the experiment. Natural sounds often have 1 / f fluctuations, which are sound fluctuations whose spectral density is inversely proportional to the frequency f, and it is said that wave sounds also include these 1 / f fluctuations. Although it was limited to the sound source used this time, the author thinks that the running sound of the car contained 1 / f fluctuation and acted on the brain waves. According to Samaki et al, it has been clarified that 1 / f fluctuation reduces stress with ultrasonic waves.[7] In other words, it is suggested that 1 / f fluctuation affects the body.

Based on this result, we interpolated the automobile noise (dB) in the city with QGIS using the data of the Ministry of the Environment, and examined where the voice of a person would have an adverse effect. [8] According to the Ministry of the Environment, it is said that a person's voice is about 50 to 61 dB when engaged in a normal conversation, but it is said to be about 88 to 99 dB when the conversation becomes loud due to excitement. In figure 5, the noise data of the car is interpolated by the reverse distance load method and contour lines are drawn. The area is where the densely populated urban areas of Moriguchi City, Kadoma City, and Neyagawa City in Osaka Prefecture are concentrated. In this figure, the bluer areas represent,- the quieter car noise, and the closer it is yellow, the louder the noise. In other words, when the blue color is dark, the noise of the person is louder than the noise of the car, and when it approaches yellow, the noise of the car is louder than the noise of the person. Judging from the results of the experiment, it may be more difficult for people living in areas close to blue to concentrate on their work. In addition, I thought that a better sound environment could be constructed by conducting such an analysis and conducting city planning.

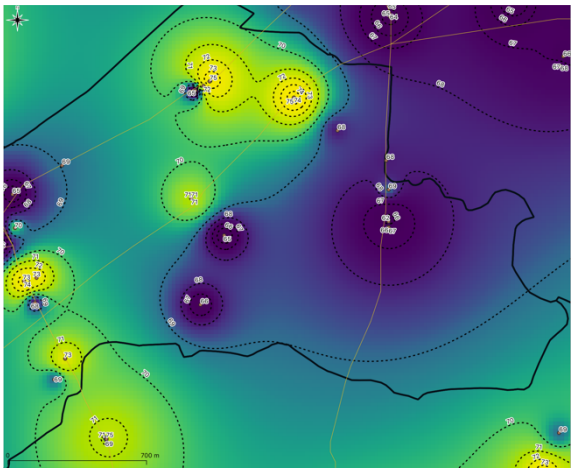

Fig. 6 Adverse Effect Zone by Human Voice for Concentration

CONCLUSION

The research results and future developments are summarized below.

Summary

In this study, in order to design a comfortable sound space, we examined comfort from two perspectives: the sound formed by the auditory image and the actual sound stimulus. As a result, it was found that the voice of a person has an adverse effect when viewed from the viewpoint of concentration. In addition, although the results were not sufficiently significant, the sound of turning paper, clocks, and chirping of birds tended to have a positive effect on concentration.

Future Tasks

We determined a car affected concentration in a psychological experiment but not in a physiological experiment, while rain and the sound of writing with a mechanical pencil, affected concentration in a psychological experiment but not in a physiological experiment. I would like to work hard to find out the cause of the discrepancy when comparing the running noise of a machine. Although it is the running noise of a car that is generally considered to be one of the causes of noise pollution, it was suggested that it improves concentration when measuring brain waves.

However, since the running sound of the car used this time was the running sound of only one car, we would like to consider how it changes with the sound of multiple automobiles running at the same time. In addition, it is necessary to consider a method that can consider 1 / f fluctuation.

REFERENCES

[1] About noise regulation law enforcement situation investigation in 2018, Ministry of Environment

[2] Hirai F., Yoshida K., Miyaji I., Comparison analysis of the thought and the memory at the learning time by the simple electroencephalograph, Multimedia, Distributed, Cooperative, and Mobile Symposium, vol.2013, no.2, pp.1441-1446

[3] Hashimoto Y., Shindo M., Tanaka Y., Considerations of a Cognition Test of Environmental Sounds, Shitugosyo Kenkyuu, Vol.9, No.4, 1989.12, pp.227-236

[4] Tahara K., Tsuneo H., Kobayashi Y., Katada A., Tyoukakushougaisya ni okeru Kankyouon no Tyoukakuimeiji ni kansuru Kenkyuu, Audiology Japan, vol.59, 2016, pp.198-206

[5] Yamazaki K., Hotta K., Saitou M., Ogawa M., Keiryuu no Oto ni fukumareru Tyouonpa ga Ningen no Seiri ni ataeru Eikyou ni tuit, Acoustical Society of Japan, Vol64, No.9, 2008, pp.545-550

[6] Shimai S., Tanaka M., Kankyouon no Kai-Fukaihyouka to Onatsu no Kankei, Acoustical Society of Japan, Vol49, No.4, 1993, pp.243-252

[7] Mori Y., Samaki Y., Tada H., Watanabe S., Shirahama N., Nakaya N., Tomita M., Effects of listening to Ultrasonic Sounds with 1/f Fluctuation for the Autonomic Nervous Activity, Biomedical Fuzzy Systems Association, Vol.19, No.1, 2017, pp.67-72

[8] Constant monitoring results of automobile noise, Ministry of the Environment

11th Int. Conf. on Geotechnique, Construction Materials & Environment, Kyoto, Japan, 3-5 November 2021, ISBN: 978-4-909106063 C3051

ON CHANGES IN THE PSYCHOLOGICAL "AFFORDANCE" IN URBAN SPACE DUE TO THE INFLUENCE OF COVID-19

Kazuki Miyake[1], Kazuknari Tanaka[2]

[1]Architecture, Civil Engineering and Urban Design, Graduate School of Engineering, Osaka Institute of Technology, 5-16-1, Omiya, Asahi-ku, Osaka, Osaka, Japan
[2]Osaka Institute of Technology, 5-16-1, Omiya, Asahi-ku, Osaka, Osaka, Japan

ABSTRACT

"Affordance" is a coined word, defined by J. Gibson and is the nature of forms and spaces. This means characteristics of forms and spaces that people get information intuitively, understand how to use it and act by just looking at and touching the shape and material without thinking.

The chair "affords" to sit and the pencil "affords" to write. Similarly, people act by getting information from their environment, such as where they can sit comfortably in a university lecture room or ride comfortably on a train. From the influence of COVID-19, telecommuting, online lectures, and delivery services became widespread. In public spaces, it is common for people to wear masks. In addition, it is recommended to avoid closed spaces, crowded places, close-contact settings etc. In urban spaces, there are physical restrictions on people's behavior, such as restrictions on admission to a store, bench usage restrictions, and requirements for disinfection and temperature measurement prior to admission. It is thought that people's psychological behavior has changed and is restricted unknowingly. In this study, we compared the behaviors of people before and after the spread of COVID-19 and investigated various "affordance" changes. The purpose is to find new actions and movements of people to design public spaces. From the behavioral surveys, we found the behavior change when people encountered a person wearing a mask. Moreover, the difference of personal space was measured. There was a clear difference between before and after the spread of COVID-19.

Keywords: Mask, COVID-19, Affordance, Personal space

INTRODUCTION

Background

"Affordance" is a coined word, defined by J. Gibson and is the nature of forms and spaces. This means characteristics of forms and spaces that people get information intuitively, understand how to use it and act by just looking at and touching the shape and material without thinking. The chair "affords" to sit and the pencil "affords" to write. Similarly, people act by getting information from their environment, such as where they can sit comfortably in a university lecture room or where they can ride comfortably on a train. Signs that indicate all perceptible signs that convey appropriate behavior to the subject are called "signifiers"

From the influence of COVID-19, telecommuting, online lectures, and delivery services became widespread. In public spaces, it is common for people to wear masks. In addition, it is recommended to avoid closed spaces, crowded places, close-contact settings etc. In urban spaces, there are physical restrictions on people's behavior, such as restrictions on admission to a store, bench usage restrictions, and requirements for disinfection and temperature measurement prior to admission. It is thought that people's psychological behavior has changed and is restricted unknowingly. In addition, it has become common for people to wear masks. So, I think the significance of masks has changed since the COVID-19 outbreak.

Purpose and Method

In this study, we compared the behaviors of people before and after the spread of COVID-19 and investigated various "affordance" changes. The purpose is to find new actions and movements of people to design public spaces. In this study, the effect that masks have on the human action is investigated from the action investigation (Experiment 1 and 2). Next, the difference before and after COVID-19 generation of the personal space is clarified by the investigation of the action space (Experiment 3).

EXPERIMENT

Experiment 1

In this study, the classification of space by Edward T. Hall is defined as being composed of four elements: proximity distance, personal distance, social distance, and public distance. The personal space is defined as the individual distance based on

the past studies and references shown in the figure below [1].

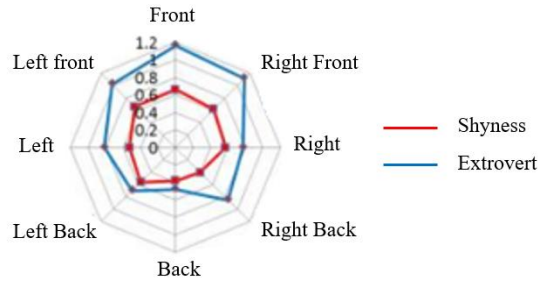

Fig. 1 Past research

In order to investigate changes in people's behavior with and without masks at proximity distances (0 ~ 45 cm), we focused on the seats of a train where the distance between each seat is 43 cm [2].

Fig. 2 Train type

We look at seat selections on trains and use the results to explore how masks can change people's behavior at close range. Questionnaires with and without masks were administered to 56 male and female university students, and questionnaires without masks were administered to 48 male and female university students. The conditions for selecting an object were defined as follows. ① We selected a photograph similar to the seat style of the Tanimachi subway line, which is familiar to students of Osaka Institute of Technology. In order to investigate the distance, bench-style seats were selected instead of facing seats. ③ As for the survey, it's conditional on being able to stand, sit, or both, rather than sit on crowded trains. ④ Option 7 means to stand. ⑤ Concerned about any age and gender bias, they used black-lacquered people. Due to concerns over the spread of COVID-19, we decided not to conduct an on-site survey, but instead to use photos obtained online. First, we investigated whether there is a difference in the behavior of sitting and standing depending on the presence or absence of a mask.

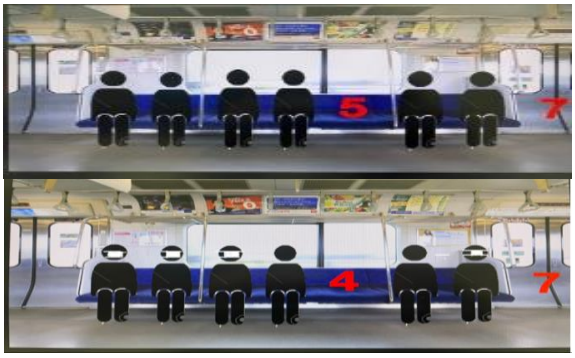

Fig. 3 Questionnaire (1)

The difference between two questionnaires was judged by t test. The results showed that there was a difference between the two, and that there were changes in people's behavior choices, such as standing or sitting, depending on whether they had masks or not.

Next, the following three questionnaires were carried out in order to examine the action selection of the seat position by the existence of a mask in close distance.

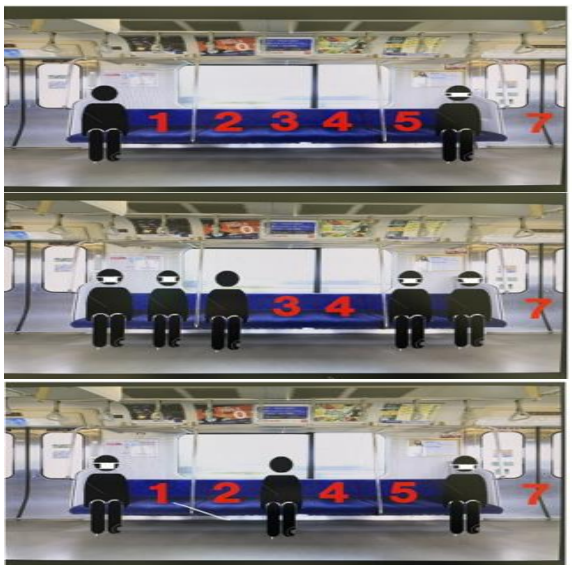

Fig. 4 Questionnaire (2)

The following table shows the distances of people wearing and not wearing a mask (The choice of do not sit is as infinity distance.)

Table 1 Experimental results

Experiment	Distance
distance from someone wearing a mask	33.7cm
distance from someone without a mask	52.2cm

From the results, it can be understood that riders want to keep a distance from people who don't wear masks. Therefore, it was proven that the existence of the mask affected the action selection in near distance.

Experiment 2

In order to investigate the behavior change of people with and without masks within the range corresponding to the individual distance (45 ~ 120 cm), we focused on the waiting position on the station platform. The difference in the distance between the waiting positions was examined according to the presence or absence of a nearby person with a mask, and was expressed numerically. A photograph was taken from the second floor of the station, and the distance was calculated by measuring the mark of the leg which shows the position of the platform. JR Osaka station was selected as an object place with many users.

Fig. 5 Home standby position

Based on the survey results, the dimensions on the photographs were measured from the actual dimensions (20.5 cm) of the foot marks indicating the positions where the platforms were lined up, and the scales were calculated to calculate the averages. The position of the person standing behind the person wearing a mask was 65.7 cm, and the position of the person standing behind them wearing a mask was 62.7 cm. In other words, there was no change in behavior selection with masks at individual distances. However, it was considered that they did not recognize the presence of a mask as information unrelated to themselves, because they did not know whether the person in front of them was wearing the mask, and because many people were focused on their mobile phones in the station.

Experiment 3

Therefore, we conducted a survey to determine the distance which you are not concerned when you are facing a person (when you can see a person's face), that is, within a personal space (individual distance). In addition to the changes in mask-induced behavior within individual distances, also revealed changes in people's personal space after the COVID-19 outbreak. In the experiment, 6 male university students and 6 female university students participated by facing each other, and the distance which the participant become worried when the counterpart walked from left side, left oblique front, front, right oblique front, right side toward the participant was measured.

Fig. 6 Experimental method

Four experiments were conducted with different subjects: when the approaching person wore a mask (3 males and 3 females) and when the approaching person did not wear a mask (3 males and 3 females). Although the experiment was scheduled to be carried out on the same station platform as the first and second investigations, it was carried out in the Osaka Institute of Technology considering space requirements for the experiment and risk of COVID-19 infection. The experimental results are shown in the diagram below.

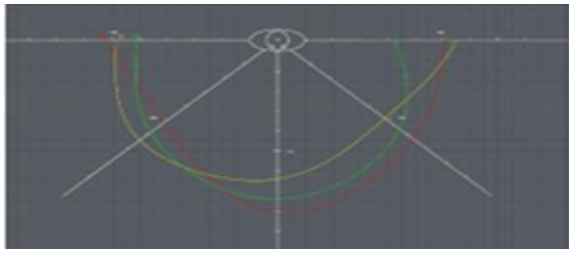

Approaching person is wearing a mask.

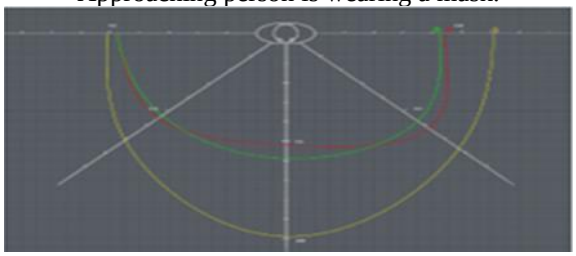

Approaching person isn`t wearing a mask

Fig. 7 Validation results

Table 2 Validation results

Direction	Mask(cm)	No mask(cm)
Left	92.33	98.67
Left front	111.67	131
Front	146	140
Right front	116	119.33
right	94.67	97.33

From the above results, it became clear that there was no change in the actions depending regarding mask wearing in the individual distance. According to past research, the average personal space before the prevalence of COVID-19 was about 60 cm, and according to the reference book, the personal space has a radius of about 70 cm from the center of the subject, and the personal space is defined as individual distance. As can be seen from this table, the personal space calculated in this study is 140 cm or more in the forward direction, which corresponds to the social distance (120 ~ 360 cm). For this reason, the definition of personal space for people after the COVID-19 epidemic corresponds to the social distance before the COVID-19 epidemic. The reason for this is thought to be that the word social distance, which is recommended around the world, has become widely known and people have become more physically distant.

3 CONCLISION

From the results of the above study, it is within individual distance that the behavior changes according to the information of the mask, and the mask indirectly affects the behavior of the person who is not wearing the mask. I think it is because of the change of feeling that wearing a mask has become normal due to the occurrence of COVID-19. In addition, it turns out that the rise of COVID-19 and the spread of social distance's terminology have changed personal space from individual distance to social distance. In the future, the team will look into the possibility of new designs based on this, while looking to identify other Afford Factors after the COVID-19 pandemic.

REFERENCES

[1] Murata S., Morihara K., and Koda T., Analyses of Effect of Personality on Personal Space in Real World and Metaverse. The Japanese journal of Psychology, Vol. 52(2), 1981, pp. 124-127.

[2] Konishi H., Nozawa K., Study on Seating Behavior in the Train; the Influence of Prediction about Crowd on Seating Behavior. The annual bulletin of Musashino University Institute of Human sciences, Vol. 7, 2018, pp. 37-39.

11th Int. Conf. on Geotechnique, Construction Materials & Environment, Kyoto, Japan, 3-5 November 2021, ISBN: 978-4-909106063 C3051

DATA MODELING WITH TRANSFORMATION IN LAPLACE AUTOREGRESSIVE MODEL USING REVERSIBLE JUMP MCMC

Suparman[1], A.M. Diponegoro[2]

[1]Department of Mathematics Education, Universitas Ahmad Dahlan, Indonesia;
[2]Department of Psychology, Universitas Ahmad Dahlan, Indonesia

ABSTRACT

Autoregressive (AR) is a model that is often used to model various types of data. For confidential data, data confusion is very important to be protected so that the data is not known by other unauthorized parties. This study aims to find data modeling with transformations in the AR model. In this AR model, noise is assumed to have a Laplace distribution. AR model parameters include AR model order, AR model coefficient, and noise variance. AR model parameter estimation is carried out in a Bayesian framework using the Markov Chain Monte Carlo (MCMC) reversible jump algorithm. This study shows that the posterior distribution of AR model parameters has a complicated equation so that the Bayes estimator cannot be determined analytically. Bayes estimators for AR model parameters are calculated using the MCMC reversible jump algorithm. This algorithm produces an AR model that satisfies the stationary conditions. The results of this research can be applied to modeling and forecasting confidential data in various sectors. The novelty of the research results is the use of transformations in the AR model which has Laplace noise. This research can be further extended to the moving average autoregressive model (ARMA).

Keywords: Autoregressive, Bayesian, Confidential data, Laplace noise, Reversible jump MCMC

INTRODUCTION

Autoregressive (AR) is one of the stochastic mathematical models. The definition and characteristics of the AR model can be found in [1]. AR models have been widely applied in various fields, including time series and signal processing. The AR model contains a noise which is assumed to have a distribution. Generally, the AR model is assumed to have a normally distributed noise, for example [2]. In order for the AR model to be applied in a wider field, several authors have developed AR models in which noise is assumed to be non-normally distributed, for example AR models with Pareto noise [3], AR models with exponential noise [4]-[5] and AR models with Laplace noise [6]. However, for confidential data, the AR model needs to be transformed. So that the confidentiality of the data is protected when the research results are published.

Variable transformation is a method to change a random variable into another random variable. This transformation is often used in parametric data analysis when parametric assumptions are not met, for example [7]. In this article, variable transformation is proposed to transform the AR model. If the AR model is transformed to another AR model, then the AR model noise is automatically transformed into another noise. The transformed noise will have a different distribution.

In this article, variable transformation is used in the AR model to protect the confidentiality of the modeled data when the research results are published. This article focuses on AR models with Laplacian noise. This Laplacian noise was chosen because the characteristics of the AR model with Laplacian noise have not been studied much. This article has several objectives, namely: (a) finding a transformation for the AR model with Laplacian noise, (b) finding an order estimation procedure for the transformed AR model, (c) finding the procedure for estimating the coefficients of the transformed AR model, and (d) finding the procedure for estimating the noise variance of the transformed AR model.

LITERATUR STUDY

Laplace Distribution

The random variable z is said to have a Laplace distribution with parameters μ and β, written as $z \sim Laplace(\mu, \beta)$, if and only if the probability density function of z is

$$\boldsymbol{f(z|\mu,\beta) = \frac{1}{2\beta} exp - \frac{|z-\mu|}{\beta}.}$$

The mean and variance of the random variable $\boldsymbol{z}$ are $\boldsymbol{\mu}$ and $\boldsymbol{2\beta^2}$, respectively. If $\boldsymbol{z \sim Laplace(\mu,\beta)}$ then the random variable $\boldsymbol{e = az + b \sim Laplace(a\mu + b, a\beta)}$.

AR Model with Laplace Noise

Let $x_1, \dots, x_n$ be a data set where n is the number of observations. The data is said to have an autoregressive model of order p, written as $AR(p)$, if this data satisfies the following stochastic equation **[1]**:

$$\mathbf{x_t} = -\sum_{i=1}^{p} \boldsymbol{\phi}_i \boldsymbol{x}_{t-i} + \mathbf{z_t}$$

where $\boldsymbol{p}$ is the order of the autoregressive model and $\boldsymbol{\phi_1}, \boldsymbol{\phi_2}, \cdots, \boldsymbol{\phi_p}$ is the coefficient of the autoregressive model. The random variable $\boldsymbol{z_1}, \dots, \boldsymbol{z_n}$ is noise. In this article, $\boldsymbol{z_t \sim Laplace(0, \beta)}$.

Variable Transformation

Variable transformation is a method to change a random variable into another random variable. Let x be a continuous random variable and $f(x)$ be a probability density function of the random variable x. If $y = h(x)$ is an increasing or decreasing function, then the random variable $y = h(x)$ has a probability density function [8]:

$$\boldsymbol{g(y) = f[h^{-1}(y)] \left| \frac{dh^{-1}(y)}{dy} \right|}.$$

Bayesian Approach

Let θ be a parameter. In the Bayesian approach, the parameter is considered as a random variable that has a prior distribution. If $y_1, \cdots, y_n$ is n random samples and $L(y_1, \cdots, y_n|\theta)$ is a probability function of random samples $y_1, \cdots, y_n$. Suppose that $\pi(\theta)$ is the prior distribution of parameter θ, then the posterior distribution of parameter θ is

$$\boldsymbol{\pi(\theta|y_1, \cdots, y_n) = \frac{L(y_1, \cdots, y_n|\theta)\pi(\theta)}{\int_{-\infty}^{\infty} L(y_1, \cdots, y_n|\theta)\pi(\theta)d\theta}}$$

if the parameter $\boldsymbol{\theta}$ is continuous.

The posterior distribution of parameter $\boldsymbol{\theta}$ is

$$\boldsymbol{\pi(\theta|y_1, \cdots, y_n) = \frac{L(y_1, \cdots, y_n|\theta)\pi(\theta)}{\sum L(y_1, \cdots, y_n|\theta)\pi(\theta)}}$$

if the parameter $\boldsymbol{\theta}$ is discrete.

Reversible Jump MCMC

Suppose E is the set of states and π is the probability on E. The reversible jump MCMC algorithm [9] produces a Markov chain on E which has a stationary probability close to the probability π. Let q be the auxiliary kernel on E. From the starting point $w \in E$, take a new point w^* according to $q(w, w^*)$. Next, the point w^* is accepted with probability

$$\boldsymbol{\rho(w, w^*) = min\left\{1, \frac{\pi(w^*)q(w^*, w)}{\pi(w)q(w, w^*)}\right\}}.$$

In the reversible jump MCMC algorithm, Markov chains can move between spaces of different dimensions.

METHODOLOGY

This article uses time series data that can be modeled as an AR model with Laplace noise. The following are the steps of data modeling. Let x_t $(t = 1, 2, \cdots, n)$ De time series data. The data is transformed by using $y_t = ax_t$, The time series data x_t is modelled as an AR model with Laplace noise. The likelihood function of times series data is determined. The prior distribution of the parameters is selected. The posterior distribution of the parameters is determined. Bayes estimators for parameters are calculated using the Reversible Jump MCMC algorithm. The data modeling procedure is given in Figure 1.

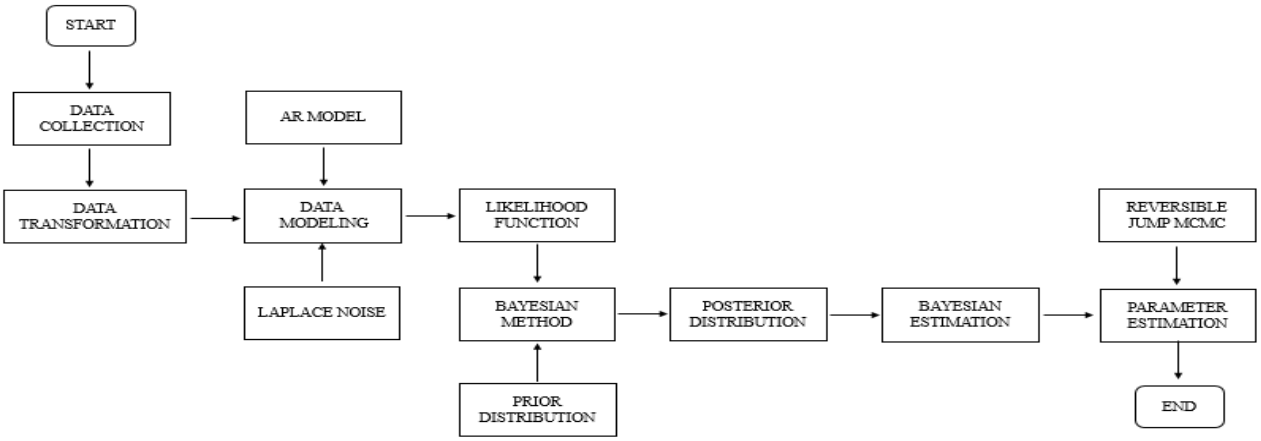

Fig. 1 Flow chart

RESULTS AND DISCUSSION

Likelihood Function

Let $x = (x_1, \dots, x_n)$ be the original data. The original data is modelled by AR model with Laplace noise. To secure the original data, the original data is transformed into new data using the equation $y = ax$. This new data is then analyzed and published. Thus, the confidentiality of the original data is protected. The statistical model for the original data can be obtained by inverse transformation on the statistical model for the new data. For example, Figure 2 plots the original data and Figure 3 plots the new data using the equation $y = 5x$.

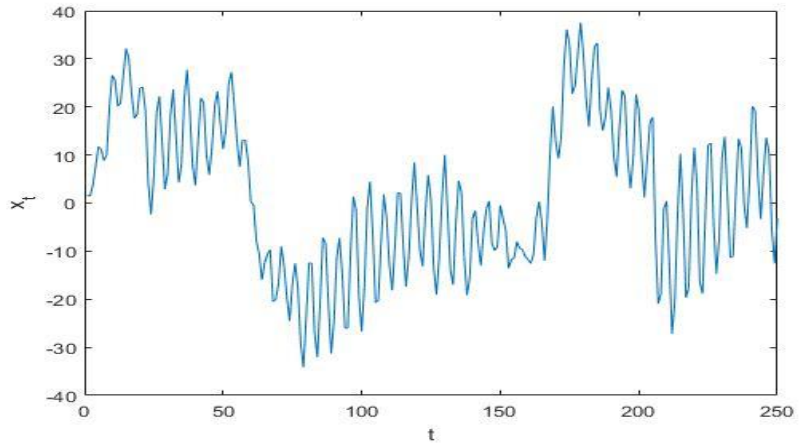

Fig. 2 Original data

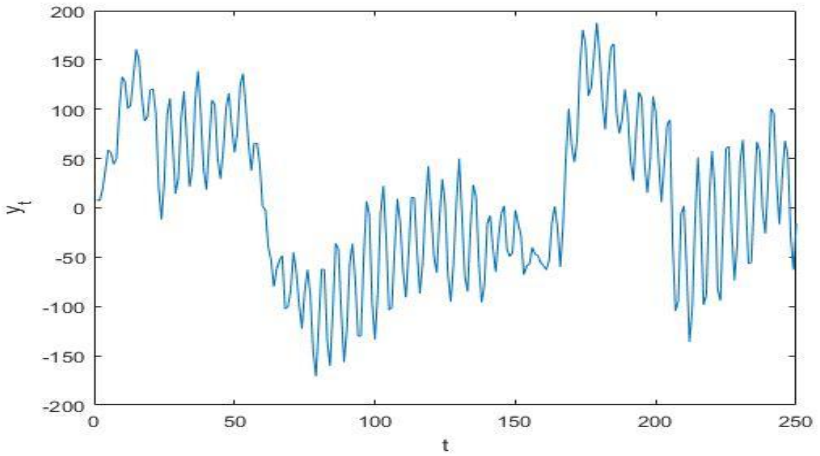

Fig. 3 New data

In this article, the noise $\boldsymbol{z_t \sim Laplace(0, \beta)}$ for $\boldsymbol{t = 1, \dots, n}$. Therefore, the probability function of $\boldsymbol{x_t}$ can be written as

$$\boldsymbol{f(x_t|\beta) = \frac{1}{2\beta}\, exp - \frac{|\sum_{i=1}^{p} \phi_i x_{t-i} + x_t|}{\beta}}$$

Time series $\boldsymbol{x_t}$ is transformed to time series $\boldsymbol{y_t = ax_t}$. Therefore, the probability function of $\boldsymbol{y_t}$ is $\boldsymbol{f(y_t|\beta) = \frac{1}{2a\beta}\, exp - \frac{|\sum_{i=1}^{p} \phi_i y_{t-i} + y_t|}{a\beta}}$.

Let $\boldsymbol{y = (y_1, \dots, y_n)}$ be the new time series that is the result of the transformation. The probability function of $\boldsymbol{y}$ is

$$\boldsymbol{f(y|p, \phi^{(p)}, \beta) = \left(\frac{1}{2a\beta}\right)^{n-p} exp - \frac{1}{a\beta} \sum_{t=p+1}^{n} \left| \sum_{i=1}^{p} \phi_i y_{t-i} + y_t \right|}$$

where $\boldsymbol{\phi^{(p)} = (\phi_1, \dots, \phi_p)}$.

AR model with order $\boldsymbol{p}$ that satisfies the stationary condition is very useful. However, the stationarity

condition is difficult to determine when the order $\boldsymbol{p}$ is large. In order to solve this problem, reparameterization of the AR model is required. Let $\boldsymbol{r_1, r_2, \cdots, r_p}$ be partial autocorrelation functions corresponding to AR model with order $\boldsymbol{p}$. Next, let $\boldsymbol{F}$ be a transformation from $(\boldsymbol{\phi_1, \ldots, \phi_p}) \in \boldsymbol{S_p}$ to $(\boldsymbol{r_1, r_2, \cdots, r_p}) \in (\boldsymbol{-1, 1})^{\boldsymbol{p}}$ where $\boldsymbol{S_p}$ is the stationarity region of the AR model [10]. In the new parameter, probability function for the time series $\boldsymbol{y}$ becomes

$$\boldsymbol{f(y|p, r^{(p)}, \beta)} = \left(\frac{\mathbf{1}}{\mathbf{2a\beta}}\right)^{\boldsymbol{n-p}} \boldsymbol{exp} - \frac{\mathbf{1}}{\boldsymbol{a\beta}} \sum_{\boldsymbol{t=p+1}}^{\boldsymbol{n}} \left| \sum_{\boldsymbol{i=1}}^{\boldsymbol{p}} \boldsymbol{F^{-1}(r_i) y_{t-i}} + \boldsymbol{y_t} \right|$$

where $\boldsymbol{F^{-1}}$ si the inverse transformation of $\boldsymbol{F}$.

Prior Distribution

The binomial distribution with parameters p_{max} dan λ is chosen as the prior distribution of the order of the AR model. While the uniform distribution on the interval $(\boldsymbol{-1, 1})^{\boldsymbol{p}}$ is chosen as the prior distribution of $\boldsymbol{r^{(p)}}$. And, the distribution $\boldsymbol{IG(2, v)}$ is chosen as the prior distribution of $\boldsymbol{\beta}$. In the prior distribution, there are parameters λ and v. The uniform distribution on the interval (0,1) is chosen as the prior distribution of λ. And, the Jeffreys distribution is chosen as the prior distribution of v. Finally, the joint prior distribution of all parameters can be written as

$$\pi(p, r^{(p)}, \lambda, \beta, v) = C_p^{p_{max}} \lambda^p (1-\lambda)^{p_{max}-p} \frac{1}{2^p} \frac{v^2}{\beta^3} exp - \frac{v}{\beta} \frac{1}{v}.$$

Posterior Distribution

Using Bayes' Theorem, the posterior distribution of $(p, r^{(p)}, \lambda, \beta, v)$ can be expressed as

$$\pi(p, r^{(p)}, \lambda, \beta, v|x) = \left(\frac{1}{2a}\right)^{n-p} \left(\frac{1}{\beta}\right)^{n-p+3} exp - \frac{1}{a\beta} \sum_{t=p+1}^{n} \left| \sum_{i=1}^{p} F^{-1}(r_i) y_{t-i} + y_t \right| C_p^{p_{max}} \lambda^p (1-\lambda)^{p_{max}-p} \frac{1}{2^p} v \, exp - \frac{v}{\beta}.$$

Reversible Jump MCMC Algorithm

The posterior distribution is simulated in 2 stages. First, simulate the conditional distribution of (λ, β, v) Ir given the value $(p, r^{(p)})$. Second, simulation of conditional distribution of $(p, r^{(p)})$ if given the value (λ, β, v). Since the conditional distribution of (λ, β, v) if given the value $(p, r^{(p)})$ can easily recognized, then the simulation of the conditional distribution of (λ, β, v) if given the value $(p, r^{(p)})$ can be done as follows:

- $\boldsymbol{\beta \sim IG\left(n-p+2, v + \frac{1}{a}\sum_{t=p+1}^{n} \left|\sum_{i=1}^{p} F^{-1}(r_i) y_{t-i} + y_t\right|\right)}$,
- $\boldsymbol{\lambda \sim B(p+1, p_{max}-p+1)}$, and
- $\boldsymbol{v \sim G(2, \frac{1}{\beta})}$.

However, the conditional distribution of $(\boldsymbol{p, r^{(p)}})$ if given the value $(\boldsymbol{\lambda, \beta, v})$ has a complex form, then the simulation of the conditional distribution of $(\boldsymbol{p, r^{(p)}})$ if given the value $(\boldsymbol{\lambda, \beta, v})$ is simulated with the reversible jump MCMC algorithm. For this purpose, the reversible jump MCMC algorithm uses 3 types of transformations, namely: changes to the coefficient of the AR model, birth of order of the AR model, death of order of the AR model [6].

The results of the study were in accordance with what was expected. Data modeling using AR model transformation so that the confidentiality of the original data is protected when the research results are published. The data used in the publication of research results is new data which is transformation data. The model for the original data is obtained by applying the inverse transformation.

If the results of this study are compared with the results of research in [2] then this study has similarities and differences. The similarity between the results of this study and the results of research in [2] is that both use the same prior distribution. But the difference between the results of this study and the results of research in Suparman is that this study uses Laplace noise while research in [2] uses Gaussian noise. If the results of the research in this article are compared with the results of research in [6] then this study also has similarities and differences. The equation is that they both use the same prior and noise distribution. However, the difference is that the results of research in [6] are a special form in this research when the transformation is identity transformation. In this study, the transformation used is the transformation $\boldsymbol{y = ax}$. In order to increase the confidentiality of the original data, this study was developed using a more complicated transformation.

Research results can be applied in a wider field because research results can not only be used in fields where data is not confidential but research results can be applied to fields where data is confidential. The results of this study are

recommended for modeling time series data that is confidential. So that when the research results are published, the confidentiality of the original data is protected.

Model Validation

The model generated by the reversible jump MCMC algorithm is validated through a simulation study. First, the values of the model parameters are set. Then, simulated data is created based on the value of this model parameter. Furthermore, the reversible jump MCMC algorithm is implemented on the simulated data to estimate the value of the model parameters. Finally, the estimators of the model parameters are compared with the predefined values of the model parameters. The model is said to be correct if the estimator of the model parameters is close to the value of the model parameters that have been set previously.

CONCLUSIONS

This article examines the AR model estimation procedure with Laplace noise to ensure the confidentiality of the data so that it is not accessed by other parties. This article uses the transform method to hide the original data. This article focuses on the transformation of the linear through the center of the coordinates. This article has not investigated the use of non-linear transformations, so this topic is interesting to be studied further. This article provides benefits on data security. This article has two advantages. The first advantage is the use of transformations to ensure data confidentiality. The second advantage is that the order of the AR model is treated as a parameter and the order of the model is estimated using data so that the AR model used is more accurate than if the order is determined subjectively. Research results can be applied to a wider field because research results can not only be used to model non-confidential data, but research can also be applied to model confidential data. For data that is confidential, it is recommended to use data modeling that protects data confidentiality.

ACKNOWLEDGMENTS

The authors would like to thank the Directorate of Research and Community Service (DRPM), Ministry of Education, Culture, Research and Technology (Indonesia) for the basic research scheme research grant that has been provided so that the research can be carried out. Furthermore, the authors also thank the reviewers of the 11th International Conference on Geotechnique, Construction Materials and Environment in Kyoto, Japan, for their comments and suggestions to improve the quality of this article.

REFERENCES

[1] G. E. P. Box, G. M. Jenkins, G. C. Reinsel, and G. M. Ljung, *Time Series Analysis: Forecasting and Control*. John Wiley & Sons, 2016.

[2] Suparman and M. S. Rusiman, “Hierarchical Bayesian Estimation for Stationary Autoregressive Models Using Reversible Jump MCMC Algorithm,” *Int. J. Eng. Technol.*, pp. 64–67, 2018, [Online]. Available: www.sciencepubco.com/index.php/IJET.

[3] J. Jureckova, H. L. Koul, and J. Picek, “Testing the tail index in autoregressive models,” *Ann Inst Stat Math*, vol. 61, pp. 579–598, 2009.

[4] L. Larbi and H. Fellag, “Robust Bayesian Analysis of an Autoregressive Model with Exponential Innovations,” *Afr. Stat.*, vol. 11, no. 1, pp. 955–964, 2016.

[5] Suparman, “A new estimation procedure using a reversible jump MCMC algorithm for ar models of exponential white noise,” *Int. J. GEOMATE*, vol. 15, no. 49, pp. 85–91, 2018, doi: 10.21660/2018.49.3622.

[6] Suparman and A. M. Diponegoro, “Mathematical Model with Laplace Autoregressive Process for Heart Rate Signals,” 2020.

[7] D. K. Lee, “Data transformation: A focus on the interpretation,” *Korean J. Anesthesiol.*, vol. 73, no. 6, pp. 503–508, 2020, doi: 10.4097/kja.20137.

[8] D. D. Wackerly, I. Mendenhall, and R. L. Scheaffer, *Mathematical Statistics with Applications*. Thomson Higher Education, 2008.

[9] P. J. Green, “Reversible jump Markov chain Monte Carlo computation and Bayesian model determination,” *Biometrika*, vol. 82, no. 4, pp. 711–743, 1995.

[10] O. Barndorff-Nielsen and G. Schou, “On the Parametrization of Autoregressive models by partial autoccorelation,” *J. Multivar. Anal.*, vol. 3, pp. 408–419, 1973.

11th Int. Conf. on Geotechnique, Construction Materials & Environment,
Kyoto, Japan, 3-5 November 2021, ISBN: 978-4-909106063 C3051

A COMPARATIVE STUDY ON THE CHANGE OF TOWNSCAPE IN HISTORICAL BLOCKS BETWEEN XI'AN AND KYOTO

Kun YUAN[1], Hirokazu ABE[2], Kensuke YASUFUKU[2],
Akira TAKAHASHI[2]

[1]Dept. of Global Architecture, Osaka University, Japan; [2] Cybermedia Center, Osaka University, Japan

ABSTRACT

This paper uses space syntax analysis to analyze similarities and differences in the urban spatial structure changes of two of the world's historical and cultural cities during the process of modernization. Axial line maps of the main urban areas of Xi'an, China, and Kyoto, Japan, are compared from the start of their respective periods of modernization to the present day. Changes in the cities' topological centers are analyzed, and the global and local relationships in their main urban areas are explored. The primary outcomes of the study are as follows:

1. With the expansion of the urban area, the topological centers of the two main urban areas also changed. From 1902 to 2020, the topological centers of Kyoto expanded outward simultaneously in both the horizontal and vertical directions. Xi'an also expanded, from one topological center centered on the bell tower in 1949 to two topological centers in 2019. In both cities, the global integration value (hereafter, Int.V global) grew (especially in Kyoto) during the period of modernization and long-distance accessibility increased, indicating that the two cities were heading toward motorization.

2. The average Int.V global change rates in the local historical blocks of the old Xi'an city show differences in the growth rates of local change and the global growth rate of urban space, which indicate the local development feature of block evolution is evident. The Int.V global change rates in the three wards of Kyoto are not significantly different from the global change rate, indicating a consistent change in global integration for Kyoto and a greater consistency of global street construction.

3. The correlation of global integration and local integration, as represented by intelligibility (R^2), increased in both Xi'an and Kyoto, indicating that the solidarity of the respective regions increased during the modernization process. This is especially true for Kyoto.

Keywords: Capital Cities, Morphological Change, Space Syntax, Xi'an, Kyoto

INTRODUCTION

Xi'an, China, and Kyoto, Japan, are ancient cultural centers whose main urban areas have developed around a chessboard network of roads. In terms of their morphology, the two have similarities, but they also have had their own distinct development features over the course of their modernization.

The Ming City District is the core area of Xi'an, which was built on the basis of the imperial city of the Sui and Tang Dynasties during the Hongwu Period of the Ming Dynasty, and which has retained many of its original areas [1]. The Ming City District is the center of Xi'an's urban human settlements, especially in its southwest area's remaining historic and cultural block of Beiyuan Gate and Sanxue Street, which inherited the best historical characteristics of the region and streets. With the founding of the People's Republic of China (1949), China began its modernization construction. [2] Since that time, Xi'an has experienced four master plans, and its urban areas have expanded dramatically to the East, South and West from the old city, growing from 13.2 to 724 square kilometers; during this period, the population has also increased, from 2.27 to 10.2 million [1]. With the rapid expansion and development of the city area, the form and structure of the main urban area within the city wall has changed significantly, and a large number of historical alleys have been rebuilt while others have disappeared in the historic blocks of the main city.

Japan began its modernization construction in the Meiji period (1868-1912), during which time the new Japanese government began to restore Kyoto [3]. A number of urban planning measures were carried out, widening streets and creating a ring road, all of which had the effect of accelerating the city's modernization. In the Showa period (1926-1989), the city merged with surrounding towns, rapidly and significantly expanding its urban area from 31 to 210 square kilometers. The population increased from 0.28 million in the Meiji period to 1.41 million [4], [5]. The city's urban development is still mainly characterized by grid planning, and the main urban

area is dominated by Kamigyo Ward, Nakagyo Ward and Shimogyo Ward. As in Xi'an, the modernization construction in Kyoto has greatly changed the urban area and street morphology of the city through urban planning.

Previous studies of the urban morphology of the two cities include a study by Onishi [2], who conducted a detailed investigation of the changes in the townscape of Xi'an's historic center and compared them to developments in Kyoto. Kang [6] studied the spatial morphology characteristics of Xi'an's Historic District using traditional spatial morphology analysis, mostly in terms of spatial layout, texture, street scale and plane form. Compared to investigative analyses that focus on traditional morphological characteristics, more recent spatial morphology analysis is mainly carried out using quantitative methods and is mainly focused on space syntax with a GIS data platform.

In an empirical and quantitative study of large-scale urban streets and roads in three separate periods, Huang [7] investigated the complex evolution of the morphological characteristics of the typical urban Hui culture from the morphological middle, street structures and network systems perspective, and examined the shift in the topological relationship between historic block space and urban whole space; however, there are few comparative studies between similar blocks.

Space syntax is important for extracting the topological structures of a city, particularly when comparing two or more cities. Kigawa [3] conducted an analysis of Kyoto's spatial configurations throughout the ages and its urban planning project based on space syntax, revealing that streets had a strong impact on Kyoto's transformation from its early modern to modern form. Kigawa [8] also used space syntax to analyze the process by which the castle cities had been reformed. In studying the process of urban modernization in several of the castle cities of Japan, he found distinct differences among the cities. In China, a comparative study of urban space based on space syntax was conducted by Wang et al. [9], who selected cities with wide differences in road networks and land configurations. Analyzing the axial line, the study explored differences and commonalities. Such studies help us to understand core area aggregation and urban morphology evolution inertia. However, comparative studies involving cities in two different countries that have a similar space structure initially but which later experience different development patterns are rare.

This paper compares the urban spatial structure changes in Xi'an and Kyoto in their respective modern city construction. In the process, we not only make a horizontal comparison of similar cities in different development stages, but also provide a vertical analysis of the relationship between their global and local aspects. Using a comprehensive quantitative analysis of the current urban development situation and its distinctive characteristics, we compare axis maps of the main urban areas of Xi'an and Kyoto in different years, and analyze the changes in their topological centers as well as the global and local relationship in their main urban areas.

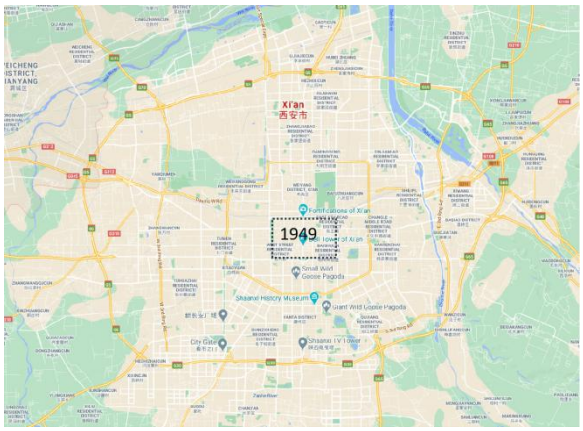

Fig. 1 Map of Xi'an (2019)

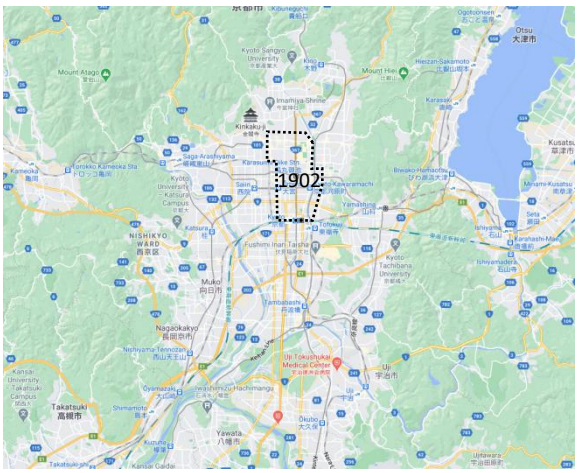

Fig. 2 Map of Kyoto (2020)

METHOD

Space syntax is a set of theories and analytical tools introduced in "The Social Logic of Space" by Hillier and Hanson in 1984 [10]. Topological analysis focuses on the connection between spaces.

We examined the street network of the historical capital districts in two steps:

First, we use an axial analysis to investigate the street network, then compare the axis maps of Xi'an and Kyoto in different years, tracing the changes in their topological centers. (The axial map is constructed by taking an accurate map and drawing a set of intersecting lines through all the spaces of the urban grid so that the grid is covered and all rings of circulation are completed.)

Because the urban morphologies of the two

cities have undergone dramatic changes in modern times, we chose the beginning period of the modernization construction of the two cities as the contrastive object. The starting point examined in this study for Xi'an is the founding of the new China in 1949; the starting point for Kyoto is the year of the earliest measured map (1902) in the Meiji period of the new Japanese government.

The study area for Xi'an focuses on the main urban areas that served as the Ming castle city (13.2 km^2). The main study area for Kyoto (21.2 km^2) consists of three districts (Kamigyo Ward, Nakagyo Ward and Shimogyo Ward). With respect to Xi'an, the key objects used in the study include four maps of narrow streets in the old city 1949 road network, together with a remote sensing image of Xi'an in 2019. In the case of Kyoto, the key objects are a field survey map from 1902 and a cadastral map from 2020.

In order to analyze the configuration layout of each city, we translated the actual spatial structure into an axial map (Fig. 3), which is the least set of longest lines drawn tangent to vertices that can see each other. For our topological analysis, the axial map was projected onto a justified graph in which the axial lines are represented as nodes, and the intersecting lines are the connections between the nodes [10].

Fig. 3 shows a justified graph that has been converted from an axial map. A justified graph is one in which a node is drawn at the base, and all the points of various depths are drawn above it. Specifically, all the points at depth 1 from the starting point are aligned horizontally immediately above it, all the points at depth 2 from that point are drawn above those at depth 1, and so on, until all levels of depth from the initial point are accounted for. The topological total depth and mean depth can then be determined from the justified graph.

A depth value represents the convenience of moving from one space to another. The topological distance between two adjacent nodes is one step. The shortest topological distance between any two nodes—that is, the number of spatial transformations—is expressed as the depth value between the two nodes. The larger the value, the deeper the element is hidden in the network of the study area.

Topological total depth (TD) is the cumulative total of the fewest topological depth paths between all pairs of nodes. MD (mean depth) is the average of the minimum number of steps from one node to all the other nodes in the system, which eliminates the effect of numbers.

Next, integration is introduced as an important result of the axis analysis. Its value is derived from the value of the topological depth, as in Fig. 4. By analyzing the integration value, it is possible to determine the degree of a street and how topologically shallow or deep the entire system is from a point on the street.

An integration value essentially describes the "accessibility" of an element in the study area network. The higher the depth value, the lower is the

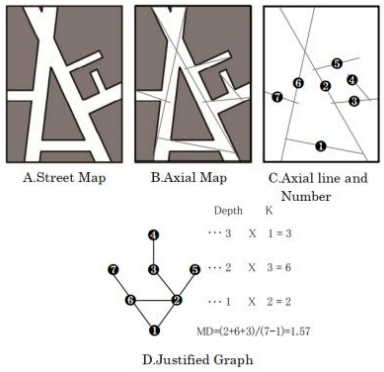

Fig. 3 Axial analysis [11]

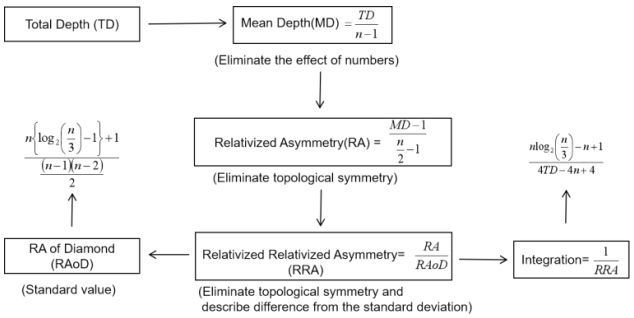

Fig. 4 Flow Chart from Depth to Integration [10]
n: total number of vertices

degree of integration, that is, the worse is the connectivity, and vice versa. More specifically, axial local integration is defined as the integration values of the axial lines at radius 3 (root plus two topological steps from the root) which can be used to represent a localized picture of integration. Axial global integration is defined as the integration values of axial lines at an infinite radius which can be used to represent the integration pattern at the largest scale.

Finally, the integration core can be used to represent the change and transfer of the topological center, consisting of the most integrating 10% of the lines [10,12].

In the second step, the results of the topological analysis conducted in the previous step are used to analyze the global and local relations of the respective main urban areas.

Axial intelligibility indexes the degree to which the number of immediate connections that a line has is a reliable guide to the importance of that line in the system as a whole. (Specifically, it is the correlation between local and global elements). Thus, intelligibility is introduced as a way to describe the

correlation between local integration and global integration and as the means to measure whether the local space and the global space environment are related and unified. This relationship indicates whether an area is intelligible in its global context [13, 14].

Intelligibility: $$R^2 = \frac{\left[\sum\left(I_3 - \bar{I}_3\right)\left(I_n - \bar{I}_n\right)\right]^2}{\sum\left(I_3 - \bar{I}_3\right)^2 \sum\left(I_n - \bar{I}_n\right)^2} \quad (1)$$

The value of intelligibility (R^2) is calculated by Equation 1, where I_n is the global integration of any axis in space, and I_3 is the three-step integration value of any axis in space. $\bar{I}_n$ and $\bar{I}_3$ are the mean values of global integration and three-step integration, respectively.

For Eq. (1), if the intelligibility of the local space is high, the indication is that the centrality of local space can be integrated into the global spatial structure. The natural movement of local space can not only bring movement economy; it can also produce a greater multiplier effect in the process of functional interaction with the movement economy of global space. On the other hand, if the intelligibility of local space is low, the indication is that the local centrality of the regional urban space cannot be integrated with the global space and is thus relatively isolated [12,15].

RESULTS AND DISCUSSION

Changes in the main urban areas of Xi'an and Kyoto

1) Main urban area of Xi'an

The two axial maps of Xi'an (1949 and 2019) shown in Fig. 5, allow us to examine the change in the urban topological center. With the development of lattice sub-trunk road planning, many narrow alleys were expanded and new roads throughout the castle district were constructed. The global integration value (Int.V global) of Lianhu Road, East 5th Road and West 5th Road to the north of the central axis, Jiefang Road and Heping Road to the east of the Central Axis is high. This suggests that the topological center of the street network has extended to the north side roads of the main road centered on the bell tower.

The remaining historical and cultural blocks of Beiyuan Gate and Sanxue Street in the western and southern areas of Ming city, with low Int.V global values, were far from the topological center of the main cross road centered on the bell tower and the northeastern part of the castle city in 1949. The average global integration values of the two historical blocks are 1.56 and 1.58, respectively, which is lower than the average global value of 1.71 in 1949. By 2019, the average global integration value had increased from 1.71 to 1.91, over which time the values for the two historical blocks increased to 1.88 and 1.74, respectively, both of which are lower than the 1.91 global average. However, the percentage change for the Beiyuan Gate block (18%) is greater than the global average (12%), while the percentage change for the Sanxue Street Block (10%) is slightly lower. The indication is that the historical blocks in the main city area experienced a high degree of local change with urban global space development. The local development in the evolution of the historic blocks is clear.

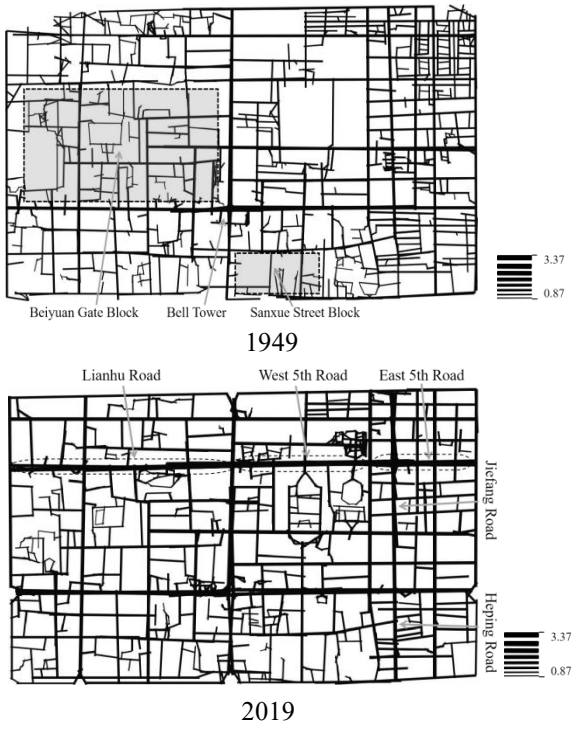

Fig. 5 Axial Maps with Global int.V for Xi'an in 1949 and 2019

2) Main urban area of Kyoto

Fig. 6 shows the 1902 and 2020 axial maps with Int.V global for Kyoto. The streets with high integration values based on the results of the axial analysis are more darkly shaded.

In 1902, the highest integration values are for Karasuma Street, Horikawa Street and San-Jyo Street, which constitute the urban topological center, as seen in the two maps. The highest vertical axial global Int.V extended outward and westward to Nishiohji street in 2020. The highest horizontal axial global Int.V expanded from San-Jyo Street to shi-Jyo Street. High connectivity is also seen for Go-Jyo Street and Shichi-Jyo Street. The topological center extended outward in both the horizontal and vertical directions simultaneously. The average global integration values of the three Kyoto wards increased from 1.38, 1.62 and 1.54, respectively, in 1902 to 2.18, 2.46 and 2.37 in 2020, corresponding to respective change rates of 55.7%, 51.8% and 53.9%. The fact that the change rates are not

substantially different from the global change rate (53.6%) indicates a strong consistency in global street construction.

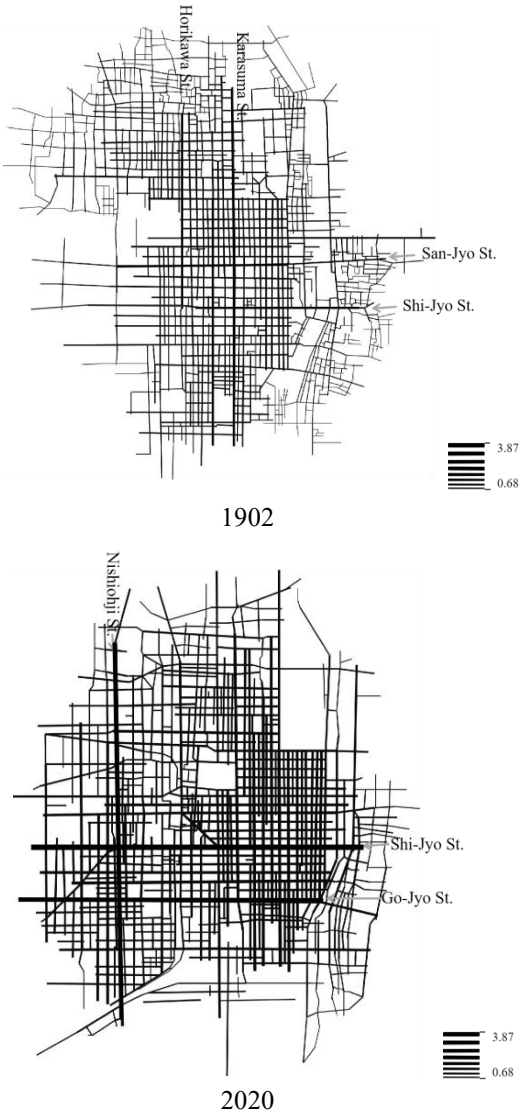

Fig. 6 Global integration values for Kyoto in 1902 and 2020

As can be seen here, the topological centers of both cities experienced an outward expansion. In the main urban area of Kyoto, the consistency of street construction is stronger and the change in global accessibility is more obvious. In Xi'an, the global change in the main city is not nearly as clear. While Xi'an's main urban area has been strongly affected by the urban expansion outside of the castle city, the residential areas inside the city wall also have obvious characteristics of local development. The external driving force of urban global space development and the internal traction of block evolution appear to have interacted with each other to jointly promote the deepening development of the structure of the historic blocks.

Scatter diagram analysis

Scatter diagrams for Xi'an showing Int.V global on the horizontal axis and Int.V local on the vertical axis are provided in Fig. 7. It is apparent that the distribution shapes of the scatter points in 1949 and 2019 show little similarity. In 1949, Int.V global was relatively low, and the scatter points are concentrated in the lower left portion of the diagram. In 2019, the concentration of the scatter points has shifted toward the middle, and the average Int.V global has increased, indicating that the Int.V global of Xi'an's axial line became stronger in the process of the city's modern urban spatial development.

Fig. 8 gives the Int.V (global and local) scatter diagrams for Kyoto. As shown, the center of the dense area of the scatter points moves rightward over the period of 1902 to 2020. The average value of Int.V global increased markedly as the global integration value of most of the scatter points was greater than 1.0. Such results indicate that Int.V global grew substantially stronger and that long-distance accessibility increased during the modernization period.

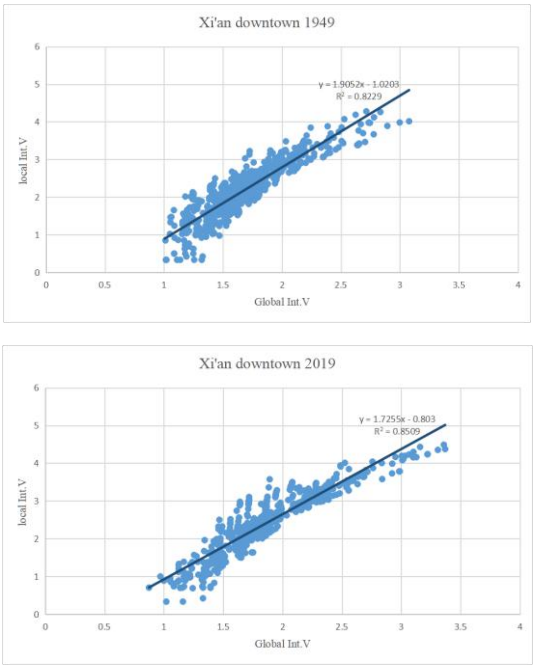

Fig. 7 Int.V (global and local) scatter diagrams for Xi'an in 1949 and 2019

Table 1 gives key parameters of the scatter plots in Fig. 7 and Fig. 8. Of particular note is the slope of the regression line fitted to the Xi'an (Fig. 7) scatter points, which decreases from 1.905 in 1949 to 1.725 in 2019. The slope of the regression line for the Kyoto scatter diagrams (Fig. 8) also decreases,

from 1.868 in 1902 to 1.454 in 2020. The fact that the slopes decrease means that the scatter points move rightward (i.e., Int.V global becomes stronger). In general, urban networks with a higher Int.V global are better suited for long-range accessibility, since Int.V global is calculated with up to all topological depths in Depthmap, and is closely related to motor vehicle traffic. In contrast, urban networks with a higher Int.V local are better suited for short-range accessibility related to pedestrian traffic. From the basic of these, it can be inferred that the modernization of the two cities was heading toward motorization.

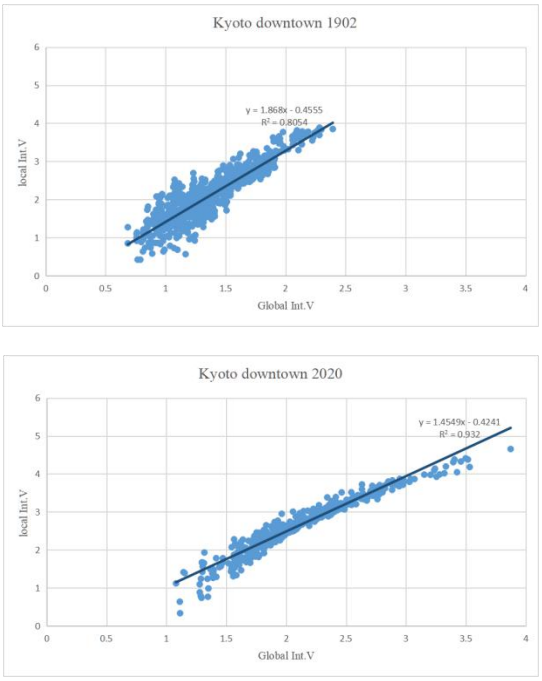

Fig. 8 Int.V (global and local) scatter diagrams for Kyoto in 1902 and 2020

Table1 Parameter comparison of Fig. 7 and Fig. 8

	1902, Kyoto	2020, Kyoto	1949, Xi'an	2019, Xi'an
Regression Line	y=1.868x+0.4555	y=1.4549x+0.4241	y=1.9052x+1.0203	y=1.7255x+0.803
R^2 (Intelligibility)	0.8054	0.9319	0.8229	0.8509
Global Int.V(mean)	1.3774	2.1162	1.711	1.9080
Local Int.V(mean)	2.1174	2.6564	2.2396	2.4893

The intelligibility (R^2) value for Xi'an increased from 0.8229 (1949) to 0.8509 (2019), while the value for Kyoto increased from 0.8054 (1902) to 0.9319 (2020). Hillier suggests that intelligibility is used to describe the correlation between local integration and global integration and measures whether the local space and the global space environment are related and unified. This relationship presents if an area is intelligible in its global context [13].

Hillier also suggests that if the intelligibility value of local space is low, the implication is that the local centrality of the regional urban space cannot be integrated with the global space and is thus relatively isolated [15]. The value of intelligibility (R^2) increases in both Xi'an and Kyoto, meaning that the solidarity of the respective regions has increased during the modernization process.

CONCLUSIONS

This paper sought to uncover similarities and differences in the evolution of the historical cities of Xi'an and Kyoto by using space syntax. Through axis analysis of the two main urban areas in different years, the topological centers and the global and local relations of the main urban areas were compared. The analysis produced three important findings:

1. With the expansion of the urban area, the topological centers changed correspondingly. The topological center in the main urban area of Kyoto clearly expanded outward from 1902 to 2020 in both the horizontal and vertical directions simultaneously. In Xi'an, the area expanded from one topological center centered on the bell tower in 1949 to two topological centers in 2019. Int.V global increased markedly for the two cities (especially for Kyoto), and long-distance accessibility increased during the period of modernization. The implication is that the modernization of the two cities was heading toward motorization.
2. The average Int.V global change rates of the local historical blocks in the old Xi'an city show a difference in the local change and the global growth of its urban space, and make evident the local development feature of block evolution. On the other hand, the Int.V global change rates for the three wards in Kyoto are similar to the global change rate, indicating a consistent change in global integration and a strong consistency of global street construction.
3. The global and local integration correlation of the two major urban areas is reinforced by the characteristic curve and index analysis, with the two exhibiting strong similarity. The intelligibility (R^2) value increases in both Xi'an and Kyoto, meaning that the solidarity of the respective regions has increased during the modernization process. In this regard, Kyoto is clearly stronger than Xi'an.

REFERENCES

[1] Xi'an Municipal Bureau of Statistics: Xi'an Statistical Yearbook, China Statistics Press, 2020.
[2] Ohnishi, K.: A Study on the Change of Townscape in the Historic Center in Xi'an City, China, Journal of the City Planning Institute of Japan, Vol.28 ,1993.
[3] Kigawa, T. and Furuyama, M.: Study on a

Vector in Kyoto's Modernization by means of Space Syntax, Journal of the City Planning Institute of Japan, Vol.40-3, pp.139-144, 2005.10.

[4] Ohnishi, K.: The Beauty of Kyoto—The Theory of Conservation and Regeneration, Kajima Institute Publishing Co., Ltd.,1992.05

[5] Kyoto Population, Japan Geographic Data Center, 2020.

[6] Yitong, K., Sunwei, L. and Wei, F.: The Beilin Historic District, Xi'an Spatial Morphology Characteristics Analysis, Journal of Architecture and Culture , Vol.9, 2017.

[7] Jiaying, H.: Study on the Construction and Morphology Transition of the Drum-tower Hui Community in Xi'an, Doctoral Dissertation of South China University of Technology, 2010.

[8] Kigawa, T. and Seo, K. W.: Using Space Syntax to trace the Japanese urban renovation from JYOKAMACHI to modern cities What formed the city, the Centre or the Boundary?, Proceedings of the 11th International Space Syntax Symposium, 2009.

[9] Jiejing, W. Fang, W. and Rui, L.: Space Syntax Based Urban Morphology Comparison, Journal of Planners, Vol.28, 2012.6.

[10] Hillier, B. and Hanson, J.: The Social Logic of Space, Cambridge University Press: Cambridge, 1984.

[11] Woochul N. A. and Abe H.: A Morphological Examination of Street Networks and Building Condition in the Old Castle District of Daegu, Korea, 15th international conference on geometry and graphics, 2012.

[12] Hillier, B., Hanson, J., Grajewski,T., and Xu,J.: Natural movement: or, configuration and attraction in urban pedestrian movement., Environment and Planning B: Planning and Design, Vol.20, pp.29-66, 1993.

[13] Hillier, B., Burdett, R., Peponis, J. and Penn, A.: Creating Life: Or, Does Architecture Determine Anything? Journal of Architecture and Behaviour , Vol.3-3, pp.237, 1987.

[14] Tuncer, E.: Perception and Intelligibility in the Context of Spatial Syntax and Spatial Cognition., Proceedings of the 6th International Space Syntax Symposium, 2007.

[15] Hillier, B.: Space is the Machine, Cambridge University Press: Cambridge, pp.149-200, 1996.

11th Int. Conf. on Geotechnique, Construction Materials & Environment,
Kyoto, Japan, 3-5 November 2021, ISBN: 978-4-909106063 C3051

MID-INFRARED SPECTRA OF CHLORIDE ION IMMOBILIZED ON CEMENT

Yu Hashimoto[1], Shinichiro Okazaki[2], Kenji Wada[3], Ichiro Ishimaru[4] and Koji Kanasaki[5]

[1]Graduate School of Engineering, Kagawa University, Japan;
[2,4]Faculty of Engineering and Design, [3]Medicine, Kagawa University, Japan;
[5] Nisshin Kikai Co.,Ltd., Japan

ABSTRACT

A strategy based on infrared spectroscopy is prospected to be used as a novel nondestructive inspection method to assess the risk of chloride attack on reinforced concrete (RC) structures. The characteristics of the infrared spectra of bound chloride ions in cement in the mid-infrared region were investigated in this study to examine the concentration of chloride ions on the surface of the concrete using the mid-infrared spectroscopic camera. The reflection FTIR technique was used to measure the infrared spectra of cement paste samples with varying chloride ion concentrations. Furthermore, multivariate statistical methods were applied to the obtained mid-infrared spectra to critically examine the wavelength bands of the peaks with characteristic values reflecting differences in chloride ion concentrations. As a result, if we can develop an instrument that can measure around 7300 nm, the wavelength that reflects the difference in chloride ion concentration may be around 7300 nm.

Keywords: Mid-infrared spectroscopy, infrared spectrum, Bound chloride ions in cement

INTRODUCTION

In recent years, various fields have made efforts to realize a sustainable society as outlined in the Sutainable Development Goals. For example, in civil engineering, infrastructures are being shifted from breakdown maintenance to preventive maintenance management to improve sustainability. In addition, various nondestructive testing methods have been developed in recent years and are actually in operation in the field.

Reinforced concrete is frequently used for the construction of infrastructure. When the sea breeze carries in chloride, it enters the concrete through cracks. When this chloride reaches the steel bars, corrosion begins, and the structure's life is cut short. To assess the degree of chloride deterioration of reinforced concrete, the chloride ion concentration at the location of the reinforcing bar must be measured, and a formula has been proposed to estimate the internal chloride ion concentration by measuring the concentration on the concrete surface [1][2].

With the establishment of the formula for calculating the internal chloride ion concentration, it became possible to predict the concentration at the bar's location by measuring the surface chloride ion concentration. Thus, focusing on measuring the concentration on the concrete surface, a method for estimating the concentration using near-infrared spectroscopy was proposed [3]. As a result of this study, it was found that there is a peak in the near-infrared spectrum around 2,266 nm that correlates with chloride ion concentration [3]. Based on these findings, various near-infrared spectrometers have been developed [4–7] and tested, but it has been noted that sunlight may interfere with outdoor measurements [8].

The authors have elemental technology related to a lightweight, compact, and vibration-resistant spectrometer (Fig. 1, hereinafter referred to as the "compact device") [9] that uses imaging 2-D Fourier spectroscopy in the mid-infrared region, which is less affected by low solar radiation. The purpose of this study is to investigate in detail the wavelengths that are correlated with the concentration of chloride ion immobilized on cement in the mid-infrared region, assuming that this device will be used, and to obtain information that will help with future measurements using this device.

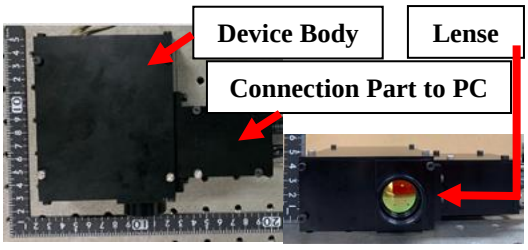

Fig.1 Spectrometer using imaging two-dimensional Fourier spectroscopy (Compact Device)

INFRARED SPECTROSCOPY

Infrared spectroscopy is a spectroscopic method based on absorption, diffuse reflection, and emission of light in the infrared wavelength range. When a material is irradiated with infrared light, the molecules that make up the material absorb the light energy, causing a state transition in molecular motion.

The energy of the infrared light transmitted or reflected from the material is smaller than that of the irradiated infrared light used for the state transition of the molecular motion. This energy is called absorbance, and it is excellent for identifying chemical substances because each molecular structure exhibits a unique waveform. The advantages of this measurement method include the fact that it is nondestructive and non-contact and that no pretreatment is required because no chemicals are needed. In addition, the measurement time is short, which makes it easy even when the number of test pieces is large.

EXPERIMENTAL METHOD

Overview of Device and Measurement Methods

In this experiment, the powdered samples were measured using Fourier Transform Infrared Spectrometer (hereafter, this is called "FTIR"). In this study, the diffuse reflection method was used for the measurement. To examine the results in more detail, the number of integrations was 64 times. The FTIR-4200 type A spectrometer manufactured by JASCO Co. was used for the measurement.

Samples

Ordinary Portland cement was used to prepare the samples, and the weight ratio of water to cement (W/C) was 50%. Two samples were prepared, one for FTIR and the other for later measurement by the Compact Device. The samples were placed in a sample form to a height of 5cm, cured for 24 hours, and then de-molded and sealed for 21 days. After curing for 24 hours, the sample was unmolded and sealed and cured for 21 days. The reason for using a 5cm sample was to facilitate measurement with the Compact Device. After the curing was completed, the samples were ground into powder using a metal mortar for FTIR analysis Although it has been confirmed that the mid-infrared region is affected by moisture, we did not completely dry the powder because it might change the physical properties.

ANALYSIS

Spectral Processing

To improve the analytical accuracy of instrumental analysis, it is necessary to remove disturbances other than the actual information that inevitably enters the analysis as much as possible. In infrared spectroscopy, environmental factors such as fluctuations in the light source and humidity at the time of measurement often cause the entire absorption spectrum to rise and fall. This is called baseline shift, and it makes it challenging to detect apparent differences. Therefore, Standard Normal Variate (SNV) is often used [10]. Let y (v, p) be the dataset of acquired spectral y(v). If the spectral variable in the p-th spectral is v, the mean value of the spectral is $\bar{y}$(p), and the standard deviation is σ(p), then SNV is expressed as

$$\boldsymbol{y_{SNV}(v,p)} = \frac{\boldsymbol{y(v,p)-\bar{y}(p)}}{\boldsymbol{\sigma(p)}} \quad (1)$$

Since this process unifies the baseline of all spectral data and makes it easier to detect apparent differences, the processed data were used in the analysis.

Analysis Methods

Multivariate analysis is used to detect apparent differences, particularly, principal component regression and partial least squares regression analyses are often used in infrared spectroscopy [10]. In this study, these two types of analysis methods were used. The analysis was performed in the range of 5000-17000 nm, including the Compact Device's wavelength range. The Unscrambler X from Camo Analytics Co. was used for the analysis.

Principal component regression analysis (PCR)

In PCR, the amount of chloride is calculated from spectral data X using the coefficient of principal component T, which is estimated to maximize the variance of X by an information compression method known as principal component analysis and by creating a regression equation using least-squares regression. The following equation expresses the model equation for principal component analysis with the weight P assigned to each wavelength:

$$X = TP^t \quad (2)$$

The superscript t represents the transpose matrix. For least-squares regression, the target variable is only the amount of chloride, so it is a simple regression. If the amount of chloride is y, the regression coefficient is q, the initial value is f; least-squares regression is expressed by the following equation, which is calculated to estimate the amount of chloride.

$$y = Tq + f \quad (3)$$

Partial least squares regression analysis (PLSR)

In PLSR, the principal component T is calculated to optimize the covariance between the spectral data X and the amount of chloride y. Thus, the model equation is E for the residual of X, q for the coefficient of the principal component, and f for the residual of y.

$$X = TP^t + E \quad (4)$$
$$y = Tq + f \quad (5)$$

The principal component T is calculated from Eq. (4) and Eq. (5). The chloride content is estimated from Eq. (5)

MEASUREMENT RESULTS

In the FTIR measurement results, each spectrum is shifted up and down, making it challenging to detect characteristic differences (Fig.2). However, by using SNV, the baseline is aligned, making it easier to see the characteristic differences in the spectra (Fig.3).

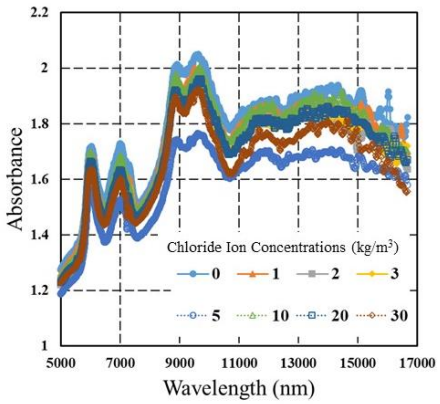

Fig.2 Original spectral data acquired by FTIR

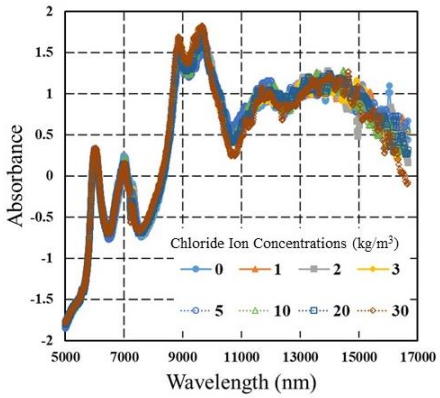

Fig.3 Spectral data acquired by FTIR after SNV processing.

ANALYSIS RESULTS

PLSR and PCR generated the regression equations, and the mean squared errors of the predictions of chloride ion concentrations were compared. The PLSR results showed a smaller mean square error than the PCR results, and the distinctive wavelengths were identified from the PLSR results.

First, comparing the predicted values based on the regression equation and the initial chloride ion concentration shows that the prediction is highly accurate (Fig.4). In addition, the factor contribution rate of this regression equation exceeds 70% at the third principal component (Fig.5).

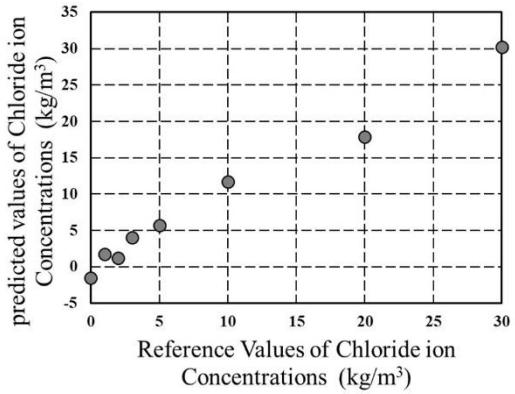

Fig.4 Comparison of standard and predicted chloride ion concentrations

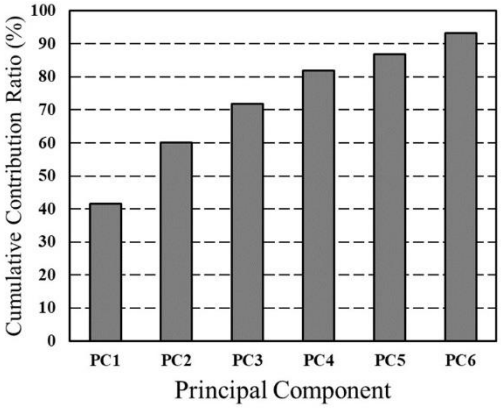

Fig.5 Cumulative contribution ratio of principal components

From Fig.3, it can be said that there is a characteristic difference in the wavelengths with large absolute values of loading among the first to third principal components. The wavelengths with particularly large absolute values are 7300, 8800, 9200, 10700, 15000, and 16300 nm (Fig.6, 7, and 8).

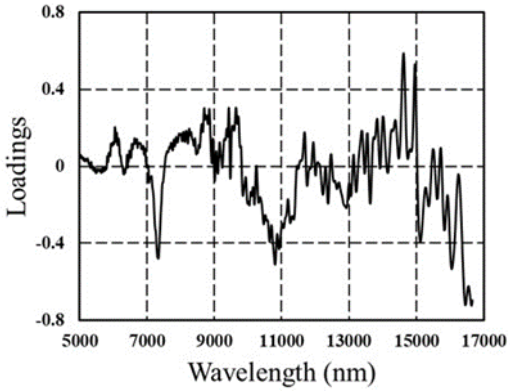

Fig.6 Loading of the first principal component

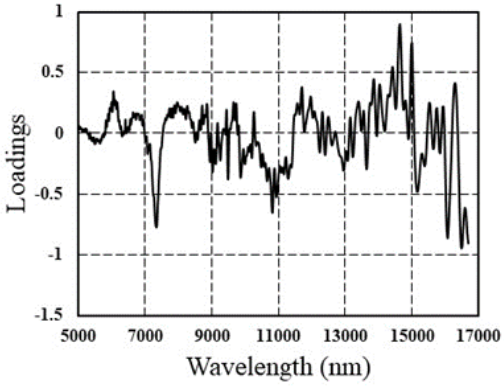

Fig.7 Loading of the second principal component

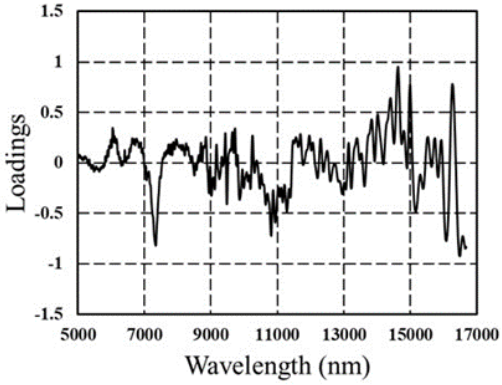

Fig.8 Loading of the third principal component

DISCUSSION OF ANALYSIS RESULTS

By comparing the spectra of the analysis results and the spectra after SNV processing, we will examine in detail where the wavelengths that reflect the differences in chloride ion concentrations are located. First, from the magnified images of the wavelengths with the largest absolute values, the absorbance of only the area around 7300 nm is arranged in order of concentration (Fig.9).

Next, the absorbance at 7339 nm, where the absolute value of loading was huge among the 7300 nm region, is negatively proportional to the chloride ion concentration (Fig.10).This suggests that 7339 nm is a characteristic wavelength that reflects the difference in chloride ion concentration.

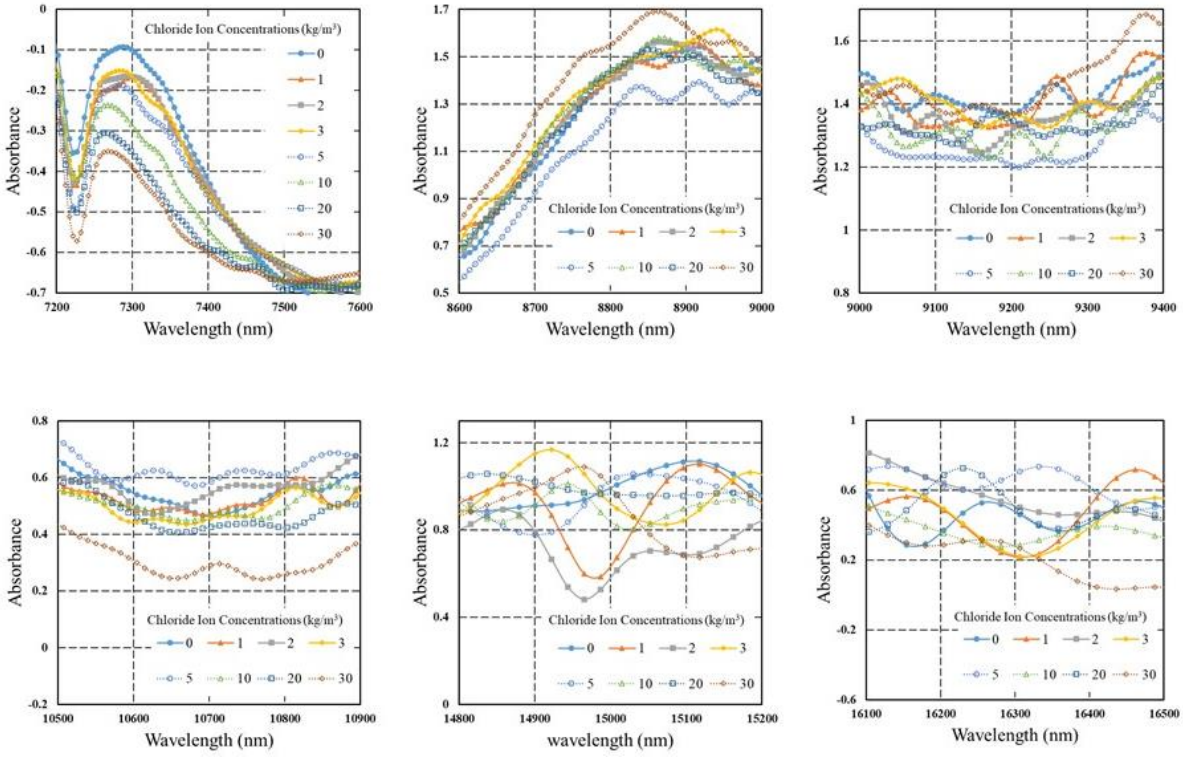

Fig.9 Absorbance near the wavelength where the absolute value of loading was large

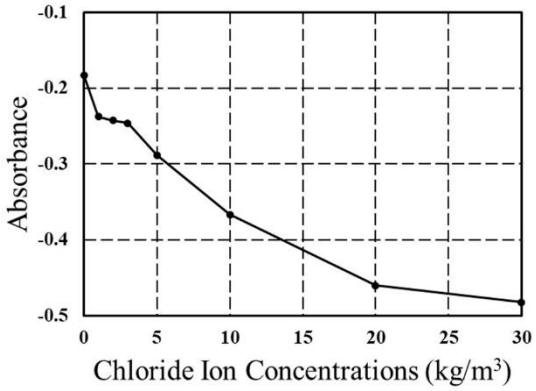

Fig.10 Relationship between absorbance and chloride ion concentration at 7339nm

MEASUREMENT BY THE COMPACT DEVICE

Experimental Method

A light source, a sample mounting apparatus, and the Compact Device were used for the measurements. The light source was a halogen lamp manufactured by HawkEye Technologies Co. The positional relationship is shown in Fig.11.

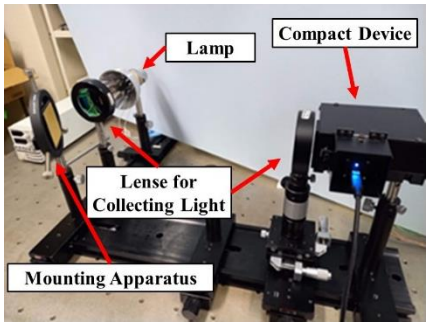

Fig.11 A scene of measurement using the Compact Device

The first step in the measurement procedure is to place an unwanted sample on the sample mounting apparatus and check and adjust whether sufficient luminance can be measured with the Compact Device. Once adequate illumination is obtained, the sample and gold plate are replaced to obtain a reference. Then, the measurement is carried out while replacing each sample. When setting up the samples, the measurement was carried out carefully so that the surface to be measured would not shift back and forth.

Measurement Results

The measurement range of the Compact Device is 8000-14000 nm, and the area around 7300 nm is barely measurable. The wavelength 8000-14000 nm showed a waveform similar to that of FTIR (Fig.12), but the area around 7300 nm was quite noisy and the absorbance was not ordered by chloride ion concentration. (Fig.13); therefore, we could not detect a clear difference in absorbance.

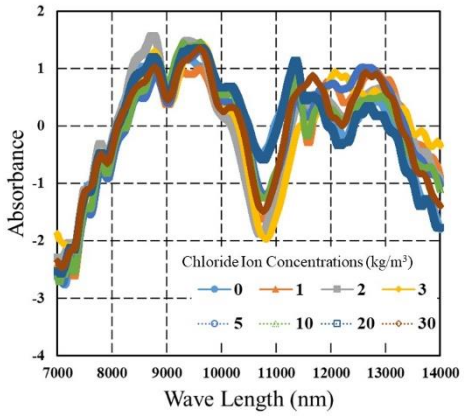

Fig.12 Spectral data acquired by the Compact Device after SNV processing

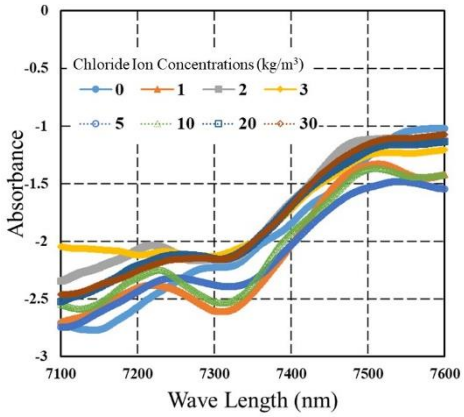

Fig.13 Spectral data around 7300 nm after SNV processing acquired by the Compact Device.

CONCLUSION

To develop and propose a chloride ion concentration detection system using mid-infrared spectroscopy as a new method for investigating chloride induced damage to RC structures, this study reports on the infrared spectra of cement paste with sequentially changing chloride concentrations using mid-infrared spectroscopy.

As a result of FTIR measurement and multivariate analysis, it was confirmed that the wavelength reflecting the difference of chloride ion concentration existed around 7300nm. At 7339 nm, the correlation between chloride ion concentration and absorbance was strong. However, as a result of measurement using the Compact Device, it was impossible to measure around 7300 nm accurately, and the difference in chloride ion concentration could not be determined. In the future, it will be necessary to develop a compact device that can accurately measure around 7300 nm.

REFERENCES

[1] T. Saeki, T. Shima, and S. Nagataki, Prediction of Chloride Penetration into Concrete by Equivalent Diffusion Coefficient, Proceedings of the Japan Concrete Institute, 20(2), 1998 pp. 859-864,

[2] G.K. Glass, and N.R. Buenfeld, The influence of chloride binding on the chloride-induced corrosion risk in reinforced concrete, Corrosion Science 42, 2000, pp. 329-344

[3] Y. Ishikawa, H. Kanada, Y. Kato, and T. Uomoto, Development of quantitative analysis of chloride content in concrete using near-infrared method, Monthly journal of the Institute of Industrial Science, University of Tokyo, 58(3), 2006, pp. 281-284

[4] Y. Nakajima, Y. Shirane, S. Suenaga, I. Hanya, and R. Sakimura, A Development on the Inspection System for Chloride Ion Content on the Concrete Surface Using Near-Infrared Spectrum and Its Application to the Maintenance of the RC Structures, Report of technical research institute, Maeda Corporation, 57, 2016, pp.06

[5] K. Toda, Y. Nakamura, and T. Kurata, System for Diagnosing Concrete Deterioration with Spectroscopic Analysis, IHI Engineering Review, 45(1) 2012, pp.31-36

[6] A. Watanabe, H. Furukawa, S Miyamoto, and H. Minagawa, Nondestructive Chemical Analysis of Water and Chlorine Content in Cement Paste using Near-infrared Spectroscopy, Construction and Building Materials, 196(30), 2019, pp.95-104

[7] K. Wada, S. Okazaki, and I. Ishimaru, Visualization of Chemical Composition and Chloride Ion Distribution by Novel NIR Imaging Spectroscopic System, Journal of the Imaging Society of Japan, 58(6), 2019, pp.664-650

[8] Y. Sakakihara, Y. Kabeyama, K. Hamada, S. Okazaki, K. Kanasaki, K Wada, I. Ishimaru and T. Saito, Development of Two-dimensional Imaging System of Surface Chloride Ion of Concrete Structure, Journal of Japan Society of Civil Engineers, Ser. B3 (Ocean Engineering), 75(2), 2019, pp. I_157-I_162

[9] N. Yamamoto, T. Saito, S. Ogawa, and I. Ishimaru, Middle Infrared (wavelength range: 8 μm-14 μm) 2-dimensional Spectroscopy (total weight with Electrical Controller: 1.7 kg, total cost: less than 10,000 USD) so-called hyperspectral camera for unmanned air vehicles like drones, Proc. SPIE 9840, Algorithms and Technologies for Multispectral, Hyperspectral, and Ultraspectral Imagery XXII, 2016

[10] K. Miyamoto, Near-Infrared Spectroscopy III. Quantitative Analysis by Near-Infrared Spectroscopy, Journal of the spectroscopical research of Japan, 53(3), pp. 192-203

11th Int. Conf. on Geotechnique, Construction Materials & Environment,
Kyoto, Japan, 3-5 November 2021, ISBN: 978-4-909106063 C3051

TILLER AND RHIZOME GROWTH ON EXCAVATED SLOPES IN TWO *Carex* SPECIES DERIVED FROM COLONIES ON LANDSLIDES

Teruo Arase[1], Tetsuo Okano[1], Tetsuoh Shirota[1], Masaaki Furuno[2] and Taizo Uchida[3]

[1]Faculty of Agriculture, Shinshu University, Japan; [2]Graduate School of Engineering, Kyusyu Sangyo University, Japan; [3]Faculty of Architecture and Civil Engineering, Kyusyu Sangyo University, Japan

ABSTRACT

To assist with the revegetation of excavated slopes, experimental revegetation sites were established using two terrestrial sedges, *Carex oxyandra* and *C. satsumensis*, that typically colonize landslides in the Kiso Mountains, Japan. The experimental design comprised a randomized block design with a two-way layout; 2 species × 2 soil types (black-colored soil and weathered granite soil) × 2 replicates. The plot size was set to 1.5 × 0.9 m. Rootstocks of the sedges were collected and 15 rootstocks per plot (1 to 3 tillers per rootstock) were transplanted in May 2019. The number of tillers per ramet was measured at one-month intervals. Rhizome growth was measured by sampling two ramets from each replicate in December 2020. Based on the increase of tillers, both species were capable of growth on both soil types; *C. oxyandra* showed superior growth on the black-colored soil, while *C. satsumensis* grew better on the weathered granite soil, and both species showed poor growth in the plot under shaded conditions. Rhizome growth was influenced significantly by species, soil type and their interaction; the total rhizome length per ramet in *C. oxyandra* and *C. satsumensis* was 15.9 to 28.6 cm and 182.1 to 746.2 cm, respectively. The former species produced short rhizomes and dense tussocks from concentrated tillers, while the latter produced numerous extremely long rhizomes and sporadic foliage from horizontally scattered tillers. Since the characteristics of growth differed between the two species, using an optimum combination of both species is considered suitable for early revegetation of excavated slopes.

Keywords: Carex oxyandra, Carex satsumensis, Tiller, Rhizome, Excavated slope

INTRODUCTION

Wild plant species that are indigenous to specific areas are attracting attention for revegetation projects given the important roles they play in the conservation of biodiversity and landscape ecology [1]. While some wild plants, such as Japanese pampas grass (*Miscanthus sinensis*) and Japanese mugwort (*Artemisia princeps*), have already been used for revegetation projects [1], using wild plant species is often complicated by the lack of basic information on their ecology, germination and growth, and reproduction. In addition, compared to cultivated pasture grasses, wild plants often show considerably less uniformity in their germination and growth patterns as they need to survive in natural areas affected by occasional disturbances. It is therefore necessary to collate information on how these wild plant species can be applied to revegetation projects.

The increased frequency of severe typhoons and heavy rainfall events in recent years has meant that landslide disasters are also increasing across Japan [2]; for example, a record of 3,459 landslide disasters occurred in the country in 2018 [3]. While saving human life and providing aid to people adversely affected by these events is a universal concern, construction work to prevent landslides is also urgently required in order to protect and stabilize susceptible areas., Revegetation projects focusing on stabilizing these areas in Japan have formerly employed exotic pasture grasses, but these species are regarded as problematic at present because their rapid and uniform growth may be difficult to limit once established. [1]. Two approaches can be adopted when using native plant species for revegetation: developing technological improvements to promote rapid vegetational succession, and searching for native species with excellent growth characteristics. In the present study, we employed the latter approach and focused on terrestrial sedges native to Japan.

Sedges, herbaceous species in the genus *Carex* (Cyperaceae), are perennials with rhizomes and tussock foliage. Sedges are very familiar to Japanese people; the foliage of some *Carex* species has been used as a traditional fiber to make straw lampshade-hats, raincoats, and sacred festoons in some areas, and variegated-leaf varieties are planted as ornamental garden plants [4]. Of the approximately 2,000 *Carex* species that have been described to date, approximately 250 species are found in Japan where they inhabit environments such as riparian areas, wetlands, grasslands, forests, alpine areas and coastal areas [5]. While the growth characteristics of sedges are relatively similar to those of grasses

(Poaceae), most revegetation projects using sedges have been limited to riparian areas and wetlands [1, 6–7].

Studies on *Carex* species have generally focused on aspects such as taxonomy and phytogeographical distribution [8–9], seed dispersal [10], growth responses to water [11–12], and vegetational succession [13]. Within the context of practical applications, some aquatic and hydrarch species have been studied for use in riparian areas and wetlands [1, 6–7], as mentioned above; however, a recent study examined the application of sedges to water purification [5]. Most of the studies that have been conducted on terrestrial sedge species in Japan have focused on their undesirable characteristics, such as the way in which they behave like weeds and cause nutritional deterioration of pasture [14], and how they can suppress the regeneration of tree seedlings in natural forests [15–16].

However, some terrestrial sedge species have been reported to be pioneer plants that colonize landslides in riparian areas [9] and bare ground in abandoned mine quarries [13]. The species that colonize disturbed areas as pioneers could potentially play an important role in maintaining plant community structure and in protecting the soil, at least in the early stages of vegetational succession. Given the broad range of habitats colonized by *Carex* species, it is considered that there must be some species that are well suited to revegetating disturbed terrestrial areas (i.e., areas in addition to riparian areas or wetlands), such as landslides or excavated slopes.

In this study, we established experimental revegetation plots using two terrestrial *Carex* species on excavated slopes. The species were selected based on the results of a previous study on *Carex* flora found in the subalpine and alpine zones of the Kiso Mountains, Central Japan [9]. By monitoring the increase in tillers and elongation of rhizomes after planting, the growth characteristics of these species were analyzed and their potential for application to revegetation projects is suggested.

RESEARCH SIGNIFICANCE

The significance of the present study is that it focuses on two native terrestrial *Carex* species and assesses whether they can be applied to practical revegetation experiments on excavated slopes in two different soil types. Specifically, the increase in aboveground tillers was measured at monthly intervals over an 18-month period after planting, and the development of underground rhizomes and buds was monitored. The obtained data and findings are considered to be useful for promoting the use of native terrestrial *Carex* species to revegetation projects.

Fig. 1 *Carex oxyandra* in natural habitat at an elevation of 1,430 m in the Kiso Mountains in May 2019.

Fig. 2 *Carex satsumensis* in natural habitat at an elevation of 1,230 m in the Kiso Mountains in May 2019.

METHODS

Carex Species Used in the Present Study

The flora and habitat of *Carex* species were previously investigated in the subalpine and alpine zones (at elevations of approximately 1,230 to 2,650 m) of the Kiso Mountains in central Japan [9]. A total of 14 *Carex* species were observed, and of these, two species (C. *oxyandra* and *C. satsumensis*) were evaluated as being potentially suitable for revegetation applications as they typically colonized areas comprising accumulated detritus or gravel associated with landslides.

Carex oxyandra (Fig. 1) had a broad vertical distribution at elevations ranging from 1,300 to 2,650 m (from low-mountain to the alpine zone) in the Kiso Mountains [9]. In addition, this species has been reported to have colonized the bare ground of an abandoned mine quarry [13]. This species has also been reported to have suppressed the growth of tree seedlings [15-16].

Compared to *C. oxyandra*, *C. satsumensis* (Fig. 2) had a narrower vertical distribution and was found at elevations of 1,200 to 1,400 m [9]. Little information is available for this sedge, except that it emerged as a pioneer species in a clearing experiment conducted in an alpine grassland [17].

Establishment of Experimental Sites

Experimental revegetation sites were established in two areas with different soil types: black-colored soil (Andosol; derived from volcanic ash) on the Campus Research Farm, and weathered granite soil in the Terasawayama Research Forest, both of which belong to the Faculty of Agriculture at Shinshu University. In each area, excavated slopes covered with almost no vegetation were selected as experimental sites.

The experimental design comprised a randomized block design with a two-way layout; 2 species × 2 soil types (black-colored soil and weathered granite soil) × 2 replicates. The plot size was set to 1.5 × 0.9 m, where 1.5 m was set along the slope direction. Table 1 shows the environmental conditions at the experimental sites.

Rootstocks of the sedges were collected from their natural habitats in the Kiso Mountains and 15 rootstocks per plot (1 to 3 tillers per rootstock) were transplanted at the end of May 2019. The experiment was started on June 1, 2019.

Table 1 Environmental conditions of the experimental plots

Soil	Plots	Elevation (m)	Slope direction	Incline (°)
Black-colored soil (Research Farm on university campus)				
	Upper slope	760	NE	25
	Lower slope	759	NE	16
Weathered granite soil (Research forest in Terasawayama)				
	Open slope	1,059	SW	36
	Shaded slope	1,061	SW	37

Plant height and number of tillers per rootstock were measured at one-month intervals from June 2019 to December 2020; no sampling was performed over the winter season as the sites were covered by snow.

To measure underground growth, two ramets per site (since the rootstocks developed rhizomes and numerous tillers after planting, we use the word 'ramet' hereafter to refer to the rootstock) were collected at the site with the black-colored soil (upper slope) and at the site with the weathered granite soil (open slope) in December 2020 i.e., 18 months after planting. The rhizomes were then untangled and straightened so that the condition of branching and the length of every rhizome section (from one bud to the next) could be recorded. The locations of apical and lateral buds on the rhizome were also recorded.

For the statistical analysis, the significance of each factor's effect (species, soil types, and their interaction) was estimated by analyses of variance (F-test). Significant differences among the averages were then estimated using Tukey's HSD test.

RESULTS AND DISCUSSION

Aboveground Growth

Each of the two species survived in both soil types during the experimental period. Colonization by each species was not observed in 2019 (i.e., 6 months after planting). Except for the plots on the shaded slope with weathered granite soil, the initial rootstocks became rather indistinguishable from each other due to an increase in foliage in 2020.

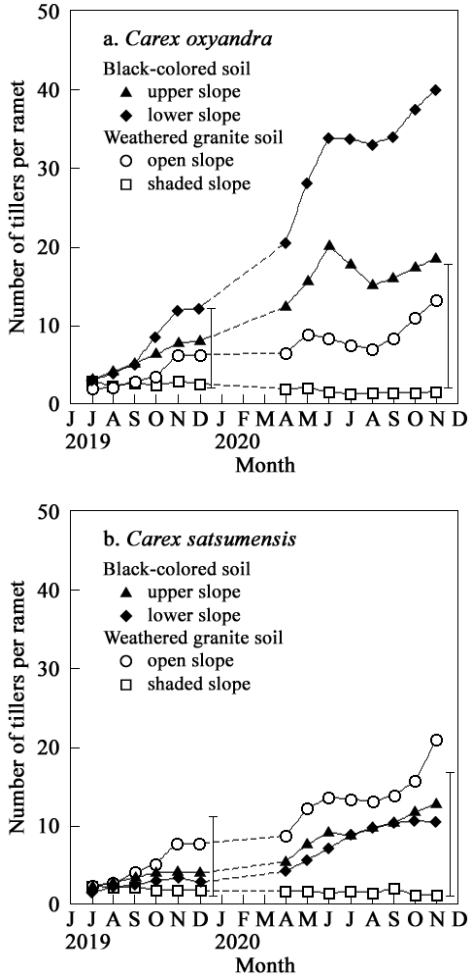

Fig. 3 Growth of tillers per ramet after planting. Vertical bars indicate the least significant difference among averages (Tukey's HSD, $p<0.05$).

Fig. 3 shows the increase of tillers per ramet in each of the two species. Based on tiller development, *C. oxyandra* showed superior growth in the black-colored soil, while *C. satsumensis* showed superior growth in the weathered granite soil; in December

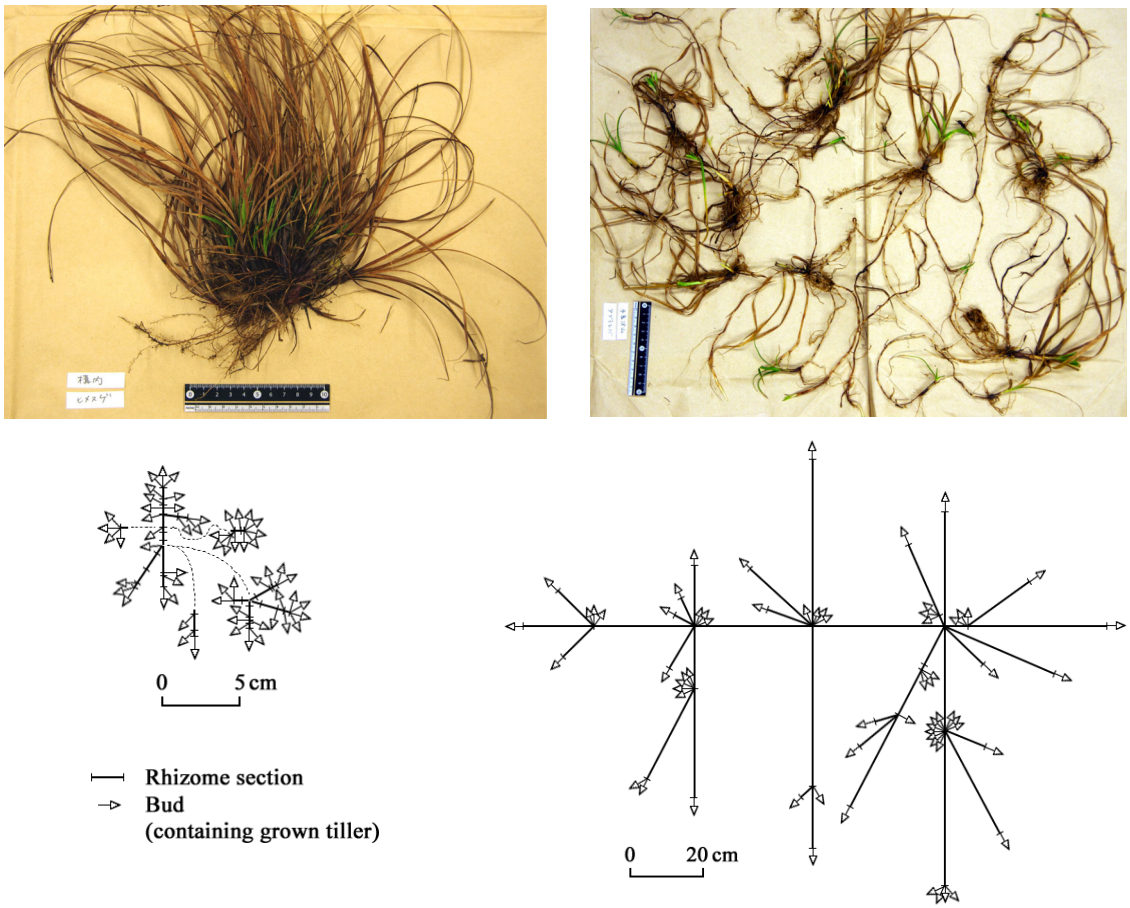

Fig. 4 Examples of ramet growth of *Carex oxyandra* (left) and *C. satsumensis* (right) at 18 months after planting. The upper row shows photos (black rulers are 10-cm long), and the lower row shows the corresponding depictions of rhizome sections and buds.

2020, the average number of tillers per ramet of *C. oxyandra* was 18.4 to 39.9 in the black-colored soil and 1.5 to 13.3 in the weathered granite soil, whereas that of *C. satsumensis* was 10.4 to 12.7 in the black-colored soil and 1.0 to 21.0 in the weathered granite soil. Each species showed poor growth in the plot on the shaded slope in the weathered granite soil.

In examining the aboveground growth of tillers, it was found that each species was able to grow for at least 18 months in both of the soil types. However, regarding long-term survival, the poor growth observed in both species in the plots under shaded conditions is considered to be problematic because, as vegetational succession advances, tall herbaceous plants and arboreal species will shade out smaller plants in the lower layer. Since the habitat of the two terrestrial *Carex* species used in the present study comprised open landslides, shady conditions might restrict their germination and growth as *Carex albata*, a weedy sedge in pasture whose seeds needs light (i.e. gap formation) for breaking the dormancy [14]. Consequently, when considering vegetational succession at disturbed sites, shade-resistant *Carex* species will be required for revegetation projects.

Rhizome Growth

Fig. 4 shows representative examples of ramet growth of *C. oxyandra* and *C. satsumensis* at 18 months after planting. Although elongation of the rhizomes did not always proceed linearly, the rhizomes depicted in the figure were extended linearly to facilitate interpretation of the differences in rhizome length.

In *C. oxyandra*, rhizome sections were densely arranged with numerous buds and tillers, whereas in *C. satsumensis*, rhizome sections were more loosely spread out with small clumps of buds and tillers scattered throughout (Fig. 4).

Table 2 shows the average measurements obtained for underground growth at 18 months after planting. The reason why the number of buds seems larger than the average number of tillers (Fig. 3) is because the former contains both developed tillers and young buds. *Carex oxyandra* showed similar underground growth patterns in both black-colored and weathered granite soils (44.0–44.5 buds and 17.7–20.8 cm-length rhizome, respectively). Conversely, *C. satsumensis* showed a markedly

superior underground growth pattern in the weathered granite soil (20.8 buds and 763.9 cm-length rhizome) than in the black-colored soil (19.5 buds and 191.1 cm-length rhizome); rhizome length and the number of buds were approximately four times larger in the weathered granite soil than in the black-colored soil. However, even in the inferior growth, the length of the rhizomes in *C. satsumensis* was several tens-of-times greater than the plant height, which is comparable to Japanese lawn grass (*Zoysia japonica*) and alang-alang (*Imperata cylindrica*) [18], both of which can be widely observed in Japan in frequent-cut grassland such as a ridge between rice fields.

Table 2 Number of buds and total rhizome length per ramet of the two *Carex* species at 18 months after planting

Item	Species	Soil	
		Black-colored soil	Weathered granite soil
Number of buds			
	C. oxyandra	44.5 ab	44.0 ab
	C. satsumensis	19.5 b	72.5 a
Total rhizome length (cm)			
	C. oxyandra	17.7 c	20.8 c
	C. satsumensis	191.1 b	763.9 a

Average values with different letters were significantly different (Tukey's HSD, $p<0.05$).

Fig. 5 shows a histogram of rhizome section length in ramets of each species. In *C. oxyandra*, the data have a lognormal distribution with a peak at $10^{-0.2}$ to $10^{-0.4}$ cm (i.e., 0.40 to 0.63 cm) in both the black-colored soil and the weathered granite soil. However, in *C. satsumensis*, the data have a bi-modal distribution, with a small peak at 10^{-1} to $10^{-0.5}$ cm (i.e., 0.10 to 0.31 cm) and a large peak at 10^{1} to $10^{1.5}$ cm (i.e., 10.0 to 31.6 cm) in both soil types. Maximum rhizome length was 55.0 cm in the weathered granite plot. These results imply that *C. satsumensis* develops two types of rhizomes, a small number of very short rhizomes and a large number of long rhizomes. This differentiation of rhizome sections is considered to correspond to the differentiation of functions in long shoots (the space-capture strategy) and short shoots (the light-capture strategy) in terms of the general shoot development patterns of trees [19].

Concerning the marked variation observed in the exceedingly long rhizome sections of *C. satsumensis*, we attempted to clarify the cause of elongation. Twelve long rhizome sections were sampled and the number of internodes (accumulation of internodes comprises a rhizome section) were counted in both soil types. Fig. 6 shows the relationship between the length of rhizome section and number of internodes. A logarithmic regression curve was obtained for each soil type, in which the number of internodes increased as the length of rhizome section increased.

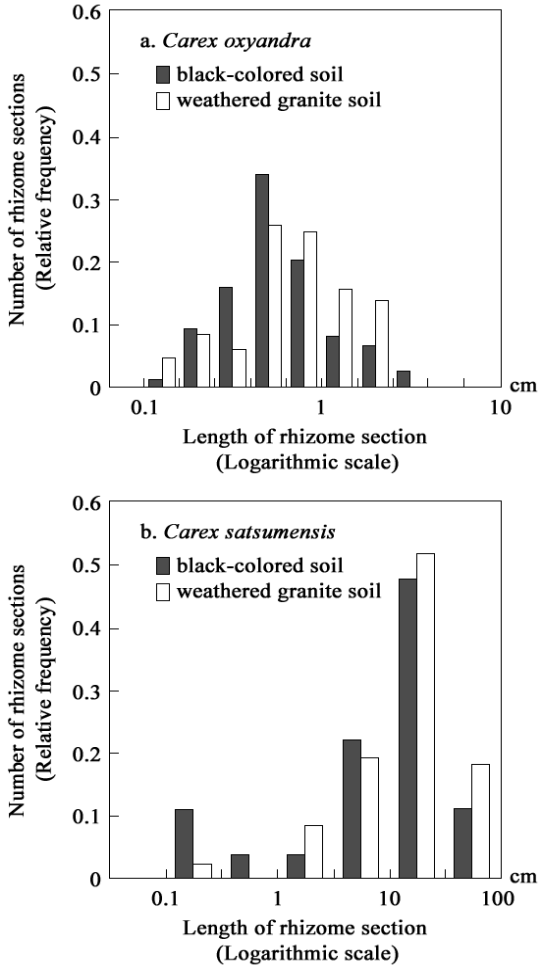

Fig. 5 Histogram of rhizome-section length in a ramet at 18 months after planting.

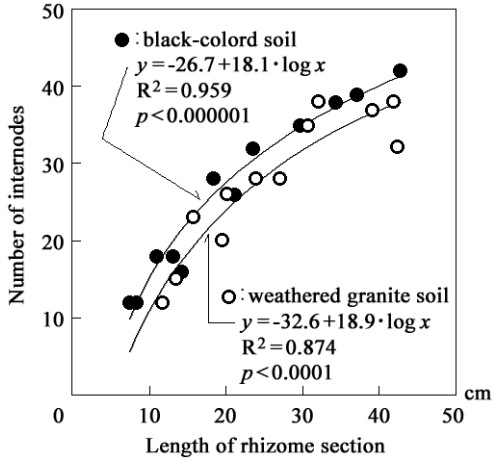

Fig. 6 Relationship between the length of rhizome section and the number of internodes in *Carex satsumensis*

An analysis of covariance detected a significant difference between the *y*-axis intercepts ($p<0.01$, F-test),with the intercept for the black-colored soil being larger than that obtained for the weathered granite soil (-26.7 and -32.6, respectively). The coefficient of log *x* was similar between the two regression curves and the difference was not significant. Thus, the relationship shown in Fig. 6 implies that the relationship between an increase in the number of internodes and rhizome elongation is almost the same in both soil types, but a larger number of internodes is likely to be produced (i.e., each internode becomes slightly smaller in the black-colored soil compared to the weathered granite soil.

These findings clarified the differences of growth properties between the two species; *C. oxyandra* benefits from steadily producing dense rhizome tillers around the mother rootstock, and underground growth showed no noticeable differences between the two soil types. Conversely, *C. satsumensis* benefits from rapidly spreading its rhizomes far from the mother rootstock, and the underground growth changed dramatically in the two soil type. This difference observed in the growth of *C. satsumensis* in different soils suggests that soil type plays an important role in deciding whether to use this species for revegetation applications. Since the persistence (i.e., life span) of *Carex* communities has been reported to differ among species [20], it is possible that differences in underground growth may be responsible. Consequently, soil type should be carefully considered when using *C. satsumensis* for revegetation purposes.

CONCLUSION

To assess whether the native terrestrial sedges *Carex oxyandra* and *C. satsumensis*, both of which have been found to colonize landslides in the Kiso Mountains of central Japan, could potentially be used to revegetate disturbed areas, this study established revegetation sites on excavated slopes in May 2019. The experimental design employed a two-way layout; 2 species × 2 soil types (black-colored soil (Andosol) and weathered granite soil) × 2 replicates. The number of tillers per ramet was measured at one-month intervals and rhizome growth was measured in December 2020. The results were as follows:

1. As to the aboveground growth and increase in tillers, each species was capable of growth on both soil types; *C. oxyandra* showed superior growth on the black-colored soil, while *C. satsumensis* grew better on weathered granite soil. However, each species showed poor growth in the plot under shaded conditions.
2. As to the underground growth of rhizomes and buds, dense rhizome sections and numerous buds developed in *C. oxyandra*, while long widely spread rhizome sections with small scattered clumps of buds developed in *C. satsumensis*. Rhizome growth in *C. satsumensis* changed dramatically according to soil type.

Thus, the characteristics of tiller and rhizome growth in the two species were markedly different; *C. oxyandra* benefits from steadily producing dense rhizome tillers around the mother rootstock, whereas *C. satsumensis* benefits from rapidly spreading its rhizomes far from the mother rootstock. Since these characteristics are considered to complement each other, using an optimum combination of both species is considered to be well suited to the early stages of revegetating excavated slopes.

ACKNOWLEDGMENTS

This study was funded by a Grant-in-Aid for Scientific Research from the Ministry of Education, Culture, Sports, Science and Technology, Japan (Grant No. 18K05723, fiscal year 2018 to 2020 to T.A.).

REFERENCES

[1] Kobayashi, T. and Kuramoto, W. eds., Handbook of Revegetation for Biodiversity Conservation. Chijin Shokan Co., Ltd., 2006, 323 pp. (in Japanese)

[2] Japan Meteorological Agency, A Search for Past Meteorological data Home Page (http: data/jma.go.jp/obd/stats/etrm/index.php). Referred in 25th May, 2021.

[3] Ministry of Land, Infrastructure, Transport and Tourism, Public Information Home Page (http:milt.go.jp/report/press/sabo02_hh_000091. html). Updated in 25th March, 2021.

[4] Saito, S., The World of Sedges –The sedges Indigenous to Fukushima Prefecture. Rekishi Shunju Publishing Co., Ltd., 2001, 162 pp. (in Japanese)

[5] Kitamura, S., Murata, G. and Koyama, T., Colored Illustrations of Herbaceous Plants of Japan III. Hoikusha Publishing Co., Ltd., 1964, pp. 256-303. (in Japanese)

[6] Tsuji, M., Yamada, K. and Hiratsuka, A., Water Purification Characteristics of Native Plant Species whose Height does not Obstruct the View in Planted Canal –A Case Study of *Carex dispalata*, *Carex thunbergii* and *Phalaris arundinacea*. Transactions of the Japanese Society of Irrigation, Drainage and Reclamation Engineering, No. 243 (Vol. 74, No. 3), 2006, pp. 33-40.

[7] Kurita, K. and Aso, M., Studies on the Revegetation Method of Snow-Patch Vegetation at Heavy Snow Montane Region. Journal of the Japanese Society of Revegetation Technology,

Vol. 20, No. 4, 1995, pp. 223-233. (in Japanese with English summary)

[8] Hoshino, T., Karyomorphological and Cytogenetical Studies on Aneuploidy in *Carex*. Journal of Science of the Hiroshima University. Series B. Div. 2, Botany, Vol. 17, 1980, pp. 155-238.

[9] Arase, T. and Uchida, T., Vertical Distribution of *Carex* Species (Cyperaceae) in the Riparian Zone in Nishikoma Research Forest at Shinshu University. Bulletin Shinshu University Alpine Field Center, No. 17, 2019, pp. 37-43. (in Japanese with English summary)

[10] Tanaka, T., Yamawo, A., and Yano, O., Seed Dispersal by Ants in *Carex oxyandra* var. *oxyandra* (Cyperaceae) from Japan. The Journal of Japanese Botany, Vol. 90, No. 2, 2015, pp. 129-133.

[11] Molina, A., Acedo, C. and Llamas, F., The Relationship between Water Availability and Anatomical Characters in *Carex hirta*. Aquatic Botany, Vol. 85, No. 3, 2006, pp. 257-262.

[12] Bubier, J. L., The Relationship of Vegetation to Methane Emission and Hydrochemical Gradients in Northern Peatlands. Journal of Ecology, Vol. 83, 1995, 403-420.

[13] Tsujimura, A., The Ecology of *Carex oxyandra* II. The Behavior of Seedling and Tillers. Ecological Research, Vol. 2, 1987, pp. 279-288.

[14] Watanabe, N., Nishiwaki, A. and Sugawara, K., Effects of Bare Ground Formed in Pasture on Dormancy Breaking of *Carex albata* Boott Seeds. Grassland Science, Vol. 45, No. 3, 1999, 233-237.

[15] Arase, T., Okano, T. and Shirota, T., Colonization and Morphological Changes of a Sedge Restricting Regeneration after Wind Damage in a Natural Forest. International Journal of GEOMATE, Vol. 12, Issue 31, 2017, pp. 100-104.

[16] Arase, T., Okano, T. and Shirota, T., Methods of Suppressing Colonizing Sedge to Help to Establish Tree Seedlings in a Natural Forest. International Journal of GEOMATE, Vol. 12, Issue 32, 2017, pp. 19－24.

[17] Chou, C. and Lee, Y. (1991) Allelopathic Dominance of *Miscanthus transmorrisonensis* in an Alpine Grassland Community in Taiwan. Journal of Chemical Ecology, Vol. 17, No. 11, 1991, pp. 2267-2281.

[18] Numata, M. and Yoshizawa, N. eds., Weed Flora of Japan Illustrated by Colour. Zenkoku Noson Kyouiku Kyokai Publishing, 1978, 414 pp. (in Japanese with English legend)

[19] Shirota, T. and Okano, T., Comparison of Shoot Design among Four ERICACEAE Understory Species in *Pinus densifolia* Forest. Bulletin Shinshu University Alpine Field Center, No. 8, 2010, pp. 1-8. (in Japanese with English summary)

[20] Arase, T. and Uchida, T., Growth and Persistency of Five Terrestrial Sedge Species Established on a Cutting Slope. Journal of the Japanese Society of Revegetation Technology, Vol. 35, No. 1, 2009, pp.119-122 (in Japanese)

11th Int. Conf. on Geotechnique, Construction Materials & Environment,
Kyoto, Japan, 3-5 November 2021, ISBN: 978-4-909106063 C3051

NUMERICAL STUDY OF PARTICLE FLOW(PM10) IN LOW-VOLUME IMPACT SEPARATOR: PARTICLE'S PATH AND COLLECTION PERFORMANCE

Pannita Phirommark[1], Watcharapong Chookaew[1], Chakrit Suvanjumrat[1], Sakchai Uapipatanakul[2], Machimontorn Promtong[1]

[1] Department of Mechanical Engineering, Faculty of Engineering, Mahidol University, Salaya, Nakorn Pathom, 73170, Thailand
[2] Kinetics Corporation Ltd. 388 Ratchadapisek Rd.32 Chandrakasem, Chatuchak Bangkok 10900, Thailand

ABSTRACT

Due to a health issue, an inspection of soot particle size quantity in ambient air is essential. This research focuses on studying the small particles (PM 1, PM10, and PM100) flow behavior while is separated by a low-volume impact separator. A computational Fluid Dynamics (CFD) method was introduced to analyze the flow complex of particle flow. In the simulation, the actual operating flow rates and considered particle sizes were adopted as the initial conditions and material properties. The flow pattern was numerically observed and evaluated the collection performance. Moreover, the particle's paths of different sizes were compared and discussed. The simulation results showed that the air velocity influenced the particle traces and their distributions in the separator PM10 head, especially the smaller sizes (PM1 and PM10). The residence time and the number of escaped particles were used to evaluate the performance. Within 5 seconds, the predicted collection performance of 1 µm,10 µm, and 100 µm were 44.2%, 37.6%, and 0%, respectively. In future work, the validation study will be performed, and the effect of the internal structure that could affect the separator performance will be further investigated. In addition, the aggregations of the particles due to the flow vorticities that could cause the dispersions will be observed as well.

Keywords: Soot Particle Flow, Computational Fluid Dynamics (CFD), Discrete Phase Modelling (DPM), Performance evaluation, Separation Technique

INTRODUCTION

Due to an impact on public health, monitoring many harmful particulates (PM10, PM2.5, PM1) suspended in the air has become a critical task. Practically, sizing and recognizing the ingredients of these particles are also another necessary task because it may give information regarding the sources, i.e., burning of crops, pollutions due to construction, and automotive. In certain circumstances, like an indoor environment, the particles could become a virus carrier (COVID-19); thus, spreading infected particles could lead to a viral infection which could directly affect the health of the living [1, 2]. Particle collectors/separators have been invented to collect harmful particles and report real-time information [3, 4]. However, to accurately classify and effectively collect the particle size, the proposed particle sizers may require investigating a collection performance [5-9].

Recently, many researchers have invented and implemented the developed techniques (i.e., cyclonic and impact methods) into the particle separators to classify the ultrafine particle sizes [6, 8]. For example, Peng [8] studied the cyclone's efficiency to isolate PM2.5 by establishing a novel static chamber system. The polydisperse aerosol was involved to evaluate the performance of separators tested the critical parameters of the system. It also compared the separation efficiency curves of three cyclone separators (VSCC-A, SCC-A, and SCC112). The results showed that the performance of the VSCC-A was optimal (with a slightly sharper cutoff curve). Tongling Xia and Chun Chen [10] studied the evolution of incense particles on nanofiber filter media. The results show that the PM2.5 removal efficiency of nanofiber filter media decreased with an increase in the incense particle loading mass. The liquid aerosols were found to interact with the nanofiber network and enlarged the pore sizes.

When the loading mass was sufficiently large, the PM2.5 removal efficiency tended to be a constant. Zhanpeng Sun [3] studied a static cyclone classifier and observed the flow characteristics. It was found that the primary flow could characterize by an upper vortex and a lower reverse vortex. The primary and secondary air occupied a separate area. Regardless of the inlet air velocity, the upward vortex represented a high flushing effect, reducing the retention of fine particles caused by higher-size particles. Prashant

Patel [11] investigated a PM2.5 high-volume impactor (HVI) with a new inlet design. Also, the optimized D50 cutoff size of 2.52 μm was investigated experimentally under the ambient conditions. The performance of the developed PM2.5 HVI sampler was investigated under various mass loading conditions. As a result, the developed PM2.5 HVI sampler gave a comparable performance compared with commercial PM2.5 high- and low-volume samplers.

Instead of experimental testing, a Computation Fluid Dynamics (CFD) method is a promising tool for investigating complex flow and use for redesigning the thermal system [12-16], and particle flow circulations[17-23]. Kaltenbach and Laurien [18] studied the diffusion of radioactive particles inside the reactor building. As mentioned, the cycle during a catastrophic accident was simulated using a CFD technique. Different droplets and particle size groups were introduced in this three-dimensional modeling.

Ahmed [24] studied the Venturi scrubber, an essential element of the Filtered and Closed Ventilation System (FCVS), which removes aerosols from polluted air. In the simulation, ANSYS CFX was used to investigate the removal efficiency of Venturi scrubbers operating in self-priming mode. Titanium oxide (TiO2) particles with a size of 1 micron were used as the size of powder particles. The removal efficiency was evaluated under the inlet air velocities of 1-3 m/s. It was found that higher inlet air velocity, removal give higher efficiency.

Peng [25] proposed a hydraulic separator to remove pollutant particles. Ansys FLUENT program was used to simulate the hydrodynamic separator under complex initial conditions. As a result, the optimal angle between the overflow tube and the inlet tube in removing the polluting particles was found. Fang [26] simulated the stone powder separator (SPS) using Ansys FLUENT software. The Discrete Phase Model (DPM) was introduced to simulate the crusher's airflow distribution and particle trajectory. The structure of the stone separation device and the suitable volume were optimized. Also, the simulation results were compared with experimental data.

This research will introduce the Discrete Phase Model (DPM) to observe the flows inside the commercial impact separator. The observation will particularly investigate how different particle sizes distributed while passing the classifying chamber. In addition, the performance of the collector in classifying the particle smaller than 10 microns (PM10) will also be discussed. In general, the objective of this research is to utilize the Computational Fluid Dynamics (CFD) technique;

i) to investigate the effect of internal configurations and the flow characteristics in a commercial impact particle separator,

ii) to capture the particle (PM1, PM10, and PM100) paths under actual operation conditions,

iii) to study the effect of particle sizes, internal configuration and address the critical factors related to particle collection performance.

Apart from the flow variables and the particle's paths, the residence time and the number of particles escaped will additionally compare to evaluate the collection performance of the impact separator. Hopefully, a more understanding regarding the current design and the possible solutions to enhance the current performance could be found and suggested.

FLUID AND PARTICLE FLOW EQUATIONS

Continuity Equation

The continuity equation reflects the fact that mass is conserved (as shown in Eq. (1)). The equation is developed by adding up the rate at which mass is flowing in and out of a control volume, and setting the net in-flow equal to the rate of change of mass within it. Since the mass velocity is continuous, this partial differential equation is usually called as the continuity equation. Sometimes the first term can be omitted when the fluid flow is in the steady state.

$$\frac{\partial \rho}{\partial t} + \rho \frac{\partial (\bar{u}_i)}{\partial x_i} = 0 \quad (1)$$

Momentum Equation

The momentum transfers within a control volume is conserved, hence the momentum equation can describe as shown in Eq. 2.

$$\frac{\partial \bar{u}_i}{\partial t} + \rho \bar{u}_j \frac{\partial \bar{u}_i}{\partial x_j} = -\frac{\partial \bar{p}}{\partial x_i} + \frac{\partial}{\partial x_j}\left[\mu\left(\frac{\partial \bar{u}_i}{\partial x_j} + \frac{\partial \bar{u}_j}{\partial x_i}\right) - \rho\overline{u_i' u_j'}\right] \quad (2)$$

Where

$$\tau_{ij} = -\rho\overline{u_i' u_j'} = \mu_t\left(\frac{\partial \bar{u}_i}{\partial x_j} + \frac{\partial \bar{u}_j}{\partial x_i}\right) - \frac{2}{3}\delta_{ij}\rho k \quad (3)$$

In Eqs. (1) - (2), ρ is a fluid density and $\bar{p}$ is the system pressure. Here $\bar{u}_i, \bar{u}_j$ are the average velocity components and $\overline{u_i' u_j'}$ is the velocity fluctuation. The x_i, x_j terms are the coordinate axis. The g_j and μ terms represent the gravitational acceleration vector and kinetic viscosity, respectively. Equation (3) shows the Reynolds-stress term ($-\rho\overline{u_i' u_j'}$)

Moreover, Boussinesq approximation is increased in term which calculated the difference property of fluid. And this equation can be resolved by turbulent models. The term of turbulence model is used RNG $k-\varepsilon$ (Re-Normalization Group k-epsilon) to calculate the air flow by value show in Eq.

(5) and Eq. (6). and then bring to calculate the viscosity due to turbulence model in Equation (4).

$$\boldsymbol{\mu_t = \rho C_\mu \frac{k^2}{\varepsilon}} \quad (4)$$

$\boldsymbol{k}$ Equation:

$$\boldsymbol{\frac{\partial}{\partial x_i}(\rho k u_i) + \frac{\partial}{\partial t}(\rho k) = \frac{\partial}{\partial x_j}\left[\left(\mu + \frac{\mu_t}{\sigma_k}\right)\frac{\partial k}{\partial x_j}\right] + P_k - \rho\varepsilon} \quad (5)$$

$\boldsymbol{\varepsilon}$ Equation:

$$\boldsymbol{\frac{\partial}{\partial x_i}(\rho\varepsilon u_i) + \frac{\partial}{\partial t}(\rho\varepsilon) = \frac{\partial}{\partial x_j}\left[\left(\mu + \frac{\mu_t}{\sigma_\varepsilon}\right)\frac{\partial \varepsilon}{\partial x_j}\right]}$$

$$\boldsymbol{+C_{1\varepsilon}\frac{\varepsilon}{k}P_k - C_{2\varepsilon}^{*}\rho\frac{\varepsilon^2}{k}} \quad (6)$$

Where

$$\boldsymbol{C_{2\varepsilon}^{*} = C_{2\varepsilon} + \frac{C_\mu \eta^3(1-\eta/\eta_0)}{1+\beta\eta^3}}$$

And

$$\boldsymbol{\eta = Sk/\varepsilon \qquad S = (2S_{ij}S_{ij})^{1/2}}$$

The model constants are

$$\boldsymbol{C_\mu = 0.0845,\ C_{1\varepsilon} = 1.42,\ C_{2\varepsilon} = 1.68,\ \eta_0 = 4.38,}$$
$$\boldsymbol{\sigma_k = 0.7194,\ \sigma_\varepsilon = 0.7194,\ \beta = 0.0012}$$

The last term in equation (6), $\boldsymbol{\rho\varepsilon}$ represents the destruction rate, and $\boldsymbol{P}$ are the shear production buoyancy production term, which are given by:

$$\boldsymbol{P = \mu_t \frac{\partial u_i}{\partial x_j}\left(\frac{\partial \bar{u}_i}{\partial x_j} + \frac{\partial \bar{u}_i}{\partial x_i}\right)} \quad (7)$$

Flow equation of particles phase

The particle motion equation is obtained by the integration of the equilibrium force acting on the particle. which is in the Lagrangian frame (Fluent 6.2 User's guide. 2005). On the left with the terms of the force acting on the particle can be written as

$$\frac{du_p}{dt} = F_D\left(u - u_p\right) + \frac{g_x\left(\rho_p - \rho\right)}{\rho_p} + F_x. \quad (8)$$

Where

- $\boldsymbol{u}$ is the fluid phase velocity
- $\boldsymbol{u_p}$ is the particle velocity
- μ is the molecular viscosity of the fluid
- ρ is the fluid density
- $\boldsymbol{\rho_p}$ is the density of the particles
- $\boldsymbol{F_x}$ is an additional acceleration
- $\boldsymbol{F_D}$ is the drag force per unit particles mass

$$F_D = \frac{18\mu}{\rho_p d_p^2}\frac{c_D R_e}{24}. \quad (9)$$

Re is the relative Reynolds number is given by

$$R_e = \left(\frac{\rho d_p\left(u_p - \mu\right)}{u}\right). \quad (10)$$

Where $\boldsymbol{d_p}$ is the particles diameter.

Turbulence model

Turbulence model is a model that helps to calculate continuity equations and the Reynolds-averaged Navier-Stokes equation (RANS) in turbulent flow. It is used to determine Reynolds stress. A good turbulence model must be able to accurately calculate various flow behaviors. The most popular turbulence model in turbulence simulation is the Launder and Spalding model called the Standard k −ε model. [27].

In this research, the Standard k - ε turbulence model was chosen because it was a turbulence model whose results were close to the reality by the Standard k - ε turbulence model equation as in Equation 11.

$$\frac{\partial}{\partial_t}(\rho k) + \frac{\partial}{\partial_{x_i}}(\rho k u_i) = \frac{\partial}{\partial_{x_j}}\left[\left(\mu + \frac{\mu_t}{\sigma_k}\right)\frac{\partial k}{\partial x_i}\right] + G_k - \rho\varepsilon \quad (11)$$

where k is the kinetic energy of turbulence, ε is the rate of reduction in kinetic energy of turbulence, $\boldsymbol{G_k}$ is the production term of turbulence kinetic energy.

$$\frac{\partial}{\partial_t}(\rho\varepsilon) + \frac{\partial}{\partial_{x_i}}(\rho u_i \varepsilon) = \frac{\partial}{\partial_{x_j}}\left(\left(\mu + \frac{\mu_t}{\sigma_\varepsilon}\right)\frac{\partial_\varepsilon}{\partial_{x_j}}\right) + c_{\varepsilon 1}\frac{\varepsilon}{k}G_k - c_{\varepsilon 2}\rho\frac{\varepsilon^{2\rho}}{k} \quad (12)$$

RESEARCH METHODOLOGY

The research methodology is illustrated in Fig. 1. Our main task is to perform the simulation of the particle flow in the particle separator. Nevertheless, before using the CFD method to simulate the particle flow, the steady-state flow's initial stage is first required (running the case without the particles). Afterward, the considered size of the particles was adopted into the simulation, and the flow's paths are monitored. The results, including the velocity pattern the motions of each particle size, the residence time, are mainly discussed regarding the separation performance. By adopting different operating conditions, hopefully, the ideas for further development and design could be found.

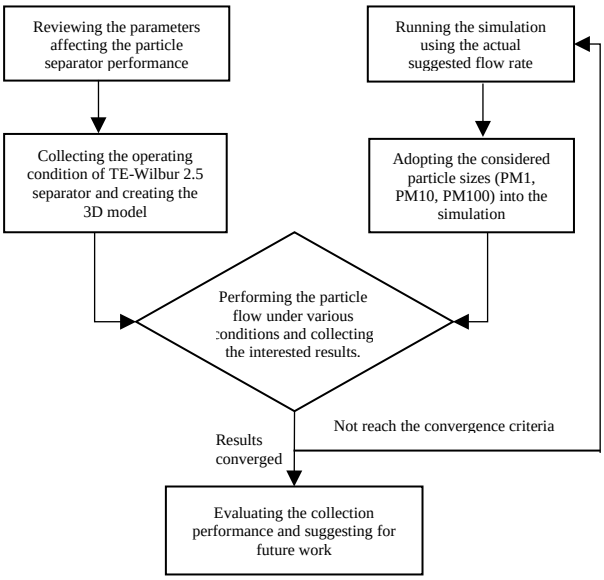

Fig. 1 The flow chart representing the research methodology

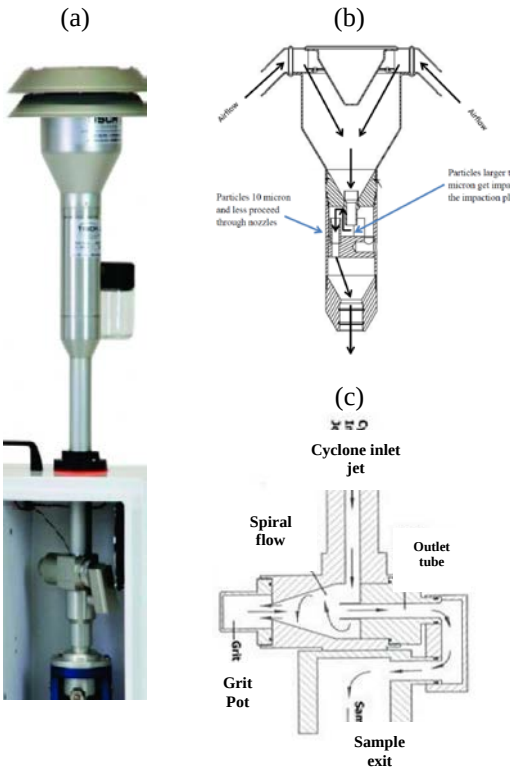

Fig. 2 PM10 and PM2.5 particle size sorting head (a) with internal structure details (b) at the PM10 size sorting point and PM2.5 size sorting point (c).

Details of the particle separator

There are two available functions of the TE-Wilbur 2.5 particle separator. The first is to collect PM10 dust (sizes from 10 microns down) and works based on the impact technique (Figure 2). Specifically, the size is equal to or smaller than PM10; when they hit the solid plate, it will bounce down to the screening tube and flow-through another function (PM2.5 dust screening unit). For the second mode, the separation of dust particles that are equal or smaller than PM2.5 size separated using the cyclonical object (based on the rotation principle). The cyclonic separator will send the particle sizes smaller than PM2.5 into the sampling room and larger sizes to the other collector.

Meshing

The 3D separation head after the meshing process is shown in Fig. 2. It should be noted that the mesh independence study was conducted, and the velocity at the center of the chamber was compared between the various number of the mesh considered. As a result (Fig. 3), the velocity was insignificantly changed when using the mesh element at about 150,000 [23]. Therefore, this number of mesh sizes was adopted for further numerical investigation. Furthermore, 16.67 L/min (0.0675 m/s) of the volumetric flow rate was adopted for the velocity inlet and this number is suggested by the manufacturer for the real operation.

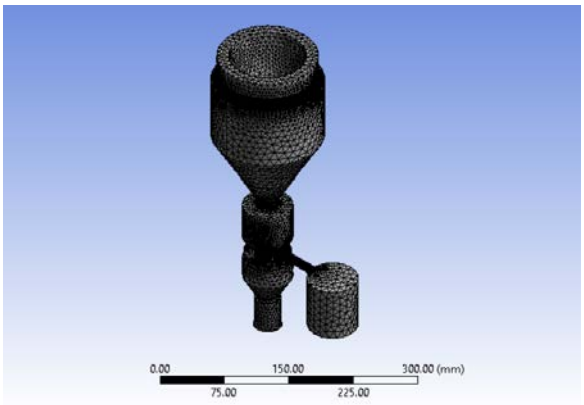

Fig. 3 The 3D separation head (PM10) after the meshing process

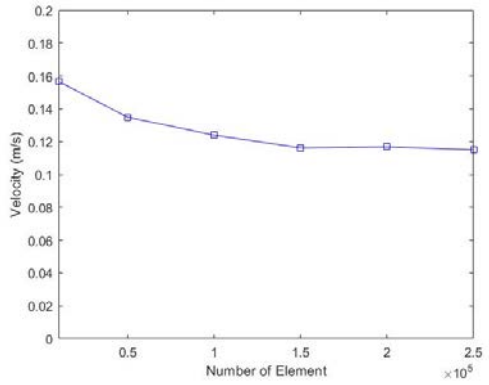

Fig. 4 Total mesh used for the separator model (the mesh independence study).

RESULTS AND DISCUSSIONS

In this section, the simulation results of the particle separator will be presented and discussed. Firstly, the velocity profiles in the separator system will be given. The section part discusses the flow paths of different particle sizes (PM1, PM10, and PM100). Last, the particle's escaped number will be discussed to evaluate the collection performance. It should be noted that only the PM10 separator system was investigated and evaluated the impact technique, especially in terms of sizing performance.

The Velocity Pattern

Usually, the local flow velocity could lead the particle's motions in the separator system, and hence observing the flow pattern in the primary chamber is necessary. The velocity streamlines of the PM10 in the separator system are shown in Fig.5. It is clearly seen that the vortexes occurred at the top of the primary chamber (see in Fig. 5a and Fig. 5b). Because Inside the system, the lower velocity appeared near the chamber surface (Fig. 5b), and when having high inlet velocity, the velocity difference could lead to a presence of the circulations [28].

It should be noted that without the suitably designed cone inside the separator head, the air circulations could not happen [29]. The maximum velocity found at the connecting tube that links to the separation chamber from the figures. The maximum velocity was about 4.30 m/s.

Fig. 5c presented the flow velocity when the inlet velocity was halved. Averagely, the velocity values in the primary chamber were reduced almost a haft. When there is a smaller gap between the inlet velocity and the near-wall velocity, the smaller vortexes were found near the top of the chamber. Moreover, the maximum velocity in the connecting tube was decreased as well.

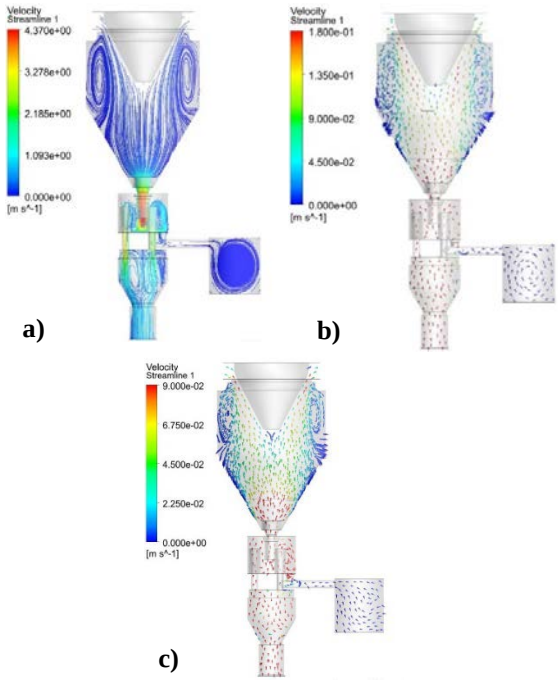

Fig. 5 Velocity streamlines a) having normal velocity b) having normal velocity c) reduced to a haft-velocity

Fig. 6 compares the flow pattern in the separation chamber when there is only a haft of the velocity inlet. As shown, when the airflow in the chamber impacts the bottom wall and flows to the wall causing the circulations inside the collecting room. Because of having a small chamber, currently, it is hard to recognize a difference in the flow circulation in the separation room.

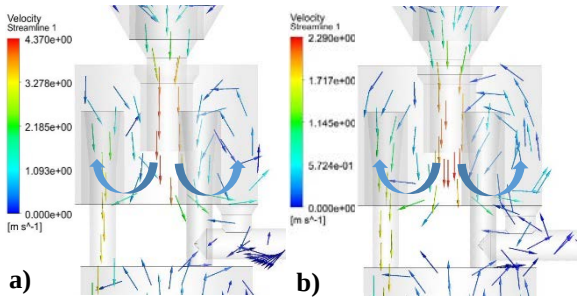

Fig. 6 Velocity streamlines in the separation chamber a) having normal velocity and b) reduced to a haft-velocity

The Particles's Path

In this section, the particle's paths of different sizes are presented (under the same operating condition). Fig.7a show the particle's path of 1 µm and 10 µm, and Fig. 7b show the particle's path of 1 µm and 100 µm. For both cases, the particles were

tracked from the inlet and the final time captured was at 5s.

It is clearly seen that when the particles were injected, the large dust particles (10 µm and 100 µm) were fallen to the middle of the primary chamber due to a dominant inlet velocity. On the other hand, the particle particles at 1 µm micron kept swirling at the top for longer than 10 µm and 100 µm near the top region of the chamber. This could be a result of being push away from the heavy-turbulent regions.

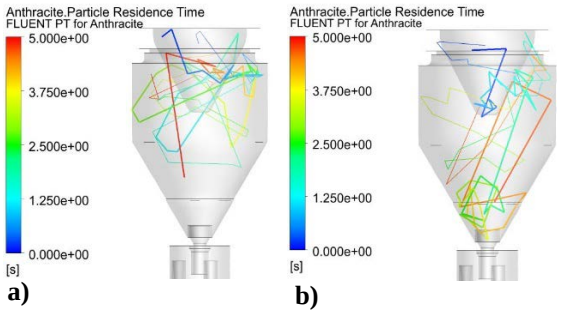

Fig. 7 The particle's path of a) 1 µm and 10 µm and b) 1 µm and 100 µm

Fig.8a and Fig. 8b present the particle's path dust of 1 µm and 100 µm. It should be noted that the case of fig. 8b, the pipe length remains only a half of the original height. According to the residence time (shown on both figures), it can confirm that the smaller particle takes a longer time (kept swirling) to leave the separation chamber in the case of having the haft-height. This could result from the height of the unsuitable collecting area, tube to collect the smaller particle. In the case of 100 µm, although the particle could enter the separation chamber, however, within 45s, the particle is still in the separation unit, not escaped out [30].

More details regarding the time required to enter the separation chamber and the time required to escape from the separator are given in Table 1. Interestingly, it shows that the escaped time required for the smaller particle for the case of having original tube length was smaller than the case of the haft-height. Nevertheless, at this point, it requires more evidence to conclude the influence of the collecting tube height.

Table 1 Comparisons for particle separation 1 µm and 100 µm

Case study	Particles	Time to enter separation chamber	Escaped time
Normal height	1 µm	19.2s	25.1s
	100 µm	4.9s	-
Half height	1 µm	39.2s	45.4s
	100 µm	2.9s	-

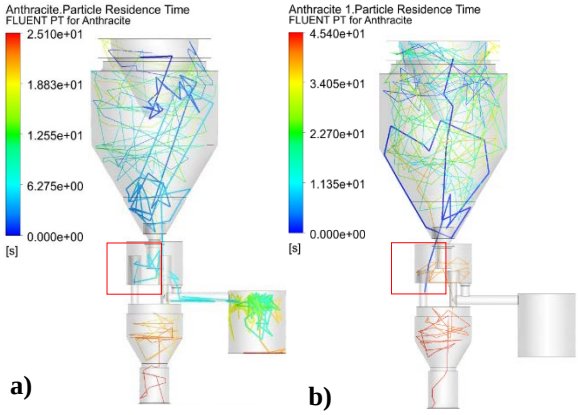

Fig. 8 The particle's path of 1 µm and 100 µm when the collecting tube has a) an original height and b) reduced to the half-height.

The Collection performance

In Fig. 9-11, the Particle Residence Times (PRT) of each particle size (1 µm, 10 µm, and 100 µm) are presented. It should be noted that the ending time for this tracking was 5s; hence it is possible to have a slight change in terms of the number of escaped and stayed particles in the separator.

Within the 5 seconds, the large particles 100 µm were unable to be separated from the separation chamber. This is also relevant to the design objective that this system should allow only the particle sizes equal and/or smaller than 10 µm flow through. This could be because the flow kept pushing the particle to flow near the floor of the separation chamber.

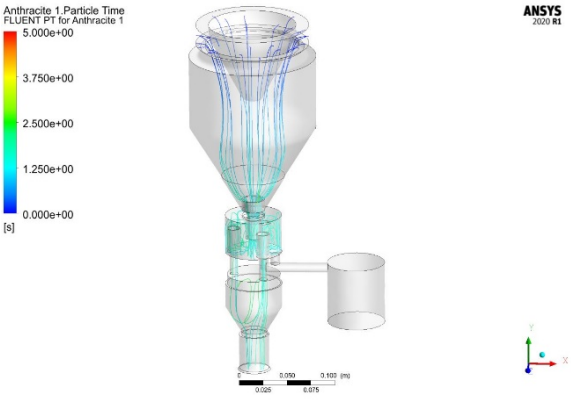

Fig. 9 Particle Residence Time (PRT) of particles size 1 µm

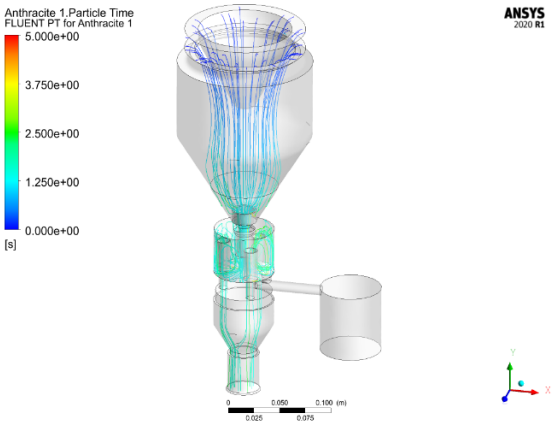

Fig. 10 Particle Residence Time (PRT) of particles size 10 µm

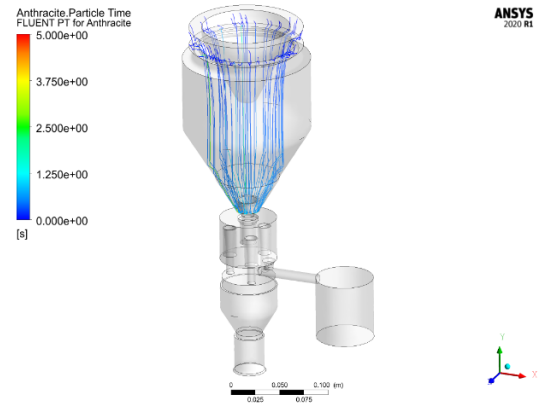

Fig. 11 Particle Residence Time (PRT) of particles size 100 µm

Table 2 The calculated collection performance when the tracking time ended at 5 seconds.

Size (µm)	No. of (#) the particles injected	# Stayed	# Escaped	Calculated collection performance
1	708	395	313	44.2%
10	706	440	266	37.6%
100	706	706	0	0%

As displayed in Table 2, some of 1 µm and 10 µm were separated and left the chamber for about 44% and 37%, respectively. More details regarding the number of particles leaving and staying in the separation chamber can be seen from the Table. 2. It should be bear in mind that the escaped number of the small particles (1 µm and 10 µm) number could increase following the times.

CONCLUSION AND FUTURE WORK

The simulation of the particle flow in the impact system of the TE-Wilbur 2.5 particle separator has been performed. In general, it was found that the particle-sized smaller than 10 microns (PM 10) can be separated by the collector, not for the 100 microns (PM100). Also, by introducing the computational Fluid Dynamics (CFD) technique, the separation performance and the particle's path could be investigated. Overall, the conclusions can be drawn as follows:

i) The secondary flow (vortexes) occurred near the top of the primary chamber. The flow circulations could result from high inlet velocity and the internal geometry of the impact system. The average velocity inside the primary chamber was less than 0.5 m/s; however, the velocity inside the connecting tube before entering the impacting room was as high as 4.37 m/s.

ii) By tracking the particle paths of PM1, PM10, and PM100, it was found that smaller particles (PM 1 and PM10) kept swirling inside the primary chamber longer than higher particles (PM100) before entry the separation chamber.

iii) When reducing the length of the separating tube (remaining only a haft) in the separation chamber, it was found that the residence time of small particles was longer than having the original length. This may be because of the velocity profiles (circulation) in the separation chamber.

iv) At the end of the collection time (5 seconds), the collection performance of the impact stem for 1 micron, 10 microns, and 100 microns particles were 44.2%, 37.6%, and 0%, respectively.

In future work, the experimental study will be conducted, and the validation study will be performed. Further investigations would be the optimization of the operating condition and internal structure of the impact and cyclonical systems of the particle separator.

ACKNOWLEDGMENTS

Many thanks to the Mechanical Engineering Department, Faculty of Engineering, Mahidol University, for allowing us to use the laboratory. Thanks to CADFEM SEA Pte. Ltd. - A certified Elite Channel Partner to ANSYS - for providing support and access to the CFD program named ANSYS Fluent 2021 R1.

Also, many thanks to Kinetics Corporation Ltd. and National Research Council of Thailand (NRCT) for financial support.

REFERENCES

[1] Vuorinen, V., et al., *Modelling aerosol transport and virus exposure with numerical simulations in relation to SARS-CoV-2 transmission by inhalation indoors.* Saf Sci, 2020. 130: p. 104866.

[2] (WHO), W.H.O. *Coronavirus disease (COVID-19): How is it transmitted?* 2020 01/05/2021]; Available from: https://www.who.int/news-room/q-a-detail/coronavirus-disease-covid-19-how-is-it-transmitted.

[3] Sun, Z., et al., *A new static cyclonic classifier: Flow characteristics, performance evaluation and industrial applications.* Chemical Engineering Research and Design, 2019. 145: p. 141-149.

[4] Mui, W., et al., *Design, simulation, and characterization of a radial opposed migration ion and aerosol classifier (ROMIAC).* Aerosol Science and Technology, 2017. 51(7): p. 801-823.

[5] Prasanna, N., et al., *CFD study on the performance of reducing pressure drop holes in cyclone separator*. Materials Today: Proceedings, 2021. 43: p. 1960-1968.

[6] Lin, W.-Y., T.-C. Hsiao, and B.-L. Hong, *Improving the removal efficiency of fine particulate matters in air pollution control devices: Design and performance of an electrostatic aerosol particle agglomerator*. Journal of the Taiwan Institute of Chemical Engineers, 2020. 107: p. 110-118.

[7] Zhang, H. and Q. Liu, *Numerical investigation on performance of moisture separator: Experimental validation, applications and new findings.* Annals of Nuclear Energy, 2020. 142.

[8] Du, P., et al., *Development of a static test apparatus for evaluating the performance of three PM2.5 separators commonly used in China.* J Environ Sci (China), 2020. 87: p. 238-249.

[9] Wang, S., et al., *Effect of the inlet angle on the performance of a cyclone separator using CFD-DEM.* Advanced Powder Technology, 2019. 30(2): p. 227-239.

[10] Xia, T. and C. Chen, *Toward understanding the evolution of incense particles on nanofiber filter media: Its influence on PM2.5 removal efficiency and pressure drop.* Building and Environment, 2020. 172.

[11] Patel, P., et al., *Theoretical and field evaluation of a PM2.5 high-volume impactor inlet design.* Atmospheric Environment, 2021. 244.

[12] Promtong, M., et al., *Experimental and Numerical Investigations into the Natural Convection of Hot Gas in a Vertical Smoking Oven: A Validation Study*, in *The 34th Conference of the Mechanical Engineering Network of Thailand*. 2020: 15 - 17 July 2020, Prachuap Khiri Khan, Thailand.

[13] Tekasakul, P. and M. Promtong, *Energy efficiency enhancement of natural rubber smoking process by flow improvement using a CFD technique.* Applied Energy, 2008. 85(9): p. 878-895.

[14] Promtong, M. and P. Tekasakul, *CFD study of flow in natural rubber smoking-room: I. Validation with the present smoking-room.* Applied Thermal Engineering, 2007. 27(11-12): p. 2113-2121.

[15] Promtong, M., *CFD study of flow in rubber smoking room and modification to improve uniformity of velocity and temperature distributions.* 2006, Prince of Songkla University.

[16] Promtong, M., et al., *CFD and Experimental Study of the Temperature Distribution in a Present Rubber Smoking Room*, in *The 19th Conference of Mechanical Engineering Network of Thailand*. 2005: 19-21 October 2005, Phuket, Thailand.

[17] Ren, J., et al., *Numerical Study of Three Ventilation Strategies in a prefabricated COVID-19 inpatient ward.* Build Environ, 2021. 188: p. 107467.

[18] Kaltenbach, C. and E. Laurien, *CFD Simulation of aerosol particle removal by water spray in the model containment THAI.* Journal of Aerosol Science, 2018. 120: p. 62-81.

[19] Xu, G. and J. Wang, *CFD modeling of particle dispersion and deposition coupled with particle dynamical models in a ventilated room.* Atmospheric Environment, 2017. 166: p. 300-314.

[20] Brusca, S., et al., *PM10 Dispersion Modeling by Means of CFD 3D and Eulerian–Lagrangian Models: Analysis and Comparison with Experiments.* Energy Procedia, 2016. 101: p. 329-336.

[21] Sajjadi, H., et al., *Computational fluid dynamics (CFD) simulation of a newly designed passive particle sampler.* Environ Pollut, 2016. 214: p. 410-418.

[22] Dickenson, J.A. and J.J. Sansalone, *Discrete phase model representation of particulate matter (PM) for simulating PM separation by hydrodynamic unit operations.* Environ Sci Technol, 2009. 43(21): p. 8220-6.

[23] Udaya Bhaskar, K., et al., *CFD validation for flyash particle classification in hydrocyclones.* Minerals Engineering, 2007. 20(3): p. 290-302.

[24] Ahmed, S., et al., *Investigation of dust particle removal efficiency of self-priming venturi scrubber using computational fluid dynamics.* Nuclear Engineering and Technology, 2018. 50(5): p. 665-672.

[25] Peng, Y., et al., *Computation fluid dynamics model of first-flush runoff through a hydrodynamic separator.* Journal of Cleaner Production, 2019. 241.

[26] Fang, H., et al., *Simulation and experimental study on the stone powder separator of a vertical shaft impact crusher.* Advanced Powder Technology, 2020. 31(3): p. 1013-1022.

[27] Mothilal, T. and K. Pitchandi, *Influence of inlet velocity of air and solid particle feed rate on holdup mass and heat transfer characteristics in cyclone heat exchanger.* Journal of Mechanical Science and Technology, 2015. 29(10): p. 4509-4518.

[28] Chen, X., J. Yu, and Y. Zhang, *The use of axial cyclone separator in the separation of wax from natural gas: A theoretical approach.* Energy Reports, 2021. 7: p. 2615-2624.

[29] Bnà, S., et al., *Investigation of particle dynamics and classification mechanism in a spiral jet mill through computational fluid dynamics and discrete element methods.* Powder Technology, 2020. 364: p. 746-773.

[30] Elsayed, K. and C. Lacor, *Numerical modeling of the flow field and performance in cyclones of different cone-tip diameters.* Computers & Fluids, 2011. 51(1): p. 48-59.

11th Int. Conf. on Geotechnique, Construction Materials & Environment, Kyoto, Japan, 3-5 November 2021, ISBN: 978-4-909106063 C3051

IMPACT OF THE GREAT EAST JAPAN EARTHQUAKE AND NUCLEAR ACCIDENT ON LAND PRICE FLUCTUATIONS

Takato Azegami[1], Akira Takahashi[2], Kensuke Yasufuku[2], Noriko Otsuka[3], Tomoko Miyagawa[4] and Hirokazu Abe[2]

[1]Takenaka Corporation, Japan; [2]Osaka University, Japan; [3]ILS Research Institute for Regional and Urban Development, Germany, [4]Wakayama University, Japan

ABSTRACT

Using a hedonic regression approach, this research aims to identify what factors affected land price fluctuations in Fukushima Prefecture following the Great East Japan Earthquake and the Fukushima Daiichi Nuclear Power Station accident in 2011. In this paper, taking a long-term perspective, the analysis focuses on Iwaki City in Fukushima, where the real estate market behaved unexpectedly following the two catastrophic events, and land price fluctuation rate were rising abnormally. Results based on analysis of data for eight-year indicate the following: The impact of radiation air dose rate and distance from the nuclear power plant on land price fluctuation rate changed significantly from the fourth year after the disaster. Being located in a reconstruction base area had a negative impact on land price fluctuation rate, while access to sewers and city gas had a positive impact. It appears that the stigma associated with the accident had a little disappeared after approximately four years.

Keywords: Land price, Hedonic Approach, Great East Japan Earthquake, Nuclear Accident

INTRODUCTION

Ten years have passed since the Great East Japan Earthquake. At this point, many of the counter-measures of the reconstruction/creation period have been completed. The number of evacuees has fallen to approximately one-tenth of the number immediately after the earthquake, and the reconstruction of housing in the damaged area has been progressing at a fairly rapid pace. The supply of new or re-constructed buildings has reached 18,000 private units and 30,000 units of public housing.

However, in Fukushima Prefecture, it has been not only the damage caused by the earthquake and tsunami, but also the radioactive contamination resulting from the Fukushima Daiichi Nuclear Power Plant accident that has had long-term effects on the physical, psychological and social well-being of the victims. This was a completely different case from past earthquakes in Japan, and unprecedented measures have been required. Given the severity of the radioactive contamination, it was impossible to respond immediately to the problems and anxieties of the residents, and many victims were forced to evacuate the area, seeking a new living base either within or outside the prefecture. Reaction to the radioactive contamination also radically affected Fukushima Prefecture's land prices.

In 2012, immediately after the earthquake, land prices in all residential and commercial areas in Fukushima Prefecture fell significantly. In 2013, land prices at all points in the commercial area continued to decrease. However, two years after the earthquake, the official land prices in Iwaki City showed an abnormal rate of increase, not only for Fukushima Prefecture but for all of Japan. This had a substantial impact on the housing supply available to victims. The radioactive contamination and the subsequent evacuation orders resulting from the nuclear accident were unique events in the world. Accordingly, attempting to understand the large fluctuations in land prices that occurred in the disaster area is a significant part of understanding the massive effects of this unprecedented catastrophe.

The purpose of this paper is to identify those factors that influenced post-disaster land price fluctuations in Iwaki City, where land prices rose abnormally following the Great East Japan Earthquake and the Fukushima Daiichi Nuclear Power Station accident.

Previous research related to earthquake disasters and land price fluctuations include a study by Nomura et al. [1], which analyzed the impact of the Great Hanshin Earthquake in 1995 on land prices using a hedonic approach. It was found that in 1996, the year immediately following the earthquake, the decrease in land prices was directly proportional to the degree of damage to buildings (i.e., the greater the damage to buildings, the lower the land price). However, in 1997, land prices stopped falling in areas where buildings had been completely destroyed or burned to the ground, while in areas with high half-destruction rates, land prices continued to fall.

Regarding the relationship between land price fluctuations after the earthquake and real estate sales in Fukushima Prefecture, Kawamura [2] pointed out that the spatial movement and settlement of many victims was a significant factor. Saito [3] analyzed the impact of accepting evacuees from the nuclear accident on city planning in Iwaki City, focusing on changes in population and land use He found that houses were scattered on a small scale and built in places that were not intended to be residential areas, pointing to the need to develop a new living environment after such a disaster.

These studies focused on factors such as the number of real estate transactions in the disaster area, the rate of increase in land prices, and changes in land use. There are few studies discussing the relationship between land prices and the stigma of radioactive contamination caused by a nuclear accident. Hirota [4] considered the outlook for the real estate market in the year of the Great East Japan Earthquake, highlighting concerns about the decline in real estate value and the associated stigma with soil pollution from diffused radioactivity. As an overseas reference example, he also introduced a research report by Gambling and Downing et al. [5] describing the impact on land prices of the Three Mile Island accident in the United States.

METHOD

As noted, the purpose of this paper is to identify how the Great East Japan Earthquake and the Fukushima Daiichi Nuclear Power Station accident affected the real estate market in the region. Focusing on fluctuations in land prices in Iwaki City, the study quantitatively analyzes the effects of various social factors caused by the earthquake from a long-term perspective using a hedonic regression approach. We first investigate changes in land price fluctuation rate and changes in the air dose (radiation dose of the surrounding environment emitted from radioactive materials) throughout Fukushima Prefecture following the disaster, and describe the position of Iwaki City within the prefecture. Next, we create a land price volatility function using multivariate analysis based on the official land prices in Iwaki City. We then establish how various factors associated with the earthquake affected land price fluctuation rate in the disaster area.

POST-EARTHQUAKE LAND PRICES AND AIR DOSES IN FUKUSHIMA

Land prices after the earthquake

Figure 1 shows the fluctuation of land prices in seven cities and towns (Fukushima City, Koriyama City, Shirakawa City, Aizu-wakamatsu City, Minami-aizu Town, Minami-soma City, Iwaki City), represented by seven regions of Fukushima Prefecture. The land price used here is the average of the official land price and benchmark land price. (The official land price is the land price announced on January 1st every year based on an appraisal by two or more real estate appraisers for each plot set by the Ministry of Land, Infrastructure, Transport and Tourism. The benchmark land price is the land price determined by the prefecture on July 1st every year based on an appraisal by one or more real estate appraisers per plot.) Land price fluctuations rate which are compared to the previous year were negative until 2011 and then turned positive in all regions except Minami-aizu in 2013 after the earthquake.

However, the movements show different patterns in each region. The fluctuation in land prices in Minami-soma and Iwaki changed significantly after the earthquake, and the fluctuation in Iwaki rose abnormally from 2013 to 2016 compared to other regions. Possible reasons for this are the acceptance of approximately 24,000 evacuees in the Futaba District and the transfer of workers who worked at the nuclear power plant while accommodated in Iwaki city during the countermeasure process. (approximately 10% of the population of Iwaki City). However, this is not sufficient to explain the complex relationship between the earthquake and nuclear plant disaster and land price fluctuations.

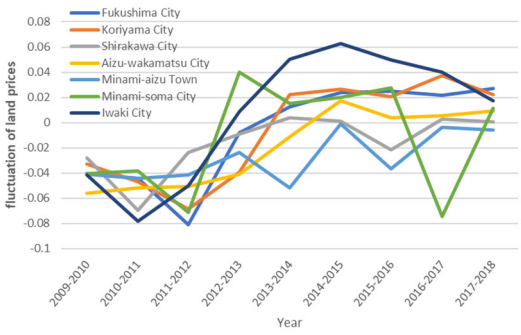

Fig. 1 Fluctuation of land prices in seven areas of Fukushima Prefecture.

On the other hand, unlike other areas, Minami-soma, where many victims were forced to evacuate due to the nuclear accident, experienced rapid changes in land price fluctuations. There were no major changes in land price fluctuations in Aizu-wakamatsu, Minami-aizu, and Shirakawa.

Air dose rate after the earthquake

Figure 2 shows the changes in the air dose rate from 2011 to 2018 in the seven representative cities of the regions of Fukushima Prefecture. We used the air dose rates (μSv/h) for the seven representative cities that were listed on the website of the Fukushima

Reconstruction Station. (Measured location is the joint-government building in each city, the prefectural north health and welfare office building in Fukushima city) On this site, the air dose rate measurement results in Fukushima Prefecture are recorded by measuring the air dose every hour in each area. Here, the average of the measurement results at 00:00 on the first day of each month of the year is taken as the air dose rate for the year.

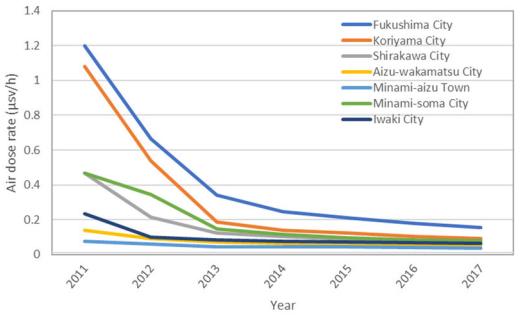

Fig. 2 Changes in air dose rate in seven areas of Fukushima Prefecture.

Since the radioactive materials diffused by the Fukushima Daiichi Nuclear Power Plant accident flowed towards the west by the wind, the values in Fukushima City and Koriyama City, which are located west of the nuclear power plant, are quite high, at more than 1.0 μSv/h. Especially in 2011, Shirakawa City, Minami-soma City, and Iwaki City had air dose rates exceeding 0.23 μSv/h. The Ministry of the Environment has determined that the requirement for an area to be included in the decontamination implementation plan is an area with an air dose rate of 0.23 μSv/h or more. This value is calculated by converting the additional exposure dose of 1 mSv/y into the radiation dose per hour and adding the natural radiation dose.

Since 2013, the air dose rate in all seven regions has decreased due to decontamination and attenuation, and in 2017, the air dose rate at the monitoring posts in the seven areas was below 0.23 μSv/h.

Table 1 shows the correlation coefficients indicating the degree of correlation between land price fluctuations and air dose rates in the seven regions of Fukushima Prefecture from 2011 to 2017. Figure 3 shows a scatter plot of the air dose rates and land price fluctuations in the seven representative cities in FY2011.

Fukushima City and Koriyama City, which had high air dose rates in 2011, saw large declines in land price fluctuations. On the other hand, the decline is small in Shirakawa City and Minami-aizu Town, where the air dose rate is low. Table 1 also shows a negative correlation between air dose rate and land price fluctuations in 2011, indicating that higher air dose rates are associated with lower land price fluctuations. However, in 2012, the correlation coefficient became quite small, after which it became slightly positive.

Table 1 Correlation coefficients measuring the correlation of land price fluctuations and air dose rates from 2011 - 2018

year	2011	2012	2013	2014	2015	2016	2017
Correlation coefficient	-0.66	0.04	0.34	0.11	0.38	0.20	0.80

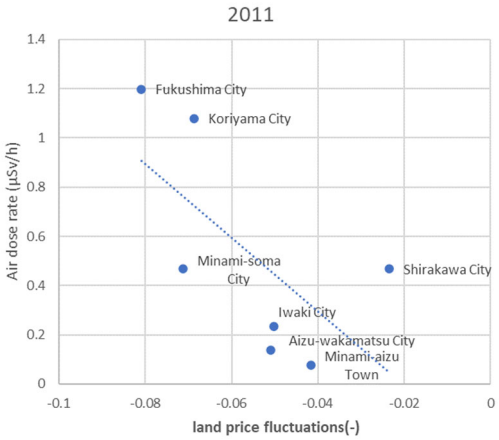

Fig. 3 Scatter plot of air dose rates and land price fluctuations in the 7 cities of Fukushima in 2011

In 2017, a strong positive correlation was found, resulting in higher land price fluctuation rate in areas with higher air doses. Immediately after the earthquake, it is probable that the anxiety caused by the lack of information on radioactive contamination and the damage it could inflict on the human body drastically reduced land price fluctuation rate.

However, by 2013 (approximately), when decontamination work and national measures/reconstruction plans were underway, the air dose rate had decreased, at least to some extent, and the land market appeared not to react significantly to the air dose rate. It can be said that the land price increased regardless of the air dose rate due to the population concentration in Iwaki City, Fukushima City, and Koriyama City, which were major destinations for residents who had received evacuation orders.

LAND PRICE FLUCTUATIONS AFTER THE EARTHQUAKE IN IWAKI CITY

It is believed that the rise in land prices in Iwaki City after the earthquake is mainly due to the

acceptance of evacuees and the presence of workers at the nuclear plant. We analyzed the situation using the hedonic approach in order to quantitatively determine what factors actually affected the land price fluctuations in Iwaki City.

Analytical method (hedonic approach)

The hedonic method is a regression technique used to estimate the prices of qualities or models that are not available on the market in particular periods, but whose prices in those periods are needed in order to be able to construct price relatives. [6]. Because the hedonic approach is based on the capitalization hypothesis, In this paper, we consider that land prices are determined by a variety of factors, including the surrounding environment, and express them as vectors for characteristics that contribute to land price [7]. Multiple regression analysis is used to implement this approach. In this study EXCEL multivariate analysis Ver.6.0, Esumi Co., Ltd. was used.

Setting surveyed sites

The surveyed sites in this paper are the standard land of the official land price set by the Ministry of Land, Infrastructure, Transport and Tourism (103 sites) and the standard land of benchmark land price set by the local government (77 sites), for a total of 180 sites in Iwaki City (2018).

Objective variables and explanatory variables

The objective variable in the hedonic approach used in this paper is the land price fluctuation (rate of land price in a given year compared to the previous year) at each surveyed site in the analysis. The explanatory variables are the various environmental factors that potentially affected the real estate market during the period from the earthquake to the reconstruction of the study site in the following criteria.

1) building and infrastructure related variables;
Land area, floor area ratio, front road condition, lifeline (city-gas or sewer), distance from the nearest station, distance to Iwaki station, along national or prefectural road, site shape, building structure, building usage status (a total of 24 items)
2) built environment related variables;
Surroundings and surveyed site surroundings (a total of 24 items)
3) different districts;
Taira district, Onahama district, Nakoso district, Joban district, Uchigo district, Yotsukura district, Tono district, Ogawa district, Yoshima district, Sanwa district, Taito district, Kawamae district, Kunohama/Oku district (a total of 13 items, all of which are converted to dummy variables)
4) variables directly related to nuclear power plant;
Air dose, distance to the nuclear power plant, tsunami inundation area, and reconstruction base area (a total of 4 items)
In total of 55 explanatory variables have been set.

Examination of each explanatory variable and multicollinearity

Among the explanatory variables above, there may be multicollinearity that could adversely affect the estimation accuracy of the model. To ensure that the hedonic function produces a highly explanatory model, the presence or absence of multicollinearity is established using a correlation coefficient table. If the value of VIF (Variance Inflation Factor) calculated after the multivariate analysis is greater than 10, then the presence or absence of the effect of that variable is re-examined.

Table 2 shows the final set of explanatory variables after excluding factors which were causing the multicollinearity. With respect to the quantitative variables shown in the table, since 12 stations besides Iwaki Station were used well, we chose to omit “distance to Iwaki station” (DS) as an explanatory variable.

Regarding air dose (AD), since the values at each survey site were not measured, we applied the air dose values at the monitoring post closest to the site. The monitoring post uses the Fukushima Prefecture Radioactivity Measurement Map operated by Fukushima Prefecture. When the closest monitoring post changes, it is changed every year. (For the measured values of air dose rate (μ Sv /h) at the monitoring post, the Fukushima Prefecture website is referred.

Among the qualitative variables shown in the table, the front road width (Road-4,6,8) at the survey site includes widths of 0 to 4 m, 4 to 6 m, and 6 to 8 m. Dummy variables are set for each range.

As for site shape (Square, Rectangle, Trapezoid), building structure (ST-W, LS, RC, S, Other) and land use (Residence, Industrial, Store, Bank, Office, Farm, Workshop), the VIF value at the time of the analysis greatly exceeded 10. Moreover, when these variables were excluded, the coefficient of determination and the p-value value were significant. Consequently, these factors were excluded from the set of

explanatory variables.

The list of explanatory variables related to surrounding buildings initially included AR-Residence (houses around the survey site), AR-Farm (farmhouses around the survey site), AR-Industrial (factories around the survey site), AR-Public (public facilities around the survey site), AR-Vacant (vacant lot around the survey site), and AR-Store (when there is a store around the survey site). However, since there were no survey sites corresponding to AR-Public, AR-Public was excluded from the final set of explanatory variables.

Table 2 Explanatory variables

		Abbreviation	Variable name	Measurement Units	Description	final decision	Reason
Objective variable		PLP	Land price	Yen/m²	Official land prices for 2010-2018	○	
Explanatory variable	Quantitative variables	AC	Land area	m²	Area of one survey site	○	
		FAR	Floor-area ratio	%/100	Ratio of maximum allowable floor area to the area of the survey site	○	
		Station	Distance to the nearest station	m	Distance from the survey site to the nearest station	○	
		DS	Distance to "Iwaki Station"	㎞	Distance to "Iwaki Station"	×	※1
		AD	Air dose rate	μsv/h	Annual average value of the monitoring post closest to survey site	○	
		DSNPP	Distance to the nuclear power plant	m	Distance to Fukushima Daiichi Nuclear Power Station	○	
	Qualitative variables	Road-4	Front road width	m	Front road width is 0-4m	○	
		Road-6	Front road width	m	Front road width is 4-6m	○	
		Road-8	Front road width	m	Front road width is 6-8m, Yes	○	
		N-P-Road	Along national or prefectural roads		Along national or prefectural roads	○	
		GOS	Lifeline dummy		Supply by city gas or sewer	○	
		Square	Site shape		The site shape is square	×	※2
		Rectangle	Site shape		The site shape is rectangular	×	※2
		Trapezoid	Site shape		The site shape is trapezoidal	×	※2
		ST-W	Architectural structure		The building structure is wooden	×	※2
		ST-LS	Architectural structure		The building structure is light steel	×	※2
		ST-RC	Architectural structure		The building structure is RC	×	※2
		ST-S	Architectural structure		The building structure is steel	×	※2
		ST-Other	Architectural structure		Other building structures	×	※2
		Residence	Land use		Land use status is residential	×	※2
		Industrial	Land use		Land use status is factory	×	※2
		Store	Land use		Land use status is store	×	※2
		Bank	Land use		Land use status is bank	×	※2
		Office	Land use		Land use status is office	×	※2
		Farm	Land use		Land use situation is rice field	×	※2
		Workshop	Land use		Land use status is the workplace	×	※2
		AR-Resid	Surrounding buildings		Dwelling in the vicinity	○	
		AR-Farm	Surrounding buildings		Farmers in the vicinity	○	
		AR-Indu	Surrounding buildings		Factories in the vicinity	○	
		AR-Public	Surrounding buildings		Public facilities in the vicinity	×	※3
		AR-Vacant	Surrounding buildings		vacant land in vicinity	○	
		AR-Store	Surrounding buildings		Stores in the vicinity	○	
		DLA	Surrounding area		located in area of house for installment sale	○	
		BUA	Surrounding area		located in Urbanized area	○	
		RA	Surrounding area		located in Residential area	○	
		ASA	Surrounding area		located in Farm village area	○	
		CA	Surrounding area		located in Commercial area	○	
		Dev-M	Surrounding area		located in Medium-scale development site	×	※3
		Dev-L	Surrounding area		located in Large-scale development site	×	※3
		Adjust	Surrounding area		located in Land readjustment	○	
		DV-TAI	District dummy		Taira district dummy	○	
		DV-ONA	District dummy		Onahama district dummy	○	
		DV-NAK	District dummy		Nakoso district dummy	○	
		DV-ZYO	District dummy		Joban district dummy	○	
		DV-NAI	District dummy		Uchigo district dummy	○	
		DV-YOK	District dummy		Yotsukura district dummy	○	
		DV-TON	District dummy		Tono district dummy	○	
		DV-OGA	District dummy		Ogawa district dummy	○	
		DV-YOS	District dummy		Yoshima district dummy	○	
		DV-SAN	District dummy		Sanwa district dummy	○	
		DV-TAJ	District dummy		Tabito district dummy	○	
		DV-KAW	District dummy		Kawamae district dummy	○	
		DV-KUN	District dummy		Hisanohama / ohisa district dummy	○	
		FD	Flooded area dummy		Tsunami inundation area	○	※4
		RD	Reconstruction base dummy		Reconstruction base	○	※5
※1	In Iwaki City, the nearest stations on the JR Joban Line and interchanges on the motorway are mainly used.						
※2	The VIF value was high, and the coefficient of determination did not change in the analysis excluding this variable.						
※3	There was no corresponding area						
※4	The damage caused by the tsunami caused by the earthquake was great in Iwaki City.						
※5	Samples belonging to the area around Onahama						

Similarly, the initial list of explanatory variables related to the surrounding area included LA (survey site is located in an area of houses for installment sale), BUA (site is in an urbanized area), RA (site is in a residential area), ASA (site is in a farm village area), CA (site is in a commercial area), Dev-M (site is in a medium-sized development area), Dev-L (site is in a large-scale development site), and Adjust (a land readjustment is involved). However, since there were no survey sites corresponding to Dev-M and Dev-L, these two variables were excluded from the final set of explanatory variables.

The inundation area dummy (FD) indicates that the survey site is within the tsunami inundation area according to data on the 2011 Great East Japan Earthquake released by the Geospatial Information Authority of Japan. The reconstruction base dummy (RD) refers to being located in the Onahama hinterland tsunami reconstruction base development project in the reconstruction plan of Iwaki City.

Table 3 shows the correlation coefficients among the quantitative explanatory variables. For the explanatory variables, there were no significantly high correlation coefficients (r > = 0.8).

Table 3 Correlation coefficients for explanatory variables

2011	PLP	AC	FAR	Station	AD	DSNPP
PLP	1.00					
AC	0.04	1.00				
FAR	0.00	0.00	1.00			
Station	-0.17	0.00	-0.32	1.00		
AD	0.06	-0.05	-0.18	0.03	1.00	
DSNPP	-0.29	0.07	0.01	0.08	-0.53	1.00

2012	PLP	AC	FAR	Station	AD	DSNPP
PLP	1.00					
AC	-0.02	1.00				
FAR	-0.17	0.00	1.00			
Station	0.11	0.00	-0.32	1.00		
AD	0.18	-0.01	-0.22	0.01	1.00	
DSNPP	-0.14	0.07	0.01	0.08	-0.63	1.00

2013	PLP	AC	FAR	Station	AD	DSNPP
PLP	1.00					
AC	-0.10	1.00				
FAR	-0.27	0.00	1.00			
Station	-0.05	0.00	-0.32	1.00		
AD	0.11	-0.04	-0.01	0.05	1.00	
DSNPP	-0.14	0.07	0.01	0.08	-0.39	1.00

2014	PLP	AC	FAR	Station	AD	DSNPP
PLP	1.00					
AC	-0.10	1.00				
FAR	-0.23	0.00	1.00			
Station	-0.10	0.00	-0.32	1.00		
AD	0.09	-0.04	0.06	-0.07	1.00	
DSNPP	-0.04	0.07	0.01	0.08	-0.41	1.00

2015	PLP	AC	FAR	Station	AD	DSNPP
PLP	1.00					
AC	-0.11	1.00				
FAR	-0.29	0.00	1.00			
Station	-0.09	0.00	-0.32	1.00		
AD	-0.05	-0.03	0.05	-0.04	1.00	
DSNPP	0.01	0.07	0.01	0.08	-0.48	1.00

2016	PLP	AC	FAR	Station	AD	DSNPP
PLP	1.00					
AC	-0.11	1.00				
FAR	-0.27	0.00	1.00			
Station	-0.07	0.00	-0.32	1.00		
AD	-0.10	-0.03	0.08	-0.05	1.00	
DSNPP	-0.06	0.07	0.01	0.08	-0.42	1.00

2017	PLP	AC	FAR	Station	AD	DSNPP
PLP	1.00					
AC	-0.11	1.00				
FAR	-0.24	0.00	1.00			
Station	-0.07	0.00	-0.32	1.00		
AD	-0.07	-0.02	0.09	-0.10	1.00	
DSNPP	-0.12	0.07	0.01	0.08	-0.48	1.00

2018	PLP	AC	FAR	Station	AD	DSNPP
PLP	1.00					
AC	-0.07	1.00				
FAR	-0.06	0.00	1.00			
Station	-0.08	0.00	-0.32	1.00		
AD	-0.09	-0.03	0.08	-0.07	1.00	
DSNPP	-0.02	0.07	0.01	0.08	-0.47	1.00

RESULTS AND DISCUSSION

Coefficient of determination and model validity

Table 4 shows the coefficients of determination, adjusted coefficients of determination, and sample sizes from 2011 to 2018. For 2011 and 2012, the coefficients of determination (R^2 values) were 0.33 and 0.22, respectively, with adjusted R-squared values (Adjusted R^2) of 0.06 and -0.07, indicating a poor goodness-of-fit for the model.

Table 4 Coefficients of determination (2011-2018)

	2011	2012	2013	2014	2015	2016	2017	2018
Coefficient determination (R^2)	0.334	0.225	0.562	0.598	0.713	0.726	0.658	0.525
Adjusted R^2	0.062	-0.063	0.403	0.468	0.630	0.647	0.567	0.402
Number of samples	125	134	136	148	161	163	171	176

This would appear to be largely due to the rapid decrease in land price in Iwaki City immediately after the earthquake. The various environmental factors that determine normal land price fluctuation rate may not have responded clearly in the turmoil of the land market during this period. On the other hand, from 2013, land price fluctuation rate show an upward trend, and the coefficients of determination for the model are all above 0.5. The adjusted coefficients of determination are also substantially higher. Thus, the model's explanatory power, as reflected in its better goodness-of-fit, appears to be much stronger. Consequently, it is considered an effective means for estimating land price fluctuations after 2013.

Multiple regression analysis

Table 5 shows the standardized partial regression coefficients and significance levels from 2011 to 2018. No significant results were produced for the land area (AC) variable during the estimation period, suggesting that the size of the land area did not affect the fluctuation in the land price during the reconstruction period.

Table 5 Standardized partial regression coefficients (2011-2018)

Explanatory variable		Coef.							
logprice		2011	2012	2013	2014	2015	2016	2017	2018
Quantitative variables	AC	0.123	-0.032	-0.031	-0.060	-0.053	-0.052	-0.046	-0.030
	FAR	-0.020	-0.070	-0.320	-0.237	-0.235	-0.201	-0.220	-0.020
	Station	0.033	0.164	0.015	-0.022	-0.140	-0.067	-0.134	-0.158
	AD	0.720	-0.148	-0.042	0.024	-0.163	-0.203	-0.191	-0.156
	DSNPP	0.159	0.177	0.778	0.287	-0.151	-0.203	-0.695	-0.557
Qualitative variables	DV-TAI	-0.342	0.211	0.525	0.300	0.414	0.232	-0.036	-0.276
	DV-ONA	-0.155	-0.027	0.050	0.165	0.452	0.349	0.323	0.083
	DV-NAK	-0.252	-0.047	-0.558	-0.183	0.159	0.044	0.180	-0.065
	DV-ZYO	-0.160	0.040	0.026	-0.054	0.035	-0.002	-0.042	-0.216
	DV-NAI	-0.310	0.176	0.123	-0.023	0.036	-0.077	-0.130	-0.228
	DV-YOK	-0.571	0.036	0.082	-0.019	-0.003	0.131	-0.140	-0.364
	DV-TON	-0.363	0.022	-0.210	-0.201	-0.107	-0.155	-0.135	-0.139
	DV-OGA	-0.024	0.133	0.147	0.046	-0.001	-0.064	-0.188	-0.200
	DV-YOS	-0.208	0.085	0.250	0.090	0.092	0.041	-0.084	-0.221
	DV-SAN	-0.451	0.037	0.009	0.037	0.067	0.007	-0.038	-0.019
	DV-TAJ	-0.457	0.066	-0.204	-0.171	-0.019	-0.085	-0.053	-0.115
	DV-KAW	-0.128	0.101	0.078	-0.096	-0.184	-0.186	-0.289	-0.307
	DV-KUN	-0.595	0.264	0.185	0.008	-0.085	-0.136	-0.262	-0.306
	FD	-0.127	0.033	-0.095	-0.085	0.063	0.062	0.113	0.161
	RD	0.124	-0.171	-0.206	-0.093	-0.175	-0.163	-0.114	-0.089
	Road-4	-0.009	-0.222	0.001	0.021	0.209	0.341	0.300	0.195
	Road-6	-0.258	-0.423	0.333	0.403	0.597	0.863	0.800	0.599
	Road-8	-0.287	-0.192	0.416	0.381	0.340	0.653	0.663	0.488
	GOS	0.043	0.095	0.334	0.310	0.226	0.281	0.176	0.161
	N-P-Road	0.088	-0.050	-0.124	-0.174	-0.114	-0.080	-0.106	-0.027
	AR-Resid	0.192	0.035	0.014	0.072	0.014	0.040	0.058	-0.016
	AR-Farm	0.117	-0.043	-0.034	-0.138	-0.112	-0.148	-0.274	-0.241
	AR-Indu	-0.021	0.103	0.078	0.041	0.043	0.046	0.065	0.133
	AR-Vacant	-0.057	-0.210	-0.159	-0.110	-0.009	-0.065	-0.100	-0.056
	AR-Store	-0.116	-0.174	-0.037	0.018	-0.043	0.018	0.042	0.123
	DLA	0.016	-0.073	-0.058	-0.083	-0.003	0.038	0.036	0.142
	BUA	-0.163	-0.068	0.023	-0.001	0.071	0.027	0.133	0.172
	RA	-0.213	0.184	0.242	0.315	0.295	0.256	0.331	0.483
	ASA	0.046	0.135	-0.007	-0.032	-0.121	-0.063	-0.027	-0.055
	CA	0.036	0.179	0.073	0.044	0.062	-0.044	0.010	-0.067
	Adjust	-0.027	-0.093	0.004	0.046	0.050	0.057	0.064	-0.005
Land price volatility rise		10%level	5%level	1%level					
Land price volatility decline		10%level	5%level	1%level					

On the other hand, the effect of the floor area ratio (FAR) was found to be negative and significant at the 1%-5% level from 2013 to 2017, thus suggesting that the floor area ratio actually had a negative impact on land price fluctuations. This would seem to run counter to what would normally be expected. Since, in general, a larger floor area ratio means that a larger floor area can be constructed, the floor area ratio is typically a variable that contributes positively to a rise in land price fluctuation rate; however, here it appears to work in the opposite way. This result is thought to be due to the high demand for low- and middle-rise housing in Iwaki City during this time.

Distance from the nearest station (Station) was shown to have a significant negative effect (at the 10% significance level) in 2015, 2017, and 2018. This result indicates that the shorter the distance from the nearest station, the greater the land price fluctuation is.

Air dose (AD) was not significant until 2014. However, it had a significant negative effect (at the 1%-10% level) between 2015 and 2018, suggesting that this environmental factor negatively impacted land price fluctuation rate. Moreover, since the standardized partial regression coefficient for air dose is rather large, it can be inferred that its influence on land price fluctuation rate was substantial. The likely reason for this is that the excessive demand for housing had begun to settle down, and air dose considerations came to constitute a large portion of the judgment factors affecting the residents' choice of a place to live.

A significant positive effect (at the 5% level) was found for distance from the Fukushima Daiichi Nuclear Power Station in 2013; however, a significant negative effect (at the 10% level) was found for this same variable in 2017 and 2018.

In 2013, the larger the distance from the Fukushima Daiichi Nuclear Power Station, the higher was the land price fluctuation. In contrast, in 2017 and 2018, the larger the distance to the Fukushima Daiichi Nuclear Power Station, the lower the land price fluctuation was. Immediately following the earthquake, evacuees were concerned about the unknown dangers of the nuclear power plant and generally looked for a place to live that was far from the Fukushima facility. However, several years after the earthquake, many became less anxious or less concerned about the dangers. It appears that the stigma associated with the accident had a little disappeared after approximately four years.

There is great variation among the district dummies (DV-TAI, ONA, NAK, ZYO, NAI, YOK, TON, OGA, YOS, SAN, TAJ, KAW, KU). In 2015 and 2016, a significant positive effect (at the 5%-10% level) was found in the Taira and Onahama areas.

These areas are among the most reconstructed areas in Iwaki City. This was also the time when many disaster-related public housing and group relocation promotion projects were completed.

A significant negative effect (at the 1%-5% level) can be seen in 2011 for areas in the northern part of Iwaki City, such as the Yotsukura, Hisanohama, and Kawamae districts; however, the coefficient of determination is quite small from 2011 to 2012, making it difficult to evaluate based on the model.

In 2017 and 2018, a significant negative effect (at the 1%-10% level) was found in most areas, with the exception of the Onahama area. As the reconstruction progressed and the demand for housing slowed down, it seems that the land market fell to the level that was seen in the local cities before the earthquake.

For the flooded area dummy (FD), no significant results were produced until 2016; thereafter, a significant positive effect (at the 5%-10% level) was found in 2017 and 2018. The positive impact of the tsunami inundation variable since 2017 may be due to the progress of the tsunami countermeasures, such as seawalls.

The Reconstruction Base Area dummy (RD) was negative significant effect (at the 5% level) in 2013, 2015 and 2016. Despite the business vision, land price fluctuation rate fell near the Onahama Port tsunami reconstruction center development project.

The influence of front road width (Road-4,6,8) was found to be positive and significant (at the 1%-5% level) in 2015, 2016 and 2017. A sufficiently wide front road is advantageous in terms of access to parking lots and day lighting conditions and thus seems to be preferred as a condition for choosing a residence.

For the lifeline dummies (GOS), a positive significant effect (at the 1% level) was found from 2013 to 2018. The construction of sewers and city gas lines is a very important factor in the rapid reconstruction of living space after a disaster, and has a great positive impact on land price fluctuations.

Among the surrounding buildings variables (AR-Residence, Industrial, Store, Bank, Office, Farm, Workshop), the effect of AR-Farm was negative and significant (at the 1%-5% level) between 2016 and 2018, and the effect of the AR-Vacant was negative and significant (at the 10% level) in 2013. This suggests that land price fluctuation rate will decrease if there are farms or vacant lots around the survey area.

Finally, Finally, regarding the area around the surveyed site (DLA, BUA, RA, ASA, CA, Dev-L, Dev-M, Adjustment).

DLA (house for installment sale area) had a significant positive effect (at the 5% level) in 2018. BUA (urbanized area) had a significant positive effect (at the 5%-10% level) in 2016/2017, and RA (residential area) had a significant positive effect (at the 1%-5% level) from 2014 through 2018. After the disaster, it seems that Iwaki City experienced an increase in demand by evacuees seeking a place of residence.

CONCLUSIONS

Focusing on Iwaki City, where the real estate market behaved unexpectedly after the Great East Japan Earthquake, and land price fluctuation rate were rising abnormally, this paper used a hedonic regression approach to identify those factors that significantly affected area land price fluctuations. The results are as follows:

1. From 2013 to 2016, when an abnormal rise in land price fluctuation rates was observed, the explanatory variables having a significant positive effect were the Taira and Onahama area dummies, Front road width, Lifeline, and Surrounding area.

2. Regarding distance from the Fukushima Daiichi Nuclear Power Station, it was found that in 2013, the larger the distance, the higher the land price fluctuation rate was. In contrast, in 2017 and 2018, the larger the distance, the lower the land price fluctuation rate was.

3. With regard to reconstruction bases (RD), land price fluctuation rates decreased in all such areas. As for the impact of lifelines (GOS), a significant positive effect was found between 2013 and 2018.

4. Air dose (AD) was not significant until 2014. However, it had a significant negative effect (at the 1%-10% level) between 2015 and 2018, suggesting that this environmental factor negatively impacted land price fluctuation rate.

The effect of the air dose and distance from the nuclear power plant variables changed significantly after the 4th year since the earthquake. On the other hand, regardless of the time of year, a negative impact on land price fluctuation rate was shown for the reconstruction base variable, while a positive impact was shown for lifelines. It suggests that the stigma for land that existed after the accident was a little resolved in roughly four years.

We have issues to be addressed in the future. Since the coefficient of determination (R^2) in 2011 and 2012 was rather small, the model for Iwaki City was ill fitting for 2011 and 2012. We intend to improve the explanatory power of the hedonic model by adding variables that reflect the regional characteristics of the

survey area, the rate of collapse of houses, and the rate of population decline.

ACKNOWLEDGMENTS

We are grateful for a Grant-in-Aid for Scientific Research (18K18602) for supporting this research.

REFERENCES

[1] Koji NOMURA, Miho OHARA and Kimiro MEGURO, Analysis of Change of Land Price After an Urban Earthquake -Case Study in Affected Area Due to The 1995 Kobe Earthquake-, Journal of Japan Society of Civil Engineers A1、Vol.65, No.1, p. 655-660, 2009

[2] Shinya KAWAMURA, Relationship between Real Estate Transactions by Fukushima Refugees and Land Price Changes after The Great East-Japan Earthquake, Proceedings of the General Meeting of the Association of Japanese Geographers, 2013a(0), 100141, Session ID : 316 , 2013

[3] Mitsuhiro Saito, An Approach to Influence on City Planning by Accepting Evacuees due to Nuclear Accident, 2018 Vol.53 Issue 3, pp.919-926

[4] Yuji Hirota, Nuclear Power Plant Accident Due to the Great East Japan Earthquake and Appraisal of Real Estate, The Appraisal Journal Summer 2011 Vol.53, No.3 pp25-40、2011.07

[5] Gamble, H.B., and R.H. Downing, "Effects of Nuclear Power Plants on Residential Property Values," Journal of Regional Science, 1982, 457-478.

[6] OECD Glossary of Statistical Terms, Organization for Economic Co-operation and Development, https://stats.oecd.org/glossary/detail.asp?ID=1225, (10th june2021)

[7] Koji Shimada, Tomohiko Yoshida, Urban and Environmental Policy Assessment for Kyoto, Osaka and Kobe City by The Hedonic Price Method, Proceedings of Annual Meeting of Environmental Systems Research, Vol.40 PP.373-378, 2012

11th Int. Conf. on Geotechnique, Construction Materials & Environment,
Kyoto, Japan, 3-5 November 2021, ISBN: 978-4-909106063 C3051

NUMERICAL INVESTIGATION INTO MOLTEN METAL FLOW AND ITS SOLIDIFICATION UNDER GRAVITY SAND MOULDING IN PLUMBING COMPONENTS: POURING TEMPERATURE AND RUNNER STRUCTURE

Sirawit Namchanthra[1], Watcharapong Chookaew[1], Chakrit Suvanjumrat[1],
Wichuphan Wijitdamkerng, and Machimontorn Promtong[1]

Department of Mechanical Engineering, Faculty of Engineering,
Mahidol University, Salaya, Nakorn Pathom, Thailand

ABSTRACT

Metal casting using the solidification of molten metal flows involves complex heat transference during production. This can cause defects on the workpiece, affecting the efficiency of production. This research will use the Computational Fluid Dynamics (CFD) technique to investigate the filling, solidification, and cooling stages of the production of a component for plumbing. The CFD program FLOW 3D CAST v5.03 tracked the leading edge of the molten metal liquid (based on the Volume of Fluid (VOF) method). A two-equation k–ε turbulence was adopted to provide a Reynold term, and it should be noted that the geometry of the molten liquid and internal chamber are the same as in the actual production line. The simulation shows how different pouring temperatures effect the runner, and that the pouring temperature influenced the behavior of the molten metal flow, resulting in defects on the workpiece. Moreover, the runner and its number affected the liquid metal flow and affected the defect's location during the solidification period. Future work will verify the results between the simulation and experiments, and further investigate possible defect locations on the surface of the workpiece, which could be a critical criterion in further discussions.

Keywords: Gravity sand casting, Solidification, Computational Fluid Dynamics (CFD)

INTRODUCTION

In the manufacturing of plumbing components, gravity sand casting is a commonly used production process. The casting process starts with the preparation of a sand mould, into which molten metal is poured [33]. The metal solidifies during the cooling processes, after which the mould is removed, and the workpiece quality checked for shape and size. If there are defects, the component cannot proceed to the finishing section, and will be recycled to save the materials cost. However, the energy and labor costs are already spent and cannot be retrieved, so this process can be more efficient. Many techniques have been proposed to enhance the economic efficiency of molten metal casting, such as the production of several castings in a single mould and the introduction of lost foam technology. [1]. This can increase the efficiency of material use and save production costs, but it requires a deep understanding of mould layout design, material pouring techniques, and physical molten metal heat transfer process.

Defects in castings may arise from poor design of the mould, an unsuitably sized runner, or carelessness during the pouring process [2, 3]. Fig. 1 shows plumbing components produced by casting as defective workpieces (Fig. 1c shows the defects (porosity) within the workpiece). The external and internal cavities affect the mechanical properties, resulting in low-quality casting that is unfit for purpose. For decades, research has investigated the influence of pouring temperature, filling rate, and pressure transfer (during the solidification period), cooling rates, mould coating material, and air entrapment behavior [1, 4-9] on the quality. Some works focused on minimizing residual stress and the healing of possible bifilms during solidification [10, 11]. Moreover, the magnetic fields added to the solidification process to eliminate shrinkage defects [12]. Because of the parameter optimization (i.e., pouring temperature and pouring time), a mathematical model based on regression analysis was proposed recently [13].

The Computational Fluid Dynamics (CFD) technique is widely used in the casting process design, especially for parametric optimization [14-22]. Basically, this promising tool can help redesign the mould layout and eliminate defects such as shrinkage, porosity, and the discovery of hot spot regions [23], significantly, the liquid phase transformation to the solid phase, which could also capture using the CFD technique. This metallurgical process could point out critical criteria of defect occurrence [20]. Some researchers have observed the effects of the feeder and discussed concerns regarding the filling characteristics [23]. Moreover, the heat

transfer and the interface between solids and liquids were identified related to various casting speeds [15]. In addition, apart from the fluctuated surface of molten metal, the temperature distribution during the filling and solidification was monitored [18]. The validation study, and especially the casting process, became mandatory tasks so the evaluation was accurate [2, 6, 24-30].

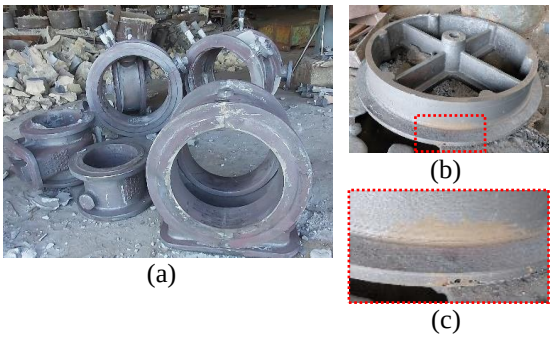

(a) (b) (c)

Fig. 1 Plumbing Joints Produced in the Plumbing Manufacturing Process (Thailand); a) An Example of a Defect, b) A Defect Causing Porosity occurrence , and c) detail view of porosity occurrence.

This research uses the Volume of Fluid (VOF) method to capture the molten metal flows in the gravity sand mould. It will observe the effects of different pouring temperatures and different internal structures on the traveling distance and filling time. In addition, the curve of average temperature during the solidification and cooling stages will be discussed. The objective of this work is to use the Computational Fluid Dynamics (CFD) technique:

i) to investigate the molten metal flows during the filling stage, as well as the influence of pouring temperature,

ii) to capture the casting process, especially the solidification, when operating under different pouring temperatures,

iii) to analyze the effects of the size and number of runners and discuss possible solutions to reduce the cavity defects.

It should be noted that a CFD program named FLOW CAST v5.03 was used to capture the filling, solidification, and cooling sequences. Therefore, the time for each stage will be included in additional discussions under the considered controlling conditions, from which insights may be observed. This will lead to suggestions for future improvements, especially reducing the cavity defects, reduction of production time, and increase in quality.

FLUID FLOW EQUATIONS AND VOLUME TRACKING METHOD

Fluid Flow Equations

To perform the casting simulation, FLOW 3D CAST will be used as it is a program that calculates based on the Fractional Area/Volume Obstacle Representation (FAVOR) method, which is based on the finite difference for the generated mesh. This technique may improve the accuracy of the numerical solution near the mould walls when compared to the standard finite difference. For an incompressible, viscous fluid study, FAVOR equations are formulated using the flowing equations:

$$\nabla \cdot (\boldsymbol{Au}) = \mathbf{0} \tag{1}$$

$$\frac{\partial \boldsymbol{u}}{\partial t} + \frac{1}{V}(\boldsymbol{Au} \cdot \nabla)\boldsymbol{u} = -\frac{1}{\rho}\nabla \boldsymbol{p} + \frac{1}{\rho V}(\nabla \boldsymbol{A}) \cdot (\boldsymbol{\mu}\nabla)\boldsymbol{u} + \boldsymbol{g} \tag{2}$$

$$\frac{\partial \boldsymbol{H}}{\partial t} + \frac{1}{V}(\boldsymbol{Au} \cdot \nabla)\boldsymbol{H} = \frac{1}{\rho V}(\nabla \boldsymbol{A}) \cdot (\boldsymbol{k}\nabla \boldsymbol{T}) \tag{3}$$

where

$$\boldsymbol{Au} = \left(\boldsymbol{A_x u_x}, \boldsymbol{A_y u_y}, \boldsymbol{A_z u_z}\right)$$

$$(\nabla \boldsymbol{A}) = \left(\frac{\partial}{\partial \boldsymbol{x}}\boldsymbol{A_x}, \frac{\partial}{\partial \boldsymbol{y}}\boldsymbol{A_y}, \frac{\partial}{\partial \boldsymbol{z}}\boldsymbol{A_z}\right)$$

$$\boldsymbol{H} = \int \boldsymbol{C}(\boldsymbol{T})\boldsymbol{dT} + \boldsymbol{L}(\mathbf{1} - \boldsymbol{f_s}) \tag{4}$$

Where A_i is the open area fraction associated with the flow in the i^{th} direction. *V, ρ, and p* are the open volume fraction, density, pressure. Where u_i is velocity component and μ is the fluid viscosity coefficient. *g* gravity, *H* fluid enthalpy, *T* fluid temperature, f_s solid fraction, *L* latent heat. *C* and *k* are the fluid-specific heat and thermal conductivity coefficient, respectively.

With regard to the temperature focus, the energy equation and form are as follows:

$$\frac{\partial \boldsymbol{T_m}}{\partial t} = \frac{1}{\rho \boldsymbol{C_m} \boldsymbol{V_c}}(\nabla \boldsymbol{A_c}) \cdot (\boldsymbol{k_m}\nabla \boldsymbol{T_m}) \tag{5}$$

where *m* indicates the parameter related to the mould and *c* indicates quantities that are complements of the volume and area fractions. At the metal/mould interface, the heat flux, *q*, is calculated by

$$\boldsymbol{q} = \boldsymbol{h}(\boldsymbol{T} - \boldsymbol{T_m}) \tag{6}$$

where *h* is the heat transfer coefficient.

Volume of Fluid (VOF) Method

In the mould filling process, the boundaries between the molten casting metal and the surrounding air can be tracked using the tracking free surface technique. In terms of numerical development, the most popular method to describe the free surfaces and deformations are the Volume-of-Fluid (VOF) method. The equation for the VOF method is represented as the *F* function, which is shown as follows:

$$\frac{\partial F}{\partial t} + \frac{1}{V}\nabla \cdot (AuF) = 0 \quad (7)$$

The boundary conditions on the free surface have no normal and tangential stresses so the time step must assess the accuracy and stability. As in Eq. 8, the accuracy of the results is constant when the time step is less than the minimum value of the calculated ratio. The time increment for stability is necessarily governed by two restrictions, firstly the fluid material cannot move through more than one cell in the one-time step because the different equations assume fluxes between adjacent cells only. Therefore, the time increment must satisfy the inequality below.

$$\Delta t < min\left\{\frac{\Delta x_i}{|u_{i,j}|}, \frac{\Delta y_j}{|v_{i,j}|}\right\} \quad (8)$$

where the mesh increments, Δx and Δx, u and v, velocity component, and the time increment, Δt. The minimum is calculated with respect to every cell in the mesh. Typically, Δt is equal to one-fourth to one-third of the minimum cell transit time. Secondly, where there is a non-zero value for kinematic viscosity, momentum must not be diffused by more than approximately one cell in one-time step. A linear stability analysis shows that this limitation by

$$v\Delta t < \frac{1}{2}\frac{\Delta x_i^2 \Delta y_j^2}{\Delta x_i^2 + \Delta y_j^2} \quad (9)$$

with Δ*t* satisfying the two inequalities above. The last parameter ensures numerical stability is *α*, the upstream differencing parameter. The proper choice for *α* is

$$1 \geq \alpha > \max\left\{\left|\frac{u_{i,j}\Delta t}{\Delta x_i}\right|, \left|\frac{v_{i,j}\Delta t}{\Delta y_i}\right|\right\} \quad (10)$$

Further information regarding the VOF method can be found in research from Hirt [31] and Aniszewski [32].

DESCRIPTION OF THE NUMERICAL STUDY

The plumbing component is used to simulate the study and it was created in the stereolithography (STL) format and imported into the FLOW 3D CAST software. The model's multi-block meshes are shown in Fig. 3, and the thermo-physical properties of the cast iron and sand mould are shown in Table 1. The surface roughness of the mould was 25 μm, and the contact angle was 180◦. The volume flow rate at the sprue was 0.0016 m^3/s, which was calculated using the total weight of the molten metal and the filling time.

RESULTS AND DISCUSSIONS

Mesh Independence Study

To minimize the calculation time, a mesh independence study was performed. In this study, the average temperature at the completion of the filling stage was derived from a comparison of different meshes. Fig. 3 shows how the multi-blocks are applied for the mesh of the plumbing component. The mesh was the smallest available size in the plumbing block (denoted by the blue box).

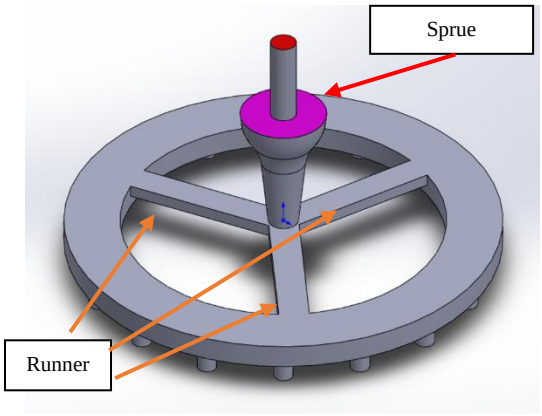

Fig. 2 A 3D Model of the Plumbing Component where the Red Area is the Cast Iron Input Boundary, and the Pink Area is the Environment Boundary.

Four different meshes (3,600,000, 1,500,000, 250,000 and 20,000 elements) were tested and their average molten cast iron temperature compared (shown in Table 2).

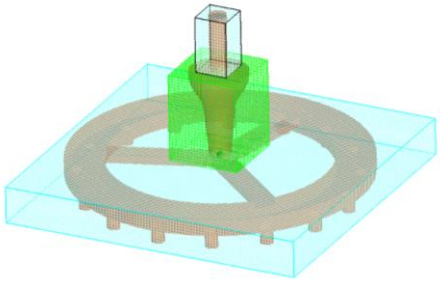

Fig. 3 The Multi-Block Meshes of the Plumbing Component (the Mould Mesh is Not Displayed).

Table 1 Thermo-Physical Properties of the Casting & Mould used in the simulations

Material	Property	Symbol	Value	Unit
Casting	Thermal Conductivity of the Liquid	k_l	39.59	W/(mK)
	Thermal Conductivity of the Solid	k_s	34.39	W/(mK)
	Specific Heat of the Liquid	C_l	897	J/(kg K)
	Specific Heat of the Solid	C_s	770	J/(kg K)
	Surface Tension Coefficient of the Liquid	σ	1.871	kg/s^2
	Kinematic Viscosity	μ	0.004516* 0.0045* 0.00448539*	m^2/s
	Density of the Liquid	ρ_l	6856	kg/m^3
	Density of the Solid	ρ_s	7100	kg/m^3
	Latent Heat	L	216	kJ/m^3
	Liquidus Temperature	T_l	1230.5	deg-C
	Solidus Temperature	T_s	1146.5	deg-C
Sand Mould	Thermal Conductivity	k_m	0.61	W/(mK)
	Volumetric Specific Heat	ρC	1700	kJ/(kg K)

* Note: Three viscosities are for Molten Cast Iron at 1329, 1429 and 1529 deg-C Respectively.

The pouring temperature was 1429 deg-C (which is relevant to the real operation), and after the liquid was poured, the average temperature was reduced to a certain value due to the heat transfer to the mould. As shown in Table 1, the average temperature created by the three different meshes are different, with the maximum approximately 0.5%. Therefore, the smallest mesh size (250,000) was introduced for further study as the plumbing part component is small so the average temperature will not have much variance.

Table 2 The Percentage Difference of the Average Temperature at the End of the Filling Stage of Different Mesh Sizes

Mesh	Average temperature on finish time (deg-C)	Error (%)
250,000	1401.49	0.447
1,500,000	1395.22	0.037
3,600,000	1394.70	-

Simulation of Plumbing Part

The filling of the molten liquid in the mould at different time are shown in Fig. 4. The cast iron melt at 1429 deg-C enters the mould at the poring cup and keep filling up the plumbing part. Fig. 4a show the filling at 1s, at this time only a small volume of the liquid gets into the plumbing region. From Fig. 4b and 4c show the melt entering to the mould cavity and then completed filling the cavity about 9s. Afterward, the liquid keeps running back to runner and completely fills the mould and ending at 10.861s (see (Fig. 4d). It should be noted that in this simulation the fill fraction criteria for stopping the calculation was set at 0.999. At the finishing time of filling process, the lowest temperature in the mould was lower than the pouring temperature about 35 deg-C.

Fig. 5. shows the solidification stage of the plumbing part, after the filling period. This process is very important because if having the entrapped air in the mould it could lead to the defect occurrence. From the figure, the melt solidification is started from bottom part, to the runner and the pouring area. As shown in Fig. 5a., reaching of 0.6 solid fraction, it takes about 324s. The solidification reaches 0.9 of the solid fractions when the time is 529s, at this time, just only the basin region is not completely solidified (see Fig. 5b). In Fig. 5c, it shows the time consumed and the solidified volume fraction. According to the graph, the solidified process slowly increases from 0 to 0.05 the beginning (0-100s) and rapidly increased from 0.05 to 0.9 (100s-500s). After that, there has a slightly increase until get 0.999 of the solid fractions (~840s or ~ 14 mins).

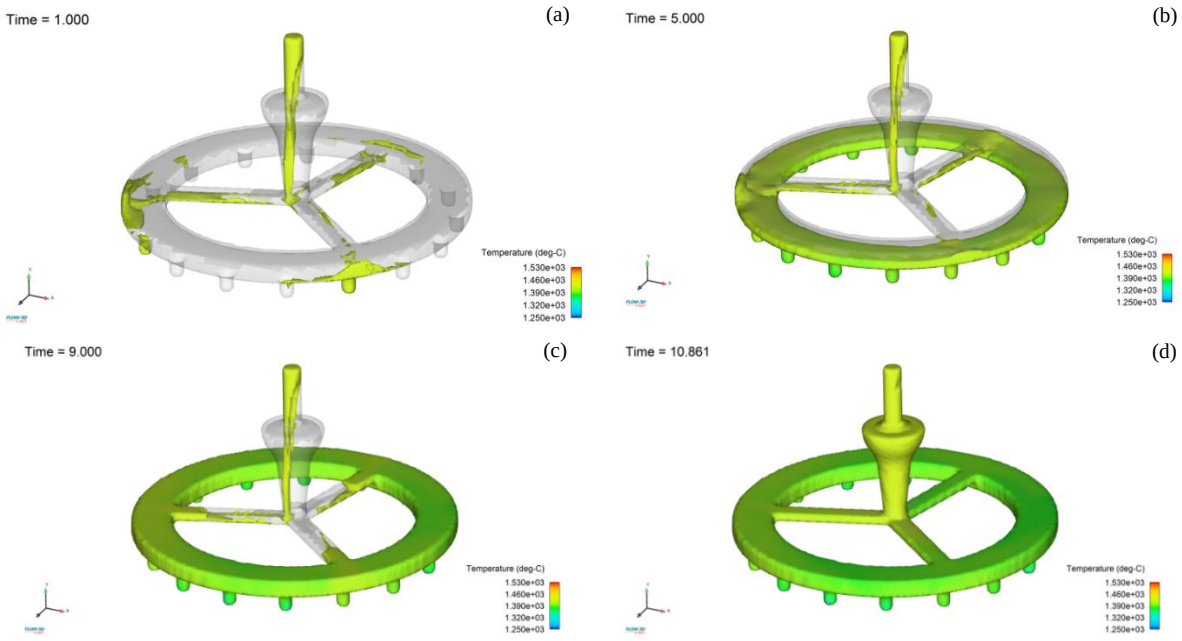

Fig. 4 The Filling for the Plumbing Component at Different Times: (a) 1sec, (b) 5sec, (c) 9sec, and (d) 10.861sec.

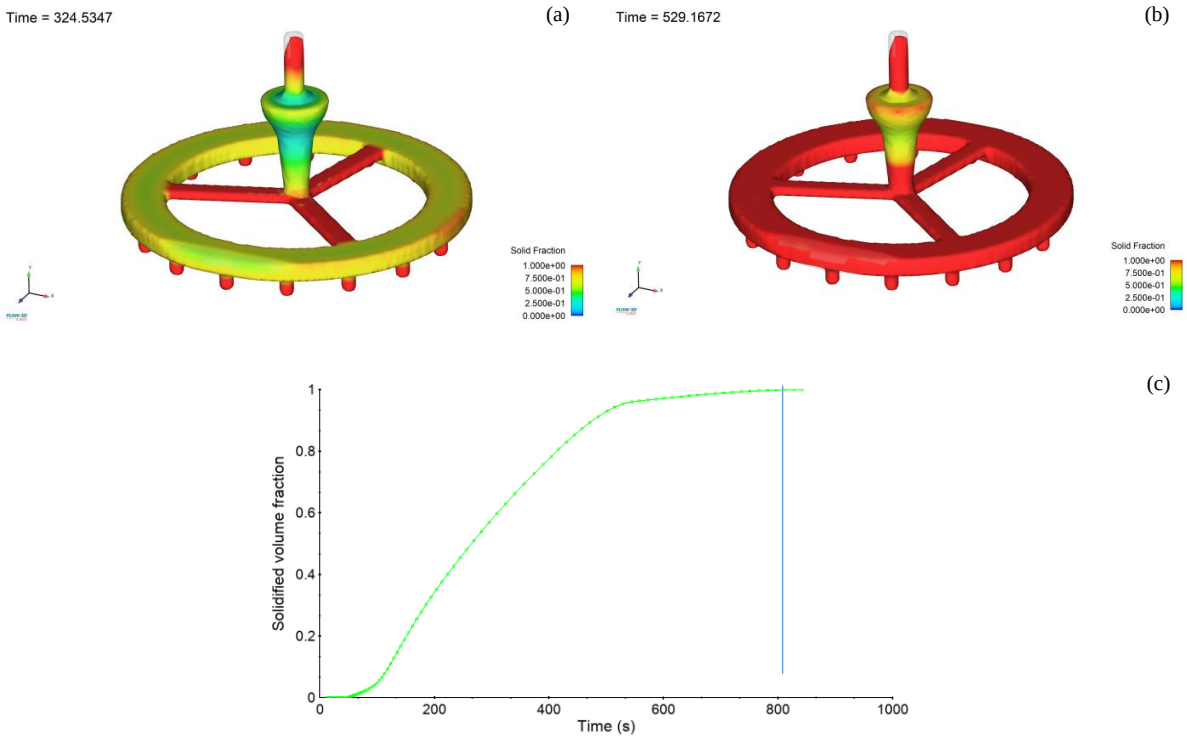

Fig. 5 The Solidification of the Plumbing Component at (a) 0.6 and (b) 0.9 Solid Fraction. The Graph Shows the Solidified Volume Fraction Through the Solidification Process

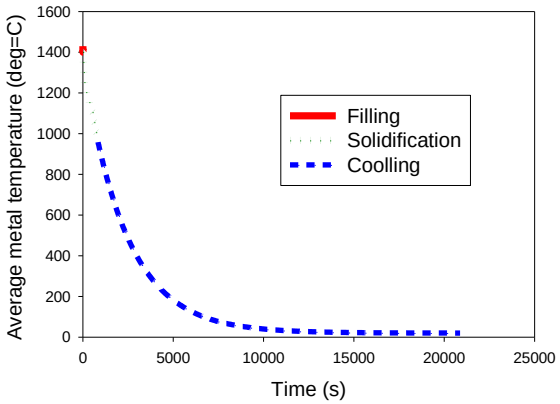

Fig. 6 Average Temperature Occurrence During the Filling, Solidification, & Cooling Stages (pouring 1429 deg-C).

Fig. 5 illustrates the average temperature and time consumed for the filling, solidification, and cooling stages. According to simulation results, the filling required 11 seconds, and the average temperature was reduced from 1429 °C to be approximately 1395 °C. During the solidification stage, 14 minutes (840 secs) were required. The solidification process was halted when the whole domain had 0.999 of the solid fractions, when the average temperature was found at 962 °C. The cooling stage was longer than the other stages at more than five and a half hours before it reached ambient temperature.

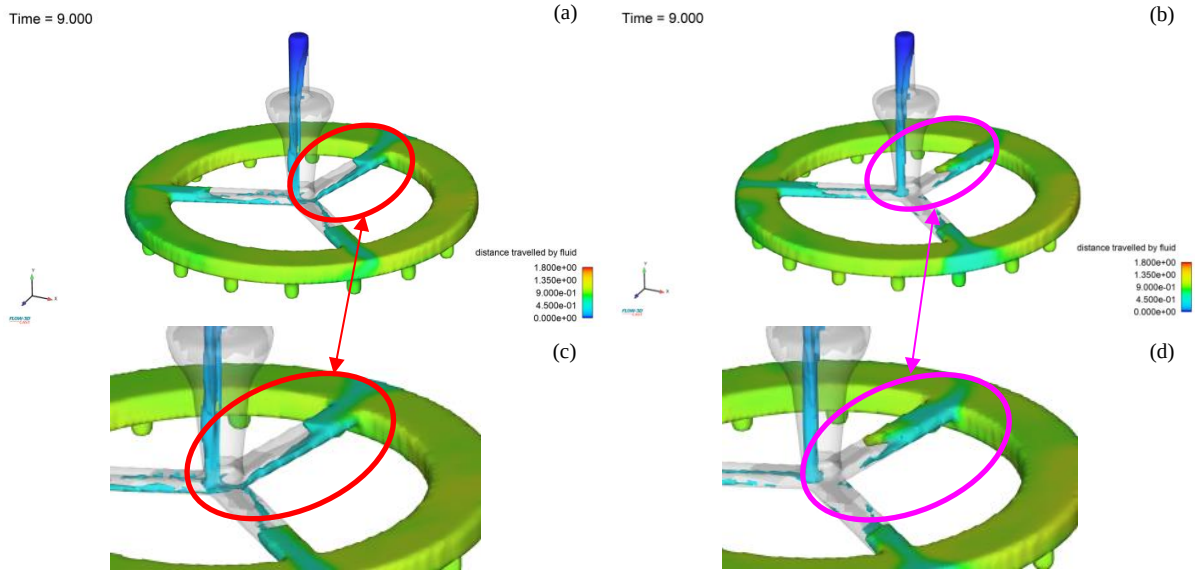

Fig. 7 Contour of Distance Traveled by the Molten Metal on 9s at (a) 1329 deg-C, (b) 1529 deg-C of the pouring temperature, (c) an up-close view of 1329 deg-C, and (d) an up-close view of 1529 deg-C

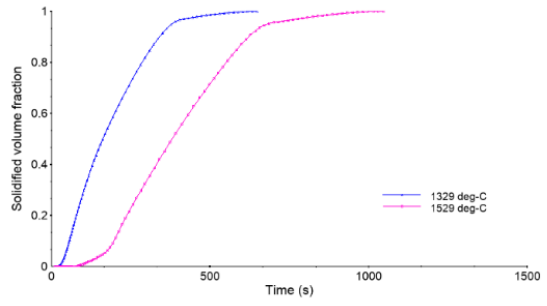

Fig. 8 Comparison of the Solidified Volume Fraction of Each Pouring Temperature Through the Solidification Process

The Influence of the Pouring Temperature

Due to a requirement to study the influence of the pouring temperature, thus, in this simulation two different cases having the temperature at 1329 deg-C and 1529 deg-C were investigated. Fig.7 shows the distance traveled by the fluid at the pouring time at 9 s. From the figures, it can be noticed the position of melted cast iron at 1529 deg-C flows faster than 1329 deg-C as confirmed by Fig. 7c and 7d. This could be because the higher pouring temperature has lower viscosity, hence the melt can flow faster.

In this study, the solidification of melt cast iron on 1329 deg-C and 1529 deg-C were also compared and discussed about the time consuming.

Table 3 The Solidification of the Plumbing Component at 0.6 and 0.9 Solid Fraction at 1329 deg-C and 1529 deg-C.

Solid Fraction	Molten Cast Iron Input Temperature (deg-C)	
	1329	1529
0.6	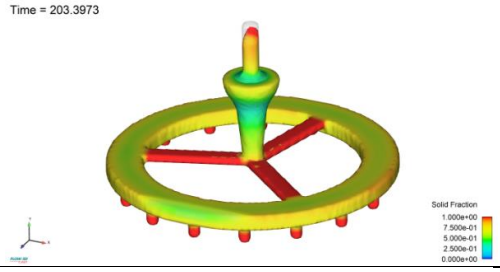	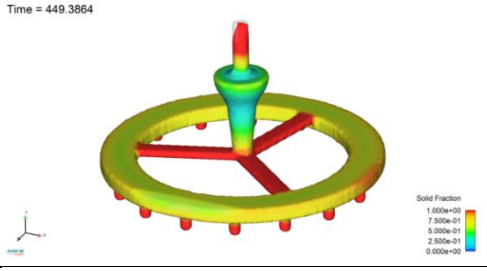
0.9	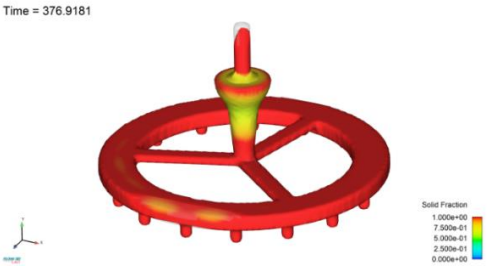	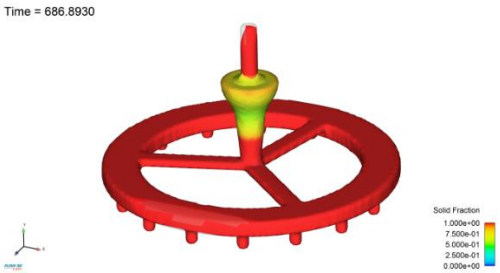

Table 3 shows the results at 0.6 and 0.9 of the solid fractions for the different pouring temperatures. The time consumed for each case to reach 0.6 of the solid fractions are approximately 200 seconds and 450 seconds respectively. For the case of reaching 0.9 of the solid fractions, the time required for the different pouring temperatures is approximately 376 seconds and 687 seconds at 1329 deg-C respectively. In general, the first solidified volume was found at the lowest point of the plumbing component, at the runner, and at the last area to solidify, as shown in Table 3. The solidification graph (Fig. 8) shows that the solidification of the two different pouring temperatures were similar. at the beginning of the period, but the higher temperature case had slower growth compared to the case of having lower pouring temperature. This can affect the quality of the final workpieces, but further study is required to confirm this prediction.

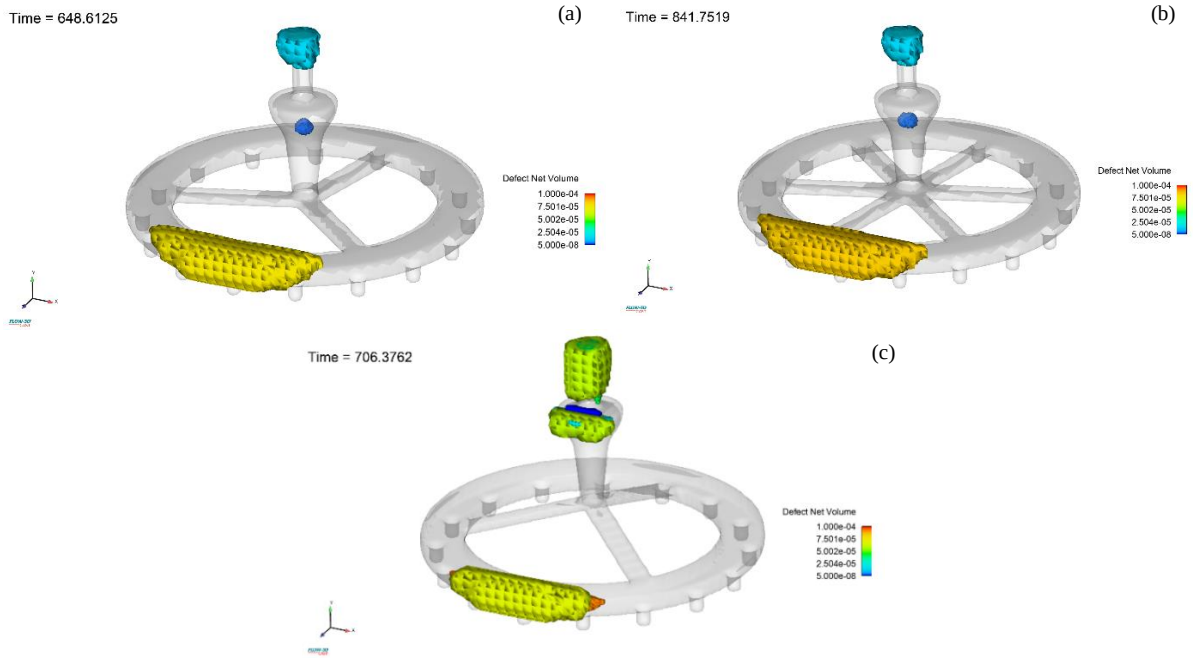

Fig. 9 Defect net volume on 1329 deg-C of the case (a) 3 branches, (b) 6 branches and (c) 15-degree inclined

Influence of the Runner Structure

The cavity found in the plumbing component was removed. Other possible defects occurred, and modifications to the runner were attempted. Three different angles were investigated, and the pouring temperature of the molten cast iron was 1329 deg-C. More details of the modified runners can be seen in Fig.9.

After the solidification was completed, the defect net volume (the volume of void) in the mould and its position were identifiable. It was found the defect location was the same in all cases, and the defect net volume was also similar, at approximately $1.0x10^{-4}$ (see Fig. 9). Therefore, the new modifications to the runner did not reduce the cavity defects in the plumbing component, possibly because of having no the riser. Further investigation regarding the runner modifications study will be conducted in future work.

CONCLUSIONS AND RECOMMENDATIONS

The simulation of casting molten iron in the plumbing component was successfully performed using the Computational Fluid Dynamics (CFD) technique. The parameters affecting the quality of casting related to the cavity defect were investigated. Overall, the conclusions are:

i) At the temperature of 1429 deg-C, the filling time required is 11 seconds, the solidification stage required 14 minutes, and the cooling time was around five and half hours.

ii) At different pouring temperatures (1329 and 1529 deg-C), the distance was travelled faster by molten cast iron with a higher temperature as it was less viscous. When comparing the solidification behavior, the time required to become solid for the case having a higher pouring temperature (1529 deg-C) was required nearly double the lower temperature.

iii) Applying three different types of runner has no effect in terms of reducing the number of defects at the present work.

In future work, the experiment of pouring temperature will be conducted, an experimental study regarding the production of plumbing components will be compared with simulation results. The parameters affecting the reasons behind the cavity defect will be discussed and a lower cost of production sought.

ACKNOWLEDGMENTS

This research was supported by the Mechanical Engineering Department, Faculty of Engineering, Mahidol University.

Thanks to CADFEM SEA Pte. Ltd. - A Certified Elite Channel Partner to ANSYS - for providing support and access to the CFD program named ANSYS Fluent 2021 R1.

Moreover, authors would like to thank Chaipong Engineering Co., Ltd. for allowing to use the facilities.

Thanks to Robert McEvoy, from the Faculty of ICT at Mahidol University for editing and proofreading the manuscript.

REFERENCES

[1] Dev, V.B., K.V. Ponomareva, O.G. Prikhodko, and S.V. Smetanyuk, *Influence of Temperatures of Melt Overheating and Pouring on the Quality of Aluminum Alloy Lost Foam Castings.* Russian Journal Of Non-Ferrous Metals, 2017. 58(4): P. 373-377.

[2] Ayar, M.S., V.S. Ayar, and P.M. George, *Simulation and Experimental Validation for Defect Reduction in Geometry Varied Aluminium Plates Casted using Sand Casting.* Materials Today: Proceedings, 2020. 27: P. 1422-1430.

[3] Borikar, G.P. and S.T. Chavan, *Optimization of Casting Yield in Multi-Cavity Sand Moulds of Al-Alloy Components.* Materials Today: Proceedings, 2020. 28: P. 819-824.

[4] Zhao, H.-D., Y.-F. Bai, X.-X. Ouyang, and P.-Y. Dong, *Simulation of Mold Filling and Prediction of Gas Entrapment on Practical High Pressure Die Castings.* Transactions of Nonferrous Metals Society of China, 2010. 20(11): P. 2064-2070.

[5] Li, Y., J. Liu, G. Zhong, W. Huang, and R. Zou, *Analysis of a Diesel Engine Cylinder Head Failure Caused by Casting Porosity Defects.* Engineering Failure Analysis, 2021. 127.

[6] Dou, K., E. Lordan, Y. Zhang, A. Jacot, and Z. Fan, *A Novel Approach to Optimize Mechanical Properties for Aluminium Alloy in High Pressure Die Casting (HPDC) Process Combining Experiment and Modelling.* Journal of Materials Processing Technology, 2021. 296.

[7] Pulisheru, K.S. and A.K. Birru, *Effect of Pouring Temperature on Hot Tearing Susceptibility of Al-Cu Cast Alloy: Casting Simulation.* Materials Today: Proceedings, 2021.

[8] Pulivarti, S.R. and A.K. Birru, *Effect of Mould Coatings and Pouring Temperature on the Fluidity of Different Thin Cross-Sections of A206 Alloy by Sand Casting*. Transactions of the Indian Institute Of Metals, 2018. 71(7): P. 1735-1745.

[9] Li, Y., J. Liu, Q. Zhang, and W. Huang, *Casting Defects and Microstructure Distribution Characteristics of Aluminum Alloy Cylinder Head with Complex Structure.* Materials Today Communications, 2021. 27.

[10] Sarkar, C., S.H. Gawande, and A.A. Keste, *Design Optimization of Precision Casting for Residual Stress Reduction.* Journal of Computational Design and Engineering, 2016. 3(2): P. 140-150.

[11] Gopalan, R. and N.K. Prabhu, *Oxide Bifilms in Aluminium Alloy Castings – A Review.* Materials Science and Technology, 2013. 27(12): P. 1757-1769.

[12] Luo, L., H.-Y. Xia, L.-S. Luo, Y.-Q. Su, C.-J. Cai, L. Wang, J.-J. Guo, and H.-Z. Fu, *Eliminating Shrinkage Defects and Improving Mechanical Performance of Large Thin-Walled ZL205A Alloy Castings by Coupling Ravelling Magnetic Fields with Sequential Solidification.* Transactions of Nonferrous Metals Society of China, 2021. 31(4): P. 865-877.

[13] Nandagopal, M., K. Sivakumar, and M. Sengottuvelan, *Process Parameter Optimization to Reduce Cold Metal Defect in Ferrous Casting Using Taguchi Technique and Regression Analysis.* Materials Today: Proceedings, 2021. 45: P. 7917-7921.

[14] Yang, W., Z. Luo, Z. Zou, C. Zhao, and Y. You, *Modelling and Analysis of Bubble Entrapment by Solidification Shell in Steel Continuous Casting Considering Bubble Interaction with a Coupled CFD-DBM Approach.* Powder Technology, 2021. 390: P. 387-400.

[15] Wei Loon, L., S. Sreekar Reddy, and P.R. A.K, *CFD Simulation of Direct Chill Casting Process of Magnesium Alloy Billets.* Journal of Manufacturing Processes, 2019. 45: P. 447-454.

[16] YIN, J., *Numerical Modelling of Centrifugal Casting Process*. 2016, KTH ROYAL INSTITUTE OF TECHNOLOGY.

[17] Reikher, A., *Numerical Analysis of Die-Casting Process in Thin Cavities Using Lubrication Approximation*. 2012, University of Wisconsin-Milwaukee.

[18] Yuwen, X.-X., L. Chen, and Y.-J. Han, *Numerical Simulation of Casting Filling Process Based on FLUENT.* Energy Procedia, 2012. 17: P. 1864-1871.

[19] Kermanpur, A., S. Mahmoudi, and A. Hajipour, *Numerical Simulation of Metal Flow and Solidification in the Multi-Cavity Casting Moulds of Automotive Components.* Journal of Materials Processing Technology, 2008. 206(1-3): P. 62-68.

[20] Vijayaram, T.R., S. Sulaiman, A.M.S. Hamouda, and M.H.M. Ahmad, *Numerical Simulation of Casting Solidification in Permanent Metallic Molds.* Journal of Materials Processing Technology, 2006. 178(1-3): P. 29-33.

[21] Reikher, A. and K.M. Pillai, *A Fast Simulation of Transient Metal Flow and Solidification in a Narrow Channel. Part I: Model Development Using Lubrication Approximation.* International Journal of Heat and Mass Transfer, 2013. 60: P. 797-805.

[22] Reikher, A. and K.M. Pillai, *A Fast Simulation of Transient Metal Flow and Solidification in a Narrow Channel. Part II. Model Validation and Parametric Study.* International Journal of Heat and Mass Transfer, 2013. 60: P. 806-815.

[23] Wang, H., G. Djambazov, K.A. Pericleous, R.A. Harding, and M. Wickins, *Modelling The Dynamics of The Tilt-Casting Process and the Effect of the Mould Design on the Casting Quality.* Computers & Fluids, 2011. 42(1): P. 92-101.

[24] Aravind, S., P. Ragupathi, and G. Vignesh, *Numerical and Experimental Approach to Eliminate Defects in Al Alloy Pump- Crank Case Processed Through Gravity Die Casting Route.* Materials Today: Proceedings, 2021. 37: P. 1772-1777.

[25] Barot, R.P. and V.S. Ayar, *Casting Simulation and Defect Identification of Geometry Varied Plates with Experimental Validation.* Materials Today: Proceedings, 2020. 26: P. 2754-2762.

[26] Promtong, M., C. Kasemjirapatara, P. Srithep, Y. Masoodi, S. Namchanthra, J. Priyadumkol, and C. Suvanjumrat, *Investigation of Aerodynamic Performance of Four Potential Airfoils for a Formula SAE Car: A 2D Validation Study,* in *the 34th Conference of the Mechanical Engineering Network of Thailand*. 2020: 15 - 17 July 2020, Prachuap Khiri Khan, Thailand.

[27] Promtong, M., K. Khunsri, K. Teachapanitvittaya, T. Trakulkumlue, S. Watechagit, and C. Suvanjumrat, *Experimental and Numerical Investigations into the Natural Convection of Hot Gas in a Vertical Smoking Oven: A Validation Study*, in *the 34th Conference of the Mechanical Engineering Network of Thailand*. 2020: 15 - 17 July 2020, Prachuap Khiri Khan, Thailand.

[28] Promtong, M., S. Cheung, G. Yeoh, S. Vahaji, and J. Tu, *CFD Investigation ff Sub-Cooled Boiling Flow using a Mechanistic Wall Heat Partitioning Approach with Wet-Steam Properties.* The Journal of Computational Multiphase Flows, 2018. 10(4): P. 239-258.

[29] Promtong, M., S. Cheung, and J. Tu, *Numerical Modelling of Subcooled Boiling Flow Based on Mechanistic Approach: A Validation Study Using Wet Steam (IAPWS) as Working Fluid Properties.* Lecture Notes in Engineering and Computer Science, 2016.

[30] Promtong, M. and P. Tekasakul, *CFD Study of Flow in Natural Rubber Smoking-Room: I. Validation with the Present Smoking-Room.* Applied Thermal Engineering, 2007. 27(11-12): P. 2113-2121.

[31] Hirt, C.W. And B.D. Nichols, *Volume of Fluid (VOF) Method for the Dynamics of Free Boundaries.* Journal of Computational Physics, 1981. 39(1): P. 201-225.

[32] Aniszewski, W., T. Ménard, and M. Marek, *Volume of Fluid (VOF) Type Advection Methods in Two-Phase Flow: A Comparative Study.* Computers & Fluids, 2014. 97: P. 52-73.

[33] J. Campbell, Castings (2nd ed.), Butterworth-Heinemann Ltd., Oxford (2003)

11th Int. Conf. on Geotechnique, Construction Materials & Environment,
Kyoto, Japan, 3-5 November 2021, ISBN: 978-4-909106063 C3051

MOTORCYCLE ACCIDENT MODEL BASED ON MOTORCYCLIST CHARACTERISTICS FOR DESIGN THE DEDICATED LANE

Sobri Abusini[1] and Lasmini Ambarwati[2]

[1]Faculty of Natural Science, Brawijaya University, Malang, East Java; [2]Faculty of Engineering, Brawijaya University, Malang, East Java, Indonesia

ABSTRACT

A motorcycle is the most popular transport mode and requires a relatively inexpensive cost for traveling within the city. The growth of the transport mode is quite high and 87% of the total vehicles overburden a large part of the highway network in Malang District, as the study case area. As a consequence, more than 70% of accident victims are motorcyclists. An accident prediction model based on motorcyclist characteristics is required in the effort to minimize the occurrence of accidents. The model is expected to predict the causalities of motorcyclists and to design dedicated lane requirements. This research aims to identify motorcyclist characteristics, to develop an accident model, and to plan the best solution in reducing motorcycle accidents. Motorcyclist characteristics were identified from questionnaires. Most respondents (±70%) had collided with other motorcycles or other vehicles with socio-economic background, i.e., male, only having motorcycle as a transport mode, traveling with a travel time of average a half-hour and once in a day, rarely carrying heavy luggage, as well often passing another vehicle from the right side. The results are found out that the motorcycle accident probability is influenced by several characteristics, i.e. age, amount of luggage, and motorcyclist knowledge. A dedicated lane for motorcycles should be prepared with a clearance distance with other vehicles of more than 2.18 m. The government should facilitate the dedicated lane standard taking into account clearance distance for safe travel.

Keywords: Accident model, Accident victims, Dedicated lane, Motorcyclist characteristics, Motorcycle interactions.

INTRODUCTION

Traffic volume in urban areas increases every year. This can be seen from increasing the density of road traffic. The increase in traffic density has an impact on raising the traffic accidents on the highway.

In Indonesia, the population of motorized vehicles in 2018 was around 141,428.052 units, 81.58% of which were motorcycles. The risk factor with the involvement of motorcycles in traffic accidents is increasing due to minimum motorcycle infrastructure and an increase in the number of motorcycles. In 2018, there were 196,457 accidents or 73.49% of traffic accidents involving motorcyclist as a victim.

According to [1], the number of vehicles increases every year, from 2012 the number of vehicles was only 196,000, while the number of vehicles had reached 779,000 in 2016 or increased almost 4 times in less than 5 years. Of these vehicles, the number of motorcycles dominates approximately 680,000 units or 87% of the total vehicles in Malang District. Based on 2016-2019 data, several black spots are Geneng Kepanjen, Sudirman/ Mojosari Kepanjen, Hayam Wuruk Gondanglegi, Raya Bululawang, Sultan Agung Kepanjen, Brigjen Abdul Manan Pujon, Mojorejo, Panglima Sudirman Batu, Raya Areng-areng and Patimura Batu Streets as the research locations.

The increase in the number of vehicles in Malang District is also followed by rising in the number of accidents. There was the largest increase in the number of accidents that occurred in 2016 with an increasing 232 incidents from 542 to 774. Based on the number of victims, the number of deaths and minor injuries also experienced a significant increase from 2015 to 2016 The number of victims who died was 219 persons and 1,031 persons suffered minor injuries.

A motorcycle is a two-wheeled motorized vehicle that is designed in such a way for the easiest and cheapest transport mode for mobility among other motorized vehicles [2]. Motorcycles with slim two-wheeled vehicles are considered to have high flexibility for the rider. On the other hand, motorcycles have a greater risk of an accident compared to four-wheeled vehicles because motorcycles are more prone to slipping or falling. Motorcycle riders are relatively in danger of being victims of traffic accidents [3]-[4].

Motorcyclist characteristics have greatly an impact on traffic accidents such as the age group of 26-59 years being the highest victim in traffic accidents [5]. A driving offense committed by motorcyclists is one factor in accidents. . Higher age groups have better levels of discipline [6]. The level of education and knowledge also affects the discipline of motorcyclists when driving. Driving knowledge are about good driving methods such as knowledge of human-vehicle-environment interaction, developing driving skills, and positively influencing driver behavior [7]. Driving experience also influences driver behavior. An experience in driving directs the extent to which the driver's ability to control his vehicle both under normal conditions and in sudden conditions that require a quick response [6]. Furthermore, This study underlies research on motorcyclists' behavior and their interactions with other vehicles.

A motorcycle accident for highland areas is influenced by geometry and traffic flow, therefore, the efforts to reduce the number of accidents should be considered with improving these factors [8]. Motorcyclists tend to ride motorcycles at higher speeds on roads with dedicated motorcycle lanes than on roads without this lane [9]. Setting and formulation of motorcycle accident models are required to predict accidents and to reduce the risk of accidents that occur [10]. In India, motorcycle accidents are increasing every day. Therefore, it is needed to identify factors causing the accident through further research analysis on the prevention of motorcycle accidents [11].

There are not many studies that understand the reduction in motorcycle accidents from the motorcyclists' behavior on roads with the requirement of dedicated motorcycle lanes. To achieve this goal, it is necessary to research motorcyclist characteristics and behavior as the basis for determining motorcycle lanes. Understanding motorcyclists' characteristics and behavior aim to reduce the number of accidents and to improve the safety of motorcyclists.

Attention to assess the factors related to motorcyclist characteristics and behavior, to develop motorcycle accidents, to design dedicated motorcycle lanes that aim to reduce motorcycle accidents as a victim. This research aims to identify motorcyclist characteristics, to develop an accident model, and to plan the best solution in reducing motorcycle accidents.

The outline of the paper is: research framework is elaborated in ‘‘Methods” section consisting of background information on the existing condition of the motorcycle accident, motorcyclist characteristics and behavior, the road accident on the certain roads as the research locations, design of dedicated lane for motorcycle. The ‘‘Results” section explains the analysis of motorcyclist characteristics and behavior as a victim, and setting up motorcycle accident models. Section ‘‘Conclusions and recommendations” presents conclusions and recommendations for further research.

METHODS

The research area is in Malang District where the city surrounding Malang Municipality in East Java Province, Indonesia. The locations of the survey are adjusted to the location of the motorcycle accident as “Black Spot”. The locations were chosen due to the high motorcycle accident rate. Traffic accident data was supported by the Malang Police Department in 2016 – 2019.

Collecting Data

The research survey was conducted by distributing questionnaires to respondents randomly on ten roads which are “Black Spots". The samples have amounted to 150 respondents who had experienced in traffic accidents or as a victim. The contents of the questionnaire include general characteristics of respondents (social-economic background), travel characteristics, and riding behavior.

Data Analysis

a. Descriptive analysis is an analysis that describes the situation or event that is only limited to describing the facts.
b. An accident model by applying the logistic regression method was developed to determine the accident probability involving motorcycle riders through the motorcyclist characteristics, travel, and behavior characteristics of motorcyclists.

The logit model is based on the formation of the cumulative logistic probability function as follows:

$$Pi = F(\beta o + \beta_1 X_{1i}) = \frac{1}{1+e^{-z}} = \frac{1}{1+e^{-(\beta o+\beta 1 X 1 i)}} \quad (1)$$

$$P_{(MCA)} = \frac{1}{1+e^{-(\beta o+\beta 1 X 1+\beta 0+\beta 2 X 2+\beta 0+\beta 3 X 3+\cdots)}} \quad (2)$$

which :
$P_{(MCA)}$ = Probability of motorcycle accident
e = natural number (2.71828)
X = explanatory variable

As seen in Fig.1, steps for developing model aims to identify a relationship between the number

of a motorcycle accident (response variable) and motorcyclist characteristic also behavior variables (explanatory variables). This study will determine a model between a response variable and explanatory variables on areas surrounding ten road sections in the city of Malang identified as black spots (the high number of motorcycle accidents). Those explanatory variables can forecast the number of motorcycle accidents for the future years. The analysis is done by using the number of motorcycle accidents (*MCA)* as the dependent variables or response variables.

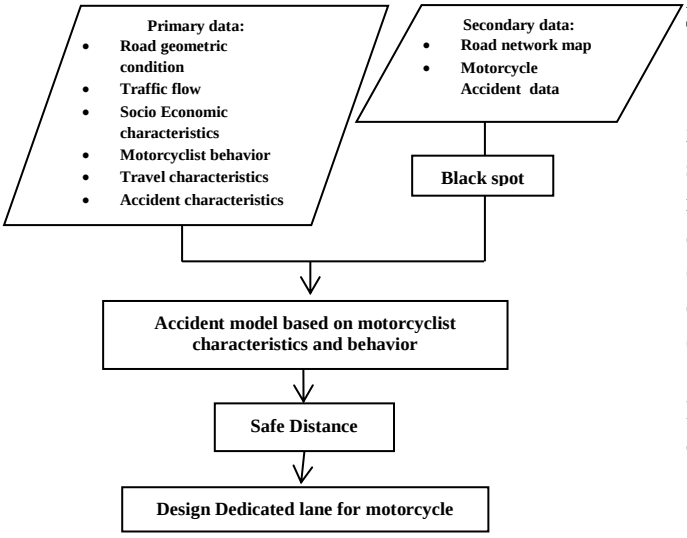

Fig. 1 The research framework

The statistical tests are explained as follow:

a. Correlation Test, the correlation coefficients are more than 0.05 then H_0 is rejected, H_1 is accepted or vice versa, which is H_0: Simultaneous independent variables have no effect on the probability of an accident, and H_1: The independent variable simultaneously affects the probability of an accident
b. Model Significance Test, a significance test of the model is defined from the results of simultaneous testing on the effect of the explanatory variables.
c. Regression Model Feasibility Test, a significance value is more than 0.05 then H_0 is accepted, H_1 is rejected or vice versa. H_0: The model used is feasible, H_1: The model used is not feasible
d. Chi-Square Test (X^2), the chi-square count should more than chi-square table, then these attributes are related to the probability of an accident or vice versa.
e. Coefficient of Determination Test. The basis for decision-making for this test is based on the statistical value of -2log-likelihood and Negelkerke R Square.
f. Formulating the model.
   After the F test and t-test, the model is formulated from all explanatory variables and a response variable (dependent variable) as the proposed model in Eq. (2).
   Factors that cause accidents should be predicted

RESULTS AND DISCUSSIONS

Motorcyclist Characteristics and Behavior, Travel characteristics

Motorcyclist characteristics are important factors in planning and design for motorcycle infrastructure such as exclusive motorcycle lanes to minimize the number of motorcycle accidents. Motorcycle characteristics are defined as explanatory variables (X1-X71) which experience in the accident with other vehicles involving motorcyclists as the victim (Y), as explained in Table 1.

The characteristics of motorcyclists in the Malang District are as follows:

a. Most of the respondents who ride a motorcycle are aged 15-25 years (58%), and most of them are male. Most of the respondents are graduated from senior high school (55%), as private employees (40%).
b. Travel Characteristics. In general, motorcyclists travel for working with frequency in every day needed average 27 minutes for traveling, so it is required good pavement condition for highway network.
c. Accident Characteristics. Fifty-six percent of respondents ever had one accident with a light injury which occurs at noon and evening. A motorcyclist has a crash with the other riders or due to their own mistake.
d. Behavior characteristics before riding. Motorcyclist always checks breaking devices, fuel, and electrical devices before riding, while they rarely check motorcycle wheel and rearview mirror.
e. Behavior characteristic during riding. Motorcyclist rarely uses a helmet, trouser, and jacket. They sometimes ride together, giving signs during overtaking and rarely using a dedicated lane for motorcycles.
f. Behavior characteristic during riding. Motorcyclist rarely uses a helmet, trouser, and jacket. They sometimes ride together, giving signs during overtaking and using a dedicated lane for motorcycles.

g. Safety knowledge. Most of the motorcyclist does not understand about the function of the dedicated lane, even though they will use the dedicated lane when the government facilitates these lanes with two lanes, designing with traffic marking, and average 2.18 meter width. The minimum and average safe distances for a motorcycle with the other vehicle are 0.75 m and 2.18 m respectively. Motorcyclists hope the government gives attention to safety infrastructures and policies for motorcycles. This distance is in line with the previous research revealed that the motorcycle interactions with the other motorcycle and car requiring critical pore space 3.12 m and 3.21 m respectively [10].

Development of Accident Model

Table 1 Significance test for explanatory variables

Explanatory variables	Notation	Significance
Socio-economic background		
Sex	X1	0.973
Income	X2	0.169
Age	X3	0.004
Education	X4	0.559
Job	X5	0.122
The age which is the first time driving	X6	0.332
Motorcycle(MC) ownership	X7	0.167
The number of MC	X8	0.301
Type of MC	X9	0.255
Family member using MC	X10	0.845
Transport cost a month	X11	0.595
Travel characteristics		
Frequency in a week	X12	0.624
Activity time	X13	0.863
Travel distance	X14	0.761
Travel time	X15	0.171
Travel propose	X16	0.268
Accompanied person	X17	0.106
Type of road	X18	0.497
Pavement condition of the road	X19	0.808
Other vehicle ownership	X20	0.735
Other vehicles used except Motorcycle (MC)	X21	0.163
Accident experience		
Frequency of accident	X22	0.999
Type of injury	X23	0.999
Cost for injury treatment	X24	0.999
Motorcycle repairing	X25	0.999
The time when the accident occurred	X26	0.999
Accident time	X27	0.999
Accident cause	X28	0.999
Other vehicle involved	X29	0.997
Motorcyclist Knowledge		
Knowledge about Motorcycle lane	X30	0.255
Requirement of motorcycle lane	X31	0.000
Willingness to use motorcycle (MC) lane	X32	0.857
Design of MC lane	X33	0.000
The number of MC lane	X34	0.000
Safe distance with other vehicles when moving	X35	0.002
Using motorcycle even though having other vehicles	X36	0.359
Checking Motorcycle equipment		
Checking rearview mirror	X37	0.999
Bell	X38	0.61
Major lamp	X39	1.000
Breaking lamp	X40	1.000
Sign lamp	X41	0.999
Speedometer	X42	0.61
Exhausted equipment	X43	0.999
Wheel	X44	0.792
Reflected light	X45	1.000
Motorcycle license	X46	0.453
Behavior before driving		
Checking the motorcycle coil and spark plug wires	X47	0.905
Checking brake condition	X48	0.83
Checking wheel condition	X49	0.653
checking the condition of motorcycle chains and gears	X50	0.856
Checking battery	X51	0.472
Checking oil	X52	0.508
Checking rearview mirror	X53	0.577
Behavior during driving		
Using helmet	X54	0.956
Using gloves	X55	0.464
Using shoes	X56	0.351
Using trousers	X57	0.876
Wearing jacket	X58	0.951
Ride with another person	X59	0.118
Riding motorcycle in a group	X60	0.111
Joking when driving	X61	0.104
Breaching traffic light	X62	0.550
Bringing heavy or big luggage	X63	0.000

Overtaking from the left side	X64	0.941
Signing when overtaking	X65	0.726
Traveling when raining	X66	0.708
Riding on motorcycle lane	X67	0.645
Motorcyclist perception to the government policy related to motorcycle safety program		
The government already consider safety program	X68	0.267
Considering other drivers	X69	0.433
Felling ignored by the other vehicle driver	X70	0.524
Requirement for a special safety program for motorcycle	X71	0.134
Ever crashing with other vehicles (experience in an accident)	Y	1.000

From Table 1, it can be concluded that the variables X3 (age) from socio-economic background is proven to be related to the experience in the accident (dependent variable). The explanatory variables from travel characteristics (X12-X21) are omitted from the model because they had a p-value of significance greater than 0.05. And all explanatory variables from accident experience (X22-X29) are omitted from the model. From motorcyclist knowledge, the variables X30 (knowledge about motorcycle lane), X32(Willingness to use MC lane), and X36 (Using a motorcycle even though having other vehicles) are omitted from the model. On the other hand, X31 (Requirement of motorcycle lane), X33 (Design of MC lane), X34(The number of MC lane), and X35 (Safe distance with other vehicles when moving) are verified on influencing to the dependent variable.

In a similar analysis, the explanatory variables from motorcycle equipment (X37-X46) are left from the model and also all variables from behavior before driving (X47-X53). Most explanatory variables from behavior during driving (X54-X67) are omitted from the model. X63 (Bringing heavy or big luggage) can be proven to influence the model. All explanatory variables from motorcyclist perception to the government policy related to the motorcycle safety program (X68-X71) are ignored from the model.

The model development is set from socio-economic characteristic (SE) is influenced by age (X3) with a positive coefficient which means that variable X3 increases the probability of an accident.

$Y_{SE} = -2.576+0.093\ X_3$, then the probability of accident due to age of motorcyclist is

$$Pi = F(\beta_o + \beta_1 X_{1i}) = \frac{1}{1+ e^{-Y}SE} = \frac{1}{1+e^{-(0-2.576+0.093\ X3)}}$$

From motorcyclist knowledge (MK), the probability of motorcycle accident is influenced by X31 (Requirement of motorcycle lane), X33 (Design of MC lane), X34(The number of MC lane), and X35 (Safe distance with other vehicles when moving). When X31, X33, X34, and X35 are analyzed together in the model, there is one variable X33 that must be deleted due to no relation to the model. Then the regression function is developed by three variables (X31, X34, and X35). The regression function is

$Y_{MK} = 3.063+4.829X_{31} - 3.28\ X_{34(1)} -3.924\ X_{34(2)} - 1.037\ X_{35}$, then the probability of accident due to variables of the requirement of motorcycle lane (X31), X33 (Design of MC lane), and X35 (Safe distance with other vehicles when moving) is

$$Pi = F(\beta_o + \beta_1 X_{1i}) = \frac{1}{1+ e^{-Y}MK} = \frac{1}{1+e^{-(3.063+4.829X31 - 3.28\ X34(1) -3.924\ X34(2) - 1.037\ X35)}}$$

From behavior during driving (BD), the probability of motorcycle accidents is influenced by X63 (Bringing heavy or big luggage). Then, the regression function is as follows

$Y_{BD} = -2.944+3.977X_{63}$, then the probability of accident is

$$Pi = F(\beta_o + \beta_1 X_{1i}) = \frac{1}{1+ e^{-Y}BD} = \frac{1}{1+e^{-(-2.944+3.977X63,)}} = \frac{1}{1+e^{\ 2.944-3.977X63,}}$$

The combination of all significant variables is set by five explanatory variables that are X3 (age), X31 (the requirement of motorcycle lane), X34(The number of MC lane), X35 (Safe distance with other vehicles when moving), and X63 (Bringing heavy or big luggage). The regression function is defined as follows:

$Y_{Comb.} = 0.662+0.008\ X_3 + 4.247X_{31} - 2.633\ X_{34(1)} - 3.489\ X_{34(2)} - 1.072\ X_{35} +2.471X_{63}$, then the probability of accident due to age of motorcyclist is

$$Pi = F(\beta_o + \beta_1 X_{1i}) = \frac{1}{1+ e^{-Y}comb.} = \frac{1}{1+e^{-(0.662+0.008\ X3 + 4.247X31 - 2.633\ X34(1) -3.489\ X34(2) - 1.072\ X35 +2.471X63)}}$$

The probability of a motorcycle rider obtain an accident P(i) is influenced by X3 (age), X31 (the requirement of motorcycle lane), X34(The number of MC lane), X35 (Safe distance with other vehicles when moving), and X63 (Bringing heavy or big luggage). From the model, the odds ratio for age is $e^{-0.008} = 0.99$, the probability of a driver having an accident is 0.99 times with adding the age of motorcyclist. Odd ratio of the requirement of motorcycle lane, $e^{-4.247} = 0.014$, the probability of facilitating motorcycle lane in an accident is 0.014 times, meaning that possibility of a motorcycle accident can increase with a small value of 0.014 by providing motorcycle lane. On the other hand, Odd ratio of the one motorcycle of $e^{-(-2.633)} = 13.9$, so the probability of the driver having an accident can be reduced by providing one motorcycle lane. Establishing two motorcycle lanes can reduce the

probability of an accident by 32.75 times. While, Odd ratio of the safe distance with other vehicles of $e^{-(-1.072)}$ = 2.92, so the probability of motorcycle accident is approximately 2.92 times with increasing clearance distance between the motorcycle and the other vehicle. The odds ratio of the carrier/loader (X63) is $e^{2.471}$ = 0.085, meaning that the driver who carries a large number of goods can increase the probability of an accident only 0,085 times.

In brief, the number of motorcycle lanes has a significant effect on reducing motorcycle accidents, and a wide distance between the motorcycle and the other vehicles also will decrease motorcycle crashing with the other vehicle.

CONCLUSIONS

The majority of motorcycle riders in Malang District have experienced an accident while riding a motorcycle by 56%. Based on socio-economic characteristics, the drivers are male (70%), aged 15-25 years (58%), high school education background (55%), and private employees (40%). Based on the travel characteristics, the most of the motorcycle riders intend to working place (78%) with an average travel time of approximately 27 minutes.

Based on behavioral characteristics, it was found that drivers always check breaking devices, fuel, and electrical devices before riding, while they rarely check motorcycle wheels. For behavior characteristics during riding, motorcyclist rarely uses a helmet, trouser, and jacket. They sometimes ride together, giving signs during overtaking and rarely using dedicated lanes for motorcycles.

The probability of accident model involving motorcycle riders is influenced by X3 (age), X31 (the requirement of motorcycle lane), X34(The number of MC lane), X35 (Safe distance with other vehicles when moving), and X63 (Bringing heavy or big luggage). The accident model involving motorcycle riders has the greatest opportunity is old riders, bringing luggage, no motorcycle lane, the narrow distance between a motorcycle or the other vehicle. The requirement of a dedicated motorcycle lane is more than 2.18 meters based on motorcyclist behavior.

This study recommends that safety campaign programs to improve the safety of motorcycle drivers in the city of Malang should be undertaken based on motorcyclist characteristics and behavior.

ACKNOWLEDGMENTS

This research has supported a grant from the Faculty of Natural Science, Brawijaya University, Malang, Indonesia. We would like to express deep thanks to the Faculty of Natural Science, Brawijaya University. We also want to thank Riski Nur Istiqomah Dinnullah, the doctoral student in the Department of Mathematics, Brawijaya University for assisting to collect and processing data.

REFERENCES

[1] Statistic Bureau of Malang City, the Figures of Malang City in 2017 (in Indonesian).

[2] Herwangi, Y., Syabri, I., & Kustiawan, I. (2015). Peran dan Pola Penggunaan Sepeda Motor Pada Masyarakat Berpendapatan Rendah di Kawasan Perkotaan Yogyakarta. Jurnal Perencanaan Wilayah dan Kota. 26(3): 166-176.

[3] Hidayati, A. & Hendrati, L.Y. (2016). Analisis Risiko Kecelakaan Lalu Lintas Berdasar Pengetahuan, Penggunaan Jalur, Dan Kecepatan Berkendara. Jurnal Berkala Epidemiologi. 4(2): 275–287.

[4] Susanto, B., Malkhamah, S., & Suparma, L.B. (2019). Risiko Kecelakaan Sepeda Motor Pada Simpang Prioritas. Jurnal Transportasi. 19(3):161-170.

[5] Ibrahim, M.M., Adi, M. S., & Suhartono. (2018). Gambaran Distribusi Kejadian Kecelakaan Lalu Lintas Pada Pengendara Sepeda Motor. Jurnal Ilmiah Permas: Jurnal Ilmiah STIKES Kendal. 8(2): 82 - 91.

[6] Lady, L., Rizqandini, L.A. & Trenggonowati, D.L. (2020). Efek Usia, Pengalaman Berkendara, Dan Tingkat Kecelakaan Terhadap Driver Behavior Pengendara Sepeda Motor. Jurnal Teknologi. 12(1): 57-64.

[7] Imanulloh, R.F., & Prihutomo, N.B. (2019). Kajian Karakteristik Pengendara Sepeda Motor Di Kota Depok. Seminar Nasional Teknik Sipil Politeknik Negeri Jakarta. 1(1): 380-386.

[8] Abusini, S., & Ambarwati, L.. (2017). Motorcycle Accident Model on the Road Section of Highlands Region by Using Generalized Linear Model. International Journal of Civil Engineering and Technology (IJCIET). 8(10):1249-1258.

[9] Ambarwati, L., Pel, A.J., Verhaeghe, R., & van Arem, B., (2014a). Empirical analysis of heterogeneous traffic flow and calibration of porous flow model. Transp.Res. Part C: Emerg. Technol. 48, 418–436.

[10] Kiran, B. N., Swamy, N. K., & Sashidhar, C. (2017). Prediction of Road Accident Modelling for Indian National Highways. International Journal of Civil Engineering and Technology (IJCIET). 8(1): 789-802.

[11] Singh, J., *et al.* 2017. Analytical Hierarchy Process for Road Accident of Motorcycle in India: A Case Study. *International Journal of Mechanical Engineering and Technology (IJMET)*, Volume 8, Issue 7, July 2017, pp. 1348–1356.

11th Int. Conf. on Geotechnique, Construction Materials & Environment,
Kyoto, Japan, 3-5 November 2021, ISBN: 978-4-909106063 C3051

STUDY OF DISTANCE AND NUMBER OF REBARS ON VELOCITY MEASUREMENT USING NON-DESTRUCTIVE TEST

Christin Remayanti Nainggolan[1], Indradi Wijatmiko[2], Hendro Suseno[3], Ananda Insan Firdausy[4]

[1,2,3,4]Department of Civil Engineering, Brawijaya University, Indonesia

ABSTRACT

The quality of constructions can be evaluated by using non-destructive test (NDT) method, one of them is an ultrasonic pulse velocity (UPV) test. Velocity is one of the parameters that can indicate density of material that will affect the strength of material. The difference in density of concrete and rebars could affect the velocity measurement of reinforced concrete. It is common knowledge as there are factors that affect the velocity measurement and some of them are the position of transducers and the number of rebars. An experiment was conducted to get better understanding on the velocity measurement of reinforced concrete determined by position of the transducers, number of rebars and distance between rebars and transducers using UPV test. The specimens were reinforced concrete beam with different number of rebars, however had the same tensile strength and diameter. The number of rebars used for specimens are 4; 8 and 12 rebars with varied position of transducers. It can be concluded that the pulse velocity of reinforced concrete when measured with perpendicular position lower than the parallel position and also the average transmission time in the parallel position was 52% faster than perpendicular. On the case of rebar parallel to pulse path, the velocity of reinforced concrete decreased as the distance between rebar and transducers increased, however the number of rebars did not affect the velocity. On the other hand, in case of rebar perpendicular to pulse path, the number of rebars resulted insignificant effect to the velocity measurement (less than 1%).

Keywords: Velocity, Rebar, Ultrasonic pulse velocity, Non-destructive test

INTRODUCTION

Every structure must be in good condition and meet the safety standard therefore it can perform a good service ability. To evaluate the condition of existing structure then it is needed reliable inspection techniques. Recently, non-destructive test (NDT) methods is an assessment technique that getting popular among engineers and often used to evaluate buildings. NDT methods represent approach of quality and condition of materials in the structure, further more they are used to diagnose and predict the structure condition. In addition, NDT methods have a major advantage in their capability to evaluate an existing building [1] and become promising techniques for in-situ examination [2]. Even now, these methods are still being developed to meet the expectation of the user.

Ultrasonic Pulse Velocity (UPV) is one of NDT methods that frequently used to evaluate the quality of materials especially concrete. Many researchers propose the relationship between UPV measurement and compressive strength to estimate the strength of concrete [3]-[6]. Therefore, it is important to know the validity of the UPV results by studying and evaluating many kinds of UPV measurements.

The basic idea of UPV methods is using pulse wave propagation which have velocity that depend on elastic properties and density of the materials. Therefore, it is a challenge to evaluate an existing structure especially reinforced concrete structure using UPV because even though this technique is easy to conduct however it is affected by various factors. These factors can be divided into two categories: (1) factors from concrete properties such as type and amount of aggregate, cement type, water-cement ratio, admixture and age of concrete, curing condition [7] [8]; and (2) other factors such as transducers contact, size of the specimen and presence of steel reinforcement. From several factors that have already been mentioned, this study discusses further specifically to the presence of steel reinforcement.

According to some research, elasticity properties and density of rebar are higher than concrete, therefore the pulse velocity in rebar is 1.4 to 1.7 times than the concrete [9]. The pulse velocity of steel medium is generally up to 5.90 km/s, however the value decreases as well as the diameter [10]. The pulse velocity of rebar at reinforced concrete is lower than the rebar in the air because it is affected by the velocity of concrete and the bond condition between rebar and concrete.

Several research on UPV measurement have been carried out on reinforced concrete and the presence of rebar commonly affected the pulse velocity of reinforced concrete. The effect can be an increase or decrease [11] in the measurement of pulse velocity where this value is also influenced by the condition of the concrete [12], the quality of the concrete and rebar

[13]. In addition, the position between the rebar and the transducers will also affect the pulse velocity value and the transmission time because at a certain position, the first pulse wave received by the receiving transducers is partly pass through the concrete and partly pass through the rebar.

There are many things that affect the measurement of the pulse velocity of reinforced concrete therefore it still needs to be studied further. This present experiment focus on the effect of rebar to the pulse velocity and the transmission time of the pulse wave of reinforced concrete based on proximity of the measurements to the rebars, the number of rebars and the position of the transducers (parallel and perpendicular to rebars).

STUDY LITERATURE

UPV measurement on reinforced concrete should not at the point where the rebar is located to prevent the pulse wave path pass through the rebar. However, if this is unavoidable, then it is needed correction due to the influence of rebar. BS 1881-203:1986 [14] provides a formula of correction factor for the pulse velocity of reinforced concrete where the approximate pulse velocity of concrete will be reduced due to the influence of rebar.

$$V_c = kV_m \tag{1}$$

Where V_c is the pulse velocity in concrete (km/s) , k is the correction factor and V_m is the measured apparent of pulse velocity (km/s)

The correction factor will be affected by the distance between the transducers and the nearest rebar, the diameter of rebar and the pulse velocity surrounding concrete. When the pulse path is parallel to the rebar then the correction factor can be obtained by the following formula:

$$k = \gamma + 2\left(\frac{a}{L}\right)\sqrt{1-\gamma^2} \tag{2}$$

in which

$$\gamma = \frac{V_c}{V_s} \tag{3}$$

Where γ is velocity ratio, V_s is pulse velocity in rebar (km/s), a is distance from the surface of the rebar to the nearest point of both transducers, L is the direct path length between transducers (mm).

If the value of a is greater than two times the distance from the end of the concrete to the end of the rebar (b) then Eq. 2 can apply, otherwise

$$k = \gamma + 2\left(\frac{\sqrt{a^2+b^2}-\gamma b}{L}\right) \tag{4}$$

If the rebar is in line with the transducers (a = 0) then

$$k = 1 - \frac{L_s}{L}(1-\gamma) \tag{5}$$

Where L_s is the length of the bar (mm).

When the position on rebar is parallel to the transducers then the velocity ratio can be obtained according to Figure 1, while Figure 2 can be used for the case when rebar perpendicular to the transducers.

The influence of rebar on reinforced concrete is considered non-existent if:

$$\frac{a}{L} > \frac{1}{2}\sqrt{\frac{V_s - V_c}{V_s + V_c}} \tag{6}$$

The effect of rebar is considered to exist when a/L < 0.5 in high strength concrete or a/L < 0.25 in low strength concrete.

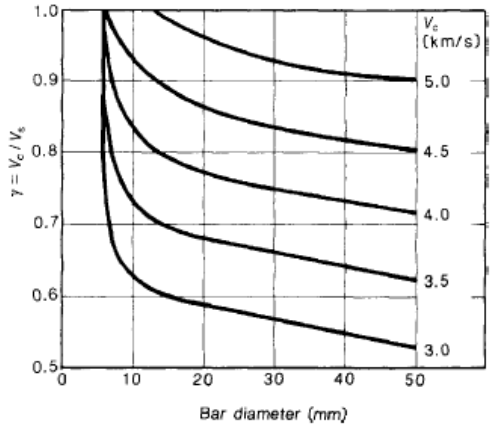

Fig. 1 Relationship between velocity ratio and bar diameter for bar parallel to pulse path [10,14]

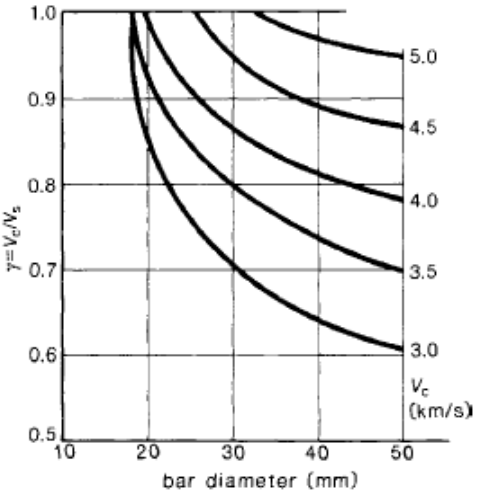

Fig. 2 Relationship between velocity ratio and bar diameter for bar perpendicular to pulse path [10,14]

EXPERIMENTAL METHOD

UPV test was conducted to the reinforced concrete and unreinforced concrete with dimensions of specimens as follows: length, 60 cm; width, 30 cm, and height, 40 cm. The rebars were deformed bar of the same diameter (22 mm) and plain bar (diameter 8 mm) as the stirrup. The rebars had the same tensile strength and the concrete had the same mixture.

The specimens differ from each other depend on the number of the bars and the arrangement of the transducers position as follows:

- ✓ BC1, unreinforced concrete beam (Fig. 3 (g)-(h))
- ✓ BC2, 4 deformed bar - Ø 22 mm as the rebar (Fig. 3 (a)-(b))
- ✓ BC3, 8 deformed bar - Ø 22 mm as the rebar (Fig. 3 (c)-(d))
- ✓ BC4, 12 deformed bar - Ø 22 mm as the rebar (Fig. 3 (e)-(f))

Figure 3 (a)-(f) show the arrangement of rebars : Fig. 3 (a), Fig. 3 (c) and Fig. (e) are the long section of the specimens and Fig. 3 (b), Fig. 3 (d) and Fig. (f) are the cross section of the specimens.

Before the UPV test was carried out, the first thing to do was perform a bar scanner on the specimens to found out the exact location of rebars. Afterward, determined the location of the transducers placement.

The UPV were tested with 2 transducers positions: (1) parallel to the rebar with a variety distance ($\boldsymbol{a}$); (2) perpendicular to the rebar.

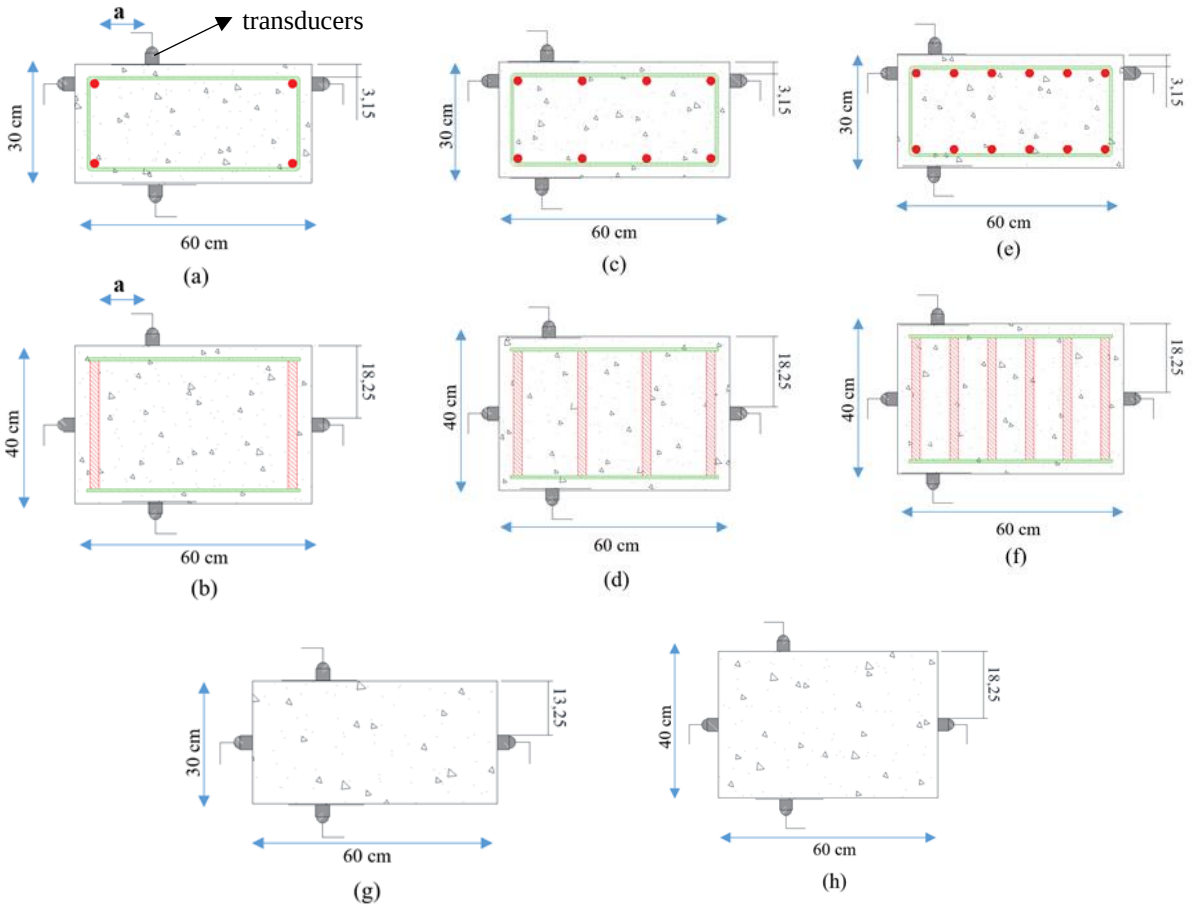

Fig. 3 (a)-(f) Reinforced concrete; (g)-(h) unreinforced concrete

RESULTS AND DISCUSSION

The pulse velocity of reinforced concrete (V) when measured with position of the rebar is parallel to the transducers can be seen in Table 1 – 3. Moreover, it can also be seen the results of the calculation of Eq. 2 – 4 for the value of correction factor. The diameter of the rebar and the pulse velocity of concrete were inserted at Fig.1 to estimate the velocity ratio and afterward, used to calculate the pulse velocity of rebar. Table 1 shows that rebar give higher effect to the pulse velocity of reinforced concrete when the transducers is in the center of rebar ($a = 0$) than the other value of a. At that point ($a = 0$), the pulse wave fully pass through the rebar as shown in Fig.4.

When it is compared to the pulse velocity of unreinforced concrete, which is 4.31 km/s, there was an increase by 13% due to the presence of rebar. Moreover, in this point, the pulse velocity of rebar was 5 km/s which is smaller than the pulse velocity of rebar in the air because of the influence of the bond between rebar and concrete that can not be define. At the measurement point where a = 12 mm, there was a decrease in pulse velocity of reinforced concrete by 9.8% compared to when a = 0 and when compared to the pulse velocity of unreinforced concrete, there was an increase by 2%. At this point, the pulse wave only pass through the concrete, however the influence of rebar was still extant and made the pulse velocity of reinforced concrete increased although not significant.

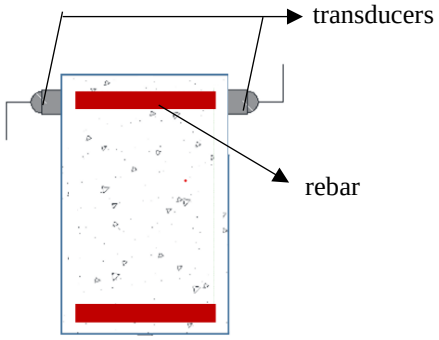

Fig. 4 Cross section of reinforcement concrete with rebar parallel to transducers

Table 1 Measurement condition: rebar parallel to transducers on specimen BC2

a (mm)	V (km/s)	k	V_c (km/s)	V_s (km/s)	a/L
0	4.89	0.84	4.1	5	0
12	4.41	0.85	3.73	4.54	0.03
32	4.41	0.89	3.9	4.75	0.08
52	4.36	0.94	4.1	4.99	0.13
72	4.31	0.96	4.13	5.03	0.18
92	4.31	1	4.29	5.23	0.23

Table 2 Measurement condition: rebar parallel to transducers on specimen BC3

a (mm)	V (km/s)	k	V_c (km/s)	V_s (km/s)	a/L
50	4.31	0.93	4.03	4.90	0.13
70	4.26	0.95	4.07	4.95	0.18

Table 2 gives information about the results of specimen BC3 when measured with condition of rebar parallel to transducers. In this specimen, the pulse velocity of reinforced concrete measured at a = 50 mm was nearly the same when it measured at a = 70 mm. As for the specimen BC4, the result can be seen at Table 3. In specimen BC4, the value of distance was 20 mm and 40 mm. This value was smaller than the specimen BC3 because of the limited space between rebar on BC4. Same as the specimen BC3, the pulse velocity of reinforced concrete slightly decreased as the distance a increased.

Table 3 Measured condition: parallel to transducers on specimen BC4

a (mm)	V (km/s)	k	V_c (km/s)	V_s (km/s)	a/L
20	4.6	0.87	4	4.81	0.05
40	4.45	0.91	4.08	4.9	0.10

Figure 5 illustrates the relationship between pulse velocity (reinforced concrete and concrete) and ratio of distance and path length. When the distance between the transducers and rebar increased, it followed by the decreased in the pulse velocity of reinforced concrete ($\boldsymbol{V}$). This happened because the position of the rebar was far from the transducers that caused the pulse wave only pass through concrete material. On the other hand, the farther the distance between rebar and transducers, the higher the pulse velocity of concrete ($\boldsymbol{V_c}$), although the value was still smaller than the pulse velocity of reinforced concrete.

At certain distance, the presence of rebar on the reinforced concrete was still considered give effect. Based on the regulation BS 1881-203:1986 (Eq. 6), there is a condition on the distance of rebar that can affect the pulse velocity of reinforced concrete. In this study, the length of the specimen had a constant value which was 40 cm, while the distance from the rebar to the transducers had a various value. From Eq. 6 was obtained the requirement value of $\boldsymbol{a/L}$ = 0.16, therefore the UPV measurements at the value of $\boldsymbol{a}$ = 70 mm, 72 mm and 92 mm were considered not affected by the presence of rebar.

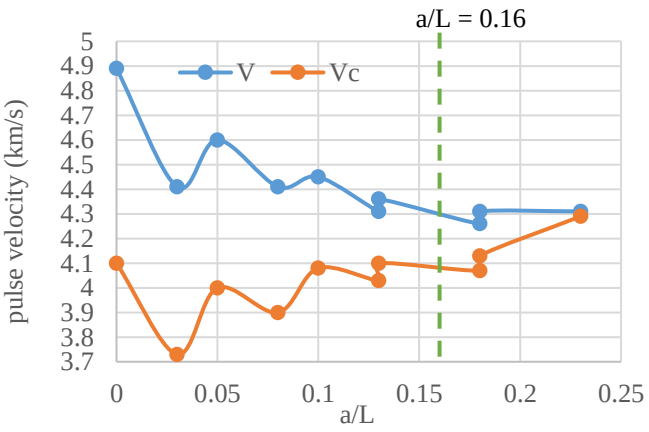

Fig.5 Relationship of pulse velocity and a/L for test condition : rebar parallel to transducers

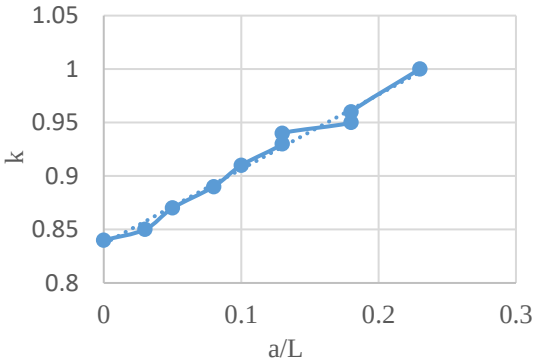

Fig. 6 Relationship of correction factor k and a/L for test condition : rebar parallel to transducers

From Fig. 6 it can be seen that as the ratio of distance and path length increases, the value of correction factor increase gradually. This could signify that the effect of rebar to the UPV measurements became smaller. Effect of correction factor can be seen in Fig. 5 where the pulse velocity of unreinforced concrete increases as the length a increases and the values is nearly the same with the pulse velocity of reinforced concrete at position a = 92 mm which the value of k = 1.

The measurement results with the position of the rebar perpendicular to the transducers can be seen in Table 4. The value of correction factor was obtained by used Eq. 5 and to obtained the value of velocity ratio, interpolation is carried out on the graph in Fig. 2.

Table 4 Measured condition: rebar perpendicular to transducers

Specimen	L_s (mm)	V (km/s)	k	V_c (km/s)	V_s (km/s)
BC2	44	4.23	0.93	3.92	4.41
BC3	88	4.27	0.85	3.64	4.06
BC4	132	4.23	0.78	3.30	3.89

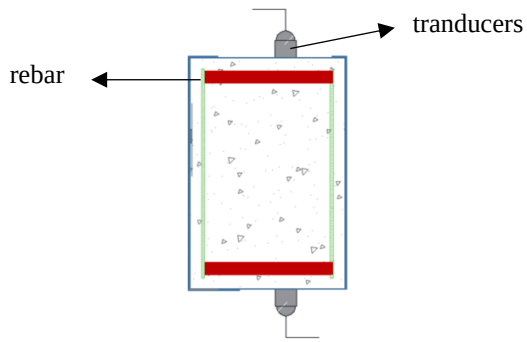

Fig.7 Cross section of reinforcement concrete with rebar perpendicular with transducers

Table 4 shows that the effect of rebar on the UPV measurements in perpendicular position is not as significant as in parallel position because the pulse wave does not completely pass through the rebar as shown in Fig. 7.

The pulse velocity of unreinforced concrete (4.32 km/s) was not much different from the pulse velocity of reinforced concrete BC2, BC3 and BC4 with decreased of 2%, 1.6% and 2% respectively. Although the pulse velocity of reinforced concrete did not differ between specimens, however the addition of more rebars gave reduction effect to the correction factor by 8,2% - 8,6%. Increased the number of rebar caused increased to the length of bars and reduced the correction factor, consequently higher effect of rebar to the UPV measurement. In this measurement position, the magnitude of rebar influence was still uncertain because there was another factor that affect the reinforced concrete which was the bond between rebar and concrete.

Table 5 Results of transmission time (T0)

Variation	L (mm)	T0 (µs)	Measurement position
BC1	600	140	Rebar perpendicular with transducers
BC2	600	142.2	
BC3	600	144.1	
BC4	600	145.1	
BC1	400	93.7	Rebar parallel to transducers
a = 0 mm	400	86.8	
a = 12 mm	400	92.4	
a = 32 mm	400	97.5	
a = 52 mm	400	96	
a = 72 mm	400	94.8	
a = 92 mm	400	96.3	

The presence of rebar in reinforced concrete also influenced the value of transmission time. Table 5 shows the transmission time when the first pulse wave detected (T0) between 2 points (transmitter transducer and receiver transducer) with different length depends on the measurement position. The smaller the value of transmission time, the faster the pulse is received by the receiver and signified that the density of material was high. The transmission time when measured with the transducers position perpendicular to the axis of rebar was higher than when measured with the transducers position parallel to the axis of rebar. This indicates that the time required to receive pulse wave in perpendicular position was longer than in parallel position. This caused by the difference in path length L as well as the homogeneity and density of the material where the pulse wave pass through when the transducers was in parallel position and perpendicular position.

The transmission time when measured on parallel

position and the rebar was in line with the transducers (a = 0) was the smallest then the other distances because in this position, the pulse wave pass through the rebar. Rebar density is higher than concrete therefore the time needed to detect pulse wave is faster than concrete. At the distance a = 12 mm, the transmission time increased because the pulse wave path only on the concrete. At several distance, the transmission time fluctuated due to the level of homogeneity of the concrete material. While on the transducers position perpendicular to the rebar, the addition of more rebars caused the transmission time increased slightly.

CONCLUSIONS

From the experiment, several conclusions were obtained:

1. When UPV measured with condition rebar parallel to the transducers:
   a) the farther the transducers from the rebar ($\boldsymbol{a}$), the pulse velocity of reinforced concrete will decreased and the other hand the value of the correction factor ($\boldsymbol{k}$) will increased and followed by the pulse velocity of concrete.
   b) with the dimension of specimen, the requirement of $\boldsymbol{a}/\boldsymbol{L}$ was 0.16, therefore the effect of rebar was considered not existed in the specimen with $\boldsymbol{a}$ = 70 mm, 72 mm and 92 mm.
   2. When UPV measured with position of the rebar perpendicular to the transducers, it was known that the addition of more rebars gave a slightly increased (less than 1%) to the pulse velocity of reinforced concrete.
3. The pulse velocity of reinforced concrete when measured with perpendicular position lower than the parallel position due to the difference in path length ($\boldsymbol{L}$) and the level of homogeneity in the pulse path.
4. The position of the transducers and the number of rebars also affect the transmission time (T0) where the average transmission time in the parallel position was 52% faster than perpendicular due to the difference in the level of homogeneity and density of the material in the pulse wave path.

REFERENCES

[1] Verma S.K., bhadauria S.S, Akhtar S., Review of Nondestructive Testing Methods for Condition Monitoring of Concrete Structures. Journal of Construction Engineering, Volume 2013, Article ID 834572, 2013, pp.1-11.

[2] Tavukçuoğlu A., Non-Destructive Testing for Building Diagnostics and Monitoring : Experience Achieved with Case Studies, MATEC Web of Conferences 149, 01015, 2018, pp.1-8.

[3] Kannan A., Relationship Between Ultrasonic Pulse Velocity and Compressive Strength of Self Compacting Concrete Incorporate Risk Husk Ash and Metakaolin, International Journal of Engineering and Applied Sciences, Volume 2, Issue 5, 2015, pp.66-71.

[4] Mahure N.V., Vijh G. K., Sharma P., Sivakumar N., Ratnam M., Correlation Between Pulse Velocity and Compressive Strength of Concrete, International Journal of Earth Sciences and Engineering, Volume 4, No. 06 SPL, 2011, pp.871-874.

[5] Hedjazi S., Castillo D., Relationship Among Compressive Strength and UPV of Concrete Reinforced With Different Types of Fibers, Heliyon 6, 2020.

[6] Aribawa, B. B., Wijatmiko I., Simatupang R. M., Effect of Concrete Quality on Concrete Strength Using Non-Destructive Test and Destructive Test, Rekayasa Sipil, Volume 13, No. 3, 2019, pp.184-192. (in Indonesian)

[7] Lorenzi A., Tisbierek F. T., Filho L. C. P. S., Ultrasonic Pulse Velocity Analysis in Concrete Specimens, Conferencia Panamericana de END Buenos Aires, 2007.

[8] Godinho J.P., De Souza Junior T. F., Medeiros M. H. F., Silva M. S. S., Factor Influencing Ultrasonic Pulse Velocity in Concrete, IBRACON Structures and Materials Journal, Vol.13, Number 2, 2020, pp. 222-247.

[9] Malhotra V.M., Carino N.J., Handbook on Nondestructive Testing of Concrete, 2nd ed., CRC Press LLC, 2004.

[10] Bungey J. H., Millard, S. G., Testing on Concrete in Structures, 3rd ed., Blackie Academic & professional An Imprint of Chapman & Hall,1996.

[11] Lencis U., Udris A., Korjakins A., Decrease of The Ultrasonic Pulse Velocity in Concrete Caused by Reinforcement, Journal of Materials Science and Engineering, A 1, 2011, pp.1016-1028.

[12] Kencanawati, N. N., Akmaluddin, Anshari B., Paedullah A. G., Shigeishi M., The Study of Ultrasonic Pulse Velocity on Plain and Reinforced Damaged Concrete, MATEC Web of Conference 195, 2018.

[13] Fodil N., Chemrouk M., Ammar A., The Influence of Steel Reinforcement on Ultrasonic Pulse Velocity Measurements in Concrete of Different Strength Ranges, IOP Conf. Series : Materials Science and Engineering 603, 2019.

[14] British Standard, BS 1881-203-1986, Testing Concrete Part 203 : Recommendations for Measurement of Velocity of Ultrasonic Pulses in Concrete, pp.7-10.

11th Int. Conf. on Geotechnique, Construction Materials & Environment, Kyoto, Japan, 3-5 November 2021, ISBN: 978-4-909106063 C3051

NON-DESTRUCTIVE EVALUATION OF VARIOUS FLOOR COATING USING ULTRASONIC PULSE VELOCITY AND ULTRASONIC PULSE ECHO: A COMPARATIVE STUDY

Indradi Wijatmiko[1], Christin Remayanti Nainggolan[2], Sugeng Prayitno Budio[3], Ming Narto Wijaya[4] and Indra Waluyohadi[5]

[1,2,3,4,5] Department of Civil Engineering, Faculty of Engineering, Universitas Brawijaya, Indonesia

ABSTRACT

The present study was conducted to evaluate the effect of floor coating on the assessment of non-destructive test (NDT). Floor coating has been known as simple and low-cost method in modifying the surface's membrane distillation (MD) to improve durability or strength, hence the coating material affect on the transmitted NDT energy has not been clearly studied. It is necessary to investigate the effect of coating material on NDT assessment to get better understanding on the quality of inspected structures. In this study, ultrasonic pulse velocity (UPV) and ultrasonic pulse echo (UPE) techniques were performed to evaluate the degree of disruption of coating material on the NDT measurement. Various floor coating was used, i.e., water shield coating, waterproof coating, cement resin coating, and floor hardener coating to investigate the differences on the waveform length, amplitude, and velocity. The comparison of waveform between with and without epoxy floor coating showed 1-2% differences of signal amplitude and wave velocity, in respect to the material coating and surface smoothness. Further, the waveform of coated ones indicates longer wavelength in term of peak and period.

Keywords: Non-destructive test, Floor coating, UPE, UPV

INTRODUCTION

The vastly growth of construction industry demanded effective and efficient method through all construction sites. The use of epoxy on floor has been a common action to provide a high-performance, smooth, and durable surface that can last many years and withstand heavy loads. One of the advantages of epoxy floor is the resistance ability to stains and water, therefore some application tended to use it as water shield and waterproof type, meanwhile some others are used it as floor hardener due to its durability. The thickness and uniformity of material coating tend to affect the quality of the structure.

Non-destructive test (NDT) has been widely used on the existing structure to monitor and assess the structure quality[1]. Moreover, there are many NDT method which depend on the material and structural condition, such as visual testing, eddy current testing, infra-red thermographic testing, acoustic emission testing and ultrasonic testing. Among of these techniques, ultrasonic testing is considered one of the most capable NDT methods used for testing of solid component, such as beam, column, and plate.

Many research reviews on the non-destructive test have been published to achieve higher accuracy on the prediction of structural quality[2],[3]. Thus, the study on the epoxy coated floor holds a few reviews article. Though the epoxy materials may create an addition layer above the structural surface, which could give significant impedance or amplify the pulse wave of NDT. In order to get better understanding on the effect of various floor epoxy coating. This study to investigate the effect of epoxy floor coating to the reading of ultrasonic pulse velocities and echoes on the non-destructive measurement.

EXPERIMENTAL SETUP

Samples

Concrete blocks of 0.5m x 0.2m x 0.2m and cylindrical samples of diameter 0.15m x 0.3m height were casted with various coating materials as seen in Table 1.

Table 1 Sample attributes.

Sample Code	Sample Shape	Coating	Hole	Unit
N.C.	Block	None	No	3
N.C.R.	Block	Cement resin (thick 5mm)	No	3
H.N.C.	Block	None	Yes	3
H.C.E1	Block	Water shield	Yes	3
H.C.E2	Block	Waterproof	Yes	3
H.C.E3	Block	Floor Hardener	Yes	3
S.N.C.	Cylinder	None	No	8

As seen in Fig.1 several concrete blocks were casted with hole to make clearer on distinguishing the

NDT reading differences between with coating and without ones.

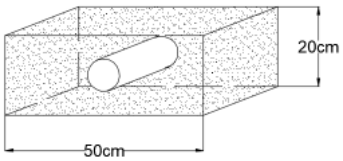

Fig. 1. Schematic view of concrete block with hole

Coating Material

Concrete blocks of 0.5m x 0.2m x 0.2m and cylindrical samples of diameter 0.15m x 0.3m height were made with various coating materials to investigate the effect of epoxy coating to the reading of non-destructive test result. The various types of epoxy coating were used to get clearer understanding, i.e., water shield, water floor, and floor hardener type. As additional comparison, cement raisin coated was also introduced on this study.

NON-DESTRUCTIVE TECHNIQUE

Ultrasonic Pulse Velocity (UPV) Testing

The propagation of sound waves requires some physical elastic medium, such as gas, liquid or solid. The propagation of ultrasonic sound waves creates stress on applied surface, which cause the internal particle to restore the system to its original equilibrium by vibrating back and forth [4][5]. The vibration of particle triggers the surrounding particles to vibrate in relation to the sound wave propagation directions continuously until the mechanic energy transmission dissipate. Ultrasonic transmission method used to detect defects in the concrete by measuring the wave acoustic parameter (amplitude and frequency) and the wave velocity parameter [6].

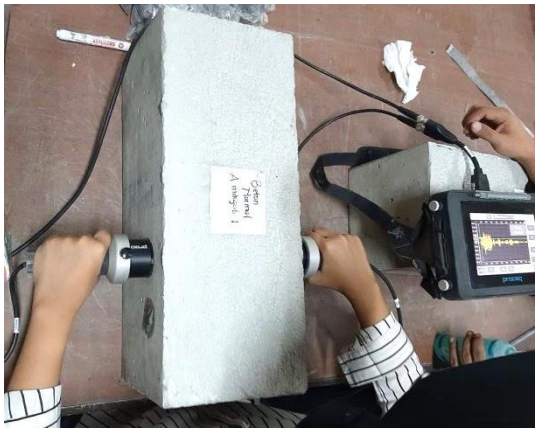

Fig. 2. The non-destructive test direct method.

In this study, the Pundit PL-200 sonicator from the Swiss company Proceq SA with 54 kHz P-wave transducers was used to measure the wave acoustic and velocity parameter, which in this case is the longitudinal wave. The compressional wave in which the particle motion is parallel to the wave propagation direction was measured by using direct method as seen in Fig. 2.

The measured ultrasonic velocity (V) is related with the Young's modulus (E), Poisson's ration (σ) and density of sample (ρ), as described on Eq. (1).

$$V = \sqrt{\frac{E(1-\sigma)}{2\rho(1+\sigma)(1-2\sigma)}} \quad (1)$$

Ultrasonic Pulse Echo (UPE) Testing

The generated propagation of the ultrasound pulse waves is being bounced back by the target into the reception to be detected. Thus, the bounce back pulse provides parameter of signal processing and repetition frequency. Echoes are generated when the ultrasound wave intercept inhomogeneities in a medium which reflect part of the incident energy back to the receiver, as seen in Fig. 3.

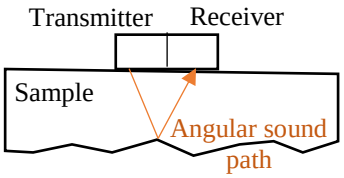

Fig. 3. The angular sound path of UPE

When an ultrasonic echo travel into a boundary between two media, a part of energy is being reflected, while the rest is being transmitted. The percentage of transmission and reflection energy is related with acoustic impedance of material, as follow-on Eq. (2).

$$Z = \rho . c \quad (2)$$

With z is the acoustic impedance (N s/m^3), ρ is the density of the material (kg/m^3) and c is the velocity of sound in the material (m/s).

The greater the impedance difference, the greater the percentage of energy that will be reflected at the interface or boundary between one medium and another. Thus, the reflection coefficient can be calculated as Eq. (3).

$$R = \left(\frac{Z_2 - Z_1}{Z_2 + Z_1}\right)^2 \quad (3)$$

Where Z_1 and Z_2 are the acoustic impedances of the two materials at the interface.

RESULT AND DISCUSSION

Compressive Strength

Table 2 show the result of compressive strength and the indicated strength from the concrete blocks by using hammer test. The compressive strength obtained from the compressive machine (Fig. 4) of cylindrical samples from each concrete mixture.

Fig. 4. Compressive test on cylindrical samples.

Table 2. Result of Compressive Strength

Sample Code	Compressive Strength (MPa)	
	Machine	Hammer Test
S.N.C.	3143	31.11
N.C.R.	32.08	31.42
H.C.E1.	32.16	32.09
	32.48	32.64
H.C.E2	32.81	32.82
	32.97	33.16
H.C.E3	34.02	33.92
	33.78	34.50

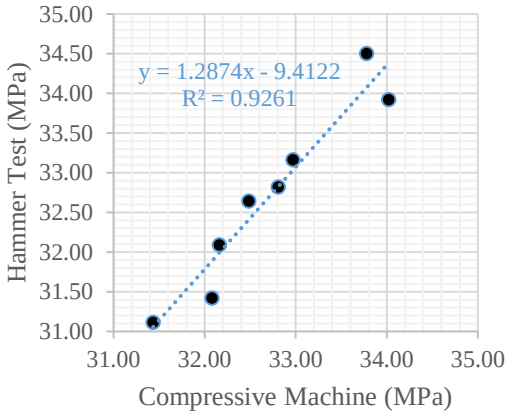

Fig. 5. Correlation value of hammer test and compressive test.

The results shown in Table 2 and Fig. 5 indicates good agreement between hammer test results and compressive test results on measuring the compressive strength of samples.

Ultrasonic Pulse Velocity

Figure 6 shows the measurement position of transducer in the sample block.

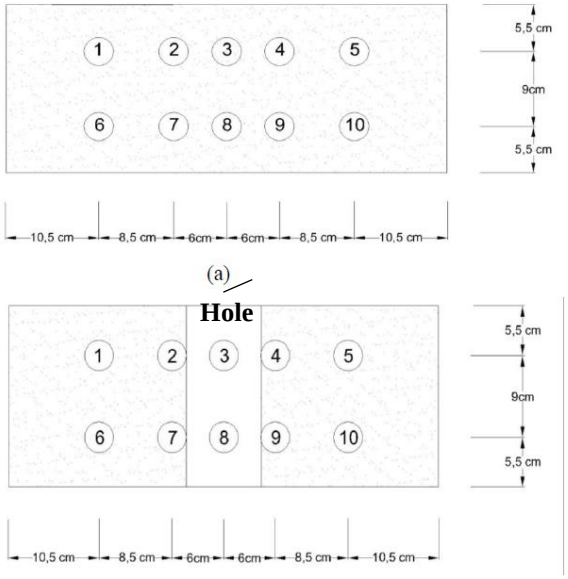

Fig. 6. Measurement position of transducer.

Direct method of UPV were used to measure the wave velocity on 10 different locations as seen in Fig.6. The result of wave velocities was compared between coated surfaces and without coated ones as illustrated on Fig. 7 and Fig. 8. The comparison in Fig.7 shows that the wave velocity of non-coated surface tended to achieve higher velocity compared to with cement resin coated. The decreasing of wave velocity may occur due to air existence between cement resin and concrete block.

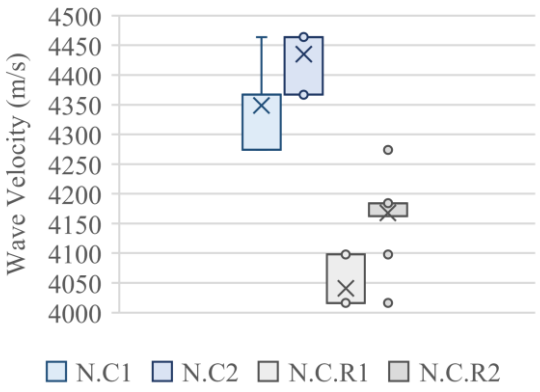

Fig. 7. Wave velocities of normal concrete and normal concrete with cement resin coated.

Meanwhile in term of epoxy coated materials, the used of epoxy as water shield, waterproof, and floor hardener purposes did not create significant effects on the wave velocity. However, among all epoxy coated, water shield epoxy type produces higher reduction of wave velocity value with approximately 3.4%.

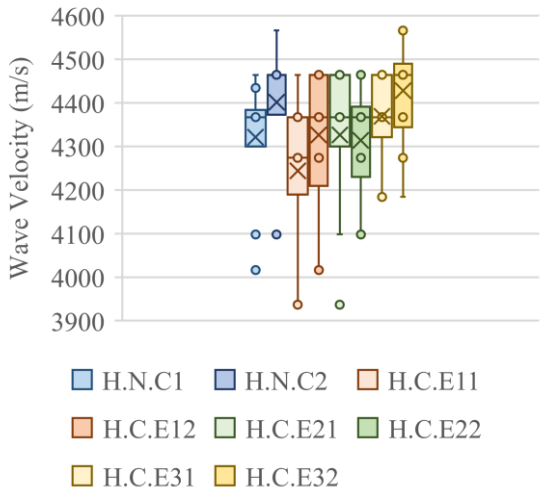

Fig. 8. Wave velocities of normal concrete with hole and various epoxy coated concrete with hole.

Figure 9 shows the measurement of initial wave on pulse waveform in the reading of non-destructive test UPV.

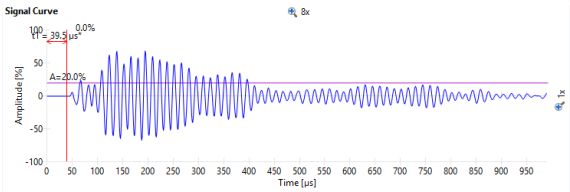

Fig. 9. Measured initial wave on the waveform.

As seen in Fig. 10, the comparison of waveform between normal concrete and concrete with cement resin coated shows that the amplitude of wave was greatly reduced due to the existence of cement resin. However, there were no significant different on the initial wave travel time.

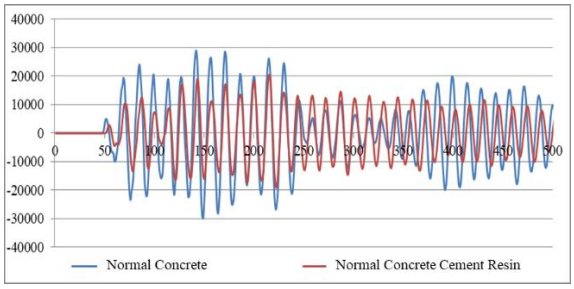

Fig. 10. Waveform comparison between normal concrete and concrete coated with cement resin.

However, the introduction of epoxy coated on the concrete did not give significant different on the waveform amplitude as seen in Fig. 11 and Fig. 12, which are the water shield and waterproof coated respectively.

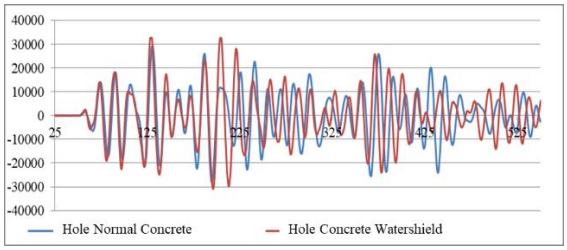

Fig. 11. Waveform comparison between normal concrete with hole and concrete water shield coated.

The wave pattern of both with and without coated in Fig. 11 and Fig. 12 did not significantly change, thus the wavelength tended to be slightly longer in case of coated ones.

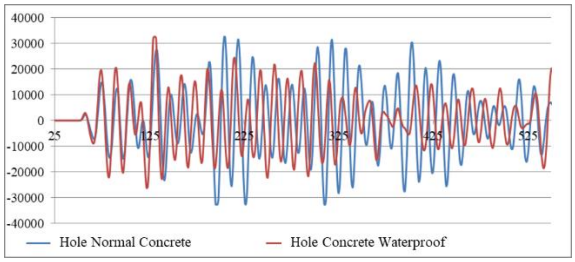

Fig. 12. Waveform comparison between normal concrete with hole and concrete waterproof coated.

The epoxy floor hardener coated have a tendency to significantly increase the wavelength, although the initial wave time trave was similar with the concrete without coated as seen in Fig. 13. Further, the epoxy coated gave slight reduce on the wave amplitude as the wave traveling longer.

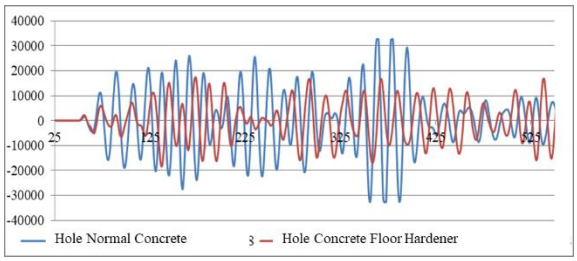

Fig. 13. Waveform comparison between normal concrete with hole and concrete floor hardener coated.

The measurement of maximum amplitude on pulse waveform has been set on the first wave maximum point, in which the placement point of non-destructive test UPV reading can be seen in Fig. 14.

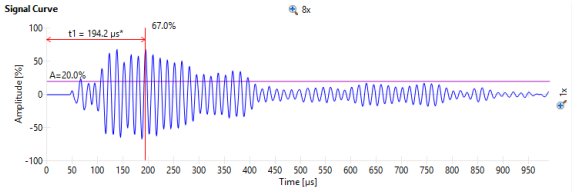

Fig. 14. Measured maximum amplitude on the waveform.

The comparison of maximum amplitude value and time can be seen in Table 3a and Table 3b.

Table 3a. Measured time of maximum amplitude

Comparison	T max (µs)		
	N.C.	N.C.R.	Diff.
N.C. vs N.C.R.	168.1	168.4	0%
Comparison	H.C.	H.C.E	Diff.
H.C. vs H.C.E1	203.3	208	2%
H.C. vs H.C.E2	215.9	205.9	-5%
H.C. vs H.C.E3	125.9	359.6	65%

Table 3b. Measured maximum amplitude

Comparison	A max (%)		
	N.C.	N.C.R.	Diff.
N.C. vs N.C.R.	86.1	38.8	-122%
Comparison	H.C.	H.C.E	Diff.
H.C. vs H.C.E1	79.2	80.3	1%
H.C. vs H.C.E2	100.1	98	-2%
H.C. vs H.C.E3	98.9	75.3	-31%

Ultrasonic Pulse Echo

The detection of backscattered pulse-echo was performed to acquire the echo waveforms which shows the spatial and contrast of each measurement. As described, the measurements were conducted horizontally perpendicular to the hole on each sample block. B-Scan method was used with the increment of 0.01m for 35 points. All signal gains and voltage on each measurement were set at the same value to get better understanding on the difference between sample comparison.

Figure 15 and 16 shows the comparison result between normal concrete and the ones with the cement resin coated. In Fig. 15, the thickness of sample block can be indicated by the yellow color between the red ones at the depth of 0.20m. Though the red color on the depth of 0.18-0.20m indicated the material were not homogeneities due to rough surface finishing. Meanwhile on the cement resin coated ones, a layer was observed on the depth of 0.0-0.02m which were separated by the thin air between cement resin and the concrete block. Thus, the thin air bounce most of the echo wave, which resulted on the less signal strength through the sample block and cause the contrast signal from the inhomogeneities materials at the bottom side became dimmer.

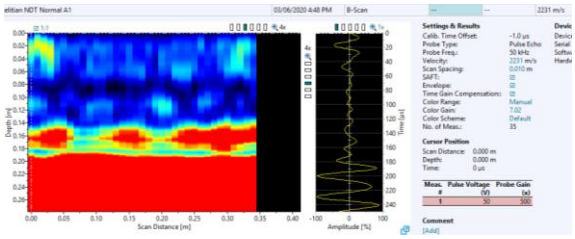

Fig. 15. UPE result on the normal concrete sample.

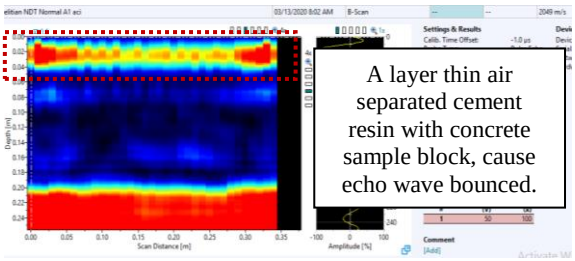

Fig. 16. UPE result on the normal concrete sample with cement resin.

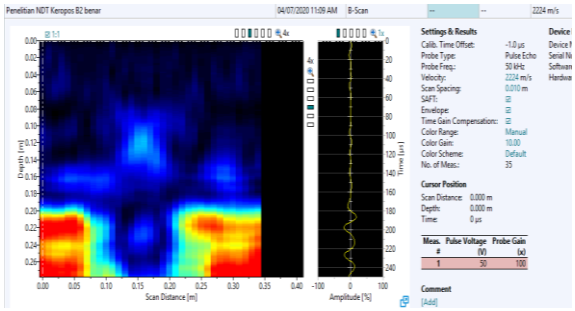

Fig. 17. UPE result on the normal concrete sample with hole.

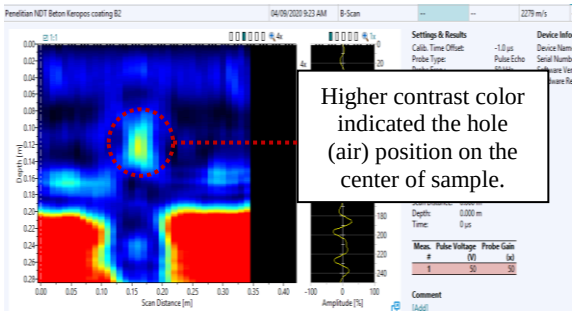

Fig. 18. UPE result on the concrete sample with hole, coated with water shield epoxy.

Both Fig. 17, Fig. 18 and Fig. 19 shows that coated epoxy materials (water shield type and waterproof type) increased the signal strength of echo

and generating higher contras color on the each inhomogeneities materials, especially the hole (air) on the center of the concrete sample. It was due to the material of epoxy reduce the impedance of echo signal and smoother the measurement surface that caused solid contact between transducer and surface.

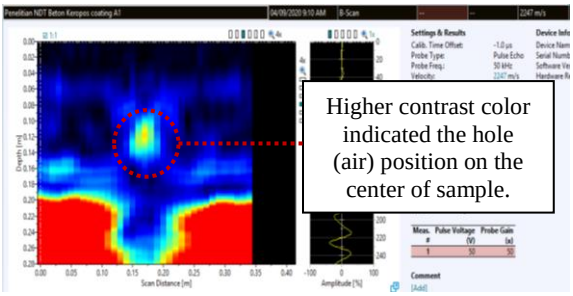

Fig. 19. UPE result on the concrete sample with hole, coated with waterproof epoxy.

Similar result can be found in the case of floor hardener epoxy coating, as seen in Fig. 21. However, the amplified signal was not as robust as water shield epoxy coated nor waterproof epoxy coated.

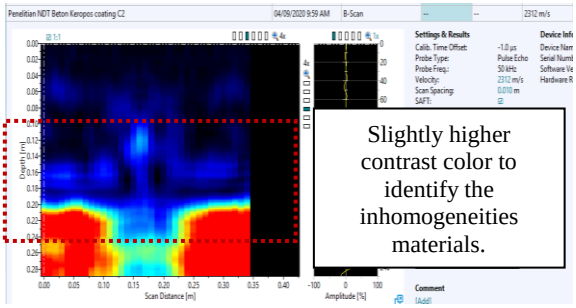

Fig. 19. UPE result on the concrete sample with hole, coated with floor hardener epoxy.

The comparison of initial echo wave time travel can be seen in Table 4a. In which it showed insignificant difference between with and without coated samples. The cement resin materials tended to reduce the echo wave velocity, in the other hand the effect on epoxy coated tended to slightly increase it.

Table 4a. The comparison of initial wave time travel

Comparison	T (µs)		
	N.C.	N.C.R.	Diff.
N.C. vs N.C.R.	230.5	225	-2.44%
Comparison	H.C.	H.C.E	Diff.
H.C. vs H.C.E1	302.7	308.7	1.94%
H.C. vs H.C.E2	313	318.3	1.67%
H.C. vs H.C.E3	307.5	311.5	1.28%

As seen in Table 4b, the significant effect can be found on the water shield and waterproof type of epoxy with the increase signal around 15-21%.

Table 4a. The comparison wave amplitude

Comparison	Amplitude (%)		
	N.C.	N.C.R.	Diff.
N.C. vs N.C.R.	45	42.2	-7%
Comparison	H.C.	H.C.E	Diff.
H.C. vs H.C.E1	68.5	86.2	21%
H.C. vs H.C.E2	60.6	71.2	15%
H.C. vs H.C.E3	73.2	75	2%

CONCLUSIONS

The used of cement resin as coated materials tended to reduce the wave velocity and reducing wave amplitude approximately 7% due to the existence of air as seen in the UPE result. Further, the cement resin coating tended to significantly decrease the maximum value of amplitude.

In the other hand, the used of epoxy coating material such as, water shield, waterproof, and floor hardener type did not create significant effect on the wave velocity (max +3.4%) and wave form pattern. However, the introduction of epoxy coating produce higher contrast on the UPE readings (+15-21%).

REFERENCES

[1] Verma S.K., bhadauria S.S, Akhtar S., Review of Nondestructive Testing Methods for Condition Monitoring of Concrete Structures. Journal of Construction Engineering, Volume 2013, Article ID 834572, 2013, pp.1-11.

[2] Bungey J. H., Millard, S. G., Testing on Concrete in Structures, 3rd ed., Blackie Academic & professional An Imprint of Chapman & Hall,1996.

[3] Aribawa, B. B., Wijatmiko I., Simatupang R. M., Effect of Concrete Quality on Concrete Strength Using Non-Destructive Test and Destructive Test, Rekayasa Sipil, Volume 13, No. 3, 2019, pp.184-192. (in Indonesian)

[4] Tavukçuoğlu A., Non-Destructive Testing for Building Diagnostics and Monitoring : Experience Achieved with Case Studies, MATEC Web of Conference 149, 01015, 2018, pp.1-8.

[5] Kencanawati, N. N., Akmaluddin, Anshari B., Paedullah A. G., Shigeishi M., The Study of Ultrasonic Pulse Velocity on Plain and Reinforced Damaged Concrete, MATEC Web of Conference 195, 2018.

[6] Malhotra V.M., Carino N.J., Handbook on Nondestructive Testing of Concrete, 2nd ed., CRC Press LLC, 2004.

11th Int. Conf. on Geotechnique, Construction Materials & Environment,
Kyoto, Japan, 3-5 November 2021, ISBN: 978-4-909106063 C3051

ANALYTICAL OF MULTI CRITERIA APPROACH FOR IDENTIFYING THE WEIGHT AND FACTOR OF RURAL ROAD MAINTENANCE PRIORITIZATION.

Pawarotorn Chaipetch[1], Chisanu Amprayn[2] Paijit Pawan[3] and Vatanavongs Ratanavaraha[4]

[1, 2, 3]School of Engineering, Sripatum University, Thailand; [4]Suranaree University of Technology, Thailand

ABSTRACT

The Department of Rural Roads' (DRR) annual budget prioritization for road maintenance is now based on a comparison of the benefits of reduced road user costs (Vehicle Operation Cost, Value of Time, and Accidental Cost) and maintenance costs, which is mainly based on two factors: traffic volume and international roughness index (IRI). As a result, the budget allocation for these factors may be inappropriate for a low-traffic road. The main objective of this paper is to modify DRR's road maintenance budget prioritization, which is related to the DRR's strategic driving plan. The factors in the study are divided into three groups in order to investigate and evaluate factors which have impact on road maintenance in rural road: economic, engineering, and social. The weight of each factor and the priority value of each strategic driving plan were found out by using the Analytic Hierarchy Process (AHP). The priority values of DRR's strategic driving plan (from highest to lowest) are strategic for logistic and integrated transport systems, strategic for reducing traffic congestion in urban areas, strategic for developing transportation to strengthen competitiveness and rural economic development, and strategic for tourism respectively. The economic factor is the most important factor that every strategy considers because it reflects the value of an investment. It involves evaluating all of the costs of maintenance and the benefits of reduced vehicle operating costs, travel time savings, and accident reduction to determine their monetary value. The Engineer calculated priority value for IRI, V/C ratio, traffic volume, volume of heavy truck, lifeline network and connectivity to other road networks, the result of engineering factor showed that connectivity to other road networks is an important factor in every strategy because it provides network connectivity and ensures traffic continuity. transporting goods and services and making public services and attractive places more accessible. While IRI is the only factor that is prioritized in the tourism strategy. Because the tourist road network must be maintained to ensure that it remains in good condition, is comfortable, and is easily accessible to tourist attractions and strategic of logistic and integrated transportation system is the only one that prioritize the volume of heavy truck as the most important factor. In terms of social factors, the number of people, tourist attractions, business centers, government offices, hospitals, and industrial areas were all counted along both sides of the road for 2 kilometers, indicated that all strategies prioritize consistent and appropriate road usage behavior, population density, tourist attractions, and business hub is a factor that every strategy prioritizes. As a result, priority factors should be investigated so that road hierarchy is consistent and appropriate budget allocation.

Keywords: Prioritization, AHP, IRI, Low Volume Road

INTRODUCTION

The World Bank considers roads to be important assets for reducing poverty levels and considers them to be keys to raising living standards. [1]. Better roads improve social outcomes by lowering transportation costs and fostering economic linkages that improve agricultural and industrial production while also facilitating access to public service facilities.

The Department of rural roads (DRR) in Thailand is responsible for road maintenance 48,974 kilometers, which includes 2,563 kilometers of concrete, 45,868 kilometers of asphalt, and 542 kilometers of gravel [2]. The deterioration of pavement is in exponential function and is affected by pavement age, traffic volume, volume of heavy truck, rainfall and topographical gradient [3,4]. DRR allocated funding for road network maintenance in accordance with road strategies and the nation's development policy, including strategic for logistic and integrated transport systems, tourism, reducing traffic congestion in urban areas, and developing transportation to strengthen competitiveness and rural economic development.

The annual budget for road maintenance is primarily based mostly on engineering and asset management criteria to guide investment and work to reduce life cycle agency and road user costs such as travel time, operating costs, and safety [5]. Benefit-cost analysis is used to assess the impact of various funding levels on the economic cost to users and agencies [6], as well as analyzing treatment alternatives from a financial perspective. Database

of existing road assets, use patterns, asset deterioration rate, project cost, user costs of deteriorated condition, and investment triggers or minimally tolerated conditions are all included in these models minimally tolerable conditions [7]. As a result, the allocated budget may be insufficient or inappropriate for maintenance needs in each area, especially the low volume road.

The most widely known method for determining the economic value of road maintenance investments is cost-benefit analysis (CBA), which involves evaluating all of the costs and benefits of projects to determine their monetary worth. The most important monetary benefits are reduced vehicle operating costs, travel time savings, and accident reduction. Chanon and Wisanu (2009) studied analytical framework of road serviceability level corresponding to road strategies found that the economic analysis approach is suitable for road that accommodate high traffic volume. According to the life cycle cost analysis, an investment with an Annual Average Daily Traffic (AADT) greater than or equal to 3,500 vehicles per day and an International Roughness Index (IRI) greater than or equal to 3.0 meters per kilometer will be effective [8]. When this criterion is compared to current AADT data from DRR, it was found that over 84 percent of roads have AADT less than 3500 vehicles per day **(**Fig.1**)**.

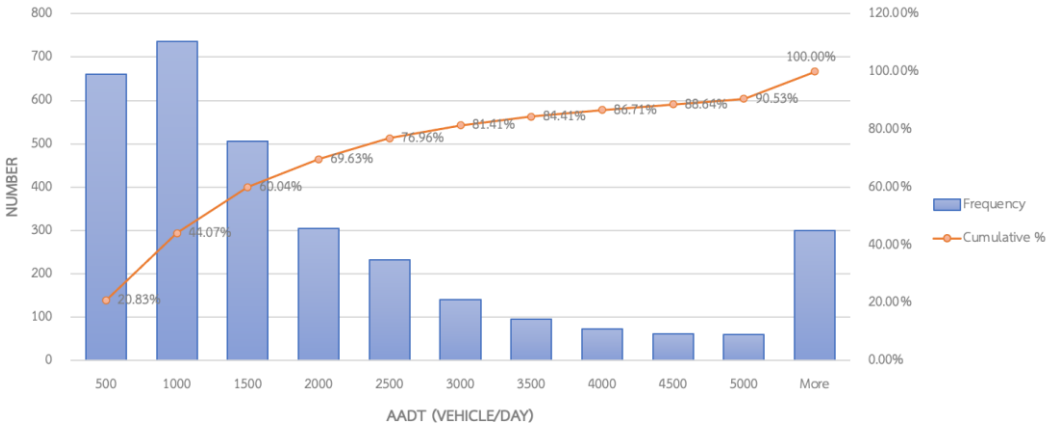

Fig. 1 Cumulative Traffic Volume of Department of Rural Road (Department of Rural Road, 2020)**.**

Because of its sole focus on economic efficiency, this method's effectiveness as a decision-making tool is limited. The effects on the environment and community, as well as the transportation factors that drive non-travel productivity, are not quantified. Because the project list included many rural road sections with lower traffic volumes, this approach was not chosen. The benefits of low-volume roads may be insufficient to justify the investments. There are various other socioeconomic benefits associated with the development of rural road. These are advantages related to increased economic activity in terms of connectivity, accessibility, regional growth, and a key component of rural development, such as access, which is important both for goods movement and labor markets, and is a contributing factor to higher income. Finally, the budget allocation should be based on the Strategic Driving Plan of DRR. As a result, priority factors should be investigated and evaluated so that road hierarchy is consistent and appropriate, considering economic, engineering, and social factors.

OBJECTIVE

The objective of the study was to use an analytical hierarchy process (AHP) to analyze the priority factors based on the Department of Rural Road's Strategic Driving Plan in Thailand, and to prioritize the main and secondary factors by considering economic, engineering, and social factors in order to classify the rural road network and apply it to appropriate budget allocation.

AN ANALYTICAL HIERARCHY PROCESS

The analytic hierarchy process (AHP), also known as the analytical hierarchy process is a structured method for organizing and analyzing complex decisions that is based on math and psychology. It was created in the 1970s by Thomas L. Saaty [9] and it has been extensively studied and refined since then. It is a precise method of quantifying the weights of decision criteria. Pair-wise comparisons are used to estimate the relative magnitudes of factors based on individual experts' experiences. Using a specially designed questionnaire, each respondent compares the relative importance of each pair of items. AHP is suitable to complex decisions involving the comparison of

difficult-to-quantify decision elements. It is based on the assumption that when challenged with a complex decision.

A LITERATURE REVIEW ON FACTOR TO PRIORITIZATION ROAD MAINTENANCE

This study examines the factor that should be considered when prioritizing road maintenance, and it is divided into three groups based on the findings of a literature review. [10,11]

Economic factor

It is an evaluating all of the costs and benefits of projects to determine their monetary value. The most important monetary benefits are reduced vehicle operating costs, travel time savings, and accident reduction compared with maintenance and rehabilitation cost. As a result, the benefit-cost ratio must be greater than 1.0.

Engineering Factor

It's a direct factor in the design, management, maintenance, and rehabilitation of a road, and it includes physical, functional, distress, condition, connectivity, and accident data. As an example,

- International Roughness Index (IRI).
- Traffic Volume and Volume of Heavy Truck.
- Volume Capacity Ratio (V/C Ratio)
- Lifeline Road.
- Connectivity to road network.
- Accident Data.

Social Factor

It's a direct factor that related to social, environment, land use, community area and attractive point of Interest. As an example,

- Population density.
- Tourist spots.
- Government office, School, Colleges and Hospital.
- Business Center, Market.
- Industrial area, Warehouse

ANALYSIS

This research is a study on the strategic, main and secondary factor analysis based on Department of Rural Road's Strategic Driving Plan in Thailand. The methodology of research was analytic hierarchy process which compared each pair of factors in matrix table. An analysis calculated the priority value for the economic factor in term of a benefit cost ratio, the engineering factor included IRI, V/C ratio, traffic volume, volume of heavy truck, lifeline network and connectivity to other road networks. Finally, social factor is the number of people, tourist attractions, business centers, government offices, hospitals, and industrial areas were all counted along both sides of the road for 2 kilometers. The population was purposive in authority of budget planning and prioritization on road maintenance or decision – making authority on planning policy, which is 20 respondents.

Analysis of Priority Strategic Factor

According to an analysis of priority strategic factors as a component of road maintenance budget allocation, the highest priority value with a priority value of 27 is strategic for logistic and integrated transport systems and strategic for reducing traffic congestion in urban areas. Second, with a priority value of 24, strategic for developing transportation to strengthen competitiveness and rural economic development, and finally, with a priority value of 22, strategic for tourism.

Analysis of Priority main and secondary Factor

An analysis of main and secondary factor is a result of priority factor of economic, engineering and social factor, including a secondary priority factor of engineering and social perspective.

Strategic for logistic and integrated transport systems. (LIS)

The highest priority factor is the economic factor, which has a priority value of 46, followed by the engineering factor, which has a priority value of 29. In descending order, the secondary factors are connectivity to the road network, heavy truck volume, accident data, traffic volume, and V/C ratio. Industrial area, population density, and tourist spots are the priority secondary factors in descending order, with a social factor having the lowest priority value of 25.

Strategic for reducing traffic congestion in urban areas. (TCA)

The highest priority factor is the economic factor, which has a priority value of 40, followed by social factor, which has a priority value of 32. In descending order, the secondary factors are population density, business center, industrial area and tourist spots.

An engineering factor is a lowest priority value of 28 with a priority secondary factor are in descending order is accident data, V/C ratio, connectivity to the road network and traffic volume.

Strategic for tourism (TSM).

Economic factor is a highest priority value of 44 and 33 for social factor with a priority secondary factor are in descending order is tourist spots, business center, hospital and population density.

Accident data, connectivity to the road network, V/C ratio, traffic volume and IRI are the priority secondary factors in descending order, with an engineering factor is lowest priority value of 23.

Strategic for developing transportation to strengthen competitiveness and rural economic development (CED).

Finally, economic is a highest priority factor same as others strategic with a value of 45, followed by the social factor, which has a priority value of 35. In descending order, business center, tourist spots, population density and industrial area.

Accident data, connectivity to the road network, V/C ratio, traffic volume and lifeline road are the priority secondary factors in descending order, with a social factor having the lowest priority value of 20.

Table 1 Summary of the analysis of Priority Factor.

Factor/Strategic	LIS Priority Value	TCA Priority Value	TSM Priority Value	CED Priority Value
	27	**27**	**22**	**24**
Economic	**46**	**40**	**43**	**45**
Engineering	**29**	**28**	**23**	**20**
IRI	-	-	13	-
V/C Ratio	17	24	21	17
Traffic Volume	19	21	16	15
Volume of Heavy Truck	21	-	-	-
Lifeline	-	-	-	14
Connectivity to the road network	23	24	25	27
Accident data	20	31	25	27
Social	**25**	**32**	**33**	**35**
Population density	19	29	17	25
Tourist spots.	18	20	40	26
Business Center	23	26	23	27
Government office.	-			-
Hospital	-		20	-
Industrial Area	40	25		22

DISCUSSION AND CONCLUSION

The Thai government has allocated funding for road network maintenance in accordance with road strategies and the nation's development policy, including strategic for logistic and integrated transport systems, tourism, reducing traffic congestion in urban areas, and developing transportation to strengthen competitiveness and rural economic development. The DRR annual budget prioritization for road maintenance is now based on a comparison of the benefits of reduced road user costs (Vehicle Operation Cost, Value of Time, and Accidental Cost) and maintenance costs, which is mainly based on two factors: traffic volume and international roughness index (IRI). As a result, the budget allocation for these factors may be inappropriate for a low-traffic road.

The benefits of low-volume roads may be insufficient to justify the investments. There are various other socioeconomic benefits associated with the development of rural road. These are advantages related to increased economic activity in terms of connectivity, accessibility, regional growth, and a key component of rural development, such as access, which is important both for goods movement and labor markets, and is a contributing factor to higher income. The budget allocation should be based on the Strategic Driving Plan of DRR. As a result, priority factors should be investigated and evaluated so that road hierarchy is consistent and appropriate, considering economic, engineering, and social factors.

This research is a study on the strategic, main and secondary factor analysis based on DRR's Strategic Driving Plan. The methodology of research was analytic hierarchy process which compared each pair of factors in matrix table. According to an analysis of priority strategic factors, the highest priority value is strategic for logistic and integrated transport systems (LIS) and strategic for reducing traffic congestion in urban areas (TCA). Second,

strategic for developing transportation to strengthen competitiveness and rural economic development (CED) and finally, strategic for tourism (TSM).

The economic factor is the most important factor that every strategy considers because it reflects the value of an investment. In terms of social factors, TCA, CED and TSM are secondary considerations because it's a factor that reflect the land use, social characteristics, and usage behavior. However, LIS is the only one with secondary engineering factor significance.

The engineering factors found that connectivity to other road networks is an important factor in every strategy because it provides network connectivity and ensures traffic continuity. transporting goods and services and making public services and attractive places more accessible. Accident data is the primary secondary factor that almost every strategy recognizes. The V/C Ratio is a secondary priority factor because it is related to the quality of traffic flow and congestion, particularly in urban areas.

Finally, secondary social factors indicated that all strategies prioritize consistent and appropriate road usage behavior, for example, LIS prioritizes industrial areas. Population density is considered important for TCA. The number of tourist spots was emphasized in TSM. The importance of business centers is strategically valued for CED. Furthermore, it was found that the secondary factor in population density, tourist spots, and business center is a factor that every strategy prioritizes, but the order of each strategy differs.

Following a detail analysis of main and secondary factors in each strategy, LIS is the only one that prioritize the volume of heavy truck as the most important component. Because roads of that strategic support the transportation of goods and services, as well as connectivity to other networks. Because routes enhance the growth of transportation of services and goods while also connecting to other networks. As a result, to develop spatial logistics management, network creation, and the connectivity of raw materials source, production base, and market to improve and increase logistics and supply chain management.

Furthermore, to decrease transportation costs and improve the efficiency of transportation services, as well as to integrate the logistic network, such as roads, rails, waterways, and air, and to strengthen the private sector's competitiveness. Furthermore, a business center and industrial area are also priority factors in the social secondary factor. Finally, according to the third Thailand logistic development plan (2017-2022) of the office of national economic and social development council, road asset management is a priority factor in the strategic of logistic and integrated transportation system to be more efficient.

Moreover, TSM as an important service sector, develop a transportation facilitation toward the tourist attraction and create value-added products and travel service and is the only one that prioritizes IRI as a maintenance management factor. Because the tourist road network must be maintained to ensure that it remains in good condition, is comfortable, and is conveniently accessible to tourist attractions. Furthermore, the tourism strategy's network has significant high traffic volume exclusively during only the festival season or during the vacation. Hospital is a secondary priority value for social factors in tourism strategy. There is a possibility and risk of an accident during the vacation season due to the high volume of traffic and increasing travel speed. Assemble the engineering factor, which prioritizes the accident data, reflects the importance of being consistent and heading in the same direction that can respond to sustainable and environmentally friendly tourism.

Private car ownership and road usage are increasing faster in urban areas and large cities than in rural areas. This implies significant traffic congestion in many large cities, as well as air pollution and car emissions. As result, the population density, business center and industrial are the most significant social factor in TCA. As a result, by integrating the v/c ratio, accident data and connectivity to the road network with traffic management and maintenance management in metropolitan areas may be more effective. These characteristics can help to reduce traffic congestion and making travel more convenient and safer.

According to the priority analysis of CED, the roads network in this strategy is a low-volume road, but it has a variety of other socioeconomic benefits associated with its development. These are benefits related to increased economic activity in terms of connectivity, accessibility, regional growth, and a key component of rural development, such as public service access, which is important for both goods movement and labor markets, and is a contributing factor to higher income.

Finally, the priority value of each factor that was analyzed by AHP was used to calculate the score and order of each road by considering economic, engineering, and social factors in order to classify the rural road network and apply it to appropriate budget allocation. Details of priority analysis of social and engineering factor shown in fig. 2 and fig. 3

ACKNOWLEDGMENTS

I would like to thank Bureau of Road Maintenance, Department of Rural Road and Center of Excellence in Infrastructure Management, Chulalongkorn University for their valuable data, expert opinion and constructive suggestions.

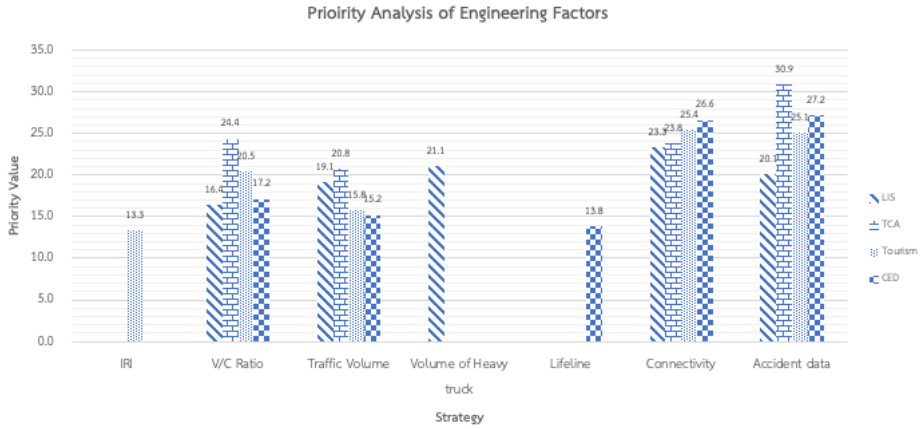

Fig. 2 Priority analysis of Engineering factors

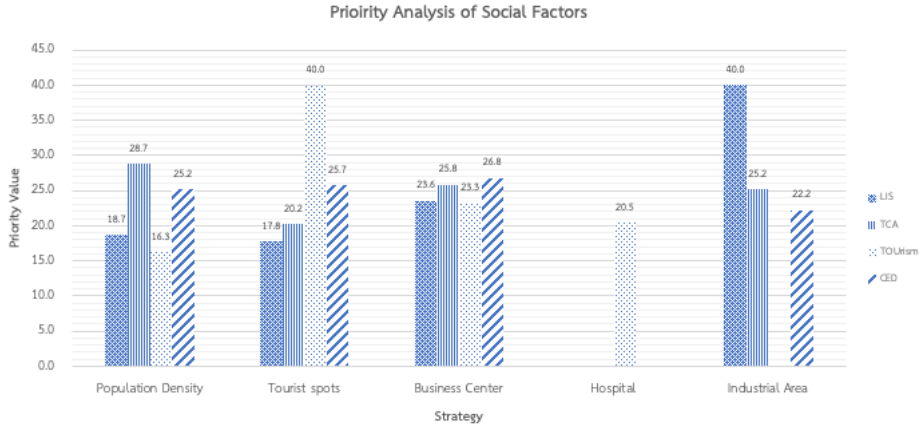

Fig. 3 Priority analysis of social factors

REFERENCES

[1] Gannon C. A., and Zhi Liu, Poverty and Transport, TWU discussion papers, TWU-30, 1997, World Bank, Washington D.C.

[2] Department of Rural Road, Annual Report of Bureau of Road Maintenance, 2020, Thailand.

[3] Subsompon, W., et. al., Road Detrioration Model based on International Roughness Index (IRI), 2000, Proceeding of the 6th National Civil Engineering Convention, Engineering Institute of Thailand.

[4] Subsompon, W., and Chaipetch, P., Work Estimation Model for Pavement Routine Maintenance, 2010, Research and Development Journal, Vol. 21, No.4.

[5] National Academics of Science. Engineering, and Medicine, Investment Prioritization Methods for Low-Volume Roads, 2018, The National Academies Press, Washington D.C.

[6] Duncan, C. and Schroeckenthaler, K., NCHRP Synthesis 510: Resource Allocation Available Funding to Programs of Work, 2015, Transportation Research Board of the National Academies, Washington, D.C.

[7] Margiotta, R., The Highway Economic Requirements System (HERS): How HERS Works, 2016, Cambridge Systematics. Presented to Committee for a Study of the Future Interstate Highway System.

[8] Amornchaisakda, C., and Subsompon, W., Analytical Framework of Road Serviceability Level Corresponding to Road Strategies, 2009, Proceeding of the 14th National Civil Engineering Convention, Engineering Institute of Thailand, pp. 635-642.

[9] Satty, L. T., Fundamental of Decision Making and Priority Theory with The Analytic Hierarchy Process, 2014, RWS Publication, USA.

[10] Moya, M., Gallego, E., Garcia, A. I., and Ayuga, F., A Proposed Methodology for the Management of Low-Volume Roads in Spain, 2011, The Baltic Journal of Road and Bridge Engineering, Vol. 6, No. 3, pp. 153-162.

[11] Menendex, J. R., Budget Allocation Planning for Small Road Systems in Peru, 2015, Proceedings of the 25th World Road Congress - Seoul 2015: Roads and Mobility - Creating New Value from Transport.

11th Int. Conf. on Geotechnique, Construction Materials & Environment, Kyoto, Japan, 3-5 November 2021, ISBN: 978-4-909106063 C3051

TRANSPORT MODE CHOICE SPLIT FOR COMMUTER LINES IN PANDEMIC COVID-19 SITUATION

Lasmini Ambarwati[1] and Achmad Wicaksono[2]

[1,2]Faculty of Engineering, Brawijaya University, Malang, East Java, Indonesia

ABSTRACT

The Covid-19 pandemic is a global disease at the end of 2019 caused by the SARS-Cov-2 virus. WHO issued that people should maintain a social distance, use masks and wash their hands to minimize the disease spread. To minimize the widespread of Covid-19, the Indonesian government executes a national lockdown program. Movement and capacity restrictions on public transport are implemented. Commuter lines that accommodate passengers in Jabodetabek (Jakarta, Bogor, Depok, Tangerang, Bekasi) are also limited to passenger capacity of up to 50%. As a result, there is a change in passenger behavior and transport mode of commuter line passengers to other vehicles. The study aims to determine passenger characteristics and passenger behavior in choosing transport mode as well to predict the split of transport mode from commuter lines to motorcycles in Bekasi City as a case study area. Data is collected by Google form that distributes to passengers of three Bekasi routes due to many passengers on the commuter lines. There is a change in passenger behavior in maintaining hygiene and health protocols when traveling on a commuter line in a Covid-19 pandemic. Changes in transportation modes occur from commuter rail to motorcycles based on travel time and cost. Humanitarian factors are also factors in choosing transport mode, i.e., social distance and health protocol. Government policies related to public transportation operational should be taken based on the factors.

Keywords: Capacity restrictions, Commuter passengers, Covid-19 pandemic, Humanitarian factors, Transport mode choice.

INTRODUCTION

Commuter line, *KRL ('Kereta Rel Listrik")* Jabodetabek (Jakarta, Bogor, Depok, Tangerang, Bekasi) has important impact on reducing traffic congestion in Jakarta and its surrounding areas. The commuter line is interested in the local community due to the consideration of travel time, punctuality of departure, mass accommodation, and affordable fares. On the other hand, the commuter line is still overcapacity in peak hours (06.00-08.00.a.m and 16.00-18.00.p.m). This situation has an impact on uncomfortable for the passengers, which is jostling without safe distance in the train carriages. This condition is contrary to the pandemic situation, which requires a social distance of 1.5-2 meters width.

Lockdown is undertaken in those areas (Jabodetabek), which decreases the number of commuter passengers. There is a split mode choice from commuter line to motorcycles due to the lockdown. During the lockdown, limitation of passenger capacity until 50% is done to reduce massive density in the train carriages as well as arranging at the station area during train departures, limitation of passenger flow at the main entrance of the station, and the implementation of health protocols. The station arrangement has led to decreased movement/mobility, long queues, long waiting times, and decreased accessibility, resulting in changes in the behavior of commuter line users.

Several variables that will affect the behavior of Commuter Line *(KRL*) users in traveling, such as time, routes, fares, comfort, and security, are the determinant factors in choosing public transportation [1]. To improve the Jabodetabek Commuter Line, the manager develops and implements high-priority technical requirements as a quality improvement strategy. This strategy is expected to improve the service quality of commuter lines as well as to increase the level of customer [2].

In Lagos, Nigeria, the manager of public transport increase tickets by 53.5%. The government should provide financial support to the public transport operator to prevent the increasing ticket which is burdensome the passengers [3]. During pandemic covid-19, there was a decline in commuter line travel by 58% for the Greater Tokyo Region [4].

During the Covid-19 pandemic, many cities worldwide have decreased air pollution and cleaner air due to lockdowns, restrictions on activities outside the home, and other physical distancing requirements. Its impact has also occurred on the transport sector on a rail, disrupting the regular rhythm of the European rail supply industry [5].

Das [6] informed that the total revenue for Indian Railways, down 41% compared to the same time last year due to the Covid-19 pandemic. There is a

change of behavior by increasing the use and dependence on cars for people's movement behavior.

In the USA, a survey of the panel revealed that of transit riders, 75% reported taking transit less since the pandemic, due to a combination of being affected by transit service changes, concerns about infection risk on transit, and trip reductions due to shelter-in-place rules. The study results have significant implications for understanding how welfare has been affected for lower-income riders during the pandemic and insight into the recovery of U.S. public transit systems [7].

COVID-19 pandemic in Bangladesh causes significant variations in transport mode preferences but minor variations in the frequency of trips. Most people continue to use the bus for health costs due to the lack of cheaper transport modes. The government should ensure proper hygiene practices on public transport and non-motorized paratransit vehicles. Information and Communication Technology (ICT), pedestrian and bicycle facilities also need to be improved [8].

Increasing the use of cars concerning with the higher risk of infection during heavy use of public transport occurred by doubled use of parking lots for school trips from February to March 2020 in the Tokyo District. More people may switch to using cars during the longer pandemic [9]. The strategy related to sustainable transportation development, improvement of P.T. systems reduces emissions rates of each emission parameter by 66% (H.C.), 71% (C.O.), and 82% (NOx) [10]. So the improvement of the P.T. system with considering healthy and humanitarian factors should be implemented during the pandemic.

Attention to assess the factors on transport mode choice and the change in the transport behavior of commuter passengers during the pandemic will be done in this study. The objectives of the study are to develop a mode choice model during normal, lockdown, and post-lockdown or new normal periods. The specific objectives are to identify passengers' characteristics and changes of commuter line user behavior for Bekasi routes during the pandemic.

METHODS

Research Framework

The impact of the Covid-19 pandemic period on the implementation of the social restriction program and health protocols on public transportation operations, especially the Commuter Line *(KRL*), is investigated. The characteristics and behavior of users of the Commuter Line from Bekasi City under different conditions, such as conditions before the pandemic or normal, lockdown, and post-lockdown or new normal conditions, are informed from the result of this study.

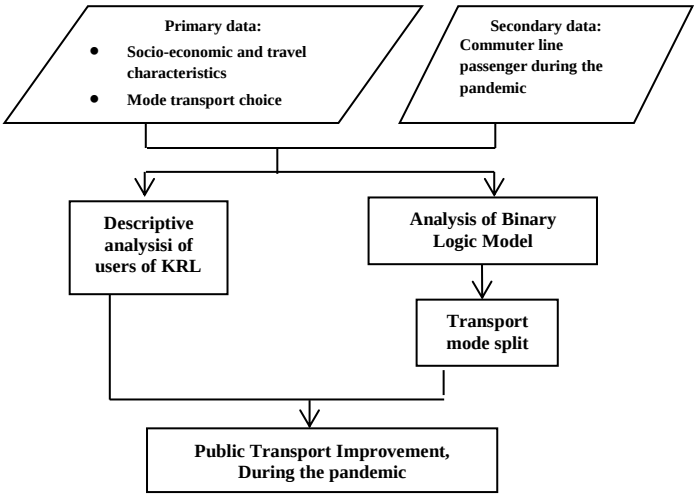

Fig. 1 The research framework

The first research steps are conducted by surveying primary and secondary data to obtain commuter line user characteristics and information about implementing social restrictions and health protocols on public transportation operations during the pandemic, as shown in Fig.1. A survey method is conducted by distributing a questionnaire or a web-based questionnaire survey. Data were obtained from 390 respondents (130 persons for each route) as a representative of the total passengers of Commuter Line from Bekasi City (298,395 passengers/day), West Java Province, Indonesia. Questionnaires are distributed to users of Commuter Line with Bekasi-Jakarta, Bekasi-Depok, and Bekasi-Bogor routes with a high number of passengers from Bekasi City. The questionnaire consists of the respondent's background about the social-economic background, trip characteristics, behavioral characteristics related to social restrictions and health protocols on public transportation operations during the pandemic, and factors influencing transport mode choice.

The Choice of Transport Mode Model

A Stated Preference (S.P.) technique is made using a numerical scale and specific information adjusted to the choice of transportation mode, i.e., between commuter line *(KRL)* and motorcycle according to some attributes influencing the choice of transport mode during the pandemic. Differences in total travel time (X_1) and cost (X_2) between commuter lines and motorcycles are factors assessed according to passengers' preferences.

Total travel time for a motorcycle includes preparation time, the delay/waiting time in traffic flow, and trip time. The total travel time for Commuters Line consist of reparation time, waiting

time, queuing time to check health protocols on public transportation operations, and traveling. Total travel costs include parking and fuel cost for a motorcycle, whereas KRL cost comprises ticket price, parking cost, or feeder transport cost from home to station and post-trip (from station to destination place).

Before analyzing the transport mode choice data, firstly, correlation coefficient test (R) and t-test were carried out. After testing the hypothesis by calculating the coefficient correlation (R) and t-test, the model of transport mode choice is carried out by applying the binomial logit model to get the respective probabilities of each transport mode. The choice probability of each mode is obtained by using the equation:

$$U1 - U2 = b0 + bn\ (\Delta X) \quad (1)$$

$$P_1 = \frac{e^{U_1}}{e^{U1} + e^{U2}} \quad (2)$$

$$P_1 = 1 - P_2 \quad (3)$$

which is

$U_1 - U_2$ = Utility function of transport mode
b_0 = constant
b_n = coefficient
ΔX = difference of each attribute
P1 = the probability of Commuter Line choice
P2 = the probability of motorcycle mode

RESULTS AND DISCUSSIONS

Motorcyclist Characteristics, Behavior and Travel Characteristics

Passengers' characteristics can be explained as informed in Table 1. Respondents are male (> 53% for each route) in 17-25 years (52.8%) and 26-35 years (42.05%), meaning that passengers can pay the ticket and as private employees and university students. They have background education graduating high school and bachelor's degrees. They have an income of 4.5-7.5 million IDR and spend transport costs in a month ± 250.00-500.00 IDR (44-47%) and 500.00- 1 million IDR (30-34%).

Passengers of Commuter Line mostly are clarified working at the private company (35.13%) and university students (38.97%) who need a morning and evening peak hour trip. This situation should be arranged by managing less waiting time and checking healthy protocol in peak hours to reduce queuing at Commuter Line stations.

Table 1 informs that the travel time required by Commuter line passengers is more than 60 minutes for one trip, i.e., 64.62% for travel time before the pandemic, 69.23% during the pandemic, and 71.79% new normal period. It means that checking healthy protocol needs 5-10 minutes for each passenger.

Transportation costs are 250,000-500.000 IDR during three conditions. However, there is an increase in travel costs below 250,000 IDR during the lockdown and new normal, due to the social restrictions causing some activities to be limited, such as office activities done from home, and so on as well as lead to lower transportation costs.

Uncertain frequency is dominated by Commuter Line passengers, approximately 61.28%, 72.31%, and 70.26% during before pandemic, lockdown, and new normal conditions. Some activities are allowed to be done during the new normal, increasing the frequency 1-2 times a week.

The reasons for respondents choosing to use the Commuter Line are cost and travel time for all conditions. In addition, respondents also paid attention to safety and health factors, humanitarian factors, especially during the lockdown, and new normal trips.

Feeder transport mode mostly used by Commuter Line passengers is online motorcycle mode, which is 62.31% before pandemic decreasing 51.79% during the lockdown and new normal trips. Furthermore, the use of motorcycles increases during the lockdown and new normal trips related to safety and health reasons and flexible transport mode. Reasons for cost and travel time also dominate respondents in choosing feeder transport mode.

Table 1 Trip characteristic of Commuter line passengers

Trip characteristic	a. Travel time (Minutes)				
	< 30	30-60	>60		
Normal	5.9 %	29.5%	64.6%		
Lock down	4.9 %	25.9%	69.2%		
New normal	4.1 %	24.1%	71.8%		
	b. Travel cost (IDR)				
	<250,000	250,00-500,000	500,000-1 million	>1 million	
Normal	16.41%	45.64%	34.36%	3.59%	
Lock down	21.28%	47.44%	30.00%	1.28%	
New normal	21.03%	44.10%	32.31%	2.56%	
	c. Frequency to use Commuter Line				
	Every day	1-2 times	3 times	>3 times	Uncer tain time
Normal	5.64%	5.62%	5.38%	22.1%	61.3%
Lock down	3.08%	7.6%	4.36%	12.6%	72.3%
New normal	3.33%	9.2%	1.54%	12.3%	71.5%
	d. Reason to choose commuter Line				
	Travel time	cost	comfort	Fix schedule	Safe and health
Normal	64.36%	81%	14.36%	37.95%	5.9%
Lock down	62.56%	81%	16.41%	36.67%	8.97%
New normal	62.05%	80%	17.95%	37.44%	9.49%
	e. Feeder transport mode				
	car	Motorcycle	bike	Online vehicle	Other modes

Normal	3.33%	27.95%	0.26%	62.31%	6.2%
Lock down	7.18%	34.87%	0.77%	51.79%	5.38%
New normal	7.18%	34.36%	0.77%	51.79%	5.90%

f. Reason to use feeder transport mode

	Travel time	cost	comfort	Fix schedule	Safe and health
Normal	74.6%	77.4%	16.67%	22.82%	9.49%
Lock down	74.4%	77.4%	16.41%	16.41%	13.59%
New normal	74.6%	75.4%	18.97%	22.56%	14.87%

g. Impact of KRL operational

	More Travel time	Less comfort & safety	Inflexible time	Queuing at station	Healthy protocol problem
Normal	74.6%	64.36%	55.1%	63.85%	14.62%
Lock down	69.5%	26.92%	51.3%	84.1%	14.62%
New normal	69.7%	24.62%	51,5%	84.1%	14.87%

h. Passenger preference to healthy protocol

	Agree	Not agree
Normal	97.18%	2.82%
Lock down	96.67%	3.33%
New normal	95.38%	4.62%

i. Realizing healthy protocol by using

	Standard mask	Keep the distance	No talk in KRL	Washing hand	Bring hand sanitizer
Normal	92.6%	51.03%	85.1%	70.77%	51.03%
Lock down	93.1%	49.74%	85.4%	72.05%	52.05%
New normal	93.9%	54.62%	86.9%	69.23%	46.15%

j. Transport mode choice due to implementing the healthy protocol

	Using KRL	Split to motorcycle	Split to other public transport
Normal	74.62%	18.46%	6.92%
Lock down	75.90%	16.15%	7.95%
New normal	64.62%	26.15%	9.23%

Based on Table 1, the pandemic's impact on the operation of the Commuter Line is the queuing at the station, increasing from 63.85% to 84.10%. Increasing queues at the stations are due to restrictions of Commuter Line operations such as transport capacity causing longer waiting time in checking healthy protocol.

Respondents' preferences for implementing social restrictions and health protocols in Commuter Line operations are agreed, 97.18% and 96.67 % during the lockdown and new normal. Health-protocols are done by passengers using a standard mask, no talk inside commuter line, washing hands, and keeping a safe distance from other passengers.

Most of the respondents' behavior due to applying health protocols in Commuter Line operation is to continue using Commuter Line. Meanwhile, there is a significant increase of some respondents using or split to a motorcycle.

The change of Transport Mode

Based on descriptive analysis of passenger characteristics in trip characteristics, cost and travel time are expected as major factors in transport mode choice. Other factors are comfort, and safe and healthy significantly increase during the lockdown and new normal because passengers consider humanitarian factors in realizing healthy protocol using commuter Line.

To develop the mode choice model, the researcher uses total travel time (X_1) and cost (X_2) to be assessed according to passengers' preferences by applying a binomial logic model.

Correlation analysis was done, and the results are informed that R values are more than 98% of travel time and cost attributes for three routes. With significance value (α), 0.05, the t-test values are more than the t-test standard, 1.9787 for travel time and cost variables for all routes. The utility model will determine the probability of each transport mode chosen between the Commuter Line and motorcycle.

A. The Change of Travel time variable (ΔX_1)

a. Bekasi-Jakarta route:

The utility function can be determined based on statistical analysis in Table 2.

Table 2. Significance values of each attribute ΔX_1

Variabel	Nilai	Std Error	t Hitung	Siginifikasi (a =0,05)	
Konstanta(b_o)	0,503	0,0380	13,376	0,0010	Signifikan
Koefisin(b_{Δ})	-0,059	0,0030	-22,232	0,0000	Signifikan
R	0,997				
R^2	99,40%				
t Tabel	1,9787				

The probability of commuter line choice is set as follows:

$$P_{KRL} = \frac{e^{0.503 - 0.059\ \Delta X1}}{1+e^{0.503 - 0.059\ \Delta X1}} \quad (4)$$

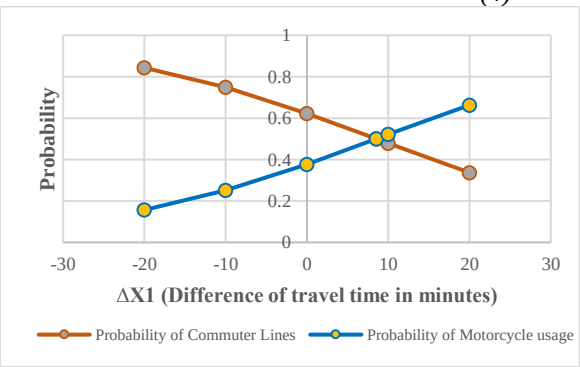

Fig. 2 Transport mode choice model based on travel time variable for Bekasi-Jakarta route

Fig. 2 explains the travel time change between Commuter Line *(KRL)* and motorcycle (MC). Passenger tends to choose KRL within the difference of travel time less than 8.525 minutes. It means that the Commuter Line system is expected to have higher speed and less waiting time than a motorcycle. This result is in line with the fact that consumers prefer to choose flexible transportation modes with minimum travel time.

b. Bekasi-Depok route:

$$P_{KRL} = \frac{e^{0.845 - 0.056\ X1}}{1+e^{0.845 - 0.056\ X1}} \quad (5)$$

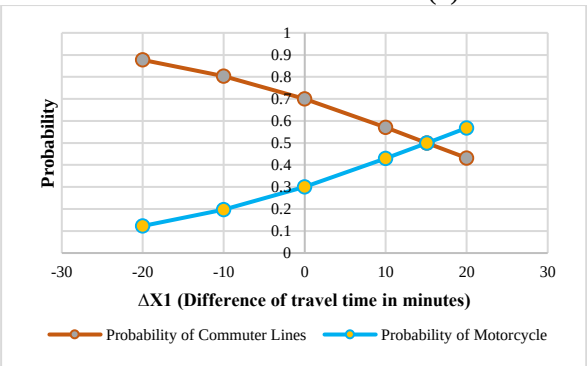

Fig. 3 Transport mode choice model based on travel time variable for Bekasi-Depok route

Fig. 3 explains that a balance situation is obtained between Commuter Line and motorcycle probability with a ratio of 50% for each transport mode if the difference in travel time (X1) is 15.09 minutes. Similar analysis with other routes, the difference of travel time between Commuter Line *(KRL)* and motorcycle (MC) less than 15.09 minutes, passengers prefer to choose KRL.

c. Bekasi-Bogor route:

$$P_{KRL} = \frac{e^{0.848 - 0.058\ X1}}{1+e^{0.848 - 0.058\ X1}} \quad (6)$$

Equation (6) explains the change of travel time between Commuter Line *(KRL)* and motorcycle (MC). Passengers tend to choose KRL within the difference of travel time approximately 0-14.62 minutes. It shows that respondents use KRL within a travel time of fewer than 15.09 minutes.

B. The Change of Travel Cost variable (ΔX_2)

a. Bekasi-Jakarta route:

Travel cost attribute affects a utility function for mode choice, which can be determined based on statistical analysis in Table 3.

Table 3. Significance values of each attribute ΔX_2

Variabel	Nilai	Std Error	t Hitung	Siginifikasi (a =0,05)	
Konstanta (b_o)	0,471	0,0160	28,595	0,0000	Signifikan
Koefisin (b_n)	-0,001	0,0000	-47,134	0,0000	Signifikan
R	0,999				
R^2	99,00%				
t Tabel	1,9787				

The probability of commuter line choice is set as follows:

$$P_{KRL} = \frac{e^{0.471 - 0.001\ \Delta X2}}{1+e^{0.471 - 0.001\ \Delta X2}} \quad (7)$$

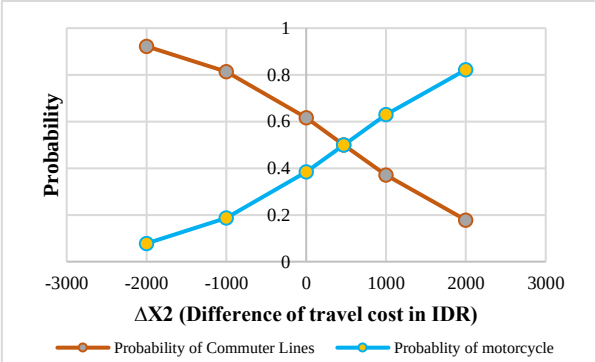

Fig. 4 Transport mode choice model based on cost variable for Bekasi-Jakarta route

Fig. 4 informs the probability of choosing KRL and motorcycles based on travel cost variables. Passengers will choose KRL with differences of travel cost minimal 471 IDR. It means that government should be subsidized Commuter Line up to passenger ability to pay the ticket.

b. Bekasi-Depok route:

$$P_{KRL} = \frac{e^{0.785 - 0.001 X2}}{1+e^{0.785 - 0.001 X2}} \quad (8)$$

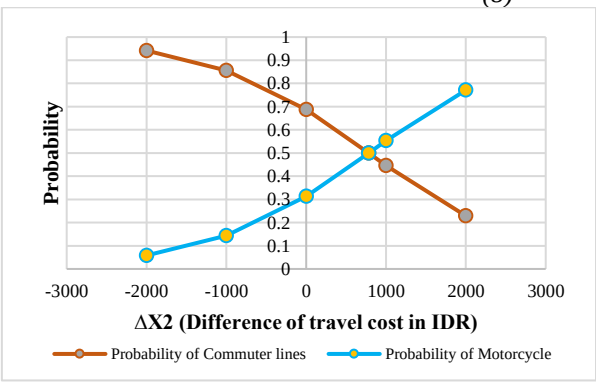

Fig. 5 Transport mode choice model based on travel cost variable for Bekasi-Depok route

Fig. 5 shows that a balance situation is obtained between Commuter Line and motorcycle probability with a ratio of 50% for each transport mode if the difference in travel cost (X2) is 785 IDR.

c. Bekasi-Bogor route:

$$P_{KRL} = \frac{e^{0.798 - 0.001 X2}}{1+e^{0.798 - 0.001 X2}} \quad (9)$$

Equation (9) explains that passengers tend to choose Commuter Line within the difference of travel cost approximately minimal 798 IDR. It

means that respondents will use Commuter Line to make a trip activity with a cost difference of less than 798 IDR.

CONCLUSIONS

The majority of Commuter Line passengers are male (> 53% for each route), aged 17-25 years (52.8%) and 26-35 years (42.05%) high school and bachelor degree for education background high school and bachelor degree. They are explained working at the private company and university students who need a trip in the morning and evening peak hour.

Travel time is more than 60 minutes for one trip for three conditions. It means that checking healthy protocol needs 5-10 minutes for each passenger. The reasons for respondents choosing to use the Commuter Line are cost and travel time for all conditions. In addition, respondents also paid attention to safety and health factors, especially during the lockdown and new normal trips. Here, the use of motorcycles increases during the lockdown and new normal trips related to safety and health reasons and as a flexible transport mode. The impact of the pandemic on the operation of the Commuter Line is the increase in queuing at the station. Increasing queues at the stations are due to restrictions of Commuter Line operations such as transport capacity causing longer waiting time in checking healthy protocol. Furthermore, the government should ensure proper hygiene practices for public transport operators.

By considering the difference of travel time and cost between Commuter Line and motorcycle, passenger tends to choose Commuter line within the difference of travel time approximately 8.525, 15.09 and 14.62 minutes, as well as travel cost minimal 471, 785 and 798 IDR for Bekasi-Jakarta, Bekasi-Depok, and Bekasi-Bogor routes respectively.

The probability choice model between the Commuter Line and other motorized vehicles can be set as a reference to operate the Commuter Line during the pandemic. The study results can be recommended for further studies in predicting the potency of passengers demand with considering humanitarian factors influencing the use of Commuter Line during the pandemic.

ACKNOWLEDGMENTS

Thanks to Rizky Pratama, the bachelor student in the Department of Civil Engineering, Brawijaya University, for collecting and process data.

REFERENCES

[1] Pratandari, S. 2019. Analysis of factors influencing people's behavior in choosing public transport Commuter Line Indonesia (Bachelor's thesis, FISIP UIN Jakarta).

[2] Dianawati, F., Hanif, H. and Maiciptaani, L. 2019. December. Strategy of service quality improvement for commuter line Jabodetabek train using integration methods of SERVQUAL and Kano Model into the house of quality. In *AIP Conference Proceedings* (Vol. 2194, No. 1, p. 020021). AIP Publishing LLC.

[3] Mogaji, E. 2020. Impact of Covid-19 on transportation in Lagos, Nigeria, *Transportation Research Interdisciplinary Perspectives* 6 (2020) 100154.

[4] Parady, G., Taniguchi, A., Takami, K. 2020. A Travel behavior changes during the Covid-19 pandemic in Japan: Analyzing the effects of risk perception and social influence on going-out self-restriction, *Transportation Research Interdisciplinary Perspectives* 7 (2020) 100181.

[5] Citroën, P. 26 March 2020. https://www.globalrailwayreview.com/article/98741/covid19-european-rail-supply-industry/ [Assessed on October 27, 2020].

[6] Das, M., New Delhi | Updated on April 22. 2020 Published on April 22, 2020. https://www.thehindubusinessline.com/economy/logistics/covid-19-impact-36-drop-in-railways-cargo-in-early-april/article31407380.ece# [Assessed on October 27, 2020] .

[7] Parker, M. E., Li, M., Bouzaghrane, M. A., Obeid, H., Hayes, D., Frick, K. T., & Chatman, D. G. (2021). Public transit use in the United States in the era of COVID-19: Transit riders' travel behavior in the COVID-19 impact and recovery period. *Transport Policy*.

[8] Anwari, N., Ahmed, M. T., Islam, M. R., Hadiuzzaman, M., & Amin, S. (2021). Exploring the travel behavior changes caused by the COVID-19 crisis: A case study for a developing country. *Transportation Research Interdisciplinary Perspectives*, *9*, 100334.

[9] Shafi, R., Delbosc, A., Rose, G., 2020. Travel attitudes and mode use among Asian international students at an Australian university. *Transportation Research Part D*, 80, 102259.

[10] Ambarwati, L. and Indriastuti, A.K. 2019. Improvement of Public Transport to Minimize Air Pollution in Urban Sprawl. *Geomate International Journal*, *17*(59), pp.43-50.

11th Int. Conf. on Geotechnique, Construction Materials & Environment,
Kyoto, Japan, 3-5 November 2021, ISBN: 978-4-909106063 C3051

PREDICTION OF THE COMPRESSIVE STRENGTH OF FOAM CONCRETE USING THE ARTIFICIAL NEURAL NETWORK

Husnah[1], Rahmat Tisnawan[2], Harnedi Maizir[3] and Reni Suryanita[4*]
Fakultas Teknik, Universitas Abdurrab, Pekanbaru, Indonesia[1,2]
Fakultas Teknik, Sekolah Tinggi Teknologi Pekanbaru, Pekanbaru, Indonesia[3]
Fakultas Teknik, Universitas Riau, Pekanbaru, Indonesia[4*]

ABSTRACT

Foam concrete experiments require a lot of time and money. Therefore, a brand new modeling system is needed. A system which is not depending on the experiments but can predict the strength of foam concrete accurately. In this study, an Artificial Neural Network (ANN) was used as a solution to predict the compressive strength of foam concrete. The ANN method uses the feed-forward backpropagation architecture and the Levenberg-Marquardt training algorithm it consists of three layers, namely the input layer, hidden layer, and output layer. The input layer consists of cement, sand, water, foam, slum flow, and density, while the output layer consists of the compressive strength of foam concrete. The number of data used in this study was 90 data. The results indicated that the Artificial Neural Network had 6 input layer neurons, 13 hidden layer neurons, and 1 output layer neurons and they had an accuracy rate of 98.7%. It can be concluded that the Artificial Neural Network method can be used to predict the strength of foam concrete with an accuracy level close to 100 percent.

Key Words: Foam Concrete, Backpropagation, Artificial Neural Network, Compresive Strength, Accuracy Level

INTRODUCTION

Foam concrete is a type of lightweight concrete widely used in building construction. The use of foam concrete is apparently the latest innovation in building construction material since foam concrete is lighter and more environmentally friendly, starting from the manufacturing process to its implementation. Foam concrete, one type of lightweight concrete, consists of Portland cement or mortar which has a hollow structure formed from air bubbles and has a specific gravity of (400 – 1,600) kg/m^2 [1]. Foam concrete is used as a temperature and sound insulation material and is easy to produce. The use of foam concrete in civil building construction should be carefully and effectively planned, as foam concrete must be able to fulfill the required technical specifications [2], therefore the right mixture composition is essentially needed to be applied to civil building construction. The composition of the foam concrete material mix will greatly affect its weight and strength, thus it is necessary to test the properties of the material and produce test samples in the laboratory [3]. The foam concrete sample is tested using a free compressive strength test. This test requires a large number of test samples, this is not efficient and it takes a long time, also this experimental test is not able to describe the relationship between the components of the foam concrete mixture and the compressive strength produced. Therefore, Artificial Neural Network (ANN) is able to classify complex input-output relationships in foam concrete mixtures accurately. The use of ANN has been researched extensively in recent years to predict lightweight concrete. However, there are not many prediction foam concrete. For instance, the use of ANN on lightweight bricks[4], high-performance foam concrete [5], and porous concrete [6] and the research on multivariate adaptive regression splines optimized by water on foamed cellular lightweight concrete (FCLC)[7], the SVM method on lightweight foam concrete (LFC)[8]–[10] and the use of genetic programming in foam concrete[11].

This study predicts the compressive strength of foam concrete with varied constituent materials consisting of mortar and foam which has a complex impact on foam concrete properties using ANN. This study used ANN as a method of predicting the composition of foam concrete constituent materials fulfilling the requirements of a density value and it is smaller than the specific gravity of water and the compressive strength of foam concrete that can be determined before being applied. Although many studies have been devoted to predicting foam concrete, we need to pay more attention to the compressive strength of foam concrete, not to that of the density of foam concrete. The foam concrete has its main advantage, the lightweight. Thus the foam concrete will float if it is immersed in water.

This paper reports the results obtained from predicting the compressive strength of foam

concrete using the ANN method which fulfills the requirements for foam concrete density thus it can be applied in fields that require light construction. The benefit of this study is that it can predict the compressive strength of lightweight foam concrete without conducting experimental research that requires a lot of costs and a long time.

LITERATURE REVIEW

Previous research that has been done to predict foam concrete is in research [7] on foamed cellular lightweight concrete, by developing and evaluating the Multivariate Adaptive Regression Splines optimized using Water Cycle Algorithm (MARS-WCA) model. which this study has a weakness in modeling optimization so that it takes an artificial intelligence-based method with an algorithm with high-speed convergence. In addition, there is also a lightweight Foamed Concrete (LFC) study with a Support Vector Machine (SVM)[8] which adopts a radial basis function characterized by a minimum mean squared error relative to other functions and traditional regression. This study reports having a minimum standard deviation so that the prediction results get high precision values at all points in the data set. The research proposed by previous researchers such as [5], [8], [9], [12], [13],[14] all predicts the compressive strength of foam concrete to study quickly and more accurately in improving the performance of methods that predict the strength of the foam concrete. Compressive strength of foam concrete without considering the effect of density on foam concrete where the predicted foam concrete not only has the targeted compressive strength of foam concrete but also lightweight foam concrete. Therefore, this study offers to explore the use of ANN with the backpropagation (BP) algorithm. The neurons have activation according to formulas (1) and (2).

$$net_k = \sum W_{kj}\, O_j \qquad (1)$$

$$Y_k = f(net_k) \qquad (2)$$

netk is the activation of k neurons, j sets of neurons in the previous layer. Wkj of the connection between neuron k and neuron j is the output of neuron j, and yk is the output that can be calculated in both sigmoid and logistic transfer functions. The ANN structure can be seen in Figure 1 Artificial neural network architecture with 3 layers, namely 6 inputs, 13 hidden nodes, 1 output

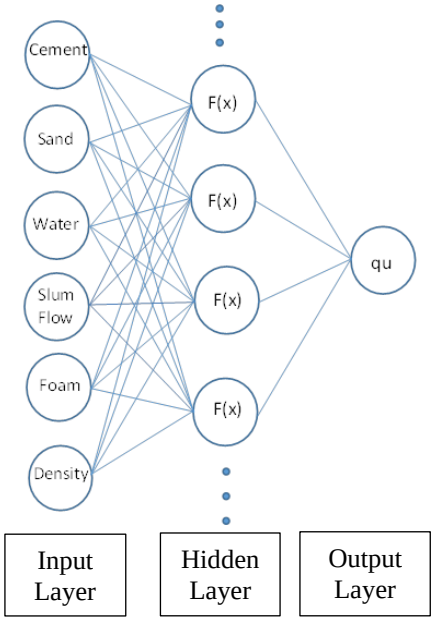

Fig. 1 Artificial neural network architecture with 3 layers, namely 7 inputs, 8 hidden nodes, 1 output

The author also refers to research [6] that uses an artificial neural network model with the Levenberg Marquardt (LM) algorithm that will be used in this study where the LM algorithm can capture complex interactions between input/output variables in a system without prior knowledge of the nature of the interaction. and without having to explicitly assume a model. The research describes the existing research data, data selection, network model training process, and validation. The results showed that the compressive strength of porous concrete can be predicted more accurately, easily, and quickly from the density of porous concrete, the ratio of sand and cement, and the distribution of sand particle size. According to [8],[15] the neural network method has good performance in overcoming the problem of nonlinear data, but the neural network has limitations in dealing with high noise data. So to solve this problem, a bagging method is needed to reduce data noise in the neural network method. In the question of estimating the compressive strength of the concrete lifted, this study combines the bagging and neural network methods to estimate the compressive strength of foam concrete.

METHODS

Experimental data were obtained from experimental research results from Abdurrab University in collaboration with Riau University. The data used in this study were 90 samples of foam concrete with variations of cement, sand, and foam which were used to test the predictive model of the ANN method. The back-propagation algorithm. This

research uses input data, namely cement, sand, water, slum flow, foam, and density. While the target is the free compressive strength of foam concrete. This input and target data are for training with ANN. Training with ANN is carried out using the MATLAB R2021a software with the following stages:

a. Initialize input and target
b. Normalization of input and target data
c. ANN initialization

The ANN used is feed-forward with a total of 13 hidden layer nodes, the activation function from the input layer to the hidden layer is tansig and the Levenberg -Marquardt ANN algorithm.

d. Determination of training parameters
e. Training process
f. Display final weight
g. Saving ANN, the Best network will be used

4. RESULTS AND DISCUSSION

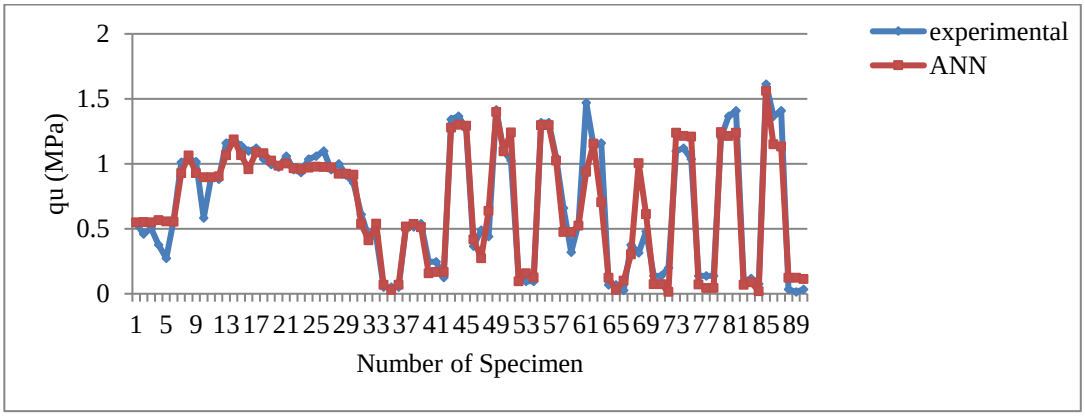

Fig. 2 ANN calculation result with experimental data

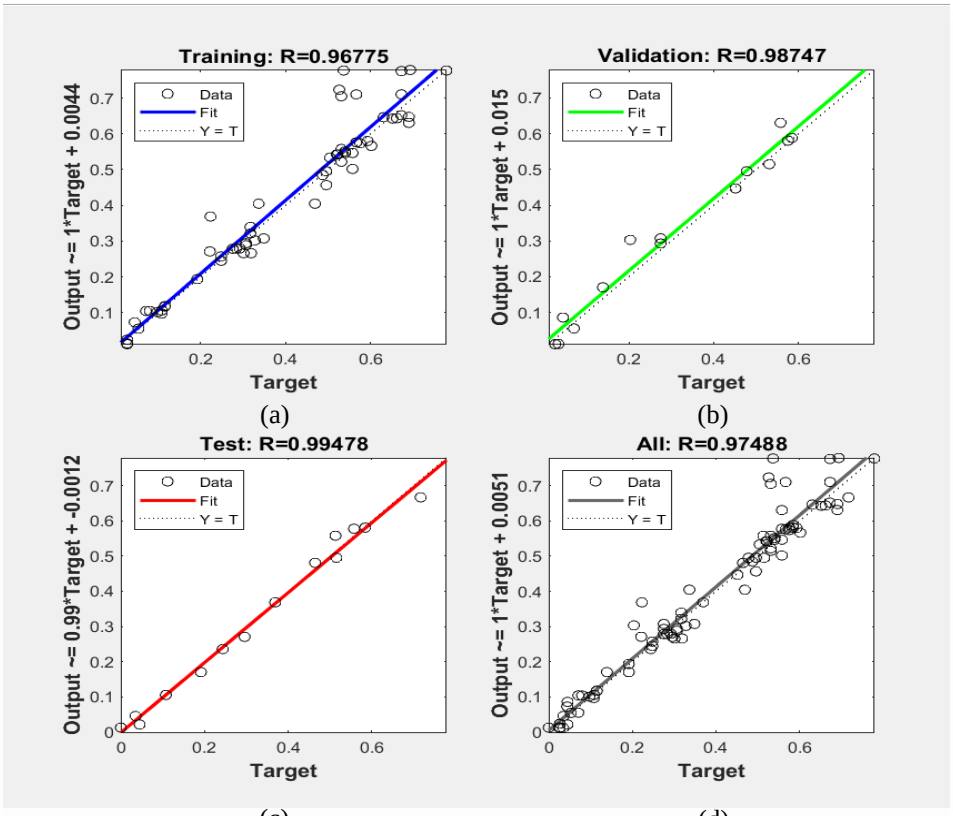

(a) (b) (c) (d)

Fig. 3 Training, validation, test and all regresion plot in matlab to predict the compressive strength of foam concrete

Figure2. shows the prediction results with experimental data using ANN with 13 hidden nodes, it can be seen that the prediction results of the compressive strength of foam concrete using

primary data as input as many as 90 samples did not deviate too far from the results of the tests carried out. This shows that the developed ANN can predict the effect of the composition of the constituent elements on the compressive strength of foam concrete with an acceptable level of accuracy.

Figure 3 shows that for training and validation with ANN using 13 hidden nodes, the R-value (coefficient of determination) is 0.96775 and 0.98747, respectively. This R-value shows the relationship between the output and the target in the training and validation process. An R-value that is more than 0.97, means that the amount of training data that has been recognized is large. So it shows that the output data generated in the training and validation is close to the target data entered in the ANN. While the blue and green fit lines which are close to the dotted line indicate that the Y value (output) is also close to the T value (target).

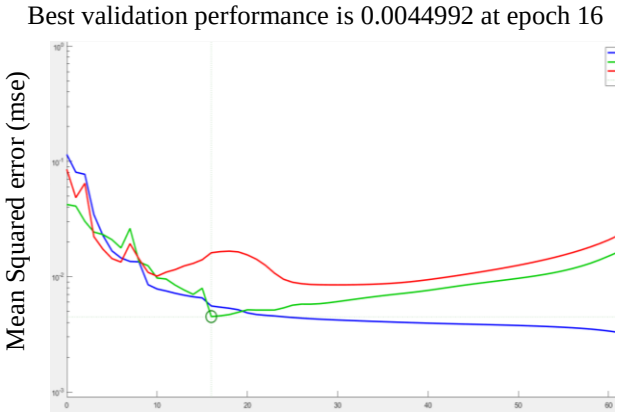

Fig. 4 Error value: Best Validation Performance vs Mean Square Error (MSE)

Figure 4 shows that the results of training and data testing using ANN have produced the best error value (Mean Squared Error, MSE) of 4.4992×10-7. ANN will be of good value if the MSE value is close to 1. From the training using input data from primary data by varying the hidden node ANN, the results of the mean square error of training and validation are obtained. as shown in figure 4. It can be seen from the training results that the number of hidden nodes 13 obtained the smallest validation mean square error, then hidden node 13 had the best training MSE value. Thus ANN can be trained to recognize the compressive strength of foam concrete with this architecture. The architecture of this network is 6 neurons in the input layer, 13 neurons in the hidden layer, 1 neuron in the output layer. Therefore, the network used in this study is a network with 13 hidden nodes. The ANN architecture used can be seen in Figure 1.

The results of this ANN research are strongly influenced by the input data and the target that becomes the learner in ANN training takes a long time to get the best training results. Forecasting research conducted [7] the most recently conducted there are limitations in terms of the combination of materials and components of the mixture. One of the drawbacks of the MARS-WCA model is that its implementation is time-consuming due to the parameter setting of modeling optimization. This study resulted in a small mse value which is shown in Figure 4, and the amount of training data that was successfully recognized was large in Figure 3.

CONCLUSIONS

Based on the research and observations that have been carried out on the ANN system for predicting the compressive strength of concrete using feed-forward backpropagation architecture and the Levenberg-Marquardt training algorithm, the best is obtained at hidden node 13, with a validation MSE of 4.4992×10-7, the authors can conclude that by The ANN method can be used to predict the compressive strength of foam concrete based on the input amount of the foam concrete-forming mixture. So that costs in planning the formation of foam concrete can be minimized because they no longer depend on concrete experts who offer services at high prices. The ANN in this study showed that the accuracy of the 90 training data tested reached 98.7%, indicating that the amount of training data that was successfully recognized was large. However, further research is needed to optimize the prediction results of lightweight foam concrete and the required compressive strength of foam concrete.

ACKNOWLEDGMENTS

Gratitude to the Ministry of education and culture research and technology of Indonesia Grant for Higher Education Cooperation Year 2021–2022, and Civil Engineering Study Program at Abdurrab University.

REFERENCES

[1] M. A. O. Mydin and Y. C. Wang, “Mechanical properties of foamed concrete exposed to high temperatures,” *Constr. Build. Mater.*, vol. 26, no. 1, pp. 638–654, 2012.

[2] S. EDARAN and M.-B. U. K. JALAN, “SALINAN.”

[3] T. Triastuti and A. Nugroho, “Pengaruh Penggunaan Abu Sekam Padi terhadap Sifat Mekanik Beton Busa Ringan,” *J. Tek. Sipil ITB*, vol. 24, no. 2, pp. 139–144, 2017.

[4] M. M. Alshihri, A. M. Azmy, and M. S. El-Bisy, "Neural networks for predicting compressive strength of structural light weight concrete," *Constr. Build. Mater.*, vol. 23, no. 6, pp. 2214–2219, 2009.

[5] T. Nguyen, A. Kashani, T. Ngo, and S. Bordas, "Deep neural network with high-order neuron for the prediction of foamed concrete strength," *Comput. Civ. Infrastruct. Eng.*, vol. 34, no. 4, pp. 316–332, 2019.

[6] R. Bayuaji and T. R. Biyanto, "Model Jaringan Saraf Tiruan Kuat Tekan Beton Porus dengan Material Pengisi Pasir," *J. Civ. Eng.*, vol. 20, no. 1, pp. 23–32, 2013.

[7] A. Ashrafian, F. Shokri, M. J. T. Amiri, Z. M. Yaseen, and M. Rezaie-Balf, "Compressive strength of Foamed Cellular Lightweight Concrete simulation: New development of hybrid artificial intelligence model," *Constr. Build. Mater.*, vol. 230, p. 117048, 2020.

[8] A. M. Abd and S. M. Abd, "Case Studies in Construction Materials Modelling the strength of lightweight foamed concrete using support vector machine (SVM)," *Case Stud. Constr. Mater.*, vol. 6, pp. 8–15, 2017, doi: 10.1016/j.cscm.2016.11.002.

[9] Z. M. Yaseen *et al.*, "Predicting compressive strength of lightweight foamed concrete using extreme learning machine model," *Adv. Eng. Softw.*, vol. 115, no. April, pp. 112–125, 2018, doi: 10.1016/j.advengsoft.2017.09.004.

[10] D. Journal, "SUPPORT VECTOR MACHINE (SVM) FOR MODELLING," pp. 29–36, 2015.

[11] B. Kiani, A. H. Gandomi, S. Sajedi, and R. Y. Liang, "New formulation of compressive strength of preformed-foam cellular concrete: an evolutionary approach," *J. Mater. Civ. Eng.*, vol. 28, no. 10, p. 4016092, 2016.

[12] D. Van Dao, H.-B. Ly, H.-L. T. Vu, T.-T. Le, and B. T. Pham, "Investigation and optimization of the C-ANN structure in predicting the compressive strength of foamed concrete," *Materials (Basel).*, vol. 13, no. 5, p. 1072, 2020.

[13] J. Y. Yoon, H. Kim, Y.-J. Lee, and S.-H. Sim, "Prediction model for mechanical properties of lightweight aggregate concrete using artificial neural network," *Materials (Basel).*, vol. 12, no. 17, p. 2678, 2019.

[14] H. Naderpour, A. H. Rafiean, and P. Fakharian, "Compressive strength prediction of environmentally friendly concrete using artificial neural networks," *J. Build. Eng.*, vol. 16, pp. 213–219, 2018.

[15] A. Behnood and E. M. Golafshani, "Predicting the compressive strength of silica fume concrete using hybrid artificial neural network with multi-objective grey wolves," *J. Clean. Prod.*, vol. 202, pp. 54–64, 2018.

11th Int. Conf. on Geotechnique, Construction Materials & Environment,
Kyoto, Japan, 3-5 November 2021, ISBN: 978-4-909106063 C3051

STUDY ON EVALUATION OF HUMAN DAMAGE FROM TSUNAMI CONSIDERED CONGESTION OF EVACUEE

Ken-ichi Fujita[1] and Harumi Yashiro[2]

[1] Faculty of Engineering, Nagasaki Institute of Applied Science, Japan
[2] School of Systems Engineering, National Defense Academy of Japan, Japan

ABSTRACT

In evacuation behavior from tsunami, street-blockage caused by building collapse due to earthquake increase the number of human damage because of decrease of walking speed by congestion of evacuee. When area-wide mesh as macro evaluation is used to evaluate the human damage, the congestion of evacuee has to be appropriately considered. In this study, the stochastically evaluation method of human damage in evacuation from tsunami using area-wide mesh proposed by the authors is extended to the method which can be considered both the congestion of evacuee and relation between the street-blockage and building damage. The congestion is assumed to be occurred from the street-blockage caused by building collapse due to earthquake. The congestion degree is defined by number of people per square meter. The decrease of walking speed in evacuation is expressed by the congestion degree. Moreover, using the proposed method, the variations of the number of the human damage in evacuating from tsunami by difference of the evacuation awareness and the congestion by the street-blockage caused by building collapse are discussed.

Keywords: Tsunami Evacuation, Human damage probability, Congestion, Street-blockage, Area-wide mesh

INTRODUCTION

The damage estimation for large-scale natural disaster caused by earthquake or tsunami which may occur in the future has been carried out in Japan. To reduce the damage caused by the natural disaster, disaster prevention and evacuation plans have been planned by using the estimation results in many municipalities. The evaluation of the human damage in the damage estimation is one of an important item. The human damage for tsunami has been usually evaluated for evacuation behavior from tsunami. However, in many studies and damage estimations on the human damage, the effects of building damage, liquefaction of the ground and street-blockage caused by earthquake have not been considered. The evaluation result of the human damage considering the effect of earthquake damage is considered to be different because walking speed of evacuee is decreased due to obstacles such as rubbles and collapsed objects on evacuation route caused by earthquake.

As the one of the most impact on evacuation from tsunami, street-blockage caused by building collapse is considered. The evaluation of the human damage considering the impact on the street-blockage to evacuation from tsunami in the previous studies can be divided into the following two methods. One is the numerical method such as the multi-agent model, and the other is the method using the area-wide mesh. The authors have proposed a stochastically evaluation method of the human damage using the area-wide mesh [1], [2]. Variances of walking speed and tsunami inundation speed have been considered in the studies. The street-blockage has been represented by decrement of sidewalk width. However, consideration of decrease of walking speed by congestion of evacuee is left for a future work.

This study presents a stochastically evaluation method on the human damage in evacuation from tsunami taking account of the congestion of evacuee. The congestion is assumed to be occurred from the street-blockage caused by building collapse due to earthquake. The congestion degree is defined by number of people per square meter. The decrease of walking speed in evacuation is expressed by the congestion degree. The area-wide mesh is used to visually represent the distribution of the human damage in evacuation from tsunami. Moreover, the variations of the number of the human damage in evacuating from tsunami by difference of the evacuation awareness and the congestion due to the street-blockage are discussed using the proposed method. The originality of this study is in the point of evaluating of the human damage in evacuating from tsunami using stochastically considering variances walking speed and tsunami run-up speed.

OUTLINE OF EVALUATION OF HUMAN DAMAGE

The area-wide mesh is used to set up evaluation conditions and to show evaluation results. Mesh size is 250m x 250m. Population, number of buildings, road network, and geographical conditions are introduced of GIS (Geographic Information System)

data. For seismic intensity and tsunami inundation depth, the average value in mesh area is adopted.

Evacuation distance from evacuation mesh to evacuation facility including the difference of elevation between mesh is assumed to be 1.5 times of length of plane distance between the centers of mesh.

The human damage probability is evaluated by using relation between the evacuation time and the tsunami arriving time after earthquake occurrence. The human damage ratio is evaluated by using the tsunami fragility [3].

The street-blockage is occurred by the building collapse due to earthquake. The blockage ratio is evaluated by using the fragility of buildings for earthquake [4].

The walking speed in evacuation assumed to be decreased by the congestion of evacuee by the street-blockage. The congestion is defined by the number of people per unit area [5].

From the above, the evaluation flow on the human damage in evacuation from tsunami can be shown in Fig.1.

The following assumptions are used in the evaluation.

1) The human damage is counted when person is caught up with tsunami.
2) The evacuation method is only walk. The walking is only permitted on sidewalk.
3) The evacuation direction is not toward to coast.
4) The evacuation facility is designated for each evacuation mesh. The damage of evacuation facilities by earthquake is not occurred.
5) Random variables with respect to speed and time are assumed to follow normal distribution.
6) Mean value of walking speed is only decreased by the effect of the congestion. Standard deviation of the walking speed is assumed to be not variable for the congestion.

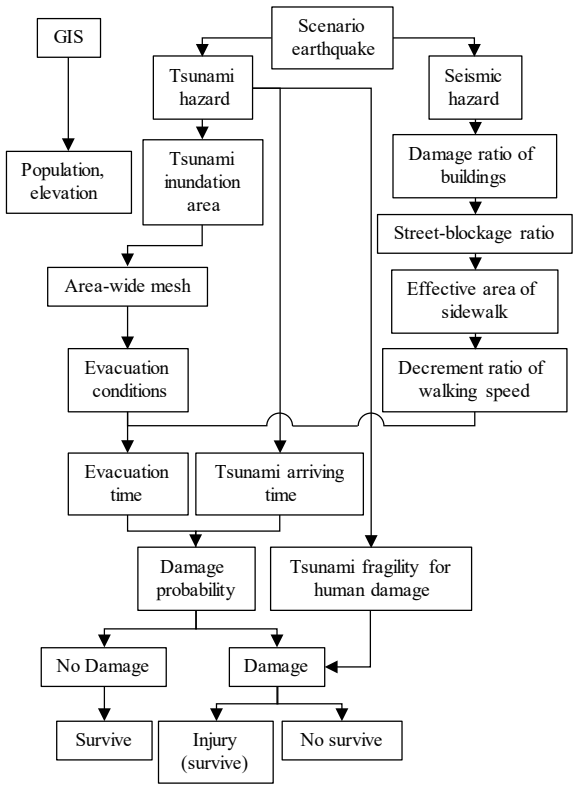

Fig.1 Evaluation flow of human damage

EVALUATION METHOD OF HUMAN DAMAGE

Human Damage Probability

The human damage in evacuation from tsunami is evaluated for each evacuation mesh. The human damage is analyzed by using the difference between total time in evacuation behavior after the earthquake occurrence $F_E(t)$ and the time from tsunami generating to arrival at evacuation facility $F_T(t)$. $F_E(t)$ and $F_T(t)$ are assumed to be follow normal distribution $N(\mu_E, \sigma_E)$ and $N(\mu_T, \sigma_T)$, respectively. It should be noted that μ_E and σ_E are the mean value and standard deviation of T_E and μ_E and σ_E are the mean value and standard deviation of T_T.

The mean values of T_E and T_T are expressed by the following equations;

$$\mu_E = t_S + t_W \tag{1}$$

$$\mu_T = t_P + t_R \tag{2}$$

where, t_S is the start time of evacuation after earthquake, t_W is the mean value of random variables of the walking time T_W obtained by the walking speed and the distance to evacuation facility, t_P is the tsunami propagation time to coast, and t_R is the mean value of random variables of the tsunami run-up time T_R obtained by the run-up speed and the distance to evacuation facility.

The mean values and the standard deviations of t_W and t_R in this study have to be evaluated as the inverse function because the walking speed in evacuation V_{WE} and the tsunami ran-up speed V_T defined as normal distributions are used. The mean value $\mu_{1/X}$ and the standard deviation $\sigma_{1/X}$ of an inverse function of a positive normal variable X with mean value μ_X and standard deviation σ_X are given by the following equations [6];

$$\mu_{1/X} = \left\{1 + \left(\frac{\sigma_X}{\mu_X}\right)^2\right\}\mu_X \tag{3}$$

$$\sigma_{1/X} = \frac{\sigma_X}{{\mu_X}^2}\sqrt{\left\{1 - \left(\frac{\sigma_X}{\mu_X}\right)^2\right\}} \tag{4}$$

The mean value and standard deviation of T_W and

T_R can be evaluated by Eq. (3) and Eq. (4), respectively.

The human damage probability P_D in evacuation can be provided by the following equation.

$$P_D = 1 - \Phi\left(\frac{\mu_M}{\sigma_M}\right) \tag{5}$$

where, Φ is the standard normal distribution function with $N(0, 1)$, μ_M and σ_M are given by the following equations;

$$\mu_M = \mu_T - \mu_E \tag{6}$$

$$\sigma_M = \sqrt{\sigma_T^2 + \sigma_E^2} \tag{7}$$

The survival probability can be obtained by 1-P_D. The survival probability curve and the probability density function of $f_E(t)$ and $f_T(t)$ of probability functions $F_E(t)$ and $F_T(t)$ are shown in Fig.2.

Decrease Ratio of Walking Speed by Congestion

Decrease of walking speed is assumed to be occurred by congestion of evacuee by street-blockage. The decrease of walking speed is evaluated for each evacuation mesh. The street-blockage is occurred by building collapse. Fragility curves of buildings for seismic motion shown in Fig.3 [7] are used to the evaluation of the street-blockage. In Fig.3, C.D. is completely destroyed, C.P.D. is completely and partially destroyed. The fragility is evaluated for each structural type, construction year, and destruction type.

The street-blockage ratio is evaluated for each mesh using destruction ratio of buildings obtained by the fragility curve. Evaluation equation for the street-blockage ratio R_d is given as follows [5];

$$R_d = \begin{cases} 1.28D_{dr} & (W_S < 3m) \\ 0.604D_{dr} & (3m \le W_S < 5.5m) \\ 0.194D_{dr} & (5.5m \le W_S < 13m) \end{cases} \tag{8}$$

where, W_S is the road width and D_{dr} is the destruction ratio given by the following equation [5];

$$D_{dr} = D_{cr} + \frac{D_{pr}}{2} \tag{9}$$

where, D_{cr} and D_{pr} is the completely and the partially destruction of building, respectively, which can be evaluated by using the fragility. The width of street-blockage W_{sb} can be obtained by multiplying D_{dr} and W_s.

The decrease ratio R_{wd} of the walking speed by the congestion is evaluated for each mesh by the following procedure.

1) Evaluating the sidewalk area in usual condition A_{sw} by subtracting the roadway area A_r and the road shoulder area A_{rs} from the total road area in mesh.
2) Evaluating the sidewalk width in usual condition W_{sw} by dividing the side walk area A_{sw} by the road length L_r in mesh.
3) Evaluating the sidewalk width by the street-blockage W_{swb} by the difference between W_{sw} and W_{sb}.
4) Evaluating the sidewalk area considered the street-blockage A_{swb} by multiplying W_{swb} and evacuation route length in mesh L_r.
5) Evaluating the congestion degree R_c by dividing population in mesh N_p by A_{swb}.

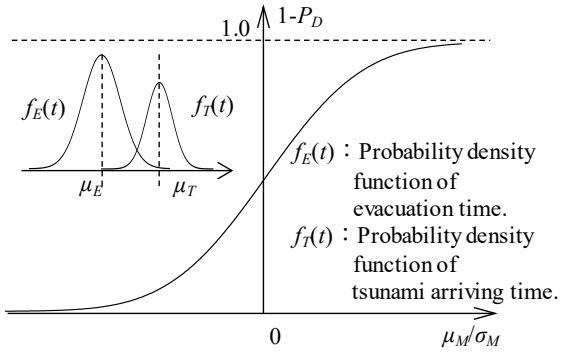

Fig.2 Survival probability curve

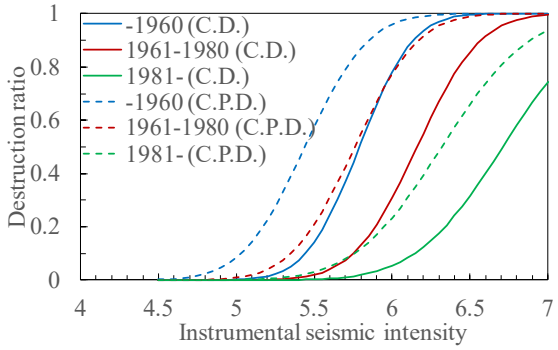

(a) Wooden structure

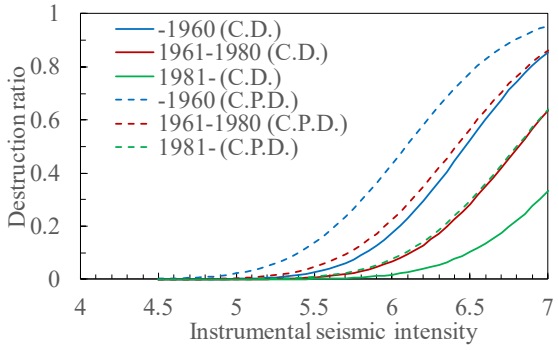

(b) Non wooden structure

Fig.3 Fragility curve for buildings

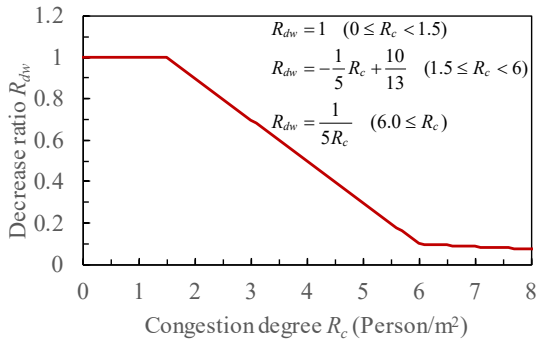

Fig.4 Decrease ratio of walking speed

6) Obtain the decrease ratio of the walking speed R_{wd} by using R_c.
7) Evaluating the mean value of walking speed in evacuation v_{WE} by multiplying the mean value of walking speed in usual condition v_W and R_{wd}.

The relation between decrease ratio of the walking speed R_{wd} and the congestion degree R_c is given by Fig.4 [5].

EVALUATION OF HUMAN DAMAGE

Evaluation Conditions

The human damage in evacuation from tsunami using the proposed method is discussed by difference of the evacuation awareness and the effect of the congestion by the street-blockage.

The area-wide mesh of a target area is shown in Fig.5. The mesh size is 250m x 250m. The population in mesh and the evacuation facilities are also shown in the figure. The population is 26,250 persons. The population is large in the west and part of the east. Building distribution is shown in Fig.6. The number of buildings is 8,088, wooden buildings is 813 and non-wooden is 7,275. In addition, geographical

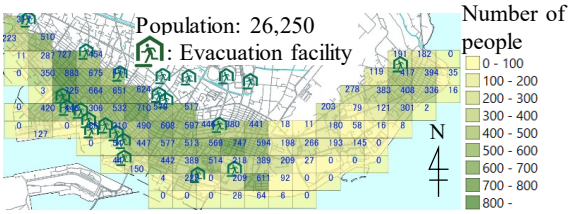

Fig.5 Area-wide mesh and population distribution

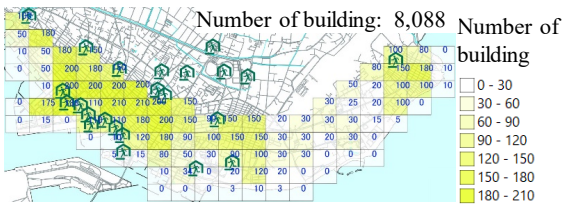

Fig.6 Building distribution

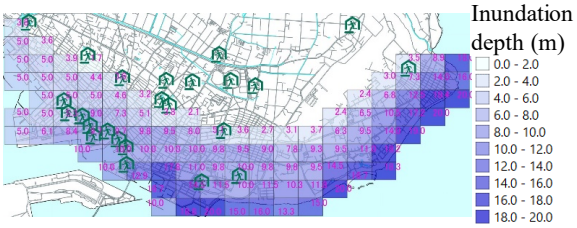

Fig.7 Tsunami inundation depth

condition, hazard map information of tsunami and seismic intensity, and statistical data of the target area are used to the mesh.

Tsunami inundation depth and seismic intensity obtained by damage estimation result for a Yaeyama islands southern offshore earthquake are used [7]. The moment magnitude of the earthquake Mw is estimated to be 9.0.

Tsunami inundation depth is shown in Fig.7. In addition, the maximum tsunami height is 22m and the arriving time of the first wave of the tsunami is 16 minutes [7]. The mean value of tsunami run-up speed v_T is evaluated by using the following equation [8];

$$v_T = 1.1\sqrt{gh} \tag{10}$$

where, g is the gravitational acceleration and h is the inundation depth. The standard deviation σ_T of the run-up speed is assumed $v_T/10$ in this study.

Seismic intensity of the area by the earthquake is 6- which indicates in the range of greater or equal 5.5 and less than 6.0 of measured seismic intensity defined by Japan Meteorological Agency. The destruction ratio of building can be obtained by using fragility curve shown in Fig.8. The destruction is large in west and part of east. The ratios are 0.1 to 0.15 for the mesh with large number of buildings and 0.05 to 0.1 for the mesh with small number of

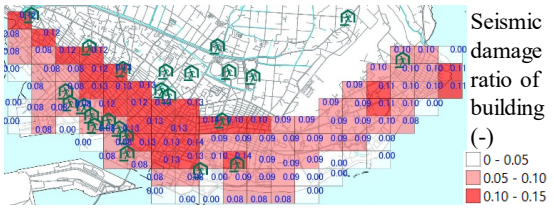

Fig.8 Destruction ratio of building

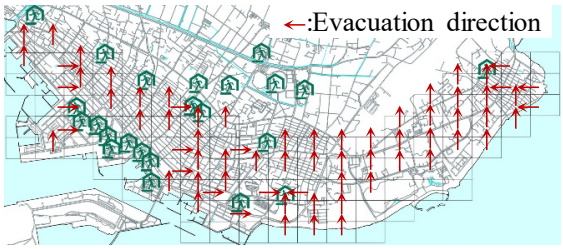

Fig.9 Evacuation route

Table 1 Population ratio for evacuation awareness

Evacuation awareness level	Evacuation behavior			
	Immediately (High)	After work (Low)	Urgency (Low)	No evacuation (Low)
High	80%	10%	5%	5%
Normal	50%	25%	15%	10%
Low	15%	35%	30%	20%

Table 2 start time of evacuation

Immediately	After work	Urgency
5 min.	15 min.	tsunami arriving time

building. The number of completely destroyed building is 404 and that of partially one is 750.

Evacuation routs are shown in Fig.9. The red arrow in the figure is the evacuation direction.

The evacuation behavior is divided into four type: evacuation immediately, evacuation after work, urgency evacuation and no evacuation. The evacuation awareness is categorized into three types; high, normal and low awareness. Population for these awareness is grouped by combining the four types of the evacuation behavior [4]. The population ratio for evacuation awareness is shown in Table 1. The start time of evacuation for several conditions is shown in Table 2.

The mean value v_W and the standard deviation σ_W of walking speeds are used statistical results for middle aged in the previous study [9]. v_W is 1.34m/s and σ_W is 0.167m/s.

Evaluation Results

Evaluation Results without Congestion

The human damage under the condition neither the congestion nor the street-blockage are discussed.

Evaluation results of the human damage distribution for different evacuation awareness are shown in Fig.10 and the number of the human damage is shown in Table 3. Number of the human damage becomes large with decreasing evacuation awareness. The number of the human damage increases in some meshes for high level of evacuation awareness. The number of the damage increases in the west and part of the east for low level of the awareness.

Evaluation Results with Congestion

Evaluation results of the human damage under the condition with the congestion by the street-blockage are discussed.

Table 3 Evaluation results of human damage

Evacuation awareness level	Damaged population (persons)	
	Without congestion	Congestion
High	7,130	9,918
Normal	13,501	15,245
Low	20,941	21,465

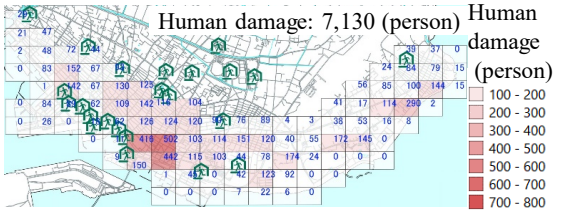

(a) High evacuation awareness

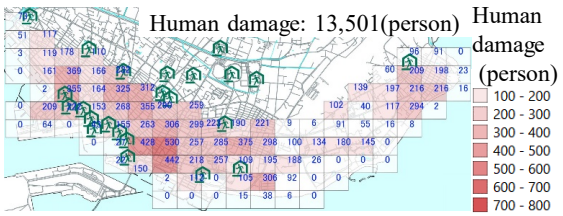

(b) Normal evacuation awareness

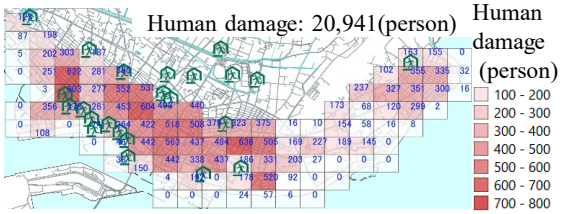

(c) Low evacuation awareness

Fig.10 Human damage distribution without congestion

The congestion degree for each evacuation mesh by the street-blockage caused by the building collapse is shown in Fig.11. The congestion tends to increase in the evacuation mesh with the large number of population and passing the route in the high damage of building. The walking speed in evacuation decreases for the applicable mesh.

Evaluation results of the human damage distribution for different evacuation awareness are shown in Fig.12 and the number of the human damage is also shown in Table 3. The human damage considering the congestion is larger than that of the result without the congestion in spite of difference of the evacuation awareness. The human damage for the high awareness is 1.39 times larger than that of the result without the congestion. For the normal awareness and the low awareness are 1.13 times and

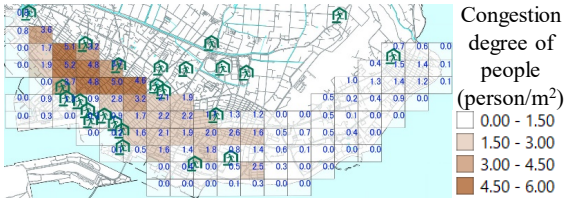

Fig.11 Congestion degree by street-blockage

1.03times larger than those of the results without the congestion. The human damage considering the congestion in the evacuation increases regardless the difference in the evacuation awareness.

CONCLUSIONS

A stochastically evaluation method of the human damage in the evacuation from tsunami considering the congestion due to the street-blockage by the building collapse was presented. The number of the human damage by difference of the evacuation awareness and the congestion are discussed.

The following conclusions can be drawn.

1) The human damage considering the congestion increases than that of the result of without the congestion regardless the difference of the evacuation awareness.
2) The impact of the congestion is especially large. Even if the evacuation awareness is high, the human damage increase due to a decrease in the walking speed.
3) To consider the congestion due to the street-blockage caused by building collapse is important in the evaluation of the human damage in evacuation from tsunami.

The future work of this study is that the validity of the proposed method is verified using comparison with the result of damage estimation using area-wide mesh published by the local government in Japan.

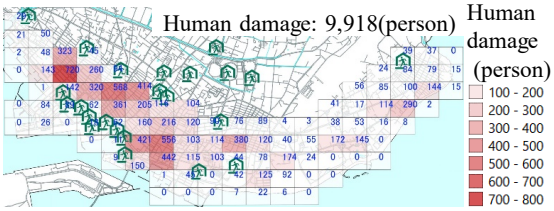

(a) High evacuation awareness

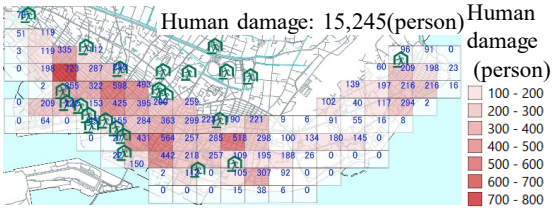

(b) Normal evacuation awareness

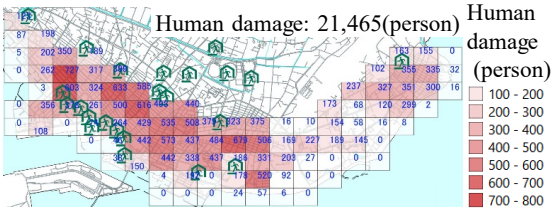

(c) Low evacuation awareness

Fig.12 Human damage distribution with congestion

REFERENCES

[1] Fujita K., and Yashiro H, A Study on Human Damage in Evacuation from Tsunami Considering Street-Blockades Caused by Destroy of Buildings, International Journal of GEOMATE, Vol. 19, Issue 72, 2020, pp.1-7.

[2] Fujita K., and Yashiro H, Human Damage Estimation in Evacuation from Tsunami Caused by a Common Scenario Trench-Type Earthquake, Proc. of the 30th European Safety and Reliability Conf. and the 15th Probabilistic Safety Assessment and Management Conf., 2020, pp.508-516.

[3] Koshimura S., Namegawa Y., Yanagisawa H., Fragility Functions for Tsunami Damage Estimation, Journal of Japan Society of Civil Engineers, ser. B, Vol.65, No.4, 2009, pp.320-331. (in Japanese)

[4] Cabinet office of Japan, Damage Estimation of Nankai Trough Earthquake (1st. Report), 2012. (in Japanese)

[5] Cabinet office of Japan, Simulation Results on Return Home Action, 2007. (in Japanese)

[6] Nakamura T., On the Moment of Positively Truncated Normal Distribution, J. of Japan Statist. Soc., Vol.10, No.2, 1980, pp.139-134. (in Japanese)

[7] Okinawa Pref., website, Report of Survey on Estimation of Earthquake damage in Okinawa Prefecture in 2013, https://www.pref.okinawa.jp/site/chijiko/bosai/h25jishinhigaisoutei.html (Reference: 2021.5.13)

[8] Shuto N, Imamura F., Koshimura S., Satake K., Matsutomi H., eds., Encyclopedia of Tsunami, Asakura Publishing Co., Ltd., 2007. (in Japanese)

[9] Matsumoto N., Kiyota S., Ito M., Relationship between the Characteristics of Streetscape and Walking Speed, Journal of Architecture and Planning, Vol.74, No.640, 2009, pp.1371-1377. (in Japanese)

11th Int. Conf. on Geotechnique, Construction Materials & Environment, Kyoto, Japan, 3-5 November 2021, ISBN: 978-4-909106063 C3051

EXPERIMENTAL STUDIES ON THE TAYLOR-COUETTE FLOW OF SHEAR-THINNING FLUIDS

Yuki TANO, Tatsuya KAWAGUCHI and Takushi SAITO

[1]Faculty of Engineering, Tokyo Tech, JAPAN

ABSTRACT

Two concentric cylinders which rotating inner cylinder make the circumferential flow with Taylor vortex under the certain Reynolds number. It is called Taylor-Couette flow. It has been focused on the extensive study for Newtonian fluids but does not for non-Newtonian fluids since flow transition mechanism is remained and its use in various industrial applications. Many kinds of apparatus using Taylor-Couette flow of redesign and scale up are still under investigation. The objective of the present study is firstly to specify the transition area of the Taylor-vortex flow and Wavy vortex flow with the non-Newtonian working fluid. In the experiment, two type of shear-thinning fluids that have different structural viscosity index. Particle Image Velocimetry (PIV) was employed as the flow visualization technique for a wide range of Reynolds number. Water solution of guar gum (n=0.7) resulted the six-cell stable mode in the range of Taylor-vortex flow and wavy-vortex flow. The other working fluid with Xanthan gum (n=0.52) resulted the vertical oval vortex enlarged to axial direction with the same Reynolds number range. Both results were significantly different from the Taylor-Couette flow with Newtonian fluid. As a conclusion, we confirm that the shear-thinning effects of working fluid affects the vertical oval vortex drafting to axial direction.

Keywords: Non-Newtonian fluids, Taylor vortex Flow, Wavy vortex Flow, Shear-thinning Fluids, Structural viscosity index

INTRODUCTION

Two concentric cylinders in which one or both are rotating make the circumferential flow with Taylor vortex under the certain Reynolds number. It is called Taylor Couette flow. Taylor Couette flow has been applied to various industries including food, chemical, medical fabrication industries and has improved many industrial applications, including filtration[1], protein shearing[2], blood detoxification[3], liquid-liquid extraction[4], bioreactors[5], emulsion polymerization[6], crystallization[7], cultivation of animal cells[5], and photocatalytic reactions[8]. Many industrial applications of Taylor-Couette flow use non-Newtonian fluids. Ashrafi[9] pointed out that in terms of study of complex fluids, Taylor-Couette flow of non-Newtonian fluids plays an important role of rheology in flow instabilities. As mentioned above, there are many case studies on complex fluids and many kinds of apparatus using Taylor-Couette flow of redesign and scale up are still under investigation. Many Taylor-Couette flow-based applications employ shear-thinning fluids and some researchers[9]-[12] have pointed out that there are insufficient experimental data on shear-thinning fluids. From that background, the purpose of this research is to figure out flow transition mechanism for non-Newtonian fluids. The theoretical equation for determining the transition Reynolds number of Taylor Couette flow in Newtonian fluids has been established, but it has not yet been established for non-Newtonian fluids. Therefore, if it becomes possible to identify the transition region and determine the transition Reynolds number theoretically, it will be useful for the design of devices in various industrial fields.

For that reason, the objective of the present study is to specify the transition area of the Taylor-vortex flow and Wavy vortex flow with the shear-thinning fluids using experimental methods.

Taylor-Couette flow has many flow regimes which are controlled by the Reynolds number and has surprisingly complex dynamics. Considering the most common condition, the inner cylinder is rotating and the outer cylinder is fixed. Reynolds number is defined below.

$$Re = \frac{\rho d r_i \Omega}{\mu_{eff}} \tag{1}$$

Where ρ is the fluid density, μ_{eff} is the effective viscosity, Ω is the rotational speed of the inner cylinder, d is the gap between the cylinders, r_i is the inner cylinder radius. One of differences between Newtonian and shear thinning flow is a

circumferential velocity gradient. The shear stress acting on the fluid is given by the following equation.

$$\tau = \mu^* \left(\frac{du}{dy}\right)^n \qquad (0 < n < 1) \qquad (2)$$

where τ is shear stress, μ^* is reference viscosity, u is velocity, y is coordinates perpendicular to the flow, n is structural viscosity index. From the above equation, the velocity gradient boundary layer increases as n decreases, that is, high shear thinning.

Andereck and Swinney[13] observed the flow transitions between states were determined by R_i and R_o(inner- and outer-cylinder Reynolds number). Fig 1[13] shows regimes observed in flow between independently rotating concentric cylinders. In this research, outer cylinder is fixed, flow regimes are Circular-Couette Flow(CCF), Taylor-Vortex Flow(TVF), Wavy-Vortex-Flow(WVF), Modulated-Wavy-Vortex-Flow(MWF) and Turbulent Taylor Vortex Flow. CCF is laminar and axisymmetric at the low Reynolds number. As the Reynolds number is increased beyond a critical value Re_{c1}, the flow becomes unstable and CCF trans to TVF. TVF is dominated by a series of steady toroidal vortices. A second critical Reynolds number Re_{c2} exists and a series of toroidal vortices becomes unsteady and pulsates at a single frequency. This state is WVF. Further increase in Reynolds number is associated with more transitions in which include MWF pulsates at two frequencies, ultimately leading to turbulence.

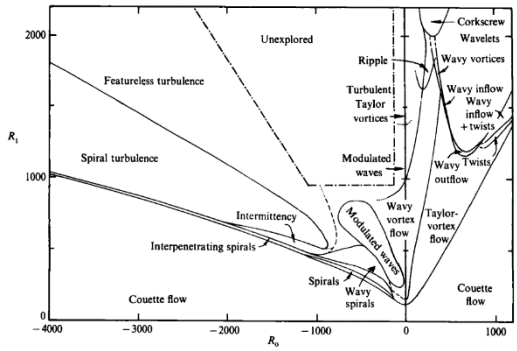

Fig.1 Flow regimes of two concentric rotating cylinder [13]

Study of Taylor-Couette flow was mainly initiated by Taylor[14] for Newtonian fluids, and has been the focus of considerable attention until now. From numerical work of Lockett, Richardson, and Worraker[15], Khali, Nebbali, and Bouhadef[16] and Alibenyahia *et al*[11], Ashrafi[9] predicted that shear thinning characteristic of working fluid lowered the critical Reynolds number for TVF compared with Newtonian fluids using a deterministic approach to analyze the nonlinear flow stability and reported results clearly show the dynamics that is completely different in Taylor-Couette flow of Newtonian fluids and is caused by the shear thinning property of the fluid. Cagney and Balabani[17] examined four fluids with different structural viscosity index(n=1, 0.68, 0.62 and 0.52). Three of them are shear thinning and viscoelastic. They confirmed that shear thinning lowered the critical Reynolds numbers for TVF and WVF compared with Newtonian case and calculated the amplitudes of inflow(moving toward the inner cylinder) and outflow(moving toward the outer cylinder) using particle image velocity measurement(PIV) for TVF and WVF. They reported results that the magnitude of vorticity and the strength of the outflow are both reduced in shear thinning fluids to relative to the Newtonian case. In the WVF for Newtonian fluids, the magnitude of inflow are lower than those at the outflow, but the magnitude of inflow and outflow both tend to be significantly larger for shear thinning fluids. They also observed slow drifts in the axial positions of vortices and spatial variations in the wavy instability which are not observed in Newtonian fluids.

The most parts of dynamics for shear thinning fluids of Taylor Couette flow are still unexplained and needed more experimental data. The previous research[17] got the critical Reynolds number of TVF and WVF for shear thinning fluids. However, elucidation of the mechanism remains an issue for flow mode transition. This paper describes the identification of transition regimes using PIV for shear thinning fluids and have consideration for them.

EXPERIMENTAL DETAILS

The appearance of the experimental device is shown in Fig.2. Cylindrical coordinates, r, θ, z

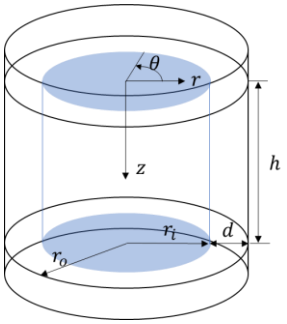

Fig.2 Schematic diagram of experimental equipment

represents the radial, the circumferential, and axial coordinates respectively. The material of the cavity is an acrylic and a water jacket is designed around the outer cylinder. Table 1 shows the dimensions of the experimental equipment. The inner cylinder is connected to the motor driver via a belt. The stepping motor is good for Taylor Couette flow device. In this paper, the velocity distribution was measured by PIV.

A schematic diagram of the PIV experiment is shown in Fig.3. The laser sheet was inserted into the vertical cross section. The tracer particles are DNTEC DYNAMIC S-HGS, Sliver Coated Hollow Glass Spheres. The particle size is 10 μm and the particle density is 0.68 g/cm^3. The shooting frame rate is 500 fps and the resolution is 1280 x 768 pixels. After confirming that the flow was steady, 2177 frames were taken.

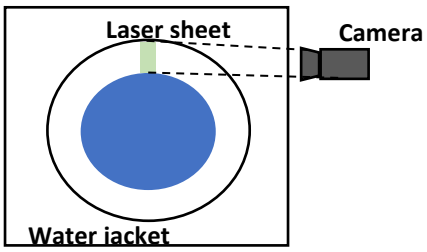

Fig.3 A schematic diagram of the PIV experiment

Table 1 Device dimensions

Parts	Unit
Radius of inner cylinder $\boldsymbol{r_i}$ [mm]	64
Radius of outer cylinder $\boldsymbol{r_o}$ [mm]	80
Height $\boldsymbol{h}$ [mm]	96
Gap $\boldsymbol{d}$ [mm]	16
Radius ratio $\boldsymbol{\eta = r_i/r_o}$	0.8
aspect ratio $\boldsymbol{\Gamma = h/d}$	6

METHOD OF DETERMINING EFECTIVE VISCOSITY

The model of shear-thinning fluid is shown by Eq(2). For Newtonian fluids, the velocity distribution and the viscosity are constant because $n = 1$. However, for shear thinning fluids, the velocity distribution is exponential and the viscosity depends on the shear rate. Determining effective viscosity is required to get effective Reynolds number because the viscosity varies depending on the positions. Masuda, Horie, Hubacz, Ohta and Ohmura [18] suggested method of determining effective shear rate in order to determinate effective viscosity. The effective shear rate is given the following equation.

$$\dot{\gamma}_{eff} = k\Omega \qquad (3)$$

where k is proportional coefficient. The proportional constant is determined by numerical work compared with experimental data. k is shown by following equation and is determined by n and η, but if $\eta \geq 0.7$ it can be effective because wider gap has larger viscosity ratio between inner and outer walls than narrow gap.

$$k(n,\eta) = 77.05n^{0.32}\eta^2 - 88.73n^{0.31}\eta + 26.85n^{0.21} \qquad (4)$$

The effective viscosity is shown using Carreau model by the following equation.

$$\mu(\dot{\gamma}) = \mu_\infty + (\mu_0 - \mu_\infty)(1 + (\lambda_c\dot{\gamma}^2)^{\frac{n-1}{2}} \qquad (5)$$

where μ_0 is zero viscosity, μ_∞ is infinity viscosity λ_c is relaxation time. From the above results, the identification of the transition region is evaluated using the Reynolds number in Eq (1).

RHELOGICAL PROPERTIES

To see how shear thinning influence flow field, two fluids are made with different structural viscosity index which are guar gum 0.1%wt(n=0.7) and xanthan gum 0.05%wt(n=0.52). The two fluids were prepared by mixing them at 700 rpm for 30 minutes using a stirrer with blades and then storing them in the refrigerator for one day. The rheological properties of both fluids were measured with a rheometer. The measurement results are shown in Fig.3 and Fig.4, and the important parameters in this paper are shown in Table 2. The shear rate band in this research is 10~150.

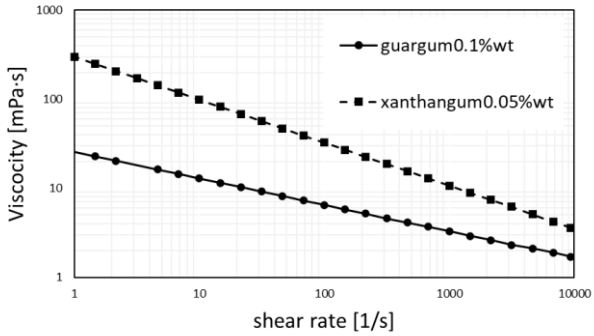

Fig.4 Viscosity v.s. shear rate.

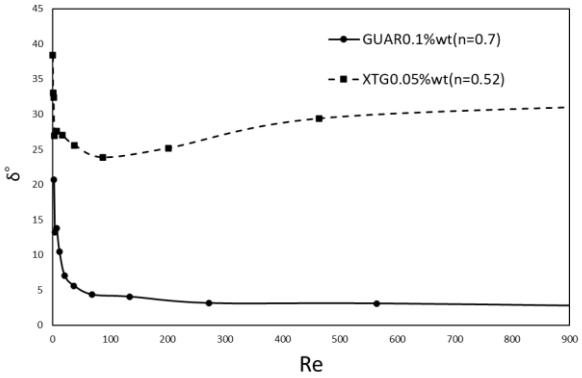

Fig.5 $\delta° = \tan^{-1} G''/G'$ v.s. the Reynolds number (G'' is elastic modulus, G' is storage modulus)

Table 2 Fluids property used in the experiment.

Fluids	n	$\mu_0[\mathbf{mPa \cdot s}]$	λ_c [s]
GUAR0.1%wt	0.7	51	0.55
XTG0.05%wt	0.52	820	0.76

RESULT OF FLOW VISUALIZATION

Each working fluid was visualized up to Reynolds numbers 650(*n*=0.52) and 850(*n*=0.7) using a visualization tracer. Fig.6 shows the flow visualization results. The Taylor vortices on the upper and lower end faces are slightly different in size due to the influence of the Ekman boundary layer. For Newtonian fluids, a series of toroidal vortices are six cells mode and the each cell size is almost same are observed at the TVF and WVF in the previous research[19]. If the cylinders are infinitely long, a series of vortex trains infinitely are expected for Newtonian fluids and a series of vortex trains which size are irregular infinitely are expected for non Newtonian fluids. For guar gum 0.1%wt fluid(*n*=0.7), the flow is beginning with a simple circumferential Couette flow and a series of steady toroidal vortices are six cells mode and the each cell size is almost same are observed at the Re=~90. At the Re=90~850, the flow becomes WVF and the each cell size fluctuates are observed. For xanthan gum 0.05%wt fluid(n=0.52), the flow is beginning with a simple circumferential Couette flow and a series of steady toroidal vortices are four cells mode and the each cell size is almost same are observed at the Re=0~65. At the Re=65~650, the flow becomes WVF and a series of toroidal vortices are significantly different with Newtonian case are observed. The

Fig.6 Flow visualization at the Re=600(above *n*=0.7, below *n*=0.52)

upper and lower roll pairs become vertically enlarged depending on the Reynolds number and the roll pair of the central cells look crushed at the WVF. The relationship between the axial vortex length of the roll pair compared with Newtonian case and the Reynolds number is shown in Fig.7. The vertical axis is the ratio of axial lengths based on the case of Newtonian fluid. The first and second vortex center positions from the top are $\boldsymbol{Z_1}$ and $\boldsymbol{Z_2}$, they offset upper depending on the Reynolds number at the WVF. The relationship between $\boldsymbol{Z_1}$ and $\boldsymbol{Z_2}$ and the Reynolds number is shown in Fig.8.

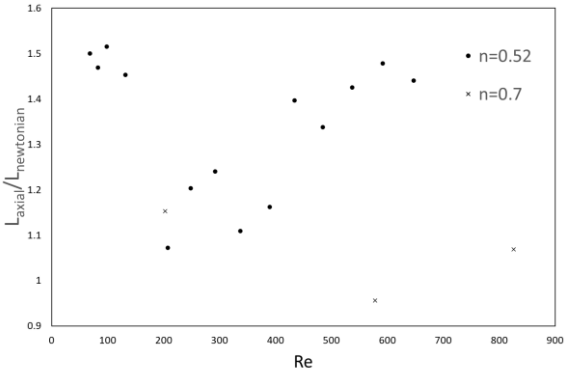

Fig.7 The ratio of axial lengths based on the case of Newtonian fluid vs Reynolds numbers

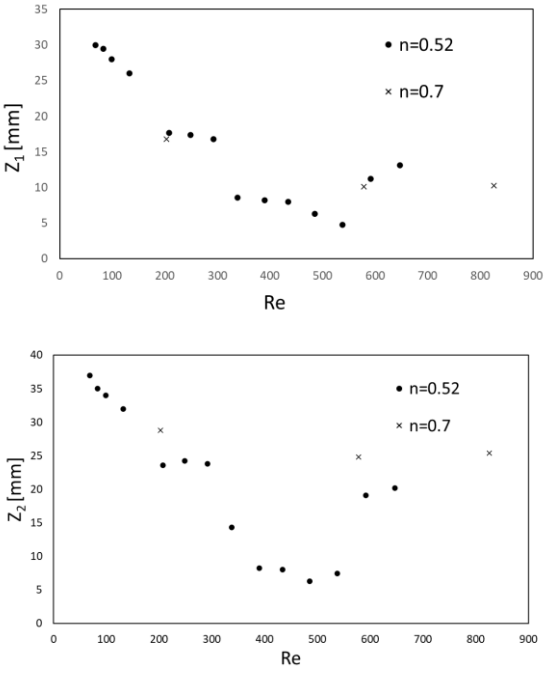

Fig.8 $\boldsymbol{Z_1}$ and $\boldsymbol{Z_2}$ vs the Reynolds numbers

DETERMING THE CRITICAL REYNOLSDS NUMBER

Velocity distributions were obtained from the images acquired by PIV in order to determinate the critical Reynolds numbers for TVF

and WVF. Here Re_{c1}, Re_{c2} are the critical Reynolds numbers for TVF and WVF respectively. Re_{c1} is determined from the velocity distribution when steady toroidal vortices are observed. The velocity distributions for both fluids are shown in Fig.9. Re_{c2} is determined from the spectrum analysis result by acquiring the velocity time series data of each window from the velocity distribution and spatially averaging it. WVF has the peak frequency and the Taylor vortex pulsates at the peak frequency. The relationship between the peak frequency and the Reynolds number is shown in Fig.10. From the above process, each critical Reynolds number is shown in table 3 compared to the Newtonian case[19].

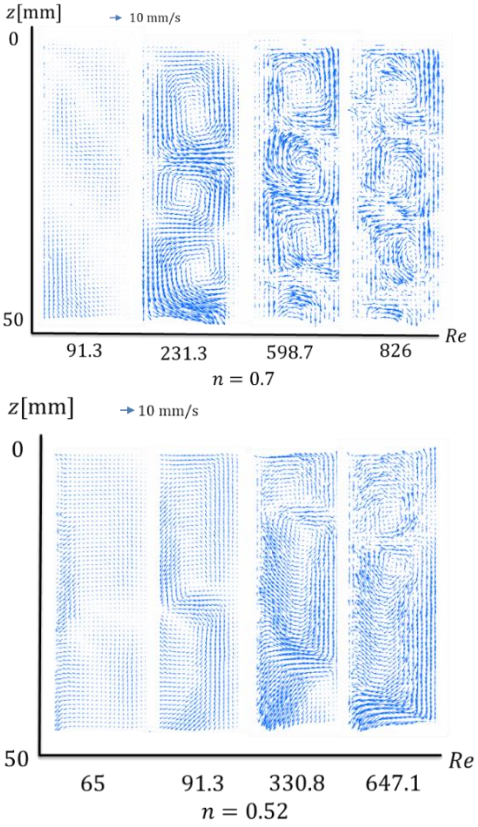

Fig.9 Velocity distributions

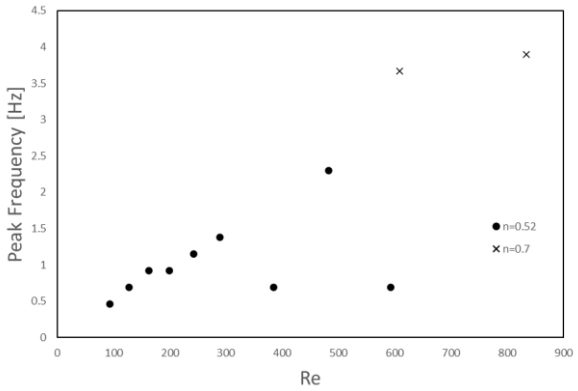

Fig.10 Peak frequency vs the Reynolds number

Table 3 Re_{c1}, Re_{c2} for both fluids

n	Re_{c1}	Re_{c2}	f(WVF) [Hz]
1	95	1330	~1
0.7	92.6	608.7	3.67
0.52	65	93.1	0.68

SPECIFAYING THE TRANSITION AREA

For shear thinning effects of working fluids, significantly different velocity fields are observed, unlike the case of the Newtonian fluids. The shape of the Taylor vortices are not the same in the axial and radial directions. Those are a tendency not seen in the case of Newtonian fluids. For n=0.52, four cell mode and the size of upper and lower cells are larger than central of the cells are observed. Fig.7 show that as the Reynolds number increases, the size of the vortex increases in the axial direction, and the core of the vortex is offset in the axial direction at the WVF. Table 3 show that the critical Reynolds numbers for shear thinning fluids and they are lower than the critical Reynolds number for the Newtonian case. Cagney and Balabani[17] got the critical Reynolds number for TVF and WVF for shear thinning fluids experimentally. A large difference was observed between the critical Reynolds number of Cagney and Balabani[17] and the critical Reynolds number of this experiment. The possible reason is their definition of the Reynolds number is different. They prepared four kinds of fluids which one of them is the Newtonian fluid and three of them have different viscosity index. They confirm that shear-thinning makes the critical Reynolds number lower than the Newtonian case, but there are no large differences. In this experiment, the critical Reynolds numbers for TVF are no large difference. However, shear-thinning make the critical Reynolds number for WVF significantly lower than the Newtonian case. Shear-thinning makes significantly increases the viscosity difference between the vicinity of the wall surface and the distance, because the velocity gradient in the circumferential direction is exponential as shown by Eq (2). The Taylor vortices become easy to pulsate when wall binding force is reduced by the larger viscosity difference.

CONCLUSIONS

We performed experiments examining Taylor Couette flow of two shear-thinning fluids, in which the Reynolds number was increased, such that the CCF, TVF and WVF were observed. The flow dynamics were examined using PIV to measure the velocity field in the vertical cross section.

The time-averaged velocity field indicated that shear thinning makes the shape of Taylor vortex vertically

long and the position of the vortex core is vertically offset as the Reynolds number increase at the WVF.

The critical Reynolds numbers for transition to TVF and WVF both showed that shear-thinning makes them lower than the case of the Newtonian fluids, especially the critical Reynolds number for transition to WVF is significantly low depending on the viscosity index. As a hypothesis, he Taylor vortices become easy to pulsate when wall binding force is reduced because shear-thinning makes the larger viscosity difference.

We analysis the flow field of vertical cross section for two shear-thinning fluids experimentally, but analysis of the circumferential velocity field is remained yet.

ACKNOWLEAGES

Sansho Co., Ltd. who provided the medicine is gratefully acknowledged.

REFERENCES

[1]U.B.Holeschovsky and C.L.Cooney, "Quantitative description of ultrafiltration in a rotating filtration device," AIChE J. 37, 1219–1226 (1991).

[2]E. K. Hill, B. Krebs, D. G. Goodall, G. J. Howlett, and D. E. Dunstan, "Shear flow induces amyloid fibril formation," Biomacromolecules 7, 10–13 (2006)

[3] G. A. Ameer, E. A. Grovender, B. Obradovic, C. L. Cooney, and R. Langer, "RTD analysis of a novel Taylor-Couette flow device for blood detoxification," AIChE J.45, 633–638 (1999).

[4] S. Vedantam and J. B. Joshi, "Annular centrifugal contactors—A review," Chem. Eng. Res. Des. 84, 522–542 (2006).

[5] B. Haut, H. Ben Amor, L. Coulon, A. Jacquet, and A. Halloin, "Hydrodynamics and mass transfer in a Couette-Taylor bioreactor for the culture of animal cells,"Chem.Eng.Sci. 58, 777–784 (2003).

[6]Kataoka, K., N. Ohmura, M. Kouzu, Y. Simamura and M. Okubo; "Emulsion Polymerization of Styrene in a Continuous Taylor Vortex Flow Reactor," Chem. Eng. Sci., 50, 1409–1416 (1995)

[7]Jung, T., W. S. Kim and C. K. Choi; "Eect of Monovalent Salts on Morphology of Calcium Carbonate Crystallized in Couette–Taylor Reactor,"Cryst.Res.Technol., 40, 586–592 (2005)

[8]Dutta, P. K. and A. K. Ray; "Experimental Investigation of Taylor Vortex Photocatalytic Reactor for Water Purication," Chem. Eng. Sci., 59, 5249–5259 (2004)

[9]N. Ashrafi, "Stability analysis of shear-thinning flow between rotating cylinders," Appl. Math. Modell. 35, 4407–4423 (2011).

[10]O. Coronado-Matutti, P. R. Souza Mendes, and M. S. Carvalho, "Instability of inelastic shear-thinning liquids in a Couette flow between concentric cylinders," J.Fluids Eng.126,385–390 (2004).

[11]B. Alibenyahia, C. Lemaitre, C. Nouar, and N. Ait-Messaoudene, "Revisiting the stability of circular Couette flow of shear-thinning fluids," J. Non-NewtonianFluidMech.183-184,37–51(2012).

[12]M. P. Escudier, I. W. Gouldson, and D. M. Jones, "Taylor vortices in Newtonian and shear-thinning liquids," Proc. R. Soc. London, Ser. A 449, 155–175 (1995).

[13]C. D A V I D ANDERECK, AND HARRY L. SWINNEY "Flow regimes in a circular Couette system with independently rotating cylinders" J . Fluid Mech (1986), vol. 164, p p . 15S183

[14]Taylor.G.I 1923 "Stability of a viscous liquid contained between two rotating cylinders." Phil. Trans. R. Soc. Lond. A 223, 289

[15]T. J. Lockett, S. M. Richardson, and W. J. Worraker, "The stability of inelastic non-Newtonian fluids in Couette flow between concentric cylinders: A finite-element study," J. Non-Newtonian Fluid Mech. 43, 165–177 (1992).

[16]S. Khali, R. Nebbali, and K. Bouhadef, "Numerical investigation of non-Newtonian fluids flows between two rotating cylinders using lattice-Boltzmann method," Int. Scholarly Sci. Res. Innovation 7, 1999–2005(2013).

[17]N. Cagney and S. Balabani "Taylor-Couette flow of shear-thinning fluids" Cite as: Phys. Fluids 31, 053102 (2019)

[18]Hayato Masuda, Takafumi Horie, Robert Hubacz, Mitsuhiro Ohta and Naoto Ohmura "Prediction of onset of Taylor-Couette instability for shear-thinning fluids" Rheol Acta (2017)

[19]Yuki Noguchi, Takushi Saito and Tatsuya Kawaguchi "Flow Structure Analysis of Taylor-Couette Flow in Low Aspect Ratio Cell Department of Mechanical Engineering, Tokyo Institute of Technology"

11th Int. Conf. on Geotechnique, Construction Materials & Environment,
Kyoto, Japan, 3-5 November 2021, ISBN: 978-4-909106063 C3051

NUMERICAL BEACH EVOLUTION MODEL CONSIDERING SEDIMENT TRANSPORT IN SWASH ZONE

Shuhei Miki[1], Masamitsu Kuroiwa[2] and Kajikawa Yuki[3]

[1,2,3] Department of Management of Social Systems and Civil Engineering, Tottori University, Tottori, Japan

ABSTRACT

The objective of this study was to develop a three-dimensional morphodynamic model that considers the sediment transport rate in the swash zone and shoreline change. First, the setting of the run-up height and equilibrium beach slope parameters in the swash zone of the sediment transport model were investigated. Next, the beach profile changes computed using the proposed sediment transport model in the swash zone were compared with previous experimental results obtained using a large wave flume, showing good agreement in patterns of beach profile erosion and sedimentation. Finally, the applicability of the proposed model to the analysis of the morphodynamics around submerged breakwaters was investigated at a field site, and the results showed good agreement with the observed erosion and sedimentation patterns.

Keywords: sediment transport, numerical model, topographic change, swash zone

INTRODUCTION

In Japan, many coastal structures such as detached breakwaters, groins, and submerged breakwaters have been built to prevent coastal erosion. However, the erosion of sandy beaches can still occur as a result of the complicated waves and nearshore currents generated around such coastal structures. In addition, beach erosion is also caused by the severe waves that accompany typhoons. The retreat of a shoreline can therefore occur as the water level rises and the wave characteristics change over time. To implement appropriate beach protection, it is necessary to improve the accuracy of numerical beach evolution models by calculating the complex waves, currents, and sediment transport rates around coastal structures and near the shoreline. Though the shoreline change model is effective for long-term prediction over a wide area, the three-dimensional morphodynamic model is more effective for predicting short-term topographic changes caused by sediment transport due to waves and currents around structures. Many laboratory experiments [1]-[3] and numerical analyses [4], [5] have been performed to study sediment transport in the swash zone. In particular, detailed numerical analyses have been performed using the discrete element method and the particle tracking method [6]. However, in practice, it is still difficult to apply these methods to local analyses of beach evolution.

The objective of this study was therefore to develop a three-dimensional morphodynamic model that considers the sediment transport rate in the swash zone as well as the shoreline change. In this study, the beach evolution model with a sediment transport model in the swash zone, developed by Miki [7], was modified and its applicability was investigated. First, to improve the accuracy of the sediment transport model in the swash zone, the appropriate expressions for the equilibrium slope and run-up height parameters were investigated as they exert a critical influence on sediment transport rates. Next, the sediment transport model was evaluated using previously obtained experimental results for various erosion and sedimentation types with a constant slope topography. Finally, the proposed model was applied to the simulations of a field site, and the computed results were compared with the observed shoreline change.

NUMERICAL MODEL

Outline of Numerical Model

The numerical beach evolution model developed by Miki [7] was modified in this study. As shown in Fig. 1, this model consists of four modules: the wave module, nearshore current module, sediment transport module, and topographic change module. The wave module is based on the wave action balance equation with energy dissipation for the wave breaking and wave diffraction terms [8]. The nearshore current module is based on a hybrid of the Q-3D and 2DH models, proposed by Kuroiwa [9].

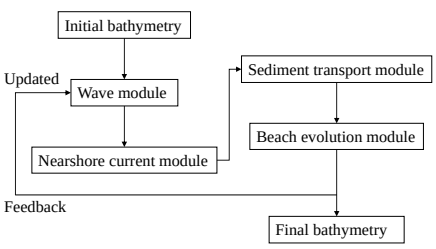

Fig. 1 Outline of numerical modeling modules

Sediment Transport Model in Swash Zone

The sediment transport model in the swash zone was based on the model developed by Leont'yev [10] to reproduce the formation of beach scarps and was improved considering the shoreline change. The model for sediment transport distribution in the cross-shore direction is shown in Fig. 2.

The swash zone was defined as the region from x_s to x_r, where x_s is the point where the water depth is the same as the offshore wave height and x_r is the maximum run-up point. x_c is the shoreline point. The total sediment transport rates in the cross-shore and alongshore directions (q_x and q_y, respectively) can then be represented by

$$q_x, q_y = \begin{cases} q_{xc}, q_{yc} & x < x_s \\ q_{xc} + q_{xr}, q_{yc} + q_{yr} & x_s \le x \le x_c \\ q_{xr}, q_{yr} & x_c \le x \le x_r \end{cases} \quad (1)$$

$$q_{xr}, q_{yr} = \begin{cases} \hat{q}_{xr} \left[\dfrac{x - x_s}{x_c - x_s} \right]^{\gamma_1} & x_s \le x \le x_c \\ \hat{q}_{yr} \left[\dfrac{x_r - x}{x_r - x_c} \right]^{\gamma_2} & x_c \le x \le x_r \end{cases} \quad (2)$$

where q_{xc} and q_{yc} represent the sediment transport rates from the offshore boundary to the shoreline, presented by Kuroiwa [9]; q_{xr} and q_{yr} are the sediment transport distributions in the swash zone; γ_1 and γ_2 are coefficients that determine the sediment transport rate distribution in the swash zone, and were set to 0.5 and 1.0, respectively; and. $\hat{q}_{xr}$ and $\hat{q}_{yr}$ are respectively determined by

$$\hat{q}_{xr} = K_R \rho \hat{u}_R^3 \ \tan\beta_{eq} - \tan\beta \quad (3)$$

$$\hat{q}_{yr} = 0.1 K_R \rho \hat{u}_R^2 \frac{R}{T} \frac{\tan\theta_w}{\tan\beta} \quad (4)$$

where tanβ is the beach slope, tanβ_{eq} is the equilibrium slope, R is the run-up height determined using the equation provided by Larson [11], K_R is the scaling coefficient, $\hat{u}_R$ is the amplitude of the wave orbital velocities at the shoreline, T is the wave period, and θ_w is the wave angle relative to the shore normal.

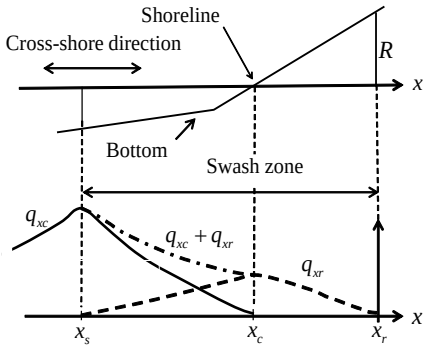

Fig. 2 Sediment transport model in swash zone

The values of tanβ and tanβ_{eq} are determined by

$$\tan\beta = \frac{H_s + R}{x_r - x_s} \quad (5)$$

$$\tan\beta_{eq} = \alpha_1 \sqrt{\frac{W_f T}{H_s}} \quad (6)$$

where W_f is the settling velocity, H_s is the wave height at x_s, and α_1 is a constant coefficient determined according to the type of beach evolution as per Horikawa and Sunamura [12]. In this study, α_1 was set to 0.06.

The value of R is determined by

$$\frac{R}{H_o} = 1.47 \times \left(\frac{\tan\beta}{\sqrt{H_o / L_o}} \right)^{0.79} \quad (7)$$

where H_o is the equivalent deepwater wave height, and L_o is the equivalent deepwater wave length.

The values of K_R and $\hat{u}_R$ are determined by

$$K_R = 0.5 \times 10^{-7} \frac{T\sqrt{gH_s}}{d} \quad (8)$$

$$\hat{u}_R = \frac{\sigma H_c}{T \sinh kh} \quad (9)$$

where d is the median sediment diameter, σ is relative angular frequency, k is wave number, h is water depth and H_c is the wave height at x_c.

VERIFICATION OF PARAMETERS

The equilibrium slope and run-up height are very important parameters for estimating the sediment transport rates in the swash zone in Eqs. (3) and (4) and for predicting beach profile changes. We accordingly investigated the influence of wave and bottom material characteristics on the estimation of the equilibrium slope in Eq. (6) and the run-up height in Eq. (7).

Equilibrium Slope

The response of the equilibrium slope calculated using the proposed model was investigated using various wave and sand particle size conditions. Thus,

the incident significant wave height H_s, wave period T, and sand grain size d were set to 0.5–2.0 m, 5.0–9.0 s, and 0.1–0.4 mm, respectively.

Figure 3 shows the relationship between the equilibrium slope and wave steepness H_s/L_o, in which it can be seen that the equilibrium beach slope increased with the applied sand grain size. Figure 4 shows the relationship between equilibrium slope and sand grain size. The coefficient of determination R^2 obtained from the relationship in Fig. 4 was 0.7006, which is similar to that obtained by Noshi [13], who also indicated that sand grain size plays an important role in determining the equilibrium slope.

Run-up Height

To investigate the accuracy of the run-up height calculation, the results computed using Eq. (7) were compared with the experimental results of Gono [14], Sawaragi [15], and Mizuguchi [16], defined as Case 1, Case 2, and Case 3, respectively, as shown in Table 1.

Figure 5 shows a comparison of the calculated and experimental results for run-up height R. In this figure, it can be observed that the R calculated using

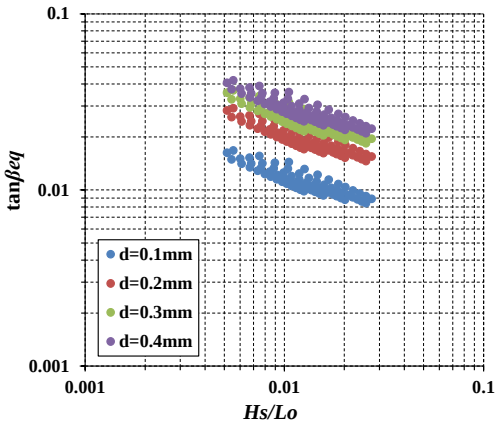

Fig. 3 Relationship between equilibrium slope and wave steepness H_s/L_o

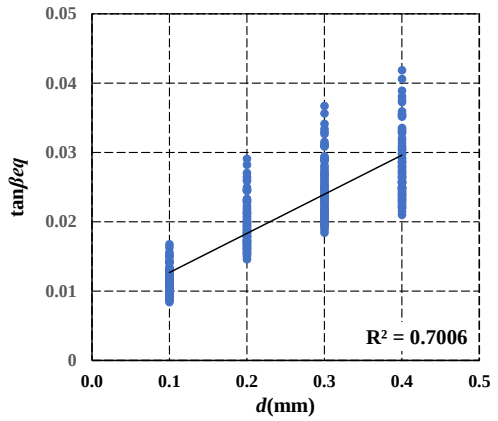

Fig. 4 Relationship between equilibrium slope and sand grain size

Eq. (7) for different beach slopes was overestimated when the beach slope was large and underestimated when the beach slope was small. In order to modify the relationship accordingly, the use of a new correction coefficient α_2 was proposed as follows:

$$\frac{R}{H_o} = 1.47 \times \alpha_2 \left(\frac{\tan\beta}{\sqrt{H_o / L_o}} \right)^{0.79} \tag{10}$$

Where correction coefficient α_2 is

Table 1 Calculation conditions

	Wave height H_s (cm)	Wave period T (s)	Beach slope
Case 1	2.30–5.10	0.80–1.25	1/20–1/5
Case 2	2.55–6.81	0.70–1.50	1/40–1/5
Case 3	24.2–77.1	4.40–10.9	1/60

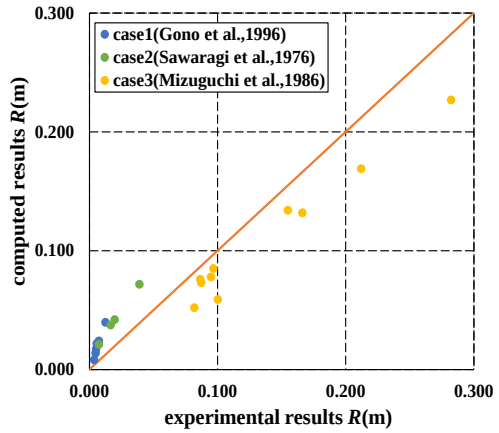

Fig. 5 Comparison between calculated results and experimental results

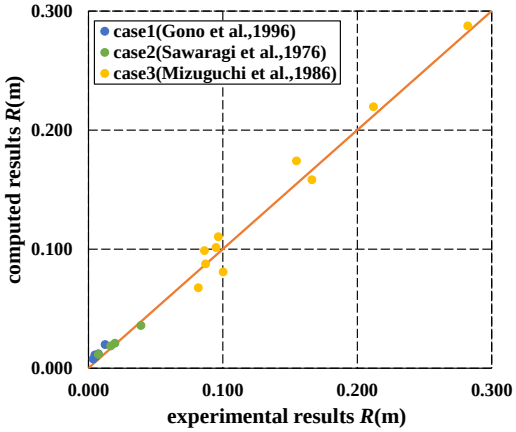

Fig. 6 Comparison between calculated results with corrected coefficients and experimental results

$$\alpha_2 = \begin{cases} 1-3.0\times \tan\beta - 0.02 & \tan\beta > 1/50 \\ 1+5.0\times 0.02 - \tan\beta & \tan\beta \le 1/50 \end{cases}$$

Figure 6 shows comparison between the calculated R obtained using Eq. (10) and the experimental results. Clearly, the use of the correction coefficient α_2 resulted in calculated run-up heights that agreed well with the experimental results.

COMPARISON WITH EXPERIMENTAL RESULTS IN THE CROSS-SHORE DIRECTION

To investigate the applicability of the proposed beach evolution model with sediment transport in the swash zone, the computed results were compared with the results of wave flume tests evaluating beach profile changes under regular waves, conducted at the Central Research Institute of Electric Power Industry [17]. The length, width, and height of the wave flume were 205, 3.4, and 6.0 m, respectively. The experimental conditions for the sedimentation and erosion types are defined in Table 2 based on Maruyama [17].

Figures 7 and 8 show the computed results after 7 h and 15 h, respectively, in Case 4. Figure 7 indicates that the experimental results did not show erosion in the swash zone, and that the computed result nearer the shoreline exhibited a large discrepancy with the experimental results. However, the computed sand bar height and position qualitatively agreed with the experimental results. After 15 h, Fig. 8 shows that the computed results agreed well with the experimental results; the presented model was able to reproduce the erosion exhibited by the experimental result in the swash zone.

Table 2 Calculation conditions in experiment of Maruyama [17]

	Wave height H_s (m)	Wave period T (s)	sand grain size d (mm)	Beach slope
Case 4	1.62	3.1	0.27	1/20
Case 5	1.61	3.1	0.27	3/100

Figures 9 and 10 show comparisons of the beach profile after 30 h for Case 4 and Case 5, respectively. In Case 4, the computed result in the swash zone was in good agreement with the experimental result. In Case 5, although the computed magnitudes of erosion and sedimentation were smaller than those of the experimental result, the numerical model shows qualitative agreement with the experimental results. Thus, the numerical model for the beach profile changes effectively agreed with the experimental results regardless of the deposition condition.

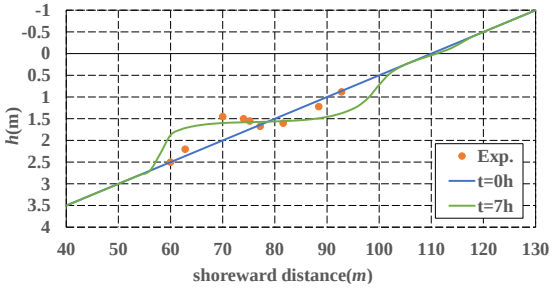

Fig. 7 Comparison of computed results with experimental results by Maruyama [17] in Case 4 (after 7 h)

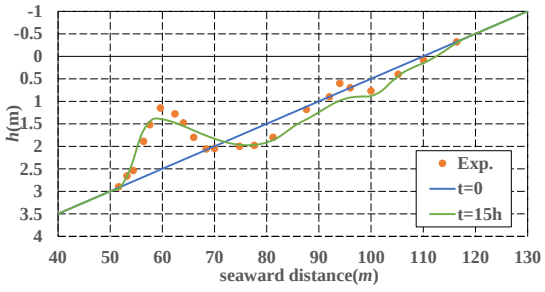

Fig. 8 Comparison of computed results with experimental results by Maruyama [17] in Case 4 (after 15 h)

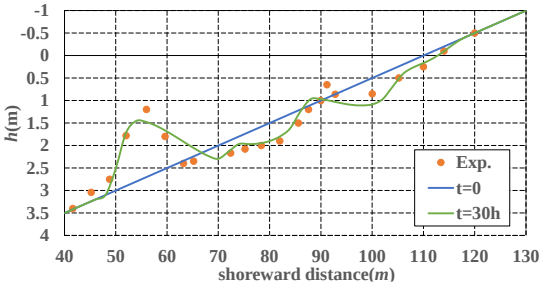

Fig. 9 Comparison of computed results with experimental results by Maruyama [17] in Case 4 (after 30 h)

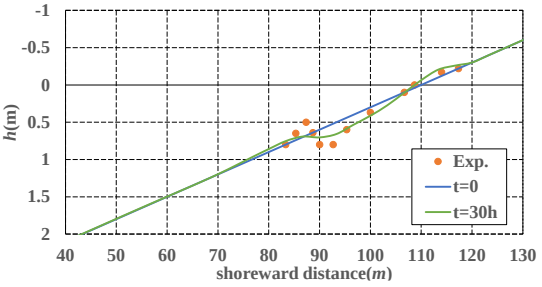

Fig. 10 Comparison of computed results with experimental results by Maruyama [17] in Case 5 (after 30 h)

APPLICATION TO FIELD SITE

The applicability of the numerical model under field conditions was investigated using field observations collected in the Tomimasu area of Kaike Beach in Tottori Prefecture, Japan from August 2017 to November 2017.

The wave conditions and time series of the observed waves are presented in Table 3 and Fig. 11. The wave conditions were based on the wave data measured offshore of the Tomimasu area; wave heights of less than 0.5 m were neglected. Until the final bathymetry was obtained by the computations, the bathymetry was updated every 1 days, and the computations were performed 45 times. The median sand particle diameter d was 0.2 mm. Figures 12 and 13 show the observed and computed erosion/deposition plots, respectively. Figure 14 shows a comparison between the computed and observed topographies in the cross-shore direction at 500 m in the alongshore direction.

The computed erosion/deposition patterns can be seen in Fig. 13 to be very similar to the observed results in Fig. 12, indicating that the computed topographical changes on the west side and behind the submerged breakwaters are reasonable. Thus, it was found that the computed result near the shoreline was in good agreement with the observed result in the swash zone. However, Fig. 14 shows that the erosion behind the sand bar was overestimated in the computed results. Still, in the swash zone, the computed result was in good agreement with the observed results. The applicability of the model was therefore confirmed by these results.

Table 3 Wave conditions

	Wave height H(m)	Wave period T(s)	Wave direction θ (・)
Wave 1	0.781	6.325	-10.0
Wave 2	1.181	6.407	-10.0
Wave 3	2.014	8.309	-10.0
Wave 4	3.089	10.025	-10.0

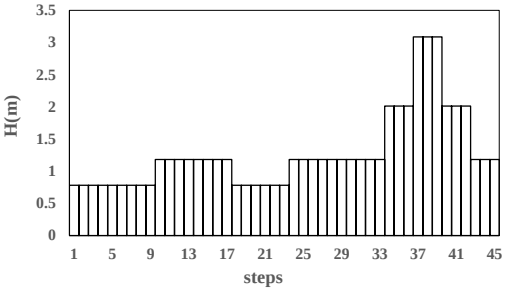

CONCLUSIONS

In this study, we first reexamined in detail the run-up height and equilibrium slope parameters of the sediment transport model for erosion and sedimentation in the swash zone. Then, the performance of the revised numerical beach evolution model including the sediment transport model was investigated on a constant slope topography. Finally, the proposed model was applied to a field site and the results were compared with field observations. The final results of this study were as follows:

(1) It was confirmed that the equilibrium slope parameter obtained from Eq. (6) yields reasonable results. The results calculated using the modified run-up height model were in good agreement with previous conventional experimental results.

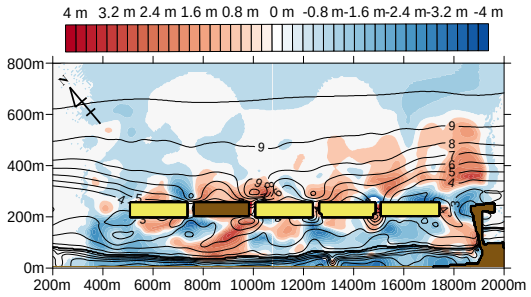

Fig. 12 Observed erosion/deposition plot

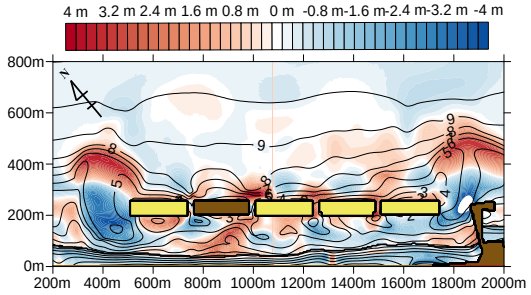

Fig. 13 Computed erosion/deposition plot

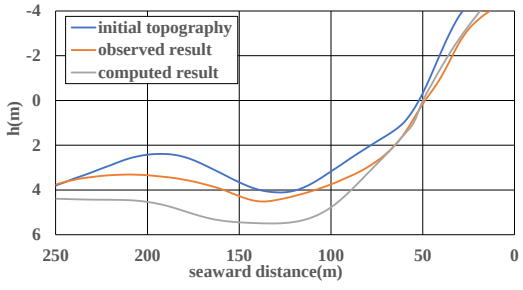

(2) The results of a comparison between the experimental and computed topography change in the cross-shore direction indicated that the proposed sediment transport model was able to accurately compute the beach profile patterns of erosion and sedimentation.
(3) A comparison between the computed results and field observations of erosion/deposition in the Tomimasu area of Kaike Beach indicated that the result obtained using the proposed model agreed reasonably well with the observed data.

REFERENCES

[1] Ruju A., Conley D., Masselink G. and Puleo J., Sediment Transport Dynamics in The Swash Zone Under Large-scale Laboratory Conditions, Continental Shelf Research, Vol.120, 2016, pp. 1-13.
[2] Alsina J.M., Caceres I., Brocchini M. and Baldock T.E., An Experimental Study on Sediment Transport and Bed Evolution Under Different Swash Zone Morphological Conditions, Coastal Engineering, Vol.68, 2012, pp. 31-43.
[3] Murakami S., Mizuguchi Y., Kaneko Y., Koyanagi Y., Nakazawa Y. and Nomoto H., Laboratory Study on Equilibrium Slope and Sedimenr Transport in Swash Zone by Nonbreaking Waves, Annual Journal of Coastal Engineering, JSCE, Vol.71, No2, 2015, pp. 535-540.
[4] Kuchiishi T., Kuroiwa M., Kato K., Matsubara Y. and Noda H., Prediction of 3D Beach Evolution with Shoreline Change Around Coastal Structures Using Q-3D Nearshore Current Model, Annual Journal of Coastal Engineering, JSCE, Vol.20, 2004, pp. 503-508.
[5] Bakhtyar R., Ghaheri A., Yeganeh-Bakhtiary A. and Barry D.A., Process-based Model for Nearshore Hydrodynamics, Sediment Transport and Morphological Evolution in the Surf and Swash Zones, Applied Ocean Research, Vol.31, No.1, 2009, pp. 44-56.
[6] Harada E. and Goto H., Numerical Simulation for Vertical Sorting in Sheetflow by Particle-Laden Turbulence Flow Model, Annual Journal of Coastal Engineering, JSCE, Vol.65, No.1, 2009, pp. 516-520.
[7] Miki S., Kuroiwa M. and Kajikawa Y., Three-dimensional Morphological Model with Shoreline Change in Consideration of Sediment Transport in Swash Zone, Annual Journal of Coastal Engineering, JSCE, Vol.76, No2, 2020, pp. 499-504.
[8] Mase H., Yuhi M., Amamori H. and Takayama T., Phase Averaging Wave Prediction Model with Breaking and Diffraction Effects in Wave-current Coexisting Field, Annual Journal of Coastal Engineering, JSCE, Vol.51, No.1, 2004, pp.6-10.
[9] Kuroiwa M., Matsubara Y., Kuchiishi T., and Kato K., Prediction System of 3D Beach Evolution with 2DH and Q3D Hydrodynamic Modes, Proceedings of 16th International Offshore and Polar Engineering Conference, 2006, pp.751-757.
[10] Leont'yev I.O., Modeling the Morphological Response in Coastal Zone for Different Temporal Scales, Advances in Coastal Modeling edited by V.C. Lakhan, 2003, pp. 299-335.
[11] Larson M. and Kraus N.C., SBEACH: Numerical Model for Simulating Storm-induced Beach Change, Report 1, Empirical foundation and model development, Technical Report CERC-89-9, US Army Engineer Waterways Experiment Station, CERC, Vicksburg, MS, 1989.
[12] Horikawa K., Sunamura T. and Kondo K., Experimental Study for 2DH Beach Changes with Waves, Annual Journal of Coastal Engineering, JSCE, Vol.21, 1976, pp. 193-199. (in Japanese)
[13] Noshi Y., Kobayashi A., Kumada T., Uda T. and Serizawa M., Calculation Method of the Local Cross-shore Slope Based on the Sediment Grain Size Composition, Annual Journal of Coastal Engineering, JSCE, Vol.51, 2004, pp. 406-410. (in Japanese)
[14] Gono K., Hattori S. and Sugimoto N., Experimental Study for Motion Mechanism of the Runup Height of Swash Waves, Annual Journal of Coastal Engineering, JSCE, Vol.43, 1996, pp. 141-145. (in Japanese)
[15] Sawaragi T., Iwata K. and Morino A., Characteristics for the Runup Height of Swash Waves on a Mild Slope, Annual Journal of Coastal Engineering, JSCE, Vol.23, 1976, pp. 164-169. (in Japanese)
[16] Mizuguchi Y., Karibe Y. and Hotta S., Runup Height of Swash Waves in Local Coast, Annual Journal of Coastal Engineering, JSCE, Vol.30, 1983, pp. 109-113. (in Japanese)
[17] Maruyama K. and Shimizu T., Verification of Improved Model for Prediction of On-Offshore Beach Change, CRIEPI Research Report, Report Number U86014, 1986.

11th Int. Conf. on Geotechnique, Construction Materials & Environment,
Kyoto, Japan, 3-5 November 2021, ISBN: 978-4-909106063 C3051

ANTIBACTERIAL ACTIVITY OF *HELIOTROPIUM INDICUM* CRUDE EXTRACTS AGAINST *STAPHYLOCOCCUS AUREUS* FROM CLINICAL AND SUBCLINICAL MASTITIS IN DAIRY COW

Duangkamol Taemchuay[1], Nareerat Phangsub[2], Kanokpon Bunya-atichart[2] and Wimonmat Boonmee[3]

[1]Department of Animal Production Technology and Fishery, School of Agricultural Technology, King Mongkut's Institute of Technology Ladkrabang, Bangkok, 10520, Thailand
[2]Department of Agricultural Technology, King Mongkut's Institute of Technology Ladkrabang, Prince of Chumphon Campus, Chumphon, 86160, Thailand
[3]Department of Biology, School of Science, King Mongkut's Institute of Technology Ladkrabang, Bangkok, 10520, Thailand

ABSTRACT

Bovine mastitis is an economic disease. The disease is affected to milk productivity and milk quality. *Staphylococcus aureus* is a contagious pathogen in clinical mastitis and subclinical mastitis in dairy cow. The conventional antibiotic treatment is intramammary infusion into infected quarters of the udder. The treatment has been caused of antibiotic residue in marketed milk. Therefore, medicinal plants are interested in a new alternative treatment from natural resources. *Heliotropium indicum* is the weed that has a wide range of medical properties. This study aimed to evaluate antibacterial activity of *H. indicum* crude extracts against *S. aureus*. The methanol extracts were prepared from leaf and whole plant of *H. indicum*. Crude extracts were tested for antibacterial activity using by disc diffusion and the modified resazurin methods. The results of disc diffusion method showed the inhibition zones of 11.58 mm for the methanol extract of leaf part and the inhibition zones of 7.33 mm for the whole plant extracted with methanol and ethyl acetate. The MIC and MBC values of the methanol extract from leaf part were 8 and 64 mg/ml, respectively. Conclusion, the leaf part of *H. indicum* with methanol extracts could impeded *S. aureus* growth from clinical mastitis and subclinical mastitis in dairy cows.

Keywords: Antibacterial activity, Heliotropium indicum, Staphylococcus aureus, Mastitis, Dairy cow

INTRODUCTION

Bovine mastitis is a disease that is primary importance in dairy cows, causing damage to dairy farmers. When the milk secretory cells are damaged resulting in decreasing milk yield and also having the cost of medicine, treatment and culling of cattle [1]. This disease is an inflammation of the mammary glands with the cause of physical trauma and pathogenic infections [2]. Clinical mastitis shows that the dairy cows have a fever, pain, anorexia, udder swollen, redness, and being able to find abnormal milk whereas subclinical mastitis shows no symptoms in udder of cow and visible unchanged in milk [3]. *Staphylococcus aureus* is often the most common infection of cow udders. The main reservoir of *S. aureus* is not only the infected quarter, but also be able to transmiss from cow to cow during milking [4]. This pathogen recognized as a causative agent of subclinical mastitis, leading to an increase a number of somatic cell count in milk [5], which cause clinical mastitis [6]. Treatment of *S. aureus* infection is quite difficult due to it is often resistant to antibiotics resulting in treatment failure [7, 8].

Therefore, traditional medicine with herbs has been the most sensible and interest source of alternative therapeutic in the bovine mastitis. *Heliotropium indicum* L. is an interesting plant to be used against *S. aureus* in mastitis. It is in the Boraginaceae family, locally also known as Yah nguang-chang in Thai [9]. *H. indicum* is a small annual with a height of 15–50 cm. The leaves are always opposite. The hairy layers cover throughtout the stem and root. The flowers are calyx green with flowering around the whole year [10]. This medicinal plant contains many phytochemical constituents such as alkaloids, flavonoids, tannins, phenols, saponins, glycosides and volatile oil. The main substances in the alkaloid group are heliotrine and indicine N-oxide, that they have been isolated from the aerial parts of *H. indicum* [11, 12]. The pharmacological substance effect depends on the extraction solvent; water, chloroform, ethanol, methanol, ethyl acetate and petroleum ether [13]. Boye et al. (2012) found that *H. indicum* was extracted by ethanol and aqueous had a potential application for analgesic treatment [14]. In addition, the methanol extract of *H. indicum* showed anti-inflammatory activity against acute paw edema and sub-acute inflammation [15], whereas the ethanol extract of whole plant showed the anti-microbial activity against *S. aureus* [16]. In Thailand, the dried and powdered plant is used for this disease treatment [17].

This research investigated appropriate solvents

and parts of plant for extraction, include antibacterial activity of *H. indicum* against *S. aureus*.

MATERIALS AND METHODS

Preparation of crude extracts

H. indicum sample was obtained from Chumphon Province in the single batch collection. The whole plants of *H. indicum* (4 kg) were cleaned with water and the leaf part (5.3 kg) got from *H. indicum* (11 kg). Then, they were dried at 50°C in the hot air oven for 24 hr. and finely grounded into powder by the cutting mill machine. After that, the powder of whole plant (615.20 g) and leaf part (612.20 g) were individual extracted with 95% ethanol, methanol, ethyl acetate (1:10) and then macerated at room temperature for 7 days. The whole plant and leaf part extracts derived from ethanol, methanol and ethyl acetate refered to EW, EL, MW, ML, EaW and EaL, respectively. The powder-solvent mixturess were hand-squeezed and filtered by using a filter paper (Whatman No.1), respectively. To obtain the crude extracts, all solvent was removed using a rotary evaporator. The crude extracts were kept at -20°C until use.

Isolation of S. aureus from bovine mastitis

One ml of milk sample was added into 10 ml of Tryptic Soy Broth (TSB) with 1% pyruvate and 10% sodium chloride. The culture was incubated at 37°C for 24-48 hr. After that, 2-3 loops of the culture were streaked onto Baird-Parker agar (BPA) and incubated at 37°C for 24-48 hr. The circular, smooth, convex, and gray to jet-black and surrounded by opaque zone indicated the colonies of *S. aureus*.

Identification of S. aureus

The coagulase positive test was used for *S. aureus* confirmation. The colonies of *S. aureus* were transferred into 2 ml of Brain Heart Infusion Broth (BHI). The culture were incubated at 37°C for 18-24 hr. The coagulase test was carried out by 20 ml of solution from BHI into 200 ml of coagulase plasma solution. After that, it was incubated at 37°C for 24 hr. *S. aureus* was also approved by Mannitol Salt Agar (MSA).

Antibacterial activity by disc diffusion test

Preparation of the crude extract by diluted in the solvent (dimethyl sulfoside; DMSO for ethanol extracts) to concentrations of 1,000, 800, 400, 200, 100 and 50 mg/ml. Thus, the concentration of each disc contained 20, 16, 8, 4, 2 and 1 mg of crude extract, respectively. Twenty µl of each crude extract was dropped on sterile 6 mm-diameter filter paper disc. After that, the discs were dried at room temperature overnight.

Preparation of bacteria, the selected colonies in to 5 ml of Mueller-Hinton broth (MHB). Then the broth were incubated at 37°C for 3-5 h until 0.5 McFarland standard turbidity using the densitometer. The suspensions of 150 µl were added to 5 ml of Mueller-Hinton agar (MHA). The final inoculum concentration was approximately 10^6 CFU/ml. The discs were transferred on MHA and incubated at 37°C 18-24 hr. Negative controls used pure DMSO, 95% ethanol, methanol, and ethyl acetate as while the positive control used cephalotin (30 µg, Oxoid) and amoxicillin-clavulanic acid (30 µg, Oxoid). The diameter of the inhibition zone were recorded and the means were calculated. The experiments were done in 6 replicates.

Determination of the MIC by the modified resazurin assay

The sterile 96 well plates (Greiner bio-one, Germany) modified resazurin assay was performed for MIC determination. Fifty µl of MHB was added into all wells. Fifty µl of the initial concentration; 1,024 mg/ml, of crude extracts prepared were added into the first well. After that, two-fold serial dilutions were done into nine consecutive wells. Fifty µl of the 0.5 McFarland cultures were added into all wells. The plates were incubated at 37°C for 18-24 hr. After incubation, growth of the bacteria was evaluated by adding 50 µl of resazurin solution; 5 mg of one resazurin tablet in sterile distilled water (50 ml). The plates were further incubation for one hour. The color change from purple to pink indicated that (was then assessed). The MIC values; the bacteria growth inhibit, the lowest concentration at which color change. DMSO, 95% ethanol, methanol and ethyl acetate were used as the negative controls.

Determination of the MBC by the Mannitol Salt Agar

The MBC; the lowest concentration that kill the bacteria. The method was determined by one loop touching from each well of MIC plate and streaking on MSA plate. The plates were then incubated at 37°C for 18-24 hr. The unchanged media color is defined as the MBC. *S. aureus* growth will turn media yellow.

Statistical analysis

The experimental designed with factorial in completely randomize design (CRD) consists of two factors. These factors of the crude extract were a concentration in 6 levels and The powder-solvent mixturess in 6 kinds.

The statistical analysis was compared the inhibition zone was performed using ANOVA with

Duncan's multiple comparison test. Inhibition zones were expressed as mean ± SD.

RESULTS

The different solvents; ethanol, methanol and ethyl acetate were used for extraction of *H. indicum*. The yields (%) were calculated based on the initial weight, 200 g of the powder of leaf and whole plant. The results showed the weight of the ethanol extracts of leaf part and whole plant were 12.43 and 13.89 g, the methanol extracts of leaf part and whole plant were 17.99 and 13.15 g, and the ethyl acetate extracts of leaf part and whole plant were 9.89 and 7.82 g (data not shown). The yields of each crude extracts of *H. indicum* from the powder of leaf part and whole plant with ethanol, methanol and ethyl acetate were 6.22, 6.95, 9.00, 6.58, 4.95 and 3.91, respectively (Table 1). The selected solvent and plant part used to obtain the crude extracts, the highest yield of the extract derived from the methanol extract solvent with the leaf part.

Table 1 Yields of crude extracts from *H. indicum*

Crude extracts	Extract yields (%)
EL	6.22
ML	9.00
EaL	4.95
EW	6.95
MW	6.58
EaW	3.91

The solvent of our experiment selected has a potential to extract active substance which have all these medicinal properties; analgesic activity, anti-inflammatory activity and anti-microbial activity [13, 14, 15 and 16].

The yield of ethanol extraction of whole plant of *H. indicum* showed the similar result [16], which our result was obtained 6.95 % and the previous reports was 7.20%.

Solvent Extraction is the separation of substances by the solubility between the solvents and the active substances in herbs. This is based on the principle of the polarity dissolving of both the solvents and the substances. Importantly, the active substances can be dissolved in any solvent only if the polarity of the active substances and the solvents are similar [18].

Due to the ethanol and methanol belong to the group of moderately polar solvents, therefore they gave higher percentage of yield than ethyl acetate, which is in the group of non-polar solvents. As the result, ethyl acetate extraction yield obtained from the leaf and the whole plant gave a lower percentage of yield.

The crude extracts showed antibacterial effect property against *S. aureus* depending on the concentration and the powder-solvent mixer which is measured from the inhibition zone diameter as shown in significantly at p- value ≤ 0.01 (Table 2).

Table 2 Antibacterial activity of the crude extracts from *H. indicum* against *S. aureus* and *S. aureus* ATCC 25923

Concentrations of crude extract (mg/disc)	Powder -solvent mixtures	Inhibition zone (mm)	
		S. aureus	*S. aureus* ATCC 25923
1	EL	6.00±0.00^{g}	6.00±0.00^{j}
	ML	6.00±0.00^{g}	6.00±0.00^{j}
	EaL	6.00±0.00^{g}	6.00±0.00^{j}
	EW	6.00±0.00^{g}	6.00±0.00^{j}
	MW	6.00±0.00^{g}	6.00±0.00^{j}
	EaW	6.00±0.00^{g}	6.00±0.00^{j}
2	EL	6.00±0.00^{g}	6.00±0.00^{j}
	ML	6.00±0.00^{g}	6.00±0.00^{j}
	EaL	6.00±0.00^{g}	6.00±0.00^{j}
	EW	6.00±0.00^{g}	6.00±0.00^{j}
	MW	6.00±0.00^{g}	6.00±0.00^{j}
	EaW	6.00±0.00^{g}	6.00±0.00^{j}
4	EL	6.00±0.00^{g}	6.00±0.00^{j}
	ML	7.50±0.45^{d}	6.00±0.00^{j}
	EaL	6.00±0.00^{g}	6.00±0.00^{j}
	EW	6.00±0.00^{g}	6.00±0.00^{j}
	MW	6.00±0.00^{g}	6.00±0.00^{j}
	EaW	6.00±0.00^{g}	6.00±0.00^{j}
8	EL	6.00±0.00^{g}	12.92±1.02^{b}
	ML	8.17±0.26^{c}	14.92±0.49^{a}
	EaL	7.17±0.26^{ef}	10.25±0.61^{e}
	EW	6.00±0.00^{g}	8.25±0.42^{g}
	MW	6.00±0.00^{g}	10.83±0.75^{d}
	EaW	6.00±0.00^{g}	9.00±0.63^{f}
16	EL	7.00±0.00^{f}	12.50±1.00^{b}
	ML	10.00±0.63^{b}	12.50±0.55^{b}
	EaL	7.33±0.26^{de}	11.83±1.13^{c}
	EW	7.00±0.00^{f}	7.17±0.41^{i}
	MW	7.08±0.20^{ef}	8.08±1.02^{gh}
	EaW	7.00±0.00^{f}	8.83±0.52^{f}
20	EL	7.33±0.26^{de}	10.17±0.41^{e}
	ML	11.58±0.49^{a}	11.42±0.49^{c}
	EaL	8.25±0.42^{c}	13.08±0.74^{b}
	EW	7.08±0.20^{ef}	7.58±0.92^{hi}
	MW	7.33±0.26^{de}	7.00±0.00^{i}
	EaW	7.33±0.26^{de}	7.83±0.52^{gh}
Concentration of crude extracts		**	**
Powder-solvent mixtures		**	**
Concentration x Powder-solvent mixtures		**	**

In column, means followed by a different letter are significantly different by $DMRT_{0.05}$

** are significantly difference at probability ≤ 0.01

The inhibition zone diameter of crude extracts gave the better result at the higher concentrations than that of the lower concentrations. The methanol extract of leaf had the highest antibacterial activity, which was at the concentration 20 mg/disc and 11.58 mm of inhibition zone diameter observed. Whereas, at 2 mg/disc of other extracts had the lowest antibacterial activity which was 6.00 mm of inhibition zone diameter.

Additionally, the antibacterial activity of the crude extracts at concentration 16, 8, 4 mg/disc had inhibition zone of the leaf extracted with methanol 10.00, 8.17 and 7.50 mm, respectively. As the result indicates that the lower concentration of crude extract the less effective antibacterial activity, and vice versa.

The antibacterial activity at concentration 16, 20 mg/disc had no significant different as the numbers show in the table 2. As the results of the experiment, it can be seen that the methanol extracts of the leaf part had better results than the whole plant of *H. indicum*.

By contrast, the leaf and the whole plant extracts obtained from ethanol and ethyl acetate showed the similar trend of inhibition zone diameter which the figure were range between 7.00-7.33 mm except the ethyl acetate extract of leaf.

The similar trend result on the antibacterial activity effect against *S. aureus* and *S. aureus* ATCC 25923 were observed in aspects of concentration and the powder-solvent mixtures (Table 2). These results emphasize the fact that the leaf extract with methanol gave the highest antibacterial activity.

The MIC values of the extracts were determined by the modified resazurin microtiterplate. The DMSO 95% ethanol, methanol and ethyl acetate used as controls showed no inhibitory effect. The MIC values were range 8-256 mg/ml for *S. aureus* and 32-512 mg/ml for *S. aureus* ATCC 25923. The results of MIC values show in Table 3.

Table 3 The MIC values of *H. indicum* crude extracts against *S. aureus* and *S. aureus* ATCC 25923

Crude extracts	MIC value (mg/ml)	
	S. aureus	*S. aureus* ATCC 25923
EL	64	64
ML	8	32
EaL	128	64
EW	128	256
MW	128	512
EaW	256	256

The MBC values of the extracts were determined on *S.aureus* and *S. aureus* ATCC 25923. The MBC values of both bacteria were identical which range between 64-1,024 mg/ml. The result of MBC values shows in Table 4.

Table 4 The MBC values of *H. indicum* crude extracts against *S. aureus* and *S. aureus* ATCC 25923

Crude extracts	MBC value (mg/ml)	
	S. aureus	*S. aureus* ATCC 25923
EL	512	256
ML	64	64
EaL	256	128
EW	512	512
MW	512	512
EaW	1,024	1,024

CONCLUSIONS

The crude extracts of *H. indicum* impeded the growth of *S. aureus* isolated from bovine mastitis. The antibacterial activity of crude extracts from *H. indicum* was observed *in vitro*. The most extensive inhibition of crude extract against *S. aureus* derived from the methanol extraction of leaf. These results will bring about our further study on *in vivo* application, and also being able to advance the teat dipping product from *H. indicum* extracts.

ACKNOWLEDGMENTS

We gratefully thank you to the staff of the Department of Veterinary Public health and Diagnostic Service and The Animal Disease Diagnostic Unit, Faculty of Veterinary Medicine, Kasetsart University, Kamphaeng Saen Campus for providing the facilities and all instruments. Finally, I would like to thank King Mongkut's Institute of Technology Ladkrabang for the grant support in this research.

REFERENCES

[1] Gomes F. and Henriques M., Control of bovine mastitis: old and recent therapeutic approaches, Curr. Microbiol, 72, 2016, pp. 377- 82.

[2] Wei N.C. and Sung G.H., Bovine mastitis: risk factors, therapeutic strategies, and alternative treatments. A review, Asian-Australas J Anim Sci, Vol. 33, No.11, 2020, pp. 1699-1713.

[3] Khan M. and Khan A., Basic facts of mastitis in dairy animals: a review, Pak Vet J, 26, 2006, pp. 204-208.

[4] Valentina M., Hans U.G., Claudia P., Paola C., Bianca C., Enriqueta B., Alejandro C.M., Laura L.R., Volker K., Nicole W., Petzer I.M., Carlos S., Jeff R., Marcos V.S., Bruna G.A., Renata P., Valerio B., Mohamed S.A., Meriam B.S., and Paolo M., *Staphylococcus aureus* Isolates from Bovine Mastitis in Eight Countries: Genotypes, Detection of Genes Encoding Different Toxins and Other Virulence Genes, Toxins, 10, 2018, pp. 247.

[5] Abebe R., Hatiya H., Abera M., Megersa B., and Asmare K., Bovine mastitis: prevalence, risk factors and isolation of *Staphylococcus aureus* in dairy herds at Hawassa milk shed, South Ethiopia, BMC Vet Res, 12, 2016, pp. 270.

[6] Vasudevan P., Nair M.K.M., Annamalai T., and Venkitanarayanan K.S., Phenotypic and genotypic characterization of bovine mastitis isolates of *Staphylococcus aureus* for biofilm formation, Vet Microbiol, 92, 2003, pp. 179-185.

[7] Rainard P., Foucras G., and Fitzgerald J.R., Knowledge gaps and research priorities in *Staphylococcus aureus* mastitis control, Transbound Emerg Dis, 2018, 65 (Suppl 1), pp. 149-165.

[8] Kappeli N., Morach M., Corti S., Eicher C., Stephan R., and Johler S., *Staphylococcus aureus* related to bovine mastitis in Switzerland: Clonal diversity, virulence gene profiles, and antimicrobial resistance of isolates collected throughout 2017, J. Dairy Sci., 2019, Vol. 102 No. 4, pp. 3274–3281.

[9] Chandan S., Milon M., Bilkis K., Monir Md., Hossain Md., Solayman H., Antoni S., Muhammad T.I., Miquel M., Manoj K., Javad S.R., Harrasi A.A., and Rawahi A.A., *Heliotropium indicum* L.: From Farm to a Source of Bioactive Compounds with Therapeutic Activity, Evidence-Based Complementary and Alternative Medicine, 2021, Article ID 9965481, 21 pages.

[10] Osungunna M.O. and Adedeji K.A., Phytochemical and antimicrobial screening of methanol extract of *Heliotropium indicum* leaf, Journal of Microbiology and Antimicrobials, 2016, Vol. 3, No. 8, pp. 213–216.

[11] Nawaz A.H., Hossain M., Karim M., Khan M., Jahan R., and Rahmatullah M., An ethnobotanical survey of Rajshahi district in Rajshahi division, Bangladesh, American-Eurasian Journal of Sustainable Agriculture, 2009, Vol. 3, No. 2, pp. 143–150.

[12] Kugelman M., Liu W.C., Axelrod M., McBride T.J., and Rao K.V., Indicine-N-oxide: the antitumor principle of *Heliotropium indicum*, Lloydia, 2015, Vol. 39, No. 2-3, pp. 125–128.

[13] Roy A., Pharmacological activities of Indian Heliotrope (*Heliotropium indicum* L.): a review, Journal of Pharmacognosy and Phytochemistry, 2015, Vol. 4, No. 3, pp. 101–104.

[14] Boye A., Koffuor G.A., Amoateng P., Ameyaw E.O., and Abaitey A.K., Analgesic activity and safety assessment of *Heliotropium indicum* Linn. (Boraginaceae) in rodents, International Journal of Pharmacology, 2012, Vol. 8, No. 2, pp. 91–100.

[15] Shalini S., Kaza R., and Shaik F., Study on the anti-inflammatory activity of *Heliotropium indicum*, Journal of Innovative Trends in Pharmaceutical Sciences, 2010, Vol. 1, No. 1, pp. 43.

[16] Premnath D. and Gomez P., Antifungal and anti-bacterial activities of chemical constituents from *Heliotropium indicum* Linn. Plant, Drug Invention Today, 2012, Vol. 4, No. 11, pp. 564–568.

[17] Suroowan S., Pynee K.B., and Mahomoodally M.F., A comprehensive review of ethnopharmacologically important medicinal plant species from Mauritius, South African, Journal of Botany, 2019, Vol. 122, pp. 189–213.

[18] Pandey A. and Tripathi S., Concept of standardization, extraction and pre phytochemical screeningstrategies for herbal drug, Journal of Pharmacognosy and Phytochemistry, 2014, Vol. 2, No. 5, pp. 115-119.

11th Int. Conf. on Geotechnique, Construction Materials & Environment, Kyoto, Japan, 3-5 November 2021, ISBN: 978-4-909106063 C3051

ANALYSIS OF LOCAL RESIDENTS' MOVEMENTS FOR DAILY LIFE IN URBAN AREAS IN JAPAN

Hibiki MOTOI[1], Yukihiro YAMASHITA[2], Daisuke KOBAYASHI [3] and Yukikazu YAMAGUCHI[4]

[1]Graduate Course in Architecture, Civil Engineering and Urban Design, Osaka Institute of Technology, Japan; [2]Himeji City, Japan; [3]Osaka City, Japan;[4]Faculty of Engineering, Osaka Institute of Technology, Japan

ABSTRACT

In recent years, as Japan's urban population and the birthrate have declined as the population has aged, the number of vacant houses in urban centers has increased. This increase in house vacancy is an urban problem that is difficult to solve using conventional town and transportation planning methods. In particular, with regard to local transportation, the number of elderly people who have difficulty traveling is increasing as public transportation services are being cut due to profitability issues. The purpose of this study was to clarify the issues affecting local transportation in daily life. The analysis considered local residents' evaluations of public transportation and an assessment of local residents' movements in Moriguchi City, Osaka Prefecture. The results of the analysis showed that local residents' satisfaction with transportation services was correlated with the distance to the nearest train or metro station, but not to the nearest bus stop. Also, the transportation network may need to be redeveloped in the future because of differences in daily activities**,** even within Moriguchi City.

Keywords: Local residents, Daily life, Local transportation, Public transportation, Transportation network

INTRODUCTION

In recent years, as the Japanese population has declined and aged, vacant houses and other underused or unused land have randomly appeared inside cities, causing economic decline and public safety problems **[1]-[2]**. On the other hand, even in areas where the population is concentrated, it is becoming difficult to maintain public transportation, as buses are being discontinued due to a decrease in the number of users. In addition, as the number of elderly drivers increases, traffic accidents have also increased, and the number of elderly people surrendering their driver's licenses is increasing, despite public transportation services often being inadequate. As a result, there are concerns about an increase in the number of people with low mobility. Furthermore, the spread of the coronavirus is expected to bring about major changes in the transportation environment in daily life, including changes in work styles and lifestyles. To date, local governments have subsidized the operation of local community buses, and demand-based transportation services [3]. It is necessary to develop a transportation system that is tailored to the specific requirements of local residents in order to ensure that they can maintain their daily activities.

The purpose of this study was to clarify the problems facing local transportation by analyzing local residents' evaluations of the current public transportation system and their travel history in Moriguchi City, Osaka Prefecture, to provide basic information for improving the existing transportation system, and to propose improvements to the existing transportation networks.

METHODOLOGY

Target Area of Case Study

The study area is Moriguchi City, Osaka Prefecture (See Fig. 1). The city, which has a population of approximately 140,000 people and an area of 12.71 km^2, has been experiencing a decline in both population and economic activity since 1975. The city is served by trains, subways, and monorails. It takes about 15 minutes to travel from Moriguchi City to the center of Osaka City and about 35 minutes to Osaka Airport. In addition, private buses and local community buses run at a frequency of about one bus every hour [4]-[5].

Questionnaire Survey on Local Residents' Movements

Table 1 shows an overview of a questionnaire survey on local residents' movements. The questions assessed whether respondents had a driver's license, private car, evaluation of their movements in the city, and their movement history. Based on data published by Moriguchi City, the city was divided into eastern, central, and southern regions [4]-[5]. The evaluation results for daily movement and movement history were analyzed.

RESULTS & DISCUSSION

Table 1 Overview of a questionnaire survey on of local residents' movements

Purpose	To understand the evaluation of local residents' movements and the history of movements in order to examine the means of transportation for the future aging population
Study Area	Moriguchi City, Osaka Prefecture
Period	September 26, 2020 - October 19, 2020
Method	By mail
Target People	1,000 residents, aged 16 or older, randomly selected from Basic resident register network system in Moriguchi City
Collection Results	1000 distributed, 244 responses. 24.4% valid response rate

Results of analysis of local residents' movements

Evaluation of local residents' movements in the city

As can be seen in Fig. 1, the questionnaire survey was conducted in Sep and Oct 2020. 1,000 questionnaires were distributed to local residents of Moriguchi City in Osaka, Japan, and 244 responses were received. Figure 2 shows the personal attributes of respondents to the survey. A total of 59% of the respondents were "female," and 55% of the respondents were aged "60 or older". The percentage of respondents who "possessed a driving license" was 55%, and the percentage of those who owned "private car" was 44%. A total of 39% of the respondents rated their movements in the city as "inconvenient" or "slightly inconvenient". As shown in Fig. 3, the number of respondents who rated transportation in the city as being "inconvenient" was 29% for "shopping", 19% for "going to the hospital", 18% for "getting from their home to the nearest station", and 16% for "entertainment/learning".

Attitudes of private car owners toward surrendering driver's license

Figure 4 shows the results of the questions on alternative means of transportation for private car owners after they surrendered their license. Among the private car owners surveyed, 53% intended to return their license, of which 32% planned to do so "by the time they were 75 years old" and 64% "by the time they were 80 years old". After returning their license, their primary mode of transportation was to be "public transportation" for 37% of the respondents, followed by a "cycling" for 19%, and "shuttle bus or lifts by family members" for 14%.

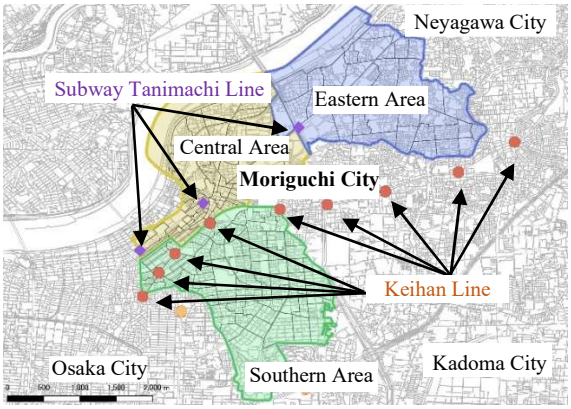

Fig. 1 The study area.

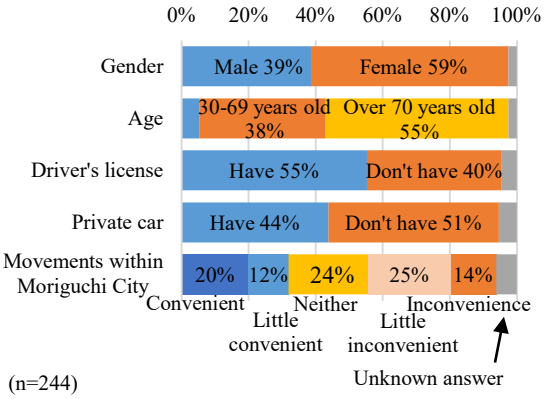

Fig. 2 The personal attributes of respondents.

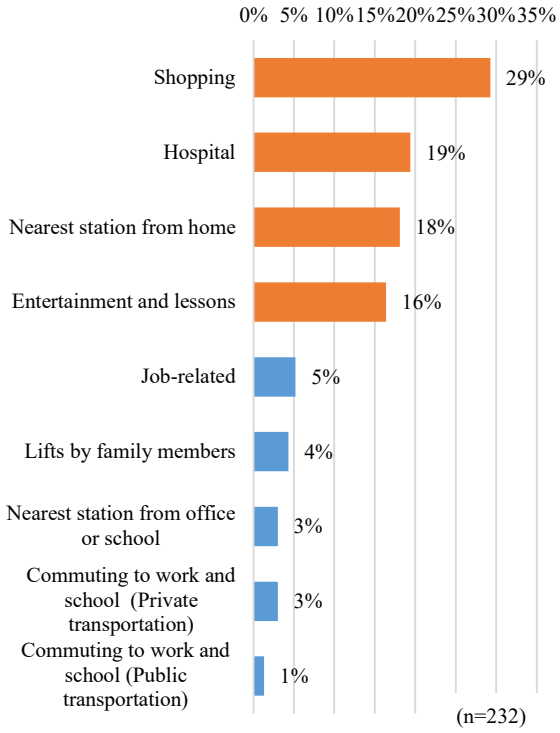

Fig. 3 The number of respondents who rated transportation in the city as being "inconvenient" / multiple answers.

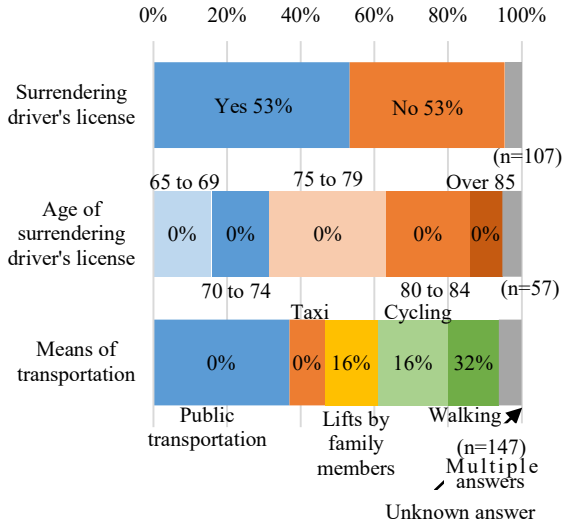

Fig. 4 alternative means of transportation for private car owners after they surrendered their license.

Figure 5 shows the reasons why private car owners selected these alternative means of transportation after surrendering their license. Most of the respondents emphasized "short travel time" and "catching transportation immediately in front of home". Those who selected public transportation placed more importance on "short travel time", while those who selected "taxi", "lifts by family members", "cycling", and "walking" placed more importance on "being able to travel immediately from in front of the home".

Evaluation of travel within the city by distance to the nearest station

Figure 6 shows the ratings obtained for the "convenience" or "inconvenience" of travel in the city as a function of distance from home to the nearest train station. The number of people who rated the distance from their home to the nearest station as "inconvenient" exceeded the number of people who rated it as "convenient" when the distance was between 600 m and 800 m.

Figure 7 shows a map of the "inconvenient" or "convenient" responses to travel by area. In the Eastern Area, most respondents rated travel within the city as being "inconvenient". This was because the average distance to the nearest station in the Eastern Area was more than 1000 m. Further, the only options available to residents in the Eastern Area are the subway located near the border with the Central Area, or the train station in Kadoma City, which lies outside Moriguchi City.

In the Eastern Area, only few stations exist, and all station are located near the boundary with the Central Area. Consequently, those residents who live near the stations tend to rate travel within the city as "convenient", while many other people rate it as "inconvenient".

In the Central Area, more respondents rated it as being "convenient" than "inconvenient". This may be since there are many subway stations in the area, and the distance between the residential area and the train station is shorter than it is in other areas.

Analysis results of local residents' movements

Purpose of travel in three areas of Moriguchi City

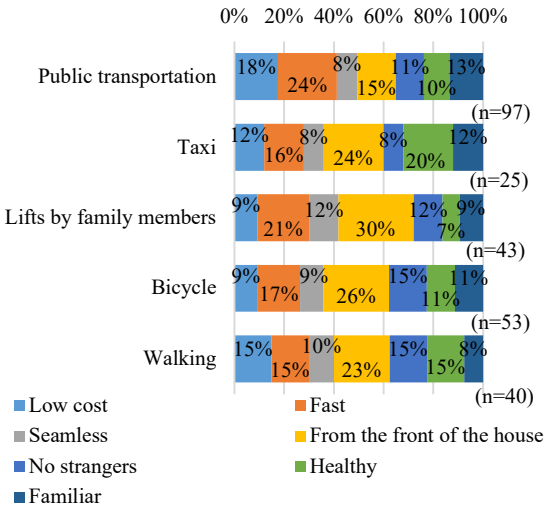

Fig. 5 Reasons why private car owners selected these alternative means of transportation after surrendering their license. (Multiple answers)

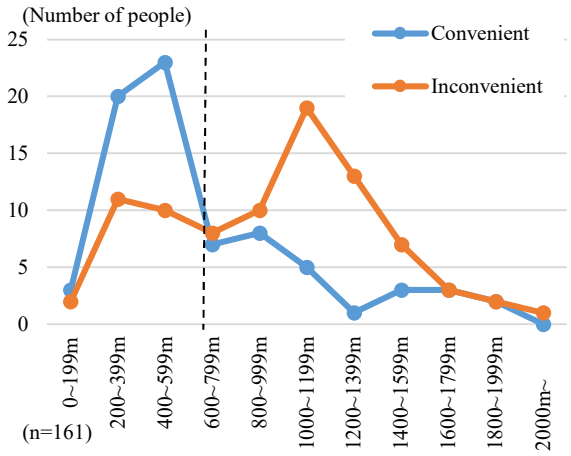

Fig. 6 The ratings obtained for the convenience or inconvenience of travel in the city as a function of distance from home to the nearest train station.

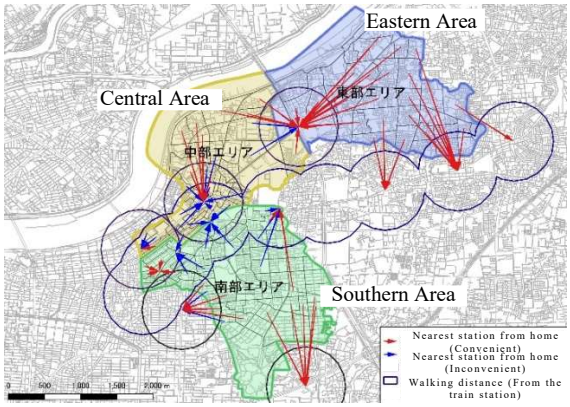

Fig. 7 Map of the inconvenient or convenient responses to travel by area.

Figure 8 shows the purpose of travel for trips in Moriguchi City only. And map of the purpose of travel for trips on weekdays and holidays are shown separately on the map in Fig. 9 and Fig. 10, respectively.

As shown in Fig. 8, “shopping” was the most common reason for travel on weekdays in all areas, followed by “commuting to work/school” and “going to hospital”. On weekends and holidays, “commuting to work/school” and “going to hospital” decrease, and “shopping” accounts for half of all trips. “shopping” was the most common activity in the Eastern Area, where there is a large commercial district, and in the Southern Area, where there are numerous department stores. “hospital visits” was the most common activity in the Central Area, where there are several regional hospitals.

Figures 9 and 10 show the following trends in travel to particular areas. On weekdays, most of the residents in Moriguchi City went to the Central Area for “hospital visits”, accounting for 44% of the total. Of these, more than 60% traveled to Matsushita Memorial Hospital. On weekdays, most “commuters” in respondents in Moriguchi City travel to the Southern Area around Moriguchi Station, accounting for 35% of all commuters in respondents. On weekends and holidays, most of the respondents went “shopping” at Dainichi Aeon Mall in the Eastern Area and Keihan Department Store in the Southern Area.

Representative means of transportation in Moriguchi City

Figure 11 shows the representative means of transportation in Moriguchi City by arrival point, and Fig. 12 and Fig. 13 shows that for travel by “train”, “subway” and “private car” for weekdays and holidays.

As shown in Fig. 11, "cycling" and "walking" account for about 60% to 70% of the means of transportation in all areas on weekdays and holidays. In addition, for both weekdays and holidays, there were more trips by “private car” to the Eastern and Central Areas than to the Southern Areas. The combined usage rate of “train” and “subway” was about 10% on weekdays and about 5% on weekends.

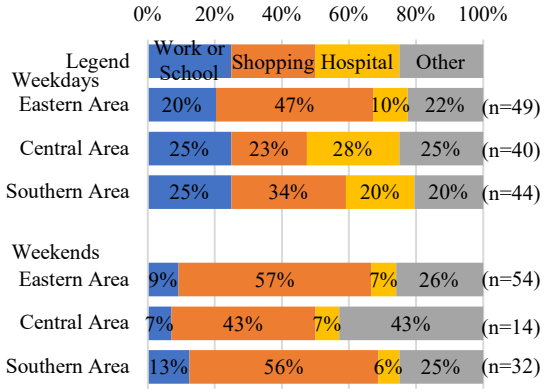

Fig. 8 Purpose of travels in Moriguchi City only.

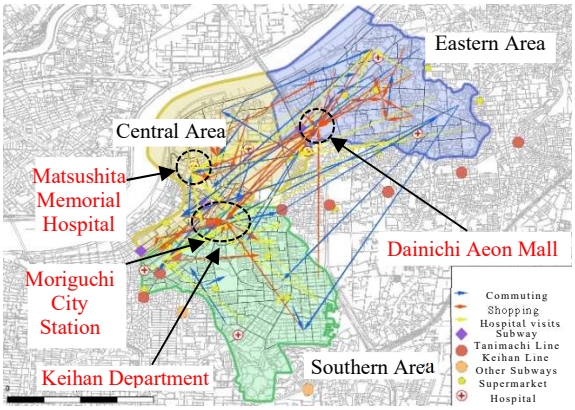

Fig. 9 Map of the purpose of travels on weekdays.

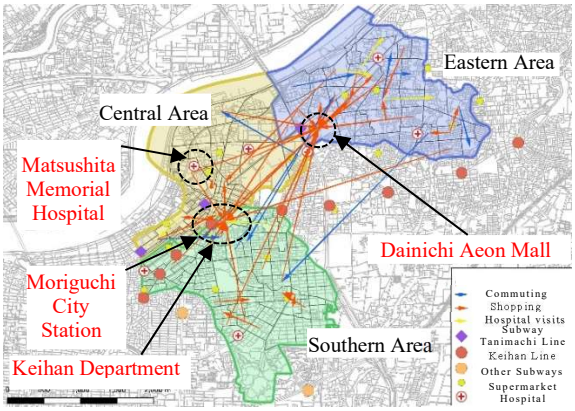

Fig. 10 Map of the purpose of travels on weekends.

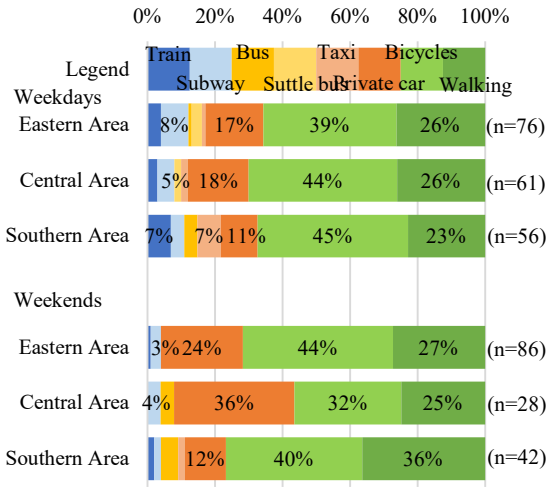

Fig. 11 The representative means of transportation in Moriguchi City by arrival point.

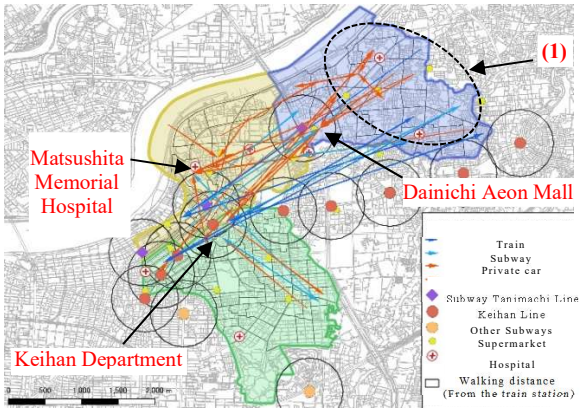

Fig. 12 Map of travels by train/subway and private car in Moriguchi City on weekdays.

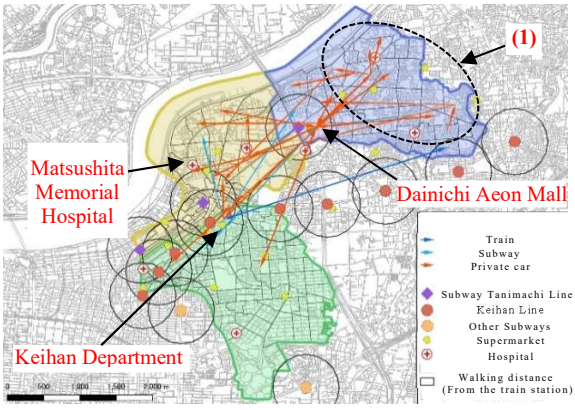

Fig. 13 Map of travels by train/subway and private car in Moriguchi city on weekends.

Figures 12 and 13 show that on weekdays, travel by "private car" were more likely to arrive at Matsushita Memorial Hospital in the Central Area and Dainichi Aeon Mall in the Eastern Area in respondents. On weekends, travel by "private car" were more likely to visit Dainichi Aeon Mall in the Eastern Area and Keihan Department Store in the Southern Area in respondents.

On weekdays, respondents that used the "train" tended to visit the areas between the Eastern and Southern Areas of the city, while respondents that used "private car" tended to move along the main street. 50 percent of the respondents that used the "train and subway" in the Eastern Area traveled from areas outside a 500 m radius of the train and subway stations, and about 60% of the respondents that used "private car" also traveled from areas outside a 500 m radius of the train and subway stations. Based on this result and the fact that the majority of the respondents will surrender their driver's license in the future, as shown in Fig. 4, it is necessary to secure a new means of transportation for zone (1) in the Eastern Area, because it will be difficult for these residents to move around in the future.

Transportation to the nearest station to get to Osaka City

We then examined "traveling from Moriguchi City to Osaka City", which is the most popular destination for commuters "going to work or school" on weekdays. Most travel on holidays was for "entertainment" or "sightseeing". Figure 14 shows the results for "travel to Osaka City" on weekdays and weekends and the means of transportation used. Figure 15 shows the mode of travel used to get to the nearest station in order to travel to Osaka City on weekdays and weekends combined, and the percentage of elderly people in 2035 by area.

Figure 14 shows that the most used mode of transport in all areas are "the train and subway". In the Eastern Area, the percentage of respondents who used "the subway" to travel to Osaka City was the highest, at 52%. On the other hand, in the Southern Area, which is relatively close to Osaka City, more people use "cycling" than any other area, at 26%.

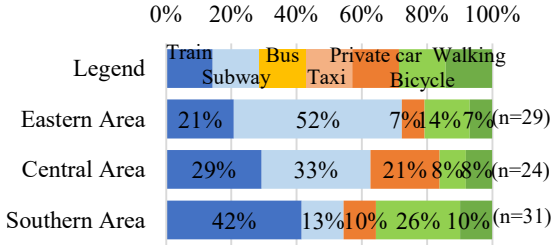

Fig. 14 The means of transportation used for "travel to Osaka City" on weekdays and weekends combined.

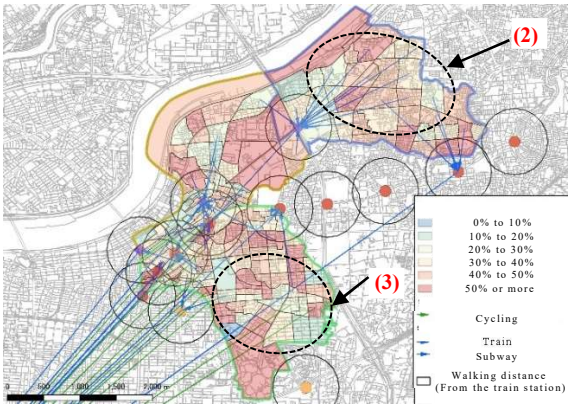

Fig. 15 The means of transportation used for "travel to Osaka City" on weekdays and weekends combined, and the percentage of elderly people in 2035 by area.

Figure 15 shows that in the Eastern Area, most people used Dainichi Station on the Osaka Metro; in the Central Area, most people used stations on the Osaka Metro; and in the Southern Area, most people used stations on the Keihan Line.

For the Eastern Area in particular, accessibility to both stations will need to be improved in the future because the future percentage of elderly people in the entire Eastern Area is estimated to be 42% and 52% of subway and rail users, respectively [6]. These people travel from areas outside a radius of 500 m from Osaka Metro Dainichi Station and Keihan Line Owada Station (See Fig. 15 (2)). On the other hand, in the Southern Area, the percentage of people traveling to the nearest station from areas outside a 500 m radius of the train or subway station is 29%, which is less than that in other areas. However, since the future aging rate for the entire Southern Area is estimated to be 40%, it is possible that those respondents who currently travel to Osaka City by cycling from areas outside a 500 m radius of a train or subway station will have difficulty in doing so due to aging or other reasons (See Fig. 15 (3)). Therefore, it is considered that accessibility to train and subway stations will need to be improved in the Southern Area in the future.

CONCLUSION

In this study, we were able to clarify the following by analyzing the current movements of local residents in Moriguchi city.

- The number of people who rated the distance from their home to the nearest station as "inconvenient" exceeded the number of people who rated it as "convenient" when the distance was between 600 m and 800 m.
- On weekdays, " shopping" was the most common reason for travel in all areas, followed by "commuting to work/school" and "going to hospital". On weekends and holidays, "commuting to work/school" and "going to hospital" decrease, and "shopping" accounts for half of all trips. On weekdays, most of the residents in Moriguchi City went to the Central Area for "hospital visits", accounting for 44% of the total. Of these, more than 60% traveled to Matsushita Memorial Hospital.
- In the Eastern and Southern Areas, accessibility to stations and subways will need to be improved in the future, as the aging of the population and other reasons may make it difficult to get around.

In the future, we would like to accumulate data on actual travel conditions and analyze changes in the number of trips and the of local residents' movements in order to consider the most sustainable means of transportation for Moriguchi City. In doing so, we hope to ensure that the transportation needs of the transportation-weak are met in an aging society.

REFERENCES

[1] Ministry of Land, Infrastructure, Transport and Tourism, Current situation and problems of vacant houses, 2014. http://www.hrr.mlit.go.jp/kensei/machi/akiya/kaisai03/02_honsho.pdf

[2] Ministry of Land, Infrastructure, Transport and Tourism, Promotion of measures against urban spongification, 2019. https://www.mlit.go.jp/common/001290033.pdf

[3] Ministry of Land, Infrastructure, Transport and Tourism, A Guide to Demand-Based Transportation, 2013. https://wwwtb.mlit.go.jp/hokushin/content/000104104.pdf

[4] Moriguchi City,2018. http://www.city.moriguchi.osaka.jp/ikkrwebBrowse/material/files/group/35/rittitekiseikakeikakuhonpen.pdf

[5] Moriguchi City,2014. http://www.city.moriguchi.osaka.jp/ikkrwebBrowse/material/files/group/13/kyotenshisetu_kihonkeikaku.pdf

[6] Ministry of Land, Infrastructure, Transport and Tourism, Future Population and Household Projection Tool V2, 2015. https://www.geospatial.jp/ckan/dataset/cohort-v2

11th Int. Conf. on Geotechnique, Construction Materials & Environment, Kyoto, Japan, 3-5 November 2021, ISBN: 978-4-909106063 C3051

THE DEDICATED LANE FOR MOTORCYCLE BASED ON MOTORCYCLIST CHARACTERISTICS AND SPACE DEMAND

Sobri Abusini[1] and Lasmini Ambarwati[2]

[1]Faculty of Natural Science, Brawijaya University, Malang, East Java; [2]Faculty of Engineering, Brawijaya University, Malang, East Java, Indonesia

ABSTRACT

A motorcyclist is the largest victim in the accident (more than 70%). The number of motorcycle increase by 3.6% every year, on the other hand, the safety of motorcyclist is still neglected. The effort to minimize motorcycle accidents should be realized by designing the demand for a dedicated lane. This study aims to develop the accident probability for the motorcyclist, to design the dedicated lanes based on the scape need, and to evaluate the existing dedicated lanes on several roads. Motorcyclist characteristics were identified from questionnaires. Evaluation of the existing dedicated lane based on the space requirements and highway performance. The results are found out that the probability of motorcycle accident is influenced by several characteristics, i.e. socio-economic characteristics, travel characteristics, and behavior characteristics. The dedicated lane requirement for motorcycle should be determined based on the innocuous movement of a motorcycle on the highway network. The existing dedicated lanes are not properly facilitated and do not pay attention to the safety and continuity of motorcycle movement. Based on the results, the government should facilitate the dedicated lane standard by considering the main factor, safety for the motorcyclists.

Keywords: Accident probability, Accident victims, Dedicated lane, Motorcycle accident, Motorcyclist characteristics.

INTRODUCTION

A motorcycle has several advantages and can move easily in traffic jams. This transport mode has efficiency in movement and low operational cost [1]. According to [2], several factors cause accidents, i.e. human, traffic, vehicle, highway, and environment. The human factor is the main factor influencing accidents approximately more than 95% because of this factor [3].

Economic development influences the growth of the number of motor vehicles by approximately 3% per year, particularly the growth of motorcycles by 5%. The number of accidents increases by 7% due to an increase in the number of motorcycles every year [4].

Motorcycle riders have a higher risk of accidents than other motorized vehicle users. First, from the stability of its movement, the motorcycle is only supported by two wheels and the balance of its movement depends on the ability of the driver to control the motorcycle. If the driver is not careful and has good skills, it is very easy to slip or crash. The second is the ability of the motorcycle to move at high speed which will result in serious injury in an accident or collision. Third, motorcycles are vehicles that are not designed to protect the rider (unprotected riders), are not equipped with covers to protect the driver, so motorcyclists must equip themselves with safety equipment such as helmets, weather-resistant jackets, and strong shoes. The impact of a motorcycle accident will result in higher losses compared to a car accident.

The phenomenon of the high number of accidents involving motorcyclists has occurred in most big cities in Indonesia, one of which is Malang District. The number of traffic accidents every year has increased. The high number of motorcycles causes a high number of accidents involving motorcyclists as victims. According to [4], the number of vehicles in Malang District increases every year, from 196,000 units up to 779,000 units, almost 4 times increase in less than 5 years (2012-2016). The number of motorcycles dominates approximately 87% of the total vehicles in Malang District. The increase in the number of vehicles in Malang District is also followed by an increase in the number of accidents. The largest increase in the number of accidents occurred in 2016. There was an increase in motorcycle accidents from 542 to 774 in 2016. Based on the number of victims, the number of deaths and minor injuries experienced a significant increase from 2015 to 2016. The death

victims and minor injuries were 219 people and 1,031 people respectively.

According to [2], Article 108 explains that slow-moving vehicles should use the left lane to ensure the safety and smoothness of traffic on the road. Motorcycle lanes are provided for the safe and smooth movement of motorcycles, improving road performance and reducing the rate and number of motorcycle accidents as victims [5]. A dedicated motorcycle lane is something that should be facilitated for each road section and the approach intersection, which separates motorcycles lanes from car lanes. With the existence of a dedicated motorcycle lane, it is expected that disturbances from motorcycles to cars can be reduced, then passenger cars and motorcycles can reach optimal speeds and for the safety of each type of vehicle [6].

The realization of dedicated motorcycle lanes in the simulation model at the intersection has an impact on reducing the average delay at the signalized intersections. The special stopping space for motorcycles in the simulation model can reduce the average delay experienced by cars. In addition, a dedicated stopping space for motorcycles is effective in reducing the average delay experienced by motorcycles [7].

Road sections with dedicated motorcycles lane influence the motorcyclist behavior in increasing speed. Here, space and minimum pore size are set in the road section to minimize the number of motorcycle accidents [6].

Generally, accidents occur based on several factors as follows: road user factors, traffic factors, vehicle factors, road factors, and environmental factors [8]. There are various relationships between the causes of road accidents. These factors make transportation safety as a focus of attention. According to [9], the behavior of male motorcyclists was recorded at 80.6% compared to other categories and needs to be considered as the cause of traffic accidents with the highest percentage compared to other identified causes.

Inadequate research concerns on behavior and characteristics of motorcyclists causing the accident by facilitating the dedicated lane based on the needs of motorcyclists for safe driving. To achieve this goal, it is necessary to investigate the need for a dedicated lane for motorcyclists based on their characteristics and behavior, as well as road performance. Understanding the need for dedicated lanes based on the characteristics and behavior of motorcyclists aims to reduce the number of accidents and to increase the safety of motorcyclists.

This study aims to identify the need for a dedicated lane by considering the safe distance of motorcycle movement based on the characteristics and behavior of motorcyclists.

The remaining paper is arranged as follows. The characteristics and behavior of motorcyclists and space requirements for designing dedicated lanes are described in Section 2. Methods, clarifying the behavior and characteristics of motorcycle and evaluating road performance in the presence of dedicated lane is described in the following sections. The Results and Discussions section explains how to describe the design of dedicated lanes related to highway performance. This section also evaluates the road performance with or without dedicated lanes. Finally, the study concludes the information and recommends the basis for the dedicated lane design by considering motorcyclist safety.

METHODS

Malang District, a city around Malang Municipality in East Java Province, Indonesia is the research area. The survey locations are adjusted to the location of the motorcycle accident as “Black Spot”. The locations were chosen because of the high rate of motorcycle accidents. Traffic accident data was supported by the Malang Police Department for 2016 – 2019 periods. The black spots are Geneng Kepanjen, Sudirman/ Mojosari Kepanjen, Hayam Wuruk Gondanglegi, Raya Bululawang, Sultan Agung Kepanjen, Brigjen Abdul Manan Pujon, Mojorejo, Panglima Sudirman Batu, Raya Areng-areng and Patimura Batu Streets as the research locations.

Collecting Data

The research survey was conducted by distributing questionnaires to respondents at random on ten roads which are “Black Spots". The samples are 150 respondents who have experienced a traffic accident or as a victim and investigated road geometry, traffic volume, and speed. The contents of the questionnaire include general characteristics of respondents (social-economic background), travel characteristics, and driving behavior.

Data Analysis

a. Descriptive analysis is an analysis that describes the condition of the road section as a black spot and the characteristics and behavior of motorcyclists.
b. Analysis of the determination/potential of motorcycle lanes, design of motorcycle lane.
c. Analysis of the need for motorcycle riding space with a pre-design of motorcycle lane including a safe space for driving when traveling alone, overtaking, and side by side with other motorcycles. Space requirement can be determined from the physical characteristics of motorcycles as well as the characteristics and behavior of motorcyclists.

d. Analysis of motor vehicle speed (heavy and light vehicles, motorcycles) on the geometry of the existing road and road condition with the design of a dedicated motorcycle lane. According to [10], road performance with service level (LOS) C is used as the basis for determining motorcycle lanes.

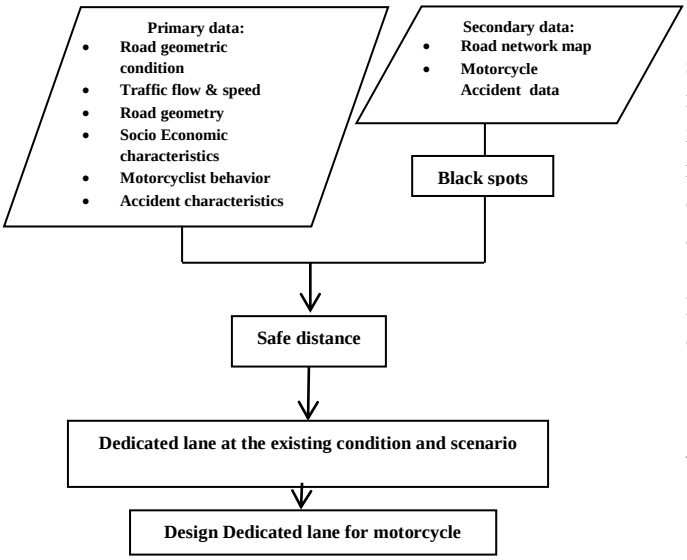

Fig. 1 The research framework

As shown in Fig.1, the design of dedicated lanes with the existing road conditions and scenarios based on the road performance on the road section as the black spot is the main analysis of this research. This study will examine the road performances without and with dedicated lane design. Analysis of road performance in scenario conditions was carried out by taking into account the existing conditions of road performance and land use at the research location as well as analysis of motorcycle space requirements and road performance before and after the scenario.

To design the dedicated motorcycle lane, it is necessary to analyze the safe distance for motorcycle movement. This study investigates the area around ten road sections in Malang District which are identified as black spots (high rates of motorcycle accidents). The survey was conducted to collect data on road geometric conditions, traffic flow, and speed, road geometry, socio-economic characteristics, motorcyclist behavior, and accident characteristics. The safe distance is based on the characteristics and behavior of motorcyclists. The design of the dedicated lane will be promoted by implementing a campaign to improve the safety of motorcycle drivers. The safety campaign programs to improve the safety of motorcycle drivers in Malang District should be carried out based on the predetermined safe distance.

RESULTS AND DISCUSSIONS

Characteristics and Behavior, and Travel characteristics of Motorcyclist

Planning and designing motorcycle infrastructure such as exclusive motorcycle lanes to minimize the number of motorcycle accidents requires information on the characteristics and behavior of motorcyclists. Their characteristics include age, sex, education, income, career, number of motorcycles, and ownership.

The characteristics of motorcyclists in Malang District are as follows:

a. Most of the respondents are aged 15-25 years (58%), and most of them are male. They graduated from senior high school (55%), as private employees (40%).
b. Accident Characteristics. Fifty-six percent of respondents have experienced at least one accident with a minor injury that occurred during the day and the evening. Motorcyclists get into accidents with other riders or through their fault.
c. Behavior characteristics before riding. Motorcyclist always checks breaking tools, fuel, and electrical tools before riding, while they rarely check motorcycle wheels and rear-view mirrors.
d. Behavioral characteristics while driving. Motorcyclists rarely use a helmet, trouser, and jacket. They sometimes ride together, giving signs when overtaking and using dedicated lanes for motorcycles.
e. Safety knowledge. Most motorcyclists do not understand the function of dedicated lanes, even though they will use dedicated lanes when the government facilitates these lanes with two lanes, designed with traffic markings, and an average width of 2.18 meters for the safety of motorcyclists. The minimum and average safe distances for motorcycles with other vehicles are 0.75 m and 2.18 m respectively. They hope that the government will pay attention to infrastructures and policies for motorcycles' safety. This distance is in line with the previous research which revealed that the interaction of motorcycles with other motorcycles and cars requires a critical pore space of 3.12 m and 3.21 m respectively [6].

Motorcyclists' knowledge of safety is taken into

consideration when designing the dedicated lane, from their knowledge, the development of an accident model is defined where the probability of motorcycle accident is influenced by the variables X31 (motorcycle lane requirements), X34 (Number of MC lane), and X35 (Safe distance with other vehicles when moving). Then the regression function is developed by three variables (X31, X34, and X35). The regression function is $Y_{MK} = 3.063+4.829X_{31} - 3.28\ X_{34(1)} -3.924\ X_{34(2)} - 1.037\ X_{35.}$ therefore the probability of accident due to the variables need for motorcycle lane (X31), X34 (Number of MC lane), and X35 (Safe distance with other vehicles when moving) is

$$Pi = F(\beta_o + \beta_1 X_{1i}) = \frac{}{e^{-Y_{MK}}} = \frac{}{e^{-(3.063+4.829X31 - 3.28\ X34(1) -3.924\ X34(2) - 1.037\ X35)}}$$

The regression function is fit because the t-test rejects the null hypothesis with a 95% confidence level. Table 1 presents the results of statistical analysis of motorcycle knowledge about safety that influences the accident. The R-squared for these variables shows a reasonable calibration fit. It is expected that the estimation model can be considered to improve motorcycle facilitation such as the existence of dedicated lanes in the highway network.

Table 1 Explanatory Variables in the model

		B	S.E.	Wald	df	Sig.	Exp(B)
Step 1[a]	X31(1)	4.829	1.001	23.283	1	.000	125.074
	X34			8.127	2	.017	
	X34(1)	-3.280	1.404	5.461	1	.019	.038
	X34(2)	-3.924	1.384	8.039	1	.005	.020
	X35	-1.037	.429	5.840	1	.016	.355
	Constant	3.063	1.590	3.712	1	.054	21.383

Table 2 Road performance before and after the design of dedicated motorcycle lane

road section	traffic volume (vehicle/hr)			speed (km/hr)	lane width (m)	shoulder width (m)	road capacity (pcu)	Volume capacity ratio		Improvement of road performance & MC safety				
	motorcycle	car	truck & bus					without MC lane	with MC lane	MC lane widh (m)		modeficatio n of lane width (m)	need to widen lane	
										scenario 1	scenario 2		scenario 1	scenario 2
Hayam Wuruk Gondanglegi	1,744	240	60	41.97	6	2.7	2,517	0.47	0.12	2.75	4.18	6.0	unnecessary widen lane	need 1.5 m widen lane each way
Raya Bululawang	3,548	840	210	42.34	6.5	1.25	2,517	1.14	0.43	2.75	4.18	6.0	need 1.25 m widen lane each way	need 2.7 m widen lane each way
Sultan Agung Kepanjen	2,498	496	124	41.22	5	3	2,517	0.75	0.34	2.75	4.18	5.0	unnecessary widen lane	need 1.2m widen lane each way
Panglima sudirman Kepanjen	2,418	804	201	40.27	5	2	2,517	0.90	0.55	2.75	4.18	5.0	need 0.75m widen lane each way	need 2.2m widen lane each way
Raya Genengan	2,176	724	181	36.24	5	1.5	2,517	0.81	0.49	2.75	4.18	5.0	widen lane	widen lane
Brigjen Abdul Manan Pujon	1,349	391	98	48.68	6	1.75	1,887	0.63	0.27	2.75	4.18	5.0	need 0.5m widen lane each way	need 2m widen lane each way
Raya Mojorejo Batu	1,681	576	144	29.51	6	1.5	2,489	0.64	0.40	2.75	4.18	5.0	need 0.75m widen lane each way	need 2.2m widen lane each way
Panglima Sudirman batu	601	206	51	50.32	9	0.5	2,766	0.21	0.09	2.75	4.18	7.0	need 1.25m widen lane each way	need 2.7m widen lane each way
Pattimura Batu	1,217	417	104	30.64	6	1	2,436	0.47	0.22	2.75	4.18	6.0	need 1.75m widen lane each way	need 3.3m widen lane each way
areng (Raya Dadaprejo/ Soekarno)	1,134	389	97	47.22	10	1	2,708	0.40	0.15	2.75	4.18	7.0	need 0.25m widen lane each way	need 2.7m widen lane each way

Table 2 describes traffic volume for each type of vehicle, speed, lane width, shoulder width, road capacity, road performance before and after the design of dedicated motorcycle lane, dedicated motorcycle width, and the modification of lane width due to the presence of motorcycle lane.

Several road performances in the existing condition have a low level of service, i.e. Raya Bululawang Kepanjen, Panglima Sudirman Kepanjen, and Raya Genengan Pakisaji Streets (VCR>0.8). This is due to the high volume of motorcycles. To improve traffic performance in the existing conditions, it is necessary to improve road performance analysis by making several scenarios.

In this study, two scenarios were created by designing a dedicated lane with a minimum distance (Scenario 1) and an average safe distance (Scenario 2) for motorcycles with the other vehicles. Scenario 1 is determined by planning the dedicated lane of 2.75 m (0.75m (minimum safe distance) + 2x 0.75m (motorcycle width) + 2 x 0,25m (distance with the barriers/ obstructions)). Scenario 2 is decided by planning the dedicated lane of 4.18 m (2.18m (average safe distance) + 2x 0.75m (motorcycle width) + 2 x 0,25m (distance with the barriers/ obstructions)). With the realization of the dedicated lane, all roads performances are at a good level as indicated by VCR <0.6 for Scenario 1 and Scenario 2.

Several roads, i.e. Hayam Wuruk Gondanglegi and Sultan Agung Kepanjen, do not require road widening with a dedicated lane width of 2.75 m. For the convenience of movement and safety of motorcycles, it is necessary to pay attention to Scenario 2 especially roads with a high volume of motorcycles. In both scenarios, there is a change in road geometry conditions.

The result of this study also supports previous research on the effort to minimize motorcycle accidents by reducing vehicle volume and speed, as well as improvement of road geometry, i.e. lane width, shoulder width, number of lanes, number of access, and walkway width [11]. The results of the previous study recommend an increase of the lane width by facilitating the dedicated lane to accommodate a high volume of motorcycles, furthermore, the movement of the motorcycle will be safe and comfortable.

The dedicated motorcycle lanes to reduce the number of accidents involving motorcycles is the result of research based on an analysis of motorcycle's safe distance when moving or interacting with other vehicles. The behavior and awareness of motorcyclists and other vehicles regarding the use of dedicated motorcycle lanes is the basis for the development and arrangement of dedicated motorcycle lanes related to motorcycle safety. It is expected that transportation safety and motorcyclist awareness will be achieved through a motorcyclist safety action program. Therefore, the government should establish the dedicated motorcycle lane for motorcycle safety and minimize motorcyclists as victims of accidents.

CONCLUSIONS

In Malang District, 56% of motorcyclists have experienced an accident while riding a motorcycle. Based on socio-economic characteristics, drivers are male (70%), aged 15-25 years (58%), high school education background (55%), and private employees (40%). Behavioral characteristics of motorcyclists were found that drivers always check breaking tools, fuel, and electrical equipment before driving, while motorcycle wheels are rarely checked. For behavior characteristics during driving, motorcyclists rarely use a helmet, trouser, and jacket. They sometimes ride together, giving signs during overtaking and rarely using dedicated lanes for motorcycles.

The study suggests that the minimum and average safe distances for a motorcycle with the other vehicles are 0.75 m and 2.18 m respectively. They hope the government to pay attention to safety infrastructures and policies for motorcycles more than 2.18 meters based on the behavior of motorcyclists.

Two scenarios are created by designing the dedicated lane with a minimum distance (Scenario 1) and an average safe distance (Scenario 2) for a motorcycle with other vehicles. Scenario 1 is set at 2.75 m and Scenario 2 is determined at 4.18 m. With the realization of the dedicated lane, all road performances are at a good level as indicated by VCR <0.6 for Scenario 1 and Scenario 2.

Scenario 2 especially roads with the high volume of motorcycles should be considered for the convenience of movement and safety of motorcycles. In both scenarios, there is a change in the condition of the road geometry. Therefore, the government should establish a dedicated motorcycle lane for motorcycle safety and minimize motorcyclists as victims of accidents.

ACKNOWLEDGMENTS

A grant from the Faculty of Natural Science, Brawijaya University, Malang, Indonesia has supported this research. We would like to express deep thanks to the Faculty of Natural Science, Brawijaya University.

We also want to thank Riski Nur Istiqomah Dinnullah, the doctoral student in the Department of

Mathematics, Brawijaya University for assisting to collect and processing data.

REFERENCES

[1] Permanawati, Sulistio, H., T. and A. Wicaksono. (2010). Motorcycle Accidents on the Highway Network, Malang: Brawijaya University, Bachelor thesis, unpublished (in Indonesian).

[2] Anonymous, Traffic Law no. 22/2009, (2009) Law of the Republic of Indonesia number 22 of 2009 concerning Road Traffic and Transportation and its implementing regulations (in Indonesian).

[3] Warpani, Suwardjoko P. (2002). Traffic Management and Road Transport: ITB (in Indonesian)

[4] Statistic Bureau of Malang City, the Figures of Malang City in 2018 (in Indonesian).

[5] Idris, M., (2010). The Criteria for Motorcycle Lane for Secondary Arterial Road (in Indonesian), Technical Report. Puslitbang Jalan dan Jembatan, Bandung.

[6] Ambarwati, L., Pel, A.J., Verhaeghe, R., & van Arem, B., (2014a). Empirical analysis of heterogeneous traffic flow and calibration of porous flow model. Transp.Res. Part C: Emerg. Technol. 48, 418–436.

[7] Zukhruf, F., Frazila, R. B., Wiowo, S. S.,(2010) Evaluation of Signalized Intersection Performance with Signalized Intersection Management Scenarios Using Micro Simulation Model, Simposium XIII FSTPT, Universitas Katolik Soegijapranata Semarang, 8-9 Oktober 2010.

[8] Enggarsasi, U. & Sa'diyah, N.K. (2017). Study of the Factors that Cause Traffic Accidents as an Effort to Improve Traffic Accident Prevention.. *Perspektif*. 22(3): 238-247 (in Indonesian).

[9] Idris, A., Hamid, H., & Hua, L. T. (2019). Factors contributing to motorcycle accidents in Malaysia. In *IOP Conference Series: Earth and Environmental Science* (Vol. 357, No. 1, p. 012039). IOP Publishing.

[10] IHCM (Indonesian Highway Capacity Manual). Department of General Work, Directorate General of Highway, 1997.

[11] Abusini, S., & Ambarwati, L. (2020). Motorcycle accident model for highlands regions by applying Generaliazed Linear Model (GLM). *Lowland Technology International*, *20* (3,Dec),331-340.

11th Int. Conf. on Geotechnique, Construction Materials & Environment,
Kyoto, Japan, 3-5 November 2021, ISBN: 978-4-909106063 C3051

FLOOD DAMAGE ASSESSMENT: A REVIEW OF MULTIVARIATE FLOOD DAMAGE MODELS

Sumiliana Sulong and Noor Suraya Romali

Faculty of Civil Engineering Technology, Universiti Malaysia Pahang, Gambang, Kuantan, Pahang

ABSTRACT

Nowadays, more emphasis is given to flood risk management for dealing with flood disaster. To assess flood risk, damage from flood is crucial component to be considered. Flood damage function is a commonly accepted approach for the estimation of flood damages worldwide, where it combines the element of hazard, vulnerability and exposure. However, this method usually considers only the flood depth and the type of buildings at risk. The effect of other flooding conditions (impact parameters) and the resistance parameters to the degree of flood damages are normally neglected. In fact, flood risk assessment should cover all damage dimensions in order to obtain an extensive description of flood damages. Multivariate damage modelling can be applied to examine the relationship between flood damages and other flood influencing factors. This paper presents a review of methods applied to generate multivariate flood damage models, which includes the Multiple Linear Regression (MLR), Bayesian Network (BN), Artificial Neural Network (ANN) and the Random Forest (RF) analysis. Moreover, the multivariate models are also found capable in generating synthetic data to counter the problems of flood damage data scarcity experienced by the developing countries. Identifying damage influencing factors especially resistance parameters is important as a comprehensive flood damage model based on the local conditions and property characteristics of study area can assist in the future damage assessment works, as well as offering decision-makers with an indispensable tool for managing strategies related to flood risk.

Keywords: Flood risk, Flood damage assessment, Flood damage influencing factors, Multivariate analysis

INTRODUCTION

Floods are the most prevalent natural catastrophes that may endanger lives, destroy property, disrupt social and economic activities, and the environment and ecology in both rural and urban regions. Global climate change and rapid urbanization are explicitly identified as major catastrophe hazard drivers in the Sendai Framework 2015 - 2030 [1]. Although boundless focus is positioned in executing structural flood mitigation approaches, non-structural measures including flood risk assessment still need to be extensively managed, since comprehension of the damage evaluation remains inadequate [2]. Flood risk assessment is concerned with the combination of the hazard and its vulnerability. Estimation of flood hazard combining two essential flood characteristics, namely flood extent and flood depth while vulnerability is a notion that includes exposure and refers to the impacts of floods. The primary tools in visualizing flood risk assessment are the flood hazard map, flood damage assessment, and flood vulnerability map [2] – [4].

Flood vulnerability assessments has become increasingly relevant all around the world. Meanwhile, flood damage assessment is one of the main tools of flood vulnerability assessment. Its framework serves as a decision support tool for decision-makers who must prioritise and execute best practices in flood risk reduction. Flood damage refers to all varieties of damages produced by floods and is categorised into two groups: tangible and intangible damages [4]–[8]. Tangible damages may be quantified in monetary terms, while intangible damages, are often measured using non-monetary metrics such as the ecosystem, the environment, health, and psychological impacts. Furthermore, each group of damage is classified further as either direct or indirect damages [9].

Penning-Rowsell and Chatterton [10] in the United Kingdom and Smith [11] from the University of New South Wales, Australia, were among the pioneer researchers on flood damage assessment. Although flood vulnerability assessment studies have begun over 40 years ago, it is still new in developing countries. Many works are to be done, which relate to several issues, such as limited knowledge on the factors influencing vulnerabilities, damage data scarcity, and uncertainties in flood damage analysis [4], [12]. Past studies on flood damage assessment typically deliberated on the relationship between flood damage and hydrological impacts parameters, such as flood depth, which has been regularly chosen as the most appropriate flood damage variable [13]. The variation of flood damages to properties could not be explained based on flood depth alone [8]. The outcomes were uncertain and did not significantly affect the total damage cost predictions. Therefore, proper estimation of flood damage is challenging and requires careful consideration of some effects such as

the effects on socio-economic conditions and the resistance parameters to the degree of flood damage, especially for loss estimation in monetary terms. Many studies have shown that the influence of resistance parameters (such as building characteristics and unitary prices) should be given more attention as it affects the accuracy of flood damage and makes the outcomes adaptable for other areas [12]. Apart from that, with appropriate modifications, flood damage assessment can also be made on other assets and properties such as building contents in residential, commercial and industrial buildings [14]. Therefore, the study on the relationship between socio-economic conditions and property characteristics that may affect the extent of flood damage should prioritised. This paper intends to deliver a concise review of the multivariate flood damage models that may aid in establishing a framework for assessing the flood damages by considering the effects of damage factors from multiple dimensions. To this end, a review of flood damage assessment framework is provided to improve the understanding of flood damage estimation.

FLOOD DAMAGE ASSESSMENT

Throughout recent decades, risk-based methods have been progressively acknowledged and utilized in managing flood risk. Flood damage assessments are important component of flood risk assessment, and the outcomes offer decision-makers with essential tools for preparing more effective approaches of reducing risk [15]. Consequently, the current understanding of flood impacts and their outcomes can be improved towards developing a more reliable damage estimation, and efficiently reduce flood risk. The effectiveness of flood damage assessment depends on its framework, which encompasses hazard, vulnerability, and exposure. The concept has been adapted by numerous studies in both developed and developing countries and has progressively obtained global reception as the standard approach for assessing urban flood damages in urban areas. The key differences among the existing methodological frameworks for damage assessment are linked to the context of flood damage assessment (purpose, required accuracy and reliability data and resource availability, time consumption, spatial scale approach (macro-, meso-, and micro-scale), exposure and element at risk analysis, damage influencing parameters, and damage categories) [9].

Two main ways of assessing the flood damage are the unit loss and the modelling approach [16]. The unit loss approach refers to the direct computation of loss to individual properties, which is then combined to create a total loss number for the event under consideration. For losses resultant of flooding, this commonly involves the estimation of the damages to each property (or unit) using a questionnaire survey on the affected populations and properties to assess the sustained damage or average values [16]. The losses for each unit (property) are then summed up to estimate the total event loss. The other method is the modelling approach method which may be divided into two main techniques: an interactive computer package model based on a web application or a stand-alone version; and statistical analysis techniques [17]–[19]. Some examples of well-known computerized model are Integrated Software Package for Flood Damage Analysis (FDA package) from United States, Rapid Appraisal Method (RAM) and ANUFLOOD from Australia and INSYDE models in Italy [14]. The statistical analysis techniques include a damage function model that utilizing the relationship between hazard parameters (hydrological characteristics), and resistance parameters such as property characteristics and socio-economics situation to the expected damages [12], [14].

Recently, several researchers have recently created multivariate flood damage models utilizing statistical approaches, such as the Multiple Linear Regression, the Bayesian Network, the Artificial Neural Network (ANN), and the Random Forest analysis [15], [20], [23]–[27]. Multivariate flood damage models have become increasingly common in data-scarce areas [19]. In addition to modelling applications, relevant new data points may be produced to counter the issues of data scarcity issues. As a result, together with subsequent works addressing the synthetic approach, model development is less reliant on accessible datasets. Therefore, creating a site-specific model that reflects the flood and socioeconomic circumstances in the data scarcity region is appropriate.

FLOOD DAMAGE MULTIVARIATE MODEL

Flood Damage Influencing Variables

Torgersen [26] asserted the necessity to identify patterns and interactions among multi-parameters that impact various damage categories for the purpose of developing reliable flood damage models that represent the relationship between flood damage and resistance parameters such as socioeconomic and property characteristics. The influencing factors of flood damage may be divided into two categories: impact (hazard) parameters; and resistance (vulnerability) parameters. Impact parameters that influence flood damage include water depth, the velocity of water flow, the duration of flood, the contamination in flood water, debris and the frequency of flooding. Meanwhile, the resistance parameters include property type, property quality, building material, property value, precautionary measures and socio-economic circumstance (e.g.,

income, educational background and ownership status).

Nevertheless, the relationship between flood damage and resistance parameters such as socio-economic and property characteristics has been insufficiently emphasized [18]. Several studies discovered that the disparity in flood damage to properties cannot be solely explicated by the depth of flood water [18]. The flood damage assessment does not depict the distribution of losses throughout a flooded area and does not reflect the total impact of the flooding since the various resistance parameters disregarded. As a result, other additional damage influencing parameters must be included in the construction of reliable flood damage modelling [28]. The multivariate flood damage model has demonstrated an improved forecast accuracy, allowing for validity with any flood occurrence and diverse locations in flood damage assessments [28].

Multivariate Flood Damage Models

Recently, flood damage models have been established with multivariate of impact parameters (e.g., water depth, flow velocity, flood duration, and contamination) and resistance parameters (e.g., building material, type of building, socio-economic status, flood warning, and preparedness) [15], [20], [23]–[27]. Table 1 summarized the techniques used by the researchers in multi variate models. Statistical analysis techniques such as Multiple Linear Regression (MLR), Bayesian Network (BN), Artificial Neural Network (ANN) and Random Forest (RF) have been used in establishing the multivariate flood damage assessment model for the purpose of identifying the importance flood damage influencing parameters and generating synthetic data for useful predictions of the flood damage estimation. The description of the techniques is further elaborated in the following sections.

Multiple Linear Regression

Multiple Linear Regression has been commonly employed to aid in flood damage assessment. Win Zin [15] established a flood loss estimation model of direct damages to residential buildings in Bago, Myanmar, using the multivariable linear regression to determine the most influencing factors to the flood damage. This model incorporates more than one factor of hazard and resistance variables that affect damage, such as the depth of floodwater, the duration of flooding, building material, age of the building, building condition, number of stories and flood level. The multiple linear regression models the linear relationship between the independent variable (hazard and resistance variables) and the dependent variable (flood damage). The coefficient of determination (R^2) value and p-value measures the significant outcome, and the output was displayed as an equation. On the other hand, Velasco [4] and Wagenaar [23] also developed a flood loss estimation model using the linear-regression-based approach compared to the other regression approaches using supervised learning techniques to identify the approach that produces the best result.

Table 1 Multivariate flood damage models techniques and variables.

Authors	Multivariate flood damage models techniques	Flood damage variables	
		Impact (hazard) variables	Resistance variables
[4]	Multiple Linear Regression, Random Forest and Artificial Neural Network	Flood depth	Building structural, building fabric, building inventory and clean-up cost
[15]	Multiple Linear Regression	Flood depth and duration of flooding	Building characteristics
[18]	Random Forest	Flood depth	Building structural, building fabric and building inventory
[23]	Multiple Linear Regression, Bayesian Network and Random Forest	Flood depth, the velocity of flood water and duration of flooding	Building characteristics
[28]	Random Forest	Flood depth	Building structural, building fabric and building inventory
[33]	Artificial Neural Network	The extent of flood, duration of flooding and flow velocity	Building material, building quality, building age, building type, location, and value of the affected buildings
[36]	Random Forest	Flood depth, duration of flooding and contamination	Size of company, emergency preparedness, building structural and equipment

Bayesian Network (BN)

Wagenaar [23] adapted the Bayesian Network (BN) technique to model flood damage and generate high-quality synthetic data as a substitute to the data-driven structure. The BN technique is a probabilistic graphical model that represents a set of random variables and provisional dependencies in a Directed Acyclic Graph (DAG) structure [35]. Every variable in the network may be perceived as a preceding probability distribution, and dependencies between variables are represented with edges representing joint probability distributions. The edges in the BN are focused on the influence of one variable that flows to the other. From this network, extrapolation can be performed to apply knowledge of one variable for predicting other variables. It demonstrates the versatility and value of combining multi-parameters to predict system behaviour for multiple data output. The ability of the BN technique to assimilate data allows them to integrate several multi-parameters simulations from developed models for a combined assessment of many scenarios and characteristics.

Wagenaar [23] performed the multi-variable flood damage model by considering the hazard variables (e.g., the depth of flood water, the duration of flooding and the velocity of flood water) and resistance variables (e.g., building characteristics). One of the most significant advantages of employing BN is due to its ability to analyse correlations between variables using data contained in conditional probability tables. Because conditional probability tables are designed with the connected relationships between variables, the BN may also be used to answer queries regarding sector behaviour [31]. By means, BN may quantify the distribution obtained in resistance parameters and assess the flood damage with the induced hazard characteristics. However, the disadvantage of the BN technique is its poor performance in cases with a limited data set and poor data quality [23].

Artificial Neural Network (ANN)

Rumelhart [34] pioneered the ANN approach, which was inspired by the way the human brain analyses information [35]. ANNs discover the connections between variables in a data collection. The model constructed using ANNs is composed of numerous (hidden) layers of neuron-like processing units coupled in a network-like model. Each neuron is linked to every other neuron in the layer immediately before and following it. Coefficients are applied to measure every value passing through the neuron. The coefficients of the neurons are computed by an optimization approach that reduces error on the training data set.

Amadio [33] applied the Artificial Neural Network (ANN) to evaluate flood damage and generate synthetic data in order to estimate the potential economic costs of flood events to residential buildings in Italy. In the study, apart from taking the flood depth into consideration, the contribution of multivariables is considered, such as the detailed hazard data (e.g., the extent of flood, its duration and its flow velocity) and comprehensive vulnerability data including building characteristics (e.g., building material, building quality, building age, building type, location, and value of the affected buildings). All of these multivariables are significantly correlated to damage factor.

ANN models are excellent for a probabilistic analysis, i.e., a procedure in which the variation in input variables may be explicitly represented in a model and may include the quantitative analysis of enormous quantities of data. Other benefit is ANN can extrapolate configuration since the output range of the model is not restricted to the range of normalized values. The input data is distributed into three unique sets at random, namely training, validation, and test. The training data set is used to calibrate the ANN model, signifying that the weight connections among neurons are changed in relation to the data set. The validation set is applied to end the training process in in the prevention of overtraining or overfitting of ANN model; thus, the test set is not supplied to the model during training since it is only utilised to check the effectiveness of a trained ANN when stipulated by new data.

Random Forest (RF)

Random Forest (RF) analysis based on regression approach is increasingly popular in modelling the flood damage assessment. Regression analysis is mainly used in understanding the relationship between dependent variables (hazard) and independent variables (vulnerability). Wagenaar [23] and Velasco [4] assessed flood damage for a variety of damage factor variables using the Random Forest (RF) regression technique. The regression tree-based model generates data for each tree using a bootstrapping resampling method [35]. Branches are created in each tree by separating the data set using binary recursive partitioning, such as partitioning data based on whether the average wind speed is greater than a specified value. The RF analysis method does not use all explanatory factors for each tree but rather pursues the optimal splits among a fixed set of explanatory variables being assessed. The number of sampled features is the square root of the total number of features in the data sets. The best splits are regression trees that separate the training data until the results do not vary as much. The mean value of the predictions from each regression tree is the anticipated value for the entire RF model. Thus, the more decision tree a random forest model includes, the more robust and accurate its result becomes.

Nafari [18], Malgwi [32], Wagenaar [35], Siege [36] and adapted the RF analysis to develop a flood damage function model for the classification and regression of continuous dependent variables. All of these researchers relate the damage to many other influencing factors including hazard and resistance parameters. Nafari [18] derived the flood damage model by considering the relationship between multi parameters, consisting of impact variables (e.g., flood depth, water contamination and flow velocity) and resistance variables which include emergency precaution, preparedness, building characteristic (e.g., building material, building quality and building size) and socio-economic situations (e.g., ownership status and household income) to flood damage. The results from the RF simulations showed that factors other than flood depth such as flow velocity, water contamination, precaution measure, size of building, the value of the affected building, and building quality also significantly influence flood damage. Apart from modelling application, this regression technique can also generate appropriate new data points to alleviate data scarcity problems [36]. Malgwi [28] reported that the RF model which use data in a site-specific region shows the same high accuracy and consistency result when tested on another region.

CONCLUSION

Nowadays, flood vulnerability assessment has become increasingly important around the world. A number of previous studies had utilized damage function approach in estimating flood damage. However, such a method relies only on a deterministic relationship between the type or use of properties at risk and the depth of the flood water. The effects of other flood influencing parameters such as the natural/socio-economic conditions and the resistance parameters to the degree of flood damages are usually neglected. From the literatures, it was discovered that the recent estimation method which applies multivariate flood damage models, has effectively relate flood damage with other influencing factors such as impact variables (e.g., flood depth, velocity, frequency, water contamination and velocity) and resistance variables inclusive of permanent resistance (e.g., emergency measures, precautionary measures, building characteristics – age of building, building material and building size) and temporal situation (e.g., preparedness and socio-economic status – ownership status, household income and educational level). Furthermore, the multivariate models are also capable of generating appropriate new data points to counter the problem of insufficient or missing data. This would be beneficial to developing countries that experience issues of data scarcity in performing damage assessment works.

ACKNOWLEDGEMENTS

The authors would like to thank Ministry of Education of Malaysia (MOE) for providing financial support under fundamental research grant No. FRGS/1/2019/TK01/UMP/02/2 (University reference RDU1901155) and Universiti Malaysia Pahang for technical support and encouragement.

REFERENCES

[1] Teitelbaum L., M. L. Ginsburg M. L., and Hopkins R. W., Sendai Framework for Disaster Risk Reduction 2015-2030, Vol. 144, No. 2, 1991, pp. 169–173.

[2] D'Ayala D., Wang K., Yan Y., Smith H., Massam A., Filipova V., and Jacqueline P., Flood Vulnerability and Risk Assessment of Urban Traditional Buildings in a Heritage District of Kuala Lumpur, Malaysia, Nat. Hazards Earth Syst. Sci., Vol. 20, No. 8, 2020, pp. 2221–2241.

[3] Romali N. S., and Yusop Z., Flood Damage and Risk Assessment for Urban Area in Malaysia, Hydrol. Res., Vol. 52, Issue. 1, 2021, pp. 142–159.

[4] Velasco M., Cabello A., and Russo B., Flood Damage Assessment In Urban Areas- Application to the Raval District of Barcelona Using Synthetic Depth Damage Curves, Urban Water J., Vol. 13, No. 4, 2016, pp. 426–440.

[5] Brémond P. and Grelot F., Review Article: Economic Evaluation of Flood Damage to Agriculture - Review and Analysis of Existing Methods, Nat. Hazards Earth Syst. Sci., Vol. 13, No. 10, 2013, pp. 2493–2512.

[6] Jonkman S. N. and Vrijling J. K., Loss of Life Due to Floods, J. Flood Risk Manag., Vol. 1, No. 1, 2008, pp. 43–56.

[7] Mohd Mushar S. H., Kasmin F., Syed Ahmad S. S., and Kasmuri E., Flood Damage Assessment: A Preliminary Study, Environ. Res. Eng. Manag., Vol. 75, No. 3, 2019, pp. 55–70.

[8] Chen A. S., Hammond M. J., Djordjević S., Butler D., Khan D. M., and Veerbeek W., From Hazard to Impact: Flood Damage Assessment Tools for Mega Cities, Vol. 82, No. 2, 2016.

[9] Scorzini A. R. and Frank E., Flood Damage Curves: New Insights From the 2010 Flood in Veneto, Italy, J. Flood Risk Manag., Vol. 10, No. 3, 2017, pp. 381–392.

[10] Penning-Rowsell E.C. and Chatterton J.B, The Benefits of Flood Alleviation: A Manual of Assessment Techniques, 1979.

[11] Smith D. I., Actual and Potential Flood Damage: A Case Study for Urban Lismore, NSW, Australia. Appl. Geogr. 1, 1981, pp. 31–39.

[12] Dottori F., Figueiredo R., Martina M. L. V., Molinari D., and Scorzini A. R., INSYDE: A Synthetic, Probabilistic Flood Damage Model

Based on Explicit Cost Analysis, Nat. Hazards Earth Syst. Sci., Vol. 16, No. 12, 2016, pp. 2577–2591.
[13] Martínez-Gomariz E., Forero-Ortiz E., Guerrero-Hidalga M., Castán S., and M. Gómez, Flood Depth-Damage Curves for Spanish Urban Areas, Sustain., Vol. 12, No. 7, 2020.
[14] Pistrika A., Tsakiris G., and Nalbantis I., Flood Depth-Damage Functions for Built Environment, Environ. Process., Vol. 1, No. 4, 2014, pp. 553–572.
[15] Zin W. W., Kawasaki A., Hörmann G., Acierto R. A., San Z. M. L. T., and Thu A. M., Multivariate Flood Loss Estimation of the 2018 Bago Flood in Myanmar, J. Disaster Res., Vol. 15, No. 3, 2020, pp. 300–311.
[16] Win S., Zin W. W., Kawasaki A., and San Z. M. L. T., Establishment of Flood Damage Function Models: A Case Study in the Bago River Basin, Myanmar, Int. J. Disaster Risk Reduct., Vol. 28, 2018, pp. 688–700.
[17] Dutta D., Herath S., and Musiake K., Direct Flood Damage Modeling Towards Urban Flood, Engineering, No. July, 2001, pp. 127–143.
[18] Nafari R. H., Ngo T., and Mendis P., An Assessment of the Effectiveness of Tree-Based Models for Multi-Variate Flood Damage Assessment in Australia, Water (Switzerland), Vol. 8, No. 7, 2016.
[19] Malgwi M. B., Fuchs S., and Keiler M., A Generic Physical Vulnerability Model for Floods: Review and Concept for Data-Scarce Regions, Nat. Hazards Earth Syst. Sci., Vol. 20, No. 7, 2020, pp. 2067–2090.
[20] Carisi F., Schröter K., Domeneghetti A., Kreibich H., and Castellarin A., Development and Assessment of Uni- and Multivariable Flood Loss Models for Emilia-Romagna (Italy), Nat. Hazards Earth Syst. Sci., Vol. 18, No. 7, 2018, pp. 2057–2079.
[21] Olesen L., Löwe R., and Arnbjerg-Nielsen K., Flood Damage Assessment - Literature Review and Application to the Elster Creek Catchment, 2016.
[22] Jamali B., Löwe R., Bach P. M., Urich C., Arnbjerg-Nielsen K., and Deletic A., A Rapid Urban Flood Inundation and Damage Assessment Model, J. Hydrol., Vol. 564, No. June, 2018, pp. 1085–1098.
[23] Wagenaar D., De Jong J., and Bouwer L. M., Multi-Variable Flood Damage Modelling with Limited Data Using Supervised Learning Approaches, Nat. Hazards Earth Syst. Sci., Vol. 17, No. 9, 2017, pp. 1683–1696.
[24] Van Ootegem L., Van Herck K. and Creten T., Exploring the Potential of Multivariate Depth-Damage and Rainfall-Damage Models, J. Flood Risk Manag., Vol. 11, 2018, pp. S916–S929.
[25] Yu I., Necesito I. V., Kim H., Cheong T. S., and Jeong S., Development of Multivariate Flood Damage Function for Flood Damage Assessment in Gunsan City, Korea, Korean Soc. Hazard Mitig., Vol. 17, No. 2, 2017, pp. 247–258.
[26] Torgersen G., Rød J. K., Kvaal K., Bjerkholt J. T., and Lindholm O. G., Evaluating Flood Exposure for Properties in Urban Areas Using a Multivariate Modelling Technique, Water (Switzerland), Vol. 9, No. 5, 2017, pp. 1–1.
[27] Wing O. E. J., Pinter N., Bates P. D., and Kousky C., New Insights into US Flood Vulnerability Revealed from Flood Insurance Big Data, Nat. Commun., Vol. 11, No. 1, 2020, pp. 1–10.
[28] Malgwi M. B., Schlögl M., and Keiler M., Expert-Based Versus Data-Driven Flood Damage Models: A Comparative Evaluation for Data-Scarce Regions, Int. J. Disaster Risk Reduct., Vol. 57, No. September 2020, 2021.
[29] Xu X., Xuesong Zhang, Hongwei Fang, Ruixun Lai, Yuefeng Zhang, Lei Huang and Xiaobo Liu, A Real-Time Probabilistic Channel Flood-Forecasting Model Based on the Bayesian Particle Filter Approach, Environ. Model. Softw., Vol. 88, Feb. 2017, pp. 151–167.
[30] Moradpouri F., Fathianpour N., Ghaedrahmati R., and Zare M., Synthetic Catalogue Simulation in Low-Seismicity Regions and Few Instrumental Records in Central Iran Based on Monte Carlo Method, Iran. J. Sci. Technol. Trans. A Sci., Vol. 43, No. 1, 2019, pp. 151–160.
[31] Sanuy M., Jiménez J. A., and Plant N., A Bayesian Network Methodology for Coastal Hazard Assessments on a Regional Scale: The BN-CRAF, Coast. Eng., Vol. 157, No. April 2019, 2020, pp. 1–10.
[32] Poelhekke L., Jäger W. S., Van Dongeren A., Plomaritis T. A., McCall R., and Ferreira Ó., Predicting Coastal Hazards for Sandy Coasts with a Bayesian Network, Coast. Eng., Vol. 118, 2016, pp. 21–34.
[33] Mattia Amadio, Anna Rita Scorzini, Francesca Carisi, Arthur H. Essenfelder Alessio Domeneghetti, Jaroslav Mysiak and Attilio astellarin, Testing Empirical and Synthetic Flood Damage Models: The Case of Italy, Nat. Hazards Earth Syst. Sci., Vol. 19, No. 3, 2019, pp. 661–678.
[34] Rumelhart D. E., Hinton G. E., and Williams R. J., Learning by Back-Propagating Errors, Nature, 1986, pp. 323, 533–536.
[35] Wagenaar D., Marc J. C. Van Den Homberg and Kreibich, H., Improved Transferability of Data-Driven Damage Models Through Sample Selection Bias Correction, Risk Anal., Vol. 41, No. 1, 2020.
[36] Siege, T., Reliability of Flood Damage Estimations Across Spatial Scales, (Dissertation) University of Postdam, Germany, 2018.

GEOMATE 2022

The 12th International Conference on

Geotechnique, Construction Materials & Environment

22-24 November 2022

Bangkok, Thailand

- The "International Journal of GEOMATE" is a Scientific Journal of the GEOMATE International Society that encompasses a broad area in Geotechnique, Construction Materials and Environment.
- The key objective of this journal is to promote interdisciplinary research from various regions of the globe.
- The editorial board of the journal is comprised of extensively qualified researchers, academicians, scientists from Japan and other countries of the world.
- It is peer-reviewed Journal that is published quarterly till 2015 and now monthly. All articles published in this journal are available online.
- Contributors may download the manuscript preparation template for submitting paper or contact to the Editors-in-Chief

[editor@geomatejournal.com].